

12th International Conference on Clouds and Precipitation

Proceedings – Volume 1

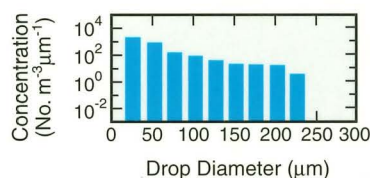
CANADIAN FREEZING DRIZZLE EXPERIMENT



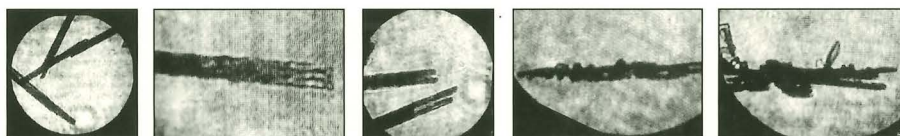
Digital Holographic Camera



Freezing Drizzle



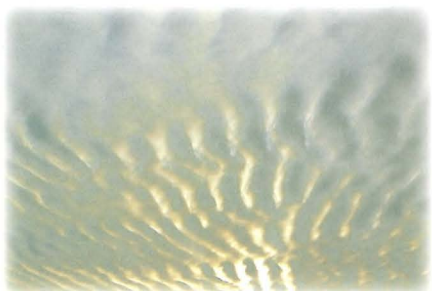
Dendrites/Plates



Needles at -6°C

Zurich, Switzerland

10-23 August 1996

*Cumulus mediocris**Cumulonimbus mamma**Cirrus spissatus**Stratocumulus stratiformis**Altostratus lenticularis**Cirrus vertebratus**Cirrus uncinus**Cumulonimbus calvus**Altostratus undulatus**Altostratus radiatus**Altostratus floccus**Cirrus aviaticus*

If you're more familiar with the difference between an "Altostratus radiatus" and a "Cirrus vertebratus" than between a high flyer and a blue chip: why not entrust your financial Banking specialists? As your he speaks your language in knows how to get the best results for you. And should your objectives change, he can help you realise them. To again give you the time and leisure to dream.

UBS Private Banking
Expertise in managing your assets

GREG MCFARQUHAR
Proceedings NCAR
Volume 1

**12th International Conference
on Clouds and Precipitation**

Sponsored by

International Commission on Clouds and Precipitation

International Association of
Meteorology and Atmospheric Science

Supported by

Royal Meteorological Society
American Meteorological Society
World Meteorological Organization
Union Bank of Switzerland

FRONT COVER PICTURE

Montage of photographs illustrating the measurement of drop sizes using a new digital holographic camera during the Canadian Freezing Drizzle Experiment.

See the paper by Lawson *et al.* on page 365 for fuller details.

Many advances in Cloud Physics have come from carefully conducted field experiments making use of state-of-the-art instruments.

Printed and bound by:

Page Bros., Norwich

12th International Conference on Clouds and Precipitation

Zurich, Switzerland

19-23 August 1996

Conference Organization

International Scientific Programme Committee

P R Jonas (UK) (Chairperson)
J-L Brenguier (France)
R T Brintjes (USA)
P Chylek (Canada)
T L Clark (USA)
A Flossmann (France)
A J Heymsfield (USA)
R A Houze (USA)
J Ogren (USA)
J-L Redelsperger (France)
A Slingo (UK)
H Sundqvist (Sweden)
T Takahashi (Japan)
A-S Wang (P R China)
M K Yau (Canada)

Local Organizing Committee

A Waldvogel (Chairperson)
E Choffat
D Hoegl
J Joss
R Luethi
H-H Schiesser
W Schmid
J Staehelin
M Waldvogel

LIST OF CONTENTS

Sessions 1.1-3.3, pages 1-697, are in Volume 1
Sessions 4.1-7.2, pages 698-1348, are in Volume 2

LIST OF AUTHORS

xxix

Session 1.1: FIELD OBSERVATIONS OF WARM CLOUD MICROPHYSICS

NEW AIRBORNE MEASUREMENTS IN ADIABATIC CORES DURING VERY EARLY COALESCENCE DEVELOPMENT IN FLORIDA CUMULI <i>R Paul Lawson, Tizhi Huang, Kim Weaver, Leigh Angus</i>	1
OBSERVED STRUCTURE AND MICROPHYSICS OF SHALLOW TROPICAL CLOUDS <i>Robert M Rauber, Marcin J Szumowski, Harry T Ochs</i>	5
DROPLET BROADENING IN STRATUS <i>James G Hudson, Seong Soo Yum</i>	7
FREEZING DRIZZLE FORMATION MECHANISM <i>G A Isaac, A Korolev, J W Strapp, S G Cober, A Tremblay, R A Stuart</i>	11
STUDIES OF THE RAINDROP SPECTRUM CHARACTERISTICS IN THREE TYPES OF PRECIPITUS CLOUDS <i>Gong Fujiu, Liu Jicheng, Li Zihua, Lu Taoshi</i>	15
MICROSTRUCTURE IN A HIGH REACHING BOUNDARY LAYER FOG <i>Wolfram Wobrock, Manfred Wendisch</i>	19
A STUDY OF THE MICROPHYSICAL STRUCTURE OF STRATOCUMULUS CLOUDS <i>Hanna Pawlowska, Jean-Louis Brenguier</i>	23
GIANT RAINDROPS OBSERVED FROM LARGE AIRCRAFT <i>Robert A Black, Paul T Willis</i>	27
SATELLITE REMOTE SENSING OF SUMMER STRATUS CLOUDS OVER THE WESTERN NORTH-PACIFIC <i>Tadahiro Hayasaka, Hiroshi Kawamura, Yuri Sato, Hiroshi Takai</i>	31
DOPPLER RADAR-DERIVED PROFILES OF RAINDROP TERMINAL VELOCITIES IN STRATIFORM RAIN <i>R Nissen, R List</i>	35
PHYSICAL CHARACTERISTICS OF SOME CLOUDS WITHIN A MOUNTAIN FOREST CANOPY <i>T P DeFelice</i>	39

Session 1.2: BASIC STUDIES OF WARM CLOUD MICROPHYSICS

LINEAR EDDY MODELING OF DROPLET SPECTRAL EVOLUTION DURING ENTRAINMENT AND MIXING IN CUMULUS CLOUDS <i>Chwen-Wei Su, Steven K Krueger, Patrick A McMurtry, Philip H Austin</i>	41
THE EFFECT OF TURBULENCE ON THE BROADENING OF THE DROPLET SPECTRUM IN CLOUDS AT THE INITIAL STAGE OF THEIR EVOLUTION <i>Mark B Pinsky, Alexander P Khain, Zev Levin</i>	45
A WIND TUNNEL INVESTIGATION OF THE EFFECTS OF TURBULENCE ON THE COLLISION GROWTH OF CLOUD DROPS <i>O Vohl, S K Mitra, H R Pruppacher</i>	49

OBSERVED VS CALCULATED RATES OF GROWTH BY COALESCENCE <i>William A Cooper, Charles A Knight, Jean-Louis Brenguier</i>	53
CONDENSATIONAL DROPLET GROWTH IN CUMULUS CLOUD <i>Jean-Louis Brenguier, Laure Chaumat</i>	57
THE DEPENDENCE OF THE DROP SIZE DISTRIBUTION SHAPE FACTOR ON PRECIPITATION EVENTS <i>Carolin Richter, John W F Goddard</i>	61
LAGRANGIAN CALCULATIONS OF RAINDROP GROWTH IN SHALLOW CONVECTIVE CLOUDS BASED ON KINEMATIC FIELDS OBTAINED FROM BOTH A CLOUD MODEL AND DUAL-DOPPLER DATA SYNTHESSES <i>Marcin J Szumowski, Harry T Ochs, Robert M Rauber</i>	65
EXPERIMENTAL STUDY OF THE EFFECTS OF MIXING ON DROPLET SPECTRA <i>Frederic Burnet, Jean-Louis Brenguier</i>	67
CONVECTIVE/STRATIFORM SORTING OF DROP SIZE DISTRIBUTIONS BASED ON COINCIDENT VERTICAL VELOCITY MEASUREMENTS <i>Paul T Willis</i>	71
FORMATION OF DROPLETS IN A MARINE STRATOCUMULUS LAYER <i>Edward E Hindman</i>	75
PRECIPITATION IN STRATIFORM CLOUDS: MODELLING RESULTS AND COMPARISON WITH OBSERVATIONS <i>Thomas Trautmann</i>	77
THREE-DIMENSIONAL DYNAMICS IN A ONE-DIMENSIONAL CONDENSATIONAL GROWTH MODEL OF CUMULUS CLOUDS <i>J R M Pasquier, P R Jonas</i>	81
COMPARISONS BETWEEN OBSERVATIONS AND NUMERICAL MODELING SIMULATIONS OF THE FORMATION OF SUPERCOOLED DRIZZLE DROPS IN STRATIFORM CLOUDS <i>Roelof T Bruintjes, Gregory Thompson</i>	85
A STOCHASTIC MODEL FOR SIMULATING COLLISION AND COALESCENCE IN WARM CLOUDS <i>Thomas Trautmann, Markus Seeßelberg, Matthias Thorn</i>	89
INFLUENCE OF TURBULENCE ON THE DROP COALESCENCE IN CLOUDS AND ON RAIN FORMATION <i>Alexander P Khain, Mark B Pinsky</i>	93
SENSITIVITY TESTS ON CLOUD DROP SIZE DISTRIBUTION PERFORMED BY 1-D FORCED TIME-DEPENDENT CONVECTIVE CLOUD MODEL <i>Mladjen Ćurić, Vlanan Vučković, Dejan Janc</i>	97
RELATIONSHIP BETWEEN RAINDROP SIZE DISTRIBUTION AND RAINFALL RATE <i>Ken-ichiro Muramoto, Kohki Matsuura, Masahiro Furukawa, Tatsuo Endoh</i>	100
MICROSCOPIC APPROACH TO CONDENSATIONAL GROWTH OF CLOUD DROPLETS <i>Paul A Vaillancourt, Man K Yau, Wojciech W Grabowski</i>	105
FORMATION OF FREEZING DRIZZLE VS SHEAR-INDUCED COLLISION-COALESCENCE NEAR CLOUD BASE <i>Ben C Bernstein, Marcia K Politovich</i>	109
THE EFFECT OF SMALL-SCALE TURBULENCE ON THE COLLISION RATES OF CLOUD DROPS <i>Anna S Koziol, Henry G Leighton</i>	113

CONDENSATION INSIDE DENSE CLUSTERS OF DROPLETS ON HYGROSCOPIC NUCLEI IN THE ATMOSPHERE <i>T Elperin, B Krasovitev</i>	117
LABORATORY MEASUREMENTS OF THE EFFECTS OF AIR PRESSURE ON THE COALESCENCE BETWEEN SMALL PRECIPITATION DROPS <i>Harry T Ochs, Kenneth V Beard, Song Liu</i>	121
LABORATORY MEASUREMENTS OF OSCILLATION AMPLITUDE FOR MODERATE-TO-LARGE RAINDROPS ACCELERATING FROM REST AND FALLING AT TERMINAL SPEED <i>Karen Andsager, Kenneth V Beard, Neil F Laird</i>	122
Session 1.3: OBSERVATIONS OF GLACIATED CLOUD MICROPHYSICS	
OBSERVATIONS OF INITIAL STAGE OF ICE DEVELOPMENT IN SUPERCOOLED CLOUDS <i>Anatoly N Nevzorov</i>	124
CLOUD MICROPHYSICS MEASUREMENTS IN COLD AIR OUTBREAKS <i>R Timm, S Bakan, V Khvorostyanov</i>	128
A COMPARISON OF MID-LATITUDE AND TROPICAL CIRRUS MICROPHYSICAL PROPERTIES AND A CONCEPTUAL MODEL OF CIRRUS CLOUD STRUCTURE <i>Andrew J Heymsfield, Larry M Miloshevich, Greg M McFarquhar</i>	131
ICE FORMATION IN WAVE CLOUDS - COMPARISON OF AIRCRAFT OBSERVATIONS WITH MEASUREMENTS OF ICE NUCLEI <i>David C Rogers, P J DeMott, W A Cooper, R M Rasmussen</i>	135
A MEASUREMENT AND MODELING STUDY OF YOUNG CIRRUS CLOUDS: PART 1, MEASUREMENTS <i>Johan Ström, Bernhard Strauss, Franz Schröder, Theodore Anderson, Jost Heintzenberg, Peter Wendling</i>	138
CIRRUS CLOUD OBSERVATIONS WITH A NEW VERSION OF HYDROMETEOR VIDEOSONDE <i>Narihiro Orikasa, Masataka Murakami, Hakaru Mizuno, Yoshinori Yamada</i>	142
IDENTIFICATION OF THE FALL MODE OF OBLATE HAIL USING MULTIPARAMETER RADAR <i>T J Smyth, T M Blackman, A J Illingworth</i>	146
THE MELTING BEHAVIOUR OF ICE PARTICLES AS OBSERVABLE BY POLARIMETRIC RADAR MEASUREMENTS <i>Igor Doelling, Peter Meischner</i>	150
THE HALLETT-MOSSOP PROCESS IN NEW MEXICAN SUMMERTIME CUMULI <i>Alan M Blyth, John Latham</i>	154
MICROPHYSICAL PROPERTIES OF ARCTIC CYCLONES <i>David R Hudak, R List, T Krauss</i>	158
SIZE DISTRIBUTION OF HYDROMETEORS THROUGH THE MELTING LAYER <i>Eszter Barthazy, Werner Henrich, Albert Waldvogel</i>	162
THEORETICAL AND FIELD INVESTIGATIONS OF THE MESO- AND MICROSTRUCTURE OF THE WINTER FRONTAL PRECIPITATION AN THE STEPPE PART OF UKRAINE <i>Nikolaj M Akimov, Anne M Pirmach</i>	166

SOME RESULTS OF MICROWAVE RADIATION OBSERVATION OF WINTER STRATIFORM CLOUD ALONG TIAN SHAN MOUNTAINS IN XINJIANG, CHINA <i>Wu Zhifang, Gao Ziyi</i>	170
STUDIES OF THE COLD POOL FOG IN BASIN <i>Shi Wenquan, Li Bin, Zhang Jianxin</i>	173
ORIENTATED ICE CRYSTALS AS OBSERVED BY LIDAR AT FIRE II <i>Wynn L Eberhard</i>	175
A COMPARISON OF THE MICROPHYSICAL CHARACTERISTICS OF CONVECTIVE CLOUDS DURING A WET SUMMER AND A DRY SUMMER <i>Jeffrey Stith, Ryan Zerr, Andrew G Detwiler, Paul L Smith</i>	179
THE HAILSTONE PARAMETERS IN THE NORTHERN PART FERGANA VALLEY <i>B Sh Kadyrov, R G Shadieva</i>	183
DISTRIBUTION OF PRECIPITATION PARAMETERS ESTIMATED FROM OBSERVATIONS WITH A DOPPLER RADAR AND A POLARIMETRIC RADAR: PART 1, RESULTS FROM VERTICAL POINTING DOPPLER RADAR OBSERVATION <i>Masayuki Maki, Koyuru Iwanami, Hiroshi Uyeda, Hiroshi Hanado, Hiroshi Kumagai</i>	186
DISTRIBUTION OF PRECIPITATION PARAMETERS ESTIMATED FROM OBSERVATIONS WITH A DOPPLER RADAR AND A POLARIMETRIC RADAR: PART 2, RESULTS FROM POLARIMETRIC RADAR OBSERVATION <i>Koyuru Iwanami, Masayuki Maki, Takeshi Sato, Masao Higashiura</i>	190
OBSERVATIONS OF MIXED PHASE CLOUD AND PRECIPITATION ON THE ANTARCTIC PENINSULAR <i>Tom Lachlan-Cope</i>	193
THE IMPACT OF REGION RELIEF ON SOME CHARACTERISTICS OF HAIL PROCESSES <i>R I Doreuli</i>	196
ICE INITIATION IN WISP SHALLOW UPSLOPE CLOUDS <i>Roy M Rasmussen, Al Cooper, Paul DeMott, Dave Rogers</i>	200
RADAR ATTENUATION IN TOGA-COARE SYSTEMS: ESTIMATION AND INTERPRETATION FROM MICROPHYSICAL DATA <i>Virginie Marécal, Sébastien Houée, Taoufik Tani, Paul Amayenc, Jacques Testud</i>	204
Session 1.4: BASIC STUDIES OF GLACIATED CLOUD MICROPHYSICS	
THEORETICAL STUDY OF THE MICROPHYSICAL STRUCTURE OF MIXED STRATIFORM FRONTAL CLOUDS AND THEIR PRECIPITATION <i>Svetlana V Krakovskaia, Anne M Pirnach</i>	208
SHEDDING BY SPONGY GROWTH OF SPHEROIDAL HAILSTONES <i>Laura Levi, Luisa Lubart</i>	212
MONODISPERSE DROPLET DISTRIBUTIONS IN THE ICE ACCRETION PROCESS <i>F Prodi, F Porcù</i>	216
LABORATORY STUDIES OF THE SCATTERING OF RADIATION BY ICE CRYSTALS <i>C P R Saunders, J Rimmer, J R Arathoon</i>	220
LATITUDINAL AND OVERALL CONVECTIVE HEAT TRANSFER FROM SMOOTH AND ROUGH SPHEROIDAL HAILSTONE MODELS <i>Guoguang Zheng, Roland List</i>	224

TIME SERIES OF A Z-R RELATIONSHIP FOR SNOWFALL AND IT'S EVALUATION <i>Ken-ichiro Muramoto, Yasushi Fujiyoshi, Koh-ichi Kitano</i>	228
RELATION BETWEEN THE CONCENTRATION OF ICE NUCLEI AND THE OCCURRENCE OF THUNDERSTORMS AND HAILSTORMS <i>A Castro, J L Marcos, J L Sánchez, R Fraile</i>	232
ON SUPERSATURATION DEPENDENT BEHAVIOR OF ICE CRYSTALS DURING VAPOR GROWTH <i>John Hallett, Charles A Knight, Riza G Oraltay, Paul Willis</i>	236
IMPORTANCE OF A -15°C TEMPERATURE LEVEL FOR THE PRECIPITATION PROCESSES IN CLOUDS <i>Tatsuo Endoh, Tsuneya Takahashi</i>	240
DERMINATION OF HAILSTONE SIZE DISTRIBUTION INSIDE A THUNDERCLOUD FROM HAILPAD MEASUREMENTS AT THE GROUND <i>Jean Dessens</i>	244
MODEL SIMULATION OF THE MELTING LAYER <i>Wanda Szyrmer, I Zawadzki, R Papagheorghe</i>	247
NUMERICAL SIMULATION OF HAILSTONE FORMATION <i>István Geresdi</i>	251
MICROPHYSICAL PROCESSES OF OROGRAPHIC SNOWFALL <i>Toshio Harimaya, Yasumi Nakai</i>	254
SELF-ORGANISATION EFFECTS IN A MODEL WITH PAREMETERIZED CLOUD MICROPHYSICS <i>Ulrike Wacker</i>	258
SOME NUMERICAL RESULTS OF FORMATION HAIL CLOUD MICROSTRUCTURE <i>B A Ashabokov, L M Fedchenko, A V Shapovalov</i>	262
ON TEMPERATURE AND MECHANISM OF HAIL EMBRYO FORMATION <i>V G Khorguani, Z V Khvedlidze</i>	264
ON THE ROLE OF ARTIFICIAL ICE FORMING REAGENTS AND RADIATIVE INTERMIXTURES IN THE VARIATION OF CONVECTIVE CLOUDS THUNDERSTORM AND HAIL ACTIVITY <i>A G Amiranashvili, T G Gzirishvili, Z A Chumburidze</i>	267
THREE-DIMENSIONAL FINE STRUCTURES OF BULLET TYPE SNOW CRYSTALS SHOWN BY STEREO- PHOTOMICROGRAPHS <i>Kunimoto Iwai</i>	271
FREE-FALL PATTERNS AND VELOCITY VARIATIONS OF RIMED PLATE-LIKE SNOW CRYSTALS <i>Masahiro Kajikawa, Kyoichi Okuhara</i>	274
A POSSIBLE RELATIONSHIP BETWEEN LIGHTNING DISCHARGE IN CLOUD AND GUSHES OF RAIN <i>Zlatko Vukovic, Mladjen Curic</i>	278
FORMATION MECHANISMS OF MULTI-BRANCHED SNOW CRYSTALS <i>Katsuhiro Kikuchi, Hiroshi Uyeda</i>	282
MICROPHYSICAL PROCESSES OF CLOUDS FORMED IN THE ARTIFICIAL CLOUD EXPERIMENTAL SYSTEM <i>Akira Sasaki, Toshio Harimaya</i>	286

MICROPHYSICAL CHARACTERISTICS OF THUNDERSTORMS AS RELATED TO STORM LIGHTNING ACTIVITY <i>Hartmut Höller, Ullrich Finke</i>	290
THE HOMOGENEOUS NUCLEATION KINETICS OF WATER VAPOR NEAR A SMALL ICE BIT <i>Sergi P Fisenko</i>	292
MICROPHYSICAL AND ELECTRICAL PHENOMENA DURING FREEZING OF WATER DROPS AND HAILSTONE GROWTH <i>A Kh Adzhiev</i>	295
SUPERCOOLED CLOUD TUNNEL STUDIES ON THE RIMING GROWTH OF SNOW CRYSTALS <i>Tsuneya Takahashi, Tatsuo Endoh</i>	297
LABORATORY EXPERIMENTS WITH SUPERCOOLED WATER DROPS IN A VERTICAL WIND TUNNEL <i>Robert R Czys, Jeffrey K Lew</i>	301
OBSERVATIONAL INVESTIGATION OF CHARACTERISTICS OF HAILSTORM ECHO SHAPE IN PINLIANG REGION <i>Zhang Hongfa, Gong Naihu, Wan Zhijun</i>	303
Session 1.5: AEROSOL MICROPHYSICS	
THE INTERACTION OF AEROSOLS WITH DEVELOPING MARITIME AND CONTINENTAL CUMULUS CLOUDS <i>Darrel Baumgardner, William A Cooper, Larry Radke</i>	308
FIELD EXPERIMENTAL DETERMINATION OF COLLISION EFFICIENCIES AS A FUNCTION OF RAINDROP AND AEROSOL PARTICLE SIZE <i>P Ebert, G Frank, M Kibler, A Mainka, T Prokop, B Tenberken, J Tschiersch, K Bachmann</i>	312
SUB-CLOUD AEROSOL CONCENTRATIONS AND CLOUD DROPLET EVOLUTION IN WARM CUMULI. IS THERE AN OBSERVABLE LINK? <i>G B Raga, P R Jonas</i>	316
RELATIONS BETWEEN AEROSOL AND CLOUD PROPERTIES IN NORTH DAKOTA CUMULUS CLOUDS <i>Paul J DeMott, Jeffrey L Stith, Ryan J Zerr, David C Rogers</i>	320
OBSERVATION AND STUDIES OF AEROSOL PARTICLES IN THE LOWER ATMOSPHERE LAYER IN XINJIANG IN WINTER <i>Shi Wenquan, Li Bin</i>	324
A MECHANISM OF FORMATION OF NONCONVECTIVE AEROSOL AND GASEOUS CLOUDS IN TURBULENT ATMOSPHERE <i>T Elperin, N Kleerorin, I Rogachevskii</i>	328
CHARGE DISTRIBUTION ON AEROSOLS CONSISTING OF PARTICLES OF DIFFERENT MATERIALS UNDER PHOTON IRRADIATION <i>O A Mikhalkova, P P Poluektov</i>	332
THE RELATIVE IMPORTANCE OF SEA-SALT AND NON-SEA-SALT SULPHATE AEROSOL TO THE MARINE CCN POPULATION <i>Colin D O'Dowd, Michael H Smith, Andrew Kaye</i>	334

Session 2.1: INSTRUMENTS AND TECHNIQUES FOR IN-SITU MEASUREMENTS

A LASER-OPTICAL DEVICE FOR MEASURING CLOUD DROPLET SIZE DISTRIBUTIONS <i>M Löffler-Mang, T Garbrecht, K D Beheng</i>	338
PROGRESS ON A NON-WETTING TEMPERATURE PROBE FOR AIRBORNE RESEARCH <i>A Rodi, R P Lawson, J Chu</i>	342
ON THE ACCURACY OF NEVZOROV AIRBORNE HOT WIRE LWC/TWC PROBE <i>A V Korolev, J W Strapp, A N Nevzorov</i>	346
AN INSTRUMENT FOR REAL-TIME CLASSIFICATION OF PARTICLE SHAPE WITHIN CLOUDS AND AEROSOLS <i>P H Kaye, E Hirst, S Saunders, D W Johnson, M A Pickering</i>	350
A BALLOON-BORNE CLOUD PARTICLE REPLICATOR FOR MEASURING VERTICAL PROFILES OF DETAILED CLOUD MICROPHYSICS: DESIGN, DATA QUALITY AND QUANTITATIVE ACCURACY ASSESSMENT <i>Larry M Miloshevich, Andrew J Heymsfield</i>	354
A NEW CLOUD CONDENSATION NUCLEI COUNTER <i>Kleiton do Carmo Mendes, Carlos Jacinto de Oliveira, Murilo Pereira de Almeida, José Carlos Parente de Oliveira</i>	358
MICROPHYSICAL SONDE <i>N A Berezinsky, L M Fedchenko, M I Tliso</i>	361
IMPROVED AIRBORNE MEASUREMENTS OF THE DROP SIZE DISTRIBUTION IN FREEZING DRIZZLE <i>R Paul Lawson, A V Korolev, Tizhi Huang, Kim Weaver, Leigh Angus, J W Strapp, G A Isaac, A G Cober</i>	365
A NEW INSTRUMENT FOR THE MEASUREMENT OF CLOUD DROPS <i>Thomas Hauf</i>	369
CAO AIRCRAFT INSTRUMENTATION FOR CLOUD PHYSICS <i>Anatoly N Nevzorov</i>	371
IMPROVEMENT OF SIZE CORRECTION TECHNIQUE FOR PARTICLES WITH SIZES LESS THAN 100MM IN DIAMETER FOR OAP-2D-GA2 <i>H Panskus, A Reuter</i>	375
FAST RESPONSE TURBULENCE MEASUREMENTS FROM AN INSTRUMENTED LIGHT AIRCRAFT <i>Robert Wood</i>	378

Session 2.2: INSTRUMENTS AND TECHNIQUES FOR REMOTE SENSING

SCATTERING AT 35.8 GHZ BY AXIALLY SYMMETRIC PARTICLES: MEASUREMENTS AND NUMERICAL CALCULATIONS <i>Orazio Stumolo, F Prodi, A Cola</i>	382
ESTIMATION OF THE LIQUID WATER CONTENT BY MULTIPARAMETER RADAR MEASUREMENTS <i>M Hagen, H Höller</i>	386

VALIDATION OF SATELLITE ESTIMATION OF PRECIPITATION USING SPARSE GROUND TRUTH DATASET IN TROPICAL AFRICA <i>Isabelle Jobard, Henri Laurent, Ana Maia, Alexandru Toma</i>	390
EXPERIMENTAL RETRIEVAL OF CLOUD OPTICAL THICKNESS DURING EUREX: COMPARISON OF THREE APPROACHES <i>J Descloîtres, H Pawłowska, J Pelon, J-L Brenguier, F Parol, J C Buriez</i>	394
PRECIPITATION RATE ESTIMATION IN CONVECTIVE TROPICAL MARITIME CLOUDS <i>Christian Asselin de Beauville, Constantin A Pontikis</i>	398
MARINE BOUNDARY LAYER CLOUD FORMATION AND CHARACTERISTIC MEASUREMENTS MADE BY LIDAR DURING ACE-1 <i>Bruce Morley, Darrel Baumgardner, Craig Walther</i>	402
AUTOMATED RADAR SYSTEM MRL-INFO <i>Ya A Ekba, M D Atabiev, A V Kapitanikov, L G Kaplan</i>	406
AIRCRAFT AUTOMATED COMPLEX <i>M Yu Pashkevich, Ya A Ekba, N A Berezinsky, A A Sinkevich, A A Malkov, A A Khorikov</i>	410
IMPROVEMENT OF LIQUID WATER CONTENT MEASUREMENT WITH COMBINED RADAR-RADIOMETER SYSTEM <i>Jinli Liu, Ling Zhang, Hong Ping Chen</i>	413
ACCURACY OF EVALUATION OF THE WIND FIELD BY SINGLE DOPPLER RADAR <i>V N Efremov</i>	417
COORDINATE METHOD OF THE WIND PROFILE EVALUATION BY DOPPLER RADAR <i>V N Efremov, K N Kim, E I Sophiev</i>	420
OBSERVATIONS OF CLOUD STRUCTURE WITH 3.2 MM-WAVE RADAR <i>Markus Quante, Olaf Danne, Ehrhard Raschke, Ivan Popstefanija, Andrew Pazmany</i>	424
COMBINED TRIPLE-CHANNEL GROUND-BASED MICROWAVE RADIOMETER FOR MEASURING ATMOSPHERIC WATER PARAMETERS IN RAINY DAYS <i>Chong Wei</i>	428
STUDY OF SPACIAL DISTRIBUTION OF PHASE AND SIZE OF HYDROMETEORS BY DUAL LINEAR POLARIZATION RADAR <i>Liu Liping, Wang Zhijun</i>	431
DETERMINATION OF EFFECTIVE RADIUS OF DROPS IN WATER CLOUDS FROM SPACE: NEW APPROACH <i>A A Kokhanovsky, E P Zege</i>	434
INVESTIGATION OF CLOUDS FROM A DUAL BEAM 95 GHZ RADAR <i>Anne Guyot, Jacques Testud</i>	438
GROUND BASED MICROWAVE MEASUREMENTS OF INTEGRAL LIQUID WATER CONTENT OF ARCTIC CLOUDS DURING BASE <i>A Koldaev, A Troitsky, J W Strapp, B E Sheppard</i>	442
DIFFERENTIATION OF FREEZING DRIZZLE FROM ICE HYDROMETEORS WITH POLARIZATION RADAR <i>Roger F Reinking, Sergey Y Matrosov, Brooks E Martner, Robert A Kropfli</i>	446

MEASUREMENT OF KINETICS AND PRECIPITATION OF STRATIFORM RAINFALL WITH AIRBORNE MULTIPARAMETER RAIN RADAR	450
<i>Nobuhiro Takahashi, Hiroshi Hanado, Shinsuke Satoh</i>	
Session 2.3: TECHNIQUES FOR DATA ANALYSIS	
OPTIMAL NON-LINEAR ESTIMATION FOR PARTICLE MEASUREMENTS	454
<i>Hanna Pawlowska, Jean-Louis Brenguier, Gerard Salut</i>	
A MODEL FOR THE FAST FSSP FUNCTIONING	458
<i>A Coelho, J-L Brenguier, T Bourrianne</i>	
DEEP CONVECTIVE CLOUD DETECTION IN A REDUCED RESOLUTION DATA SET	462
<i>Ines Velasco, Patricia Rodaro</i>	
ASPIRATION DISTORTIONS OF AEROSOLS: INVESTIGATION BY PHOTON CORRELATION SPECTROSCOPY	466
<i>V I Jakimchuk, N Kh Kopyt</i>	
SNOWFALL RATE DETERMINED BY IMAGE PROCESSING DATA	470
<i>Ken-ichiro Muramoto, Toshio Harimaya, Toru Shiina</i>	
Session 3.1: STRUCTURE OF BOUNDARY-LAYER CLOUD FIELDS	
OBSERVATIONS OF DIVERGENCE AND VORTICITY DURING ACE-1	474
<i>Steven T Siems, Donald H Lenschow, Ashley J Bainbridge, Paul B Krummel</i>	
TRANSITION OF A STRATOCUMULUS INTO A CUMULUS-TOPPED BOUNDARY LAYER AS OBSERVED DURING THE FIRST LAGRANGIAN OF ASTEX: MEAN STATE AND TURBULENCE	478
<i>S R de Roode, P G Duynkerke</i>	
THE INTERACTION BETWEEN CUMULUS AND STRATOCUMULUS CLOUDS IN THE MARINE BOUNDARY LAYER	482
<i>G M Martin, P R Jonas, D W Johnson</i>	
ON THE DIURNAL CHARACTERISTICS OF CLOUD STRUCTURE IN THE MARINE STRATOCUMULUS TRANSITION REGION	486
<i>Mark A Miller</i>	
LIDAR OBSERVATIONS OF FAIR-WEATHER CLOUDS	490
<i>I Kolev, O Parvanov</i>	
ON THE FORCING OF WINDWARD ISLAND RAINBANDS IN HAWAII	494
<i>R E Carbone, J Tuttle, W A Cooper, V Grubisic, W-C Lee</i>	
CONTINENTAL STRATUS CHARACTERISTICS FROM SURFACE-BASED REMOTE SENSING SYSTEMS	498
<i>Bruce Albrecht, Gerald G Mace, William J Syrett, Daniel Thomas, Christopher Ruf, Justin Bobak</i>	
COASTAL STRATUS OBSERVATIONS WITH AIRBORNE RADAR	502
<i>G Vali, S Haimov, D Leon, J French, R D Kelly</i>	
SMALL-SCALE STRUCTURES OF ARCTIC STRATUS CLOUDS DURING SUMMERTIME	506
<i>Andreas Reuter, Frank Albers</i>	
STRUCTURE OF TEMPERATURE FIELD IN SMALL CUMULI ON A CENTIMETER SCALE	510
<i>Krzysztof E Haman, Szymon P Malinowski</i>	

SUMMARY OF SOME CLOUD TRANSPORT AND DISPERSION EXPERIMENTS USING A GASEOUS TRACER AND RADAR CHAFF <i>Paul L Smith, Trace A Bowen, Andrew G Detwiler, Jeffrey L Stith, Brooks A Martner, Roger F Reinking</i>	514
BOUNDARY LAYER ROLLS AND CLOUD BANDS: AIRCRAFT OBSERVATIONS AND MODELLING RESULTS <i>Ian M Brooks, David P Rogers, John W Glendening</i>	518
LIDAR FOR POLARIZATION STUDIES OF CLOUDS IN THE LOW ATMOSPHERE <i>I Kolev, B Tatarov, B Kaprielov</i>	522
ANISOTROPY IN CLOUD-CLEAR AIR MIXING IN SMALL SCALES <i>Szymon P Malinowski, Piotr Banat</i>	526
CALCULATION OF PARAMETERS OF A CUMULONIMBUS CLOUD TAKING INVOLVEMENT INTO CONSIDERATION <i>Ya A Ekba, M R Vatiashvili, R G Zakinian, M K Zhekamoukhov</i>	530
TURBULENT ENTRAINMENT INTO CUMULUS CLOUDS <i>Jacques R M Pasquier, Samantha A Smith, Peter R Jonas</i>	532
AN ANALYSIS FOR THE PRECIPITATING OF THE STRATIFORM CLOUD SYSTEM IN NORTH CHINA <i>Duan Ying, Wu Zhihui, Shi Lixin</i>	536
THE NORTHEAST OF BRAZIL WARM CUMULUS CLOUD: AN OBSERVATIONAL AND THEORETICAL STUDY <i>Antônio José da Costa Sampaio, Carlos Jacinto de Oliveira, Alexandre Araujo Costa, José Carlos Parente de Oliveira</i>	540
Session 3.2: STRUCTURE OF DEEP CONVECTIVE CLOUD SYSTEMS	
INITIATION OF DEEP CONVECTION BY SHORT GRAVITY WAVES <i>Ulli Finke, Thomas Hauf</i>	544
CHARACTERISTICS OF CLOUDS, CLOUD CLUSTERS AND A SUPERCLUSTER OBSERVED ON NOVEMBER 10-12, 1992 DURING THE TOGA COARE IOP <i>Md Nazrul Islam, Hiroshi Uyeda, Osamu Kikuchi, Katsuhiro Kikuchi</i>	546
RETRIEVED THERMODYNAMIC STRUCTURES OF MESOSCALE CONVECTIVE SYSTEMS OBSERVED IN THE WESTERN TROPICAL PACIFIC <i>Shinsuke Satoh, Daisuke Abe, Masayuki Kawashima, Tomoki Ushiyama, Kensuke Tateuchi</i>	550
LIQUID WATER IN STORM-EMBEDDED OROGRAPHIC GRAVITY WAVES <i>Roger F Reinking, Jack B Snider, Roelof T Brientjes, Janice Coen, Terry L Clark</i>	554
A MULTI-SCALE SIMULATION OF A CASE OF OUTBREAK OF SEVERE CONVECTION OVER THE ALBERTA FOOTHILLS <i>M K Yau, C Li</i>	558
MESOSCALE AND MICROSCALE STRUCTURE OF SHALLOW SNOW BANDS OVER THE SEA OF JAPAN <i>Masataka Murakami, Yoshinori Yamada, Takayo Matsuo, John D Marwitz, Glenn Gordon</i>	562
TURBULENCE PARAMETERS AND VERTICAL DRAFTS IN TROPICAL CONVECTIVE CLOUDS OVER CAMAGUEY, CUBA <i>Daniel Martinez Castro</i>	566

STRUCTURE AND FORMATION MECHANISM OF A TERRAIN-TRAPPED RAIN STORM <i>Yasushi Fujiyoshi, Biao Geng, Naohiro Yoshimoto, Sachie Kanada, Takao Takeda</i>	570
INTERNAL STRUCTURE OF THE CLOUD BAND OFF THE WEST COAST OF HOKKAIDO ISLAND, JAPAN, ANALYZED WITH SSM/I AND RADAR DATA <i>Masaki Katsumata, Hiroshi Uyeda, Katsuhiro Kikuchi</i>	573
A TORNADIC THUNDERSTORM IN SWITZERLAND EXHIBITING A RADAR-DETECTABLE LOW-LEVEL VORTEX <i>Wolfgang Linder, Willi Schmid</i>	577
REGULATION OF CONVECTIVE ACTIVITY BY UPPER TROPOSPHERE RELATIVE HUMIDITY: INTERACTIONS BETWEEN TURBULENCE, MICROPHYSICS AND LARGER-SCALE CONVECTIVE DYNAMICS <i>Nenad M Aleksic, Chris J Walcek, Bosko T Telenta, Bob A Iacovazzi</i>	581
MESO-GAMMA SCALE CHARACTERISTICS OF VORTICES IN SNOW CLOUDS ANALYZED WITH DOPPLER RADAR <i>Hiroshi Uyeda, Keisuke Ueno, Yoshio Asuma, Katsuhiro Kikuchi</i>	585
RETRIEVED DYNAMIC AND THERMODYNAMIC STRUCTURE OF TROPICAL CONVECTIVE SYSTEM IN WEAK WIND PHASE IN TOGA-COARE IOP <i>Tomoki Ushiyama, Daisuke Abe, Shinsuke Satoh, Kensuke Takeuchi</i>	589
AEROSYNOPTICAL AND THERMODYNAMICAL CONDITIONS FOR HAIL-PROCESS FORMATION WITH SIMILAR RADAR STRUCTURE AND DEVELOPMENT DYNAMICS <i>M V Barekova, Z A Gazaeva, V S Makitov, A I Taumurzaev</i>	593
PRECIPITATION CAUSED BY CONVERGENCE AND CONVECTION AT THE MIDDLE LEVEL IN STRATIFORM REGION OF TROPICAL CLOUD CLUSTER <i>Shuji Shimizu, Hiroshi Uyeda, Warner L Ecklund, Kenneth S Gage</i>	597
ON THE SPATIAL AND TEMPORAL DISTRIBUTION OF THUNDERSTORMS IN SOUTHERN GERMANY <i>Thomas Hauf, Ulli Finke</i>	601
THE RESEARCH ON THE POSSIBILITY OF INVERSION LAYERS PIERCING THROUGH BY THE GROWING CONVECTIVE CLOUDS <i>Ya A Ekba, M D Atabiev, R G Zakinian</i>	604
PECULIARITIES OF CONVECTIVE CLOUDINESS ORIGIN IN THE EASTERN DROUGHTY AREAS OF THE STAVROPOL REGION <i>L I Kachaturova, Ya A Ekba</i>	608
SOME INVESTIGATION RESULTS OF AIRFLOW STRUCTURE EXAMINATION IN HAILSTORMS <i>M Yu Pashkevich, O S Bogomolov, N A Kharakhonova</i>	612
3D-ANIMATIONS OF A TORNADO-PRODUCING MULTICELLULAR HAILCLOUD <i>Willi Schmid, David Bresch</i>	614
THE RESULTS OF INVESTIGATING THE CONVECTIVE CLOUD THERMAL REGIME WITH INFRARED THERMOMETER <i>A A Sinkevich</i>	617
STRUCTURES AND MEANDERING BAND CLOUDS OBSERVED BY DUAL-POLARIZATION DOPPLER RADAR DURING THE BASE PERIOD IN CANADA <i>Y Asuma, K Kikuchi, H Uyeda, T Shimamura, S Iwata, R Kimura, K Tsuboki, R E Stewart, D R Hudak, E Hudson, G W K Moore</i>	621

APPLICATION OF NUMERICAL MODELS FOR TO STUDY THE CLOUD DYNAMICS AND STRUCTURE OF THE WINTER FRONTAL RAINBANDS <i>Anne M Pirmach</i>	625
THE ANALYSIS OF THE PRECIPITATION RESOURCES IN NORTH CHINA BY A DUAL FREQUENCY MICROWAVE RADIOMETER <i>Duan Ying, Wu Zhihui, Shi Lixin</i>	629
Session 3.3: STRUCTURE OF FRONTAL AND CIRRUS CLOUD	
OBSERVATIONS OF TURBULENCE IN CIRRUS CLOUDS <i>Samantha A Smith, Peter R Jonas</i>	633
PRELIMINARY RESULTS OF THE VERTICAL STRUCTURE OF TROPICAL (20°S-20°N) SUBVISUAL CLOUDS FROM SAGE II OBSERVATIONS <i>Pi-Huan Wang, M Patrick McCormick, Patrick Minnis, Geoffrey S Kent, Glenn K Yue, Kristi M Skeens</i>	637
STUDY OF CIRRUS MULTI-SCALE STRUCTURE <i>Yangang Liu, W Patrick Arnott, John Hallett</i>	641
FEATURES OF FRONTAL CLOUDINESS STRUCTURE OVER UKRAINE IN WINTER SEASONS <i>Ludmila V Palamarchuk, Svetlana V Krakovskaia</i>	645
OROGRAPHIC INFLUENCE ON THE DISTRIBUTION OF ACCUMULATED RAINFALL FOR DIFFERENT WIND DIRECTIONS <i>Hermann Gysi</i>	649
FRONTAL PRECIPITATION FIELD MORPHOLOGY AND IT'S APPLICATION TO FORECAST <i>N A Bezrukova, A Y Naumov</i>	653
CONVECTIVE VERSUS STRATIFORM RAINFALL - REVISITING THE DYNAMICAL AND MICROPHYSICAL BACKGROUND <i>Matthias Steiner, James A Smith</i>	657
CHARACTERISTICS OF THE CLOUD AND PRECIPITATION DURING THE DRY SUMMER SEASON IN SOUTH CHINA <i>Zeng Guang-Ping, Tang Yu, Feng Hong-Fang, Zhu Ding-Hua</i>	662
STUDIES ON THE CHARACTERISTICS OF PRECIPITATION PHENOMENA OBTAINED BY RADAR OBSERVATIONS AT SYOWA STATION, ANTARCTICA <i>Hiroyuki Konishi, Makoto Wada, Tatsuo Endoh</i>	664
REMOTE MEASUREMENTS OF SUPERCOOLED LWC SPACE DISTRIBUTION IN WINTER FRONTAL CLOUD SYSTEMS <i>A Koldaev, A Chernikov, Yu Melnichuk</i>	668
THE DEVELOPMENT PROCESS OF A CONVECTIVE SNOW CLOUD DURING THE WINTER MONSOON SURGE ALONG THE WEST COAST OF HOKKAIDO, JAPAN <i>Hiroyuki Yamada, Hiroshi Uyeda, Micheal A Menshov, Yoshio Asuma, Katsuhiko Kikuchi, Masayuki Maki, Koyuru Iwanami</i>	672
THE SPATIAL DISTRIBUTION CHARACTERISTICS OF MICROSTRUCTURE IN FRONTAL CLOUDS <i>Tamara N Zabolotskaya</i>	676
SOME CHARACTERISTICS OF THE CLOUDS AND PRECIPITATION OF THE TRANSITIONAL SEASONS OF THE YEAR ON THE TERRITORY OF UKRAINE <i>Iraida A Ocokina, Savelii V Khusid</i>	679

THE RESULTS OF INVESTIGATING CLOUDS AND PRECIPITATION REGIME OF THE COLD PERIOD IN Leningrad Region	683
<i>Yu A Dvlgalyuk, E V Orenburgskaya, A M Pirnach, D D Stalevich, A A Sinkevich, V D Stepanenko</i>	
COUPLED ATMOSPHERIC-FIRE MODELLING: ROLE OF THE CONVECTIVE FROUDE NUMBER AND DYNAMIC FINGERING AT THE FIRE LINE	686
<i>Mary Ann Jenkins, Terry L Clark, Janice Coen, David Packham</i>	
A CASE STUDY OF SNOW CLOUDS INFLUENCED BY TOPOGRAPHY OBSERVED IN THE TOHOKO DISTRICT OF JAPAN	690
<i>Sento Nakai, Yoshinori Yamada, Masahiro Kajikawa</i>	
A STUDY OF PRECIPITATING CLOUDS IN THE VICINITY OF THREE FRONTS AND A CYCLONE OBTAINED FROM OBSERVATIONS OF MICROWAVE RADIOMETER AND VERTICALLY POINTING RADAR IN SVALBARD, ARCTIC	694
<i>Makoto Wada, Hiroyuki Konishi</i>	
Session 4.1: MODELLING OF BOUNDARY-LAYER CLOUDS	
EXPLORATORY CLOUD-RESOLVING SIMULATIONS OF COLD-SEASON ARCTIC STRATUS CLOUDS	698
<i>William R Cotton, Tamir G Reisin, Sonia M Kreidenweis, Graham Feingold, Peter Q Olsson, Jerry Y Harrington</i>	
MULTILEVEL SIMULATION OF RADIATIVELY DRIVEN STRATOCUMULUS ENTRAINMENT	701
<i>David E Stevens, Christopher S Bretherton</i>	
DECOUPLING, CUMULIFORM PENETRATIVE ENTRAINMENT AND THE SIMULATED BREAKUP OF MARINE STRATOCUMULUS CLOUDS	705
<i>Matthew C Wyant, Christopher S Bretherton, Hugh A Rand, David E Stevens</i>	
SIMULATIONS OF THE ASTEX LAGRANGIAN EXPERIMENTS WITH 1D AND 2D BOUNDARY LAYER MODELS	709
<i>Steven K Krueger, Ching-Hsuan Chen, Matthew C Wyant, Christopher S Bretherton</i>	
THE INCEPTION OF DRIZZLE IN MARINE STRATOCUMULUS: A MONTE-CARLO SIMULATION OF CONVECTIVE CORES	713
<i>Jorgen B Jensen, Sunhee Lee, Reinout Boers, Paul Krummel, James Hudson</i>	
A CASE STUDY OF WINTERTIME OROGRAPHIC PRECIPITATION IN THE NORTHERN MOUNTAINS OF ARIZONA, FEB 14 1995	717
<i>W D Hall, R Bruintjes, J Coen, T L Clark</i>	
CASE STUDY OF STRATOCUMULUS-TOPPED BOUNDARY LAYER USING A LARGE EDDY SIMULATION MODEL WITH EXPLICIT MICROPHYSICS	721
<i>Y L Kogan, M P Khairoutdinov</i>	
A MICROPHYSICAL MODEL OF THE CLOUD TOPPED MARINE BOUNDARY LAYER	725
<i>Andreas Bott</i>	
EQUILIBRIUM STATES IN DRIZZLING VERSUS NON-DRIZZLING STRATOCUMULUS	729
<i>Bjorn Stevens, William R Cotton, Graham Feingold</i>	
ROLE OF RADIATIVE AND EVAPORATIVE COOLING IN THE ENTRAINMENT LAYER OF STRATOCUMULUS	733
<i>Margreet C van Zanten, Peter G Duynkerke</i>	

STUDY OF AEROSOL PROCESSING IN STRATOCUMULUS CLOUDS USING LES EXPLICIT MICROPHYSICAL MODEL WITH THE AEROSOL TRACKING OPTION <i>Qingfu Liu, Yefim Kogan</i>	737
HAWAIIAN RAINBANDS: EFFECTS OF THERMAL FORCING ON THE RAINBAND DYNAMICS <i>Vanda Grubisic, Roy M Rasmussen, Piotr K Smolarkiewicz, Richard E Carbone</i>	741
LARGE EDDY SIMULATION OF DEUTERIUM IN THE STRATOCUMULUS-TOPPED BOUNDARY LAYER <i>Hui He, David E Stevens, Ronald B Smith</i>	744
A RADIATION CLOUD MODEL WITH A DETAILED TREATMENT OF THE MICROPHYSICS <i>Christian Issig, Uwe Ritzmann, H D Schilling</i>	748
CLOUD-RESOLVING SIMULATIONS OF WARM-SEASON ARCTIC STRATUS CLOUDS: EXPLORATORY MODELLING OF THE CLOUDY BOUNDARY LAYER <i>Peter Q Olsson, Graham Feingold, Jerry Y Harrington, William R Cotton, Sonia Kreidenweis</i>	752
Session 4.2: MODELLING OF CONVECTIVE CLOUDS	
A STATISTICAL STUDY OF WARM RAIN FORMATION IN SHALLOW, TROPICAL CONVECTION <i>Marcin J Szumowski, Wojciech W Grabowski, Robert M Rauber, Harry T Ochs</i>	756
NUMERICAL SIMULATIONS OF DEEP TROPICAL CONVECTION USING A CLOUD ENSEMBLE MODEL WITH AN IMPROVED EXPLICIT MICROPHYSICS <i>Tamir Reisin, Leo Donner, Richard Hemler, Charles Seman</i>	758
THERMODYNAMICAL BUDGETS OF AN EXPLICITLY SIMULATED DEEP CONVECTIVE CLOUD SYSTEM <i>Francoise Guichard, Jean-Philippe Lafore, Jean-Luc Redelsperger</i>	762
RADAR OBSERVATIONS AND NUMERICAL SIMULATIONS OF A TOGA COARE SQUALL SYSTEM <i>Brad S Ferrier, Jeffrey B Halverson, Robert Pasken, Wei-Kuo Tao, Joanne Simpson</i>	766
CLOUD-RESOLVING MODELING OF TROPICAL CLOUD SYSTEMS AND ITS APPLICATION TO THE CLOUD-CLIMATE INTERACTIONS <i>Wojciech W Grabowski, Xiaoqing Wu, Mitchell W Moncrieff</i>	770
ICE DEVELOPMENT IN CUMULUS CLOUDS: A CASE STUDY USING A 3-D MODEL WITH EXPLICIT ICE AND WARM RAIN MICROPHYSICS <i>M V Ovtchinnikov, Yefim L Kogan, Alan M Blyth</i>	774
NUMERICAL SIMULATION OF WINTERTIME PRECIPITATION DEVELOPMENT IN GRAVITY WAVE AND UPSLOPE FLOW IN ARIZONA'S VERDE VALLEY <i>Janice L Coen, Roelof T Bruintjes, William D Hall, Terry L Clark, Roger F Reinking</i>	778
A TWO-DIMENSIONAL CLOUD MODEL: DESCRIPTION AND NUMERICAL EXPERIMENTS <i>Alexandre Araujo Costa, Antonio José da Costa Sampaio</i>	782
HAIL SIZE SPECTRUM DOMAIN INFLUENCE ON THE SIMULATED CLOUD LIFE <i>Mladjen Ćurić, Dejan Janc, Vlanan Vučković</i>	786
EXTENDED COMPARISON BETWEEN AIRBORNE DOPPLER RADAR DATA AND THREE-DIMENSIONAL SIMULATIONS OF A TROPICAL SQUALL LINE OBSERVED DURING TOGA-COARE <i>Thibaut Montmerle, Jean-Luc Redelsperger, Jean-Philippe Lafore, Gilles Sommeria, Y Lemaître</i>	790

ON THE NUMERICAL SIMULATION OF THE 10 MAY 1993 HAIL STORM USING THE UNIVERSITY OF BUENOS AIRES TWO DIMENSIONAL CONVECTIVE MODEL <i>Marcela Torres Brizuela, Matilde Nicolini</i>	794
A SENSITIVITY STUDY ON THE MESOSCALE CHARACTERISTICS OF SQUALL-LINE SYSTEMS TO ENVIRONMENTAL CONDITIONS: IMPLICATION OF ANVIL CIRRUS PARAMETERIZATION <i>Hung-Neng Steve Chin</i>	797
NUMERICAL SIMULATIONS OF TROPICAL CONVECTIVE CLOUDS OVER CUBA USING A ONE-DIMENSIONAL AND TIME-DEPENDENT CLOUD MODEL <i>Lester Alfonso, Daniel Martinez, Carlos A Perez</i>	801
THE ROLE OF ICE GENERATION IN PRECIPITATION FORMATION AS SEEN FROM THE RESULTS USING A MIXED-PHASE CLOUD MODEL WITH SPECTRAL MICROPHYSICS <i>I L Sednev, A P Khain, D Rosenfeld</i>	805
ON THE TEMPERATURE OF EVAPORATING PRECIPITATION <i>G Ragette, G Wotawa</i>	809
KINEMATICS OF CLOUD-SCALE LOCAL ATMOSPHERIC PROCESSES <i>L G Kaplan</i>	812
DYNAMICS OF A CLOUD-SCALE VORTICAL ATMOSPHERIC PROCESS <i>L G Kaplan</i>	816
DYNAMICS OF A STRONG ASCENDING FLOW JET IN ATMOSPHERE <i>L G Kaplan</i>	818
 Session 4.3: MODELLING OF FRONTAL AND CIRRUS CLOUDS	
OBSERVATIONAL AND CLOUD-SCALE NUMERICAL MODEL STUDIES OF ANVIL CIRRUS CLOUD <i>Philip R A Brown, Hugh Swann</i>	822
NUMERICAL MODELLING CONTRAIL FORMATION AND MODULATION OF RADIATION FIELD WITH USE OF MESOSCALE MICROPHYSICAL CLOUD MODEL <i>V Khvorostyanov, S Bakan, H Grassl</i>	826
LARGE-EDDY-SIMULATION OF CONTRAILS <i>A Chlond</i>	831
OBSERVATIONS AND PARAMETERIZATION OF MIXED-PHASE CLOUDS DURING THE CANADIAN FREEZING DRIZZLE EXPERIMENT <i>Andre Tremblay, Stewart G Cober, Anna Glazer, George A Isaac</i>	835
A MEASUREMENT AND MODELING STUDY OF YOUNG CIRRUS CLOUDS: PART 2, MODEL PREDICTIONS <i>Hong Lin, Kevin J Noone, Johan Strom, Andrew J Heymsfield, Larry Miloshevich</i>	839
EFFECTS OF VOLCANIC AEROSOLS ON CIRRO-FORM CLOUDS <i>Naihui Song, Dave O'C Starr</i>	842
PRECIPITATION FORMATION IN FRONTAL STRATIFORM CLOUDS WITH SEVERAL CRYSTAL FORMS <i>Boris A Dorman, Vladimir P Bakhanov</i>	846
THE NUMERICAL MODEL STUDY OF CONVECTIVE-STATIFORM MIXED CLOUD AND PARAMETERIZATION OF MICROPHYSICAL PROCESSES <i>Hong Y anchao</i>	850

MESO- AND MICROSTRUCTURE OF STRATIFORM FRONTAL CLOUDS AND MECHANISMS OF PRECIPITATION FORMATION IN FRONTAL SYSTEMS OVER UKRAINE <i>V P Bakhanov, A A Manzharova, V T Kozhuk</i>	854
 Session 4.4: TECHNIQUES FOR CLOUD MODELLING	
A NEW APPROACH TO PARAMETERIZATION OF CLOUD DROPLET FREEZING PROCESSES IN NUMERICAL CLOUD MODELS <i>I P Mazin, M V Gurovich</i>	858
EXPLICIT CLOUD MICROPHYSICS AND CODE PARALLELIZATION: POSSIBLE STRATEGIES AND FIRST EXPERIENCES ON A MASSIVELY PARALLEL SUPERCOMPUTER <i>Thomas Trautmann, Erich Strohmaier</i>	862
APPLICATION OF THE VOLUME OF FLUID METHOD TO THE ADVECTION-CONDENSATION PROBLEM <i>Jon Reisner, Len Margolin, Piotr K Smolarkiewicz</i>	866
THE APPLICABILITY STUDY OF THE Γ DISTRIBUTION OF RAINDROP SIZE <i>Gong Fujii, Liu Jicheng, Chen Weidong, Li Zihua</i>	870
CONSTRUCTION OF THE VARIOUS NUMERICAL MODELS FOR RESEARCH OF DYNAMICS AND MICROPHYSICS OF CLOUD AND PRECIPITATION IN WINTER FRONTAL CLOUD SYSTEMS <i>Anne M Pirnach</i>	874
3-D SIMULATION OF CLOUDS ACCOUNTING FOR SUBGRID FLUCTUATIONS OF TEMPERATURE AND HUMIDITY <i>L Levkov, B Rockel, H Schiller, L Kornbluh</i>	878
SEMI-LAGRANGIAN/EULERIAN CLOUD MODEL <i>Piotr K Smolarkiewicz, Wojciech W Grabowski, Vanda Grubisic</i>	882
A CLOUD-RESOLVING MODEL WITH THE RADIATION SCHEME BASED ON THE MONTE CARLO METHOD <i>Darko Koraćin, Vlad Isakov, Luis Mendez-Nuñez</i>	885
AEROSOLS AND TURBULENCE IN CLOUD-SCALE PROCESSES <i>G M Teptin, L V Morozova, P N Douraguine</i>	889
COMPARISON OF NUMERICAL MODEL SIMULATIONS AND SATELLITE OBSERVATIONS OF AN UPSLOPE CLOUD SYSTEM. <i>Gregory Thompson, Roelof Brientjes, James F Bresch</i>	892
NUMERICAL SIMULATIONS OF ALTOCUMULUS USING AN EDDY RESOLVING MODEL AND A MIXED LAYER MODEL <i>Shuairan Liu, Steven K Krueger</i>	895
NON-STATIONARY MODEL OF ADMIXTURE DISTRIBUTION IN THE CLOUDY ATMOSPHERE <i>I E Naats, Ya A Ekba, L G Kaplan, M R Vatiashvili, E A Semenchin</i>	899
DEVELOPMENT AND VALIDATION OF A DOUBLE-MOMENT MICROPHYSICS SCHEME USED FOR SIMULATING CUMULUS CLOUDS <i>H A Swann, P R A Brown</i>	901
INITIALIZATION OF A NON-HYDROSTATIC CLOUD MODEL WITH AIRBORNE DOPPLER RADAR DATA <i>Soline Bielli, Frank Roux</i>	905

MASS CONSERVING FRAGMENT DISTRIBUTION FUNCTIONS <i>Philip S Brown, Jason A Walde</i>	909
A NEW NUMERICAL TREATMENT FOR THE DRAG COEFFICIENT LAW USED IN HAIL TRAJECTORY SIMULATIONS <i>Olga B Nasello, Nesvit E Castellano</i>	913
AN APPROXIMATION FORMULA FOR DROP/DROP COLLISION EFFICIENCIES <i>K D Beheng</i>	917
THE MODIFIED KOVETZ AND OLUND METHOD FOR THE NUMERICAL SOLUTION OF STOCHASTIC COALESCENCE EQUATION <i>Elena N Stankova, Mikhail A Zatevakhin</i>	921
Session 5.1: AEROSOLS AND RADIATIVE PROPERTIES OF CLOUDS	
SOUTHERN OCEAN CLOUD EXPERIMENT: OBSERVATIONS OF MARINE STRATOCUMULUS IN AN UNPOLLUTED ENVIRONMENT <i>R Boers, J B Jensen, J L Gras, P B Krummel, S-H Lee</i>	924
STUDY OF THE ANTHROPOGENIC SULFATE AEROSOLS INDIRECT EFFECT IN MARINE STRATOCUMULUS CLOUDS <i>Z N Kogan, Y L Kogan, D K Lilly</i>	928
ROLE OF ATMOSPHERIC AEROSOL IN THE INDIRECT CLIMATE COOLING MECHANISM <i>M H Smith, A Jones, J A Lowe, C D O'Dowd</i>	932
PREDICTING CLOUD DROPLET EFFECTIVE RADIUS AND INDIRECT SULPHATE AEROSOL FORCING USING A GENERAL CIRCULATION MODEL <i>Andy Jones, Anthony Slingo</i>	936
IMPACT OF ANTHROPOGENIC SULFUR EMISSIONS ON CLOUD-CLIMATE INTERACTIONS <i>Catherine C Chuang, Joyce E Penner</i>	939
EFFECT OF REPEATED CLOUD EVENTS ON AEROSOL PARTICLES AND THEIR DIRECT AND INDIRECT RADIATIVE PROPERTIES <i>Andrea I Flossmann, Nikos Hatzianastassiou, Wolfram Wobrock</i>	943
RETRIEVAL METHODS FOR THE EFFECTIVE RADIUS IN NUMERICAL MODELS <i>Klaus Wyser</i>	947
THE CONDENSATION COEFFICIENT REDUCTION AS A MAJOR FACTOR FOR ALBEDO ENHANCEMENT IN POLLUTED CLOUDS <i>N Fukuta, Y S Zou, N Xu</i>	951
THE EFFECTS OF AEROSOL ON WARM STRATOCUMULUS CLOUD LAYER MICROPHYSICS: AN INVESTIGATION USING SHIP TRACK EMISSIONS <i>D W Johnson, S R Osborne, J P Taylor</i>	955
ARTIFICIAL ENHANCEMENT OF PRECIPITATION AND CHANGE OF THE CLIMATE IN THE REGION <i>G Kh Badakhova</i>	959
THE RADIATIVE PROPERTIES OF INHOMOGENEOUS CLOUD FIELDS <i>Paul F Coley, Peter R Jonas</i>	963
A MODELING STUDY OF THE EFFECT OF DRIZZLE PRODUCTION ON CLOUD OPTICAL DEPTH <i>Graham Feingold, Reinout Boers, Bjorn Stevens, W R Cotton</i>	967

Session 5.2: LARGE-SCALE PROPERTIES OF CLOUD FIELDS

GLOBAL CLOUD MICROPHYSICAL PROPERTIES DERIVED FROM MULTISPECTRAL AVHRR DATA <i>P W Heck, D F Young, S Mayor, P Minnis</i>	971
CLIMATOLOGY AND MICROPHYSICS CHARACTERISTICS OF THE CUMULUS CLOUDS OF THE CEARA STATE IN NORTHEAST REGION OF BRAZIL <i>Carlos Jacinto de Oliveira, Alexandre Araujo Costa, Antonio José da Costa Sampaio, José Carlos Parente de Oliveira</i>	975
CLOUD-CLIMATE FEEDBACK MECHANISMS: RESULTS FROM A GROUND-BASED CLOSURE EXPERIMENT <i>V K Saxena, P A Durkee, S Menon, John Anderson, K E Nielsen</i>	978
MEASUREMENTS OF THE MICROPHYSICS OF LOW STRATUS AND THE RADIATION ABOVE, IN AND BELOW CLOUD <i>C M Banic, W R Leitch, G A Isaac, M C Couture, K B Strawbridge, J W Strapp, H W Barker, I Gulpepe, A V Korolev, J I MacPherson</i>	982
COMPARISONS OF AIRCRAFT AND LANDSAT OBSERVATIONS OF CLOUDS: IMPLICATIONS FOR CLOUD-CLIMATE INTERACTIONS <i>I Gulpepe, B A Wielicki, W R Leitch, G A Isaac, C M Banic, J W Strapp, A Korolev</i>	986
LABORATORY FTIR MEASUREMENTS OF ICE CRYSTAL AND WATER DROPLET CLOUDS: PARTICLE SIZE SPECTRUM INVERSION <i>W Patrick Arnott, Carl Schmitt, Yangang Liu, John Hallett</i>	990
THE EFFECTS OF LONGWAVE RADIATION IN A SMALL CUMULUS CLOUD <i>H Guan, M K Lau, R Davies</i>	993
THE IMPACT OF CLOUD LAYERS OVERLAPPING ON ESTIMATION OF CLOUD AMOUNT IN ANY LAYER BASED ON THE GROUND AND SATELLITE-BORNE OBSERVATIONS <i>A L Kosarev, I P Mazin</i>	997
ON THE INFLUENCE OF CONVECTIVE CLOUDS ON SOME CLIMATE FORMING FACTORS <i>V A Amiranashvili, R I Doreuli, T V Kheladze, K A Tavartkiladze</i>	1000
EVIDENCE FOR CLOUD-CLIMATE INTERACTIONS DUE TO ATMOSPHERIC ELECTRICITY EFFECTS ON ICE NUCLEATION <i>Brian A Tinsley</i>	1004
ON THE CLIMATIC IMPACT OF CONTRAILS <i>Bernhard Strauss, Ralf Meerketter, Bruno Wissinger, Peter Wendling</i>	1008
CONDITIONS OF ATMOSPHERIC CONVECTIVE PRECIPITATION IN STAVROPOL REGION <i>G Kh Badakhova, Ya A Ekba, L K Golouz, Yu K Lashmanov, R G Zakinyan</i>	1012
CLOUDINESS CLIMATOLOGY OF THE CENTRAL PART OF THE NORTH CAUCASUS <i>G Kh Badakhova, Yu K Lashmanov, Ya A Ekba</i>	1016
CLOUD SIMULATIONS WITH THE MAX PLANCK INSTITUTE FOR METEOROLOGY GENERAL CIRCULATION MODEL ECHAM4 AND COMPARISON WITH OBSERVATIONS <i>Cheng-Ta Chen, Erich Roeckner</i>	1020
SECULAR REGIME OF CLOUDINESS IN GEORGIA <i>V G Khorguani, R A Gvazava</i>	1024

SENSITIVITY OF CLOUD MICROPHYSICS ON THE SOLUBILITY OF ATMOSPHERIC AEROSOL PARTICLES: NUMERICAL CASE STUDIES USING NEW EXPERIMENTAL DATA <i>Sabine Wurzler, Cornelia Eichel, Martina Kramer, Lothar Schutz</i>	1024
ICE PARTICLE DENSITY EFFECT ON THE REFLECTANCE AND TRANSMITTANCE OF CIRRUS <i>Chun-lei Liu, Anthony J Illingworth, Peter R Jonas</i>	1026
Session 6.1: IMPACT OF CLOUDS ON AIR CHEMISTRY	
THE INFLUENCE OF IN-CLOUD CHEMICAL REACTIONS ON OZONE FORMATION IN CLOUDY ATMOSPHERES <i>Chris J Walcek, Hong-H Yuan</i>	1030
SIZE-DEPENDENT CHEMISTRY OF FOG DROPLETS <i>Sandro Fuzzi, Paolo Laj, Loretta Ricci, Axel Berner, Dieter Schell, Wolfram Wobrock, Manfred Wendish</i>	1034
NUMERICAL SIMULATION ON PHOTOCHEMISTRY OF STRATIFORM CLOUDS <i>Qin Yu, Zhang Yuanhang</i>	1038
OBSERVATIONS IN AND NEAR ANVILS OF NEW MEXICO THUNDERSTORMS: INFLUENCE ON UPPER TROPOSPHERIC COMPOSITION BY TRANSPORT, NO _x PRODUCTION BY LIGHTNING AND OTHER MECHANISMS <i>J E Dye, B A Ridley, J G Walega, J Zheng, F E Grahek, B Rison</i>	1042
EFFECTS OF NITRIC ACID VAPOR ON CLOUD AND HAZE FORMATION <i>Dennis Lamb, Alfred M Moyle</i>	1044
A LABORATORY INVESTIGATION ON THE UPTAKE OF TRACE GASES BY SINGLE SNOW CRYSTALS <i>C Diehl, S K Mitra, H R Pruppacher</i>	1047
A THEORETICAL MODEL FOR SO ₂ UPTAKE INTO PACKED ICE BEDS <i>Thomas Huthwelker, Thomas Peter, Dennis Lamb, Marcia Baker, Brian Swanson</i>	1050
FACTORS INFLUENCING THE ENTRAPMENT OF HYDROGEN PEROXIDE AND MOLECULAR OXYGEN IN RIME ICE <i>Jefferson R Snider, Jun Huang</i>	1054
IN-SITU TRACE GAS OBSERVATIONS IN DISSIPATING THUNDERCLOUDS DURING POLINAT <i>H Huntrieser, H Schlager, P Schulte, H Ziereis, U Schumann, F Arnold, J Ovarlez</i>	1058
THE ACCURACY OF APPROXIMATE NUMERICAL SOLVER TECHNIQUES IN SOLVING THE GAS-AQUEOUS CHEMICAL SYSTEM <i>Mary Barth, Peter Hess, Sasha Madronich</i>	1062
RESULTS OF RAIN WATER CHEMICAL CONTENT INVESTIGATION IN ALAZANI VALLEY <i>L Sh Abesalashvili, A G Amiranashvili, G D Supatashvili</i>	1066
ACID BUFFERING CAPACITIES OF FOG AND CLOUDWATER <i>X Rao, A Bator, K Hoag, O Graf, E Sherman, J Collett</i>	1070
THE INTERACTION OF AMMONIA WITH CLOUD <i>M Wells, J N Cape, T W Choularton, K N Bower</i>	1074
THE ORGANIC COMPONENT OF FOG DROPLETS <i>Sandro Fuzzi, Sergio Zappoli</i>	1077

A SIMULTANEOUS STUDY OF ACID PRECIPITATION IN THE RAPIDLY DEVELOPING AREAS OF XIAMEN, QUANZHOU, ZHANGZHOU AND TONGAN IN THE SOUTHEAST COAST OF CHINA <i>Shaocai Yu, Xiaojing Cheng, Zhemian Cheng, Shuentian Cheng, Jian Xiao, Wenxian Ye</i>	1080
A FIELD STUDY OF THE REACTION BETWEEN SULFUR DIOXIDE AND HYDROGEN PEROXIDE IN CLOUDS <i>Liaquat Husain, V D Dutkiewicz, B Rajasekhar</i>	1084
CHEMICAL MASS BALANCES IN MIXED PHASE CLOUDS <i>Margit Schwikowski, Olga Poulida, Urs Baltensperger, Heinz W Gaggeler</i>	1087
TRANSPORTS OF CHEMICAL CONSTITUENTS BY A FIELD OF TRADE-WIND CUMULI <i>Bruce Albrecht, Terri Faber</i>	1091
SIMULATIONS OF MARINE STRATIFORM CLOUD PHYSICO-CHEMISTRY <i>J A Lowe, S L Clegg, M H Smith, C D O'Dowd, P Brimblecombe</i>	1095
CHEMICAL HETEROGENEITY AMONG CLOUD DROP POPULATIONS AND ITS EFFECTS ON SULFUR OXIDATION <i>J Collett, X Rao, A Bator</i>	1099
COMPARISON AND ANALYSIS OF THE CHEMICAL CHARACTERISTICS OF PRECIPITATION IN CHINA, JAPAN AND USA <i>Huang Meiyuan, Cheng Xinjin, Wang Zifa</i>	1103
SIZE-DEPENDENT STRATOSPHERIC DROPLET COMPOSITION IN MESOSCALE TEMPERATURE FLUCTUATIONS AND THEIR POTENTIAL ROLE IN PSC FREEZING <i>Thomas Peter, Stefanie Meilinger</i>	1106
A WIND TUNNEL AND THEORETICAL INVESTIGATION OF THE UPTAKE OF NH ₃ , SO ₂ , AND CO ₂ IN FALLING WATER DROPS <i>A U Hannemann, S K Mitra, H R Pruppacher</i>	1110
CALCULATION OF THE IN-CLOUD CONCENTRATION OF TRACE COMPOUNDS IN RAIN BY SAMPLING RAINDROPS AT THE GROUND <i>P Ebert, K Baechmann, M Kibler, A Mainka, T Prokop, B Tenberken</i>	1114
FIELD EXPERIMENTAL DETERMINATION OF COLLISION EFFICIENCIES AS A FUNCTION OF RAINDROP AND AEROSOL PARTICLE SIZE <i>P Ebert, G Frank, M Kibler, A Mainka, T Prokop, B Tenberken, J Tschiersch, K Bachmann</i>	1118
EFFECTS OF CLOUD COVER IN GAS-PHASE CHEMICAL REACTIONS <i>Wang Tijian</i>	1122
ANALYSIS OF SEVERAL CHEMICAL COMPOSITION OF THE STRATUS IN NORTH ALONG MT. TIANSHAN IN XINJIANG IN WINTER <i>Li Bin, Shi Wenquan</i>	1125
MEASUREMENT AND RESEARCH ON CLOUDWATER CHEMISTRY OVER SEVERE ACID RAIN AREAS OF CHINA <i>Shen Zhilai, Wu Yuxiao, Huang Meiyuan, Xiao Hui, Lei Henchi</i>	1128
SCAVENGING OF SO ₂ AND NH ₃ DURING GROWTH OF ICE <i>G Santachiara, F Prodi, R Udisti</i>	1130
THE EFFECTS OF CLOUD MICROPHYSICAL PARAMETRIZATION ON MODEL PREDICTIONS OF GAS SCAVENGING BY WARM CONVECTIVE CLOUDS <i>Sabine Wurzler</i>	1134

PERTURBATION INDUCED BY CLOUDS ON OZONE DIURNAL VARIATIONS IN THE MARINE BOUNDARY LAYER OVER THE INDIAN OCEAN: MEASUREMENTS AND SIMULATIONS <i>P J Bremaud, A M Thompson, F Taupin, N Chaumerliac</i>	1138
A WIND TUNNEL AND THEORETICAL INVESTIGATION OF THE UPTAKE OF NH ₃ , SO ₂ AND CO ₂ IN FALLING WATER DROPS <i>A U Hannemann, S K Mitra, H R Pruppacher</i>	1141
SCAVENGING ALONG A MOUNTAIN SLOPE: EXPERIMENTAL AND MODEL COMPARISON <i>J Orb, J Staehelin, A Waldvogel</i>	1142
Session 6.2: IMPACT OF CLOUDS ON AEROSOL CHEMISTRY	
A STUDY OF THE AEROSOL MODIFICATION GENERATED BY PASSAGE THROUGH AN OROGRAPHIC CLOUD <i>T W Choularton, K N Bower, M W Gallagher, C Bradbury, M Wells, A Wiedensohler, W Birmili, B Martinsson, E Swietliki</i>	1145
PRECIPITATION SCAVENGING IN A COUPLED CHEMISTRY/CLIMATE MODEL OF SULFATE AEROSOL <i>C R Molenkamp, J E Penner, J J Walton, C J O'Connor</i>	1149
ORGANIC AEROSOLS AS CCN IN CARIBBEAN TRADE WINDS <i>T Novakov, C E Corrigan, J E Penner, C C Chuang, O Rosario, O Mayol Bracero</i>	1153
SEASONAL VARIATION OF CLOUD LIQUID WATER CONTENT AND ACTIVATED AEROSOL FRACTION AT A HIGH-ALPINE SITE <i>Urs Baltensperger, Margit Schwikowski, Dieter T Jost, Stephan Nyeki, Heinz W Gäggeler</i>	1157
CLOUD PROCESSING OF AEROSOL IN THE STRATOCUMULUS CAPPED MARINE BOUNDARY LAYER <i>Sonia M Kreidenweis, Graham Feingold, Bjorn Stevens, William R Cotton</i>	1161
THE INFLUENCE OF CONVECTIVE CLOUDS ON THE TRANSPORT OF GASES AND PARTICLES <i>Andrea I Flossmann</i>	1165
AEROSOL-CLOUD INTERACTIONS IN THE MARINE CLOUDY BOUNDARY LAYER <i>R Majeed, D Hegg, P Yuen, M Baker</i>	1169
OBSERVATIONS AND MODELLING STUDIES OF CHEMICAL CLOUD PROCESSING BY MARINE STRATOCUMULUS <i>Colin D O'Dowd, Jason A Lowe, Michael H Smith</i>	1172
CHEMICAL AND MICROPHYSICAL PROPERTIES OF CLOUD DROPLET RESIDUAL PARTICLES IN MARINE STRATOCUMULUS CLOUDS OBSERVED DURING THE MAST EXPERIMENT <i>Kevin J Noone, Elisabeth Öström, Robert A Pockalny, Lieve De Bock, Rene van Grieken</i>	1176
EFFECT OF RAINDROP BREAKUP ON SUBCLOUD SCAVENGING OF AEROSOLS OF 1 TO 5 MM <i>Gustavo G Carrio</i>	1179
SULFUR CHEMISTRY IN THE NCAR COMMUNITY CLIMATE MODEL <i>Mary Barth, Phil Rasch, Brian Eaton, Natalie Mahowald</i>	1181
A MODELLING STUDY OF AEROSOL PROCESSING BY STRATOCUMULUS CLOUDS <i>Keith N Bower, Tom W Choularton</i>	1184

CLOUD-PROCESSING AND MORPHOLOGICAL RESTRUCTURING OF SOOT AGGLOMERATES SAMPLED AT THE JUNGFRAUJOCH HIGH-ALPINE RESEARCH STATION (3454 M), SWITZERLAND <i>S Nyeki, V Lavanchy, D Lewis, U Baltensperger, I Colbeck, H W Gäggeler</i>	1188
ON THE INFLUENCE OF ACTIVITY COEFFICIENTS ON THE SIZE DEPENDENT CLOUD DROP CONCENTRATION DEVELOPMENT <i>F Müller</i>	1192
THE EFFECTS OF SEA-SALT AEROSOL ON THE PRODUCTION OF SULPHATE IN THE MARINE ATMOSPHERIC BOUNDARY LAYER AND ITS EFFECT ON STRATIFORM CLOUDS <i>J A Lowe, M H Smith, C D O'Dowd, S L Clegg</i>	1196
CLOUD CYCLING OF SOLUBLE AND INSOLUBLE SUBSTANCES: FIELD STUDIES ON MOUNTAIN KLEINER FELDBERG, FRG <i>Cornelia Eichel, Martina Kramer, Matthias Schule, Lothar Schutz, Dieter Schell</i>	1200
COMING INTO THE QUESTION OF AEROSOLS CHEMICAL AND PHYSICAL PROPERTIES INFLUENCE UPON DISASTROUS HAIL FORMING. <i>M R Vatiashvily, I R Preis, Kh M Kalov</i>	1208
AEROSOL EXCHANGE IN THE CLOUD-AMBIENT AIR SYSTEM <i>N A Berezinsky, G V Stepanov</i>	1212
PARAMETERIZATION OF IN-CLOUD SULPHATE PRODUCTION <i>Quingyuan Song, H G Leighton</i>	1216
Session 7.1: PARAMETRIZATION OF CLOUD PROPERTIES	
PARAMETERIZATION OF THE DROPLET EFFECTIVE RADIUS OF WARM CLOUDS <i>Constantin A Pontikis, Elizabeth M Hicks</i>	1220
THE EFFECTIVE RADIUS OF STRATIFORM CLOUD PARTICLES IN MIDDLE LATITUDES (EMPIRICAL DATA) <i>I P Mazin, V F Shugaev, N A Monakhova</i>	1224
INFLUENCE OF DIFFERENT PARAMETERIZATIONS OF ICE CLOUDS ON CLIMATE SENSITIVITY IN A GENERAL CIRCULATION MODEL <i>Ulrike Lohmann, Erich Roeckner</i>	1228
PARAMETERIZATION OF TROPICAL CIRRUS ICE CRYSTAL SPECTRA AND IMPLICATIONS FOR RADIATIVE TRANSFER <i>Greg M McFarquhar, Andrew J Heymsfield</i>	1232
THE MODELLING OF SECONDARY ICE PRODUCTION IN STRATIFORM CLOUDS BY USE OF A ONE DIMENSIONAL MIXED LAYER MODEL <i>D S Morris, T W Choularton</i>	1236
A PARAMETERIZATION FOR PREDICTING FRACTIONAL CLOUDINESS IN THE TRADE CUMULUS BOUNDARY LAYER <i>Alistair Fraser, Christopher S Bretherton</i>	1240
PARAMETERIZATION OF CLOUD DROPLET CONDENSATIONAL GROWTH <i>Alan M Gadian, Jean-Louis Brenguier, Wojciech Grabowski</i>	1244
PARAMETRIZATION OF CCN CONCENTRATION BASED ON THE CALCULATION OF THE VERTICAL PROFILE OF AEROSOL PARTICLES <i>J Phelps, M H Smith, C D O'Dowd</i>	1247

THE SENSITIVITY OF A LAM MODEL TO THE INCLUSION OF A CLOUD FRACTION IN AN EXPLICIT REPRESENTATION OF CONVECTION: PRELIMINARY RESULTS <i>A Celeste Saulo, Matilde Nicolini</i>	1251
A COMPARATIVE ANALYSIS OF TWO BULK MICROPHYSICS PARAMETERIZATIONS USED IN A MESO-B-SCALE NON-HYDROSTATIC METEOROLOGICAL MODEL <i>N Molders, A Raabe, G Kramm, M Laube</i>	1254
CALCULATION AND PARAMETRIZATION OF THE EFFECTIVE RADIUS OF ICE PARTICLES USING AIRCRAFT DATA <i>S J Moss, P Francis, D W Johnson</i>	1255
Session 7.2: APPLICATIONS OF CLOUD PHYSICS	
APPLICATION OF CLOUD MODEL TO PREDICTING THE TORRENTIAL RAIN IN CENTRAL CHINA <i>Hu Zhijin, Liu Gongbo</i>	1263
APPLICATION OF CLOUD AND PRECIPITATION IN SCIENTIFIC SYSTEM ON NATURAL DISASTER REDUCTION <i>Wang Ang-Sheng, Liang Bi-Jun, Dong Jia-Rui, Feng Qiang, Wang Zhuo</i>	1267
RAINBAND PRECIPITATION PROCESSES IN DIFFERENT CLIMATOLOGICAL AREAS <i>Tsutomu Takahashi</i>	1271
PHYSICAL CHARACTERISTICS OF HAIL FROM NATURALLY DEVELOPED AND SEEDDED CLOUD PROCESSES: RECOMMENDATIONS ON MODIFICATION OF PRESENT HAIL SUPPRESSION METHODS <i>M I Tlisov, B M Khuchunaev</i>	1275
THE GLOBAL PROPERTIES AND ENVIRONMENT OF MESOSCALE CONVECTIVE COMPLEXES <i>Arlene G Laing, J Michael Fritsch</i>	1277
VALIDATION OF SATELLITE-DERIVED CLOUD PROPERTIES DURING TOGA-COARE <i>David R Doelling, R Palikonda, J K Ayres, P Minnis, T P Ackerman, J D Spinhirne</i>	1281
NUMERICAL SIMULATIONS OF HYGROSCOPIC SEEDING FOR RAINFALL ENHANCEMENT <i>Zailiang Hu, Roelof T Buijntjes, Eric A Betterton</i>	1285
THE STRUCTURAL CHARACTERISTICS OF THE CLOUD AND PRECIPITATION FIELDS IN CENTRAL ASIA (TURAN CLIMATIC REGION) <i>B Sh Kadyrov, V P Kurbatkin, V Ph Ushintseva</i>	1289
NUMERICAL SIMULATION OF NDTP CASE 3.1 (JUNE 18, 1989) <i>Xiong Huanan, Feng Shuchang, Chen Yuan</i>	1293
NUMERICAL SIMULATION OF THE PRECIPITATION DEVELOPMENT ON CUMULUS MERGERS IN CHANGSHA OF CHINA <i>Xiong Huanan, Feng Shuchang, Han Siying</i>	1296
THE CHARACTERISTICS OF THE ATMOSPHERIC WATER OVER TROPICAL WESTERN PACIFIC "WARM POOL" DURING TOGA-COARE IOP <i>Chong Wei, Xuan Yuejian</i>	1300
THE INFLUENCE OF SURFACE PARAMETERS ON RAINFALL DEVELOPMENT IN MESO- γ -SCALE MODELS; A SENSITIVITY STUDY <i>J Thielen, W Wobrock, J-D Creutin, P Mestayer</i>	1303

DRYING OUT OF ARAL SEA AND A REGIME OF CLOUD AND PRECIPITATION <i>B A Kamalov</i>	1307
SYSTEMATIC VARIATIONS OF RAINDROP SIZE DISTRIBUTION MEASURED IN NORTHERN GERMANY DURING 7 YEARS <i>Igor G Doelling, Johann Riedl, Jurg Joss</i>	1310
APPLICATION OF CLOUD AND PRECIPITATION IN FLOOD-WATERLOGGING DISASTER MODEL <i>Wang Ang-Sheng, Dong Jia-Rui</i>	1314
AIRCRAFT ICING FROM SUPERCOOLED DRIZZLE <i>Stewart G Cober, George A Isaac, J Walter Strapp</i>	1318
A SEMI-ANALYTICAL MODEL OF GLOBALLY-AVERAGED ATMOSPHERIC RESPONSE TO ENHANCED GREENHOUSE WARMING WITH CLOUDS <i>Krzysztof Szilder, Edward P Lozowski, Gerhard W Reuter</i>	1322
MICROPHYSICAL RESPONSE OF SUMMER CONVECTIVE CLOUDS IN WEST TEXAS TO AGI "DYNAMIC" SEEDING <i>Daniel Rosenfeld, William L Woodley</i>	1325
LATE PAPERS	
HIGH EFFICIENCY AEROSOL GENERATORS FOR CLOUD PHYSICS RESEARCHES <i>Anatoly V Savchenko, Vladimir V Smirnov, Michail B Anipko, Valentin S Kayro, Sergey M Kontush, Leonid M Makalsky</i>	1329
INVESTIGATION OF INTERACTION BETWEEN DROPLET AND DUST-SALT CLOUDS <i>Vladimir V Smirnov, D A Gillette, G S Golitsyn, I G Granberg, A A Pronin, A V Savchenko</i>	1333
INVESTIGATION OF THE RELATIVE ROLE OF DIFFERENT ICE CRYSTALS FORMATION MECHANISMS IN CONVECTIVE CLOUDS USING A MODEL WITH DETAILED MICROPHYSICS <i>Zev Levin, Tamir Reisin, Shalva Tzivion</i>	1337
ESTIMATION OF CIRRUS MICROPHYSICAL PARAMETERS FROM MULTISPECTRAL MEASUREMENTS IN THE NEAR INFRARED <i>Stephan Bakan, Claudio Costanzo</i>	1341
FORMATION AND INFLUENCE OF PRECIPITATION-SIZED DROPS IN CUMULUS CLOUDS <i>John Latham, Alan M Blyth, Paul R Krehbiel, Rasmus E Benestad</i>	1345

LIST OF AUTHORS

ABE D	550 589	BERNER A	1034	CHEN Y	1293
ABESALASHVILI L SH		BERNSTEIN B C	109	CHENG S T	1080
	1066	BETTERTON E A	1285	CHENG X J	1080 1103
ACKERMAN T P	1281	BEZRUKOVA N A		CHENG Z M	1080
ADZHIEV A KH	295		653	CHERNIKOV A	668
AKIMOV N M	166	BIELLI S	905	CHIN H-N S	797
ALBERS F	506	BIRMILI W	1145	CHLOND A	831
ALBRECHT B	498 1091	BLACK R A	27	CHONG W	428 1300
ALEKSIC N M	581	BLACKMAN T M		CHOULARTON T W	
ALFONSO L	801		146		1074 1145
ALMEIDA M P DE		BLYTH A M	154 774 1345		1184 1236
	358	BOBAK J	498	CHU J	342
AMAYENC P	204	BOERS R	713 924	CHUANG C C	939 1153
AMIRANASHVILI A G		BOGOMOLOV O S		CLARK T L	554 686 717
	267 1000 1066		612		778
ANDERSON J	978	BOTT A	725	CLEGG S L	1095 1196
ANDERSON T	138	BOURRIANNE T	458	COBER S G	11 365 835
ANDSAGER K	122	BOWEN T A	514		1318
ANGUS L 1	365	BOWER K N	1074 1145	COELHO A	458
ANIPKO M B	1329		1184	COEN J L	554 686 717
ARATHOON J R	220	BRADBURY C	1145		778
ARNOLD F	1058	BREMAUD P J	1138	COLA A	382
ARNOTT W P	641 990	BRENGUIER J-L	23 53 57 67	COLBECK I	1188
ASHABOKOV B A			394 454 458	COLEY P F	963
	262		1244	COLLETT J	1070 1099
ASSELIN DE BEAUVILLE C		BRESCH D	614	COOPER W A	53 135 200
	398	BRESCH J F	892		308 494
ASUMA Y	585 621 672	BRETHERTON C S		CORRIGAN C E	1153
ATABIEV M D	406 604		701 705 709	COSTA A A	540 782 975
AUSTIN P H	41		1240	COSTA SAMPAIO A J DA	
AYRES J K	1281	BRIMBLECOMBE P			540 975 782
BABB D	498		1095	COSTANZO C	1341
BADAKHOVA G KH		BRINKMANN J	1200	COTTON W R	698 729 752
	959	BRIZUELA M T	794		1161
BADAKHOVA G KH		BROOKS I M	518	COUTURE M C	982
	1012 1016	BROWN P R A	822 901	CREUTIN J-D	1303
BAECHMANN K	1114 1118	BROWN P S	909	ĆURIĆ M	97 278 786
BAINBRIDGE A J	474	BRUINTJES R T	85 554 717	CZYS R R	301
BAKAN S	128 826 1341		778 892 1285	DANNE O	424
BAKER M	1050 1169	BURIEZ J C	394	DAVIES R	993
BAKHANOV V P	846 854	BURNET F	67	DE BOCK L	1176
BALTENSPERGER U		CAI X P	1080	DEFELICE T P	39
	1087 1157	CAPE J N	1074	DEMOTT P J	200 135 320
	1188	CARBONE R E	494 741	DESCLOITRES J	394
BANAT P	526	CARMO MENDES K DO		DESSENS J	244
BANIC C M	982 986		358	DETWILER A G	179 514
BAREKOVA M V	593	CARRIO G G	1179	DIEHL C	1047
BARKER H W	982	CASTELLANO N E		DOELLING D R	1281
BARTH M	1062 1181		913	DOLLING I G	150 1310
BARTHAZY E	162	CASTRO A	232	DONG J R	1267 1314
BATOR A	1070 1099	CASTRO D M	566 801	DONNER L	758
BAUMGARDNER D		CHAUMAT L	57	DOREULI R A	1000
	308 402	CHAUMERLIAC N		DOREULI R I	196
BEARD K V	121 122		1138	DORMAN B A	846
BEHENG K D	338 917	CHEN C T	1020	DOURIAGUINE P N	
BENESTAD R E	1345	CHEN C-H	709		889
BEREZINSKY N A		CHEN H P	413	DOVGALYUK YU A	
	361 410 1212	CHEN W	870		683

DUAN Y	536 629	GOLOUZ L K	1012	HUANG M Y	1103 1128
DURKEE P A	978	GONG F	15 870	HUANG T	1 365
DUTKIEWICZ V D		GONG N H	303	HUDAK D R	158
	1084	GORDON G	562	HUDAK D R	621
DUYNKERKE P G		GRABOWSKI W W		HUDSON E	621
	478 733		105 756 770	HUDSON J G	7 713
DYE J E	1042		882 1244	HUNTRIESER H	1058
EATON B	1181	GRAF O	1070	HUSAIN L	1084
EBERHARD W L	175	GRAHEK F E	1042	HUTHWELKER T	1050
EBERT P	1114 1118	GRANBERG I G	1333	IACOVAZZI B A	581
ECKLUND W L	597	GRAS J L	924	ILLINGWORTH A J	
EFREMOV V N	417 420	GRASSL H	826		146 1026
EICHEL C	1024 1200	GRUBISIC V	494 741 882	ISAAC G A	11 365 835
EKBA YA A	406 410 530	GUAN H	993		982 986 1318
	604 608 899	GUICHARD F	762	ISAKOV V	885
	1012 1016	GULTEPE I	982 986	ISLAM MD N	546
ELPERIN T	117 328	GUROVICH M V	858	ISSIG C	748
ENDOH T	100 240 297	GUYOT A	438	IWAI K	271
	664	GVAZAVA R A	1024	IWANAMI K	186 190 672
FABER T	1091	GYSI H	649	IWATA S	621
FEDCHENKO L M		GZIRISHVILI T G		JAKIMCHUK V I	466
	262 361		267	JANC D	97 786
FEINGOLD G	698 729 752	HAGEN M	386	JENKINS M A	686
	967 1161	HAIMOV S	502	JENSEN J B	713 924
FENG H-F	662	HALL W D	717 778	JOBARD I	390
FENG Q	1267	HALLETT J	236 641 990	JOHNSON D W	350 482 955
FENG S	1293 1296	HALVERSON J B	766		1255
FERRIER B S	766	HAMAN K E	510	JONAS P R	81 316 482
FINKE U	290 544 601	HAN S	1296		532 633 963
FISENKO S P	292	HANADO H	186 450		1026
FLOSSMANN A I		HANNEMANN A U		JONES A	932 936
	943 1165		1110 1141	JOSS J	1310
FRAILE R	232	HARIMAYA T	254 286 470	JOST D T	1157
FRANCIS P	1255	HARRINGTON J Y		KACHATUROVA L I	
FRANK G	1118		698 752		608
FRASER A	1240	HATZIANASTASSIOU N		KADYROV B SH	183 1289
FRENCH J	502		943	KAJIKAWA M	274 690
FRITSCH J M	1277	HAUF T	369 544 601	KALOV KH M	1208
FUJIYOSHI Y	228 570	HAYASAKA T	31	KAMALOV B A	1307
FUKUTA N	951	HE H	744	KANADA S	570
FURUKAWA M	100	HECK P W	971	KAPITANIKOV A V	
FUZZI S	1034 1077	HEGG D	1169		406
GADIAN A M	1244	HEINTZENBERG J		KAPLAN L G	406 812 816
GAGE K S	597		138		818 899
GÄGGELER H W	1087 1157	HEMLER R	758	KAPRILOV B	522
	1188	HENRICH W	162	KATSUMATA M	573
GALLAGHER M W		HESS P	1062	KAWAMURA H	31
	1145	HEYMSFIELD A J		KAWASHIMA M	550
GAO Z Y	170		131 354 839	KAYE A	334
GARBRECHT T	338		1232	KAYE P H	350
GAZAEVA Z A	593	HICKS E M	1220	KAYRO V S	1329
GENG B	570	HIGASHIURA M	190	KELLY R D	502
GERESDI I	251	HINDMAN E E	75	KENT G S	637
GILLETTE D A	1333	HIRST E	350	KHAIN A P	45 93 805
GLAZER A	835	HOAG K	1070	KHAIROUTDINOV M P	
GLENDENING J W		HÖLLER H	290 386		721
	518	HONG Y C	850	KHARAKHONOVA N A	
GODDARD J W F		HOUEE S	204		612
	61	HU Z	1285 1263	KHELADZE T V	1000
GOLITSYN G S	1333	HUANG J	1054		

KHORGUANI V G		LAU M K	993	MANZHARA A A	
	264 1024	LAUBE M	1254		854
KHORIKOV A A	410	LAURENT H	390	MARCOS J L	232
KHUCHUNAEV B M		LAVANCHY V	1188	MARÉCAL V	204
	1275	LAWSON R P	1 342 365	MARGOLIN L	866
KHUSID S V	679	LEAITCH W R	982 986	MARTIN G M	482
KHVEDLIDZE Z V		LEE S	713	MARTINSSON B	1145
	264	LEE S-H	924	MARTNER B A	514
KHVOROSTYANOV V		LEE W-C	494	MARTNER B E	446
	128 826	LEI H C	1128	MARWITZ J D	562
KIBLER M	1114 1118	LEIGHTON H G	113 1216	MATROSOV S Y	446
KIKUCHI K	282 546 573	LEMAÎTRE Y	790	MATSUO T	562
	585 621 672	LENSCHOW D H	474	MATSUURA K	100
KIKUCHI O	546	LEON D	502	MAYOL BRACERO O L	
KIM K N	420	LEVI L	212		1153
KIMURA R	621	LEVIN Z	45 1337	MAYOR S	971
KITANO K	228	LEVKOV L	878	MAZIN I P	858 997 1224
KLEEORIN N	328	LEW J K	301	MCCORMICK M P	
KNIGHT C A	53 236	LEWIS D	1188		637
KOGAN Y L	721 737 774	LI B	173 324 1125	McFARQUHAR G M	
	928	LI C	558		131 1232
KOGAN Z N	928	LI Z	15 870	McMURTRY P A	
KOKHANOVSKY A A		LIANG B J	1267		41
	434	LILLY D K	928	MEERKETTER R	1008
KOLDAEV A	442 668	LIN H	839	MEILINGER S	1106
KOLEV I	490 522	LINDER W	577	MEISCHNER P	150
KOLEZHUK V T	854	LIST R	35 158 224	MELNICHUK YU	668
KONISHI H	664 694	LIU C L	1026	MENDEZ-NÚÑEZ L	
KONTUSH S M	1329	LIU G B	1263		885
KOPYT N KH	466	LIU J	15 413 870	MENON S	978
KORACIN D	885	LIU L	431	MENSHOV M A	672
KORNBLUEH	878	LIU Q	721 737	MESTAYER P	1303
KOROLEV A V	11 346 365	LIU S	121 895	MIKHALKOVA O A	
	982 986 997	LIU S R	1103		332
KOZIOL A S	113	LIU Y	990	MILLER M A	486
KRAKOVSKAIA S V		LIU Y G	641	MILOSHEVICH L M	
	208 645	LÖFFLER-MANG M			131 354 839
KRAMER M	1024 1200		338	MINNIS P	637 971 1281
KRAMM G	1254	LOHMANN U	1228	MITRA S K	49 1047 1110
KRASOVITOV B	117	LOWE J A	932 1095 1172		1141
KRAUSS T	158		1196	MIZUNO H	142
KREHBIEL P R	1345	LOZOWSKI E P	1322	MOLDERS N	1254
KREIDENWEIS S M		LU T	15	MOLENKAMP C R	
	698 752 1161	LUBART L	212		1149
KROPFLI R A	446	MACE G G	498	MONAKHOVA N A	
KRUEGER S K	41 709 895	MACPHERSON J I			1224
KRUMMEL P B	474 713 924		982	MONCRIEFF M W	
KUMAGAI H	186	MADRONICH S	1062		770
KURBATKIN V P	1289	MAHOWALD N	1181	MONTMERLE T	790
LACHLAN-COPE T		MAIA A	390	MOORE G W K	621
	193	MAINKA A	1114 1118	MORLEY B	402
LAFORE J-P	762 790	MAJEED R	1169	MOROZOVA L V	889
LAING A G	1277	MAKALSKY L M		MORRIS D S	1236
LAIRD N F	122		1329	MOSS S J	1255
LAI P	1034	MAKI M	186 190 672	MOYLE A M	1044
LAM D	721	MAKITOV V S	593	MÜLLER F	1192
LAMB D	1044 1050	MALINOWSKI S P		MURAKAMI M	142 562
LASHMANOV YU K			510 526	MURAMOTO K	100 228 470
	1012 1016	MALKOV A A	410	NAATS I E	899
LATHAM J	154 1345			NAKAI S	690

NAKAI Y	254	POLUEKTOV P P	332	SAULO A C	1251
NASELLO O B	913	PONTIKIS C A	398 1220	SAUNDERS C P R	220
NAUMOV A Y	653	POPSTEFANIJA I	424	SAUNDERS S	350
NEVZOROV A N	124 346 371	PORCÙ F	216	SAVCHENKO A V	1329 1333
NICOLINI M	794 1251	POULIDA O	1087	SAXENA V K	978
NIELSEN K E	978	PREIS I R	1208	SCHELL D	1034 1200
NISSSEN R	35	PRODI F	216 382 1130	SCHILLER H	878
NOONE K J	839 1176	PROKOP T	1114 1118	SCHILLING H D	748
NOVAKOV T	1153	PRONIN A A	1333	SCHLAGER H	1058
NYEKI S	1157 1188	PRUPPACHER H R	49 1047 1110	SCHMID W	577 614
O'CONNOR C J	1149		1141	SCHMITT C	990
O'DOWD C D	334 932 1095	QIN Y	1038	SCHRÖDER F	138
	1172 1196	QUANTE M	424	SCHULE M	1200
	1247	RAABE A	1254	SCHULTE P	1058
OCHS H T	5 65 121 756	RADKE L	308	SCHUMANN U	1058
OCOKINA I A	679	RAGA G B	316	SCHUTZ L	1024 1200
OKUHARA K	274	RAGETTE G	809	SCHWIKOWSKI M	1087 1157
OLIVEIRA C J DE	358 540 975	RAJASEKHAR B	1084	SEDNEV I L	805
OLSSON P Q	698 752	RAND H A	705	SEEBELBERG M	89
ORALTAY R G	236	RAO X	1070 1099	SEMAN C	758
ORB J	1142	RASCH P	1181	SEMENCHIN E A	899
ORENBURGSKAYA E V	683	RASCHKE E	424	SHADIEVA R G	183
		RASMUSSEN R M	135 200 741	SHAPOVALOV A V	262
ORIKASA N	142	RAUBER R M	5 65 756	SHEN Z L	1128
OSBORNE S R	955	REDELSPERGER J-L	762 790	SHEPPARD B E	442
OSTROM E	1176		446 514 554	SHERMAN E	1070
OVARLEZ J	1058	REINKING R F	778	SHI L X	536 629
OVTCHINNIKOV M V	774		698 758 1337	SHI W Q	173 324 1125
		REISIN T	866	SHIINA T	470
PACKHAM D	686	REISNER J	375 506	SHIMAMURA T	621
PALAMARCHUK L V	645	REUTER A	1322	SHIMIZU S	597
		REUTER G W	1034	SHUGAEV V F	1224
PALIKONDA R	1281	RICCI L	61	SIEMS S T	474
PANSKUS H	375	RICHTER C	1042	SIMPSON J	766
PAPAGHEORGHE R	247	RIDLEY B A	1310	SINKEVICH A A	410 617 683
PARENTE DE OLIVEIRA J C	358 540 975	RIEDL J	220	SKEENS K M	637
		RIMMER J	1042	SLINGO A	936
PAROL F	394	RISON B	748	SMIRNOV V V	1329 1333
PARVANOV D	490	RITZMANN U	878	SMITH J A	657
PASHKEVICH M YU	410 612	ROCKEL B	462	SMITH M H	334 932 1095
PASKEN R	766	RODARO P	1020 1228		1172 1196
PASQUIER J R M	81 532	RODI A	328		1247
		ROECKNER E	135 200 320	SMITH P L	179 514
PAWLOWSKA H	23 394 454	ROGACHEVSKII I	518	SMITH R B	744
PAZMANY A	424	ROGERS D C	478	SMITH S A	532 633
PELON J	394	ROGERS D P	1153	SMOLARKIEWICZ P K	741 866 882
PENNER J E	939 1149 1153	ROODE S R DE	805 1325		
PEREZ C A	801	ROSENFELD D	905	SMYTH T J	146
PETER T	1050 1106	ROUX F	454	SNIDER J B	554
PHELPS J	1247	SALUT G	232	SNIDER J R	1054
PICKERING M A	350	SANCHEZ J L	1130	SOMMERIA G	790
PINSKY M B	45 93	SANTACHIARA G	286	SONG N	842
PIRNACH A M	166 208 625		190	SONG Q Y	1216
	683 874	SASAKI A	31	SOPHIEV E I	420
POCKALNY R A	1176	SATO T	450 550 589	SPINHIRNE J D	1281
POLITOVICH M K	109	SATO Y		STAEHELIN J	1142

STALEVICH D D	683	TOMA A	390	WU Y X	1128
STANKOVA E N	921	TRAUTMANN T	77 89 862	WU Z F	170
STARR D O'C	842	TREMBLAY A	11 835	WU Z H	536 629
STEINER M	657	TROITSKY A	442	WURZLER S	1024 1134
STEPANENKO V D	683	TSCHIRSCH J	1118	WYANT M C	705 709
STEPANOV G V	1212	TSUBOKI K	621	WYSER K	947
STEVENS B	729 1161	TUTTLE J	494	XIAO H	1128
STEVENS D E	701 705 744	TZIVION S	1337	XIAO J	1080
STEWART R E	621	UDISTI R	1130	XIONG H	1293 1296
STITH J L	179 320 514	UEDA H	1103	XU N	951
STRAPP J W	11 346 365	UENO K	585	XUAN Y J	1300
	442 982 986	USHINTSEVA V PH	1289	YAMADA H	672
	1318	USHIYAMA T	550 589	YAMADA Y	142 562 690
STRAUSS B	138 1008	UYEDA H	186 282 546	YAU M K	105 558
STRAWBRIDGE K B	982		573 585 597	YE W X	1080
STROHMAIER	862		621 672	YOSHIMOTO N	570
STRÖM J	138 839	VAILLANCOURT P A	105	YOUNG D F	971
STUART R A	11	VALI G	502	YU S C	1080
STURNIOLO O	382	VAN GRIEKEN R	1176	YUAN H H	1030
SU C-W	41	VAN ZANTEN M C	733	YUE G K	637
SUPATASHVILI G D	1066	VATIAHSVILY M R	530 899 1208	YUEN P	1169
SWANN H A	822 901	VELASCO I	462	YUM S	7
SWANSON B	1050	VOHL O	49	ZABOLOTSKAYA T N	676
SWIETLIKI E	1145	VUČKOVIĆ V	97 786	ZAKINIAN R G	530 604 1012
SYRETT W J	498	VUKOVIC Z R	278	ZAPPOLI S	1077
SZILDER K	1322	WACKER U	258	ZATEVAKHIN M A	921
SZUMOWSKI M J	5 65 756	WADA M	664 694	ZAWADZKI I	247
SZYRMER W	247	WALCEK C J	581 1030	ZEGE E P	434
TAKAHASHI N	450	WALDE J A	909	ZENG G-P	662
TAKAHASHI T	240 297 1271	WALDVOGEL A	162 1142	ZERR R J	179 320
TAKAI H	31	WALEGA J G	1042	ZHANG H F	303
TAKEDA T	570	WALTHER C	402	ZHANG J X	173
TAKEUCHI K	589	WALTON J J	1149	ZHANG L	413
TANG Y	662	WAN Z J	303	ZHANG Y H	1038
TANI T	204	WANG A S	1267 1314	ZHEKAMOUKHOV M K	530
TAO W-K	766	WANG P-H	637	ZHENG G	224
TATAROV B	522	WANG T J	1122	ZHENG J	1042
TATEUCHI K	550	WANG Z	1103 1267	ZHU D-H	662
TAUMURZAEV A I	593	WANG Z J	431	ZIEREIS H	1058
TAUPIN F	1138	WEAVER K	1 365	ZOU Y S	951
TAVARTKILADZE K A	1000	WELLS M	1074 1145		
TAYLOR J P	955	WENDISCH M	19 1034		
TELENTA B T	581	WENDLING P	138 1008		
TENBERKEN B	1118 1114	WIEDENSOHLER A	1145		
TEPTIN G M	889	WIELICKI B A	986		
TESTUD J	204 438	WILLIS P	236		
THIELEN J	1303	WILLIS P T	27 71		
THOMAS D	498	WISSINGER B	1008		
THOMPSON A M	1138	WOBROCK W	19 943 1034		
THOMPSON G	85 892		1303		
THORN M	89	WOOD R	378		
TIMM R	128	WOODLEY W L	1325		
TINSLEY B A	1004	WOTAWA G	809		
TLISOV M I	361 1275	WU X	770		

Volume 1

Sessions 1.1-3.3

NEW AIRBORNE MEASUREMENTS IN ADIABATIC CORES DURING VERY EARLY COALESCENCE DEVELOPMENT IN FLORIDA CUMULI

R. Paul Lawson, Leigh J. Angus, Tizhi Huang, Kim A. Weaver
SPEC Incorporated, Boulder, CO USA

Alan M. Blyth
Department of Physics, New Mexico Technical University, Socorro, NM USA

1. INTRODUCTION

The Small Cumulus Microphysics Study (SCMS) took place in Cocoa Beech, Florida from 17 July - 13 August 1995. The field project focused on aircraft and radar studies of small cumuli and the very early initiation of the warm rain (coalescence) process believed to be active in these clouds. The small cumulus clouds initially contain a continental drop size distribution that appears to rapidly broaden and develop into drizzle drops via the coalescence process (Knight and Miller 1993). Here we discuss aircraft data collected with a new cloud drop spectrometer (Lawson and Cormack 1995). Measurements were made from about 50 \rightarrow 2000 m above cloud base in adiabatic and mixed regions of clouds.

2. INSTRUMENTATION

Three aircraft were used: A C-130 operated by the National Center for Atmospheric Research (NCAR), the University of Wyoming (UW) King Air and a Merlin operated by the Centre National De Recherches Meteorologiques (CNRM) of France. The NCAR C-130 was extensively instrumented for making microphysical measurements. Along with the standard PMS (Knollenberg 1981) and hot-wire cloud liquid water content (LWC) King et al. (1978) probes, the PVM-100 LWC instrument (Gerber et al. 1994) and the CNRM fast forward scattering spectrometer probe (FFSSP) described by Brenguier et al. (1993) were installed.

A new optical instrument built by SPEC Incorporated, called a cloud drop spectrometer (CDS), was flown for the first time on the C-130. The design and preliminary wind-tunnel tests of the CDS are described by Lawson and Cormack (1995). The CDS measures the forward scattered light from an ensemble of drops. The measurement is made from $0.15^\circ \rightarrow 9^\circ$ using a CCD detector with 512 pixels, producing an angular measurement resolution of 0.017° . In the CDS, the raw measurements are recorded and LWC is computed in software by assigning appropriate weights to the angular measurements. The technique of optically weighting the basis functions, pioneered by Chittenden (1976) and reported by Blyth et al. (1984), is also the method used in

the Gerber instrument. The CDS differs in that it measures the scattered light and weights the measurements in software. The CDS also computes drop size from the same raw scattered light data by inverting the measurements and this is not possible with the Gerber instrument. The mathematics of the drop sizing technique was originally developed by Chin et al. (1955) and is similar to the drop-sizing method used in the Malvern particle analyzer (see Riley and Agrawal 1991 for a discussion of similar particle sizing techniques).

The CDS is the first airborne instrument to measure both cloud LWC and drop size distribution from an ensemble of drops. The measurement has inherent advantages over single-particle sizing and counting used in the FSSP and the Phase Doppler Particle Analyzer (Bachalo and Houser 1984). The sample volume of the CDS is 6 cm^3 and the measurement is independent of airspeed. Thus, coincidence and dead-time errors inherent in the FSSP (Baumgardner et al. 1985) are not a problem in the CDS. The CDS was installed in a standard PMS canister under the right-wing pod of the C-130. Since the raw (optically unweighted) scattered light measurements are acquired, the baseline can be maintained and data are processed using various techniques. The measurements are processed using different algorithms which are optimized for different applications. For example, if it is determined in a first pass through the data that there are no drops $> 100 \mu\text{m}$ in the sample volume, weighting functions and bin sizes which are limited to the maximum drop size can be used to produce better-conditioned results. The CDS is capable of measuring drops from about $2 \rightarrow 200 \mu\text{m}$ in diameter.

An example of theoretical and measured scattering patterns for polystyrene spheres ranging from $5 \rightarrow 200 \mu\text{m}$ that were suspended in an aqueous solution in the laboratory is shown in Figure 1. The theoretical scattering patterns are exact Mie functions scaled only by the gain of the CDS. The overall agreement in Mie theory and the measured light scattered from the solutions of spheres with known diameters is excellent. The slight discrepancies are most likely due to uncertainties in the actual size distributions of the spheres and the gain function of the CDS. The very strong correlation between theory and measurements in Figure 1 provides a solid

foundation for development of the drop-sizing algorithm. The technique used here to recover drop size distribution from the patterns of scattered light is called the estimate maximize (EM) method. The EM and the EMS (smooth) methods are particularly suited to poorly posed systems of linear equations. In the CDS, the scattered light measurements are used to determine the shape of drop size spectra and LWC separately, then the LWC is used to compute a linear scale factor which gives absolute number concentrations for each drop size bin.

The EM and EMS methods have been commonly used in emission tomography and stereology. (See Latham and Anderssen 1994 for the mathematics and further discussion of applications). However, to our knowledge, this is the first published use of this technique in cloud drop sizing.

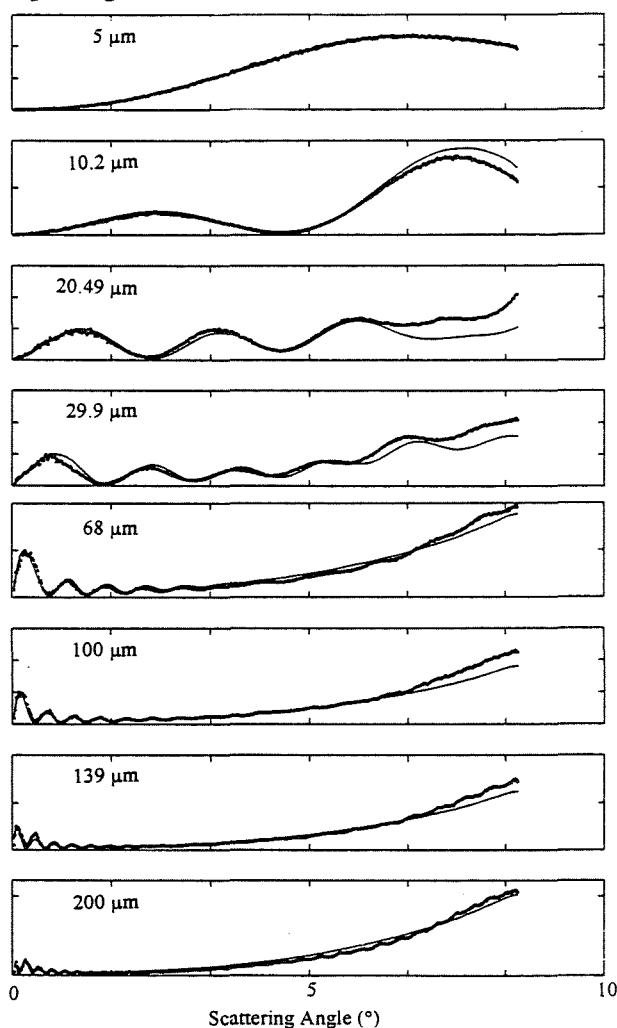


Figure 1. Comparison of Mie theoretical (light line) and CDS measured (heavy line) distributions of light scattered from aqueous solutions of polystyrene spheres.

3. OBSERVATIONS IN ADIABATIC CORES

3.1 Liquid Water Content

The CDS was installed on the C-130 for selected portions of the SCMS field experiment. Data from

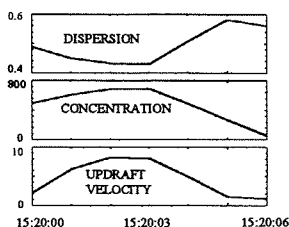


Figure 2. FSSP drop dispersion, concentration and updraft velocity measurements from the air motion system in adiabatic region of cloud on 22 July 1995.

above cloud base on 22 July. Data points at 152002 and 152003 show a region where the (unsaturated) FSSP-100 drop concentration is a maximum and flat, the dispersion is a minimum and flat and there is a relatively flat (8.2 m s^{-1}) peak in updraft velocity. Measurements with this combined pattern are very typical of those found in adiabatic cores in cumulus clouds (see, for example, measurements in Lawson and Cooper 1990).

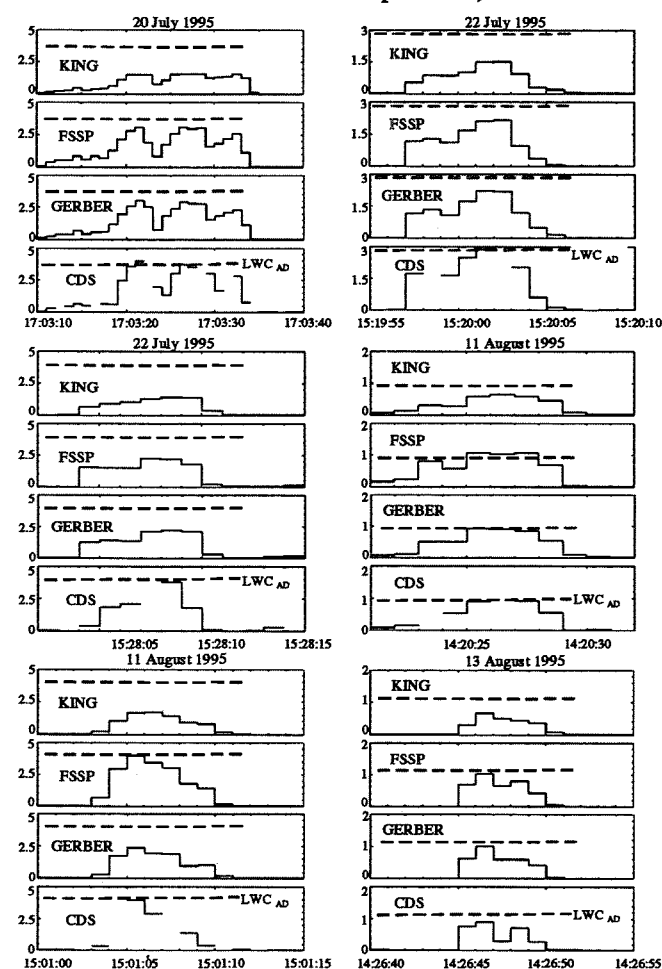


Figure 3. LWC measurements in adiabatic cores. LWC_{AD} is the adiabatic LWC computed from cloud base measurements. For 20 July: $P_{BASE}=905 \text{ mb}$, $T_{BASE}=22^\circ\text{C}$, $P_{OBS}=730 \text{ mb}$; 22 July (1520): $P_{BASE}=942$, $T_{BASE}=23$, $P_{OBS}=816$; (1528) $P_{OBS}=760$; 11 August (1420): $P_{BASE}=950$, $T_{BASE}=23$, $P_{OBS}=912$; 11 August (1501): $P_{BASE}=942$, $T_{BASE}=23$, $P_{OBS}=754$; 13 August: $P_{BASE}=960$, $T_{BASE}=23$, $P_{OBS}=912$. The missing CDS data are due to dropouts in the data acquisition system.

Figure 3 shows observations of LWC and the corresponding adiabatic values for cloud penetrations on 20 and 22 July, 11 and 13 August where the pattern of the measurements were similar to those shown in Figure 2. The LWC corresponding to adiabatic ascent was computed from cloud base pressure and temperature measurements made by the Wyoming King Air on 20 and 22 July and from earlier C-130 measurements at cloud base on the other days. In Figure 3, the CDS LWC measurements are very close to the adiabatic values at all elevations. The Gerber and FSSP LWC measurements also agree well with the adiabatic value 50 mb (~0.5 km) above cloud base. As distance above cloud base increases, however, the Gerber probe appears to proportionately underestimate the adiabatic LWC. The FSSP, corrected for activity (Baumgardner, personal communication), also tends to underestimate adiabatic LWC higher in the cloud except for the 11 August cloud pass at 1501. The King LWC measurements are significantly sub-adiabatic at all elevations above cloud base.

3.2 Drop Size Distribution

The cloud penetrations about 0.5 km above cloud base on 11 and 13 August shown in Figure 3 are of particular interest for studies of the condensational growth of cloud drops. Fitzgerald (1972) showed that theoretical calculations and measurements of drop size spectra near cloud base are very narrow. However, Cerni (1983) and others have found that instrumentation limitations of the FSSP typically broaden the measured drop size spectra.

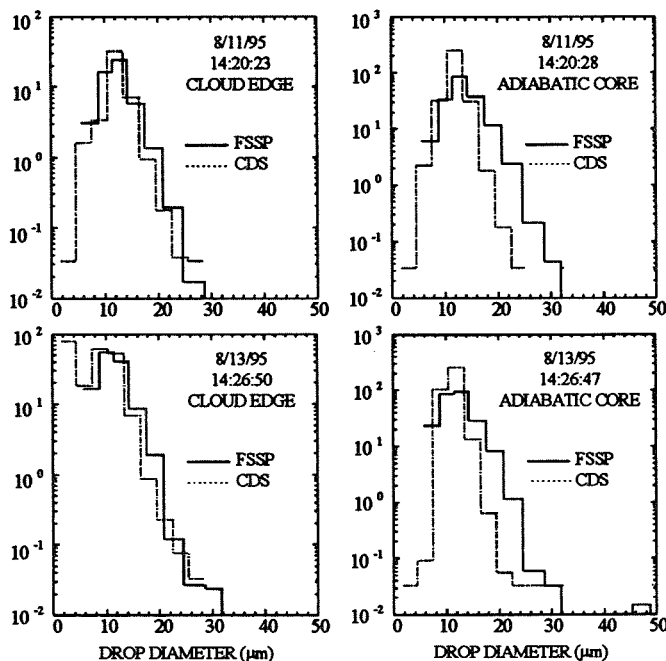


Figure 4. FSSP and CDS measurements 0.5 km above cloud base at edges and in adiabatic regions of cloud.

Figure 4 shows FSSP and CDS measurements of drop size taken 50 mb above cloud base at the edges and in the adiabatic cores of the 11 and 13 August clouds. The FSSP

has fifteen equal size bins with the first bin centered at 3 μm . For the data presented here, the CDS measurements of scattered light were solved using the EM algorithm for 33 equal size bins with the first bin centered at 3 μm . The general agreement between drop size spectra measured by the CDS and FSSP is very good. The FSSP drop spectra, however, is almost always broader than the CDS (with the exception of measurements in the smallest size bin near the edge of cloud). In the adiabatic regions shown in Figure 4, the CDS drop spectra is about 6 μm (2 full size bins) narrower than the FSSP. The width of drop size spectra measured 0.5 km above cloud base by the Merlin FFSSP in other clouds was intermediate between the CDS and FSSP measurements.

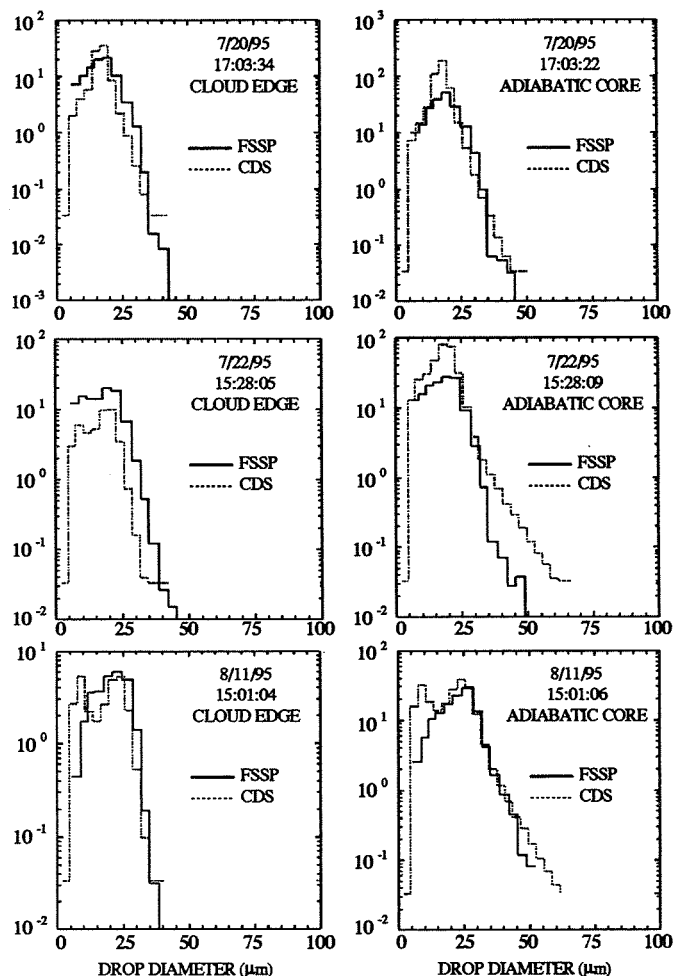


Figure 5. As in Figure 4 except 2 km above cloud base.

Figure 5 shows drop size measurements from the CDS and FSSP¹ probes in three cloud passes with adiabatic cores at about 2 km above cloud base. In all three adiabatic regions shown in Figure 5, when compared with the CDS measurements, the FSSP shows smaller concentrations of large drops. In the 22 July data, FSSP measurements show nearly an order of magnitude fewer drops at 45 μm (the largest size bin of the FSSP-100).

¹ In Figure 5, the first channel of the CDS is set to zero and the first channel of FSSP is not plotted.

The trend is not purely systematic, however, because the CDS spectra is noticeably more narrow than the FSSP near cloud base in adiabatic regions (as shown in Figure 4) and higher in cloud near the edges shown in Figure 5.

4.0 DISCUSSION

The new cloud drop spectrometer (CDS) reliably measured the adiabatic value of LWC 0.5, 1 and 2 km above cloud base in undiluted updraft cores in small Florida cumuli. The FSSP-100 and Gerber PVM-100 were in good agreement with adiabatic LWC 0.5 km above cloud base, but generally underestimated (by about 20 - 40%) the adiabatic LWC at 1 and 2 km above cloud base. Underestimates by the Gerber instrument appeared to be systematic while the FSSP did measure the adiabatic value of 4 g m^{-3} at 1501 on 11 August. The King hot-wire device typically measured sub-adiabatic values at all elevations in the clouds.

The CDS drop size distribution in adiabatic cores at 0.5 km above cloud base was about $6 \text{ }\mu\text{m}$ narrower than the FSSP. The validity of the CDS drop size measurements are strengthened by: 1) condensational drop growth theory predicts very narrow drop size spectra near cloud base (Fitzgerald 1972) and 2) the FSSP is known to artificially broaden the drop size distribution (Cerni 1983).

The drop size distribution in the higher regions of these clouds often had "tails" which were much larger than predicted by condensational growth theory. The CDS showed about an order of magnitude more $45 \text{ }\mu\text{m}$ diameter drops than the FSSP in one adiabatic updraft core about 2 km above cloud base. While no explanation is offered for the existence of the large tails in adiabatic regions, the combination of very high (up to 4 g m^{-3}) LWC and the broadened drop size distribution in adiabatic cores provide a strong catalyst for the very early development of coalescence and the rapid development of warm rain.

Acknowledgments. The authors wish to thank the NCAR Research Flight Facility. We are indebted to Dr. Darrel Baumgardner of NCAR and Rick Igau of Texas A&M for valuable support during the field project. We also wish to thank Dr. Jean-Louis Brenguier for making available FFSSP measurements.

5.0 REFERENCES

- Bachalo, W. D. and M. J. Houser, 1984: Phase/Doppler spray analyzer for simultaneous measurements of drop size and velocity distributions. *Optical Eng.*, **23**, 583-590.
- Baumgardner, D., W. Strapp, and J. E. Dye, 1985: Evaluation of the forward scattering spectrometer probe. Part II: Corrections for coincidence and dead-time losses. *J. Atmos. Oceanic Technol.*, **2**, 626-632.
- Blyth, A. M., A. M. I. Chittenden, and J. Latham, 1984: An optical device for the measurement of liquid water content in clouds. *Quart. J. Roy. Meteor. Soc.*, **110**, 53-63.
- Brenguier, J.-L., D. Trevarin, R. Peytavi, and P. Wechsler, 1993: New electronics for FSSP: The fast FSSP. *J. Atmos. and Oceanic Tech.*, **10**, 27-33.
- Cerni, T. A. 1983: Determination of the size and concentration of cloud drops with an FSSP. *J. Clim. & Appl. Meteorol.*, **22**, 1346-1355.
- Chin, J. H., C. M. Sliepcevich and M. Tribus, 1955: Particle size distributions from angular variation of forward-scattered light at very small angles. *J. Phys. Chem.*, **59**, 841-844.
- Chittenden, A. M. I., 1976: The determination of cloud droplet size distributions by light scattering. Ph.D. dissertation, University of Manchester, England.
- Fitzgerald, J. W., 1972: A study of the initial phase of cloud droplet growth by condensation. Ph.D. thesis, University of Chicago.
- Gerber, H., B. G. Arends, and A. S. Ackerman, 1994: New microphysics sensor for aircraft use. *Atmos. Res.*, **31**, 235-252.
- King, W. D., D. A. Parkin, and R. J. Handsworth, 1978: A hot wire liquid water device having fully calculable response characteristics. *J. Appl. Meteor.*, **17**, 1809-1813.
- Knight, C. A., and L. J. Miller, 1993: First radar echoes from cumulus clouds. *Bull. Amer. Meteor. Soc.*, **74**, 179-188.
- Knollenberg, R. G., 1981: Techniques for probing cloud microstructure. In: *Clouds, Their Formation Optical Properties and Effects*. Eds: P. V. Hobbs and A. Deepak. Academic Press, New York. 15-92.
- Latham, G. A., and R. S. Anderssen, 1994: On the stabilization inherent in the EMS algorithm. *Inverse Problems*, **10**, 161-183.
- Lawson, R. P., and W. A. Cooper, 1990: Performance of some airborne thermometers in clouds. *J. Atmos. Oceanic Technol.*, **7**, 480-494.
- Lawson, R. P. and R. H. Cormack, 1995: Theoretical design and preliminary tests of two new particle spectrometers for cloud microphysics research. *Atmos. Res.*, **35**, 315-348.
- Riley, J. B. and Y. C. Agrawal, 1991: Sampling and inversion of data in diffraction particle sizing. *Appl. Optics*, **30**, 4800-4817.

OBSERVED STRUCTURE AND MICROPHYSICS OF SHALLOW TROPICAL CLOUDS

Robert M. Rauber¹, Marcin J. Szumowski^{1,2}, and Harry T. Ochs III^{1,2}

¹ Department of Atmospheric Sciences, University of Illinois, Urbana, IL

² Illinois State Water Survey, Champaign, IL

1. INTRODUCTION

The Hawaiian Rainband Project (HaRP), conducted in July and August of 1990, employed aircraft, radar, surface and upper air measurements to investigate the formation, and dynamical and microphysical structure of rainbands offshore of the Big Island. One goal of HaRP was to study the warm rain process by relating the microphysical evolution of these rainbands to their dynamical structure. HaRP employed the 5 cm wavelength National Center for Atmospheric Research (NCAR) CP3 and CP4 Doppler radar systems as well as the NCAR Electra aircraft. This paper focuses on the evolution of the structure and kinematics of hawaiian rainbands in relation to their microphysical structure.

2. RAINBAND CHARACTERISTICS

Typical characteristics of the Hawaiian rainbands and their environment include: 1) a 300 to 400 m deep mixed surface layer; 2) a Lifting Condensation Level near 600-700 m; 3) cloud depth between 1.5 and 3.5 km, with clouds top temperatures $> 5^{\circ}\text{C}$; 4) an isothermal layer or an inversion, with base between 2 and 4 km and a dry layer above, that limits vertical development of convection; 5) a conditionally unstable environment within the marine layer below the inversion. Typical CAPE calculated in the three cases ranged from 35 and 100 J/kg allowing for maximum (adiabatic) updrafts between 8.6 and 14.0 ms^{-1} . In general, the vertical wind shear was generally less than 2 $\text{ms}^{-1} \text{ km}^{-1}$ and the airflow in the convective updrafts was nearly vertical. The outflow just below the inversion was nearly symmetric.

Rainbands were the typical organization of precipitation upstream of the island. Rainbands first appeared on radar as continuous lines of low reflectivity with embedded cells of higher reflectivity, or as lines of cells separated by echo free regions. The higher reflectivity cells were always associated with the strongest updrafts. The capping effect of the inversion led to locally strong outflow regions centered above the strongest updrafts. The strong outflow just below the inversion led to the formation of a radar echo overhang surrounding the cells (Fig. 1). With time, the base of

the overhang descended to the surface, leading to an overall increase in the width of the rainband. Typically, the strongest updrafts, and highest reflectivities, occurred early in the development of the rainband as the band organized and intensified. As the band approached shore, updrafts spread laterally and weakened, producing more continuous lines of more uniform precipitation. High reflectivity cores were much less common in the latter part of rainbands' life cycles.

Reflectivities exceeding 50 dBZ were associated with the strongest updraft regions. Peak reflectivities exceeded 60 dBZ in each of the three cases. The horizontal dimensions of these high reflectivity cores were typically 1-2 km. They occupied a small volume fraction of the entire precipitating rainband. A typical lifetime of an individual high reflectivity core was about 10-15 minutes. Reflectivities > 50 dBZ typically formed in the middle or upper part of the cloud, then expanded to occupy most of cloud depth, and finally collapsed as the updraft weakened. All high reflectivity cores could be associated with updraft cores. A local updraft core developed approximately 10 minutes prior to the appearance of the corresponding high reflectivity core. Generally reflectivities between 20-35 dBZ were observed between 1 and 2.5 km above the ocean surface when the local updraft maximum first appeared. The updraft reached peak intensity approximately 5 minutes before the development of the high reflectivity core, and remained close to its peak speed until the core first appeared. The peak updraft always preceded the appearance of peak reflectivities. High reflectivity cores generally first appeared in the middle or upper part of the cloud, depending on the magnitude of the peak updraft. The high reflectivity core expanded horizontally and vertically in the minutes following the formation, reaching its peak intensity as the updraft weakened. The locally strong updraft subsequently disappeared as the high reflectivity core collapsed to the surface. The dissipating stage of a high reflectivity core typically lasted about five minutes. The magnitude of the peak reflectivity in a high reflectivity core was not necessarily proportional to the magnitude of the peak updraft. Despite the range of peak updraft speeds (4.5 to 8.8 ms^{-1}), the peak reflectivities in three cases were very similar, ranging from 60.2 to 62.7 dBZ.

3. MICROPHYSICAL IMPLICATIONS

The evolution of the vertical motion and corresponding reflectivity fields in these clouds allowed us to make inferences concerning the formation and evolution of both the larger raindrops which comprise high reflectivity regions, and the smaller raindrops which occupy weaker reflectivity areas. The evolution of those fields suggests that growing raindrops present near the top of the rising cloud turrets remain suspended in the strengthening, nearly vertical updrafts as the cloud depth increased. As a result, the higher reflectivity first appeared in the middle part of the cloud shortly after the cloud reached its maximum height and vertical velocity. As the updraft reached its peak intensity large raindrop formation continued higher in the cloud for a period of several minutes. During this time, the larger raindrops present in the middle of the cloud fell through cloud base to the surface, while new raindrops, which had formed near cloud top, fell through the strong updraft to cloud middle levels. These raindrops, which were exposed to largest cloud liquid water content, were generally responsible for the extremely high (> 60 dBZ) reflectivities observed in most intense high reflectivity cores. As updrafts weakened, the larger raindrops fell rapidly to the surface, leaving smaller raindrops and drizzle in the previous location of the high reflectivity core. At the same time, smaller raindrops ejected from the primary updraft core near cloud top, also fell to the surface, creating the broad area of weaker reflectivity.

A close correspondence between the shape and location of highest reflectivity and strongest updraft was evident in most cases after the vertical motion field from earlier times had been advected with the mean cell motion to the position of the high reflectivity core. The correspondence between the two implied that the raindrops that eventually grew to the largest sizes and contributed significantly to the magnitude of the reflectivity, began their growth within the strongest updrafts several minutes prior to the development of the highest reflectivities. The lower portion of a high reflectivity core was generally found directly below the location of the strongest updraft advected forward from 7.5 minutes earlier, while the upper portion of a high reflectivity core tended to be located approximately below the location of the strongest updraft advected forward from 2.5 to 5 minutes earlier. The evolution of the reflectivity field suggests that, on average, the mean differential fall speed (mean terminal velocity less the mean updraft speed) of the large raindrops between the time of peak updraft and peak reflectivity was about 4 ms^{-1} . Based on aircraft observations of raindrop concentrations and size spectra in Hawaiian rainbands, raindrops with diameters 4 mm and greater are present in the high reflectivity cores. Raindrop terminal velocities range from 6.5 ms^{-1} for a 2 mm diameter drop to 8.8 ms^{-1} for a 4 mm drop. Cells must maintain updrafts with speeds greater than these terminal

velocities to suspend, or carry upward, raindrops of these sizes.

An increase in the width of the radar echo coverage near the inversion was initially evident in many vertical cross-sections through developing high reflectivity cores. The spreading of the reflectivity pattern below the inversion is related to strong outflow at that location. Transport of raindrops away from the developing cells within the strong outflow just below the inversion led to the formation of the radar echo overhang in the outflow. Smaller raindrops were carried further from the main updraft in the divergent flow, while larger raindrops fell closer to the cell. This led initially to a sloped base of the overhang. As raindrops composing the overhang fell, the base of the overhang descended to the surface, leading to an overall increase in the width of the rainband. Raindrops at the core of the updraft experienced the least lateral force as air diverged at the inversion, and were exposed to the largest (closest to adiabatic) liquid water content. These raindrops, which grew the fastest and were suspended the longest, apparently produced the observed high reflectivities. Based on the radar analyses, 5 to 7.5 minutes typically passed between cell's peak in vertical motion and a corresponding maximum in the reflectivity field. This time lag is consistent with the concept that raindrops grow most rapidly to large sizes when suspended within a region of strong updraft, and then fall out through the cloud as their terminal velocities exceed the updraft speed. Since the outflow at the inversion transports smaller raindrops out of the area where the larger raindrops are growing, it, in effect, reduces the probability of collisions between the largest drops and smaller raindrops, reducing the rate of breakup for the largest raindrops.

4. ACKNOWLEDGEMENTS

We thank everyone at NCAR who contributed to the Hawaiian Rainband Project data acquisition and processing. We also wish to thank L. Jay Miller and Bill Anderson for their assistance with radar data analyses software. Computing time was provided by the NCAR, which is sponsored by the National Science Foundation. This research was sponsored by the NSF under grants NSF ATM 9020245 and NSF ATM 9223165.

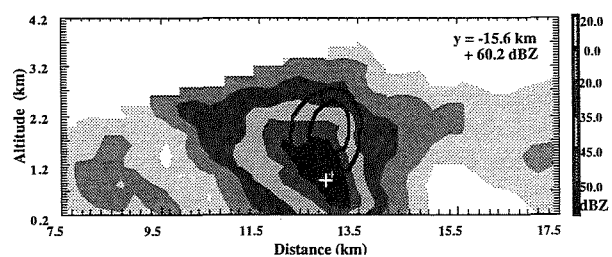


Fig. 1: Example of a developing rainband containing a high reflectivity core and overhang region. Overlaid are the 2.5 and 3.5 ms^{-1} vertical motion contours.

DROPLET SPECTRAL BROADENING IN STRATUS

James G. Hudson and Seong Soo Yum

Atmospheric Sciences Center
Desert Research Institute
University and Community College System of
Nevada, Reno, Nevada

1. INTRODUCTION

Without the ice phase, condensation alone can not produce precipitation. This requires autoconversion, which depends on the relative sizes of the droplets, which depends on the width of the droplet spectrum, which we characterize by the standard deviation of the droplet diameter, σ_d . We present data from three maritime projects: 1) FIRE (First ISCCP Regional Experiment), June and July, 1987 (Albrecht et al. 1988); 2) ASTEX (Atlantic Stratocumulus Transition Experiment), June, 1992 (Albrecht et al. 1995); and 3) SOCEX (Southern Ocean Cloud Experiment), July, 1993.

Measurements were from the PMS forward scattering spectrometer probe (FSSP) and 260X probe. These are discussed by Hudson and Svensson (1995), and Dye and Baumgardner (1984). We distinguish between droplets from the FSSP (2-50 μm) and drops from the 260X (50-620 μm).

2. RESULTS

Figure 1 shows average values of σ_d vs. droplet mean diameter, MD, for the 43 ASTEX soundings.

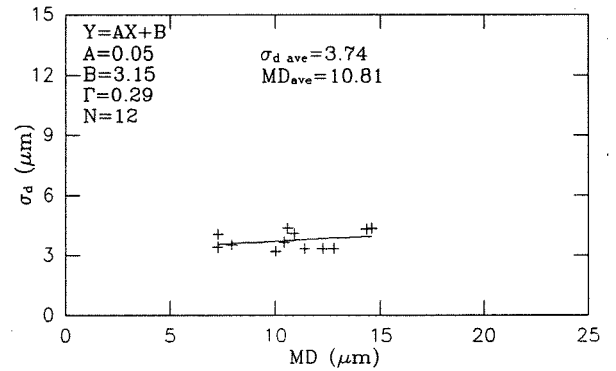
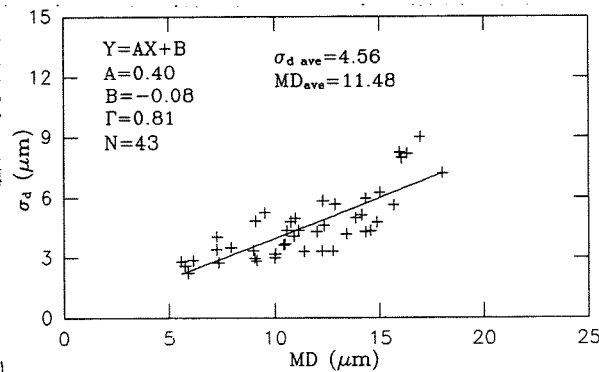


Fig. 2. As Fig. 1 except only for MzL_c in ASTEX.

The soundings were divided on the basis of being monotonic with height, z . These soundings are called MzL_c; the others, which are less adiabatic are called NzL_c. The MzL_c soundings (Fig. 2) show less broadening with MD. Average values of σ_d over 1 μm wide MD bins are plotted for all of the one second data points in Fig. 3. Again MzL_c is flat while σ_d increases with MD for NzL_c.

Figure 4 and Table 1 show that there is less drizzle in the MzL_c and increasing drizzle with MD

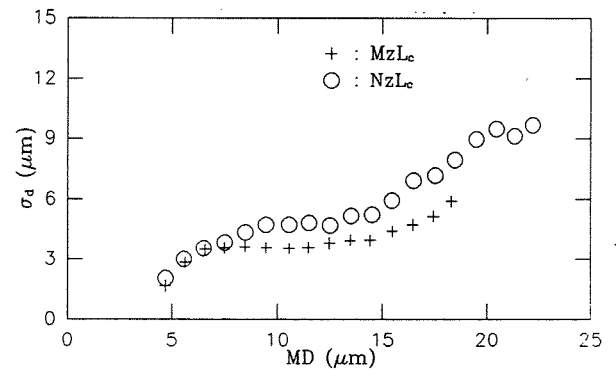


Fig. 3. One μm wide MD bin averages of σ_d for MzL_c and NzL_c in ASTEX.

Table 1. Averages of σ_d and MD for the two cloud LWC soundings for various amounts of drizzle, LWC_d.

ASTEX			
LWC _d [gm/m ³]		σ_d [μ m]	MD [μ m]
MzL _c	0.03	3.9	11.5
NzL _c	LWC _d =0	4.0	9.3
	LWC _d >0	5.5	12.7
	0 <LWC _d <0.02	5.1	11.6
	0.02<LWC _d <0.05	5.0	11.8
	0.05<LWC _d <0.10	5.4	12.8
	0.10<LWC _d <0.30	6.3	14.7
	0.30<LWC _d	7.2	15.3

for NzL_c. This increase happens at the same MD that σ_d increases (Fig. 3).

Data in all three projects show a similar tracking of drizzle and σ_d with MD. These results echo Gerber (1996), who found constant droplet spectral shapes with height in ASTEX for clouds with less than 0.01 g m⁻³ LWC_d and a threshold MD for drizzle (Hudson and Svensson 1995).

Table 1 summarizes the relationship between σ_d and MD for the two LWC profiles in ASTEX; it was similar for FIRE and SOCEX. This shows broader droplet spectra in NzL_c especially for greater amounts of drizzle. The increase in the average σ_d and MD with increased drizzle was apparent in all projects.

3. ADIABATIC THEORY

Figure 5 displays the narrowing of the droplet spectrum with MD for most adiabatic predictions. Table 2 contrasts a clean spectrum with a polluted

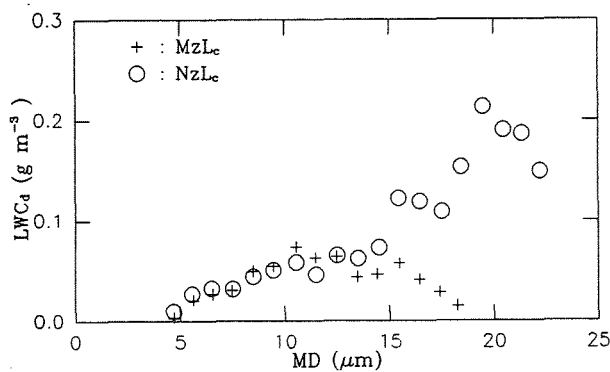


Fig. 4. As Fig. 3 except drizzle liquid water content, LWC_d.

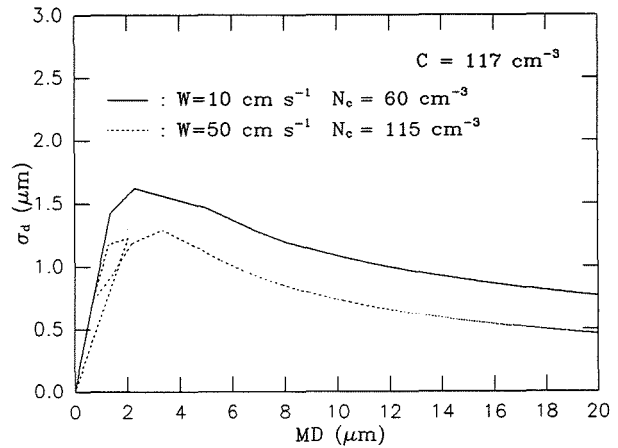


Fig. 5. Standard deviation of the droplet diameters, σ_d , vs. the mean diameter, MD, calculated from a clean CCN spectrum using the model by Robinson (1984).

spectrum. Both CCN spectra were from Hudson and Li (1995); they were typical of the clean and polluted CCN in ASTEX. The lower updraft velocities, W,

Table 2. Characteristics of droplet spectra predicted for two CCN spectra and two W and a mixture of parcels with these two W. N_c is the concentration of activated cloud droplets.

	C=117, high k	C=669, low k
	N_c	N_c
W = 10 cm/s	60	195
σ_d & slope @ MD = 10 μ m	1.04	2.2
σ_d & slope @ MD = 20 μ m	0.8	2.9
W = 50 cm/s	115	504
σ_d & slope @ MD = 10 μ m	0.72	1.4
σ_d & slope @ MD = 20 μ m	0.48	1.2
W is 50-50 mix of 10 & 50 cm/s parcels	88	350
σ_d & slope @ MD = 10 μ m	1.6	2.4
σ_d & slope @ MD = 20 μ m	2.6	4.0

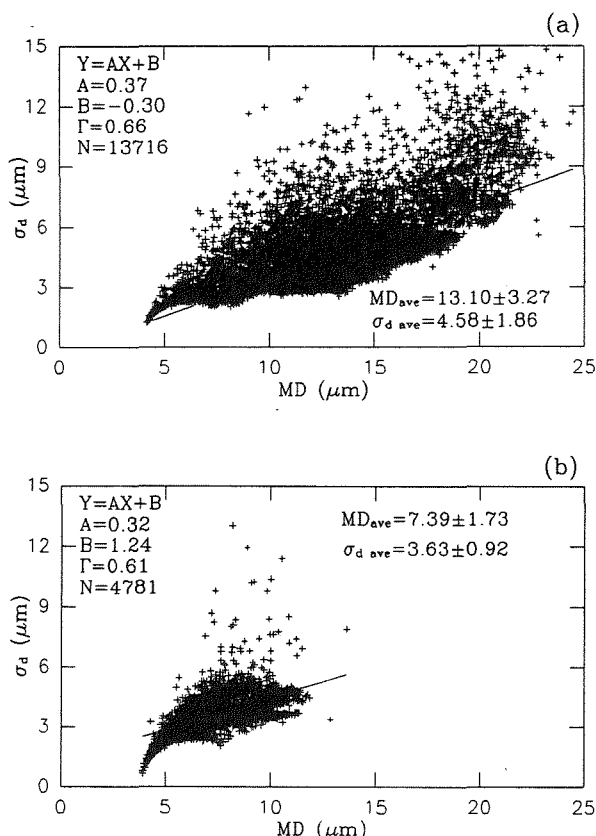


Fig. 6. As Fig.1 except that all of the one second data points are shown for clean(a) and polluted(b) clouds in ASTEX.

produced lower cloud droplet concentrations, N_c , and higher σ_d as shown by Srivastava (1991). On the other hand for both W the polluted CCN spectra result in higher σ_d in spite of the higher N_c . The polluted spectra also show less narrowing of the droplet spectra with increasing MD. Broader spectra for higher N_c is contrary to observations of lower σ_d in polluted air (e.g. Alkezweeny et al. 1993; Hudson and Li 1995).

The polluted and clean CCN spectra differed not only in concentration, C (@ 1% S_c) but also in shape-- k . The clean spectrum had a higher k (Hudson and Li 1995). We sorted out the relative contributions of C and k by constructing artificial CCN spectra. The

Table 3. Average values of various parameters for the clean and polluted clouds in ASTEX.

ASTEX, horizontal					
	N_c [#cm ⁻³]	MD [μm]	σ_d [μm]	LWC _c [gm/m ³]	LWC _d [gm/m ³]
clean	97±55	13.1	4.58	0.18	0.06
pollut	208±116	7.4	3.63	0.10	0.02

results showed that higher C and lower k make larger σ_d and less narrowing with MD.

None of these predicted adiabatic spectra have as high a σ_d as were actually measured (e.g. Fitzgerald 1972). However, some of the observed σ_d is composed of instrumental broadening (Cerni 1983; Politovich 1993), which amounts to 2-4 μm.

4. CLEAN vs. POLLUTED OBSERVATIONS

N_c was higher and MD and σ_d were lower in the polluted clouds than in the clean clouds of ASTEX (Table 3). Figure 6 shows σ_d vs. MD for all one second data points for ASTEX clean and polluted clouds. The clean clouds had a larger σ_d than polluted clouds in agreement with Alkezweeny et al. (1993) and Hudson and Li (1995). However, when equal size ranges are considered--6 to 11 μm MD and 1 μm wide bins are used--the average σ_d is 3.56 μm for the clean and 4.01 μm for the polluted.

5. MIXING

Hudson and Svensson (1995) suggested that droplet spectra can be broadened by internal mixing among parcels with different cloud base W , which activate different proportions of the CCN spectrum. Lower W produce lower N_c , which results in larger MD. If the parcels remain somewhat distinct while the droplets grow and then mix together they will display larger σ_d (Cooper 1989). This is displayed in Fig. 7 and the last panel of Table 2, which represents a 50-50 mixture of the two updrafts--10 and 50 cm/s.

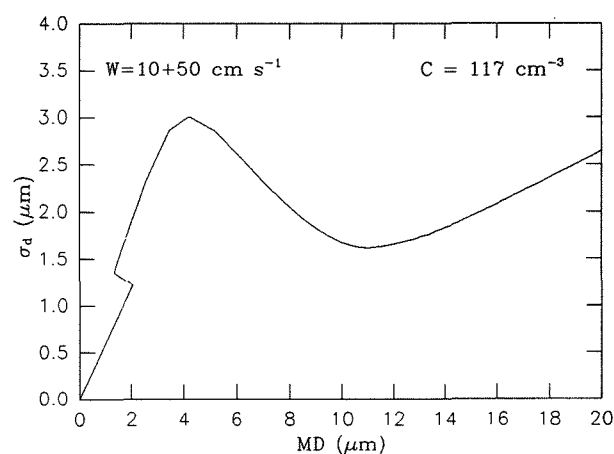


Fig. 7. As Fig. 5 except for a 50-50 mixture of the two parcels considered in Table 2.

Internal mixing causes more broadening for higher k because of the greater differences in concentration with S_c , which results in more variability in N_c for the same range of W . But the most important difference is that internal mixing makes an increasing σ_d with MD especially with a higher k CCN spectrum.

6. CONCLUSIONS

- 1) σ_d does not always increase with MD.
- 2) σ_d is susceptible to both the C and k of the CCN spectrum. The concentration of low S_c CCN is the most important factor for σ_d .
- 3) Polluted clouds have smaller σ_d mainly because they have smaller MD.
- 4) Polluted clouds have larger σ_d for over an equal small MD range.
- 5) σ_d can be increased by internal mixing of cloud parcels.

ACKNOWLEDGMENTS

Support came from NASA Grants NAG-1-1113 and NAGW-3753, DOE Grants DE-FG08-90ER61012 and DE-FG03-93ER61647, and ONR Grant N00014-91-J-1090.

REFERENCES

- Albrecht, B.A., D.A. Randall, and S. Nicholls, 1988: Observations of marine stratocumulus during FIRE. *Bull. Amer. Meteor. Soc.*, **69**, 618-626.
- Albrecht, B.A., C.S. Bretherton, D. Johnson, W.H. Schubert, and A.S. Frisch, 1995: The Atlantic Stratocumulus Transition Experiment--ASTEX. *Bull. Amer. Meteor. Soc.*, **76**, 889-904.
- Alkezweeny, A.J., D.A. Burrows, and C.A. Grainger, 1993: Measurements of cloud-droplet-size distributions in polluted and unpolluted stratiform clouds. *J. Appl. Meteorol.*, **32**, 106-115.
- Cerni, T.A., 1983: Determination of the size and concentration of cloud drops with an FSSP. *J. Climat. and Appl. Meteorol.*, **22**, 1346-1355.
- Cooper, W.A., 1989: Effects of variable droplet growth histories on droplet size distributions. Part I: Theory. *J. of Atmos. Sci.*, **46**, 1301-1311.
- Dye, J.E., and D. Baumgardner, 1984: Evaluation of the Forward Scattering Spectrometer Probe. Part I: Electronic and optical studies. *J. Atmos. Ocean. Technol.*, **1**, 329-344.
- Fitzgerald, J.W., 1972: A study of the initial phase of cloud droplet growth by condensation: Comparison between theory and observation. Dissertation for Ph.D. in Geophysical Sciences. University of Chicago, published as Tech. Note 44 of the University of Chicago, Cloud Physics Laboratory, June 1972.
- Gerber, H., 1996: Microphysics of marine stratocumulus clouds with two drizzle modes. *J. Atmos. Sci.* in press.
- Hudson, J.G., and G. Svensson, 1995: Cloud microphysical relationships in California marine stratus. *J. Appl. Meteorol.*, **34**, 2655-2666.
- Hudson, J.G., and H. Li, 1995: Microphysical contrasts in Atlantic stratus. *J. Atmos. Sci.*, **52**, 3031-3040.
- Politovich, M.K., 1993: A study of the broadening of droplet size distributions in cumuli. *J. Atmos. Sci.*, **50**, 2230-2244.
- Robinson, N.F., 1984: The efficient numerical calculation of condensational cloud drop growth. *J. Atmos. Sci.*, **41**, 697-700.
- Srivastava, R. C., 1991: Growth of cloud drop by condensation: effect of surface tension on the dispersion of drop sizes. *J. Atmos. Sci.*, **48**, 1596-1605.

FREEZING DRIZZLE FORMATION MECHANISMS

G.A. Isaac, A. Korolev, J.W. Strapp, S.G. Cober, A. Tremblay
Cloud Physics Research Division
Atmospheric Environment Service
Downsview, Ontario, Canada, M3H 5T4

and

R.A. Stuart
Weather Research House
Willowdale, Ontario, Canada, M2N 2V9

1. INTRODUCTION

Freezing drizzle occurs infrequently, but often enough to cause problems. For example, hazardous road conditions can result, power lines can accumulate large amounts of ice, and aircraft performance can be affected while in-flight, during landing, or while preparing to take-off. The Canadian Freezing Drizzle Experiment was conducted during March 1995 out of St. John's, Newfoundland to determine the mechanisms whereby freezing drizzle occurs, to document the characteristics of freezing drizzle, and to develop better methods for forecasting freezing drizzle. This paper will discuss the mechanisms of drizzle formation. Other papers at this conference will discuss the characterization of the icing environment (Cober et al. 1996), the forecasting problems (Tremblay et al. 1996), and instrumentation problems related to measuring cloud microphysics associated with freezing drizzle (Korolev et al. 1996 and Lawson et al. 1996).

2. CLIMATOLOGY

A climatology of freezing precipitation across North America has been produced showing maxima in terms of occurrence near the Great Lakes and over Newfoundland. The maximum frequency of occurrence reaches 150 hours of freezing precipitation (drizzle and rain) and 110 hours of freezing drizzle per year in eastern Newfoundland. Fig. 1 shows the percentage of hours with freezing precipitation in Atlantic Canada during March. It is clear that there are large variations over short distances in Newfoundland, strongly suggesting mesoscale influences on formation mechanisms.

The occurrence of freezing precipitation is also strongly dependent on local wind direction. Freezing rain occurs at St. John's over 7 per cent of the time with wind directions from the southeast, and freezing drizzle occurs over 9 per cent of the time with wind directions from the

east. In contrast, when winds are from the west, the most frequently occurring direction, the frequency of occurrence is less than 0.5%.

For stations around Hudson's Bay, there are strong maxima in April and June when winds are off the ice over the Bay. The forecasters at St. John's have correlated the occurrence of freezing drizzle with winds from northeasterly directions off the sea ice. This appears to agree with the analysis around Hudson's Bay. Perhaps the appropriate boundary layer conditions are generated with winds from this direction. Cloud formation could also be enhanced by lifting as the air reaches the shoreline. There

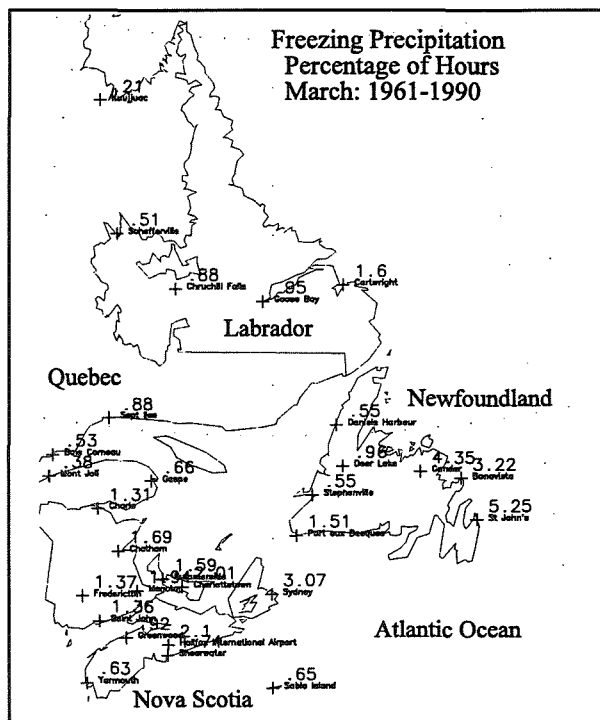


Fig. 1: Climatology of freezing precipitation (drizzle and rain) during March for Atlantic Canada.

is also the possibility of isobaric cooling which could generate long lifetimes for stratus with winds from this direction.

3. CLASSICAL VERSUS NON-CLASSICAL

Fig. 2 shows the frequency of occurrence of freezing rain and drizzle as a function of surface temperature and maximum upper air temperature for St. John's. Approximately 15% of the freezing rain events, and 60% of the freezing drizzle events have no warm tongue aloft with temperatures warmer than 0°C. An analysis of the individual temperature profiles also shows that many of the freezing precipitation events that occurred with a warm layer aloft formed in cloud that was entirely at temperatures colder than 0°C.

The classical mechanism for formation of freezing precipitation is through ice crystals or snow flakes falling into a warm layer, melting, and then supercooling in a colder layer near the surface. This mechanism has been described in detail by Stewart (1992). However, it appears that a considerable fraction of freezing precipitation forms entirely at temperatures colder than 0°C. Although similar observations have been made in other studies (e.g. Huffman and Norman 1988), the non-classical mechanism has never received full recognition.

4. FORMATION MECHANISMS FOR NON-CLASSICAL

There are very few studies which have attempted to explain the occurrence of drizzle which forms entirely at temperatures below 0°C. Besides having the right dynamical situations, which might be very specific as indicated in Fig. 1, there must be suitable microphysical conditions for the formation of large droplets. Some possible mechanisms are suggested as follows:

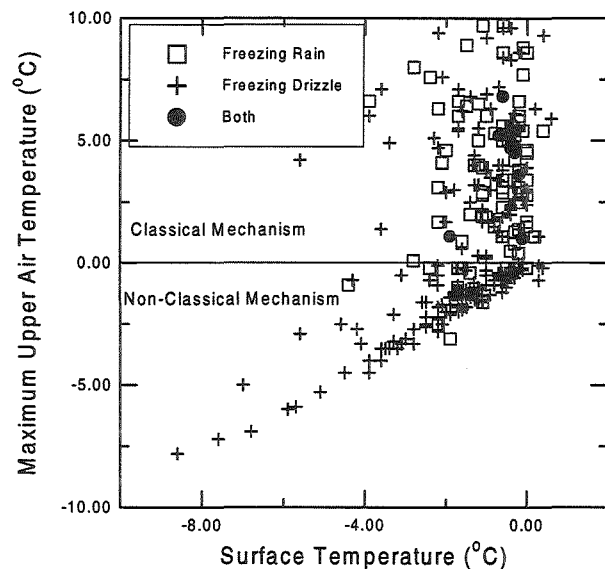


Fig. 2: Frequency of occurrence of freezing precipitation as a function of surface temperature and maximum upper air temperature.

a.) Giant Aerosol might accelerate the formation of freezing drizzle by creating a critical number of large droplets.

b.) Wind Shear might lead to entrainment and inhomogeneous mixing near the top of a stratiform cloud, which could generate large drops. This mechanism was recently proposed by Pobanz et al. (1995) as explaining many events which were qualitatively identified as possibly containing large droplets.

c.) Long Droplet Lifetimes in stratiform clouds, might be a sufficient explanation of the generation of large droplets. Mazin (1963) discussed the question of droplet lifetimes in stratiform clouds. Some droplets, driven by turbulent vertical fluctuations, might undergo several cycles of ascents and descents, and these fluctuations can promote the growth of larger drops (Korolev 1995).

d.) High Supersaturations can generate large droplets (50-100 μm) in a relatively short time. Zones of high supersaturations can arise in layers with temperature inversions which are frequently observed near the tops of stratiform clouds. A turbulent parcel may ascend or descend some distance before mixing with the cloud environment. The turbulence needed to drive the cloud parcel up and down may be generated by wind shear. If the vertical motion occurs without mixing, the temperature inside the parcel will change along the wet adiabat. In the presence of an inversion, the vertical displacement of a cloud parcel will lead to a difference in temperature between the environment and the parcel (Fig. 3). The mixing of two saturated parcels having different temperatures results in a higher supersaturation than in either of these parcels. Fig. 4 shows that, depending on the temperature difference, the supersaturation may reach several percent. With $S=2\%$, Fig. 5 shows that droplets of 50 μm can grow in 5 min. This time may be accumulated by a droplet during several ascents or descents. The probability of such an event is not high, but may be enough to explain the concentrations of drizzle observed.

These mechanisms are being examined through the use of data from the Canadian Freezing Drizzle Experiment. Illustrations of the generation of freezing

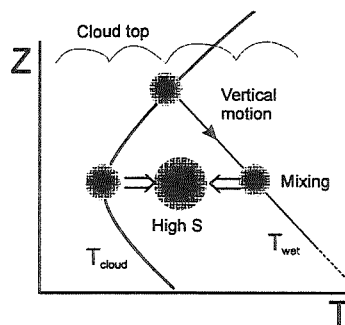


Fig. 3: Formation zones of high supersaturation in the presence of temperature inversions.

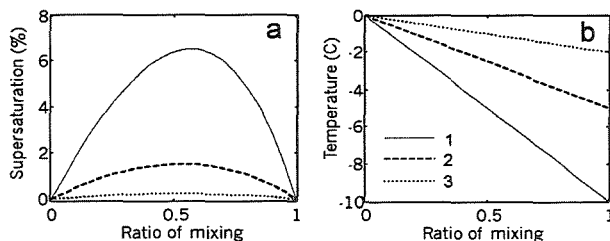


Fig. 4: Supersaturation (a) and temperature (b) resulting from mixing two parcels with initial temperatures (1) $T = 0$ and -10°C , (2) $T = 0$ and -5°C and (3) $T = 0$ and -2°C . Both parcels were initially saturated.

precipitation entirely by droplet condensation/coalescence have been provided by other authors such as: Cober et al. (1995a,b), Rasmussen et al. (1995), and Vali et al. (1995).

Clearly, none of the above mechanisms can be successfully included in a numerical weather prediction model unless a mixed phase cloud scheme is at least considered (e.g. Tremblay et al. 1996).

5. CASE STUDY OF 9 MARCH 1995

The NRC Convair-580 flew north of St. John's, Newfoundland, on 9 March 1995 sampling in freezing precipitation on the north side of a warm front situated near 0°C with a substantial surface wind shift. Fig. 6 shows one of the profiles done to 2500m from 18:34 to 18:52 GMT which clearly shows the warm layer just above freezing near 2000m while the surface temperatures were near -10°C . Another profile was made to 6000m 30 minutes later showing the cloud was topped by a thin layer at 2800m not shown in Fig. 6. No ice was found in any of these clouds. The difference shown between the Nevzorov total water probe and the liquid water probe in Fig. 6 clearly indicates the presence of freezing drizzle (see Korolev et al. 1996). The PMS 2D images showed droplets up to $800\text{ }\mu\text{m}$, with many circular images greater than $200\text{ }\mu\text{m}$ (Fig. 7). Average (120 s) spectra from the profile of Fig. 6, obtained using the method of Cober et al. (1996), are shown in Fig. 8. The cloud droplet concentrations were typically 100 cm^{-3} , the total water contents reached 0.3 g m^{-3} and the droplet concentration greater than $200\text{ }\mu\text{m}$ was typically greater than 4 l^{-1} between 1825 to 1840 GMT.

Freezing drizzle was formed in this case by a non-classical mechanism, in the presence of significant wind shear.

6. SUMMARY

During the March 1995 field project, there were flights on 4 days with classical freezing precipitation and 7 days with non-classical freezing precipitation. All days with classical freezing precipitation had significant wind shear, while there were 2 days with little or no shear

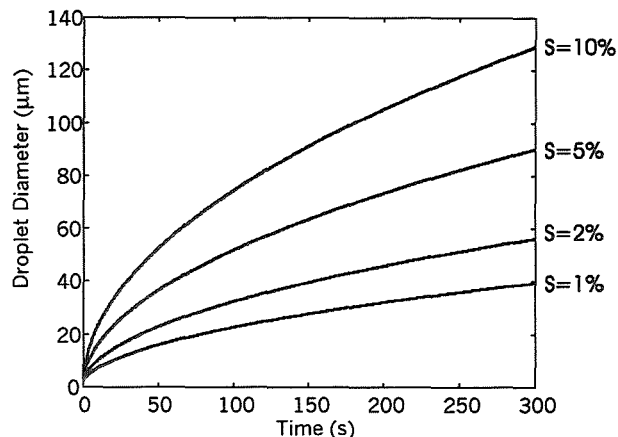


Fig. 5: Droplet growth by condensation at different supersaturations.

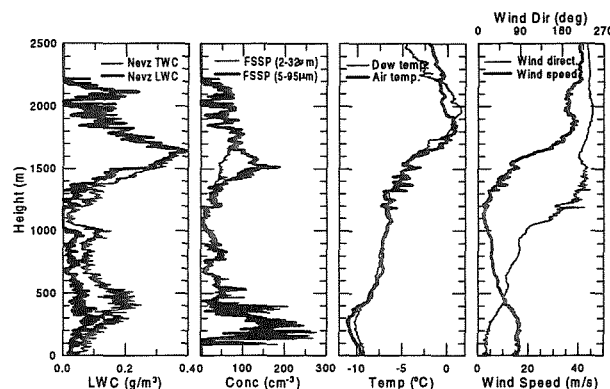


Fig. 6: Profile from March 9, 1995

during non-classical freezing precipitation. Most of the events appeared to have inversions near cloud top. For both classical and non-classical events, the cloud droplet size number concentration for 5 minute averages varied from low values ($< 20\text{ cm}^{-3}$) to values greater than 250 cm^{-3} . Although most events occurred with northeasterly to southeasterly winds, consistent with the climatology, there were examples of non-classical events with westerly to southwesterly winds. There were many examples where the freezing drizzle appeared to originate at cloud top, but others indicated drizzle formation further within the cloud deck. On one occasion, non-classical freezing drizzle drops up to $150\text{ }\mu\text{m}$ formed in a shallow deck less than 300 m thick.

In short, there does not appear to be one mechanism for producing freezing drizzle near St. John's, Newfoundland. There is a distinct correlation between easterly winds and the occurrence of drizzle, suggestive of a mesoscale dynamical influence. In addition, most events appear to have inversions and wind shear near cloud top which would favour large droplet formation.

7. ACKNOWLEDGMENTS

This work received funding from the Canadian National Search and Rescue Secretariat, and Transport

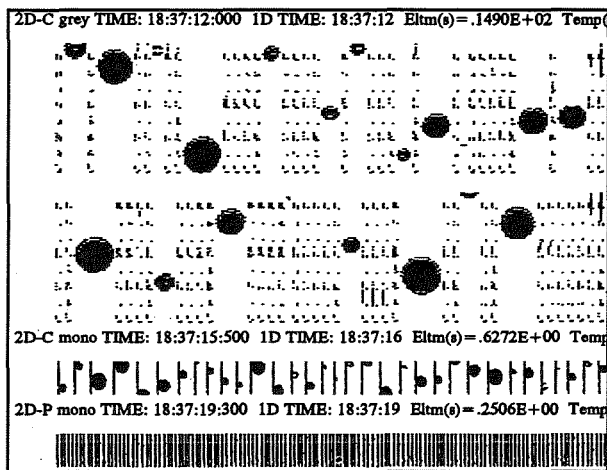


Fig. 7: PMS 2D images at 18:37 GMT from the 2D grey, 2D-C and 2D-P probes.

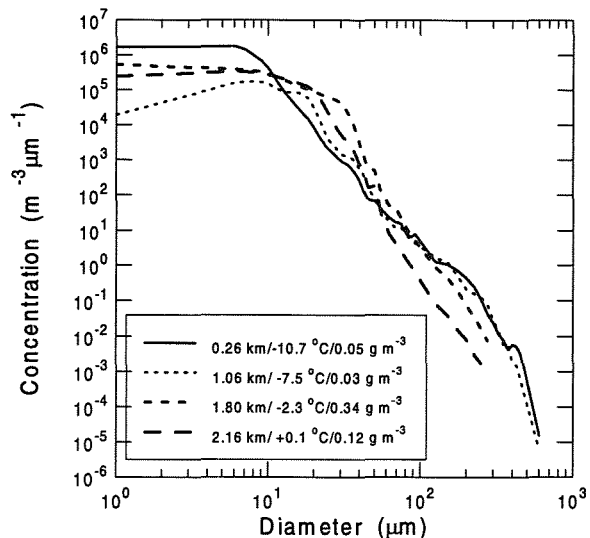


Fig. 8: Particle spectra obtained during the profile of Fig. 6 on 9 March 1995.

Canada. The Canadian Freezing Drizzle Project was jointly conducted by the Atmospheric Environment Service (AES) and the Institute for Aerospace Research of the National Research Council of Canada (NRC). The authors would like to especially thank David Marcotte of NRC and the many technicians of AES/NRC for their invaluable assistance.

8. REFERENCES

- Cober, S.G., J.W. Strapp and G.A. Isaac, 1995a: A case study of freezing drizzle formed through a condensation coalescence process. AMS Conf. Cloud Physics, Dallas, Texas, 286-291.
- Cober, S.G., G.A. Isaac and J.W. Strapp, 1995b: Aircraft icing measurements in east coast storms. *J. Appl. Meteor.*, 34, 88-100.
- Cober, S.G., G.A. Isaac and J.W. Strapp, 1996: Aircraft icing from supercooled drizzle. Proceedings of 12th Intl. Conf. Clouds and Precipitation.
- Hudson, J.G. and C.F. Rogers, 1986: Relationship between critical supersaturation and cloud droplet size: Implications for cloud mixing processes. *J. Atmos. Sci.*, 43, 2341-2359.
- Huffman, G.J. and G.A. Norman, Jr., 1988: The supercooled warm rain process and specification of freezing precipitation. *Mon. Wea. Rev.*, 116, 2172-2182.
- Korolev, A.V., J.W. Strapp and A.N. Nevzorov, 1996: On the accuracy of Nevzorov airborne hot wire LWC/TWC probe. Proceedings of 12th Intl. Conf. Clouds and Precipitation.
- Korolev, A.V., 1995: The influence of supersaturation fluctuations on droplet size spectra formation. *J. Atmos. Sci.*, 52, 3620-3634.
- Lawson, R.P., T. Huang, G.A. Isaac, J.W. Strapp and S.G. Cober, 1996: Improved airborne measurements of the drop-size distribution in freezing drizzle. Proceedings of 12th Intl. Conf. Clouds and Precipitation.
- Mazin, I.P., 1963: The lifetime of droplets in stratiform clouds. *Trudi TsAO*, 47, 24-32.
- Pobanz, B.M., J.D. Marwitz and M.K. Politovich, 1994: Conditions associated with large-drop regions. *J. Appl. Meteor.*, 33, 1366-1372.
- Rasmussen, R.M., B.C. Bernstein, M. Murakami, G. Stossmeister and J. Reisner, 1995: The 1990 Valentine's Day Arctic outbreak. Part I: Mesoscale and microscale structure and evolution of a Colorado front range shallow upslope cloud. *J. Appl. Meteor.*, 34, 1481-1511.
- Stewart, R.E., 1992: Precipitation types in the transition region of winter storms. *Bull. Amer. Meteor. Soc.*, 73, 287-296.
- Tremblay, A., S.G. Cober, A. Glazer and G.A. Isaac, 1996: Observations and parameterization of mixed -phase clouds during the Canadian Freezing Drizzle Experiment (FDE). Proceedings of 12th Intl. Conf. Clouds and Precipitation.
- Tremblay, A., A. Glazer, W. Yu and R. Benoit, 1996: A mixed-phase cloud scheme based on a single prognostic equation. *Tellus*, In Press.
- Vali, G., R.D. Kelly, A. Pazmany, R.E. McIntosh, 1995: airborne radar and in-situ observations of a shallow stratus with drizzle. *Atmos. Res.*, 361-380.

STUDIES ON THE RAINDROP SPECTRUM CHARACTERISTICS IN THREE TYPES OF PRECIPITUS CLOUDS

Gong Fujiu¹ Liu Jicheng² Li Zihua² Lu Taoshi¹

¹ Liaoning Weather Bureau, Shenyang, P.R.C.

² Nanjing Institute of Meteorology, Nanjin, P.R.C.

1. INTRODUCTION

During the period of July-August 1994, we used GBPP-100 ground raindrop spectrograph manufactured by the American PMS Company for continuous measurement of several rainfalls in Shenyang. The instrument can make total spectrum measurement by using optical arrays on the scale of 0.2-12.4mm divided into 60 intervals with 0.2mm spacing for each. Owing to computer recording, measurements were performed without stopping.

In this paper, the ground raindrop spectra in the cumulus, stratiformis and Cu-St merging cloud rainfall on three rain days are used for the analysis of the spectrum patterns and characteristic quantities of the three types of precipitus rainfall and the laws governing their evolution, and for the study of their correlation with the M-P and Γ distributions.

2. CHOICE AND MANIPULATION OF DATA

Owing to continuous measurements, the sampling time is taken from 10 to 30 seconds, depending on rain density. Altogether 1270 samples have been obtained. In order to reduce accidental errors, we take 5-minute averaging for all the data used for calculating the characteristic parameters. Thus, 127 copies of data are selected for the three types of rainfall, 31 for the cumulus rainfall, 34 for the stratiformis rainfall and 62 for the Cu-St merging cloud rainfall. The characteristic parameters calculated are space number density N , rain intensity I , mean diameter D_1 , diameter of mean cubic root D_3 , volume medium diameter D_0 and spectrum width.

The M-P and Γ distribution fitting is made for each copy of data and their distribution formulas are

respectively as

$$N(D) = N_0 e^{(-\lambda D)} \quad D_{\min} \leq D \leq D_{\max} \quad (1)$$

$$N(D) = N_0 D^\mu e^{(-\lambda D)} \quad D_{\min} \leq D \leq D_{\max} \quad (2)$$

3. RAINDROP SPECTRUM ANALYSIS

3.1 Mean raindrop spectrum diagrams

Fig. 1 shows the mean raindrop spectra of the three types of precipitus rainfall. It is seen that the stratiformis raindrop spectrum is rather narrow and the maximum raindrops are 4mm in diameter, while the cumulus and Cu-St merging cloud spectra are very wide and the maximum raindrops reach 6mm in diameter. The three curves intersect at about 1.5mm. On the left side of the raindrops smaller than 1.5mm, the number density of the stratiformis raindrops is large and that of cumulus raindrops is small, while on

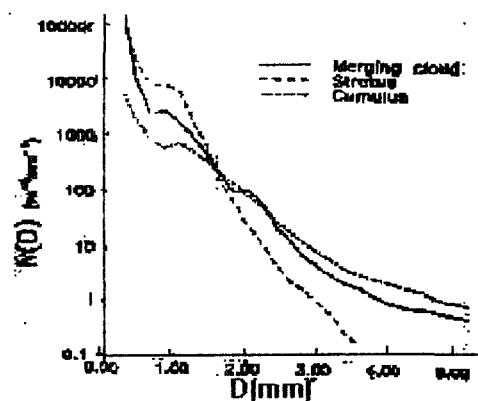


Fig. 1. Mean raindrop spectrum of the three types of precipitus cloud

the right side of the raindrops larger than 1.5mm, the number density of the cumulus raindrops is large and that of the stratiformis raindrops is small. The number density of the Cu-St merging cloud raindrops is

magnification of this system has been set for a size range of 0.2 to 12.4 mm. It has been tested that both the precision and the reliability of the instrument are relatively high for non-showery precipitation.

3. COMPUTATIONAL METHODOLOGY

3.1 About N(D)

In July-August 1994, successively observation of every type of precipitation have been done in Shenyang. With the rainfall intensity differing, the sample interval varies from 10 to 30 seconds. In this papper, average of two minutes has been done for all data.

The calculating formula of N(D) is

$$N(D) = n(D) / (s(D) \cdot v(D) \cdot t) / \Delta D \quad (3)$$

where N(D) is the number of raindrops, s(D) is the sample area, v(D) is the terminal velocity, ΔD is the interval of diameter which is 0.2 mm.

3.2 About the parameters of Γ distribution

Eq.(2), after a logarithmic transformation, can be expressed as

$$\ln(D) = \ln N_0 + \mu \ln D - \lambda D$$

Let $X = D$, $Y = \ln D$, $Z = \ln N(D)$, $A = \ln N_0$, $B = -\lambda$,

$C = \mu$, then one has

$$Z = A + BX + CY$$

By using the least squar method ,A, B and C meet:

$$B = (\sum YZ \sum XZ - \sum XZ \sum Y^2) / [(\sum XZ)^2 - \sum X^2 \sum Y^2]$$

$$C = (\sum XZ \sum XY - \sum YZ \sum X^2) / [(\sum XZ)^2 - \sum X^2 \sum Y^2]$$

$$A = \bar{Z} - B\bar{X} - C\bar{Y}$$

Baed on the value of A, B and C, we can calculate N_0 , μ and λ .

3.3 About the parameters of M-P distribution

Samely, eq.(1) can be transformed as

$$\ln N(D) = \ln N_0 - \lambda D$$

Let $Y = \ln N(D)$, $X = D$, $A = \ln N_0$, $B = \lambda$, then we have

$$Y = A - BX$$

In the same way, we can get

$$B = (n \sum XiYi - \sum Xi \sum Yi) / [(n \sum Xi)^2 - (\sum Xi)^2]$$

$$A = \bar{Y} - B\bar{X}$$

then N_0 and λ can be easily calculated.

4. RESULTS AND ANALYSES

4.1 Fitting and analysing of Γ distribution

Table 1 shows the fitted results of three parameters in Γ distribution. From table1, one can see that the range of N_0 is very large with a minimum value of 4.12、 maximum value of 3710.56 and a mean value of 832.69; having a mean value of -1.0571 and only one positive value, μ fluctuates around -1. Most of λ is between 1 and 2 with a mean value of 1.1605. Therefore, the mean Γ distribution in Shenyang in summer can be expressed by

$$N(D) = 832.69 D^{-1.0571} \exp(-1.1605D),$$

$$D_{\min} \leq D \leq D_{\max}$$

The fitting significancy of Γ distribution is tested by F test. The calculating formula is

$$R^2 = U / S_{zz}$$

where Szz is the sum of squares of deriations and U is quadratic sum of regression

$$S_{zz} = \sum (Zi - \bar{Z})^2$$

$$U = \sum (Zi - \bar{Z})^2$$

Generally, the value of R varies between 0 to 1; the nearer to 1, the better the fitting significancy is.

Because R is subject to the number of the variables in regression equation, m, and the sample size n, and has a reasonable value onlyif $n \gg m$, so it is not suitable to test the fitting significancy with R. A more rational statistic is

$$F = (U/m) / [Q/(n-m-1)] = [R^2/m] / [(1-R^2)/(n-m-1)]$$

where Q, the residual sum of squares, is expressed by

$$Q = S_{zz} - U$$

In model $Y = \beta_0 + \beta_1 X_1 + \beta_2 X_2 + \dots + \beta_m X_m + \varepsilon$

hypothesis H_0 :

$$\beta_1 = \beta_2 = \dots = \beta_m = 0$$

It hints that Y is not relevant to each of all the m variables. Statistic F submits to $F(m, n-m-1)$ distribution and take values on the left of F distribution with a large probability. For a given significance level α , if $F > F(m, n-m-1)$, we can give up the hypothesis and deem that those variables are significantly relevant to Y. $1 - \alpha$ expresses the level of reliability. Obviously, the larger F is, the better fitting significance is.

Table 1 also shows the values of R, F and α . From table 1, we can see that in 10 out of all the 20 cases, R's are significant at $\alpha=0.01$. In only one case, the correlation is not significant even let $\alpha=0.1$. This means that Γ distribution is a relatively good distribution function to fit the DSD in Shenyang in summer.

4.2 A comparison between Γ distribution and M-P distribution

To make a comparison on fitting efficiency between Γ distribution and M-P distribution, relative error ε_n is calculated according to its definition

$$\varepsilon_n = (1/n) \sum_{i=1}^n \frac{|\hat{N}(Di) - N(Di)|}{N(Di)}$$

where $\hat{N}(Di)$ is the fitting distribution function of diameter; $N(Di)$ is real distribution density, n is the sample size. The value of ε_n reflects efficiency of fitting equation; the less ε_n is, the better the fitting efficiency.

Table 1. The fitting significance of Γ distribution

date	N_0 ($\text{mm}^3 \text{m}^{-1}$)	μ	λ (mm^{-1})	R	F	α
7-13 20:00	1868.56	-1.08	1.52	0.71	9.27	0.01
7-13 21:00	5341.61	-0.54	1.92	0.77	12.25	0.01
7-18 06:00	1405.34	-1.12	2.33	0.65	3.35	0.1
7-18 06:30	1320.48	-0.10	2.32	0.57	7.54	0.01
7-18 07:00	184.43	-0.56	1.20	0.79	5.73	0.05
7-18 07:30	88.47	-0.88	0.94	0.78	4.38	0.1
8-06 19:00	17.62	-1.35	-0.32	0.67	3.37	0.1
8-08 19:00	3716.56	-0.44	2.28	0.50	553.33	0.01
8-08 19:30	145.68	-1.05	0.86	0.83	3.75	0.1
8-08 12:10	380.75	-0.98	1.08	0.57	4.66	0.05
8-08 12:20	379.42	-1.29	1.00	0.71	14.78	0.01
8-08 12:30	300.84	-1.09	1.14	0.69	8.09	0.01
8-08 12:40	115.87	-1.49	0.58	0.77	2.53	---
8-15 06:00	4.12	-2.33	-0.42	0.97	5.82	0.05
8-15 14:00	75.14	-0.81	1.17	0.96	24.29	0.01
8-15 14:30	203.42	-0.29	2.08	0.82	6.42	0.05
8-16 02:00	75.31	-1.00	1.53	0.90	9.47	0.01
8-16 07:00	73.11	-2.73	-0.48	0.63	11.47	0.01
8-16 08:00	138.28	-1.93	0.16	0.51	5.43	0.05
8-25 00:00	818.29	0.01	2.23	0.92	43.38	0.01

Table 2. The comparison of fitting significance between Γ distribution and M-P distribution

No.	date	M-P distribution		Γ distribution	
		α	$\varepsilon_n(\%)$	α	$\varepsilon_n(\%)$
1	7-13 20:00	--	49.71	0.01	45.49
2	7-13 21:00	0.05	57.47	0.01	58.29
3	7-18 06:00	--	42.51	0.1	42.58
4	7-18 06:30	--	57.97	0.01	57.34
5	7-18 07:00	--	18.83	0.05	16.62
6	7-18 07:30	--	28.31	0.1	25.39
7	8-06 19:00	--	53.12	0.1	44.53
8	8-08 19:00	0.01	24.01	0.01	22.05
9	8-08 19:30	--	38.41	0.1	32.08
10	8-08 12:10	--	36.34	0.05	36.15
11	8-08 12:20	--	43.16	0.01	40.87
12	8-08 12:30	--	27.25	0.01	22.01
13	8-08 12:40	0.1	32.61	--	18.38
14	8-15 06:00	--	32.69	0.05	8.09
15	8-15 14:00	0.1	39.24	0.01	36.52
16	8-15 14:30	--	40.59	0.05	41.14
17	8-16 02:00	--	32.07	0.01	18.91
18	8-16 07:00	--	70.47	0.01	18.20
19	8-16 08:00	--	64.66	0.05	49.32
20	8-25 00:00	0.01	54.95	0.01	55.03

Table 2 shows the value of ε_n and the significance level of equation. We can see that ε_n from M-P distribution is larger than that from Γ distribution in 16 cases. So, only in 4 cases the Γ distribution is worse than the M-P distribution. The mean value of ε_n from M-P distribution is 42.4%, whereas that of Γ distribution is 34.45%. Even worse, there are as many as 15 cases in which the fitted M-P function are not significant. So Γ distribution is evidently superior to M-P distribution to describe the spectrum in Shenyang in summer not only at ε_n aspect but also at significance level aspect

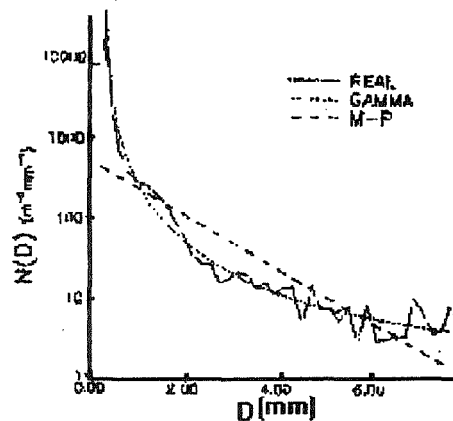


Fig.1 The comparison of real and fitting spectra between Γ distribution and M-P distribution

Fig.1 shows the mean real spectra, mean Γ distribution and mean M-P distribution which has a expression of

$$N(D) = 487.4 \exp(-0.774D), \quad D_{\min} \leq D \leq D_{\max}$$

From Fig.1, We can see that fitting efficiency of Γ distribution is relatively good in whole diameter range, whereas the M-P distribution is well fitted only in middle area; in the ends of spectra, the fitting value has a evident difference from the real data. The reason is that Γ distribution has a factor of D^μ which has a beneficial adjustment to the ends of spectrum.

4.3 The applicability of Γ distribution in different rainfall intensity.

Table 3. The comparison of fitting significance with rainfall intensity(I) differing

I(mm/h)	M-P distribution		Γ distribution	
	R	ε_n (%)	R	ε_n (%)
0-5	0.7912	52.45	0.8505	43.78
5-10	0.8829	71.21	0.9091	62.40
10-15	0.4829	70.20	0.8771	54.58
15-20	0.2890	108.25	0.6718	72.13
20-25	0.3107	93.78	0.9379	82.18
25-30	0.2095	83.77	0.8377	41.96
30-35	0.3321	97.11	0.5711	58.12
35-40	0.2536	86.47	0.6312	36.43
40-45	0.1980	96.62	0.6662	20.33
45-50	0.1231	91.43	0.7143	28.50

Table 3 shows the comparison of fitting efficiency between Γ distribution and M-P distribution for different rainfall intensities. For Γ distribution, complex coefficient of correlation fluctuates slightly in middle area and the relative error is relatively little and stable. So the fitting efficiency of Γ distribution for different type of precipitation is the same by and large. For M-P distribution, the complex coefficient of correlation decreases evidently as rainfall intensity increases and the relative error

increases with rainfall intensity at the beginning. When the rainfall intensity is higher than 15 mm/h, all of the relative error are higher than 80%. So the fitting efficiency of M-P distribution is relatively good if the rainfall intensity is less than 15 mm/h, other wise, the M-P distribution function is not suggested. The difference in fitting efficiency between Γ distribution and M-P distribution is related to the efficiencies in various diameter range. Generally speaking, the larger the rainfall intensity is, the broader the spectral width is. Γ distribution fits the real data quite well in any diameter range, whereas M-P distribution is applicable only in the middle area; with the rainfall intensity increasing, the fitting efficiency become worse because of the broad spectral width. So we can draw a conclusion that M-P distribution only fits the stable stratus clouds precipitation which has a narrow spectral width and little rainfall intensity and do not fit the unstable cumulus precipitation which has a broad spectral width and large rainfall intensity.

5. CONCLUSION

1. Γ distribution satisfactorily fits the observed drop spectrum in Shenyang in summer and is superior to M-P distribution;

2. There is no evident difference of fitting efficiency for Γ distribution with rainfall intensity differing.

REFERENCES

1. Marahall. J. S. and Palmer. W. Mck., The distribution of raindrop with size, J. Met. S., 5, 165-166, 1948
2. Waldvogel. A., The No jump of raindrop spectra, J. Atmos. Sci., 31, 1067-1078, 1974
3. Carlton W.U., Natural variation in the analytical form of the raindrop size distribution, J. climate Appl. Meter., 22, 1764-1775, 1993

MICROSTRUCTURE IN A HIGH REACHING BOUNDARY LAYER FOG

Wolfram Wobrock¹ and Manfred Wendisch²

¹ Laboratoire de Météorologie Physique, Université Blaise Pascal, 63177 Aubière, France

² Institut für Troposphärenforschung, Permoserstr. 15, 04303 Leipzig, Germany

1. INTRODUCTION

During the field experiment *ChemDrop*, November 1994 in the Po-valley in Northern Italy a quite high reaching fog layer persisted over several days. The rawin soundings reported typically fog heights between 250 to 500 m, but in some cases also up to 1000 m. Although the objectives of the experiment were devoted to study the size dependent *Chemistry of Droplets* an extensive equipment for turbulence, micrometeorological, and microphysical measurements was also available.

Most of the observational results presented here concentrate on a 30 min. time period during a long lasting fog night wherein also drizzle occurred. This short episode illustrates many characteristics of this fog event, e.g. the structure of the foggy surface layer, the droplet spectra, and the turbulence.

2. EXPERIMENTAL SETUP

Observations were performed with three sonic instruments measuring the three components of wind and the wet bulb temperature with a time resolution of 10 (or 20) Hz. The instruments were located in 2, 25m, and 50m height. Next to them three fast sensors for the monitoring of the LWC (PVM-100, 300) were installed. A fourth fast LWC-sensor was also located at the ground level in 2 m, but 15 m upwind of the mast to study the horizontal differences in the LWC field. The field site of San Pietro Capofiume (44.7° N, 11.6°E) is located in a very flat and almost horizontally homogeneous terrain of grassland and harvested fields and thus favorable for turbulence measurements. Inhomogeneities for the flow were only created by the large instrumental equipment and a 51 m high reaching meteorological tower.

Microphysical measurements for the fog droplet spectra in the size range from 2-47 μm were performed with two PMS/FSSP-100, one located in ground level, another one in 30 m. By means of a Ground Based Precipitation Probe (PMS/GBPP-100) which was located 3.5 m above the ground also the precipitating droplet spectra were observed. The GBPP-100 is an optical array probe, which resolves droplet sizes from

142 μm to 12.4 mm in 62 channels. Each channel has a width of 200 μm (Yangang and Laiguang, 1994). Both the FSSP and the GBPP were carefully calibrated using a monodisperse drop generator (Wendisch et al., 1996). The FSSP data were corrected for coincidence and electronic dead.

3. OBSERVATIONAL RESULTS

3.1 Meteorological observations

Starting on 13 Nov. 1994 a high reaching boundary layer fog formed over the first 300-350 m. This fog dissipated during daytime of 14 Nov. and hazy conditions with relative humidities close to saturation

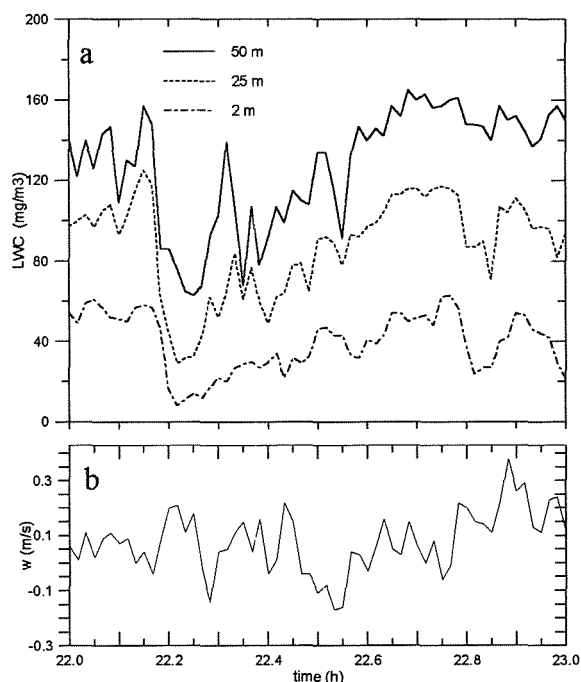


Fig. 1a: LWC in 2, 25, and 50 m. 1b: vertical wind speed in 25 m (time resolution = 1min.)

prevailed in the first 300 m. From the evening of 14 Nov. until the late morning of 15 Nov. 1994 fog evolved again on the field site of San Pietro Capofiume. Several soundings during this night reported a fog top varying between 240-400 m. The fog formed under extremely low wind conditions (0.5 m/s) in the first 50

m. After 21.30 the wind speeds increased to 2-3 m/s for the rest of the night. In the surface layer we found a slightly unstable stratification, with a stability length of -100 to -500 m. The increase of the temperature next to the ground level is also reflected in the decrease of the observed LWCs from 50, 25, to 2 m. For the time period from 22.00 to 23.00, 14 Nov. 94, Figs. 1a and b illustrate the time evolution of the LWC in 3 levels and the vertical windspeed in 25 m in time steps of 1 min. Due to the higher temperatures next to the surface fog droplets started to evaporate in the surface layer. It is also surprising to see that this weak instability is connected with a predominating updraft velocity. The vertical winds observed are in general quite low, but in periods when temperature and LWC gradients intensified vertical velocities between 10- 20 cm/s were observed.

The reason for the unstable stratification in the surface layer is obvious: The high reaching boundary layer fog (Fitzjarrald and Lala, 1989) heats by its significant downwelling longwave radiation the earth surface, from where the temperature is transported upward by turbulent diffusion. Consequently, positive vertical turbulent heat fluxes of a few W/m^2 were observed most of the time.

3.2 Microphysics

From previous Po-valley fog experiments (Wobrock et al., 1992) we know that fog droplet spectra can be quite large, covering the entire size range of a FSSP-100 up to 47 μm diameter. This is also true for the measuring period on 14/15 Nov. 1994. Figs. 2a and b display the mass density distribution function for the fog droplet spectra observed in 2 m. The six spectra present 1 minute averages in the period from 22.32 to 22.48. Except for curve 1 all other observations show droplets up to 47 μm . This is very surprising as the PVM observations for the LWC in 2 m (see Fig. 1a) only reported 40 - 60 mg/m^3 for this time period. From the integration of the FSSP spectra in Fig. 2a and b, however, we receive the following LWCs: curve 1 = 52 mg/m^3 , curve 2 = 76 mg/m^3 , curve 3 = 143 mg/m^3 , curve 4 = 97 mg/m^3 , curve 5 = 87 mg/m^3 , and curve 6 = 81 mg/m^3 . The comparison of these values with the PVM observations (Fig. 1a) suggests that the PVM probably did not correctly detect droplets larger than 25-30 μm diameter, which are most responsible for changes in LWC during this time interval.

Another interesting feature of this observational period is the appearances of drizzle from 22.37 to 22.58. Fig. 1c gives the mass density distribution of the precipitating drops, observed with the GBPP. We can see that mainly diameters between 100 to 300 μm are responsible for the drizzle mass. But also drizzle or rain drops up to 700 μm appeared. Drizzle occurred several times during this fog night and showed in both cases the same behavior in the microphysical observations: as displayed in Fig. 2a some minutes before drizzle the

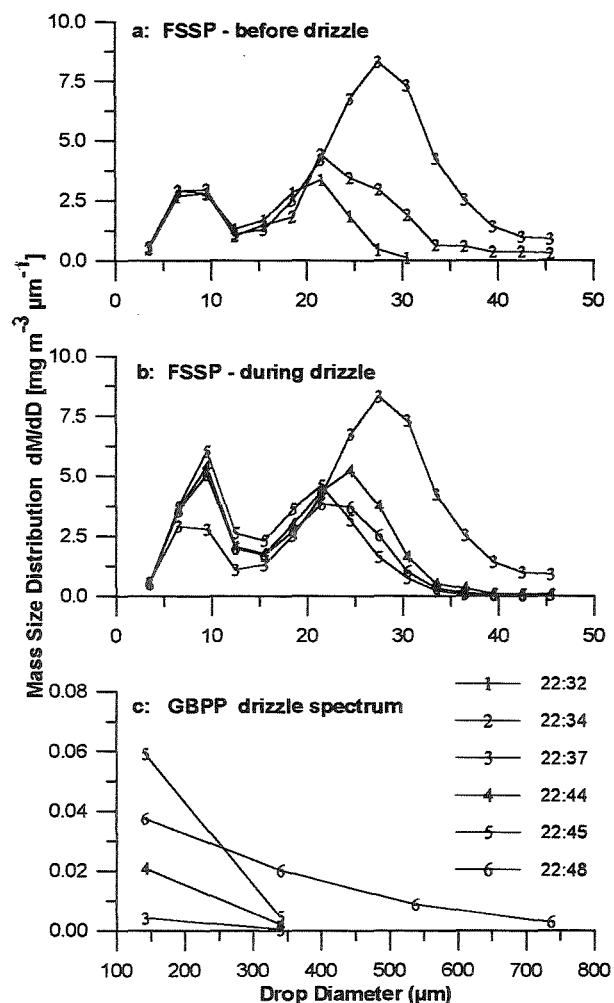


Fig. 2a-c: Fog droplet and drizzle spectra observed at ground level on 14 Nov. 94.

number of large droplets increased significantly (see curve 1 and 2). When the size distribution reached its maximum (curve 3 in Fig. 2a) weak drizzle (curve 3, Fig. 2c) started. During drizzle the number of large fog droplets with diameters $> 25 \mu m$ decreased rapidly (curve 4 to 5). Considering also the droplet spectra in the time span between curve 3 and 4 (not displayed here), one can see that the disappearance of droplets in the fog spectrum first occurred in the range from 35-45 μm and then after 5-10 min proceeded to the smaller diameters around 20-25 μm .

This observed time evolution of the fog droplet spectrum agrees qualitatively quite well with the results of numerical simulations of the collision - coalescence process for typical convective cloud droplet spectra (Beheng and Doms, 1990). Applying these calculations to a broad fog droplet spectrum with LWCs around 0.5 g/m^3 , drizzle spectra result after 30-40 minutes of simulation, which are similar with those displayed in Fig. 2c (Wobrock, 1988). However, as the LWC of the strongest observed fog spectrum only counted 0.143 g/m^3 and drizzle occurred already at the same time, we can exclude, that this droplet spectrum (curve 3, Fig. 2a)

was responsible for the drizzle formation. From the presence of the strong LWC gradients (Fig. 1a) we can assume that the drizzle formation probably took place in higher fog levels where significantly higher LWCs prevailed. The presence of the extremely broad droplet spectrum at 22.37 in the ground level can possibly be explained by the down-mixing of air from higher fog layers. Fig. 1b indicates that just around 22.30 to 22.34 the strongest 'downward' motion for this time period occurred. Thus, the spectrum indicated by curve 3 could reflect the shape of the spectra in higher levels, which trigger drizzle formation.

3.3 Turbulence observations

In the following Figs. 3 to 5, the variance or energy (power) spectra $S(f)$ of the velocity, temperature, and LWC - fluctuations are illustrated. The 10 Hz data set of these parameters were detrended for the time period from 22.30 to 22.58 and analyzed by FFT. The resulting 2^{13} frequencies of the FFT - analysis were integrated over 20 logarithmic equally spaced frequency intervals.

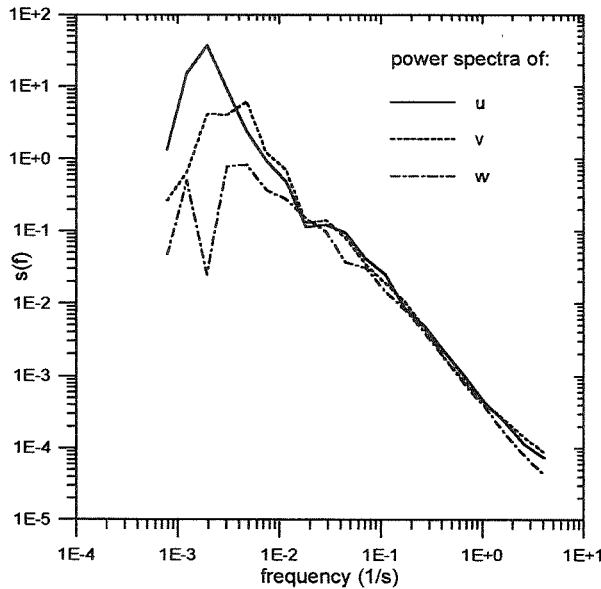


Fig. 3: Power-spectra $S(f)$ (m^2/s) of the three wind components in 25 m (14 Nov. 94, 22.30-23.00)

Fig. 3 displays the power spectra for the wind components u , v , and w in 25 m. For all frequencies $f > 0.01 - 0.1$ Hz we can see the typical $-5/3$ slope of the power spectrum for the eddy sizes in the inertial subrange.

In contrast, the power spectra determined from the fast measurements of temperature and LWC for the same time period in 25 m show a different behavior, especially for the smallest fluctuations resolved (Fig. 4). While the LWC - power spectrum differs from the power law only for frequencies above 2 Hz, an increase of the temperature spectrum already started for larger eddy sizes at 0.5 Hz. The appearance of this

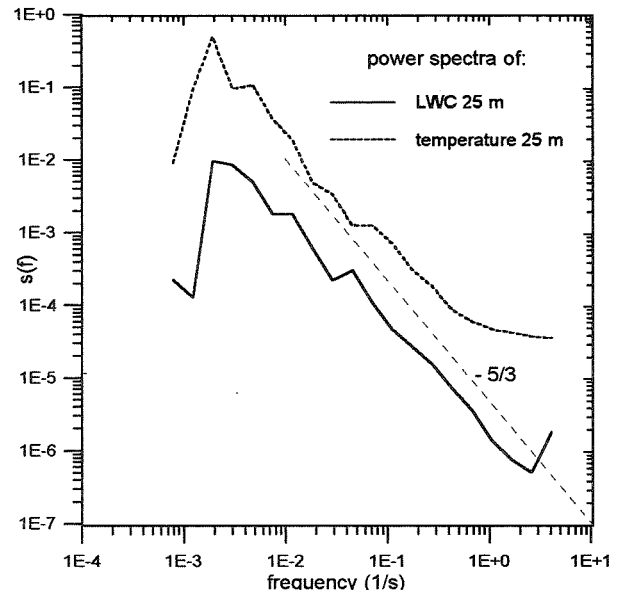


Fig. 4: Power-spectra $S(f)$ of temperature in $\text{K}^2 \text{s}$ and LWC in $(\text{g cm}^{-3})^2 \text{s}$ for $z=25$ m (14 Nov. 94, 22.30 - 23.00)

white noise in temperature and LWC - power spectra occurred quite often during this fog night and even started at smaller frequencies (see power spectra in 2 m in Fig. 5). An instrumental error or another technical failure which might have caused an aliasing can be excluded as also several power spectra of T and LWC which were analysed for this fog night agree very well with the $-5/3$ power law for all frequencies > 0.01 Hz.

In Fig. 5 the power spectra of the LWC fluctuations are displayed for four different locations in the surface

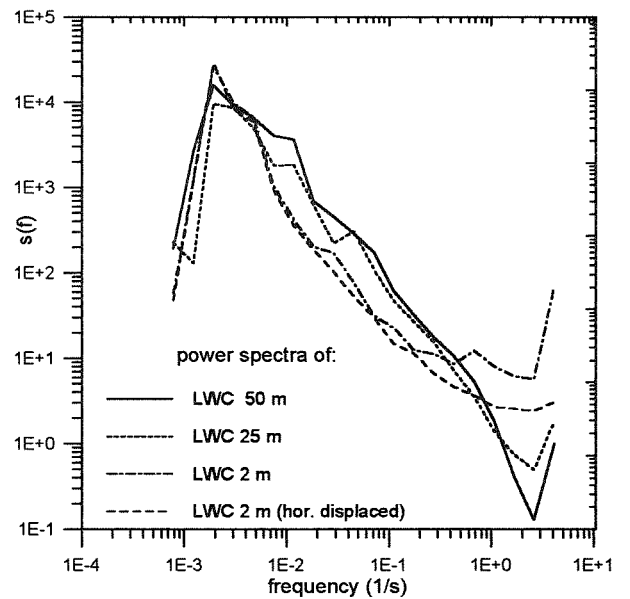


Fig. 5: Power-spectra $S(f)$ of LWC in $(\text{g m}^{-3})^2 \text{s}$ for 4 different locations in fog (14 Nov. 94, 22.30-23.00)

layer. We can detect herein that all LWC sensors located along the 50 m tower show the same increase for frequencies $> 2\text{Hz}$. The fourth sensor, however, which was 15 m upwind of the tower displays a power spectrum with a shape similar to the T spectrum in Fig. 4. An explanation for this observational result is not obvious, as an influence of the tower on the fluctuations in LWC should not be expected. Instrumental errors or differences of the 4 PVM sensor can also be excluded. During a calibration period in fog (13 Nov. 94) all four sensor were operated next to each other resulting in 4 identical power spectra.

Although the form of the LWC - power spectra were quite variable during the entire fog night, Fig. 5 illustrates very good the typical differences between the 2, 25, and 50 m level: for the frequency range from 0.01 to 0.5 Hz nearly all observations confirm a gradient in the power spectra. $S(f)$ decreased from the 50 m to 25 m level and even stronger down to 2 m. For small eddies, however, the value of $S(f)$ increased significantly next to the surface. While the LWC - power spectra observed in the 25 and 50 m level still showed the characteristics of the inertial subrange, most observations in 2m during this fog night displayed a constant behavior of $S(f)$ for frequencies $> 0.5\text{Hz}$.

4. SUMMARY AND CONCLUSIONS

During a high reaching boundary layer fog strong vertical gradients of temperature and LWC associated with weak but predominant updraft velocities were observed in the surface layer. Also drizzle occurred several times in this fog night. Shortly before the onset of drizzle the number of droplets with diameters between 25 and 47 μm increased significantly. After a few minutes of drizzle the large droplet sizes in the fog spectrum disappeared successively starting with the largest diameters, while the spectrum of the drizzle drops extended.

The variance or power spectra of the velocity fluctuations showed in all situation a quite good agreement with the $-5/3$ power law for the inertial subrange indicating a steady state turbulent flow. Temperature and LWC - power spectra, however, gave a constant or even increasing $S(f)$ spectrum for the highest frequencies resolved. The vertical profiles of the LWC - power spectra indicate that this behavior is most pronounced for the ground observations. As the air adjacent to the ground level experienced the strongest heating by the surface we can speculate that the air became subsaturated leading to drop evaporation. This process seemed to have contributed mostly to the increase in the LWC fluctuations for the highest frequencies.

5. ACKNOWLEDGEMENTS

The authors want to thank Dr. S. Fuzzi and his coworkers from FISBAT-CNR, Bologna, who hosted the CHEMDROP field campaign, 1994. This research was supported by the EC Environment and Climate Research Programme (contract EV5V-CT- 0314, Climatology and Natural Hazard) .

6. LIST OF REFERENCES

- Beheng K.D. and G. Doms, 1990: The time evolution of a droplet spectrum due to collision-coalescence: a numerical case study on the effect of selfcollection, autoconversion and accretion. *Meteorol. Rdsch.*, 42, 52-61.
- Fitzgarrauld, D.R. and G.G. Lala, 1989: Hudon Valley fog Enivornments. *J. Appl. Meteor.*, 28, 1303-1328.
- Wendisch M, A. Keil and A.V. Koroloev, 1996: FSSP characterization with monodisperse water droplets. submitted to *J. Atmos. Oceanic Technol.*
- Wobrock, W., 1988: Numerische Modellstudien zur Simulation von Strahlungsnebel unter besonderer Berücksichtigung spektraler Wolkenmikrophysik. *PhD Thesis, Berichte des Inst. für Meteorologie und Geophysik*, Nr. 78, Universität Frankfurt.
- Wobrock W., D. Schell, R. Maser, M. Kessel, W. Jaeschke, S. Fuzzi, M.C. Facchini, G. Orsi, M. Marzorati, P. Winkler, B. Arends and J. Bendix (1992): Meteorological characteristics of the Po-valley fog. *Tellus* 44B, Nr. 5, 449-469.
- Yangang, L. and Y. Laiguang, 1994: Error analysis of GBPP-100 probe. *Atmos. Res.*, 34, 379-387.

A STUDY OF THE MICROPHYSICAL STRUCTURE OF STRATOCUMULUS CLOUDS

Hanna Pawlowska^{1,2} and Jean-Louis Brenguier¹

¹ METEO-FRANCE (CNRM/GMEI), Toulouse, France

² on leave from Institute of Geophysics, University of Warsaw, Poland

1. INTRODUCTION

Clouds are very inhomogeneous and anisotropic phenomena in the atmosphere, and the parameterization of their effects is still a challenge. The microphysical properties are driven by small scale processes, smaller than the cloud scale, while forecast or climate models are only able to represent much larger scales. The interactions between dynamics, thermodynamics and microphysics are so complex, that it has not yet been possible to relate directly the mean dynamical fields to the mean cloud properties at the meso or the large scale. However, the coupling between dynamics and microphysics is better understood at the scale of an updraft, so that it seems more feasible to parameterize the coupling at this scale and then extend the result to larger scales by parameterizing the statistics of the process. The approach proposed in this paper aims at the description of the microphysical properties of a stratocumulus in order to parameterize its radiative properties. The methodology is based on the coupling of in-situ measurements of the cloud parameters and remote sensing of the cloud radiative properties.

In-situ measurements are generally not well suited for the description of the statistical properties of an extended system because measurements are limited to a very thin sampling section along the aircraft trajectory and a long period of measurements is needed in order to get a satisfactory statistical significance from these measurements. The case study presented here is particularly interesting because the situation remained stationary during the whole duration of the experiment (2.5 hours). The objective is thus to describe the main characteristics of the microphysical fields, to identify parameters that are crucial for the radiative properties and finally to document their statistical distribution from the smallest scale to the scale of the whole system.

The droplet size distribution is a critical parameter for the calculation of the cloud radiance. The in-situ measurements have been performed on board the Météo-France Merlin-IV with the Fast FSSP (Brenguier et al, 1996; Coelho et al, 1996) that provides a much better accuracy than the standard probe.

Small scale variations of the droplet size distributions have been obtained from the data by using the optimal estimator described in Pawlowska et al (1996-a and -b).

2. THE EUCREX-94 EXPERIMENT

The experiment, performed in April 1994 at Brest (France), was dedicated to the study of the radiative properties of extended warm clouds over the ocean. Three instrumented aircraft contributed to the project. The Météo-France Merlin-IV for in-situ measurements, and two aircraft for remote sensing from above the cloud: the INSU-ARAT Fokker-27 equipped with the POLDER and the LEANDRE (Descloîtres et al, 1996) and the DLR Falcon-20 equipped with the OVID and a second POLDER.

On April 18 (mission 206), a high was located west of Brittany maintaining a stationary North-Easterly flow over the Channel, with an extended stratocumulus at the southern edge. The system was particularly interesting because the cloud depth was decreasing slowly from the South (point M (48.37N, 4.77W)) to the North (point A (49.33N, 5.6W)) where the cloud deck was progressively broken. Further North, the air was completely clear. This slow gradient remained unchanged during the whole duration of the experiment (2.5 hours), so that it has been possible to analyze extensively the related trend in the cloud radiative properties.

2.1 Sampling strategy

Our primary objective, with in-situ measurements is to document the processes responsible for the evolution of the droplet size distribution. In such a cloud, this evolution is mainly determined by convective organisation, i.e. by vertical motions. Vertical sampling is not possible with an aircraft but rapid ascents and descents (zooms) provide satisfactory sampling of the vertical evolution of the droplet spectra. With a cloud depth of the order of 400 m, the aircraft moves by about 5 to 10 km horizontally during the zoom. Therefore, while it is feasible from

outside the cloud to select a convective cell, the aircraft is not certain to remain in the cell during the whole figure. The first series of zooms have been extended 100 m below cloud base and above cloud top in order to document the thermodynamics outside the cloud layer. The last series has been limited to the cloud layer in order to increase the number of zooms along the leg. The main limitation of this strategy is that it has a poor statistical representativity (from 8 to 12 zooms per leg).

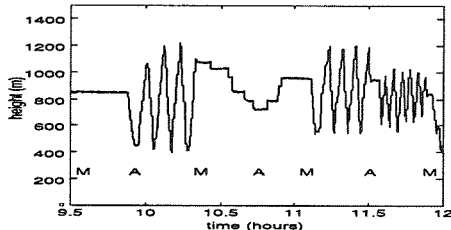


Fig.1 Vertical profile of the Merlin-IV flight.

Our secondary objective is to relate in-situ measurements and remote sensing of the cloud radiative properties at all scales. Because it is not feasible to co-ordinate precisely the three aircraft on the same spot, this comparison can be made only on a statistical basis. With the instruments on board the ARAT-F27 or the DLR-Falcon20, these properties were described with a resolution of the order of 100 m. Only horizontal legs in the cloud are suited for a continuous description of the microphysics at this scale. The cloud top has been selected as the most critical sampling region for the comparison with remote sensing. Therefore, two legs were flown horizontally, with flight level changing step by step in order to stay at the cloud top.

This strategy, illustrated in Fig 1, shows the series of figures for the whole flight: long zooms, two horizontal legs, long zooms and finally, short zooms.

3. DESCRIPTION OF THE CLOUD STRUCTURE

3.1 General features

The stratocumulus layer had a relatively stable base located at about 700 m, slightly descending northward. The cloud top covered by a strong inversion was more inhomogeneous because of the convective cells but its mean level was decreasing from 1100 m at the southern edge (M) to 900 m at the northern edge. These features are illustrated by the contours of the temperature measured during the series of long zooms. The region limited by the -0.5 C contour corresponds to the cloud layer, that is also exhibited by the superimposed dots corresponding to the sections of the flight legs where liquid water was measured. The apparent structure in the boundary and in the inversion layers have no physical mean-

ing and are only due to the scarce sampling with the zooms outside the cloud layer.

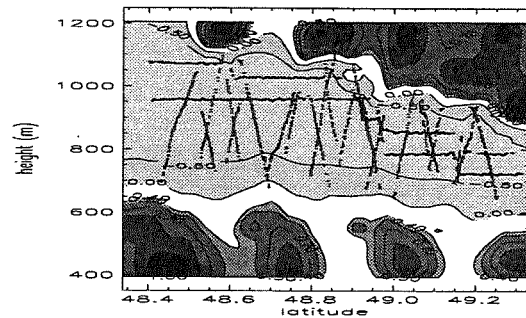


Fig.2 Temperature contours along the M-A axis. Superimposed dots represent sections of the flight legs where liquid water was measured. The structure below and above the layer is due to sparse sampling outside the cloud layer.

3.2 Vertical profiles

Figures 3, 4 and 5 show vertical profiles of the total droplet concentration (in the 2-45 microns range) in (a), the LWC in (b) and the effective diameter ϕ^3/ϕ^2 in (c). Each dot corresponds to Fast FSSP measurements averaged over 1 second. 25 zooms were performed during the flight. Some of them display an adiabatic profile (solid line in (b)), but most of them are characterized by values below the adiabatic with fluctuations of LWC due to fluctuations in both the concentration and the effective diameter. In the adiabatic cases, the LWC and the effective diameter increase linearly with altitude, so that their ratio, which is used for the calculation of the cloud optical thickness, can be represented by a linear function of the altitude above cloud base. In addition, the adiabatic profiles correspond to convective cells so that the cloud optical thickness, proportional to the integral of LWC/D_{eff} in a vertical column can be expressed as a function of the cloud depth ΔZ or the maximum value of LWC/D_{eff} that corresponds to the cloud top: $(LWC/D_{eff})_{max} = \Delta Z/8500$

$$\begin{aligned} \delta &= k \int_{Z_{base}}^{Z_{top}} \frac{LWC}{D_{eff}(z)} dz \approx k \frac{k^*}{2} (Z_{top} - Z_{base})^2 \\ &\approx \frac{k}{2k^*} \left(\frac{LWC}{D_{eff}} \right)_{top}^2 \end{aligned} \quad (1)$$

Sub-adiabatic values are measured when the aircraft is sampling a region of mixing between the convective cells and the dry air from above, and this circumstance can occur any time during the zoom. Therefore, the zoom procedure provides information about the maximum values of LWC/D_{eff} that can be encountered in the stratocumulus but it cannot provide information on the statistics of these values in the cloud. These must be obtained by analysing the horizontal legs.

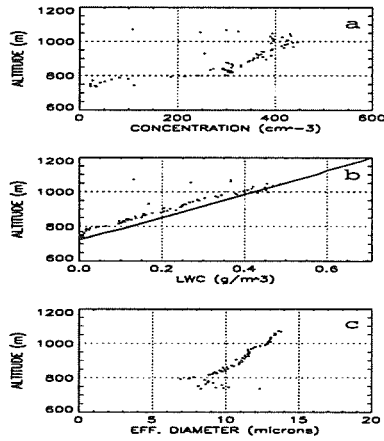


Fig.3 Vertical profiles of the total droplet concentration (a), the LWC (b) and the effective diameter (c). The adiabatic LWC profile is represented by a solid line in (b). Data collected at 10h05', 48.9N.

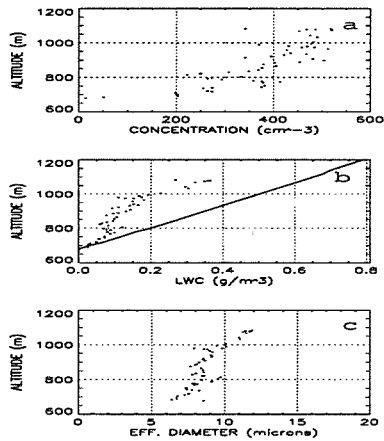


Fig.4 Vertical profiles as in Fig.3. Data collected at 10h11', 48.65N.

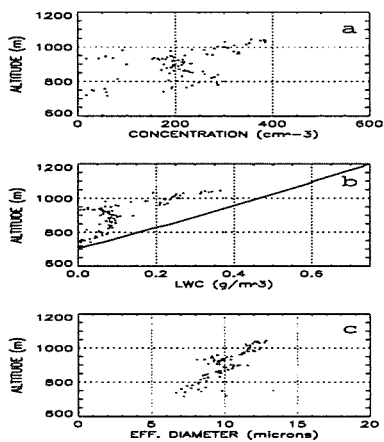


Fig.5 Vertical profiles as in Fig.3. Data collected at 11h10', 48.45N.

3.3 Horizontal statistics

As shown in Fig.2, the cloud top altitude was decreasing by steps and the horizontal sampling consisted of a series of horizontal sections in order to stay a few tens of meters below the top. The 1 second averaged values of the ratio LWC/D_{eff} are represented in Fig.6 as a function of the position along the leg. The solid line represents the variation of the maximum values derived from Eq. 1 for a cloud depth decreasing linearly from 380 m at the southern edge (M) to 180 m at the northern edge (A). Diamonds show the maximum values retrieved from the zooms. This figure shows that the maximum values encountered along the horizontal sections are in agreement with the linear relation derived from the vertical profiles, the underestimation being due to the fact that the flight level is slightly below the cloud top. Few values from the zooms (diamonds) at the northern edge are above the general trend. They correspond to sampling in few convective cells ascending higher than the mean cloud top. This procedure thus provides detailed information about the statistics of the LWC/D_{eff} values at a fixed level. However, this information cannot be directly used for calculation of the statistics of the cloud optical thickness. For example, the aircraft might be flying across an entrainment region, with a downdraft penetrating below the flight level, so that the value measured by the aircraft is close to 0 while, just below the flight level, the value of LWC/D_{eff} might be much higher. A complete description of these statistics will be derived from the coupling of the statistics presented here for the microphysics and the statistics of the cloud top altitude derived from the remote sensing with the lidar (LEANDRE) or the radiometers (POLDER and OVID).

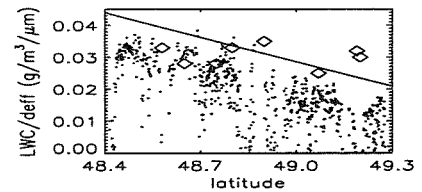


Fig.6 The ratio of LWC to effective diameter calculated from the measurements between 10h20' and 10h45' (see text).

4. UP-SCALING

The final step in this study will be to evaluate precisely the contribution of the fluctuations in the microphysics to the averaged radiative properties at the cloud scale. It is not yet clear what is the smallest significant scale for this contribution and it is crucial to process microphysical data with the finest spatial resolution. This has been made possible with the optimal estimation of the size distribution developed by Pawlowska et al (1996-a and -b), which provides

a much better spatial resolution from the series of counts measured with the Fast FSSP.

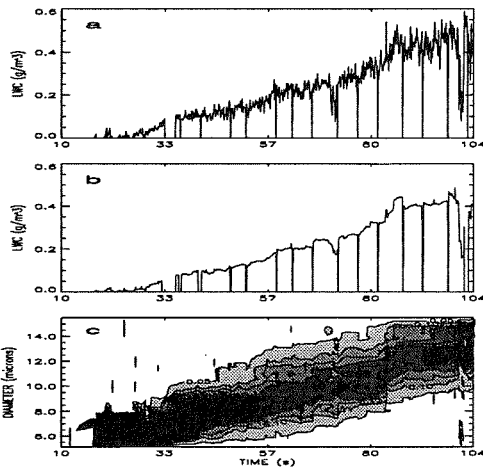


Fig.7 Ascent at 10h05', 48.9N. a - LWC calculated by cumulating counts over 0.1s, b - LWC calculated using optimal estimation, c - time evolution of the droplet size distribution.

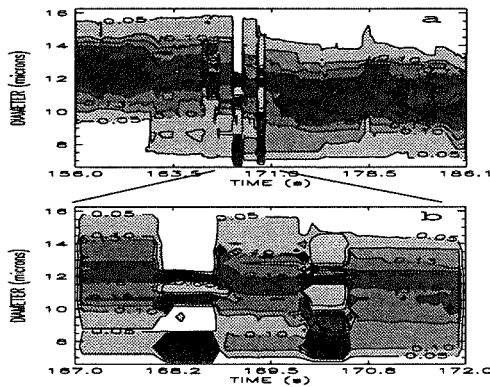


Fig.8 Time evolution of the droplet spectra during a horizontal leg at cloud top. Time counted from 10h21'. b - details of the series on a 5 seconds section.

Spatial resolution is particularly important when processing a zoom because time is directly related to the change in altitude, so that time resolution corresponds to the resolution in the vertical profile. For example, Fig. 7-a shows the LWC profile from data processed at 10 Hz with the current method. The fluctuations in LWC are typical of the Poisson noise when the sampling period becomes too short. Fig. 7-b shows the same parameter after optimal estimation. The Poisson noise has been removed but the vertical profile still shows many details. This is particularly significant for the vertical profile of the size distribution as shown in Fig. 7-c. Another example is displayed in Fig.8 for a short section of a horizontal leg. The figure shows that optimal estimation is very efficient for getting information on the size of the diluted regions where droplets are smaller.

4. CONCLUSIONS

In-situ measurements have been performed within stratocumulus for the study of the cloud radiative properties. Two sampling procedures have been performed: series of ascents and descents throughout the cloud depth, for documenting the vertical profiles, and horizontal legs at the cloud top, for deriving the statistics of the microphysics at the cloud scale. Both strategies are complementary. The zooms have shown that the LWC and the effective diameter increase linearly with altitude in the adiabatic regions, which correspond to the maximum values within the cloud. A simple parameterization has been deduced that allows estimation of the cloud optical thickness as a function of the cloud depth for these maximum values. Horizontal legs have shown that the maximum values of LWC/D_{eff} encountered close to the cloud top are in agreement with this simple parameterization. They also provide information about the distribution of the sub-adiabatic values. These will be coupled with the statistics of the cloud top altitude measured by remote sensing to derive statistics of the cloud optical thickness. Finally, examples of a new processing method (optimal estimation) for microphysical data have been shown. The method provides very detailed information about the fine scale variations of the droplet size distributions and it will be particularly useful for studying the contributions of the sub-adiabatic regions to the radiative properties.

5. ACKNOWLEDGEMENTS

The authors are grateful to the team of the Centre d'Aviation Météorologique for their active collaboration during the flights and to the group of Mesures Météorologiques Aéroportées for the aircraft data processing. This research was supported by Météo-France and INSU under grant D13570.

6. REFERENCES

- Brenguier, J.L., D. Trevarin, R. Peytavi, A. Coelho, P. Wechsler, and J. Isbert, 1996: New electronics for the Forward Scattering Spectrometer Probe: The Fast FSSP. Accepted to *J.Atmos.Oceanic Technol.*
- Coelho, A., J.L. Brenguier, and T. Bourianne, 1996: A model for the Fast FSSP operation. Proceedings of the ICCP 1996.
- Desclotres, J., H. Pawlowska, J. Pelon, J.L. Brenguier, F. Parol, J.C. Buriez, and P. Flamant, 1996: Experimental retrieval of cloud optical thickness during EU-CREX: comparison of three approaches. Proceedings of the ICCP 1996.
- Pawlowska H., J.L. Brenguier, and G. Salut, 1996: Optimal non-linear estimation for particle measurements. Submitted to *J.Atmos.Oceanic Technol.*
- Pawlowska, H., and J.L. Brenguier, and G. Salut, 1996: Optimal non-linear estimation for particle measurements. Proceedings of the ICCP 1996.

Giant Drops observed from large aircraft

Robert A. Black and Paul T. Willis

NOAA/AOML/ Hurricane Research Division
Miami, FL 33149, USA

1. INTRODUCTION.

Giant raindrops (nominal mean diameter $> \sim 5$ mm) are relatively rare in nature, yet their influence upon the radar reflectivity and rain rate is substantial, thus it is important to determine the circumstances in which they are observed. Most observations of such drops have been made by small aircraft in the tropics, most notably in Hawaii (Beard et al, 1986) and in south Florida (Baumgartner and Colpitt, 1995). However, only large aircraft have the range to properly survey most oceanic convection, and only they can safely study hurricanes far from land.

The advent of the Particle Measuring Systems, Inc. 2-dimensional (2-D) optical array probes in 1975 (Knollenberg, 1981) revolutionized cloud microphysical measurements. In that year, NOAA installed two of these probes on the NOAA DC-6 aircraft. While making a low altitude (~ 300 m) penetration into a strong convective cell in Hurricane Gladys, the earliest known 2-D images of naturally occurring giant drops (Fig. 1) were observed.

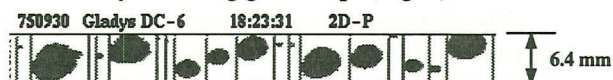


Figure 1. Selected giant drops observed with the 2D-P in Hurricane Gladys (1975).

After that season, the DC-6 was retired and the 2-D probes were installed on the WP-3D aircraft. This aircraft's penetration speed is about 140 ms^{-1} , compared with $\sim 100 \text{ ms}^{-1}$ for the DC-6. For many years, we have been concerned about the shape of raindrop images as observed from the WP-3D aircraft. NOAA operates two of these aircraft, and the 2-D probe mounting was identical on both aircraft through March 1993. In the summer of 1993, a new pylon was constructed for one aircraft because the original pylon developed cracks. This new pylon has a slightly different shape, but it is mounted at the same place on the wing as the original.

The first images we obtained from these probes on the WP-3D showed that raindrop images were typically elliptical, with a preferred orientation, whereas ice particle images showed no evidence of distortion, although columnar ice crystals frequently showed a preferred orientation roughly parallel to the major axes of the elliptical drops. We have used this fact to

successfully discriminate between graupel and raindrops (Black and Hallett, 1986, Houze et al, 1992) in our data.



Figure 2. A 2D-P image observed by NOAA-43 in Hurricane Olivia. In this and all subsequent images, time advances from left to right. The large image is a possible large drop in the process of breaking up.

Since 1977, we have collected hundreds of flight-hours of data in numerous hurricanes, mostly in rain. In all that time, we found very few raindrop images whose equivalent circle diameter (ECD) was > 4 mm. Because of this, we had a suspicion that the larger drops were in fact breaking up before we could sample them. When we found the image shown in Figure 2, we were almost certain that drops were in fact being disrupted. Therefore, we embarked on an informal experiment to determine the degree to which raindrops were being distorted by flow around the WP-3D 2-D probe mount. Additionally, we obtained data from NOAA-42 to refute the hypothesis that the large drops were being systematically disrupted. But first, a word about the 2-D probes and their characteristics.

A 2-D probe functions by illuminating a photodiode array with a laser that passes between two cylindrical tips. Particles that occult the laser beam cast a shadow on the photodiode array, whose state is sampled at such a rate that the array moves forward its own depth between samples. In this manner, a 2-dimensional image of the shadow is obtained as the aircraft flies.

We define the coordinates for these probes (during level flight) such that the x-direction is normal to the long axis of the diode array and parallel to the airspeed vector. The y-direction is parallel to the long axis of the diode array, which is horizontal when the probe tips occupy the x-z plane (the normal probe orientation on the WP-3D). The z-axis is parallel to the Earth's gravity vector, as usual.

In their normal orientation, particle fallspeed produces no measurable distortion of the images. However, the 2-D probes can also be mounted with the probe arms in the horizontal (x-y) plane. In this orientation, the long axis of the diode array is parallel to

the z-axis. In such cases, the particle fallspeed produces particle motion parallel to the long axis of the diode array, which produces about an 8-10% shape distortion for the largest drops.

The WP-3D carries two 2-D probes mounted on either side of a pylon located about 1.5 m from the wingtip that extends approximately 1 m below the wing; the probe tips are about 0.2 m behind the leading edge of the wing. The outboard 2-D mount (closest to the wingtip) usually holds the 2D-C, whereas the inboard mount usually holds the 2D-P.

NOAA 2-D PROBE CHARACTERISTICS		
PROBE	RESOLUTION (mm)	ARRAY WIDTH mm (pixels)
2D-C (mono)	0.05	1.6 (32)
2D-P (mono)	0.2	6.4 (32)
2DG-C (grey)	0.03	1.92 (64)
2DG-P (grey)	0.15	9.60 (64)

Table 1. The NOAA 2-D optical array probe characteristics.

2-D probes come in 2 basic mechanical configurations, and they have 2 electronic versions: "mono" and "greyscale". The mono versions have a 32-diode array, and provide one bit of shadow information per diode; a shadow is registered when the illumination of a diode is reduced by 50% or more. The greyscale (grey) version has a 64-diode array with 2 bits of shadow information, representing threshold values of 0, 25%, 50%, or 75% reductions in the unshadowed diode illumination level. The abbreviation and characteristics of the probes used in this study are given in Table 1. A "G" in the name signifies a greyscale probe.

2. METHOD OF STUDY

The data presented here were collected in various tropical cyclones and summer convective rain showers in the vicinity of Miami, FL. Most of the data we present were obtained with the 2-D Greyscale probes in the late summer of 1995, except where noted. Information on the distorted shape of the drops was obtained by mounting the 2-D probes with the arms in both the vertical and horizontal orientations, and flying through rain. Data were not gathered for all possible probe orientations on both NOAA WP-3D aircraft, nor were all data obtained at the same altitude.

To objectively determine the orientation of the images, we employed an ellipse-fitting routine. This routine treats the image points as "x-y" data points and computes a least-squares fit to them. The intersection of the fit line with the actual image defines the major axis of the ellipse, and the center is defined to be the center of the line segment between the intersection points. The minor axis length and eccentricity are determined by the requirement that the ellipse area equal the image area. If the "minor" axis is longer than the major axis, the axis

definitions are interchanged. These results were saved both as data points for individual images, and as averages over several minutes as a function of image size.

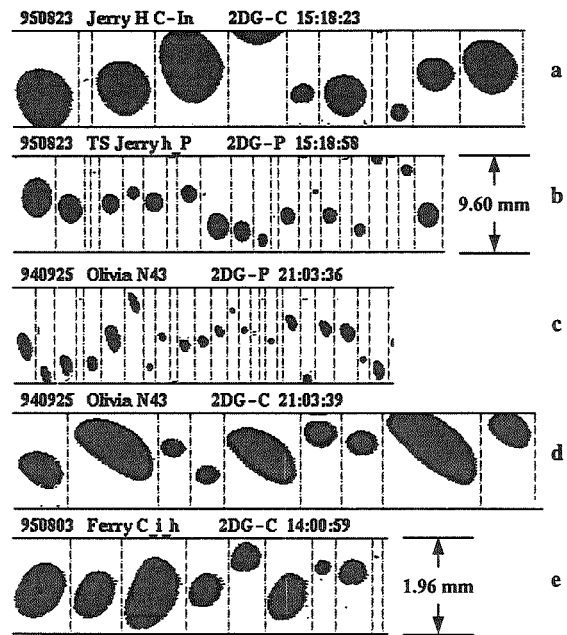


Figure 3. 2-D greyscale probe images for selected probe mounts on the two WP-3D aircraft. a) Vertical arm cloud probe, inboard mount, NOAA-42. b) Horizontal arm precipitation probe, outboard mount, NOAA-42. 2DG-P length scale is 9.6 mm. c) Vertical arm precipitation probe, inboard mount, NOAA-43. d) Vertical arm cloud probe, outboard mount, NOAA-43. e) Horizontal arm cloud probe, inboard mount, NOAA-43. 2DG-C length scale is 1.96 mm.

3. RESULTS

The data presented in the graphs below can best be understood with the aid of a few representative 2-D images. The values in the graphs are mean values, and there is significant scatter, although the standard deviations of the points for diameters < 3 mm is small. Selected 2-D greyscale probe images (Fig. 3) show typical examples of the drops observed without showing the copious noise in these data.

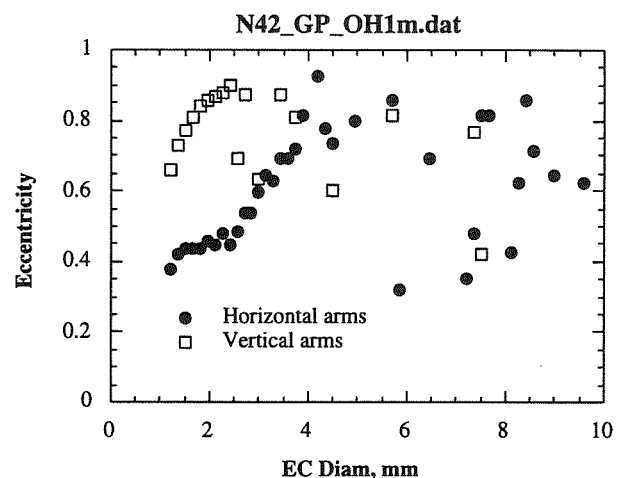


Figure 4. Eccentricity as a function of diameter for the outboard probe mount on Noaa-42. Data are from the 2DG-P probe.

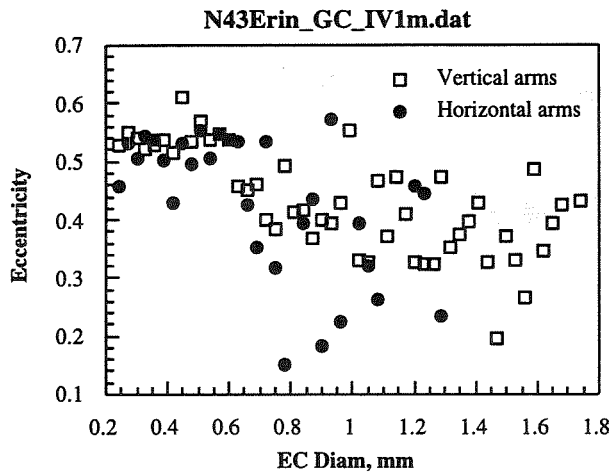


Figure 5. Eccentricity for the 2 probe orientations at the inboard probe mount on NOAA-42. Data obtained by the 2DG-C probe.

The differences in the computed eccentricities of the drops observed by the 2DG-P at the outboard position on NOAA-42 is shown in Figure 4 for the two probe orientations available. These plots are mean values computed for drops observed over several minutes, or as long as data are available. The data for the different orientations necessarily came from different flights, and

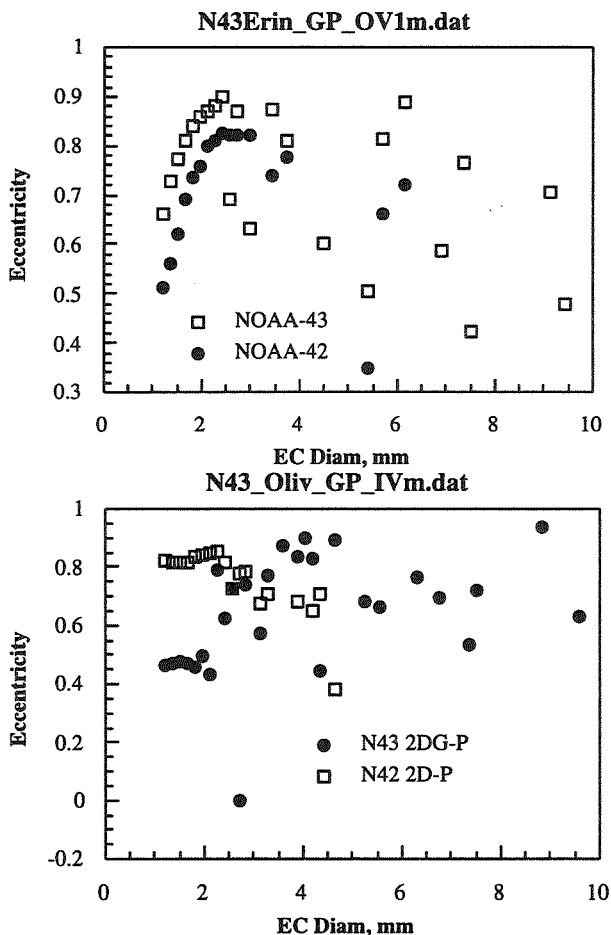


Figure 6. Differences in image eccentricity between aircraft with the probe arms vertical. A) 2DG-P probe images from the outboard mount. B) NOAA-43 2DG-P and NOAA-42 2D-P images from the inboard mount.

there are different numbers of particles available for each. The trend lines for these data become noisy at the point where insufficient numbers of drops were observed in that size. It is apparent that the elongation of the images is most severe when the probe arms are vertical, and for the larger sizes of drops at the same probe orientation.

For the inboard mounting position, the distortions are less severe. These are shown in Figure 5 for the cloud probe on NOAA-43. As can be seen, the inboard mount suffers considerably less from distortion than does the outboard mount, and there is no significant difference between the two available probe orientations.

Another goal of these tests was to determine if the droplet distortions were different between the two WP-3D aircraft. The engineers that first tested the new pylon on NOAA-43 thought that the drops seen from the newer pylon were more elongated than on the old one. Eccentricity versus diameter of 2DG-P images from the outboard mounts on both WP-3D aircraft, and the NOAA-43 2DG-P and the NOAA-42 2D-P inboard mount are given in Figure 6. There are sufficient points to characterize the differences in the mounts up to about 3 mm diameter. As can be seen, images from the outboard

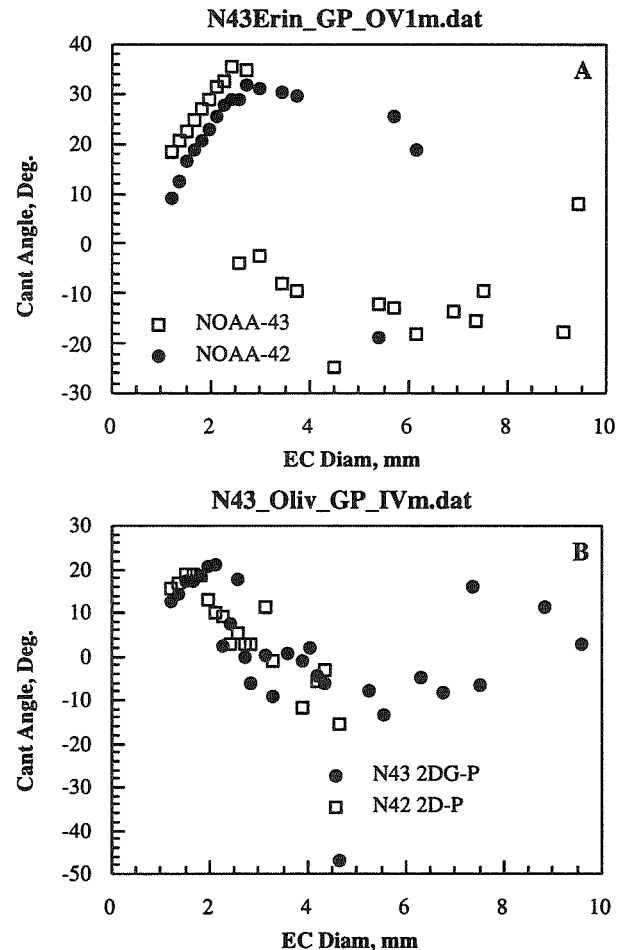


Figure 7. Orientation angle of drop images observed with the 2-D probe arms vertical. A) Drop images observed from the outboard probe mount with the 2DG-P. Images are canted at a steeper angle for NOAA-43 for any given size up to about 3 mm diameter. B) Drops observed at the inboard mounts of NOAA-43 (2DG-P) and NOAA-42 (2D-P)

mount on the new pylon of NOAA-43 are slightly more distorted than those from the original style pylon on NOAA-42. Surprisingly, 2D-P images from the inboard mount on NOAA-42 are more elongated than 2DG-P images from NOAA-43. In fact, they are elongated almost as much as the images from the outboard mount of NOAA-43. At this time, we do not have sufficient data to determine if the 2DG-P image data from the inboard mount on the old style pylon will show the same characteristics as the old 2D-P.

We also measured the orientation angle (Fig. 7) of these images; in this case, an angle of 0° represents an image oriented normal to the diode array; a positive value represents an image oriented from upper left to lower right, and a negative value from lower left to upper right (e.g. Fig. 9a). In addition to being slightly more elongated at any given size, the images from the outboard mount on NOAA-43 are also slightly more steeply canted than those from NOAA-42. The inboard positions (Fig. 7b) are similar in this respect for both aircraft.

4. SUMMARY

Clearly, these distortions are serious, but this is not sufficient evidence to conclude that large drops are being systematically disrupted on either WP-3D. The fact remains that the lack of giant drops in the NOAA hurricane data archive may be an artifact of where and at what altitude the majority of WP-3D flights have occurred. Nearly all of the rain data collected with the 2D-P was obtained with the probe in the inboard mount

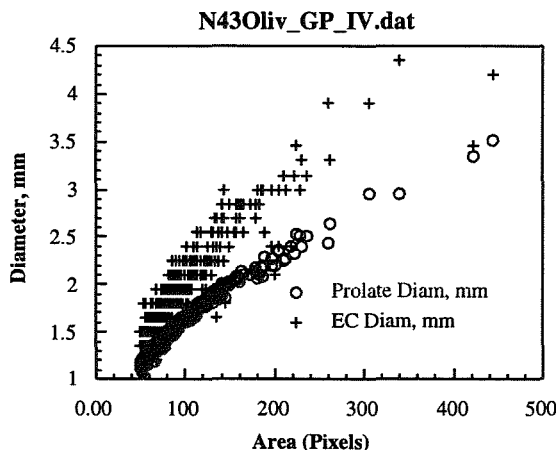


Figure 8. Prolate spheroid and EC diameters as a function of image area. Data from a 2DG-P in the inboard mount with the arms vertical.

of the old style (NOAA-42) pylon.

These distortions should be accounted for when computing rain rate and radar reflectivity from 2-D droplet spectra. Figure 8 shows the difference between using the ECD and assuming that the image is a prolate spheroid with major and minor axes as defined by the elliptical 2-D image. The ECD clearly overestimates the diameter by as much as 25% for images of about 200 pixels area, equivalent to a 2-3 mm diameter raindrop for the 2DG-P. The results are similar if the image is

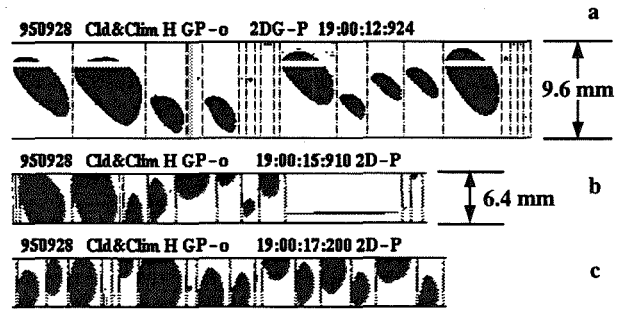


Figure 9. A selection of giant drops observed from NOAA-42. The 2DG-P was mounted in the outboard position, the 2D-P was inboard. Both probes were mounted with their arms vertical. a) 5-8 mm drops from the 2DG-P. The gap was caused by an electronic problem with the probe. b) and c) 4-8 mm drops from the 2D-P.

assumed to be an oblate spheroid.

New data (Fig. 9) from NOAA-42 obtained during low level (< 500 m) passes through the rain shaft of a small oceanic cumulus encountered near Marathon in the Florida keys, about 110 km south of Miami, was found to contain giant drops. The aircraft carried a 2DG-P in the outboard mount, and the 2D-P in the inboard mount on this flight. As both probes observed giant drops, and this pylon was found to distort the drops almost as much as the one on NOAA-43, we conclude that large drops can indeed be observed by the NOAA WP-3D aircraft. Further, we conclude that the absence of large drops in the WP-3D hurricane data archive is the result of meteorological factors such as wind shear and turbulence, rather than to drop breakup in the air ahead of the 2-D probe mount. However, these data also show that the effect of drop shape needs to be accounted for in order to properly characterize the particle size distribution.

5. REFERENCES

- Baumgartner, D. and A. Colpitt, 1995: Monster drops and rain gushes: Unusual precipitation phenomena in Florida marine cumulus. *Preprints, Conf. on cloud physics., 15-18 January, 1995, Dallas, TX, Amer. Meteor. Soc.*, 344-349.
- Beard, K. V., D. V. Johnson, and D. Baumgardner, 1986: Aircraft observations of large raindrops in warm, shallow, convective clouds., *Geophys. Res. Lett.*, **13**, 991-994.
- Black, R. A., and J. Hallett, 1986: Observations of the distribution of ice in hurricanes. *J. Atmos. Sci.*, **43**, 802-822.
- Houze, R. A., F. D. Marks, and R. A. Black, 1992: Dual-aircraft investigation of the inner core of Hurricane Norbert. Part II: Mesoscale distribution of ice particles. *J. Atmos. Sci.*, **49**, 943-962.
- Knollenberg, R. G., 1981: Techniques for probing cloud microstructure. *Clouds, their formation, optical properties, and effects*, P. V. Hobbs and A. Deepak, eds., Academic Press, 15-91.

SATELLITE REMOTE SENSING OF SUMMER STRATUS CLOUDS OVER THE WESTERN NORTH-PACIFIC

Tadahiro Hayasaka, Hiroshi Kawamura, Yuri Sato and Hiroshi Takai

Center for Atmospheric and Oceanic Studies, Tohoku University,
Sendai 980-77, JAPAN

1. Introduction

Low level stratus clouds are frequently observed over the western North-Pacific off the coast of Japan during summer. Cold air mass system including these clouds bring cold summer in the north-east area of Japan. It is inferred from satellite images that these clouds extend homogeneously larger than 1000 km with the cloud top height lower than 1 km. As shown by Warren et al. (1988), these clouds are considered to be a part of large scale cloud system in the central North-Pacific in this season. However, their physical and radiative properties have not been investigated sufficiently in contrast to the clouds over the eastern North-Pacific off the coast of California during the same season.

In the present study, optical thickness and effective droplet radius of the stratus clouds over the western North-Pacific during the summer of 1993 are retrieved from NOAA-11 and NOAA-12 Advanced Very High Resolution Radiometer (AVHRR) data. Atmospheric conditions related to the clouds are also discussed using ECMWF objective analysis data.

2. AVHRR Data Analysis

An algorithm for retrieving cloud optical thickness and effective droplet radius is based on a comparison of bidirectionally reflected solar radiation measured by AVHRR ch1 and ch3 with those calculated (Hayasaka et al., 1994). Calibration constant of ch1 was corrected by using Abel et al. (1993) and Platnick and Valero (1995). In deriving ch3 reflected radiance, an influence by thermal emission was corrected with ch4 infrared data.

Reflected radiance in visible region is mainly determined by the optical thickness while that in near infrared strongly depends on the size of cloud droplet. Figure 1 shows the calculated relationship between the reflected radiance at wavelength $\lambda = 0.64 \mu\text{m}$ (ch1) and $\lambda = 3.7 \mu\text{m}$ (ch3) for various values of the cloud optical thickness τ at $\lambda = 0.64 \mu\text{m}$ and effective droplet radius r_e . Corresponding data from AVHRR measurements are superimposed on the figure. Optical thickness and effective radius are thus obtained and also liquid water path (LWP: vertically integrated liquid water content)

is obtained from the approximated relationship for large particle as follows (Stephens, 1978),

$$\tau = \frac{3LWP}{2\rho r_e} \quad (1)$$

where ρ indicates the density of liquid water.

In the theoretical calculation, the atmosphere model was provided from ECMWF objective analysis data. Cloud was assumed to be single homogeneous layer with the cloud top at 900 hPa and 50 hPa in thickness. Cloud layer includes liquid water droplet particles expressed by a log-normal size distribution.

Theoretical calculations were performed for each 48 km x 48 km area where solar zenith angle and viewing angle from the satellite were constant. Radiances at $\lambda = 0.64 \mu\text{m}$ and $\lambda = 3.7 \mu\text{m}$ are both calculated monochromatically. However, in the spectral region of ch3 response function there are several gaseous absorption bands so that a relationship between the monochromatic calculation and exact one was established in advance, and the monochromatically calculated radiance was corrected with the relationship.

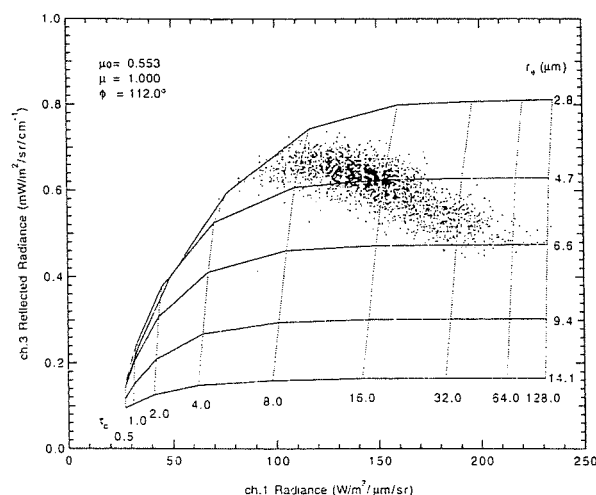


Fig. 1. The relationship between the reflected radiance at $\lambda = 0.64 \mu\text{m}$ (ch1) and $\lambda = 3.7 \mu\text{m}$ (ch3) for various values of the cloud optical thickness and effective droplet radius r_e . AVHRR data are superimposed on the figure.

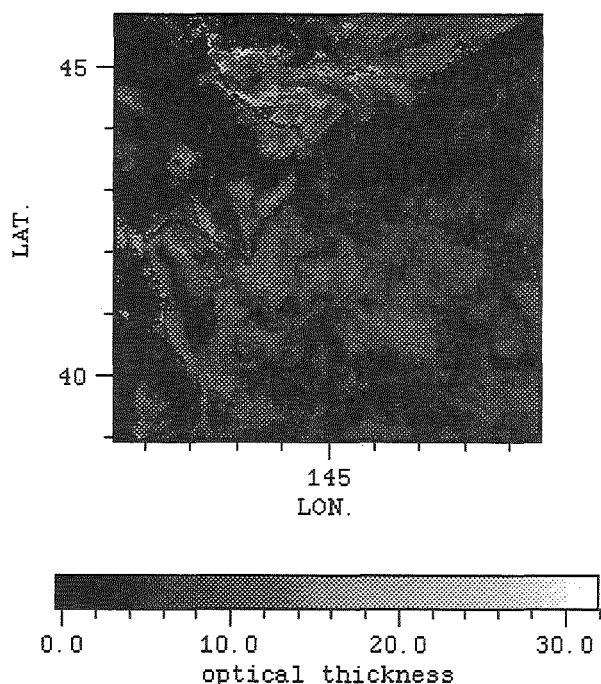


Fig. 2a. Optical thickness of low level clouds on Aug. 5, 1993 retrieved from AVHRR analysis.

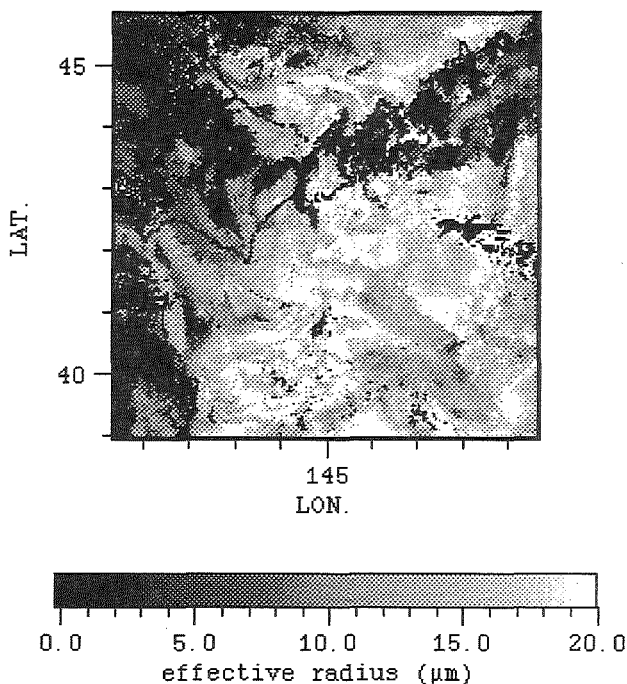


Fig. 2b. Effective droplet radius of low level clouds on Aug. 5, 1993 retrieved from AVHRR analysis.

3. Results from AVHRR Data Analysis

We have analyzed 10 images of AVHRR in which 2 images cover 750 km x 750 km centered at 42.5°N, 145°E and the others cover 1500 km x 1500 km centered at 45°N, 150°E mainly over the ocean of western North-Pacific. As an example of the results, optical thickness and droplet effective radius obtained for Aug. 5, 0800LST are shown by Figs. 2a and 2b, respectively, where the north part of Japan is superimposed. It is distinctive from the figure that there are cloud droplet particles of larger effective radius, as well as the other results in this study. It is also found that distribution and microphysics of clouds are influenced by topography of land or islands since

the cloud top level is low. In the upper part of Fig. 2a, for example, the cloud has larger value of optical thickness with larger cloud particles.

The relationship between cloud optical thickness and effective droplet radius is shown by Fig. 3 corresponding to Figs. 2a and 2b. It is inferred that optical thickness is not so dependent on the effective radius. This feature suggests that the cloud with larger particles contains larger liquid water path. Most of the results show the similar tendency except a few cases. Although Nakajima et al. (1991) suggested that there is a positive correlation between optical thickness and effective radius in small optical thickness cases and a weak negative correlation in large optical thickness cases. However, it is not so obvious in this study.

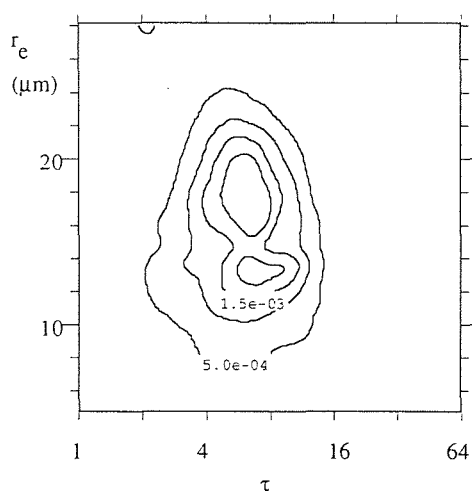


Fig. 3. The relationship between cloud optical thickness and effective droplet radius is shown by Fig. 3 corresponding to Figs. 2a and 2b.

Table 1. Average values of optical thickness, effective radius, and liquid water path obtained in this study.

Date & Time	τ	r_e (μm)	LWP (g/m^3)
AUG.05 08	6.19 ± 3.19	14.4 ± 4.6	59.3 ± 34.0
AUG.06 07	8.29 ± 5.13	11.4 ± 3.8	68.7 ± 54.7
JUL.28 07	8.27 ± 4.81	14.7 ± 5.2	79.5 ± 51.0
JUL.29 07	10.1 ± 5.9	15.2 ± 4.3	102 ± 62
JUL.29 15	15.6 ± 11.2	13.5 ± 4.3	143 ± 115
JUL.30 15	14.4 ± 10.2	15.0 ± 5.3	145 ± 113
AUG.02 07	8.66 ± 5.04	14.0 ± 4.7	79.6 ± 49.0
AUG.02 14	11.8 ± 8.8	12.6 ± 4.6	103 ± 87
AUG.03 07	7.69 ± 4.92	13.3 ± 4.8	68.8 ± 48.9
AUG.07 07	7.61 ± 4.15	12.4 ± 4.7	68.0 ± 47.8

Average values of optical thickness, effective radius, and liquid water path obtained in this study are summarized in Table 1. According to Han et al. (1994), global average values of optical thickness and effective radius of low level clouds over ocean are 6.9 and 11.8 μm , respectively. The optical thickness retrieved in this study is slightly larger than the global average and the effective radius is also larger than the global average. Cloud droplet size distribution is closely related to cloud condensation nuclei (CCN). Since airmass of the clouds in this study comes from ocean, the number of CCN is limited and then cloud particle might be grown up to larger size. In winter season, on the other hand, small cloud droplets are frequently observed over ocean around Japan. This is ascribed to the airmass transported from China which contain aerosols of high concentration in number (e. g. Ishizaka et al., 1995).

4. Discussion with ECMWF Data Analysis

The cloud microphysical properties are related to the cloud formation, maintenance and dissipation processes. It is found from every 1 hour Geostationary Meteorological Satellite (GMS) data that the clouds observed in this study are transported from the northern part of central North-Pacific or from the Sea of Okhotsk. The ECMWF objective analysis data were used to investigate atmospheric and oceanic conditions of the area including the clouds.

Backward trajectory analysis was carried out with wind data at 10 m above the sea surface. Although the used data are close to surface, these data are consistent with measurements by ERS-1/AMI scatterometer. The trajectory analysis results are consistent with those from GMS data. Along the trajectory line, sea surface temperature (SST), surface air temperature, and relative dew point temperature are investigated for several cases. The results revealed that both SST and air temperature are almost same (about 10°C) in the Bering Sea off the coast of Kamchatka

Peninsula and the both temperatures increase with reaching the coast of Japan where SST is slightly higher than air temperature. This change of relationship between SST and air temperature might be related to cloud droplet particle formation observed by satellite. The dew point temperature is 1~2°C lower than the air temperature so that relative humidity just above the sea surface is more than 90% in almost all area of the Bering Sea in July and August 1993.

Corresponding to the two types of trajectory lines as mentioned, a composite of surface pressure pattern was made from ECMWF data for each case. The result suggests that movement of the cloud is attributed to the Okhotsk high and also on a large scale low pressure system located in the central North-Pacific or relatively small low pressure around the Kamchatka Peninsula. Schematics of these patterns are shown by Figs. 4a and 4b, respectively. Advection pattern shown in Fig. 4a was observed in July 1993 and that shown in Fig. 4b was observed in August 1993. These pressure patterns are also found at 500 hPa level and therefore stable. This mechanism efficiently brings cold air mass and low level stratus clouds to Japan for more than 1 month.

5. Summary

Optical thickness and effective droplet radius of the stratus clouds over the western North-Pacific during the summer of 1993 are retrieved from NOAA-11 and NOAA-12 AVHRR data. Also the large scale atmospheric condition is analyzed with ECMWF objective analysis data. The satellite data analysis indicates that the cloud optical thickness in this region tends to be larger than the global average value of maritime low level clouds reported previously. The effective droplet radius is generally large and sometimes becomes larger than 15~20 μm and changes in time and space. This large effective radius might be related to the cloud formation, maintenance and dissipation processes. Since the clouds observed in this

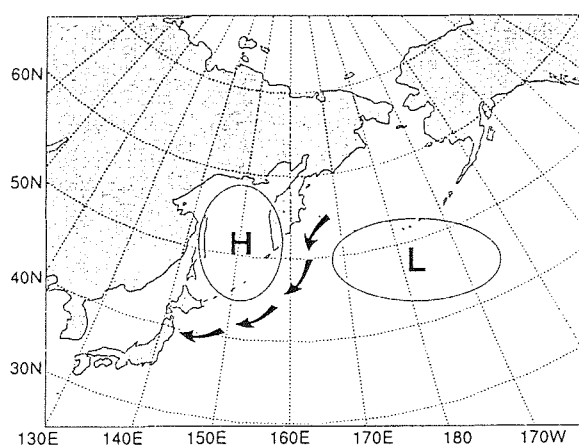


Fig. 4a. Advection pattern and high and low pressure system observed in the second half of July 1993.

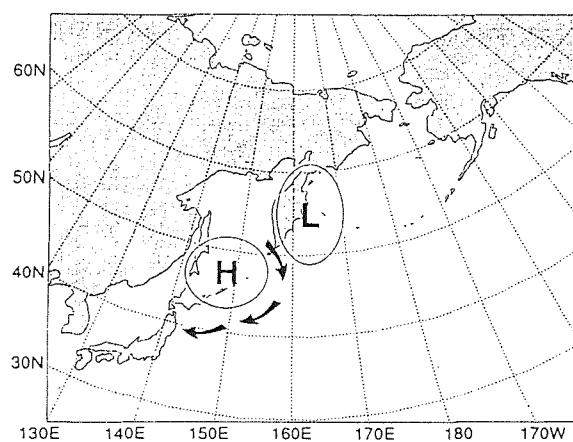


Fig. 4b. Same as Fig. 4a except for the period, the first half of August 1993.

study are transported from the northern part of central North-Pacific, CCN concentration is considered to be low. Therefore larger cloud droplet particles might be observed. The ECMWF objective analysis data suggested that movement of the cloud is attributed not only to the Okhotsk high but also to the low pressure system in the North-Pacific.

Acknowledgments: We would like to thank M. Kuji for his helpful comments on the AVHRR data analysis. We are also grateful to M. Tanaka for his valuable discussion. The AVHRR data used in this study were received in Center for Atmospheric and Oceanic Studies, Faculty of Science, Tohoku University.

References

- Abel, P., B. Guenther, R. N. Galimore and J. W. Cooper, 1993: Calibration results for NOAA-11 AVHRR channels 1 and 2 from congruent path aircraft observations. *J. Atmos. Oceanic Tech.*, 10, 493-508.
- Han, Q., W. B. Rossow and A. A. Lacis, 1994: Near-global survey of effective droplet radii in liquid water clouds using ISCCP data. *J. Climate*, 7, 465-497.
- Hayasaka, T., M. Kuji, T. Nakajima, and M. Tanaka, 1994: Satellite remote sensing and air-truth validation of cloud liquid water path and droplet effective radius. *Proceedings of the 8th Conference on Atmospheric Radiation*, 23-28 January 1994, Nashville, Tennessee, American Meteorological Society, 421-422.
- Ishizaka, Y., Y. Kurahashi, H. Tsuruta, 1995: Microphysical properties of winter stratiform clouds over the Southwest Islands area in Japan. *J. Meteor. Soc. Japan*, 73, 1137-1151.
- Nakajima, T., M. D. King, J. D. Spinhirne and L. F. Radke, 1991: Determination of the optical thickness and effective radius of clouds from reflected solar radiation measurements. Part II: Marine stratocumulus observations. *J. Atmos. Sci.*, 48, 728-750.
- Stephens, G. L., 1978: Radiation profiles in extended water clouds. II: Parameterization schemes. *J. Atmos. Sci.*, 35, 2123-2132.
- Platnick, S. and F. P. J. Valero, 1995: A validation of a satellite cloud retrieval during ASTEX. *J. Atmos. Sci.*, 52, 2985-3001.
- Warren, S. G., C. J. Hahn, J. London, R. M. Chervin and R. L. Genne, 1988: Global distribution of total cloud cover and cloud type amounts over ocean. NCAR/TN-317+STR, also DOE Tech. Rep. ER/0406, National Center for Atmospheric Research, Boulder, Colorado. 42pp.

DOPPLER RADAR-DERIVED PROFILES OF RAINDROP TERMINAL VELOCITIES IN STRATIFORM RAIN

R. Nissen and R. List

Department of Physics, University of Toronto, Toronto, Ontario, Canada M5S 1A7

1. INTRODUCTION

Frequently in cloud physics research it is desirable to know raindrop size distributions (RSDs) aloft. RSDs are the link between reflectivities measured by radar and rainrates, which are of importance for hydrologic applications. Variations in RSDs with height and time may provide insights into the raindrop collision process. However, direct measurements using aircraft instrument platforms are not operationally feasible.

The advent of microwave radar has allowed for measurements of rain intensity to be made at frequent intervals in space. In particular, with Doppler radar the vertical component of velocities can be related to raindrop fall speeds, which are strongly dependent on drop size.

One approach has been to point a Doppler radar straight up. If Rayleigh scattering dominates, the normalized signal power density S_n at a frequency corresponding to radial speed ($w_a - V_t$) is related by (e.g. Doviak and Zrnić, 1984):

$$S_n(w_a - V_t) dV_t = D^6 N(D) dZ Z^1 \quad (1)$$

where V_t is the drop terminal velocity (positive downward), w_a is the vertical air speed (positive upward), D is drop diameter, $N(D)$ is the number concentration per diameter interval, and Z is the radar reflectivity factor. The two main limitations to this approach are that vertical air speeds are combined with drop terminal velocities, and the sampling volume is rather limited for deriving the full spectrum.

A different scheme involves processing data from sweeping radar scans (Plan Position Indicators, or PPIs) to derive more precise Doppler mean fall speeds within certain conditions. Lhermitte and Atlas (1961) pioneered the Velocity Azimuth Display (VAD) analysis, where for a ring of data at constant range and low elevation angle α a fit to the variation of radial velocity V_R with azimuth β is made:

$$V_R = a_0 + a_1 \sin \beta + b_1 \cos \beta \quad (2)$$

It is assumed that the wind field is constant with time during the sweep, particle fall speeds W_p vary only in the vertical, and horizontal wind components vary linearly in the horizontal. These constraints are generally satisfied in steady, stratiform rain, more so with greater confinement of the analysis in the horizontal. The divergence of the horizontal wind $\nabla \cdot U_H$ is obtained from:

$$\frac{2 a_0}{r \cos \alpha} = \nabla \cdot U_H + \frac{2 \tan \alpha}{r} W_p \quad (3)$$

where r is the radius of the VAD circle.

Srivastava et al (1986) developed the Extended Velocity Azimuth Display (EVAD) algorithm. Here Equation 3 is applied to several elevation angles of a volume scan for a given height interval. Plotting $[2 a_0 / (r \cos \alpha)^{-1}]$ versus $[2 \tan \alpha / r^{-1}]$ yields a slope of W_p and an intercept of $\nabla \cdot U_H$. Vertical air speeds are derived through an integration of the anelastic continuity equation:

$$\rho_a \nabla \cdot U_H + \frac{\partial(\rho_a w_a)}{\partial z} = 0 \quad (4)$$

where ρ_a is the air density (obtained from sounding data) and z is the height above the ground. The Doppler mean terminal velocity is then calculated from

$$V_t = w_a - W_p \quad (5)$$

Thus, a profile of terminal velocities representative of the larger drops is obtained. Matejka and Srivastava (1991) refined the algorithm by incorporating statistical weighing factors.

2. IMPLEMENTATION

Volume scans were performed using the University

of Toronto X-band Doppler radar. When the pulse repetition frequency (PRF) was set at 2000 Hz, the resolution of radial velocity was 0.125 ms^{-1} and the unambiguous velocity v_a 16 ms^{-1} .

Two data sets were used for the analysis. The first was acquired from September 25 to November 4, 1990 in Penang, Malaysia during the Tropical Rain Experiment in collaboration with the Malaysian Meteorological Service. The other data set was collected at the University of Toronto in Toronto, Canada from March 27 to November 1, 1991. For both locations, ground clutter effects were mainly confined to elevation angles of 7° or less.

Velocity Azimuth Display (VAD) fits were performed using the least squares method of Rabin and Zrnić (1980). The Extended VAD (EVAD) analyses were based on Srivastava et al (1986) and Matejka and Srivastava (1991). Sounding data were used to determine the air density profile for the EVAD calculations. Hodographs of VAD-derived horizontal winds were plotted to check for self-consistency. For each volume scan, derived values of particle fall speed, vertical air speed, and terminal velocity were evaluated using decreasing allowances for gaps ($\geq 30^\circ$) in the VAD data rings, and errors assessed.

For many events vertically pointing radar data were also acquired. Doppler mean velocities were compared with derived values from preceding and subsequent volume scans.

Profiles of terminal velocities for raindrops of constant diameter were calculated using the equations of Best (1950), Foote and du Toit (1969), and Beard (1976). These profiles incorporated the sounding data and were compared with those of the EVAD-derived terminal velocities.

At ground level, RSDs were determined using a disdrometer of the type described in Joss and Waldvogel (1967). The data were electronically grouped into 1024 size categories according to the calibration that appears in McFarquhar and List (1993). In light rain, drop diameters of 0.25 to 5.0 mm could be measured. However, in very heavy rain only drops larger than 1.0 mm were detected. A plot of diameter versus time for each drop was constructed to determine time periods with reasonably constant drop size spectra. Time-averaged spectra were then used to determine the Doppler mean terminal velocity $\langle v \rangle$ according to the following equation:

$$\langle v \rangle \equiv \int_0^\infty v Z'(v) dv \left[\int_0^\infty Z'(v) dv \right]^{-1} \quad (6)$$

where Z' is the reflectivity factor per velocity interval

dv .

For two events in Penang, data collected aloft by a King Air research aircraft (owned by the Malaysian Meteorological Service) were available. The Particle Measuring System (PMS) 2DP laser spectrometer probe had an array of 32 photodiodes, each representing $200 \mu\text{m}$ for a maximum image size of 6.4 mm. Image data were processed using a center-in scheme. As for the disdrometer (JWD) data, Doppler mean velocities were calculated from time-averaged spectra using Equation 6. Variations in static pressure, as measured by a Rosemount 1201 Altitude Transducer, with temperature, as measured by a Rosemount probe, were consistent with sounding data. Thus, the sounding data and the measured static pressure were used to determine the aircraft height above ground. Flight course notes, and the true air speed evaluated from dynamic pressure values, were used for horizontal positioning.

3. RESULTS

Differences between the sets of terminal velocity equations did not significantly affect the results within the resolution of the analysis. Thus, the equations of Beard (1976) were consistently used for the terminal velocity profiles of constant drop diameter in the figures below. Some sample case results follow.

Figure 1 displays a particle fall speed profile derived from a volume scan commencing at 18:44 local time (Greenwich Mean Time plus 8 hours), November 2, 1990 in Penang, Malaysia. There were insufficient elevation angles to perform an EVAD analysis. However, with an elevation angle of 70° and stratiform conditions, the divergence term in Equation 3 is much less than the second term, and Equation 3 simplifies to:

$$W_p = a_0 (\sin \alpha)^{-1} \quad (7)$$

Radial velocities were determined to the nearest 0.125 ms^{-1} and the range resolution was 125 m, thus, the height resolution was $125 \text{ m} / (\sin 70^\circ)$, or 133 m. As expected, fall speeds increase sharply in the layer of enhanced reflectivities (bright band) where ice particles are melting. Below the melting layer, the fall speed profile from the radar data closely follows that of a 2.0 mm diameter raindrop. Faster fall speeds aloft are due to the lower pressure. This correlation suggests very little evolution of the RSD at least among the larger drops. JWD data were averaged for the period 18:40 to 18:50, and aircraft 2DP data for the period 18:46:05 to 18:46:19. The latter period coincided with the time the aircraft was traversing the VAD circle at this height above ground (1640 m). The derived Doppler mean fall speeds for both the JWD and the 2DP data were also close to that of a 2.0 mm diameter drop. Thus, the three instruments, operating with different measuring principles and data reduction schemes, gave results consistent with very little evolution of the large drop

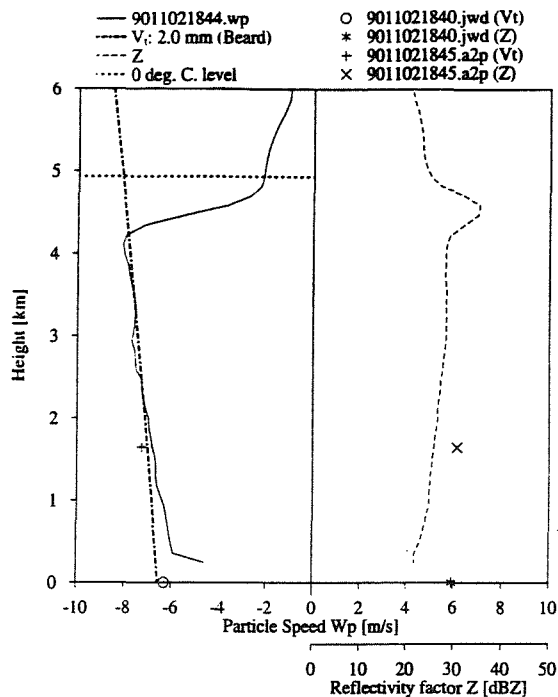


Figure 1: Profile of VAD-derived vertical speed (solid line) and radar reflectivity (dashed line) from the 70° elevation angle of the volume scan beginning at 18:44 on November 2, 1990. The dash-dot line is the calculated terminal velocity profile for a 2.0 mm diameter drop. Derived values for JWD data (○) and aircraft 2DP data (+) are also included. The horizontal dotted line represents the 0°C level.

spectrum below the melting layer.

Figure 2 displays EVAD-derived terminal velocities for a volume scan commencing at 19:44 on October 25, 1990, also at Penang. Data were collected at elevation angles of 62.0°, 50.6°, 34.7°, and 17.0°. The vertical resolution of the EVAD analysis was 250 m. Between 1.7 and 3.5 km height there is a very close correspondence between the EVAD-derived terminal velocities and those expected for a drop of 2.5 mm diameter. This is also in good agreement with the averaged value for the JWD data for the period 19:49 to 19:57. The smaller terminal velocities below 1.0 km height correspond to the onset of heavier precipitation, a pattern confirmed by analysis of preceding and subsequent volume scans. There is a blip of higher terminal velocities just below the melting layer. This pattern is also evident in earlier and later volume scans and by inspection of the radial velocity field for the higher elevation PPIs. It appears very large drops which have melted from large ice particles are quickly depleted by collisions with smaller drops. The rapid evolution occurred despite moderate rainrates of 3 mm h⁻¹. When the most collisionally unstable large drops are depleted, subsequent spectral evolution is much slower.

In Figure 3, a similar pattern can be detected with data taken on October 28, 1990 with the radar pointed

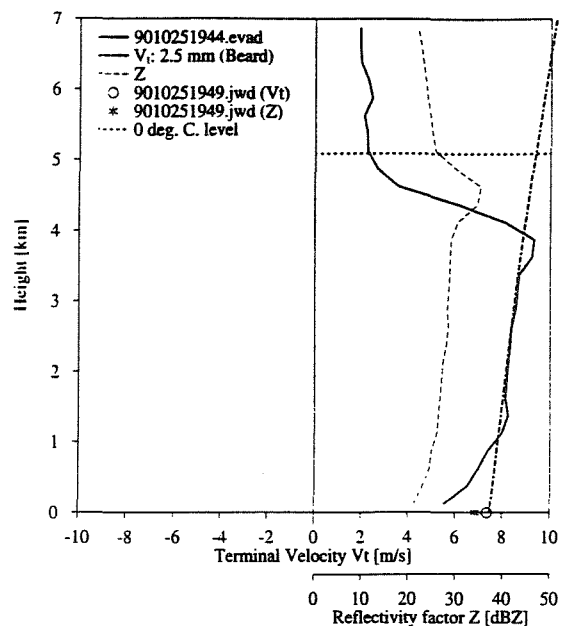


Figure 2: As in Figure 1 but for EVAD-derived terminal velocities (solid line) from the volume scan beginning at 19:44 on October 25, 1990. Dash-dot line is the calculated terminal velocity profile for drops of diameter 2.5 mm.

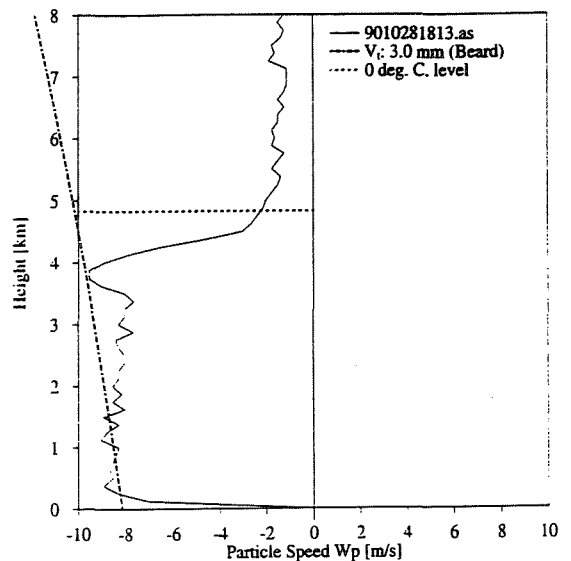


Figure 3: Profile of particle fall speeds for a vertically-pointing scan taken at 18:13 on October 28, 1990. The dash-dot line is the calculated terminal velocity profile for 3.0 mm diameter drops. The horizontal dotted line represents the 0°C level.

vertically. Here the vertical resolution was 125 m. The fall speeds are likely enhanced by a downdraft as this event was more convective and rainrates of 15 mm h⁻¹ were calculated from JWD data.

Data collected in Toronto on June 15, 1991 illustrate

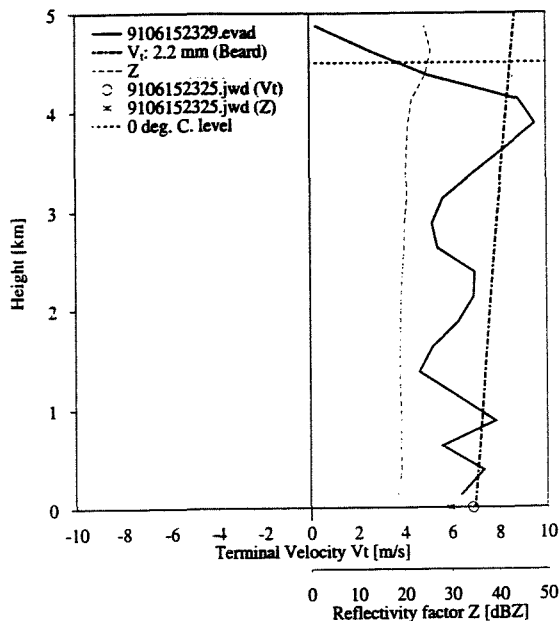


Figure 4: As in Figure 2 except for the volume scan beginning at 23:29 on June 15, 1991. The dash-dot line is the calculated terminal velocity profile for 2.2 mm drop diameters.

how important differences in sampling volumes can be. In Figure 4, the EVAD-derived profile for the volume scan commencing at 23:29 local time (Greenwich Mean Time minus 4 hours) is presented. Data were collected at elevation angles from 5° to 75° at intervals of 5° , with radial velocity resolution of 0.25 ms^{-1} and range resolution of 250 m. Though statistical errors are somewhat larger than for the events presented earlier, there is still an indication of very large drop breakup just below the melting layer. However, data from a vertically pointing scan taken at 23:22 do not show a pattern caused by large drop breakup. Inspection of the velocity and reflectivity PPIs revealed that larger drops at the melting layer base passed by to the south of the radar. They were close enough to be detected by the volume scans, but were missed by the vertically pointing scans.

4. SUMMARY

Doppler radar-derived profiles for raindrop terminal velocities have been generated for raindrop terminal velocities using an Extended Velocity Azimuth Display analysis of volume scan data. These closely follow expected profiles for raindrops of constant diameter. Comparisons with Doppler mean terminal velocities derived for disdrometer data obtained at the ground and

laser spectrometer data acquired aloft further support the scenario of very slow evolution of the large drop spectrum below the melting layer in cold stratiform rain of light to moderate intensity. More rapid spectral evolution briefly occurs if very large drops emerge from the melting layer. Comparisons with data from vertically pointed scans indicate the potential for large sampling differences.

Acknowledgments This research was sponsored by the Atmospheric Environment Service, AES. Considerable assistance for the data set collected in Malaysia was provided by the Malaysian Meteorological Service. Additional help was supplied by Dr. David Hudak, Greg McFarquhar, and Dr. Paul Lawson. One of the authors (RN) is indebted to AES and the Walter Sumner Foundation for postgraduate scholarships.

REFERENCES

- Beard, K.V., 1976: Terminal velocity and shape of cloud and precipitation drops aloft. *J. Atmos. Sci.*, **33**, 851-864.
- Best, A.C., 1950: Empirical formulae for the terminal velocity of water drops falling through the atmosphere. *Quart. J. Roy. Meteor. Soc.*, **76**, 302-311.
- Doviak, R.J., and D.S. Zrnić, 1984: *Doppler Radar and Weather Observations*, Academic Press, San Diego, U.S.A., 458 pp.
- Foote, G.B., and P.S. du Toit, 1969: Terminal velocity of raindrops aloft. *J. Appl. Meteor.*, **8**, 249-253.
- Joss, J., and A. Waldvogel, 1967: Ein Spektrograph für Niederschlagstropfen mit automatischer Auswertung. *Pure Appl. Geophys.*, **68**, 240-246.
- Lhermitte, R.M., and D. Atlas, 1961: Precipitation motion by pulse-Doppler radar. *Proc. 9th Conf. Radar Meteorology*, Kansas City, Amer. Meteor. Soc., 218-223.
- Matejka, T.J., and R.C. Srivastava, 1991: An improved version of the extended velocity-azimuth display analysis of single-Doppler radar data. *J. Atmos. Oceanic Technol.*, **8**, 453-466.
- McFarquhar, G.M., and R. List, 1993: The effect of curve fits for the disdrometer calibration on raindrop spectra, rainfall rate, and radar reflectivity. *J. Appl. Meteor.*, **32**, 774-782.
- Rabin, R., and D. Zrnić, 1980: Subsynoptic-scale vertical wind revealed by dual Doppler-radar and VAD analysis. *J. Atmos. Sci.*, **37**, 644-654.
- Srivastava, R.C., T.J. Matejka, and T.J. Lorello, 1986: Doppler radar study of the trailing anvil region associated with a squall line. *J. Atmos. Sci.*, **43**, 356-377.

PHYSICAL CHARACTERISTICS OF SOME CLOUDS WITHIN A MONTANE FOREST CANOPY

Tom DeFelice

ASG, Lapham Hall, UWM, Milwaukee, Wi. 53211, USA

1. INTRODUCTION

The microphysical characteristics of the within canopy clouds that traversed a predominantly Fraser Fir and Red Spruce forest in the Mt. Mitchell State Park, NC on Mt. Gibbs (2,006 m ASL and ≈ 3.3 km southwest of the 2,038 m MSL summit of Mt. Mitchell - $35^{\circ}44'05''$ N, $82^{\circ}17'15''$ W) were measured between 2 - 22 June 1993. The latter measurements are needed to help validate acidic deposition fluxes to forests that are derived from above canopy measurements.

2. BACKGROUND

Standard meteorological, physical and chemical data have been monitored (≈ 17.5 m above ground level, AGL) above a Fraser Fir and Red Spruce stand (average top ≈ 7.5 m AGL) at the Mt. Gibbs site since the summer of 1986. The above canopy platform includes a passive string cloudwater collector (ASRC), and an optical droplet sizing probe (FSSP-100). The within canopy sampling platform is similarly equipped, except there were no windfield, pressure, nor radiation instruments.

The FSSPs were calibrated before and after the field season by their manufacturer. The alignment of the optics was checked before and after each event, but neither realignment nor significant correction to the pre-season calibration were necessary.

The June 1993 canopy FSSP data are continuously acquired every second by a software controlled pulse height analyzer, accumulator that typically sent 12 s totals to disk. The only available FSSP data for the concurrent above canopy cloud are in the form of an

average of 1 to 4 15 min values.

3. RESULTS AND DISCUSSION

The average within canopy cloud had ≈ 250 (± 65) drops cm^{-3} , an ave. diameter of ≈ 9.5 (± 2.9) μm , and a liquid water content, LWC, of ≈ 0.11 (± 0.08) g m^{-3} during 8 events (out of 11 total) between 13 and 22 June 1993. The events lasted between 1.5 h to ≈ 24.5 h (21-22 June 1993), or a total of ≈ 41 h. The concurrent average above canopy cloud had ≈ 600 (± 250) drops cm^{-3} , an ave. diameter of ≈ 6.5 (± 0.7) μm , and a LWC of ≈ 0.23 (± 0.17) g m^{-3} .

The within canopy cloud acquired, statistically significant modes within $\approx 1\text{-}2$ μm and $\approx 4\text{-}9$ μm , herein arbitrarily termed the 'canopy-induced' cloud mode during calmless portions (student t-test: $\geq 99\%$ or 97% confidence for the 5 or 15 min ave. 12 s data) of this sampling campaign. The canopy-induced cloud mode was intermittently observed in time, and occurred independent of precip. presence (Fig. 1).

The temporal measurements of N_d , LWC, especially, indicate periods of well correlated LWC & N_d during sampled events (Fig. 1). Choularton et al. (1986, QJRMS 112, 131-148) found LWC & N_d to be well correlated at 4 m above the ground, due to droplet loss to the ground. The canopy N_d , LWC and within canopy volume distribution were split into 3 groups (i.e. Present, Transitional and Absent as outlined below), with the intent that Absent is expected to be predominant if the measured cloud structure is primarily due to droplet loss to ground. Present- The within canopy cloud exhibits the 'canopy-induced' modal structure during 15 min.

periods of non-positively correlated N_d & LWC data points. Short periods of no correlation between N_d & LWC may be included. Transitional- 'canopy-induced' modal structure exists when the N_d & LWC were not always pos. correlated during a concurrent 15 min. period. Absent- The 'canopy-induced' modes were absent during concurrent periods of pos. correlated N_d & LWC.

The within canopy cloud structure becomes Transitional after the onset of water loading on the canopy. Eventually the water load reaches a supercritical amount and is shed, or resuspended. The expelled water might then be collected by the collector and/or by other trees, and otherwise

contribute to the formation of the 'canopy-induced' mode of the within canopy cloud (Present). Once the canopy trees are below their subcritical loadings (this does not necessarily mean that they are water free), the 'canopy-induced' mode is modified (Transitional) and then disappears (Absent), and the process repeats. The latter could ultimately be coupled with present cloud deposition models to study cloud - canopy acid deposition related issues for example, and consequently warrants further investigation.

Acknowledgements - The UWM Graduate School Research Committee Grant 1993-1994. Dr. V.K. Saxena for use of his site.

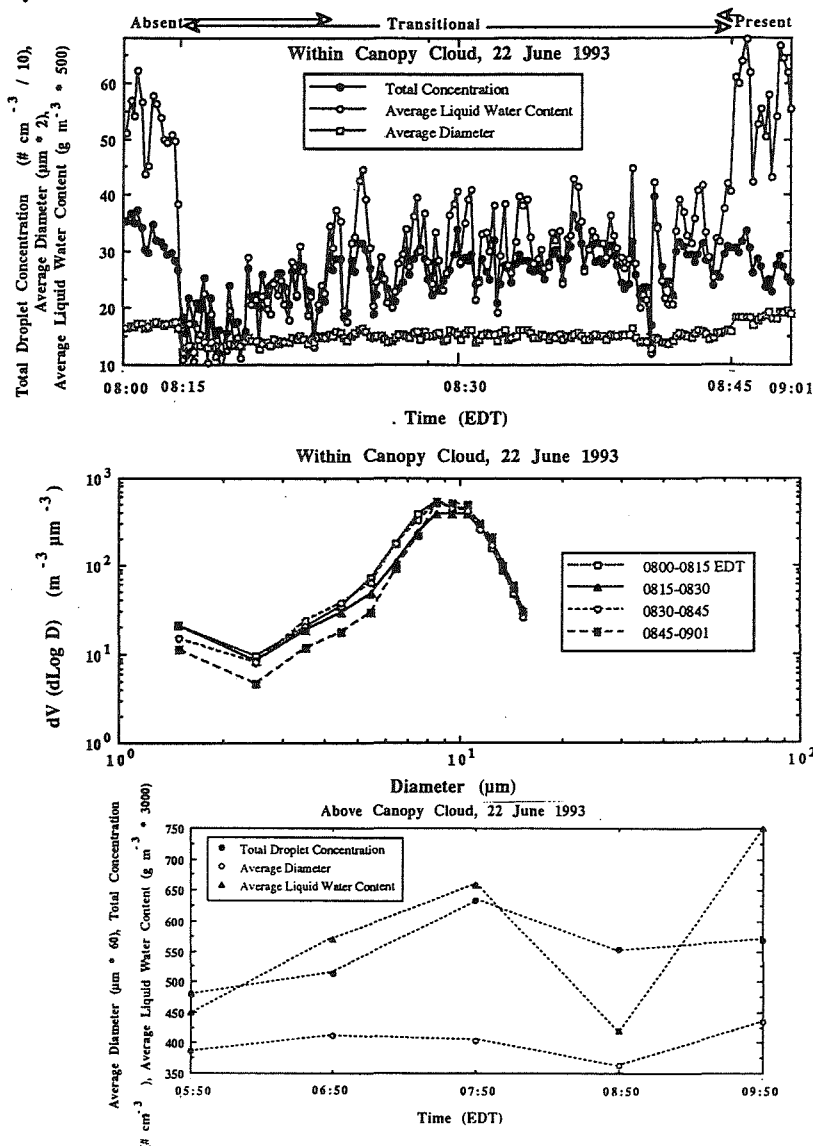


Fig. 1 Representative example of the temporal microstructure of the within canopy cloud during a cloud only period. Example is based on 12 s data for the within canopy cloud between 08:15 & 08:45 EDT 22 June 1993. Prior to 08:15 EDT and after 08:45 EDT the data are based on 60 s data. The available above canopy data point represent averages of 1 to as many as 4 15 minute averaged data.

LINEAR EDDY MODELING OF DROPLET SPECTRAL EVOLUTION DURING ENTRAINMENT AND MIXING IN CUMULUS CLOUDS

Chwen-Wei Su¹, Steven K. Krueger¹, Patrick A. McMurtry¹ and Philip H. Austin²

¹University of Utah, Salt Lake City, UT84112

²University of British Columbia, Vancouver, British Columbia, Canada

1. INTRODUCTION

Entrainment and mixing plays an important, yet not clearly quantified, role in the evolution of cloud droplet spectra. In many previous studies, researchers have assumed that mixing between a parcel of cloudy air and entrained environmental air is instantaneous. Recent observations (e.g., Brenguier 1993) indicate that a more detailed analysis must be considered. Such observations suggest the following conceptual picture of mixing: A cloud engulfs discrete blobs of clear air. Subsequent to this entrainment, deformation and stretching occur, reducing scalar length scales at a finite rate. As the length scales decrease, molecular mixing increases as a result of increased scalar gradients.

The effects of finite-rate mixing on droplet spectra have been debated for many years. Jensen and Baker (1989) studied droplet spectral evolution in a parcel of cloudy air after a single entrainment event. They used a simplified mixing model to implement the finite-rate mixing process. Grabowski (1993) used a similar approach. Su et al. (1995) used a more sophisticated turbulent mixing model, the linear eddy model (LEM) (Kerstein 1988; Krueger 1993) to study a similar problem. Recently this approach has been extended to include multiple entrainment events as a parcel rises as part of a cumulus cloud and to include entrainment of cloud condensation nuclei (CCN). In this paper we present results from a number of simulations using this approach regarding the effects of entrainment and mixing, entrained CCN, and droplet sedimentation on droplet spectral evolution in cumulus clouds.

2. THE MODEL

In a cumulus cloud, a parcel of cloudy air containing cloud droplets rises from cloud base to cloud top. As the parcel rises, it intermittently entrains blobs of environmental air. Meanwhile, turbulent deformation and molecular diffusion are on-going,

while cloud droplets grow or evaporate depending on their local microphysical environments.

To study entrainment and mixing in cumulus clouds, we have combined an entraining parcel model with explicit treatments of two distinct physical processes: turbulent mixing and condensation (or evaporation). Turbulent mixing is carried out by the LEM. Condensation (or evaporation) is performed by a droplet growth equation.

The LEM simulates the mixing process by explicitly representing turbulent stirring and molecular diffusion over a linear domain. Molecular diffusion is treated by solving a 1D diffusion equation. The key to realistically representing the effects of turbulent stirring in one spatial dimension is the manner in which the deformation processes is treated. This is done by spatial rearrangement of the scalar field in the linear domain. The rearrangement events are defined by (1) a length distribution characteristic of inertial range turbulence which represents the eddy size distribution in the turbulent flow under consideration, and (2) a frequency parameter that describes the rate of the rearrangement events. The rearrangement events affect a region of the domain determined by randomly sampling the length distribution. The length scale distribution and the rate parameters can be determined by the parameters: L (integral length scale), η (Kolmogorov scale) and D_T (turbulent diffusivity). Given the initial scalar distribution and the mixing parameters, the mixing process is simulated by solution of the diffusion equation, interrupted by discrete rearrangement events. Because the domain is restricted to a 1D representation, it is affordable to resolve all the relevant length scales of the flow field, even for relatively high Reynolds-number flows.

In our parcel model, entrainment occurs in discrete events. During each event, a region of the parcel is replaced with environmental air. The size of the entrained blob is a specified parameter and the mean frequency of entrainment is chosen to be consistent with the observed fractional rate

of entrainment. Krueger et al. (1995) combined this entrainment parameterization with the LEM and a simple bulk condensation scheme. They used the resulting “explicit mixing” parcel model (EMPM) to calculate the properties of observed Hawaiian cumulus clouds. The EMPM was able to realistically predict the in-cloud scalar means and variances.

The current model is the same as the EMPM except that it explicitly calculates each droplet’s diffusional growth following Fukuta and Walter (1970):

$$r_j \frac{dr_j}{dt} = \frac{S - A_1 + A_2}{A_3 + A_4},$$

where r_j is the radius of the j th droplet; S is the supersaturation ratio; A_1 and A_2 are the correction factors for curvature and solution effects; A_3 and A_4 are the heat conduction and the vapor diffusion terms. In the current model, in which the domain is 20 m long and has a cross-sectional area equal to the square of the grid size which is 1.7 mm, the growth of several thousand individual cloud droplets is predicted based on each droplet’s local microphysical environment. The latter is determined by the effects of both mixing and droplet growth.

3. RESULTS

We are using our model to calculate the evolution of droplet spectra in Hawaiian cumulus clouds. For these simulations, the parcel ascent rate is 2 m/s, the integral scale is 20 m, the Kolmogorov scale is 1 cm, and the turbulent dissipation rate is $0.01 \text{ m}^2/\text{s}^3$. We can determine the turbulent diffusivity, which is required by the LEM, from the dissipation rate (Krueger 1993). Because we found that droplet sedimentation has no significant impact on droplet evolution, most of the calculations reported in this section did not include droplet sedimentation. Unless otherwise stated, entrained air contains CCN.

3.1 Effects of entrainment and mixing

Figure 1 shows the droplet spectral evolution for 3 different cases: adiabatic ascent (no entrainment), instant mixing (with discrete entrainment events), and finite-rate mixing. Each frame in a column shows the droplet spectrum at a different height, from cloud base to 1.5 km above cloud base. For the instant mixing and finite-rate mixing cases, the fractional entrainment rate is 1.0 km^{-1} , the entrained blob size is 2 m, and 17 separate entrainment events occur between cloud base at 450 m and cloud top at 1550 m.

The adiabatic case exhibits a narrow droplet spectrum that simply shifts to larger droplet sizes as the parcel rises. The middle column shows the evolution of the droplet spectrum for the instant mixing case. The predominant feature of this case is the development of multiple isolated peaks. Upon entrainment of dry air, evaporation can occur, but as the parcel rises, small droplet growth is rapid as a result of the instant mixing of entrained CCN that are activated after entrainment. Because the pre-existing droplets are much larger than the newly activated ones, the development of isolated peaks results. For finite-rate mixing (third column), very broad droplet spectra develop. This occurs because the finite mixing rate leads to significant fine-scale structure which allows individual droplets to experience quite different local environments, resulting in different growth rates.

We also performed the similar simulations as Figure 1 but without entraining CCN. The droplet spectra become narrower and droplets grow bigger for both cases. This is because the droplet number decreases each time the parcel replaces a blob of clear air. For the instant mixing, it does not have isolated peaks anymore. For the finite rate mixing, it still has a slightly broadened droplet spectrum because of the activation of a few totally evaporated droplets.

3.2 Effects of entrained CCN

Figure 2 shows the effects on droplet spectral evolution of including CCN with the entrained air. To illustrate this effect, sequences from two simulations are presented: one with entrained CCN and one without. To isolate the effect of the entrained CCN from other effects, only one entrainment event is allowed (at 250 m above cloud base) and all other parameters are identical in the two simulations. Figure 2a shows the spectrum before the entrainment events. After the entrainment event, the spectra begin to broaden due to evaporation while some droplets totally evaporate (Figure 2b). As the parcels continue to rise, the entrained CCN, as well as CCN from some of the totally evaporated drops, are activated (Figure 2c). Figure 2d indicates that smaller droplets exist with entrainment of CCN. This is a result of more droplets in the entrained CCN case competing for the same amount of water vapor.

3.3 Effects of sedimentation

The effects of droplet sedimentation were also studied. Figure 3 shows that sedimentation has no significant impact on droplet evolution for the cases studied here, which are similar to the finite-

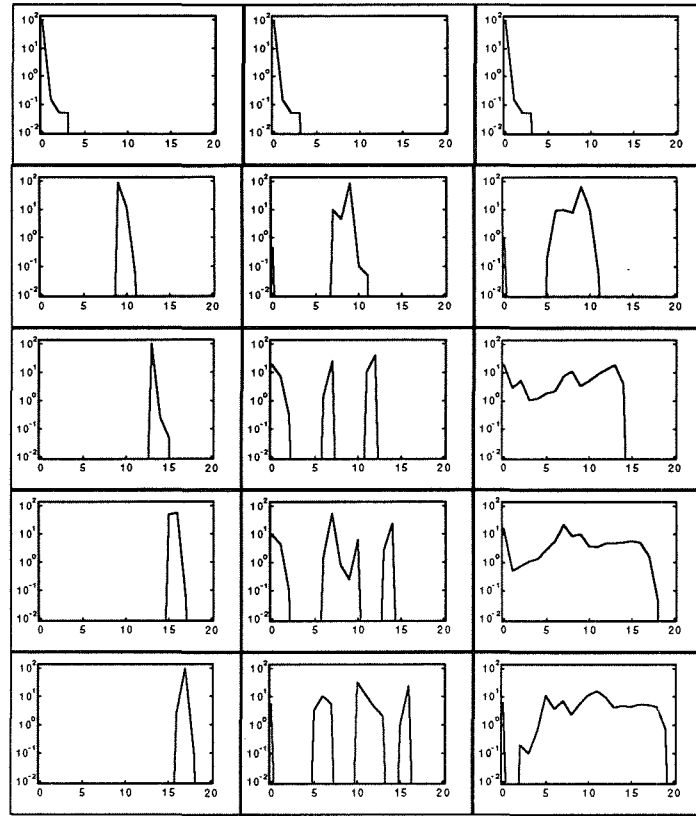


Figure 1. Droplet spectral evolutions at different heights from cloud base to 1100 *m*. The left, middle and right columns are adiabatic, instantaneous mixing and finite rate mixing cases, respectively. The vertical axis is the droplet concentration ($\#/cm^3 \cdot \mu m$), the horizontal axis is the droplet radius (μm).

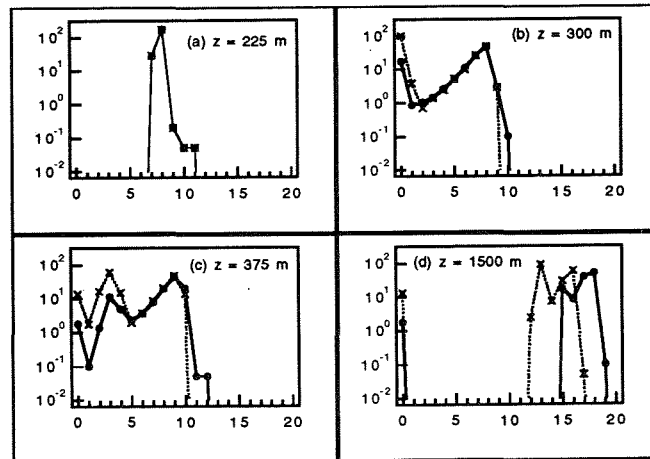


Figure 2. The spectral comparisons at different heights. One entrainment event at 250 *m* above cloud base. Dotted line - parcel with entrained CCN. Solid line - parcel without entrained CCN. The labels and units are the same as Figure 1.

rate mixing case shown in Figure 1. A few cases were run with artificially large terminal velocities (for example, 0.21 m/s). In these cases, including sedimentation produced narrower droplet spectra. This suggests that sedimentation tends to lessen the differences between the *average* environments that droplets experience.

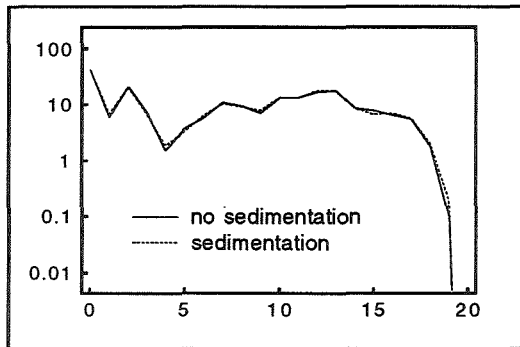


Figure 3 Almost identical droplet spectra for with sedimentation and without. The height is 1500 m above cloud base. The labels and units are the same as Figure 1.

4. CONCLUSIONS AND FUTURE STUDIES

By combining droplet microphysics and a parametrization of entrainment with the LEM, we have developed a useful tool for studying droplet spectral evolution in growing cumulus clouds. Our results show that 1) entrainment and mixing can broaden droplet spectra; 2) after entrainment, entrained CCN and the CCN from totally evaporated droplets can be activated when the parcels continue to rise; and 3) droplet sedimentation has no major effects on droplet spectral evolution. Additional parametric studies are currently in process. Preliminary comparisons with observations of Hawaiian cumulus clouds show qualitative agreement.

5. ACKNOWLEDGEMENTS

This work was supported in part by NSF Grant No. CTS9258445 and ONR grant N00014-91-J-1175. Our studies in mixing are also supported by the Advanced Combustion Engineering Research Center and the Utah Supercomputer Institute. Funding for the Combustion Center is received from the National Science Foundation, the State of Utah, 26 Industrial participants, and the U.S. Department of Energy. The Utah Supercomputer Institute is funded by the State of Utah.

6. REFERENCES

- Brenguier, J.-L., 1993: Observations of cloud microstructure at the centimeter scale. *J. Appl. Meteor.*, **32**, 783-794.
- Fukuta, N., and L.A. Walter, 1971: Kinetics of hydrometeor growth from a water spherical mode. *J. Atmos. Sci.*, **28**, 1160-1172.
- Grabowski, W. W., 1993: Cumulus entrainment, fine-scale mixing, and buoyancy reversal. *Quart. J. Roy. Meteor. Soc.*, **119**, 935-956.
- Jensen, J.B., and M.B. Baker, 1989: A simple model of droplet spectral evolution during turbulent mixing. *J. Atmos. Sci.*, **46**, 2812-2829.
- Kerstein, A.R., 1988: Linear eddy modeling of turbulent scalar transport and mixing. *Comb. Sci. and Technol.*, **60**, 391-421.
- Krueger, S.K., 1993: Linear eddy modeling of entrainment and mixing in stratus clouds. *J. Atmos. Sci.*, **50**, 3078-3090.
- Krueger, S.K., C.-W. Su, and P.A. McMurtry, 1995: Linear eddy modeling of entrainment and mixing in cumulus clouds. *Preprints, Conference on Cloud Physics*, Dallas, Texas, Amer. Meteor. Soc., 559-564.
- Su, C.-W., S.K. Krueger, P.H. Austin and P.A. McMurtry, 1995: Linear eddy modeling of droplet spectral evolution during turbulent mixing in cumulus clouds. *Preprints, Conference on Cloud Physics*, Dallas, Texas, Amer. Meteor. Soc., 565-568.

THE EFFECT OF TURBULENCE ON THE BROADENING OF THE DROPLET SPECTRUM IN CLOUDS AT THE INITIAL STAGE OF THEIR EVOLUTION

Mark B. Pinsky¹, Alexander P. Khain¹ and Zev Levin²

¹Department of Atmospheric Sciences, the Hebrew University of Jerusalem, Israel

²Department of Geophysics and Planetary Sciences, Tel Aviv University, Israel

1. INTRODUCTION

Observed size distributions of droplets are considerably broader than those computed for ascending isolated air parcels cooled adiabatically (Warner, 1969a,b). Such models fail to produce droplets of $r > 20 \mu\text{m}$ unless one assumes the presence of giant condensation nuclei (e.g., Mason and Chien, 1962). The problem becomes ever more complicated, if we take into account the fact that diffusional growth under uniform supersaturation makes the initial spectrum narrower (Roger and Yau, 1989) reducing the growth by coagulation even of relatively large but similar size drops.

Mixing with the surroundings is usually thought to be one of most likely mechanisms for spectrum broadening. Two main mechanisms of mixing were suggested: lateral homogeneous mixing (e.g. Warner 1973; Mason and Jonas, 1974), and inhomogeneous mixing (e.g., Baker and Latham 1982; Jensen and Baker, 1989). Note, that the mechanisms of cloud air mixing with the unsaturated surrounding air retard the increase in the maximum drop size. For example, the maximum radii of drops obtained in the studies of Manton and Warner (1982), Jensen and Baker (1989) do not exceed $12 \mu\text{m}$, while the adiabatic drop size is larger by about $1 \mu\text{m}$ to $2 \mu\text{m}$. Hence, the problem of large drops formation cannot be resolved using the mixing mechanisms mentioned above.

Although many mechanisms have been suggested, the presence of giant and ultragiant CCN is still thought to be the main source of large cloud drops (Beard and Ochs, 1993). However, such an outstanding role of giant and ultragiant CCN seems doubtful. The concentration of giant and ultragiant CCN greatly decreases with height. Besides, in spite of the enormous variability in the CCN spectra in the atmosphere, a substantial consistency of the shape of small droplets size distributions can be seen from observed data characteristics of droplet size spectra in clouds (e.g., Johnson et al, 1992; Levin, 1992, Garrett and Hobbs, 1995; Politovich, 1993).

Note, that Politovich and Celik (1995) revealed the existence of high correlation between the presence of large drops at the base of stratiform clouds and the intensity of turbulence.

In this paper we analyze possible effects of small-scale turbulence on the formation of the cloud droplet size spectrum under diffusional growth. It is known that clouds are the areas of enhanced turbulence. The

intensity of turbulence varies widely depending on the type of clouds and their age. Thus, Mazin et al. (1984,1989) observed in stratus clouds a turbulent energy dissipation rate $\epsilon \approx 10 \text{ cm}^2\text{s}^{-3}$ as compared to $\epsilon \approx 100 \text{ cm}^2\text{s}^{-3}$ in small cumuli.

2. MECHANISM OF THE DROPLET SPECTRA FORMATION

We assume that there is a horizontal cloud layer with preset supersaturation referred to as an external parameter. The simplified geometry of the problem is satisfactory enough to simulate the droplet spectrum evolution within an unmixed updraft or within the layer of about one hundred meter depth above the cloud base, where the contribution of lateral mixing with the surroundings is negligible. We will take into account three processes of the formation of the droplet size spectra: condensational growth of droplets, mean velocity updraft and turbulent diffusion of small cloud droplets. The velocity of the air is looked upon as a superposition of a horizontally uniform updraft and the turbulent velocity fluctuation field. Activation of drops is assumed to take place in the vicinity of the condensation level. Then the drops move within a turbulent flow. As the mean flow velocity is directed upward, most of the drops are lifted and exit from the top of the cloud layer considered.

We will determine droplet size distribution at any cloud level according to the sizes of drops crossing the level for the first time. It is obvious, that due to turbulent diffusion droplets released at the cloud base reach a particular level within the cloud at different time instances. Thus, there is a distribution of "ages" in these droplets. Differences in the droplets history cause differences in the size of droplets reaching a particular level above the cloud base.

The experiments were carried out as follows. One thousand drops of a certain radius (or a certain initial size distribution) are initially located at the base of the cloud layer. The turbulent diffusion of droplets is simulated by the Monte Carlo method. The tracks of drops within the layer were calculated using the drop motion equation (Khain and Pinsky, 1995) with a time step of 0.01 s. The diffusional growth of moving drops was calculated as in Rogers and Yau (1989). Turbulent velocity fluctuation field was generated by a model of homogeneous and isotropic turbulence (Pinsky and Khain, 1995a,b). To take into account the changes of a turbulent flow during the

drop motion, a new realization of the turbulent velocity field was generated each 20 s of the drop motion. Droplet size distributions at any cloud level obtained, when using this approach, can be interpreted as distributions obtained by time or spatial averaging or by averaging over an ensemble of clouds with similar characteristics. These averaged spectra should be close to those measured by aircraft flying across a cloud, when the spectra are calculated using spatial averaging over scales greater than an external turbulence scale (several tens of meters).

3. RESULTS

The droplet size spectrum (histogram) at the distance of 100 m above the cloud base (and their approximations by "shifted" gamma-distribution) resulting under the conditions typical of stratiform clouds with a mean vertical updraft of 0.25 m s^{-1} , the low magnitudes of supersaturation (0.05%) and weak turbulence $\varepsilon = 10 \text{ cm}^2 \text{ s}^{-3}$ is presented in Fig. 1. This spectrum resulted from the initial delta-distribution with drops of $1 \mu\text{m}$ -radius. The width of the droplet spectra reaches $5 \mu\text{m}$.

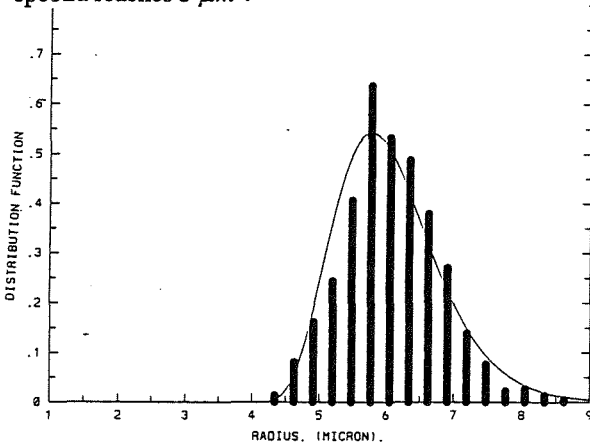


Figure 1. Droplet spectrum at the distance of 100 m above cloud base of a "stratiform" cloud

Fig. 2 illustrates the droplet size spectra at 100 m resulting from conditions, typical of early cumulus clouds: the mean vertical velocity is set 1 m/s , the dissipation rate $\varepsilon = 50 \text{ cm}^2 \text{ s}^{-3}$ and the supersaturation 0.2%. One can see that at 100 m above cloud base the radii of the largest drops are greater than $8 \mu\text{m}$. The modal radius at this level is about $6 \mu\text{m}$. The spectrum measured by Warner at 150 m above the base of a maritime cumulus cloud is presented (in relative units). A good agreement of the measured spectrum with the calculated drop size distribution can be seen.

Note, that due to the turbulence effect, the maximum drop radius substantially exceeds the modal value, which in its turn, seems to be close to the value reached under the adiabatic ascent within a non-turbulent flow. This is a most important result, because all mixing mechanisms lead to a decrease of the maximum drop size as compared to the adiabatic ascent value. Curves approximating the size

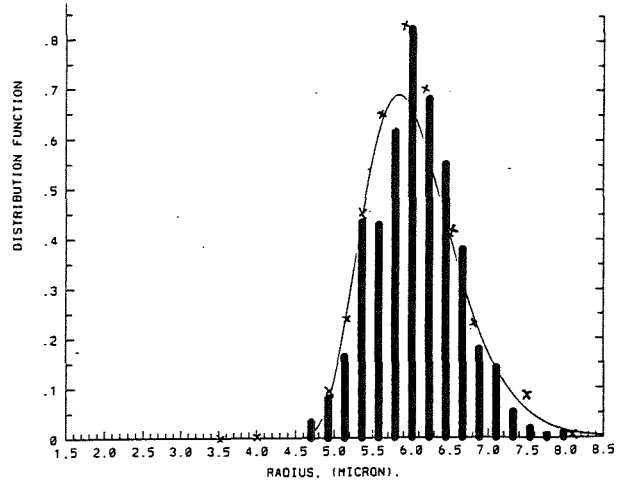


Figure 2. Size droplet spectra at 100 m resulting from conditions, typical of early cumulus clouds. The spectrum measured by Warner at 150 m above the base of a maritime cloud is drawn by crosses.

distributions were plotted using the "shifted" gamma-distribution function:

$$n(r) = \frac{(r - r_o)^\alpha \exp[-(r - r_o)/\beta]}{\Gamma(\alpha + 1)\beta^{\alpha + 1}}, \quad (1)$$

if $r \geq r_o$ and $n(r) = 0$, if $r < r_o$. In (1) r is the droplet radius, r_o is the smallest droplet radii at a given level and $\Gamma(\alpha + 1)$ is the gamma-function. Parameters of (1) have been evaluated using the method of maximum likelihood.

In Fig. 3 we plot the vertical profile of dispersion σ/\bar{r} obtained in the calculations at the supersaturation of 0.2%, and the dissipation rate of $100 \text{ cm}^2 \text{ s}^{-3}$, along with vertical profiles measured during adiabatic ascents through the base and updraft core of a growing cumulus sampled 28 June 1981 (Politovich, 1993). In the calculations a shifted gamma distribution spectrum (1) with the modal value of $2.8 \mu\text{m}$ and $r_o = 1.8 \mu\text{m}$ was used. The mean vertical velocity was taken as 3 m s^{-1} , which is close to the measured value at the top of the ascent.

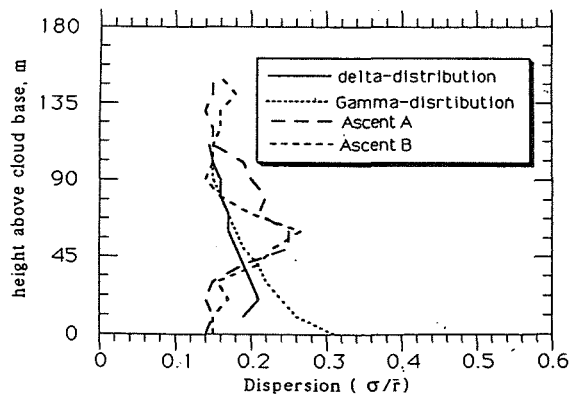


Figure 3. Vertical profiles of dispersion in droplet size distribution obtained in the calculations as well as measured within updraft core of a growing cumulus (Politovich, 1993)

Taking into account that existing theories are unable to predict even the order of the dispersion value in an unmixed ascent area (see discussion in Politovich, 1993) the agreement of the results of the calculations with the observed data can be considered to be quite satisfactory. The values of the dispersion are high near cloud base, then they gradually decrease with height. At 100 m above the cloud base the values of the dispersion are close to 0.15, both in the observations and calculations. The vertical profiles of the mean radius, calculated under the same conditions as in Fig. 3 as well as those measured by Politovich (1993) within updraft core of a growing cumulus agree satisfactory as well (not shown).

As it was demonstrated above, the evolution of the spectrum of droplets ascending within an unmixed cloud core is determined by two opposite mechanisms. The first one is related to different rates of diffusional growth of droplets of different sizes and tends to make the initial size distribution narrower. The second mechanism is related to the turbulent droplet diffusion and leads to the spectrum broadening due to different "ages" of droplets. The comparable contribution of these mechanisms to the evolution of the initial spectrum depends on the parameters of the initial droplet spectrum itself, on the value of supersaturation, the intensity of turbulence and the vertical velocity of the flow. Under low intense turbulence and large vertical velocities, the droplet spectrum will be determined mainly by the initial spectrum of activated droplets and will tend to become narrower as was considered by Mordy (1959). Under initial narrow spectrum and low mean vertical updraft velocity, the droplet spectrum at some distance above the cloud base will be determined mainly by the impact of turbulence. One can expect, that under some conditions the contributions of the two mechanisms can compensate each other, so that standard deviation will not change with height. These three possible results are illustrated in Fig. 4, where the standard deviations of droplet size distribution are shown as a function of the distance above cloud base. All curves in Fig. 4 were calculated from the initial narrow gamma-distribution spectrum with the modal radius of $1 \mu\text{m}$ under the supersaturation 0.1%, the vertical mean velocity of 0.5 m/s and different values of the dissipation rate: 0, 20, 50 and $100 \text{ cm}^2\text{s}^{-3}$.

Note, that all these values (except the case of zero turbulence) can be regularly observed in clouds of different types. One can see, that the drop size distribution becomes narrower under zero turbulence, small intense turbulence (up to $10 \text{ cm}^2\text{s}^{-3}$) makes this narrowing weaker. Under $\epsilon = 20 \text{ cm}^2\text{s}^{-3}$ the width of the droplet spectrum remains nearly constant with height. Turbulence with the dissipation rate $\epsilon > 30 \text{ cm}^2\text{s}^{-3}$ is able to make the initial spectrum broader. In the first four cases the spectrum at 100 m above the cloud base is determined mainly by the initial size distribution, while in the last case the contribution of turbulence is substantial. In Fig. 5 we present the drop size spectra at 100 m above cloud

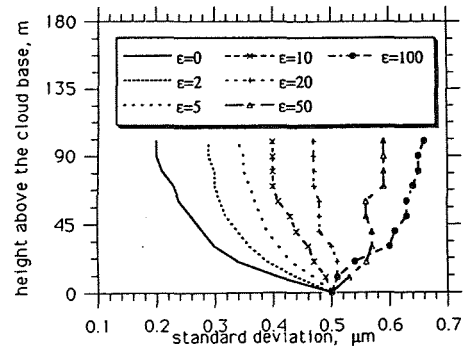


Figure 4. Standard deviations of droplet size distribution as a function of the distance above cloud base under different values of the dissipation rate: 0, 20, 50 and $100 \text{ cm}^2\text{s}^{-3}$.

base resulting from the different initial drop size distributions described by (a) the delta-type size distribution with drops of $1 \mu\text{m}$ radius, (b) the gamma-distribution function (1) with $\alpha = 2$ and the mean radius of $1.7 \mu\text{m}$ respectively. As can be seen, the spectra are similar and, therefore, in this case the final spectrum at 100 m above the cloud base "forgets" the initial distribution.

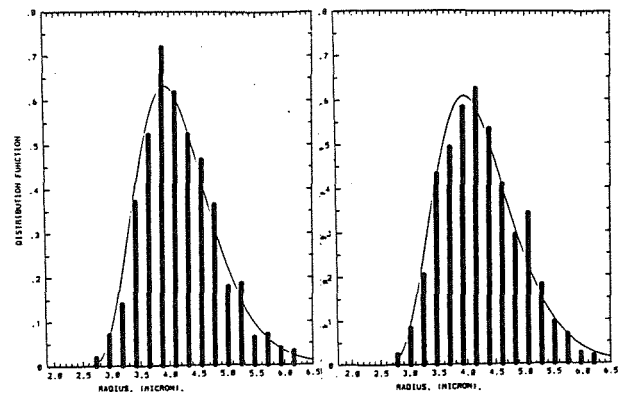


Figure 5. Drop size spectra at 100 m above the cloud base resulting from the different initial drop size distributions described by (a) the delta-type size distribution with drops of $1 \mu\text{m}$ radius, (b) the gamma-distribution function (3.1) with $\alpha = 2$ and mean radius of $1.7 \mu\text{m}$, respectively.

In Fig. 6 a histogram of the droplet size distribution at 100 m above cloud base resulting from the initial delta-function type spectrum with $5 \mu\text{m}$ - radius droplets is presented. The conditions of the runs were as follows: supersaturation of 0.5%, vertical updraft of 0.5 ms^{-1} and the dissipation rate of $\epsilon = 100 \text{ cm}^2\text{s}^{-3}$. This last example shows that under the conditions mentioned the radii of drops can reach a value as large as $20 \mu\text{m}$. The formation of drops of this size is usually attributed to the activation on the giant CCN.

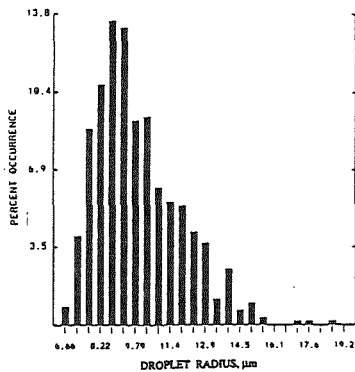


Figure 6. Histogram of the droplet size distribution under supersaturation of 0.5% and the dissipation rate of $\varepsilon = 100 \text{ cm}^2 \text{ s}^{-3}$.

4. CONCLUSIONS

Turbulent diffusion is shown to be an effective mechanism leading to the broadening of the spectrum of cloud droplets in clouds. Droplets move within the turbulent flow along different tracks. As a result they cross the same levels within the cloud having different ages and, consequently, different sizes. In contrast to the mechanisms of spectrum broadening related to mixing with the surrounding air, turbulent diffusion provides droplets larger than those growing within an adiabatic non-turbulent ascent. Under vertical velocities and supersaturations typical to stratiform maritime clouds and early cumulus clouds (at 100 m above cloud base), the drop size spectrum was found to be rather wide, containing drops with radii of up to $20 \mu\text{m}$. This spectrum contains large drops, whose formation had been attributed earlier only to the nucleation of giant CCN particles. Note, that turbulence intensity usually increases with height. Besides, the areas of enhanced turbulence exist along lateral cloud boundaries and cloud top. The spectrum broadening must be especially pronounced in these areas. Of course, in the vicinity of cloud boundaries the effects of mixing with the surrounding air become very important.

The role of turbulence in the initial drop spectrum broadening has to be taken into account in numerical cloud models. As a matter of fact, the increments of finite-difference grids in cloud models in the vertical are usually greater than 200 m. Thus, at the lowest model level above cloud base, the size drop spectrum has been already formed and it differs from the spectrum of drops just activated.

5. ACKNOWLEDGMENTS

This study was supported by the Israel Science Foundation administered by The Israel "Academy of Sciences and Humanities" and by Lady Davis Foundation of the Hebrew University of Jerusalem.

6. REFERENCES

- Baker, M.B. and J. Latham, 1982: A diffusive model of the turbulent mixing of dry and cloudy air. *Quart. J. Roy. Met. Soc.*, **108**, 871-898.
- Beard, K., V., and H. T. Ochs III, 1993: Warm-rain initiation: an overview of microphysical mechanisms. *J. Appl. Meteor.*, **32**, 608-625.
- Jensen, J.B., and M.B. Baker, 1989: A simple model of droplet spectral evolution during turbulent mixing. *J. Atmos. Sci.*, **46**, 2812-2829.
- Khain A. P., and M. B. Pinsky, 1995: Drops' inertia and its contribution to turbulent coalescence in convective clouds: Part 1: drops fall in the flow with random horizontal velocity. *J. Atmos. Sci.*, **52**, 196-206.
- Levin, Z., 1992: Effects of aerosol composition on the development of rain in the Eastern Mediterranean-potential effects of global warming, WMO Workshop on Cloud Microphysics and Applications to Global Change., 10-14 August, Toronto. WMP Report, No 19, 115-120.
- Manton, M.J. and J. Warner, 1982: On the droplet distribution near the base of cumulus clouds. *Quart. J. Roy. Met. Soc.*, **108**, 917-928.
- Mason, B.J. and C.W. Chien, 1962: Cloud-droplet growth by condensation in cumulus. *Quart. J. Roy. Met. Soc.*, **88**, 136-142.
- Mason, B.J. and P.R. Jonas, 1974: The evolution of droplet spectra and large droplets by condensation in cumulus clouds. *Quart. J. Roy. Met. Soc.*, **100**, 23-38.
- Mazin, I. P., V. I. Silaeva, and M. A. Strunin, 1984: Turbulent fluctuations of horizontal and vertical wind velocity components in various cloud forms. *Izvestia, Atmospheric and Oceanic Physics*, **20**, 6-11.
- Mazin, I. P., Khrgian, A. Kh. and Imyanitov, I. M., 1989: *Handbook of Clouds and Cloudy atmosphere*. Gidrometeoizdat, 647 p.
- Mordy, W., 1959: Computations of the growth by condensation of a population of cloud droplets. *Tellus*, **11**, 16-44.
- Pinsky M. B. and A. P. Khain, 1995: A model of homogeneous isotropic turbulence flow and its application for simulation of cloud drop tracks *Geophys. and Astr. Fluid Dynamics (in press)*
- Pinsky M. B. and A. P. Khain, 1995b: Simulations of drops' fall in a homogeneous isotropic turbulence flow *Atmosph. Research*. (in press).
- Politovich, M. K., 1993: A study of the broadening of droplet size distributions in cumuli. *J. Atmos. Sci.*, **50**, 2230-2244.
- Politovich, M.K., and F. Celik, 1995: Large droplet formation in stratiform clouds sampled during WISP 94. *Conference on Cloud Physics*, January 15-20, 285.
- Rogers R. R. and M. K. Yau, 1989: *A Short Course in Cloud Physics*, Pergamon Press., 293 p.
- Warner, J., 1969a: The microstructure of cumulus cloud. Part 1: general features of the droplet spectrum. *J. Atmos. Sci.*, **26**, 1049-1059.
- Warner, J., 1969b: The microstructure of cumulus cloud. Part 2: The effect on droplet size distribution of cloud nucleus spectrum and updraft velocity. *J. Atmos. Sci.*, **26**, 1272-1282.
- Warner, J., 1973: The microstructure of cumulus cloud: Part 4: The effect on the droplet spectrum of mixing between cloud and environment. *J. Atmos. Sci.*, **30**, 256-261.

A WIND TUNNEL STUDY OF THE EFFECT OF TURBULENCE ON THE COLLISIONAL GROWTH OF WATER DROPS

O. Vohl, S.K. Mitra, and H.R. Pruppacher

Institut für Physik der Atmosphäre, Joh.-Gutenberg Universität Mainz

1. INTRODUCTION

Observations show the intensity of turbulence in clouds varies widely between energy dissipation rates of 20 up to $2 \cdot 10^3 \text{ cm}^2 \text{ s}^{-3}$ depending on the type of cloud and their age. A plot of observed values for the turbulent spectral energy density inside and outside atmospheric clouds is given in Figure 1.

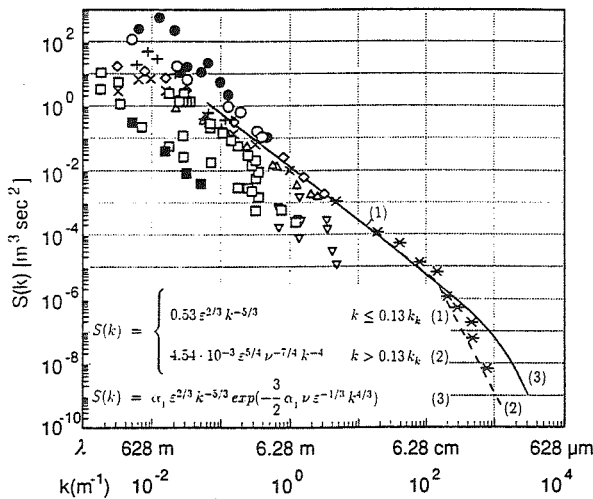


Figure 1: Turbulent energy spectra of vertical velocities as a function of wavenumber(k) and wavelength(λ), based on a large number of observers. Lines give theoretical formulations (1) and (2) based on Townsend(1976); (3) from Tennekes and Lumley(1972) based on Pao(1965)

Arenberg (1939) was perhaps the first to point out that turbulence in clouds may affect the collision of drops. However, he confined himself in his theoretical study to simple sinusoidal motions, a model also used later by Gabilly (1949). East and Marshall

(1954) and East (1957) extended Gabilly's work by incorporating in their treatment the random character of the turbulent motion, neglected however, the spatial variability of the drops. Saffmann and Turner (1956) included the spatial variability of drops and also improved the characterization of the turbulent field, concentrated however, only on the behavior of nearly equal size drops. A subsequent effort along the same lines can be found in the work of Levin and Sedunov (1966).

About 10 years later de Almeida (1979a,b) studied the effect of turbulence on collision efficiency of drops based on the fact that a turbulent, unsteady flow imports a degree of randomness to the drop trajectories as the drops interact hydrodynamically. Based on the work of Basset (1910) and Tchen (1947), de Almeida formulated the equations of motion for a pair of drops interacting hydrodynamically, while falling under gravity in turbulent air, assuming that the drag on a drop as given by Klett and Davis (1973), forces the relative motion. To simulate the random flow of the air past the drop a Monte Carlo method was employed. As constraints on the components of the random flow vector a velocity correlation applicable to the inertial subrange was formulated. Again about 10 years later Grover and Pruppacher (1985) used a one dimensional model to study the effects of vertical velocity fluctuations of the air on efficiencies with which spherical particles collide while falling from one turbulent eddy to the next. The turbulent char-

acteristics of the air were assumed to be described by the empirical, one-dimensional, longitudinal turbulent energy spectrum of Townsend (1976) for the viscous subrange. A few years later Reuter et al. (1988) formulated a model for computing the collection kernel of drops colliding in turbulent air based on stochastic diffusion equation. With these he determined the displacements of drops assumed originally to be contained in spatially separated eddies which at a later stage overlap. To compute collection kernels the collision efficiency itself was assumed to be not affected by turbulence, and to be given by the laminar efficiencies. Seven years had to pass before the problem of turbulent effects on the collisional growth of drops was again taken up this time by Khain and Pinsky (1995) and Pinsky and Khain (1995,1996, pers. comm.). These authors formulated a turbulent model to determine the effect of turbulence on the growth rate of drops growing by collision. They showed that turbulence can cause a significant broadening of the drop size spectrum as a result of the turbulence induced relative velocities between the drops and the surrounding air due to differences in the drop's inertia, the latter causes an increase in the number of collisions per unit time.

Unfortunately, none of the four recent models is able to treat the problem of drop collision in turbulent air with all its facets and therefore cannot withstand considerable criticism (see e.g. Grover and Pruppacher, 1985; Cooper and Baumgardner, 1989; Pruppacher and Klett, 1978, 1996). In addition the models voice completely opposing views. Thus de Almeida (1979) found considerable enhancement of the collision efficiency in turbulent air even at moderate values of ϵ , Grover and Pruppacher (1985) found turbulent enhancement only at the highest possible atmospheric values for ϵ and for drops with radii less than $50 \mu m$, a result essentially also obtained by Reuter et al. (1988) from their model for the collision kernel. In con-

trast, again, the model of Khain and Pinsky (1995) produced large effects of turbulence on the collisional growth of drops even at moderate values of ϵ .

Unfortunately, till today no experiments have been carried out to verify or reject the various theoretical turbulence models, except for the experiments of Woods et al. (1972), and Jonas and Goldsmith (1972) who found rather significant effects of laminar shear flows on the collision efficiency of drops if the drops were smaller than $25 \mu m$ in radius.

2. THE PRESENT EXPERIMENT

In order to make a more detailed attempt to determine the effect of turbulence on the collisional growth of drops, we carried out experiments in the Mainz vertical wind tunnel. After numerous tests we were able to show that drops could be freely floated in this tunnel, despite the presence of turbulent air stream, as long as the turbulence was confined to the "core" of the air stream. We also were aware of the fact that, in order to be somewhat realistic, the turbulent energy spectrum, produced by the turbulence forming body, had to resemble the energy spectrum observed in the atmosphere. In addition, since the interaction distances between colliding drops in clouds are of the order of centimeter or less (see Grover and Pruppacher, 1985), the turbulent energy spectrum in the tunnel core had to resemble the atmospheric spectrum particularly at wavenumbers larger than $100 m^{-1}$ (see Figure 1). The turbulent energy spectrum at the level of observation used for the present collisional growth studies is given in Figure 2. We note that this spectrum meets reasonably well the requirements for $k > 100 m^{-1}$. Drops of radii between $50 \mu m$ and $500 \mu m$ were injected into the tunnel air (turbulent or laminar) which carried a continuous stream of smaller drops produced by a battery of ultrasonic nebulizers. The drop size spec-

trum produced was peaked at 4 to 6 μm radius, and the liquid water content of the drop cloud was 1 to 3 g m^{-3} inferred from the dewpoint of the completely evaporated cloud sucked out of the tunnel. The laminar flow had a low turbulence level of less than 0.3 %. With this setup the growth rate of a drop of given size in laminar flow was compared to the growth rate of the same drop size in turbulent flow.

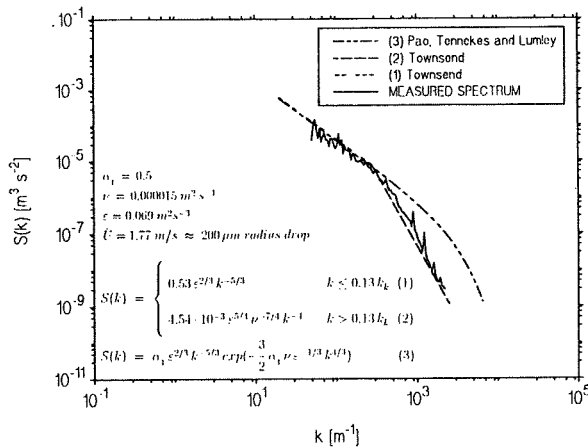


Figure 2: Variation of the turbulent energy spectrum with wavenumber. Comparison of windtunnel data with theoretical formulations of Townsend(1976), Tennekes and Lumley(1972) and Pao(1965).

3. RESULTS

From figures which will be presented during the conference (clarity would require an oversize) we can deduce the following conclusions from our experiments:

- (1) For values of ϵ of the order of a few hundred $\text{cm}^{-2} \text{s}^{-3}$ drops of radii near 100 μm grow at the expense of smaller drops ("continuous growth") at a rate which progressively increases with time above the rate in laminar flow.
- (2) Inclusion of our experimental conditions in the turbulent model of Khain and Pinsky produces the same trend

but affects the growth rate somewhat less than that observed. However in the model of Khain and Pinsky shear effects (which were present in our wind tunnel experiments) were at the time of writing this abstract not yet included. Also in the model the collision efficiency was taken to be that for laminar flow.

- (3) Although the observed and theoretical effects of turbulence on the "continuous growth" were found to be significant but small, large effects are expected to result if drops are allowed to grow stochastically in an ensemble of drops. This conclusion is in agreement with the computations of Khain and Pinsky.

ACKNOWLEDGEMENTS

Fundings for this study were provided by the SFB 233 (Project B8) supported by the DFG.

REFERENCES

- Arenberg, D., 1939: Turbulence as the major factor in the growth of cloud drops. *Bull. Amer. Meteor. Soc.*, **20**, 444-448
- de Almeida, F.C., 1979a: The collision problem of cloud droplets moving in a turbulent environment. Part II: Turbulent collision efficiencies. *J. Atmos. Sci.*, **36**, 1564-1576
- de Almeida, F.C., 1979b: The effects of small-scale turbulent motions on the growth of a cloud drop spectrum. *J. Atmos. Sci.*, **36**, 1557-1563.
- Basset, A.B., 1910: *Quart. J. Pure Appl. Math.*, **41**, 369.
- Cooper, W.A., and D. Baumgardner, 1989: Comment on "The collection kernel for two falling cloud drops subjected to random perturbations in a turbulent air flow: A stochastic model". *J. Atmos. Sci.*, **46**, 1165-1167.

- East, T.W.R., and J.S. Marshall, 1954: Turbulence in clouds as a factor in precipitation. *Quart. J. Roy. Meteor. Soc.*, **80**, 26-471
- East, T.W.R., 1957: An Inherent Precipitation Mechanism in Cumulus Clouds. *Quart. J. Roy. Meteor. Soc.*, **83**, 61-76
- Gabilly, A., 1949: On the role that turbulence can play in the coalescence of cloud droplets. *Ann. Geophys.*, **5**, 233-234
- Grover, S.N., and H.R. Pruppacher, 1985: The effect of vertical turbulent fluctuations in the atmosphere on the collection of aerosol particles by cloud drops. *J. Atmos. Sci.*, **42**, 2305-2318.
- Jonas, P.R., and P. Goldsmith, 1972: The collection efficiencies of small droplets falling through a sheared air flow. *J. Fluid Mech.* **52**, 593-608.
- Khain, A.P., and M.B. Pinsky, 1995: Drop inertia and its contribution to turbulent coalescence in convective clouds. Part I: Drop fall in the Flow with random horizontal velocity. *J. Atmos. Sci.*, **52**, 196-204.
- Klett J.D., and M.H. Davis, 1973: Theoretical collision efficiencies of cloud droplets at small Reynolds numbers. *J. Atmos. Sci.*, **30**, 107-117.
- Levin, L.M., and Yu.s. Sedunov, 1966: Gravitational coagulation of charged cloud drops in turbulent flow. *it Pure Appl. Geophys.*, **63**, 185-196.
- Pao, Y.H., 1965: Structure of turbulent velocity and scalar fields at large wave numbers. *Physics of Fluids*, **8**, 1063-1075.
- Pruppacher H.R., and J.D. Klett, 1978: *Microphysics of Clouds and Precipitation*, Reidel, 714 pp.
- Pruppacher H.R., and J.D. Klett, 1996: *Microphysics of Clouds and Precipitation*, Reidel, 2nd ed.
- Reuter, G.W., R. de Villiers and Y. Yavin, 1988: The collection kernel for two falling cloud drops subjected to random perturbations in a turbulent air flow: A stochastic model. *J. Atmos. Sci.*, **45**, 765- 773.
- Saffman, P.G., and J.S. Turner, 1956: On the collision of drops in turbulent clouds. *J. Fluid Mech.*, **1**, 16-30.
- Tchen, C.M., 1947: *Ph.D. Thesis*, Den Haag, Holland.
- Tennekes H., and J.L. Lumley, 1972: *A First Course in Turbulence*, MIT Press, 300pp.
- Townsend, A.A., 1976: *The Structure of Turbulent Shear Flow*, 2nd ed., Cambridge University Press, 93-99.
- Woods, J.D., J.C. Drake and P. Goldsmith, 1972: Coalescence in a turbulent cloud. *it Quart. J. Roy. Meteor. Soc.*, **99**, 758-763.

OBSERVED VS CALCULATED RATES OF GROWTH BY COALESCENCE

William A. Cooper,¹ Charles A. Knight,¹ and Jean-Louis Brenguier^{2†}

¹National Center for Atmospheric Research,* Boulder, CO, USA

²METEO-FRANCE (CNRM/GMEI), Toulouse, France

1. INTRODUCTION

The objective of this study is to determine if conventional calculations of growth by condensation and coalescence are adequate to explain the observed rates of precipitation development in warm clouds. Measurements from radar are used to determine the elapsed times between the appearance of clouds and the appearance of precipitation in those clouds. In situ measurements of the hydrometeor size distributions in the same clouds, collected by three instrumented aircraft, documented the sizes of drops responsible for the observed echoes.

The observations are from the Small Cumulus Microphysics Study (SCMS), conducted from 15 July to 13 August 1995 in eastern Florida at a site on the Kennedy Space Flight Center. Key instruments were the NCAR CP-2 radar (cf. Knight and Miller 1993), used to measure the radar reflectivity at 3 and 10 cm wavelength, three instrumented aircraft (the NCAR C-130, the Meteo-France Merlin, and the University of Wyoming King Air), and ground-based and airborne video recorders. At X-band, the NCAR CP-2 radar has 200 kW peak power, 44.5 dB antenna gain, and 0.95° beamwidth. RHI scans were used in sectors that spanned target cells or clusters of cells, with spacing between scans of 1–2°. Clouds within about 20 km of the radar were emphasized to ensure good sensitivity and resolution in the radar data, and the aircraft concentrated on clouds for which there was early documentation of cloud development by the radar.

2. CALCULATED COALESCENCE RATES

The calculations used in this paper represent the effects of condensation and coalescence during adiabatic ascent of a closed parcel. The technique used was described by Cooper et al. (1994). Growth by condensation was treated by allowing the size assigned to each bin to change without any reassignment of droplets to new bins, and a modified Kovetz

and Olund (1969) scheme was used to represent the effects of coalescence.

The CCN concentration was assumed to be 300 cm^{-3} at 1% supersaturation, and to increase as (supersaturation)^{0.7}, because these values produced reasonable agreement with observed droplet concentrations and are consistent with other estimates of CCN concentrations in this location. However, this functional form must be modified for the largest particles. The aerosol size distributions measured during this experiment showed a slope approximately consistent with that of a "Junge" spectrum for diameters from about 0.1–10.0 μm ; for soluble particles this shape would require that the CCN concentration be proportional to (supersaturation)² in this size range. For particles larger than 10 μm in diameter, the concentration decreased still more rapidly with size, so that for soluble particles the CCN concentration at very small supersaturations would vary as (supersaturation)⁴. Therefore, the natural CCN size distributions used in this paper include three regions to represent these three different variations with supersaturation.

The collision efficiencies were taken to be those of Klett and Davis (1973). For radii larger than 70 μm , the Beard and Grover (1974) representations of the collision efficiencies were used. Coalescence efficiencies as parameterized by Beard and Ochs (1984) were included in these calculations, but the detailed size distributions resulting from break-up were not; instead, collisions not resulting in coalescence were assumed to preserve the initial drop sizes.

Conditions were selected to represent the ascent of an unmixed parcel in the measured sounding for 10 August 1995, a day for which there are good observations available from the SCMS. That sounding was sufficiently unstable that an unmixed parcel would ascend from the cloud base (observed to be at a pressure of 926 mb, temperature 21.3°C, and altitude 730 m MSL) to well above 500 mb. However, observed clouds were confined initially to below about 2 km, apparently breaking through that level only after the early turrets had brought sufficient moisture to that level. Many of the turrets

*Sponsored by the National Science Foundation.

†Also Affiliate Scientist, NCAR.

studied by the research aircraft had core regions that appeared unmixed or only slightly mixed, but they were also quite small (1–2 km in diameter) and so formed skinny turrets that rapidly rose to a level where mixing inhibited further ascent.

The resulting drop size distributions are shown in Fig. 1. The parcel reached an altitude of 1.8 km after 200 s, and 4.5 km after 400 s. The calculated radar reflectivity factors were -12 dBZ after 200 s, -5 dBZ after 320 s (at 3.0 km), and 0 dBZ after 400 s.

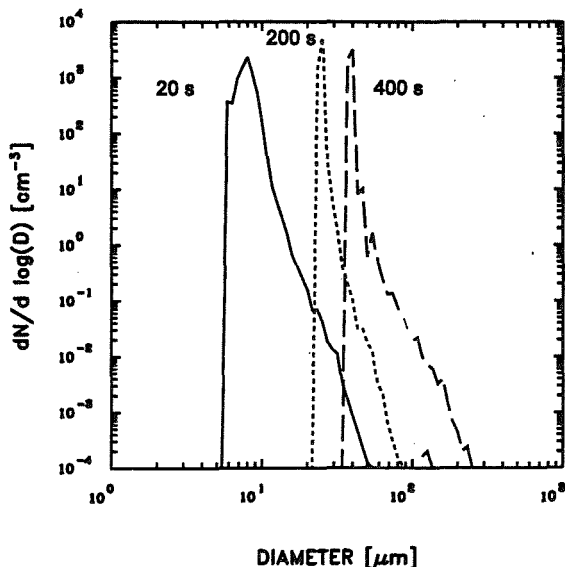


Fig. 1: Drop size distributions calculated after 20, 200, and 400 s of ascent from cloud base.

3. OBSERVATIONS

From about 14:30 to 17:30 UTC, the radar and the three research aircraft conducted coordinated studies of developing clouds located within about 20 km of the CP2 radar. The time-height history of the maximum X-band radar reflectivity for one of these clouds is shown in Fig. 2. After about 14:55, the descending contours suggest the formation of precipitation having significant fall speeds, and at the end of the study reflectivities exceeding 40 dBZ were measured even though the cloud top barely reached 4.5 km (which was also the freezing level).

The aircraft passes through this cloud at 14:43 and 14:45 were through short-lived turrets that appeared to dissipate and be replaced by other connected turrets in a pulsing structure. The radar reflectivity slowly increased as the altitude of cloud top increased, until precipitation (suggested here by descending contours) began shortly before 15:00. Particularly interesting is the speed of precipitation

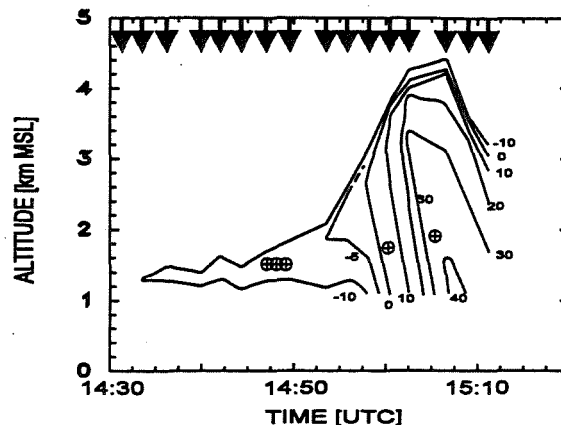


Fig. 2: History of the altitudes at which the indicated contours of radar reflectivity factor [dBZ] were observed as one cloud developed from 12–20 km from the radar on 10 August 1995. The arrows at the top of the plot show the times for which radar RHI scans through the cloud were available from which to construct this history of the maximum reflectivity, and the circled-plus symbols show the altitudes and times of passes through the cloud by the C-130 research aircraft.

development from 14:56 to 15:01, during which time the maximum reflectivity in the cloud increased from about -3 dBZ to 15: dBZ as the cloud top rose from 2.6 to 3.8 km. The rate of ascent of the cloud top corresponded to an average updraft of 4 m/s, similar to the updrafts measured in turrets in this vicinity (and in this cloud) during the aircraft passes. The video records from the research aircraft show that at 15:00–15:05 the cloud was a small-diameter single turret that rose rapidly to an altitude well above other turrets in the vicinity. There were no descending contours before about 14:56, and there was apparently no significant formation of precipitation before then. The rate of descent of the 10 dBZ contour after 15:01 corresponds to about 10 m/s, consistent with the fall of large raindrops.

All three aircraft carried Forward Scattering Spectrometer Probes (FSSPs) to measure the cloud droplet size distribution, and all carried Optical Array Probes (OAPs) for the detection of hydrometeors larger than cloud droplets. In the cases of the C-130 and King Air, the OAPs included two PMS 2D spectrometers (a 2DC and a 2DP) for measurement of drops having sizes from about 50–800 and 200–6400 μm , respectively. All three aircraft carried 1D spectrometer probes that covered the intermediate size range from about 30–300 μm . The Merlin also carried the Fast FSSP (Coelho et al. 1996).

The droplet size distributions measured near cloud base were very narrow, with typical diameters 80 m above cloud base of $10 \pm 1 \mu\text{m}$ and concentrations of about $200\text{--}300 \text{ cm}^{-3}$. The droplet size distribution measured at 14:43 UTC, at 1.5 km altitude and about 780 m above cloud base, was still quite narrow, and there were no droplets detected larger than $60 \mu\text{m}$ in diameter. The radar reflectivity calculated from the measured size distribution was about -16 dBZ .

The measurements at 15:01 UTC indicated a 1-km region with liquid water content near the value expected for adiabatic ascent and with a steady droplet concentration and low value of turbulence as expected for an unmixed region of cloud. The droplet size distribution measured in this region is shown in Fig. 3. The radar reflectivity factor calculated from the measured size distribution was still only about -10 dBZ , but in nearby regions of the cloud some $500\text{--}\mu\text{m}$ drops were encountered that gave a calculated radar reflectivity of about 10 dBZ . The size distribution of Fig. 3 contained more than $3/L$ drops with diameters larger than $80 \mu\text{m}$, so there was significant drizzle production by this time.

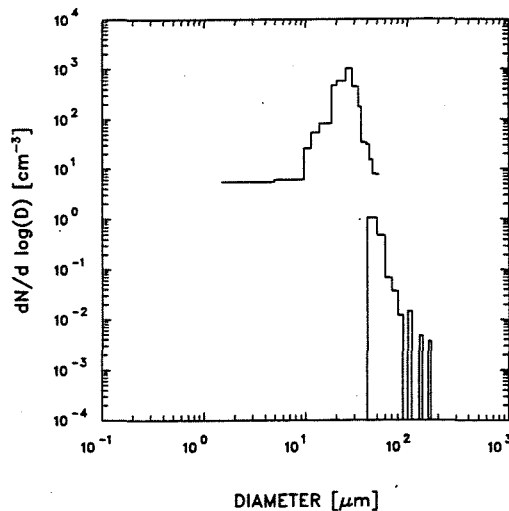


Fig. 3: Drop size distribution measured at 15:01 UTC, at an altitude of 1.7 km MSL. The smaller sizes were measured by an FSSP-100 and the larger sizes by a PMS 260X optical array probe.

On the last pass through the cloud, the size distribution contained still more drizzle, as shown in Fig. 4. The drizzle droplets were located on the edges of the region with highest updraft and highest liquid water content; in the core of the cloud, there was only a very low concentration of drizzle. The 2D spectrometers on the aircraft detected raindrops in a concentration large enough

to produce a calculated radar reflectivity factor of about 30 dBZ at this time, approximately consistent with the radar observations. This reflectivity was produced by a low concentration of large drops, however; the spectrum of Fig. 4 only represents a reflectivity of about -8 dBZ . Figure 2 shows that the cloud was far above the altitude of the aircraft at this time, so that it was possible for the larger droplets to have fallen from upper regions of the cloud.

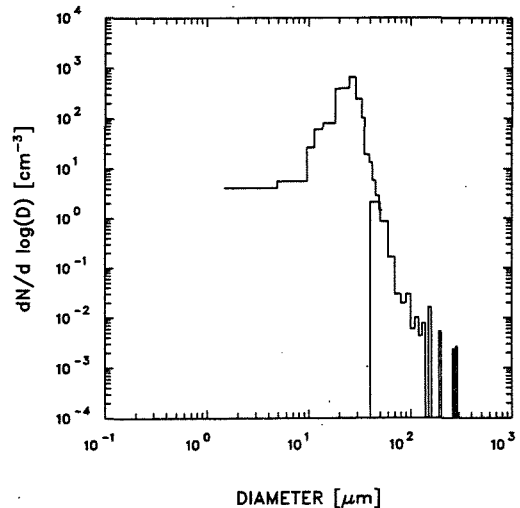


Fig. 4: Droplet size distribution, as in Fig. 3, for the cloud pass at 15:05 UTC and altitude 1.8 km MSL.

4. COMPARISON

The distribution labeled "200 s" in Fig. 1 shows the calculated result for altitudes near those of the observations shown in Figs. 3 and 4. The general shapes of the size distributions are similar, but there are significant differences. The development of drizzle drops (with diameters near $100 \mu\text{m}$) is more pronounced in the observations than in the calculations, and the main peak in the droplet size distribution is broader and includes more small droplets in the observations. However, it is known that the size resolution of the FSSP is inadequate to resolve narrow peaks such as those shown in Fig. 1, so the latter discrepancy may be mostly the result of instrumental deficiencies.

In the calculations for adiabatic ascent, radar reflectivity factors of -12 , -5 , and 0 dBZ were produced at altitudes of 1.8, 3.0, and 4.5 km, respectively. These altitudes are significantly higher than the altitudes at which the corresponding reflectivities were first measured by the radar, which were about

1.2 km for -10, 2 km for -5, and 2.6 km for 0 dBZ. The lower appearance of increased radar reflectivity apparently does not arise from more rapid coalescence than calculated, because these observed reflectivity factors are far above those calculated from measurements in the nearly unmixed regions of cloud. They also cannot arise solely from continued evolution with time once the cloudy parcels mix with the environment, because the calculations indicated that if parcels were mixed with the environmental air in proportions that gave neutral or negative buoyancy then the liquid water content was reduced so much that further growth by coalescence was insignificant. Even arbitrarily slowing the parcels to 25% of their updraft speed while maintaining adiabatic liquid water content only produced minor changes in the association between radar reflectivity and altitude.

A possible origin of this discrepancy might be the use of unrealistically narrow cloud droplet size distributions in the calculations. To investigate this possibility, the calculated droplet size distributions were artificially broadened to maintain a size dispersion of at least 0.2. This change lowered the altitudes at which the -5 and 0 dBZ reflectivities first appeared to 2.6 and 3.7 km, still substantially above the observed levels. The narrow size distributions measured by Brenguier and Chaumat (1996) are further indications that broadening substantially more than this did not occur in unmixed parcels. It therefore appears that underestimating the breadth of the droplet size distribution in unmixed parcels does not account for the discrepancy in the altitudes at which thresholds in the radar reflectivity first appear.

Because the observations in unmixed parcels do not support a much faster evolution than calculated, and because dilution slows the rate at which coalescence proceeds, it appears that mixing and sedimentation may be required to introduce drizzle drops, clearly produced in high concentrations during adiabatic ascent, into regions with liquid water content high enough to support the growth to raindrops. Indeed, raindrops that could account for the observed radar reflectivity were observed on the edges of the nearly unmixed regions encountered at 15:01 and 15:05, although not in their centers. Also, the drizzle concentrations were clearly higher at the edges of these regions than in their centers. This suggests that a recirculation mechanism may be needed to account for the rate at which rain appeared in this cloud.

5. CONCLUSIONS

Although the appearance of drizzle drops in rapidly ascending parcels of this cloud was slightly faster than predicted from the calculations, these results do not appear to indicate any major deficiencies in predictions of coalescence rates. In the framework used for these calculations, they fail to account for the rate of production of rainfall in this cloud, but that may be the fault of inadequate representation of the dynamics and especially of the possibilities of mixing and recirculation. These results are preliminary, and further investigation of these possibilities is needed and will be possible with the SCMS data set.

REFERENCES

- Beard, K. V., and S. N. Grover, 1974: Numerical collision efficiencies for small raindrops colliding with micron size particles. *J. Atmos. Sci.*, **31**, 543-550.
- Beard, K. V., and H. T. Ochs III, 1984: Collection and coalescence efficiencies for accretion. *J. Geophys. Res.*, **89**, 7165-7169.
- Brenguier, J.-L., and L. Chaumat, 1996: Condensational droplet growth in cumulus clouds. (This conference.)
- Coelho, A., J. L. Brenguier, and T. Bourrianne, 1996: A model for the Fast FSSP operation. (This conference.)
- Cooper, W. A., R. T. Bruintjes, and G. K. Mather, 1994: Some calculations pertaining to hygroscopic seeding with flares. Sixth WMO Scientific Conference on Weather Modification, Paestum, Italy, WMO, 677-680.
- Klett, J. D., and M. H. Davis, 1973: Theoretical collision efficiencies of cloud droplets at small Reynolds numbers. *J. Atmos. Sci.*, **30**, 107-117.
- Knight, C. A., and L. J. Miller, 1993: First radar echoes from cumulus clouds. *Bull. Amer. Meteorol. Soc.*, **74**, 179-188.
- Kovetz, A., and B. Olund, 1969: The effects of coalescence and condensation on rain formation in a cloud of finite vertical extent. *J. Atmos. Sci.*, **26**, 1060-1065.

CONDENSATIONNAL DROPLET GROWTH IN CUMULUS CLOUDS

Jean-Louis Brenguier^{1,2}, and Laure Chaumat¹

¹ METEO-FRANCE (CNRM/GMEI), Toulouse, France

² Affiliate Scientist at NCAR/ATD+MMM

1. INTRODUCTION

Since the contributions of Warner in the sixties (Warner, 1969), droplet spectrum broadening has become an active subject of interest in microphysics. According to the diffusion growth equation in a uniform updraft, uniform in the sense that the supersaturation is the same for all the droplets, the droplet size distribution should become narrower, while all the observations performed in clouds have always shown broad spectra. To avoid any ambiguity, it must be specified that this statement applies when the solute salt and the surface tension effects are negligible, namely in convective clouds, with a short life time. In stratus clouds, with low supersaturations and small vertical velocities, these effects can produce a significant broadening with time (Korolev, 1995).

If the diffusion growth equation for a single droplet is correct, then the spectrum broadening reflects the fact that, in real clouds, droplets in an ascending parcel are not exposed to the same supersaturation. There is a simple equation for the evolution of the mean supersaturation in a cloudy parcel, but it has not yet been possible to derive the complete set of equations for each droplet separately (Srivastava, 1989). It is more feasible to start with the statistics of the process by evaluating the various contributions to the variance of the supersaturation, or more precisely to the variance of its lagrangian integral for the ensemble of droplets (Manton, 1979; Cooper, 1989). All scales of the turbulence are likely to affect the droplet growth and their coupling with the microphysics is extremely complex. This explains why there is still no complete formalism for the condensation droplet growth in convective clouds. In addition, the broadening itself is poorly documented because the size resolution of airborne spectrometers is too coarse.

Our objective in this study is to document precisely the spectrum broadening with the Fast FSSP which provides a much better size resolution, in order to support efforts to improve the formalism.

2. EXPERIMENTAL METHODOLOGY

Dynamical structure at the cloud scale contributes significantly to spectrum broadening by mix-

ing of droplet populations that have followed different trajectories before their mixing with each other. Their condensation growth can be different either because the total concentration is different and/or because the amount of condensed water is different. For example, Telford and Chai, (1980) have shown that the recycling of droplet populations after dilution by mixing produces a significant broadening. Brenguier and Grabowski (1993) have simulated, with a 2-D model of cumulus cloud, the mixing of droplets ascending from the cloud base with droplets that have been activated much higher up at the edge of the cloud. The resulting spectrum is bimodal and evolves progressively to a broad spectrum when these mixing events are accumulated. However, it is always assumed in these studies that droplets following the same trajectory evolve according to the diffusion growth equation, and the broad spectra are obtained by the combination of narrow spectra. It is implicitly assumed that the droplet populations have grown separately before they are observed. Otherwise, the differences in the parameters governing the droplet growth would have no broadening effects. Consequently, there should be a significant chance of observing narrow spectra with an aircraft, especially when flying in an updraft with a LWC close to the adiabatic value.

Such spectra have never been observed but it was not possible to conclude that they were not present in clouds because of the uncertainties in the size distribution measurements, especially in terms of instrumental broadening of the measured spectra. In the Fast FSSP, the instrumental broadening has been considerably reduced. The instrument was flown in cumulus clouds during the SCMS experiment in 1995, and after complete analysis of the data, it can be concluded that the narrowest spectra observed throughout the cloud depth are still too broad when compared to the spectra predicted by uniform diffusion growth. The mixing of air parcels with different trajectories is therefore not sufficient to explain real size distributions. The contribution of the small scale turbulence must be considered too as in Cooper (1989) and Srivastava (1989).

Our methodology for quantifying this process is the following: all the cloud penetrations have been analysed. For each flight a typical narrow spectrum

measured at a low level (preferably at the cloud base) is selected as a reference. The narrowest spectra observed at higher levels are then compared to an adiabatic spectrum that is derived from the reference spectrum by adiabatic growth between the level of reference and the observation level.

Starting from the simplified equation for diffusional growth, where solute salt and surface tension effects are neglected,

$$\phi \frac{d\phi}{dt} = A(P, T) S, \quad (1)$$

where ϕ is the droplet diameter and S the supersaturation in the vicinity of the droplet, the general equation for the evolution of a spectrum of droplets growing in a uniform parcel can be written as:

$$f(\phi^2, z) = f(\phi^2 - \beta^2(z), z_0), \quad (2)$$

with $\beta^2(z) = 2 \int_{z_0}^z A S(z) dz$.

When the ascent from the reference level z_0 and the observation level z is adiabatic, the adiabatic value of the integral of supersaturation β_A^2 can be derived from the adiabatic amount of condensation between these two levels ΔLWC_A , by:

$$\frac{\pi}{6} \rho_w \int_0^\infty \phi^3 f(\phi^2 - \beta_A^2, z_0) d\phi^2 = \Delta LWC_A, \quad (3)$$

If the parcel is not uniform, or more precisely if the integral of supersaturation is not the same for all the droplets, the spectrum is broadened (Cooper, 1989). This broad spectrum $g(\phi^2)$ can be simply expressed as a function of the probability density function of the integral of supersaturation, $\Psi(\beta^2) d\beta^2$ (Brennguier, 1990), as:

$$g(\phi^2, z) = \int_0^{\beta_{max}^2} \Psi(\beta^2) f(\phi^2 - \beta^2, z_0) d\beta^2 \quad (4)$$

Our objective is to document this probability density function in cumulus clouds. When a reference spectrum is known, it is possible to derive the probability density function of the integral of supersaturation for any measured spectrum by inversion of Eq.4. However, as a first step, a simple parameterization of the function Ψ has been tested, with two degrees of freedom, the average integral of supersaturation $\bar{\beta}^2$ and its standard deviation $\sigma_{\beta^2} = \sqrt{2} \sigma_{\beta^2}^*$:

$$\Psi(\beta^2) = \exp \left[-\left| \frac{\beta^2 - \bar{\beta}^2}{\sigma_{\beta^2}^*} \right|^2 \right] \quad (5)$$

3. DATA ANALYSIS

The total droplet concentration is a crucial parameter for droplet growth. For the same spectral shape, and the same amount of condensed water, numerous droplets grow less than few droplets according to Eq.3. The total concentration is mainly determined by the CCN background and by the intensity

of the updraft at the CCN activation levels. During one flight, the measured concentrations are comparable but not exactly the same and the spectra measured at different levels are not directly comparable. In the analysis presented here, the reference spectrum f_0 is chosen at the cloud base among the narrowest measured spectra and its total concentration N_0 is calculated. A second spectrum is then selected among the narrowest spectra observed at a higher level and its total concentration N is also calculated. The reference spectrum is then rectified by preserving its shape but in such a way that its total concentration is equal to N : $f(\phi^2, z_0) = N/N_0 f_0(\phi^2, z_0)$

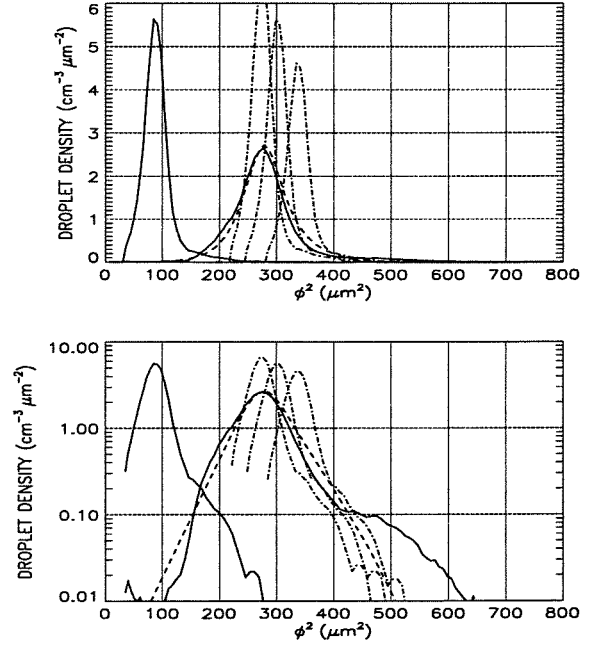


Fig.1 Comparison between a selected spectrum and the spectrum predicted by Eq.4, on a linear scale (a) and log scale (b). Solid lines represent the reference spectrum and the selected one. The dashed line corresponds to the predicted spectrum $g(\phi^2, z)$. Dot-dashed lines represent the adiabatic spectra for (from left to right) β_{A+}^2 , β^2 and β_{A-}^2 .

$z_0 = 714 \text{ m}$; $z = 989 \text{ m}$; $N_0 = 104 \text{ cm}^{-3}$; $N = 276 \text{ cm}^{-3}$; $\Delta LWC_A = 0.65 \text{ g m}^{-3}$; $\bar{\beta}^2 = 192 \text{ μm}^2$; $\sigma_{\beta^2}^* = 32 \text{ μm}^2$; $\beta_{A+}^2 = 187 \text{ μm}^2$; $\beta_A^2 = 214 \text{ μm}^2$; $\beta_{A-}^2 = 250 \text{ μm}^2$.

Fig.1 shows an example of the method (linear scale in (a), log scale in (b)) for spectra sampled on August 10, 1995, during the SCMS experiment. The reference spectrum, on the left, and the selected spectrum, on the right, are represented by solid lines. The reference spectrum was sampled at an altitude of 714 m. The selected spectrum, with a total concentration of 276 cm^{-3} was sampled at an altitude of 989 m. The difference in adiabatic LWC between these two levels was $\Delta LWC_A = 0.65 \text{ g m}^{-3}$. The adiabatic integral of supersaturation β_A^2 is calculated according to Eq.3 for a total concentration equal to N , $N-50$ (β_{A-}^2), and $N+50$ (β_{A+}^2) and the correspond-

ing spectra (Eq.2) are reported in Fig.1 (dot-dashed lines). Finally, the values of $\bar{\beta}^2$ and $\sigma_{\beta^2}^*$ are calculated in order to fit $g(\phi^2)$, as given by Eq.4, with the selected spectrum. The value of $\bar{\beta}^2$ is approximated by the difference between the mode of the selected spectrum and the mode of the reference spectrum; $\sigma_{\beta^2}^*$ is approximated by the difference between the spectral half-width at $1/e$ of the selected spectrum and the half-width of the reference spectrum. The resulting spectrum $g(\phi^2)$ is represented by a dashed line.

Fig. 2 illustrates another example for a much larger difference in altitude, with the same altitude for the reference spectrum and 2170 m for the selected one, that results in a difference of adiabatic LWC of $\Delta LWC_A = 3.11 \text{ g m}^{-3}$.

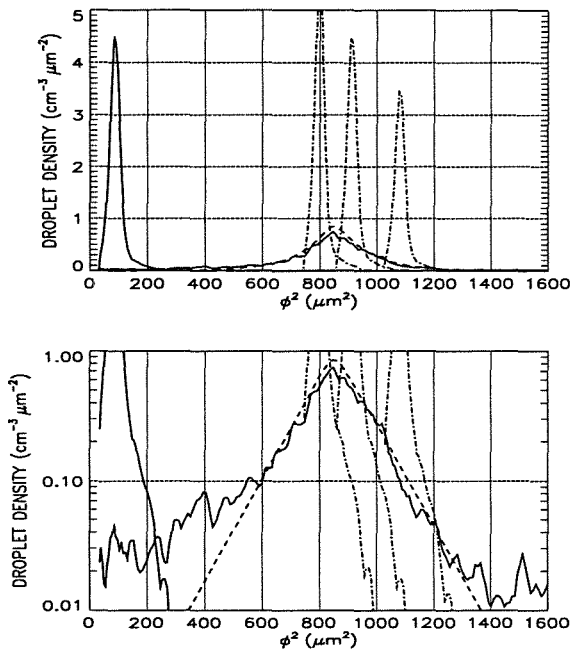


Fig.2 Same as Fig.1 for a spectrum selected at a higher level.

$z_0 = 714 \text{ m}$; $z = 2170 \text{ m}$; $N_0 = 104 \text{ cm}^{-3}$; $N = 219 \text{ cm}^{-3}$; $\Delta LWC_A = 3.11 \text{ g m}^{-3}$; $\bar{\beta}^2 = 762 \mu\text{m}^2$; $\sigma_{\beta^2}^* = 110 \mu\text{m}^2$; $\beta_{A+}^2 = 711 \mu\text{m}^2$; $\beta_A^2 = 825 \mu\text{m}^2$; $\beta_{A-}^2 = 993 \mu\text{m}^2$.

The total concentration in the selected spectrum was $N = 219 \text{ cm}^{-3}$. The two figures demonstrate that the choice of the function Ψ is satisfactory. For example, a Gaussian distribution has been tested but the resulting spectral density was found to decrease too rapidly on the sides, compared to the selected spectrum. It can be noted too that the density in the selected spectra decreases less rapidly than the calculated ones, at high ϕ^2 values. This feature is quite common in most of the selected spectra. But it is likely that it arises only from coincidences of droplets in the laser beam of the instrument.

The figures also show that the spectra have been selected in regions of the cloud with nearly adiabatic

LWC. Fig. 3 summarizes, for the whole campaign, the comparison between the integral of supersaturation for the selected spectra $\bar{\beta}^2$ and the adiabatic estimations. On the error bars, the intermediate value corresponds to β_A^2 and the extremes correspond respectively to β_{A+}^2 (bottom) and β_{A-}^2 (top). This figure demonstrates that all the spectra have been selected in nearly adiabatic regions.

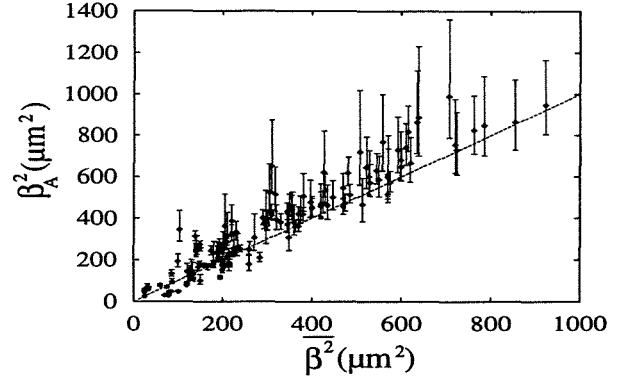


Fig.3 The values of the integral of supersaturation: adiabatic values, β_{A+}^2 , β_A^2 , β_{A-}^2 (from bottom to top on error bars), versus values derived from the selected spectra, $\bar{\beta}^2$.

4. DISCUSSION

Figure 4 summarises this experimental study of the spectral broadening. It represents the estimated $\sigma_{\beta^2}^*$ as a function of the estimated $\bar{\beta}^2$. It is obvious that the broadening is proportional to the mean condensational growth and that a broadening of $\sigma_{\beta^2}^* \approx 0.15 \bar{\beta}^2$ is a minimum. Broader spectra have been observed, in fact much broader than the spectra selected for this study, but narrower spectra have never been observed. The broader spectra can be explained in term of mixing between populations of droplets following different trajectories, but the reason for a limit to the narrowing is difficult to interpret.

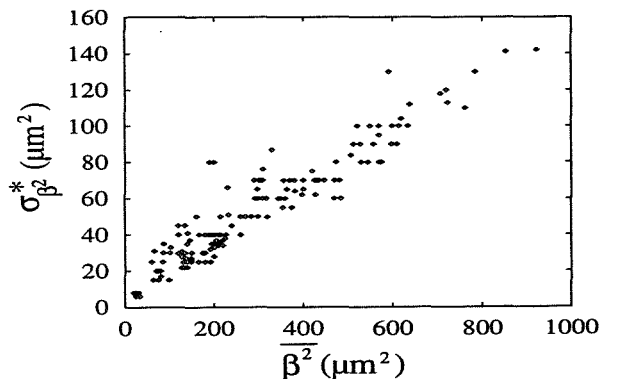


Fig.4 Spectrum broadening: $\sigma_{\beta^2}^*$ versus $\bar{\beta}^2$ (see text and Eq. 5.) for all the selected spectra.

There is still some doubt concerning the performance of the instrument for measuring narrow spectra. The narrowest spectra measured by the Fast

2. CASE STUDIES

Drops size spectra recorded with a disdrometer (Joss and Waldvogel, 1967) for 12 precipitation events, a total of 4000 data samples, in Southern England were used to derive the shape factor μ of an appropriate Gamma distribution and to estimate the parameters of an exponential drops size distribution by fitting methods.

The precipitation events could be categorised into two main meteorological situations.

Firstly, precipitation related to a cold front, which is advecting cold or cooler air masses. The precipitation initiated by abruptly descending air masses, causing intensive condensation and evaporation processes, was characterised in general by stratiform rain with outbursts of heavy showers.

The second situation is a warm frontal system, advecting warm or warmer air masses. The warm air slides over cooler air and is slowly lifted. This causes cooling by adiabatic expansion and hence condensation processes which initiated a broad band of continuous precipitation, often ceasing after embedded convective rain sequences.

Time series of rain rate R , the deviation of the median drop diameter from the actual value ΔD_0 and the shape factor μ , all recorded in 30 s intervals, are shown in Figures 2 and 3.

The rain rates derived by an exponential fit (circles) and a Gamma fit (dotted line) are presented in the top figures and compared with the actual rain rate (solid line) as measured with the disdrometer.

As an indicator for the deviation of the actual drop size shape from an assumed exponential shape, the difference ΔD_0 (circles) between the median diameter derived by exponential fitting and the actual disdrometer D_0 is shown in the middle figures. The smaller the difference between the exponential fit and the disdrometer, the more accurate is the exponential assumption of the drop size shape. A quality control for the Gamma fit procedure is given by the difference between D_0 (dotted line) as a result of the Gamma fit, and the disdrometer value. The closer the value is to zero the more reliable is the Gamma fitting.

The time series of μ in the bottom figures was smoothed additionally with a moving average of 20 minutes to more readily recognise trends and to eliminate noise.

2.1 COLD AIR ADVECTION

The event on the 17-01-1995 is taken as example to show the main characteristics of rain initiated by cold air approach. A stratiform light to moderate rain sequence is interrupted by heavy showers (Fig. 2, top).

The disdrometer (actual) rain rate is in average underestimated by the exponential (by 16%) and Gamma shaped (by 3%) model distributions. The

percentage deviation of the median drop diameter, ΔD_0 value is a good indicator of whether the applied fits are close to the actual distribution. The variance of ΔD_0 (circles), as estimated by exponential fitting from the disdrometer D_0 , is larger (66%) than the corresponding deviation between the Gamma and disdrometer estimated D_0 (16%) (dotted line) (Fig. 2, middle). But the large variance of ΔD_0 based on exponential fitting can get small as well which coincides with a decrease of the initially positive value of μ from an average of 8 to -1 (Fig. 2, bottom).

A general explanation of the positive shape factor over a long time interval is that the advected cold air and related descending air mass causes evaporation of the smaller drops. Additionally, intensive condensation processes which are related to cold fronts, caused by quickly lifted warm humid air masses, lead to a more intensive production of larger rain drops. The change to negative shape factors can be explained that (as weather charts have indicated) warmer air masses have reached the test site and caused condensation processes supporting the growth of cloud drops.

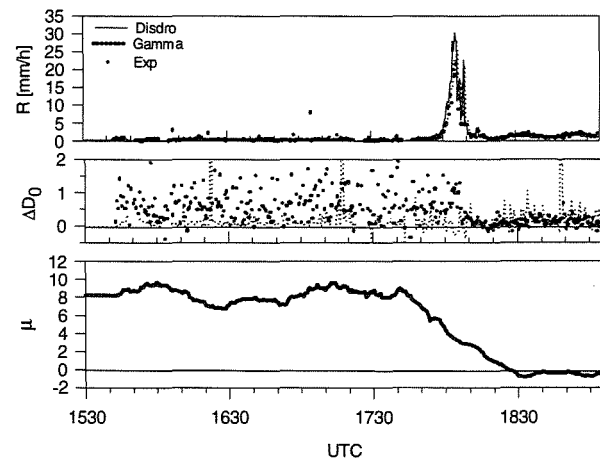


Figure 2: Top: Rain rate R as measured with disdrometer, exponential (Exp) fit and as estimated with Gamma fit. Middle: Difference of the median diameters ΔD_0 , which means difference between exponential fit derived D_0 and disdrometer measured D_0 and difference between Gamma derived D_0 and disdrometer measured D_0 . Bottom: Shape factor μ on the 17 January 1995, Chilton.

2.2 WARM AIR ADVECTION

This case was recorded on 24-02-1995 while the test site was influenced by warm air related to a warm front system. The initiated precipitation is characterised by a continuous rain band with embedded convective rain cells (Fig. 3, top).

The percentage difference ΔR between the fitting methods and the disdrometer (solid line) shows an

underestimation of rain fall rate for the exponential fit (circles) by 7% and for the Gamma fit (dotted line) by 2%. The large value ΔD_0 of 55%, related to exponential fitting (circles), is caused by the increasing variance at 0330 UTC. Compared to the case in section 2.1, the ΔD_0 values estimated by both techniques are smaller. This event here is characterised by a sudden change of signs of the shape factor, from negative, $\mu = -2$, to positive values of in average $\mu = 4$. As in the earlier case, the reason is a change of weather conditions which means here a change from warmer to cooler air masses.

In general, the shape factor is negative from the beginning of the precipitation events. The negative shape factor signifies a large number of small rain drops produced by the condensation processes related to the slow lifting of air masses as warmer air reaches cooler areas.

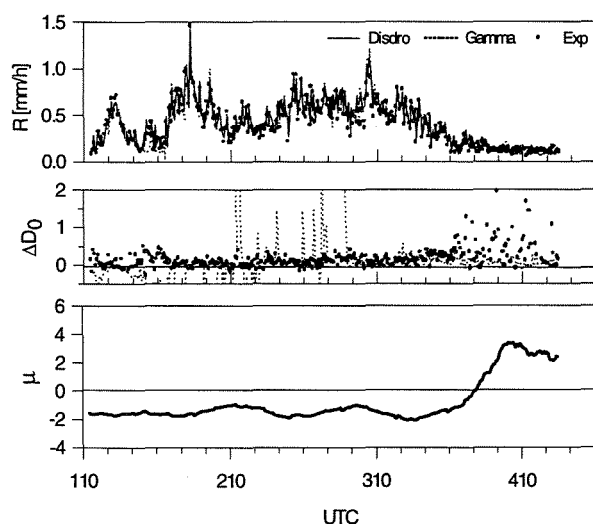


Figure 3: Top: Rain rate R as measured with disdrometer, exponential (Exp) fit and as estimated with Gamma fit. Middle: Difference of the median diameters ΔD_0 , which means difference between exponential fit derived D_0 and disdrometer measured D_0 and difference between Gamma derived D_0 and disdrometer measured D_0 . Bottom: Shape factor μ on the 24 February 1995, Chilton.

3. SUMMARY OF RESULTS FOR ALL CASE STUDIES

The study of all 12 analysed precipitation events (Richter, 1996) leads to the following results:

Rain rates derived by drops size spectra modelled by a Gamma fit deviate less from the actual measured rain rate than the one derived by an exponential fit. This is confirmed by the small ΔD_0 values related to Gamma

fitting which support the plausibility of the Gamma fit compared to the exponential one.

The histogram in Figure 4 shows the distribution of rain rate in 1 mm/h intervals. The comparison of exponential (dark grey) and Gamma fit (light grey) techniques with the disdrometer values (black) gives detailed information about the quality of the fit.

For cold air advection cases (Fig. 4, top) the Gamma fit is closer to disdrometer measurements than the exponential fit for $0 < R \text{ mm/h} < 2.5$. For rain rate intervals between 3 and 7 mm/h there is no big discrepancy between both fitting methods but for $R > 7$ mm/h Gamma fittings are again better.

For the warm air advection events (Fig. 4, bottom) in the intervals between 0 and 9 mm/h the exponential fits come closer to the disdrometer values.

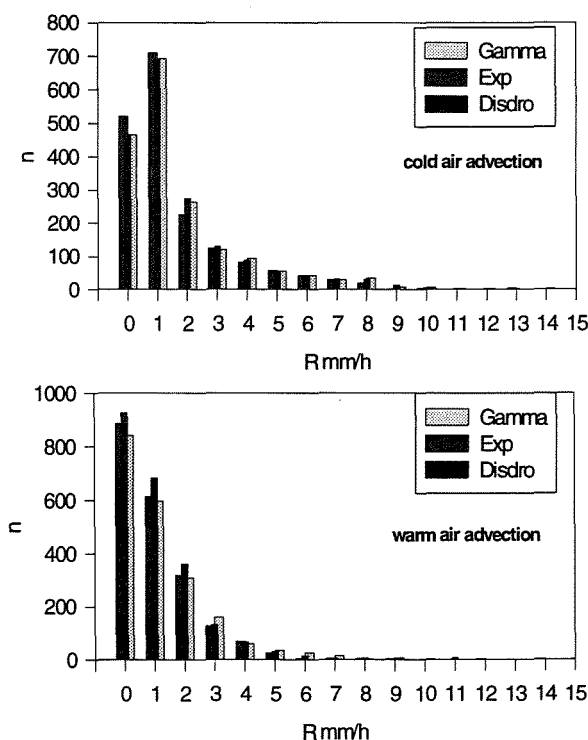


Figure 4: Top: Histogram of rain rate R mm/h as derived by disdrometer (black), exponential (Exp) fitting (grey) and Gamma fitting (light grey) for n single measurements related to cold air advection. Bottom: Histogram of R mm/h related to warm air advection.

For the cases related to cold air advection, it is significant that the average value for the shape factor μ is positive, that is the processes responsible for rain drop formation produce a greater number of large drops than small ones.

For the warm air advection cases the average shape factor is negative, which indicates that the number of smaller drops dominates the number of larger drops.

Figure 5 is the distribution of the shape factor for n single measurements in the range between -4 and 12 for interval steps of $\Delta\mu = 1$.

The histogram, which gives a comprehensive overview of the single cases, shows clear differences between warm (black) and cold (grey) air advection events.

For the warm air advection events the maximum of the distribution can be found around -1 (the interval $-1.5 < \mu < -0.5$). A second peak can be found in the next interval around the value of -2 ($-2.5 < \mu < -1.5$).

In contrast, for cold air events the distribution of the μ -value is broader. Nearly equally distributed μ -values can be found between -1 and 3 . The number of measurements for $\mu > 4$ is far larger for warm than for cold air events.

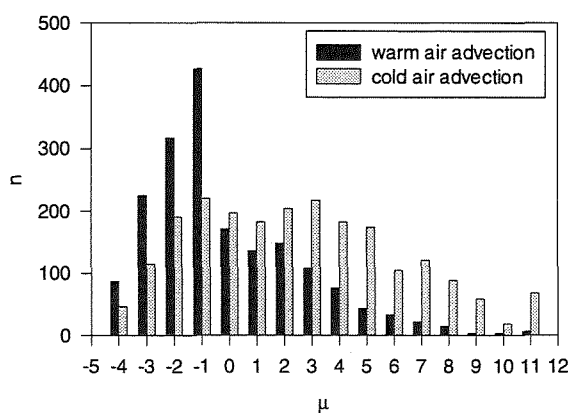


Figure 5: Histogram of shape factor μ corresponding to warm air (black) and to cold air advection (light grey).

As Figure 6 reveals, a change in rain rate does not cause a change of the shape factor. Hence, a specific rain rate can be derived by many various forms of dropsize distributions. Rain intensities cannot be estimated accurately by using a linear relationship between R and μ .

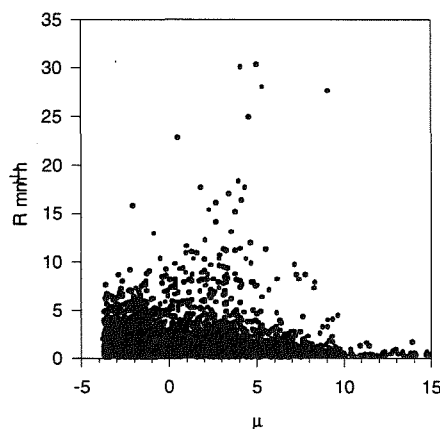


Figure 6: Scatterplot of R versus μ for 12 events (4000 data samples).

In the end, for a specific area and a particular synoptic situation an appropriate choice of the shape parameter could improve operational services in radar rainfall estimations.

4. ACKNOWLEDGEMENTS

This work was supported by the Human Capital and Mobility (HCM) program financed by the European Commission

5. REFERENCES

- Joss, J. and A. Waldvogel, 1967: Ein Spektrograph für Niederschlagstropfen mit automatischer Auswertung, Pure Appl. Geophy., 68, 240-246.
- Richter, C., 1996: On the Parameterisation of Drop Size Distributions - Case Studies with Disdrometer, submitted to J. Appl. Meteor.
- Willis, P.T., 1984: Functional fits to some observed drop size distributions and parameterisation of rain, J. Atm. Sc., 41(9), 1648-1661.

LAGRANGIAN CALCULATIONS OF RAINDROP GROWTH IN SHALLOW CONVECTIVE CLOUDS BASED ON KINEMATIC FIELDS OBTAINED FROM BOTH A CLOUD MODEL AND DUAL-DOPPLER DATA SYNTHESSES

Marcin J. Szumowski^{1,2}, Harry T. Ochs III^{1,2}, Robert M. Rauber¹, Wojciech W. Grabowski³

¹ Department of Atmospheric Sciences, University of Illinois, Urbana, IL, USA

² Illinois State Water Survey, Champaign, IL, USA

³ National Center for Atmospheric Research, Boulder, CO, USA

1. INTRODUCTION

Radar and aircraft data collected in Hawaiian rainband clouds suggests that the dominant microphysical process responsible for the rapid formation of giant ($d > 4$ mm) raindrops is accretion of cloud water. The role that cloud dynamics play in the microphysical evolution of these shallow convective clouds has been a subject of debate. Giant raindrops could grow during a simple up-down trajectory through the cloud; however, some of the radar and aircraft data suggests that eddy motions on scales on the order of 100 meters may substantially influence the evolution of the raindrop spectra. These eddy rolls could significantly enhance drop growth by recirculation into the main updraft, especially near cloud top regions, as hypothesized in a conceptual model by Rauber *et al.* (1991).

In this paper we present the results of a Lagrangian drop-growth trajectory model, initialized with both dual-Doppler radar data as well as the kinematic and thermodynamic fields from the Clark anelastic, nonhydrostatic cloud model. Two Hawaiian Rainband Project (HaRP, 1990) case studies (10 and 22 August) have been used in this study. Relatively vigorous convective cells which produced rainshafts characterized by unusually high radar reflectivity factors (maximum > 60 dBZ) were observed in off-shore rainbands on both days (Szumowski *et al.* 1996a).

2. DUAL-DOPPLER RADAR DATA

Radial velocity measurements from NCAR CP3 and CP4 five cm wavelength Doppler radars have been synthesized on a Cartesian (0.3 km horizontal and 0.2 km vertical) grid. Vertical motion was calculated from the divergence field at each level using the anelastic continuity equation, prescribed boundary conditions, and the variational integration method. Radar volumes had been synthesized every 2.5 to 5 minutes and the gridded data were interpolated in time at 10 second

intervals for drop growth calculations. While the synthesized three-dimensional Doppler kinematic data provides a good estimate of the evolution of the flow on spatial scales of 500 m or greater and time scale of minutes, both its temporal and spatial resolution are inadequate to address the issue of the hypothesized recirculation mechanism. Additionally, the spatial distribution and peak values of cloud liquid water have to be prescribed based on limited aircraft observations, model output and theoretical calculations.

3. THE CLOUD MODEL

The Clark model was initialized with thermodynamic data collected on 10 and 22 August and forced with a broad weak convergence with random perturbation in temperature and moisture fields. Grid nesting provided sufficient resolution (25 meters) to investigate the small scale eddy motions. Two-dimensional framework was chosen to obtain fine resolution and enhance the feasibility of multi-drop trajectory calculation. The data used in the Lagrangian drop-growth trajectory model has 25 meter spatial and 8 second temporal resolution. The rain and cloud water fields have been calculated using bulk microphysics with Berry parametrization.

4. THE TRAJECTORY MODEL

In the Lagrangian drop-growth model the trajectories are initialized at various positions in the lower part of the cloud. A range of initial droplet sizes with diameters between 30 and 150 μm are used. The gridded velocity data interpolated to the position of the particle using a second-order-accurate scheme are used in a second-order-accurate predictor-corrector scheme to calculate drop-growth trajectories. The simplified microphysical formulation of the model includes a growth rate equation for the large drop collecting smaller cloud droplets:

$$\frac{dM_i}{dt} = \pi R_i^2 E(R_i, r) \chi \rho_a [v(R_i) - v(r)]$$

where R_i and r are the sizes of large and small drops, respectively, and $v(R_i)$ and $v(r)$ are their respective terminal velocities. χ is the liquid water mixing ratio, $E(R_i, r)$ is collection efficiency and ρ_a is the density of air. The effects of the sedimentation of the cloud droplets are neglected. We also neglect the condensational growth of the collector drop, as it should be negligible for particles greater than 30 μm . Collision-coalescence and breakup processes are assumed to have negligible effects on the drop growth rate. Stochastic coalescence, important in early stages of drop's growth, may effect the location and time of formation of a drop of approximately 50 μm . However, in our model we assume that drops of this size already exist in the cloud. Based on JHWRP microphysical data and some of the previous studies breakup processes appear to have no limiting effect on the size to which a raindrop could grow (Beard *et al.* 1986). Some preliminary results of raindrop growth calculations in the Doppler kinematic fields from the 22 August under the above assumptions are illustrated in Figure 1. The fundamental suggestion of these calculations is that large raindrops (> 4 mm diameter) can form through accretion of cloud water alone in simple one cycle up-down trajectories, provided the core of the updraft is close to adiabatic

5. CURRENT RESEARCH

Currently we are using both the Doppler radar and cloud model fields to calculate multiple trajectories of growing raindrops. We vary the initial location and size of the collector drops as well as test the sensitivity to the prescribed cloud water distribution (in case of the radar kinematic fields) and the collection efficiency. Other issues such as probability of breakup and statistical significance of the eddy recirculation mechanism are addressed in another paper in this volume (Szumowski *et al.* 1996b).

6. ACKNOWLEDGEMENTS

We thank everyone at the National Center for Atmospheric Research who contributed to the Hawaiian Rainband Project data acquisition and processing. We also wish to thank L. Jay Miller and Bill Anderson for their assistance with radar data analyses software and Terry Clark and William Hall for the assistance with the cloud model. Computing time was provided by the National Center for Atmospheric Research, which is sponsored by the National Science Foundation. This research was sponsored by the National Science Foundation under grants NSF ATM 9020245 and NSF ATM 9223165.

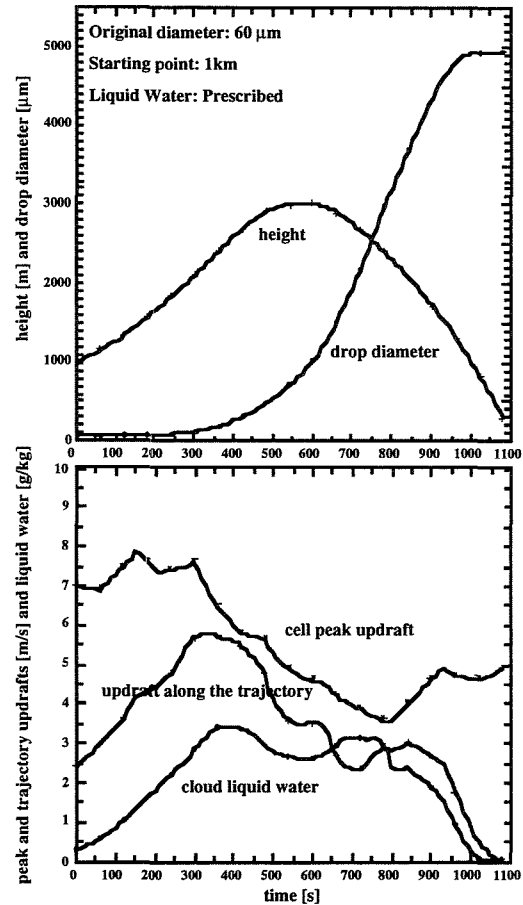


Figure 1. Parameters along a sample drop trajectory in a prescribed liquid water field and 22 August dual-Doppler temporally evolving kinematic field. Top panel: drop height and diameter. Bottom panel: Cloud liquid water and updraft speed.

7. REFERENCES

- Beard, K. V., D. B. Johnson, and D. Baumgardener, 1986: Aircraft observations of large raindrops in warm, shallow, convective clouds. *Geophys. Res. Lett.*, **19**, 991-994.
- Raubert, R. M., K. V. Beard, and B. M. Andrews, 1991: A mechanism for giant raindrop formation in warm, shallow, convective clouds. *J. Atmos. Sci.*, **48**, 1791-1797.
- Szumowski, M. J., R. M. Rauber, H. T. Ochs, and L. J. Miller, 1996a: The microphysical structure and evolution of Hawaiian rainband clouds. Part I: Radar observations of rainbands containing high reflectivity cores. *J. Atmos. Sci.*, submitted: April 1996.
- Szumowski, M. J., W. W. Grabowski, R. M. Rauber, H. T. Ochs, , 1996b: A Statistical study of warm rain formation in shallow, tropical convection. Preprints, 12th International Conference on Clouds and Precipitation, Zurich, Switzerland.

EXPERIMENTAL STUDY OF THE EFFECT OF MIXING ON DROPLET SPECTRA

Jean-Louis Brenguier^{1,2}, and Frederic Burnet¹

¹ METEO-FRANCE (CNRM/GMEI), Toulouse, France

² Affiliate Scientist at NCAR/ATD+MMM

1. INTRODUCTION

The mixing between a convective cloud and its dry environment strongly affects the droplet size distributions. The process has been clearly described by Baker et al (1980): if the dry air is instantaneously mixed with the cloudy air, down to the smallest scale, all the droplets are exposed to the same sub-saturation and they are evaporated according to the diffusion equation (the rate of evaporation is inversely proportional to the droplet size); if the evaporation is much faster than the mixing, all the droplets at the interface between dry air and cloudy air are totally evaporated until the mixture reaches the saturation, and the remaining droplets are no longer affected. The first scenario is referred to as homogeneous mixing and the second one as inhomogeneous.

In fact, the real process combines both kinds of mixing. Brenguier (1993) documented an example of interface between a convective cloud and its environment shorter than a few centimeters. Droplets in the cloudy part were not affected by the vicinity of the dry air and mixing was strongly inhomogeneous. On the opposite, many cases of diluted cloud cells with small droplets can be observed, generally in decaying turrets. In fact, the distinction between homogeneous and inhomogeneous mixing has no meaning when considering single mixing events. The main question is to understand the accumulated effect of these events. For example, Baker et al (1980) proposed a model based on the hypothesis that the mean effect can be represented by a inhomogeneous scheme.

The objective of this paper is to document the statistics of the microphysical parameters, as measured during cloud traverses, in order to validate this hypothesis.

2. METHODOLOGY

The liquid water content, or LWC, (q_c) in convective clouds at a given altitude above cloud base, fluctuates between 0 and a maximum value called the adiabatic LWC or q_{cA} . Throughout this paper q_c refers to the condensation droplets since the above statement is no longer valid for precipitations. q_{cA} is equal to the difference between the water vapor saturation mixing ratio at the cloud base $q_{vs}(z_0)$ and its value at the level of reference $q_{vs}(z)$. Because of

entrainment of dry air and mixing with cloudy air, $q_c(z) \leq q_{cA}(z)$. Assuming that the initial conditions are characterized by:

$$q_c = q_{cA} \quad , \quad q_v = q_{vs}(T_0) = q_{vs0} \quad , \quad q_{ve} < q_v,$$

where the indice e refers to the environment, the values of the parameters can be calculated after mixing between percentages α of cloudy air and $1 - \alpha$ of environmental air as:

$$q_v = q_{vs}(T)$$

$$q_c = \alpha (q_{vs0} + q_{cA}) + (1 - \alpha) q_{ve} - q_{vs} \quad (1)$$

Both equations are coupled by the release of latent heat during the evaporation from q_{cA} to q_c . For simplicity, the temperature in the environment is assumed to be equal to the temperature in the cloud and the mixing is assumed to occur at constant pressure.

The parameterization of the mixing process aims at the description of this dilution mechanism in term of droplet spectrum evolution. As a first step, let us consider only the mean volume diameter ϕ_v for characterizing the droplet spectrum. This parameter is simply related to q_c and to the droplet concentration c by:

$$q_c = \pi \rho_w c \phi_v^3 / 6 \quad (2)$$

If the mixing is purely inhomogeneous, some droplets of all sizes are completely evaporated and the spectral shape remained unchanged. It follows that the mean volume diameter is constant throughout the mixing. The concentration is thus diluted as:

$$c = c_0 \frac{q_c}{q_{cA}} \quad (3)$$

If the mixing is purely homogeneous, the final spectrum depends on the humidity in the environment. When the environment is saturated (assuming the temperature in the environment is the same as in the cloud), there is no evaporation and the spectrum is unchanged. The mean volume diameter is constant and the concentration is diluted as:

$$c = c_0 \frac{q_c}{q_{cA}} = \alpha c_0 \quad (4)$$

When the environment is subsaturated, all the droplets are evaporated according to the vapor diffusion growth equation and the evolution of the spectrum can be calculated by integration of this equation. However, the dilution of the concentration can

still be directly expressed as a function of the percentage of cloudy air in the mixing as:

$$c = \alpha c_0, \quad (5)$$

except when the droplets are becoming so small that some are totally evaporated. The mean volume diameter is thus derived from the final LWC as:

$$\phi_v = \left(\frac{q_c}{\pi \rho_w c / 6}\right)^{1/3} = \left(\frac{q_c}{\pi \rho_w \alpha c_0 / 6}\right)^{1/3} \quad (6)$$

This brief presentation of the mechanism and of its parameterization shows that a diagram of concentration versus mean volume diameter provides information about the nature of the mixing process. In this paper, the mean volume diameter is represented on a ϕ^3 scale so that the product of the two coordinates is proportional to the LWC. Finally, in order to compare more easily samples with different droplet concentrations, the concentration is normalized by the maximum concentration measured in the cloud c_0 ($C = c/c_0$) and the mean volume diameter is normalized by ϕ_{v0} ($\Phi = \phi_v/\phi_{v0}$) such that $\pi \rho_w c_0 \phi_{v0}^3 / 6 = q_{cA}$

Figure 1 shows such a diagram of Φ versus C . The dot-dashed lines correspond to the isolines of q_c from q_{cA} to $0.1q_{cA}$ every 10%. The dashed line at $\Phi = 1$ represent the possible values during an inhomogeneous mixing process or a homogeneous process of mixing with a saturated environment. The dashed curves marked 99, 90, 80, and 70 % represent the possible values for a homogeneous mixing process with a relative humidity in the environment as indicated by the labels.

By linearizing the Clausius Clapeyron equation for the saturation vapor pressure, the relation between C and Φ can be approximated by:

$$\Phi = 1 - a \left(\frac{1 - C}{C} \right), \quad (7)$$

where $a = (q_{vs0} - q_{ve}) / (q_{cA}(1 + k))$, and $k = (L^2 q_{vs}) / (C_p R_T T^2)$. L is the latent heat of condensation, C_p is the heat capacity of water vapor, R_T is the specific gas constant for water vapor, and T is the temperature.

Eq.7 shows that the slope $d\Phi/dC$, at the beginning of the mixing process ($\Phi \approx 1$ and $C \approx 1$) is proportional to the difference between the vapor mixing ratio in the cloud and its value in the environment.

3. DATA ANALYSIS

The Small Cumulus Microphysics Study (SCMS) has been organized by NCAR/MMM+ATD in Florida from July 14 to August 15, 1995 for the study of the formation of precipitation in convective clouds. The instrumental setup included a dual frequency cm radar (CP2) at the ground and three instrumented aircraft: the NCAR C-130, the U. of Wyoming K/A, equipped with a millimetric radar and the Météo-France Merlin-IV, equipped with the

Fast FSSP (Brennguier et al, 1996; Coelho et al, 1996). The data shown in this paper have been collected with the Fast FSSP and processed at 10 Hz.

3.1 Case study August 10, 1995

The first case is a cloud cell that was selected for its convective activity and its sharp contour at the cloud top (2200 m). However, the cell was rapidly detached from the cloud base and collapsed in less than 10 minutes. Fig.1 shows the iso-contours of the measured frequency distribution of Φ versus C for the six traverses performed by the Merlin-IV from 15:26:48 to 15:34:07 (UTC). At the beginning of the procedure, the measured LWC was close to the adiabatic value and then it decreased rapidly with time. During the last traverse, the LWC was less than 10% of the adiabatic. Most of the mean volume diameters were between 90 and 100% of the adiabatic value, except for very diluted values of the concentration. At this high level of dilution, the $\{\Phi; C\}$ values still lie between the 90 and the 99% humidity mixing curves.

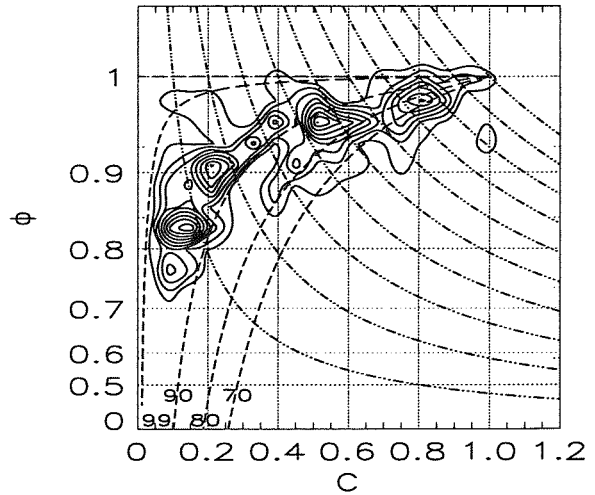


Fig.1 Iso-contours of the frequency distribution of Φ versus C , measured in a cloud cell on August 10, 1995, from 15:26:48 to 15:34:07 UTC. The dot-dashed lines represent the isolines of LWC from q_{cA} to $0.1 q_{cA}$, every 10%. The dashed lines represent the variation of Φ versus C during homogeneous mixing with environmental air characterized by a relative humidity as indicated by the labels.

Another example is shown in Fig. 2, for 11 traverses in a more active cell from 15:42:11 to 15:57:39 (UTC). Most of the values at high dilution are between the 90 and the 99% humidity mixing curves. The two other cells sampled in this cloud field are showing the same characteristics. The maximum droplet concentration during this mission was between 250 and 350 cm^{-3} , and the water vapor deficit at cloud top was 4 g kg^{-1} (from $q_{vs0} = 13 \text{ g kg}^{-1}$ in the cloud to $q_{ve} = 9 \text{ g kg}^{-1}$ in the environment), at the beginning of the convective development. After dilution, the cell was colder, because of mixing with the environment and evaporation of liquid wa-

ter, and its water vapor mixing ratio was decreased to $q_{vs0} = 11 \text{ g kg}^{-1}$.

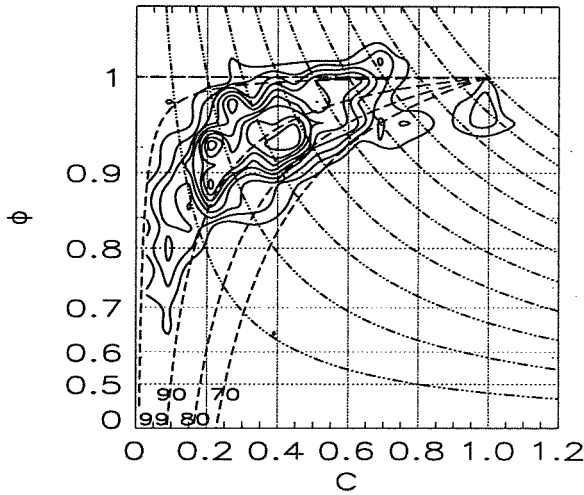


Fig.2 Same as Fig.1, for 11 traverses in a cell sampled on August 10, 1995, from 15:42:11 to 15:57:39.

This example suggest that the mixing process is close to the inhomogeneous type. Thermodynamics has been simplified in the above equations but a detailed calculation, including the temperature difference between the cloud and its environment shows that homogeneous mixing in this case should be characterized by $\{\Phi; C\}$ values around the 70% humidity mixing curve. The analysis of the time series for the water vapor and the liquid water mixing ratios shows that the close environment of the cloud is humidified by previous mixing events during which all the droplets have been evaporated. The visible cloud appears to be surrounded by a humid shell, void of droplets, and further dilution of the cloud cells with this humidified air affects slightly the droplet size distribution.

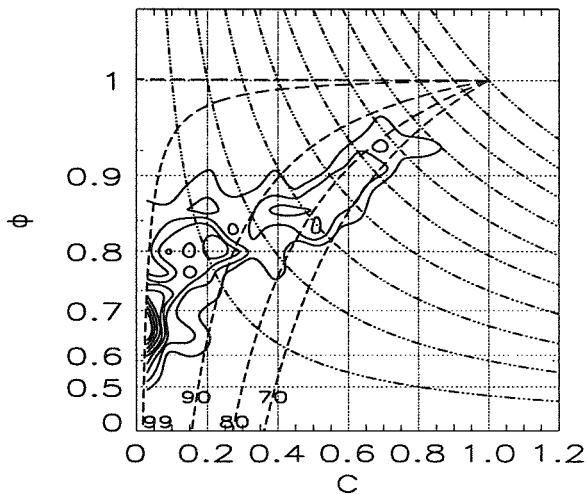


Fig.3 Same as Fig.1 for a cell sampled on August 8, 1995, from 17:23:06 to 17:36:11.

3.2 Case study August 8, 1995

Fig.3 shows the Φ versus C frequency isocontours for penetrations at cloud top (1850 m) in a series of pulsating cells (from 17:23:06 to 17:36:11 UTC). At this time the convection was blocked by a dry layer at 810 hPa. During this mission, the droplet concentration was larger than in the previous case (between 900 and 1300 cm^{-3}), probably because of pollution from ground fires.

Fig. 4 shows a similar case sampled much higher (2450 m) when the clouds were more vigorous and were passing through the dry layer (from 18:30:35 to 18:39:49 UTC).

Both figures, as well as all the cells sampled during this mission, are showing a $\{\Phi; C\}$ frequency distribution different from the one displayed above for August 10. At the highest levels of dilution ($q_c < 0.1 q_{cA}$), the mean volume diameter is between 60 and 90% of the adiabatic value against 70 to 95% for August 10, but the main difference appears for intermediate values of dilution, ($0.1 q_{cA} < q_c < 0.3 q_{cA}$): Φ is between 70 and 90% of the adiabatic value instead of 85 to 100% for August 10.

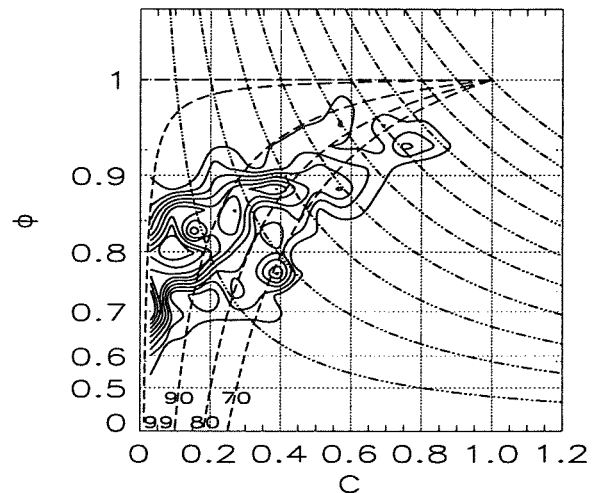


Fig.4 Same as Fig.1 for a cell sampled on August 8, 1995, from 18:30:35 to 18:39:49.

4. DISCUSSION

The main differences between the two cases discussed here are the droplet concentrations (250 cm^{-3} for August 10 and more than 1000 cm^{-3} for August 8) and the vertical profiles of temperature and humidity in the environment. There is no simple speculation on how the difference in droplet concentration could be responsible for the observed difference in the statistics of the $\{\Phi; C\}$ in diluted cells. On the contrary, it is obvious that the humidity in the environment is actively involved in the mixing process.

The vertical profiles of temperature and dew point for the two cases discussed in this paper are shown in Fig. 5 and 6, with the adiabatic profiles from the cloud base.

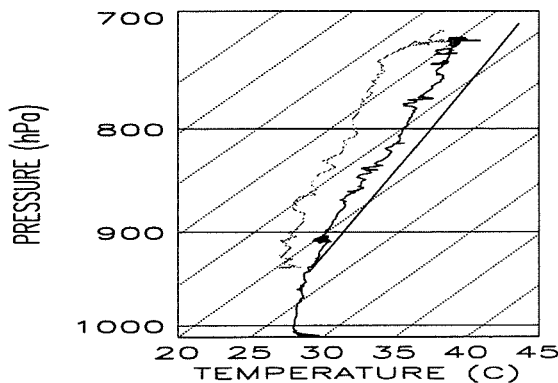


Fig.5 Temperature and Dew-Point vertical profiles on August 10, 1995. The solid line is the adiabatic profile from the cloud base.

For August 10, the layer was slightly unstable and uniformly humid (≈ 60 to 70% relative humidity) well above the cloud layer, with no noticeable inversion. The convection was only limited by the mixing with the environment. Evaporation of early clouds was moistening the layer, the most active cells had a temperature close to the adiabatic value and finally the last sampled cell at 16 UTC started to develop up to the 600 hPa level.

For August 8, the temperature profile above 900 hPa was more unstable up to 810 hPa, where the convection was blocked by a dry layer with a slight temperature inversion. This inversion was topped by a second unstable and moist layer up to 740 hPa. The first example (Fig.3) has been sampled below the inversion layer and the second example (Fig.4) has been sampled above. It can be noted that, for the two examples in August 8, the largest values of LWC are lower than 70% of q_{cA} and the temperature is well below the adiabatic value. For an adiabatic cell, the water vapor saturation mixing ratio would be 18 g kg^{-1} at 1850 m and 16 g kg^{-1} at 2450 m. With a value in the environment as low as $\approx 8 \text{ g kg}^{-1}$, i.e. the water vapor deficit is of the order of 10 g kg^{-1} , much larger than the 4 g kg^{-1} measured on August 10.

5. CONCLUSION

This preliminary study of the effects of mixing on the droplet size distribution in convective clouds has shown that the process cannot be simply parameterized as homogeneous or inhomogeneous. At a low dilution ratio ($q_c > 0.6 q_{cA}$), both types are observed with regions where the mean volume diameter is not affected at all and regions where it is reduced according to the homogeneous scheme. At a higher dilution ratio ($0.3 < q_c/q_{cA} < 0.6$), the moistening of the cloud environment by previous mixing events counteracts further droplet evaporation and the mean volume diameter is less diminished than during a homogeneous mixing process with an unmodified environment.

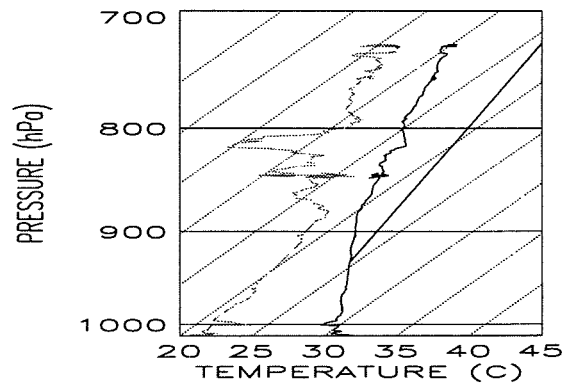


Fig.6 Temperature and Dew-Point vertical profiles on August 8, 1995.

Two cases have been shown: when the vapor deficit in the environment is not important, the moistening is sufficient for the mixing to affect very little the droplet sizes; when the deficit is higher, the droplets are progressively evaporated as during homogeneous mixing with a humidity in the environment slightly higher than its value far from the cloud. Finally, at very high dilution ($q_c < 0.3 q_{cA}$), the moistening of the environment becomes important, even for a dry environment, and the cloud remnants are characterized by very low concentrations but mean volume diameters that are still larger than 60% of the adiabatic value.

6. ACKNOWLEDGEMENTS The authors are grateful to the NCAR team and especially to C. Knight for the co-ordination of the SCMS experiment. Thanks are due to the participants from the *Centre d'Aviation Météorologique* for their active collaboration during the flights and to the group *Mesures Météorologiques Aéroportées* for the aircraft data processing. This research was supported by Météo-France and INSU under grant D13570.

7. REFERENCES

- Baker, M.B., R.G. Corbin and J. Latham, 1980: The influence of entrainment on the evolution of cloud droplet spectra: I. A model of inhomogeneous mixing. *Quart. J. Roy. Meteor. Soc.*, **106**, 581-598.
- Brenguier, J.L., 1993: Observations of cloud microstructure at the centimeter scale. *J. Appl. Meteor.*, **32**, 783-793.
- Brenguier, J.L., D. Trevarin, R. Peytavi, A. Coelho, P. Wechsler, and J. Isbert, 1996: New electronics for the Forward Scattering Spectrometer Probe: The Fast FSSP. Accepted to *J. Atmos. Oceanic Technol.*
- Coelho, A., J.L. Brenguier, and T. Bourianne, 1996: A model for the Fast FSSP operation. Proceedings of the ICCP 1996.

CONVECTIVE/STRATIFORM SORTING OF DROP SIZE DISTRIBUTIONS BASED ON COINCIDENT VERTICAL VELOCITY MEASUREMENTS

Paul T. Willis¹

¹CIMAS, U. of Miami, Miami, FL 33149

1.0 INTRODUCTION

Ever since the widespread introduction of satellites in the late 1950's, and as the result of earlier tropical experiments (Line Islands, Zipser 1969, GATE 1974), it has been recognized that virtually all deep tropical convection occurs in systems that exhibit some degree of mesoscale organization. Even a cursory examination of radar data in these systems indicates that, in addition to the convective precipitation, these systems are characterized by extensive mesoscale regions of stratiform precipitation, and bright band. For tropical systems the separation, and accurate radar measurement of the two types became important when it was realized that the vertical profiles of latent heat release of the two types were both important and significantly different (Leary and Houze, 1979, Zipser, 1969). Although the rainfall rates are typically much less in the stratiform precipitation, the typically very large areal coverages make correct measurement of this component important.

It is the purpose of this paper to attempt to separate a sample of TOGA COARE airborne drop size distribution measurements into a convective and stratiform sample based on concurrent measurements of vertical velocity.

2.0 DATA

For this study we use a sample of data from TOGA COARE on 14 Dec 92, consisting of 6s mean rain drop size distributions and 6s mean vertical velocities measured on the NCAR Electra Aircraft. The data from this day are typical of the larger data set, covering a range of convective and stratiform conditions.

3.0 PRECIPITATION PROCESSES IN TROPICAL CONVECTIVE SYSTEMS

3.1 Convective Precipitation

The environment within which all tropical convective systems with deep convection grow is characterized by essentially the same copious boundary layer moisture content, and virtually the same low convective cloud base. The typically clean tropical maritime air is characterized by low concentrations of cloud condensation nuclei. The copious moisture being made available, and the maritime aerosol spectrum fosters rapid development of the stochastic coalescence process (warm rain). For several reasons the updraft velocities tend to be only moderate (6-12 m/s), even in

deep convection, so that convective parcels arrive at ice levels with well developed convective rain drop size distributions. As these updrafts ascend to levels where ice processes become important graupel develops, probably largely on frozen drop embryos, and this rapidly falling melted graupel contributes to the convective rain component. As the updraft continues to ascend, rapid ice nucleation is fostered by the broad maritime drop size distributions arriving, and much of the condensate made available by the updrafts above these levels forms on relatively small slowly falling ice hydrometeors. These ice hydrometeors are advected away from the active convection and provide a particle flux into the stratiform rain and the anvil. In tropical, and in mid latitude systems, there is often a rainfall minimum, or moat, immediately adjacent to the heavy convective precipitation. Although the melted graupel is involved in the convective precipitation, far and away the majority of the convective rain in mesoscale tropical systems has its origins in the stochastic coalescence process.

After the initial rain formation the convective drop size distributions are the result of a balance, or equilibrium, between the coalescence process and the collision breakup process (Low and List, 1982). Most of the convective rain falls in fairly close proximity to the convective updrafts responsible for its formation. Downdrafts are also involved in the convective rain reaching the surface.

A significant fraction of the overall convective rainfall in the tropics occurs in wholly warm convective clouds. This rainfall component is usually not a significant part of mesoscale deep convective systems. The drop size distributions in these clouds will be the same as in the convective regions of the systems that produce both precipitation types. These wholly warm clouds do not produce regions of stratiform precipitation.

3.2 Stratiform Precipitation

Virtually all of the stratiform precipitation in tropical convective systems is formed by ice processes. Aggregation is most prominently involved in the formation of stratiform rain that reaches the surface, as most of the single crystals do not fall rapidly enough to make a survivable trip to the surface. It is well known that the deep convective updrafts continue up to very high, very cold levels. Here additional ice processes-nucleation, deposition growth, and accretion produce

copious ice hydrometeor concentrations. These hydrometeors are advected into the anvils and stratiform precipitation, and do not fall in close proximity to the convective updrafts and downdrafts. These ice particles form the origins of much of the stratiform precipitation observed in association with the deep convection in these systems.

Considerable aggregation may well start in the updrafts and occur before the ice descends back to warmer levels (-10°C). The dendritic growth maximum around -15°C in the updrafts may well be a region of initiation of considerable aggregation. The details of the ice processes in tropical convection at these levels are not well documented.

The initial stratiform rain drop size distributions are formed in the melting layer. A considerable fraction of the condensate originated in the deep convection, but additional deposition growth, and some accretion is provided by widespread mesoscale ascent. Precisely what fraction of total stratiform condensate is advected from the convection, and what is added by mesoscale ascent in the stratiform regions, is a current research topic. Although under certain conditions some breakup does occur upon melting, the melting layer is more often a region of enhanced aggregation. The stratiform drop size distributions are characterized by relatively fewer small drops, and relatively more large drops for a given rainfall rate. Understandably the stratiform rainfall rates tend to be much lower, because the total condensate made available on their trajectories after they leave the convection is much less than that made available in the updrafts. Below the melting layer the rain drop size distributions are shaped, as in the convective case, by a balance between collision coalescence and collision breakup. But, the approach to an equilibrium distribution in stratiform rain is very much slower than in the convective case. So the stratiform rain distributions maintain their relative dearth of small drops, and relative higher concentration of larger drops, on their trajectories to the surface. The concentration of small drops is much less than in the convective case, firstly because there is no prolific supply of small raindrops continually being supplied from new condensation and stochastic coalescence, as is the case in the convective updraft. Also, in mesoscale systems the layers below the melting layer tend to be regions of mesoscale descent. Consequently, these layers may be regions of evaporation and thus sinks for small drops. Secondly, and probably more importantly, the collision breakup of the large drops is much slower because the all important concentration of the critical small to medium drops is much less. Thus, collision breakup process is much less effective and relatively more of the large drops survive the trip to the surface.

3.3 Convective vs Stratiform Drop Size Distributions and Z-R Relations

The convective drop size distributions are the equilibrium distributions. They are in equilibrium, or near equilibrium, as the convective updrafts arrive at the

level of ice processes. Once this equilibrium is attained it tends to be maintained on the fall to the surface, in neutral conditions, or in weak downdrafts. Exceptions are strong shear sorting, and first drops out of a cell. Hu and Srivastava (1995) have numerically modeled equilibrium distributions, and their 10 min distribution is compared to a similar water content mean distribution from "TOGA COARE in Fig. 1. The agreement is

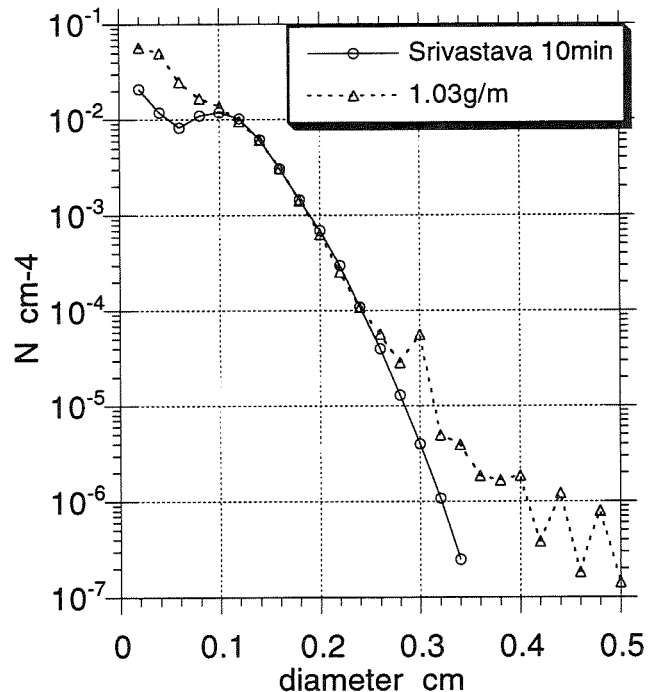


Fig. 1 Lu and Srivastava 1995 10 min equilibrium distribution (EXPM .92 g/m³) and observed mean DSD 1.23 g/m³ from TC 12/14/92.

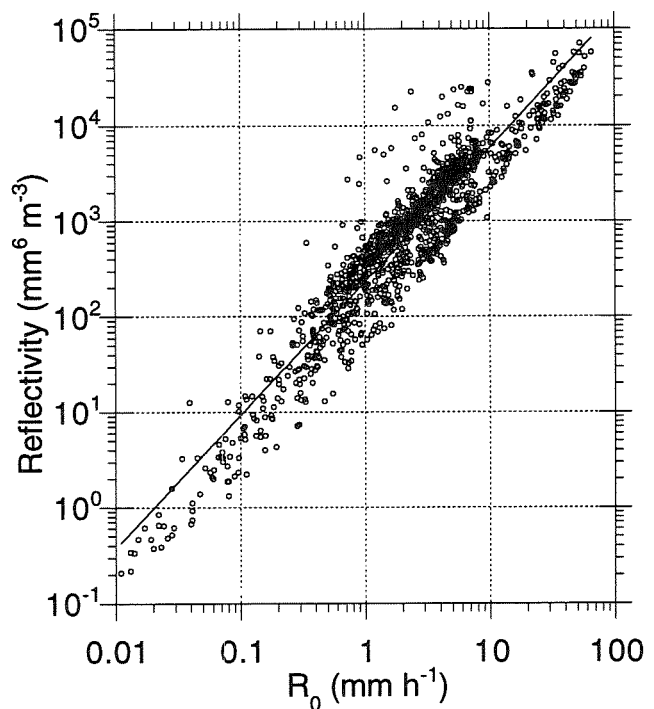


Fig. 2 Z vs R for all data on TC 12/14/92 Fit line is $Z = 231.6 R^{1.398}$.

almost perfect through the middle sizes ($d=1-3\text{mm}$). The theoretical distribution has a lower concentration of small drops than this convective distribution probably because the theoretical distribution did not have the continuous supply of small raindrops that are being made available in the convective updrafts in the observed case. Also the observed distribution has a tail of large

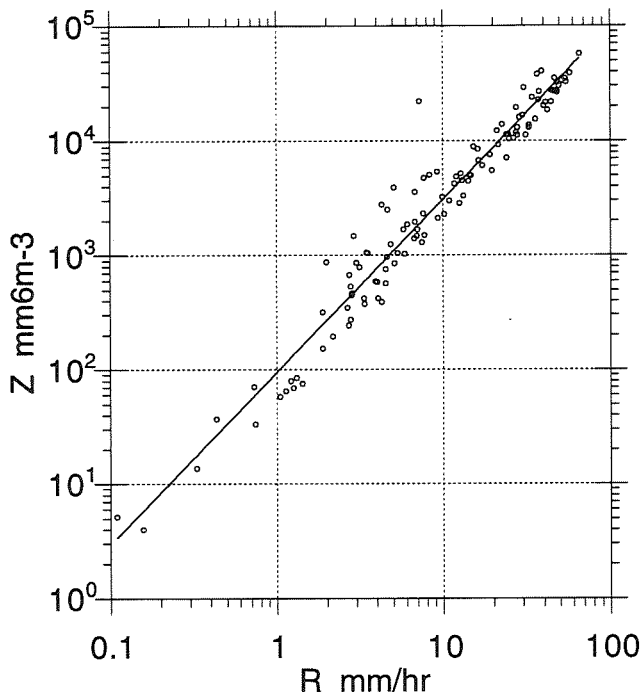


Fig. 3 Z vs R for convective sample, fit is $Z = 95.6 R^{1.509}$.

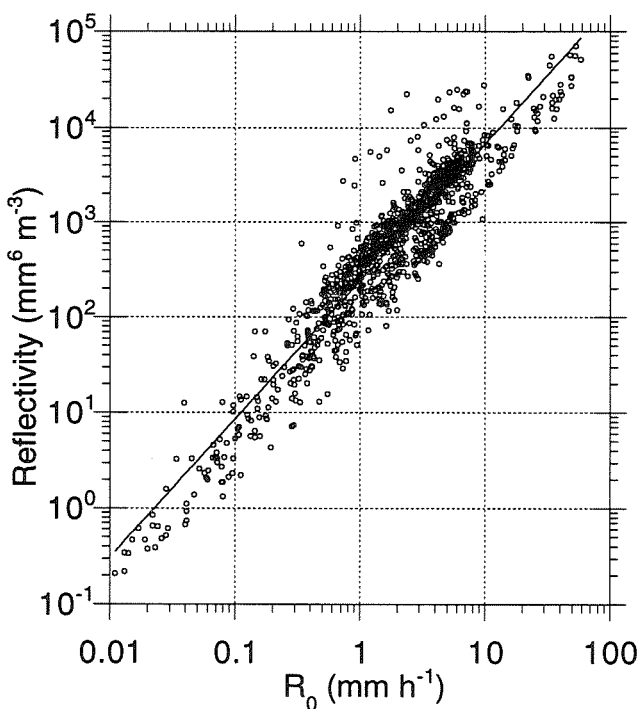


Fig 4 Z vs R for Stratiform sample (all not identified as convective), fit is $Z = 240.1 R^{1.445}$.

drops, some of which may be artifacts of the observations, but, some of which are real. That some of these larger drops survive may indicate that the collision breakup efficiencies may be slightly overestimated in the numerical calculations. Also, some non-equilibrium distributions may be included in the bin averaging of the observed distributions, i.e. it may not be a pure convective sample.

The stratiform rain distributions are not in equilibrium as they are formed in the melting layer, and typically do not reach equilibrium on their trajectories to the surface. Shear sorting of the drops may further accentuate the departure from equilibrium of the stratiform distributions. Waldvogel (1974) has related changes in the shape of the distributions below the melting layer to the degree of riming of the crystals and aggregates above the melting layer. Although this increase in riming is due to some slight increase in convection, it is probably far from what we are considering as convection here.

The Z vs R plot for the entire sample is presented in Fig. 2. The sample appears to divide into two fairly distinct Z-R populations. This is due to differences in the drop size distributions, presumably stratiform and convective. Tokay and Short (1996), in ground based distrometer sample, have used the shapes of the DSD's to separate their sample into convective and stratiform distributions. They find the convective and stratiform Z-R relations of $Z = 139R^{1.43}$ and $Z = 367R^{1.30}$ respectively, in agreement with the data of Fig. 2.

A major difference between stratiform and convective rain distributions is related to the vertical air motions involved in their development. Historically a separation into stratiform and convective distributions has been done based on the variance of the radar reflectivity field. Tokay and Short's separation based on the distributions themselves, although probably correct, is not based on independent evidence. So, in this study we attempt to separate the sample into stratiform and convective based on concurrent measurements of vertical air velocity and raindrop distributions.

We have separated the convective sample requiring: 1) $w > 1$ m/s, or 2) $w < 1$ m/s and $|\Delta w| > 0.65$ m/s, where w is the 6s mean and $|\Delta w|$ the change in w from 6s before to 6s after the sample. The Z vs R for this convective sample is plotted in Fig. 3. Requiring concurrent in situ convective vertical velocity of this magnitude makes this a nearly pure convective sample, i.e. virtually no stratiform samples are included. The remainder of the sample was labelled stratiform, and is plotted in Fig. 4. This is not a pure stratiform sample, i.e. numerous convective samples are included. The lack of concurrent convective air motions at a point does not ensure stratiform conditions. In many cases the samples could have been formed by convective motions in fairly close time and space proximity. And, once an equilibrium condition is reached it should be maintained, unless the distribution is seriously perturbed by sorting, etc.

Since the variance of the radar reflectivity factor has historically been used to separate convective and stratiform precipitation, the change in Z computed from the 6s mean drop size distributions was explored as a parameter to separate the sample. Fig. 5 is a plot of $|\Delta Z|$, the change in Z from 6s prior to 6s after the sample, vs a parameter $Z-Z_0$. A line $Z_0=169R^{1.43}$ separates the data of Fig. 2 into a presumably stratiform and convective sample. The plotted parameter is the $\log Z - \log Z_0$, so that above the line is stratiform, and below convective. The parameter $|\Delta Z|$ does not appear to show much skill as a separator of stratiform and convective precipitation. Part of the deficiency may be that it is only along one dimension, and the precipitation structure is at least two dimensional.

The mean drop size distributions for rain rate categories were computed for the sample above the Z_0 line (stratiform) and the sample below the line (convective). These two mean drop size distributions for the R' interval from 1 - 7 mm/hr are plotted in Fig. 6. The stratiform distribution has much lower concentrations of drops smaller than $d=1.4$ mm, and a higher concentration of larger drops. The suggestion of a tail at diameters larger than $d=4.5$ mm may be in part due to drops slipping through the artifact rejection, but the data reduction of both halves of the sample was identical, and the drops are not there in the convective sample.

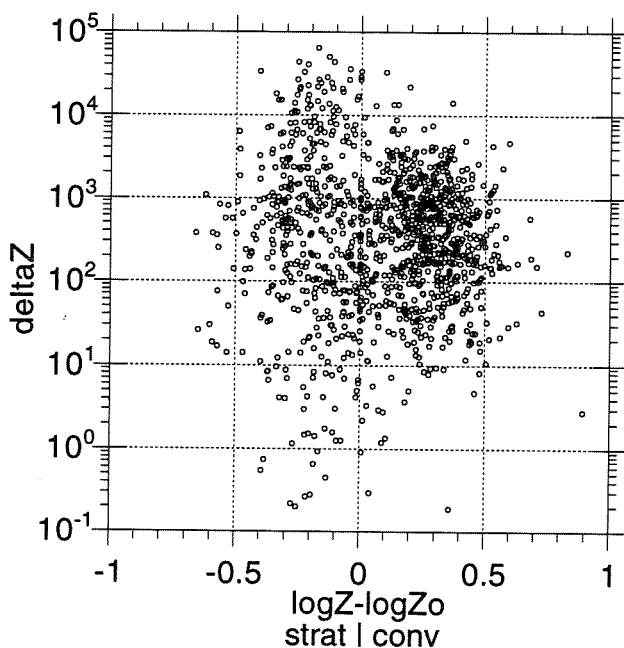


Fig 5 Change in Z from 6s sample before to 6s sample after vs $\log Z - \log Z_0$. Z_0 is fit line on Fig2 separating stratiform and convective samples. Values <0 - convective, >0 stratiform.

4.0 REFERENCES

Hu, Zailiang, and R. C. Srivastava, 1995: Evolution of raindrop size distribution by coalescence, breakup, and evaporation: Theory and observations. *J. Atmos. Sci.*, **52**, 1761-1783.

Leary, C. A., and R. A. Houze, 1979: The structure and Evolution of Convection in a Tropical Cloud Cluster, *J. Atmos. Sci.*, **36**, 437-457.

Low, T. b., and R. List, 1982: Collision, coalescence and breakup of raindrops, Parts a and B, *J. Atmos. Sci.*, **39**, 1591-1618.

Tokay, A., and D. A. Short, 1996: Evidence from tropical raindrop spectra of the origin of rain from stratiform and convective clouds. *J. of Appl. Meteor.*, in press.

Waldvogel, A., 1974: The No jump of raindrop spectra. *J. Atmos. Sci.*, **31**, 1067-1078.

Zipser, E. J., 1969: The role of organized unsaturated downdrafts in the structure and rapid decay of an equatorial disturbance. *J. of Appl. Meteor.* **8**, 799-814.

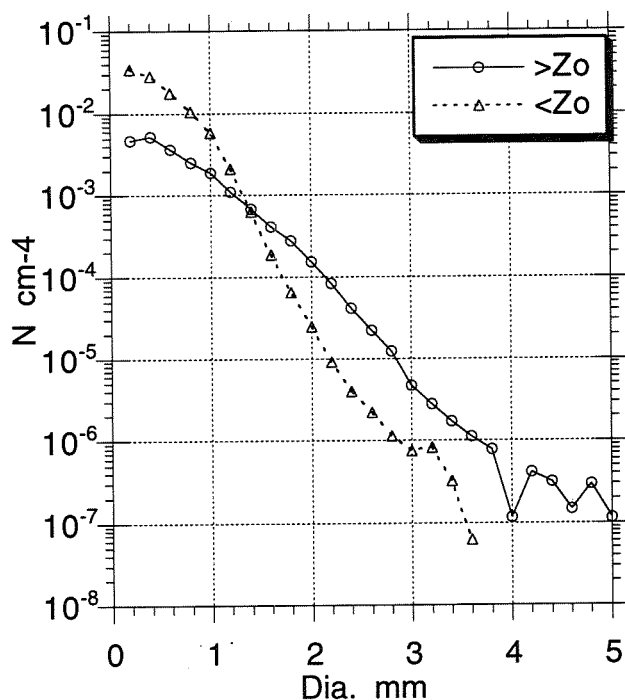


Fig. 6 Mean drop size distributions for the rain rate interval from 1 - 7 mm/hr, above Z_0 stratiform, below Z_0 convective.

FORMATION OF DROPLETS IN A MARINE STRATOCUMULUS LAYER

Edward E. Hindman*

Central Department of Meteorology
Tribhuvan University
Kirtipur, Nepal

1. INTRODUCTION

Fitzgerald (1974) showed that droplet spectra measured near the bases of continental and marine cumulus clouds could be reproduced using a one-dimensional, adiabatic parcel model with measured cloud condensation nuclei (CCN) and updrafts. Hindman and Bodowski (1996) showed that mean-droplet sizes in marine stratocumulus, estimated from satellite-detected radiance, could be reproduced using a similar model with measured CCN and assumed updrafts. Recently, droplet and CCN measurements have been obtained from a marine stratocumulus layer. We employ these measurements to test the limits of the model.

2. MEASUREMENTS

On 21 June 1994, an oil-fired vessel steamed offshore Monterey, CA underneath a thin, broken stratocumulus layer which topped a well-mixed, buoyancy-driven boundary layer as determined from airborne vertical profiles of sensible and latent heat and buoyancy fluxes (Brooks, Johnson and Rogers, 1995, personal communication). No ship-track attributable to the vessel was detected in the $3.7 \mu\text{m}$ radiation reflected from the cloud layer measured by a NOAA satellite (Durkee, 1995, personal communication). Ship-tracks are anomalous linear features detected in $3.7 \mu\text{m}$ satellite images of marine stratocumulus layers caused by steaming ships (e.g., Hindman, et al, 1994). Tracks contain more and smaller droplets than the nearby ambient cloud and, thus, differentially affect the $3.7 \mu\text{m}$ radiation (Coakley, et al., 1987).

Experimental evidence that no ship-track was produced comes from airborne condensation nucleus (CN) and droplet spectrometer (FSSP) measurements (Hobbs, 1995, personal communication). Distinct and systematic elevated CN concentrations were measured in the cloud layer indicating the presence of the ship's plume but no corresponding perturbation to the cloud droplet spectra was detected. Further, no significant differences in cloud droplet-residue particles from the airborne counterflow virtual impactor (CVI) measurements (Noon, 1995, personal communication) were detected between the region of the cloud layer affected by the plume and the ambient region. This result

indicates the CCN produced by the ship were too small to nucleate additional cloud droplets. Supporting the finding with the CVI, the airborne CCN measurements (Hudson, 1995, personal communication) show concentrations in the plume with critical supersaturations greater than about 0.2% were not larger than concentrations in the nearby ambient air (Fig. 1).

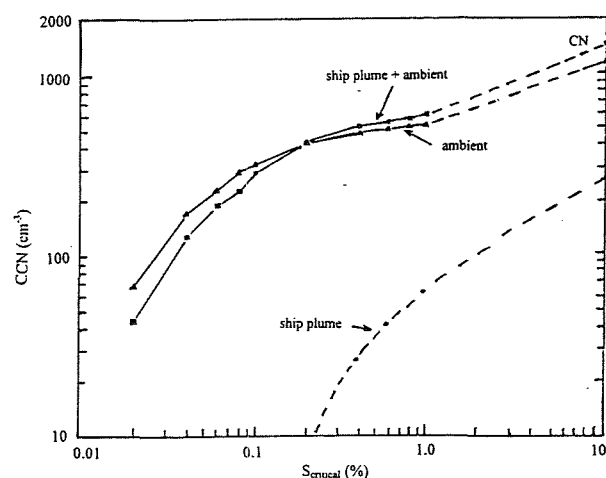


Figure 1. CCN measurements made from the UW C131 aircraft on 21 June 1994 at 1144 PDT using the chamber of Hudson and Frisbee (1991). The values at 10% are from a condensation nucleus instrument. The measurements were obtained 5 miles from the vessel.

3. CALCULATIONS

Numerical simulations of the measured cloud features were performed using an adiabatic, one-dimensional cloud model (Hindman and Bodowski, 1996). The ambient CCN spectra (Fig. 1), the airborne, subcloud temperature (T) and dew point measurements (T_d) (Hobbs, 1995, personal communication) and an assumed updraft were used to initialize the model. The calculations proceeded until the calculated cloud liquid water content (LWC) corresponded to the average value measured from the aircraft near the top of the layer. At this point, the calculations were terminated. The resulting droplet effective radius (D_e) and droplet concentration (N) were remarkably close to the airborne measurements in the ambient cloud (Fig. 2a). This result indicates the model reasonably simulated cloud formation in the ambient conditions.

*On sabbatical leave from The City College of the City University of New York, USA

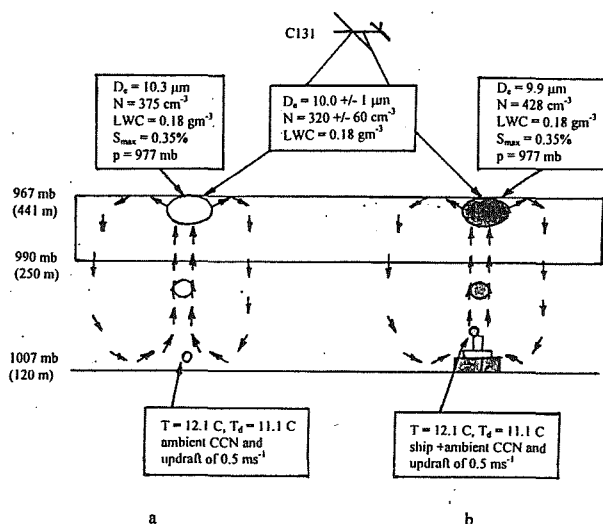


Figure 2. Results of calculations using the cloud model: a) ambient parcel and b) parcel containing ambient plus ship CCN. The symbols are defined in the text.

The ambient CCN values, then, were replaced with the values measured in the ship's plume (Fig. 1, ship plume + ambient) and the calculations were repeated. The resulting droplet effective radius reduced $0.4 \mu\text{m}$ and the concentration increased by 53 cm^{-3} from the ambient results (Fig. 2b), changes within the variations of the measurements. Hence, the model calculations confirm that the ship did not produce sufficient CCN with critical supersaturations small enough to nucleate significant numbers of droplets and produce a ship-track in the stratocumulus layer.

The measured average droplet spectrum near the top of the cloud layer is compared with the calculated spectrum in Figure 3. The spectra agree in mean droplet size and number concentration but the width of the measured spectrum is considerably broader than the calculated spectrum. The model did not include activation of new droplets accounting for the absence of the small droplets. Further, apparently coalescence was occurring in the cloud because of the large droplets that were not reproduced in the calculations; coalescence was not considered in the model. Nevertheless, the model reproduced two of three spectra parameters; namely mean droplet size and number concentration.

4. CONCLUSIONS

Cloud droplet formation in a marine stratocumulus layer was investigated using a 1D adiabatic parcel model and measured initial conditions. The calculations confirmed the observation that a steaming ship did not produce a ship-track, caused by numerous small droplets, even though its plume reached the cloud layer. The plume contained no CCN with critical supersaturations smaller than the calculated cloud maximum supersaturation (S_{max}). Further, the calculated cloud

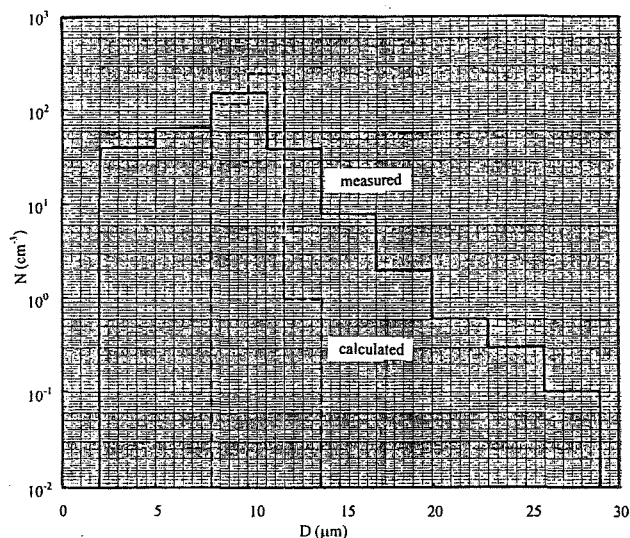


Figure 3. Average cloud droplet spectrum measured during the first penetration of the ship's plume imbedded in the stratocumulus layer (solid line) and the calculated spectrum (dashed line).

droplet mean diameter and number concentration were close to the measured values. However, the width of the calculated spectrum was smaller than measured. These results indicate the 1-D parcel model can simulate reasonable features of marine stratocumulus droplet spectra. Activation of new droplets and droplet coalescence will have to be included to simulate more representative spectra.

5. ACKNOWLEDGMENTS

The research was sponsored by the ONR. Robert Bodowski performed the model simulations and droplet analyses.

6. REFERENCES

- Coakley, Jr., J. A., R. L. Bernstein and P. A., Durkee, 1987: Effect of ship-stack effluents on cloud reflectivity. *Science*, **237**, 1020-1022.
- Fitzgerald, J. W., 1974: A study of the initial formation of droplets in marine and continental cumuli. *Ph. D. Thesis*, Univ. Chicago.
- Hindman, E. E., W. M. Porch, J. G. Hudson and P. A. Durkee, 1994: Ship-produced cloud lines of 13 July 1991. *Atmos. Environ.*, **28**, 3393-3403.
- Hindman, E. E. and R. J. Bodowski, 1996: A marine stratus layer modified by nuclei from a ship plume. *J. Appl. Meteor.*, in press.
- Hudson, J. G. and P. R. Frisbee, 1991: Cloud condensation nuclei near marine stratus *J. Geophys. Res.*, **96**, 20975-21008.

PRECIPITATION IN STRATIFORM CLOUDS: MODELING RESULTS AND COMPARISON WITH OBSERVATIONS

Thomas Trautmann

Inst. für Physik der Atmosphäre, Johannes Gutenberg-Universität, 55099 Mainz, Germany

1. INTRODUCTION

Stratiform boundary layer clouds cover a large area of the Earth and thus play a dominant role in both the global radiation budget as well as the hydrological cycle. Since this cloud type typically has a depth of only a few hundred meters, small variations in the optical properties may have a large effect on the albedo of these cloud systems. Various field experiments revealed that a delicate balance between radiative cooling, droplet growth, sedimentation of droplets and turbulence effectively controls the evolution of stratus and stratocumulus clouds. In this paper the interaction of microphysics, turbulence and radiation in boundary layer clouds is addressed with the aim to investigate the occurrence of drizzle in stratiform clouds.

2. MODEL DESCRIPTION

To explore these issues, the one-dimensional thermo-hydrodynamic cloud model MISTRA is used which is described in a companion paper at this conference (Trautmann and Strohmaier, 1996). MISTRA solves prognostic equations for the horizontal wind components, the potential temperature and the specific humidity. As turbulence closure the level 2.5 model of Mellor and Yamada (1982) is applied in which a prognostic equation for the turbulent kinetic energy is solved. Droplet growth by condensation and coalescence are treated in detail for a two-component system consisting of aerosol material and liquid water. The evolution of the spectral number concentration $f(a, r)$ of particles (aerosols and/or droplets) is then governed by

$$\frac{\partial f}{\partial t} = \frac{\partial}{\partial z} \left(K_h \frac{\partial f}{\partial z} \right) - \frac{\partial}{\partial z} ((w + w_t) f) - \frac{\partial}{\partial r} (\dot{r} f) + \frac{\partial f}{\partial t} \Big|_{COAL},$$

where w_t represents the terminal velocity of the particles (sedimentation term), w is a prescribed sub-

sidence velocity and \dot{r} is the growth velocity due to condensation/evaporation.

Solving the coalescence equation for a two-component system is a rather complicated task. Here we attempt to find a solution by applying a simple discrete bin approximation to the continuous coalescence equation as described in Seeßelberg *et al.* (1996). Firstly, one introduces an appropriate set of radius bins Δa_k and Δr_i for discretizing the aerosol and water components, respectively. The number concentration, N_{ik} , of particles in the two-dimensional bin $\Delta r_i \Delta a_k$ is then defined as

$$N_{ik}(t) = f(a, r, t) \Delta r_i \Delta a_k.$$

One can then show that the discrete bin approximation of the coalescence equation can be formulated as

$$\begin{aligned} \frac{\partial N_{ik}(t)}{\partial t} = & \frac{1}{2} \sum_{l=1}^{N_r} \sum_{m=1}^{N_r} \sum_{r=1}^{N_a} \sum_{s=1}^{N_a} W_{ilm}^r W_{krs}^a N_{lr} N_{ms} K_{lr,ms} \\ & - N_{ik} \sum_{l=1}^{N_r} \sum_{r=1}^{N_a} N_{lr} K_{ik,lr}, \end{aligned}$$

where N_a and N_r are the total number of radius bins for aerosol and water, respectively. The quantity $K_{ik,lr}$ is an average value of the coalescence kernel for the involved radius bins. The triple-index quantities W_{ilm}^r and W_{krs}^a are defined in a manner that both the number concentration as well as the particle mass are treated physically consistent (i.e. consistent number and mass balance). The evaluation of the four-fold sum is extremely CPU time intensive. However, it can be shown that due to the pairwise interaction of the particles this sum can be effectively reduced to a double summation.

4. NUMERICAL ISSUES

The lower 1000 m of the boundary layer are discretized with a resolution of $\Delta z = 10$ m. Between

1000 and 2000 meters a logarithmically expanding grid is chosen. A constant model atmosphere allows one to extend the radiation calculations up to a height of 50,000 meters.

For the cloud microphysical grids 60 radius bins for the aerosol mass between $0.05 \leq a \leq 2.2 \mu\text{m}$ were chosen. A total number of 70 radius bins for covering the water mass of the particles is used, which covers the radius range $0.05 \leq r \leq 1045 \mu\text{m}$. The coalescence equation is solved using a time step of $\Delta t = 5 \text{ s}$, whereas the dynamical equations are integrated forward in time with $\Delta t = 10 \text{ s}$. The optical properties of the cloud-topped boundary layer and the radiative fluxes in the solar and terrestrial wavelength region are updated every 60 s.

4. DESCRIPTION OF A CASE STUDY

In the following section we present results for a marine, stratiform cloud layer evolution for a case in which the occurrence of precipitation-sized drops has been reported. The data of flight 526 on 22 July 1982 as presented by Nicholls (1984) were chosen. In the lower cloud half and beneath the cloud the OAP (optical array probe) registered drops with radii up to $150 \mu\text{m}$ in significant concentrations. Table 1 list the initial and boundary conditions that were used for the model simulation.

Table 1: Summary of the initial and boundary conditions employed.

Parameter	
$z_{inv} \text{ (m)}$	830
$v_g \text{ (m s}^{-1}\text{)}$	8.5
$D = \frac{\partial w}{\partial z} \text{ (s}^{-1}\text{)}$	4.5×10^{-6}
$\Delta T_{inv} \text{ (K)}$	6
$q(z > z_{inv}) \text{ (g kg}^{-1}\text{)}$	4
$N_{CN} \text{ (cm}^{-3}\text{)}$	180
$\sigma_{CN} \text{ (s}^{-1}\text{)}$	1.16×10^{-5}
$T_w \text{ (K)}$	288.15

In Table 1 z_{inv} denotes the initial height of the inversion, v_g is the modulus of the geostrophic wind, D is the divergence rate of the horizontal wind field, ΔT_{inv} is the temperature jump at z_{inv} , $q(z > z_{inv})$ denotes the specific humidity above the inversion, N_{CN} is total concentration of condensation nuclei (CN),

and T_w is the sea surface temperature.

The CN production rate, σ_{CN} , corresponds to a replenishment of the initial CN distribution within 24 hours. This production is necessary, since continuing coalescence represents a sink for droplets. In essence it achieves that the total droplet concentration is approximately steady over time.

5. RESULTS

Figure 1 presents a contour plot of the liquid water content as a function of height and time. The contour levels are 0.01, 0.05, 0.1 to 0.7 (with spacing 0.1). The model has been initialized at midnight. It can be clearly seen that the cloud exhibits a strong day-night variability which is primarily caused by the absorption of solar radiation within the cloud. During night-time precipitation reaches the lower boundary of the model. The maximum liquid water content is 0.75 g m^{-3} .

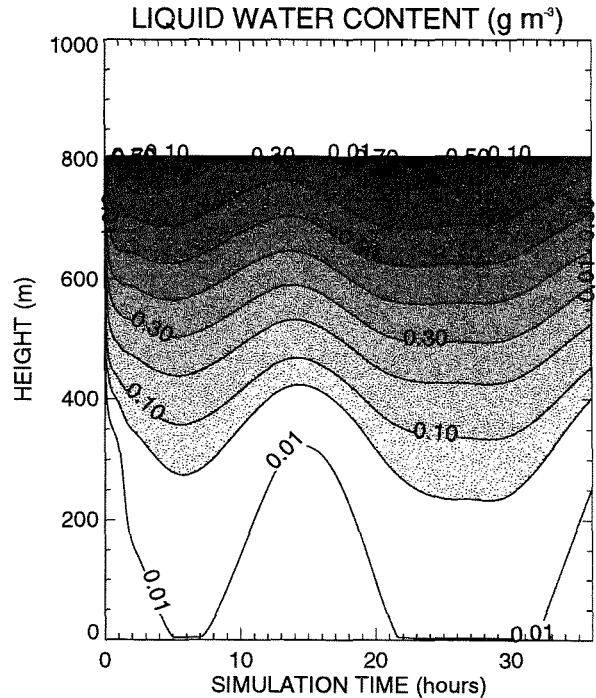


Figure 1: Contour plot of the cloud water content as a function of height and time.

Figure 2 shows the vertical profile of cloud water at 11 h model time. The diamond symbols represent the measurements taken by Nicholls (1984) during a descent at the same local time. The model results match the observed data quite well.

In Figures 3 and 4 we present a comparison of the droplet size distributions at the altitudes 730 and 90 m. Good agreement between modeled and measured

data is found for small droplets and in the precipitation tail of the spectra. A mismatch can be noted in the intermediate size range ($25 < r < 70 \mu\text{m}$) where the model predicts higher droplet concentrations.

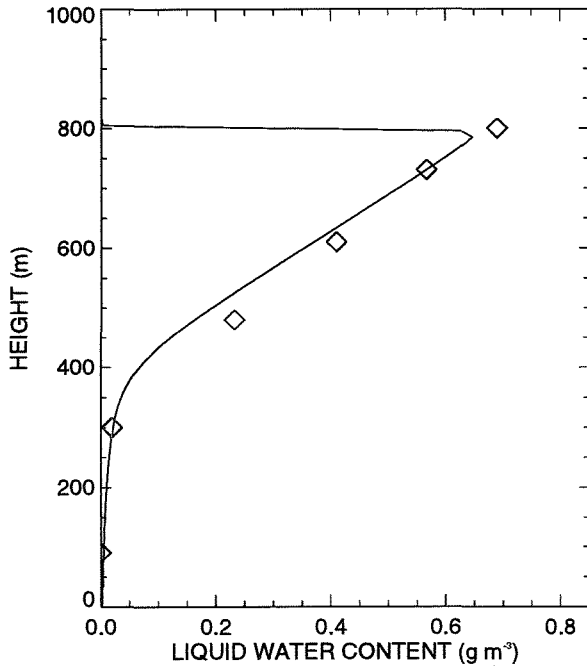


Figure 2: Modeled (at 11 h model time) and measured (diamonds) profile for the cloud water content.

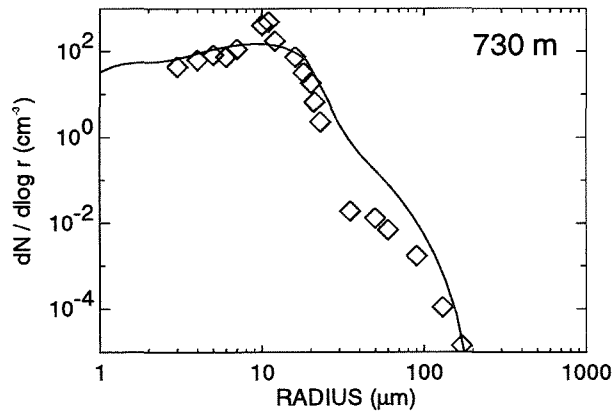


Figure 3: Comparison of the measured and simulated (11 h) droplet size distributions at altitude $z = 730$ m.

The precipitation flux is presented in Figure 5, also for 11 h model time. In the computed results a separation of the contributions from cloud droplets (FSSP range) and precipitating droplets (OAP range) has been made. The large diamond symbols are data calculated from the observed FSSP

and OAP spectra. Below cloud there is good agreement between the computed and measured drizzle rates. Within cloud the predicted precipitation fluxes are more than twice as high as the observed data. One reason for this is that the model cloud contains considerably more medium-sized droplets, see Figure 3. A sensitivity test revealed that this size region has the largest impact on the resulting drizzle rates. With his numerical experiments Nicholls (1987) arrived at a similar conclusion. Finally, re-

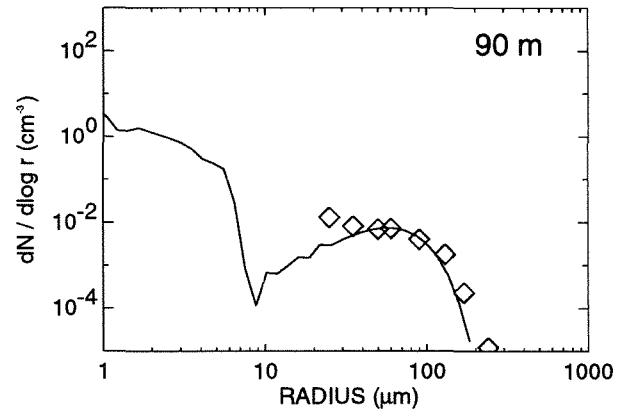


Figure 4: Same as Fig. 3, but for $z = 90$ m.

sults for the mean volume radius are shown in Figure 6. Here again a distinction is made for computed results in the FSSP and OAP size ranges. It can be seen that the modeled data compare very well with the observations. The secondary maximum at 200 m altitude is due to drizzle droplets.

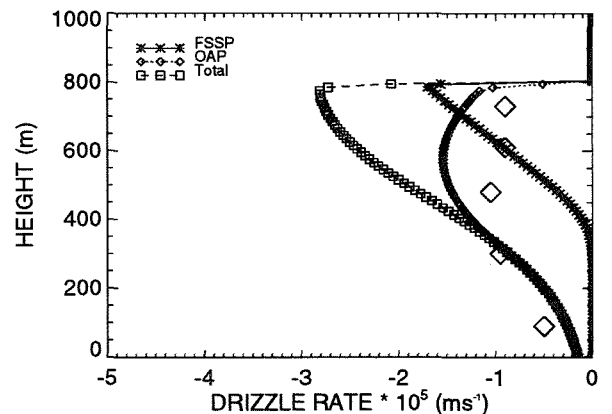


Figure 5: Drizzle rate as a function of altitude. Measured (large diamonds) and modeled results (11 h).

6. CONCLUSIONS

The presented one-dimensional, microphysical model of the cloud-topped boundary layer is capable

of reproducing the main characteristics of dynamics, radiation and microphysics. Due to the inclusion of coalescence the model results also reproduce the production of drizzle as observed by Nicholls (1984). Coalescence causes a considerable reduction in total cloud water. Without invoking precipitation formation the cloud would attain much higher cloud water contents as measured. The simulated droplet spectra agree well with measurements and also exhibit a large droplet tail extending up to about $200\text{ }\mu\text{m}$ in radius.

The modeled drizzle fluxes are larger than the data derived from the observations. This can be attributed to the fact that the model predicts higher droplet concentrations in the radius region from 20 to $70\text{ }\mu\text{m}$ within the cloud. An inspection of figure 9 in Nicholls (1987) reveals that the measurement ranges of the FSSP and OAP probe do not overlap in this region. The absence of an overlap between these two parts of the spectrum is believed to be caused by the OAP probe undercounting smaller particles (c. f. Nicholls, 1987). Drizzle rates derived from such spectra thus are prone to underestimation. To clarify this point, further investigations will be carried out by using other sources of measurements.

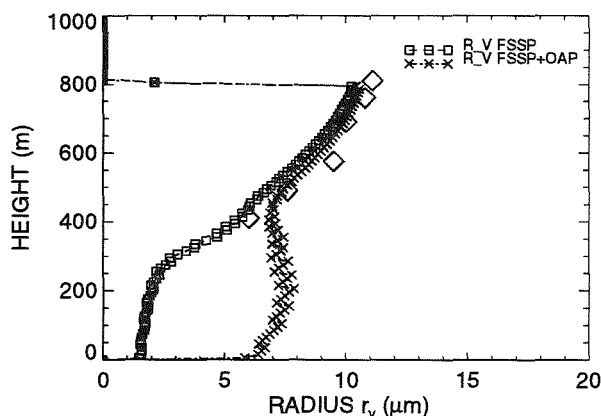


Figure 6: Same as Fig. 5, but for the mean volume radius of the droplets.

7. REFERENCES

- Bott, A., T. Trautmann, and W. Zdunkowski, 1995: A numerical model of the cloud topped planetary boundary layer: Radiation, turbulence and spectral microphysics in a marine stratus. *Quart. J. of the Royal Meteor. Soc.* (in print).
- Hoppel, W. A., and G. M. Frick, 1990: Submicron aerosol size distributions measured over the tropical and south Pacific. *Atmos. Environ.*, **24A**, 645–659.
- Mellor, G. L., and T. Yamada, 1982: Development of a turbulence closure model for geophysical fluid problems. *Rev. Geophys. Space Phys.*, **20**, 851–875.
- Nicholls, S., 1984: The dynamics of stratocumulus clouds: aircraft observations and comparisons with a mixed layer model. *Quart. J. Roy. Meteor. Soc.*, **110**, 783–820.
- Nicholls, S., 1987: A model of drizzle growth in warm, turbulent, stratiform clouds. *Quart. J. Roy. Meteor. Soc.*, **113**, 1141–1170.
- Seefeldberg, M., T. Trautmann, and M. Thorn, 1996: Stochastic simulations as a benchmark for mathematical methods solving the coalescence equation. *Atmosph. Research* (in print).
- Trautmann, T., and E. Strohmaier, 1996: Explicit cloud microphysics and code parallelization: Possible strategies and first experiences on a massively parallel supercomputer. (These proceedings)
- Zdunkowski, W. G., W.-G. Panhans, R. M. Welch, and G. J. Korb, 1982: A radiation scheme for circulation and climate models. *Beitr. Phys. Atmosph.*, **55**, 215–238.

THREE-DIMENSIONAL DYNAMICS IN A ONE-DIMENSIONAL CONDENSATIONAL GROWTH MODEL OF CUMULUS CLOUDS.

Jacques R.M. Pasquier and Peter R. Jonas

Dept. of Physics, U.M.I.S.T., Manchester, M60 1QD, UK.

1. INTRODUCTION

In this study, the microphysical characteristics of cumulus clouds were investigated. Observations were compared with calculations of the growth of droplets due to condensation made using two separate numerical models. The first model was a three-dimensional (3D) large-eddy simulation (LES) of a field of cumulus clouds in which parcels of air were released in the thermals and their subsequent trajectories were followed to ascertain the origin of in-cloud air. The dynamical results from these representative parcels were then used to impose the vertical motions of a parcel in a one-dimensional microphysical model of condensational growth (MCG) with the same environment conditions as for the LES runs.

2. OBSERVATIONS

The observations of the turbulent fluxes in marine cumulus cloud fields obtained from Meteorological Office Research Flight A119 are presented in Smith and Jonas (1995). Table 1 shows the microphysical characteristics of the cumuli observed during the three-level in-cloud runs of this flight. The two lower levels have two sets of values indicating the two runs made at different times and therefore in different clouds.

The liquid water content increased with height to a maximum at cloud top of 0.973 gkg^{-1} . This is about 18 % of the adiabatic liquid water content for a cloud of around 1400 m deep. The mean droplet radius and effective droplet radius increased with height in accordance with Raga and Jonas (1993) but in contrast with observations of continental cumuli in which the effective radius does not vary with

z /(m)	q_l /(gkg^{-1})	r /(μm)	r_{eff} /(μm)	n /(cm^{-3})
1016	0.124	5.680	7.143	31.470
1016	0.061	5.625	6.985	18.840
1829	0.387	7.108	9.858	35.010
1829	0.142	6.785	9.883	12.570
2133	0.973	7.143	10.830	40.740

Table 1: Cloud characteristics of Flight A119. The values represent the average over all in-cloud points and are :- z - flight height; q_l - mean liquid water content; r - mean droplet radius; r_{eff} - mean effective radius; n - mean droplet number concentration.

height above cloud base. This was a consequence of the weaker updraughts found in the maritime cumuli (typically less than 4 ms^{-1} at cloud top in A119) while those in continental cumulus are several times larger than this. Hence, the updraughts were not strong enough for the supersaturation to rise sufficiently to activate large numbers of entrained nuclei.

The variations in the mean droplet number concentration are more difficult to quantify. In Raga and Jonas (1993), the averages over all the in-cloud points for all four flights showed no clear trend with height in contrast to what is observed in marine stratocumuli. The results for A119 show a significant difference in droplet number concentration, based on whether it was the first or second leg of the level flight (in different clouds), although the data suggested a maximum near cloud top. Due to the more vigorous entrainment in cumulus clouds, there is much greater variability than in stratocumuli which resulted in the differences in droplet concentration.

3. SIMULATIONS

3.1 The LES model

The Meteorological Office LES model (Mason, 1989), which uses a bulk-water parametrisation microphysical scheme, was used for the simulation of an observational study of fields of small, warm (ice-free) cumulus clouds. The initial profiles of potential temperature and total water content used for the simulations were based on the initial sounding from Flight A119. Prescribed latent and sensible surface heat fluxes were applied constantly throughout the simulations. A circular perturbation in the centre of the domain, of magnitude 0.1K, was included at the start to initiate a thermal and subsequent convective motions. The turbulent transport in the simulated cumulus-capped boundary agreed reasonably well with the observations. Further details of initial conditions and turbulence statistics can be found in Pasquier and Jonas (1995). The model was extended to permit the release of parcels (57 in 2D and 54 in 3D) from three different levels after two hours of simulation time, ie. when the LES model approached a quasi-steady state. An analysis of the trajectories in the LES domain was carried out and representative ones were chosen.

3.2 The microphysical model

The MCG (Mason and Jonas, 1974) considered a rising thermal as an expanding spherical mass mixing with its surroundings by turbulent motions generated within the thermal. A critical assumption was that the mixing transferred droplets from the cloud to the drier environment where they evaporated and were replaced by fresh condensation nuclei of the same nucleus mass. In this application, the vertical ascent was prescribed by the LES trajectories while temperature, supersaturation, radius and liquid water content of the thermal were determined from the conservation equations of the MCG. The radii and concentration of the droplets were also explicitly determined, with an initial condensation-nucleus spectrum consisting of 60 nuclear mass classes of sodium chloride, ranging from 1.46×10^{-20} kg to 5.28×10^{-14} kg. Entrainment processes were taken as inho-

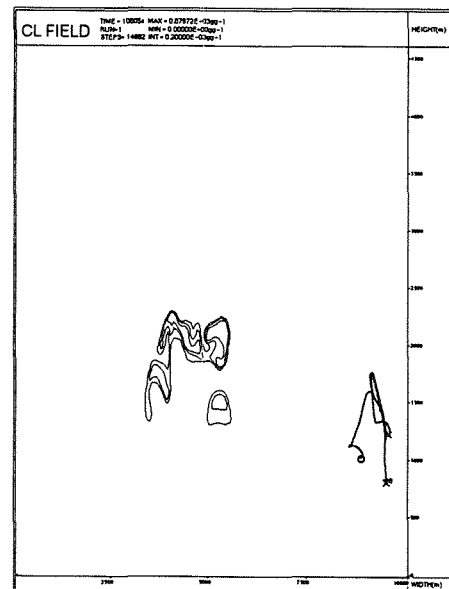


Figure 1: Vertical cross-section of the liquid water field in the 10×4.7 km² domain. The contour interval and lowest contour are 0.2 g kg^{-1} and 0.1 g kg^{-1} . The dark line is the trajectory of the parcel released at a height of 800 m. The numbered cross is the point of release and the circle denotes its position after one hour. The thicker regions of the line show when the parcel was in-cloud.

mogeneous. The vertical profiles of temperature and humidity from the LES were used to represent the environmental conditions in the MCG. These statistics were horizontally-averaged over the domain and time-averaged over the third hour of simulation from the LES to represent the mean environment in which the LES parcel was transported. One of the MCG runs will be discussed below to describe the microphysics of the simulated cumuli.

4. RESULTS AND DISCUSSION

4.1 Evolution of the parcels

The 2D and 3D trajectories provided similar patterns. Twenty-one of the parcels were found to enter cloud during the 2D LES runs, but only one will be considered here for the microphysical runs. A brief summary of the trajectories simulated may be found in Jonas *et al* (1996). The parcel considered here was released at a height of 800 m and its subsequent motion, shown in Fig. 1, indicates that it was

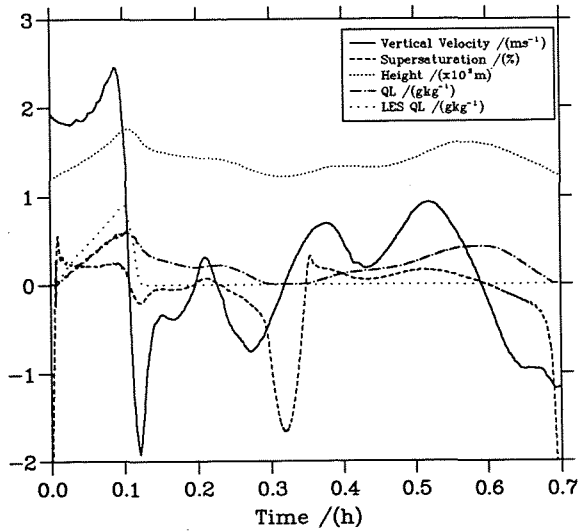


Figure 2: Evolution of the vertical velocity, supersaturation, height and liquid water content for a start height of 1200 m in the MCG simulations. The liquid water content for the corresponding LES parcel is also shown.

initially in a cloudy updraught but then was detrained from the cloud, finishing about 800 m from its point of origin after one hour.

This parcel released from below cloud base was in-cloud after 200 s. A thermal was initiated from this condensation level with a radius (R) of 625 μm , based on the size of LES clouds at the same height. The evolution of the thermal properties is shown in Fig. 2. Condensation occurred at the same time as the LES parcel but, characteristically for these comparisons, the peak liquid water content was greater for the LES runs. The peak supersaturation was about 0.55 %, which is quite high for these clouds. The maximum vertical velocity (W) was 2.5 ms^{-1} . Based on an entrainment rate of $(0.6W/R)$, the thermal attained a maximum liquid water content of 0.57 gkg^{-1} at the top of the first ascent at 1760 m, which contrasted with the LES value of 0.8 gkg^{-1} . This was higher than the mean value from the observations but only accounts for one thermal. Once caught in a downdraught, the cloud began to evaporate as it mixed with the subsaturated environmental air, causing the drop in supersaturation. The thermal then descended, reaching a minimum velocity of -1.9 ms^{-1} . The LES parcel then completely evaporated while the MCG parcel remained saturated. The lifetime of the cloudy

parcel in the MCG was approximately 20 mins.

In the second significant, but weaker, updraught, the MCG parcel attained a height of 1580 m, with a maximum vertical velocity of 0.9 ms^{-1} , a peak liquid water content of 0.42 gkg^{-1} and a peak supersaturation for this ascent of 0.3 %. The values for this second ascent were lower than the first because the thermal was initially mixing with air which had been dried by the earlier thermals.

4.2 Microphysical characteristics

The MCG parcel's microphysical characteristics were followed and comparisons were made with observations. The initial spectrum in the MCG was critical in the development of the microphysics that were simulated. The observations did not describe the nucleus spectra and there are limitations in the range over which droplet sizes can be measured by the probes. As a consequence, quantitative comparisons were difficult and the analysis was restricted to the general variation of data with height and to a common range for droplets of diameter $2 \mu\text{m}$ to $45 \mu\text{m}$.

The droplet spectra for the first and second thermals described in the previous section are shown in Fig. 3. The initial spectrum developed a bimodal structure at the top of the first ascent with 230 activated nuclei. There was evaporation of the larger droplets in the descent, thereby reducing the number of activated nuclei. At the top of the second ascent, the droplet spectrum has further broadened as some droplets have grown to a radius of $19 \mu\text{m}$. The bimodal structure is preserved with the double peak occurring at radius of $10 \mu\text{m}$. For MCG parcels which reached the inversion (not shown), the spectrum also exhibited bimodality, but with a larger number droplets in the middle part, with a peak at $12\text{--}13 \mu\text{m}$ and the largest droplets reaching $20 \mu\text{m}$ in size.

The mean droplet radius was found to increase from an initial value of $2.65 \mu\text{m}$ to $6.05 \mu\text{m}$ at the top of the second thermal. The mean effective radius also increased from $4.06 \mu\text{m}$ to $7.44 \mu\text{m}$. These values are smaller

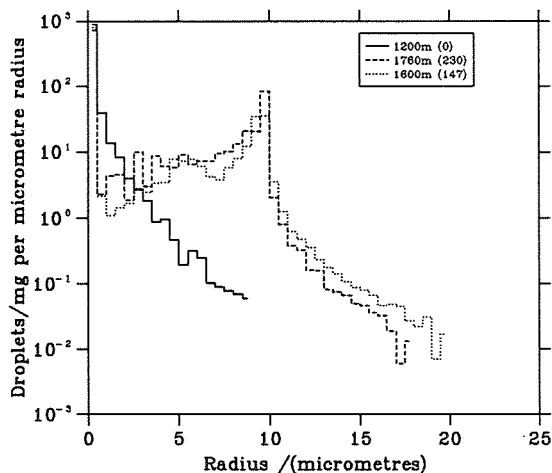


Figure 3: The evolution of the droplet spectrum with height for successive thermals. The initial spectrum (solid line) was determined by assuming that the concentrations of sodium chloride nuclei varied inversely as the nuclear mass. The first thermal (dashed) reached 1760 m and the second (dotted) reached 1600 m. The number in the parentheses represents the number of droplets (activated nuclei) per mg of air.

than the observations but show similar variations with height. A possible explanation for the discrepancies in effective and mean radii is that the assumed initial spectrum did not contain enough large nuclei, thereby leading to the growth of the smaller sized droplets at the expense of larger ones. The mixing rates were also calculated to understand the exchange mechanisms occurring between the cloud and the environment. Regions of strong exchanges were consistent with the onset of evaporation as the entrainment of drier environmental air resulted in reduction in the liquid water content.

5. CONCLUSIONS

The observed microphysics of the cumuli in this study agree well with previous observational studies. The initial development of the clouds in the MCG was consistent with the simulated LES clouds, although the liquid water was underestimated and the cloudy thermal life-time was longer than the time the LES parcel spent in-cloud. This demonstrates the difficulty in using 1D models which do not allow horizontal variations of the imposed LES statistics.

The simulated results demonstrate the condensational growth of droplets leads to a broadening of the spectra which exhibited a bimodal nature. This process is thought to account for the creation of large droplets which are necessary for the initiation of coalescence. Given the limitations of the initial conditions discussed in 4.2, the variations of the mean droplet radius and droplet mean effective radius with height in the simulations were consistent with the observed characteristics. The droplets were growing with successive thermals to sizes approaching those observed. Further details will demonstrate the effect of the initial spectrum and some three-dimensional parcel trajectories. The effect of entrainment processes on the microphysical characteristics of various parcels will be analysed and further application of this work is considered.

6. REFERENCES

- Jonas, P. R., J. R. M. Pasquier and S. A. Smith, 1996: Turbulent entrainment into cumulus clouds. *Proc. 12th Int. Conf. on Clouds and Precip., Zurich, 19-23 August 1996*.
- Mason, B. J., and P. R. Jonas, 1974: The evolution of droplet spectra and large droplets by condensation in cumulus clouds. *Quart. J. Roy. Meteor. Soc.*, **100**, 23-38.
- Mason P. J., 1989: Large-eddy simulation of the convective atmospheric boundary layer. *J. Atmos. Sci.*, **46**, 1492-1516.
- Pasquier, J. R. M., and P. R. Jonas, 1995: Large eddy simulations of fields of cumulus clouds. *Proc. Conf. Cloud Phys., AMS, Dallas, 15-20 January*, 575-576.
- Raga, G. B., and P. R. Jonas, 1993: Microphysical and radiative properties of small cumulus clouds over the sea. *Quart. J. Roy. Meteor. Soc.*, **119**, 1399-1417.
- Smith, S. A., and P. R. Jonas, 1995: Observations of the turbulent fluxes in fields of cumulus clouds. *Quart. J. Roy. Meteor. Soc.*, **110**, 783-820.

COMPARISONS BETWEEN OBSERVATIONS AND NUMERICAL MODEL SIMULATIONS OF THE FORMATION OF SUPERCOOLED DRIZZLE DROPS IN STRATIFORM CLOUDS

Roelof T Brientjes and Gregory Thompson

Research Applications Program, NCAR*
P.O. Box 3000, Boulder, CO 80307

1. INTRODUCTION

Regions of large drops in clouds, especially supercooled drizzle size drops can be a severe icing hazard to aviation. Politovich (1995) found based on data analyses from in-situ research flights that the presence of large droplets (median volume diameter ($MVD > 30 \mu m$) alone, was not sufficient. Liquid water contents $> .2 g m^{-3}$ were needed to substantially affect the performance of aircraft. This was further confirmed by Rasmussen et al. (1995) who found that liquid water contents $> .25 g m^{-3}$ were needed to initiate an effective coalescence process to produce drizzle size droplets in a winter storm along the Colorado Front Range. Politovich (1995) also found that with high liquid water contents at temperatures warmer than $-10^{\circ}C$ can result in extreme performance degradation. The mass of ice accumulating due to supercooled liquid water (SLW) is highly dependent on the relatively few large drops in the spectrum, since they are more likely to impinge and freeze on the airframe. SLW increases rapidly when the number of large droplets increases, however air parcels with similar amounts of SLW but different drop-size distributions, could pose significantly different aircraft icing hazards. Generally, cloud ice and snow do not adhere to the airframe when in flight, and graupel and small hail may actually help remove accreted ice. However, cloud ice, snow and graupel are the main depleters of SLW in the atmosphere and therefore are important parameters in the problem of aircraft icing.

In a study by Vilcans (1989), occurrences of freezing rain (ZR) or freezing drizzle (ZL) at 110

airports around the United States were related to surface observations and data from radiosonde (RAOB) launches at these airports. During a period of 23 years ZL- was reported at Denver on seventeen different days. Results from this study indicate that although the temperature profiles are similar to that of freezing rain situations (with warm air overrunning cold air), it is seldom warmer than $0^{\circ}C$ aloft, even though ZL- is being reported. The freezing precipitation usually consisted of light freezing drizzle rather than freezing rain and was often associated with some snow grains. The ZL conditions were almost always accompanied by low cloud bases or ceilings; and the clouds often consisted of a single low layer with tops between 0.5 km and 1.5 km AGL and capped by an inversion with drier air above. Occasionally the cloud layers were as much as 2.0 to 2.5 km deep. Often surface temperatures were between $-2^{\circ}C$ and $-8^{\circ}C$, while the lowest temperatures within the cloud layer ranged between $-5^{\circ}C$ and $-10^{\circ}C$, with a few cases reaching as low as $-13^{\circ}C$. Many of these cases correspond to the typical upslope stratiform cloud layers associated with an arctic air outbreak on the east side of the Rocky Mountains.

Numerical mesoscale models that would allow model vertical motions to produce cloud water, and to deplete the so produced cloud water by ice crystal growth and other processes such as turbulent mixing has been used to forecast cloud microphysical variables. This approach has been extensively used in cloud models based on explicit microphysical schemes, with relatively good success for convective, summertime storms. Winter storms, however, typically require larger scale models for proper simulation, including the incorporation of time-dependent lateral boundary conditions and synoptic scale forcing. The recent studies by Rasmussen et al. (1995), and Brientjes et al., (1994) amongst others have shown good success in simulating the dynamics of winter storms using mesoscale models. Recently, Reisner et al. (1996) evaluated the predictions of icing using the Penn State/NCAR MM5 mesoscale model with a newly developed microphysical scheme which explicitly predicts regions of SLW in clouds.

* This research is sponsored by the National Science Foundation through an Interagency Agreement in response to requirements and funding by the Federal Aviation Administration Aviation Weather Development Program. The views expressed are those of the authors and do not necessarily represent the official policy or position of the U.S. Government.

Corresponding author address: Roelof T. Brientjes, NCAR, P.O. Box 3000, Boulder, CO 80307

The purpose of this paper is to describe a case study of an event in a typical Colorado Front Range winter storm in which an active coalescence process with large amounts of supercooled drizzle drops was observed. This event (7 March 1994) occurred during the 1994 Winter Storms and Icing Program (WISP) field program. Numerical simulations with the MM5 model will be used to compare with the observations.

2. 7 MARCH 1994 CASE STUDY

2.1 Observations

This day was characterized by an arctic front moving south through western Nebraska, eastern Wyoming and north-eastern Colorado. While temperatures ahead of the cold front in the cloud layer were initially above 0°C, this changed to below 0°C in the post-frontal airmass. The post-frontal upslope cloud was clearly evident on the visible satellite images as an advancing large area of stratus clouds covering western Nebraska, eastern Wyoming and northeastern Colorado. The front moved through the Nebraska, Colorado and Wyoming triple-point around 15:00 GMT and reached the Palmer Divide by 21:00 GMT. In

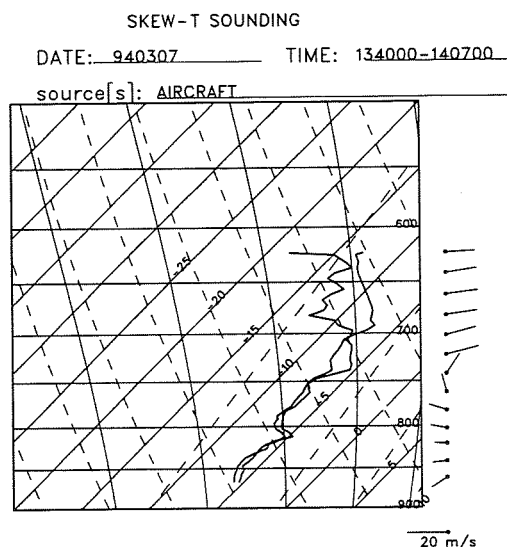


Figure 1. Aircraft sounding near Scottsbluff, NE.

addition to the low-level stratus associated with the post-frontal airmass, there was another cloud deck above and linked to the low-level cloud deck observed by the research aircraft. The higher cloud deck formed due to warmer southerly winds overriding the colder air around 750 hPa. This is evident from the aircraft sounding conducted near Scottsbluff, Nebraska shown in Fig. 2. Cloud bases were generally only a few hundred feet above the ground and fog was observed at many surface stations.

The extent of supercooled water in the clouds was widespread and very little ice was observed by

the aircraft. The primary precipitation process was a coalescence process operating at temperatures below 0°C. Both the NCAR research aircraft and the University of Wyoming aircraft reported mostly liquid water with numerous large drops in the cloud layer.

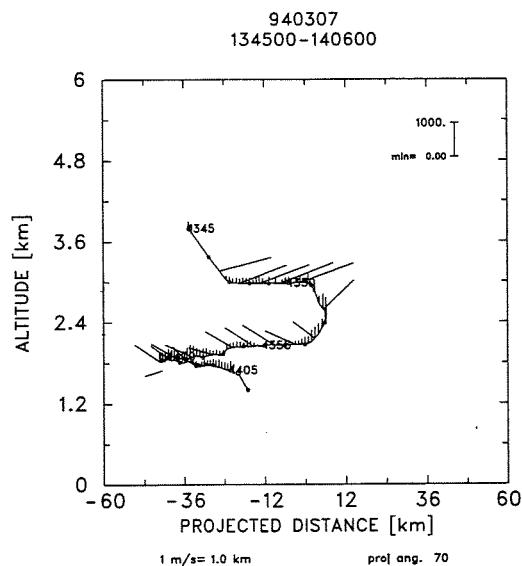


Figure 3. NCAR Electra aircraft track during descent through the cloud deck into Scottsbluff airport. The wind vectors are also plotted on the track and the vertical bars represent areas where cloud droplets were encountered by the PMS-FSSP probe.

As the front moved through eastern Colorado freezing drizzle was reported by all the surface stations and numerous volunteer snow observers that participated in the WISP field program. Data from the additional rawinsonde launches as part of WISP showed temperatures between -5 and -10°C in the cloud layer with cloud tops around 700 hPa. Aircraft coming into Denver all experienced icing during this period.

Icing was also consistently reported by the two WISP research aircraft during flights on this day. The NCAR Electra conducted a research flight in the Scottsbluff area and experienced the worst icing conditions it has flown through; with more than six inches of ice collected on some instrumentation on the aircraft during a descent through the cloud deck at Scottsbluff. Most of the research instrumentation was iced up to such an extent that measurements were unreliable after the descent and the aircraft had to land at Scottsbluff to de-ice and clear ice off the instrumentation. Streaks of ice build-up were also visible on the bottom of the tailwing section. Figure 3 shows a vertical profile of the flight track through the cloud on a missed approach into Scottsbluff airport. The wind vectors are plotted on the track and the vertical bars represent areas where cloud droplets

were encountered by the PMS-FSSP probe.

While easterly to southeasterly winds were evident in the lowest layer, the winds in the layer between 2.5 and 3.0 km MSL were southerly to southwesterly with westerly winds aloft in the dry air above the cloud deck. Concentrations of cloud droplets as measured by the FSSP were between 100 to 200 cm^{-3} near cloud top with LWC around 0.2 g m^{-3} ; the concentrations increased to around 300 cm^{-3} around 2.4 km MSL with LWC around 0.4 g m^{-3} . Measurements from the PMS-260X probe, which measures particles in the size range between 10 μm and 610 μm , indicated low concentrations (between 1 and 10 L^{-1}) of particles in the size range around 100 μm near cloud top. These increased significantly (around

100 L^{-1}) in the middle part of the cloud around 2.4 km MSL. Figures 4a to d display the combined particle spectra of the Aerosol Probe (ASASP), the FSSP, and the PMS-260X during different stages of the descent into Scottsbluff airport. The times correspond to the times plotted on the flight track in Fig. 3. It is clearly evident from these figures that an active coalescence process was operating in this cloud system with high concentrations of drizzle size drops produced in the lower part of the cloud deck.

The general meteorological conditions on this day support the earlier findings of Vilcans (1989) and Pobanz et al. (1994). In addition, wind shear was evident within the cloud layer which may also have enhanced the coalescence process. In addition, cloud condensation nuclei measurements

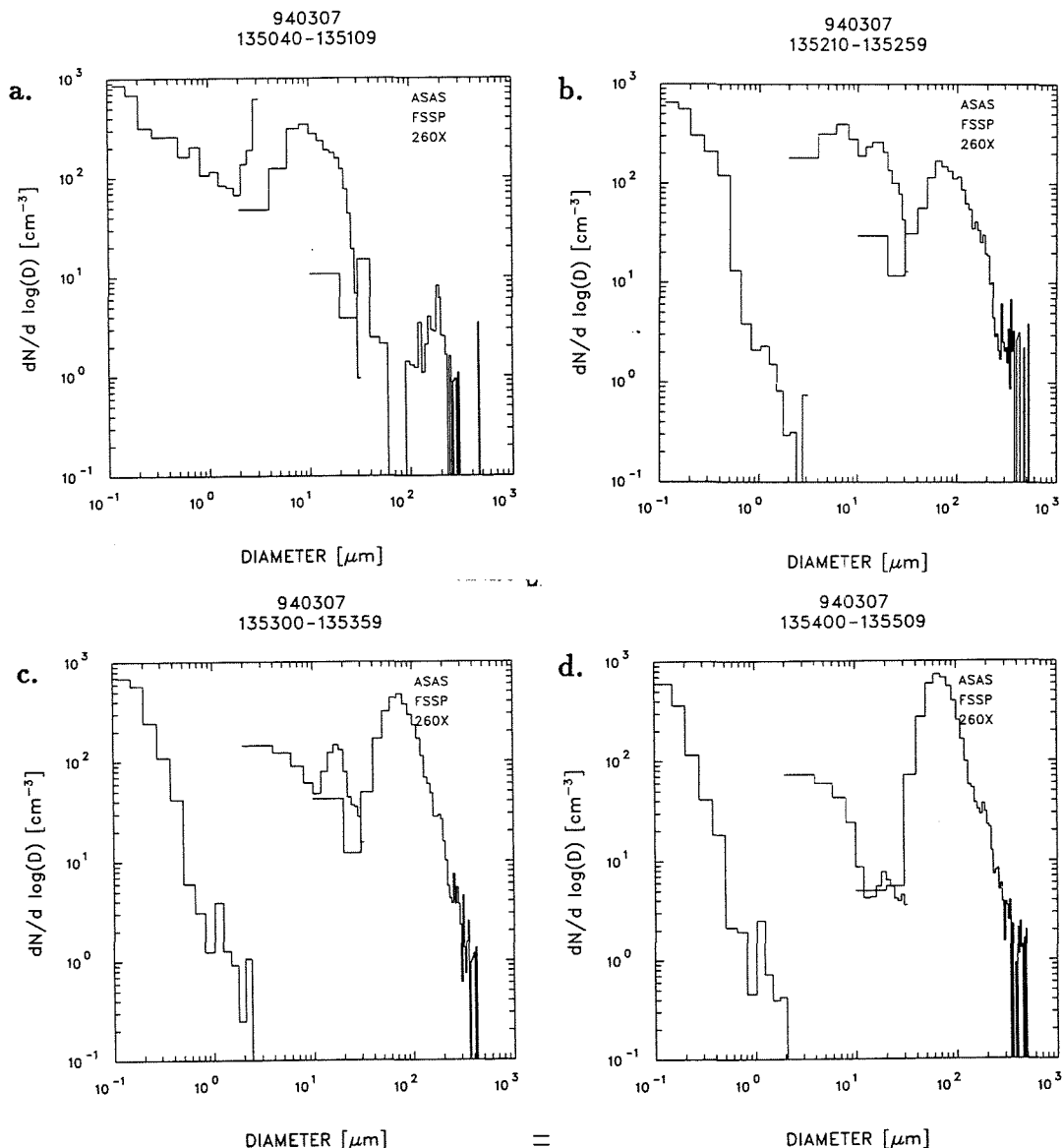


Figure 4. Combined particle spectra as measured by the PMS-ASASP, PMS-FSSP, and PMS-260X probes. Concentrations of the PMS-ASASP and PMS-FSSP are in cm^{-3} while the units for the PMS-260X probe are in L^{-1} .

(not shown here) indicated two different CCN distributions in the lower level and higher levels of the cloud. We are currently conducting a modeling study with a detailed microphysical model to study how this would effect the coalescence process. The results will be presented at the conference.

2.2 Modelling results

The NCAR/Penn State MM5 mesoscale model with explicit microphysics was also run for this case. Figure 4 shows two vertical cross-sections of the cloud liquid water mixing ratio in g kg^{-1} from the MM5 model simulation for 1500 UTC and 1800 UTC. It is clear from Fig. 5 that in several areas CLW values were in excess of 0.3 g kg^{-1} which is about the threshold that was found by Rasmussen et al. (1995) to initiate a coalescence process. Additional results will be presented at the conference including simulations from the detailed model.

3. DISCUSSION

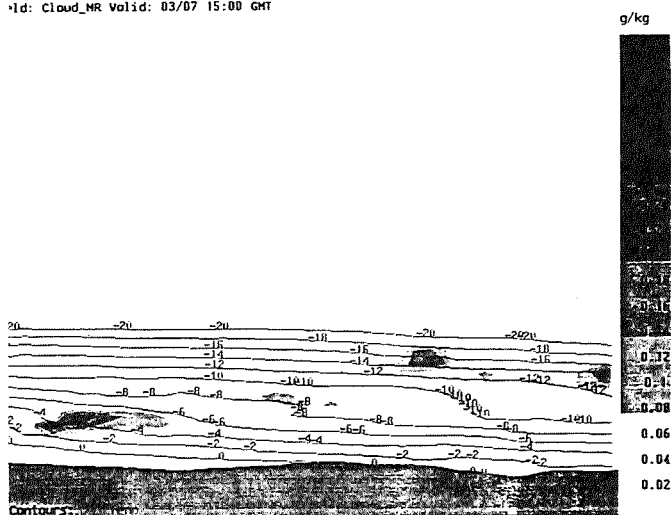
This case study presents a typical situation where icing could be hazardous to aircraft. It is therefore important to be able to identify such situations in order to provide adequate warning for such events. Comparing the observations and modeling results for this case study, showed that the model did well in diagnosing the freezing drizzle scenario and associated icing hazard.

Future work will concentrate on evaluating how consistently the model can detect similar situations. In addition, studies are ongoing to also use satellite data to detect and verify some of the modeling results.

4. REFERENCES

- Bruintjes R.T., T.L. Clark and W.D. Hall, 1994: Interactions between topographic airflow and cloud and precipitation development during the passage of a winterstorm in Arizona. *Journal of Atmospheric Sciences*, **51**, 48-67.
- Politovich, M.K., 1995: Effect of icing on a research aircraft and evaluation of a severity index. *J. Aircraft*, In press.
- Pobanz, B.M., J.D. Marwitz and M.K. Politovich, 1994: Conditions associated with large-drop regions. *J. Appl. Meteor.*, **33**, 1366-1372.
- Rasmussen, R.M., B.C. Bernstein, M. Murakami, G. Stossmeister, J.M. Reisner and B. Stankov, 1995: The 1990 Valentine's Day arctic outbreak Part I: Mesoscale and Microscale Structure and Evolution of the Colorado Front Range Shallow Upslope Cloud. Accepted for publication in the *J. Appl. Meteor.*, **34**, 1481-1511.
- Reisner, J., R.T. Bruintjes and R.M. Rasmussen, 1993: Preliminary comparisons between MM5

Id: Cloud_MR Valid: 03/07 15:00 GMT



Id: Cloud_MR Valid: 03/07 18:00 GMT

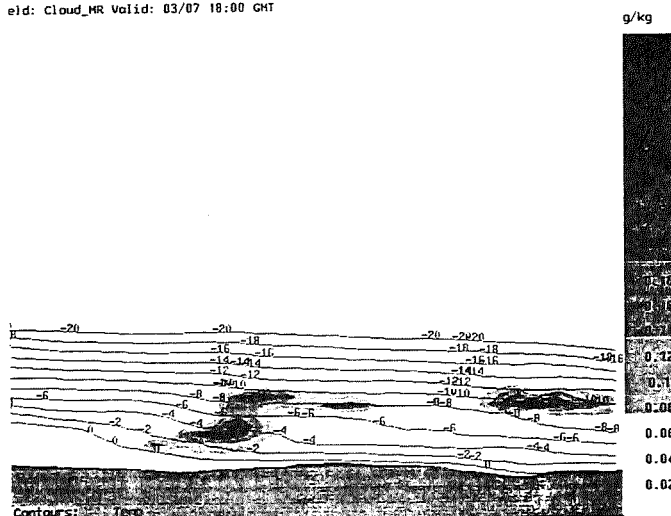


Figure 5. Vertical cross-sections between Denver and Scottsbluff of cloud liquid water mixing ratio in g kg^{-1} from the MM5 model simulation for 1500 UTC (a) and 1800 UTC (b)

NCAR/Penn State model generated icing forecasts and observations. *Preprints, 5th Int. Conf. on Aviation Weather Systems*, Vienna, VA, 2-6 August. Amer. Meteor. Soc., Boston, 65-69.

Vilcans, J, 1989: Climatological study to determine the impact of icing on low level windshear alert system. Report No. DOT-TSC-FAA-89-3, Volpe Transportation Systems Center, Cambridge, MA 02142.

A STOCHASTIC MODEL FOR SIMULATING COLLISION AND COALESCENCE IN WARM CLOUDS

Thomas Trautmann¹, Markus Seeßelberg² and Matthias Thorn²

¹Inst. für Physik der Atmosphäre, Johannes Gutenberg-Universität, 55099 Mainz, Germany

²Fakultät für Physik, Albert-Ludwigs-Universität, 79104 Freiburg, Germany

1. INTRODUCTION

Common mathematical methods for the treatment of the collision and coalescence process attempt to approximate the coalescence equation in various manners. Some of these methods may yield different results when realistic kernels are applied.

In this paper we present a modification of Gillespie's stochastic simulation algorithm. Since this technique provides a direct simulation of the physical process it does not rely on numerical approximations to evaluate the collision integrals. Therefore this algorithm can be used to perform benchmark calculations in order to test the quality of faster numerically-based solution methods. Two examples for these numerically-based methods will be considered, namely the integration scheme of Berry and Reinhardt and a very fast discrete bin technique.

2. MODEL DESCRIPTION

The stochastic simulation model is a simple but significant modification of Gillespie's (1975) algorithm. Details can be found in Seeßelberg *et al.* (1996).

First, droplet classes i ($i = 1, \dots, n$) are introduced which contain all droplets with radii between radii R_{i-1} and R_i . For the examples presented in Section 5 the grid $R_i = i \mu\text{m}$ with $R_0 = 0 \mu\text{m}$ is employed.

After a random waiting time τ the next coalescence event occurs at time $t + \tau$. This time interval is generated by picking a uniformly distributed random number $\eta \in [0, 1]$ and by putting $\tau = -D_0^{-1} \ln \eta$

and

$$D_0 \stackrel{\text{def}}{=} V^{-1} \sum_{\substack{r,s=1 \\ r \leq s}}^n K_{rs} N_r N_s + V^{-1} \sum_{r=1}^n K_{rr} \frac{N_r(N_r - 1)}{2}, \quad (1)$$

where D_0 is the total rate for any possible coalescence event, K_{rs} is the value of the coalescence kernel for a pair of droplets from classes r, s and V is the cloud volume.

The probability D_{rs} that the next coalescence will involve droplets of classes r and s , $r \leq s$, is given by

$$D_{rs} \stackrel{\text{def}}{=} \begin{cases} V^{-1} K_{rs} N_r N_s / D_0 & \text{if } r \neq s \\ V^{-1} K_{rr} \frac{N_r(N_r - 1)}{2 D_0} & \text{if } r = s \end{cases} \quad (2)$$

Due to the introduction of radius classes, only the mean mass $\bar{m}_i \stackrel{\text{def}}{=} M_i / N_i$ of all droplets which belong to a particular class i is known, where M_i, N_i are the total mass and number of the droplets in class i and in volume V . The mass m_i of the droplet which finally takes part in the coalescence event, and thus will be removed from the class it belongs to, is determined by choosing another uniformly distributed random number $m_i \in [\bar{m}_i - \Delta m_i, \bar{m}_i + \Delta m_i]$ where the width of the interval is defined as

$$\Delta m_i \stackrel{\text{def}}{=} \text{Min} \left\{ \left(\frac{4}{3} \pi \varrho R_i^3 - \bar{m}_i \right), \left(\bar{m}_i - \frac{4}{3} \pi \varrho R_{i-1}^3 \right) \right\}$$

It should be noted that Δm_i is chosen in this particular manner, since after removing a droplet with mass m_i from class i the resulting mean droplet mass in that class should still lie within the mass bounds which correspond to the class boundaries R_{i-1}, R_i .

The computational steps are now as follows:

- S1 Evaluate D_0 and determine τ . Replace time t by $t + \tau$.
- S2 Choose drop class indices r, s with probability D_{rs} . Determine the coalescing drop masses m_i ($i = r, s$) as described above.
- S3 Remove the drops with mass m_i ($i = r, s$) by replacing N_i by $N_i - 1$ and M_i by $M_i - m_i$. Determine the class of the drop with mass $m_r + m_s$, which is supposed to be the class u . Replace N_u by $N_u + 1$ and M_u by $M_u + m_r + m_s$.
- S4 Continue with step 1 until the total simulation time has elapsed.

As in the case of Gillespie's algorithm physical quantities of interest can be estimated from several realizations of the coalescence process.

3. NUMERICALLY-BASED METHODS

As typical representatives for numerically-based methods for solving the quasi-stochastic coalescence equation

$$\frac{\partial f}{\partial t} = \int_0^{x/2} f(x-x')K(x-x',x')f(x')dx' - f(x) \int_0^\infty K(x,x')f(x')dx' \quad (3)$$

we have used a very fast discrete bin technique (Trautmann, 1996), D-scheme for short, and the well-known integration scheme of Berry and Reinhardt (1974), BR-scheme for short. Details can be found in these references. In the above equation $f = f(x, t)$ is the droplet number density as a function of droplet mass x .

4. KERNEL DATA

Two different kernels have been used. Firstly, for a comparison with Golovin's analytical solution, the sum of mass kernel

$$K(x, x') = b(x + x'),$$

with $b = 1500 \text{ cm}^3 \text{ g}^{-1} \text{ s}^{-1}$ is employed.

As second kernel we have used the realistic hydrodynamic coalescence kernel for which the coalescence efficiency has been set equal to 1 for all droplet sizes. The collision efficiencies have been adopted from Hall (1980) with minor changes. The modifications include a more detailed treatment of small droplets whose radii are below $30 \mu\text{m}$ radius (Davis, 1972, Jonas 1972) and wake capture effects for larger collector droplets in the radius range $70 \mu\text{m} < r \leq$

$300 \mu\text{m}$ (Lin and Lee, 1975). For details the reader is referred to Seeßelberg *et al.* (1996). Fig. 1 shows a contour plot of the hydrodynamic coalescence kernel.

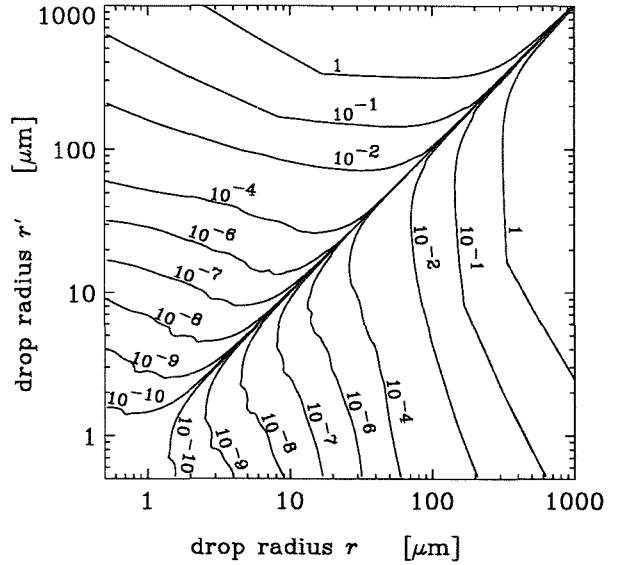


Figure 1: Contour plot of the hydrodynamic coalescence kernel. The contour lines are in $\text{cm}^3 \text{ s}^{-1}$.

5. RESULTS

For the numerically-based methods logarithmically equidistant grids are employed. For the D-scheme the center mass of each class doubles for every fourth grid point, whereas for the BR-scheme a mass doubling for every second grid point is used. The time steps are chosen as follows: $\Delta t = 5 \text{ s}$ for the D-scheme and $\Delta t = 2 \text{ s}$ for the BR-scheme.

The initial condition is given by a drop distribution which varies exponentially with droplet mass. Initial total droplet number N_0 , liquid water content L and the mean initial droplet mass x_0 are related by $x_0 = L/N_0$.

For the presentation of the results we use the mass concentration $M(J, t)$ in class J which for the grid $x(J+1) \stackrel{\text{def}}{=} \sqrt{2}x(J)$ is defined as

$$M(J, t) \stackrel{\text{def}}{=} \ln \sqrt{2} x(J)^2 f(x(J), t), \quad J \geq 1. \quad (4)$$

Firstly, the results for the sum of mass kernel will be described. The initial parameters are $N_0 = 300$

cm^{-3} and $L = 1 \text{ g cm}^{-3}$.

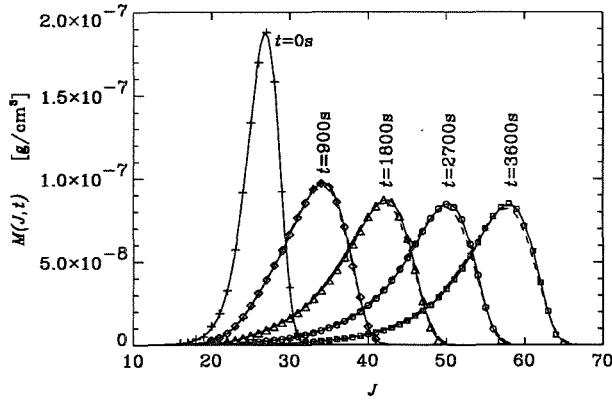


Figure 2: Droplet mass concentration $M(J,t)$ versus J at different times for the sum of mass kernel. Solid lines: analytical solution. Dashed lines: discrete method. Symbols: stochastic simulation.

Fig. 2 depicts the analytical solution as well as the results for the D-scheme and for the stochastic algorithm at different times. It is clearly seen that the results of the stochastic simulation are in perfect agreement with the analytical solution. Also the results of the D-scheme reasonably agree with these predictions although there are small deviations which slightly increase with time. The results of the BR-scheme are not plotted since they virtually coincide with the analytical solution. At this stage, however, one cannot decisively conclude that the D-scheme is generally less accurate than BR-scheme.

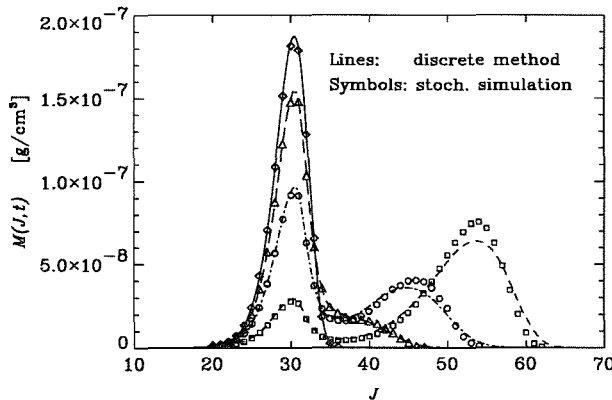


Figure 3: Same as Fig. 2, but for the hydrodynamical kernel. Lines/symbols: discrete/stochastic method (solid/rhombs: $t = 0\text{s}$, long-dashed/triangles: $t = 600\text{s}$, dash-dotted/circles: $t = 900\text{s}$, dashed/squares: $t = 1200\text{s}$.)

Now we turn our attention to the results for the

realistic hydrodynamical kernel. The initial condition is again chosen as an exponential distribution, but now with $N_0 = 87 \text{ cm}^{-1}$ and $L = 1 \text{ g cm}^{-3}$ so that a substantial amount of rain drops will be produced.

Figs. 3 and 4 present the results for the different mathematical methods in comparison to the results obtained by the stochastic simulation. Fig. 3 reveals discrepancies between the D-scheme and the stochastic simulation which increase with increasing time. The D-scheme produces a somewhat lower maximum for the large droplet mode, and, at the same time, exhibits a certain amount of numerical diffusion in the tail of the distribution.

In contrast to this, Fig. 4 shows that the results of the BR-scheme are consistent with the stochastic simulation data. Clearly the BR-scheme is more accurate than the D-scheme.

Finally, we wish to compare the CPU time requirements of the methods used. The stochastic simulation algorithm is very CPU time demanding. For the results presented a total number of 10 realizations has been used. Each realization required approximately 5 hours of CPU time on a IBM RS6000/550 workstation. The D-scheme and the BR-scheme on the other hand require less than 1 minute of CPU time for an one hour simulation.

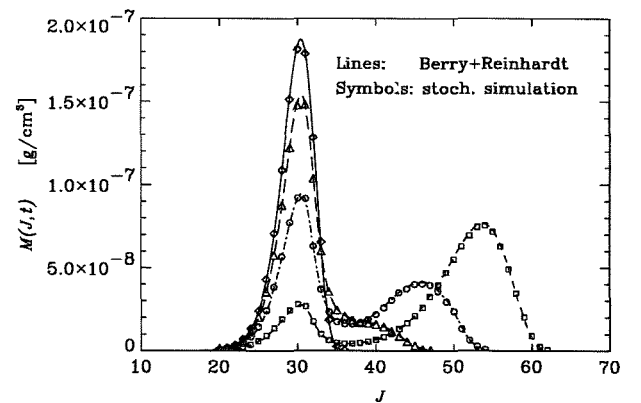


Figure 4: Same as Fig. 3, except for the lines which show the results for the integration scheme of Berry and Reinhardt.

6. CONCLUSION

The main topic of this paper is the development of a stochastic algorithm which can serve as a benchmark tool for testing numerically-based solu-

tion methods. Such a stochastic method is predestinated for this purpose since it offers a direct physical realization of the coalescence process and thus does not rely on numerical approximations for evaluating rapidly varying integrands.

In the future we plan to perform similar tests with other numerical techniques. Another interesting topic is to study the sensitivity of the produced drop spectra as a function of different formulations for the kernel data in regard to collision efficiencies and turbulence effects.

7. REFERENCES

- Berry, E. X., and R. L. Reinhardt, 1974: An analysis of cloud drop growth by collection: Part I. Double distributions. *J. Atmos. Sci.*, **31**, 1814–1824.
- Davis, M. H., 1972: Collisions of small cloud droplets: Gas kinetic effects. *J. Atmos. Sci.*, **29**, 911–915.
- Gillespie, D. T., 1975. An exact method for numerically simulating the stochastic coalescence process in a cloud. *J. Atmos. Sci.*, **32**, 1977–1989.
- Hall, W. D., 1980: A detailed microphysical model within a two-dimensional dynamic framework: Model description and preliminary results. *J. Atmos. Sci.*, **37**, 2486–2507.
- Jonas, P. R., 1972: The collision efficiency of small drops. *Quart. J. Roy. Meteor. Soc.*, **98**, 681–683.
- Lin, C. L., and S. C. Lee, 1975: Collision efficiency of water drops in the atmosphere. *J. Atmos. Sci.*, **32**, 1412–1418.
- Seeßelberg, M., T. Trautmann, and M. Thorn, 1996: Stochastic simulations as a benchmark for mathematical methods solving the coalescence equation. *Atmosph. Research* (in print).
- Trautmann, T., 1996: Reformulation of a fast discrete bin method for solving the droplet coalescence equation. Submitted to *Atmosph. Research*.

INFLUENCE OF TURBULENCE ON THE DROP COALESCENCE IN CLOUDS AND ON RAIN FORMATION

Alexander P. Khain and Mark B. Pinsky

Dept. Atmos. Sciences, the Hebrew University of Jerusalem, Israel

1. INTRODUCTION

In spite of the complexity of the microphysical processes, the geometry of drop collision is assumed to be rather simple: the larger drop falls faster than drops of a smaller mass, and collisions take place in the vertical direction due to the difference in their terminal fall velocities, which are considered to be the function of the drop mass only. The values of terminal velocities generally used have been calculated under the assumption of still air environment. The corresponding collision kernel is assumed to be proportional to the difference between the terminal fall velocities of interacting drops. These simplifications are based on the assumption that drops inertia is negligible. Gravitational effects are considered to be much more important than those resulting from differential response due to their different inertia.

As is known, clouds are the areas of enhanced turbulence. The intensity of turbulence varies widely depending on the type of clouds and their age. Thus, Mazin et al. (1984, 1989) observed in stratus clouds a turbulent energy dissipation rate $\epsilon \approx 10 \text{ cm}^2\text{sec}^{-3}$ as compared to $\epsilon \approx 100 \text{ cm}^2\text{sec}^{-3}$ in small cumuli. Weil et al. (1989) observed in heavy cumulonimbi values of ϵ up to $2 \cdot 10^3 \text{ cm}^2\text{sec}^{-3}$.

We are going to demonstrate that 1) the inertia of drops moving within a turbulent media leads to significant deviations of drop velocity from that of the surrounding air. It will be shown that for small drops and typical values of cloud turbulence, the relative velocity is several times greater than their still air terminal velocity; 2) due to the differences in drop inertia, turbulence impact results in the formation of relative velocity between falling drops. It will be shown that for small drops the relative velocity between drops induced by turbulence is greater than that induced by gravity. Possible influence of turbulence on the drop coalescence in clouds and on rain formation will be discussed as well.

2. MECHANISMS OF THE FORMATION OF DROP VELOCITY DEVIATIONS

Let us consider two simple examples: drop fall within a linearly sheared air flow (Fig. 1a) and drop motion within a curved turbulent flow (Fig. 1b). In the first case the drop velocity deviations are determined by the tendency to conserve drop momentum in the horizontal direction. In the second case drop velocity deviations are induced by inertial

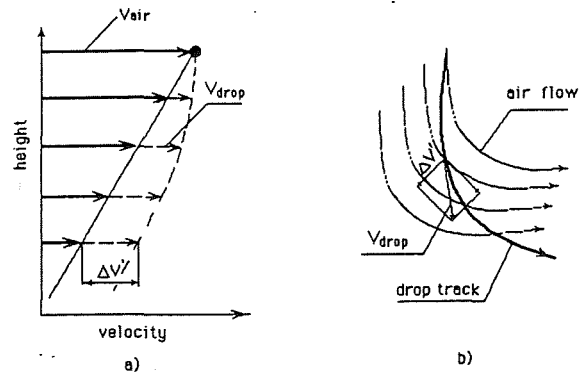


Figure 1. Drop motion within a linearly sheared air flow (a) and within a curved turbulent flow (b).

acceleration (centrifugal forces). What is most important is the fact, that after a short relaxation period [whose duration is the same as in case of still air (Wang and Pruppacher, 1977; Khain and Pinsky, 1995)] the adjusted values of drop velocity deviations are not equal to zero, but are determined by the drop mass (inertia) and the properties of the air flow (by the values of the shear, curvature of air parcel tracks, flow velocity, etc.). In case of linear wind shear (Khain and Pinsky, 1995) the adjusted values of drop velocity deviations can be written as $\Delta V = -\frac{\alpha}{g} V_t^2$, where V_t is the terminal fall velocity of a drop in still air and α is the constant vertical shear of the flow. For example, for the wind shear $\alpha = 0.5 \text{ s}^{-1}$ the adjusted values of drop velocity relative to the air are 0.15 ms^{-1} and about 3.75 ms^{-1} for drops of $200 \text{ }\mu\text{m}$ and $2000 \text{ }\mu\text{m}$ radii, respectively.

In case of drop motion within a curved flow the adjusted value of the velocity of small drops relative to the air is proportional to the inertial acceleration of the flow. In case of air rotation with an air velocity V_a , the drop velocity deviation is determined by a balance between centrifugal and friction forces. In this case $\Delta V = -\frac{V_a^2}{R} \tau_d$, where $\tau_d = V_t/g$ is the characteristic adaptation time, and R is the curvature radius. Typical values of ΔV for drops with the radius of $10 \text{ }\mu\text{m}$ are $1-2 \text{ cm/s}$, which is of the same order or greater than their terminal fall velocity, induced by gravity.

Taking into account that the duration of relaxation periods is short as compared to the

characteristic times of turbulent flow fluctuations (especially for small drops), the changes of drop velocity deviations can be regarded as transitions from one adjusted state to a subsequent one. It means, that adjusted drop velocity deviations change with the characteristic time scales of the surrounding air flow and are never equal to zero. Thus, due to the drop inertia, drop fall within a spatially inhomogeneous flow always leads to the formation of deviation of the drop velocity relative to the air.

Main mechanism of the formation of the relative velocity between drops falling in a turbulent flow is their differential response to the inertial accelerations of the flow. Due to centrifugal forces, droplets tend to leave turbulent eddies with different velocities. Another mechanism is the differential response of droplets with different inertia to the shears of the air flow. In the example mentioned above, the relative velocity in the horizontal direction between 200 and 2000 μm radii drops is equal to 3.6 ms^{-1} .

3. SIMULATION OF DROP VELOCITY DEVIATIONS USING A TURBULENCE MODEL

Drop motion in a turbulent flow is studied using a model of homogeneous and isotropic turbulence (Pinsky and Khain, 1995a,b). The model permits us to generate different realizations of the random two dimensional velocity field component with given latitudinal and lateral correlation functions and a spatial structure which obeys the Kolmogorov theory. The structure function of the flow (Batchelor, 1951) which describes the spectrum of turbulence both in the viscous and inertial subranges was used. In Fig. 2 an example of time dependence of drop velocity deviations for drops of $10 \mu\text{m}$ radii in the vertical direction is presented. One can see, that the amplitudes of these velocity deviations for small droplets can be several times greater than their still-air terminal velocities. The statistical characteristics of a drop movement in a turbulent flow are studied using the Monte Carlo method. The contribution of turbulence (inertia) effects as compared to the effect of gravity has been evaluated calculating the ratio of the root-mean-square drop velocity deviation (induced by turbulence) to the terminal velocity (induced by gravity), $\langle V'^2 \rangle^{1/2}/V_t$.

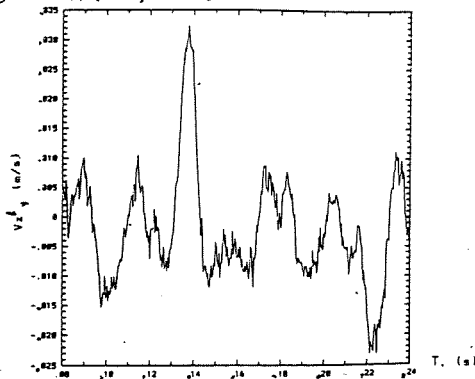


Figure 2. Time dependence of drop velocity deviations for drops of $10 \mu\text{m}$ radii

The dependence of $\langle V'^2 \rangle^{1/2}/V_t$ on the drop size under the turbulence dissipation rate \mathcal{E} of $100 \text{ cm}^2\text{sec}^{-3}$ is presented in Fig. 3. The maximum value of $\langle V'^2 \rangle^{1/2}/V_t$ is of the order of 1 and is attained for small drops.

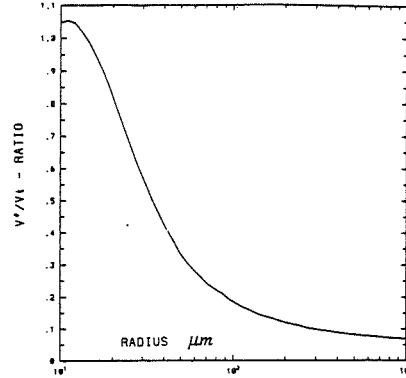


Figure 3. Dependence of $\langle V'^2 \rangle^{1/2}/V_t$ on the drop size ($\mathcal{E} = 100 \text{ cm}^2\text{sec}^{-3}$)

4. ANALYTICAL CALCULATIONS OF THE DROP VELOCITY DEVIATIONS

To calculate the statistical characteristics of drop velocity deviations and those of the relative velocity between drops falling within a three-dimensional turbulent flow, an analytical study has been carried out. The statistical properties of a turbulent flow velocity field were described by the latitudinal structure function (Batchelor, 1951), which describes the spectrum of turbulence both in the viscous and inertial subranges. Using the statistical characteristic of the velocity field, the statistical characteristics of the vertical velocity shear and inertial acceleration were calculated. Corresponding terms in (1) play the role of "forcing" leading to the formation of drop velocity deviations relative to the air flow. The Millionshchikov zero-fourth-cumulant hypothesis (Monin and Yaglom, 1975) was used while carrying out the calculations.

Using the drop motion equation (Pinsky and Khain, 1996)

$$\frac{\partial \vec{V}'}{\partial z} + \frac{g}{V_t^2} \vec{V}' = - \frac{\partial \vec{V}_a}{\partial z} - \frac{1}{V_t} (\vec{V}_a \cdot \nabla) \vec{V}_a \quad (1)$$

and the statistical characteristics of the terms on the right side of (1), the spectral characteristics of drop velocity deviations were calculated. In (1) \vec{V}_a is the air velocity, \vec{V}' is the deviation of the drop velocity from \vec{V}_a . By integrating the drop velocity deviation spectrum, the root mean square values $\langle V'^2 \rangle^{1/2}$ of velocity deviations were determined. Fig. 4 shows the dependence of ratio $\langle V'^2 \rangle^{1/2}/V_t$ on the drop radius under different values of the turbulence dissipation rate \mathcal{E} : $10 \text{ cm}^2\text{sec}^{-3}$ (curve A), $50 \text{ cm}^2\text{sec}^{-3}$ (B); $100 \text{ cm}^2\text{sec}^{-3}$ (C); $200 \text{ cm}^2\text{sec}^{-3}$ (D); $400 \text{ cm}^2\text{sec}^{-3}$ (E) and $\mathcal{E} = 600 \text{ cm}^2\text{sec}^{-3}$ (F). One can see that the amplitude of drop velocity deviations for drops that are not very

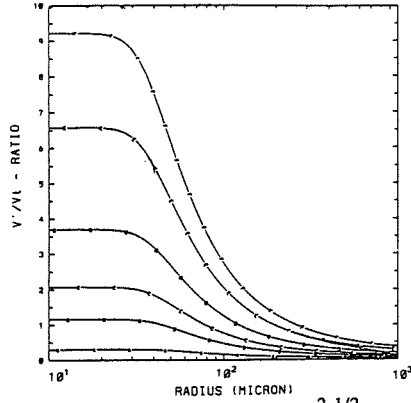


Figure 4. Dependence of ratio $\langle V^2 \rangle^{1/2} / V_t$ on the drop radius for different \mathcal{E} .

large is significantly greater than still air terminal velocity by means of which the parameters of gravitational coalescence are usually calculated. Comparison with Fig. 3 shows that in case of the 3-D velocity field the ratios $\langle V^2 \rangle^{1/2} / V_t$ are greater than in case of a 2-D velocity field. The analytical and numerical results reveal the same features: turbulence induced velocity deviations are significant, their maximum being reached for small drops.

In the same way (Khain and Pinsky, 1996), the statistical characteristics of relative velocity between two drops about to collide ($\Delta \vec{V} = \vec{V}_2 - \vec{V}_1$) were calculated. The contribution of turbulence effects as compared to gravitational effects to relative velocities between drops will be characterized by the ratio $\langle \Delta V^2 \rangle^{1/2} / \Delta V_t$, where $\Delta V_t = V_{t2} - V_{t1}$ is the relative velocity induced by gravity. The dependence of the ratio $\langle \Delta V^2 \rangle^{1/2} / \Delta V_t$ on the sizes of drops is shown in Fig. 5 for $\mathcal{E} = 100 \text{ cm}^2 \text{sec}^{-3}$. The magnitude of this ratio for small drops reaches values as large as 2.0. Thus, the relative velocity of drops with $30 \mu\text{m}$ radii and less induced by turbulence is nearly twice as large as the difference in their still air terminal velocities even for small intense turbulence.

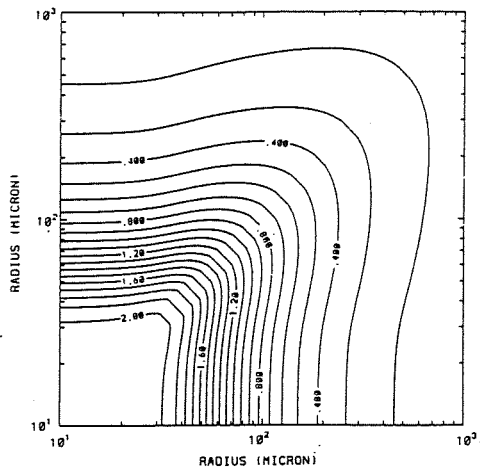


Figure 5. The dependence of the ratio $\langle \Delta V^2 \rangle^{1/2} / \Delta V_t$ on the sizes of drops for $\mathcal{E} = 100 \text{ cm}^2 \text{sec}^{-3}$.

5. COLLISION KERNEL AND THE DROP SIZE SPECTRUM EVOLUTION

The increase of relative velocity leads to an increase of the collision kernel in several ways. The first mechanism is related to the increase of the swept volume and, consequently, to the increase of the number of collisions per unit of time. This mechanism is illustrated by schemes of mutual motion of drops about to collide in cases a) relative velocity is induced by gravity only (Fig. 6a) and b) additional relative velocity is taken into account (Fig. 6b). We expect that the second mechanism is related to the increase of collision efficiency between drops, because the increase in relative velocity must lead to a change of the track of one drop within the boundary layer of the other (Fig. 6c).

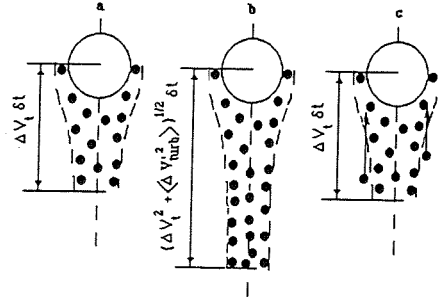


Figure 6. Schemes of mutual motion of drops in cases a) relative velocity is induced by gravity only and b) additional relative velocity is taken into account; c) impact on the collision efficiency

Below the first mechanism will only be analyzed. Collision efficiencies will be used as in case of still air (the classic approach). A possible effect of turbulence on the broadening rate of the drop size spectrum is illustrated by solving the stochastic coalescence equation for the water drop size distribution function using the Berry and Reinhard (1974) method. To describe the drop spectrum, 33 mass categories were used, the minimum value of the drop radius set equal to $1 \mu\text{m}$. Our problem consists in correcting the collision kernel, to include the turbulence effects discussed. Due to the drop inertia the relative velocity between drops is greater than the difference in their terminal velocities. Strictly speaking, it appears that the classical theory of coagulation in clouds ought to be refined, to take into account three-dimensional drop tracks and their possible spatial intersections under different angles. Useful "non-classical" definitions of the collision kernel were proposed by Almeida (1979) and Reuter et al. (1988), and further studies are needed. Here, as a first approximation, we simply replace the still air terminal velocity difference $|\Delta V_t|$ in the well known expression for the collision kernel by the difference in the mean square relative velocities between drops $\{\Delta V_t^2 + \langle \Delta V^2 \rangle\}^{1/2}$. The applicability of this replacement, in our opinion, can be explained by the

fact that the spectrum of relative velocity between drops of different radii depends mainly on the mass of the larger drop in a drop pair (see Fig. 5). Velocity deviations of the larger drop from the velocity of the flow are greater because of a greater inertia. The increase of the swept volume (which is close in our case to the increase of the drop track length relative to the surrounding turbulent flow) depends mainly on the velocity of the larger drop, and the situation appears similar to the classical approach.

In Fig. 7 the drop size spectrum resulting toward 24 min. from initial distribution is demonstrated with different values of \mathcal{E} from $50 \text{ cm}^2\text{sec}^{-3}$ to $400 \text{ cm}^2\text{sec}^{-3}$. The spectrum evolution for $\mathcal{E} = 0$ (no turbulence) is presented as well (curve A). One can see that turbulence impact is very significant: the formation of rain drops with the radii of $100 \mu\text{m}$ takes about 12 min for $\mathcal{E} = 200 \text{ cm}^2\text{sec}^{-3}$ (not shown) and about 24 min for $\mathcal{E} = 50 \text{ cm}^2\text{sec}^{-3}$. In case of zero turbulence impact, no rain drops are being formed during this period.

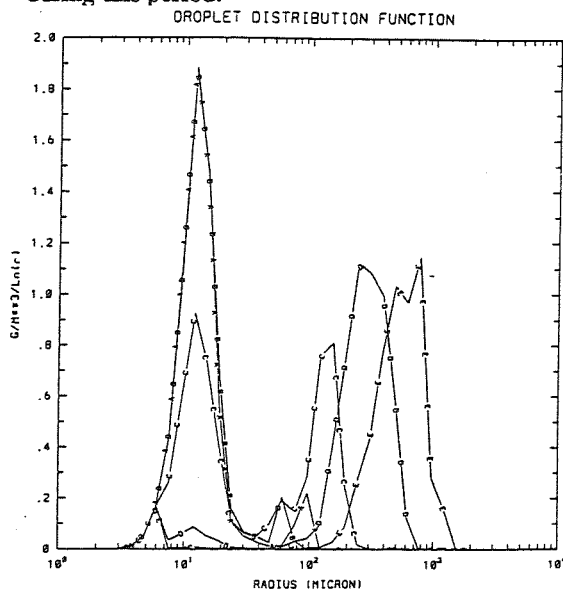


Figure 7. Drop size distribution at 24 min. under different intensity of cloud turbulence.

6. CONCLUSIONS

It was demonstrated that drops inertia leads to the formation of a significant relative velocity between drops, which for small droplets can be greater than gravity driven velocity difference. An increase of relative velocity between drops leads to an increase of the swept volume and the collision kernel. As a result, the rate of generation of large drops is substantially increased by cloud turbulence.

In case of ice particles interaction, as well as ice-water drops collisions (riming) in clouds turbulent effects must be more pronounced than in case of water drops. It can be explained by the fact that the comparably high inertia of ice particles is accompanied by their relatively small still air terminal velocity.

7. ACKNOWLEDGMENTS

This study was supported by the Israel Science Foundation administered by The Israel "Academy of Sciences and Humanities" and by the Lady Davis Foundation of the Hebrew University of Jerusalem.

8. REFERENCES

- Almeida, F. C., 1979: The collisional problem of cloud droplets moving in a turbulent environment-part II: Turbulent collision efficiencies. *J. Atmos. Sci.*, **36**, 1564-1576.
- Batchelor, G.K.: Pressure fluctuations in isotropic turbulence. *Proc. Cambr. Phil. Soc.*, **47**, 359-374 (1951).
- Berry, E. X., and R. L. Reinhard, 1974: An analysis of cloud drop growth by collection: part 1. Double distributions. *J. Atmos. Sci.*, **31**, 1814-1824.
- Khain A. P., and M. B. Pinsky, 1995: Drops' inertia and its contribution to turbulent coalescence in convective clouds: Part 1: drops fall in the flow with random horizontal velocity. *J. Atmos. Sci.*, **52**, 196-206.
- Khain, A.P. and M. B. Pinsky, 1996: Turbulence effects on collision kernel Part 2: Increase of the swept volume of colliding drops (Submitted to *QJRM*S).
- Mazin, I. P., V. I. Silaeva, and M. A. Strunin, 1984: Turbulent fluctuations of horizontal and vertical wind velocity components in various cloud forms. *Izvestia, Atmospheric and Oceanic Physics*, **20**, 6-11.
- Mazin, I. P., Khrgian, A. Kh. and Imyanitov, I. M., 1989: *Handbook of Clouds and Cloudy atmosphere*. Gidrometeoizdat, 647 p.
- Monin, A. S. and A. M. Yaglom, 1975: *Statistical fluid mechanics: Mechanics of turbulence*, v.2, p.874. MIT Press.
- Pinsky M. B. and A. P. Khain, 1995: A model of homogeneous isotropic turbulence flow and its application for simulation of cloud drop tracks *Geophys. and Astr. Fluid Dynamics (in press)*
- Pinsky M. B. and A. P. Khain, 1995b: Simulations of drops' fall in a homogeneous isotropic turbulence flow *Atmosph. Research.*, **81**, 33-55.
- Pinsky, M.B. and A. P. Khain, 1996: Turbulence effects on the collision kernel. Part 1: Formation of velocity deviations of drops falling within a turbulent three-dimensional flow (submitted to *QJRM*S).
- Reuter, G.W., R. de Villiers, and Y. Yavin, 1988: The collection kernel for two falling cloud drops subjected to random perturbations in a turbulent air flow: a stochastic model. *J. Atmos. Sci.*, **45**, 765-773.
- Wang, P. K., and H. R. Pruppacher: Acceleration to terminal velocity of cloud and raindrops. *J. Appl. Meteor.*, **16**, 275-280 (1977).
- Weil J.C., R. P. Lawson, and A. R. Rodi: Relative dispersion of ice crystals in seeded cumuli. *J. Appl. Meteor.*, **32**, 1055-1073 (1989).

SENSITIVITY TESTS ON CLOUD DROP SIZE DISTRIBUTION PERFORMED BY 1-D FORCED TIME DEPENDENT CONVECTIVE CLOUD MODEL

Mladjen Ćurić, Dejan Janc and Vladan Vučković

Institute of Meteorology, University of Belgrade, Belgrade, Yugoslavia

1. INTRODUCTION

The choice of the size distributions in numerical models with bulk microphysics has been received increased attention in recent years (Verlinde et al., 1990; Ćurić and Janc, 1995b). The sensitivity experiments with solutions of the integrand form of the stochastic collection equation clearly show that the major differences in computations would be made if we change the size distributions of the elements interacting. Therefore, the choice of the size distribution is an important decision. Since the size distributions of elements are the end products of the cloud microphysics, cloud dynamics and interactions that affect the precipitation processes, it is instructive to see how the size distribution influence the modeled cloud life.

We shall conduct the sensitivity experiments by two versions of the 1-D forced time-dependent model (Ćurić and Janc, 1993) to show the effects of the cloud drop size distribution on cloud microphysical fields. The first version includes the monodisperse size distribution of cloud droplets and the Marshall-Palmer one for raindrops, (hereafter called MMP), while the second one uses the Khrgian-Mazin size distribution for both water fractions (hereafter called KM).

2. DROP SIZE DISTRIBUTIONS IN BULK MICROPHYSICS SCHEMES

A characteristic shape of the cloud

droplet size distribution can be approximated well by either the lognormal or gamma distribution functions. One of the most common used expression is that introduced by Khrgian and Mazin (1963). Despite of its good characteristics, it is still rarely employed in numerical models with bulk microphysics (Ćurić and Janc, 1995a).

The Marshall-Palmer exponential size distribution is most widely used approximation of the raindrop spectrum owing to its attractive simplicity. Meanwhile, it tends to overestimate the number of both the smallest and the largest drops (Torres et al., 1994). Therefore, the more sophisticated size distributions based on complementary observational data as generalized exponential, gamma, lognormal or Weibull distribution functions have been introduced later. Nearly 70% of used formulations for raindrop spectra belong to those of gamma type (Torres et al., 1994).

Despite of it, most convective cloud models use the simple monodisperse size distribution for cloud droplets due to the minor errors in computations of some of the production terms for interactions between elements via gravitational coagulation and the Marshall-Palmer one for rain water (e.g. Ćurić and Janc, 1993). Farley and Orville (1986) indicated that the Marshall-Palmer treatment generates the rain for a case when it was not observed.

Verlinde et al. (1990) pointed out the need for inclusion of the other size

distributions favourable for some model simulations in existing bulk microphysics schemes besides classical treatment. Herein, we shall introduce the unique Khrgian-Mazin size distribution for both water fractions in order to avoid the unnatural gap at the lower limit of raindrop spectrum. The arbitrary limit between two parts of the spectrum is taken to be $D_{\text{MIN}}=100\mu\text{m}$. Such approach is already employed by Ćurić and Janc (1995a;1995b). They indicated that the Khrgian-Mazin size distribution produces more small raindrops than the Marshall-Palmer one, where both have the same rain water mixing ratio. On the other hand, it generates more large cloud droplets compared to the monodisperse size distribution under the same other conditions.

3. SENSITIVITY EXPERIMENTS

Experiments were performed by KM and MMP versions of the 1-D forced time dependent model (Ćurić and Janc,1993). The KM one is derived by implementation of the corresponding production terms with the Khrgian-Mazin size distribution instead of those with the monodisperse and the Marshall-Palmer size distributions. In experiments the mean cloud drop spectrum diameter of

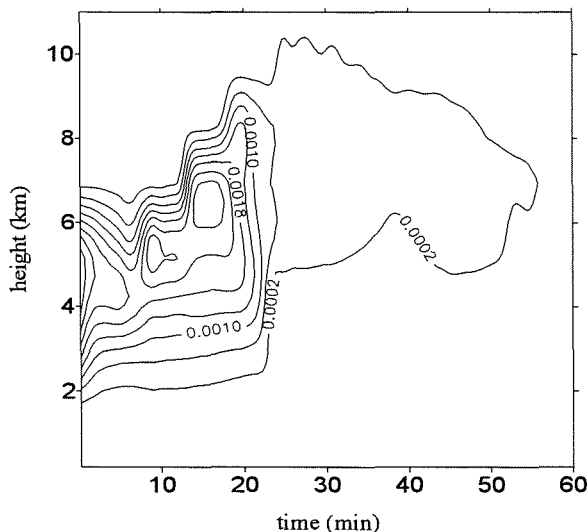


Fig. 1. Time-height cross-sections of cloud water mixing ratio (in kg/kg) for KM version of the model. Height is in km above ground level.

$R_M=10\mu\text{m}$ is used. The influence of the cloud drop size distribution is investigated for a simulated storm based on the 23 June 1985 sounding in Belgrade.

The time-height cross-section of cloud water mixing ratio is depicted in Fig. 1 for the KM version of a model. As can be seen, the model cloud generates the large cloud water mixing ratios at first 20min of integration time with the peak value of $3.7 \times 10^{-3} \text{kgkg}^{-1}$ at height of 5km when model simulation starts. After $t=20\text{min}$, the rapid ascent of the cloud base occurs. In contrast, the MMP one produces smaller cloud water contents at first 20min of integration time, but the model solution is rather stationary after $t=20\text{min}$ with the cloud base level around $z=4\text{km}$ (Fig. 2).

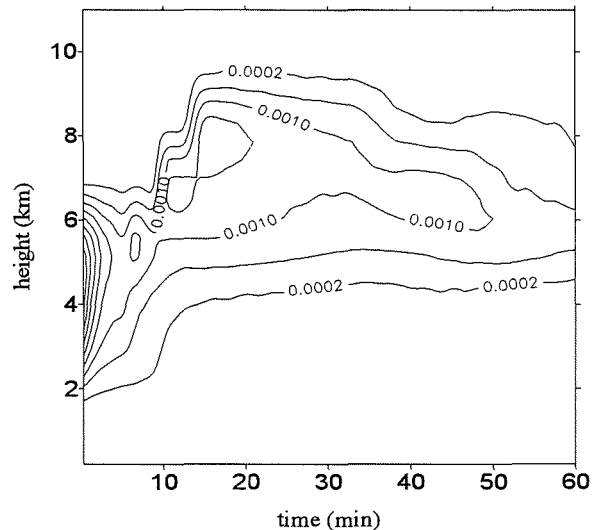


Fig. 2. Same as in Fig. 2 but for the MMP model version.

The field of rain water for the KM model version differ significantly from that for the MMP one (Figs. 3 and 4). For the KM version the rain water content is generally smaller than for the MMP one inside the cloud. Further, it produces the rain shower around $t=25\text{min}$ of integration time (the peak value of rain water mixing ratio greater than $7 \times 10^{-3} \text{kgkg}^{-1}$ at $z=3\text{km}$) contrary to MMP version which simulates the precipitation continually after $t=10\text{min}$ of integration time

The KM size distribution shows profound effects on hail fields compared to the MMP version as can be seen from Figs. 5 and 6. Then the hail forms nearly 20min later compared to the MMP version. This is primarily induced by the immersion freezing because the KM model version tends to underestimate it highly.

Finally, the fields of cloud ice for both model versions are shown in Figs. 7 and 8. An

anvil begins to form after 25min of integration time for the KM version (Fig.7) and somewhat earlier for the MMP one (Fig. 8). The KM version produces smaller amounts of the cloud ice because the hail collects it more effectively than in the MMP version.

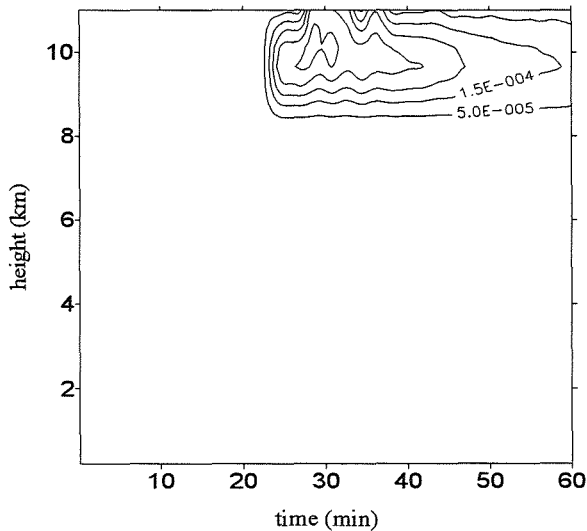


Fig. 7. As in Fig. 1 but for cloud ice mixing ratio.

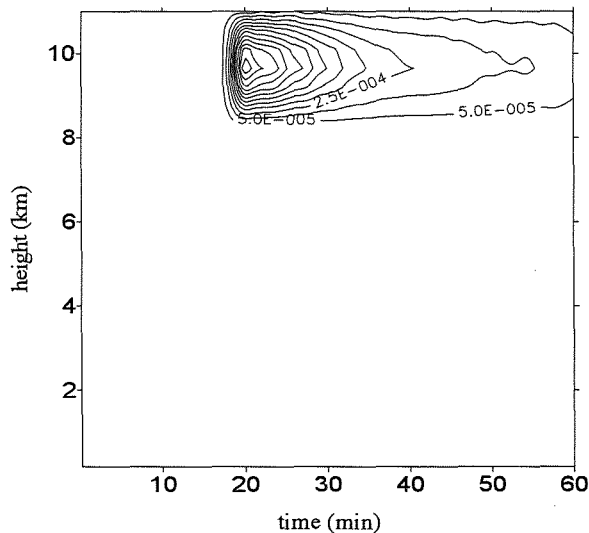


Fig. 8. As in Fig. 7 but for the MMP model version.

4. CONCLUSIONS

The Khrgian-Mazin size distribution leads to profound effects on cloud fields. For a simulated storm, the KM version gives

different model cloud compared to that for the MMP one. It produces more cloud water in the first half of the cloud life, smaller rain and cloud ice contents and more hail compared to MMP version. In addition, the KM version simulates shower-type precipitation where the solid component prevails. These differences are primarily induced by different hail formation times.

REFERENCES

- Ćurić, M., i D. Janc, 1993: Predictive capabilities of a one-dimensional convective cloud model with forced lifting and a new entrainment formulation. *J. Appl. Meteor.*, 32, 1733-1740.
- Ćurić, M., i D. Janc, 1995a: On the consumption of AgI seeding agent dependence on the liquid water content in seeding zone. *J. Wea. Mod.*, Vol. 27, 17-20.
- Ćurić, M., i D. Janc, 1995b: On the sensitivity of the continuous accretion rate equation used in bulk-water parameterization schemes. *Atmos. Res.*, 39, 313-332.
- Farley, R.D., i H.D. Orville, 1986: Numerical Modeling of hailstorms and hailstone growth. Part I: Preliminary model verification and sensitivity tests. *J. Climate Appl. Meteor.*, 25, 2014-2035.
- Khrgian, A., i I.P. Mazin, 1963: Cloud Physics. Israel Prog. Sci. Transl., Jerusalem, 392pp.
- Torres, D. S., J.M. Porra i J.-D. Creutin, 1994: A general formulation for raindrop size distribution. *J. Appl. Meteor.*, 33, 1494-1502.
- Verlinde, J., Flatau, P.J., i W.R. Cotton, 1990: Analytical solutions to the collection growth equation: comparison with approximate methods and application to cloud parameterization schemes. *J. Atmos. Sci.*, 47, 2871-2880.

RELATIONSHIP BETWEEN RAINDROP SIZE DISTRIBUTION AND RAINFALL RATE

Ken-ichiro Muramoto¹, Kohki Matsuura¹, Masahiro Furukawa¹, Tatsuo Endoh² and Toshio Harimaya³

¹Faculty of Engineering, Kanazawa University, Kanazawa 920, Japan

²Institute of Low Temperature Science, Hokkaido University, Sapporo 060, Japan

³Graduate School of Science, Hokkaido University, Sapporo 060, Japan

1. INTRODUCTION

Raindrop size distributions associated with rainfall rate are important for understanding the mechanism on rainfall formation in the field of cloud physics. In addition, it contributes to evaluate the radar reflectivity factor Z and the rainfall rate R for use in the Z - R relationship (e.g., Stout and Mueller, 1968). From the defining equation of the radar, Z depends on the drop size distribution and is very sensitive to the large drop component of the distribution.

The raindrop size distribution is often found to the negative exponential law and the slope factor which is depended on rainfall rate (Marshall and Palmer, 1948). The formula has frequently been used as a standard distribution. However, the raindrop size distributions in intense rainfall are deferent from Marshall-Palmer's distribution (Waldvogel, 1974; Willis and Tattelman, 1989). Furthermore, size distribution during short period are often far from exponential (Fujiwara, 1965; Joss and Gori, 1978). In order to examine rainfall phenomena, simultaneous and short sampling observation of size and rainfall should be done.

In this paper, a new system to determine the size and fall velocity of rainfall is proposed. Photographed and recorded images of falling raindrops by VTR (video tape recorder) are analyzed using a personal computer with an image-analysis board. Contribution of ratio of raindrop size to rainfall rate are calculated from the image

processing data. The relationships between raindrop size distribution and rainfall rate are investigated during short period.

2. METHODS

2.1 System for measuring the size and velocity of raindrops

Since the system which measures the size and fall velocity of raindrops has been reported (Muramoto, 1995), a brief explanation will be provided. The measuring system and hardware diagram are shown in Fig. 1. The apparatus consists of a light source and two TV cameras. Images of raindrops that have

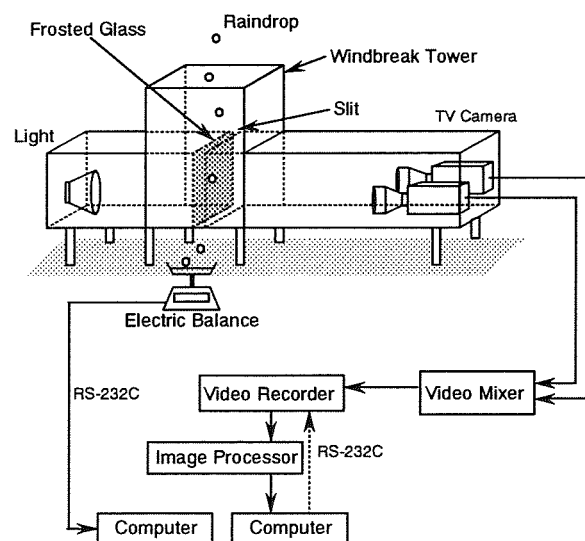


Fig. 1 Schematic for the simultaneous measurement of the physical parameter of raindrops and rainfall rate.

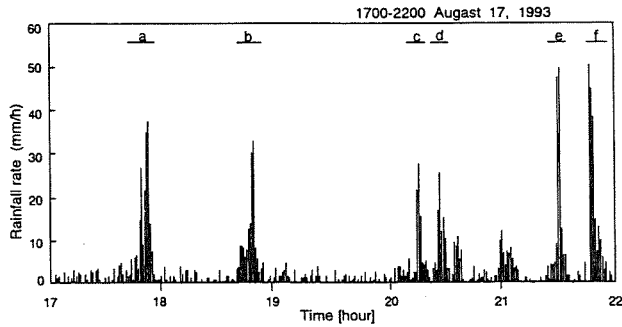


Fig. 2 Temporal changes of rainfall rate measured by electric balance from 1700 to 2200 in August 17, 1993.

fallen through a slit are observed on a frosted glass plate as enlarged shadow figures. One of the cameras has a high speed of shutter of 1/20000 s for measuring the dimension of raindrop. The other has a 1/2000 s shutter speed for measuring the fall velocity of the same raindrop. Two images of a raindrop and the vertical displacement of the same raindrop were taken by two different video cameras simultaneously every 1/30 s and combined again by a video mixer to form a single pair of images in order to synchronize the time. The images of raindrops were converted into digital form with an image analysis board installed on a personal computer. The area of cross section A of a raindrop is obtained from the number of pixels inside the region of the high speed projection. The equivalent diameter D of raindrop is calculated from the area of cross section A , i. e., $D = 2 (A / \pi)^{1/2}$.

Since each falling raindrop produced a short streak during the 1/2000 s time interval, its velocity is calculated from the vertical length.

2.2 Direct measurement of rainfall rate

Since raindrop has a density of 1.0 g/cm³, it

follows that rainfall rate can be measured by weight of rainfall. A high sensitive instrument for measuring rainfall rate will be developed using an electric balance and computer system. This weighing gauge measures the amount of rainfall directly without delay or error due to surface tension or evaporation. The data were acquired by personal computer with an RS-232C interface at preset time intervals.

2.3 Calculation of rainfall rate using image processing data

Rainfall rate is the flux of rainfall through a horizontal surface. It is measured in terms of the volume flux of water. Assuming spatial distribution to be constant and the shape of a raindrop to be approximately spherical, rainfall rate was determined from the diameter and velocity of raindrops. The rainfall rate can be calculated as

$$R = \sum_{i=1}^n \frac{4}{3} \pi \left(\frac{D_i}{2} \right)^3 \frac{v_i}{kV} 120 \quad (1)$$

where D is diameter (mm), v is velocity (mm/s), k is number of photographs taken per s (1/s), V is photographing space (mm³) and 120 is the constant for converting R from per 30 s to mm per h.

3. RESULTS AND DISCUSSION

The present study was conducted in Kanazawa situated centrally on the Japan Sea coast on August 17, 1993. A cold front passed Kanazawa on that day, and the amount of rainfall rate was heavy.

Table 1 Lists of the characteristics of rainfall obtained by the image processing data.

	Distribution		Peak of rainfall			Duration of rainfall (min)			Rainfall rate (mm/h)			Total	Rainfall rate per min (mm/(h · min))		
	No	λ	rate (mm/h)			0-1.0	1.0-1.5	1.5-	0-1.0	1.0-1.5	1.5-		0-1.0	1.0-1.5	1.5-
			0-1.0	1.0-1.5	1.5-										
a	31.5	14.5	38.3 (8.9	4.0	25.4)	11.5	7.0	4.0	44.4	71.8	89.9	206.1	3.9	10.3	22.5
b	27.2	10.3	36.8 (2.6	5.5	28.8)	12.5	9.0	3.5	33.0	65.4	77.9	176.3	2.6	7.3	22.3
c	19.2	8.7	28.1 (3.8	11.8	13.5)	11.5	5.0	2.0	43.0	57.4	38.3	138.7	3.7	11.5	19.2
d	17.4	8.2	26.6 (4.2	4.8	17.6)	9.0	5.0	3.0	52.3	60.3	60.1	172.7	5.8	12.6	20.0
e	51.5	28.4	46.9 (8.5	11.8	26.6)	10.0	5.5	3.0	55.2	63.8	81.6	200.6	5.5	11.6	27.2
f	43.0	22.3	49.7 (11.4	11.1	27.2)	10.0	8.0	3.0	70.8	133.7	80.8	285.3	7.1	16.7	26.9

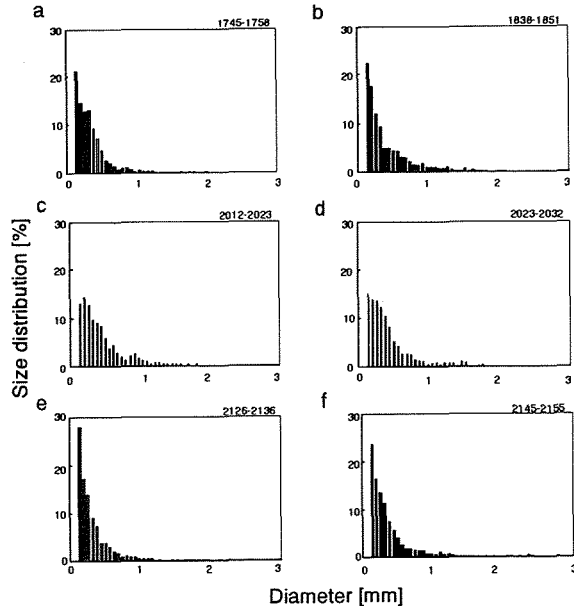


Fig. 3 Six cases of the percentage of the raindrop size distribution. a: 1745-1758. b: 1838-1851. c: 2012-2023. d: 2023-2032. e: 2126-2136. f: 2145-2155.

3.1 Rainfall rate measured by a balance directly

Rainfall rates measurement by an electric balance from 1700 to 2200 in August 17, 1993 are shown in Fig. 2. Although the period for this measurement was short (30 s), rainfall was often spiky. Six cases of rainfall features were examined in detail.

3.2 Physical parameters of raindrops measured by image processing

Since number of all observed raindrops was depended on the duration of observation. Shape of size distribution was normalized by total number of raindrops. Percentage of size distribution of all observed raindrops for six cases is shown Fig. 3. Size distribution of snowflakes $N(D)$ can be expressed from diameter as following equation (Marshall and Palmer), where N_0 and λ are constant.

$$N(D) = N_0 \exp(-\lambda D) \quad (2)$$

The value of N_0 and λ for each case were shown Table 1. Data indicate that N_0 and λ were proportionally increased with the peak of rainfall rate.

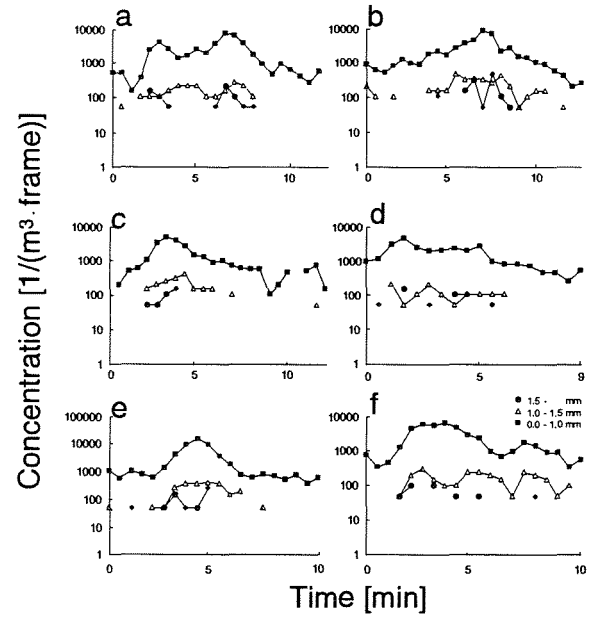


Fig. 4 Temporal changes of number concentration of raindrops in the size range of three groups. The duration is as for the case in Fig. 3.

Temporal changes of the number concentration of raindrops in the size range of three groups (0-1.0 mm, 1.0-1.5 mm and more than 1.5 mm) were calculated. Fig. 4 shows the number concentration at 30-s intervals for each case. Although smaller raindrops fell almost constantly, larger ones fell occasionally.

3.3 Rainfall rate calculated by image processing data

Rainfall rate at 30-s interval for each size was calculated using Eq.(1). Fig. 5 shows the contribution of raindrop size to rainfall rate. Rainfall rate was almost constant for smaller raindrop size. Intense rainfalls were mainly caused by larger size, but usually they did not continue long period. Details for the peak of rainfall rate were shown in Table 1. More than half of rainfall rate was occurred by larger size on the time of peak in five of six cases. Rainfall rates per min were calculated using duration of rainfall and rainfall rate for each size. Mean and SD of the rainfall rate per min were 4.8 ± 1.5 , 11.7 ± 2.8 and 23.0 ± 3.1 mm/(h · min) for smaller, middle and larger size, respectively. Since each value of SD was small, rainfall rates would be

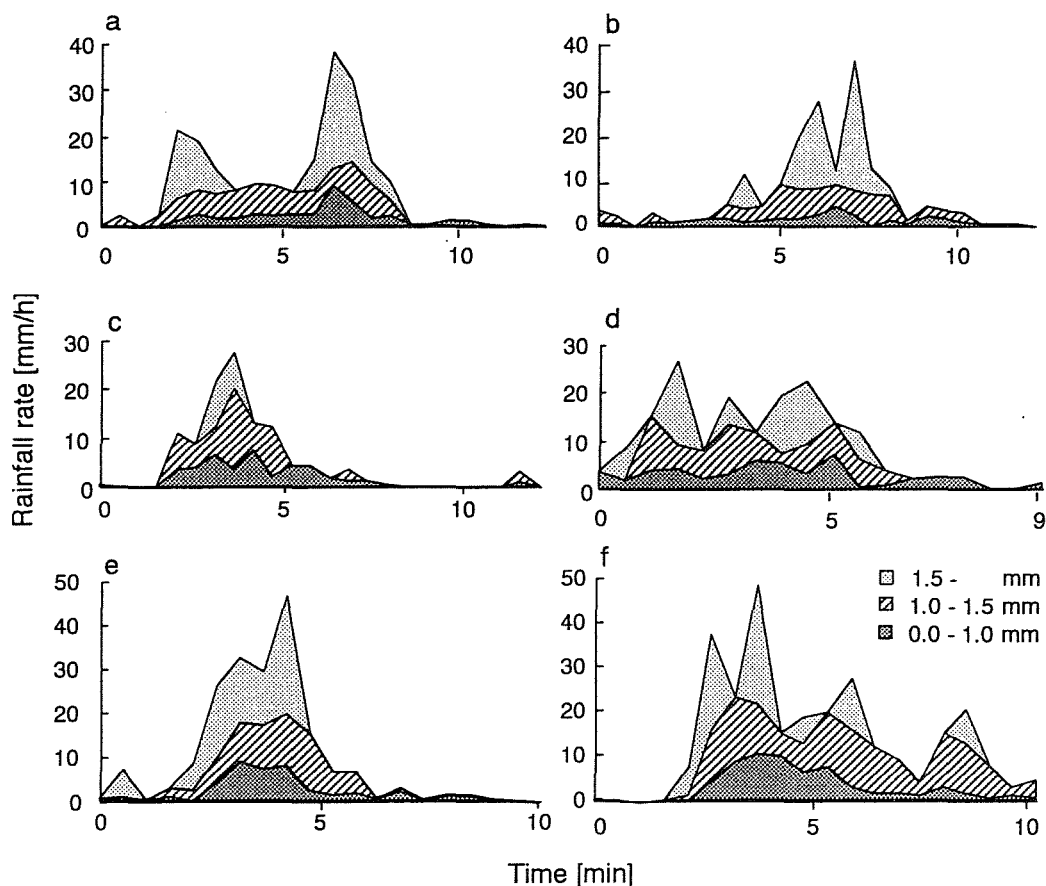


Fig. 5 Temporal changes of contribution of raindrop sizes to rainfall rate calculated by image processing data. The duration is as for the case in Fig. 3.

constant for each size. Total rainfall rates for individual event will depend to the duration of rainfall of each size.

4. CONCLUSION

The raindrop size distribution and rainfall rates during short period were observed using image processing method. Value of N_0 and λ of size distribution curve were related to the peak of rainfall rate. Contribution of raindrop size to rainfall rate were examined. Rainfall rate per min was constant for each size. Although the raindrops of larger size fell occasionally, its raindrops contributed to intense rainfall rate.

5. REFERENCES

- Fujiwara M., 1965: Raindrop-size distribution from individual storms. *J. Meteor.*, **22**, 584-591.
- Joss, J., and E.G. Gori, 1978: Shape of raindrop size distributions. *J. Appl. Meteor.*, **17**, 1054-1061.
- Marshall J.S., and W.M. Palmer, 1948: The distribution of raindrops with size. *J. Meteor.*, **5**, 165-166.
- Muramoto K., 1995: Determination of shape and fall velocity of raindrops by image processing. *IEICE Trans. Inf. Syst.*, **E78-D**, 1051-1057.
- Stout, G.E., and E.A. Mueller, 1968: Survey of relationships between rainfall rate and radar reflectivity in the measurement of precipitation. *J. Appl. Meteor.*, **7**, 465-474.
- Waldvogel, A., 1974: The No jump of raindrop spectra. *J. Atmos. Sci.*, **31**, 1067-1078.
- Willis P.T., and P. Tattelman, 1989: Drop-size distributions associated with intense rainfall. *J. Appl. Meteor.*, **28**, 3-15.

MICROSCOPIC APPROACH TO CONDENSATIONAL GROWTH OF CLOUD DROPLETS

Paul A. Vaillancourt¹, Man K. Yau¹ and Wojciech W. Grabowski²

¹ McGill University, Montreal, Quebec, Canada

² NCAR, Boulder, Colorado, USA

1 Introduction

Before reaching a radius of approximately $25\mu\text{m}$, cloud droplets grow mainly by condensation. Traditionally, the growth of a cloud droplet population is calculated using values of the environmental conditions that represent averages over large volumes, the so called macroscopic conditions. However, the growth rate of an individual droplet should be a function of the temperature and the vapor pressure in its immediate environment, the so called microscopic conditions. These quantities vary from droplet to droplet and vary with time because of the spatial and temporal variations in the size of the droplets, the local concentration of the droplets and the vertical velocity. Our concern here is on the variations caused by the random nature of the spatial distribution of cloud droplets which are being constantly re-shuffled by sedimentation and small scale turbulence. We are not considering the variability that may occur on larger scales due to entrainment (Cooper 1989).

Srivastava (1989) pointed out that in most theoretical and numerical studies of clouds, the hypothesis is implicitly made that droplet to droplet variability is not important when calculating the growth of an ensemble of droplets. This hypothesis could only be justified if either the difference between the microscopic and the macroscopic supersaturation is negligible or the difference in the time integral of these supersaturations is negligible. Based on analytical calculations, Srivastava (1989) concluded that both the random spatial distribution of droplets and variations in the vertical air velocity could cause non-negligible deviations of the microscopic supersaturation from the macroscopic value and can affect the growth of an ensemble of cloud droplets. However, this conclusion is tentative as he did not include the possible effects of turbulence and sedimentation. It is the objective of this work to include these effects in numerical experiments and determine the possible effect of microscopic supersaturations on the growth of an ensemble of cloud droplets.

2 Approach

Ultimately, to solve this problem properly, it would be necessary to solve the water vapor and temperature diffusion equations with the appropriate boundary conditions at the surface of all the droplets. If many droplets in motion are considered, this direct approach becomes impractical. Simplifications are possible because there is a separation in spatial scale and time scale between the changes in temperature and water vapor mixing ratio fields due to condensational growth and those due to the turbulent flow. Gradients in the temperature and water vapor mixing ratio fields due to the presence of droplets are significant within a distance of the order of ten times the droplet's radius (Sedunov 1974), typically $\approx .1\text{mm}$. The diffusive time scale associated with the approach to steady state for such scales is $\approx 10^{-5}\text{s}$. The smallest structures in these fields due to the turbulent flow are of the order of the Kolmogorov length scale, which for typical values of eddy dissipation rate measured in clouds (MacPherson and Isaac 1977) is a few mm's. The time scale associated with changes in these structures is the turnover time for eddies of that size which is $\approx .1\text{s}$. Fukuta (1992) proposed some changes to the droplet growth equation to take into account the fact that the distance, from a droplet, at which gradients in the scalar fields are zero is not infinity, as implicitly assumed in the usual formulation, but at some midpoint distance between droplets. He shows that the impact of this modification becomes negligible for low concentrations of cloud droplets. To avoid this difficulty and to minimize the occurrence of droplets coming close enough to each other to modify their growth rates, we will use low average concentrations of cloud droplets in our experiments. Because of the spatial and time scale separation discussed above, and because we will use low concentrations of cloud droplets we can assume that the droplets grow in isolation surrounded by spherically symmetric fields of temperature and water vapor which are regarded as quasi-stationary.

Our approach is to use a 3D turbulence model coupled with a model that follows several thousands of cloud droplets. The turbulence model predicts local velocity fields and local thermodynamic fields, whereas the cloud droplet growth model predicts the trajectories and growth of the individual droplets in their local environment. The local environment is given by the grid values of temperature and water vapor mixing ratio in which the droplet under consideration is located. The grid size is chosen to be small enough such that only a fraction of the grid points contain one or more droplet but big enough such that the grid values are representative of conditions at a distance greater than a few tens of droplet radius. The small grid size ($\approx 1mm$) necessarily imply that we are restricted to domain sizes of several centimeters. We impose a uniform constant updraft on the entire domain to provide forcing for the droplet growth.

Physically, our simulations correspond to conditions found in an adiabatic updraft near the core of a developing cumulus cloud far from entrainment regions. These adiabatic cloud cores have been observed at a few Km's from cloud base and contain broad droplet distributions (Brenguier and Chau-mat 1996).

3 Model equations

The set of equations solved by the two models is the following:

$$\frac{d\vec{\omega}(\vec{x})}{dt} = \nu \nabla^2 \vec{\omega}(\vec{x}) \quad (1)$$

$$\frac{dT(\vec{x})}{dt} = \frac{L}{c_p} C_d(\vec{x}) + \Gamma w(\vec{x}) + \kappa \nabla^2 T(\vec{x}) \quad (2)$$

$$\frac{dq_v(\vec{x})}{dt} = -C_d(\vec{x}) + D_v \nabla^2 q_v(\vec{x}) \quad (3)$$

$$C_d(\vec{x}) = AS(\vec{x}) \sum_0^{i \text{ box}(\vec{x})} R_i \quad (4)$$

$$\frac{dR_i^2}{dt} = 2KS(\vec{x}_i) \quad (5)$$

$$\frac{d\vec{x}_i}{dt} = \vec{U}(\vec{x}_i) - \mathbf{k}V_{Ti} \quad (6)$$

The first equation is the vorticity equation for an incompressible fluid assuming that there is no stratification inside the domain and no feedback effect of latent heat release. The velocity field can be uniquely retrieved from the vorticity field because of incompressibility. The second and third equations are the thermodynamic equations for temperature and water vapor mixing ratio. Γ is the dry adiabatic lapse rate and $C_d(\vec{x})$ is the condensation rate at gridpoint (\vec{x}), calculated using (4), where the parameter A is the combination of several factors and can be assumed constant in the experiments we perform. The sum appearing in this

equation is over all droplets present in the grid-point. Equation (5) represents diffusional growth for droplet i as a function of the supersaturation at its location (\vec{x}_i). The last one is the equation of motion for droplet i as a function of the local velocity field and its terminal velocity, V_{Ti} . This simple form is valid when inertial effects and interactions between droplets can be neglected. To close this system of equations we use the hydrostatic equation and calculate the supersaturation using an iterative procedure presented in Hall (1980).

The turbulence model is a pseudo-spectral model. Advection terms are calculated in real space. To force the flow in the domain we use a common technique which consists in, at each timestep, adding an amount of energy at small wavenumbers equal to that which is dissipated at high wavenumbers at the previous timestep. This ensures that the flow is stationary in the sense that the total kinetic energy varies about a constant value. The general procedure to solve the above system of equations is to first-solve the first three equations excluding the condensation rate terms to obtain temporary values for the scalar fields. Time stepping is done using the leapfrog scheme and the Crank-Nicolson method is used for the diffusive terms. We then use those temporary values to solve the last 3 equations and proceed with the microphysical adjustment of the scalar fields. Periodical boundary conditions are used for all variables as well as for the moving droplets. Our macroscopic results are obtained by solving equations (2) to (5), without the diffusion terms, considering the whole domain to be one gridpoint. In the following, when we talk about the perturbation in supersaturation (S') we mean the difference between the microscopic and macroscopic supersaturations.

4 Results

We present results from two experiments. In experiment 1, we consider a fixed configuration of droplets. We turn off advection in the thermodynamic equations and we do not allow sedimentation. This unrealistic experiment serves as an upper bound for the effects of microscopic supersaturations. Furthermore, it serves as a test case for the model since we can compare our results to analytical results obtained by Srivastava (1989). In experiment 2 we used a frozen velocity field. We ran the turbulence model with all microphysics turned off for several integral scale turnover times until a stationary isotropic flow was obtained. We then turn on the microphysics and use this flow without allowing it to evolve further. The rms velocity of the flow is 2.5 cm s^{-1} . An examination of the spectra of the kinetic energy and of the variance of temperature perturbation show a dependence on

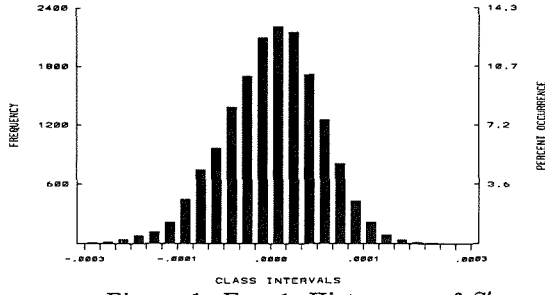


Figure 1: Exp 1, Histogram of S'

wavenumber typical of the dissipation range.

The grid size is $.1158\text{cm}$, the number of grid-points is $60 \times 60 \times 60$. The entire domain is submitted to an updraft of 2ms^{-1} . The experiments last for 215s and the timestep used is $.006\text{s}$. We put 16770 droplets in the domain for an average concentration of 50cm^{-3} . The initial position of the droplets is calculated with a uniform deviate random number generator while their initial size is randomly generated to follow a Gaussian distribution centered at $8\mu\text{m}$ and with a standard deviation of $.75\mu\text{m}$. In both experiments the final average radius and standard deviation obtained with the macroscopic approach are $18.45\mu\text{m}$ and $0.35\mu\text{m}$ respectively.

In experiment 1, since only diffusion is acting, the droplets are submitted to a constant S' . Figure 1 shows a histogram of S' for all the droplets. Values vary between ± 0.0003 which corresponds to a deviation of $\pm 7\%$ from the macroscopic value. The effect of these perturbations on the growth of the individual droplets can be seen in figure 2. This figure is a histogram of $R_{mic\ i} - R_{mac\ i}$, where $R_{mic\ i}$ is the final radius of droplet i with the microscopic approach and $R_{mac\ i}$ is the same from the macroscopic approach. This distribution is negatively skewed and the values fall between $-.4$ and $.24\mu\text{m}$. In other words, the droplet that happens to be in the highest concentration region grew to a size of $-.4\mu\text{m}$ smaller than if its growth had been calculated with the macroscopic approach.

After 215s of growth, the standard deviation of the microscopic spectrum is 3% greater than that of the macroscopic spectrum. Figure 3 displays $\sigma_{mic} - \sigma_{mac}$ as a function of time for both experiments. σ is the standard deviation. Curve 1, corresponding to experiment 1, shows that the broadening is increasing with time.

In contrast to experiment 1, droplets in the second experiment see a variable environment. They are carried by the flow and they sediment. Figure 4 shows S' along the trajectory of one partic-

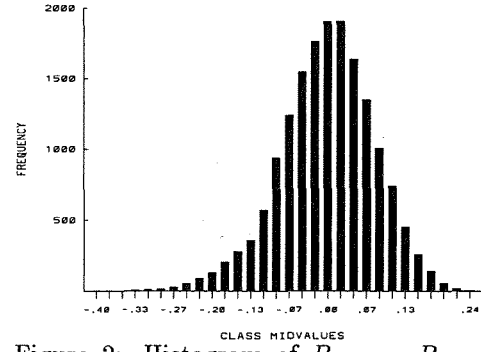


Figure 2: Histogram of $R_{mic\ i} - R_{mac\ i}$ (μm) \forall droplets for Exp. 1

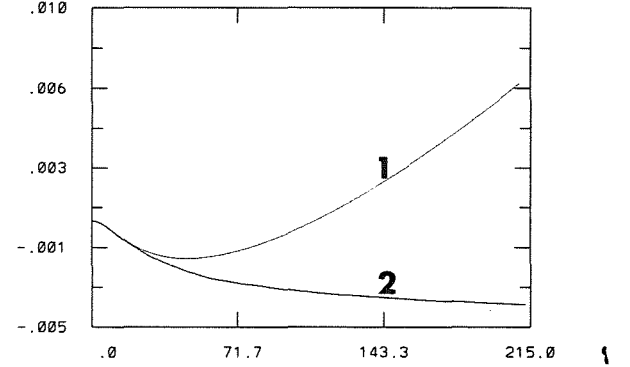


Figure 3: Difference in final standard deviation (μm) between spectrum obtained by microscopic and macroscopic calculations for Exp's 1 (curve 1) and 2 (curve 2)

ular droplet for half the simulation. This droplet evolved in an environment where the local concentration was generally higher than the average since the time integral of S' is slightly negative. Figure 5 shows the histogram of S' for all the droplets at the final time. Comparison with figure 1 shows that this distribution is narrower and more strongly negatively skewed. The resultant effect on the evolution of the individual droplets and on the spectrum is less important than in Exp 1 and is not very significant.

Curve 2 in figure 3 shows that the standard de-

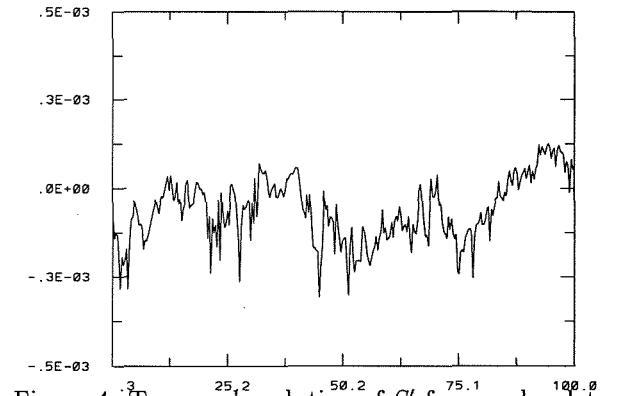


Figure 4: Temporal evolution of S' for one droplet

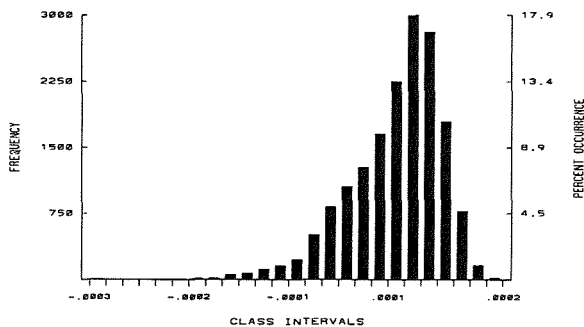


Figure 5: Exp. 2, Histogram of S'

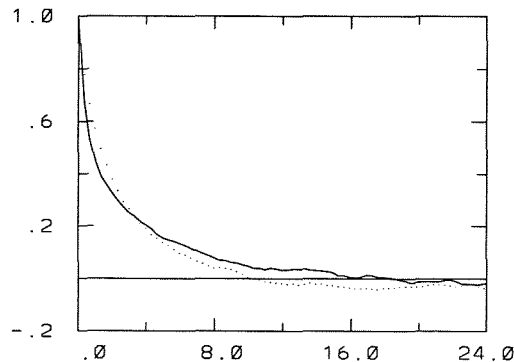


Figure 6: Autocorrelation coefficient as a function of time lag (s)

viation of the microscopic spectrum stays slightly lower than that of the macroscopic spectrum. Eventhough S' as seen by a particular droplet is very variable, it is not random. Figure 6 shows the autocorrelation coefficient for S' as a function of the lag time. These curves represent averages over 20 droplets. The continuous line is from experiment 2 and the dotted line is from a similar experiment except for the sedimentation which has been turned off. It is seen that the decorrelation time is of the order of 10s in both cases.

5 Conclusion

The results we have presented from experiment 1 are compatible with the analytical results obtained by Srivastava (1989) and show that the variable spatial concentration of droplets does influence the evolution of individual droplets and of the spectrum. In more realistic conditions, i.e when droplets experience a variable environment due to the fact that they are moving with the flow and are sedimenting our results show no broadening effect. The perturbations experienced by the droplets tend to be smaller and their time integral is very small.

However, the results presented here are tenta-

tive in the sense that for such experiments to be conclusive, many experiments with varying conditions have to be conducted to gain statistical significance. Furthermore, we need to conduct experiments with a varying flow field. We intend to do that in the near future.

Acknowledgments

The authors thank Dr. P. Bartello for providing his turbulence model.

References

- Brenguier, J.-L. and Chaumat, L. (1996). Condensational droplet growth in a homogeneous updraft. In *Proc. 12th Int. Conf. on Clouds and Precip.*
- Cooper, W. A. (1989). Effects of variable droplet growth histories on droplet size distributions. part i: Theory. *Journal of the Atmospheric Sciences*, 46:1301–1311.
- Fukuta, N. (1992). Theories of competitive cloud droplet growth and their application to cloud physics studies. *Journal of the Atmospheric Sciences*, 49:1107–1113.
- Hall, W. D. (1980). A detailed microphysical model within a two-dimensional framework: Model description and preliminary results. *Journal of the Atmospheric Sciences*, 37:2486–2507.
- Kerr, R. M. (1994). Deterministic forcing of homogeneous, isotropic turbulence. *Phys. Fluids*, 6:1612–1614.
- MacPherson, J. I. and Isaac, G. A. (1977). Turbulent characteristics of some canadian cumulus clouds. *J. Applied Meteor.*, 16:81–90.
- Sedunov, Y. S. (1974). *Physics of the drop formation in the atmosphere*. John Wiley & Sons.
- Srivastava, R. C. (1989). Growth of cloud droplets by condensation: A criticism of currently accepted theory and a new approach. *Journal of the Atmospheric Sciences*, 46:869–887.

FORMATION OF FREEZING DRIZZLE VIA SHEAR-ENHANCED COLLISION-COALESCENCE NEAR CLOUD BASE

Ben C. Bernstein and Marcia K. Politovich
Research Applications Program
National Center for Atmospheric Research
Boulder CO 80307

1. Introduction

On 5-7 March 1994, a shallow, supercooled liquid water cloud was in place over northeastern Colorado (CO). This cloud was undercut by a dry, secondary cold front late on 7 March, causing a shear layer to form at the secondary frontal interface (near cloud base). Within an hour, large freezing drizzle (ZL) drops were observed within wavelike structures near cloud base and at the surface soon thereafter. The ZL persisted for more than 6 hours across parts of the Winter Icing and Storms Project (WISP; Rasmussen et al 1992) domain. In this paper, research aircraft, ground-based Doppler radar, balloon-borne sounding and surface weather observations will be combined to show that the intrusion of the secondary cold front may have led to the formation of Kelvin-Helmholtz (K-H) waves at cloud base, and the subsequent broadening of the droplet size spectra to include drizzle by enhancing the collision-coalescence process.

2. Synoptic Overview

At 1500, 5 March (05/1500; all times UTC), a surface cold front extended from a weak low pressure center over southern Saskatchewan to the CO/WY(Wyoming) border. The front was associated with a broad high pressure area centered off the Washington coast. By 07/1200, the active cold front moved southward to the Texas panhandle, as the high pressure area nosed into the Dakotas, bringing moist upslope flow to the northeast CO (see Fig. 1). At this time, a strong, secondary cold front moved southward to Nebraska. Ahead of this front, 5 ms^{-1} east and southeast winds persisted, while temperatures and dew points were $2\text{-}5^{\circ}\text{C}$. Behind the secondary cold front, winds were from the north, while temperatures and dew points were -7 to -1°C . The front entered the WISP domain just after 07/1500 and passed through by 08/0000. This motion coincided with the gradual passage of a trough axis at 500 and 700 mb.

3. Observations of the Cloud and Wave Structures

3.1 Mesoscale analysis

Before the secondary cold front entered CO from the north, light to moderate rain showers were occurring along the CO/WY border, with reflectivities up to 30 dBZ (not shown) indicated by the NCAR CP4 radar located in Roggen, CO (see Fig. 2). These showers were associated with weak upper level disturbances passing through the area, and dissipated by 14Z. As the front moved southward into CO, temperatures fell to near freezing, winds increased in speed and shifted to northeasterly. A sharp southern edge to the reflectivity was roughly collocated with the position of the surface

front just south of the CO/WY border at 07/1540 (not shown). Peak reflectivities behind the front were ~ 30 dBZ. Observations from a sounding site at Briggsdale (BGD) noted showers of graupel and aggregates at this time, followed by rapid clearing and an increase in visibility from near zero to ~ 15 km. Ceiling and visibility data from Platteville, Greeley and Fort Collins/Loveland (PTL, GXY and FNL) all showed that cloud base increased by $\sim 150\text{m}$ and visibility increased dramatically following frontal passage. The front moved roughly southward through the WISP network, reaching Denver (DEN) at 07/1830.

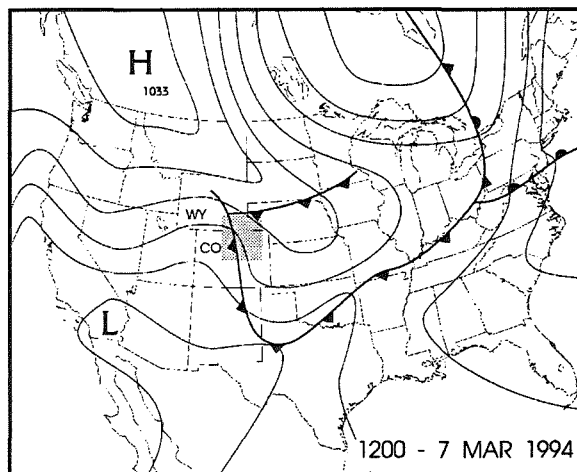


Fig. 1: United states synoptic-scale surface map for 07/1200. Contours of surface pressure are every 4 mb. Standard symbols are used to identify fronts, high and low pressure centers. Stippled area indicates the 1994 WISP domain.

An area of -10 to 0 dBZ reflectivity began to form between DEN, FNL and GXY by 07/2000, as surface winds in that area shifted to due E. Winds ~ 700 m above the surface were from the NE in the 07/2100 Hudson sounding (not shown). Elsewhere in the mesonet, winds had not begun to shift, and were still parallel with the NE flow aloft. Beginning at 07/2200, weak waves became apparent in the 0.5° PPI scans from CP4 (Fig. 3a). These waves were only visible within 60 km of the radar, and were located over the NOAA K_a -band radar (NOAA-K) and Hudson. The waves were oriented WSW-ESE (perpendicular to the low-level shear), had a wavelength of ~ 3 km, and caused bands of 0 dBZ reflectivity interspersed with -5 dBZ to form. These wave features were located very near cloud base initially, but the precipitation associated with them and their appearance in the reflectivity

tivity field descended to reach the surface by 07/2200.

Surface observations at NOAA-K indicated light drizzle (L-) at this time, while a volunteer observer at nearby Erie reported freezing drizzle (ZL). At ~07/2240, L- changed to ZL- at NOAA-K and DEN. Several other observers reported ZL- beginning about the same time that the waves in reflectivity became apparent over their sites. ZL- was also reported at, but waves were not apparent over Fort Collins and Loveland. This was likely due to the shallow nature of the waves, since the CP4 0.5 degree scan was above 2.0 km MSL (the top of the waves) at distances of 60 km or more (FNL was 70 km from CP4 - see Fig. 2).

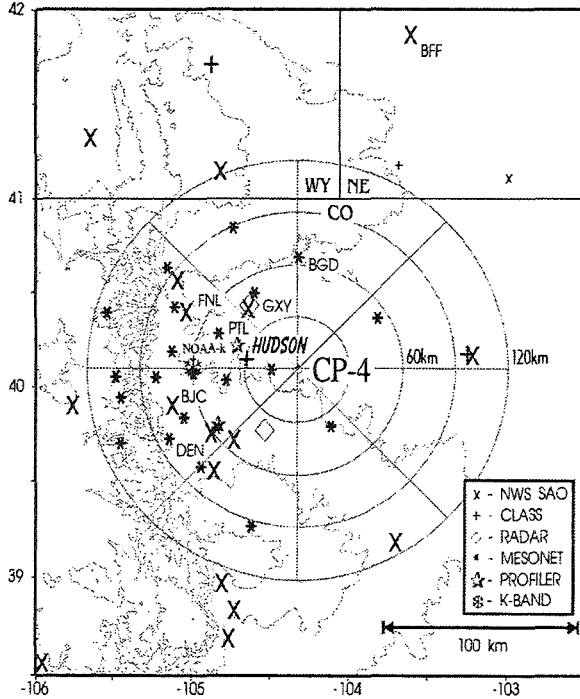


Fig. 2: WISP94 project network. Symbol legend given in figure. NCAR CP4 radar range rings every 30 km, azimuths every 45°, and correspond to those in Fig. 3. Topography contours every 1000 ft (304.8 m), beginning at 5000 ft (1524 m) MSL.

By 07/2350 (not shown), the waves were very apparent from just south of FNL to southeast of DEN. With time, they appeared throughout the Denver area as low-level shear developed there (Fig. 3b). No precipitation of any type was reported more than 20 km north and east of the radar, where no large areas of reflectivity or waves existed. The waves in the reflectivity field were confined to those locations where surface winds differed significantly from those seen above 2 km MSL. Surface winds in these areas may have been turning due to blocking of the stably stratified boundary layer air by the foothills of the CO Rockies. Overall, it appears that the formation of low level shear may have been critical to the formation of freezing drizzle to the south and west of CP4.

3.2 NOAA-K Doppler radar measurements

Over-the-top RHI scans performed by NOAA-K at 08/0000 show that reflectivity values increased gradually with decreasing height to 1-2 dBZ at ~2.0 km (0.5 km AGL, the height of the waves), where they suddenly increased to > 5 dBZ (Fig. 4). It is at this same level that a marked increase in

the downward vertical velocity (a mixture of terminal velocity and true vertical wind speed) was measured. This feature is clearly visible directly above the radar as a maximum of about 1.3 ms^{-1} in downward (toward) radial velocity at that height. With the knowledge that this was occurring in a gentle upslope wind of $5\text{-}10 \text{ ms}^{-1}$, and that conditions were stable and stratiform in nature, vertical wind speeds ($\sim 10 \text{ cm s}^{-1}$) were likely to be rather small in comparison to the fall speeds, thus the Doppler velocity field at 90° elevation (looking up) essentially indicated the fall speed of the precipitation.

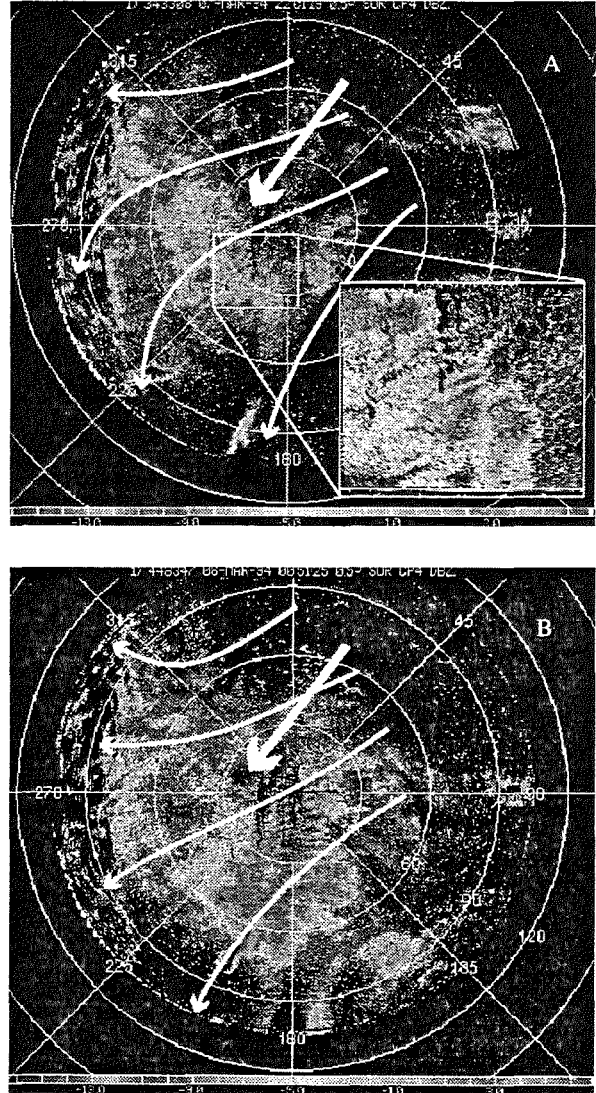


Fig. 3: NCAR CP4 radar reflectivity and surface mesonet streamlines (thin arrows) for a) 07/2201 and b) 08/0051. Reflectivity values, range rings (every 30 km) and azimuth angles are indicated. Thick arrows indicate the 700 m AGL winds from the a) 07/2100 and b) 08/0010 Hudson soundings.

The corrected values near 1.4 ms^{-1} correlate with $\sim 250\text{-}400 \text{ }\mu\text{m}$ diameter droplets (Gunn and Kinzer, 1949). Aircraft microphysical probe data discussed in the next section will reveal that such droplet sizes were common in this portion of the cloud. Waves at the low-level shear interface were not clearly visible in the RHI data, though some weak regular undulations in the reflectivity and velocity fields were dis-

cernible, and strong wind shear was evident at 2 km (~ 0.5 km AGL). More obvious structures in the reflectivity and velocity fields, as well as wind shear, were visible near cloud top.

Breaking K-H waves have been suggested by Pobanz et al. (1994) to be associated with creation of drizzle-sized droplets in shear layers at cloud top. In this case, there was a shear layer near the cloud top, but the most pronounced increase in drop size occurred at the shear layer nearest to cloud base, at 2 km. The upper shear layers may have played a role in the initial broadening of the cloud droplet spectrum to observed maximum sizes $> 100 \mu\text{m}$ in the upper cloud layers. Martner and Ralph (1993) documented two cases where NOAA-K observed K-H waves at or near cloud top. However, the authors of this paper are unaware of any published observations of K-H waves embedded within a cloud layer.

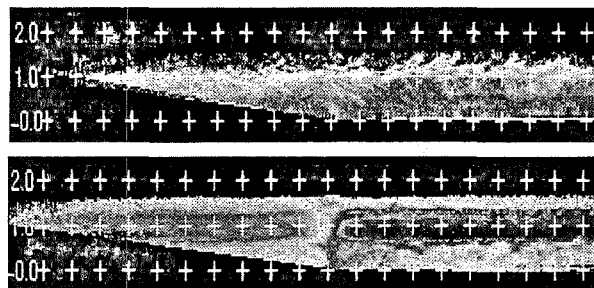


Fig. 4: a) Reflectivity and b) radial velocity data from NOAA-K for 07/2358. Darker greys indicate higher values on reflectivity plot, darkest greys and whites indicate the strong toward and zero values on radial velocity plot. Heights (km AGL) are indicated on the left.

3.3 Aircraft measurements

From 07/2358 through 08/0034, the University of Wyoming King Air (N2UW) conducted a sounding from 1.5 to 3.7 km MSL, including brief level flight legs at 2.1, 2.4 and 2.7 km. The flight track was roughly a triangle connecting FNL, GXY and NOAA-K. The sounding revealed a complex atmospheric structure, with cloud extending from 1.5–3.0 km, as shown in Figs. 5a and b. It is not clear whether the temperature inversions noted at 2.4 and 2.7 km represent differences in airmasses or are due to horizontal differences since the aircraft flew extended level flight legs at those altitudes. The air was stable throughout the cloud, with potential temperature increasing with height at all levels. All hydrometeors observed during this portion of the flight were water droplets. They may be roughly partitioned by size by the individual probes: the FSSP (3–45 μm), 1D-C (12.5–187.5 μm), 2D-C (25–800 μm) and 2D-P (200–6400 μm). Since the 2D-C size range overlaps those of the 1D-C and 2D-P probes, these measurements are not included in Fig. 5b.

The strongest shifts in wind direction were at 1.9 and 2.7 km MSL, and occurred in shallow shear layers with depths < 100 m. These shear layers divided the cloud into three distinct layers. The highest FSSP-measured liquid water content of 0.98 g m^{-3} was at the top of the middle layer, at around 2.7 km. This layer also had the highest 1D-C droplet concentration, with values exceeding the maximum of 600 l^{-1} shown on the diagram. In the top cloud layer, liquid water values reached $0.3\text{--}0.4 \text{ g m}^{-3}$, with FSSP-measured droplet concentrations near 100 cm^{-3} , 1D-C concentrations around 200 l^{-1} , and very few 2D-P droplets. Wind speed shear and a

strong (nearly 4°C) temperature inversion existed at the very top of the cloud.

The lower-level wind shift corresponds with the shear layer noted in the sounding and radar data, where the tops of the bands of higher reflectivity were located. The wind shift was below the temperature inversion base. Below 1.9 km, winds were from the east-southeast at 6 ms^{-1} , with $3\text{--}6 \text{ ms}^{-1}$ north-northeasterly winds above. The shear vector in this case was nearly due north, which corresponds with the east-west oriented waves observed by CP4. The Richardson number calculated for this layer was only 0.14, clearly within the range where breaking K-H waves could be produced.

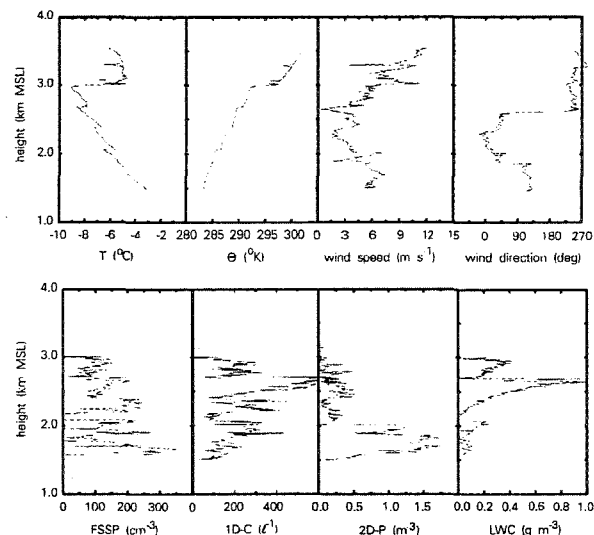


Fig. 5: Measurements obtained from N2UW between 07/2358 and 08/0035. a) Temperature (T), potential temperature (θ), wind speed and direction. b) Droplet concentrations from FSSP, 1D-C, 2D-P and liquid water content from the FSSP (LWC). All measurements are 1-s values.

The lowest cloud layer had the lowest FSSP-measured liquid water content. The 2D-P concentrations were highest here, and this is in agreement with the enhanced reflectivity and fall speeds in the NOAA-K data. This is consistent with an active coalescence process, by which drops grow rapidly to precipitation size and deplete the smaller, FSSP-sized droplets. ZL-sized droplets could not be detected by the FSSP, thus the FSSP-derived LWC values did not include the LWC that was contained within the larger sized droplets.

Droplet size distributions for all four particle sizing probes (FSSP, 1D-C, 2D-C and 2D-P) were derived for 50-m vertical intervals throughout the sounding. From these, the median, 5%, 25%, 75%, and 95% mass-weighted diameters were calculated, as well as the total liquid water content. The distribution of sizes as a function of height is shown in Fig. 6. In general, there was an increase in droplet size as well as broadening of the distribution downward with height in all three cloud layers. However, the most pronounced increase, both in droplet size and spectral breadth, occurred just below the lower shear interface.

Liquid water content from the FSSP-only and from the entire droplet spectrum are shown for the 50-m intervals in Fig. 7. In the upper two cloud layers, most of the liquid was in cloud droplet sizes well-measured by the FSSP, but below, most of the liquid was in larger sizes. Characterizing the liq-

uid water content of the cloud by FSSP measurements alone can thus be misleading.

This cloud may not be well represented by a simple 1-D parcel model. The cloudy layers have different origins (lowest from the south-southeast, middle from the north-northeast, and upper from the west-southwest). However, drizzle droplets formed in the upper cloud layers can certainly fall into the lower layers and interact with them through a collision-coalescence process, depleting liquid and creating larger droplets. Three shear layers existed in this cloud: one at the top (3 km) and two embedded within (2.7 and 2 km). The marked increase in droplet size below 2 km cannot be attributed to simple growth of a droplet falling into an enhanced LWC environment alone, since the corrected LWC values at this level were still well below the maximum values measured in this cloud.

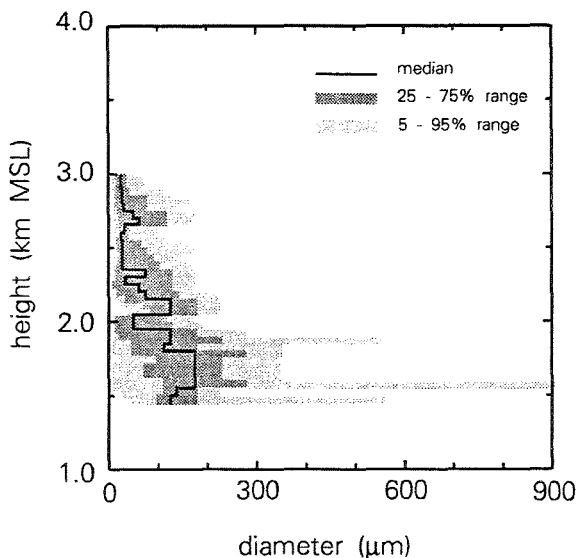


Fig. 6: Median (solid line), 25-75% range (dark shading) and 5-95% range (light shading) of mass-weighted droplet diameters from the four measurement probes on board N2UW. Measurements were obtained during the sounding shown in Fig. 5, and are divided into 50-m vertical increments.

4. CONCLUSIONS

The data presented here point toward the existence of supercooled water droplets of the size range 100-250 μm throughout the entire depth of a supercooled liquid water cloud, and sudden broadening of the droplet size distribution well within the cloud. This broadening appears to be related to the existence of a marked shear layer, where wavelike structures in radar reflectivity were clearly identified. The origins of the drizzle droplets in the upper cloud layer, the relation of K-H waves to spectral broadening, and the interaction between the cloudy layers, are topics for further study.

ACKNOWLEDGEMENTS

Thanks to NOAA's Environmental Technology Laboratory for supplying the authors with NOAA K_a -band radar data, and to Brooks Martner of NOAA for his help with interpretation of that data. Aircraft data were provided by the University of Wyoming.

This research is sponsored by the National Science Foundation through an Interagency Agreement in response to requirements and funding by the Federal Aviation Administration's Aviation Weather Development Program. The views expressed are those of the authors and do not necessarily represent the official policy or position of the U.S. Government.

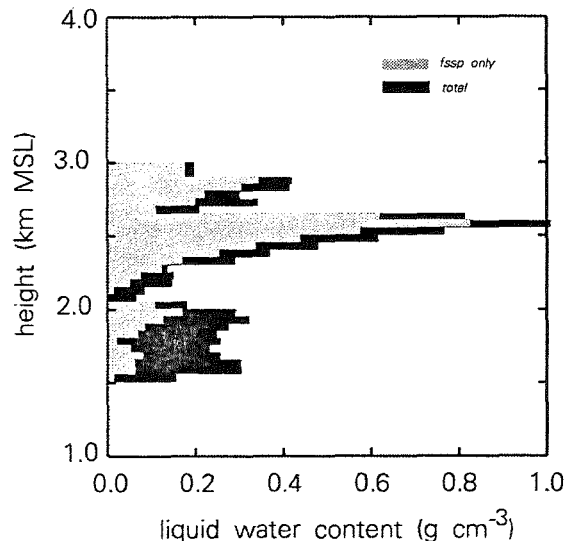


Fig. 7: Liquid water content from the FSSP (light shading) and from all probes (dark shading) for 50-m vertical increments of the sounding shown in Figs. 5 and 6.

REFERENCES

- Gunn, R. and G.D. Kinzer, 1949: The terminal velocity of fall for water droplets in stagnant air. *J. Meteor.*, **6**, 243-248.
- Martner, B.E. and F.M. Ralph, 1993: Breaking Kelvin-Helmholtz waves and cloud-top entrainment as revealed by K -band Doppler radar. *Preprints*, Ninth Conference on Atmospheric and Oceanic Waves and Stability. San Antonio, Texas, 10-14 May. Amer. Meteor. Soc.
- Pobanz, B.M., J.D. Marwitz and M.K. Politovich, 1994: Conditions associated with large-drop regions. *J. Appl. Meteor.*, **33**, 1366-1372.
- Rasmussen, R., M. Politovich, J. Marwitz, W. Sand, J. McGinley, J. Smart, R. Pielke, S. Rutledge, D. Wesley, G. Stossmeister, B. Bernstein, K. Elmore, N. Powell, E. Westwater, B. Stankov and D. Burrows, 1992: Winter Icing and Storms Project (WISP). *Bull. Amer. Meteor. Soc.*, **73**, 951-974.

THE EFFECT OF SMALL-SCALE TURBULENCE ON THE COLLISION RATES OF CLOUD DROPS

Anna S. Koziol¹ and Henry G. Leighton²

¹Atmospheric Environment Service, Dorval, Québec H9P 1J3, Canada

²Dept. of Atmospheric and Oceanic Sciences, McGill University, Montréal, Québec H3A 2K6, Canada

1. INTRODUCTION

For over fifty years, the influence of turbulence on the collision-coalescence of cloud drops has been discussed in the cloud physics community. Over these years no agreement has been reached on whether or not turbulence is a major factor in the collisional growth of cloud droplets. Here, we consider the effects of turbulence which are limited to small scales only (of the order of the Kolmogorov length scale). Turbulence on such scales is homogeneous, isotropic and stationary. We also restrict the drop sizes of the collector (i.e. larger) drops to the range 10–20 μm .

Historically, the first attempts to account for the influence of small scale turbulence on the collisional growth of cloud drops were concentrated on the effect of drop inertia, most comprehensively by East & Marshall (1954). Later, however, Saffman and Turner (1956) noticed that this effect (i.e. different drop motions relative to the air) is only one possible effect of turbulence, the other being due to different drop motions with the air. While the former effect is determined by the r.m.s. turbulent velocity, the later is governed by the rate of energy dissipation. According to Saffman & Turner, the effect of the motion relative to the air is small except for drops of significantly different sizes, and the effect of the motion with the air might be significant only for strong turbulence (e.g. for the rate of energy dissipation, ϵ , of the order of 1000 $\text{cm}^2 \text{s}^{-3}$.) Neither Saffman & Turner nor the earlier researchers included the effect of hydrodynamic interactions in their estimates. It was not until 1975 that the effect of hydrodynamic interactions was incorporated. De Almeida (1976, 1979) developed a method of calculating collision rates on the basis of modelling individual trajectories. He found that the effect of weak turbulent fields ($\epsilon = 1$ and 10 $\text{cm}^2 \text{s}^{-3}$) on collision rates was very strong, and affected profoundly the development of cloud spectra. However, subsequent work (Pruppacher & Klett, 1980) questioned some of de Almeida's assumptions and the results were never fully accepted.

This research is inspired by the work of Saffman

& Turner (1956), and of de Almeida (1976, 1979). In particular, the flux method presented in the next section is based on the work by Saffman & Turner, and in the use of individual drop trajectories to calculate collision rates we follow de Almeida.

2. THE MODEL

Following the ideas of Smoluchowski (1916) for Brownian coagulation, and those of Saffman & Turner (1956), we calculate the collision rate of drops '1' and '2' as a flux of droplets '2' through the sphere of radius R . Let R be a minimum radius beyond which the effect of hydrodynamic interactions between drops on their relative displacement can be neglected in comparison to the effects of turbulence. We are interested in the flux of drops '2' entering the sphere of radius R that subsequently collide with drops '1' at the origin. The flux through a surface element of the sphere, dS , is represented by

$$dP = -\mathbf{j} \cdot d\mathbf{S} \delta t P(\mathbf{S}), \quad (1)$$

where \mathbf{j} is the average current of droplets '2', and $P(\mathbf{S})$ is the probability that drop '2' will collide with drop '1'. Because $\mathbf{j} = n_2 \mathbf{w}$, \mathbf{w} being the average relative velocity of drops '1' and '2', and n_2 the concentration of drops '2',

$$P = -n_2 \delta t \int_S P(\mathbf{S}) \mathbf{w} \cdot d\mathbf{S}. \quad (2)$$

Provided that the separation between drops is not too large, and for the strengths of turbulence considered here, the average relative velocity of the drops is dominated by their terminal velocities and so

$$\mathbf{w} \cdot d\mathbf{S} = -(v_1 - v_2) dS \cos \theta \quad (3)$$

for all values of θ with significant probability of collision. (v_1 and v_2 are the respective terminal velocities of the drops, and θ is the azimuthal angle for spherical coordinates.) The largest values of θ for which there is a significant probability of collision occur for large radius ratios ($r_2/r_1 > 0.9$) and strong

turbulence ($\epsilon = 100 \text{ cm}^2 \text{ s}^{-3}$) but even then $\theta < 40^\circ$. Inserting this approximation in (2) we get

$$\mathcal{P} = 2\pi n_2 \delta t R^2 (v_1 - v_2) \int_0^\pi P(\theta; R) \cos \theta \sin \theta d\theta, \quad (4)$$

where, because of symmetry, $P(\mathbf{S}) = P(\theta; R)$.

We can interpret \mathcal{P} as the probability that a droplet '2' collides with a droplet '1' during the time δt . This interpretation allows us to relate \mathcal{P} to the collision kernel in the Stochastic Growth Equation, K_{12} (Gillespie 1975)

$$K_{12} n_2 \delta t = \mathcal{P}. \quad (5)$$

Finally,

$$K_{12} = \pi R^2 (v_1 - v_2) \int_0^\pi P(\theta; R) \sin 2\theta d\theta. \quad (6)$$

By analogy to the case of laminar settling in a still fluid we can define the collision efficiency for the turbulent case

$$E_{12} = K_{12} / [\pi(r_1 + r_2)^2 (v_1 - v_2)]. \quad (7)$$

From many independent trajectory calculations, the probability of collision is estimated as

$$P(\theta; R) = N_{\text{coll}} / N_{\text{exp}}, \quad (8)$$

where N_{coll} is the number of trajectories which resulted in collisions, and N_{exp} is the total number of experiments—trajectories. Trajectory calculations are performed with our hydrodynamic model. We numerically integrate the initial value problem for two hydrodynamically interacting drops in the external turbulent field. The collector drop is placed initially at the origin, and the collected drop on the surface of the sphere of radius R at a specified angle θ . Generally R is taken to be $20r_1$.

The drop equations of motion are obtained on the basis of the resistance problem for the time-independent Stokes flow. This assumption is correct because the Reynolds and Strouhal number based on the length and time scales characterizing the drops, and their terminal velocities are small. Farther, because the length scale of the two-drop problem is of the order or smaller than the Kolmogorov length scale, we expand the ambient turbulent velocity field, $u_i(\mathbf{x})$ in a Taylor series as follows

$$u_i(\mathbf{x}) = u_i(\mathbf{x}_0) + \frac{\partial u_i}{\partial x_j} \delta x_j + o(\delta^2 x). \quad (9)$$

Introducing the rate of stress, $E_{ij}^\infty = \mathbf{E}_\infty$, and the solid body angular velocity $\Omega_k^\infty = \mathbf{\Omega}_\infty$, (9) can be written

$$u_i = u_i(\mathbf{x}_0) + \mathbf{E}_\infty \cdot \delta \mathbf{x} + \mathbf{\Omega}_\infty \times \delta \mathbf{x}. \quad (10)$$

Now, after Kim & Karrila (1991), the drop equations of motion can be written as

$$m_\alpha \frac{dv_i^\alpha}{dt} = F_i^\alpha + m_\alpha g_i, \quad (11)$$

$$I_\alpha \frac{d\Omega_i^\alpha}{dt} = T_i^\alpha, \quad \frac{dx_i^\alpha}{dt} = v_i^\alpha, \quad (12)$$

where

$$\begin{aligned} F_i^\alpha &= \mu A_{ij}^{\alpha\alpha} [u_j(\mathbf{x}^\alpha) - v_j^\alpha] + \mu A_{ij}^{\alpha\beta} [u_j(\mathbf{x}^\beta) - v_j^\beta] \\ &\quad - \mu \tilde{B}_{ij}^{\alpha\alpha} (\Omega_j^\alpha - \Omega_j^\infty) - \mu \tilde{B}_{ij}^{\alpha\beta} (\Omega_j^\beta - \Omega_j^\infty) \\ &\quad + \mu G_{ijk}^{\alpha\alpha} E_{jk}^\infty + \mu G_{ijk}^{\alpha\beta} E_{jk}^\infty, \end{aligned} \quad (13)$$

$$\begin{aligned} T_i^\alpha &= \mu B_{ij}^{\alpha\alpha} [u_j(\mathbf{x}^\alpha) - v_j^\alpha] + \mu B_{ij}^{\alpha\beta} [u_j(\mathbf{x}^\beta) - v_j^\beta] \\ &\quad - \mu C_{ij}^{\alpha\alpha} (\Omega_j^\alpha - \Omega_j^\infty) - \mu C_{ij}^{\alpha\beta} (\Omega_j^\beta - \Omega_j^\infty) \\ &\quad + \mu H_{ijk}^{\alpha\alpha} E_{jk}^\infty + \mu H_{ijk}^{\alpha\beta} E_{jk}^\infty, \end{aligned} \quad (14)$$

μ is the dynamic viscosity, α and β are the drop indicators, and m_α and I_α are respectively the drop mass and moment of inertia. The coefficients $A_{ij}^{\alpha\beta}$, $B_{ij}^{\alpha\beta}$, $\tilde{B}_{ij}^{\alpha\beta}$, $C_{ij}^{\alpha\beta}$, $G_{ijk}^{\alpha\beta}$, and $H_{ijk}^{\alpha\beta}$ depend only on two nondimensional parameters, the radius ratio, and the parameter, $2D/(r_1 + r_2)$, where D is the distance between centers. The coefficients were calculated as in Jeffrey & Onishi (1984), and Jeffrey (1992).

The turbulent velocity field, u_i is represented in the form of random Fourier modes (Kraichnan, 1970)

$$\begin{aligned} u_i(\mathbf{x}, t) &= \sum_{n=1}^N [b_i^{(n)} \cos(\mathbf{k}^{(n)} \cdot \mathbf{x} + \omega^{(n)} t) \\ &\quad + c_i^{(n)} \sin(\mathbf{k}^{(n)} \cdot \mathbf{x} + \omega^{(n)} t)]. \end{aligned} \quad (15)$$

After Maxey (1987), we let the wavenumbers, \mathbf{k} , and the frequencies, ω be random variables with the probability density functions $p_1(\mathbf{k})$ and $p_2(\omega)$ respectively. The coefficients $b_i^{(n)}$ and $c_i^{(n)}$ must be chosen in such a way that the flow is incompressible, and the two-point velocity correlation corresponds to the desired energy spectrum. This condition is satisfied for coefficients of the form

$$b_i^{(n)} = \Gamma(k, \omega) \left(\delta_{ij} - \frac{k_i^{(n)} k_j^{(n)}}{k^{(n)2}} \right) \hat{b}_j^{(n)}. \quad (16)$$

The function $\Gamma(k, \omega)$ scales the coefficients so as to obtain the desired energy spectrum, while the coefficients $\hat{b}_j^{(n)}$ are random Gaussian variables with zero mean and unit variance (similar relations hold for $\hat{c}_j^{(n)}$). Maxey (1987) showed that

$$\Gamma^2(k, \omega) = \frac{\mathcal{E}(k, \omega)}{4\pi k^2 N p_1(\mathbf{k}) p_2(\omega)}, \quad (17)$$

where the four-dimensional spectrum $\mathcal{E}(k, \omega)$ is calculated as

$$\mathcal{E}(k, \omega) = E(k) \frac{1}{\sqrt{2\pi}\sigma_\omega} \exp\left[-\frac{(\omega - \bar{\omega})^2}{2\sigma_\omega^2}\right]. \quad (18)$$

We assume that the energy spectrum, $E(k)$ has the form of the Pao spectrum (Pao 1965)

$$E(k) = \alpha \epsilon^{\frac{2}{3}} k^{-\frac{5}{3}} \exp\left(-\frac{3}{2} \alpha \nu \epsilon^{-\frac{1}{3}} k^{\frac{4}{3}}\right), \quad (19)$$

where α is a constant. The spectrum given by (19) reduces to the $-5/3$ law for small wavenumbers. Fung et al. (1992) assume that

$$\sigma_\omega = \bar{\omega} = \epsilon^{\frac{1}{3}} k^{\frac{2}{3}}. \quad (20)$$

The numerical calculation of Fung et al. shows that the above choice of $\mathcal{E}(k, \omega)$ results in the Eulerian-Lagrangian time spectrum $\chi_{ii} = \beta \epsilon \omega^{-2}$, where β is a constant. Finally, we assume that $p_1(k)$ and $p_2(\omega)$ are uniformly distributed in their respective ranges.

3. RESULTS

We systematically examined collector drops with three different radii: 10, 15, and 20 μm . The selected rates of energy dissipation were 1, 10, and 100 $\text{cm}^2 \text{s}^{-3}$. Figs. 1–3 compare the values of the collision efficiencies for the laminar and turbulent cases for the same collector drop. Statistical uncertainties are also included. (Because of our representation of the hydrodynamic forces, our laminar calculations can be compared with the results of Hocking & Jonas, 1970 for $\delta = 0.001$)

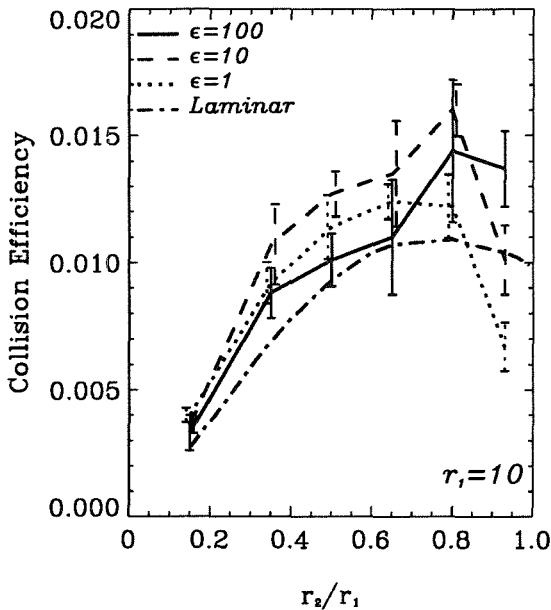


Fig. 1 Comparison of the collision efficiencies for different strengths of turbulence with the laminar collision efficiencies for 10 μm collector drops.

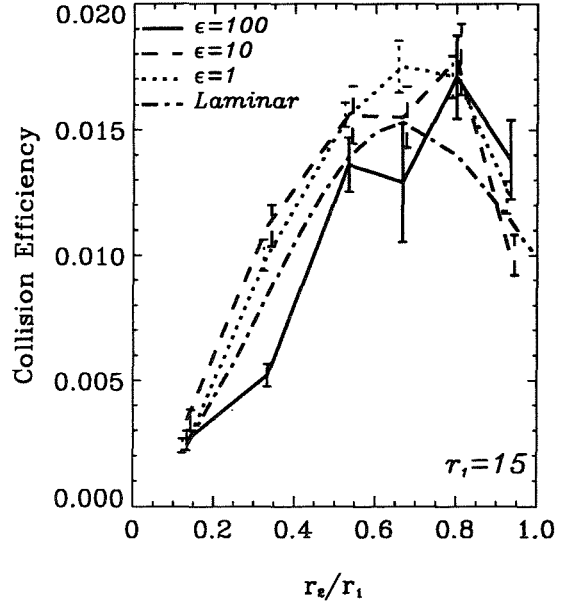


Fig. 2 Comparison of the collision efficiencies for different strengths of turbulence with the laminar collision efficiencies for 15 μm collector drops.

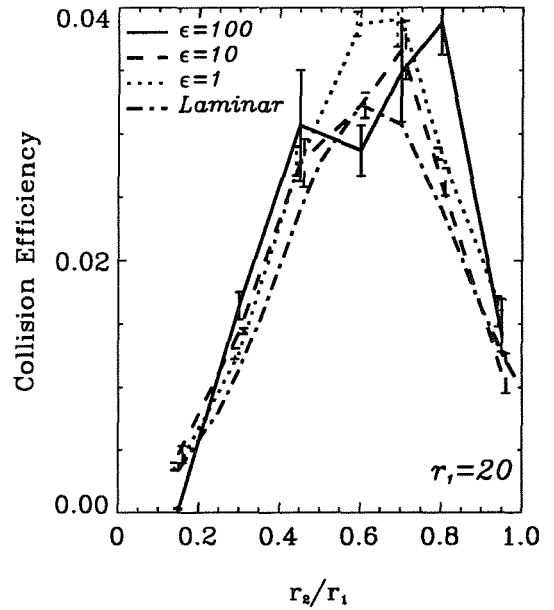


Fig. 3 Comparison of the collision efficiencies for different strengths of turbulence with the laminar collision efficiencies for 20 μm collector drops.

For a 10 μm collector drop a general increase in the collision efficiency is observed. The maximum increase is 50% for collisions with 8 μm drops, and $\epsilon = 10 \text{ cm}^2 \text{s}^{-3}$. For $\epsilon = 1$ and $10 \text{ cm}^2 \text{s}^{-3}$ and for large drop radius ratios the collision efficiency decreases as r_2/r_1 increases but for $\epsilon = 100 \text{ cm}^2 \text{s}^{-3}$ no such trend is evident. The shape of the collision efficiency curves for 15 μm and 20 μm collector drops is similar to that for 10 μm collector drop except that for large r_2/r_1 the collision efficiency decreases with increasing r_2/r_1 when $\epsilon = 100 \text{ cm}^2 \text{s}^{-3}$. For a 15 μm

collector drop the effect is generally weaker than for a 10 μm collector drop, especially for $\epsilon = 10$ and 100 $\text{cm}^2 \text{s}^{-3}$. The largest relative increase in collision efficiency (60%) is found for 20 μm collector drops collecting 16 μm drops with $\epsilon = 100 \text{ cm}^2 \text{s}^{-3}$. The maximum in the collision efficiency curves for $\epsilon = 1 \text{ cm}^2 \text{s}^{-3}$ occurs at about the same value of r_2/r_1 as for the laminar collision efficiency for all three values of r_1 . For stronger turbulence the maxima in the collision efficiency curves are shifted to larger values of r_2/r_1 relative to the maxima for laminar flow. Statistical errors are between 5% and 20%, generally larger for stronger turbulence and large radius ratios.

4. CONCLUSIONS

Presently, the only systematic and comprehensive examination of the influence of turbulence on collision efficiencies is that by de Almeida (1976, 1979). The effect of turbulence which de Almeida's drops experienced was dramatic—the increase of collision efficiencies being ten fold and larger. Such large increases were not found here. Our model predicts moderate, at maximum 1.5-fold increases; and, for some combinations of drop radii and rate of energy dissipation our model even predicts decreases in the collision efficiency.

A detailed interpretation of the shapes of the collision efficiency curves is not justified because of the relatively large statistical uncertainties. Nevertheless, it is worth noting that part of the complexity of the curves may be due to the fact that within the present framework turbulence can influence the collision process either through its effect on gravitational settling, or as a result of its direct effect on the hydrodynamic interactions. Each of these mechanisms may depend in a complicated way on the droplet radii and strength of the turbulence. To gain a more complete understanding of the shapes of the curves many more lengthy and computationally expensive experiments would be required. In view of the relatively small influence that turbulence of the intensity considered here has on the collision rates of small drops, further experimentation is not warranted. Our interest is in the potential of turbulence to influence the development of drop size spectra. We do not expect a pronounced effect of these new collision efficiencies on the growth of droplet spectra because the values of the turbulent collision efficiencies differ relatively little from the values for laminar flow. The differences between the laminar and turbulent collision efficiencies are, for example, smaller than those resulting from the introduction of gas kinetic effects by Davis (1972), which were subsequently shown to have only a small impact on cloud droplet spectrum evolution (Leighton 1977).

REFERENCES

- Almeida de, F. C., 1976: The collision problem in cloud droplets moving in a turbulent environment—Part I: A method of solution. *J. Atmos. Sci.*, **33**, 1571–1878.
- Almeida de, F. C., 1979: The collisional problem of cloud droplets moving in a turbulent environment—Part II: Turbulent collision efficiencies. *J. Atmos. Sci.*, **36**, 1564–1576.
- Davis, M. H., 1972: Collisions of small cloud droplets: Gas kinetic effects. *J. Atmos. Sci.*, **29**, 911–915.
- East, T. W. R., and J. S. Marshall, 1954: Turbulence in clouds as a factor in precipitation. *Quart. J. R. Met. Soc.*, **80**, 26–47.
- Fung, J. C. H., J. C. R. Hunt, N. A. Malik, and R. J. Perkins, 1992: Kinematic simulation of homogeneous turbulence by unsteady random Fourier modes. *J. Fluid Mech.*, **236**, 281–318.
- Gillespie, D. T., 1972: The stochastic coalescence model for cloud droplet growth. *J. Atmos. Sci.*, **29**, 1496–1510.
- Hocking, L. M., and P. R. Jonas, 1970: The collision efficiency of small drops. *Quart. J. R. Met. Soc.*, **96**, 722–729.
- Jeffrey, D. J., 1992: The calculation of the low Reynolds number resistance functions for two unequal spheres. *Phys. Fluids A*, **4**, No. 1, 16–29.
- Jeffrey, D. J., and Y. Onishi, 1984: Calculation of the resistance and mobility functions for two unequal rigid spheres in low Reynolds number flow. *J. Fluid Mech.*, **130**, 261–290.
- Kim, S., and S. J. Karrila, 1991: *Microhydrodynamics: Principles and Selected Applications*. Butterworth-Heinemann, Boston, 507 pp.
- Kraichnan, R. H., 1970: Diffusion by random velocity field. *Phys. Fluids*, **13**, no. 1, 22–31.
- Leighton H. G., 1977: Collision efficiency and cloud spectrum evolution. *J. Atmos. Sci.*, **34**, 2005–2006.
- Maxey, M. B., 1987: The gravitational settling of aerosol particles in homogeneous turbulence and random flow fields. *J. Fluid Mech.*, **174**, 441–465.
- Pao, Y.-H., 1965: Structure of turbulent velocity and scalar fields at large wavenumbers. *Phys. Fluids*, **8**, No. 6, 1063–1075.
- Pruppacher, H. R., and J. D. Klett, 1980: *Microphysics of Clouds and Precipitation*. D. Reidel Publishing Company, Dordrecht, 714 pp.
- Saffman, P. G., and J. S. Turner, 1956: On the collision of drops in turbulent clouds. *J. Fluid Mech.*, **1**, 16–30.
- Smoluchowski, M., 1916: Drei Vorträge über Diffusion Brownsche Molekularbewegung und Koagulation von Kolloidteilchen. *Physik. Z.*, **17**, 557–571.

CONDENSATION INSIDE DENSE CLUSTERS OF DROPLETS ON HYGROSCOPIC NUCLEI IN THE ATMOSPHERE.

Tov Elperin and Boris Krasovitev

The Pearlstone Center for Aeronautical Engineering Studies
Department of Mechanical Engineering, Ben-Gurion University of the Negev
P.O. Box 653, Beer-Sheva 84105
Israel

1. INTRODUCTION.

Evaporation (condensation) of a dispersed phase in an ambient gas occurs frequently in numerous atmospheric processes. The applications include atmospheric condensation and evaporation in clouds, artificial modifications of clouds, natural fogs decomposition, etc. (see Mason, 1971; Seinfeld, 1986). Condensational droplet growth on nuclei consisting of hygroscopic substances is very important in such fields as separation of submicron particles from gases and scavenging of the pollutants (Heidenreich and Ebert, 1995). Single drop evaporation models yield the parameters and evaporation characteristics of the individual droplets. In reality the clusters of droplets which are encountered in various environmental applications have a large concentration of droplets. In this case the droplets behave quite different from the single droplets. The importance of droplet interaction effects has not gone unrecognized in the literature.

State-of-the art in the methods used in present for the treating of interactive problems was reviewed by Annamalai and Ryan (1992), Annamalai *et al.* (1993), Elperin and Krasovitev (1994), (1995). The previous theoretical studies deal primarily with droplet evaporation in various limiting cases, such as: regular structure of cluster, finite array, dilute clusters, monosized clusters etc. The method of expansions into irreducible multipoles which was developed in our previous investigations (Elperin and Krasovitev, 1994, 1995) is applicable to more realistic problems and is particularly suitable for dense random clusters of droplets.

The effects of interactions on the evaporation (condensation) rate are estimated using the correction factor which for a cluster of pure droplets can be determined as follows:

$$\eta = \frac{\dot{m}}{\dot{m}_{iso}} \quad (1)$$

where \dot{m} is the mass loss rate of an interacting particle, \dot{m}_{iso} is the mass loss rate of an isolated particle in an infinite atmosphere.

It is well known that interactive effects could both retard and enhance the rate of evaporation of the

interacting droplets. It was shown previously (see e.g., Labowsky, 1980; Annamalai *et al.*, 1993) that the latter occurs under some restrictive conditions such as buoyant convective effects and when droplets of dissimilar composition are considered. In case when interactive effects retard the rate of evaporation, the correction factor is less than 1 ($\eta < 1$, "negative" interactions) and in case when the interactive effects enhance the rate of evaporation the correction factor is greater than 1 ($\eta > 1$, "positive" interactions).

However, the above mentioned theoretical results were obtained for constant droplet diameters, compositions and center-to-center distances. In reality, the compositions and sizes of droplets change with time. The latter implies that the correction factor η depends on time and, therefore, could give rise to the mass and heat sources and sinks inside the cluster. In this study it is showed that heat and mass sinks and sources within the cluster of multicomponent droplets containing volatile and a nonvolatile components can occur also in a case of condensation on hygroscopic nuclei inside the cluster. The first theoretical investigation of the transient problem where the sizes of particles inside a random cluster of char/carbon particles change with time was performed by Elperin and Krasovitev (1995).

The purpose of the present study is to develop the theory of evaporation (condensation) of dense random clusters of droplets with dissimilar compositions.

2. INTERACTIVE EVAPORATION (GROWTH) OF DROPLETS CONTAINING SOLUBLE PARTICLES.

Consider a cluster containing N spherical droplets composed of hygroscopic nuclei and volatile component whose centers are located at $\mathbf{r}_0^{(i)}$ and which have radii R_i where $i = \overline{1, N}$. The location of each droplet is fixed in a system of coordinate X, Y, Z the origin of which can be located in the center of each droplet. The location of j -th droplet can be determined in the system of coordinate X_j, Y_j, Z_j which is connected with the center of each droplet by the vector \mathbf{L}_{ij} . Similarly the location of i -th droplet can be determined in the coordinate system X_j, Y_j, Z_j by the vector $\mathbf{L}_{ji} = -\mathbf{L}_{ij}$. It is assumed that the temperature differences in the neighbourhood of each

droplet are small. Assume also that the characteristic times of heat and diffusive relaxation are small and we can consider a steady state evaporation. Under the above assumptions the system of mass and energy conservation equations in the domain exterior to N arbitrary located droplets reads:

$$\operatorname{div} \tilde{C} = 0, \quad \operatorname{div} \tilde{T} = 0 \quad (2)$$

where $\tilde{C} = C_1 - C_{1,\infty}$, $C_{1,\infty} = \lim_{r_i \rightarrow \infty} C_1$ ($r_i = |\mathbf{r}_i|$, $\mathbf{r}_i = \mathbf{r} - \mathbf{r}_0^{(i)}$), $C_k = n_k^{(e)} / \sum_k n_k^{(e)}$ is a relative concentration of k -th species ($n_k^{(e)}$ is the number of molecules of k -th species per unit of volume, $k=1$ denotes volatile species), $\tilde{T} = T - T_\infty$, $T_\infty = \lim_{r_i \rightarrow \infty} T$, T is the temperature. Note that in order to simplify notations hereafter we omit index i near the solutions \tilde{C} and \tilde{T} . Boundary conditions for conservation equations (2) read:

$$\tilde{C}|_{S_i} = \tilde{C}_s, \quad \tilde{T}|_{S_i} = \tilde{T}_s \quad (3)$$

$$Lm_1 n^{(e)} D \left(\nabla \tilde{C} \mathbf{n}_r \right) \Big|_{S_i} + k \left(\nabla \tilde{T} \mathbf{n}_r \right) \Big|_{S_i} = 0 \quad (4)$$

where L is the latent heat of evaporation, k is the coefficient of thermal conductivity, D is the diffusion coefficient and $n^{(e)} = n_1^{(e)} + n_2^{(e)}$.

Conditions at infinity read:

$$\tilde{T}|_{r_i \rightarrow \infty} \rightarrow 0, \quad \tilde{C}|_{r_i \rightarrow \infty} \rightarrow 0 \quad (5)$$

Note that in the case of small temperature differences in the neighbourhood of each droplet we can expand the dimensionless vapor concentration at the gas-liquid interface in Taylor series and keep only the linear term:

$$\tilde{C}|_{S_i} = \tilde{C}_s = C_s^i(T_\infty) + \frac{\partial C_s^i}{\partial T_s^i} \Big|_{T_s^i=0} \tilde{T}_s + \dots$$

where $C_s^i = C_{1,s}^i - C_{1,\infty}$ and $\tilde{T}_s^i = T_{i,s} - T_\infty$. For ideal solutions the concentrations $C_{1,s}^i$ can be determined by the Raoult's law. In case of evaporation (growth) of droplets containing soluble particles the concentration $C_{1,s}^i$ can be determined by the following formula (see Mason, 1971, pp. 24–30):

$$C_{1,s}(T_s) = C_{1,s}^{(0)}(T_s) \left(1 + \frac{2\mu_v \tilde{\sigma}}{\rho R_g T_s} \frac{1}{R} - \frac{3i\mu_v}{4\pi\rho\mu'} \frac{M'}{R^3} \right)$$

where $\tilde{\sigma}$ is the surface tension, ρ is the density of solvent, μ_v and μ' are the molar masses of vapor of the solvent and of soluble hygroscopic nucleus, i is van't

Hoff's factor which depends on the chemical nature and the degree of dissociation (i.e., on the concentration) of the solute and M' is the mass of a soluble hygroscopic nucleus.

In accordance with the modified method of expansion into irreducible multipoles (see Elperin and Krasovtsov, 1994, 1995) the field functions in the domain outside the droplets can be represented as follows:

$$\tilde{T} = T^i + \delta T^i, \quad \tilde{C} = C^i + \delta C^i \quad (6)$$

where

$$C^i = \sum_{n=0}^{\infty} A_{v_1 \dots v_n}^i x_i^{-(2n+1)} \overbrace{x_{v_1}^i \dots x_{v_n}^i} \quad (7)$$

$$\delta C^i = \sum_{n=0}^{\infty} B_{v_1 \dots v_n}^i \overbrace{x_{v_1}^i \dots x_{v_n}^i}$$

$$T^i = \sum_{n=0}^{\infty} M_{v_1 \dots v_n}^i x_i^{-(2n+1)} \overbrace{x_{v_1}^i \dots x_{v_n}^i} \quad (8)$$

$$\delta T^i = \sum_{n=0}^{\infty} Q_{v_1 \dots v_n}^i \overbrace{x_{v_1}^i \dots x_{v_n}^i}$$

Substituting equations (7)–(8) into the boundary conditions (3)–(4) we can obtain the following system of linear algebraic equations for determining the tensors

$A_{v_1 \dots v_n}^i$ and $M_{v_1 \dots v_n}^i$, via the tensors $B_{v_1 \dots v_n}^i$ and $Q_{v_1 \dots v_n}^i$:

$$A_{v_1 \dots v_n}^i = \lambda_n^{i(0)} \delta_{0n} + B_{v_1 \dots v_n}^i \lambda_{bn}^i + Q_{v_1 \dots v_n}^i \lambda_{qn}^i \quad (9)$$

$$M_{v_1 \dots v_n}^i = \varphi_n^{i(0)} \delta_{0n} + B_{v_1 \dots v_n}^i \varphi_{bn}^i + Q_{v_1 \dots v_n}^i \varphi_{qn}^i \quad (10)$$

where $\lambda_n^{i(0)} = \frac{(C_{1,s}^i(T_\infty) - C_{1,\infty})k}{k + \gamma^i D n^{(e)} L m_1}$, $\lambda_{bn}^i = -\frac{\lambda_n^{i(0)}}{C_{1,s}^i(T_\infty) - C_{1,\infty}}$

$$\lambda_{qn}^i = \frac{(2n+1)k\gamma^i}{(n+1)(k + \gamma^i D n^{(e)} L m_1)}, \quad \gamma^i = C_{1,s}^i(T_\infty) \frac{L\mu_1}{R_g T_\infty^2},$$

$$\varphi_n^{i(0)} = \frac{(C_{1,\infty} - C_{1,s}^i(T_\infty)) L m_1 n^{(e)} D}{k + \gamma^i D n^{(e)} L m_1},$$

$$\varphi_{bn}^i = \frac{\varphi_n^{i(0)}}{C_{1,\infty} - C_{1,s}^i(T_\infty)}, \quad \varphi_{qn}^i = -\frac{nk + (n+1)Lm_1 n^{(e)} D \gamma^i}{(n+1)(k + \gamma^i D n^{(e)} L m_1)}$$

Using the approach developed by Elperin and Krasovtsov (1994), (1995) the temperature and concentration distributions in the neighbourhood of the i -th droplet can be obtained as follows:

$$\tilde{C} = C^{i(0)} + \sum_{n=0}^{\infty} \left(B_{v_1 \dots v_n}^i (1 + x_i^{-(2n+1)} \lambda_{bn}^i) + Q_{v_1 \dots v_n}^i x_i^{-(2n+1)} \lambda_{qn}^i \right) \overline{x_{v_1}^i \dots x_{v_n}^i} \quad (11)$$

$$\tilde{T} = T^{i(0)} + \sum_{n=0}^{\infty} \left(Q_{v_1 \dots v_n}^i (1 + x_i^{-(2n+1)} \varphi_{qn}^i) + B_{v_1 \dots v_n}^i x_i^{-(2n+1)} \varphi_{bn}^i \right) \overline{x_{v_1}^i \dots x_{v_n}^i} \quad (12)$$

where $C^{i(0)} = x_i^{-1} \lambda_n^{i(0)} \delta_{0n}$ and $T_e^{i(0)} = x_i^{-1} \varphi_n^{i(0)} \delta_{0n}$ are non perturbed fields of concentration and temperature generated by i -th droplet.

The unknown coefficients $B_{v_1 \dots v_n}^i$ and $Q_{v_1 \dots v_n}^i$ can be found from the following system of equations:

$$B_{v_1 \dots v_n}^i = B_{v_1 \dots v_n}^{i(0)} + \sum_{j=1}^N \sum_{k=0}^{\infty} \left(\lambda_{bk}^j B_{\mu_1 \dots \mu_k}^j + \lambda_{qk}^j Q_{\mu_1 \dots \mu_k}^j \right) \omega_{nk} \varepsilon_j^{k+1} \varepsilon_i^n \Omega_{v_1 \dots v_n \mu_1 \dots \mu_k} (L_{ij}) \quad (13)$$

$$Q_{v_1 \dots v_n}^i = Q_{v_1 \dots v_n}^{i(0)} + \sum_{j=1}^N \sum_{k=0}^{\infty} \left(\varphi_{bk}^j B_{\mu_1 \dots \mu_k}^j + \varphi_{qk}^j Q_{\mu_1 \dots \mu_k}^j \right) \omega_{nk} \varepsilon_j^{k+1} \varepsilon_i^n \Omega_{v_1 \dots v_n \mu_1 \dots \mu_k} (L_{ij}) \quad (14)$$

where $B_{v_1 \dots v_n}^{i(0)} = \sum_{j=1}^N \lambda_0^{j(0)} \omega_{k0} \varepsilon_j^k \varepsilon_i^k \Omega_{v_1 \dots v_n} (L_{ij})$ and

$$Q_{v_1 \dots v_n}^{i(0)} = \sum_{j=1}^N \varphi_0^{j(0)} \omega_{k0} \varepsilon_j^k \varepsilon_i^k \Omega_{v_1 \dots v_n} (L_{ij}).$$

The solution of the above system of coupled linear algebraic equations can be found by Jacobi-Zeidel iterations with successive underrelaxation and can be calculated with any accuracy of the n -th power of the small parameter ε . All the calculations in this study were performed with accuracy $O(\varepsilon^5)$.

As was suggested by Labowsky (1976) for evaporating clusters it is more convenient to represent the obtained results in terms of correction factor. In the notions of the present solution the heat and mass correction factors could be determined as follows:

$$\zeta_i = -\frac{1}{4\pi R_i \varphi_0^i} \int (\nabla \tilde{T} \mathbf{n}_r) \Big|_{S_i} R_i^2 \sin \vartheta_i d\vartheta_i d\varphi_i \quad (15)$$

$$\eta_i = -\frac{1}{4\pi R_i \lambda_0^i} \int (\nabla \tilde{C} \mathbf{n}_r) \Big|_{S_i} R_i^2 \sin \vartheta_i d\vartheta_i d\varphi_i \quad (16)$$

where $\varphi_0^i = \varphi_n^{i(0)} (n=0)$ and $\lambda_0^i = \lambda_n^{i(0)} (n=0)$.

Keeping only the first term in expansions (11), (12) we obtain:

$$\zeta_i = 1 + \frac{\varphi_{b0}^i}{\varphi_0^i} B_0^i + \frac{\varphi_{q0}^i}{\varphi_0^i} Q_0^i, \quad \eta_i = 1 + \frac{\lambda_{b0}^i}{\lambda_0^i} B_0^i + \frac{\lambda_{q0}^i}{\lambda_0^i} Q_0^i \quad (17)$$

Finally the rate of evaporation can be found from the following equation:

$$\frac{dM_d}{dt} = -m_1 \oint_{S_i} n D \nabla \tilde{C} dS \quad (18)$$

3. RESULTS AND DISCUSSION.

Interactive growth of droplets on hygroscopic nuclei is encountered in various environmental applications. In particular, small aerosol soluble particles acts as nuclei for droplet condensation in atmospheric clouds. In this case the mixture of volatile component and soluble nonvolatile component constitutes the non-ideal solution. In this connection the evaporation of a binary array comprising a pure droplet and droplet consisting of volatile and nonvolatile soluble nucleus was considered. The results of calculation of evaporation rate of a pure water droplet located in the neighbourhood of a droplet consisting of water and a hygroscopic nucleus of NaCl are presented in Fig. 1.

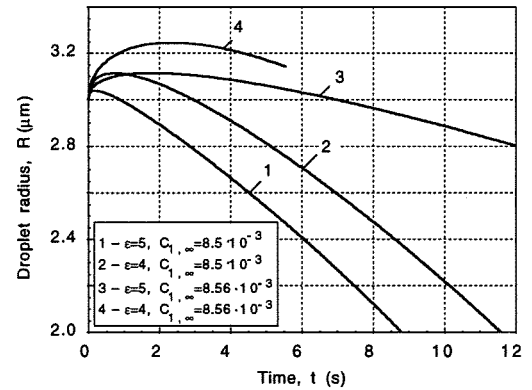


Fig. 1. Evaporation rate of pure water droplet located in the neighbourhood of droplet consisting of water and hygroscopic nucleus of NaCl.

The calculations were performed for droplets with the radius 3 μm and for the ambient temperature $T_\infty = 278$ K, pressure $p = 1$ atm, mass of soluble nucleus $M' = 10^{-10}$ g and various ambient concentrations of volatile species and center-to-center distances (in this plot ε is the L_{ij}/R ratio). As can be seen from this plot for the considered values of the center-to-center distances and ambient concentrations of volatile species the pure water droplet grows first and only then the droplet begins to evaporate. In this instance, the droplet containing soluble nucleus (droplet 1) acts as a heat source and a mass sink that causes an increase of vapor concentration in the

neighbourhood of the droplet. Thus the pure water droplet (droplet 2) located in the vicinity droplet 1 grows. When the radius of the pure water droplet increases, the concentration of the solution within the droplet containing soluble nucleus (droplet 1) increases. The latter retards the condensation rate at the pure droplet and decreases vapor concentration in the vicinity of the droplets. Thus inside the dense clusters and clouds containing pure droplets and droplets containing soluble nuclei heat and mass sources and sinks can occur. Therefore when dense cloud contains both, pure water droplets and droplets containing soluble nuclei, interaction between temperature and concentration fields causes the growth of some droplets in a cluster and evaporation of other droplets. In the case of a finite symmetrical arrays of compositionally dissimilar interacting droplets this phenomena was originally predicted by Labowsky (1980) who used the method of images. Later the theoretical model of recondensation in multicomponent droplet arrays was developed using the point sources method by Annamalai (1993).

The dependence of mass flux on the radius for the array of two identical droplets containing hygroscopic nuclei of NaCl is shown in Fig. 2.

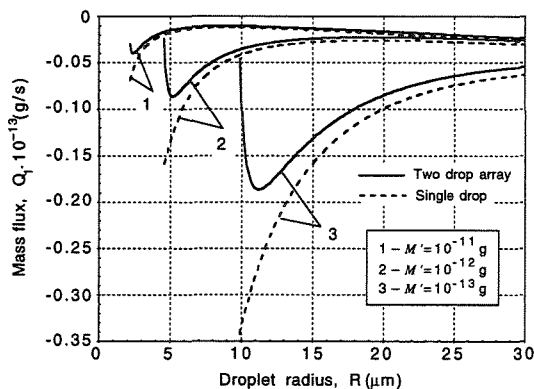


Fig. 2 Mass flux versus radius. Comparison the results obtained for a growing two monosized drop array and single drop contain hygroscopic nuclei NaCl (M' – the mass of hygroscopic nucleus).

In this plot the solid lines denote the interacting droplets and the dashed lines denote the single droplets. The calculations were performed for the ambient temperature $T_\infty = 278$ K, ambient pressure $p = 1$ atm, dimensionless concentration of volatile species $C_{1,\infty} = 0.009$ and various values of the nuclei' mass. As it can be seen from this plot the dependence of the mass flux on droplet radius has the minimum in a case of interactive evaporation of droplets. The negative values of mass flux mean that condensation of droplets containing soluble nuclei occurs. Thus, in the case of monosized cluster of droplets the radius of hygroscopic nuclei which enables the growth of the droplets in the cluster can be calculated. In clusters with droplet size distribution, the size distribution of hygroscopic nuclei which enables growth of droplets in a dense cluster can be determined using the developed theory.

Variation of the average correction factor $\bar{\eta}_p$ for the primary pure water droplet which is located in the center

of the cluster versus droplet volume fraction for cluster with log-normally distributed radii and uniformly distributed droplets in space is shown in Fig. 3.

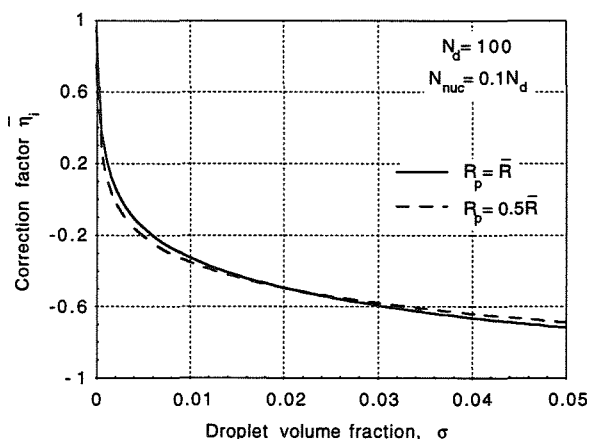


Fig. 3. Variation of the correction factor vs. droplet volume fraction.

Calculations were performed for the clusters containing $N_d = 100$ droplets 10% of which contain the soluble nuclei NaCl. It is assumed that the cluster immersed into the ambient air with humidity 65%. The solid line is plotted for the primary droplet with the radius which is equal to the average radius of droplets and the dashed line is plotted for the primary droplet with the radius that is equal to 0.5 of average radius. It was assumed that the radii of droplets ranges from 5 to 50 μm . Notably, when the primary droplet contains of hygroscopic nucleus the correction factor increases significantly, e.g., up to $\bar{\eta}_p \approx -14$ for $\sigma \approx 0.05$.

4. REFERENCES.

- Annamalai, K., and Ryan, W., 1992: Interactive processes in gasification and combustion. Part I: Liquid drop arrays and clouds. *Prog. Energy Combust. Sci.*, **18**, 221–295.
- , Ryan W., and Chandra, S., 1993: Evaporation of multi-component drop arrays. *J. Heat Transfer*, **115**, 707–716.
- Eperin, T., and Krasovitsov, B., 1994: Analysis of evaporation and combustion of random clusters of droplets by a modified method of expansion into irreducible multipoles. *Atomization and Sprays*, **4**(1), 79–97.
- , and Krasovitsov, B., 1995: Combustion of cylindrical and spherical random clusters of char/carbon particles. *Comb. Sci. Tech.*, **102**(1–6), 168.
- Heidenreich, S., and Ebert, F., 1995: Condensational droplet growth as a preconditioning technique for the separation of submicron particles from gases. *Chem. Eng. Process.*, **34**, 235–244.
- Labowsky, M., 1976: The effects of nearest neighbourhood interactions on the evaporation rate of clouds particles. *Chem. Eng. Sci.*, **31**, 803–813.
- , 1980: Transfer rate calculations for compositionally dissimilar interacting particles. *Chem. Eng. Sci.*, **35**, 1041–1048.
- Mason B. J., 1971: *The Physics of Clouds*, 2nd ed., Clarendon Press, Oxford.
- Seinfeld, J. H., 1986: *Atmospheric Chemistry and Physics of Air Pollution*, John Wiley & Sons Inc., New York.

LABORATORY MEASUREMENTS OF THE EFFECTS OF AIR PRESSURE ON THE COALESCENCE BETWEEN SMALL PRECIPITATION DROPS

Harry T. Ochs III, Kenneth V. Beard, and Song Liu

Illinois State Water Survey, Champaign, Illinois, USA
Department of Atmospheric Sciences, Urbana, Illinois, USA

1. INTRODUCTION

Laboratory studies have been conducted on collisions between precipitation size drops in free fall to obtain the collection efficiencies needed to calculate the rates for self collection, a process that controls the spreading of the raindrop size distribution and the intensification of the radar reflectivity.

2. EXPERIMENT

Figure 1 shows the experiment. The Plexiglass fall column and gravity feed reservoir are maintained at reduced pressure. Isolated drops fall at terminal velocity from the two computer controlled drop generators (one for each drop size) and collide in front of orthogonally positioned cameras. The computer also controls the camera shutters. Collisions occur at a rate of about 1 s^{-1} . Streak photographs are analyzed using a microscope to determine the horizontal offset of the drops just before collision which is then used to calculate the coalescence efficiency.

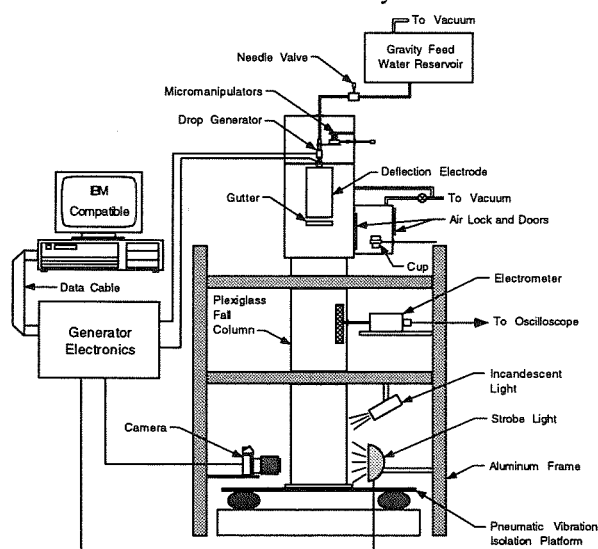


Figure 1. Experiment diagram.

3. RESULTS

New measurements have been obtained for the collision efficiencies for small precipitation drops between 425 and 200 μm radius at pressures of 1000,

700, and 500 mb. As an example, the coalescence efficiency for a drop pair of 425 and 300 μm radius, having negligible charge, increases from 14 to 38% as the air pressure was reduced from 1000 to 500 mb. This outcome appears to contradict the previous result of List and Fung (1982) who found that reduced air pressure had no effect on the collisional breakup of larger precipitation drops. Based on our recent scaling law for collision dynamics (Beard and Ochs 1995), we would predict a decrease in coalescence efficiency as pressure is reduced. When a new scaling factor is included for the effect of pressure on the film drainage time, the predicted coalescence efficiencies agrees with our data. The new results are consistent with our previous finding for the change in film drainage time for drops cooled by evaporation at low relative humidities (Ochs et al. 1995). The more general scaling law for collision dynamics and film drainage can be used to extend our results to a wider range of drop sizes and environmental conditions.

7. ACKNOWLEDGMENTS

This material is based on work supported by the National Science Foundation under grants ATM 9020959 and ATM 9421735. Any opinions, findings, and conclusions or recommendations expressed in this material are those of the authors and do not necessarily reflect the view of the National Science Foundation.

4 REFERENCES

- Beard, K. V., and H. T. Ochs, 1995: Collisions between small precipitation drops. Part II. *J. Atmos. Sci.*, **52**, 3977-3996.
- List, R., and C. Fung, 1982: The effect of pressure on the breakup of one pair of raindrops. *Atmos.-Ocean*, **20**, 17-27.
- Ochs, H. T., K. V. Beard, R. R. Czys, N. F. Laird, D. J. Holdridge, and D. E. Schaufelberger, 1995: Collisions between small precipitation drops. Part I. *J. Atmos. Sci.*, **52**, 2258-2275.

LABORATORY MEASUREMENTS OF OSCILLATION AMPLITUDE FOR MODERATE TO-LARGE RAINDROPS FALLING AT TERMINAL SPEED

Karen Andsager¹, Kenneth V. Beard^{1,2} and Neil F. Laird¹

¹ Cloud & Precipitation Research, Illinois State Water Survey, Champaign, IL 61820

² Department of Atmospheric Sciences, UIUC, Urbana, IL 61801

1. INTRODUCTION

The use of a differential radar reflectivity (Z_{DR}) was proposed by Seliga and Bringi (1976) to improve estimates of rainfall rate based on the assumption of a single, equilibrium axis ratio (α_0) at each drop size (Pruppacher and Beard 1970). Raindrops, however, oscillate because of drop collisions (Beard et al. 1983) and vortex shedding (Beard et al. 1989, Beard and Tokay 1991, Tokay and Beard 1996), thereby producing a dispersion in axis ratios at each raindrop size with a time average axis ratio ($\bar{\alpha}$) that is significantly larger than α_0 . For example, Kubesh and Beard (1993) found that the average axis ratio for moderate size water drops at terminal velocity of diameters $D = 2.0$ and 2.5 mm, had average axis ratios that would reduce a Z_{DR} for these sizes by 30%. Evidence for a decrease in Z_{DR} was found previously in the radar study of Goddard and Cherry (1984) by comparison of measurements of Z_{DR} with values calculated from raindrop size distributions measured below the radar pulse volumes.

In the present work, the natural oscillations of moderate-to-large raindrops were studied in a seven-story fall column with shape data obtained from multiple-strobe photographs. Measurements were made at a fall distance of $z = 27$ meters for drops of $D = 2.5$, 2.9 , 3.6 , and 4.0 mm. Additional measurements were made at intermediate distance to assess the oscillation decay and the steady state oscillation behavior.

2. RESULTS

Our axis ratio measurements showed that the initial oscillations from the drop generator died away by $z = 3$ m, but then increased again as the drops attained terminal speed near $z = 10$ m. The oscillation amplitude was essentially constant the lower portion of the fall column ($z = 10 - 27$ m) where the drops were at terminal speed. These steady state oscillations produced a distribution of axis ratios, scattering above and below the equilibrium axis ratio (α_0) for non-

oscillating drops. All four raindrop sizes had a peak in the distribution near α_0 , characteristic of the axisymmetric mode of the fundamental frequency, mode (2,0). The sizes at $D = 2.9$ and 4.0 mm, however, also had a peak above α_0 with a mean axis ratio above equilibrium, $\bar{\alpha} - \alpha_0 \approx 0.01 - 0.03$. This behavior is expected for the transverse modes of the lowest two frequencies, modes (2,1) and (3,1) (Beard and Kubesh 1991). The steady state oscillations for all sizes had a standard deviation in axis ratio of $\sigma_\alpha \approx 0.02 - 0.03$ and a range of $\Delta\alpha \approx 5\sigma_\alpha/2 = 0.05 - 0.08$.

3. DISCUSSION

In this experiment, because the original oscillation energy was dissipated by viscosity, the persistent oscillations from $z \approx 10 - 27$ m must have been forced by an intrinsic aerodynamic mechanism. The likely forcing is resonance with the transverse vortex shedding by the transverse modes (2,1) and (3,1), a conclusion consistent with recent laboratory findings for raindrops of 1 mm diameter and above (Beard et al. 1991). The presence of the axisymmetric mode (2,0) is not too surprising when considering that mode (2,0) needs only one-hundredth the oscillation energy to have the same axis ratio amplitude ($\Delta\alpha$) as mode (2,1) (Beard and Kubesh 1991).

In light-to-moderate rains, where the time between collisions is much longer than the oscillation decay time (see Beard et al. 1983), the ensemble mean axis ratio for these raindrop sizes ($D = 2.5 - 4.0$ mm) would be dominated by a shift of $\bar{\alpha} - \alpha_0 \approx 0.01 - 0.03$. The magnitude and direction of this axis ratio shift are consistent with findings from field studies (Chandrasekar et al. 1988, Goddard and Cherry 1984). In heavier rains the larger amplitude oscillations from the decaying collisional energy would dominate producing an axis ratio shift through mode (2,0) exceeding 0.03 (see Jones 1959, Jameson and Beard 1982, Beard and Johnson 1984).

4. APPLICATION

The changes in average axis ratio for raindrops discussed here amount to a reduction in Z_{DR} of 0.2 to 0.4 dB for raindrop size distributions having a reflectivity mean drop size of $\bar{D} = 2$ to 4 mm (see Jameson 1983). These corrections are consistent with the higher axis ratios obtained from field measurements (Goddard and Cherry 1984, Chandrasekar et al. 1988). Two approaches can be used to make the adjustment. The method of Goddard and Cherry, whereby the axis ratios are increased, has the advantage of a drop-size dependent correction factor. Alternatively, the apparent reflectivity mean drop size (\bar{D}) can be reduced by about 0.1 - 0.2 mm diameter for $\bar{D} = 1.0$ - 1.5 mm and by as much as 0.5 mm for $\bar{D} = 2$ - 4 mm.

5. REFERENCES

- Beard, K. V., and D. B. Johnson, 1984: Raindrop axial and backscatter ratios using a collisional probability model. *Geophys. Res. Lett.*, **11**, 65-68.
- Beard, K. V., D. B. Johnson, and A. R. Jameson, 1983: Collisional forcing of raindrop oscillations. *J. Atmos. Sci.*, **40**, 455-462.
- Beard, K. V., H. T. Ochs, and R. J. Kubesh, 1989: Natural oscillations of small raindrops. *Nature*, **342**, 408-410.
- Beard, K. V., R. J. Kubesh and H. T. Ochs, 1991: Laboratory measurements of small raindrop distortion. Part 1: Axis ratios and fall behavior. *J. Atmos. Sci.*, **48**, 698-710.
- Beard, K. V., and R. J. Kubesh, 1991: Laboratory measurements of small raindrop distortion. Part 2: Oscillation frequencies and modes. *J. Atmos. Sci.*, **48**, 2245-2264.
- Beard, K. V., and A. Tokay, 1991: A Field Study of Raindrop Oscillations: Observations Of Size Spectra And Evaluation Of Oscillation Causes *Geophys. Res. Lett.*, **18**, 2257-2260.
- Chandrasekar, V., W. A. Cooper and V. N. Bringi, 1988: Axis ratios and oscillations of raindrops. *J. Atmos. Sci.*, **45**, 1323-1333.
- Goddard, J. W. F., and S. M. Cherry, 1984: The ability of dual-polarization radar (copolar linear) to predict rainfall and microwave attenuation. *Radio Sci.*, **19**, 201-208.
- Jameson, A. R., 1983: Microphysical interpretation of multi-parameter radar measurements in rain. Part I: Interpretation of polarization measurements and estimation of raindrop shapes. *J. Atmos. Sci.*, **40**, 1792 - 1802.
- Jameson, A. R., and K. V. Beard, 1982: Raindrop axial ratios. *J. Appl. Meteor.*, **21**, 257-259.
- Jones, D. M. A., 1959: The shape of raindrops. *J. Meteor.*, **16**, 504-510.
- Kubesh, R. J., and K. V. Beard, 1993: Laboratory measurements of spontaneous oscillations for moderate-size raindrops. *J. Atmos. Sci.*, **50**, 1089-1098.
- Pruppacher, H. R., and K. V. Beard, 1970: A wind tunnel investigation of the internal circulation and shape of water drops falling at terminal velocity in air. *Quart. J. Roy. Meteor. Soc.*, **96**, 247-256.
- Seliga, T. A., and V. N. Bringi, 1976: Potential use of radar differential reflectivity measurements at orthogonal polarizations for measuring precipitation. *J. Appl. Meteor.*, **15**, 69-76.
- Tokay, A. and K. V. Beard, 1996: A Field Study of Raindrop Oscillations. Part 1: Observations of size spectra and evaluation of oscillation causes. *J. Appl. Meteor.* **5** (in press).

6. ACKNOWLEDGMENTS

This material is based on work supported by the National Science Foundation under grants ATM 87-22688 and ATM 91-21698. Any opinions, findings, and conclusions or recommendations expressed in this material are those of the authors and do not necessarily reflect the view of the National Science Foundation.

OBSERVATIONS OF INITIAL STAGE OF ICE DEVELOPMENT IN SUPERCOOLED CLOUDS

Anatoly N. Nevzorov

Central Aerological Observatory
Dolgoprudny 141700, Russia

1. INTRODUCTION

It is generally agreed that a dominant mechanism of ice initiation in supercooled clouds is the freezing of droplets, followed by rapid growth of so formed ice particles under high vapor supersaturation relative to ice. To explain super-high cloud crystal concentrations as compared with the known freezing nuclei at moderate supercoolings, proposals were offered for ice enhancement mechanisms such as effects of drop - crystal collision, crystal fragmentation, contact nucleation etc. (e. g. Mosson, 1985; Hobbs and Rangno, 1985). However, none of above concepts has in fact objective proofs, and none works well in view of essential independence of cloud crystal concentration of temperature (Hobbs and Rangno, 1985).

There appears to exist more realistic explanation for such "anomalies" in cloud crystal concentration, which has nothing to do with the freezing nuclei. Rosinski (1991) and Rosinski and Morgan (1991) have recently experimentally found that homogeneous remainders or condensation nuclei, just released from evaporated supercooled droplets, can take on new properties of nuclei of ice deposition. Since no ice was nucleated on these before, it becomes clear that the water condensation-evaporation process can result in reactivation of some part of condensation nuclei with transforming them into secondary ice-forming nuclei (SIFN). If so, this nucleus reactivation process can far dominate over drop freezing pro-

cess to produce ice particles in explainable concentrations.

What additionally stays in need for explanation, is many-hours existence of supercooled stratiform clouds without observable signs of ice, in spite of well known permanent presence of freezing nuclei in atmospheric air as well as of potential SIFN within these clouds. Hobbs and Rangno (1985) reasoned, on the ground of their measurements, that there is a period for growing of cloud droplets until their sizes allow for the most probable freezing with mechanisms discussed in their paper. Unfortunately, the FSSP data carried no information on the phase state of particles of size spectra preceding the occurrence of directly detectable large crystals, that does not exclude their alternative interpretation in support of above presumptions as well.

Using unique airborne instrumentation for measuring various cloud microphysical parameters, we have recently obtained more comprehensive results which reinforce and further develop the suggested conception. The techniques and principal results of the study have been described in detail before (Nevzorov and Shugaev, 1992a). In this paper we outline and discuss the most characteristic peculiarities of the results.

2. INSTRUMENTATION

The measurements were made aboard the CAO IL-18 research aircraft, with the instrumentation briefly described

earlier by Nevzorov and Shugaev (1992a, 1992b) and here by Nevzorov (1996). A central place in this study was held by the measurements of liquid and total (liquid plus ice) water content (LWC and TWC, respectively) described by Korolev et al. (1996). Parallel measurements of the cloud extinction enabled to estimate effective or volume-modal droplet sizes as well as to correct the LWC measurements for the drop collection efficiency (Nevzorov and Shugaev, 1992a).

The photoelectric particle phase/size analyser (PPSA) has been used in this study for detection of ice crystals larger than $20\text{ }\mu\text{m}$ in equivalent cross-sectional diameter, and the large particle meter (LPM) for any particles of more than $200\text{ }\mu\text{m}$ in mean linear size.

3. APPROACH

Let W_L and W_T denote instrumental readings of LWC and TWC meters, respectively. In the general case,

$$\begin{aligned} W_L &= C_L \cdot LWC, \\ W_T &= C_T \cdot LWC + k \cdot IWC, \end{aligned}$$

where IWC is the ice water content, C_L and C_T are the drop collection efficiencies of the respective probes, k is a factor for IWC responsivity of the TWC probe. For typical clouds, the C_L value is close to 1. The value of $C_T < C_L$ was determined via the ratio $R_0 = W_T/W_L$ obtained at $IWC=0$ in warm non-precipitating clouds. The measurements of R_0 were well described as a function of the ratio W_L/E where E is the extinction coefficient (Nevzorov and Shugaev, 1992a).

In obviously mixed clouds, the experimental points $R = W_T/W_L$ fell above the derived curve, i. e. we had $R > R_0$ and most commonly $R > 1$, that would follow from $k > 0$ and $IWC > 0$.

Unexpectedly related result was obtained for most (>70%) space of supercooled stratiform clouds where no ice crystals of $>20\text{ }\mu\text{m}$ in size were

detected at all. In this case, the inequality $R > R_0$ or often $R > 1$ readily implies that $TWC > LWC$; that is, rather fine-dispersed ice phase is already present in such clouds. This statement is supported by the fact that zones with directly detected ice crystals often not exceeding $50\text{ }\mu\text{m}$ were in places embedded within or adjacent to such so-called "latent-mixed" zones.

Real sensitivity of the described technique suggests reliable detection of the cloud fine-dispersed ice only if its content is not less than 0.1 - 0.15 of TWC. This gives no assurance that lesser contents of ice are not present in supercooled clouds or zones where all above criteria do not work.

4. OBSERVATIONAL EVIDENCE

The data to be summarized have been collected at spring periods of 1988 (Bulgaria) and 1989 (Uzbekistan) in total penetration of about 1000 km of supercooled water clouds of various layer types. The effective cloud droplet diameters ranged typically between $3\text{ }\mu\text{m}$ and $15\text{ }\mu\text{m}$, with the largest droplets not exceeding $80\text{ }\mu\text{m}$ in limiting cases. The low-level liquid clouds occurred only at $T > -10^\circ\text{C}$. Among the middle-level clouds (between 2 km and 7 km), the events of absence of ice crystals $>20\text{ }\mu\text{m}$ were followed down to about -20°C . At lower temperatures, all investigated clouds exhibited ice crystals $>20\text{ }\mu\text{m}$ in direct PPSA readings (Nevzorov and Shugaev, 1992b), although in some rare instances their sizes scarcely achieved $50\text{ }\mu\text{m}$.

In that clouds where no crystals $>20\text{ }\mu\text{m}$ were detected, the "latent-mixed" structure revealed itself with the criterion $R > R_0$ as frequently as in 73% of total cloud extent without distinct dependence on cloud level and temperature. As follows from the foregoing, the "latent-mixed" cloud structure as defined constitutes most likely markedly more than 75 percent

of the total space of conventionally supercooled liquid clouds. In turn, these latter amount to nearly 30% of all stratiform clouds at 0°C to -20°C range, suggesting long enough durability of "latent-mixed" state relative to total cloud lifetime.

The horizontal extents of both pronounced "latent-mixed" and "none-ice-detected" zones of stratiform clouds (including proper cloud dimensions) varied over wide ranges from less than 1 km to 60 km for the former and to 35 km for the latter. Average extents were 11.5 km (over 66 selected zones) and 9.6 km (over 29 zones), respectively. Nearly 70% of all zones did not exceed 10 km. The peak of occurrence fell at 5 to 10 km reaching 41% for the "liquid-apparent" zones, and at 1 to 5 km (39%) for the "latent-mixed" zones.

In the "latent-mixed" clouds, estimated values of IWC ran from 10% to 30% of TWC. Obviously undervalued assessment of the concentrations of ice particles, assuming them compact and sized close to 20 μm , came to units and tens per cubic centimetre. It is significant that, as a rule, positive spatial correlation took place between IWC and LWC, except in scarce cases of pronounced negative correlation (Nevzorov and Shugaev, 1992a).

5. DISCUSSION

The reported results throw light, above all, on the phenomenon of anomalous viability of purely water clouds at negative temperatures. It turns out that ice phase already exists in these clouds, quite possible during their total lifetime, in the form of ice particles comparable in both sizes and concentrations with the bulk of cloud droplets. It follows from this evidence that such particles grow in many orders slower than considered before. The obvious reason for that is the molecular-diffusion mode of ice deposition while a particle remains small enough to be essentially immobile with respect to

even moving air. This statement needs still theoretical examination. In any case, an evidence is available that abruptly faster growth of crystals begins from their sizes of order of 20 - 50 μm .

All available facts including extremely low fall velocity of smallest crystals show that ice forming process goes on throughout a cloud, i. e. has local nature. It has been proposed in Section 1 that responsible for the initial formation of the bulk of cloud ice crystals is the droplet condensation-evaporation process as producing secondary IFN. However, typical positive spatial correlation of IWC with LWC cannot be reconciled with the droplet evaporation concept. On the contrary, this points that the ice initiation occurs preferably in developing parts of a cloud where collective droplet evaporation seems highly improbable.

We postulate, then, that the dominant contributors of SIFN are not common cloud condensation nuclei but nonhygroscopic nuclei, capable of adsorption of water only under high supersaturations occurring in just originating cloud portions, and then releasing from water as supersaturation falls with droplet growing. That is, the main ice-forming mechanism would be water adsorption on and then evaporation from such nuclei. This does not exclude that collective droplet evaporation can happen, for instance, in descending air movements. Moreover, we consider that this is just the case when negative IWC-LWC correlation was observed.

6. CONCLUSIONS

The experimental evidence summarized and discussed in this paper offers a clue to adequate understanding of micro- and macroprocesses responsible for ice generation and initial growth in supercooled clouds. The revealed "latent-mixed" state of conventionally supercooled water clouds, with super-high concentrations of fi-

ne-dispersed ice particles as opposed to the freezing nuclei, obviates the necessity for the existing hypotheses for droplet freezing as well as ice enhancement in cloud phase evolution. Instead, that supports the postulated concept of ice initiation by deposition on latent, or secondary-formed nuclei produced by the water condensation-evaporation process. The most possible source of these nuclei is bound to be mainly nonhygroscopic particles. The extremely slow initial growth of the originated ice particles as well as their considerable reduction in concentration in subsequent obviously mixed clouds have yet to be explained.

REFERENCES

- Hobbs, P.V., and A.L. Rangno, 1985: Ice particle concentration in clouds. *J. Atm. Sci.*, **42**, 2523-2549
- Korolev, A.V., J. W. Strapp, and A. N. Nevzorov, 1996: On the accuracy of Nevzorov airborne hot wire LWC/TWC probe. *Rep. pres. at this Conf.*
- Mossop, S. C., 1985: The origin and concentration of ice crystals in clouds. *Bul. of Am. Met. Soc.*, **66**, 264-273
- Nevzorov, A. N., 1996: CAO aircraft instrumentation for cloud physics. *Rep. pres. at this Conf.*
- , and V. F. Shugaev, 1992a: Observation of the initial stage of ice phase evolution in supercooled clouds. *Soviet Met. and Hydr.*, No 1, 69-76
- , ----, 1992b: Experimental studies of the phase-disperse structure of stratiform clouds at negative temperatures. *Soviet Met. and Hydr.*, No 8, 41-51
- Rosinski, J., 1991: Latent ice-forming nuclei in the Pacific Northwest. *Atm. Res.*, **26**, 509-523
- , and G. Morgan, 1991: Cloud condensation nuclei as a source of ice-formation nuclei in clouds. *J. Aerosol Sci.*, **22**, 123-133

CLOUD MICROPHYSICS MEASUREMENTS IN COLD AIR OUTBREAKS

R. Timm¹, S. Bakan¹, and V. Khvorostyanov²

¹ Max-Planck-Institut für Meteorologie, Bundesstraße 55, D-20146 Hamburg, Germany

² Central Aerological Observatory, Moscow, Russia

1. INTRODUCTION

Cold air outbreaks from the ice over the ocean are frequent during winter time. They contribute significantly to the heat exchange between ocean and atmosphere, yielding occasionally very high fluxes of sensible and latent heat. Intense vertical mixing is organized in parallel boundary layer rolls, which eventually become visible as clouds streets. These transform into cellular convection several hundred kilometres downstream. Our aim is to document in field campaigns and to understand with numerical models the observed phenomena and their implication on atmospheric development. This paper concentrates on aspects of cloud microphysics, which are of importance for the humidity balance and radiative properties.

During March 1993 the field campaign ARKTIS'93 was conducted near the ice edge west of the Spitsbergen island to study these cold air outbreaks (Brümmer 1993). Two research airplanes operated in different heights and different distances from the ice edge to document the fields of mean and turbulent meteorological quantities, e.g., wind speed and direction, temperature, moisture, etc., and of cloud microphysical properties. Their measurements were supported by three research vessels, one of which – the POLARSTERN – took a position within the sea ice area in order to document the conditions of the air mass on the ice side.

Cold air outbreaks occurred several times during the campaign, starting with near surface temperatures of down to -40°C over the ice. Near the ice edge fog was observed. Downstream, the boundary layer grew rapidly in depth and the cloud base lifted up to a few hun-

dred meters, leaving a mesoscale organized stratocumulus deck below the capping inversion.

2. MICROPHYSICAL MEASUREMENTS

Two aircraft (DO-128, TU Braunschweig, and FALCON, DLR) were used to conduct in situ measurements of mean and turbulent quantities as well as of cloud microphysics. Each of them was equipped with two PMS particle probes for different size ranges, a Forward Scattering Spectrometer Probe FSSP 100 (range $2 - 47\ \mu\text{m}$) and an Optical Array 2D-C Probe (range $25 - 800\ \mu\text{m}$) or 2D-Greyprobe (range $10 - 640\ \mu\text{m}$), respectively. The two airplanes flew horizontal legs and vertical profiles at different positions to cover the whole cloud evolution from the ice edge up to about 250 km over open water.

2.1 Results

The analysis of the microphysical measurements at distances of about 250 km south of the ice edge shows that

- the maximum number density in clouds is always about $120\ \text{cm}^{-3}$.
- the mean particle diameter in clouds is $5\ \mu\text{m}$ at cloud base and increases with height to about $10\ \mu\text{m}$.
- the water content is very low. Cloud particles with diameters between 2 and $47\ \mu\text{m}$ contribute less than $0.05\ \text{gm}^{-3}$, those in the size range 10 to $620\ \mu\text{m}$ in some cases more.
- the increase with height of the LWC is considerably less than expected for an adiabatic

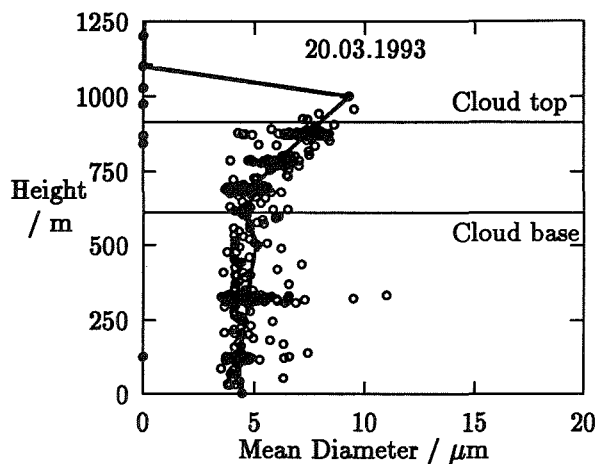


Fig. 1: Profile of the measured mean particle diameter, March 20. The thick line marks the average over the whole measurement, the dots indicate individual 10 seconds averages.

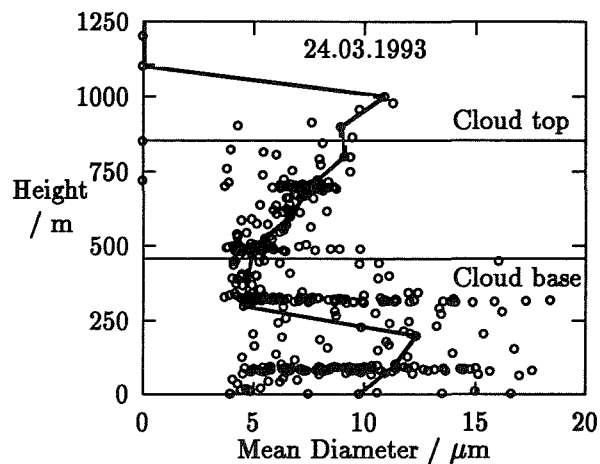


Fig. 4: Profile of the measured mean particle diameter as in fig. (1), but for March 24. Large ice particles beneath cloud shift the average to higher values of up to 15 μm .

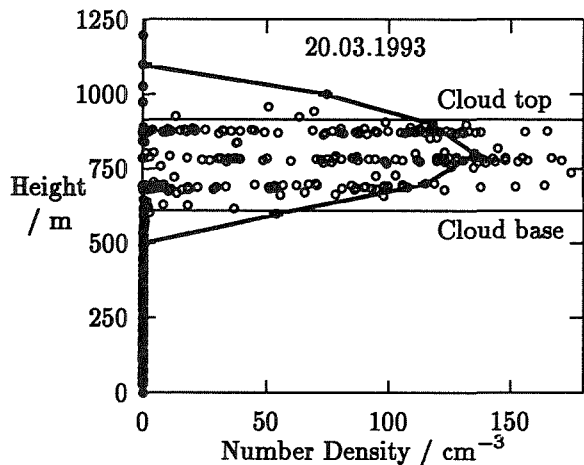


Fig. 2: Profile of the measured particle number density. The average (thick line) was calculated considering the cloud elements only.

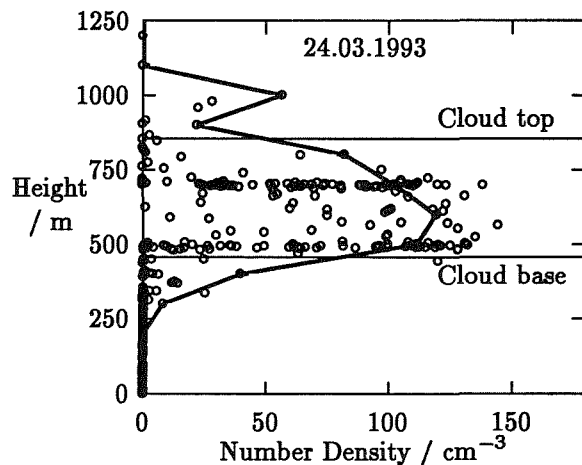


Fig. 5: Profile of the measured particle number density as in fig. (2), but for March 24.

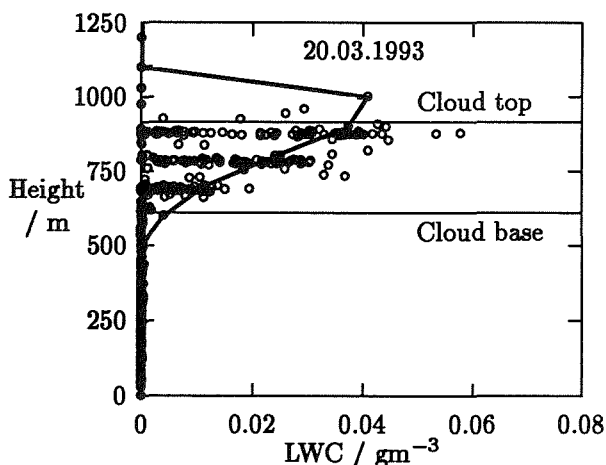


Fig. 3: Profile of the measured water content. No difference is made here between liquid and ice water.

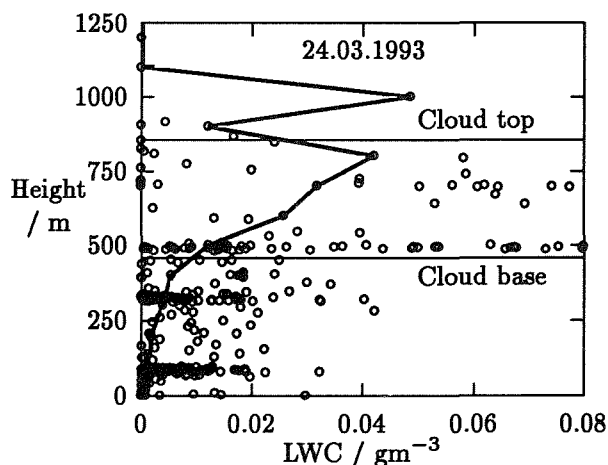


Fig. 6: Profile of the water content measured with the FSSP as in fig. (3), but for March 24.

ascent. Entrainment of dry air from above the inversion may be an important factor for this behavior.

- despite of the very low LWC in some cases there are drizzle-like particles beneath cloud. The mean diameter of these particles is generally much higher than that of the cloud particles. Greyprobe images show that these bigger particles are mostly frozen.

This is shown for two days in figures (1) to (6).

3. NUMERICAL MODELING

A set of 2D/3D cloud-resolving models with explicit microphysics has been developed at the Central Aerological Observatory (CAO), Moscow, for the simulation of various types of clouds (Khvorostyanov 1994). For the simulation of cloud streets a 2D version of the model was selected and further improved. The model domain represents a plane perpendicular to and moving with the wind, in order to study the time development during the formation of the streets. The model accounts for non-hydrostatic dynamics, applying the equations for the vorticity and for the stream function. Cloud microphysics is considered explicitly by solving the kinetic equations for the droplet and crystal size distribution functions for 30 radius intervals for both droplets and crystals between $1\text{ }\mu\text{m}$ and $3.5\text{ }\mu\text{m}$. An additional integro-differential equation for the supersaturation with respect to water and ice is used. Radiative transfer calculations are performed, accounting for cloud particle radius and phase state. Heat and moisture exchange with the underlying surface is considered.

3.1 Results

- near the ice edge advective fog develops due to strong evaporation from the sea surface and advective cooling. Not much horizontal structure is exhibited. The layer is capped by a strong temperature inversion in 200 - 400m height. Mean droplet radius is calculated to 4 - 6 μm . The corresponding albedo reaches 60 - 70 % due to the small droplet size.

- further downwind a convective boundary layer forms, which consist of narrow bands of saturated updrafts (2 - 3 km diameter) with vertical velocities of $0.3 - 1.5\text{ ms}^{-1}$, separated by considerably wider downdraft regions.
- condensation is found in the updrafts with mostly small droplets and LWC below $0.05 - 0.1\text{ gm}^{-3}$. A small droplet fraction becomes big enough to precipitate out, creating a very thin drizzle.
- some droplets freeze to crystals, which grow very fast. The large crystals precipitate and can survive even outside the cloud streets, because supersaturation with respect to ice is calculated to be positive in a much larger domain than with respect to water.

4. MODEL MEASUREMENT INTERCOMPARISON

Arctic cold air outbreaks during wintertime were studied in a field campaign and in a numerical model. Measurements at a distance of 250 km off ice edge and model runs are in a good agreement. The model reproduces the observed cloud structure reasonably well. Differences occur in the details of the particle size distributions.

The intercomparison between model runs and measurements still has to be intensified. Also we want to include measurements made closer to the ice edge to study the cloud evolution.

6. REFERENCES

- B. Brümmer (editor), 1993: ARKTIS 1993. Report on the Field Phase with Examples of Measurements *Berichte aus dem Zentrum für Meeres- und Klimaforschung, Hamburg, Reihe A, Nr. 11.*
- V. I. Khvorostyanov, 1995: Mesoscale processes of cloud formation, cloud radiation interaction, and their modelling with explicit cloud microphysics. *Berichte aus dem Zentrum für Meeres- und Klimaforschung, Hamburg, Reihe A, Nr. 14.*

A COMPARISON OF MID-LATITUDE AND TROPICAL CIRRUS MICROPHYSICAL PROPERTIES AND A CONCEPTUAL MODEL OF CIRRUS CLOUD STRUCTURE

Andrew J. Heymsfield, Larry M. Miloshevich, Greg M. McFarquhar, and Janine Goldstein
National Center for Atmospheric Research,*
Boulder, Colorado

Sam Oltmans
NOAA Climate Modeling and Diagnostic Laboratory
Boulder, Colorado

1. INTRODUCTION

Cirrus clouds cover more than 20% of the Earth's land area and 10% of the Oceanic areas, and have a major influence on the Earth's climate through their effects on incoming solar and outgoing longwave radiation. In recent years, the mathematical treatment of cirrus in climate models has become more sophisticated, using prognostic equations which advect water vapor and condensate between grid cells. Advances are limited, however, because there is a lack of critical information on the clouds themselves, including knowledge of the ambient relative humidity conditions required to initiate cirrus crystals (and hence cirrus clouds), which affects cirrus cloud coverage and knowledge of cirrus ice crystal sizes and shapes, influencing their radiative properties. Other researchers also require more information on cirrus properties: meteorologists and engineers studying the direct effects of aircraft-generated contrails on cloudiness and aircraft detectability; mesoscale modelers needing an accurate representation of the upper-tropospheric latent heat release in mesoscale and climate scale numerical models; and hydrologists using models to account for the various terms in water budgets.

The goal of this study is to obtain a better description of cirrus microphysical properties as a function of latitude, using data from mid-latitude, tropical, and Arctic field programs. Based on the mid-latitude measurements, a conceptual model is developed which describes the initiation and evolution of non-anvil cirrus.

2. COMPARISON OF MICROPHYSICAL PROPERTIES

Microphysical data were acquired with research aircraft in cirrus anvils during CCOPE (1981) in Montana USA; in synoptically generated cirrus during FIRE I and II (1986, 1991) in Wisconsin and Kansas, USA; in convectively-generated tropical cirrus at Kwajalein, Marshall Islands (1974-1975), during TOGA COARE and CEPEX (1993); and in the Arctic during BASE (Beaufort and Arctic

Seas Experiment) (see Heymsfield 1993; Heymsfield and Miloshevich 1995; Heymsfield and McFarquhar 1996; BASE data kindly furnished by Dr. Judith Curry). Size distributions for particle sizes above approximately $> 50 \mu\text{m}$ were measured with PMS 2D-C and 2D-P probes. The distributions between 5 and $100 \mu\text{m}$ dimension during FIRE II and CEPEX were measured with an impactor-type Video Ice Particle Sampler (VIPS). Ice water content (IWC) was derived from the size spectra, cross-sectional area per unit volume A was measured from the 2D and VIPS images, and effective radius r_e (see later discussion) was derived from IWC and A .

IWC from the various experiments are plotted according to temperature in Fig. 1. Three points are noteworthy:

- IWC increases by approximately two orders of magnitude over the 70°C temperature range considered. Data points which are markedly different than those in the same temperature interval include the high values for CEPEX in the -60 to -70°C interval within vigorous convection, the high and nearly temperature-independent values for the vigorous convective cells associated with CCOPE, the decreasing values of IWC above -20°C from FIRE I and II

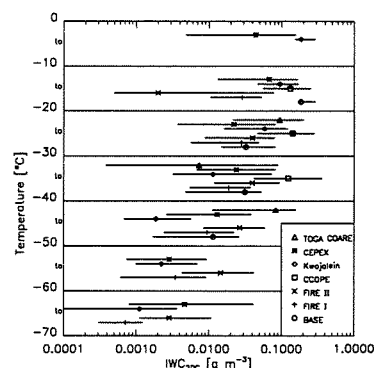


Figure 1. IWC averaged in 10°C temperature intervals from FIRE I and II, CCOPE, Kwajalein, TOGA COARE, CEPEX, and BASE. The end-points of the horizontal bars represent the lowest and highest 25% of the data points in each temperature interval and the symbols represent the median values.

* The National Center for Atmospheric Research is sponsored by the National Science Foundation.

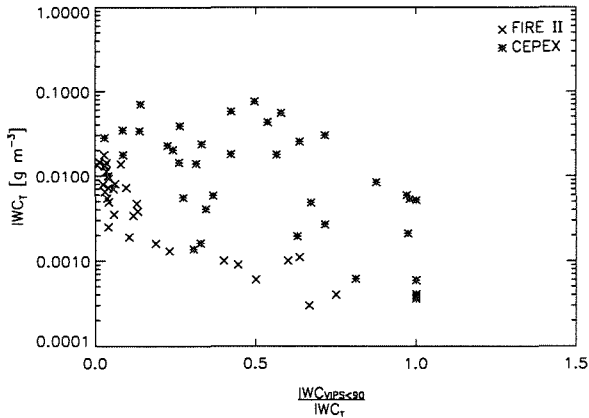


Figure 2. Total IWC as a function of the fraction of the total IWC contained in particles $90 \mu\text{m}$ and below (see text), from CEPEX and FIRE II.

associated with ice-subsaturation regions, and the large values of IWC noted in the Arctic data at warm temperatures.

- The highest IWC are found in the mid-latitude anvils.
- The length of the horizontal bars in Fig. 1 illustrate that there is a great deal of natural variability among clouds.

The fraction of the IWC in small particle sizes can be examined as a function of the “total” IWC, using sizes $< 90 \mu\text{m}$ from the VIPS, IWC_{VIPS} , and sizes $> 90 \mu\text{m}$ from the 2DC, $\text{IWC}_{2\text{DC}}$: $\text{IWC}_T = \text{IWC}_{\text{VIPS}} + \text{IWC}_{2\text{DC}}$. The fraction of IWC in sub- $90 \mu\text{m}$ (“small”) ice particles from CEPEX and FIRE II is in general inversely proportional to IWC_T (Fig. 2). Figure 2 shows that the small particles contribute fractionally the most when the IWC is below 10^{-2} g m^{-3} . Considerably greater variability is also noted in the CEPEX data, a difference which can be attributed to the cloud formation mechanisms—cirrus elements in varying stages of decay produced by convection were sampled during CEPEX, versus developing cirrus produced by large scale ascent sampled during FIRE II. Note that while the cirrus from CEPEX were generated as a result of convection, the measurements in Fig. 2 are acquired in regions removed from convection, primarily in extended and detached anvils. It is therefore stressed that the CEPEX small particle data apply primarily to non-convective regions; small ice crystals are likely to make a much greater contribution to the IWC in regions within and adjacent to convection.

Effective radius (r_e , the third moment of the particle size spectrum of equivalent area spheres divided by the second moment) is a parameter used in representing particle size for radiative transfer calculations. A plot of IWC vs A is useful for climate modeling studies and provides information on how r_e varies with IWC. Francis et al. (1994) show that $A \approx \frac{1.1\text{IWC}}{r_e}$ while from Ebert and Curry (1992) it can be shown that $A \approx \frac{1.22\text{IWC}}{r_e}$.

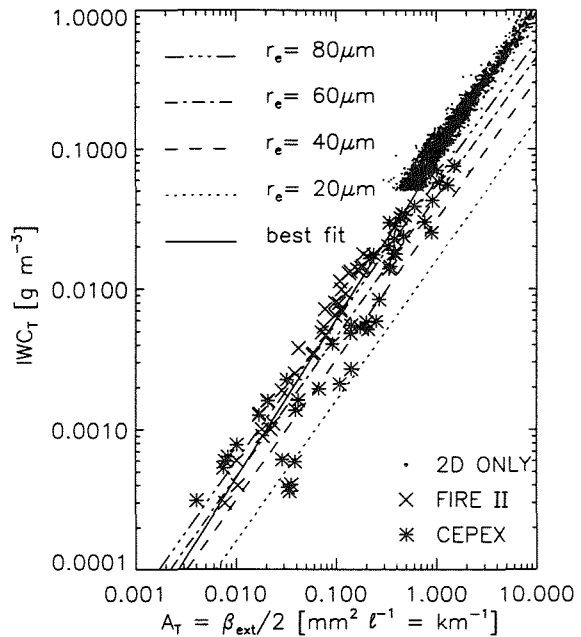


Figure 3. IWC versus A for particle sizes $> 5 \mu\text{m}$ from CEPEX and FIRE II cases when VIPS data has been processed, and from the 2D data whenever $\text{IWC} > 0.05 \text{ g m}^{-3}$. A least squares curve fit through data, $A = 12.15\text{IWC}^{0.883}$, is the solid line. Lines of constant r_e are based on Ebert and Curry (1992), are shown for reference.

A linear relationship between A and IWC indicates that r_e is nearly constant while a power-law relationship indicates that r_e either increases or decreases with increasing A and IWC. Figure 3 shows that IWC_T and A from CEPEX and FIRE II data are well-correlated and that r_e generally increases with increasing IWC. Note that the data points in Fig. 3 above 0.05 g m^{-3} are derived from the CEPEX 2D data alone, to augment the small particle data set. The data below 0.05 g m^{-3} suggests that small particles are likely to contribute minimally above 0.05 g m^{-3} .

3. CONCEPTUAL MODEL OF NON-CONVECTIVELY PRODUCED CIRRUS

A three-layer conceptual model of the structure of “non-convectively” generated cirrus is developed in this section based on the FIRE data sets. In addition, data are used from aircraft in orographic wave clouds and balloon-borne cloud particle replicators (Miloshevich and Heymsfield 1996) in cirrus are used, acquired near Boulder, Colorado, USA in 1990 and 1994. The conceptual model applies to cirrus which form by synoptic-scale uplift, shallow convection, or wave-induced motions in the upper troposphere, and not to cirrus anvils which form by outflow associated with convection rooted in the boundary layer. This restriction does not exclude an important subset of tropical cirrus clouds which *can* form by large-scale uplift, and is presumably applicable to Arctic cirrus as well.

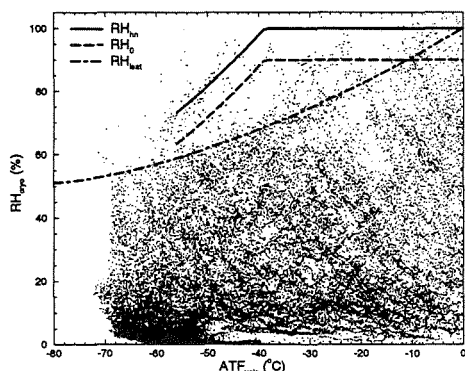


Figure 4. Relative humidity versus temperature as measured by balloon-borne cryogenic hygrometers launched in the vicinity of Boulder, Colorado. Eqs. (1) and (2) and ice saturation curves are shown for reference.

a. Conditions Required for Ice Crystal Formation

The dynamically and microphysically simpler, quasi-steady state orographic wave clouds sampled by Heymsfield and Miloshevich (1995, hereafter HM) provide relatively ideal conditions for measuring the ambient conditions when haze and water droplets freeze. As the aircraft penetrated the clouds at constant altitude along the wind direction, the measurements at temperatures between -30 and -60°C showed a rapid transition from solution droplets to ice crystals characteristic of homogeneous ice nucleation. Relative humidity RH was measured by a cryogenic hygrometer with an estimated accuracy of 4%. The RH at which the supply of water vapor due to lifting in the air parcel is offset by the rate of removal of water vapor due to droplet and ice crystal growth RH_{hn} , a transient state observed during rapidly increasing numbers of ice crystals associated with homogeneous ice nucleation, decreases monotonically from water-saturation at -39°C to about 70% at -56°C . The following curve was fit to the data by HM:

$$\text{RH}_{hn}(\%) = 188.92 + 2.81T + 0.013336T^2, \quad (1)$$

where temperature T is in $^{\circ}\text{C}$.

Aircraft observations of ice-supersaturated regions in clear-air using the cryogenic hygrometer during FIRE II set a *lower* bound on the RH required for ice initiation in cirrus, given by

$$\text{RH}_0(\%) \cong \text{RH}_{hn} - 10. \quad (2)$$

Additional RH measurements were acquired from launches of balloon-borne cryogenic hygrometers (Oltmans and Hofmann 1995) near Boulder, Colorado, from 1991 to the present (Fig. 4). The data set was biased toward cloud-free conditions as launches into cloud were intentionally avoided when possible; however, cirrus were emphasized in three of the recent launches. The upper boundary of the RH-T data points shows a trend similar to Eqs. (1) and (2), with a few data points exceeding the RH_{hn}

curve; specifics of these situations are under examination.

b. Layer 1: Ice Crystal Initiation Zone

Data from our balloon-borne ice crystal replicators provided information on ice crystal size distributions and shapes for sizes $15\text{ }\mu\text{m}$ as a function of height within six cirrus during FIRE II and three cirrus sampled near Boulder, Colorado. Rawinsondes on the balloons gave coincident temperature and RH information; the Vaisala sondes appeared to give systematically and unrealistically low RH measurements, limiting the reliable RH information to those launches with the cryogenic hygrometers.

Six of the replicator launches showed predominantly small ice crystals located near cloud top, with concentrations order of $10^2\text{ }\ell^{-1}$. In these 100–150 m deep regions, most ice crystals were $\leq 100\text{ }\mu\text{m}$ diameter (HM). The recent Boulder launches showed RH comparable to those required to nucleate ice crystals given by (2), and numerous small ice crystals were found at cloud top (Fig. 5).

The top layer in cirrus, *Layer 1*, is the generation region, where the RH is sufficiently high to allow nucleation of new ice crystals (see Fig. 6). Presumably, vertical motions are strong enough to generate a sufficiently high RH, otherwise nucleation will not occur; strong radiative cooling might also lead to sufficiently high RH. The balance between vapor depletion by the size distribution of ice particles and a sufficient vapor supply for the nucleation of additional crystals may be very delicate and transient.

c. Layer 2: Growth Zone

The measurements imply that a minimum vertical displacement above the level of ice saturation, ΔZ , is needed for ice nucleation to commence; as cirrus crystals fall through this layer of ice supersaturation they deplete the water vapor excess above ice saturation and the required ΔZ for ice nucleation increases. Assuming a dry adiabatic lapse rate of $9.8^{\circ}\text{C km}^{-1}$ and an RH for ice nucleation given by (2), $\Delta Z = 340\text{ m}$ at -40°C , 310 m at -50°C , and 280 m at -60°C .

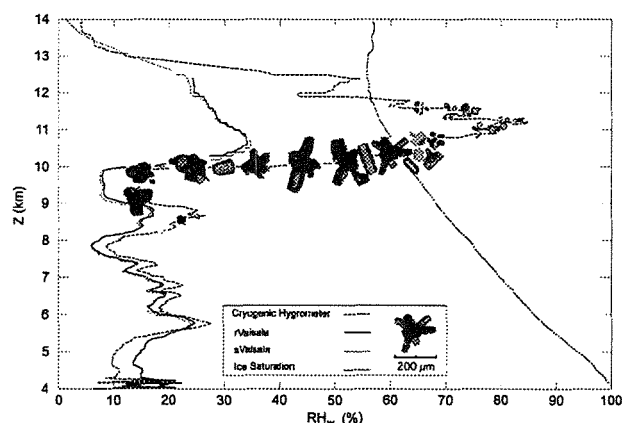


Figure 5. Data collected from replicator, radiosondes and cryogenic hygrometer during balloon ascent in October 1994. Ice crystal images are representative examples.

Schematic Depiction of Dynamically Active Cirrus Layer

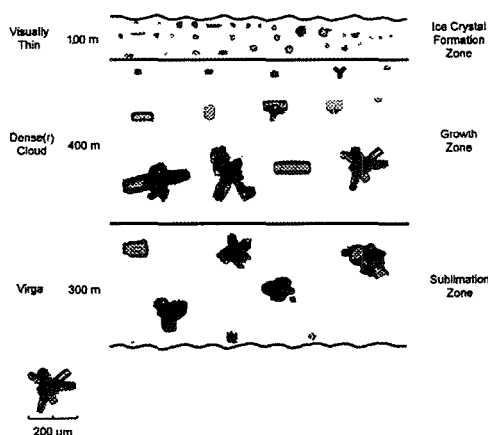


Figure 6. Schematic depiction of three-layer conceptual model of cirrus cloud structure.

Layer 2 is therefore a deeper region of ice supersaturation, where ice crystals can grow from tens of microns to hundreds and even a thousand microns (Fig. 6). The presence of ice supersaturated regions should not be surprising: frequently, individual cirrus elements are observed to be growing prior to falling into sublimation zones, producing the familiar cirrus class known as uncinus; also, contrails form and merge into extensive cirrus sheets in the absence of natural cirrus.

c. Layer 3: Sublimation Zone

Ice crystals can fall great distances through dry layers (Fig. 5 and Heymsfield and Donner 1990), where they moisten the local environment and act to transport upper-tropospheric moisture downwards. The smaller ice crystals, which contain most of the mass, disappear quickly while the larger crystals may break apart to produce numerous smaller ice crystals.

Layer 3, therefore, is the sublimation zone, where ice crystals generated aloft fall into dry air, lowering the cloud base and moistening the air below (Fig. 6). The thickness of Layer 3 is dependent upon the IWC and particle sizes near the base of layer 2 and the RH and temperature profiles in Layer 3.

4. SUMMARY AND CONCLUSIONS

Measurements in cirrus which form as the result of either deep convection or large-scale ascent were examined using measurements from mid-latitude and Arctic continental locations and over the warm pool of the tropical central and western Pacific. In general, the IWC increased from order of 10^{-3} to order 10^{-1} g m^{-3} over the 70°C temperature range of the measurements, but differences are noted between locations, and substantial variability exists at all temperatures at each location. Small particles, between 5 and $100 \mu\text{m}$, give the greatest

relative contributions to the IWC when it is $<10^{-2} \text{ g m}^{-3}$; additional data are needed to confirm these findings.

Using our mid-latitude measurements, a three-layer conceptual model describing the nucleation and development of ice crystals produced in cirrus by layer lifting is developed: an upper nucleation layer, a middle growth layer, and a lower sublimation zone. The model provides a framework for calculating the development and evolution of cirrus in mesoscale and climate models, and for evaluating the effects of jet aircraft on upper-level cloudiness.

5. ACKNOWLEDGEMENTS

The assistance of Steve Aulenbach and Rick Graves in the data analysis and preparation of this manuscript is greatly appreciated. Original data were kindly provided by Prof. Judith Curry of the University of Colorado. This research was supported by the NASA FIRE Program and by the NSF through the Center for Clouds, Climate, and Chemistry (C4).

REFERENCES

- Ebert, E. E., and J. A. Curry, 1992: A parameterization of ice cloud optical properties for climate models. *J. Geophys. Res.*, **97**, 3831–3836.
- Francis, P. N., A. Jones, R. W. Saunders, K. P. Shine, A. Slingo, and Z. Sun, 1994: An observational and theoretical study of the radiative properties of cirrus: Some results from ICE'89. *Quart. J. Roy. Meteor. Soc.*, **120**, 809–848.
- Heymsfield, A. J., 1993: Microphysical structures of Stratiform and Cirrus Clouds. *Chapter 4, Aerosol-Cloud-Climate Interactions*, edited by P. Hobbs, Published by Academic Press, Inc, 97–121.
- Heymsfield, A. J., and L. J. Donner, 1990: A scheme for parameterizing ice cloud water content in general circulation models. *J. Atmos. Sci.*, **47**, 1865–1877.
- Heymsfield, A. J., and L. M. Miloshevich, 1995: Relative humidity and temperature influences on cirrus formation and evolution: Observations from wave clouds and FIRE-II. *J. Atmos. Sci.*, **52**, 4302–4326.
- Heymsfield, A. J., and G. M. McFarquhar, 1996: On the high albedos of cirrus in the tropical Pacific warm pool: Microphysical interpretations from CEPEX and from Kwajalein, Marshall Islands. *J. Atmos. Sci.*, in press.
- Miloshevich, L. M., and A. J. Heymsfield, 1996: A balloon-borne cloud particle replicator for measuring vertical profiles of cloud microphysics: Instrument design and performance. *Proc. Int. Conf. on Cl. and Precip.*, Zurich.
- Oltmans, S. J., and D. M. Hofmann, 1995: Increase in lower-stratospheric water vapor at a mid-latitude northern hemisphere site from 1981 to 1994. *Nature*, **374**, 146–149.

ICE FORMATION IN WAVE CLOUDS –

COMPARISON OF AIRCRAFT OBSERVATIONS WITH MEASUREMENTS OF ICE NUCLEI

David C. Rogers¹, Paul J. DeMott¹, W.A. Cooper², and R.M. Rasmussen²

¹Department of Atmospheric Science, Colorado State University, Fort Collins, CO, USA

²National Center for Atmospheric Research, Boulder, CO, USA

1. INTRODUCTION

A wide variety of observations were made during the 1994 Winter Icing and Storms Project along the eastern front range of Colorado mountains (Rasmussen et al., 1992). Primary goals of the project were to improve the understanding of the formation of liquid water and the initiation of ice in supercooled clouds. These were studied by several different, complementary approaches: remote sensing (radar and radiometers), in situ observations by instrumented aircraft and measurements of ice nucleating aerosols. This focus of this paper is to compare the aircraft observations of ice crystal concentration in wave clouds with measurements of ice nucleating aerosols (IN) of air samples collected from the inflow regions of the clouds.

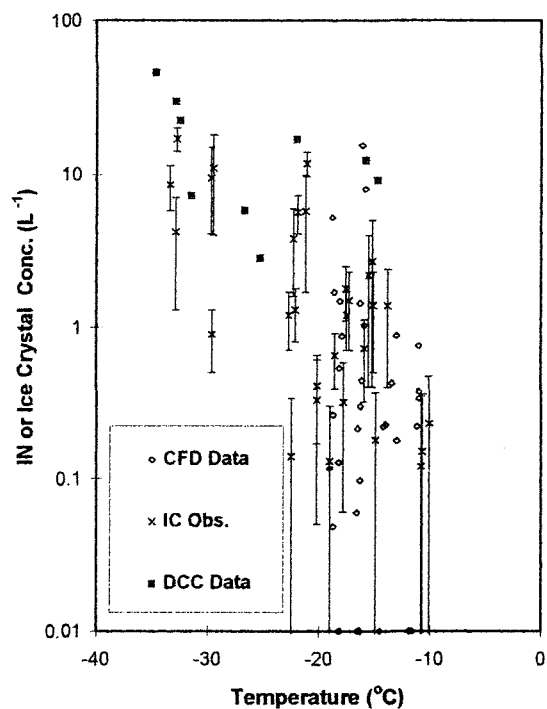
2. AIRCRAFT DATA

Wave cloud and IN studies were done on 10 days in February and March 1994. The aircraft made several cloud penetrations along upwind-downwind directions. Ice concentration was estimated from "shadow-OR" counts from a Particle Measuring Systems (PMS) 2DC probe. In some cases, the concentration was also estimated from a 1D probe, the PMS 260X. The two estimates ranged from about the same value to twice as high for the 260X. The differences are probably a consequence of the ways that sample volumes are determined for these probes. For crystals larger than about 100 μ m, the two estimates agreed.

In all of the clouds studied here, the ice concentration rose rapidly downwind from the upwind edge and reached a relatively steady value through the body of the cloud. This feature is consistent with earlier orographic wave cloud studies (e.g., Cooper and Vali 1981; Heymsfield and Milosevich 1993). For this study, the plateau ice concentration was used as a representative value, along with the average temperature during the cloud penetration. For the colder clouds, a second region of ice formation was detected near the downwind cloud edge where evaporation is occurring;

that feature has been described in a separate paper (Cooper 1995).

A summary of the aircraft ice crystal measurements is shown in Figure 1. Altitudes of the wave clouds ranged from 3.8 to 6.5km MSL, with temperatures -10 to -33C and ice crystal concentrations 0.2 to 17 per liter. Measurements of ice nuclei from the bag samples are also shown on this figure.



1. AEROSOL SAMPLING

2.1 Collection

Bag samples (~300L per bag) were collected by NCAR and University of Wyoming aircraft near the inflow areas of orographic wave clouds. Two metal bellows pumps were used in parallel to fill bags on the aircraft. Filling time was ~10 minutes. The bag samples were delivered to local airports and taken to the lab for analysis. CN concentration was used to monitor the loss

of aerosol in bag samples and to estimate correction factors. This loss was well described by $N(t) = N_0 \exp(-t/\tau)$, where time is in minutes, and τ is ~180 to 360. All measurements from the bag samples were corrected for this decay back to the time of collection. Most bag samples were analyzed within < 2 hours of collection, and particle losses were usually < 25%. The bags were made of electrically conductive plastic (Velostattm, 3M Corp.).

2.2 Dynamic Cloud Chamber (DCC)

The CSU dynamic (controlled expansion) cloud chamber was used to simulate adiabatic parcel rise, condensation, and ice formation for ground-level and aircraft bag samples. The simulation experiments extended from cloud formation (-10 to -23°C) through the homogeneous freezing regime. Descriptions of the dynamic cloud chamber (DCC) and examples of experiments are in DeMott and Rogers (1990), DeMott (1990) and DeMott et al. (1990). The cloud chamber consists of a 2.0 m³ stainless steel outer pressure vessel containing a thin cylindrical inner temperature-controlled copper liner which is vented to the pressure vessel by small holes in the top and bottom plates. Total experimental working volume is 1.19 m³. Air is evacuated to produce expansion cooling of the sample air. Simulated ascent rates corresponded to updrafts measured by the aircraft. The simulated ascents are based on equations for dry adiabatic expansion until cloud forms and moist adiabatic expansion thereafter.

Cloud droplets are measured with a (PMS) FSSP-100. Ice crystal concentration in the chamber volume is measured at the bottom in two ways: single particles are counted by extinction in a laser beam; and an aspirated PMS 1D probe (OAP-230X, 30 size bins 10-300µm). The first two channels (10-30µm) of PMS 1D data were not counted, in order to avoid the possibility of incorrectly counting large droplets as ice crystals. The minimum detectable crystal concentration in the DCC is about 1 per liter.

The volume of the DCC is ~4 times larger than a 300 L bag, so the bag samples were added to preconditioned air already in the chamber. The preconditioned air was dry and filtered to remove all particles. Then water vapor was added in order to achieve cloud point at the same pressure and temperature observed by the aircraft. In a few cases, ammonium sulfate CCN were added to the preconditioned air to bring the expected droplet concentration up to that observed by the aircraft, in order to limit the peak supersaturation. Experiments confirmed that ammonium sulfate CCN aerosols could be added to the DCC without causing additional ice formation in natural air to at least -28°C.

The particular ice nucleation mode dominant in DCC experiments is not readily apparent. Deposition

nucleation is indicated when ice appears below water supersaturation during ascent; condensation-freezing nucleation should show a dependence on supersaturation; and immersion-freezing is the likely mode if all of the available CN are nucleated as cloud droplets. In some experiments, cloud evaporation was induced in order to study the potential effect on ice initiation. Ice formation by apparent homogeneous freezing occurred in some experiments when the expansion was allowed to continue to -35°C or colder.

2.2 Continuous Flow Diffusion chamber (CFD)

The CFD is the same instrument described in Rogers (1988; 1994), with some minor modifications. In the CFD, air flows in the annular space between two ice-coated cylinders which are at different temperatures. Ice crystals form on active IN, grow to ~5µm, and are counted at the outlet. The ranges of temperature and water supersaturation (SSw) in the CFD were: -8 to -20°C, -10 to +20% SSw. The CFD was operated in a batch sampling mode, accumulating counts over a fixed time interval of 5 to 10 minutes (sample volume 5 to 10 L). Temperature and supersaturation were kept constant during each sample period and were changed for subsequent samples. Several measurements were made from each bag, from a few percent subsaturated to a few percent supersaturated. The highest SSw values were deliberately chosen very high (> 10%) to ensure that water saturation was exceeded.

2.3 Other Aerosol Measurements

Concentration of CN was measured using a Thermo-Systems Incorporated (TSI) Model 3020 Condensation Nuclei Counter. CCN were measured with a Mee Industries Model 130 CCN counter (a static thermal gradient diffusion chamber), modified by adding laser-illumination and CCD-video counting of the droplets. CCN concentrations were measured at supersaturations of 0.50, 1.0 and 2.0%, with occasional values inside and outside this range.

3.0 RESULTS

Since ice nucleation is a strong function of temperature and supersaturation, the laboratory measurements attempted to expose the aerosol to temperatures and supersaturations that were expected in the wave clouds. This was not always possible, due to equipment limitations.

As shown in Figure 1, CFD measurements of IN ranged from -11 to -19°C, and IN concentrations were 0 to 22 per liter. CFD water supersaturations were -3 to +14%. DCC experiments went from cloud formation (-10 to -23°C) to the onset of homogeneous freezing (~-35°C), with concentrations 0 to 40 per liter.

The DCC and CFD use quite different techniques. The CFD is sensitive to deposition, condensation-freezing, and immersion-freezing nucleation. The DCC is sensitive to these mechanisms plus contact-freezing. The CFD has greater sensitivity to low IN concentrations because all of the sample air passes through its sample volume, whereas the DCC collects only a small fraction of the crystals which form. The DCC is capable of measurements to about -50C, whereas the CFD's cold limit was -20C. In the DCC, the ambient dew point temperature determines the temperature where cloud forms, whereas, in the CFD, the condensation point is entirely controlled by the wall temperatures. In spite of these numerous differences, the measurements showed reasonable agreement with each other in the temperature region where the instruments overlap. Comparison with the aircraft measurements shows a substantial amount of overlap also. A tentative conclusion from the consistency of the DCC and CFD measurements is that these techniques respond to the same aerosol. The general agreement with aircraft data suggests that IN measurements represented the dominant ice nucleation mechanisms.

4.0 CONCLUSIONS

Ice crystal and IN concentrations increased rapidly with colder temperatures and as the humidity rose above water saturation. In situations where the production of ice could be attributed to primary nucleation, the IN measurements compared favorably with aircraft observations of cloud ice crystal concentration at the same temperature. Measurements with the DCC and the CFD showed reasonable agreement, although the range of temperatures was limited where these instruments overlap. These results suggest that IN aerosol measurements have diagnostic value for predicting cloud microphysical properties.

5.0 ACKNOWLEDGEMENTS

This research was supported by National Science Foundation (Grants ATM-9103748, ATM-9317405 and ATM-9311616). Additional support and equipment loans came from NCAR/Research Applications Program and the University of Wyoming.

6.0 REFERENCES

- Cooper, W.A. and Gabor Vali, 1981: The origin of ice in mountain cap clouds. *J. Atmos. Sci.*, 38, 1244-1259.
- Cooper, W.A., 1995: Ice formation in wave clouds: Observed enhancement during evaporation. Preprints, American Meteorological Society Conference on Cloud Physics, 15-20 January, Dallas, TX, 147-152.
- DeMott, P.J., 1990: Quantifying ice nucleation by silver iodide aerosols. Ph.D. Dissertation, Paper No. 466,

Department of Atmospheric Science, Colorado State University, Fort Collins, CO, 252 pp.

DeMott, P.J. and D.C. Rogers, 1990: Freezing nucleation rates of dilute solution droplets measured between -30 and -40C in laboratory simulations of natural clouds. *J. Atmos. Sci.*, 47, 1056-1064.

DeMott, P.J., D.C. Rogers, and R.P. Lawson, 1990: Improvements to the CSU controlled-expansion cloud chamber. Preprints of the AMS Conference on Cloud Physics, 23-27 July, San Francisco, CA., 126-149.

Rasmussen, R., M. Politovich, J. Marwitz, W. Sand, J. McGinley, J. Smart, R. Pielke, S. Rutledge, D. Wesley, G. Stossmeister, B. Bernstein, K. Elmore, N. Powell, E. Westwater, B. Stankov, and D. Burrows, 1992: Winter icing and storms project (WISP). *Bull. Amer. Meteor. Soc.*, 951-974.

Rogers, D.C., 1988: Development of a continuous flow thermal gradient diffusion chamber for ice nucleation studies. *Atmospheric Research*, 22, 149-181.

Rogers, D.C., 1994: Detecting ice nuclei with a continuous flow diffusion chamber --some exploratory tests of instrument response. *J. Atmos. Ocean. Techn.*, 11, 1042-1047.

A MEASUREMENT AND MODELING STUDY OF YOUNG CIRRUS CLOUDS: PART 1, MEASUREMENTS

Johan Ström¹, Bernhard Struss², Franz Schröder², Theodore Anderson³, Jost Heintzenberg⁴ and Peter Wendling²

¹Dept. of Meteorology, Stockholm University, Stockholm, Sweden

²DLR, Inst. for Atmospheric Physics, Wessling, Germany

³Dept. of Atmospheric Science, University of Washington, Seattle, USA

⁴Inst. for Tropospheric Research, Leipzig, Germany

1. INTRODUCTION

Cirrus clouds are acknowledged as being very important in the Earth's radiation balance, but at the same time we know comparatively little about these high altitude and cold clouds. What processes are important during cirrus formation and what factors are controlling the crystal number concentration, size distribution and crystal habits? As a step towards answering these questions we were able to study the cloud microphysical and aerosol properties in-situ during four flights in what we interpreted to be young cirrus clouds. These flights were conducted on 18, 22, and 25 (two flights) March 1994. The missions were flown mainly over southern Germany in a sector roughly bounded by latitude 47°N and 50°N, and longitude 11°E and 15°E. During the measurement period the synoptic weather over central Europe was such that in the free troposphere the airflow was from west or northwest except on the 21 March when a "cut-off low" over France disturbed the flow pattern. In this case the air flow was from the north over the measuring area during 22 March. On 23 March the wind pattern was restored again to a westerly air flow.

2. INSTRUMENTS

All instruments were operated on board the DLR (German Aerospace Research Establishment) research aircraft Falcon. For details of the instrumentation for meteorological and wind data on the Falcon we refer to Schumann et al., (1995). In addition to the standard instrumentation, humidity was measured by a cryogenically cooled frost point mirror.

Two different PMS (Particle Measuring System) cloud probes mounted on wing pods were carried on board the aircraft: a two-dimensional optical array probe (PMS 2D-C) to obtain information about crystals with dimensions between 50 and 800 μm , and a forward scattering spectrometer probe (FSSP-100) which unfortunately did not working properly and is excluded from the analyses

Another instrument to measure crystal distribution and habit working on a completely different physical principal is the ice-replicator, designed and built by J. Hallet (Desert Research Institute, Reno, USA). This device is built into the same type of wing pod as the PMS-probes. A film coated with chloroform formvar is exposed to the ambient air through a slit facing the flight direction. Cloud particles that enter the slit and impact on the film leave a replica of their shape in the formvar. The sampling characteristics of the replicator are not well known. However, simple calculations yield a 50% sampling efficiency of around 4 μm aerodynamic diameter. The upper detection limit is mainly determined by the breakup by large crystals as they impact on the film which causes difficulties in data interpretation. This problem becomes significant for particles with dimensions larger than 100 μm .

To obtain information about the phase partitioning of aerosols in the cloud we samples particles through two complementary inlets. These are the Counterflow Virtual Impactor (CVI) or supermicrometer inlet, and the interstitial inlet or submicrometer inlet. The submicron inlet, is a 1/4" stainless steel tube which is tapered to give an effective opening cross section of 3.8mm². The opening of the inlet is turned opposite to the flight direction which results in cloud particles not being sampled due to their inertia carrying them past the inlet. The upper cut-off for this inlet is estimated to be just under 1 μm diameter. The CVI is a device that inertially separates cloud elements larger than a certain aerodynamic size from the surrounding atmosphere into a warm, dry and particle free air (Ogren et al., 1985). Water vapor and residue particles left behind by the evaporated cloud elements, are subsequently sensed and sampled by other instruments working downstream of the CVI. The calculated 50% sampling efficiency for the probe used in this experiment is 4.5 μm aerodynamic diameter.

Inside the aircraft the sample air from the two inlets is distributed to different sensors. The concentration of ambient aerosol and residual particles larger than 0.018 μm diameter was measured by two TSI-3760 condensation particle counters (TSI Inc., St.

Paul MN, USA) modified for aircraft use. Assuming that each crystal leaves behind only one residue particle, these measurements yield an equivalent crystal number concentration for cloud particles having an aerodynamic radius larger than the lower cut size of the CVI. The size distribution of the sampled aerosol and residual particles between 0.12 to 3.5 μm diameter was measured by a PMS PCASP (Passive Cavity Aerosol Spectrometer) working alternatively on both inlets. A dual-beam Lyman- α was used to measure the evaporated water from the sampled crystals, which corresponds to the condensed water content (CWC) in cloud particles larger than the lower cut size of the CVI.

3. RESULTS AND DISCUSSION

Unless stated otherwise all values are reported as 3 second averages and concentrations are normalised to standard temperature and pressure, STP (273.15 K and 1013.25 hPa) values.

3.1 Flight on the 18th of March 1994

On the 18th the first part of the flight was conducted over the Alps in virtually cloud-free air. After three flight legs over the Alps the aircraft flew east and then turned north-northwest almost directly into the wind. The aircraft entered a cirrus cloud at 8800 m pressure altitude (top level) marked as A in Figure 1. After two descents to 8500 m at point B (middle level) and 8200 m (bottom level) at point (C) the aircraft finally exited the cloud at point (D). The average temperatures on these levels were -53.3 , -51.2 and -48.8°C , respectively.

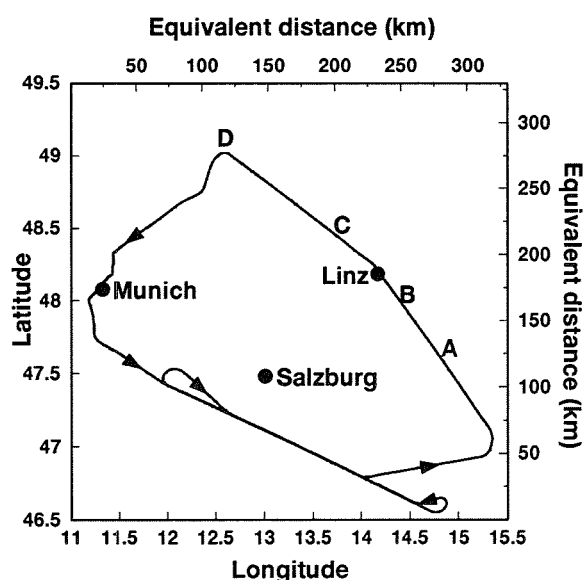


Figure 1. Flight track on 18 March 1994. The letters A-D indicate cloud penetration and level changes.

As the aircraft approached the cirrus cloud on the top level the relative humidity increased from near ice saturation to near water saturation. The crystal concentration and CWC did not show a significant increase until the RH_w (relative humidity over water) had reached about 80 %. At that time the concentrations were about 1 cm^{-3} and 1 mg m^{-3} , respectively. On the middle level crystal concentrations ranged between 0.5 and 3.5 cm^{-3} , and CWC ranged between 1 and 6 mg m^{-3} . The highest values were observed on the bottom level for both crystal concentration ($2\text{--}10 \text{ cm}^{-3}$) and CWC ($5\text{--}30 \text{ mg m}^{-3}$). The average RH_w increased from 95 % to a slightly higher value of 97.5% between the middle and bottom level. The high relative humidity observed in the cloud suggests that the crystals probably nucleated through freezing of solution droplets. The accuracy of the frostpoint and ambient temperature measurements results in an absolute uncertainty of the calculated average RH of about $\pm 10\%$. Nevertheless, at the observed temperatures in the cloud of about -50°C the observed humidities are still well above ice saturation.

Analyses of the potential temperature and the measured vertical wind speed was used to reach information about the dynamical structures in the cloud. We recreate the vertical component of the streamlines by integrating the vertical wind speed along the horizontal wind as suggested by Ström and Heintzenberg, 1994. At the first approximation the potential temperature deviation around a mean is inversely proportional to the vertical motion of an air parcel. A 30 m change in altitude for an air parcel corresponds to a change in temperature of approximately 0.3. The potential temperature and the calculated vertical component of the streamlines are consistent with each other and suggests that the dynamic forcing was due to waves with an amplitude of 25 to 50 m. We estimate an apparent wave length from the data of 40 to 50 km, which yields a period of about 15 minutes at a horizontal wind speed of 50 m s^{-1} . This value is consistent with the Brunt-Väisälä period for this part of the atmosphere (12-13 min).

The 2D-probe did not observe any significant concentration of crystals during the cloud penetration. The upper bound of the crystal size distributions should therefore not exceed 50 μm diameter. The diameter of mean mass (DMM) calculated from CVI measurements show values between 10 and 20 μm increasing toward lower altitudes. The crystal size distributions deduced from replicator data appeared to be grouped into two regimes. From these two subjectively divided groups we then calculated averages and standard deviations. The result is presented in Figure 2 as envelopes of one standard deviation plus and minus the mean for the two regimes. The number mode is clearly associated with crystals smaller than 10 μm diameter. The effective diameter calculated from the average size distributions yield values of 11.9 μm (solid line) and 7.7 μm (dotted line).

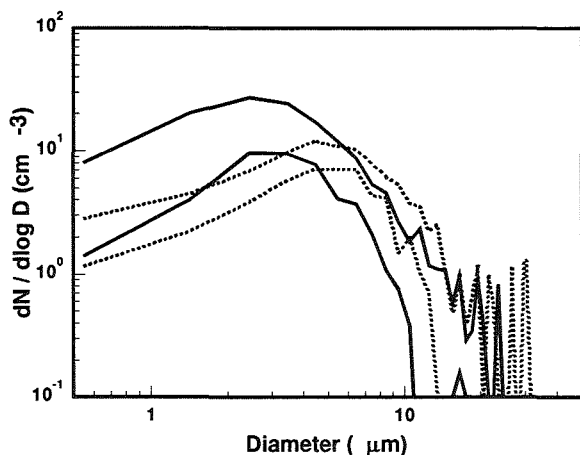


Figure 2 Crystal size distribution as measured by the replicator. The envelopes shows the arithmetic mean plus/minus one standard deviation. The solid and dotted line represents two observed regimes.

The habits of the smallest crystals measured by the replicator are mostly irregularly shaped spheres, much like potatoes. According to Ohtake (1969) this shape is attributed to the fast freezing of haze droplets which does not allow for the development of normal hexagonal and rectangular faces. With increasing crystal size the shapes become more and more hexagonal, and plates, columns and bullet rosettes can be observed for the largest crystals (20 to 30 μm).

In young cirrus clouds, where processes like coagulation and aggregation are of little importance, we can assume that the residual particle which remains after evaporating a crystal is the same as that upon which the crystal first nucleated.

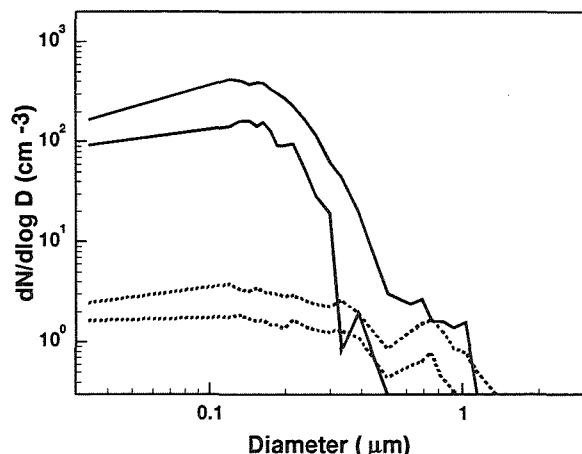


Figure 3. Average size distribution of interstitial aerosol and cloud residues as solid and dotted lines, respectively.

Thus, the residual size distribution represents the part of the ambient aerosol that took part in cloud formation. Figure 3 show two-minute averages of the residual and interstitial size distributions from a more

dense part of the cloud. Because the payload only carried one PCASP instrument, the averages had to be done sequentially. The concentration of residual particles display a number mode around 0.1 μm and a local maximum at about 0.7 μm diameter. Jensen et al. (1994) argued that the fraction of aerosol particles less than 0.6 μm diameter nucleating into crystals are too few and do not affect ice nucleation in midlatitude cirrus. The data presented in this paper and in Ström et al. (1994) and Noone et al. (1993) do not support that statement. Actually more than 90% of the residual particles were smaller than 0.6 μm in the cloud discussed here. This information has important implications for the possible climate forcing due to anthropogenic emissions of particles and precursor gases, which may perturb the aerosol size distribution and thus the cloud formation.

An interesting observation is that the shape of the residual size distribution changed very little with total crystal concentration. A reason for this can be homogeneous mixing and entrainment, but also the way crystals are nucleated in the cloud. At a given saturation level, temperature, and chemical composition of the aerosol, the fraction or probability of solution droplets freezing per unit time have a power-law dependence with decreasing probability of freezing for decreasing particle size (DeMott et al., 1994).

3.2 Statistics over four flights

The three flights on the 22nd and 25th were not suitable for a similar detailed study as for the 18th because of the flight legs being much shorter and not along the horizontal wind. However, since the weather situations were similar and we believe that these clouds also belong to the category of young cirrus, we combined the data from all the flights in order to present statistics for all flights. Only CVI data from straight and level flight segments are included in this analysis. Furthermore, only in-cloud data points are included in the data analyses, defined as an ambient crystal concentration greater than 3 L^{-1} as measured by the CVI. At this concentration the counting error for the CVI is 25-30 % depending on flow settings. The data set of 3 second averages contain a total of 2336 data points of which data from the 18th represents 16 %. The ambient temperatures for this data set range between -35 and -60 $^{\circ}\text{C}$.

On average the vertical wind in cloudy air, show no preference of sign. The bulk of the observations fall within $\pm 0.35 \text{ m s}^{-1}$ of zero, and the maximum values are less than 1 m s^{-1} . The frequency distribution of RH_w values shows a clustering of data points near water saturation with a median of 90%. The 25 and 75 percentiles were 78% and 99%, respectively. It should be mentioned that a 3 second average for the CR-1 instrument is too short with respect to the low ambient temperatures. The instrument over-shoot and oscillates around the true value at cold temperatures and when

exposed to sudden changes in the humidity. This is a likely cause for very high values measured above water saturation. With the estimated uncertainty presented above it is possible that our humidity data is overestimated by 10% on average. Nevertheless, the humidity is well above ice saturation for almost all data points at ambient temperatures, which supports the idea that nucleation by freezing of solution drops is a very important process.

The observed values of CWC and crystal concentration displayed large variations over several orders of magnitude as can be seen from the probability plot in Figure 10. Median values of 2.6 cm^{-3} and 6 mg m^{-3} serve as typical concentrations.

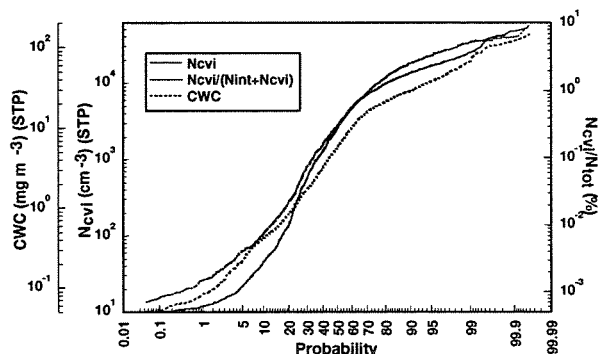


Figure 4. Probability plot of cloud water content, crystal concentration and scavenging ratio as measured by the CVI in four cirrus clouds.

Cloud water content and crystal concentrations usually show covariation in time which is depicted in the rather narrow frequency distribution of the diameter of mean mass. The DMM distribution exhibits a narrow mode at $16 \mu\text{m}$ diameter and is skewed towards larger sizes.

Clearly only a small fraction of the ambient aerosol is scavenged by the cloud as can be seen in Figure 4. This scavenging efficiency, which has a median value of 0.32 %, appears to asymptotically reach 10 %.

3. SUMMARY

The results presented in this paper add to the increasing number of observations where high number concentrations of crystals, typically smaller than $30 \mu\text{m}$ diameter, have been measured. Median values of crystal concentration and cloud water content from our observations in four clouds were 2.6 cm^{-3} and 6 mg m^{-3} (STP), respectively.

Although aerosol particles around $0.1 \mu\text{m}$ which were found scavenged in ice crystals represent only a small fraction of the total aerosol concentration, they control the number of residual particles and thus play an important role in cirrus formation. The high relative humidities near water saturation observed in the clouds also support the idea that the most important nucleation process is spontaneous freezing of haze droplets.

Clearly small aerosol particles must be included in any conceptual model for how cirrus clouds are formed.

The variations in microphysics, potential temperature and analysis of the vertical wind suggests that the dynamic forcing for the cloud on the 18th was due to waves having a period similar to the calculated Brunt-Väisälä frequency. The vertical displacement experienced by an air parcel in the wave relative to the unperturbed air appear to be only 25 to 50 m. This indicates that only a small uplift is necessary to produce a cirrus cloud with high crystal concentrations.

The crystal habits and size distributions measured by the ice replicator show striking similarities to observations made in ice-fogs at comparable temperatures. In both cases the number modes are at sizes smaller than $10 \mu\text{m}$ diameter and the crystals shapes are droxtals or amorphous spheres

4. REFERENCES

- DeMott, P.J., M.P. Meyers, and W.R. Cotton, 1994: Parameterization and impact of ice initiation processes relevant to numerical model simulations of cirrus clouds. *J. Atmos. Sci.*, **51**, 77-90.
- Jensen, E.J., O.B. Toon, D.L. Westphal, S. Kinne, and A.J. Heymsfield, 1994: Microphysical modeling of cirrus 1. Comparison with 1986 FIRE IFO measurements. *J. Geophys. Res.*, **99**, 10421-10442.
- Noone, K.B., K.J. Noone, J. Heintzenberg, J. Ström and J.A. Ogren, 1993: In-situ observations of cirrus cloud microphysical properties using the counterflow virtual impactor. *J. Oceanic Atmos. Technol.* **10**, 294-303.
- Ohtake, T., 1969: Unusual crystal in ice fog. *J. Atmos. Sci.*, **27**, 509-511.
- Ogren, J.A., J. Heintzenberg, and R.J. Charlson, 1985: In-situ sampling of clouds with a droplet to aerosol converter. *Geophys. Res. Lett.*, **12**, 121-303.
- Schumann, U., P. Konopka, R. Baumann, R. Busen, T. Gerz, H. Schlager, P. Schulte, and H. Volkert, 1995: Estimate of diffusion parameters of aircraft exhaust plumes near the tropopause from nitric oxide and turbulence measurements., *J. Geophys. Res.*, in press.
- Ström, J., and J. Heintzenberg, 1994: Water vapor, condensed water and crystal concentration in orographically influenced cirrus clouds. *J. Atmos. Sci.* **51**, 2368-2383.
- Ström, J., J. Heintzenberg, K.J. Noone, K.B. Noone, J.A. Ogren, F. Albers and M. Quante, 1994: Small crystals in cirrus clouds: their residue sized distribution, cloud water content and related cloud properties. *J. Atmos. Res.* **32**, 125-141.

CIRRUS CLOUD OBSERVATIONS WITH A NEW VERSION OF HYDROMETEOR VIDEOSONDE

Narihiro Orikasa, Masataka Murakami, Hakaru Mizuno and Yoshinori Yamada

Meteorological Research Institute, Tsukuba 305, JAPAN

1. INTRODUCTION

High-level ice clouds are thought to strongly influence the global energy budget by affecting infrared radiation emitted by the earth's surface, and in their turn to have a great impact on climatic change (e.g., Liou, 1986). In order to understand climate system, it is necessary to increase our knowledge about microphysical, radiative, and optical properties of cirrus clouds. *In situ* measurements on microphysical structures of cirrus clouds were made by using special aircraft. Therefore, limited studies have been made to date. 2-D Optical Array Probes, which are often used for aircraft measurements of cloud particles, do not have sufficient resolution to discriminate between cloud droplets and ice crystals at sizes smaller than about 100 μm , and cannot detect details of crystal habits.

To overcome these difficulties, a special sonde called Hydrometeor Videosonde (HYVIS) was developed (Murakami and Matsuo, 1990). When applying this HYVIS to cirrus cloud observations (Mizuno et al., 1994), it is necessary to obtain sufficient sampling volumes in cirrus clouds with low ice crystal concentrations. Moreover, weakness of downward scattered lights makes it necessary to improve the way of illumination using natural lights. To meet these requirements, we have improved on the original HYVIS. About 10 units of the new version of HYVIS have been launched in recent cirrus observations.

2. OUTLINE OF NEW HYDROMETEOR VIDEOSONDE

A cut-out view of the new HYVIS is shown in Fig. 1. It has two video cameras with different magnifications to take pictures of hydrometeors from 7 μm to 5 mm in size. Hydrometeors are sucked through particle inlet (1 cm in diameter) and collected on a section of transparent 35 mm leader film over which silicon oil is applied. For the first 6 s, the microscopic camera takes pictures of small ice crystals of the order of 10 to 100 μm in size. During

the beginning of the shooting of the close-up camera, the film is moved at a distance between the two cameras. Then the close-up camera takes pictures of larger ice crystals of the order of 100 μm to 1 mm for another 4 s.

A ground receiving system for the new HYVIS is the same as for the original HYVIS. Images of hydrometeors taken by two small video cameras are transmitted over a 1687 MHz microwave to a ground station in real time so that it does not need to be retrieved later. At the same time, meteorological data are transmitted at a frequency of 1673 MHz.

3. DESCRIPTION OF THE IMPROVEMENTS

3-1. The addition of a suction fan

As shown in Fig. 1, the new HYVIS with a small suction fan (V484M, Micronel) forces hydrometeors to fall through the particle inlet (cylindrical nozzle). The velocity of air flow at the condition of normal temperature and 1 atm. is approximately 12 ms^{-1} at the base of the nozzle, which corresponds to a flow rate of about 1 ls^{-1} ,

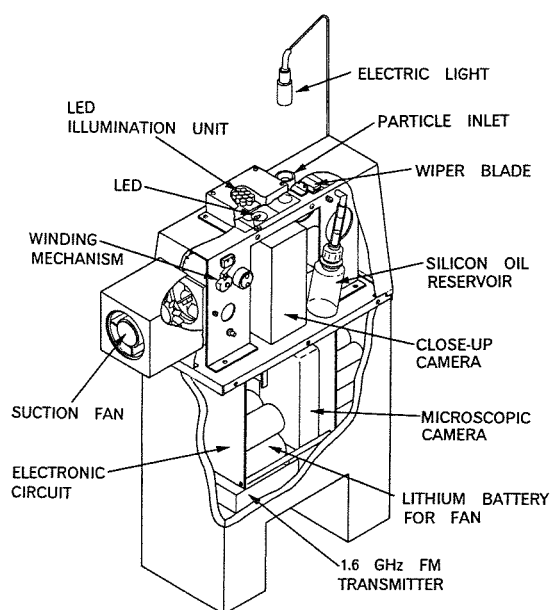


Fig. 1 Cutout view of the new version of HYVIS.

five times as voluminous as the rate of the original ventilation type. As a result of the addition of the fan, the following things were devised:

- (a) Applying silicon oil to the sampling film to prevent ice crystals from rebounding on it.
- (b) The precise movements of the film from the sampling position to the position over the close-up camera.
- (c) Monitoring of flow rates with changes of environmental conditions.

3-2. Illumination

In order to get higher quality images of ice crystals in cirrus clouds where downward scattered lights are weak, it is necessary to reform the illumination for close-up camera using natural lights. Then, a LED illumination unit and a diffusion plate with high quality are equipped over the close-up camera.

4. DETERMINATION OF THE SAMPLING VOLUME AND THE COLLECTION EFFICIENCY

In order to deduce number density of ice crystals from the number of them collected on the film, it is necessary to estimate the flow rate of air and the collection efficiency of particles.

Experiments in a decompression chamber were carried out to estimate the flow rate at altitudes where cirrus clouds occur. The flow rate did not significantly change at a constant rotation rate of the fan until the pressure is reduced to about 200 hPa. Although, beyond 200 hPa, it was difficult to exactly estimate the flow rate, it is suggested that the flow rate is probably constant at altitudes where cirrus clouds occur.

Since the relation between the rotation rates of the fan and the flow velocity is linear, the monitoring of the

rotation rate by using a microphoto sensor enables us to evaluate a flow rate.

Ambient air speed is another factor which has an influence on the flow velocity. The ambient air flow accelerates the velocity of inflow air through the nozzle. On the basis of wind tunnel experiments, we will assume the following relationship between the flow velocity v and the ambient air speed U_∞ :

$$v = (0.88v_s - 2.74) + (0.025v_s + 0.55)U_\infty, \quad (1)$$

where v_s is the flow velocity at $U_\infty = 5$.

To determine the collection efficiency of the new HYVIS for ice crystals, theoretical treatment was carried out on the basis of the collection efficiency of particles for round jet obtained by Ranz and Wong (1952). Figure 2 shows the calculated collection efficiencies of a spherical droplet, a hexagonal plate (aspect ratio 0.2), and a hexagonal cylinder (aspect ratio 2). Since the aspect ratio of a nascent ice crystal around 10 μm in size is considered not to deviate from unity, it is reasonable to assume that all ice crystals larger than 10 μm are collected.

5. SOME EXAMPLES OF CIRRUS CLOUD OBSERVATIONS WITH NEW HYVIS

The new version of HYVIS is attached to a balloon with a rawinsonde and a radiation sonde (Asano et al., 1994) and they are launched in clouds. This combination provides us with vertical profiles of microphysical, thermodynamic, and radiation properties in cirrus clouds. This section will concentrate on the microphysical properties obtained from new HYVIS observation. The microphysical structure of cirrostratus associated with a stationary (Baiu) front was observed over the Tsukuba Area, Japan, on 8 June 1995. The balloon with the above combination was launched at 1030 JST and 1631 JST. Figure 3 shows profiles of temperature, relative humidity, and wind observed with the HYVIS launched at 1030 JST. On the observation day, the tropopause existed at almost the same altitude as the cloud tops (~13.5km) and a jet core was located about 200 km north of the site.

Figures 4 (1030 JST) and 5 (1631 JST) show the vertical distributions of ice water content and number concentrations of ice crystals computed from particle images. They were obtained using the same method as Murakami and Matsuo (1990). The sizes of particles which were analyzed for microscopic and close-up images are under 200 μm and above 50 μm , respectively. It was common in Figs. 4 and 5 that, in middle and lower levels, ice water content held values under 0.01 gm^{-3} and number concentrations from microscopic and close-up images were several to several tens per liter and about 10^2

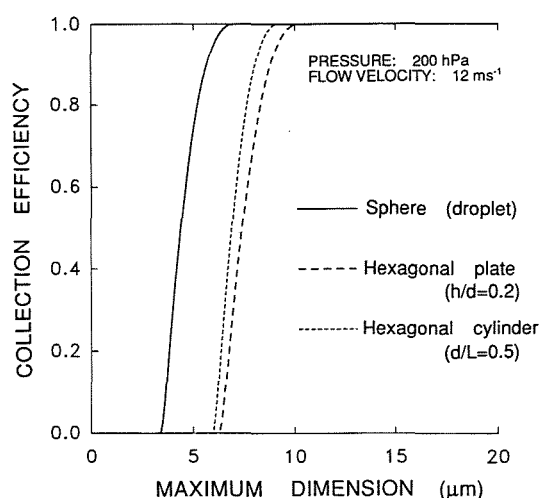


Fig. 2 Calculated collection efficiencies of the new HYVIS for three types of particles.

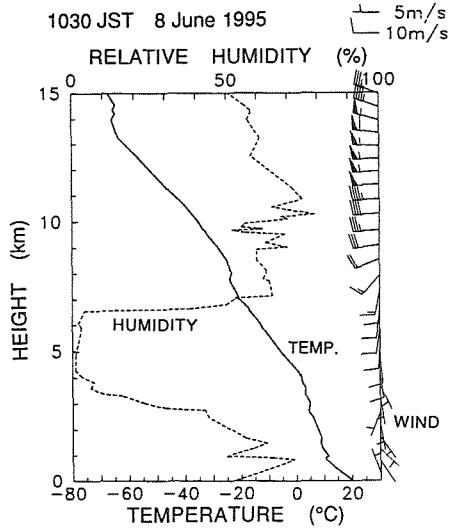


Fig. 3 Vertical profiles of temperature, relative humidity and wind measured by a rawinsonde launched at 1030 JST on 8 June 1995.

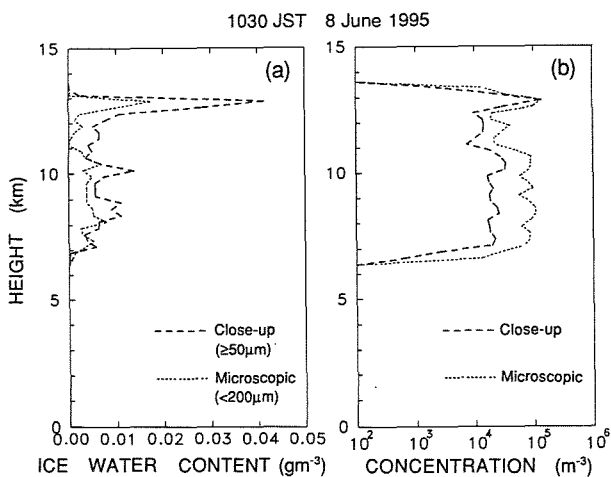


Fig. 4 Vertical structures of the cirrostratus measured by the new HYVIS launched at 1030 JST on 8 June 1995: (a) ice water content; (b) number concentration of ice crystals.

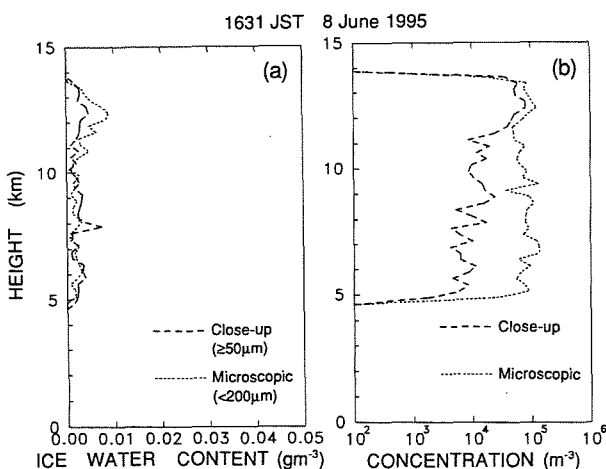


Fig. 5 As in Fig. 4 except for at 1631 JST.

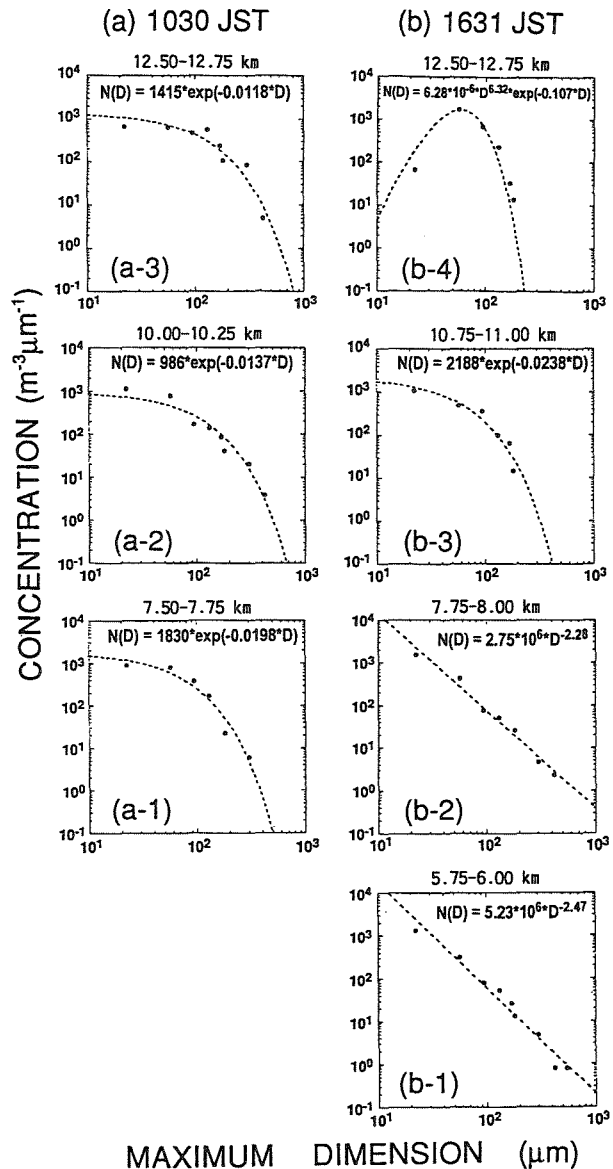


Fig. 6 Change in size distributions of ice crystals along the ascent of the new HYVIS: (a-1), (a-2) and (a-3) for the 1030 case; (b-1), (b-2), (b-3) and (b-4) for the 1631 case. Dashed lines in each panel are regression curves and their formulae are shown at the top of each panel.

per liter, respectively. High concentrations of ice crystals were confined to the upper layer of about 300 m deep for the 1030 case, while to the upper layer of about 2 km deep for the 1631 case.

Size distributions from close-up and microscopic images were combined at 250 m intervals and their vertical changes are shown in Fig. 6. Every size distribution could be approximated by an inverse-exponential function in the 1030 case, while in the 1631 case, the size distributions were of gamma distribution form in the upper levels, of power law form in the lower levels, and of inverse-exponential in the middle levels.

Major shapes of ice crystals observed in the clouds were bullets, columns, bullet rosettes, combinations of columns and plates.

For both cases, high concentrations (more than 100 particles per liter) of ice crystals were found near the cloud tops. Main component of the crystals observed there was bullet (and bullet rosette) of 100-250 μm in size in the 1030 case while it was nascent bullet rosette of about 50 μm in the 1631 case. Examples of microscopic images are shown in Fig. 7.

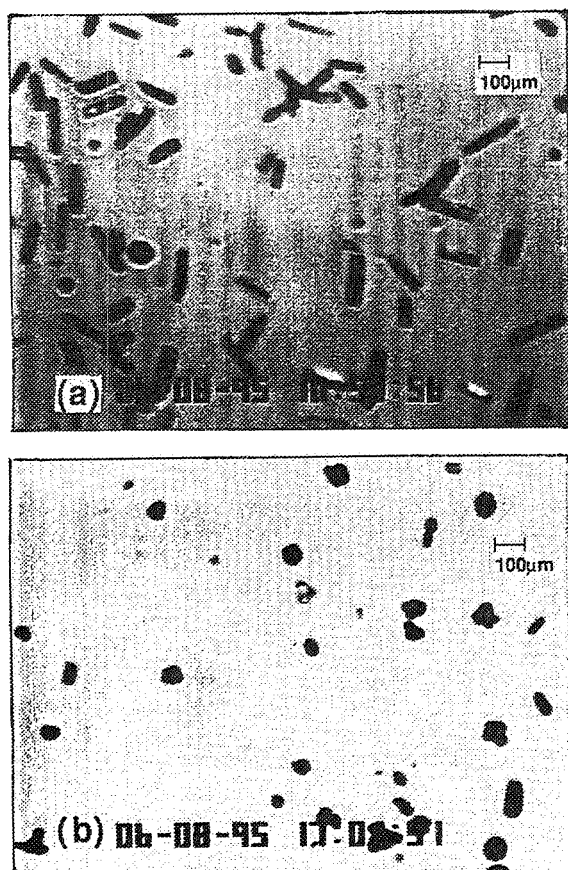


Fig. 7 Examples of microscopic images: (a) at 12.8 km MSL (-59°C) for the 1030 case; (b) at 12.8 km MSL (-57°C) for the 1631 case.

6. CONCLUSIONS

A new version of Hydrometeor Videosonde for measuring cirrus clouds was described. By adding a suction fan, sufficient sampling volumes could be obtained in cirrus clouds with low ice crystal concentrations to determine the form of size distributions at 250 m intervals. The new HYVIS enabled us to obtain reliable size distributions of ice crystals larger than 10 μm .

The new HYVIS measurements also provide us with the information on detailed shapes of ice crystals. They should lead to advanced studies on microphysical structures and radiative properties in cirrus clouds and increase our understanding of mechanisms for the formation and maintenance of cirrus clouds.

Acknowledgments. This work was done as a part of the JACCS/MRI program which is supported by the Science and Technology Agency of Japanese Government.

REFERENCES

- Asano, S., JACCS/MRI Research Group, 1994: Japanese Cloud Climate Study (JACCS): Research plan and preliminary results. Preprint of *the 8th Conf. Atmos. Radiation* (23-28 Jan. 1994, Nashville, TN), Amer. Meteor. Soc., 282-284.
- Liou, K. N., 1986: Influence of cirrus clouds on weather and climate processes: A global perspective. *Mon. Weather Rev.*, **114**, 1167-1199.
- Mizuno, H., T. Matsuo, M. Murakami and Y. Yamada, 1994: Microstructure of cirrus clouds observed by HYVIS. *Atmos. Res.*, **32**, 115-124.
- Murakami, M. and T. Matsuo, 1990: Development of the Hydrometeor Videosonde. *J. Atmos. Ocean. Tech.*, **7**, 613-620.
- Ranz, W. E. and J. B. Wong, 1952: Impaction of dust and smoke particles on surface and body collectors. *Ind. Eng. Chem.*, **44**, 1371-1381.

IDENTIFICATION OF THE FALL MODE OF OBLATE HAIL USING MULTIPARAMETER RADAR

T. J. Smyth, T. M. Blackman and A. J. Illingworth

Department of Meteorology, University of Reading, UK

1 Introduction

In this paper we report on coincidental dual-linear polarised radar and in situ measurements of a summer hailstorm which occurred in southern England on 10th July 1995. The hailstorm was remotely sensed at a range of 30 to 50km by the S-band ($\lambda = 9.75\text{cm}$) Chilbolton radar facility, the narrow (0.28° beam width) allowing excellent resolution of the storm structure. The storm was tracked for about 30 minutes (between 1700 and 1730GMT), within which time it moved in a broadly northerly direction, although individual cells had a more northeasterly trajectory. The radar data was coincidental with in situ verification of the presence of hail by more than 80 observers and by the collection of 55 hailstones, which were subsequently measured. Closer examination of the radar data has allowed an insight into the fall mode of the hailstones which is a determining factor in their resulting shape.

2 Theory.

2.1 Radar

Four radar parameters were used in this study to detect the hail; reflectivity factor, Z_H , differential reflectivity, Z_{DR} , linear depolarisation ratio, L_{DR} , and the differential phase shift ϕ_{DP} .

Differential reflectivity is defined as (Seliga and Bringi, 1976) :

$$Z_{DR}(\text{dB}) = 10\log_{10}\frac{Z_H}{Z_V} \quad (1)$$

where Z_H and Z_V are the backscattered reflectivity in the horizontal and vertical polarisations respectively. Z_{DR} is a measure of the reflectivity weighted oblateness. Raindrops are oblate to a degree which depends upon their size, and fall with their minor axis oriented vertically. High positive values of Z_{DR} are associated with large oblate raindrops. Regions containing ice particles tend to be characterised by lower values of Z_{DR} because of their lower refractive index and tendency to tumble i.e. are isotropic. Algorithms to detect the presence of hail using the Z_H/Z_{DR} pair exploit the difference between the isotropic hail and the anisotropic rain media (e.g. Aydin *et al.*, 1986). Regions of heavy rain, characterised by high values of Z_H and Z_{DR} , can be distinguished from regions of hail, which have high values of Z_H but near zero values of Z_{DR} . L_{DR} is defined as:

$$L_{DR}(\text{dB}) = 10\log_{10}\frac{Z_{VH}}{Z_H} \quad (2)$$

where Z_H is the normal co-polar return measured with horizontal polarisation and Z_{VH} is the cross-polar return measured in the horizontal for a vertically polarised transmitted signal. L_{DR} senses particle fall mode, finite values of L_{DR} occurring for oblate particles which cant or tumble as they fall. Because of the effect of the dielectric constant wet particles have higher values of

L_{DR} . The differential phase shift, ϕ_{DP} , refers to the difference in phase between the co-polar radar returns measured with vertical and horizontal polarisation ($\phi_V - \phi_H$). ϕ_{DP} is made up of three contributions; propagation (K_{DP}), differential phase shift on backscatter (δ) and a constant hardware offset (ϕ_o).

$$\phi_{dp}(r) = \int_0^r K_{DP}(r')dr' + \delta(r) + \phi_o \quad (3)$$

K_{DP} is the propagation component of ϕ_{DP} and has units of $^\circ \text{ km}^{-1}$. As the incident wave propagates through a region of rain the horizontally polarised wave lags progressively behind the vertical one, because raindrops display a high degree of anisotropy. This causes a positive differential phase shift. In rain the value of K_{DP} , at S-band, is approximately proportional to the rain-rate, R (Blackman and Illingworth, 1994).

$$K_{DP} = 0.012R^{1.37} \quad (4)$$

At S-band, the backscatter component of ϕ_{DP} , δ , is usually considered to be very small only occurring when there is Mie scattering. In this paper we will show that this is not a valid assumption for large, wet, oblate hailstones that have an aligned fall mode. δ is only measurable if hail has a preferred orientation but not if it is randomly oriented (McCormick *et al.*, 1979). It is important to note that δ can be larger than the contribution to ϕ_{DP} from the propagation effect, thus introducing ambiguity in the interpretation of the signal. The ϕ_o contribution from the hardware can be measured and subtracted. T-matrix code calculations were carried out to model the radar response to varying size, axial ratio and dielectric constant of the hailstones. The dielectric constant was varied to account for different compositions of ice and water within the hailstone structure.

2.2 Hail Fall Modes

The amplitude of the horizontal and vertical backscatter of the radar signal is directly af-

fected by the fall mode of the hailstones as this determines the average orientation of the long dimension be it in the vertical, horizontal or in a random direction. There seems to be little consensus though on the fall mode of oblates. List (1959) concluded that oblate hail falls with the shortest axis vertical acquiring maximum drag and minimum speed. Browning and Beimers (1967) modified this by introducing a flip in the fall mode to preserve symmetry. Knight and Knight (1970) postulated that to produce the major symmetries of the hailstones, any tumbling motion would have to be both systematic and fairly complex. Kry and List (1974) carried out theoretical calculations which produced a class of solutions termed symmetric gyration. This work was built on by a laboratory study by Thwaites *et al.* (1977) who grew artificial hail to a similar shape and structure to natural oblate hail by using this fall mode. The most likely conclusion to reach is that there are many hail fall modes, these depending upon axis ratio, size and ambient conditions. This paper reports on a postulated fall mode which may or may not be peculiar to the ambient conditions.

3 Results and Discussion

Figure 1 shows a schematic composite horizontal radar scan of Z_H' , Z_{DR} and ϕ_{DP} , with three regions of interest labelled (A), (B), (C). The height of the radar cross section at a range of 45km is 700m which is 2.3km below the melting layer. The hail was observed at 44km range from the antenna, the position marked 'T' in figure 1. Photographic evidence shows that there was a remarkably low number concentration of hailstones ($N \sim 10^{-3} \text{ m}^{-3}$) that fell in a 5 minute period characterised by purely hailfall. The hailstones themselves displayed a degree of triaxiality, a mean axial ratio of 0.6, and an equivalent sphere diameter of between 16 and 22mm.

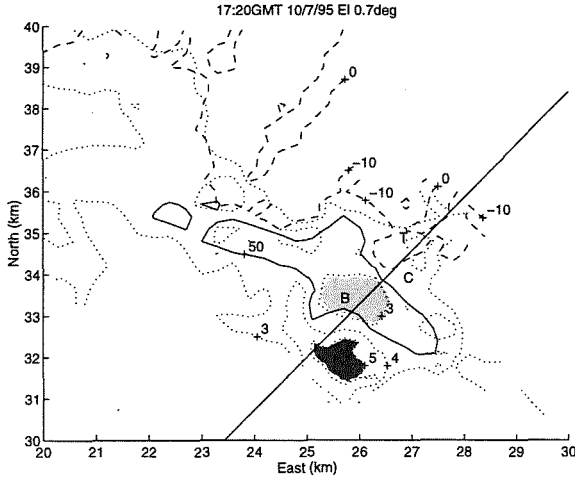


Figure 1: Radar Composite of (solid) 50dBZ Z_H , (dotted) Z_{DR} (3, 4, & 5dB) and (dashed) ϕ_{DP} (-10° & 0°)

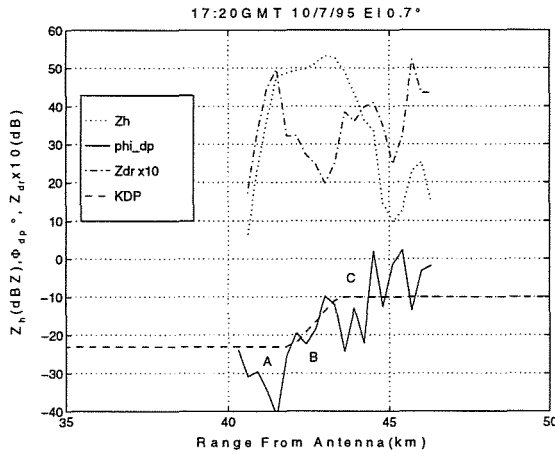


Figure 2: Fields Along a Ray Az 37.77°

Figure 2 is a ray profile along the azimuth shown in figure 1 and shows the variation of the separate fields with range. The dashed line represents an estimate of the K_{DP} (propagation) response starting at the system offset of -23° which was determined from background ϕ_{DP} values in light precipitation. Figure 2 clearly shows the difference between the K_{DP} and δ components. K_{DP} is a cumulative phase shift as the wave propagates through the precipitation whereas δ displays excursions from the smoothly varying background. Region (A) is characterised by high values of Z_{DR} (~ 5 dB) and negative δ

($\sim -7^\circ \rightarrow -13^\circ$). This is consistent with a small concentration of large (and hence oblate) raindrops with a diameter of between 7 and 8mm (axial ratio ~ 0.5). The corresponding values of L_{DR} near the antenna limit of -32 dB also indicate the presence of rain. Region (B) is within the 50dBZ contour and has $Z_{DR} \leq 3$ dBZ. Here the L_{DR} is between -28 and -26 dB indicating wet tumbling or canting particles (Frost *et al.*, 1991). The precipitation population is likely to be mixed rain and hail. Hail is present because of the sharp reduction in Z_{DR} , indicative of tumbling, combined with an increase in Z_H . The hail does not contribute to K_{DP} because of its low number concentration ($\sim 10^{-3}\text{m}^{-3}$) or to δ because it is tumbling, so we interpret the phase shift here as due to the K_{DP} of rain. The estimated K_{DP} values in this region are $\sim 6.5^\circ\text{km}^{-1}$ which from (4) gives a rainrate of $\sim 100\text{mmhr}^{-1}$. The hail detection algorithm of Aydin *et al.* (1986) was not triggered in this region because the minimum values of Z_{DR} were 2dB, this being due to the presence of both rain and hail.

Region (C) is characterised by large values of δ ($\sim \pm 13^\circ$) and high values of Z_{DR} (~ 4 dB). L_{DR} varied between -28 dB to -20 dB towards the leading edge of the storm. This implies wet hail with axial ratio 0.6 and a canting angle of $\pm 10^\circ \rightarrow 20^\circ$. The low Z_H values in a region of large hailstones is consistent with their low concentration. Such a low concentration cannot produce significant K_{DP} , so we interpret the phase observed as large values of δ ($\pm 13^\circ$). Scattering calculations show that spongy hail (30% water) or wet hail with a diameter of between 16 and 22mm and axial ratio of 0.6 is capable of producing the values of δ observed. The hailstones that were collected showed both evidence of spongy and wet growth by the presence of trapped air bubbles and transparent regions respectively. Finite δ can only be produced by hydrometeors with a degree of alignment; addition-

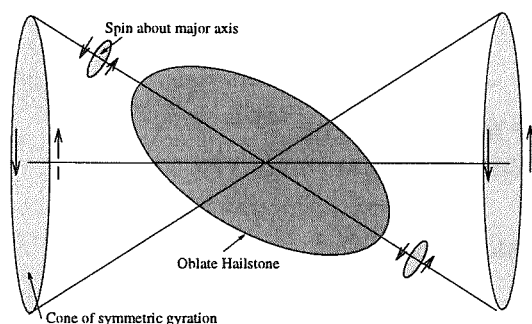


Figure 3: Tumbling Motion of Oblate Hailstone Viewed Side On

ally the positive values of Z_{DR} imply that the alignment was on average in the horizontal. A possible fall mode to produce both the observed symmetry and radar response is one where the hailstones are rotating about their major axes, whilst at the same time moving in a conical manner about the horizontal, similar to the fall modes suggested by Thwaites *et al.* (1977). This is shown in figure 3.

4 Conclusions

The coincidence of ground truth and radar observations has allowed the identification of a possible fall mode for oblate hail. The established hail detection methods failed for two reasons. Firstly in the region of tumbling hail the signal was contaminated with rain. Secondly in region (C) the hailstones were oblate and had a fall mode which had a degree of horizontal alignment. This hail signal is therefore useful only in regions where the precipitation is purely hail and where that hail is tumbling randomly. Large hail is generally more oblate and therefore is likely to display a systematic fall mode implying that the Z_{DR} techniques will often fail. In such circumstances care is needed when deriving rain rates from K_{DP} because of differential phase shift on backscatter.

5 Acknowledgements

This work was supported by NERC grant GRT/02/718. We thank J.Vivekanandan for the T-Matrix code.

References

- Aydin, K., Seliga, T., and Balaji, V. (1986). Remote sensing of hail with a dual linear polarisation radar. *J. Climate Appl. Meteor.*, **25**, 1475–1484.
- Blackman, T. M. and Illingworth, A. J. (1994). Improved measurements of rainfall using differential phase techniques. In *Cost 75*, pages 662–671, Brussels, Belgium.
- Browning, K. A. and Beimers, J. G. D. (1967). The oblateness of large hailstones. *J. Appl. Meteor.*, **6**, 1075–1081.
- Frost, I. R., Goddard, J. W. F., and Illingworth, A. J. (1991). Hydrometeor identification using cross polar radar measurements and aircraft verification. In *25th Conference on Radar Meteorology*, pages 658–661, Paris, France. Amer. Met. Soc.
- Knight, C. A. and Knight, N. C. (1970). The falling behaviour of hailstones. *J. Atmos. Sci.*, **27**, 672–681.
- Kry, P. R. and List, R. (1974). Aerodynamic torques on rotating oblate spheroids. *Phys. Fluids*, **17**, 1807–1092.
- List, R. (1959). Zur aerodynamic von hagelkörnern. *Z. angew. Math. Phys.*, **10**, 143–159.
- McCormick, G. C., Allan, L. E., and Hendry, A. (1979). The backscatter matrix of ice samples: its relation to the identification of hail by radar. *J. Appl. Meteor.*, **19**, 77–84.
- Seliga, T. A. and Bringi, V. N. (1976). Potential use of radar differential reflectivity measurements at orthogonal polarizations for measuring precipitation. *J. Appl. Meteor.*, **15**, 69–76.
- Thwaites, S., Carras, J. N., and Macklin, W. C. (1977). The aerodynamics of oblate hailstones. *Quart. J. Roy. Meteor. Soc.*, **103**, 803–808.

THE MELTING BEHAVIOUR OF ICE PARTICLES AS OBSERVABLE BY POLARIMETRIC RADAR MEASUREMENTS

Igor G Doelling¹ and Peter Meischner²

¹Deutscher Wetterdienst, Meteorologisches Observatorium, D-82383 Hohenpeissenberg, Germany

²DLR Oberpfaffenhofen, Institut für Physik der Atmosphäre, PO Box 1116, D-82230 Wessling, Germany

1. INTRODUCTION

The melting of ice particles during their fall in precipitating cloud systems causes different physical quantities of the particles to change in a characteristic manner. These are changes in shape and size, causing alterations in the fall behaviour as e. g. from tumbling motions to helical shaped motions and refractive index changes from that of pure ice via an ice-water mixture to pure water. These physical quantities in turn are sensitive to the backscattering of polarimetric radar radiation.

By model calculations applying the well known T-matrix method it will be shown, how to separate the different physical effects by using a combination of different measurable polarimetric radar parameters as Z , Z_{DR} , LDR , CDR , Apparent Degree of Orientation $ORTT$, Differential Propagation Phase K_{DP} and Differential Attenuation ΔA . The particles were modelled to be oblate spheroids changing in size, axial ratio, dielectric constant and tumbling behaviour. The dielectric constant was modelled according to different mixing rules as described by the extended Maxwell Garnet theory and by the Bruggeman theory (Bohren and Battan, 1980 and 1981).

The modelling results are discussed in comparison with in situ measurements within a melting layer of a heavily precipitating stratiform system observed during the field experiment CLEOPATRA 1992 (Meischner et al. 1993).

2. POLARIMETRIC RADAR SCATTERING CALCULATIONS

For different simplified model precipitations we computationally investigated the sensitivity of polarimetric radar parameters in dependence on particle and ensemble characteristics. We used a modified computer program based on the Extended Boundary Condition Method (T-Matrix-Method) for axisymmetric scatterers and C-band radar.

The backscattering from a hydrometeor ensemble depends on two classes of characteristics: the charac-

teristics of the individual particles and the statistical characteristics of the ensemble. For a given wavelength, four parameters determine the backscattering of an individual particle: size, shape, orientation and dielectric constant. The ensemble characteristics can principally be described by properly defined probability functions integrated over particle distributions. Our sensitivity studies presented here have the aim of differentiating between melting or refractive index changes and changes of tumbling behaviour, both influencing polarimetric backscatter.

The input parameters for the calculations were particle size, shape, dielectric constant and orientation in space and their statistical characteristics. We calculated T-matrices for oblate (plate-like) and prolate (needle-like) spheroids with axis ratios varying between 0.5 and 2.0 and for different equivolume diameters D ranging from 1 mm to 15 mm. The wavelength was $\lambda=5.5$ cm (POLDIRAD, Schroth et al. 1988). The hydrometeors were assumed to be mixtures of water and ice with volume fractions of ice f from 100% to 0% in 1%-steps. For T-matrix-calculations we used an extended Maxwell Garnet mixing rule with water as matrix and a Bruggeman mixing rule (Bohren and Battan, 1980 and 1981). The temperature was assumed to be 0°C.

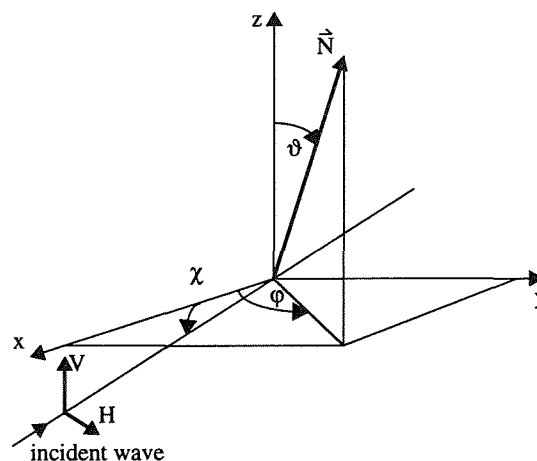


Fig. 1. Scattering geometry in general case where \vec{N} is the symmetry axis of the scatterer. χ is the conventional radar elevation angle. For calculations in presented study: $\chi=0^\circ$, $\phi=90^\circ$, \vec{N} lies in the yz -plane.

The scattering geometry in general case is shown in Fig. 1. The radar parameters were calculated from the T-matrices assuming a monodisperse distribution in size, shape, dielectric constant and φ , but Gauss-distributed in ϑ . The volume concentration was one particle per m^3 . The incident wave propagates along the minus x-axis, i.e. the elevation is $\chi=0^\circ$. The angle φ was fixed with $\varphi=90^\circ$. Therefore the angle ϑ and the symmetry axis \vec{N} of the scatterer lie in the yz-plane. The distribution in ϑ was assumed to be a 2σ -truncated Gauss-distribution. The standard deviation angle σ is from nearly 0° to 40° in 1° -steps.

With the assumptions given above, the reflectivity factor at horizontal H-polarization $Z \equiv Z_{HH}$ is defined as

$$Z = \frac{\lambda^4}{0.93 D} \int_{-2\sigma}^{2\sigma} d\vartheta p(\vartheta) \sigma_{HH}(D, \vartheta, \varphi) [\text{mm}^6 \text{m}^{-3}] \quad (1)$$

with

$$p(\vartheta) = \frac{1}{\sqrt{2\pi} \sigma} \exp \left[-\frac{1}{2} \left[\frac{\vartheta - \bar{\vartheta}}{\sigma} \right]^2 \right], \quad (2)$$

$$D = \text{const.}, \varphi = \text{const.} = 90^\circ. \quad (3)$$

The backscattering cross sections σ_{HH} are derived from T-matrices for a constant volume fraction of ice f and a constant axis ratio using the extended Maxwell Garnet mixing rule. Results for Bruggeman mixing rule are given in *Doelling and Meischner (1994)*. The qualitative behaviour of the radar parameters as the effect of resonances as shown in Fig. 2 in dependence on these two different mixing rules are similar. The quantitative behaviour on the other hand is quite different (e.g. different locations of resonances and different absolute values of calculated radar parameters).

We assumed the falling behaviour of particles related to the ϑ -distribution in accordance with aerodynamics, i.e. the mean canting angle $\bar{\vartheta}$ is 0° for oblate spheroids and 90° for prolate spheroids. Following the results of *Barge and Isaac (1970)* concerning the size and shapes of collected hailstones we investigated only oblate spheroids. The integrations over the angle ϑ and computations of the radar parameters were performed based on formulas given by *Holt (1984)* and *Vivekanandan et al. (1990)*.

The well known Differential Reflectivity factor Z_{DR} , the Linear Depolarization Ratio LDR, the Circular Depolarization Ratio CDR and the Apparent Degree of Orientation ORTT are calculated using the backscattering cross sections σ_{VV} , σ_{VH} , σ_{LR} or σ_{RR} which are as well as σ_{HH} derived from T-matrices.

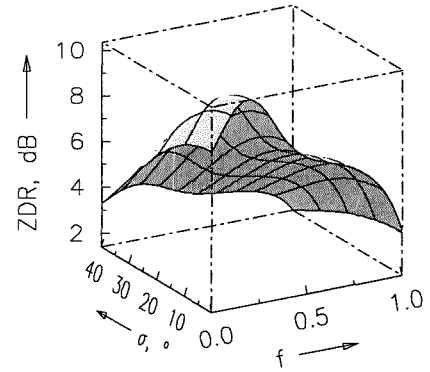
The specific differential phase shift K_{DP} is defined as the difference between the phase shift for V-polarization and the phase shift for H-polarization in the forward direction and given in $^\circ$ per km. In analogy to

K_{DP} the differential attenuation ΔA is defined as the difference between the attenuation for V-polarization and the attenuation for H-polarization in the forward direction. The differential attenuation is given in dB per km. Note that K_{DP} and ΔA are specific (per km) values. The absolute values can be derived from integration over the considered range.

3. DISCUSSION OF COMPUTATIONAL RESULTS

For a given shape and size we present three-dimensional diagrams of the radar parameters in dependence on σ and the ice volume fraction f (e.g. Fig. 2). The equivolume diameter D , the axis ratio a/b , $\bar{\vartheta}$ and φ are fixed for each diagram. Some radar parameters for large equivolume diameters show resonances like Mie resonances, but in dependence on the melting behaviour (volume fraction of ice f). Generally, deviations from Rayleigh scattering are obtained for wet particles with equivolume diameter larger than roughly 2mm. Further the behaviour of radar parameters for ensem-

$$D = 7.0 \text{ mm}, a/b = 0.5, \bar{\vartheta} = 0^\circ, \varphi = 90^\circ, \text{SEIW}$$



$$D = 7.0 \text{ mm}, a/b = 0.8, \bar{\vartheta} = 0^\circ, \varphi = 90^\circ, \text{SEIW}$$

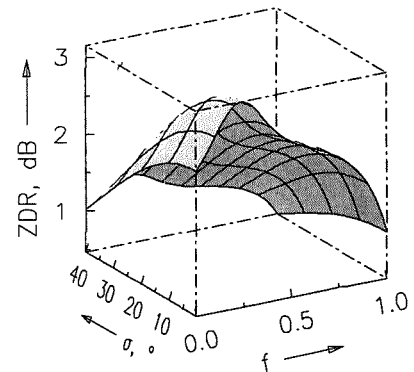


Fig. 2. Z_{DR} as a function of angle σ in $^\circ$ and ice volume fraction f , $f=0.00$ for water and $f=1.00$ for ice. The maximum tumbling angle for a given σ is 2σ . The parameters D , a/b , $\bar{\vartheta}$ and φ are printed for each diagram; SEIW stands for extended Maxwell Garnet mixing rule.

bles with different fixed maximum tumbling angles σ and melting states is presented by two-dimensional diagrams (e.g. Fig. 4).

For Z the dependences on tumbling and axis ratio are not very strong, and the most sensitive dependance is on equivolume diameter. Computational results for Z_{DR} are shown in Fig. 2 for two axis ratios and one equivolume diameter. Z_{DR} depends on all investigated parameters, and without further information it is impossible to use it for identifying or classifying particles. The differential reflectivity clearly decreases with tumbling. An interesting fact is the resonance behaviour of large particles from $D=6\text{mm}$ on. The surfaces in the diagrams for a fixed equivolume diameter D , but for different axis ratios a/b , are similar in shape, but quite different in absolute values of Z_{DR} .

$D = 7.0\text{ mm}$, $a/b=0.8$, $\bar{\vartheta} = 0^\circ$, $\varphi = 90^\circ$, SEIW

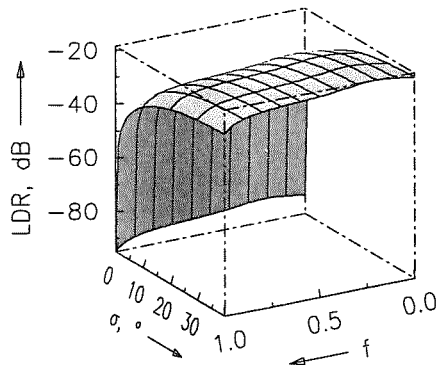


Fig. 3. Same as in Fig. 2, but for LDR and only for the axis ratio $a/b=0.8$.

The results for LDR are shown in Fig. 3. We clearly see that LDR is much more sensitive to tumbling than to melting for σ up to approximately 10° . For σ between 10° and 40° the maximum amount of change of LDR with f is in the same order as for σ , approximately 10dB. The surfaces in the diagrams for all axis ratios a/b and all equivolume diameters D are similar except the occurrence of small resonance peaks. For particle sizes from $D=7\text{mm}$ on again small resonances are observed. Because LDR is not very sensitive to size we only show the case of a fixed D in Fig. 3. For typical values for LDR of -15dB as in a bright band the angle σ should be at least 20° , i.e. the maximum tumbling angle should be at least 40° . For rain σ does not exceed 5° to 10° (e.g. Vivekanandan *et al.* 1990). The tumbling behaviour of melting particles in agreement with our calculations is quite different from those of raindrops. Further we see by our simplified model calculations that tumbling as a secondary effect of melting in a bright band exceeds the pure melting (dielectric constant changes) effects on LDR.

The qualitative behaviour of CDR is comparable to the behaviour of Z_{DR} in the sense that CDR shows extreme resonances in dependence on melting (beginning with $D=6\text{mm}$) and also depends on all influencing parameters except on tumbling. As for Z_{DR} the surfaces are similar for different axis ratios but fixed equivolume diameter D ; as for Z_{DR} the absolute values differ. ORTT depends only on the tumbling and is independent on all other parameters concern.

For C-band propagation effects are important. In precipitations we must also consider forward scattering. For the VH-polarization, on its way to the measurement region the pulse can be changed differently in phase and amplitude for each polarization. To examine such effects we investigated the forward scattering polarimetric radar parameters K_{DP} and ΔA . Again we obtain extreme resonance effects for large particles (beginning with $D=5\text{mm}$ for K_{DP} and $D=6\text{mm}$ for ΔA). In contrast to the other radar parameters we obtained two local extremas for K_{DP} and ΔA for several diameters D in dependence on melting. The behaviour of K_{DP} and ΔA for a given D but different axis ratios is the same as for Z_{DR} , LDR and CDR, i.e. the surfaces are similar but the absolute values differs. But different from the other radar parameters relevant effects on K_{DP} and ΔA are only caused by large particles and smaller axis ratios, in dependance on the melting state. The dependence of K_{DP} on equivolume diameter D shows that the effects for water can be neglected because the sizes of water drops do not exceed about 6mm, but we cannot neglect effects for a mixture and for large pure ice (Fig. 4). For ΔA effects for pure ice and water can be neglected, but not for melting particles. Note that Fig. 4 is given for a monodisperse particle size distribution with one particle per m^3 . For more than one large drop in a m^3 the K_{DP} - and ΔA -values will be larger.

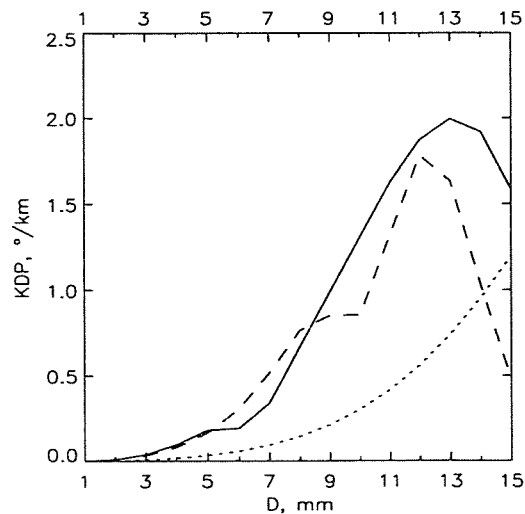


Fig. 4. K_{DP} as a function of diameter for nontumbling particles with $a/b=0.8$. The curves are for water (solid line), $f=0.5$ (dashed) and ice (dotted).

4. COMPARISON OF CALCULATIONS WITH RADAR AND AIRBORNE IN SITU MEASUREMENTS IN A BRIGHT BAND

The calculations were compared with measurements performed on 11 July 1992 during Cleopatra 1992 for a melting layer in a stratiform case (Hagen *et al.* 1993). Measurements were taken with the DLR C-band polarimetric Doppler radar POLDIRAD (Schroth *et al.*, 1988) located at Oberpfaffenhofen scanning in RHI mode in coordination with the DLR FALCON jet equipped with optical PMS 2D cloud and precipitation probes. The FALCON jet was flying along a radial from Oberpfaffenhofen at several altitudes ranging from 6690m to 1550m above ground. The 0°C layer was located near 2400m above ground.

Measured radar values for LDR were in the bright band up to -15dB, above and below the bright band between -25dB and -30dB. For Z_{DR} we found values up to 3dB in the bright band and 0dB outside, for heights above 4km values up to 1dB. Typical values for CDR were about -13dB in the bright band and outside between -26dB and -18dB.

Computational Z_{DR} -, LDR- and CDR-values for the two axis ratios $a/b=0.5$ and $a/b=0.8$ and for equivalent diameters between 1mm and 8mm in 1mm-steps were used for comparison with experimental results. The calculations show that LDR-values of -15dB in the bright band only are possible for tumbling particles with an angle σ greater than roughly 20°. Therefore, in the bright band we expect the particles to tumble with large amplitudes greater than 40°. The values of -13dB for CDR in the bright band can only be explained for axis ratios $a/b=0.5$ and melting particles. For an ensemble of hydrometeors with σ greater than 20° (large tumbling angles derived from LDR) the values of 3dB for Z_{DR} can only be obtained for axis ratios $a/b=0.5$ and melting or ice particles. Generally, the calculated values for CDR and Z_{DR} for axis ratio $a/b=0.5$ are somewhat higher than the measured radar values. With increasing a/b in the calculations the values for CDR and Z_{DR} decrease, and for axis ratios somewhat larger than 0.5 the values for CDR and ZDR should better fit to the measured radar data. Nevertheless, the axis ratio $a/b=0.5$ derived from a combination of calculations and radar measurements gives a good approximation.

In situ measurements at 2170m AGL showed mean particle sizes between 3mm and 4mm, some particles exceeding 6mm. The axis ratios were found between 0.5 and 1. Most particles had axis ratios somewhat larger than 0.5 which is in good agreement with the above results.

5. CONCLUSIONS

Our calculations showed that the radar parameters Z_{DR} , LDR, CDR, ORTT, K_{DP} and ΔA are extremely dependent on different melting and tumbling states of the investigated particle ensembles. The resonance effects in dependence on melting for large particles cannot be neglected. Further, it is of interest that LDR is nearly exclusively depending on tumbling for angles σ less than roughly 10°. The behaviour of radar parameters Z_{DR} , LDR, CDR, ORTT, K_{DP} and ΔA as functions of particle and ensemble input parameters seems to be physically realistic described. For the considered stratiform case the combination of radar measurements and sensitivity studies gives similar results for axis ratio as found by in situ measurements.

6. REFERENCES

- Barge, B.L., and G.A. Isaac, 1970: Shape, size, and surface characteristics of hailstones collected in Alberta. Conference on Cloud Physics, Ft. Collins, Amer. Meteorol. Soc., pp. 83-84.
- Bohren, C.F., and L.J. Battan, 1980: Radar Backscattering by Inhomogeneous Precipitation Particles. J. Atmos. Sci., **37**, pp. 1821-1827.
- Bohren, C.F., and L.J. Battan, 1981: Backscattering of microwaves by spongy ice spheres. 20th Conf. Radar Meteorol., Amer. Meteorol. Soc., pp. 385-388.
- Doelling, I.G., and P.F. Meischner, 1995: Computational sensitivity studies and comparison with experiment for polarimetric radar parameters. COST75 Weather Radar Systems, International Seminar, Brussels, 20-23 September 1994, Report EUR 16013 EN.
- Hagen, M., J. Hubbert, C. Richter, V.N. Bringi, and P. Meischner, 1993: Bright band observations with radar and aircraft. 26th Conf. Radar Meteorol., Amer. Meteorol. Soc., pp. 304-305.
- Holt, A.R., 1984: Some factors affecting the remote sensing of rain by polarization diversity radar in the 3- to 35-GHz frequency range. Radio Sci., **19**(5), pp. 1399-1412.
- Meischner, P.F., M. Hagen, T. Hauf, D. Heimann, H. Höller, U. Schumann, W. Jaeschke, W. Mauser, and H.R. Pruppacher, 1993: The Field Project CLEOPATRA, May- July 1992 in Southern Germany. Bulletin of the Amer. Meteorol. Soc., **47**(3), pp. 401-412.
- Schroth, A.C., M.S. Chandra, and P.F. Meischner, 1988: A C- band coherent polarimetric radar for propagation and cloud physics research. J. Atmos. Ocean. Techn., **5**, pp. 803-822.
- Vivekanandan, J., V.N. Bringi, and R. Raghavan, 1990: Multiparameter Radar Modelling and Observations of Melting Ice. J. Atmos. Sci., **47**(5), pp. 549-564.

THE HALLETT-MOSSOP PROCESS IN NEW MEXICAN SUMMERTIME CUMULI

Alan Blyth (1) and John Latham (2)

(1) Physics Dept., NMIMT, Socorro, NM 87801, USA

(2) MMM Division, NCAR, Boulder, Colo 80307, USA

1. INTRODUCTION

The Hallett-Mossop process of secondary ice-particle production (H-M) has been found to be of primary importance in the glaciation of various cloud-types, including continental summertime cumuli, studied in New Mexico by in a host of detailed field experiments.

However, there exists no good quantitative representation of H-M in clouds, nor an acceptable understanding of the influence of specified cloud parameters on the glaciation process resulting from it. This is, in our view, largely because the treatment of glaciation has not been placed in an accurate dynamical context. We decided, therefore, to take advantage of the detailed dynamical information available on these New Mexican clouds to construct a computational model of their glaciation via H-M. A major objective of this programme of work was to achieve a quantitative understanding of the sensitivity of the glaciation process to the dynamical (and also microphysical) characteristics of the clouds.

2. THE GLACIATION MODEL

The airborne and ground-based field experiments cited earlier have shown that these summertime cumuli possess a

multi-thermal structure in which a series of bubbles rise sequentially - with quiescent intervals between them - through the existing cloud at a speed w typically between 3 and 10m/s. Each one, having penetrated the cloud mass, stops and then descends to a point at which its summit is at some general cloud-top level. These bubbles are typically about 2km wide and 3km deep. The upper regions of these thermals are characterised by lateral outflow, at the outer extremities of which downdraughts occur. These downdraughts - and hydrometeors contained within them - may subsequently mix with the inner regions of the cloud (ascending thermals or quiescent regions, according to its stage of development). Radar and airborne measurement shows that when the clouds have become well established, graupel pellets exist within them at all levels above the 0C isotherm.

All the above-mentioned features are reproduced in rather simple form in our model. The cloud consists of four regions: the main updraught; the quiescent (or debris) region, characterised by zero updraught velocity; the cloud top; and the downdraught region. The values of updraught speed w and liquid-water-content L in each of these regions are prescribed, the values selected being based on field observation.

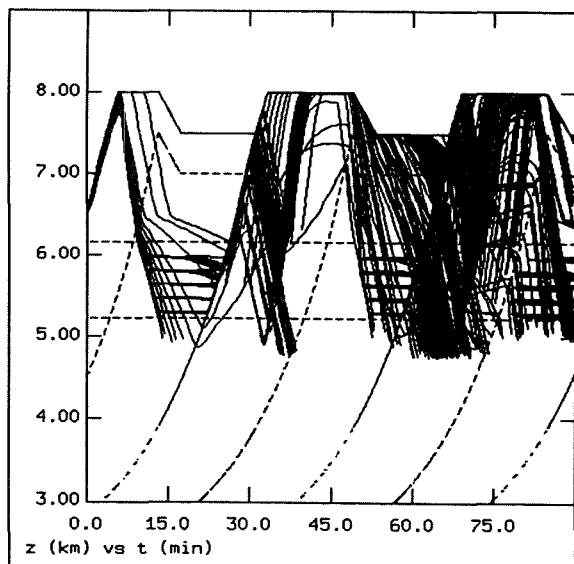


Figure 1. Characteristic set of ice particle trajectories.

At zero-time no ice crystals exist in the cloud, and graupel pellets of a range of sizes are introduced at a specified level (z_i) consistent with radar observations of the origins of the earliest precipitation particles. These follow a variety of trajectories dependent on their size (fall-speed) and the value of w in their locality. They grow by accretion of supercooled water droplets, and when they pass through the H-M temperature band (-3 to -8°C) they generate ice crystals at a rate - determined from laboratory experiments - dependent on their accretion rate. The crystals so created grow first by vapor diffusion and subsequently by riming - at which point they are themselves capable of generating splinter progeny when in the H-M zone.

The growth equations for these ice particles and assumed expressions for the terminal velocities V of the graupel pellets are of the standard forms. Prior to entering the riming stage of growth, the ice crystals are assumed to possess

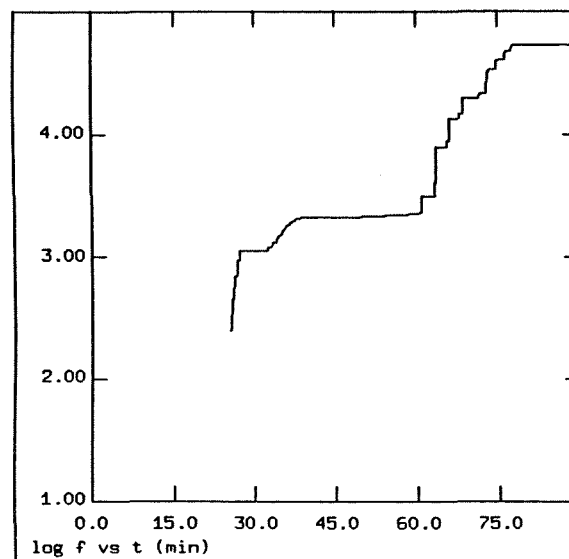


Figure 2. Typical plot of multiplication factor f versus time.

zero fall-speed.

Parameters which we expected to exercise a significant influence on the development of glaciation via H-M include: w ; L ; L/L_{ad} (the ratio of the actual to the adiabatic liquid-water-contents); H , the thermal depth; X , the inter-thermal interval; the sizes D and number concentrations N_g of the graupel pellets at time $t=0$. We also envisaged that the rate of glaciation will vary according to whether or not mixing between the downdraughts and the central regions of the cloud is allowed.

Figure 1 presents a typical set of computed ice-particle trajectories over a period of about 80 minutes following the introduction (at time $t=0$ and altitude z_i) of graupel pellets into a thermal. We see that as they ascend in the updraught, they become vertically displaced according to their sizes (the larger ones having greater terminal fall-speeds, V). The smaller ones reach cloud-top, reside there for a while before being carried to lower altitudes

by the downflow of air and then - once out of the downdraught - falling more slowly (as evidenced by the sharp increase of trajectory gradient revealed in the figure). The larger pellets are seen to achieve values of $w = V$ (the condition for descent) before they reach cloud-top. Thus, at this stage, all graupel pellets are falling through the quiescent region towards ground, growing (and falling faster) as they do so. Figure 1 shows that as the largest pellets fall through the Hallett-Mossop zone (H-M) they generate ice splinter progeny which reside at their level of creation for a while. Their parents fall out of the cloud. The second thermal now ascends into the cloud, sweeps up the ice splinters and then the smaller graupel pellets, which have not yet fallen to the H-M region. All these particles are transported upwards, the splinters and the smallest remaining primary graupel pellets up to the cloud top; the large pellets for some more limited distance before falling down again, into the H-M zone and generating further splinters. Such patterns of trajectory are duplicated as further thermals ascend through the cloud.

Figure 2 shows the associated time-development of the glaciation process, expressed in terms of a multiplication factor f , defined as the ratio of the number of ice particles in the cloud at time t to that at $t=0$. The curves for f are seen to reflect strongly the multi-thermal nature of the cloud.

Such pairs of curves were produced for a large range of values of all salient parameters, covering the ranges observed in these New Mexican summertime cumuli, in a series of field experiments over the past few years.

3. DISCUSSION

Analysis of the kind outlined in the preceding section revealed that the ice-particle trajectories and the concomitant glaciation rate via the Hallett-Mossop process are sensitive - to different degrees - to all the parameters examined. The liquid-water-content L in the updraught region of the model cloud appears to be the parameter which exerts most influence upon the glaciation rate via H-M, as expressed by the multiplication factor f . This is because as L increases the graupel pellets grow faster and thus enter the H-M zone and start producing ice splinters sooner. The significant sensitivity of f to the liquid-water-content in the debris region is attributable to the same argument.

Overall, it appears that the most rapid ice-particle multiplication is produced by combinations of parameter values which produce rapid growth of graupel pellets, high thermal frequency and efficient transport between cloud-top and the Hallett-Mossop temperature band. The pronounced degree of structure revealed by examination of the figures illustrating the variation with time of the multiplication factor f is strongly indicative of the importance in the glaciation process of the dynamical (multi-thermal) nature of the New Mexican summertime cumulus clouds.

The role of downdraughts - in some circumstances - in expediting secondary ice particle production is similar in principle to that which the reported large supercooled drops of drizzle- or raindrop dimensions may play in these clouds. In the case of the drops, their function is to intercept ice crystals and immediately freeze

to become riming agents (graupel pellets) capable (when in the H-M band) of producing splinter progeny. Thus - in this case - the glaciation process is enhanced because the lengthy process of vapour-growth of an ice crystal to a size at which it can rime efficiently is instantaneously circumvented. It is intended at some later stage explicitly to introduce large supercooled drops into the model, both to take account of their above-mentioned role in shortening the process of graupel formation, and to encompass the possibility that they may further enhance ice particle multiplication by ejecting ice

splinters as they freeze.

It is also planned both to examine the extent to which the predictions of our model are in conformity with field evidence obtained in studies of the glaciation of these New Mexican clouds; and to utilise further versions of this model to examine other cloud types, such as the tropical cumuli studied in the Toga Coare experiment.

ACKNOWLEDGEMENTS

This work was supported by the UK Meteorological Office (Hadley Centre).

MICROPHYSICAL PROPERTIES OF ARCTIC CYCLONES

David Hudak¹, Roland List² and Terry Krauss³

¹Atmospheric Environment Service, Downsview, Ontario, M3H 5T4, Canada

²Department of Physics, University of Toronto, Toronto, Ontario, M5S 1A7, Canada

³Atmospheric Environment Service, Saskatoon, Saskatchewan, S7N 3H5, Canada

1. INTRODUCTION

During the autumn in the western Canadian Arctic, cyclones are a common occurrence. They can bring hazardous weather and alter the ice coverage in the Beaufort Sea. How the location, occurrence and severity of these storms may change as a result of global change is a major concern. The goal of this study is to better understand the microphysical properties of the cloud systems associated with these storms so that ultimately their impacts are properly represented within climate predictions.

The autumn is the time when the general circulation changes from Pacific control to Arctic control and the meteorological elements are experiencing profound changes (Hudak et al., 1995). The experimental area is shown in Figure 1. Pacific disturbances that affect the area typically redevelop after they leave the Gulf of Alaska and cross the mountains of the Yukon. Extensive cloud systems and warming at all levels are characteristics of their approach. There is also a major west to east storm track along 70°N. When active, cyclones of Arctic origin move rapidly along the coast. Their cloud systems are typically shallower and prone to changes in surface features such as sea ice and snow cover.

There appear to be some fundamental differences in the microphysical evolution and precipitation development within these two types of systems. This study is designed to quantify these differences in a manner suitable for inclusion in numerical models.

2. EXPERIMENTAL DESIGN

The Beaufort and Arctic Storms Experiment (BASE) was conducted in the autumn of 1994 over the southern Beaufort Sea and northern Mackenzie Basin. Environment Canada was the lead agency for the project. The other main participants included the University of Toronto and Hokkaido University in Japan.

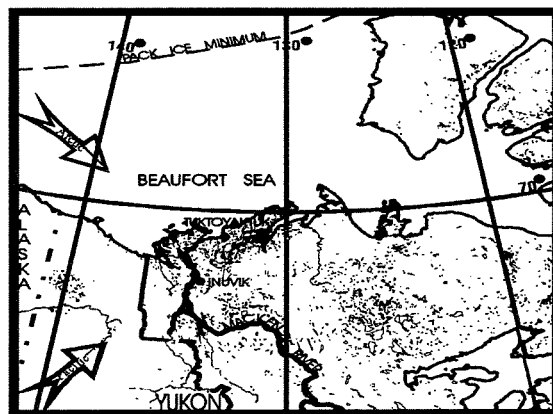


Figure 1: A map of the experimental area. The arrows indicate the influence of the Arctic and Pacific air streams.

The research aircraft deployed was a Convair-580 operated by the National Research Council of Canada. In addition to an extensive suite of cloud physics instrumentation, the aircraft also had a dropsonde capability. The main observing site was Inuvik (Figure 1). There, the facilities included an X-band Doppler radar, a network of five mesonet stations, precipitation observations with two PMS laser imaging ground probes, two microwave radiometers and the chemical analysis of precipitation samples. At the operations centre in Inuvik there was a HRPT satellite system to receive AVHRR data from the NOAA polar orbiting satellites. In addition, near real time results from the Mesoscale Compressible Community model (MC2) were received via a dedicated satellite uplink to help with project planning (Benoit, 1996). The model was run once per day with a horizontal resolution of 15 km out to 30 hr. A second observation site was at Tuktoyaktuk (Figure 1). There, an X-band Doppler radar with dual linear polarization was operated along with a surface mesonet station and an upper air station (Asuma et al., 1996).

A summary of the 13 Intensive Operational Periods (IOPs) is given in Table 1. The experiment collected unprecedented information on a wide variety of cloud systems over the Canadian Arctic.

Table 1: A summary of the Intensive Operating Periods (IOPs) on BASE.

IOP	TIME PERIOD (UTC)	DESCRIPTION
1	1800 Sept. 3 - 1800 Sept. 4	WEAK LEE CYCLOGENESIS
2	2100 Sept. 4 - 0000 Sept. 6	TROUGH AND UPSLOPE SNOWFALL
3	1200 Sept. 8 - 1200 Sept. 9	BEAUFORT MESOSCALE SYSTEM & CLOUD CHARACTER
4	1800 Sept. 14 - 1200 Sept. 16	PERSISTENT RAIN AND ICE PELLETS
5	0000 Sept. 18 - 1200 Sept. 19	CYCLOGENESIS NEAR NORMAN WELLS
6	0000 Sept. 21 - 0000 Sept. 22	UNEXPECTED SNOWFALL
7	0600 Sept. 24 - 1800 Sept. 26	DEEP, STABLE CLOUDS
8	1800 Sept. 26 - 2200 Sept. 26	PRECIPITATION BANDS ALONG CASTLINE
9	1700 Sept. 27 - 2200 Sept. 27	COLD CORE OF ARCTIC AIR
10	1730 Sept. 29 - 2300 Oct. 1	SERIES OF MESOSCALE VORTICES
11	0600 Oct. 3 - 0130 Oct. 5	TROUGH AND VERTICAL CLOUD PROFILES
12	0600 Oct. 6 - 0000 Oct. 7	HEAVY SNOW
13	0300 Oct. 9 - 0000 Oct. 11	PROLONGED SNOW IN LOW CENTRE

3. CASE STUDY (IOP 7)

In this section the observations taken at Inuvik during IOP 7 are summarized. This cyclone, significant in that it was associated with a strengthening of the circumpolar vortex, was the first of a series of Arctic disturbances moving along the Arctic coast (Hanesiak et al., 1996). This marked the beginning of the final phase of the freeze-up of the Beaufort Sea. During the event, 6.6 cm of snowfall over 30 h was recorded at Inuvik.

Figure 2 gives a time series of the vertical profiles from the vertical scans of the Doppler radar. The shading indicates the intensity of the echo as a function of height and fall velocity. Precipitation was initially detected around 5 km, or -25°C at 2340Z on September 24. Figure 2 shows the sequences of events over the next 4 h leading to the onset of precipitation at the ground by 0328Z on September 25. Initially, light drizzle was observed at the surface, but it quickly changed to light snow.

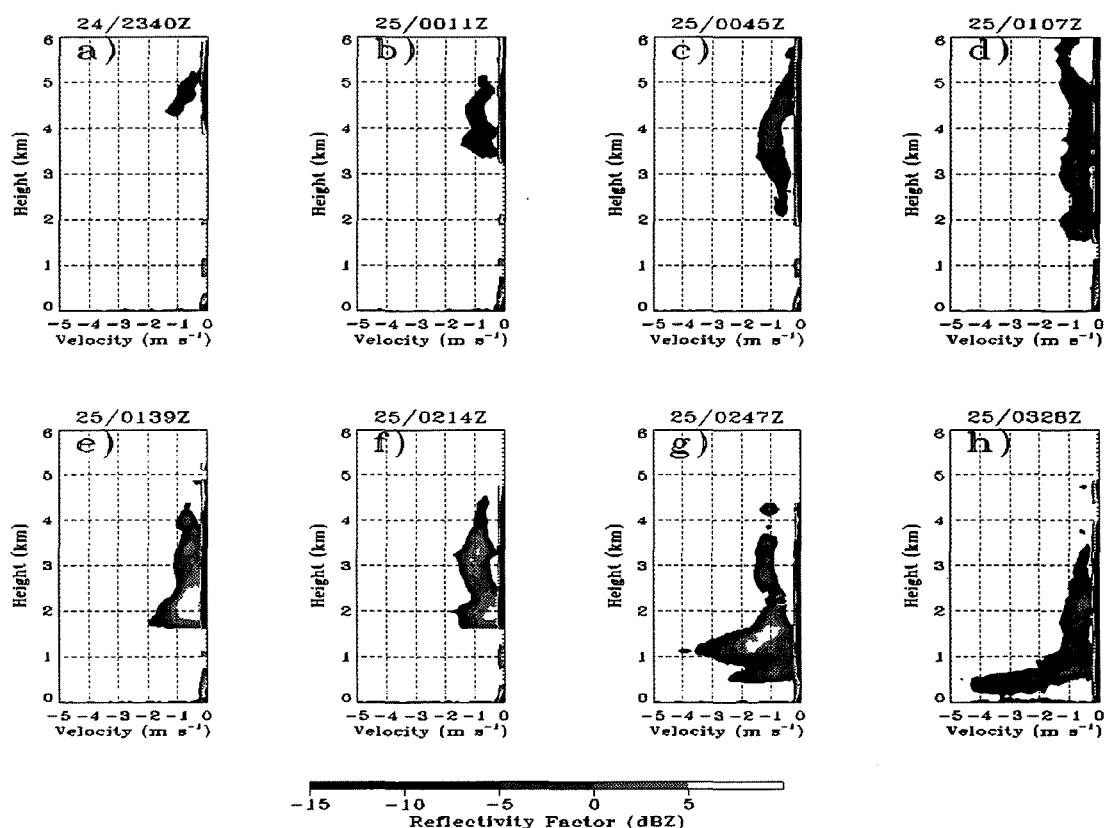


Figure 2: A time series of vertical profiles of Doppler radar reflectivity. The shading represents the intensity of the echo as a function of fall velocity.

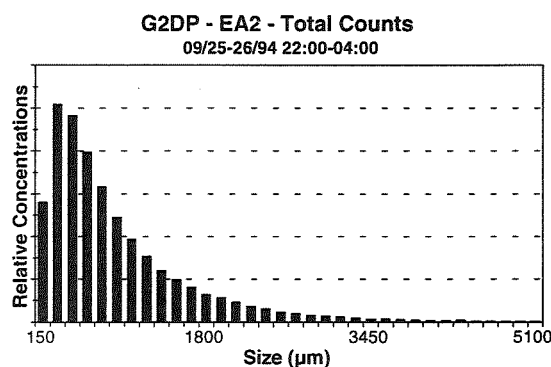
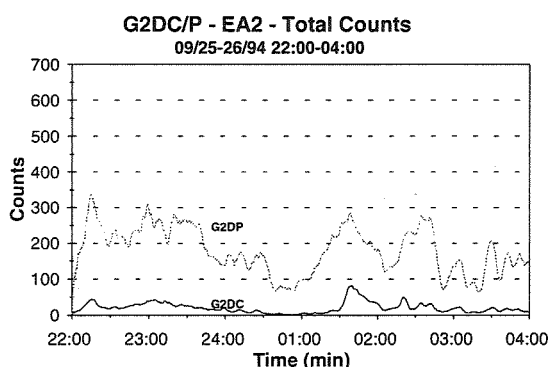
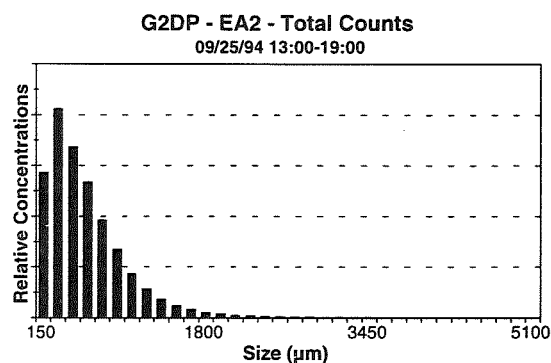
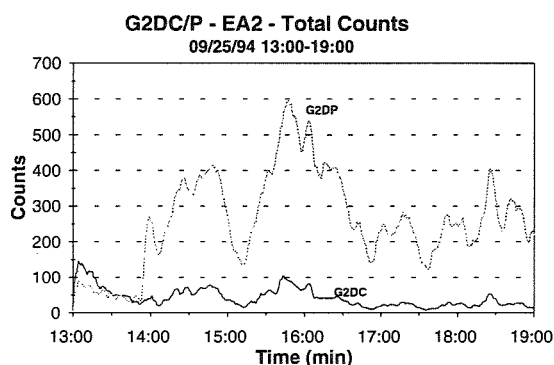
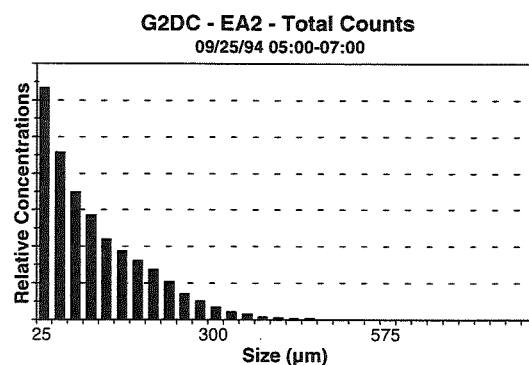
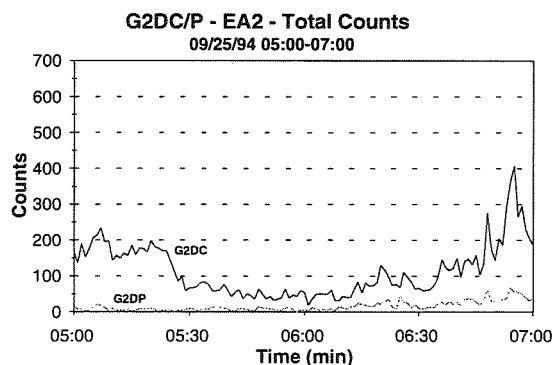


Figure 3: A time series of particle counts by the PMS optical array 2D-C and 2D-P ground probes, a) period one (top), b) period two (middle), and c) period three (bottom).

There were three distinct periods of significant snowfall associated with this event. Figure 3 gives the total counts as observed by the PMS 2D-C and 2D-P ground probes during these three periods. The former probe sizes particles up to 1.6 mm, and the latter probe to 9.6 mm. Figure 4 gives the associated particle size spectra. The spectra were derived using the extended area technique (Heymsfield and Parrish, 1978). Figure 5 gives the vertically pointing Doppler radar data during the final two periods.

Figure 4: Average particle size spectra as observed by the PMS optical array ground probes, a) period one for the 2D-C(top), b) period two for the 2D-P (middle), and c) period three for the 2D-P(bottom).

The first period occurred very close to the cyclone centre. It was characterized by small particles, up to 0.3 mm (Figure 3a, 4a). The images from the probe revealed that the particles were irregular in shape, i.e., no discernible crystal type was detected, with evidence of accretion. This was supported by the microwave radiometer that showed significant amounts of supercooled liquid present.

The second period took place in the strong northerly winds behind the low. The particles were larger during this time, up to 2 mm in size (Figure 3b, 4b). The images showed evidence of accretion

with the dominant crystal types being plates and columns. The vertical profile of radar reflectivity (Figure 5a) indicates that the accretion was occurring in the lowest km where the mean fall velocity of the particles increased from 1 m s^{-1} to 2 m s^{-1} (Hudak and Nissen, 1996).

The final phase was associated with weakening winds and a gradually thinning cloud deck ahead of an approaching ridge of high pressure. The precipitation particles were the largest during this period, up to 3 mm (Figure 3c, 4c). Before 0000Z on September 26, large aggregates were present with the only discernible crystal shape being dendritic. It was during this period that the maximum snowfall accumulation occurred. Later on, large plates became the dominant crystal type. The vertical profile of radar reflectivity (Figure 5b) indicated mean terminal velocities less than 1 m s^{-1} . This is consistent with the hypothesis that aggregational and diffusional growth were now the dominant mechanisms.

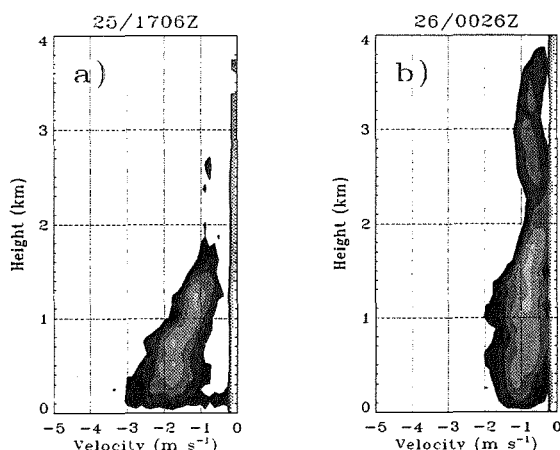


Figure 5: A time series of vertical profiles of Doppler radar reflectivity during a) period two, and b) period three. The scale is the same as Figure 2.

The vertical moisture flux was estimated from the vertically pointing Doppler radar scans using appropriate empirical relationships to convert reflectivity to water content (Battan, 1973). It showed the following pattern across the storm system. As the disturbance approached, the level of the maximum downward vertical precipitation flux gradually lowered. It reached its minimum height just to the rear of the low at a height of 0.5 km, then rose again further from the low.

4. SUMMARY

The results of such diagnostic, observationally-based studies will lead to conceptual models on precipitation formation in the Arctic where it is well known that models and remote sensing have

difficulties. These studies also have the benefit of bringing together all the relevant information into a consistent data set that can be used for model validation. To be able to identify, understand, and quantify the critical processes that influence water and energy cycles in high latitudes will be an important contribution to our understanding of global climate issues.

5. ACKNOWLEDGMENTS

The authors wish to acknowledge the assistance of Mr. Jim M.C. Young, Mr. Alan Thomson, and Ms. Tatiana Potylitsina in this work. The funding was provided in large part by the Program on Energy, Research and Development of Natural Resources Canada and is gratefully acknowledged.

6. REFERENCES

- Asuma Y., K. Kikuchi, H. Uyeda, S. Iwata, T. Shimamura, S. Iwata, R. Kimura, K. Tsuboki, R. Stewart, D. Hudak, E. Hudson, and G. Moore, 1996: 'Structures of meandering band clouds observed by dual-polarization Doppler radar during the BASE period'. *12th Intl. Conf. on Clouds and Precipitation*, Zurich, Switzerland, 19-23 August, 1996.
- Battan, L.J., 1973: 'Radar Observations of the Atmosphere'. *University of Chicago Press*, Chicago, Illinois, 324 pp.
- Benoit, R., S. Pellerin, and W. Yu, 1996: 'MC2 model performance during the Beaufort and Arctic Storm Experiment'. *Atmos.-Ocean*, accepted.
- Hanesiak, J.M., R.E. Stewart, K.K. Szeto, D.R. Hudak and H.G. Leighton, 1996: 'The structure, water budget and radiational features of a high latitude warm front'. *J. Atmos. Sci.*, submitted.
- Heymsfield, A.J., and J.L. Parrish, 1978: 'A computational technique for increasing the effective sampling volume of the PMS two-dimensional particle size spectrometer'. *J. Appl. Meteor.*, 17, 1566-1572.
- Hudak, D.R., and R. Nissen, 1996: 'Doppler radar applications in major winter snowstorms'. *Atmos. Research*, in press.
- Hudak, D.R., R.E. Stewart, G.W.K. Moore, and E.T. Hudson, 1995: 'Synoptic considerations of storms in the southern Beaufort Sea - expectations for BASE'. *Proc. 4th Conf. on Polar Meteor. and Oceanography*, Dallas Texas, 234-237.

SIZE DISTRIBUTION OF HYDROMETEORS THROUGH THE MELTING LAYER

Eszter Barthazy, Werner Henrich and Albert Waldvogel

Atmospheric Science, ETH, CH-8093 Zürich, Switzerland

1 INTRODUCTION

The melting, aggregation and breakup of ice particles and snowflakes within the melting layer are important processes in stratiform precipitation systems. Many radar measurements with different radar parameters have been made in stratiform precipitation systems. Some of them were combined with simultaneous in situ measurements within the melting layer to improve the interpretation of the measurements (e.g. Hagen *et al*, 1993, Stewart *et al*, 1984). In spite of all these efforts, the aggregation and breakup of snow within the melting layer are quantitatively not understood very well. One of the reasons is the lack of extensive in situ measurements of the size distribution of hydrometeors through the melting layer.

This study presents for the first time simultaneous measurements of the bright band with radars, of drop size distribution with a disdrometer, and of snow size distribution with a snow spectrometer for stratiform precipitation. The experiment was carried out on February 17, 1995 near Zürich. The aim of this study is to give an overview of the first results.

2 INSTRUMENTATION AND EXPERIMENTAL SETUP

We used a snow spectrometer to measure the size distribution and velocities of hydrometeors, especially snow. The instrument was developed and built at the Institute of Atmospheric Science at the ETH in Zürich. A light source (an incandescent lamp) illuminates a one-dimensional array of photoelements which is read with a frequency of 7.3 kHz. The array consists of 256 elements and yields a horizontal resolution of 235 μm (maximum particle size is 31.5 mm). Each particle falling through the measuring plane casts a shadow on the array and produces a pseudo-two-dimensional image consisting of a number of rows depending on the fall velocity and size of the particle and the read-out frequency. The image and the exact recording time of each particle are stored and processed later. The horizontal extension of the particle is given by the row with the largest number of covered elements. Assuming a certain ratio for the vertical to the horizontal extension, the fall velocity of the particle can be deduced. For raindrops, this ratio is a function of the drop diame-

ter (deformation due to friction). For snowflakes we used a ratio of 1.

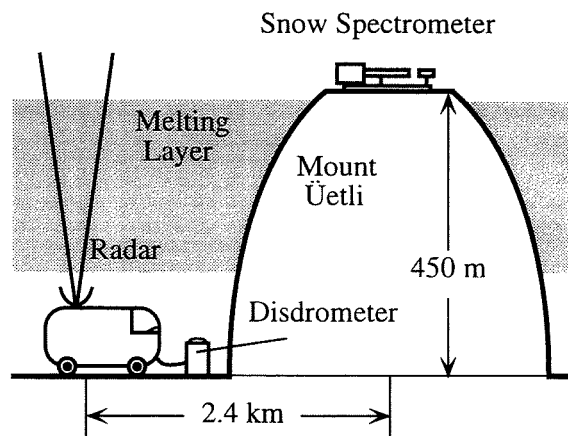


Figure 1: *Experimental setup. The picture shows the situation at the end of the measuring period (melting layer between snow spectrometer and disdrometer).*

Fig. 1 gives an overview of the experimental setup. The snow spectrometer was placed on top of a mountain (top station). A vertically pointing X-band Doppler radar and a disdrometer (Joss and Waldvogel, 1967) were located ~ 2 km southeast and 450 m below the spectrometer (bottom station). This radar had a height-resolution of 50 m, a Nyquist velocity of 32 m/s, and a velocity-resolution of $\Delta v = 0.5$ m/s. A second Doppler radar (C-band, not visible in fig. 1) was located in a distance of 5.7 km and was operated in RHI and PPI modes to survey the evolution of the precipitation.

3 CASE STUDY

On the evening of February 17, 1995 a weak cold front passed the measuring site. At the beginning of the measurements the melting layer was above the top station. During the following five hours the melting layer was descending slowly and steadily and at the end it was located between the top and the bottom station. The snow spectrometer at the top station was first measuring rain, then melting snow and at last snow. The disdrometer at the bottom station was measuring rain all the time, no melting snow was observed visually. The PPI and RHI scans

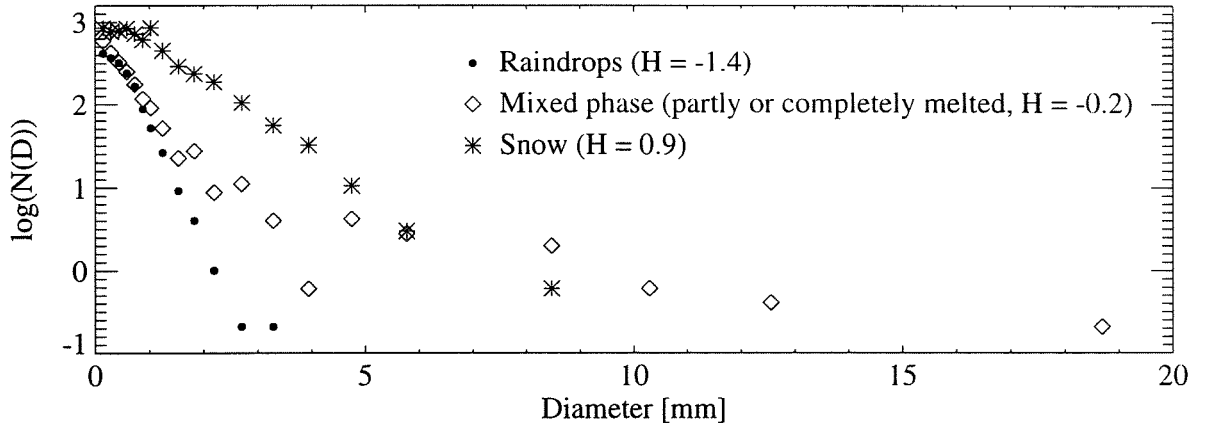


Figure 2: Particle size distribution $N(D)$ ($\text{m}^{-3}\text{mm}^{-1}$) measured by the snow spectrometer (integrated over 5 minutes). The parameter H gives the position of the snow spectrometer relative to the bright band (see text).

of the C-band radar reveal stratiform and homogeneous structures of the precipitation. The precipitation region had an extension of ~ 100 km with the center located at the measuring site. Nevertheless there were some small variations with time, the intensity of the precipitation was somewhat increasing during the first two hours (from 1 to 4 mm/h) and then decreasing again (to 1 mm/h).

The vertically pointing radar gives profiles of reflectivity with a resolution in time of 30 s. The bright band was well developed and had an extension between 300 m and 550 m. These profiles were used to determine the position of the snow spectrometer wi-

Since the horizontal distance between top and bottom station was very short and the precipitation showed well developed stratiform structures it seems to be justified to compare size distributions of hydrometeors measured at different altitudes and times. Therefore we used this position to transform the time-dependent measurements into position-dependent data within the melting layer. The parameters of the position were chosen to be $H = 0$ at the maximum of radar reflectivity and $H = 1$ at the top of the bright band. Fig. 3 shows a typical profile of radar reflectivity. The solid horizontal line is the position of the maximum of radar reflectivity ($H = 0$) and the dashed line gives the top of the bright band ($H = 1$). The position of $H = -1$ (dotted line) is chosen in the same vertical distance below the maximum of radar reflectivity as is the top of the bright band above the maximum. All profiles of reflectivity were very similar and nearly symmetric relative to the maximum. Therefore we find that the parameter $H = -1$ represents the bottom of the bright band quite well. From now on all results of the experiment are given not as time-dependent data but as position-dependent data.

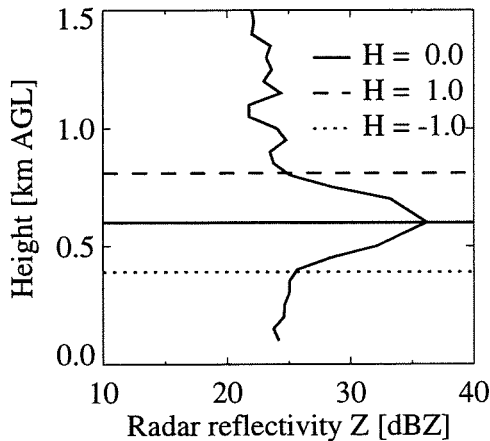


Figure 3: Radar reflectivity profile with a well developed bright band. The three horizontal lines indicate three possible positions of the snow spectrometer with the corresponding values of H : $H = 0$ maximum of radar reflectivity, $H = 1$ top of the bright band, $H = -1$ "bottom" of the bright band (see text for further explanation).

thin the melting layer, i.e. relative to the maximum in radar reflectivity.

Fig. 2 shows the particle size distribution for selected positions within the melting layer. At the beginning of the experiment the snow spectrometer was measuring rain. The drop size distribution is given by dots. At the end of the experiment there was dry snow and these data are given by stars. Both particle size distributions (rain and snow) can be approximated by an exponential size distribution ($N(D) = N_0 e^{-\Lambda D}$). Fig. 4 gives the fall velocities of the hydrometeors. Again, as in fig. 2, the rain drops are given by dots and the snowflakes given by stars. The fall velocities of the snowflakes as measured by the snow spectrometer are in good agreement with the literature (e.g. Locatelli and Hobbs, 1974) as well as the fall velocities of the rain drops. Data given by open diamonds show as well in fig. 2 as

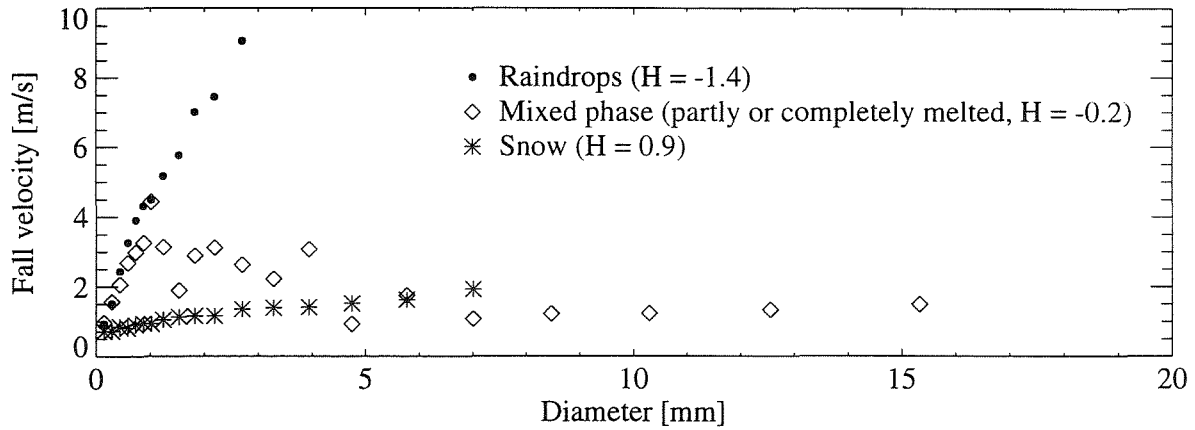


Figure 4: Particle fall velocities measured by the snow spectrometer (integrated over 5 minutes). For the parameter H see text.

in fig. 4 the measurements for partly melted snow mixed with rain drops. Note the bend in both, the particle size distribution and the fall velocity. Two parts may be identified, the first part corresponds to the completely melted particles ($D < 1$ mm) and the second part to the partly melted particles. The size distribution of the first part is very similar to the one of rain (dots) and can be approximated by

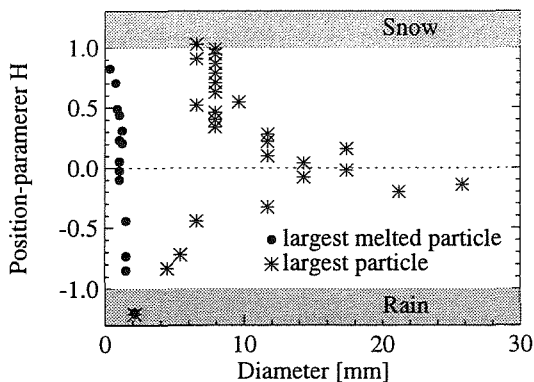


Figure 5: Largest measured particle by the snow spectrometer and largest melted particle (i.e. rain drop) within the melting layer.

an exponential DSD. The position of the bend in the size distribution and in the fall velocity gives a limit for the diameter of the largest completely melted drops. This limit depends on the position of the spectrometer within the melting layer. Fig. 5 gives the sizes of these largest melted particles (i.e. rain drops) in dependence of the parameter H . Also included in fig. 5 are the largest (unmelted) particles as measured by the snow spectrometer. The largest particles throughout the entire experiment were measured approximately at the height of the maximum of radar reflectivity. The temperature at this height was 1–2°C. Stewart *et al* (1984) give profiles of ice

particle maximum size and radar reflectivity through the melting layer. The largest particles are reported at temperatures of approximately 1°C. This corresponds very well with our findings. The maximum in radar reflectivity is reported not to coincide with the largest particles, they observe the maximum of the bright band ~ 200 m below the largest particles. In contrast to this stand the findings of Zrnić *et al* (1993). They measure the largest particles in stratiform precipitation a few hundred meters below the maximum in radar reflectivity.

Fig. 6 shows the flux densities of particles (total number per square meter and per minute) as measured by the snow spectrometer and the disdrometer. The flux densities are more or less equal for both instruments except for a short period when the snow spectrometer was at the height of the maximum of radar reflectivity. The particle flux at the spectrometer was during this period by a factor of 2–3 smaller than the particle flux at the disdrometer. Since this is coincident with the occurrence of the largest particles ($D > 15$ mm), this effect is most probably due to enhanced aggregation in the the melting layer. To be exact, the decrease of particle flux during the above mentioned period (see fig. 6 (a)) is most probably due to aggregation dominating over breakup and the following increase (fig. 6 (b)) likely due to breakup dominating over aggregation. Furthermore, the surprising agreement of particle fluxes at the end of the experiment (i.e. the snow spectrometer was measuring snow at at the top of the melting layer, the disdrometer was measuring rain at the bottom of the melting layer) seems to imply that, whatever is happening within the melting layer, one snowflake yields one raindrop.

4 CONCLUSION

From the results of our measurements in section 3, we can conclude the following:

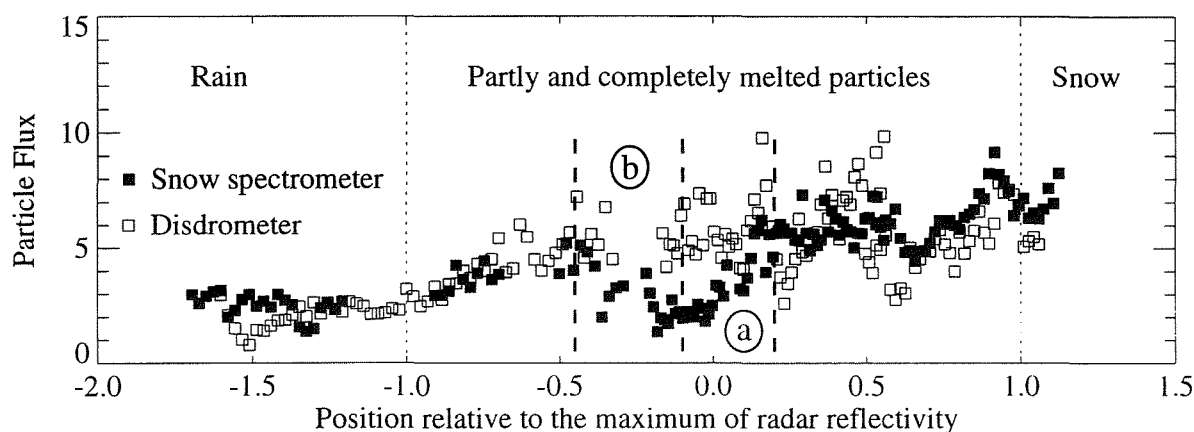


Figure 6: Particle flux density ($10^4 \text{ m}^{-2} \text{ min}^{-1}$) for the snow spectrometer and the disdrometer. Note the difference in the flux density for the part labeled (a) where aggregation dominates over breakup and the part labeled (b) where breakup dominates over aggregation.

1. The largest particles are observed approximately at the maximum of radar reflectivity of the vertically pointing Doppler radar.
2. In the middle of the melting layer the size distribution of the hydrometeors is significantly different from an exponential shape. Two parts may be identified, the first part corresponds to the completely melted particles and the second part to the partly melted particles. The first part (i.e. the melted drops) can be approximated by an exponential DSD. A maximum size for these completely melted drops can be identified.
3. Considering the particle size distributions and the flux densities within the bright band aggregation seems to dominate over breakup in the upper part of the melting layer. The same arguments can be used to show that breakup is dominating over aggregation in the lower part of the melting layer (see fig. 6 (a) and (b)).
4. The flux densities of particles measured with the snow spectrometer just above the bright band and the disdrometer just below the bright band show an astonishing agreement. This might imply that one snowflake yields one raindrop.

6 ACKNOWLEDGMENT

The authors wish to express their appreciation to D. Högl and R. Lüthi for developing, building and te-

sting the snow spectrometer. Furthermore, we also would like to thank M. Semmler for valuable calculations.

7 REFERENCES

- Hagen, M., J. Hubbert, C. Richter, V. N. Bringi, P. Meischner, 1993: Bright band observations with radar and aircraft. *Preprints, 26th Conf. on Radar Meteor., Norman, Oklahoma, Amer. Meteor. Soc.*, 304–305
- Joss, J., and A. Waldvogel, 1967: Ein Spektrograph für Niederschlagstropfen mit automatischer Auswertung. *Pure Appl. Geophys.*, **68**, 240–246
- Locatelli, J. D., and P. V. Hobbs, 1974: Fall speeds and masses of solid precipitation particles. *J. Geophys. Res.*, **79**, 2185–2197
- Stewart, R. E., J. D. Marwitz, J. C. Pace, and R. E. Carbone, 1984: Characteristics through the melting layer of stratiform clouds. *J. Atmos. Sci.*, **41**, 3227–3237.
- Zrnić, D. S., N. Balakrishnan, C. L. Ziegler, V. N. Bringi, K. Aydin, T. Matejka, 1993: Polarimetric signatures in the stratiform region of a mesoscale convective system. *J. Appl. Meteor.*, **32**, 678–693

THEORETICAL AND FIELD INVESTIGATIONS OF THE MESO- AND MICROSTRUCTURE OF THE WINTER FRONTAL PRECIPITATION IN THE STEPPE PART OF UKRAINE

Anne M. Pirnach and Nikolaj M. Akimov, UHRI, Kiev, Ukraine

1. INTRODUCTION

Investigation of the microstructure of precipitation conducted over Meteorological Proving Ground (MPG) of Ukrainian Hydrometeorological Research Institute (UHRI) beginning from 1976 and continued to present time. The analysis of the natural and artificially modified precipitation measurements were carried out. The special rainfall measurements; the aircraft, radar, rawinsonde and network data; the numerical models and spectral analysis were used for this goal (see Akimov et al. 1974, 1984; Akimov 1977; Pirnach and Krakovskaya, 1994).

A hundred and more experiments were conducted. Precipitation rate, concentration of cloud and precipitation crystals and snowflake, number of crystals in one snowflake, periodic change of precipitation, ice concentration and other characteristics were defined.

The spectral and cross-spectral analysis of the precipitation rate were carried out for analysis of the precipitation measurements. The 5-minutes resolution data were used. The periodic structure of frontal precipitation are discussed.

2. FIELD INVESTIGATION OF WINTER PRECIPITATION MICROSTRUCTURE

The many years observation have shown that the frontal snowfall contained many shapes of ice particles (see Fig.1, in x-direction the particles forms are given in its frequency succesion). Especially, this

feature occurred for Sc where the precipitation generating layers located on the different heights with different temperature and supersaturation. The form crystal investigation have shown during period of snowfalls the highest precipitation rate (j_m) in 40% cases the basic crystal shapes are dendrites. At $j_m > 1.0$ mm/h the aggregates and the rimed ice particles occurred. The maximum precipitation rate during the observation period for these particles was 3.6 mm/h. In cases of presence of two crystals forms the precipitation intensity was more strong and ranged from 1.0 to 4.2 mm/h. Probability of combination of column and plane crystals falling was the same as snow palletes and was about 20%. The

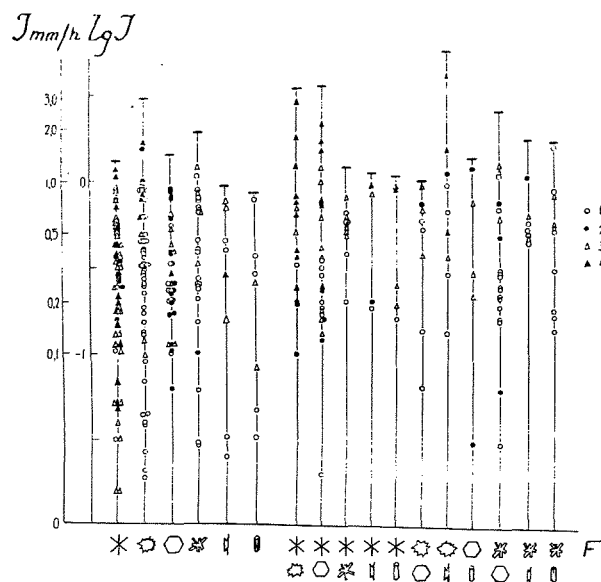


Fig.1. Influence on precipitation rate of ice particles form in MPG-region. 1) Single crystals; 2) riming crystals; 3) aggregates; 4) riming aggregates.

cells of needles were falling at $j_m > 1.5$ mm/h and snow palletes did at $j_m > 1.8$ mm/h. Their maximum intensities were 1.9 and 5.8 mm/h respectively. Palletes were falling in 16% cases. In the half of these cases the occurrence of other ice particles shapes took place. Maximum of precipitation rate for these forms was 0.8 mm/h. The needles and collomns as a basic form were found in 6% cases. Maximum intensity for these cases was 0.6 mm/h. Snowflake concentration in snowfall reached $10^3 - 10^4$ m⁻³. It was two times lower than ice crystal concentration in Ns (see Akimov et al.1974).

Total picture of measurement characteristics feature given data of observation on 4 March 1994 (see Fig.2). In this case

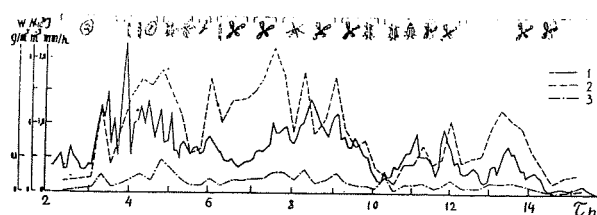


Fig.2. Time changing of intensity, j (1), particles concentration, N (2), water content, w (3), and ice particle shape. 4 March 1994.

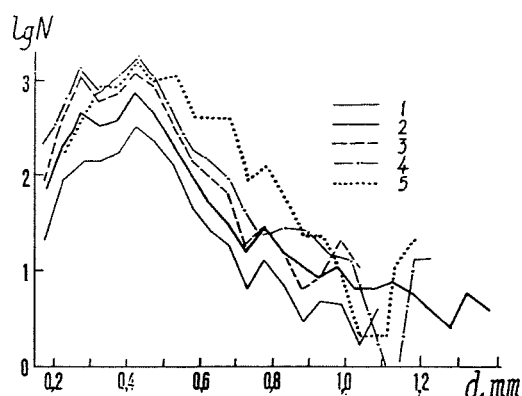


Fig.3. Snow particle spectra at the different intensity of precipitation. 1) $j < 0.30$ mm/h; 2) $j = 0.31 - 0.60$ mm/h; 3) $j = 0.61 - 0.90$ mm/h; 4) $j = 0.91 - 1.2$ mm/h; 5) $j > 1.2$ mm/h.

over MPG the snowfall from Ns connected with occluded front occurred. There are measurements of precipitation intensity, water content, concentration, shape and equivalent diameters of precipitation particles are depicted in Fig.2. It is found a simultaneous changing of precipitation and ice particles concentration. In Fig.3 ice particles spectra at different precipitation rate have shown. Because ice particles (palletes and collomns, Fig.2) have close basic sizes the influence of snowflake types on the spectrum curve was neglected. For interval from 0.3 to 1.2 mm/h an increasing of the ice concentration, N , caused an increasing of precipitation rate at conservation of a mean equivalent diameter, d_e . After $j = 1.6$ mm/h ice concentration in interval of size from 0.5 to 0.8 increased that caused increasing the mean size. An analysis of the equivalent diameter snow particles distribution $f(d_e)$ shown that the two parameter size γ -distribution occurred. For the 4 March experiment was found

$$f(d) = 9.3 d_e^{0.75} \exp(d_e/0.29)$$

The water content of the snowfall precipitation have the same range as the water content in Ns and it changed from 0.06 to 0.50 g/m³.

The frontal widespread snowfall was characterized by a strong precipitation rate oscilation. It caused spots and bands of precipitation on the ground found at analysis of network data (see Leonov and Perelet, 1967). Sizes of rainbands and spots of cloud caused a periodic change of precipitation were 30 - 50 km. Sometime they exceeded of 100 km (see Akimov and Leskov, 1977).

3. THEORETICAL STUDY OF WAVE STRUCTURE OF PRECIPITATION RATE

The spectral analysis of the 5-min discrete precipitation data is performed using the Fast Fourier Transform method. Description of the using relations is taken from Shakina 1985, etc.

Snowfalls with the longest time passing over MPG were considered. These heaviest and longest precipitation was connected with warm fronts moving northward and occluded

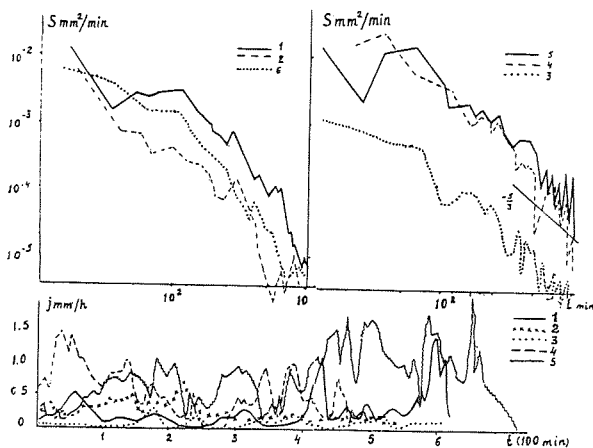


Fig.4. Rain intensity, j , and spectra of the warm fronts rain intensity, S . 1) 8 March 1987; 2) 3 March 1988; 3) 11 March 1988; 4) 19 February 1983; 5) 20 February 1981; 6) 9 March 1987.

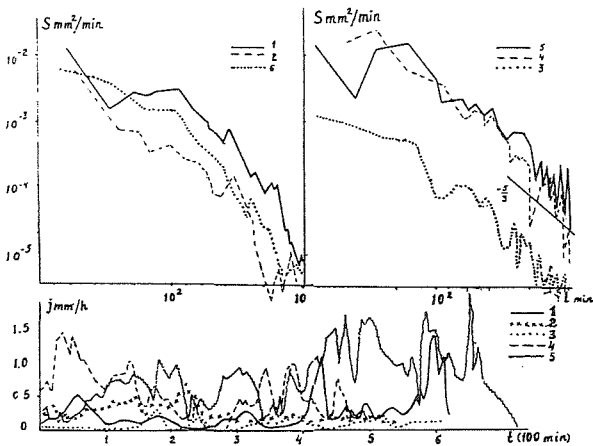


Fig.5. Rain intensity, j , spectra of occluded fronts rain intensity, S , and amplitudes, A . 1) March 17, 1976; 2) January 25, 1988; 3) January 18-19, 1988; 4) January 6, 1976; 5) March 4, 1994; 6) March 5, 1994.

ones moving eastward. In Figs. 4,5 depicted rain intensity and spectrum features of the fronts. The rain intensities and their spectrum characteristics oscillated in time and presented rainbands of a different time passing. There will be considered the precipitation measurements of 5 warm fronts and 3 occluded ones. Four warm fronts presented in Fig.4 connected with cyclones and one was moving with pressure trough (Case 5).

In mostly cases the clear periodic component appears. From chosen warm fronts heaviest precipitation was connected with front associated with pressure trough moving from South (Case 5). Two clear defined bands were located ahead front. Their time passing were 200 min and 100 min. Other two bands located in leading part of warm air mass were wider and presented practically one band with the time passing about 400 min. On spectrum these wavelength peaks presented with period $t_p > 400$ min, $t_p > 160$ min and most shorter wavelength with periods about 70, 50, 40 and 20 min, and turbulent part of spectrum at $t_p < 20$ min. As we can see from Fig.4 the spectrum with $t_p < 90$ min have slope about $-5/3$ and perhaps presented turbulent regime.

Case 1 (Fig.4) presented warm front of the southern cyclone. There are three clearly defined rainbands were found. Their time passing were 100, 40 and 60 min (from left to right). Its spectrum have peaks at $t_p > 300$ min and about 200, 90 and 35 min that perhaps presented time passing of above rainbands. The shortest wavelength presented by peaks with t_p about 25 and less 20 min. In this Case the turbulent regime rather was not found. The cases of warm front with turbulent regime were presented in Fig.4 (the right side, top row). The smallest intensity of rain was found in Case 3 (the warm front of the southern cyclone). Both wave and

turbulent regime occurred in this case. The wavelengths are with peaks at $t_p > 120$, about 70, 45 and less 40 min. The slope of spectrum about $-5/7$ take place at $t_p < 100$ min. Therefore the wavelengths on different scales occurred in considered spectra: frontal scale, large mesoscale, small mesoscale and cumulus scale, the turbulent regime occurred in several cases too (see Hobbs 1981; Shakina 1985).

The spectrum of the occluded frontal snowfall intensity presented in Fig.5. The heaviest precipitation was associated with Case 2 presented occluded front and dissipated cyclonic field. The peaks are not pronounced in the spectrum and turbulent behavior almost over all the frequencies occurred. The peaks of spectra clearly pronounced for Cases 3 and 4 that presented occluded front connected with the northwestern cyclones. They have $t_p > 300$ min, about 200, 60, 35, 25 and less 20 min. In Case 3 the rain intensity pronounced rainbands structure. There is found the prefrontal rainband with intensity maximum $j_m = 2$ mm/h. One have about the 100 min time passing with maximum intensity reached $j > 0.7$ mm/h. Three other bands with time passing about 100, 70 and 50 min occurred. Cases 1 and 4 described more detailed in Akimov et.al, 1984.

4. CONCLUSIONS

The special measurements of precipitation were fulfilled at MPG during period from 1975 to 1994. The investigation their meso- and microstructure were conducted. The ice crystal shape correspond to the concrete value of maximum precipitation intensity. It found that the snowflake concentration in snowfall reached $10^3 - 10^4$ m⁻³. In the most cases the two-parameter γ -distribution was found. The water content of snowfall is the same range as

the water content in Ns.

Spectral and cross-spectral analysis of precipitation rate were carried out for several warm and occluded fronts.

The clear periodic components were found on the different periods (up to about 8 hours). The slopes of spectra closed to $-5/3$ (the typical turbulence behavior) were found on short periods.

5. REFERENCES

- Akimov, N.M., 1977: About a snowflake formation at natural and artificial snowfall. Tr. UHRI, 162, 82-90 (in Russian).
- Akimov, N.M. and Leskov, B.N., 1977: About periodicity of particles concentration changing and intensity of solid precipitation. Tr. UHRI, 162, 91-96 (in Russian).
- Akimov, N.M., Palamarchuk, L.V. and Pirnach, A.M., 1984: Investigation of intensity and microstructure of winter frontal precipitation for real synoptic situation. Tr. UHRI, 203:56-69 (in Russian).
- Akimov, N.M., Volkov, A.D. and Leskov, B.N., 1974: Ice particles concentration in Ns. Tr. UHRI, 133, 102-109 (in Russian).
- Hobbs, P.V., 1981: Mesoscale structure in midlatitude frontal systems. Proc. JAMAP symposium, Hamburg, August 1981: 1-8.
- Leonov, M.P. and Perelet G.I., 1967: Active influence on winter clouds. Gidrometeoizdat, Leningrad, 150 pp. (in Russian).
- Pirnach, A.M. and S.V. Krakovskaya, 1994: Numerical studies of dynamics and cloud microphysics of the frontal rainbands. Atmos. Res., 33, 333-365.
- Shakina, N.P., 1985: Dynamics of atmospheric fronts and cyclones. Gidrometeoizdat, Leningrad, 263 pp. (in Russian).

SOME RESULTS OF MICROWAVE RADIATION OBSERVATION OF WINTER STRATIFORM CLOUD ALONG TIAN SHAN MOUNTAINS IN XINJIANG, CHINA

Wu Zhifang

Gao Ziyi

(The Weather Modification Office in Xinjiang, China)

1. Introduction

The potential for enhancing snowfall in winter stratiform cloud is associated with the presence of supercooled liquid water (SLW). It is very important for the researches and operations of increasing snowfall to continuously monitor the variation of SLW in clouds. Historically, this parameter has been difficult to measure by aircraft with a high cost and low efficiency. The introduction of the microwave radiometer has made the direct and continuous measurement of SLW has less difficult and more common.

This paper simply describes the method of measurement total vapor water content in atmosphere and integrated liquid water content in cloud by means of dual-channel ground-based microwave radiometer. Some results are analysed, which were observed in winter stratiform cloud along Tian Shan mountain in Xinjiang, China

2. The method of measurement of water vapor and liquid

The radiometer is a passive instrument which senses brightness temperatures emitted from water vapor and liquid along the beam path. The quantity of water vapor and liquid is measured by the magnitude of the brightness temperature at specific microwave frequency. The radiometer used in Xinjiang senses brightness temperatures at two wave length. Water vapor is sensed by 22.235 GHz (1.35 cm) channel while 25.3 GHz (8 mm) channel is used to measure liquid water. The actual measurement of water vapor and liquid is given as integrated amounts of equivalent depths in millimeters.

According to the sensitivity experiment and simulated calculation, there is nearly linear correlation between brightness temperature and water in atmosphere and clouds. The quadratic and crossing item are introduced into statistic expression because their relationship are not completely linear.

3. Results

3.1 The integrated SLW content in cloud associated with cold front passage

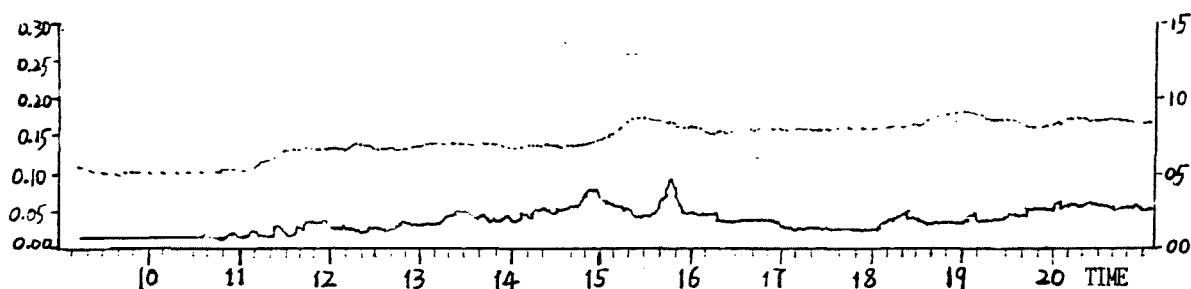


Fig. 1. Integrated quantities of vapor in mm (dashed) and liquid in mm (solid) measured by the radiometer on 24 December, 1992.

The storm of 24 December 1992 was spawned from trough which was positioned in the Middle Asia. Moderate and heavy snow occurred along Tian Shan mountain which was synonymous with a cold front passage. During this weather process, the total amount of precipitation was 6.1 mm at Changji station and 4.0 mm at the airport.

The radiometer was located at an airport, 20 kilometer from Changji, Xinjiang. It is always colder than 0°C during winter that any measurement of liquid water could be assumed to be supercooled.

SLW shown Fig. 1 indicates a gradual increase in response to the approaching system and then quick decrease by 15:42 when snowfall on the ground began. SLW maintained lower value over an hour as snow got more and more. This may be attributed to crystal sublimation exhausting a lot of SLW, which was consistent with the fact observed by aircraft. Raising SLW was again observed after cold

front passage by 20:00, Which would be in part due to the lifting effect of the post-frontal airflow by the orographic influence, resulting in the production of SLW in the norther slope of Tian Shan. The observation ceased at 21:00 because snow water permeated into the antenna of radiometer.

3.2 The integrated liquid water content in low cloud

Low cloud, referred to one of winter stratiform cloud, often appears in Zhungeer Basin, xinjiang. Its presence causes scheduled flight to be cancelled or aircraft to be forced to return. On the other hand, low cloud plays attention to the meteorological department, which would be used to increase snowfall. Low cloud system emerges after the cold air rush into basin causing snow. The vapor water in low cloud come from the evaporation of the perpetual snow on the surface of the ground.

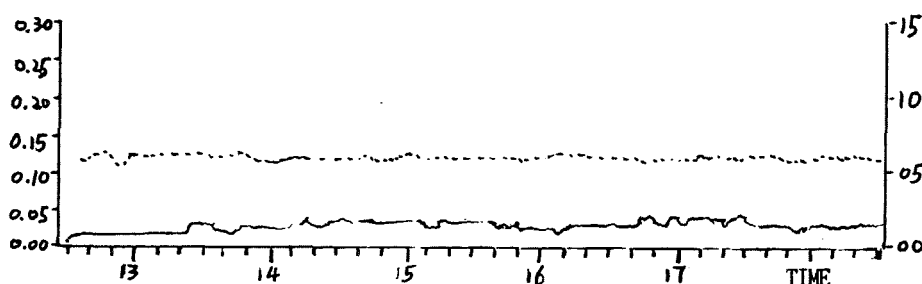


Fig. 2. Integrated quantities of vapor in mm (dashed) and liquid in mm (solid) measured by the radiometer on 13 December, 1992.

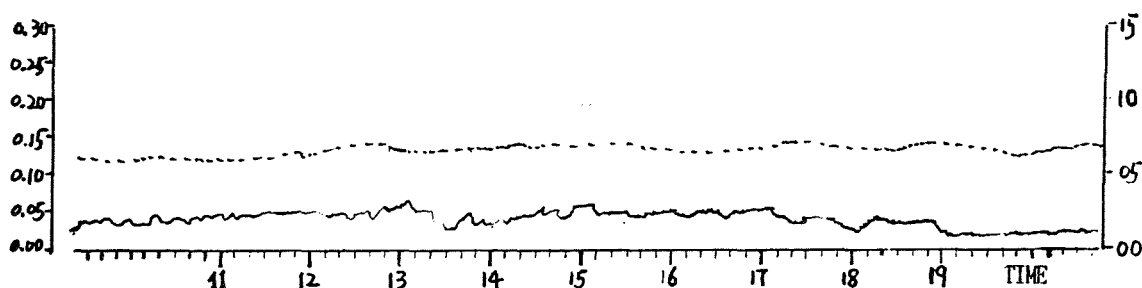


Fig. 3. Integrated quantities of vapor in mm (dashed) and liquid in mm (solid) measured by the radiometer on 31 December, 1992.

Fig. 2 and Fig. 3 shows the integrated liquid water in low cloud on 13 and 31 December, 1992. SLW had a very slow change and a little variable range, while the curve had a small wave which was associated with the light snow. Meanwhile, heavy fog was observed on both days and daily precipitation amounts were 0.4 mm and 0.3 mm, separately.

TABLE. 1 The mean integrated SLW and daily precipitation amount on the ground for four weather process in December, 1992

DATE	24	13	25	31	Means for three low cloud (mm)
mean of SLW (mm)	0.051	0.039	0.034	0.027	0.033
Daily precipitation amount(mm)	6.1	0.4	0.0	0.3	

Table. 1 shows the mean of integrated SLW content for every weather process. The value of 0.05 mm shows that there is plentiful SLW in the cold prefrontal and post-frontal precipitation cloud.

Low cloud also contains a lot of SLW (0.027~0.039 mm) and the mean of SLW for three weather process is 0.033 mm, which is nearly identical with those measured by PMS particle measurement system.

4. Summary

The slow accumulation of SLW occurs in prefrontal precipitation cloud before snow. SLW quickly decreases as the precipitation intensity increases, which is in accord with the fact observed by aircraft. Both of cold prefrontal and post-frontal precipitation cloud contain abundant SLW. The mean of integrated SLW content is 0.05 mm.

The integrated SLW in low cloud has only a little change and a mean of 0.033 mm, which is in conformity with those measured by PMS particle measurement system. It is less than the cold prefrontal precipitation cloud, but it is still large.

The dual-channel radiometer has allowed exact observation of SLW in weather systems which have not been feasible by conventional means (i.e. aircraft). The continuous operation of the radiometer has accelerated our understanding of SLW in winter stratiform cloud.

Acknowledgment The author wishes to express thank Hu chengda, and Zhang chunliany for their help.

REFERENCES

- Zhu yuanjing and Hu chengda, 1994: Application of microwave radiometer in weather modification researches, Cloud physics and artificial precipitation technology researches, The meteorological press, 207 - 215.
- Liu yubao, You Laiguang and Hu Zhijing, 1988: A study of the frontal snowfall in Zhungeer Basin of Xinjiang in winter. Part I: Precipitation pattern, J. Academy Meteor. sci., Vol. 3, NO. 1, 36 - 45.
- Gu Fuying, Ma Peibing and You Laiguang, 1985: The researches on low cloud in the Zhungeer Basin, Xinjiang, The collected meteorological scientific and technology papers, NO. 9, The meteorological press, 18 - 23.

STUDIES OF THE COLD POOL FOG IN BASIN

Shi Wenquan Li Bin Zhang Jianxin

(Xinjiang Weather Modification Office, Urumqi, Xinjiang, P.R.China)

In this paper, the studies of the lower clouds and the overcast fog in Zhunger Basin in Xinjiang in winter have been made by several observing methods. A new type of fog-the cold pool fog in basin (CPFB) has been put forward. Apart of cold air often stays in the basin after a precipitation weather. The cold basin is usually covered with a strong inversion layer which prevents the vapour from escaping out of the basin, so humidity in the basin is high and the stratification becomes neutral weak instability (Fig.1). The vapour from the surface of snow (or the surface of moist earth) condenses at a some altitude of the basin through the topographic lift or the turbulent exchange. It then gradually accumulates and grows. Finally, it contacts the earth and becomes fog. This kind of fog is defined as CPFB.

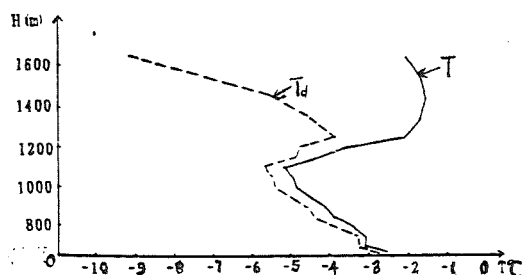


Fig.1. The distributions of temperature (T) and humidity (Td) in Urumqi in Nov.20 1987.

The main results of studies are as follows:

1. The major background conditions for CPFB are the inversion layer and the neutral weak stratification over the cold basin. The evaporation from the surface of snow (or the surface of moist earth) in the basin is the main vapour source for CPFB.

2. The major characteristics of CPFB are that the fog layer is thicker and stabler, covers large areas, even the whole basin, and usually emerges at the temperature range from -5°C to

-10°C . It mainly consists of supercooled water and sometimes makes micro snowfall (Fig.3).

3. The micro structure and the characteristics of the vertical distribution of CPFB are as follows: The particles' spectrum is narrow near the earth, but widens with height. The particles' mean scale and water content increase with height, and get the maximums near the top of the fog layer. The maximum particles' concentration is at the up-middle of the fog layer (Fig.2).

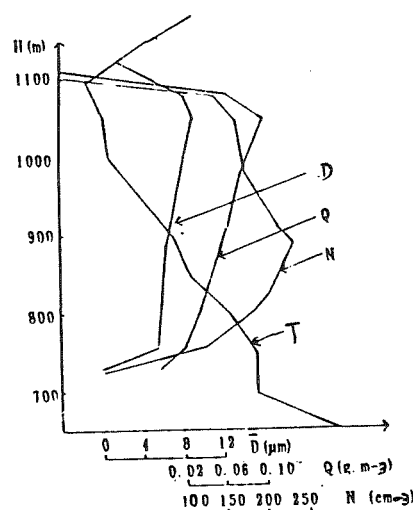


Fig.2. The vertical distributions of mean diameters (D), water contents (Q) and cloud particles' concentrations (N) ($D \geq 2 \mu\text{m}$).

4. The evolution of CPFB is closely related to lower clouds. When the bottom of the inversion layer is higher, the lower clouds are first formed and grows, then it contacts the earth and becomes fog. The area covered with fog will extend when the growth keeps, otherwise, it will reduce. The fog layer grows lower clouds while it entirely separates from slopes. The lower clouds and overcast fog will be over with the destruction of inversion by the weather system invasion.

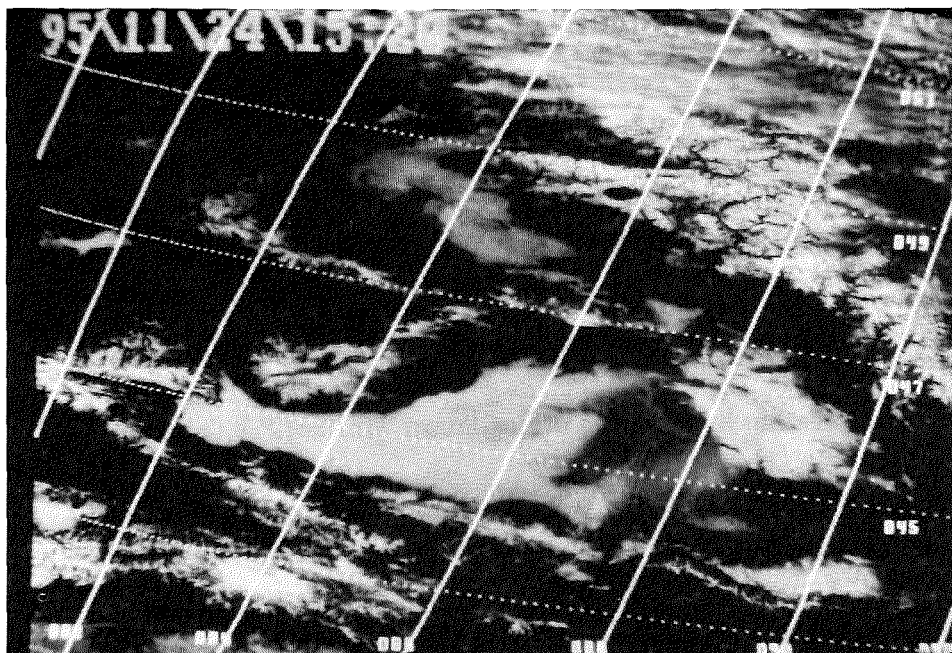


Fig.3.The satellite cloud picture ofthe lower clouds and the overcast fog in Zhunyer Basin in Xinjiang in winter.

ORIENTED ICE CRYSTALS AS OBSERVED BY LIDAR AT FIRE II

Wynn L. Eberhard

NOAA Environmental Technology Laboratory, Boulder, Colorado

1. INTRODUCTION

Many nonspherical ice particles have a Reynolds number such that they tend to orient with the long axis in the horizontal. This preferred orientation significantly affects a number of cloud properties. For radiative transfer, orientation increases vertical optical depths and the particles' effect on radiative fluxes. Orientation can affect particle terminal velocity. Orientation also alters signals obtained by remote sensors. An understanding of the signature from oriented particles can be important for proper interpretation of the remote sensor signal. This signature can also provide information on the oriented particles themselves.

2. LIDAR ZENITH-ENHANCED BACKSCATTER

Lidars often detect a strong enhancement in lidar backscatter near zenith, i.e., zenith-enhanced backscatter (ZEB). It is commonly accepted that highly-oriented, pristine plates in ice clouds can cause this phenomenon (Platt et al., 1978; Thomas et al., 1990). It is less well recognized that highly-oriented, pristine columns and needles can cause a weaker enhancement, especially at the CO₂ lidar wavelength of 10.6 μm where ice particles strongly absorb and backscatter is dominated by reflection from the first surface (Eberhard 1993a, 1993b, 1995).

Eberhard (1993a) and Popov and Shefer (1994) theoretically approximate the elevation-angle dependence of ZEB from perfectly oriented plates by assuming Fraunhofer diffraction through a circular aperture with the same area as the face of the plate (Fig. 1). The flux in the ZEB peak is determined by the geometrical-optics reflection of the laser light from the face.

Aerodynamically forced orientation of columns and needles holds the long axis horizontal, but azimuthal alignment is random. The dynamic forces for orientation in the other degree of freedom (roll about the long axis) are much weaker, so columns very likely have random roll orientation. The ZEB model (Eberhard, 1993a) for this case and for needles determines the flux in the ZEB peak using reflection per unit length from infinitely long cylinders. The elevation-angle shape is calculated by assuming diffraction through a narrow slit, followed by

an average over a uniform azimuthal distribution (Fig. 1).

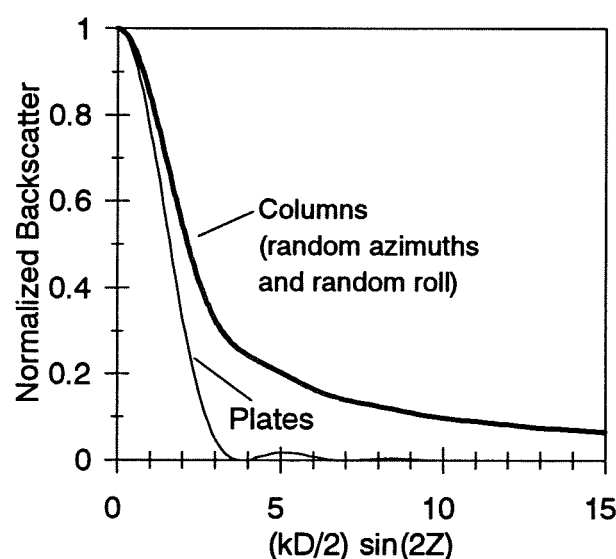


Fig. 1. Theoretical model of lidar ZEB backscatter signature, normalized to the peak at zenith, for perfectly oriented crystals as a function of lidar wavenumber k ($=2\pi/\lambda$, where λ is wavelength), particle maximum dimension D , and lidar zenith angle Z . For $D=200 \mu\text{m}$, $\lambda=10.6 \mu\text{m}$, and $Z=1^\circ$, the value of the abscissa is 2.1.

For crystals with perfect shape and orientation, diffraction determines the width of the ZEB peak, which is proportional to the wavelength and inversely proportional to the maximum dimension of the crystal. In practice, imperfect particle shapes and orientations widen the peak. The causes include particle flutter, small-scale turbulence, imperfect shapes which cause slight canting, and surfaces that are not optically flat. The width of the ZEB peak for the many particles sampled by the lidar is a convolution of all these effects.

3. MEASUREMENTS

ZEB was investigated by repeatedly scanning a lidar about zenith during the FIRE II [First ISCCP

(International Satellite Cloud Climatology Project Regional Experiment] during early winter 1991 in southeastern Kansas. The lidar wavelength was 10.6 μm , the pulse rate was 4 Hz, and the range resolution was 75 m. In order to minimize the uncertainty introduced by heterogeneous cloud density, the scan plane was aligned parallel to the wind advecting the cloud, and time averaging (typically 500 s, but sometimes shorter) of several oscillations was used during processing. Some examples of elevation-angle pattern of ZEB peaks are shown in Fig. 2. Elevation-angle plots like these were made for short height intervals, and these were examined along with time-height plots to select vertical layers throughout which the ZEB peak shapes were approximately constant.

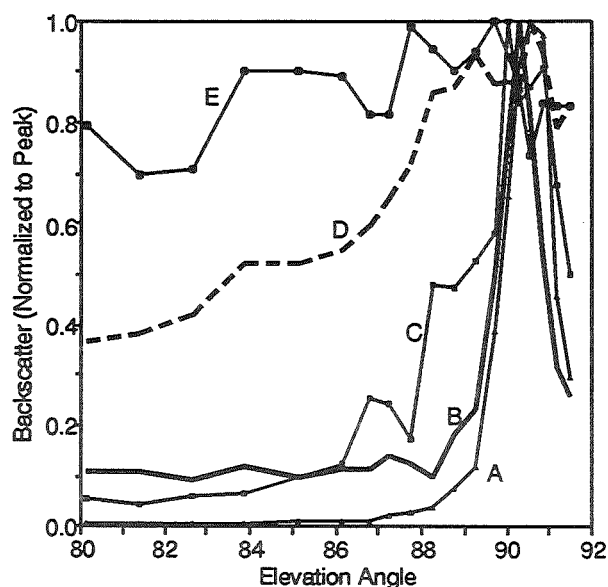


Fig. 2. Examples of observed ZEB: A) Strong ZEB, consistent with a significant fraction of highly oriented plates); B) Consistent with a few highly oriented plates among a much larger number of randomly oriented crystals; C) Consistent with a very small fraction of oriented plates or a significant fraction of oriented columns; D) As in © but with a smaller fraction oriented; E) Interpreted as no ZEB within uncertainties of measurement, but could indicate some crystals roughly oriented.

4. INFERRED CLOUD CHARACTERISTICS

Application of the scattering models (Eberhard 1993a, 1993b, 1995) permits estimation of several cloud properties related to highly oriented crystals.

The width of the ZEB peak, if particles are perfectly shaped and oriented, reveals the maximum dimension of the particles. However, the observed width gives only a lower bound on this size, because imperfect orientation and shape widen the peak.

More importantly, by integrating the area under the

peak and comparing to the backscatter where the shoulder becomes flat, the fraction of particles in the cloud which are oriented can be determined. Unfortunately, a major ambiguity exists between plates and columns/needles because of their radically different signatures. If we assume only plates cause ZEB, then the fraction of cloud particles that are highly oriented in the FIRE II data is shown in Fig. 3. These statistics are for 50 h of measurements.

These results indicate that the frequency of occurrence of highly oriented plates is small. However, this interpretation gives only a lower bound on the fraction of particles that may be roughly oriented, say within 10° of horizontal. This is partly due to instrumental and sampling limitations. The following all tend to underestimate the fraction of particles that are horizontally oriented: the limited range of angle scan; the restricted dynamic range of the lidar in strong ZEB; a conservative extrapolation to the shoulder value; the over idealization of the scattering model; and the assumption of defect-free crystal faces. Finally, average deviations from pure horizontal of even a few degrees spread the ZEB peak so far that the ratio of peak area to shoulder value is biased strongly downward, and the fraction of particles oriented can be considerably underestimated.

The peak-to-shoulder ratio is larger than is consistent with the columns-with-random-roll model in roughly 1/4 of the FIRE II events. Disregarding these cases, the fraction of highly oriented particles assuming needles or columns with random roll orientation is given in Fig. 4. When this crystal shape is assumed, the fraction of particles oriented is much higher than when only plates are assumed.

5. DISCUSSION

These results thus place a lower bound on the fraction of particles that can be considered oriented in the horizontal. Although rough orientation (standard deviation of long axis from the horizontal more than approximately 4°) almost washes out the ZEB signature, these particles will affect solar and infrared fluxes almost the same as if they were perfectly oriented.

Comparison of these ZEB results with simultaneous replicator measurements of crystal habits and sizes are underway, and results will be reported at the conference. Although replicator data do not reveal the orientation of crystals, the union of lidar and replicator data should reveal useful information about aerodynamic orientation. One objective is to demonstrate whether columns and needles can indeed cause ZEB. Another is to attempt to remove the plate-column ambiguity in at least some of the data. Finally, the comparison should indicate how many more particles are likely to be oriented, at least roughly, compared to the lower bound found from the lidar data. This will hopefully demonstrate to what

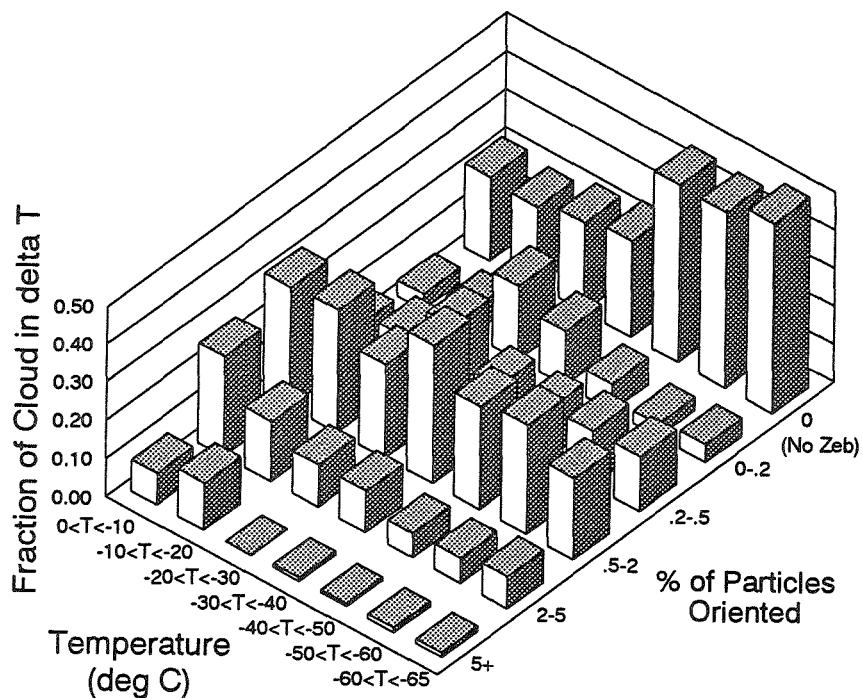


Fig. 3. Statistics for fraction of cloud particles oriented in the FIRE II data assuming plates. Data were segmented into 10° bands according to temperature at the top of a layer of approximately constant shape in ZEB signature. Of the cases within each temperature band, the probabilities were calculated for a range of inferred fraction of oriented particles. Thus, for $0 < T < -10^\circ\text{C}$, 22% of the clouds had no ZEB, and 9% had at least a fraction of 0.05 highly oriented.

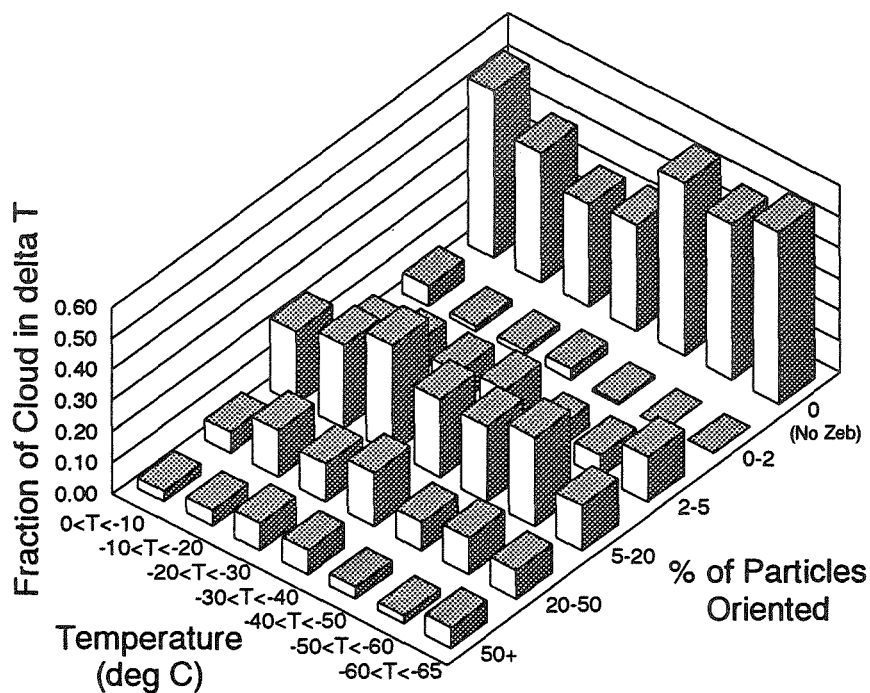


Fig. 4. As in Fig. 3, except for cases consistent with the column model. Note the change in scale for fraction of oriented particles.

extent ice particles orient and how concerned radiative transfer modelers and remote sensing practitioners should be concerned about this behavior.

6. ACKNOWLEDGEMENTS

Funding is through grants from the NASA FIRE program, the NOAA Office of Global Programs, and the DOE Atmospheric Radiation Measurement program. Replicator data are being provided by A. Heymsfield, M. Poellet, and J. Hallet and their colleagues.

7. REFERENCES

- Eberhard, W.L., 1993a: Progress in interpreting CO₂ lidar signatures to obtain cirrus microphysical and optical properties. *NASA Conference Publication 3238*, FIRE Cirrus Science Conf., Breckenridge, Colorado, June 14-17, 1993, 63-66.
- Eberhard, W.L., 1993b: Cirrus properties deduced from CO₂ lidar observations of zenith-enhanced backscatter from oriented crystals. *NASA Conference Publication 3238*, FIRE Cirrus Science Conf., Breckenridge, Colorado, June 14-17, 1993, 9-12.
- Platt, C.M.R., N.L. Abshire, and G.T. McNice, 1978: Some microphysical properties of an ice cloud from lidar observation of horizontally oriented crystals. *J. Appl. Meteor.*, **17**, 1220-1224.
- Popov, A.A., and O.V. Shefer, 1994: Theoretical and numerical investigations of the intensity of the lidar signal specular reflected from a set of oriented ice plates. *Appl. Opt.*, **33**, 7038-7044.
- Thomas, L., J.C. Cartwright, and D.P. Wareing, 1990: Lidar observations of the horizontal orientation of ice crystals in cirrus clouds. *Tellus*, **42B**, 211-216.

A COMPARISON OF THE MICROPHYSICAL CHARACTERISTICS OF CONVECTIVE CLOUDS DURING A WET SUMMER AND A DRY SUMMER

Jeffrey L. Stith¹, Ryan J. Zerr¹
Andrew G. Detwiler² and Paul L. Smith²

¹University of North Dakota, Grand Forks, ND, USA

²South Dakota School of Mines and Technology, Rapid City, SD, USA

1. INTRODUCTION

The lifetimes of most individual convective clouds ranges from a few minutes to about an hour. During this relatively short lifetime the cloud characteristics evolve dramatically. For example, the mixture of air in a cloud at the end of its lifetime is much different from that at the start. In larger clouds, precipitation develops and glaciation of the upper cloud region occurs. The precipitation, often in the form of ice, descends through the cloud levels and mixes with younger, ascending cloud elements. Larger particles, such as graupel, develop and they may in turn initiate secondary ice formation. Consequently, the chance of finding ice and precipitation in the cloud depend, to a large degree, on the age of the cloud and the location in the cloud. Other cloud characteristics, such as vertical velocity, also undergo a similar evolution with time and cloud location.

Airborne in situ measurements have been the method of choice for determining many of the important characteristics of convective clouds, such as the concentrations and sizes of hydrometeors, the internal turbulent structure, and the electrical properties of the cloud. In some sense, characterization of convective clouds from in situ aircraft data is an impossible task due to the short time that the aircraft is in the cloud and the extremely small amount of the cloud that is actually sampled during the pass (about one part in 10^{10} to 10^{12} , for data from a probe such as the Particle Measuring Systems 2DC probe). For example, one experimental approach used to follow the development of ice in a cloud involves repeated aircraft sampling of a particular cloud region (e.g. the cloud top). However, the region may lose its identifying features between aircraft passes as it mixes with adjacent cloud or clear air. The region can be better sampled or identified by the use of onboard wind computations to aid the return to the drifting parcel, or by tagging the region with a tracer (e.g. Stith, et al., 1994), but this does not solve the problem. Increasing ice concentrations might be observed in the region, but

there is no way to be certain whether the ice that is measured was formed in the sampling region or was formed elsewhere in the cloud and then mixed into the region.

In this paper we use a different approach. Instead of focusing on individual cloud passes, we examine the composite data from a large number of cloud sampling passes by two research aircraft during two six week summertime field programs conducted in central North Dakota. The first summer (1989) was a very dry year with about half the normal precipitation in the project area and the second, (1993) was a very wet year with about 150% of normal precipitation. This composite data set contains data from many locations and stages in cloud lifetimes and should therefore exhibit much of the wide variations in cloud properties that were present during each summer in the clouds sampled. The objectives are to determine how comparable the results from the two summers are and to better define the general properties of convective clouds in this region. Characterization of the average and ranges of cloud properties should more likely correspond to remote sensing measurements that average over a much larger fraction of cloud than can be sampled by aircraft.

2. DESCRIPTION OF THE INSTRUMENTATION AND THE DATA SET

The field programs were the 1989 North Dakota Thunderstorm Project (NDTP; Boe, et al. 1992) and the 1993 North Dakota Tracer Experiment (NDTE; Boe et al., 1994). Both of these programs utilized a number of similar flight patterns (described in the above references) to follow the transport and dispersion of material in cumuli and the development of ice in summertime clouds near Bismarck, North Dakota. Most of the sampling was associated with convection in developing or mature stages. A wide variety of cloud sizes were investigated, ranging from cumulus congestus to mature thunderstorms.

The data were collected by two research aircraft, the South Dakota School of Mines and Technology armored T-28 and the University of North Dakota Citation. They carried similar instrumentation for microphysical measurements, including Particle Measuring Systems, Inc., (PMS) probes (2DC, FSSP, and others), liquid water measuring instruments (Johnson Williams for the T-28; CSIRO for the Citation during the NDTE and Johnson Williams for the Citation during the NDTP) and standard instrumentation for measurement of pressure and temperature. Citation wind measurements are obtained from an Inertial Navigation System/gust probe and T-28 vertical wind measurements utilize the techniques described in Kopp (1985).

Data for eight days from the NDTP during the period 23 June to 17 July, 1989 and sixteen days from the NDTE during the period 22 June to 27 July, 1993 are included. Cloud regions to be included were automatically determined by selecting data from regions that were at least 100 mb above the estimated cloud base (determined from Cross-chain LORAN Atmospheric Sounding Stations, NWS soundings and pilot observations) that had FSSP measured droplet concentrations above 10 cm^{-3} or total concentrations from the 2DC probe above 0.5 per liter. This procedure allowed both ice and liquid clouds to be included in the data set, as well as some regions of precipitation. It produced about 10800 data points, each representing a 5-s average of in-cloud data, for the NDTE (approximately 5000 km of in-cloud data) and about half as many data points for the NDTP.

Previous 2DC imagery from North Dakota convective clouds (Stith et al., 1994 and references therein) indicates that ice crystals are the predominant 2DC image type for cold (below 0°C) regions. Thus the total particle concentration from the 2DC probe is an indicator of the concentration of ice particles for these regions. (This is often referred to as the "shadow-or" count; it includes small particles that are able to trigger the probe but do not create images.) However, it may also include some ice or large droplets (on the order of $50 \mu\text{m}$) that are able to trigger the probe. The main disadvantage of this variable is that it also includes some instrumental artifacts, such as water shedding from probe tips.

Occasional artifacts were observed in the vertical winds due to icing of the true airspeed probe (Citation) or occasional shifts in the baseline of the pressure transducer on the T-28 that produced spikes in the computed vertical wind. These artifacts were few in number and present on only a few days. They were removed by limiting the data to vertical wind values between -25 and $+25 \text{ m s}^{-1}$, for those computations that used the vertical wind data.

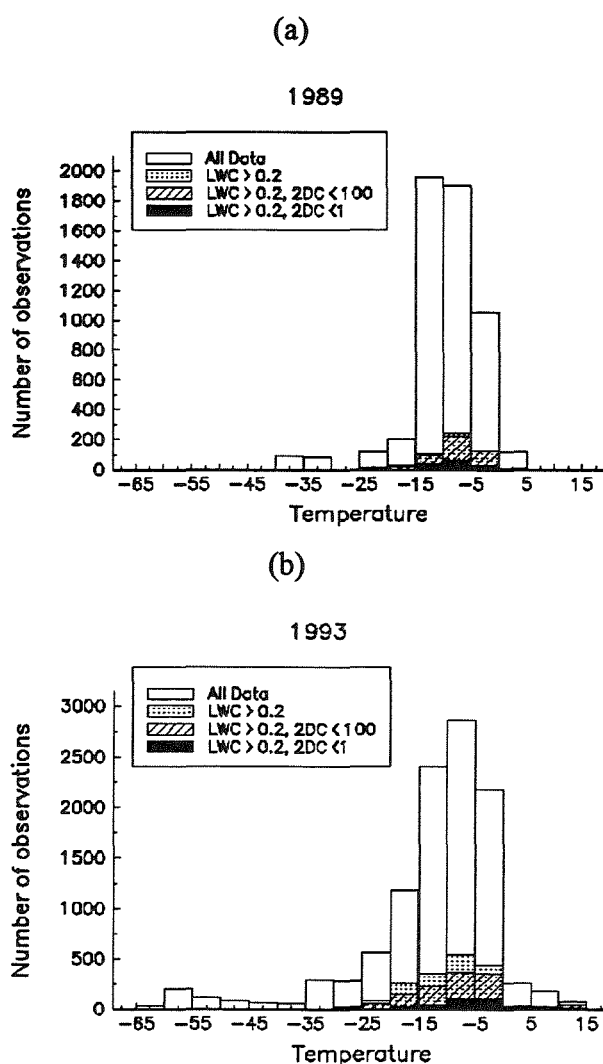


Figure 1. The frequency distribution of 5 s average in-cloud observations with temperature for (a) 1989, and (b) 1993. Samples with liquid water (g m^{-3}) and various concentrations of 2DC measured ice particles (per liter) are indicated.

3. RESULTS

The frequency distributions of the data points for various levels of liquid water and PMS 2DC concentrations are given in Fig. 1. The general distribution over temperature levels is driven by the sampling strategies, but it is clear from this figure that most of the data were obtained in cloud regions containing less than 0.2 g m^{-3} of liquid water for both years. Regions with both high liquid water and low 2DC concentrations were comparatively rare and found between 0 and -25°C , with a similar proportions of these regions in both years. Fewer data are available from 1989 than from 1993 and the earlier data do not cover as wide a range of temperatures. Because there are similar amounts of data for the range of -5 to -15°

C, this subset is chosen for comparison of cloud characteristics between the two years.

Figure 2 compares the frequency distribution of vertical wind and 2DC concentrations observed in that temperature range for the two years. The frequency distribution of vertical winds in 1993 exhibits slightly more positive values than the 1989 distribution. Only a few percent of observations came from verticals drafts greater than 10 m s^{-1} in magnitude. The 1989 data (for the dry summer) had a higher proportion of clouds with 2DC concentrations less than 1 per liter and 1993 had a greater proportion of clouds with high 2DC concentrations (100 to 1000 per liter). The 2DC concentrations were poorly correlated with vertical wind, except that high 2DC concentration regions were favored in regions of stronger updrafts (Fig. 3). 2DC concentrations were poorly correlated with temperature or height above cloud base (r^2 values were between 0.05 and 0.08).

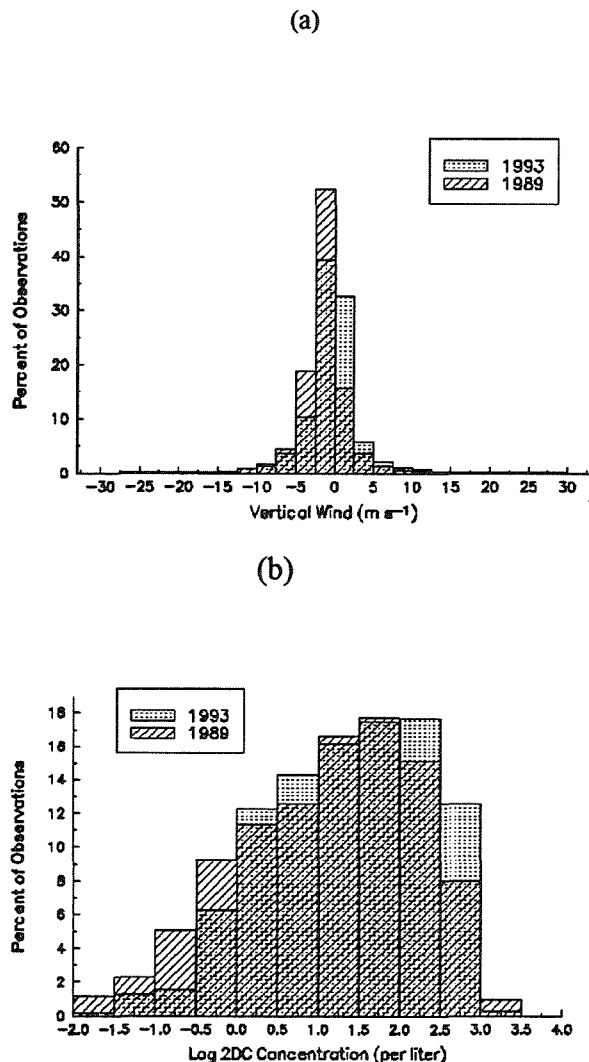


Figure 2. The relative frequency distributions of (a) vertical wind, and (b) 2DC particle concentrations, for 1989 and 1993 for cloud regions between -5 and -15°C .

4. DISCUSSION

Some of the major points of this study are:

- Even though the sampling procedures favored growing regions of the cloud between 0 and -15°C , which should be ideal regions for finding liquid water, a majority of the observations in these regions had low amounts of liquid water. This may be a result of the depletion of cloud water by the large amounts of ice that are produced in most of these clouds, which were associated primarily with strong thunderstorms. Another factor may be that these storms produce a large volume of rather dilute cloud regions with low concentrations of both ice and water. These areas are often ignored in airborne studies of convective clouds, because attention tends to be focused on the more active

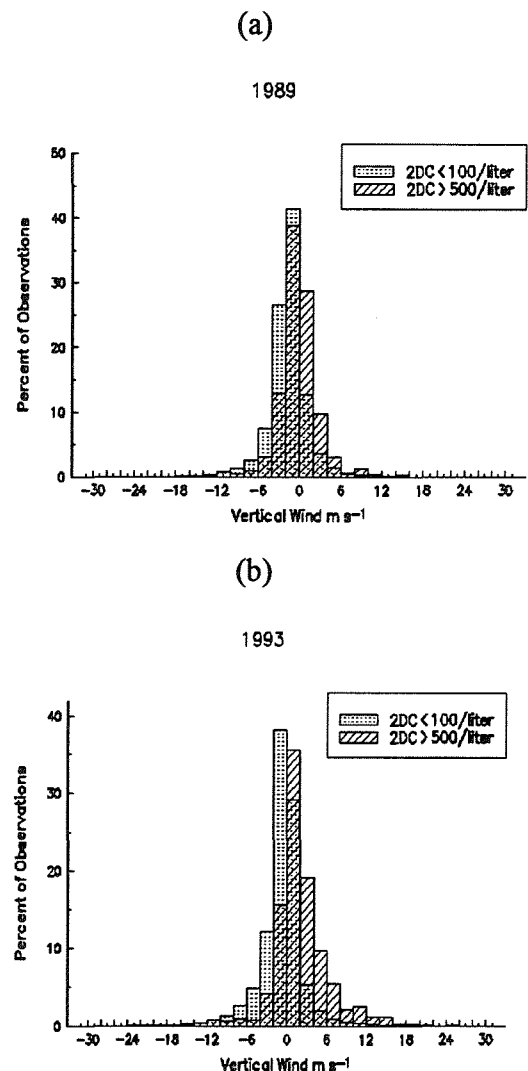


Figure 3. The relative frequency distributions of vertical wind for regions with high and low 2DC concentrations for (a) 1989 and (b) 1993.

regions.

- *Regions of updraft (which were also observed to have low fractions of adiabatic liquid water) are favored regions for high ice concentration (as represented by the 2DC concentration). This is a reasonable and expected result, since the ice is less likely to evaporate in updraft regions and the presence of the ice tends to deplete the liquid water. However, there is a great deal of scatter in the data.*
- *The data from the dryer year of 1989 had a slightly higher proportion of regions with low ice concentrations than did the data from the much wetter year of 1993, which had more regions with ice concentrations between 100 and 1000 per liter. This may simply be due to differences in the kinds of cloud regions that were sampled in 1989 compared to those in 1993. However, DeMott et al. (1996, this conference) have shown that the concentrations of ice nuclei were unusually high during the 1993 season; this might also be a factor in explaining the results. This suggests that more effort should be given to comparisons between nuclei measurements and cloud microphysics in such investigations.*

Acknowledgments:

This work is funded in part by cooperative agreement NA47RA0184 with the National Oceanic and Atmospheric Administration through the North Dakota Atmospheric Resource Board, State Water Commission. The views expressed herein are those of the authors, and do not necessarily reflect the views of NOAA or any of its sub-agencies. Additional support is provided by the National Science Foundation through cooperative agreements ATM-9104474 and ATM-9401117 and grant ATM-9221528. The authors wish to express their gratitude to the many field participants that worked to provide these data.

REFERENCES

- Boe, B. A., J. L. Stith, P. L. Smith, J. H. Hirsch, J. H. Helsdon, Jr., A. G. Detwiler, H. D. Orville, B. E. Martner, R. F. Reinking, R. J. Meitin, and R. A. Brown, 1992: The North Dakota Thunderstorm Project: A Cooperative Study of High Plains Thunderstorms. *Bull. Amer. Meteor. Soc.*, **73**, 145-160.
- Boe, B. A., P. L. Smith, and R. E. Rinehart, 1994: The North Dakota Tracer Experiment: Studies of Transport, Dispersion, and Hydrometeor Development in Cumuliform Clouds, WMO Sixth Scientific Conference on Weather Modification, Paestum, Italy, 263-266.
- Kopp, F. J., 1985: Deductions of vertical motion in the atmosphere from aircraft measurements. *J. Atmos. Ocean. Technol.*, **2**, 684-688.
- Stith, J. L., D. A. Burrows, and P. J. DeMott, 1994: Initiation of Ice: Comparison of Numerical Model Results with Observations of Ice Development in a Cumulus Cloud, *Atmos. Resch.*, **32**, 13-30.

**THE HAILSTONE PARAMETERS IN THE NORTHERN PART OF
FERGANA VALLEY
12th INTERNATIONAL CONFERENCE ON CLOUDS AND
PRECIPITATION**

B.Sh. Kadyrov¹, R.G. Shadieva²

¹Central Asian Research Hydrometeorological Institute
Tashkent, Republic of Uzbekistan

²Service for Hydrometeorological Processes Modification,
Namangan city, Republic of Uzbekistan.

Despite the fact that investigation of hail processes in Fergana valley is being carried out since the end of 60-s, the study of microphysical hail parameters wasn't paid necessary attention. The main reason was the absence of special measuring equipment. In 1991 by initiative of SANIGMI together with Alpine Geophysical Institute (AGI) there was organized the network for the hail precipitation measurement. The next year the testing of AGI technique was initiated.

The paper presents the results of observational data processing of the hail precipitation parameters obtained for the period of 1992-1993.

The measurements using passive hail indicators (PHI) made it possible to get hailstone concentration and distribution by their sizes which served as input information for the estimation of hail kinetic energy. The data on kinetic energy is very important for the assessment of hail damage to plants.

1. Measurement techniques

The possibility of measuring microphysical hail characteristics using PHI follows from the following hypothesis: hail layer, precipitated to the ground surface is concentrated in the column of the super-cooled cloud sector, and inertia of the hail

falling over this location doesn't change (Sulakvelidze G.K., 1967). The feasibility of such assumption proceeds from the scheme of hail formation by Sulakvelidze, implying that hail precipitates as the result of fast fall of the hailstones accumulated in cloud. This assumption can be substantiated by the well-known fact that hail precipitates during the short period of time when the cloud top sinks rapidly. Besides, the duration of the hail precipitation is comparable with the time period for the hailstone pass from the cloud to the ground surface. At the same time, this assumption is to a certain extent questionable and, finally, involves also the mechanism of hail formation in a whole.

Passive hail indicator is presented by a polystyrene square form (30x30cm) under-base covered by aluminum foil, installed on special metal frame fixed at the height of 1.5m over the ground surface.

Small and big ellipse diameters are defined by the traces for determination of the hailstone sizes.

In the course of measuring hail fall characteristics using PHI some errors arise related to the pillow and sampling volume (Khorguani V.G., 1974, 1976) which we considered in the data processing.

2. Calculations of measurements

In 1992-1993 the 25 prints of hail precipitated on PHI were identified. 20 of them were processed, the remaining ones could't be processed for the strong deformation of the hail pillow caused by the long and heavy hail fall. In 10 cases of 19 the hail was registered by one point, and in the rest cases it was recorded by others.

Summarized results of PHI data processing obtained in 1992-1993 are presented in table 1.

In average, the time of hail duration was 5-6 min and maximum period of hail precipitation - 18 min.

Total kinetic energy was from tens J/m^2 up to hundreds J/m^2 , the maximum value being 1680 J/m^2 .

According to the report of the hail suppression service on the results of hail-protection activities, in 1993 about 36 ha were damaged. The comparison by hail fall data showed that the significant damage was caused in days when the total kinetic hailstone energy per unit area was more than 400 J/m^2 .

Table 1. Summarized hailstone characteristics for separate hail precipitation processes during 1992-1993

Data	T min	$D_{aver.}$ mm	D_{max} mm	N m^2	M_{total} kg/m^2	E_{total} J/m^2
14.06.92	6	8.0	14	1440	3.50	112.70
14.06.92	2	3.4	12	2610	4.72	95.00
02.05.93	1	8.9	18	920	4.37	106.58
05.05.93	2	4.7	12	14120	8.01	109.52
11.05.93	4	5.5	20	4550	5.66	116.50
12.05.93	6	5.6	16	6320	9.87	124.02
21.05.93	1	7.1	18	4530	9.96	178.78
25.05.93	3	6.8	10	1900	3.60	59.80
31.05.93	13	9.0	10	3640	11.80	203.42
31.05.93	10	13.0	26	4270	51.63	1497.50
02.06.93	2	6.4	10	1450	2.33	38.44
07.06.93	3	13.6	26	800	11.79	381.44
07.06.93	4	10.8	20	690	5.10	140.80
15.06.93	17	9.7	14	7860	35.80	738.76
15.06.93	2	8.1	14	2070	6.70	134.46
16.06.93	7	8.5	16	1120	5.80	102.06
10.07.93	2	8.1	16	680	2.80	51.04
29.07.93	18	9.5	20	5650	33.70	840.56
19.08.93	8	10.2	20	8280	59.44	1676.84
24.08.93	3	5.8	16	6950	9.79	432.20

Note: T - time of hailstones precipitation, $D_{aver.}$ - average hailstones diameter, D_{max} - maximum hailstones diameter, N - hailstones number per unit area, M_{total} - total mass of hailstones fallen during one hail precipitation event; E_{total} - total kinetic energy of hailstones.

Hailstones concentration varied from 680 up to 14120 per m^2 while the maximum hailstone size was 2.6 cm.

It is seen from the hailstone spectrum averaged by size for the whole season (fig.1), that the most frequent hailstone size is 2-

4 mm. It is consistent with AGI results (Khorguani V.G., 1974, 1976), where for statistically substantiated spectra, D - value calculated by (Abshaev M.T., 1966) varied from 1.26 to 2.2 mm (with mean value of 2 mm). Besides, in our measurements the size of 93% of all hailstones didn't exceed 6 mm.

Radar data of the hail clouds observations were widely used in the course of revealing the character of the areal hail distribution.

By our observations in 1993 when the active processes were being observed, the number of days with solid precipitation was 21 (the considerable damage was recorded in 4 cases). Thus, the number of cases with solid precipitation was near mean long-term value, which is consistent with data in (Imamdzhanoz H.A., 1984).

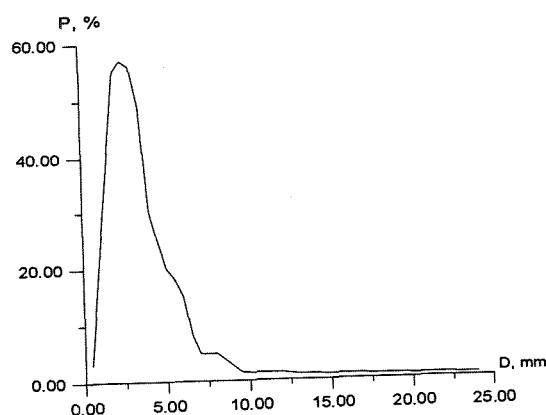


Fig.1. Frequency of hail-stones distribution by size.

3. Basic results

1. The hailstones spectrum for 1993 is obtained. In particular, it was estimated that diameter of 93% of all precipitation hailstones wasn't more than 6 mm.

2. Concentration of hailstones precipitated on 1 m^2 for the whole period of the cloud pass through the point of PHI varied from 680 up to 14120. In average, their number didn't exceed 3500-4000 per m^2 .

3. In heavy hail fall processes it is necessary to improve the order of measurements using PHI, because strong deformation of the hail pillows doesn't allow the measurements of the hail microparameters.

References

- Abshaev, M.T. , 1966: On concentration of hailstones and hail embryos in thick cumulus clouds. *Proc. AGI*, **23(5)**, 191-196.
- Imamdzhanoz, H.A. , and B.Sh. Kadyrov, 1984: Some peculiarities of the meteorological phenomena distribution in Fergana valley. *Proc. Goskomgidromet SANII*, **100(181)**, 83-89.
- Khorguani, V.G. , and M.I. Thisov, 1976: On the nature of hail embryos and hailstones concentration in clouds. *DAS of USSR*, **227**, 1108-1111.
- , ———, 1974: On the function of hailstones distribution by their sizes. *Physics of Atmosphere and Ocean*, *Izv. AS of USSR*, **100**, 440-444.
- Sulakvelidze, G.K. , 1967: Shower type precipitation and hail. L., *Gidrometeoizdat*, 412 pp.

DISTRIBUTION OF PRECIPITATION PARAMETERS ESTIMATED FROM OBSERVATIONS WITH A DOPPLER RADAR AND A POLARIMETRIC RADAR: PART I, RESULTS FROM VERTICAL POINTING DOPPLER RADAR OBSERVATION

Masayuki Maki¹, Koyuru Iwanami², Hiroshi Uyeda³, Hiroshi Hanado⁴ and Hiroshi Kumagai⁴

¹ NIED, Tennodai 3-1, Tsukuba, Ibaraki 305, Japan

² NIED, Suyoshi, Nagaoka, Niigata 940, Japan

³ Hokkaido Univ., Sapporo, Hokkaido 060, Japan

⁴ CRL, Hirai 893-1, Kashima, Ibaraki 314, Japan

1. INTRODUCTION

Although the estimation of precipitation parameters such as hydrometeor size distribution (hereafter noted HSD), liquid water content, precipitation intensity is a classical theme, it is still important and unsolved problems in cloud physics and radar meteorology. To know the vertical profiles of the precipitation parameters and to know their time evolution are important to study the precipitation mechanism. The other motivation of the present study is to provide the ground truth data for the Tropical Rainfall Measurement Mission (TRMM). Not only the horizontal distribution of rainfall amount but also the vertical profiles of precipitation parameters is necessary for understanding the mechanism of tropical precipitation system and the quantitative analysis of the heat and water budget in the tropical area. The purposes of the present studies are 1) to develop an algorithm for the estimation of precipitation parameters by using a vertical pointing Doppler radar and a polarimetric radar, and 2) to reveal the precipitation mechanism from the estimated distribution of precipitation parameters. In part I, the results of the analysis of the vertical pointing Doppler radar data is shown. The results of the analyses of polarimetric radar data will be shown in the part II of this studies (Iwanami *et al.*, 1996).

2. OBSERVATIONS

Observations were made in November 1994 in the Ishikari Plane, Hokkaido, Japan. Two x-band radars of the National Research Institute for Earth Science and Disaster Prevention (NIED) were used. One of the radars has polarimetric capability and the other is a Doppler radar operating with the vertical pointing mode. The radar operations are shown schematically in Fig. 1. RHI and PPI data of reflectivity factor, and two polarimetric parameters (Z_{DR} , LDR) were measured every 5 minutes by radar 1. Vertical profiles of reflectivity factor and Doppler velocity were measured every 20 seconds with the height interval of 62.5m by radar 2. The raindrop size distribution was also measured by a disdrometer at the same site of radar 2. The disdrometer data was used for the radar calibration and for the ground truth data of the radar-retrieved raindrop size distribution.

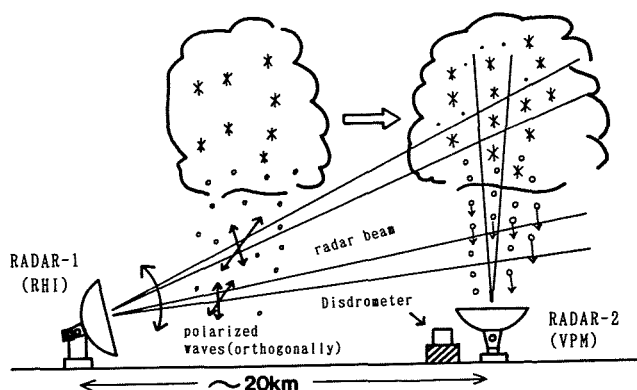


Fig.1 Schematic picture showing the radar measurements of precipitation.

3. METHODS

Several techniques for deducing HSD from the measurements by vertical pointing Doppler radar have been proposed (Atlas *et al.*, 1973). The method used in the present study is similar to Rogers (1964) and based on the following assumptions.

(1) Vertical air velocity is related with Doppler velocities and radar reflectivities. One of the serious obstacles for deducing HSD is the difficulties for precise estimation of vertical air motions. According the experimental findings obtained by Joss and Waldvogel (1970), the vertical air speed \bar{w}_a is expressed as

$$\bar{w}_a = \bar{V}_D - 2.6 Z^{1/9.3} \quad (1)$$

where Z the reflectivity factor. Equation (1) can be applied to raindrops below the melting layer. Above the melting layer, the equation proposed by Atlas *et al.*(1973),

$$\bar{w}_a = \bar{V}_D - 0.817 Z^{0.063} (\rho_0/\rho)^{0.4} \quad (2)$$

was used assuming all the precipitation particles are snowflakes.

(2) The HSD is expressed by the modified gamma

function (Ulbrich, 1983),

$$N(D) = N_0 D^\mu \exp[-G(D/D_0)] \quad (3)$$

where, $N(D)$ is the number of raindrops of diameter D per unit volume, D_0 the median-volume diameter defined as the drop size above which half the liquid water is found, μ the parameter empirically determined, G is the constant calculated by μ .

(3) The terminal velocity of the precipitation particles depends on the particle diameter and can be expressed by

$$w_t(D) = a D^b (\rho_0/\rho)^{0.4} \quad (4)$$

where the term $(\rho_0/\rho)^{0.4}$ represents the effect of air density change with height. Parameters, a and b , are constants dependent on the type of precipitation particles. $a=386.6$, $b=0.67$ for raindrop (Atlas and Ulbrich, 1977) and $a=8.34$, $b=0.31$ for snow flakes (Gunn and Marshall, 1958).

(4) The size of hydrometer is much smaller than the radar wavelength so that Rayleigh scattering can be assumed.

Under these assumptions, the mean Doppler velocity at vertical incidence V_D can be expressed as

$$\bar{V}_D = a \left(\frac{D_0}{G} \right)^b \left(\frac{\rho_0}{\rho} \right)^{0.4} \frac{\Gamma[b+\mu+7]}{\Gamma[\mu+7]} + \bar{w}_a \quad (5)$$

The radar reflective factor Z is

$$Z = N_0 (D_0/G)^{7+\mu} \Gamma[7+\mu] \quad (6)$$

The exponential distribution is a special case ($\mu=0$) of the modified gamma distribution. In this paper $\mu=0$ was assumed. Once the HSD can be estimated from (5) and (6), the other precipitation parameters such as the liquid water content and the precipitation rate can be calculated.

4. RESULTS

During the observation period, two rainfall events were observed. The first one was observed November 6, 1994 (case 1), the other November 11, 1994 (case 2). Both events were associated with the passage of depressions and developed in the warm sector.

4.1 Precipitation band of November 6, 1994 (Case 1)

The GMS images and radar PPI images showed a clear precipitation band passing over the site of radar 1 from 17:30 to

22:30 JST. According to the radio sounding at Sapporo, which was made just before the passage of the rainband, the thermal stratification was convectively unstable from 0.1 km to 2.5 km in height. Average profiles of Doppler velocity and reflectivity factor during the passage of the rainband is shown in Fig. 2. The melting layer is clearly recognized from 2.1 km to 2.6 km in height. The high value of the averaged reflectivity factor at the height of 2.3 km corresponds to the bright band which is one of the signature of stratiform precipitation.

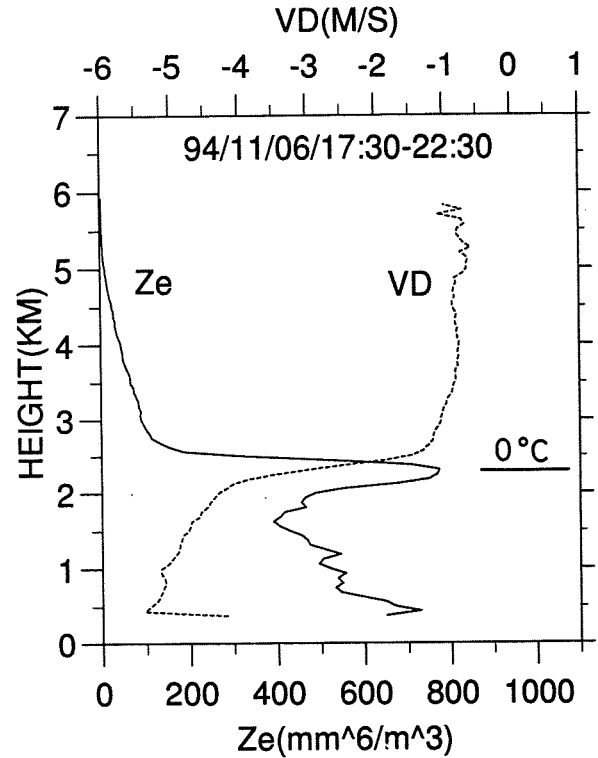


Fig. 2 Vertical profiles of the average Doppler velocity (VD) and the average effective reflectivity factor (Ze) in the case 1.

Time height cross sections of reflectivity factor and Doppler velocity are shown in Fig. 3. Four precipitation cells were observed: C1 (18:00 JST), C2 (18:30 JST), C3 (18:45-20:15 JST) and C4 (20:30-22:15 JST). The reflectivity pattern shows the bright band at the height of 2.3 km. Below this level, due to the melting of snowflakes, the rapid increase in Doppler velocity can be seen.

Time-height cross sections of estimated vertical air velocities and D_0 are shown in Fig. 4 and Fig. 5, respectively. The updraft larger than 1 m/s existed in the precipitation cell from 18:45 to 20:15 JST. On the other hand the downdraft of about 1 m/s existed just above the melting layer from 21:00 to 22:00 JST. In the center of each precipitation cells, D_0 decreases with height. Comparison between radar estimated D_0 and disdrometer measured D_0 (Fig. 6) shows good agreements with each other except small value of D_0 to which radar is not sensitive. In the case of vertical air velocity assumed to be

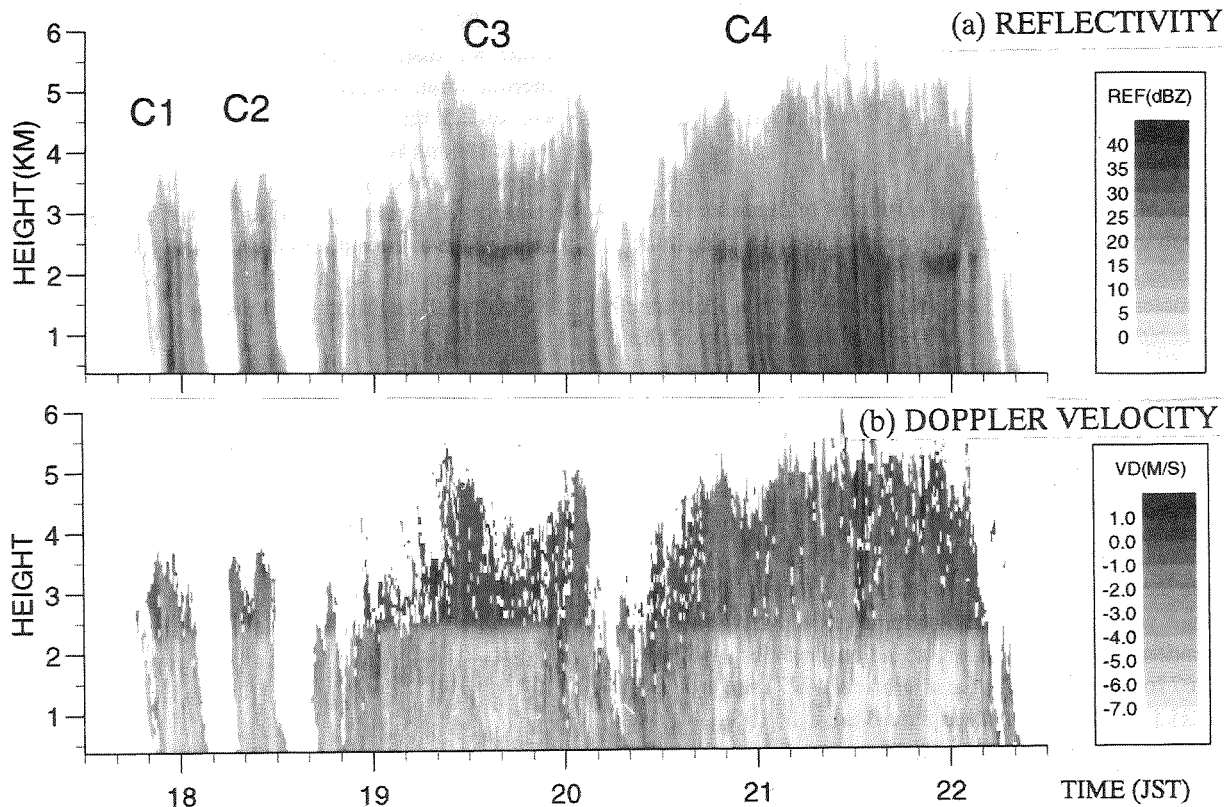


Fig. 3 Time height cross section of reflectivity factor (a) and Doppler velocity (b) of the warm-sector rainband observed November 6, 1994 (Case 1).

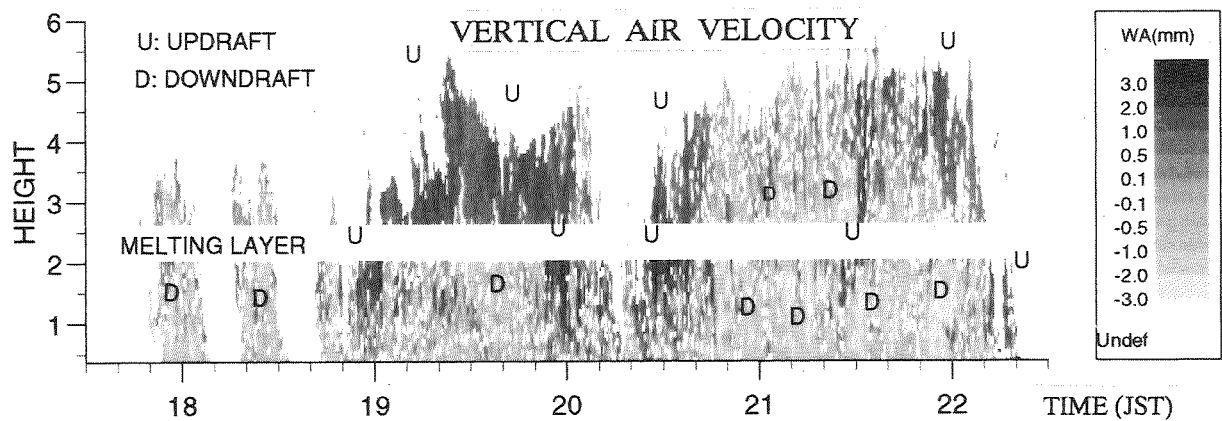


Fig. 4 As in Fig. 3 but with estimated vertical air velocities in the case 1.

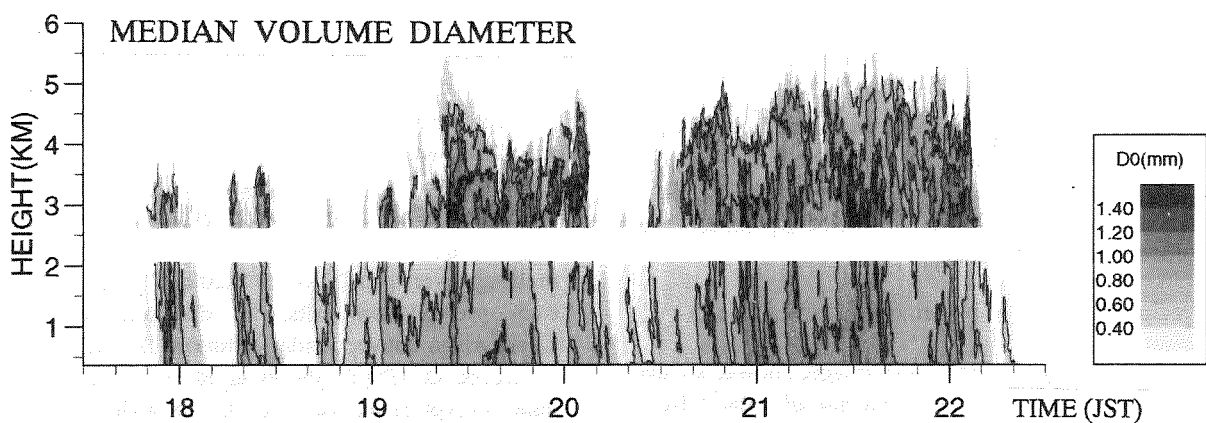


Fig. 5 As in Fig. 3 but with estimated D_0 in the case 1.

0, the calculated D_0 is about 2 times larger than disdrometer measured D_0 (not shown here).

4.2 Precipitation band of November 11, 1994 (Case 2)

Although this case was also prefrontal precipitation band type, it was more convective compared to the case 1. The updraft existed above the bright band during almost all the period when the band was passing over the radar site. Comparison between radar derived D_0 and D_0 measured by a disdrometer showed some discrepancy. The radar estimation of D_0 was underestimated especially D_0 was large. This is due the estimation error of vertical air velocity. The accuracy of Eq.(1) is $\pm 1\text{m/s}$ (Joss and Waldvogel, 1970). This will cause about 30% error in calculating D_0 for the particles falling with the terminal velocity of 5 m/s.

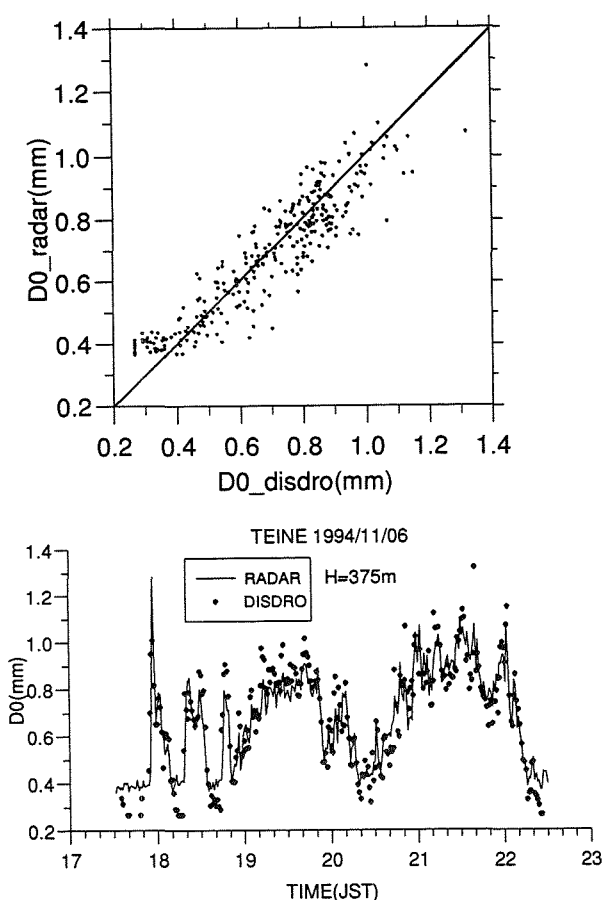


Fig. 6 Comparison of radar estimated D_0 with D_0 measured with a disdrometer in the case 1.

5. DISCUSSION

It was confirmed that the estimation technique of precipitation parameter from vertical pointing Doppler radar observations works well in the stratiform precipitation. However, the estimation error arised in the convective precipitation (case 2) where vertical air speed was not weak. In that case, vertical air speed should be estimated more precisely. When we assume the exponential distribution for HSD, there are three unknown parameters which should be estimated; HSD parameters (N_0 and D_0) and vertical air speed (w_a). One of the possible technique is to use polarimetric information to estimate D_0 . Once, D_0 is obtained from Z_{DR} , then the other parameters (N_0 and w_a) will be calculated from Eq. (5) and (6) without using empirical formula (1) and (2). The estimation of D_0 from Z_{DR} is presented by Iwanami *et al.*(1996).

ACKNOWLEDGEMENTS. The authors would like to express thanks to Sapporo local government for giving every convenience for radar observations in Teine and Mr. Kanemura of Sapporo Information Network Inc. for the use of surface meteorological data.

REFERENCES

- Atlas, D., R.C. Srivastava and R.S. Sekhon, 1973. Doppler radar characteristics of precipitation at vertical incidence. *Rev. of Geophys. Space Phys.*, 11, 1-35.
- Atlas, D. and C.W. Ulbrich, 1977. Path- and area-integrated rainfall measurement by microwave attenuation in the 1-3 cm band. *J. Appl. Meteorol.*, 16, 1322-1331.
- Gunn, K.L.S., and R.S. Marshall, 1958. The distribution of size of aggregate snowflakes. *J. Meteor.* 15, 452-466.
- Iwanami K, M. Maki, T. Sato and M. Higashiura, 1996. Distribution of precipitation parameters estimated from observations with a polarimetric radar, Part II, results from polarimetric radar observation. *Preprint, 12th ICCP, 19-23 August, 1996, Zurich, Switzerland.*
- Joss J. and A. Waldvogel, 1970. Raindrop size distributions and Doppler velocities. *Preprint, 14th Radar Meteor. Conf.*, 153-156. Boston: Amer. Meteor. Soc.
- Rogers, R.R., 1964. An extension of the Z-R relation for Doppler radar. *Proc. World Conf. Radar Meteor.*, 1964, 158-161.
- Ulbrich, C.W, 1983. Natural variations in the analytical form of the raindrop size distribution. *J. Climate Appl. Meteor.*, 22, 1764-1775.

DISTRIBUTION OF PRECIPITATION PARAMETERS ESTIMATED FROM OBSERVATIONS WITH A DOPPLER RADAR AND A POLARIMETRIC RADAR: PART 2, RESULTS FROM POLARIMETRIC RADAR OBSERVATION

Koyuru Iwanami¹, Masayuki Maki², Takeshi Sato³ and Masao Higashiura³

¹Nagaoka Institute of Snow and Ice Studies, National Research Institute for Earth Science
and Disaster Prevention (NIED), Nagaoka, Niigata 940 JAPAN

²Atmospheric and Hydrospheric Science Division, NIED, Tsukuba, Ibaraki 305 JAPAN

³Shinjo Branch of Snow and Ice Studies, NIED, Shinjo, Yamagata 996 JAPAN

1. INTRODUCTION

The precipitation clouds observation was carried out in November 1994 in the Ishikari Plain, Hokkaido, Japan with two Doppler radars and a disdrometer in order to estimate precipitation parameters (drop size distribution, liquid water content, precipitation intensity) and vertical air flow in precipitation clouds. It is important to know distributions of such parameters in order to improve the understanding of precipitation mechanisms in various types of precipitation clouds. It is considered that evaluation of drop size distribution from radar data leads to precise estimation of rainfall rate that is useful for disaster prevention and can serve as the ground truth for TRMM.

The Part 1 of this study deals with the precipitation parameters and vertical air flow evaluated from the reflectivity and Doppler velocity data obtained from vertically pointing observation with a Doppler radar. The results from a polarimetric radar observation are described in this Part 2.

2. OBSERVATION

Two X-band Doppler radars that belong to NIED were set up at an interval of 20.7 km. One of them is the dual polarization radar (radar-1) and mainly carried out RHI observation in polarization mode, and the other one (radar-2; Maki et al., 1989) vertically pointing observation in Doppler mode. A disdrometer was set up at the same site as the radar-2 and the raindrop size distributions were measured with it.

This observation was the first one with the NIED dual

polarization Doppler radar after the development and measurements in various combinations of the polarization patterns were carried out. It was unfortunately difficult to estimate cross-polarization signals precisely because of the isolation problem of polarization switch, but we could derive the distributions of differential reflectivity ZDR. The main specifications of the NIED polarimetric radar are listed in Table 1.

Table 1: Specifications of NIED dual polarization radar.

Transmitting Peak Power	40 kW
Transmitting Frequency	9,445 MHz
Polarization	Horizontal or Vertical
Beam-width	≤ 1.25 degree
Pulth-width	0.5 μs (Doppler) 1.0 μs (Polar.)
Pulth Repetition Frequency	2,000/1,500Hz (Doppler) 1,000 Hz (Polar.)
Min. Detectable signal	≤ -110dBm

3. ESTIMATION OF MEDIAN VOLUME DIAMETER

A truncated exponential raindrop size distribution, $N(D)=N_0\exp(-3.67D/D_0)$, $D\leq 0.8$ cm, is assumed. The relationships of differential reflectivity ZDR and normalized horizontal reflectivity $10\log(Zh/N_0)$ to median volume drop diameter D_0 were calculated by the method of Seliga and Bringi (1976) and Seliga et al. (1981). Figure 1 illustrates the results of the calculation for radar wavelength of 3.18 cm and refractive index of water at 10 °C. Values of D_0 were estimated from observed ZDR using the calculation results and compared with the results from disdrometer measurements.

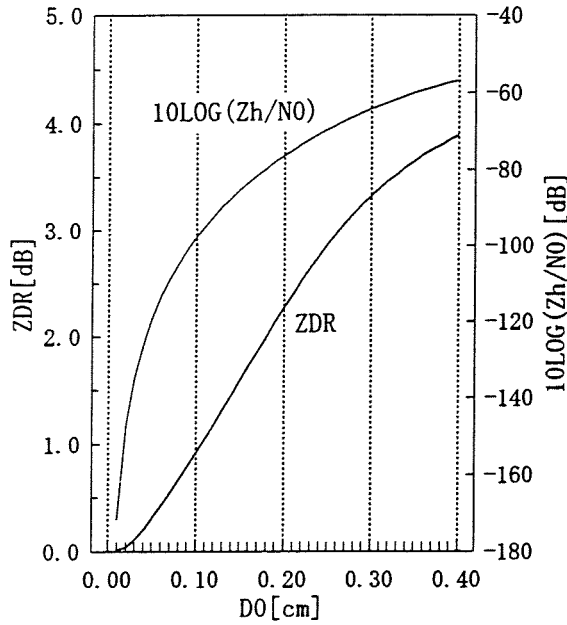


Fig. 1: Differential reflectivity ZDR and normalized horizontal reflectivity $10\log(Zh/N_0)$ as a function of median volume drop diameter D_0 .

4. RESULTS

Two rainfall events on November 6 and 11 were observed and they were associated with the passage of the low pressures. The observed stratiform precipitation clouds were located in the warm sectors. The bright bands appeared at the height of about 2.1 km and 1.4 km, respectively. The maximum positive values of ZDR were observed at the height near the maximum values of horizontal reflectivity Zh for the periods when the bright bands were clear.

Figure 2 indicates the time series of median volume drop diameter D_0 derived from the disdrometer and ZDR observation from 19:00 to 20:00 JST on November 6. D_{0dis} denotes D_0 estimated from disdrometer measurements and D_{0zdr} estimated from ZDR using the calculation results described in section 3. ZDR values in the mesh of 500 m in horizontal \times 250 m in vertical at the height of 625 m on RHI above the radar-2 site were used for the estimation, and values of D_{0dis} were averaged for two minutes in consideration of the falling time of raindrops. Rainfall rates in one minute ranged from 0.15 to 2.80 mm/h for this period.

The tendency of both time variations of D_{0dis} and

D_{0zdr} shows very good agreement, although D_{0zdr} values are about twice as much as D_{0dis} . It seems that the errors of loss measurements of our radar system and the effects of attenuation might be reasons of the discrepancy. We assumed that D_{0dis} values were true and the correlation between D_{0dis} and D_{0zdr} , $D_{0dis} = 0.383D_{0zdr} - 0.0195$, was derived. D_{0zdr} values were corrected by this relationship in the following analysis.

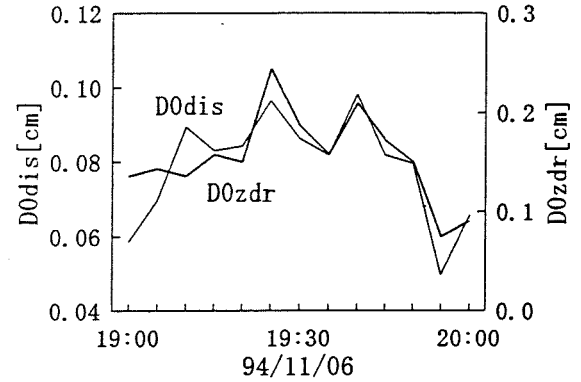


Fig. 2: Time series of median volume drop diameter D_0 . D_{0dis} and D_{0zdr} were estimated from disdrometer measurements and ZDR.

Figures 3 and 4 shows the vertical profiles of horizontal reflectivity Zh and median volume drop diameter D_0 at 19:35 and 21:30 JST on November 6. D_0 values were estimated from ZDR above the radar-2 site selected from the observed RHI data and then corrected by the method mentioned above. Rainfall rates at each time measured by the disdrometer were 2.05 and 7.53 mm/h, respectively. D_0 is displayed for the range of height below the bright band where hydrometeors were expected to be raindrops.

The bright band where the maximum Zh was 11.6 dBZ appeared at the height of 2.25 km and ZDR had maximum value (2.5 dB) at 2.0 km at 19:35 JST in Fig. 3. The profile of Zh shows small variation below the bright band and D_0 decreased from 0.103 to 0.080 cm with lowering height. It is suggested that raindrops partially evaporated and the raindrop size distribution became narrower.

On the other hand, the bright band was not clear and Zh increased with lowering height and reached to the maximum value (20.4 dBZ) at the height of 1.0 km at 21:30 JST in Fig. 4. Although the ZDR value at 2.0 km was the same as at 19:35 JST, maximum ZDR value (3.2 dB) was observed at the height of 0.75 km in the lower layer. Since Zh and D_0 show the tendency to increase with lowering

broadening of drop size distribution by convection occurred in the lower layer.

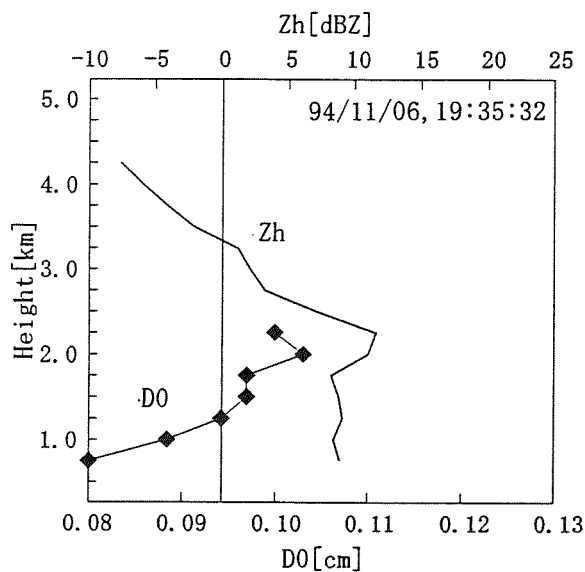


Fig. 3: Vertical profiles of horizontal reflectivity Z_h and median volume drop diameter D_0 estimated from ZDR above the radar-2 site selected from the RHI data observed at 19:35 JST on November 6.

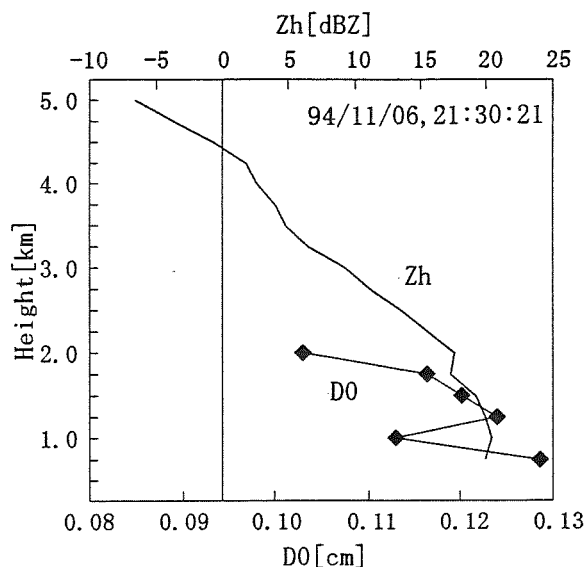


Fig. 4: As in Figure 3, but for 21:30 JST on November 6.

5. CONCLUSION

Rainfall clouds observation was carried out in November 1994 with two NIED X-band Doppler radars and a disdrometer. The median volume drop diameter D_0 was estimated from differential reflectivity ZDR observed with the dual polarization radar. Two processes of the change of raindrop size distribution were found in the lower layer in the stratiform precipitation clouds from the comparison of the vertical profiles of Z_h and D_0 . One was the narrowing of drop size distribution by partial evaporation of raindrops when the bright band was clear. The other was the broadening of drop size distribution accompanied with the growth of raindrops by convection when the bright band was not clear. It is considered that rainfall rate on the ground was low in the former case and high in the latter in result.

6. ACKNOWLEDGEMENTS

The authors would like to thank Communications Research Laboratory, Japan and Waterworks Bureau of Sapporo city, Hokkaido, Japan for their cooperation to this observation.

REFERENCES

- Maki, M., T.Yagi and S.Nakai, 1989: The Doppler Radar of NRCDP and Observations of Meso-Scale Weather Systems. *Report of the National Research Center for Disaster Prevention*, No.44, 61-79.
- Seliga, T.A. and V.N.Bringi, 1976: Potential Use of Radar Differential Reflectivity Measurements at Orthogonal Polarizations for Measuring Precipitation. *Journal of Applied Meteorology*, Vol.15, 69-76.
- Seliga, T.A., V.N.Bringi and H.H.Al-Khatib, 1981: A Preliminary Study of Comparative Measurements of Rainfall Rate Using the Differential Reflectivity Radar Technique and a Raingage Network. *Journal of Applied Meteorology*, Vol.20, 1362-1368.

OBSERVATIONS OF MIXED PHASE CLOUD AND PRECIPITATION ON THE ANTARCTIC PENINSULA

Tom Lachlan-Cope

British Antarctic Survey, Cambridge, CB3 0ET, UK

1. INTRODUCTION

Very few measurements have been taken within Antarctic clouds because of the problems of using advanced instrumentation in the Antarctic and the lack of access to research aircraft. However these measurements are needed if we are to model correctly the effect of possible global climate change in the Antarctic. In particular, to model and understand any change in precipitation over Antarctica it is necessary to understand which cloud microphysical processes are important with Antarctic cloud. Also, in-situ measurements are needed to help interpret remote sensing measurements of clouds at high southern latitudes.

During the 1995/96 southern summer, observations of cloud and precipitation were made over a twenty day period from a field camp at an altitude of 1853m on the Avery Plateau (66° 50.34'S 65° 29.58'W) which is in the middle of the Antarctic Peninsula about 70km northeast of Rothera Station (see figure 1 for places referred to in the text). This area is situated within the circumpolar trough and is crossed by large mid-latitude weather systems. The high ground of the Peninsula acts as a barrier to these systems and only a few cross completely. The precipitation at this site comes from many sources including frontal systems crossing the peninsula, precipitation from a clear sky and from orographic cloud.

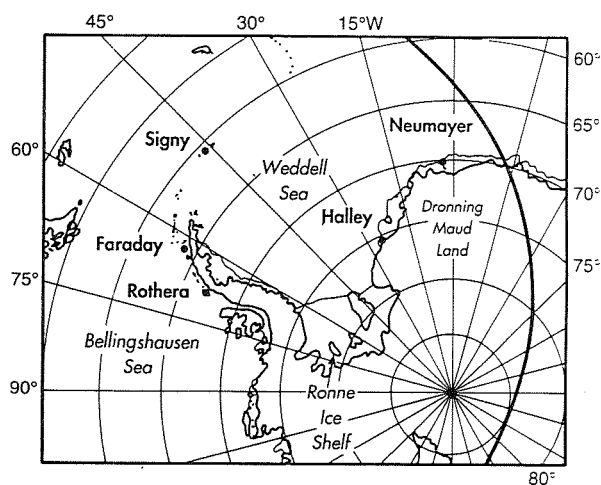


Figure 1. Map showing the Antarctic Peninsula.

Warren et al (1988), in their climatology of cloud cover, found a maximum in the zonally averaged percentage cloud cover at around 60° S in a band corresponding to the circumpolar trough. The observations in this paper were taken on the Antarctic Peninsula at 66°S where Warren's climatology would put the cloud cover at around 50%. However the Peninsula is an area where frontal systems tend to become slow moving as they approach from the west so we would expect the percentage cloud cover to be higher than the zonal average.

2. Observations.

During the field campaign, replicas of the cloud particles near the ground were taken using Formvar for later analysis. The method used was to coat a slide with a 1% (by weight) solution of Formvar in 1-2 dichloroethane. Enough solution, for the campaign, was made up at Rothera before deploying to the field site. It is normally considered better to use a fresh solution and to keep it at a temperature above -5° C to prevent ice crystals forming in the solution, but this was not possible in this case due to the difficult field conditions. A small tent was put up and the Formvar solution and slides were kept in the tent to allow them to reach a temperature close to the outside air temperature. The collection of samples required two people. One person, in the tent, coated the slides with the Formvar solution using a normal household paintbrush. The slide was then passed to the person outside who exposed the slide to the cloud particles. In this study it was found sufficient to hold the slide vertically into the wind and allow the cloud particles to be blown onto the slide. On one occasion the wind was too light for this method and a small 12v vacuum cleaner was used to pull air past the slide. The exposure time was varied according to the wind speed and density of the cloud and was normally around 10 to 30 seconds. The slides were then passed back into the tent and left to dry. A small pocket microscope was available to view the slides in the field. This method has been used before by Hogan (1975) to collect samples of diamond dust falling at the South Pole.

This method of collecting cloud particles was very time consuming. Over the 25 days that were spent on the

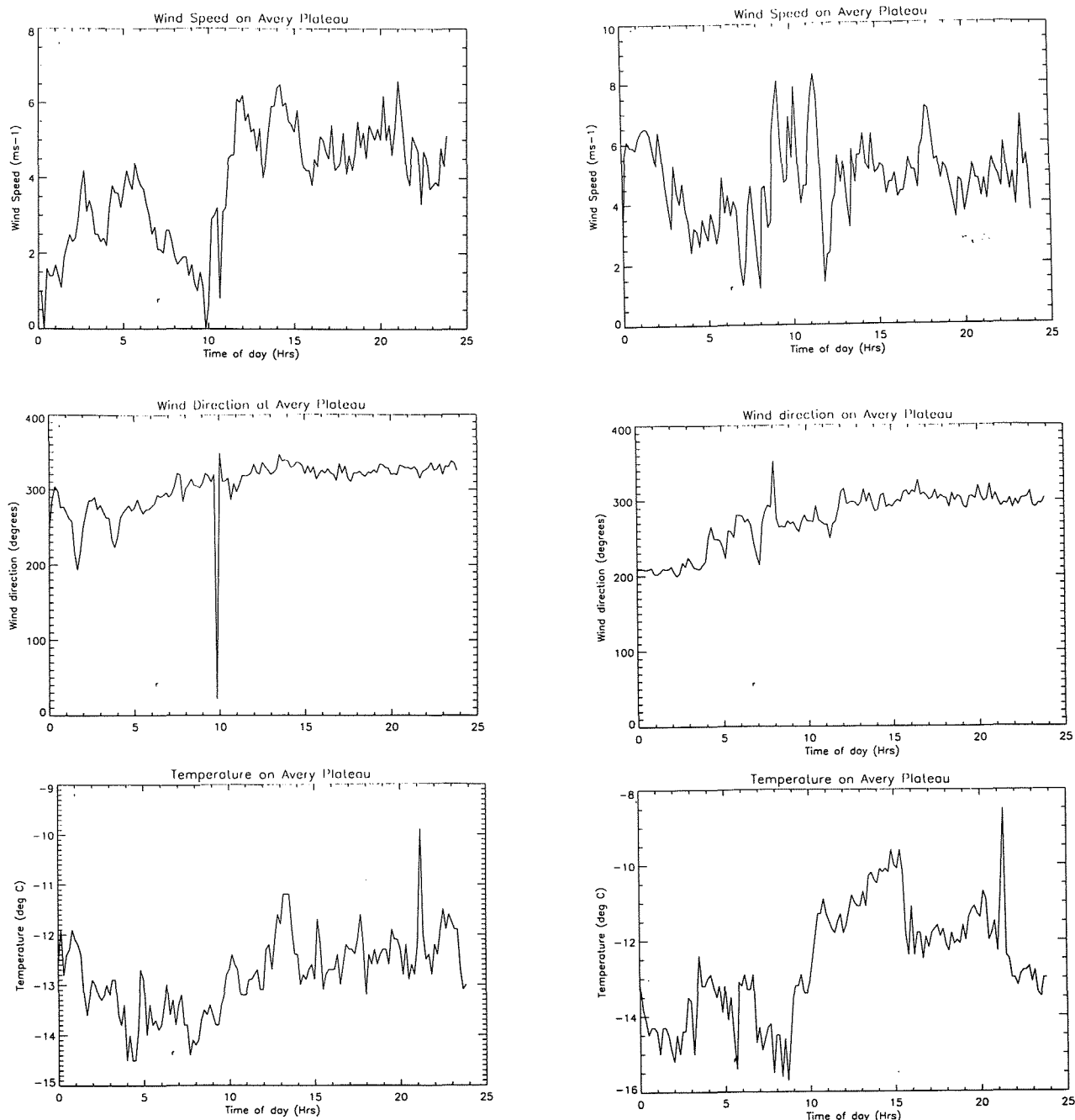


Figure 2. Wind speed, wind direction and temperature for the Avery Plateau. The graphs on the left are for the 1 December 1995 and the those on the right are for the 7 December 1995.

Avery Plateau, 140 slides were collected in a range of conditions. The analysis of these slides, initially, has been carried out manually using a microscope.

The precipitation was measured using a disdrometer which measures the size of precipitation particles. This is an optical device developed by the University of Manchester Institute of Science and Technology (UMIST) and this was run to give a continuous record of the particle size distribution on the snow falling. The

instrument is interfaced to an IBM compatible PC and this PC and the interface unit had to be kept above freezing to allow them to work. This equipment was therefore only run when someone was available to check on the paraffin 'Tilley' lamp used to heat the tent.

The snow accumulation was measured with two sets of snow stakes located to the west and south west of the camp. The accumulation was measured on alternate days to prevent the snow around each pole compacting.

It had been expected that the prevailing winds would be westerly so that any drift from the camp would not affect the snow stakes. However, the first high winds of the study period did come from the east, but it was felt that the stakes were far enough away and were not effected by drift.

Atmospheric profiles of temperature and humidity were obtained from radio sonde ascents. These ascents were made during snowfall and not at standard reporting hours. Surface meteorological measurements were also made using an Automatic Weather Station (AWS). Satellite data from the NOAA polar orbiting weather satellites were also used to obtain some cloud top measurements.

3. RESULTS

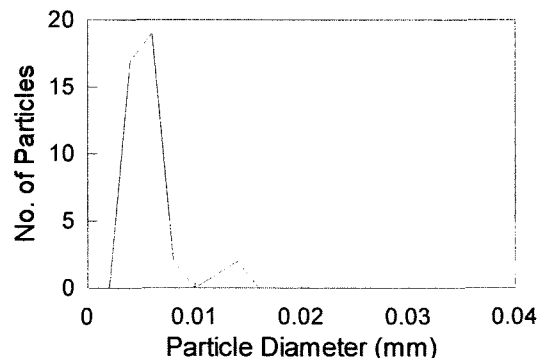
Two occasions when mixed phase clouds were observed are investigated in this paper. These were on the 1 December and the 7 December 1995. On both these occasions the field site was in a weak ridge of high pressure just in front of a developed frontal system approaching from the west. The pressure gradient over the site was relatively weak. On these occasions the precipitation is likely to be due to orographic effects. The wind speed, wind direction and temperature for these two days are shown in figure 2. It can be seen that the conditions are similar on both days; the only real difference being that the wind is slightly more easterly on the 7 December.

Figure 3 shows the size distribution of liquid droplets for two occasions on the 1 December and on the 7 December. The vertical axes in these plots are in arbitrary units. It can be seen that the distribution is biased towards the smaller drops on the 1 December. The slides were also capable of recording ice particles and for the 1 December case no particles were recorded, while some were recorded on the 7 December.

The results reported here are a small subset of those available. The two size distributions shown only give a snap shot of the distribution of the clouds being measured, although they are typical of those recorded throughout those two days. For this reason, caution has to be taken when drawing conclusions, however, the large number of ice crystals present on the 7 December relative to the number present on the 1 December, may explain the relative lack of small drops on the 7th as the small water drops could have evaporated as the crystals grow. It is possible that the more easterly winds on the 7th had brought more ice nuclei with them, although no measurements are available to confirm this. The ice crystals could possibly have been generated by the clouds being in contact with the snow covered surface of the plateau (see Rodgers and Vali 1987). The more northerly winds on the 1st would mean that the cloud would have arrived at the site over ground that rose

steeply towards the site and so would have had less contact with the site.

Slide 27 1/12/95 1247z



Slide 91 7/12/95 at 1525z

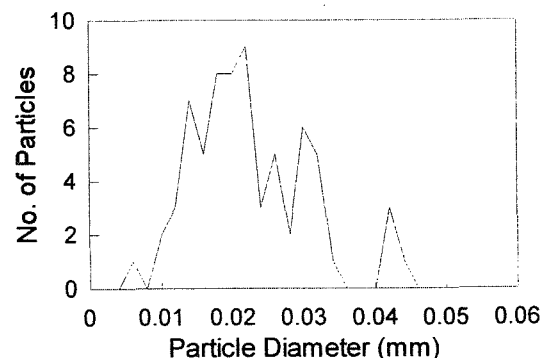


Figure 3. Cloud droplet distributions for 1 December 1995 (top) 7 December 1995 (bottom)

4. FUTURE WORK

This work is still at a very early stage and the data are still being analysed. At the moment the particles are being counted by eye with a microscope but it is planned to image the slides and use pattern recognition software to count the particles. It is hoped to compare all the data that has been collected and then use computer models to reproduce the cloud microphysics.

5. REFERENCES

- Hogan, A.W., 1975: Summer ice crystal precipitation at the south pole. *J. Appl. Met.*, **14**, 246-249.
- Rodgers, D.C., and G. Vali, 1987: Ice Crystal Production by Mountain Surfaces. *J. Clim. and Appl Met.*, **26**, 1152-1168
- Warren, S.G., C.J. Hahn, J. London, R.M. Chervin, and R.L. Jenne, 1988: Global distribution of total cloud and cloud type amounts over the ocean. *NCAR Technical Note TN-317+STR/DOE Technical Report ER/0406*, NCAR, Boulder.

THE IMPACT OF REGION RELIEF ON SOME CHARACTERISTICS OF HAIL PROCESSES

R.I. Doreuli

Geophysics Institute, M. Aleksidze 1, Tbilisi, Georgia

In haildangerous situations over various areas of a hailed region, under the influence of the relief and regional orographic conditions, the dynamics of the development and travel of cumulus - rain clouds are different. Hence the carrying out of a detailed radiolocation investigation of haildangerous clouds over these regions is of high importance both in scientific and practical aspects.

In this work the results of an investigation of the region relief height influence on the potential degree of haildanger and repetitiveness of haildangerous cloud initiation with allowance to their travel direction in various areas of the investigated territory are presented.

Analysed are the data of radiolocation observations, carried out by Geophysics Institute of Georgian Academy of Science from 1966 to 1981 in Kakheti region of Georgia, comprising Alazani valley and Iori plateau including Gombori ridge and the southern slopes of Main Caucasian ridge.

On the abovementioned territory in points Ruispiri, Gurdjaani, Tsiteli - Tskharo and Badiauri four ARS - 3 and MRL - 5 type radiolocators were installed. Every 1 - 2 minutes, the whole day round, radioecho parameters actually from all big convective clouds appearing on the territory were detected. During each series of measurements of all the parameters mentioned in work [1], values of the maximum radiolocation reflectivity multiplier (Z_m) with spatial-temporal coordinates were also measured. The air temperature, velocity and

direction of air masses travel in the atmosphere at the corresponding levels were determined by means of the data from radiosonds launched from point Ruispiri 3 times a day.

By means of the abovementioned parameters the value of cloud haildanger potential degree (K), which has been used during the last 20 years as a main criterium of haildanger in Georgia, was determined.

The direction of the maximum radiolocation reflectivity zones travel was considered as a cloud travel direction.

The investigated territory was divided into 334 equal squares with areas 25 Km^2 . As a relief mean height (H_R) the height of the earth surface above the sea level, averaged in every square on 5-6 points, was considered.

From the abovementioned radiolocation observations, by using the condition $K \geq 0.41$, on the total 1709 haildangerous and hail clouds were selected.

In each square the haildangerous cloud initiation meanannual repetitiveness (\bar{n}), the mean value of the cloud haildanger potential degree (\bar{K}), the mean velocity and predominating cloud travel direction (α°) were determined. After that, maps of the distribution of the abovementioned characteristics of haildangerous clouds over Kakheti region were built (Fig. 1 and 2).

Fig. 1 shows that haildangerous clouds over lowlands and open areas travel mainly from the South - West to North-East, whereas over the peaks

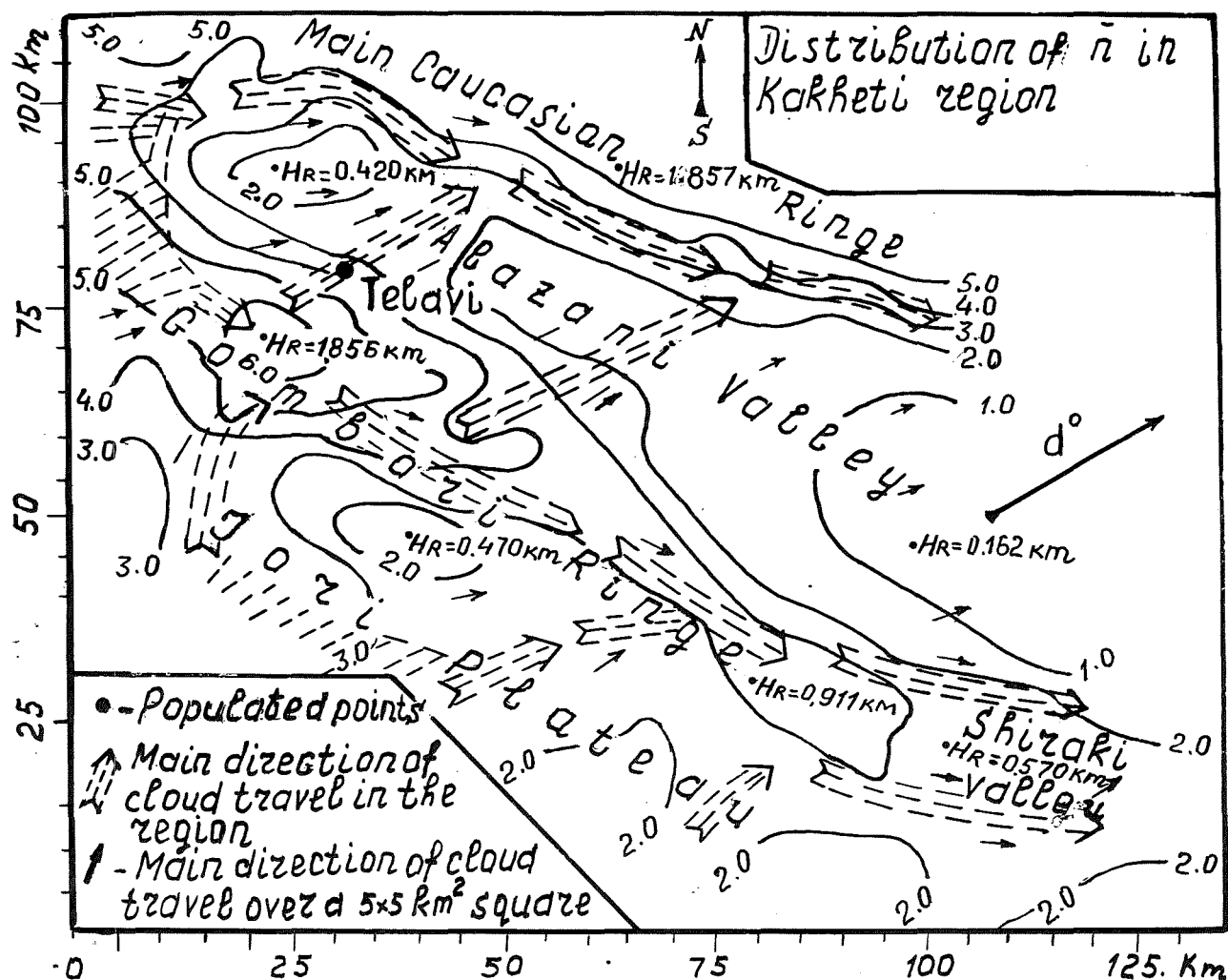


Figure 1

Distribution of mean annual repetitiveness (\bar{n}) of haildangerous clouds and their travel in Kakheti region

of Gombori ridge and southern slopes of Main Caucasian ridge - along the crest.

Over the observed territory in a layer 5.2 - 8.4 km above the sea level (the range of the maximum radiolocator reflectivity height variations) air masses travel mainly from the South - West to North - East ($d^\circ = 240^\circ$). Over plains and open areas the deviation of the predominating haildangerous cloud travel direction from the air masses travel direction is small ($\pm 10^\circ$). Big deviations are observed over the mountainous region ($\pm 45^\circ$).

As it follows from Fig.1 and 2, smaller values of \bar{n} and \bar{K} are observed over low and open locations.

With an increase in the region height H_R the values of \bar{n} and \bar{K} increase. High values of these parameters are observed over ridges and their spurs.

We tried to find correlation both between \bar{n} and H_R and between \bar{K} and H_R .

Fig.3 and 4 show the dependence of the haildangerous cloud

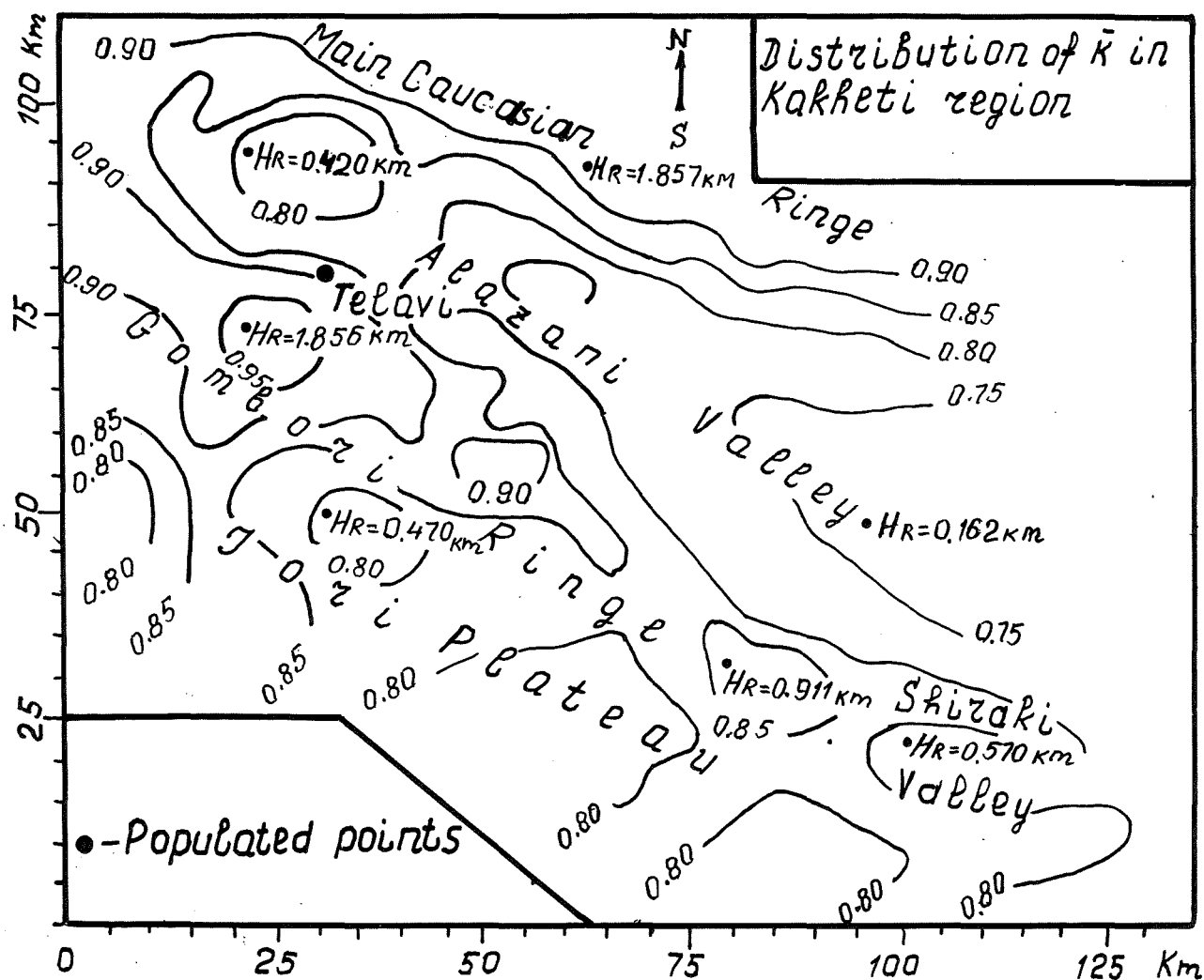


Figure 2

Distribution field of cloud potential haildanger mean values (\bar{K}) in Kakheti region.

meanannual reflectivity and cloud potential haildanger on the region height. Both dependence curves calculated by means of the below regression equations are also

represented here.

$$\bar{n} = -0.24 H_R^3 + 4.09 H_R + 0.15$$

$$\bar{K} = -0.008 H_R^3 + 0.151 H_R + 0.728$$

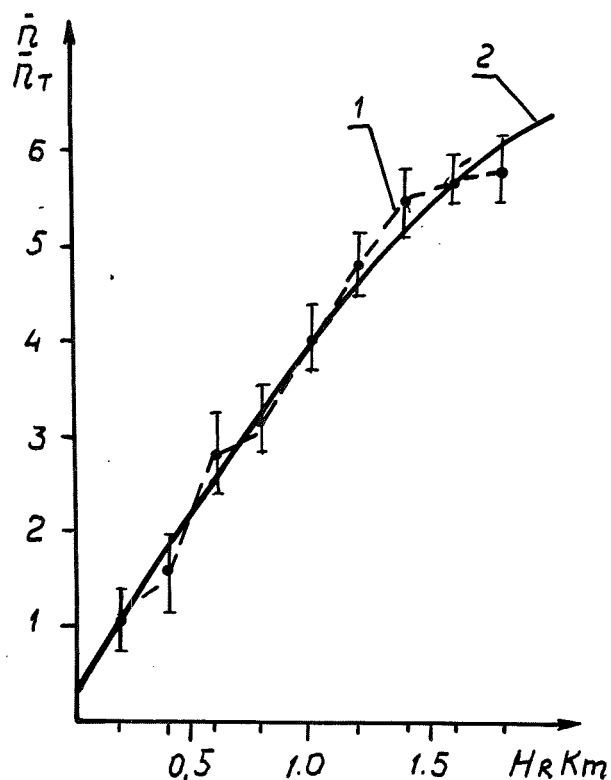


Figure 3

Dependence of \bar{n} on H_R
(1 - experimental, 2 - calculation curves)

The divergence between experimental and calculated values of \bar{n} and \bar{K} for all areas of the investigated territory amounted to not more than 10%.

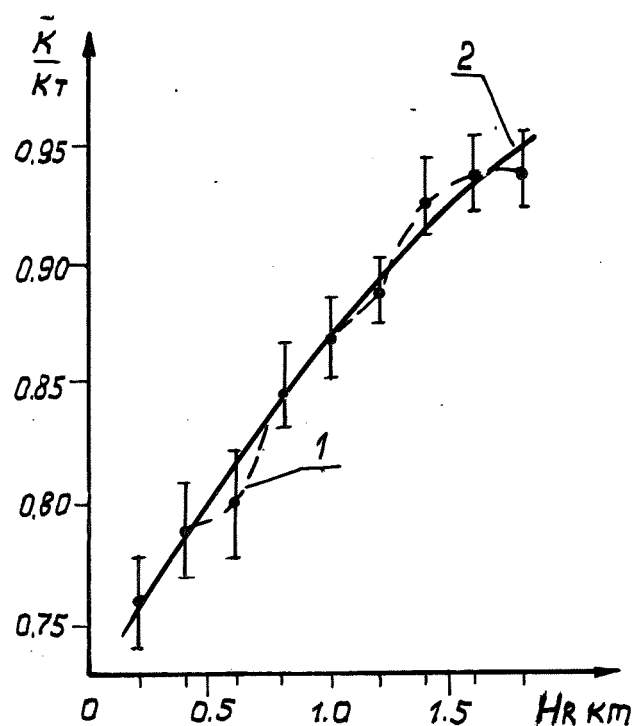


Figure 4

Dependence of \bar{K} on H_R
(1 - experimental, 2 - calculation curves)

REFERENCES

1. Salukvadze T.G., Radiolokatsionnie kharakteristiki gradovikh oblakov s uchotom ikh sezonnoy khoda., Tr. Instituta Geofiziki AN GSSR, Tbilisi, 1973. p. 123 - 133.

ICE INITIATION IN WISP SHALLOW UPSLOPE CLOUDS

by

Roy M. Rasmussen and William A. Cooper
National Center for Atmospheric Research *

Paul DeMott and Dave Rogers
Colorado State University
Ft. Collins, Colorado

1. Introduction

How ice initiates in the atmosphere remains one of the fundamental unanswered questions in cloud physics today (Rasmussen 1995). The initiation and subsequent growth of ice crystals leads to much of the world's precipitation. The diffusional growth of ice depletes water vapor, while riming growth depletes cloud droplets. Thus, ice plays an important role in the redistribution of both vapor and cloud water within a cloud system. The Winter Icing and Storms Project (WISP) conducted a major field program (WISP94) during the winter of 1993-94 focussed on the initiation of ice in winter storms, and its role in the production and depletion of supercooled liquid water. An instrument test program, called WISP Instrumentation Test (WISPIT), was conducted the year prior to the main field program in order to test some of the critical instrumentation planned for use during WISP94. Both programs focussed on two main cloud types: wave clouds forming over orographic terrain and shallow upslope clouds forming when cold continental air moves southward over the High Plains. In this paper we address two main questions on ice initiation in shallow upslope clouds: 1) the cause of the one-to-two order of magnitude variation in crystal concentration observed at a given temperature (Cooper 1986), and 2) the relationship between ice nuclei concentration and ice crystal concentration. We will consider one case in detail, and then compare the detailed case study to the upslope case observed during WISP and attempt some generalization.

2. 24 February 1993 Case Study

A shallow upslope cloud formed in the Front Range region of Colorado on 24 February 1993, causing widespread cloudiness. Two aircraft flights were

conducted during this event using the NCAR King Air as part of the WISPIT program. In Fig. 1 we present vertical profiles of temperature, liquid water content, ice crystal concentration, θ_e , and condensation nuclei concentration from the aircraft during a missed approach to Greeley (60 km north of Denver, Colorado). The ice crystal concentration was calculated from 2D-C data only considering crystals larger than 150 microns in order to avoid spurious counts from large cloud droplets.

The data clearly reveal the presence of two thermodynamically and microphysically distinct cloud layers. The upper layer is located between 1.8 and 2.4 km, and contains FSSP-measured liquid water over 0.4 gm^{-3} , and no measurable ice crystals greater than $150 \mu\text{m}$ in size (Fig. 1a). The lower layer is separated from the upper layer by a temperature inversion and is located below 1.8 km down to the ground. This lower layer contains low values of supercooled liquid water (less than 0.05 gm^{-3}), and approximately $1\text{-}2 \text{ L}^{-1}$ of ice (Fig. 1a). The temperature in the lower layer ranges between -8 and -9°C , while the temperature in the upper layer ranges from -7 to -10°C (Fig. 1a). The lower layer also contains higher CN counts than the upper layer (Fig. 1b), and lower ozone concentration (not shown). The wind speed in the lower layer is nearly constant at $4\text{-}5 \text{ m s}^{-1}$ northeasterly at 1.8 km MSL to nearly 9 m s^{-1} north-northwesterly at the top of the layer (not shown). The vertical profile of θ_e in the lower layer is only weakly stable, suggesting that this layer can be associated with the atmospheric boundary layer (Fig. 1b). The high value of CN also supports this suggestion. The most remarkable feature of this cloud, however, is the two-layer structure in the ice crystal concentration, with ice crystals up to 2 L^{-1} in the lower cloud layer, and no measurable ice crystals in the upper layer, all in a cloud system with temperatures no colder than -10°C . A similar structure was observed in the 1990 St. Valentine's Day shallow upslope storm (Rasmussen et al. 1995) (Table 1). During that study, however, no ice nuclei measurements were made, preventing us from establishing any link to the vertical distribution of ice nuclei. During WISPIT and WISP94 ice nuclei measurements were

* NCAR is sponsored by the National Science Foundation.

made via in-situ bag sampling and in-situ filter sampling, as well as some ground-level sampling at the Colorado State University Cloud Simulation and Aerosol Laboratory. On 2/24/93 an in-situ bag sample was collected above the cloud top near the end of the flight. The aircraft landed at Ft. Collins/Loveland Airport following the mission, and the bag sample was processed within two hours using a Continuous Flow Diffusion Chamber (Rogers 1988) and an expansion cloud chamber (DeMott and Rogers 1990). Losses to the side-walls of the bag were slight and have been accounted for. Results of this analysis are given in Table 2 for 2/24/93 as well as from upslope days during WISP94. An in-situ filter sample was processed by Jan Rosinski in a thermal diffusion chamber (Langer and Rogers 1975) at the approximate temperature of the cloud. In the current case we have ice nuclei data from filter sampling and the CFD (both ground and airborne samples) (see Table 2).

A ground sample was obtained at Ft. Collins at 0034 UTC, and processed by the CFD. The concentration of ice at the surface near Ft. Collins was 0.84 L^{-1} at -16.7°C , water saturation from the CFD chamber. Since the processing temperature was nearly 7°C colder than the cloud, actual ice nuclei concentration at the cloud temperatures (-7 to -10°C) is likely much less than the observed ice crystal concentration ($1\text{--}2 \text{ L}^{-1}$). Since Ft. Collins was located on the west side of the storm, this sample may not be representative of the air producing upslope cloud near Greeley (located 50 km east of Ft. Collins). The high values of ice in the lower layer sug-

gest that the boundary layer was sufficiently turbulent to provide a continuous source of ice nuclei to that layer.

The bag sample collected above cloud was processed by the CFD at a temperature of -16.8°C , and the filter sample at -10.5°C . The Rosinski filter processing technique found an ice nuclei concentration above cloud of 0.9 L^{-1} at -10.5°C , while the CFD processing found 1.13 L^{-1} at -16.8°C , both at water saturation.

The lack of ice in the upper layer suggests that the flux of ice nuclei into the layer from aloft or below was insufficient to keep up with the depletion of ice nuclei through ice crystal nucleation and subsequent growth and fallout. The temperature inversion at 1.8 km MSL likely inhibited the flux of ice nuclei from below, while the strong inversion at 2.4 km (Fig. 1a), likely limited the flux of ice nuclei from aloft (through entrainment and mixing). A calculation of Richardson number near cloud top using the aircraft data gives a value of 3.1, indicating a dynamically stable layer. Thus, the upper layer was relatively isolated from ice nuclei sources both above and below the layer, consistent with the low concentration of ice observed.

3. Comparison to Results from WISP90 and WISP94

As mentioned above, the two layer thermodynamic and microphysical structure described above is very similar to the structure of the shallow upslope cloud occurring 12–14 February 1990 during WISP90 (Rasmussen et al.

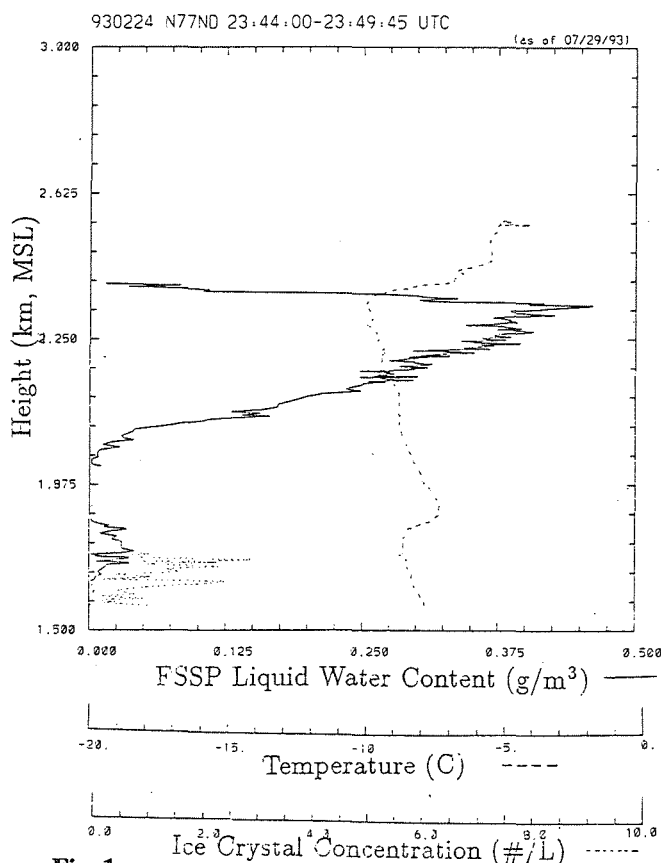


Fig. 1a

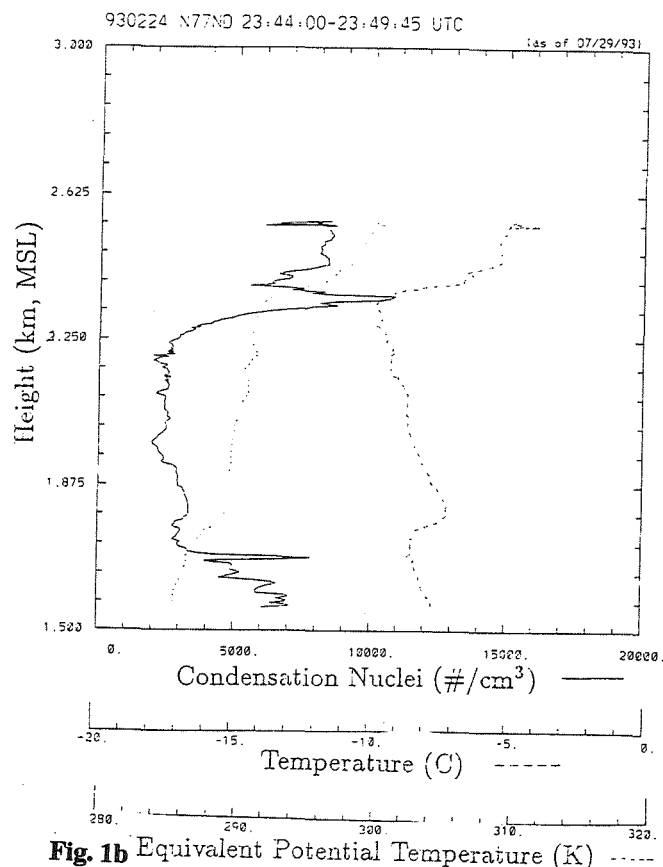


Fig. 1b

IN Temperature Spectra (Upslope Clouds)

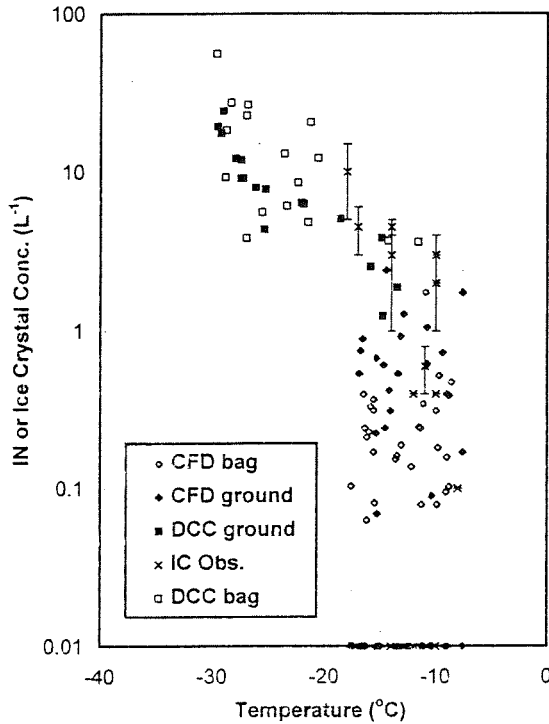


Fig. 2

1995) (Table 1). Low ice crystal concentrations were also observed in the upper layer, with 1-5 L⁻¹ ice crystal concentration in the lower layer. The lower layer was also well-mixed thermodynamically, and contained low values of supercooled liquid water. In contrast to the current case, the Richardson number near the top of the upper layer was less than 0.25, suggesting that the upper layer was dynamically unstable, and could have had a large flux of ice nuclei into the layer. The low ice crystal concentrations observed suggest that the concentration of ice nuclei may have been low above cloud top in this case. No ice nuclei measurements were available during

WISP90 to confirm this suggestion. During WISP94, however, bag samples were collected aloft and continuous samples were collected at the ground near CSU and processed by either the CSU cloud chamber or the CFD. Fig. 2 presents the IN or ice crystal concentration as a function of processing temperature for both ground (solid symbols) and airborne samples (open symbols). The results in the temperature range typical of upslope clouds (-8 to -18° C) show on average an order of magnitude higher IN concentration near the ground than aloft. Thus, the lack of ice aloft in upslope clouds may well be due to lack of IN aloft as postulated in Rasmussen et al. (1995).

In order to generalize this conceptual model further, we analyzed the vertical structure of 10 shallow upslope events observed during WISP94 using data from the NCAR Electra and the Wyoming King Air aircraft. Bag samples and ice nuclei filters were also collected with the Electra. Of the 10 upslope events sampled, 7 had a double layer structure, while the remaining 3 did not. Table 1 summarizes the depth, temperature range, ice crystal concentration, and maximum liquid water content in both the upper and lower layers. The upslope clouds on 2/19/94, 2/21/94, and 2/22/94 only contained a lower, well-mixed boundary layer. The ice crystal concentrations (Fig. 2) show reasonable agreement with the IN measurements, suggesting that primary ice nucleation may be the primary ice initiation mechanism in these types of clouds.

4. Conclusions

The aircraft vertical profiles obtained during 12 shallow upslope storms during WISP90, WISPIT and WISP94 show the presence of a two-layer structure in 9 cases. The lower layer is near neutral stability, and contains low values of supercooled liquid water and relatively high concentrations of ice crystals. The upper layer is usually thermodynamically stable, and contains higher amounts of supercooled liquid water and relatively lower

Table 1
Summary of Aircraft Microphysical Observations in WISP Upslope Storms

Date	A/C	Time Period/UTC	Upper Cloud Layer					Lower Cloud Layer				
			Thickness (m)	Temp Range (°C)	Ice Crystal conc (#/L)	Max Liquid Water content (gm ⁻³)	Precip Type	Thickness (m)	Temp Range (°C)	Ice Crystal conc (#/L)	Max Liquid Water content (gm ⁻³)	Precip Type
2/13/90	W	1700-1915	800	-12 to -14	0.0	0.15	water	800	-8 to -14	4-5	0.05	ice
2/24/93	N	2344-234945	600	-7 to -10	0.0	0.45	water	225	-8 to -9	1-2	0.03	ice
2/7/94	E	1905-192030	200	-13 to -14	0	0.13	ice	300	-13 to -14	1-5	0.01	ice
2/8/94	E	1704-171030	200	-17 to -5	3-6	0.16	ice	500	-14 to -18	5-15	0.04	ice
2/8/94	W	2230-223430	350	-12	0.4	0.3	ice	700	-11 to -14	4-5	0.0	ice
2/19/94	W	221500-222000	-	-	-	-	-	200	-2° C	0	0.25	water
2/21/94	W	213600-214000	-	-	-	-	-	600	-5 to -10	1-3	1.0	freezing drizzle
2/22/94	W	203400-204900	-	-	-	-	-	100	-5 to -10	0.4	0.05	ice
2/28/94	W	175000-180900	350	-2 to -3	0.5	0.45	drizzle	250	-2 to -3	0.5	0.2	freezing drizzle
3/6/94	E	1433-1441	800	-5 to -11	0.4 to 0.8	0.2	graupel	600	-3 to -6	1-5	0.35	freezing drizzle
3/7/94	E	210000-210600	700	-8 to -10	0.01	0.05	unknown	600	-8 to -10	0.1	0.375	graupel
3/12/94	E	1526-1530	900	-7 to -10	0	0.02	water	500	-5 to -8	0.01	0.25	graupel

W - Wyoming King Air
N - NCAR King Air
E - NCAR Electra

Table 2

Sample Date Time (UTC)	Above or Below Cloud	Type of Processing	Bag or Filter	Ice Nuclei Concentration #/L	Processing Temperature ° C	Water Supersaturation (%)
2/24/93 005318	Above	CFD	Bag	1.13	-16.8	1.9
2/24/93 003400	Below	CFD	Ground Sample	0.84	-16.7	0.1
2/24/93 005318	Above	Rosinski TDC	Filter	0.9	-10.5	1
2/8/94 195532	Above	CFD	Bag	0.35	-15.6	6.7
2/8/94 194719	Below	CFD	Bag	0.09	-15.5	6.8
3/6/94 183300	Above	CFD	Bag	0.01	-11.3	4.1
3/7/94 211135	Above	CFD	Bag	1.45	-9.6	1.5
3/7/94 205633	Below	CFD	Bag	0.59	-9.7	1.4
3/12/94 150030	Above	CFD	Bag	0.31	-11.5	3.1
3/12/94 151312	Below	CFD	Bag	0.1	-11.3	2.8

ice crystal concentrations. The above-described vertical structure is consistent with the lower layer having as its source for ice nuclei the surface, with eddy transport providing a sufficiently rapid vertical flux of ice nuclei to maintain the observed concentration against depletion by fallout. The lower ice crystal concentration in the upper layer is consistent with the upper layer being dynamically isolated from the lower layer, and the overlying air mass being either dynamically isolated, or containing lower ice nuclei concentration. In most cases, the temperature of both the upper and lower layers is nearly the same, providing a significant source for ice crystal variation at a given temperature.

5. Acknowledgments

This research is sponsored by the National Science Foundation through an Interagency Agreement in response to the requirements and funding by the Federal Aviation Administration's Aviation Weather Development Program. Support for CSU's ice nuclei measurements was provided by NSF grants ATM-9103748 and ATM-9317405. The views expressed are those of the authors and do not necessarily represent the official policy or position of the U.S. Government.

6. References

- Cooper, W.A., 1986: Ice initiation in natural clouds. In "Precipitation Enhancement - A Scientific Challenge," *Meteor. Monogr.*, No. 443, Amer. Meteor. Soc., Boston, 29-32.
- DeMott, P.J., 1992: Quantifying ice nucleation by cloud seeding aerosols for use in conceptual and numerical models. Symposium on Planned and Inadvertent Weather Modification, Amer. Meteor. Soc., Atlanta, 148-155.
- DeMott, P.J. and D.C. Rogers, 1990: Freezing nucleation rates in laboratory simulations of natural cloud formation. *J. Atmos. Sci.*, **47**, 1056-1064.
- Langer, G. and J. Rodgers, 1975: An experimental study of the detection of ice nuclei on membrane filters and other substrata. *J. Appl. Meteor.*, **14**, 560-570.
- Rasmussen, R.M., 1995: Research in cloud and precipitation physics: Review of U.S. theoretical and observational studies, 1991-1994. *Rev. Geophysics*, 1995 Supplement, 795-809.
- Rasmussen, R.M., B. Bernstein, M. Murakami, G. Stossmeister, J. Reisner and B. Stankov, 1995: The 1990 Valentine's Day arctic outbreak Part I: The mesoscale and microscale structure and evolution of a Colorado Front Range shallow upslope cloud. *J. Appl. Meteor.*, **34**, No. 7, 1481-1511.
- Rogers, D.C., 1988: Development of a continuous flow thermal gradient diffusion chamber for ice nucleation studies. *Atmos. Research*, **22**, 149-181.

RADAR ATTENUATION IN TOGA-COARE SYSTEMS : ESTIMATION AND INTERPRETATION FROM MICROPHYSICAL DATA

Virginie Marécal, Sébastien Houée, Paul Amayenc, Taoufik Tani and Jacques Testud

Centre d'études des Environnements Terrestre et Planétaires
Issy-les-Moulineaux, France

1. INTRODUCTION

Estimation of the rain rate (R) is an important goal of the TOGA/COARE experiment (Webster and Lukas, 1992). It can be made from radar reflectivity measurements. Those provided by the airborne radars at 14 and 10 GHz during the experiment clearly showed evidence of along-path integrated attenuation (PIA) due to rain in convective regions (e.g. Oury et al., 1995, Amayenc and Tani, 1995). Attenuation effect can lead to a large underestimation in the rain rate R when converting the measured "apparent" reflectivity factor Z_m uncorrected for PIA (instead of the true Z) into R by means of a "Z-R relation".

Several algorithms have been developed to correct for PIA effect. This is the case for a class of algorithms proposed by Marzoug and Amayenc (1994) which determine first the Z- or K-profile using primarily a Z-K relation, then, the R-profile using K-R or Z-R relation, where K is the attenuation coefficient due to rain. Amayenc and Tani (1995) have defined a method (AT-method) which may lead to a bulk adjustment of the Z-K relation from downward-looking rain radar measurements over a set of paths. The method also involves surface echo data below and outside rain (as a reference) to estimate of the total PIA in the rain layer.

In this study, we compute relations between Z, K and R from drop size distributions (DSD) data of the PMS-2D probe mounted on board the Electra/NCAR aircraft in TOGA-COARE. These relations are compared with those adjusted by the AT-method applied to data of the downward-looking Airborne Rain-Mapping Radar (ARMAR) installed aboard the DC8/NASA aircraft (Durden et al., 1994). As TRMM radar simulator, ARMAR (13.8 GHz) performs $\pm 20^\circ$ cross-track scanning in 2 s with along-track sampling every 440 m.

2. EXPERIMENT AND DATA

Observations were taken on 6 Feb. 1993 over ocean within a NW-SE oriented rainband at periphery of hurricane Oliver. The rain system lasting for several hours without major change in its global structure was composed of a series of convective cells embedded within stratiform precipitation. This case study was selected because of good coincident samplings by both instruments. **Fig. 1** displays the Electra and DC8 trajectories together with a composite (1630 to 1930 UT) of reflectivity measured by the ELDORA/ASTRAIA tail radar (10 GHz) aboard Electra.

The DC8 flight altitude was 9.4 km. The involved "rain" time sequences S1 (163107 to 164345 UT), and S2 (180204 to 181220 UT) both correspond to about 150-km leg along the rainband. Data for "reference" surface echo in clear air were gathered from 175715 to 180202 UT just before gathering rain data of S2.

The microphysical data were collected at 3.2 km altitude from 1630 to 2000 UT within rain while the Electra crossed over the rainband several times.

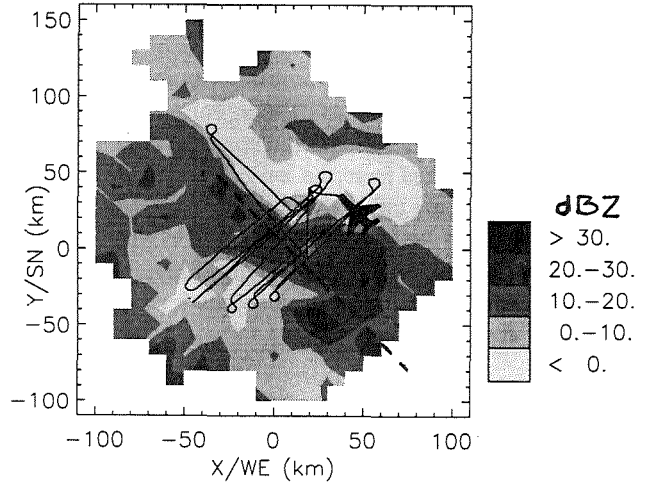


Fig. 1: Radar reflectivity composite between 1630 and 1930 UT at 3.2 km altitude. The solid and dashed lines correspond respectively to the Electra (1630-1930 UT) and to the DC8 (1802-1812 UT) trajectories.

3. MICROPHYSICAL DATA PROCESSING

The integrated parameters K and Z (13.8 GHz), and R were calculated from each measured DSD ($N(D)$ in m^{-4}) using:

$$Z(mm^6 m^{-3}) = \frac{\lambda^4 \times 10^{18}}{\pi^5 |K|^2} \int_D N(D) \sigma_b(D) dD \quad (1)$$

$$K(dB km^{-1}) = \frac{10^4}{\ln(10)} \int_D N(D) \sigma_a(D) dD \quad (2)$$

$$R(mm h^{-1}) = 3.610^6 \times \frac{\pi}{6} \int_D N(D) v(D) D^3 dD \quad (3)$$

In (1), Z is the equivalent reflectivity factor since for 13.8 GHz, the Rayleigh approximation is not valid and $|K|^2 = 0.93$ is related to the water refractive index. In (3), $v(D)$ is the terminal fallspeed (in $m s^{-1}$) of raindrops given by Gunn and Kinzer (1949). In (1) or (2), $\sigma_b(D)$ and $\sigma_a(D)$ (in m^2), represent respectively the raindrop

backscattering and absorption cross-section, and depend on the drop temperature, and the incident wave frequency and polarization. They can be computed using Mie diffusion theory while assuming spherical raindrops. It is known, however, that a raindrop flattens when its size increases, owing to aerodynamical effects. Here, we choose to consider raindrops as spheroids with the small axis oriented vertically. Thus, σ_b and σ_a were computed using the T-Matrix approach (Waterman, 1965), and the nadir-looking geometry to simulate ARMAR. The raindrop temperature was assumed to be 10°C (close to the air temperature at 3.2 km altitude).

The PMS-2D probe samples particles with diameter ranging from 0.2 mm to 6.4 mm. The DSD's were calculated using 6-s time samples. The larger particles provide a major contribution to K, Z or R. The probability that the probe records a very large particle is very low, and not statistically significant. Thus, such "marginal" large particle measurements were eliminated in N(D) data.

We selected DSD's corresponding to $R \geq 5 \text{ mmh}^{-1}$ since the AT-method was applied to ARMAR data fulfilling approximately this condition. This led us to select 126 DSD's. The Z, K and R derived from these N(D) data were fitted by using 3 power-law relations:

$$Z = a_1 K^{b_1}; Z = a_2 R^{b_2}; K = a_3 R^{b_3} \quad (4)$$

To determine the (a_i, b_i) coefficients, we looked for the best linear fit of the data plotted in a log-log scale. The "standard" least square (LS) fit between any variable pair is usually performed by selecting arbitrarily a dependent variable (including errors to be minimized) and an independent error-free variable. There is, however, a natural scatter in all three involved variables. Thus, we choose to apply an "orthogonal" LS fit minimizing the perpendicular distance from the data point to the fit line. To avoid dependency of the results on unit scales, every fit was performed over normalized range interval [0-1] for all variables. This method has two sound advantages compared to "standard" fits: i) any relationship can be analytically inverted; ii) the 3 relations are self-consistent since the analytical combination of any relation pair recovers the third relation. In all cases, the "orthogonal" fit line stands between the X(Y) and the Y(X) "standard" fit lines. Under these conditions, the obtained relations are:

$$Z = 2.24 \cdot 10^4 K^{1.375} \quad \rho = 0.97 \quad (5)$$

$$Z = 94.7 R^{1.593} \quad \rho = 0.91 \quad (6)$$

$$K = 0.0182 R^{1.171} \quad \rho = 0.98 \quad (7)$$

where ρ is the linear correlation coefficient. The correlation between the variables is generally good. The more scattered results around the fit is for Z-R.

In **figs 2a (2b)** are plotted the Z-K (Z -R) results using "orthogonal" fit. The data points extend up to nearly 50 dBZ and there are enough large Z values to get a representative relation for intense convection.

Also in **fig. 2b** are shown the two "standard" LS fits for Z-R and R-Z. The three fits yield different results. For instance, the maximum value for R (64 mmh⁻¹) corresponds to 47.6 dBZ for the Z-R fit, 49.9 dBZ for R-Z fit, and 48.5 dBZ for the orthogonal fit which takes into account the scatter of both variables.

Until now, we considered particles with $D \geq 200 \mu\text{m}$ which is the minimum size detectable by the 2D-P

probe. In the calculation of K, Z, and R, the precipitating particles dominate. Nevertheless, cloud particles with high concentration may have a significant contribution. To test the impact of particles with $D < 200 \mu\text{m}$, we used the 2D-C probe data involving cloud particles with D down to 25 μm . The coefficients of the relationships obtained combining the 2D-C and 2D-P data differ from those of relations (5) to (7) by less than 0.5 %. Hence, the contribution of cloud particles to Z, K and R may be neglected.

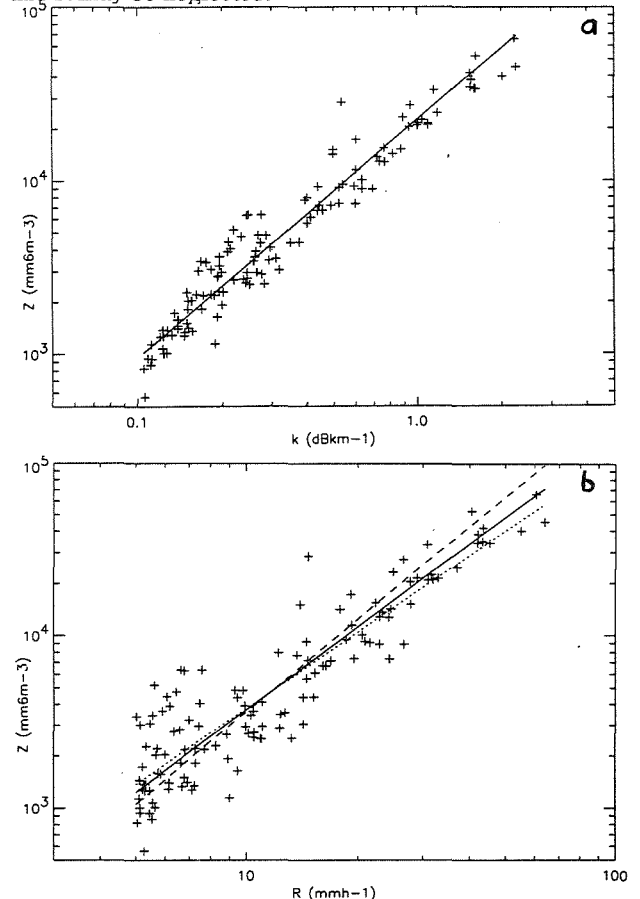


Fig. 2: Scatter plot of (a) Z versus K and (b) Z versus R. The solid line corresponds to the orthogonal fit line. In (b), the dotted and dashed lines corresponds to the standard Z-R and R-Z fits, respectively.

The previous test also proves that large size particles are dominant in the calculation of the integrated parameters. To show the effect of the procedure used for eliminating "marginal" large particles, the relations were computed with the genuine DSD data including all recorded particles, yielding :

$$Z = 3.05 \cdot 10^4 K^{1.476} \quad \rho = 0.89 \quad (8)$$

$$Z = 96.6 R^{1.683} \quad \rho = 0.80 \quad (9)$$

$$K = 0.0194 R^{1.157} \quad \rho = 0.98 \quad (10)$$

The two K-R relations (7 and 10) are closed to each other. Differences increase for the other two relations. For instance, the maximum value of K (2.26 dB km⁻¹) corresponds to 48.4 dBZ with (5), and 50.1 dBZ with (8). The Z-K and Z-R relations involve Z which is much more dependent than R and K on the concentration of larger particles. This yields lower ρ and more scattered data for (8) and (9) (see **fig. 3**).

Hence, elimination of "marginal" large particles is a major point in the computation of the relationships.

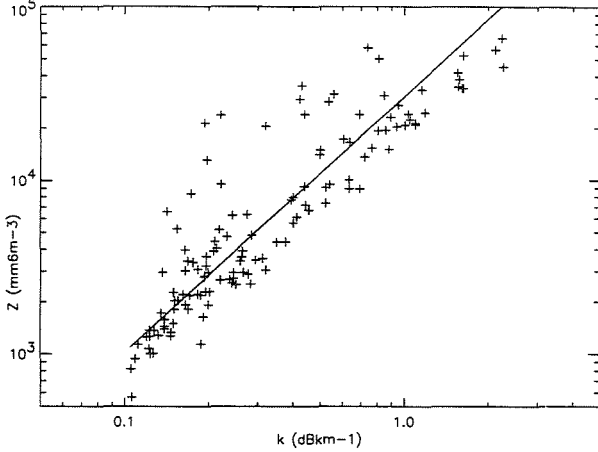


Fig. 3: As Fig. 2a except that the large particles elimination procedure is not applied to the DSDs.

4. ARMAR DATA PROCESSING

The AT-method (see Amayenc and Tani, 1995) uses a linear LS fit to minimize the deviation between the total PIA factors $A = [1 - (\gamma f_B \alpha)^{-1/\beta} S]^\beta$ derived from rain echoes, and A_t derived from the ratio of surface echo power outside rain and below rain, assuming no change in the surface backscatter coefficient σ^0 (due to surface wind or drop impact over ocean). This allows to get a bulk correction factor f_B according to :

$$f_B = \delta\alpha\delta C = \gamma\alpha^{-1} \left[\sum_{i=1}^N S_i^2(r_0, r_s) / \sum_{i=1}^N (1 - A_{t,i}^{1/\beta}) S_i \right]^\beta \quad (11)$$

where r_0 and r_s are the rain top and surface ranges, respectively; $\gamma=0.46/\beta$; α and β (β is assumed to be a known constant) are the coefficient of the reference relation $Z=\alpha K^\beta$ used in the analysis; i is the path index; A_t is the total PIA factor (<1) derived from surface echo data, and $S(r_0, r_s) = \int_{r_0}^{r_s} Z_m^{1/\beta}(r) dr$; $\delta\alpha$ and δC represent possible errors in α coefficient, or in the radar calibration constant C , respectively. Every error term δx is defined as a (positive) multiplying factor of x -value chosen as reference.

f_B barely depends on β (which is mainly a norm in (11)). It is determined over a set $\{N\}$ of N radar beam paths within the rain system. Equ. (11) shows that the α coefficient in Z-K relation may be adjusted provided that $\delta C \approx 1$ (i.e. negligible radar calibration error).

For every rain sequence S1 and S2, we selected three $\{N\}$ sets, corresponding to beam incidence $\theta=0^\circ$ (nadir), 10° off nadir (left + right azimuths), and 18° off nadir (left + right azimuths), respectively. Only the paths for which the rain top was at least 5 km altitude, and $PIA > 1$ dB (i.e. the typical rms error in σ^0 estimate outside rain) were selected for the fit.

5. RESULTS AND DISCUSSION

As case 1, we used a reference Z-K relation associated with a standard exponential DSD with

$N_0 = N_{0MP} = 0.8 \cdot 10^7 \text{ m}^{-4}$ (Marshall-Palmer, 1948) which corresponds to the relation set:

$$Z = 4.45 \cdot 10^4 K^{1.40} \quad (12)$$

$$Z = 345 R^{1.60} \quad (13)$$

$$K = 0.0314 R^{1.14} \quad (14)$$

Results for f_B are given in Table 1. The number of paths N , along with the r.m.s. deviation and the linear correlation coefficient ρ of the fit are also indicated. Results are very stable with a mean value $f_B = 0.5$.

As case 2, results for f_B using the PMS-derived relation (5) are given in Table 2. Again, results are very stable with a mean value $f_B = 0.985$. Illustration of the correlation between PIA (from rain and surface echo) obtained for the sequence S2 (nadir) after the f_B adjustment is shown in fig. 4.

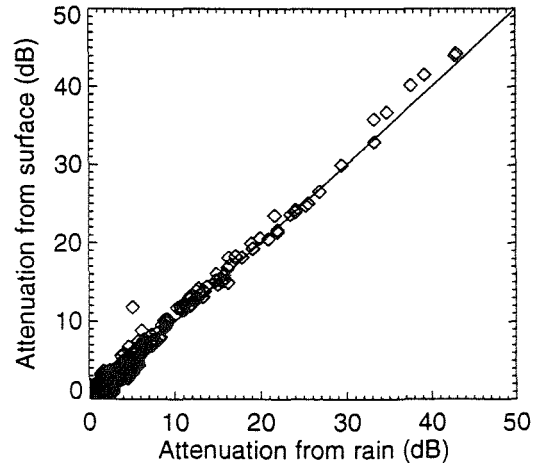


Fig. 4: Scatter plot of total PIA deduced from rain versus total PIA deduced from surface echo after adjusting f_B for sequence S2 and $\theta=0^\circ$ (nadir).

There is good indication from the data that the radar calibration error is negligible ($\delta C \approx 1$). This is based on the observed stable agreement (within 0.5 dB) between radar-derived σ^0 in clear air, and model predictions or other data (Tani et al., 1995) at $\theta=10^\circ$ where σ^0 is insensitive to surface wind. In these conditions, f_B may be interpreted primarily as α -adjustment of the $Z=\alpha K^\beta$ relation. The a coefficient of any other relations between integrated parameters X and Y , $X=aY^b$, may also be adjusted (to a') from f_B using, in each case:

$$a' = a (\alpha'/\alpha)^{(1-b)/(1-\beta)} \quad \text{with } (\alpha'/\alpha) = f_B \quad (15)$$

This equation derives from analytical considerations showing that, for Γ -shaped DSD, assuming changing N_0 to N_0' implies:

$$N_0'/N_0 = f_B^{1/(1-\beta)} \quad (16)$$

In the first case ($f_B=0.5$), referring to MP DSD, the ARMAR-adjusted relations

$$Z = 2.23 \cdot 10^4 K^{1.4} \quad (17)$$

$$Z = 122 R^{1.6} \quad (18)$$

$$K = 0.0246 R^{1.14} \quad (19)$$

are close to the PMS-derived relations (5) to (7), especially the primary adjusted relation Z-K (5). Note that attenuation effects implied by Z-K and K-R

relations (17 and 19), are severely increased when compared to the MP case relations (13 and 15).

In the second case ($f_B = 0.985$), referring to the PMS-derived DSD, the ARMAR-adjusted relations

$$Z = 2.21 \cdot 10^4 K^{1.375} \quad (20)$$

$$Z = 92.6 R^{1.593} \quad (21)$$

$$K = 0.0181 R^{1.171} \quad (22)$$

are almost identical to the PMS-derived relations. There is no need to modify significantly the PMS relations.

Results for the MP, the PMS-derived, and the ARMAR-adjusted (case 1 and 2) Z-K relations are illustrated in fig. 5.

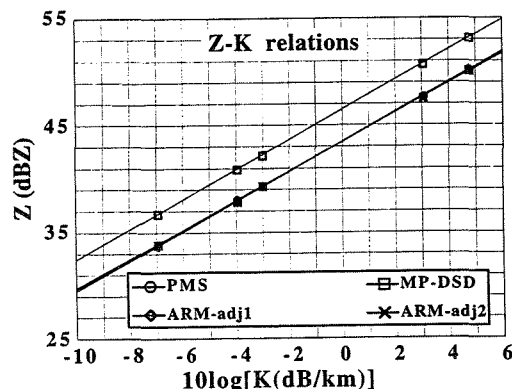


Fig. 5: Z-K relations: MP-DSD (12); PMS-derived (5); ARMAR-adjusted from MP (17) "case 1" or from PMS (20) "case 2". The range for K corresponds to a range of about (5-100 mm/h) for R according to (7).

sequ. / $\theta(^{\circ})$	N	rms(dB)	ρ	f_B
S1 / 0°	122	0.69	0.94	0.51
/ 10°	271	1.04	0.90	0.49
/ 18°	252	0.90	0.84	0.50
S2 / 0°	252	1.14	0.79	0.52
/ 10°	526	1.14	0.77	0.49
/ 18°	354	0.90	0.80	0.49

Table 1: f_B results for S1 and S2 rain sequences, and various incidences θ with MP Z-K relation.

sequ. / $\theta(^{\circ})$	N	rms(dB)	ρ	f_B
S1 / 0°	122	0.71	0.94	1.03
/ 10°	271	0.95	0.90	0.97
/ 18°	252	1.28	0.84	0.98
S2 / 0°	252	0.99	0.80	1.01
/ 10°	526	1.15	0.77	0.95
/ 18°	354	0.91	0.80	0.97

Table 2: f_B results for S1 and S2 rain sequences, and various incidences θ with PMS-derived Z-K relation.

In addition, note that the median N_0 value derived from the PMS data (using exponential-shaped DSD's) is $4.4 \cdot 10^4 \text{ m}^{-4}$ which implies $N_0/N_{0MP} = 5.5$. This is in good agreement with the value 5.7 which may be derived from (16) with $f_B = 0.5$. This also points out the self-consistency of the results.

6. CONCLUSION

We derived relations at 13.8 GHz between K, Z and R using DSD from airborne PMS data within a rain event observed during TOGA-COARE. The use of the orthogonal linear fit appears more appropriate than standard LS fit to account for the natural scatter of all variables. In the present case, cloud droplets contributed negligibly to the integral parameters. The marginal very large particles, however, should be eliminated since their detection is not statistically significant but modify substantially the results.

The PMS relations were compared to the relations adjusted by using the AT-method applied to ARMAR radar data (13.8 GHz). This method provides primarily a bulk correction factor for the Z-K relation, and infers correction factors for the other ones. Comparison between the PMS-derived and the ARMAR-adjusted relations provides very good results which proves the self-consistency of the approach. A major conclusion is that attenuation effects are more important by a factor of 2 for Z-K, and 1.5 to 1.6 for K-R (in the 5-50 mm/h range) than those which could be predicted with relations derived from "standard" MP DSD's. Analysis of other events using the same approach is required before claiming that this is a general feature of tropical oceanic rain systems in TOGA-COARE.

7. REFERENCES

- Amayenc P., and T. Tani, 1995: Tests of algorithms for range-profiling of the rain rate from ARMAR data in TOGA-COARE, *Proc. 27th Conf. on Radar Meteorology*, pp 789-791, A.M.S., Vail, Co, USA, 9-13 October 1995.
- Durden S. L., Im E., Li K., Ricketts W., Tannier A., and W. Wilson, 1994: ARMAR: An Airborne Rain-Mapping Radar, *J. Atmos. Ocean. Technol.*, 11, 727-737.
- Gunn R. and G. D. Kinzer, 1949: The terminal velocity of fall for water drops in stagnant air, *J. Meteor.*, 6, 243-248.
- Marshall J. S., and W. M. K. Palmer, 1948: The distribution of raindrops with size, *J. Meteor.*, 5, 165-166.
- Marzoug M., and P. Amayenc, 1994: A class of single and dual-frequency algorithms for rain rate profiling from a spaceborne radar-I. Principle and tests from numerical simulations, *J. Atmos. Ocean. Technol.*, 11, 1480-1506.
- Oury S., Testud J. et V. Marécal, 1995: Application of the stereoradar analysis to a real data set from the TOGA/COARE experiment, *Proc. 27th Conf. on Radar Meteorology*, pp 700-702, A.M.S., Vail, Co, USA, 9-13 October 1995.
- Tani T., Amayenc P., and M. Ali-Mehenni, 1995: Radar return from the ocean surface and path-integrated attenuation at 13.8 GHz as derived from ARMAR data in TOGA-COARE, *Proc. 27th Conf. on Radar Meteorology*, pp 694-696, A.M.S., Vail, Co, USA, 9-13 October 1995.
- Waterman P. C., 1965: Matrix formulation of electromagnetic scatterings, *Proc. IEEE*, 53, 805-812.
- Webster P. J., and R. Lukas, 1992: TOGA-COARE: The Coupled Ocean- Atmosphere Response Experiment, *Bull. Amer. Soc.*, 73, 1377-1416.

8. ACKNOWLEDGMENTS

The authors express their appreciation to F. Marks, P. Willis and R. Black of NOAA/AOML, Miami, for providing the experimental DSD data. We acknowledge E. Obligis and C. Klapisz for providing us with the T-matrix results.

THEORETICAL STUDY OF THE MICROPHYSICAL STRUCTURE OF MIXED STRATIFORM FRONTAL CLOUDS AND THEIR PRECIPITATION

Svetlana V. Krakovskaia and Anne M. Pirnach

Ukrainian Hydrometeorological Research Institute, 37 Nauki Av., Kiev-252028, Ukraine

1. INTRODUCTION

Microphysical and dynamical processes in winter stratiform clouds are subjects of continuous theoretical investigations for many years in UHRI (Buikov and Dehtyar 1968, Buikov and Pirnach 1976, Pirnach 1976, Khvorostyanov 1987, Pirnach and Krakovskaya 1994, etc.). The theoretical studies mixed stratiform clouds with aid of detailed microphysical numerical models have shown the models are good tools in the study internal structure and physical processes into cloudiness particularly frontal one.

In the presented research one-dimension numerical models with the detail description of an evolution of cloud particles (droplets, raindrops, crystals, cloud nuclei, etc.) are used to study the microphysical processes in supercooled winter frontal clouds.

Number runs of mixed supercooled clouds have explored to how extent the different microphysical processes (such as collection, aggregation, freezing, accretion, riming, etc.) and thermodynamical conditions (such as surface temperature and updrafts) can influence on the cloud and precipitation developments.

2. SHORT DESCRIPTION OF THE MODEL

In this section only the necessary for full understanding of presented results and separated steps of the model construction will be described. The reader is referred to Buikov and Dehtyar (1968), Buikov and Pirnach (1976), Pirnach (1976), (1979), Pirnach and Krakovskaya (1994) and Akimov et.al. (1984) for a detailed presentation of the methodology, set of equations and numerics.

In the below investigations the spectrum of liquid cloud drops is divided into two parts: droplets (< 20 mkm) and raindrops (> 20 mkm). The spectrum of cloud droplets is suggested to form due to condensation, turbulent diffusion and motion of drops. Besides the above processes the spectrum of raindrops is formed by collection for droplets additionally. The size distribution function of the ice particles is assumed to form due to sublimation, turbulent diffusion, motion, riming, glaciation (heterogeneous freezing), accretion and aggregation.

The set of the basic model equations is as follows:

$$\begin{aligned} \frac{df_i}{dt} + \frac{\partial}{\partial r} \left(\dot{r}_i f_i \right) - v_i \frac{\partial f_i}{\partial z} &= I_{ai} \pm I_{fi} - \delta f_i + \Delta f_i, \\ \frac{df_j}{dt} + \frac{\partial}{\partial r} \left(\dot{r}_j f_j \right) + \frac{\partial}{\partial r} \left(\dot{r}_{cj} f_j \right) - v_j \frac{\partial f_j}{\partial z} &= \pm I_{fj} + \Delta f_j, \\ \frac{dT}{dt} &= -\gamma_a w + \sum_{k=1}^4 \alpha_k \varepsilon_k + \Delta T, \\ \frac{dq}{dt} &= -\sum_{k=1}^4 \varepsilon_k + \Delta q, \quad \alpha_k = L_k / C_p, \end{aligned} \quad (1)$$

where $i=k=1$ for droplets; $i=k=2$ for cloud ice particles, $j=1, k=3$ for raindrops and $j=2, k=4$ solid precipitation; f_i and f_j are cloud (CP) and precipitation particles (PP) size distribution functions; \dot{r}_i and \dot{r}_j are rates of CP's and PP's growth due to condensation (sublimation); \dot{r}_{ci} is rate of continuous coagulation growth of PP; δf_i describes decreasing of CP by collection; I_{ai} are values which describe generation of the cloud condensation and ice nuclei; I_{fi} and I_{fj} are values which describe freezing of droplet and raindrop; ΔS_i ($S_i = f_i, f_j, T, q$) describe turbulent transfer; v_i and v_j are velocity of CP and PP falling; T and q are the temperature and specific humidity of air; ε_k are rates of water vapor condensation (sublimation); w are updrafts; γ_a is the dry-adiabatic temperature gradient; L_k are the condensation (sublimation) heats; C_p is the specific heat at constant pressure of dry air. Updrafts in the model have elliptic profile and are simulated in a layer $0 < Z_m < 4$ km, where $Z_m = 2$ km is a height of maximum updrafts (w_m). Updrafts, surface temperature and humidity are constant during a cloud evolution. The calculated values f_i give full descriptions of cloud microphysics and allow to derive integrated characteristics, such as concentrations of the particles (N_i), the water (ice) contents (q_i) and the total precipitation rate (j):

$$N_i = \int_0^{R_i} f_i dr, \quad q_i = \frac{4\pi\rho_i K_{li}}{3} \int_0^{R_i} r_i^3 f_i dr, \quad (2)$$

$$j = \sum_{i=1}^n \frac{4\pi\rho_i K_{li}}{3} \int_0^{R_i} v_i r_i^3 f_i(r) dr,$$

where ρ_i are the water (ice) densities; K_{li} are the corrected coefficients of CP form; n is the number of the sorts of CP (Buikov and Pirnach 1976, Pirnach and Krakovskaya 1994).

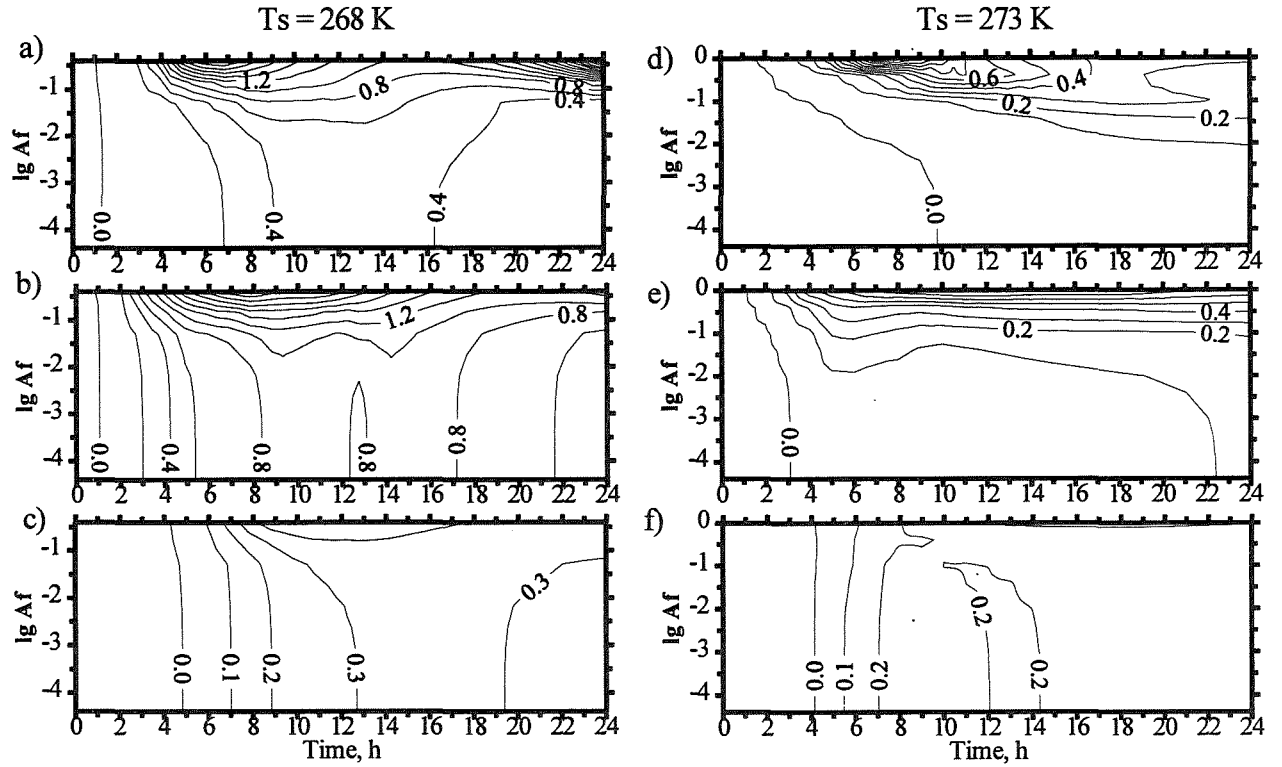


Fig.1. Precipitation intensities j (mm/h) in dependence on surface temperature T_s , freezing coefficient A_f and time of evolutions at $w_m = 2$ cm/s: a) and d) ice precipitation without accretion accounting; b) and e) ice precipitation with accretion accounting; c) and f) liquid precipitation with collection accounting.

3. NUMERICAL EXPERIMENTS

3.1. Study the effects of droplets collection by raindrops and ice particles

In the numerical runs presented in this section, the kernel of gravitational collection and coefficients of accretion for solid and liquid precipitation are calculated as in Shishkin (1964):

$$E_{ci} = \left[1 - \frac{RR_0^3}{4r^2|R^2 - r^2|} \right]^2, R_0 = 14.5 \text{ mkm}$$

where R , r and R_0 are raindrop's (or ice crystal's), droplet's and minimal possible for collection process radiuses respectively (i is as in Eq.1).

Fig.1 shows precipitation rates in dependence on time of cloud evolution and A_f -- freezing coefficient in:

$$I_{fi} = A_f \exp(B_f T_f) r_i^3 f_i \Theta(T_f), T_f = 273.15 - T,$$

where A_f and B_f are the empirical constants (Buikov and Pirnach 1976); $\Theta(T_f) = 1$ for $T_f > 0$ and $\Theta(T_f) = 0$ for $T_f < 0$.

The study was conducted for surface temperatures $T_s = 268^\circ \text{ K}$ and $T_s = 273^\circ \text{ K}$ and at very insignificant dynamics ($w_m = 2$ cm/s). Nevertheless, the accretion accounting in the simulation increases precipitation rate in two times at $T_s = 268^\circ \text{ K}$ and accelerates start of precipitation on 7 h at $T_s = 273^\circ \text{ K}$. At the same time the collection accounting allows to estimate the contribution of liquid precipitation in a total sum. Thus,

for $T_s = 268^\circ \text{ K}$ the averaged for all A_f contribution of liquid precipitation is 17% of total sum (with the maximum of 34%). For $T_s = 273^\circ \text{ K}$ the same value achieves 49% (with the maximum of 84%). Thus, even at so insignificant dynamics ($w_m = 2$ cm/s) the accounting of accretion ice particles and collection raindrops for droplets is necessary.

Results of many numerical runs with aim to estimate effects of thermodynamic characteristics on precipitation intensity are presented on Fig.2a. It shows, while maximum updraft in the middle of simulated cloud determines liquid precipitation intensity, surface temperature T_s do not affect on liquid phase of precipitation in chosen limits practically. At the same time the solid precipitation rate more depends on T_s than on w_m and with temperature falling the angle of the isolines intends to be 90° . Nevertheless, for $T_s > 273^\circ \text{ K}$ influence of w_m on solid precipitation is significant: at $T_s = 275^\circ \text{ K}$ the precipitation intensity grows from 0.1 at $w_m = 2$ cm/s up to 0.8 mm/h at $w_m = 10$ cm/s.

Fig.2b shows differences of solid and liquid precipitation rates. Isoline 0.0 shows equal contributions in precipitation rate of solid and liquid phases. It is interesting for investigation more frequent winter surface temperatures from 268° to 275° K . It is clear from the diagram that accounting of droplet collection for raindrops is undoubtedly important in the above temperature limits. But for more low temperatures the isolines are almost along with the ordinate axis (see

Fig.2b), liquid precipitation rates > 1 mm/h less than solid ones and may be excluded from simulation.

Fig.3 presents an example of one run used for constructing the diagrams in Fig.2. It shows evolution of microphysical characteristics into the cloud and its solid and liquid precipitation rates. The initial conditions correspond to the point at the 0.0 isoline in Fig.2b with equal contributions to precipitation amount of different water phases. They are $T_s = 271^\circ \text{K}$, $w_m = 6$ cm/s and $A_r = 2 \cdot 10^{-3}$. Other numerics are as in Pirnach (1979), Pirnach and Krakovskaya (1994).

The maximum of ice content q_{cr} and solid precipitation rate I_{cr} (see Fig.3) with 2-h delay corresponds to the ice concentration maximum ($N_{cr} > 7 \cdot 10^3 \text{ m}^{-3}$ at the top of cloud $Z = 4$ km at $t = 7$ h of the cloud development). Alike the maximum of raindrops' concentration ($N_{dr} > 0.9 \cdot 10^6 \text{ m}^{-3}$ at $t = 9$ h) with 2-h outstripping corresponds to q_{dr} and I_{dr} maxima. Note, N_{dr} is two orders greater than N_{cr} . A quite rapid falling of I_{cr} after $t = 12$ h may be explained by realization of latent heat of condensation, sublimation and freezing processes (at an absence of melting and evaporation ones due to $T < 273^\circ \text{K}$) and hence appearance of temperature inversion in the low troposphere after $t = 12$ h.

Note, that w_m about 10 cm/s and cloud deepness of 4 km are quite rare events for winter stratiform clouds especially at $T_s < 268^\circ \text{K}$. Hence precipitation intensities > 3 cm/s for each water phase in the upper left corner of Fig.2 seem to be more like as for cumulus clouds or embedded convection in stratus ones.

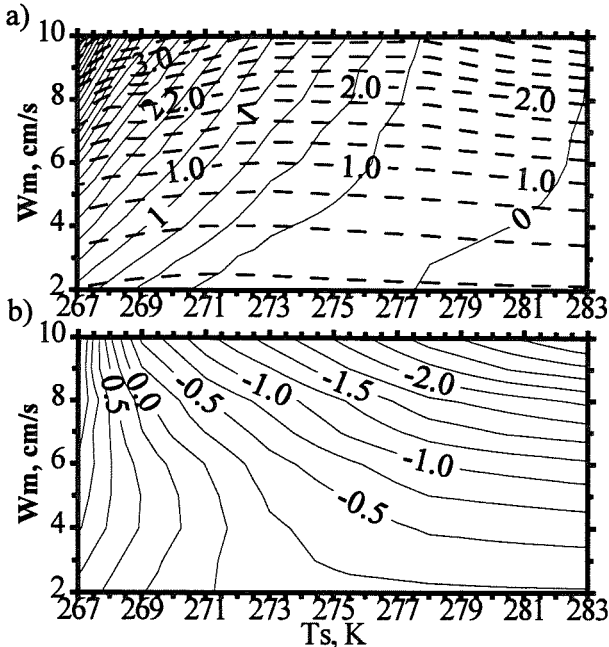


Fig.2. Diagrams of solid and liquid precipitation intensities averaged on 24-h evolutions and their differences in dependence on thermodynamic characteristics. (a) numbers in lines are solid and liquid (smashed line) precipitation rates; (b) differences of solid and liquid precipitation rates.

3.2. Influence on the winter precipitation of collection by solid precipitation particles of cloud particles

As example, there will be considered a case of frontal cloudiness observed in the field experiments at January 6, 1976, that is more detail presented in Akimov and Leskov (1977), Pirnach (1979), Akimov et al. (1984).

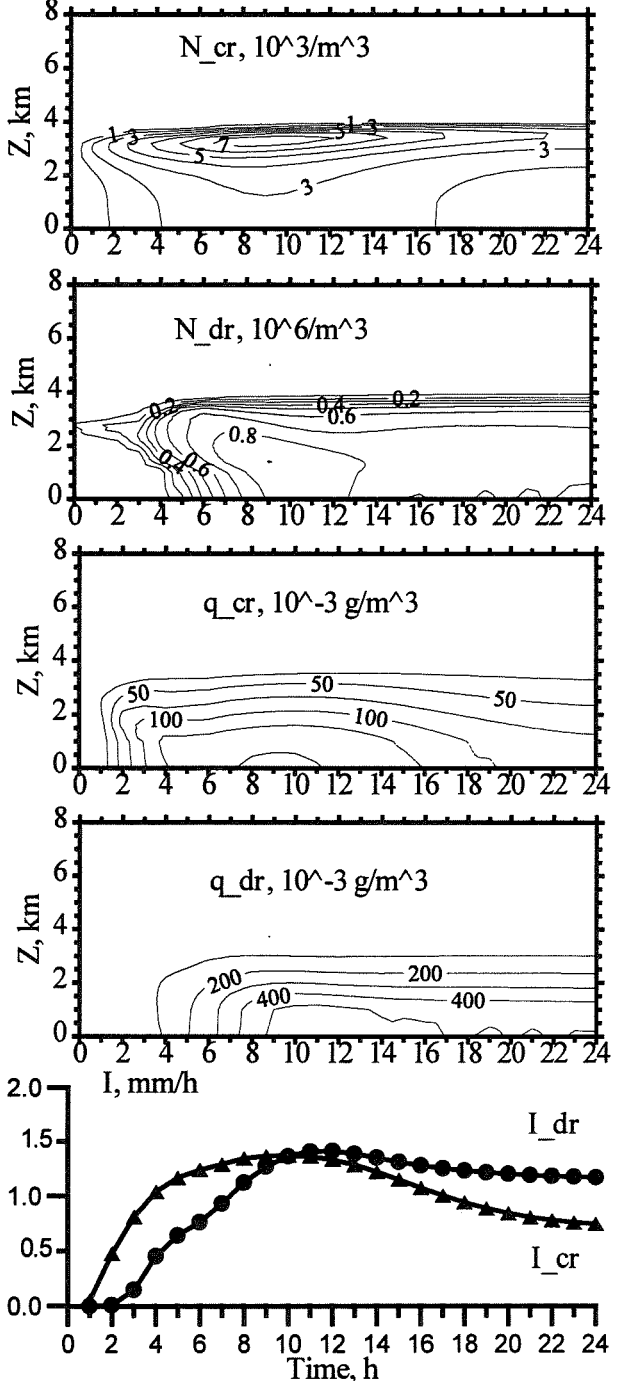


Fig.3. Vertical cross sections of ice (N_{cr}) and raindrop (N_{dr}) concentrations, ice (q_{cr}) and water (q_{dr}) contents and intensities of liquid (I_{dr}) and solid (I_{cr}) precipitation during cloud simulation at $T_s = 271^\circ \text{K}$ and $w_m = 6$ cm/s.

For numerical simulation the one-dimensional model described in Pirnach (1979) was used. The constants and parameters were taken from Pirnach (1979). The initial fields were constructed by interpolating of rawinsonde data. The temperature was decreasing from -10° to -36° at $0 < Z < 5$ km and moisture was of $> 90\%$ in a start time of run. The plate crystals and snowflakes were presented chiefly. These forms were used for modeling.

The numerical simulation shows that mixing cloud located at $1 < Z < 3$ km and above the narrow mixing layers occurred. Presence of depth mixing cloud caused precipitation formation by sublimation and coagulation. The mixing layer disappeared during short time (about 1 h), next time the cloud was crystallized both in field situation and in cloud simulation. Sometimes the mixing layers appeared and forced a high short time activity of aggregation processes.

Table 1 shows the precipitation rate and amount for different precipitation mechanisms. There one can see the strongest influence on precipitation rate of riming processes. The role of snowflake is very neglected if the riming mechanism was working. The appearance the mixing layer stimulated the riming and aggregation processes and appearance of the highest precipitation rate. The precipitation amounts defined by cloud dynamics chiefly. The influence of microphysical mechanisms is significant if there is lack of their total activity to realize all moisture capable for sublimation. There is a question which a precipitation formation mechanism has the best condition to work. At absence of the one mechanism the others are starting and can form the precipitation successfully enough.

4. CONCLUSIONS

The numerical investigations of the microphysical structure of mixed winter frontal clouds have shown:

At all studied parameters and selected conditions the liquid precipitation of supercooled mixed clouds may be significant especially at $T > 273^{\circ}$ K and their averaged value in total precipitation amount is about one thirds.

The influence on liquid precipitation of updraft values is great, while the surface temperature affects liquid phase of precipitation slightly.

Opposite for solid precipitation, the temperature is a principal factor, while the updrafts affect solid precipitation only at quite high temperatures.

Study observed frontal cloudiness has shown that every precipitation formation mechanism is important. While one such mechanism is absent, others are starting with more activity and can form the precipitation successfully enough.

Acknowledgment

This work was supported in part through Grant No. PSU052071 of International Soros Science Education Program (ISSEP).

Table 1
Precipitation intensity, j 10^{-1} mm/h, and twenty-hours total precipitation at different precipitation formation mechanisms

No*	t, h										Σ , mm
	1	2	3	4	5	6	9	12	15	18	
1	13	7	5	4	1	6	3	1	3	4	7.7
2	12	7	5	4	1	6	4	1	3	4	7.5
3	14	7	4	4	1	7	4	2	1	1	7.8
4	4	9	5	4	3	1	7	4	3	0	7.2
5	7	7	4	4	3	2	6	5	1	1	7.5
6	5	7	4	4	3	1	5	5	5	5	6.2

* 1) Sublimation, riming, aggregation (the coagulation coefficient for riming, $E_r = 1$, for aggregation, E_a was computed as in Rogers, 1974); 2) sublimation, riming;; 3) as number 1 and $E_a = 1$; 4) as 1 and nucleation occurred if ice supersaturation $\Delta_s > 0$ **; 5) sublimation, aggregation; 6) sublimation.

** In Cases 1, 2, 3, 5, 6 nucleation occurred if liquid water supersaturation $\Delta_l > 0$.

5. REFERENCES

- Akimov, N.M. and Leskov, B.N., 1977: About periodicity of particles' concentration changing and intensity of solid precipitation. Tr. UHRI, 162, 91-96 (in Russian).
- Akimov, N.M., Palamarchuk, L.V. and Pirnach, A.M., 1984: Investigation of intensity and microstructure of winter frontal precipitation for real synoptic situation. Tr. UHRI, 203: 56-69 (in Russian).
- Buikov, M.V. and M.I. Dehtyar, 1968. Stratiform clouds theory. Tr. UHRI, 70: 21-49 (in Russian).
- Buikov, M.V. and A.M. Pirnach, 1976. Influence on precipitation formation into mixing stratiform clouds of coagulation processes. Tr.UHRI, 144; 3-13 (in Russian).
- Khvorostyanov, V.I., 1987. A three-dimensional numerical model of cloud crystallization under seeding with solid carbon dioxide. Meteorol.Hydrol., 4: 29-38 (in Russian).
- Pirnach, A.M., 1976. Influence on mixing cloud microstructure of a collection by solid precipitation particles of cloud drops. Tr.UHRI, 144: 20-24 (in Russian).
- Pirnach, A.M., 1979. Study of aggregation in stratiform mixing clouds (numerical experiment). Tr.UHRI. 170: 32-43 (in Russian).
- Pirnach, A.M. and Krakovskaya S.V., 1994. Numerical studies of dynamics and cloud microphysics of the frontal rainbands. J. Atmos. Res., 33; 333-365.
- Rogers, D., 1974. The aggregation of natural ice crystals. Report No. AR 110: 35 pp.
- Shishkin, N.S., 1964. Clouds, precipitation and thunderstorm electricity. Gidrometeoizdat: 280 pp. (in Russian).

SHEDDING BY SPONGY GROWTH OF SPHEROIDAL HAILSTONES

Laura Levi¹ and Luisa Lubart

Servicio Meteorológico Nacional, Centro de Física de la Atmósfera, 1427 Buenos Aires, Argentina

¹ Consejo Nacional de Investigaciones Científicas y Técnicas (CONICET)

1. INTRODUCTION

It is usually admitted that rain drops can be formed in convective clouds by liquid water shed both, during hailstone growth in spongy regime and during hailstone or graupel melting. According to the characteristics of the wind field, these drops can either directly contribute to rain precipitation or can be recirculated in the cloud, reaching levels where they freeze and become new hailstone embryos.

The process of shedding from melting graupel and from hail growing in spongy regime has been studied by Rasmussen and Heymsfield (1987a,b,c; hereafter RHa,b,c). This authors applied the experimental results obtained by Rasmussen et al. (1984; hereafter RLP), completed in the case of spongy growth, with evaluations of the frozen fraction of collected water derived from Lesins et al. (1980) for accreted cylinders.

The accretion process on spheroidal collectors has been investigated in wind tunnel experiments where atmospheric conditions have been simulated and values have been found for the main parameters involved in the process (Lesins and List, 1986; García-García and List, 1992; Zheng and List, 1994; List et al., 1995). Among these papers, that of García-García and List (hereafter GL) will be especially considered here and the results will be applied to discuss spongy growth shedding and the related drop formation in a cloudy environment.

2. WET GROWTH AND SHEDDING EFFECT FOR SPHEROIDAL PARTICLES

2.1 Onset of wet growth and of shedding regime

The conditions for the onset of wet growth and of shedding regime were studied by GL for gyrating spheroids that grew in a wind tunnel on ice models of diameter $D = 2$ cm and aspect ratio $\alpha = 0.67$. To simulate the environmental conditions of natural hailstones, the air temperature T_a and pressure P_r

were coupled in the tunnel, using average data from hail day radio-soundings. The airspeed was set equal to the free-fall speed V of the particle

$$V = (4 g \rho_i D \alpha / 3 \rho_a C_D)^{1/2} \quad (1)$$

where: ρ_i and ρ_a are the densities of the hailstone and air, respectively; g the acceleration due to gravity and, for the drag coefficient, it was adopted the value $C_D = 0.29$ (Lesins and List, 1986). The airspeed was calculated for the model initial size, though D increased, in some cases, up to 4 cm. The results were considered useful to improve numerical simulations of clouds where most common hailstones, with diameters in the range of $2 < D < 4$ cm, are found to grow. However, since according to Eq. (1), V is proportional to $D^{1/2}$, when D is duplicated, V increases by about 40%. Thus, since the amount of water collected by a particle in a given time Δt is proportional to V , it can be expected that, for free-falling particles, the conditions for the onset of wet growth and for shedding should change substantially in the mentioned range.

In the present work, the GL results have been taken into account for $D = 2$ cm. For increasing values of D , the parameters have been modified using a numerical simulation of hailstone growth (Levi and Lubart, 1991) and assuming the environmental conditions as those used by GL. The hailstone spheroidal shape and the value of C_D have been maintained and the Nusselt number derived by Zheng and List (1994), has been used. As for the surface temperature T_s , it has been calculated using the Schuman-Ludlam equation and the transition to wet growth has been set at $T_s = 0^\circ\text{C}$, instead of using the results of GL that place this transition at $T_s < 0^\circ\text{C}$. Notwithstanding, for $D = 2$ cm, the calculated onset of wet growth occurred for critical values W_{fI} of the liquid water content W_f , which are nearly the same as those of GL. The results obtained for W_{fI} as a function of D were subsequently used to obtain the values of W_f corresponding to the onset of shedding, W_{fe} , by assuming the ratio W_{fI} / W_{fe} independent of D .

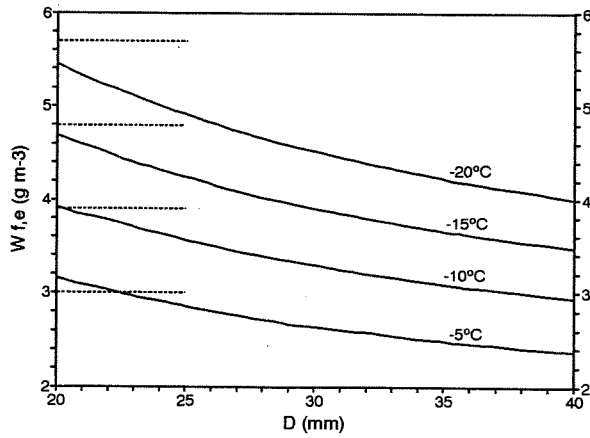


Fig. 1 - Curves for $W_{f,e}$ as a function of D , for different T_a . Straight horizontal lines give $W_{f,e}$ from GL parameterization.

In Fig. 1 $W_{f,e}$ is plotted as a function of D for different values of T_a , using both, the present results and the GL's ones, independent of D . The curves obtained here show a noticeable decrease of $W_{f,e}$ for increasing D . For each T_a , the curves of both families meet at $D = 2$ cm while for $D = 4$ cm they differ by about 25%. Equation (2) was fit to the calculated curves

$$W_{f,e} = 1.227 - 0.062 T_a + (23.32 - 1.82 T_a) / D \quad (2)$$

where D is given in mm.

2.2 Net collection efficiency

List et al. (1980) have defined the net collection efficiency E_{net} as the fraction of the initially collected water that is not returned to the environment. It results from the definition of $W_{f,e}$ that it is $E_{net} < E$ when $W_f > W_{f,e}$. When this condition is satisfied the empirical values of E_{net} , for gyrating spheroids have been adjusted by GL with the equation

$$E_{net} = E / (1 + KE (W_f - W_{f,e})) \quad (3)$$

where $W_{f,e}$ and the parameter KE are calculated from Eqs. A14 and A15 of GL, respectively.

In the present work equation (3) has been extended to particles of different diameters by calculating $W_{f,e}$ from Eq. (2) and by deriving E from Beard and Grover (1974), so that its dependence on D is taken into account.

In Fig. 2, E_{net} is plotted as a function of W_f for different values of T_a and for $D = 2$ and 4 cm. The good agreement of the calculated curves in Fig. 2a with the experimental ones of GL, confirms that the modifications in the parameters E and $W_{f,e}$ do not

affect the results, as far as $D = 2$ cm. On the other hand the comparison between Fig. 2a and Fig. 2b shows that the main effect of the diameter increase on the curve shape is due to the decrease of $W_{f,e}$ shown in Fig. 1.

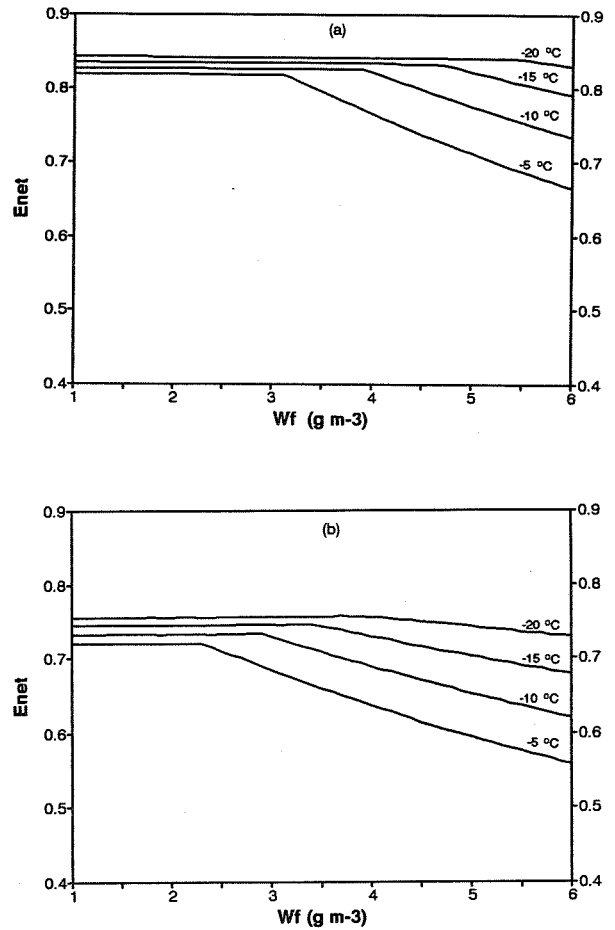


Fig. 2 - E_{net} as a function of W_f for various T_a . (a) $D = 2$ cm; (b) $D = 4$ cm.

3. DROP SHEDDING IN SPONGY GROWTH

In order to evaluate the water mass shed by a particle during both, melting and spongy growth, in RHa, a parameterized equation is used that gives the mass of water on the ice core's M_{wert} , just before shedding occurs, as a function of the core's mass M_i . In RHb, the authors use the mentioned equation to study how shedding, determined by melting of precipitating ice particles, depends on the particle size and density and on the environmental conditions. The results are represented as vertical profiles of the number $N(d)$ of 1 mm drop shed per km per particle ($N(d) \text{ km}^{-1}$) and show that, as soon as shedding due to

melting starts, this variable increases rapidly to the order of magnitude of 10^3 .

In the case of spongy growth, the authors assumed that the particle core consisted of soaked dendrites, using in their calculations the results obtained by Lesins et al. (1980) for the ice fraction found in rotating cylinders grown at normal air pressure. This method was applied in RHc to obtain the vertical profile of $N(d) \text{ km}^{-1}$, for a hailstone falling to the ground from the 7 km level. The profile shows that, though, at the altitude of about 5 km, the transition occurs from spongy growth to melting, no abrupt variations occur of the shed water amount and that $N(d) \text{ km}^{-1}$ reaches values near 10^3 km^{-1} , in the studied region.

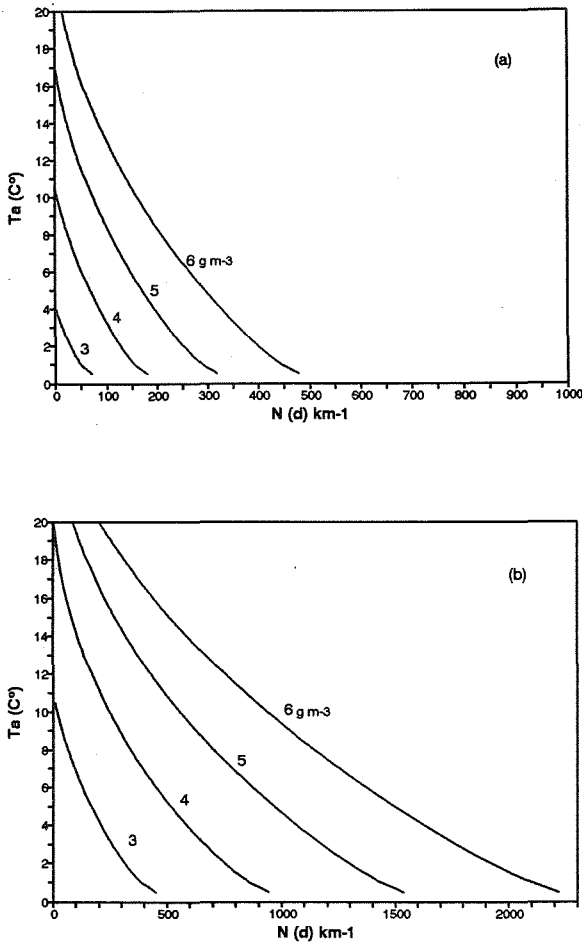


Fig. 3 - $N(d) \text{ km}^{-1}$ as a function of T_a for various W_f
(a) $D = 2 \text{ cm}$; (b) $D = 4 \text{ cm}$.

The study of shedding in spongy growth will now be revised on the light of data provided by GL, that should adjust better than those of Lesins et al. the phenomenon as it occurs for atmospheric particles. This can be done using a growth model where both E

and E_{net} are calculated. Actually the shed mass is given by

$$\Delta M / \Delta t = (E - E_{net}) W_f V A \quad (4)$$

where A is the cross section area of the particle respect to the flux.

Fig. 3 is representative of the results obtained for both, $D = 2$ and 4 cm when, in the growth model described in Section 2.1, E_{net} is calculated using Eq. (3) with W_{fe} from Eq. (2). The hailstones are assumed to precipitate in an environment with a given value of W_f and an updraft speed adjusted so to obtain a precipitation speed of 10 m s^{-1} . Following RHbc, $N(d) \text{ km}^{-1}$ is given on the x-axis while T_a instead of the altitude is given on the y-axis. In the figure curves are shown corresponding to different values of W_f . In Fig 3a, negligible shedding effect is observed up to $W_f = 3 \text{ g cm}^{-3}$ and, even for $W_f = 6 \text{ g m}^{-3}$, $N(d) \text{ km}^{-1}$ only approaches 500 km^{-1} near the melting level. In Fig. 3b, a much larger shedding effect is obtained. The values of $N(d) \text{ km}^{-1}$ are of the order of 10^2 for $W_f = 3 \text{ g m}^{-3}$ and for $W_f = 6 \text{ g m}^{-3}$ values of the order of 10^3 km^{-1} are already found near the -8°C level. Just above the melting level it is $N(d) \text{ km}^{-1} > 2000 \text{ km}^{-1}$.

4. STEADY-STATE CONCENTRATION OF SHED DROPS

It has been noted by RHc that, during spongy growth or melting, hailstones can operate both as drop source and sink, the latter effect occurring due to drop collection by larger particles. The steady-state number concentration of drops present in the atmosphere, $N(d)$, that could eventually become new hailstone embryos should consequently be derived from the simultaneous consideration of both these effects.

The authors assumed hailstones with diameters from 1.8 to 2.2 cm (mean diameter $D = 2 \text{ cm}$) and they calculated $N(d)$ at the 6 km level where spongy growth occurs. They found that the number of drops shed per particle and per second in the cloud model they used would be, at this level, of $9 \times 10^{-7} \text{ drops cm}^{-3} \text{ sec}^{-1}$, while the collection rate ($\text{drops cm}^{-3} \text{ sec}^{-1}$) would be $5.85 \times 10^{-3} N(d)$, thus resulting

$$9 \times 10^{-7} = 5.85 \times 10^{-3} N(d) \quad (5)$$

$$N(d) = 1.54 \times 10^{-4} \text{ drops cm}^{-3} \text{ sec}^{-1} \quad (6)$$

Comparing $N(d)$ with the number per cm^3 of hailstones with diameter D in the assumed range, $N(D)$, they concluded that it would be $N(d) \sim 2000 N(D)$, noting that this large value of $N(d)$ per hailstone would justify the activity of drops as

hailstone embryos. However, they also observe that, for the studied storm, aircraft penetration data indicated a drop concentration in the updraft, at the considered level, about one order of magnitude smaller.

Calculations have been presently reconsidered of drops shed per hailstone per sec, taking as a basis the results of Fig. 3a. For $W_f \leq 4 \text{ g m}^{-3}$ it is found, at all temperatures, $N(d) \leq 200 \text{ km}^{-1}$ and, for $T_a = -6^\circ\text{C}$, $N(d) < 100 \text{ km}^{-1}$. Since, according to aircraft penetration data, the assumed condition for W_f was valid, these results indicate that $N(d)$ values found from the present calculations agree with observations better than with those presented by RHc.

5. CONCLUSIONS

The study of accretions grown in conditions that simulate those existing in clouds, carried out by GL, has permitted us to analyze the process of shedding during spongy growth in a more straightforward way than it had been done before (RH_a), using as a basis the E_{net} expression.

The results indicate that shedding due to spongy growth could only determine significant effects for large hailstones with $D > 2 \text{ cm}$. For smaller diameters shedding due to melting would prevail.

The analysis performed here of this effect will be completed in future work using a cloud model as a frame.

Acknowledgements. The authors are thankful to Pablo Fuente Salas for technical help and to CONICET for economical support.

6. REFERENCES

- Beard, V. and S. N. Grover, 1974: Numerical collision efficiencies for small raindrops colliding with micron size particles. *J. Atmos. Sci.*, 31, 543-550.
- García-García, F. and R. List, 1992: Laboratory measurements and parameterizations of supercooled water skin temperatures and bulk properties of gyrating hailstones. *J. Atmos. Sci.*, 49, 2058-2073.
- Lesins, G. B., P. I. Joe and R. List, 1980: Ice Accretions, Part I: Testing of new atmospheric icing concepts. *J. Rech. Atmos.*, 14, 347-356.
- , and R. List, 1986: Sponginess and drop shedding of gyrating hailstones in a pressure-controlled icing wind tunnel. *J. Atmos. Sci.*, 43, 2813-2825.
- Levi, L. and L. Lubart, 1991: Analysis of hailstones from a severe storm and their simulated evolution. *Atmos. Res* 26, 191-211.
- List, R., G.B. Lesins and P.I. Joe, 1980: Cylinder icing, Part I: Dependence of net collection rate and sponginess on rotation rate. *Proceedings VIII Inter. Conf. Cloud Phys.*, July 15-19, Clermont-Ferrand.
- , B. J. W. Greenan and F. García-García, 1995: Surface temperature variations of gyrating hailstones and effects of pressure-temperature coupling on growth. *Atmos. Res.* 38, 161-175.
- Rasmussen, R. M., V. Levizzani and H. R. Pruppacher, 1984: A wind tunnel and theoretical study of the melting behaviour of atmospheric ice particles. III: Experimental and theory for spherical ice particles of radius $> 500 \text{ }\mu\text{m}$. *J. Atmos. Sci.*, 41, 381-388.
- , and A. J. Heymsfield, 1987a: Melting and shedding of graupel and hail. Part I: Model physics. *J. Atmos. Sci.*, 44, 2754-2763.
- , and -----, 1987b: Melting and shedding of graupel and hail. Part II: Sensitivity Study. *J. Atmos. Sci.*, 44, 2764-2782.
- , and -----, 1987c: Melting and shedding of graupel and hail. Part III: Investigation of the role of shed drops as hail embryos in the 1 August CCOPE severe storm. *J. Atmos. Sci.*, 44, 2783-2803.
- Zheng, G. and R. List, 1994: Preliminary investigation of convective heat transfer of hailstone models. *Atmos. Res.* 32, 75-83.

MONODISPERSE DROPLET DISTRIBUTIONS IN THE ICE ACCRETION PROCESS

Franco Prodi^{1,2} and Federico Porcù¹

¹ FISBAT-CNR, Clouds and Precipitation Group, Bologna, Italy

² Physics Dept., University of Ferrara, Ferrara, Italy

1. INTRODUCTION

The polydispersion of droplet spectra in ice accretion studies has always been considered unavoidable, to the point of forgetting how this is a complicating factor in the understanding of the process. In fact since a natural phenomenon (either hail formation or icing on structures) is considered polydisperse distributions of droplets are always involved. On the other hand the difficulty connected with the generation of monodisperse droplets in sufficiently high concentrations have hindered laboratory investigations.

The droplet size distribution is important in:

- aerodynamic capture by the obstacle. The droplet trajectory is determined by the droplet Stokes number; when polydisperse distributions are accreted, the resulting droplet trajectories intersect close to the obstacle so that a given obstacle surface area collects droplets with a distribution different from the one at infinity.
- the freezing time of droplets. At equal liquid water content and shape, heat dissipation by convection is favored among smaller sizes.
- the spreading factor. Larger droplets have higher spreading factors and the density of the resulting deposits is affected.

Thus it is no wonder that results of experimental accretions differ among the various authors, so much so that it is difficult to find a common ground for comparison (a droplet spectrum is difficult to standardize). As an example of this difficulty, Levi *et al.* (1991), investigating low density accretions on a fixed obstacle, have shown the effect of the droplet spectrum on the density profile with the growth angle and on the transition in growth parameters from concave to convex profiles. Moreover, they compared their results with those of Personne (1988) and found that the transition from concave to convex profiles was at different values of the significant parameters (Stokes number, Reynolds number, Macklin's parameter); they explained the difference in terms of the different droplet spectra used in the two experiments.

However, the experimental difficulty of generating monodisperse droplets in high concentration has been

overcome (Prodi and Prodi, 1984), and recent accretions (Prodi *et al.*, 1996) have proved that the role of a single parameter (impact velocity V) can be isolated and evidenced. It has been proved that the use of monodisperse particles enhances the differences in the resulting deposit and contributes to identifying the critical conditions in which the other mechanisms, such as droplet spreading, are effective.

In this work, the analysis of the role of monodispersion in accretions is carried forward along two main lines. In the first part more experimental evidence is provided, from deposits obtained with monodisperse droplets, that shows that a sharp transition is produced with a minor change of growth parameters. The second part presents a new computational method capable of simulating these transitions. Compared to previous numerical models it simulates the spreading of droplets and, though not including the thermodynamics, it relates the density to the growth conditions.

2. GROWTH OF ACCRETED ICE DEPOSITS

Tests were performed inside a cold two-room laboratory, one room at 3 °C containing the droplet generator, based upon the principle of controlled condensation. The other room, where the droplets accrete, is maintained at -15 °C. Details on the generator, the accretion conditions, droplet characterization and deposit replica system are described in Prodi *et al.* (1996). The general results, for same conditions of temperature and droplet radius and concentration, for four different values of flow velocity, indicate that at decreasing impact velocity structures become more and more distinct and separate from each other, from a conical fan-like structure to isolate feathers and, then, isolated fingers.

Here, in order to evidence the role of monodispersion, we concentrate on details at two conditions not very different as regards the impact velocity, which is 8.0 m s⁻¹ and 4.1 m s⁻¹. The other conditions are the diameter of collecting wire (R) 130 μ m and the radius of monodisperse droplets (r) 4 μ m. Relevant growth parameters for the deposits are the Stokes number K and Maklin's parameter X defined as

follows:

$$K = \frac{2 \cdot r^2 \cdot \rho_w}{9 \cdot R \cdot \eta} V \quad X = -\frac{V \cdot r}{T_d}$$

where ρ_w the water density, T_d the deposit temperature and η the air viscosity. For the two deposits shown in figure 1, we have: $K = 6.4$ and $X = 1.6$ (1a); $K = 3.2$ and $X = 0.8$ (1b).

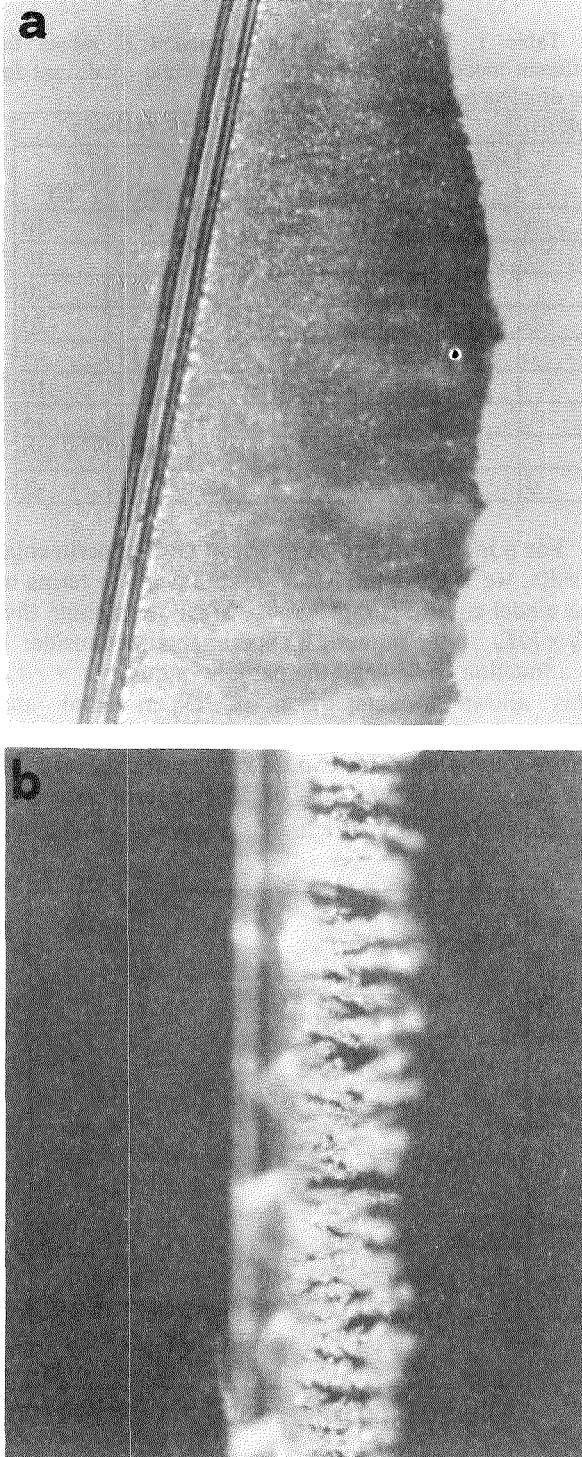


Figure 1. Side view of deposits of accreted ice obtained by impinging monodisperse supercooled droplets ($T_d = -10^\circ\text{C}$). The two deposit conditions differ only in flow velocity, which is 8.0 m s^{-1} (a) and 4.1 m s^{-1} (b).

From the comparative observation of the two pictures, we note that the reduction by half in the flow velocity when monodisperse droplets are used produces an abrupt change in the morphology:

- the shape of the deposit changes from a triangular section (fig. 1a) to a line (fig. 1b);
- the continuous structure changes to individual feathers, separated by large gaps;
- a non negligible density changes to a very low density, that is even difficult to define.

These observations are explained by a change in the spreading factor of the individual droplets and in the collection efficiency of the obstacle.

3. NUMERICAL MODEL

The model simulates the accretion of ballistic droplets on a plane perpendicular to the particle path. The simulation is bi-dimensional and the particles are disks moving on an x, y plane along y .

Circular particles are fired randomly and they hit a flat obstacle: the particle has a circular core that freezes immediately as it touches the obstacle. The rest of the particle mass is assumed to remain in the liquid phase and to have the possibility of moving a little and freezing in subsequent steps.

The positions of the single elements of liquid water on the deposit are determined by minimizing a distance function, depending on the distances of the element from both the ice core and the obstacle (or deposit).

3.1 Model parameters.

The model has three control parameters:

1. P_f percentage of the total droplet mass that freezes instantaneously, as the droplet touches the deposit: it is responsible for the density of the aggregate and affects the droplet's freezing position on the deposit and the relative strength of the shadow effect;
2. W_p weight of the distance of the droplet's liquid part from the frozen core surface, D_p : it affects the tendency of the liquid to freeze on the ice core surface;
3. W_d weight of the distance of the droplet's liquid part from the deposit surface, D_d : it affects the tendency of the liquid to freeze on the deposit surface.

The distance function chosen to be minimized is the sum of D_p and D_d multiplied by their weight W_p and W_d . If $W_d > W_p$ the model will describe experiments with higher T_d , particle temperature, T_p , and impact speed: higher values of the spreading parameters and higher density values of the deposit are expected. Conversely, when $W_d < W_p$, we simulate the low impact speed—low T_d and T_p : the particle freezes in very short time, the liquid part freezes closer to the ice

core, the droplet deformation is lower and the density of the deposit is lower. The droplet deformation is measured by S , defined as the ratio between the initial droplet radius r and the maximum radius of the frozen droplet.

The sensitivity of the model with respect to P_f variations is very low: when P_f is made to range between 0.05 and 0.2, S varies by less than 5% in the worst case. We run the model using W_d as single parameter, because in the difference function the relative balance between D_d and D_p is important and not their numerical values. Therefore we set $P_f = 0.1$ and $W_p = 1$, varying only W_d from values below 1 to values around 10, in order to describe lowest and highest cases of S , respectively.

We assume that W_d depends on V (directly) and T_d (inversely), and completely describes the droplet's spreading by means of the most effective parameters. In this model we are not able to probe deeper into the complex mechanism of droplet freezing: we merely parameterize the balance of two effects, one (impact speed) forcing the water to spread far away from the impact position on the deposit, and the other (temperature of the deposit) forcing the water to freeze near the impact position. We will use the distance as a parameter carrying information on both V and T_d .

3.2 Model results

Laboratory experiments carried out in various conditions suggest that the spreading process is mainly affected by T_d and V , while T_p and r are less crucial in determining S values (Macklin and Payne, 1969, hereafter referred as MP69). The density of the deposit is more sensitive to the r value and depends on X .

There are two features of both numerical and experimental deposits that can be compared: the spreading factor for the single droplet S and the mean density of the deposit. In fig.2 four droplets frozen on an ice substrate are shown for different values of W_d (0.5, 1.0, 2.0 and 4.0).

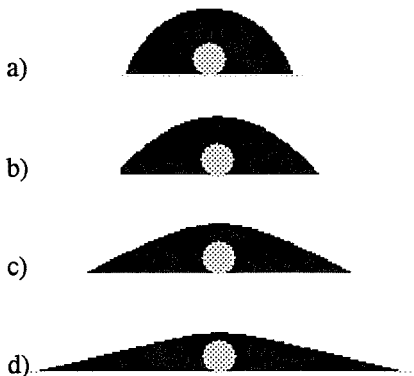


Figure 2. Droplets frozen on a flat ice substrate: the ice core (shaded) and the frozen liquid part (black) are shown.

Experimental and theoretical studies have reported that the density of a deposit can be described in terms of X (Macklin, 1962), which relates the mean volume droplet radius with the impact velocity and the deposit temperature. Experimental values for V , T_d and r , from MP69, are reported in table 1 for droplets with the nearest S value (S^*), with the corresponding W_d value for each droplet.

Table 1. Numerical and experimental S values for different model parameters and experimental conditions for the droplets in fig 2.

MODEL			EXPERIMENTS (MP69)			
#	W_d	S	S^*	V (m/s)	r (μm)	T_d ($^{\circ}\text{C}$)
a	0.5	1.58	1.6	2.5	17	-10
			1.6	4.3	54	-10
			1.6	15.0	17	-20
b	1.0	1.93	1.8	23.0	17	-20
c	2.0	2.52	2.4	2.5	17	-3
			2.4	23.0	17	-10
			2.4	4.3	54	-3
			2.4	18.0	54	-20
d	4.0	3.43	3.4	18.0	54	-3

For a more effective comparison with experimental results, we express the Macklin parameter in terms of the model control parameter W_d . Since we assume that $W_d = V/T_d$, in the numerical experiments we consider X as a function of W_d and the particle radius r : $X = rW_d$. This allows a comparison of experimental and numerical spreading values. In fig 3 and 4 S values versus X are plotted for two different particles' size: 17 μm (fig. 3) and 54 μm (fig. 4). The experimental data are from MP69 with particles temperature $T_p = -22^{\circ}\text{C}$.

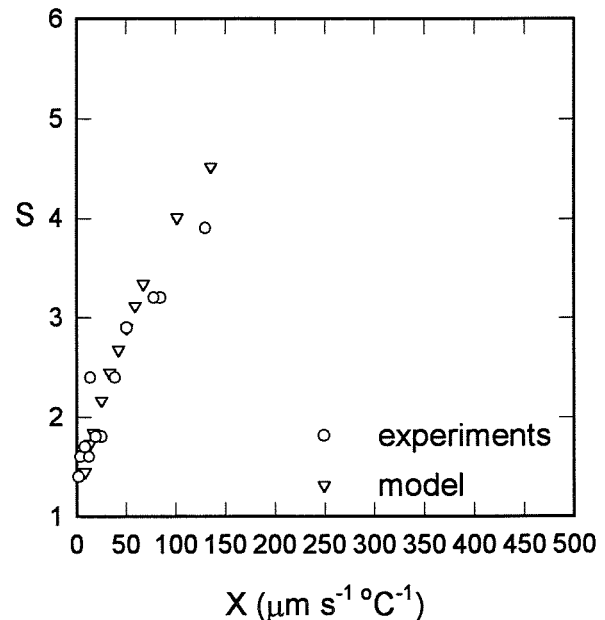


Figure 3. Experimental (MP69) and numerical S value for $r = 17 \mu\text{m}$

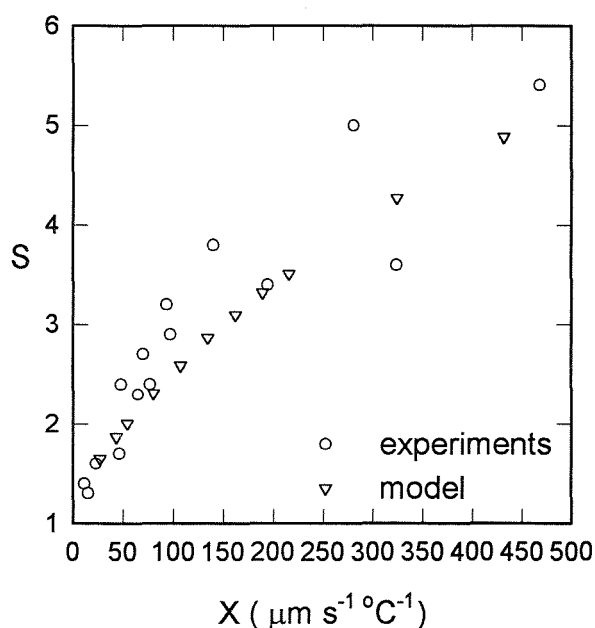


Figure 4. Experimental (MP69) and numerical S value for $r = 54 \mu\text{m}$.

In fig 5 and 6, numerical deposits with different W_d values are shown. In the deposit of fig 5 the droplets spread as in fig 2b, in fig 6 as in fig. 2d. It is qualitatively clear how the variation in W_d affects the density of the deposit.

Further studies are needed to test the capabilities of the model in describing the density of the deposits and its dependance on the growth parameters.

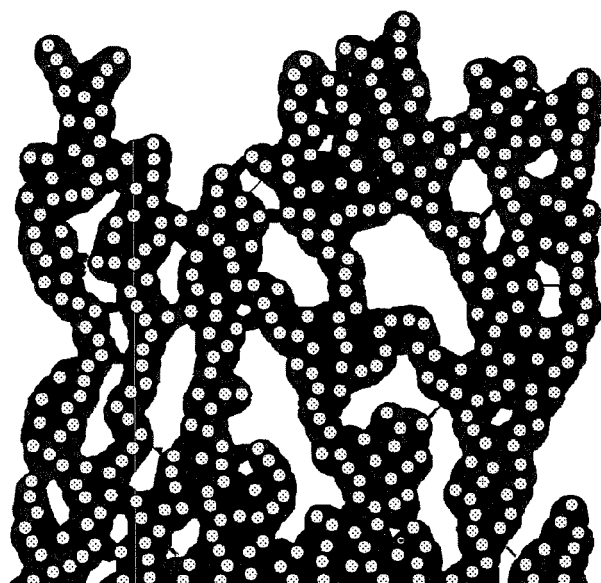


Figure 5. Numerical deposit with $W_d = 1.0$, $W_p = 1.0$, $P_f = 0.2$.

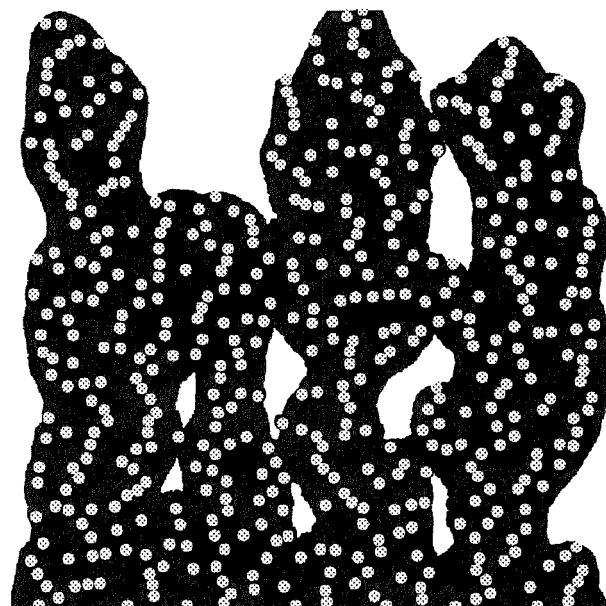


Figure 6. Numerical deposit with $W_d = 4.0$, $W_p = 1.0$, $P_f = 0.2$.

4. ACKNOWLEDGEMENTS

This work is partially funded by the Italian Space Agency (ASI). The assistance of M. Tercon and M. Maschio in performing the accretion experiments is gratefully acknowledged.

5. REFERENCES

- Levi, L., O. B. Nasello and F. Prodi, 1991: Morphology and density of ice accreted on cylindrical collectors at low values of impaction parameters. I: fixed deposits. *Quart. J. Roy. Meteor. Soc.*, **117**, 761-782.
- Macklin, W. C., 1962: The density and structure of ice formed by accretion. *Quart. J. Roy. Meteor. Soc.*, **88**, 30-50.
- , and G. S. Payne, 1969: The spreading of accreted droplets. *Quart. J. Roy. Meteor. Soc.*, **95**, 724-730.
- Personne P., 1988: Effect de la rugosité sur la croissance du givre à faible vitesse: résultats expérimentaux et modélisation. PhD dissertation, Univ. Blaise Pascal, Clermont Ferrand, 405 pp.
- Prodi, F., and V. Prodi, 1984: Generation of high concentration Monodisperse water aerosols. *Aerosols*, Liu, Pui and Fissan, Eds., Elsevier Sci. Pub., 705-708.
- , F. Porcù, M. Maschio and G. Santachiara, 1996: Laboratory study and computer simulation of the accretion of monodisperse droplets on a thin wire. *Proceedings of the 7th Int. Workshop on Atmospheric Icing of Structures*. Chicoutimi, Canada. In press.

LABORATORY STUDIES OF THE SCATTERING OF RADIATION BY ICE CRYSTALS

C P R Saunders, J Rimmer and J R Arathoon

Physics Dept., UMIST, Manchester M60 1QD, UK

1. INTRODUCTION

A knowledge and physical understanding of the scattering and absorption properties of atmospheric ice in the solar and infrared spectral bands is of great importance to studies in the two key areas of climate research and remote sensing. Ice clouds make up a large proportion of the total cloud area when viewed from above and so are important in their influence on studies of cloud reflectance using satellite data. Ice clouds also have an influence on the radiative budget of the earth, however the details of this influence have yet to be determined. The use of active and passive remote sensing techniques to determine both the macroscopic and microscopic properties of ice clouds would be enhanced if the relationships between their optical properties and general physical properties were known with greater certainty.

In order to increase our understanding of the role played by cirrus clouds in influencing world climate, experimental work has been performed in the laboratory in UMIST, Manchester. A temperature controlled cloud chamber houses a scattering chamber in which radiation in the visible band interacts with a cloud of ice crystals.

The ice crystals are grown in the chamber from a cloud of supercooled water droplets so that scattering measurements may be made for an all water cloud, a mixed phase cloud and an all ice crystal cloud. By controlling the temperature, the crystal habit is controllable and by levitation in the chamber the lifetime

and hence the size of the ice crystals is also controlled. The cloud particles are sampled by a Knollenberg 2D Greyscale probe from which crystal sizes and concentration data are available.

The objective of the experiments is to analyse the scattering of the radiation caused by the cloud particles. To this end, a photo-diode detects the input and output beam from a Helium-Neon laser, and a further photo-diode on a rotatable platform is mounted in the cloud chamber. The angle at which the scattered radiation is detected is therefore adjustable and the scattering of the beam is detected as a function of scattering angle.

2. THE APPARATUS

Figure 1 shows the circular scattering chamber within the cloud chamber inside the cold room. Laser light enters and leaves the chamber via ports and is detected by aligned photo-diodes. The scattering detector is a photo-diode mounted on a table that can be rotated by means of a stepper motor under computer control providing an angular resolution of about 0.1° per step. The detectors are two-colour Silicon-Germanium types with a measurement range of $0.4\ \mu\text{m}$ to $1.8\ \mu\text{m}$ when used in combination with a quartz halogen lamp and a monochromator. The detectors are also mounted at the entry and exit ports in order to measure cloud extinction.

Droplets are formed in the cloud chamber from a boiler; they supercool and provide the

vapour source for the growth of ice crystals introduced by a seeding technique. Air drawn slowly out of the top of the cloud chamber levitates the crystals and so increases their lifetime. The crystals are then drawn down through the scattering chamber to be sampled by the Knollenberg 2D probe.

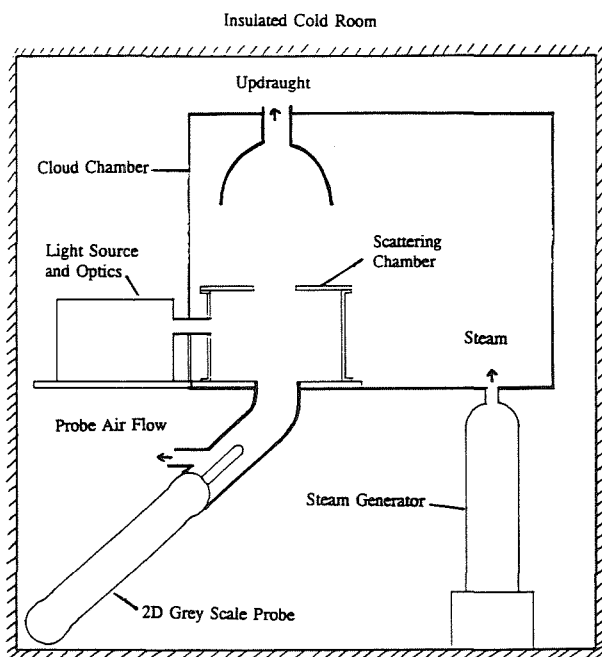


Figure 1. Diagram showing the basic experimental set up.

3. RESULTS

Figure 2 shows some scattering measurements using a He-Ne Laser of wavelength $0.63 \mu\text{m}$ as the light source. Several scans were made just after a supercooled water cloud was seeded with microscopic ice crystals. Each scan from 10° to 170° takes about 30 seconds. The first trace shows the scattering due to the supercooled water cloud; as time goes on, the scans show the enhanced scattering near 90° due to the growing ice crystals. The general reduction in the measured intensity over time is due to a combination of the water cloud dissipating and the ice particles growing quickly and then falling out of the cloud. The temperature used for this experiment was -7°C and the ice crystals were a mixture of columns and plates of not more than $50 \mu\text{m}$ maximum dimension.

Figure 3 shows how detectors can be mounted on the entry and exit ports and used to sample the light before and after it has passed through the cloud. Due to the small path length (0.45 metres) extinction measurements are limited to relatively optically thick clouds. Extinction above values of 30 per km can be measured. Using an 18.2 m path length transmissometer built at UMIST, Mackay (1992) measured the extinction of a range of cap clouds and obtained values of up to 100 per km. Water clouds produced in the cold room can easily have extinctions of over an order of magnitude greater than this. Figure 4 shows how the cloud extinction varied over a particular run. A steam generator was used to produce a cloud over the first 100 seconds or so, then the steam generator was switched off to allow the cloud to reach an ambient temperature of -15°C . The cloud was seeded with ice crystals by inserting a thin liquid nitrogen cooled rod into the cloud for a few seconds, just before the peak in the extinction curve at around 280 seconds. The ice cloud grows very quickly at the expense of the water cloud and the measured extinction drops off very quickly and becomes unmeasurable in about a minute and a half.

Measured angular scattering intensities can be made independent of particle concentration, at this wavelength, by dividing them by simultaneously measured beam extinction. The second curve in Figure 4 shows that when the scattered intensity at 112° is divided by extinction the result is almost independent of the widely varying water cloud extinction. However this changes very quickly when the ice crystals begin to grow; this is mainly because ice crystals scatter light around this angle much more effectively than equivalent sized water drops.

The scattering from a cloud of ice crystals has now been measured in the laboratory over a range of particle sizes and concentrations. The integrated intensity of light scattered between 5° and 175° was also determined in

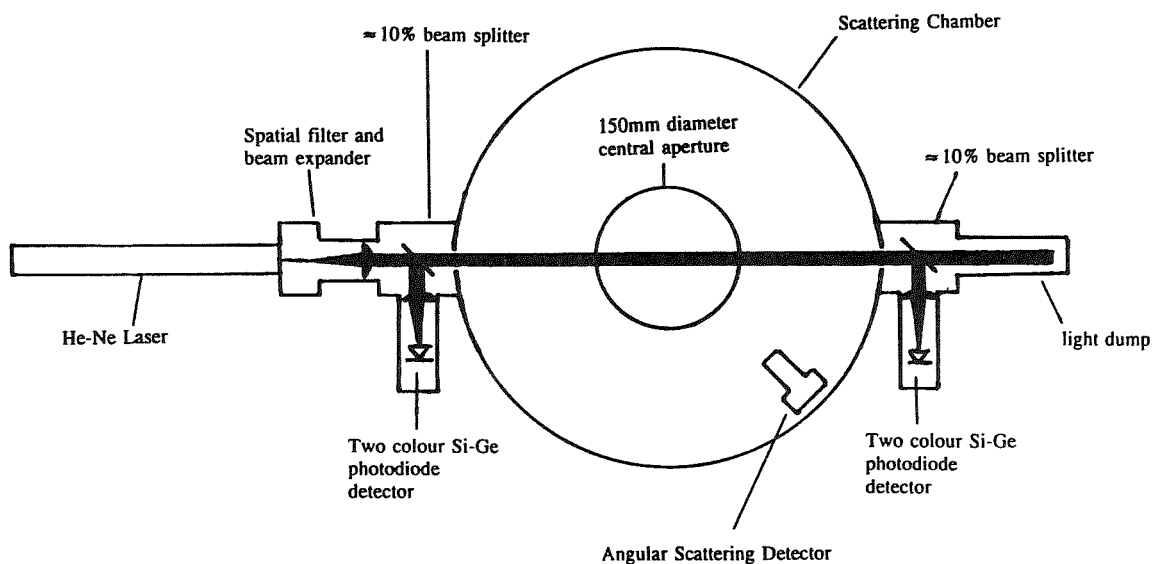
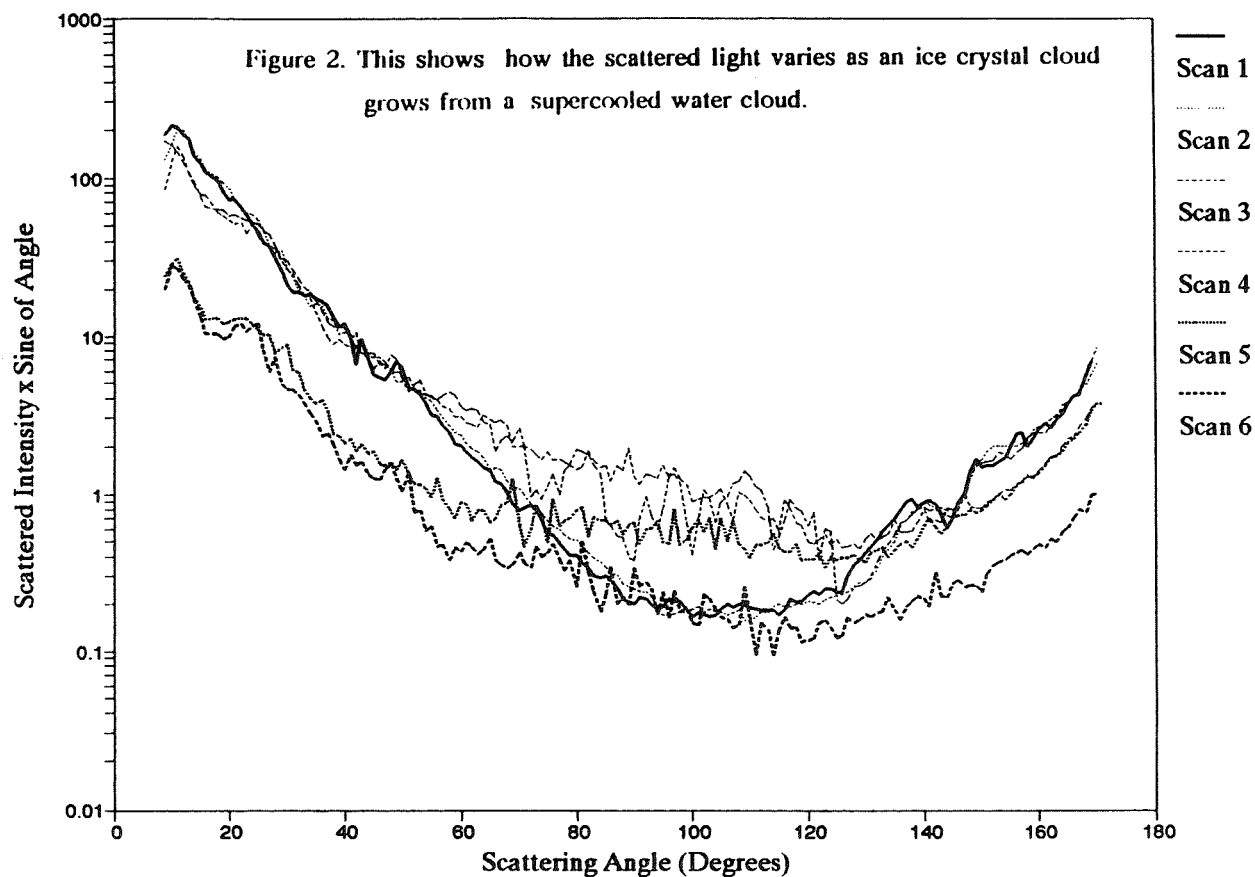


Figure 3. Diagram showing how the input and output port detectors are mounted for the measurement of cloud extinction.

Combined Scattering and Extinction Measurements

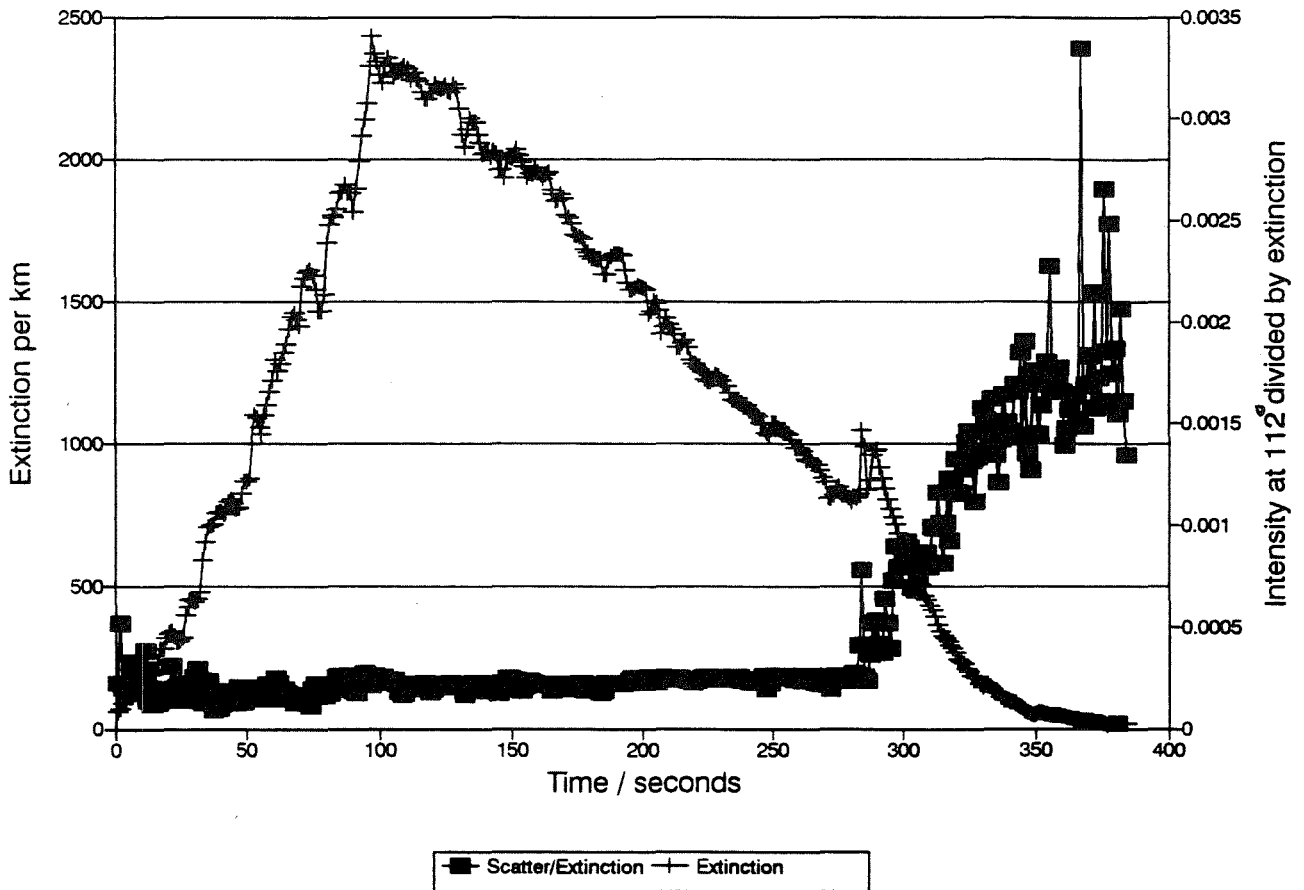


Figure 4. Graph showing water and ice cloud extinction measurements and combined scattering and extinction measurements.

order to provide an estimate of the total light scattered away from the forward direction. In general, the integrated scattered intensity increases with particle concentration as may be expected when more particles in the sample volume lead to more scattering. Other effects were also evident. With increase in crystal concentration, the scattering with increasing angle becomes smoother due to multiple scattering. At crystal concentrations below about 10^5 l^{-1} , several features were visible in the phase functions; in particular the 22° and the 46° haloes appeared. Also visible is a feature at about 150° . At even lower concentrations, around 10^3 l^{-1} , peaks were observed in the phase function at 42° , 120° , 135° and 170° . A predicted peak at 72° was not detected because the signal is lost in the noise.

In the low concentration regime there is a correlation between the effective radius, $(\Sigma r^3 / \Sigma r^2)$, and the integrated scattered intensity for phase functions produced by crystal clouds having similar particle concentrations. This relationship breaks down as the concentration increases above about 10^5 crystals per litre.

4. REFERENCE

MacKay, R. (1992). An Experimental Investigation Into Cloud Radiative Properties, PhD Thesis, *Pure and Applied Physics Department, UMIST*.

LATITUDINAL AND OVERALL CONVECTIVE HEAT TRANSFER FROM SMOOTH AND ROUGH SPHEROIDAL HAILSTONE MODELS

Guoguang Zheng and Roland List

Department of Physics, University of Toronto, Toronto, Ontario, CANADA, M5S 1A7

1. INTRODUCTION

The most commonly observed shapes of larger hailstones (i.e., $D \geq 2$ cm), which often have a flattening on the surface and smoothly rounded edges, can be approximated by spheroidal form (List, 1958; Barge and Isaac, 1973; Macklin, 1977; Matson and Huggins, 1980). These hailstones typically have various types and degrees of the surface roughness, including an irregular lobed structure (List, 1958; Browning, 1966; Macklin, 1977). Measurements have revealed that shape and roughness have significant contributions to the heat and mass transfer of hailstones (List *et al.* 1969; Macklin, 1977; Zheng and List, 1995a and b). Although the heat and mass transfer from smooth and rough spherical particles was experimentally examined, very few experiments have been addressing the transfer from rough spheroidal particles over the Reynolds number range applicable to natural hailstones. Since the heat and mass transfer plays an essential role in the hailstone growth processes, this investigation is of considerable importance for hail study. In order to give a deeper insight into the heat and mass transfer processes of hailstones with realistic shapes, the effect of the deformation of hailstones on the heat and mass transfer is also needed to be examined. In this investigation, the surface temperature distributions of rotating smooth and rough (pure and deformed) spheroidal hailstone models during cooling in an airflow were remotely measured with an Infrared Thermal Imaging System. The local and overall heat transfer coefficients were then determined.

2. EXPERIMENT

The convective heat transfer of hailstone models were measured in the University of Toronto Cloud Physics Wind Tunnel. It is a vertical, closed-circuit wind tunnel with controllable air temperature, velocity, pressure and liquid water content, which can simulate natural cloud conditions and aerodynamic motion of hailstones (List *et al.* 1987). The experiments were carried out in the tunnel measuring section with a horizontal dimension of 17.8×17.8 cm². The test models were ice particles with different surface roughness. They were prepared by freezing distilled water in rubber molds that were cast from specially designed master forms (Zheng, 1994). Only hemispherical surface roughness elements were studied because it is easy to characterize them and to control their heights. The roughness elements, which were ball bearings with various diameters, were glued to the semi-spheroidal cylinder base. Casting produced hollow semi-spheroidal rubber molds with outside major axis diameters of ~ 2 cm. The two halves of the mold were sealed together, water was injected and the PVC stem was inserted through a 3.2 mm diameter hole in the top half. The mold

was then placed in a freezer at $\sim -20^\circ\text{C}$. The produced particles were spheroids with outside major axis diameters (D_o) of ~ 2 cm, axis ratios (α) of 0.67, and surface roughness of 0, 2.0, 3.5, 5.5, 8.0 and 11%. Some smooth deformed spheroidal particles ($D_o = 2$ cm, $\alpha = 0.67$) were also produced in order to examine the effect of the deformation of the hailstones on the heat transfer. A diagram of the cross-sections through the minor axes of the test particles is shown in Figure 1.

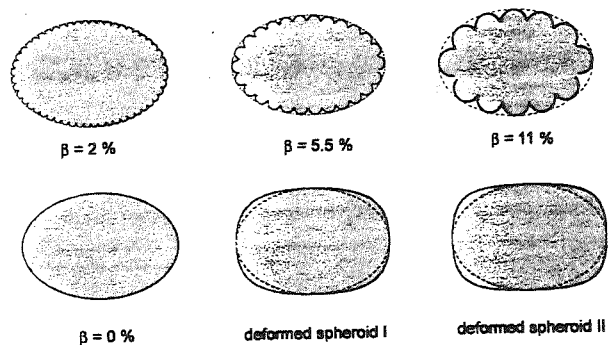


Figure 1 Configuration of the cross-sections through the minor axes of the particles ($\alpha = 0.67$) used in the present experiments. (β : surface roughness of the particles; dashed line: the perimeter of the pure spheroid.)

The experiments were started by exposing the warmed ice particle ($\sim -6^\circ\text{C}$) into a cold airflow with no supercooled water droplets. The tunnel air temperature (T_a) was set to -21°C , and the air speed (V_a) was varied from 6.3 to 24 m s⁻¹, corresponding to Reynolds numbers of $1.1 \times 10^4 \leq Re \leq 4.4 \times 10^4$. Although symmetric gyration is the most general motion for freely falling spheroidal hailstones (Kry and List, 1974), only rotation mode was chosen in the present investigation since rotation produces a latitude-dependence of the local heat transfer coefficients similar to gyration and the difference of the overall transfer coefficients is very small for the rotating and gyrating particles (Zheng and List, 1995a). In the present experiments, the test particles were forced to rotate at a rate of 10 Hz about the minor axis perpendicular to the airflow. The surface temperature of the models were remotely scanned with an "AGEMA 800" Thermal Imaging System during cooling in the airflow. The AGEMA system has a sensitivity of 0.13°C and a scanning speed of 28 frames per second, and provides real-time images of the particle surface temperature distributions. Calculations of the penetration depth of the infrared radiation indicated that 98% of the incident radiation is absorbed within the top 40 μm of the ice (Hobbs, 1974). This means that the temperatures

measured by the AGEMA system are representative of values very close to the particle surface. All experiments were performed at laboratory pressure ($\sim 100\text{kPa}$). Each experiment was performed at least twice to check for consistency.

3. HEAT TRANSFER COEFFICIENT

Since the particles rotate, the surface and internal temperature distributions are symmetric about the rotation axis. This allows a reduction of the heat conduction problem to two dimensions with a heat transfer only dependent on latitude ϕ (Figure 2). The time-evolving internal temperature distributions were established by using a numerical scheme with the measurements of surface temperature distributions of the particles (Zheng and List, 1995b). They were used to determine the conductive heat flux within the particles and, therefore, the heat transfer at the particle surface. The local Nusselt number, Nu_ϕ , is averaged latitudinally over a series of roughness elements, and can be determined by the heat balance equation at the given latitude ϕ of the particle surface

$$k_i \left(\frac{\partial T}{\partial n} \right)_{s\phi} = \frac{k_a Nu_\phi}{D_o} (T_{s\phi} - T_a) + \dot{q}_{s,esd} + \dot{q}_{s,r} \quad (1)$$

where k_i and k_a are the thermal conductivities of ice and air, T_a is the air temperature, $T_{s\phi}$ is the surface temperature averaged latitudinally over a series of roughness elements, and $\left(\frac{\partial T}{\partial n} \right)_{s\phi}$ is the numerically calculated, longitudinally averaged temperature gradient at the surface, but in the particle, at latitude ϕ . $\dot{q}_{s,esd}$ and $\dot{q}_{s,r}$ represents the heat flux at the surface of ice by phase changes through evaporation, sublimation/deposition and by thermal radiation, respectively. However, since these two terms are small ($<3\%$ and 1% , respectively) compared to others in (1) within the temperature range and conditions of the present experiments, they can be neglected. For a given particle in a known environment, k_i , k_a , D_o and T_a in (1) are constants. The two unknowns, the surface temperature $T_{s\phi}$ and temperature gradient $\left(\frac{\partial T}{\partial n} \right)_{s\phi}$ need to be established to calculate Nu_ϕ . $T_{s\phi}$ is directly measured as a function of time with the AGEMA

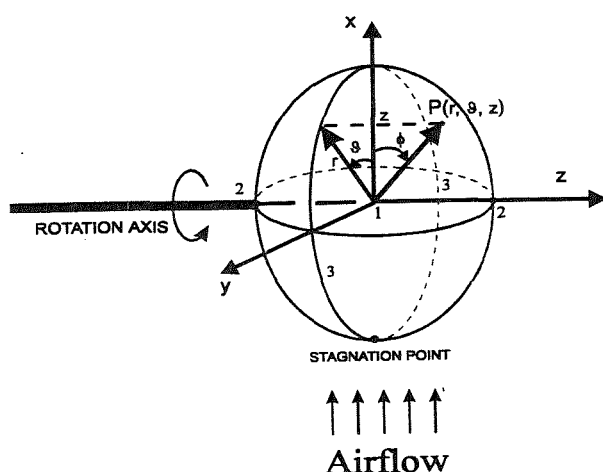


Figure 2 Configuration of rotation axis and suspension stem of the test particles, with cylindrical polar coordinates (r, θ, z). (1: particle center; 2: poles; 3: equator; ϕ : latitude; and θ : longitude.)

system while $\left(\frac{\partial T}{\partial n} \right)_{s\phi}$ is computed from the internal temperature field by solving the heat conduction equation. Since all temperature measurements were repeated at least twice, and averages were used to calculate the heat flux, the uncertainties of Nu_ϕ are less than 10% (Zheng and List, 1995b).

The overall Nusselt number, \overline{Nu} , is determined by integrating the area-weighted latitudinal Nu_ϕ

$$\overline{Nu} = \frac{\int_0^\pi Nu_\phi A(\phi) d\phi}{\int_0^\pi A(\phi) d\phi} = \frac{1}{A_s} \int_0^\pi Nu_\phi A(\phi) d\phi \quad (2)$$

where $A(\phi)$ is the average surface area between latitude ϕ and $\phi+d\phi$, while A_s is the total surface area (both determined for spheroids with an outside major axis diameter D_o).

4. RESULTS AND DISCUSSION

4.1 Local Nusselt number

The locally average Nusselt number, Nu_ϕ , for rotating spheroids with $\beta = 0, 2, 3.5, 5.5, 8$ and 11% are presented as function of latitude ϕ at $Re = 2.5 \times 10^4$ in Figure 3. It indicates that the Nu_ϕ - ϕ curves are wavelike and symmetric about $\phi = 0^\circ$. This is caused by the configuration of rotation. The maximum values are reached at $|\phi| = 35-45^\circ$, and a minimum is at $\phi = 0^\circ$. Figure 3 also shows that Nu_ϕ increases with β . The latitudinal variation of Nu_ϕ becomes smaller with increasing β , i.e., the Nu_ϕ variations of rough particles are larger than that of smooth one. The maximum value of Nu_ϕ is shifted from 35° to 45° as β increases from 0% to 11% . Physically speaking, the presence of roughness elements alters the drag coefficient, increases the particle surface area, and causes the airflow around the particles to be more turbulent because each element may create its own wake (Achenbach, 1977). Although no general correlation was found to link β to Nu_ϕ , it is obvious that surface roughness affects the boundary-layer flow, enhances the heat transfer and influences the variation of Nu_ϕ . Thus, the effect of surface roughness on heat transfer depends on size and characteristics of the roughness elements.

The effect of the deformation of the spheroid on Nu_ϕ

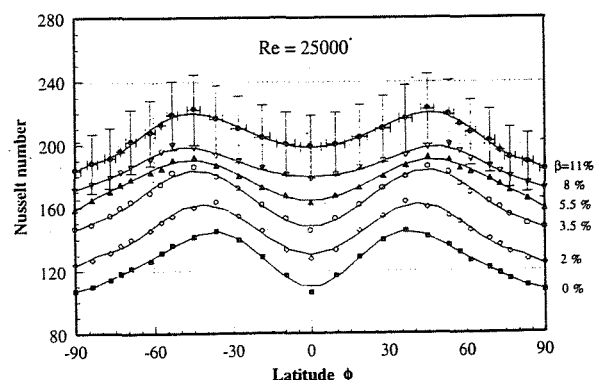


Figure 3 Latitude-dependent Nusselt number, Nu_ϕ , of rotating spheroidal particles ($\alpha = 0.67$, $f_1 = 10$ Hz) with $\beta = 0, 2, 3.5, 5.5, 8$ and 11% , as function of latitude ϕ at $Re = 2.5 \times 10^4$.

is described in Figure 4. It can be seen that the latitudinal variations of Nu_ϕ for the deformed spheroids are also wavelike similar to that of the undeformed one. The maximum value of Nu_ϕ is shifted from 35° to 50° as the

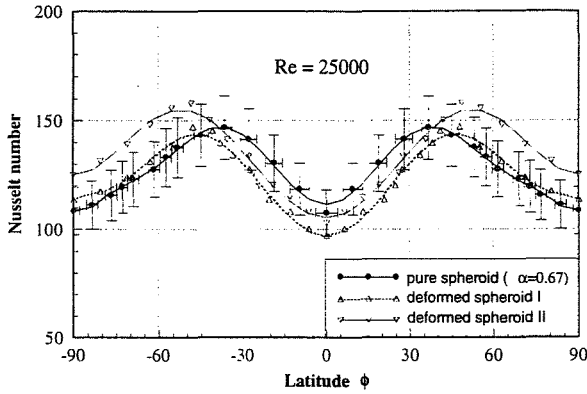


Figure 4 Latitude-dependent Nusselt number, Nu_ϕ , of deformed and undeformed (pure) spheroidal particles ($\alpha = 0.67$), rotating at $f_1 = 10$ Hz, as function of latitude ϕ at $Re = 2.5 \times 10^4$.

particle is expanded outward by keeping the constant axis ratio ($\alpha = 0.67$). It is expected that the deformation causes the airflow around the particle and the surface area to be changed and, therefore, affects the latitudinal variation of Nu_ϕ . However, this process is complicated since the influence of the deformation on heat transfer is a result of the combination of the induced flow change in the boundary layer and the increased surface area. The latter increases the heat transfer with a larger value of Nu_ϕ whereas the former can cause either a higher or smaller Nu_ϕ . As shown in Figure 4, there exists no obvious relationship between Nu_ϕ and the degree of the deformation. The Nu_ϕ - ϕ curve of the deformed spheroid I is lower than those of the undeformed and the deformed II spheroids although the difference is slight larger than or close to the experimental error. It indicates that the influence of the variation of the boundary-layer flow on Nu_ϕ could be more significant than of the increased surface area as the particle is expanded outward in this case.

4.2 Overall Nusselt number

For applications to hail studies, one is interested in the overall Nusselt number, \overline{Nu} , as defined in equation (2). \overline{Nu} of rotating rough spheroidal particles with $\beta = 0$ –11% are presented as function of Re in Figure 5. The results of rotating spherical particles (Zheng and List, 1995b) are also given for comparison. It can be seen that \overline{Nu} increases as β and Re increase. Increasing surface roughness from 0% to 11% produces an increase in \overline{Nu} up to 90%. \overline{Nu} increases exponentially with Re for the particles with different surface roughness. As Re and β increase, \overline{Nu} of rough spheroids will approach that of spherical ones with the same diameter and roughness. The relationships between \overline{Nu} and Re for spheroids with different β can be fitted to $\overline{Nu} = C Re^m$ (Figure 5). From the determination of the coefficients C and m , \overline{Nu} is expressed as a function of Re and β

$$\overline{Nu} = (0.316 + 0.103\beta) Re^{(0.587 - 0.0095\beta)} \quad (3)$$

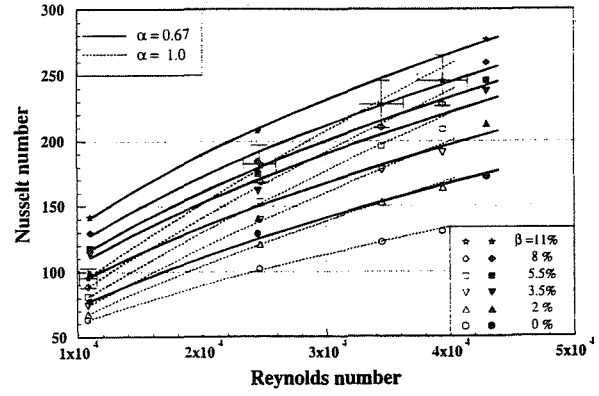


Figure 5 The overall Nusselt number, \overline{Nu} , of rotating ($f_1 = 10$ Hz) spheroidal particles ($\alpha = 0.67$) with various surface roughness β , as function of Reynolds number Re . The curves are geometrically fitted to $\overline{Nu} = C Re^m$. The data of Zheng and List (1995b) for rotating rough spheres are also displayed for comparison.

with the average correlation coefficients of $\log(\overline{Nu})$ vs. $\log(Re)$ and $\log(\overline{Nu})$ vs. β being 0.991 and 0.935, respectively. Obviously, C and m in (3) are dependent on β . C increases with increasing β whereas the power factor m of Re decreases with β . It is contrary to the result of spherical particles (Zheng and List, 1995b) although \overline{Nu} for both spherical and spheroidal particles increases with increasing β . For spherical particles, C decreases and m increases as β increases, and the β -dependence of C and m is more significant than for spheroidal ones. For a smooth spheroidal particle ($\beta = 0\%$, $\alpha = 0.67$), $\overline{Nu} = 0.316 Re^{0.587}$ with the correlation coefficient of $\log(\overline{Nu})$ vs. $\log(Re)$ being 0.999.

Figure 6 shows \overline{Nu} of the deformed and undeformed smooth spheroidal particles as a function of Re . It can be found that the deformed spheroids produce \overline{Nu} lower than that of the undeformed one with the same axis ratio. As the particle is expanded outward more, \overline{Nu} does not decrease, i.e., \overline{Nu} for the deformed II is $\sim 10\%$ larger than that for the deformed I whereas $\sim 5\%$ smaller than for the undeformed

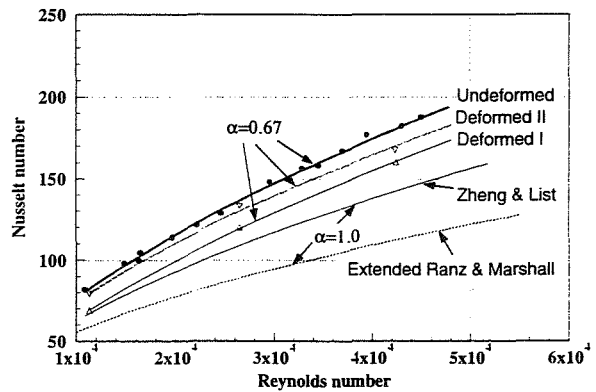


Figure 6 The overall Nusselt number, \overline{Nu} , of smooth deformed and undeformed spheroidal particles ($\alpha = 0.67$), rotating at $f_1 = 10$ Hz, as function of Reynolds number Re . The curves are geometrically fitted to $\overline{Nu} = C Re^m$. Results of the extended Ranz and Marshall (1952) and Zheng and List (1995a) for smooth spheres ($\alpha = 1.0$) are also displayed for comparison.

one. The fitting expressions of the \overline{Nu} vs. Re curves summarized in Table 1 also indicate no relations between the coefficients C and m and the degree of the deformation.

Table 1 Relationships between \overline{Nu} and Re for smooth sphere, deformed and undeformed (pure) spheroids

Particle	\overline{Nu} vs. Re relationship
sphere	$\overline{Nu} = 0.330 Re^{0.570}$
pure spheroid ($\alpha=0.67$)	$\overline{Nu} = 0.316 Re^{0.587}$
deformed spheroid I	$\overline{Nu} = 0.178 Re^{0.638}$
deformed spheroid II	$\overline{Nu} = 0.371 Re^{0.575}$

Figure 6 also illustrates \overline{Nu} of smooth spherical particles, which were given by the extended Ranz and Marshall formulation (1952) and Zheng and List's data (1995a) over the Re range applicable to natural hailstones, for comparison. It can be seen that \overline{Nu} of Zheng and List is approximately 30% larger than that predicted by the extended Ranz and Marshall formulation commonly used in hail studies. By considering the effects of shape and surface roughness, \overline{Nu} of natural hailstones will be significantly larger than that of the extended Ranz and Marshall. For example, a rough spheroidal hailstone with $\alpha = 0.67$ and $\beta = 3.5\%$ has \overline{Nu} approximately 100% higher than that of the extended Ranz and Marshall. This is important because an increase in heat transfer will delay the onset of wet growth and shedding which limit hail growth and, therefore, will allow large hailstones to be produced with shorter residence times in the clouds.

5. SUMMARY AND CONCLUSIONS

The surface temperatures of smooth and rough spheroidal hailstone models, rotating at a rate of 10 Hz, were remotely scanned as function of latitude with an Infrared Thermal Imaging System. The roughness-averaged, latitude-dependent (Nu_ϕ) and overall (\overline{Nu}) heat transfer coefficients of the models with hemispherical surface roughness elements of $0 \leq \beta \leq 11\%$ were determined over the Reynolds number range of $1.1 \times 10^4 \leq Re \leq 4.4 \times 10^4$. The following conclusions were drawn:

(1) Surface roughness affects the *local* or *latitudinal* heat transfer, Nu_ϕ , of rotating spheroidal particles. Generally, rough surfaces cause smaller latitudinal variation of Nu_ϕ than smooth surface.

(2) The heat transfer coefficient, reflecting the *overall* transfer, \overline{Nu} , of a rotating spheroidal particle is significantly affected by the presence of surface roughness; \overline{Nu} is increasing with increasing roughness and Reynolds number. Increasing surface roughness from 0% to 11% produces increase in \overline{Nu} up to 90%. \overline{Nu} can be expressed as a function of Re and β in exponential form over the Re range of $1.1 \times 10^4 \leq Re \leq 4.4 \times 10^4$.

(3) \overline{Nu} for a rough spheroid is higher than for a rough sphere with the same diameter and surface roughness. The difference becomes small as Re and β increase.

(4) The deformation of smooth spheroidal particles has an influence on the latitudinal variation of Nu_ϕ and causes decrease of the overall heat transfer up to 15% over the Re range concerned. However, more deformation does not indicate more decrease of \overline{Nu} .

The latitudinal heat transfer coefficients of rough spheroidal particles will contribute to more reasonable explanation of some specific forms of hailstones and give a deeper insight into the microphysical processes of hail growth with more realistic shapes. The parameterizations can now used to adjust the growth equations for smooth spherical hailstones to more general shapes (deformed spheroids) and surface roughness. It will also help to better interpret growth experiments with artificial hailstones and improve the parameterization of the computer models of hail evolution.

Acknowledgments. This work was sponsored by the Natural Sciences and Engineering Research Council of Canada (NSERC). This work would not have been possible without the AGEMA Infrared Temperature Scanning System which was gracefully made available by the Ontario Lightwave and Research Centre (OLLRC) at the University of Toronto.

REFERENCES

- Achenbach, E., 1977: The effect of surface roughness on the heat transfer from a circular cylinder to the cross flow of air. *Int. J. Heat Mass Transfer*, **20**, 359-369.
- Barge, B. L., and G. A. Isaac, 1973: The shape of Alberta hailstones. *J. Rech. Atmos.*, **7**, 11-20.
- Browning, K. A., 1966: The lobe structure of giant hailstones. *Quart. J. Roy. Meteor. Soc.*, **92**, 1-14.
- Hobbs, P. V., 1974: *Ice Physics*. Oxford University Press, Oxford, 837pp.
- Kry, P. R., and R. List, 1974: Angular motions of freely falling spheroidal hailstone models. *Phys. Fluids*, **17**, 1093-1102.
- List, R., 1958: Kennzeichen atmosphärischer Eispartikeln. 2. Teil. *Z. Angew. Math. Phys.*, **9a**, No.3, 217-234.
- List, R., U. W. Rentsch, P. H. Schuepp, and M. W. McBurney, 1969: The effect of surface roughness on the convective heat and mass transfer of freely falling hailstones. *Preprints 6th Conf. Severe Local Storms*, Chicago, Amer. Meteor. Soc., 267-269.
- List, R., G. B. Lesins, F. García-García and D. B. McDonald, 1987: Pressurized icing tunnel for graupel, hail and secondary raindrop production. *J. Atmos. Oceanic Technol.*, **4**, 454-463.
- Macklin, W. C., 1977: The characteristics of natural hailstones and their interpretation. *Hail: A Review of Hail Science and Hail Suppression*. Meteor. Monogr. **16**, Amer. Meteor. Soc., Boston. 65-88.
- Matson, R. J., and A. W. Huggins, 1980: The direct measurement of the sizes, shapes, and kinematics of falling hailstones. *J. Atmos. Sci.*, **37**, 1107-1125.
- Ranz, W. E., and W. R. Marshall, 1952: Evaporation from drops. *Chem. Eng. Prog.*, **48**, 141-146, 173-180.
- Zheng, G. G., 1994: *An experimental investigation of convective heat transfer of rotating and gyrating hailstone models*. Ph.D. thesis, University of Toronto, 122pp.
- Zheng, G. G., and R. List, 1995a: Convective heat transfer of rotating spheres and spheroids with non-uniform surface temperatures. *Int. J. Heat Mass Transfer*, (in press).
- Zheng, G. G., and R. List, 1995b: Latitudinal and overall convective heat transfer of rotating and gyrating rough spheres with non-uniform surface temperatures. accepted by *J. Atmos. Oceanic Technol.*

TIME SERIES OF A Z-R RELATIONSHIP FOR SNOWFALL AND ITS EVALUATION

Ken-ichiro Muramoto¹, Yasushi Fujuyoshi² and Toru Shiina³

¹Faculty of Engineering, Kanazawa University, Kanazawa 920, Japan

²Institute for Hydrospheric-Atmospheric Science, Nagoya University, Nagoya 464-01, Japan

³Toyama National College of Technology, Toyama 939, Japan

1. INTRODUCTION

In order to determine Z-R relationship for snowfall, radar reflectivity factor (Z) by cloud and snowfall rate (R) on the ground have been measured by many methods (e.g. Gunn and Marshall, 1958; Sekhon and Srivastava, 1970). This relation is often expressed the form $Z = BR^\beta$, where B and β depend upon the snow particle size distribution, fall velocity and density. The values of B and β are not universally constant, but considerably change with time. Many attempts have been made to obtain values of B and β for snowfalls from quasi-simultaneous measurements of radar reflectivity and ground data on snowfall rate or accumulation (Boucher and Wieler, 1985; Carlson and Marshall, 1972; Gunn and Marshall, 1958). These works are not sufficient, however, because of poor accuracy and long interval measurement.

In this paper, radar reflectivity factor at X band and snowfall rate were measured simultaneously to obtain the best-fit Z-R relations for each snowfall events. Furthermore, effects of number concentration, size distribution and fall velocity of snow particles for the Z-R relationship were examined using snow particle data on the ground.

2. METHODS

2.1 Measurement of radar reflective factor

An RHI radar was used to measure the amount of snowfall and ice water content in the atmosphere continuously. The data of this radar were sampled from ground level to 5.0 km in altitude with height

resolution of 500 m every 10 s. In this study, data of 500 m height were used for reflectivity factor. A detailed description of the radar used in this study may be found in a paper by Fujiyoshi et al (1990).

2.2 Measurement of snowfall rate, and size and fall velocity of snow particles

Snowfall rates were measured every minute by weighing the amount of snowfall using an electric balance system. Size and fall velocity of snow particles were measured by image processing method (Muramoto et al., 1994).

2.3 Analysis of Z-R relation

When intensity of R was lower than 0.05 mm/h, then the data were neglected. Time series of data on Z and R collected every minute were cross correlated. The time difference giving the best correlation between Z and R was less than 5 min.

3. RESULTS

3.1 Observation

Observations were carried out through February 1992 at Ooyama in Toyama prefecture at the foot of Mt. Tateyama, Japan. The surface observation site was located about 3.2 km toward the west of the radar site. Two snowfall events which continued for several hours were analyzed. Case A was from 1700 on February 8 to 0100 on February 9 and case B was from 1900 on February 10 to 2400 on February 10, respectively.

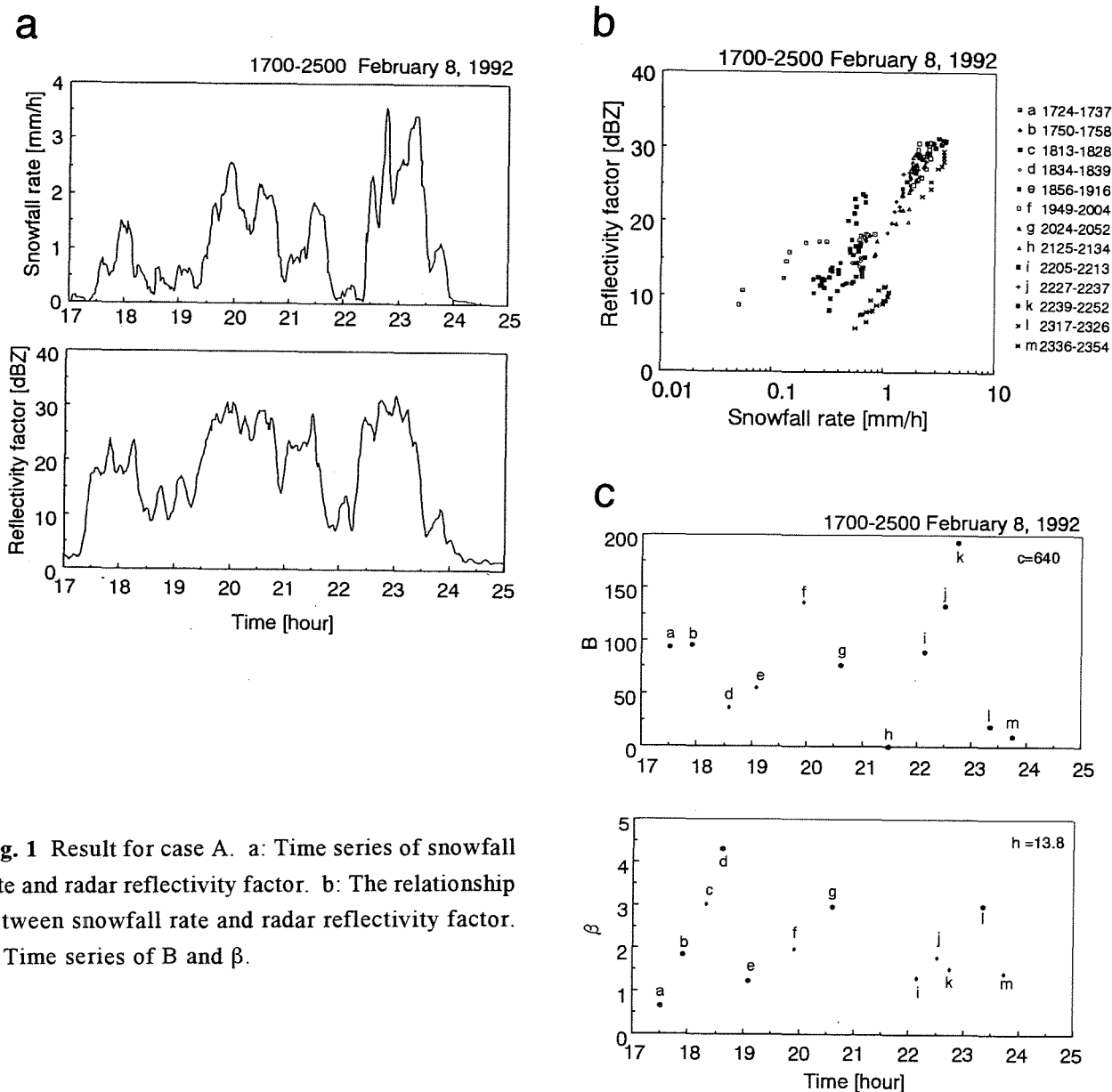


Fig. 1 Result for case A. a: Time series of snowfall rate and radar reflectivity factor. b: The relationship between snowfall rate and radar reflectivity factor. c: Time series of B and β .

3.2 Z-R relation

Figs. 1a and 2a show the time series data of snowfall rate and radar reflectivity factor. After the calculation of the time difference between the radar data (Z) and the ground data (R), all pairs of the data of Z and R were plotted as shown Figs. 1b and 2b. The coefficients of B and β in the equation of $Z = B R^\beta$ were obtained from plotted data. In case A (Fig. 1b), although three (a, c and m) of 13 events were deferent regression lines, the other were almost on the same line. In case B (Fig. 2b), regression lines were classified to five groups: (a, f), (b, c, g), (e, d, h), (j, k, m) and (i, l). Figs. 1c and 2c show the time series of the coefficients of Z-R

relationships in these two cases.

3.3 Number concentration, size and fall velocity

Time series of number concentration, diameter and fall velocity of snow particles of the two cases are shown in Figs. 3 and 4. In the case A, diameter and fall velocity were almost constant, but these data were changed with time in case B.

4. DISCUSSION

The coefficient B in the Z-R relation is the radar reflectivity factor on the regression line when the snowfall rate is 1 mm/h. The radar reflectivity will

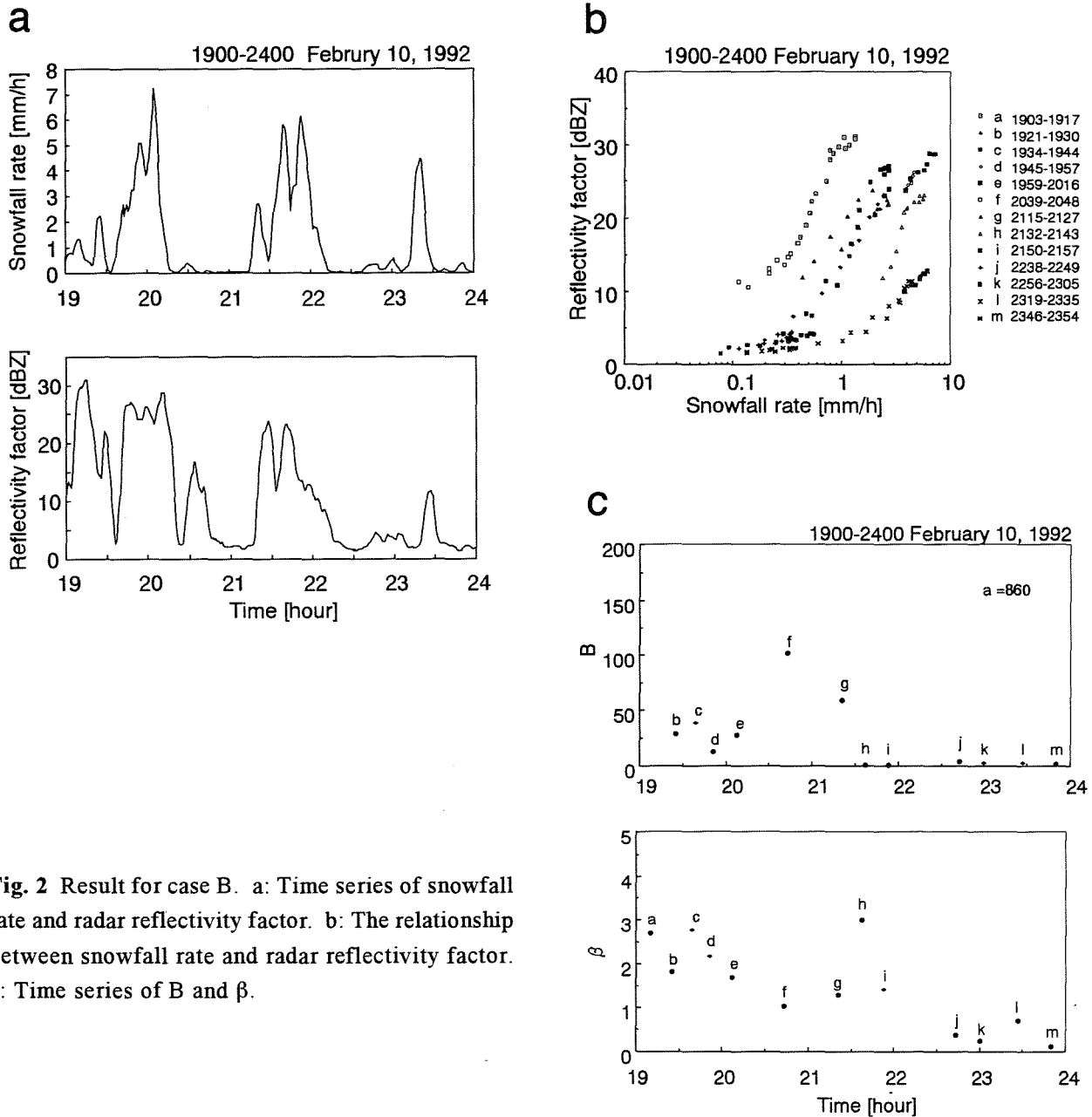


Fig. 2 Result for case B. a: Time series of snowfall rate and radar reflectivity factor. b: The relationship between snowfall rate and radar reflectivity factor. c: Time series of B and β .

become large when the snow particle size increases by coalescence because the radar reflectivity factor is proportional to the sixth power of the diameter of snow particle. The coefficient of B in case A was larger compared to case B. This result agreed with the data in terms of the diameter (Figs. 3 and 4). When diameter and fall velocity were almost constant, the coefficient of determination of Z-R relationship was high (case A). On the other hand, when diameter and fall velocity were changed abruptly, the coefficient was low (case B). In case B, since the snowfall rate and the reflectivity factor changed so fast, short time interval correlation was more effective.

5. CONCLUSION

From the results, we note three important points in determining a Z-R relationship at any given place:

- 1) R and Z should be measured at intervals of 1 min or less;
- 2) the local precipitation characteristics (especially the number concentration, diameter and fall velocity) should be studied;
- 3) each snowfall period should be determined using not only the snowfall rate but also the precipitation characteristics.

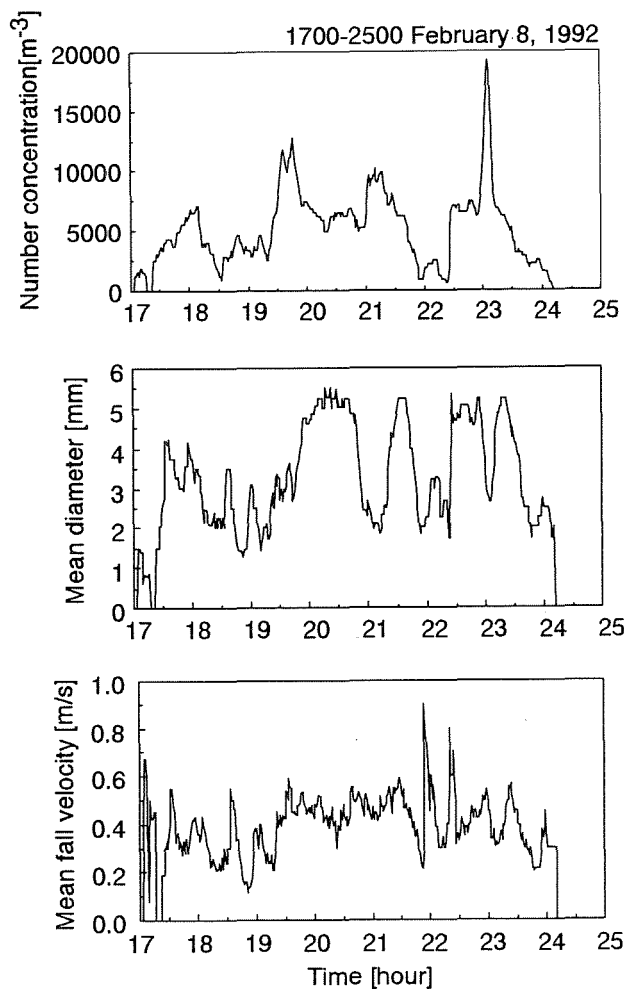


Fig. 3 Time series of number concentration, diameter and fall velocity in case A

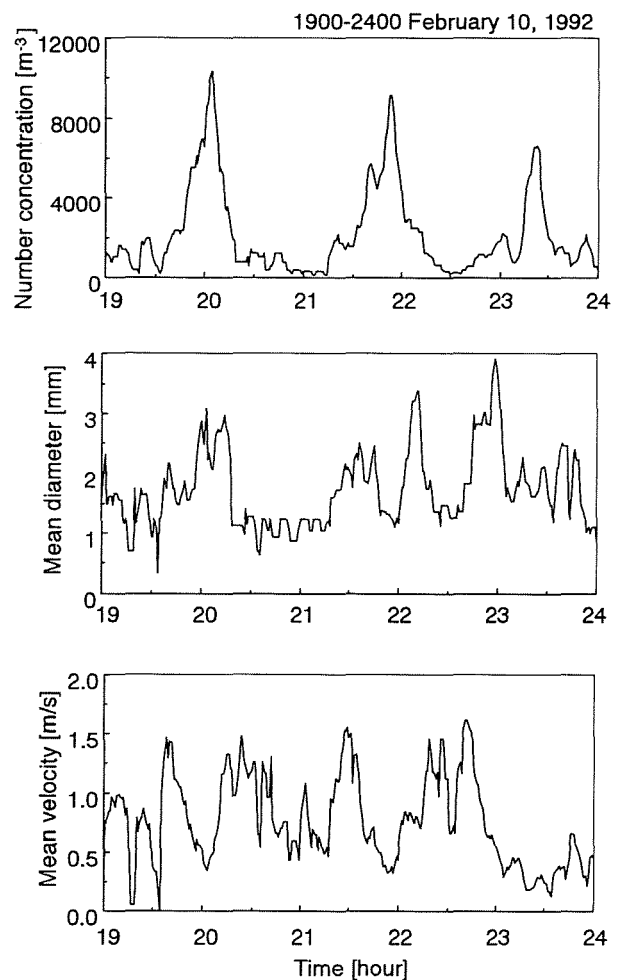


Fig. 4 Time series of number concentration, diameter and fall velocity in case B

6. REFERENCES

- Boucher, R.J., and J.G. Wiener, 1958: Radar determination of snowfall rate and accumulation. *J. Climate Appl. Meteor.*, **24**, 68-73.
- Carlson, R.E., and J.S. Marshall, 1972: Measurement of snowfall by radar. *J. Appl. Meteor.*, **11**, 494-500.
- Fujiyoshi, Y., T. Endoh, T. Yamada, K. Tsuboki, Y. Tachibana and G. Wakahama, 1990: Determination of a Z-R relationship for snowfall using a radar and high sensitive snow gauges. *J. Appl. Meteor.*, **29**, 147-152.
- Gunn, K. L. S., and J. S. Marshall, 1958: The distribution with size of aggregate snow particles, *J. Meteor.*, **16**, 452-461.
- Marshall, J.S., and K.L.S. Gunn, 1952: Measurement of snow parameters by radar. *J. Atmos. Sci.*, **9**, 322-327.
- Muramoto, K., K. Matsuura, T. Harimaya and T. Endoh, 1993: A computer database for falling snow particles, *Ann. Glaciol.*, **18**, 11-16.
- Sekhon, R. S., and R. C. Srivastava, 1970: Snow size spectra and radar reflectivity. *J. Atmos. Sci.*, **27**, 299-307.

RELATION BETWEEN THE CONCENTRATION OF ICE NUCLEI AND THE OCCURRENCE OF THUNDERSTORMS AND HAILSTORMS

A. CASTRO*, J.L. MARCOS*, J. DESSENS**, J.L. SÁNCHEZ* AND R. FRAILE*

* *Laboratorio de Física de la Atmósfera. Universidad de León, 24071 León. Spain.*

** *Laboratoire d'Aérodynamique, UMR CNRS/UPS 5560, 65300 Campistrous. France.*

1. INTRODUCTION

The formation of ice crystals from supercooled cloud drops in cold clouds is importantly connected with the nature and concentration levels of the ice nuclei (IN) which are present in the air. During the convective processes which occur during thunderstorms, when the natural concentration of IN is insufficient to facilitate the freezing of supercooled cloud drops, the latter grow in the liquid state until very low temperatures are reached, which increases the probability of their reaching a large enough size to cause a precipitation of hail (Cotton and Anthes, 1989).

However, given that convective storms are primarily fed from the lower air levels, determining the concentration of IN at ground level allows a better understanding of the mechanisms at work in the process of precipitation. Numerous natural processes are at work in the formation of hail, but it is well known that the introduction of high concentrations of small ice particles in and below the hail growth zone (HGZ) can be expected in general to diminish the amount of supercooled water available for hail growth. The presence of an increased number of embryos reduces the mass of supercooled water and therefore results in the formation of smaller ice particles in the HGZ. Since the number of embryos is a function of the number of IN present in the atmosphere, it is hoped that by increasing the number of IN, the amount of supercooled water will be diminished.

The aim of this study has been directed towards the methodology of determining the concentration of natural IN at ground level, under the different meteorological conditions prevailing during the course of two measuring sessions carried out in the summer months of 1994 and 1995.

2. DESIGN OF EXPERIMENTAL PROCESS

2.1 Cloud Chamber Studies

Numerous studies have been made using the cloud chamber in order to measure the concentration of IN in

the air (Song and Lamb, 1994a and 1994b). For the present study, a chamber formed of three identical but independent tanks was employed. In each of these, the temperature and conditions of study could be controlled. Air samples were introduced into the containers and cooled until a predetermined temperature was reached; water vapor was likewise introduced until the enclosed air reached saturation. Previous research studies established suitable working temperatures for air masses, the nucleation period and the methodology to be followed. In line with other authors (Rogers et al., 1994; Pérez et al., 1985), specific temperatures were selected for study, which in this case were -15°C and -19°C.

2.2 Target Area

Since 1986 a network of almost 500 observers has been on site in the Province of León (North-west Spain), in order to detect thunderstorm activity and possible hailfalls. The study zone is composed of relatively flat land, mainly devoted to agriculture, which has an area of some 6,825 km² and which is surrounded by various mountain ranges with a maximum altitude of 2,100 m.

3. DATABASES AND METHODOLOGY

During the summer periods, the observation network allowed a high frequency of thunderstorm phenomena, accompanied on occasions by hailfalls, to be detected. Thanks to the density of the network, it has been possible to confirm that the area affected by hailfall did not exceed 10 km² per hailfall in 30% of cases.

The databases collected from the Project have allowed the climatology of the study zone to be well characterized and defined (Sánchez et al., 1994).

At the same time as the storm and hail detection network provided data, measuring campaigns (June, July and August 1994 and 1995) were being carried out to discover the levels of IN at ground.

For the duration of the first campaign, readings were taken at 9, 12 and 15 GMT. Taking $X_{T, H, Y}$ as the set of

measurements for each temperature (T), hour of the day (H) and year (Y), it may be seen that six series are formed: $X_{-19^{\circ}\text{C}, 9\text{GMT}, 1994}$, $X_{-19^{\circ}\text{C}, 12\text{GMT}, 1994}$, $X_{-19^{\circ}\text{C}, 15\text{GMT}, 1994}$, $X_{-15^{\circ}\text{C}, 9\text{GMT}, 1994}$, $X_{-15^{\circ}\text{C}, 12\text{GMT}, 1994}$, $X_{-15^{\circ}\text{C}, 15\text{GMT}, 1994}$. However, it could be seen that the number of IN in the atmosphere on each day did not vary greatly between 9 and 15 GMT, so the Kruskal-Wallis (K-W) test was applied to the data to test the homogeneity of the three series $X_{-19^{\circ}\text{C}, H, 1994}$. The results indicated that they were homogenous, giving therefore the single series $X_{-19^{\circ}\text{C}, 1994}$, taking the average value of the three measuring times for each day.

By analogy, the homogeneity of the three series $X_{-15^{\circ}\text{C}, H, 1994}$ was confirmed, and in the same way the series $X_{-15^{\circ}\text{C}, 1994}$ was constructed.

Because the 1994 data were seen to be independent of the time of day when measuring took place, in 1995 only one reading was taken daily, at 12 GMT. Thus the four data series were constructed: $X_{-19^{\circ}\text{C}, 1994}$, $X_{-15^{\circ}\text{C}, 1994}$, $X_{-19^{\circ}\text{C}, 1995}$ and $X_{-15^{\circ}\text{C}, 1995}$.

To establish if it would be possible to unite the four series $X_{T,Y}$ into two only, which may be called X_T , the K-W test was again applied to the 1994 and 1995 series. Once again, the results showed that they were indeed homogenous, with no significant differences between the two campaigns. Consequently the data series were merged, giving the series $X_{-15^{\circ}\text{C}}$ and $X_{-19^{\circ}\text{C}}$, each one composed of 158 data.

In looking for a correlation between the number of IN measured in the study zone, and the origin of the air

masses traversing it, a clear difference could be made between maritime and continental air masses. Using the synoptic charts provided by the European Meteorological Bulletin (850 hPa level) the provenance of the air entering the study zone was analyzed on each day for which IN was measured.

Table 1 gives a breakdown of the situations recorded, according to whether the air mass was continental or maritime, storms and/or hail were recorded, and for all permutations of the above.

4. RESULTS

Various kinds of analysis were made of the data, and the results may be considered under the following headings:

a) Analysis of IN active at -15°C and -19°C .

In the course of analyzing the IN series, a considerable dispersion among the data could be seen, owing to the high values applying on certain summer days: a dispersion which has also been detected in latitudes similar to the Province of León (Admirat, 1963, in the South-west of France; Pérez et al., 1985, Province of Valladolid, Northern Spain). On applying the Kolmogorov-Smirnov test, it became apparent that the distributions were exponential—probability density function of type $\beta \exp(-\beta n)$ —for the two temperatures of -15°C and -19°C . The results are shown in Table 2

b) Analysis of IN in Situations classified according to Maritime and Continental origin of Air Mass

From the results offered in Table 3, it may be seen that this particular study zone is more affected by maritime than by continental air masses, but that the number of IN active is higher under the influence of continental air masses. As early as 1954, Rau (cited by Fletcher, 1962), encountered the same pattern con-

TABLE 1. Number of situations, and corresponding percentage of total, recorded during IN measuring sessions.

Classification	No of situations (%)
Continental Air Masses	38 (24%)
Maritime Air Masses	120 (76%)
Storm	52 (33%)
No Storm	106 (67%)
Hail	23 (15%)
No Hail	135 (85%)
Storm with Maritime Air Masses	34 (65%)
Storm with Continental Air Masses	18 (35%)
No Storm, with Maritime Air Masses	86 (81%)
No Storm, with Continental Air Masses	20 (19%)
Hail with Maritime Air Masses	16 (70%)
Hail with Continental Air Masses	7 (30%)
No Hail with Maritime Air Masses	104 (77%)
No Hail with Continental Air Masses	31 (23%)

TABLE 2. Distributions of the no. of IN per liter at the two working temperatures; value β of exponential distribution, and value for the median for each distribution.

Temperature ($^{\circ}\text{C}$)	-15	-19
No of data	158	158
Distribution	exponential	exponential
β (liters/ No of IN active)	0.055	0.016
Median (IN active/ liter)	7	35

TABLE 3. Distributions of the no. of IN per liter at the two working temperatures; value β of exponential distribution, and value for the median of each distribution for days with Maritime or Continental Air Masses.

Temp. (°C)	Maritime		Continental	
	-15	-19	-15	-19
No of data	120	120	38	38
exponential distribution	yes	yes	yes	yes
β (liters/IN active)	0.055	0.017	0.067	0.014
Median (IN active/liter)	5	29	11	45

firming what Bertrand and Baudet (1973) have to say in their reports on West African projects, particularly in affirming that IN concentration levels are influenced by the origin of air masses. Nevertheless Hobbs (1993) recorded more nuclei in maritime than in continental clouds.

The non-parameter K-W test was applied to facilitate a comparison between the samples of IN active in situations with continental, as opposed to those with maritime, air masses. Within a significance level of 5%, differences were only to be found at $T = -19^{\circ}\text{C}$; for $T = -15^{\circ}\text{C}$ the differences were negligible. The result for the test at -15°C was $H=2.76$, while at -19°C , $H=4.64$.

As a result, it maybe seen that the nuclei begin to act uniformly at -15°C , but as the temperature falls, the IN in the maritime air masses begin to become active in a different way from —and more effectively than— the IN in the continental masses.

c) Analysis of the IN active on storm and non-storm days

The distributions for the quantity of IN per liter on days with storm activity are not exponential (Table 4). This may be attributable to the fact that the meteorological conditions connected with the actual dynamics of convectivity provoke some kind of “alteration” in the nuclei of the atmospheric layers, which would need to be studied in greater detail than the present study affords.

TABLE 4. Distributions of the no. of IN at the two working temperatures; value β of exponential distribution, and value for the median of each distribution for Storm/Non-storm days, and for Hail days.

Temperature (°c)	Non-storm days		Storm days		Hail days	
	-15	-19	-15	-19	-15	-19
No of data	106	106	52	52	23	23
Exponential distribution	yes	yes	no	no	no	no
β	0.067	0.017	—	—	—	—
Median (IN active/ liter)	5	30	11	41	13	45

For the days of storm activity in this study zone, the number of nuclei active is in general higher than that for either of the two test temperatures on non-storm days. Nevertheless, on applying the non parametric K-W test to compare the samples of IN active on storm days with those on non-storm days, it transpired that there were only significant differences at -15°C ($H=10.00$). This means that at lower temperatures, the glaciogenic nuclei act in equal numbers on days with and without storm activity.

d) Analysis of IN active on classified Hail and Non-hail days

It is worth emphasizing that almost half of the days when storm presence was detected in this study zone, hail fell as a result.

Once again applying the K-W test to the samples, this time from hail and non-hail days, it emerged that there were important differences in the number of IN detected on days when there was hail as opposed to liquid precipitation, i.e. rain. Indeed a comparative study of both samples produced similar results to those given in the previous section: at -15°C there were significant differences ($H=4.55$) between hail and non-hail days, while at the lower temperature of -19°C the glaciogenic nuclei appear to activate in equal numbers ($H=2.75$).

It should be stressed that, at the two test temperatures, the distributions were exponential for non-hail days. This is in line with the results found in the previous section for days when no storm activity —and hence no hail— was recorded.

5. CONCLUSIONS

From this analysis of the data generated after two summers of measuring the concentration of IN as part of the León WM project, the following conclusions have been drawn:

1. The distributions of IN active at -15°C and -19°C are exponential.

2. There is a higher incidence of maritime than of continental air masses over the study zone in question.
3. There is a higher probability of storm activity on days when continental rather than maritime air masses traverse the study zone.
4. The IN become active uniformly (irrespective of the air mass from which they originate) at -15°C , whereas at -19°C those which derive from continental air masses become more active.
5. The assertion was verified that concentration of IN is a direct function of the degree of convectivity, the greater the latter, the higher the concentration of IN in the atmosphere.

6. ACKNOWLEDGEMENTS

This work was supported by Excma. Diputación Provincial de León and Consejería de Agricultura (Junta de Castilla y León) as a part of P.A.L.A.

7. REFERENCES

- Admirat, P., 1963: Extensions horizontale et verticale des anomalies estivales du pouvoir glaçogène de l'air. *Journal de Recherches Atmosphériques*, **1**, 1-18.
- Bertrand, J. and J. Baudet, 1973: Seasonal variations and frequency distributions of ice nuclei concentrations at Abidjan, West Africa. *J. Appl. Meteor.*, **12**, 1191-1195.
- Cotton, W.R. and R.A. Anthes, 1989: *Storm and Cloud Dynamics*. Academic Press, San Diego, 883 p.
- Fletcher, N.H., 1962: *The physics of rainclouds*. Cambridge at the University Press.
- Hobbs, P.V., 1993: *Aerosol-Cloud-Climate Interactions*. Ed. Academic Press, Inc., San Diego, 233.
- Levi, Y., D. Rosenfeld and B. Herut, 1994: Relationship between the occurrence of dust, ice nuclei concentrations and rain chemical composition in Israel. *Sixth WMO Scientific Conference on Weather Modification*, Paestum. WMO/TD, Vol 2, Nº 596, 565-568.
- Mossop, S.C., 1985: The origin and concentration of ice crystals in clouds. *Bulletin of the American Meteorological Society*, **66**, 264-273.
- Mizuno, H. and N. Fukuta, 1994: Natural ice nucleus measurement under ice supersaturation. *Sixth WMO Scientific Conference on Weather Modification*, Paestum. WMO/TD, Vol 1, Nº 596, 303-306.
- Pérez, P.J., J.A. García and J. Casanova, 1984: Estudio del ajuste de distintas distribuciones estadísticas a datos de concentraciones de IN. *Rev. de Geofísica*, **40**, 135-140.
- Pérez, P.J., J.A. García and J. Casanova, 1985: Estudio de la variación temporal de una población de IN y análisis de posibles anomalías. *Rev. de Geofísica*, **41**, 237-242.
- Rogers, D., P.J. DeMott and L.O. Grant, 1994: Concerning primary ice nuclei Concentrations and water supersaturations in the atmosphere. *Atmos. Res.*, **33**, 151-168.
- Sánchez, J.L., A. Castro, J.L. Marcos, M.T. de la Fuente and R. Fraile, 1994: Criteria for a remote ground generator network in León (Spain). *J. Wea. Mod.*, **26**, 83-88.
- Song, N. and D. Lamb, 1994b: Experimental investigations of ice supercooled clouds. Part II: scavenging of an insoluble aerosol. *J. Atmos. Sci.*, **51**, 104-116.
- Song, N. and D. Lamb, 1994a: Experimental investigations of ice supercooled clouds. Part I: system description and growth of ice by vapor deposition. *J. Atmos. Sci.*, **51**, 91-103.
- Soulafe, G., 1964: Un analyseur de pouvoir glaçogène simple pour un réseau de stations de mesure. *Journal de Recherches Atmosphériques*, **2**, 95-100.
- Zivanovic, M., M. Huter, D. Grujic, and Z. Dimitrijevic, 1981: Isothermal cloud chamber for studying the ice crystal nucleation. *Fizika*, **13**, 141-145.

ON SUPERSATURATION DEPENDENT BEHAVIOR OF ICE CRYSTALS DURING VAPOR GROWTH

John Hallett¹, Charles A. Knight²,
Riza G. Oraltay³ and Paul Willis⁴

¹Desert Research Institute, Reno, Nevada 89506-0220,

²National Center for Atmospheric Research, Boulder, Colorado 80307, USA

³University of Marmara , Istanbul, Turkey

⁴CIMAS/AOML, University of Miami, Florida 33149

1. INTRODUCTION

The Bergeron-Findeisen process for the production of ice phase precipitation works because of the vapor pressure (density) excess of water over ice which drives growth of ice as the environmental droplets either evaporate or are maintained by release of water vapor during updraft cooling. Thus, in a sense they 'lock' the saturation at just above water saturation (by at most 1%) and give an ice supersaturation primarily determined by temperature through the equilibrium vapor pressure excess of water over ice (Fig. 1). From the local viewpoint of the growing ice crystal, the region near water saturation is determined by the rate of evaporation of droplets in its neighborhood. The approach of such droplets to the surface of the crystal, as the conditions approach those required for impact, lead to the transition to rime formation and the subsequent growth of a graupel particle. We examine the role of supersaturation in determining the growth of the precipitating ice particle. Two situations are considered:

- i) Growth of an ice particle with the surface temperature below 0°C.
- ii) Growth of a particle by liquid condensation, with the surface temperature at or in excess of 0°C depending on its proximity to internal ice particles.

It is possible that (i) may be further subdivided from a physical view point related to whether there is a significant surface layer (Furakawa et al, 1987).

2. LABORATORY STUDIES

Such situations can be simulated in the laboratory by means of a dynamic thermal diffusion chamber. This consists of two horizontal ice or water covered plates separated by about 3 cm, with the top plate warmer than the base plate to give thermal stability. Crystals are grown, evaporated or melted on a vertical fiber, subject to controlled flow. The chamber is set to give a designated central (mean) temperature and a designated supersaturation at this level by the difference between top and bottom plates. This set-up can be arranged in the complete absence of droplets by making the chamber nucleus free. With the chamber incorporated in a closed circuit wind tunnel, an arrangement to study ice growth is set up when all three parameters - temperature, supersaturation and velocity are subject to independent control. (Keller and Hallett, 1982). Such experiments have shown that the transition from column to needle and plate to dendrite take place as supersaturation increases (Alena et al 1990, Hallett and Knight, 1994).

These studies imply that conditions exist such that increase of supersaturation can be made equivalent to an increase of ambient air velocity - at least as far as the growing tip of the crystal is concerned. As the air velocity (equivalent to the crystal fall velocity) is increased, the region of water supersaturation is moved closer to the crystal tip, and eventually, at a distance near the neighborhood of one mean free path, the ambient supersaturation is approached.

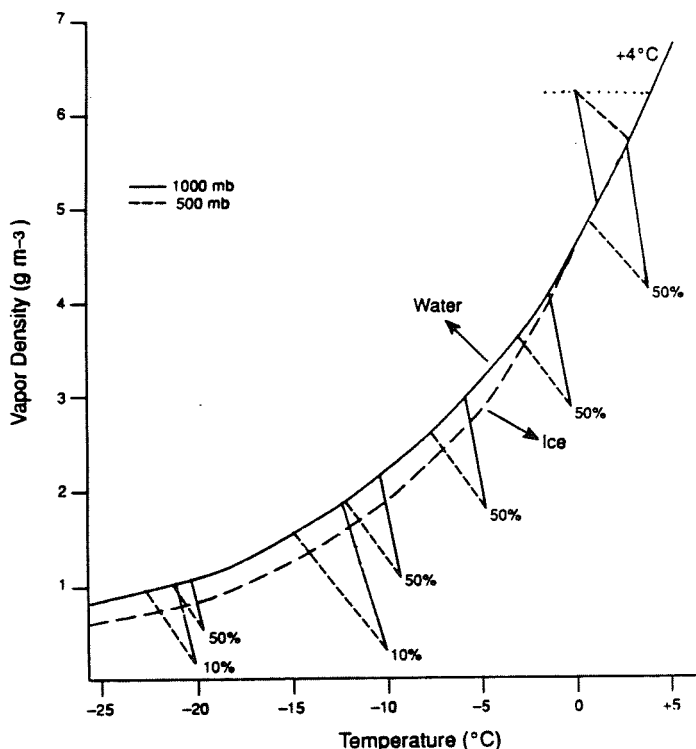


Figure 1: Water vapor density curves for ice and water. The lines through the various points represent the slope of the vapor/heat flow equations, ignoring any effect of the difference of ventilation at different pressure levels. Evaporation produces cooling of a few degrees; condensation of vapor from droplets at 4°C on ice at 0°C gives a supersaturation of some 40% and substantial potential for rapid melting, with a nominal temperature excess of a few degrees.

3. SURFACE STRUCTURE

Elbaum et al (1993) point out that in the presence of air there is no finite wetting angle for water on ice single crystals, as exists in the absence of air (Knight, 1971), so that more complete uniform melting of facets might be expected as condensation begins. This is investigated in the laboratory by passing saturated air at temperatures above 0°C over pregrown crystals as in the earlier experiment. The consequences of this behavior for influencing crystal shape, size and break up is examined, and is of interest in that droplets form on columns during evaporation, although such behavior is not observed on plates.

In particular, it appears that water saturation is always necessary to give a skeletal structure, with non

faceted growing tips (Fig. 2). It is found that at least water saturation is required for skeletal growth, irrespective of air velocity giving dendrites as the air velocity approaches a value between 15 and 35 cm s⁻¹ (Dong et al, 1995). The observations show that the growing tip of the crystal, at least within the resolution of the optical system (some 5 μm) are non-faceted, implying a surface mobility of the molecules and the lack of stability of faceted surfaces. Thus the shape is determined by an equilibrium between diffusion of heat and vapor through the air with crystallographic effects having some influence on shape, particularly back from the tip where the supersaturation is lower. The shape is independent of defects as well as any facet stability resulting from larger growth at such as occur at lower supersaturation. This concept may hold only in specific crystal directions. For plate growth in the "a" axis direction (normal to the "c" axis), but not necessarily in the "c" axis direction itself. For needle growth this situation is reversed. It was shown that very thin disc crystals showed a plate habit but with circular periphery, a result interpreted in terms of an enhanced high local supersaturation (McKnight, et al 1980).

4. ICE VAPOR GROWTH

These transitions are examined between -3 and -30°C, examining the transitions plate/dendrites near -15°C; column/needles near -4°C and below -25°C. High supersaturation (> 100%) gives spikes at 0° to the near -4°C.

4.1 The Melting Region

A further case of interest arises when ice particles fall below the 0°C level and begin to melt. In general it is observed that, ice remnants exist in precipitation when the ambient temperature is as high as +4°C. Should the dew point lie above 0°C, condensation on the ice will occur and may result in melting.

Figure 1 shows equilibrium lines through the various points representing the slope of the vapor/heat flow equations, (ignoring any effect of the difference of ventilation). Evaporation produces cooling of a few degrees; condensation of vapor from droplets at 4°C on ice at 0°C gives a supersaturation of some 40% and substantial potential for rapid melting.

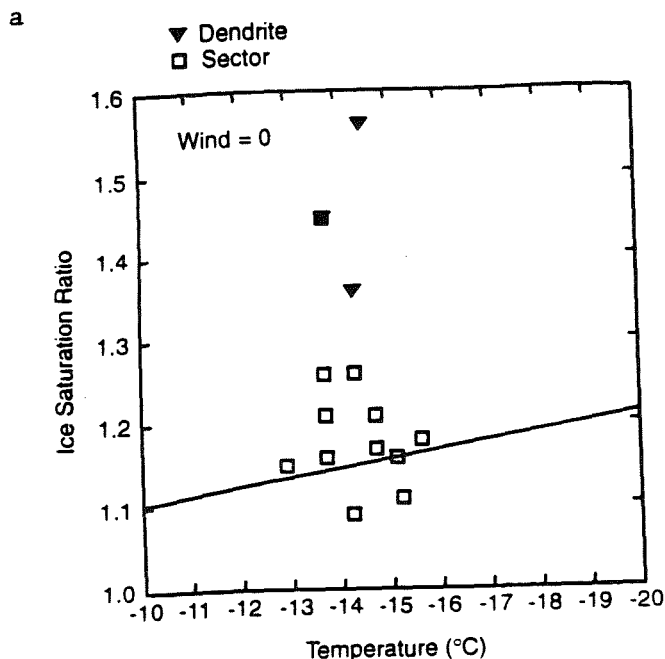
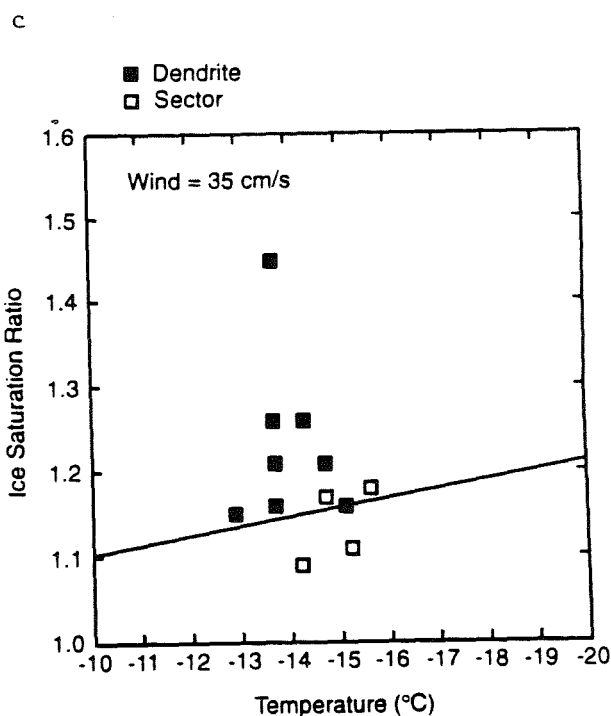
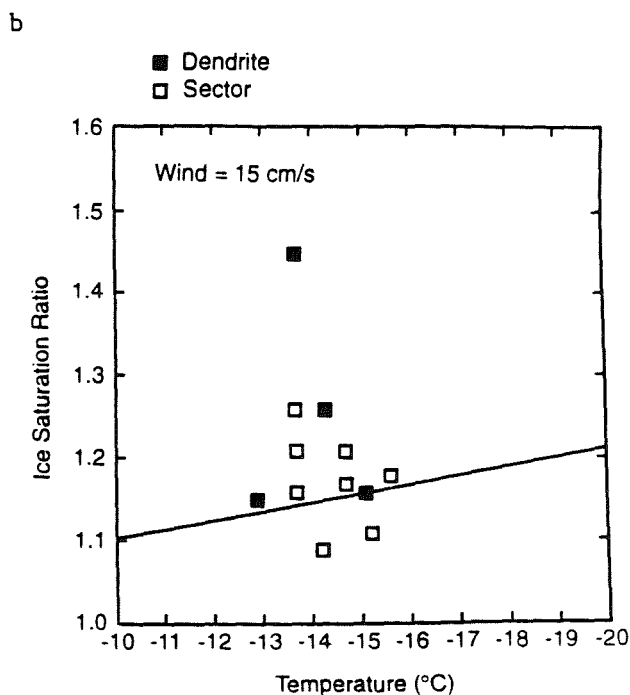


Figure 2: Occurrence of faceted crystals (plate, sectors) and dendrites, dendrites rounded (tips) depending on ventilation velocity and supersaturation at temperature near -15°C . Uncertainties arise because of local shielding, supersaturation ± 0.02 ; velocity $\pm 2 \text{ cm s}^{-1}$. Straight line is water saturation.

The straight lines on this curve represent the slope of the growth/evaporation equation for a sphere, in balance with the heat and mass flow equations at designated saturations. It is assumed for simplicity that the ventilation factors balance and that the surface is at its equilibrium vapor pressure, given by surface temperature. Thus evaporation gives cooling of a few degrees (more at lower pressures). Condensation gives warming, as shown by the curves top right where it is assumed that an environment saturated at $+4^{\circ}\text{C}$ condenses on ice particles. Scenarios can obviously occur where liquid condensation occurs at ambient temperatures below 0°C , but surface temperature above 0°C because of latent heat release.

Melting behavior for drier air has been investigated in the dynamic diffusion chamber by Oraltay and Hallett (1989) who found that complex behavior with interaction between airflow and melt water lead to local protection of ice submerged in water. In these studies the criterion was related to wet bulb temperature. The question arises as to how condensation occurs on such ice crystals, and how melting takes place when the primary source of heating is condensation latent heat at temperature above 0°C at local sites on the falling ice particle. The behavior of ice crystals near 0°C level under different



conditions of relative humidity (wet bulb temperature) is important in understanding motions at these levels driven in part, by melting and condensation latent heat, and interpreting the structure of the melting band.

We currently investigate the mechanism of condensation drop formation during condensation. The reality of these phenomena in terms of humidity structure of real melting layers is yet to be determined in as far as the temperature structure is difficult to measure by either sonde or descending aircraft spirals; the humidity structure is even more difficult to determine. Wet snow in either a temperature or humidity sensor can give major

problems of interpretation. Nevertheless, the local vertical motion as induced by weak convection above the melting level or weak stabilization below the melting level may be interactive with the cloud physical processes taking place. (Szeto et al, 1988(a), (b); Stewart, 1984(a), (b); Heymsfield and Willis, 1989; Clough and Franks, 1991.). These effects influence the structure of melting ice containing particles differently at different levels which in turn influences particle break-up and fall velocity through change of shape.

5. ACKNOWLEDGMENT

John Hallett was supported under Grant #ATM9413437, Meteorology Program, National Science Foundation, Washington, D.C. Riza G. Oraltay was partly supported from a NATO Collaborative Research Grants Program, Grant No.CRG950770.

6. REFERENCES

- Alena, T., J. Hallett and C.P.R. Saunders, 1990:
On the Facet-Skeletal of snow crystals: Experiments in high and low gravity. *J. Cryst. Gr.*, **104**, 539-555.
- Clough, S.A. and R. A. A. Franks, 1991: The evaporation of frontal and other stratiform precipitation, *Q. J. R. Meteorol. Soc.*, **117**, 1057-1080.
- Furukawa, Y., M. Yamamoto, T. Kuroda, 1987: Ellipsometric Study of the Transition Layer on the Surface of an ice crystal. *J. Cryst. Gr.*, **82**, 665-677.
- Elbaum, M., S.G. Lipson and L.G. Dorak, 1993: Optical Study of sulfur melting on Ice. *J. Cryst. Gr.*, **129**, 491-505.
- Hallett, J., Y. Y. Dong, and C. Knight, 1995: Water saturation control of the dendrite - plate transition. Dallas, Texas Conference, 118-121.
- Dong, Y.Y., J. Hallett and A.C. Knight, 1995: Snow Dendrite Growth. AMS Conference on Cloud Physics, January 15-20, Dallas, Texas, 118-121.
- Dong, Y.Y., R. G. Oraltay and J. Hallett, 1994: Ice particle generation during evaporation. *Atmos Res.*, **32**, 45-53.
- Heymsfield, A. J. and P. T. Willis, 1989: Structure of the Melting layer in Mesoscale Convective System Stratiform Precipitation. *J. Atmos. Sci.*, **46**, 2008-2025.
- Elbaum, M., S.G. Lipson and J. G. Dorak, 1993: Optical study of surface melting on ice. *J. Cryst. Gr.*, **129**, 491-505.
- Keller, V., and J. Hallett, 1982: Influence of air velocity on the habit of ice crystal growth from the vapor. *J. Cryst. Gr.*, **49**, 458-464.
- Keller, V., C.V. McKnight and J. Hallett, 1980: Growth of ice discs from the vapor and the mechanism of habit change of ice crystals. *J. Cryst. Gr.*, **49**, 458-464.
- Knight, C. A., 1971: Experiments on contact angle of water on ice. *Phil. Mag.*, **23**, 153-165.
- Knight, A.C. and J. Hallett, 1994: On the Symmetry of snow dendrites. *Atmos. Res.*, **32**, 1-11.
- Oraltay, R.G. and J. Hallett, 1989: Evaporation and Melting of Ice Crystals: A Laboratory Study. *Atmos. Res.*, **24**, 169-189.
- Stewart, R.E., 1984(a): Characteristics through the melting layer of stratiform clouds. *J. Atmos. Sci.*, **45**, 1642-1650.
- Stewart, R.E., 1984(b): Deep 0°C isothermal layers within precipitation bands over southern Ontario. *J. Geophys. Res.*, **89**, 2567-2572.
- Szeto, K.K.; C.A. Lin and R.E. Stewart, 1988(a): Mesoscale circulations forced by melting snow. Part I: Basic simulations and dynamics. *J. Atmos. Sci.*, **45**, 1629-1641.
- Szeto, K.K.; Stewart, R.E.; Lin, C.A., 1988(b): Mesoscale circulations forced by melting snow. Part II: application to meteorological features. *J. Atmos. Sci.*, **45**, 1642-1650.

IMPORTANCE OF A -15°C TEMPERATURE LEVEL ON PRECIPITATION PROCESSES IN CLOUD

Tatsuo Endoh¹ and Tsuneya Takahashi²

¹ Institute of Low Temperature Sci., Hokkaido Univ., Sapporo 060, Japan

² Hokkaido University of Education, Sapporo 002, Japan

1. INTRODUCTION

It is well known that the growth rate of ice crystals is greater at -15°C than that at other temperatures in vapor diffusional processes in laboratory experiments. Takahashi et al.(1991) measured the quantitative value of the diffusional growth rate in free fall and its fall velocity in a cold vertical wind tunnel at saturation. They reported that the growth rate at -15°C is particularly greater than that at other air temperatures by up to 2 orders due to the ventilation effect. On the other hand, fall velocity of crystals at -15°C is lower than that at other temperatures by one order or less at least. Development of activity in precipitation processes are considered to be directly and inversely proportional to growth rate and fall velocity, respectively.

In this work, some evidence supporting these hypotheses has been found out from natural phenomena. Furthermore, a tentative speculation is argued in comparison with "upper-bright bands and snow-generating cells" discussed by Dennis and Hitschfeld (1990).

2. METHODS

Some observations were carried out to study the microphysical structure of snow clouds by means of a dual Doppler radar system and a balloon launching method

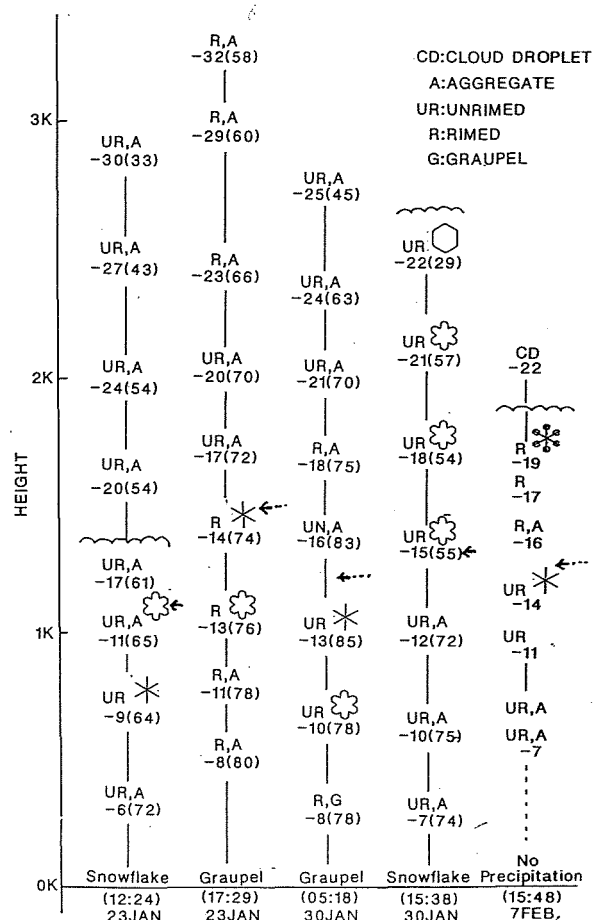
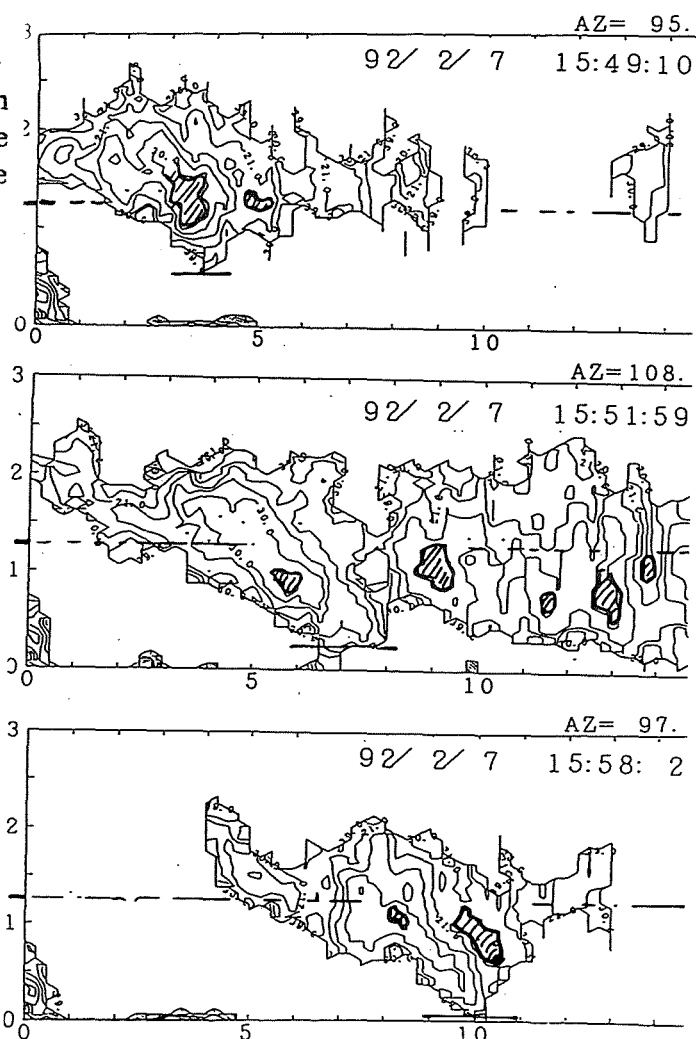


Figure 1 Vertical distribution of snow crystal shapes with schematics and the information on snow particle type e.g. aggregate(A), graupel(G) and rimed(R) or unrimed(UR). The heights of -15°C level are shown by each arrow. Numbers are air temperature and relative humidity(in parentheses). Precipitation at the surface is noted at the root of each vertical axis.

Figure 2 Radar reflectivity in RHI for an alignment of lee side echoes above a point in February 7, 1992. Most intensive parts are hatched in each echo cell which were progressing left to right in the figure. Broken lines show the heights of -15°C temperature level.



that included a specially designed sonde HIVIS. This sonde was developed by Murakami and Matsuo(1990) over the Ishikari plains northwest from Sapporo, Japan, in January and February of 1992.

3. RESULTS

Figure 1 shows five vertical distributions of snow crystal shapes and/or the information of a type e. g. aggregate(A), graupel(G) and rimed(R) or unrimed(UR). Each -15°C temperature level is shown as an arrow on the vertical axis. Around that level, it may be noted that a few single crystals were found out to be unbroken in spite of their fragility. Their crystal shapes were stellar and broad branch types of dendritic crystals which are noted again to have the highest growth rate and the lowest falling velocity from the experimental results by Takahashi et. al. (1991).

Figure 2 shows a time series of three RHI radar reflectivity. An alignment of geographical downstream cellular echoes were taken along the bands directing an almost same azimuth. The height of peak values of radar reflectivity in every echo cells were observed in almost same or slightly less than -15°C temperature level.

Figure 3 shows almost same as Fig. 2, but it was taken across the band during their decay stage of the life cycle. In this case, the lee side echoes is remarked that lee side echoes were seen to continue horizontally with same height as echo tops

which were at -15°C temperature level.

4. DISCUSSION

A simple numerical estimation has been performed by use of these values. Accordingly, the weak convective condition with updraft limited below 0.3 m/sec is calculated to be the most effective for ice crystals at the -15°C level. Here the crystals grow abruptly and are accumulated in high concentrations, resulting aggregation growth. On the other hand, only small size crystals may be brought from the lower layer as an additional supply of new ice nuclei by this updraft velocity, and grown to make moreover higher concentration for aggregation. These phenomena are occasionally observed as an enhancement of radar reflectivity as shown in Figs. 2 and 3. In the case of higher updraft velocity, only large dendritic crystals grown well may be suspended in the -15°C layer. Smaller crystals will be carried higher layer where there is little diffusional growth, but they can grow by riming or/and aggregation. Being height limited by cloud top, they are expected eventually to return to the -15°C level after undergoing further.

Some supporting evidence is available from various cases of our field observations. When snow crystal sondes were launched into snow clouds as shown in Fig. 1, the images of snow crystals revealed only at -15°C level some single dendritic crystals, frequently without any fragmentations. This meant higher generation rate and abundant existence in spite of their fragility.

In a case of radar echo of RHI as shown in Fig. 2, several intensive echoes with maximum intensity were observed to be generated one after another around -15°C level. And they started to descend downward from the level due to their increasing mass.

In another example during the decay stage of a cloud as shown in Fig. 3, a train of

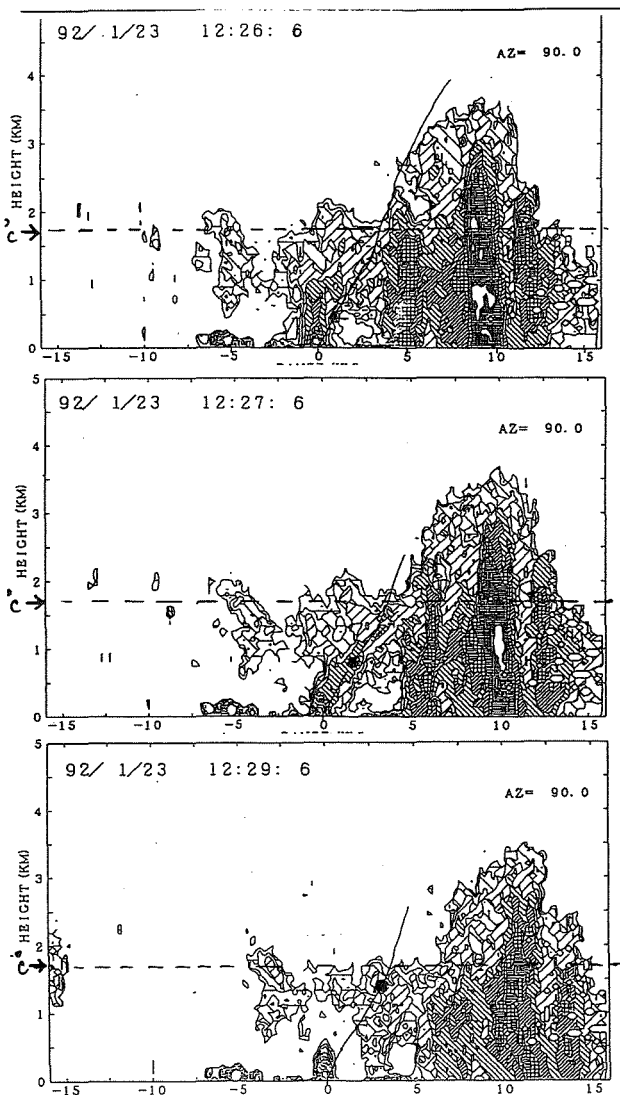


Figure 3 Same as Fig. 2 for in the case of transversal mode clouds in their decay stages. It was taken to the rear of the echo.

echoes was observed to be aligned horizontally along the constant level where air temperature was -15°C , as determined from sounding data. It may be considered that the effect of the generating layer survived in spite of the decay stage.

Consequently these phenomena are seen as evidence of the important effect of -15°C level on precipitation processes.

5. CONCLUDING REMARKS

According to the previous discussions, it is expected that there are some probable relationships between these phenomena and the earlier discussions of "upper-bright band and (snow-) generating cells". And here again, it is remarked that some parts of "(snow-)generating cells" are formed essentially at the -15°C level which can be termed the "(snow-) generating level".

6. REFERENCES

- Dennis, A. S. and W. F. Hitschfeld, 1990:
Advances in precipitation physics
following the advent of weather radar.
, Radar in Meteorology (ed. D. Atlas),
98-108.
- Murakami, M. and T. Matsuo, 1990:
Development of the hydrometeor
videosonde. J. Atmos. Ocea. Tech., 7
, 613-620.
- Takahashi, T., T. Endoh, G. Wakahama and N.
Fukuta, 1991: Vapor diffusional growth of
free-falling snow crystals between -3
and -23°C . J. Meteor. Soc. Japan, 69
, 15-30.

7. ACKNOWLEDGEMENTS

The authors wish cordially to express their thanks for the cooperation and advice by Professor K. Kikuchi of Hokkaido University, Professors R. List and G. W. Kent Moore of University of Toronto and Dr. D. Hudak of Atmospheric Environment Service.

DETERMINATION OF HAILSTONE SIZE DISTRIBUTION INSIDE A THUNDERCLOUD FROM HAILPAD MEASUREMENTS AT THE GROUND

J. Dessens¹, Roberto Fraile² and José Luis Sanchez²

¹Laboratoire d'Aérodynamique, UMR CNRS/UPS 5560, 65300 Campistrous, France,

²Laboratorio de Física de la Atmósfera, Universidad de León, 24071 León, Spain.

1. INTRODUCTION

A large-scale hailpad network has been operating since 1987 in southwestern France in relation with the ANELFA hail prevention project. The network and the data processing are described in Dessens and Fraile (1994). In 1995, 970 hailpads were distributed over an area of about 40,000 km². The data now consist of 1777 hailpads recorded from 1987 to 1995, and the hailstone size distributions have been determined for each of the 1147 hailpads having hailstones larger than 1 cm. These measured hailfalls have occurred on 405 different haildays.

It is in general acceptable to represent the size distribution of the hailstones fallen at a given location by an exponential relation (Crow et al., 1979). Such a distribution is characterized by two parameters, one relative to the hailstone concentration (the "concentration parameter"), and the other to the respective numbers of small and large hailstones (the "slope parameter"). For a given day, these distribution parameters are different from a location to another, even if the hailfalls are produced by a same storm. In Dessens and Fraile (1994), the distribution parameters of the cumulated hailstones fallen in different locations on a given day were considered, and a significant correlation was found between the daily concentration parameter and the altitude of the 0°C level. Now that we have several cases with a large number of hailpads recorded on a same day, we may check if it is justified to define such a daily distribution. For that purpose, we will compute two separate sub-distributions for a same day, and will compare the two sub-distributions.

We will also compare the correlations between the distribution parameters and the altitude of the 0°C level computed from daily distributions and from individual distributions.

2. DATA PROCESSING

The dents left by the hailstones on the extruded polystyrene pads are counted by diameter range (Lozowski and Strong, 1978), so that we can determine for each hailpad:

- A concentration parameter, N_T , which is the total number of hailstones with diameters larger than 0.7 cm (hailstones with smaller diameters are undercounted):

$$N_T = \sum_{0.7 \text{ cm}}^{D_{\max}} N_D ,$$

where D_{\max} (in cm) is the diameter of the largest hailstone fallen on the pad, and N_D the number of hailstones (in cm⁻¹ m⁻²) of diameter D (in cm).

- A mean diameter D_M :

$$D_M = \frac{\sum_{0.7 \text{ cm}}^{D_{\max}} N_D \times D}{\sum_{0.7 \text{ cm}}^{D_{\max}} N_D} .$$

In most of the cases, the distributions can be approximated by the classical exponential relation:

$$N_D = N_{0.7} e^{-\lambda(D-0.7)} ,$$

where $N_{0.7}$ (in cm⁻¹ m⁻²) is the number of hailstones of 0.7 cm diameter, and λ (in cm⁻¹) is the slope of the distribution.

$N_{0.7}$ and λ are related to N_T and D_M by the following expressions:

$$N_{0.7} = N_T / (D_M - 0.7)$$

$$\lambda = 1 / (D_M - 0.7)$$

For comparison with distributions given in the literature, the theoretical number N_0 of hailstones of diameter $D = 0$ is related to $N_{0.7}$ by the relation:

$$N_0 = N_{0.7} e^{0.7\lambda} .$$

3. DAILY DISTRIBUTIONS

A daily distribution for all the hailstones fallen in the different hailfalls is computed for the days when at

least 15 hailfalls have occurred in the network area. Table 1 gives for these days the number of processed hailpads, the concentration and slope parameters, and the altitude of the 0°C level.

In a few cases, the number of point hailfalls is large enough to separately consider two hailfall samples for different periods of the day, or for different areas. We observe that for cases 1, 9, 10 and 13 the concentration parameters are nearly identical for the two samples, while they are not for cases 6, 7 and 12. The slope parameter (the inverse of $D_M^{-0.7}$) is in general different from a sample to another, except for cases 7 and 12. In consequence, we must consider that the daily concentration parameter computed with a set of hailfalls has more chance to be representative of the environmental conditions than the slope parameter.

With the global daily distributions given in Table 1, the correlations between the different parameters are the following:

Correlation between N_T and D_M , $r = +0.05$
 - N_T - $h_{0^\circ C}$, $r = -0.56$
 - D_M - $h_{0^\circ C}$, $r = +0.24$,
 where $h_{0^\circ C}$ is the altitude of the 0°C level.

The correlation between the concentration parameter and $h_{0^\circ C}$ is significant at a level better than 0.01. The linear fitting between N_T and $h_{0^\circ C}$ (Fig. 1) gives, for a daily distribution, the value of N_T at the 0°C level from the value of N_T at the ground:

$$(N_T)_{0^\circ C} = (N_T)_{\text{ground}} \times \frac{3088}{3088 - 532 h_{0^\circ C}}$$

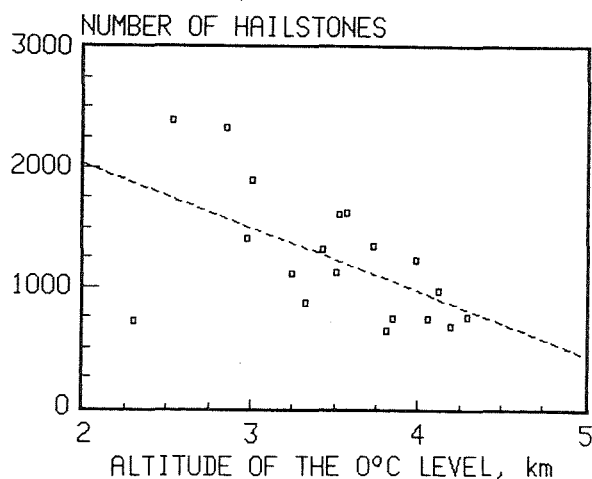


Figure 1. Relation between the altitude of the 0°C level and the total number of hailstones per hailfall (m^{-2}) for 19 major hail days.

This relation is nearly the same as the relation found with a preliminary set of daily distributions, each relative to a smaller number of hailpads (Dessens and Fraile, 1994). However, 5 distributions used in the

present paper have already been used in the first computation. In Fig. 1, the point far from the linear fitting is relative to case 11. For that day, the surface temperature in the hailed areas was 4 to 5°C warmer than the surface temperature at Bordeaux, the radiosonde station, so that the real value of $h_{0^\circ C}$ for this day is probably higher.

Table 1: Mean parameters of the hailstone size distribution for 19 major hail days. N_T is the total number of hailstones larger than 0.7 cm and D_M is the mean diameter of these hailstones. The last column gives the altitude of the 0°C level.

Day	Number of pads	N_T (m^{-2})	D_M (cm)	$h_{0^\circ C}$ (km)
6 Jul 1989	20	704	1.005	4.19
	19	632	0.952	-
	39	669	0.981	-
23 Jul 1989	20	968	1.112	4.12
17 May 1990	10	945	0.957	3.24
	10	1260	0.897	-
	22	1115	0.921	-
13 Aug 1990	20	633	0.953	3.81
31 Aug 1991	15	1334	0.931	3.72
23 May 1992	13	3110	1.077	2.85
	12	1777	0.944	-
	28	2333	1.023	-
31 May 1992	12	1843	0.979	2.97
	10	1008	0.978	-
	23	1404	0.978	-
31 Jul 1992	16	1225	0.984	3.98
	11	644	0.930	4.29
	29	796	0.996	-
8 Aug 1992	40	754	0.971	-
27 Sept 1992	10	2427	1.101	2.53
	14	2357	0.996	-
	24	2386	0.989	-
27 May 1993	18	714	0.931	2.30
1 Jun 1993	11	597	0.962	3.32
	11	1125	0.982	-
	22	861	0.975	-
28 Jun 1993	19	715	1.059	4.05
	25	723	1.022	-
	35	740	1.038	-
5 Jul 1993	15	731	1.106	3.84
14 Aug 1993	15	1619	0.932	3.57
18 Jun 1994	17	1614	1.034	3.52
31 Jul 1994	17	1312	0.956	3.42
1 Jul 1995	15	1128	0.934	3.50
2 Jul 1995	23	1888	1.048	3.00

Table 2: Correlations for 563 hailfalls between the number N_i of hailstones in each diameter range and respectively the total number of hailstones N_T , the mean diameter D_M , and the altitude of the 0°C level.

Diameter range (cm)		0.7-0.9	0.9-1.1	1.1-1.3	1.3-1.5	1.5-1.7	1.7-2.1	2.1-2.5	2.5-2.9	2.9-3.3	3.3-3.7	3.7-4.1	4.1-4.5
Correlation	N_i/N_T	-.28	-.11	0	0	0	0	0	0	0	0	0	0
-	N_i/D_M	+.91	+.95	+.76	+.65	+.50	+.41	+.27	+.19	+.13	+.06	+.05	+.07
-	$N_i/h_{0^\circ\text{C}}$	-.10	+.17	+.38	+.48	+.54	+.52	+.52	+.41	+.37	+.29	+.22	+.13

4. POINT DISTRIBUTION

Since it appears that the representativeness of daily distributions is doubtful, we also may compute correlations using the concentration and slope parameters of each individual distribution. A preliminary study with a set of 563 distributions relative to 63 days during the years 1989 to 1994 gives the following correlation coefficients:

$$\begin{array}{lll} \text{Correlation between } N_T \text{ and } D_M, & r = +0.14 \\ - & N_T - h_{0^\circ\text{C}}, & r = -0.19 \\ - & D_M - h_{0^\circ\text{C}}, & r = +0.22 \end{array}$$

The correlation between N_T and $h_{0^\circ\text{C}}$ gives a very similar relation to that found with the daily distributions:

$$(N_T)_{0^\circ\text{C}} = (N_T)_{\text{ground}} \times \frac{2526}{2526 - 427 h_{0^\circ\text{C}}}$$

There is now a significant correlation between D_M and $h_{0^\circ\text{C}}$:

$$(D_M)_{0^\circ\text{C}} = (D_M)_{\text{ground}} \times \frac{0.784}{0.784 + 0.046 h_{0^\circ\text{C}}}$$

The correlation between N_T and D_M is also significant at the 0.01 level. In order to better understand these correlations, we may compute them in each class of diameters (Table 2). We observe that only the first two classes of diameter contribute to the negative global correlation between $h_{0^\circ\text{C}}$ and the concentration parameter N_T , while the positive global correlation between $h_{0^\circ\text{C}}$ and the inverse of the slope parameter is driven by all the classes but the first one. A physical interpretation of these results is that most of the hail situations with large hail are related to high values of the altitude of the 0°C level (warm temperature at the ground), when the lower classes of hailstones are subject to melting.

5. CONCLUSION

The study of hailstone distributions at the ground in order to better understand the physical processes of hail formation comes up against two problems:

1- Considering a regional daily distribution with a set of hailfalls is valid in some cases, but in other cases the subdivision of the daily distribution into two distributions leads to different values of the parameters.

2- Considering all the individual distributions introduces the statistical shortcoming that the data are not independent, with sets of distributions relative to the same meteorological situations.

However, a similar relation is found between the concentration parameter and the altitude of the 0°C level, considering either the daily distributions or the individual ones. It is then possible to compute, for each hailfall, a concentration parameter at the 0°C level from the parameter at the ground. The relation between the slope parameter and $h_{0^\circ\text{C}}$ needs to be checked with more daily distributions.

In conclusion, we reinforce our preliminary results obtained with a limited sample of hailfalls, confirming that, according to the model of Ludlam (1980), hail in southwestern France mainly falls within downdrafts.

6. REFERENCES

- Crow, E. L., A. B. Long, J. E. Dye and C. W. Ulbrich, 1979: Results of a randomized hail suppression experiment in northeast Colorado. Part III: Analysis of hailstone size distributions for seeding and yearly effects. *J. Appl. Meteorol.*, 18, 1559-1568.
- Dessens, J., and R. Fraile, 1994: Hailstone size distributions in southwestern France. *Atmos. Res.*, 33, 57-73.
- Lozowski, E. P., and G. S. Strong, 1978: Further reflections on the calibration of hailpads. *Atmos. Ocean*, 16, 69-80.
- Ludlam, F. H., 1980: *Clouds and Storms. The behavior and effect of water in the atmosphere*. The Pennsylvania State University Press, University Park and London, 405 pp.

MODEL SIMULATION OF THE MELTING LAYER

W. Szyrmer⁽¹⁾, R. Papageorghe⁽¹⁾ and I. Zawadzki⁽²⁾

(1) Université du Québec à Montréal

(2) J. S. Marshall Radar Observatory, McGill University

1.- Introduction

In previous work, radar observations of the melting layer have been used to describe the morphology of the bright band using an X-band vertically pointing radar and a UHF Doppler profiler (Fabry et al 1994).

Here, the melting layer is modeled within a dynamic framework in which all processes, dynamic, thermodynamic and microphysical, are fully coupled. The microphysical processes are simplified into a "bulk parameterization" in which hydrometeors classes are characterized by the water content of the class and, in the case of melting snow, by the snow content and the minimum diameter of melting snowflakes. The UHF/RASS measured profiles of temperature and fall velocities provide a convenient validation on the model output.

2.- Parameterization of snow melting

We assume an inverse exponential particle size distribution for snow. Inspired by the observations of Mitra et al (1990) we assume in addition that: i) all melted water remains within the particle. We also ii) neglect aggregation or break-up of particles, and assume that iii) a particle is transferred from the melting snow category to that of rain when the volume of the melting particle equals the volume of the non melted fraction of the snowflake. At this point the ice is completely contained within the liquid water.

Let f be the fraction of melted mass at time t , V_m the volume of the melting particle, ρ_m its density and V_s the volume of the initial snowflake and ρ_s its density (taken here to be 0.1 g/cm^3). The density of the melting particle is defined by:

$$\rho_m = \frac{\rho_s V_s}{V_m} = \frac{\rho_w V_w}{V_m}, \quad (1)$$

where V_w is the completely melted volume. The melted fraction of the particle is

$$f = \frac{m_m}{\rho_s V_s} = \frac{V_s - V_m}{V_s} \quad (2)$$

Condition iii) stipulates that the transfer from snow to rain is made when $V_m = V_w$.

Since $V_m = (1-f)V_s$ the particle density is

$$\rho_m = \frac{\rho_s}{1-f} \left\{ \begin{array}{ll} \text{if } f \leq \frac{\rho_w - \rho_s}{\rho_w} \\ \rho_m \approx \rho_w \end{array} \right. \quad \text{otherwise} \quad (3)$$

After the particle is transferred into the rain category, we neglect the difference in density between pure water and mixture of ice and water.

For a spherical particle the rate of mass melting can be expressed as

$$L_f \frac{dm_m}{dt} = \quad (4)$$

$$2\pi D_m (K \delta T + D L_v \delta \rho) F = 2\pi D_m \delta Q F$$

where δT is the temperature difference between the air and the particle (equal to air temperature in $^{\circ}\text{C}$, if the particle is at 0°C); $\delta \rho$ is the difference between the ambient water vapor pressure and the saturation value at the surface of the particle; F the ventilation coefficient and K, D the heat conductivity and water vapor diffusion coefficients, respectively.

For simplicity, we will neglect the condensed mass although the latent heat of condensation is taken into account.

There is no observations of the ventilation coefficient for $0 < f < 1$. Rather than adopt some average value, independent of size, we

approximate the ventilation coefficient of melting particles by,

$$F = 25.2 \frac{D_w^{1.6}}{D_m}, \quad (5)$$

where the numerical constants were determined by least square fit to the values of ventilation coefficients for rain and snow. For $D_s > 1$ mm the fit is within 15% and provides a realistic dependence of the ventilation coefficient for melting particles. As a result, the rate of melting becomes a function of the initial size and independent of f :

$$\frac{dm_m}{dt} = \frac{50.4\pi}{L_f} \delta Q D_w^{1.6} \quad (6)$$

At any time, the melting snow (rain) particle size distribution is truncated at a minimum (maximum) diameter d_m (d_w). Snow particles below this size are transferred into the rain category. The rate of melting for the whole distribution can be obtained by integration of (6) over all the particles in the melting snow category:

$$\frac{dM}{dt} = \frac{50.4\pi}{L_f} \delta Q \int_{d_w}^{\infty} D_w^{1.6} N_m(D_w) dD_w \quad (7)$$

where $N_m(D_w)$ is the size distribution of the melting particles expressed in terms of the completely melted diameter. It can be shown that δQ can be expressed as a function of d_w :

$$\delta Q = \frac{L_f(\rho_w - \rho_s)}{302.4\Delta t} d_w^{1.4} \quad (8)$$

$[\delta Q \Delta t]$ is the heat exchange during Δt along the trajectory of the precipitation parcel. From advected d_w , δQ can be calculated at each time step.

On the other hand, the fall velocities of rain and snow in m/s are given respectively by

$$U_w = aD_w^b \quad U_s = U_s(D_w) = \alpha_w D_w^\beta \quad (9)$$

$a = 4.25$; $\alpha_w = 0.68$; $b = 0.6$; $\beta = 0.42$

when D_w is in mm. For melting snow the terminal fall velocity is expressed as

$$U_m = U_w \gamma(f) + U_s \{1 - \gamma(f)\} \quad (10)$$

where

$$\gamma(f) = \frac{U_m - U_s}{U_w - U_s} = 0.3f^{1.5} + 0.7f^{7.2} \quad (11)$$

is the best fit to the values of Mitra et al (1990). The melted fraction f , can be calculated from (6) and (8)

$$f = \frac{\rho_w - \rho_s}{\rho_s} \left(\frac{d_w}{D_w} \right)^{1.4} \quad (12)$$

During melting the fall speed of particles increases and consequently the number of particles per unit volume decreases, that is, $N_m(D_w)$ changes in time as follows:

$$N_m(D_w) = (U_s / U_m) N_s(D_w) \quad (13)$$

It can be shown that the ratio U_s / U_m may be approximated by the expression:

$g(f) = 1 + c_1 f + c_2 f^2$. Thus, introducing (8) to (7), the liquid water content of melting snowflakes, M , can be found

$$M = \frac{\pi}{6} (\rho_w - \rho_s) d_w^{1.4} g(\bar{f}) \int_{d_w}^{\infty} D_w^{1.6} N_s(D_w) dD_w \quad (14)$$

where \bar{f} is the melted fraction averaged over the melting snow distribution.

For n integer, the truncated n th moment of distribution $N_s(D_w) = N_0 e^{-\lambda D_w}$ is

$$\int_{d_w}^{\infty} D_w^n N_s(D_w) dD_w = N_0 e^{-d_w \lambda} \sum_{k=0}^n \frac{n!}{k!} \frac{d_w^k}{\lambda^{n-k+1}}.$$

The left-hand side can be approximated by $A e^{-n\Lambda}$. Hence, the integral in (14) can be calculated as

$$\left[\int_{d_w}^{\infty} D_w^2 N_s(D_w) dD_w \right]^{0.6} \left[\int_{d_w}^{\infty} D_w N_s(D_w) dD_w \right]^{0.4}$$

Equations (8), (10) and (14) form the basis for the description of the melting process of snow and graupel.

3.- The model

Microphysical processes are driven by the dynamic model described by Robert (1993). Its characteristic is the semi-Lagrangian semi-implicit numerical scheme.

The coupling between the dynamics and the microphysics is done through the conservation equation for water substance. For any substance (rain, snow, cloud), with mass q per unit volume, the conservation is written as

$$\frac{\partial q}{\partial t} + \bar{\nabla}_h \cdot [q \bar{V}_h] + \frac{\partial}{\partial z} [q(w - U)] = S_q \quad (15)$$

where S_q is the source/sink term, (u, v) and w are the components of the air velocity vector, and U the mass weighted terminal fall speed of q , the subscript h indicates horizontal components. The source/sink term contains

all the microphysical processes. Equation (15) is applied to all water categories: rain liquid water content, q_R ; cloud liquid water content, q_C ; snow liquid water content, q_S ; etc.

4.- Simulations

The simulation described here was done with the following boundary conditions:

- Periodic at lateral boundaries;
 - Rigid at the upper and lower boundary ;
 - Grid spacing: 45 m in horizontal and 30 m in vertical; time steps: 2 sec;
 - Domain of the model: two-dimensional, 21.6 km horizontal X 4.2 km vertical (241 x 141 grid points);
 - Initialization: pseudoadiabatic lapse rate with a ground temperature of 15 C;
 - Saturation with respect to water where $T > 0$ C, with respect to ice where $T < 0$ C.
- At 3 km and above, radar observed snow is introduced.

The simulations show that the non uniformity of the snow content creates convective cells within the melting layer. Through condensation in updraft and evaporation in downdraft these cells introduce a modulation in the rate of melting. If the snow input above the zero degree isotherm is maintained constant in time an equilibrium situation develops. The equilibrium is arrived at after approximately 450 time steps, at about the same time as the precipitation reaches ground. Additional 150 time steps were performed to insure the equilibrium. The snow input is from a vertically pointing high resolution radar observations made on the 1 November 1994 between 1536 and 1544 h. Some selected results of the equilibrium state are shown in Figs. 1 through 3.

In Fig. 1. the melting rate is shown. The vertical extent of the melting layer is just short of 500m which is the width of the observed bright band at the time. This result is encouraging as it indicates that no special tuning of the model seems to be necessary.

Figure 2a shows the vertical velocity generated by the heat exchange during melting. The stronger downdrafts are associated with the larger snow contents. The maximum velocities are relatively weak with maxima around 14 cm/sec. There are reports from aircraft that the air is "bumpy" under the bright band. The horizontal velocities are shown in Fig. 2b. The convergence-divergence zones

associated with the convection are seen to be linked with the larger snow content.

The horizontally averaged fraction of the melted water contained in the melting particles is shown in Fig. 3a. We see an initial slow change of f with height followed by a most pronounced increase at the bottom of the melting layer. This kind of information is of direct interest to the problem of EM propagation and scattering. The simulated (dot line) and the Doppler radar measured reflectivity weighted fall speed (solid line) is shown on the figure 3b. The effect of the heat exchange on the ambient air is depicted in Fig. 3c. The cooling associated with melting leads to the quasi-isothermal temperature profile as was observed by the UHF/ RASS profiler in cases of low level bright bands.

REFERENCES

- Fabry, F., and I. Zawadzki, 1995: Long term radar observations of the melting layer of precipitation and their interpretation. *J. Atmos. Sci.*, **52**, 838-851.
- Ferrier, B.S, 1994: A double moment multiple phase four class bulk ice scheme. Part I: Description. *J. Atmos. Sci.*, **51**, 249-280.
- Mitra, S.K., O. Wohl , M. Ahr, and H.R. Pruppacher, 1990: A wind tunnel and theoretical study of the melting behavior of atmospheric ice particles. IV: Experiment and theory for snowflakes. *J. Atmos. Sci.*, **47**, 584-591.
- Pellerin, P., R. Laprise and I. Zawadzki, 1995: The performance of semi-Lagrangian transport scheme for the advection-condensation problem. Submitted
- Pruppacher, H. R. and J. D. Klett: "Microphysics of Clouds and Precipitation", pp 714.
- Robert, A., 1993: Bubble convection: Experiments with a semi-implicit formulation of the Euler equations. *J. Atmos. Sci.*, **50**, 1865-1873
- Sekhon, R.S., and R.C. Srivastava, Doppler radar observations of drop-size distribution in a thunderstorm, *J. Atmos. Sci.*, **28**, 983-994, 1971.)

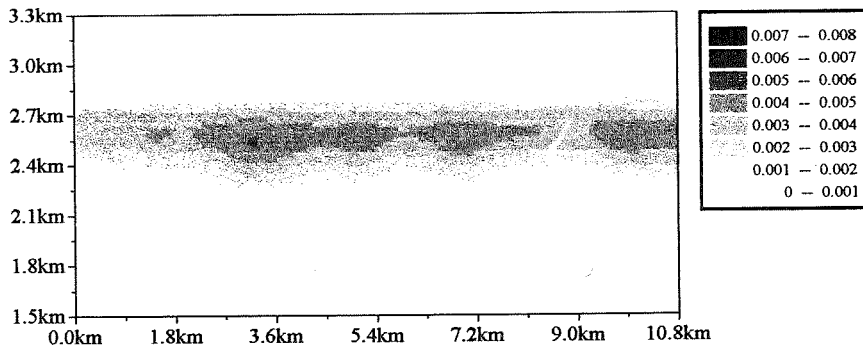


Fig. 1. Melting rate; the gray scale indicates values in $\text{g}\cdot\text{m}^{-3}\cdot\text{s}^{-1}$.

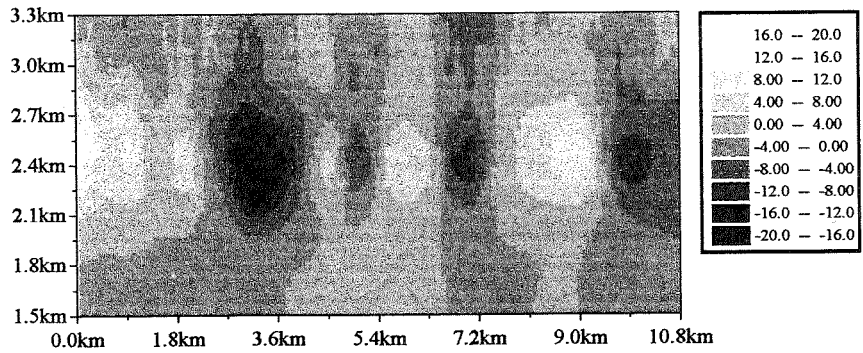


Fig. 2a. Air vertical velocity; the gray scale indicates values in $\text{cm}\cdot\text{s}^{-1}$.

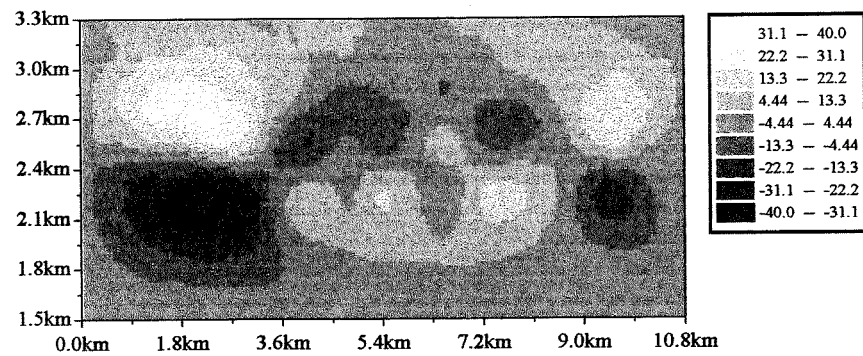


Fig. 2b. Air horizontal velocity; the gray scale indicates values in $\text{cm}\cdot\text{s}^{-1}$.

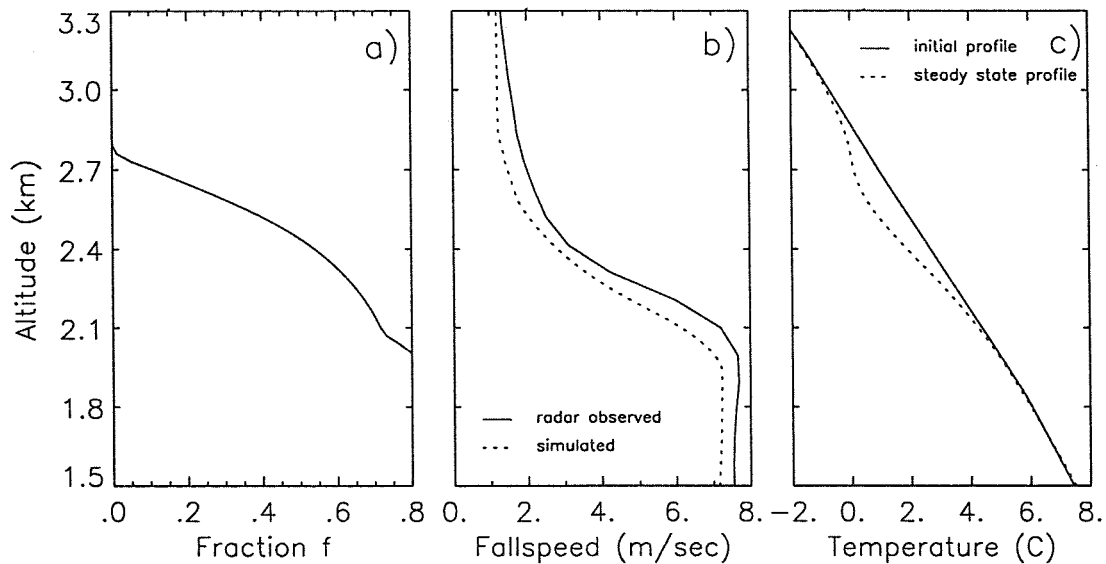


Fig. 3 a. Horizontally averaged melted fraction within the melting particles.
b. Horizontally averaged particles fall speed.
c. Horizontally averaged temperature profile.

NUMERICAL SIMULATION OF THE HAILSTONE FORMATION

István Geresdi

Department of Physical Geography, JPTE, Pécs, Hungary

1. INTRODUCTION

The freezing of the supercooled water drops has been investigated mainly in laboratories (e.g. Gorbunov et al. 1980; Deshler and Vali 1992; DeMott 1995). These experiments have been able to concentrate only on limited parts of the complex process of hailstone formation. Numerical experiment were made to get a more comprehensive picture.

2. DESCRIPTION OF THE MODEL

Detailed microphysics and very simple parcel method for the dynamics were used to simulate the hailstone formation. The updraft velocity linearly increased from 5 to 10 m/s. Beside the adiabatic expand of the parcel the release of latent heat of fusion and condensation was taken into consideration to calculate the air temperature. The effect of vapor saturation were investigated by two assumption. The calculation were made by supposing no mixing with the environment (the saturation was near constant, about 1.02) and by changing the vapor content randomly (± 5 %) about the saturation vapor mixing ratio.

Four type of particles were considered: submicron size solid particles which can act as immersion and contact nuclei, "clear" and "contaminated" water drops and hail particles. The role of nucleus size in ice forming was investigated by using three different nucleus radii (0.01, 0.1 and 1.0 μm). The water drops which captured a nucleus are defined as "contaminated" ones. The size distribution of the water droplets and hail particles

were categorized into 67 (between 1.9 μm and 3.2 mm) and into 55 intervals (between 10 μm and 5.9 mm), respectively. The nuclei are captured by the water drops due to Brownian motion, phoretic transport and gravitational collection. The formulas given by Young (1973) were used to calculate Brownian and phoretic collection rate. Collision efficiencies suggested by Beard and Grover (1974) were used to give gravitational collection rate. The evolution of the size distribution is effected by condensation, freezing, deposition and coalescence. The freezing process was initiated by contact and immersion nucleation. Collision of an active nuclei with supercooled water drops initiate the freezing by contact nucleation. The immersion nucleation was caused by activation of captured nuclei in the "contaminated" droplets. The rate of the active nuclei in both processes depends on the nucleus size and the temperature (Deshler and Vali 1992 and Gorbunov et al. 1980). Terminal velocities and collision efficiencies suggested by Beard (1976) and Hall (1980) were used to calculate the kernel function for drop-drop collision. The coalescence efficiency was supposed to be unity. The collision induced breakup was described by the formulas found in the paper of Brazier-Smith et al. (1973). After the breakup induced by collision of "clear" - "contaminated" or "contaminated" - "contaminated" drops only one drop remain "contaminated" the others get "clear". The probability of involving nucleus depended on drop volume. The hail particle formed by freezing of supercooled droplets grew by collection of water drops and deposition. The terminal velocity given by Rasmussen and Heymsfield (1988) for dry hailstones and Langmuir's (1948) formulas for collision

efficiency were used to calculate the collection rate. Following the collision all of the collected water droplets freeze and the temperature of the hailstones remained below the 0 C. The more correct calculation of this process may modify partly the result. The calculation of the hailstone temperature and making the wet growth possible are planned in the next phase of the research.

The air parcel started at 800 mb, the air temperature and vapor mixing ratio were 10 C and 9.45 g/kg, respectively. The initial mass density distribution of the water drops is characterized by mean radius of 6 μ m and relative dispersion of 1. Initially the

air parcel contains only "clear" drops with mixing ratio of 0.5 g/kg and number concentration of 500 db/cm³. The initial concentration of the nuclei was 10 1/l when the radius was 0.01 and 0.1 μ m and it was only 1 1/l when the radius was 1 μ m.

Technique developed by Kovetz and Olund (1969) was applied to calculate the change of the number concentration in the size categories. Simple Eulerian method was used for the time integration. The time step was 1 sec. , except for calculation of the condensation when a much smaller time step (0.05 sec.) was used.

Table 1. Evolution of the hail spectra in the investigated cases. The sizes (nucleus size: r_a , mean size and predominant size of hail particles: r_f and r_g) are given in μ m, the dimension of the concentration (n) is 1/kg and that of the mixing ratio (q) is g/kg. In the last two columns the concentration of the nuclei (n_a) at 0. min. and at 10. min. are written.

r_a		8. min.				10. min.				n_a	
		r_f	r_g	n	q	r_f	r_g	n	q		
0.01	no fluc.	105	774	522	0.01	641	1168	3020	3.00	10000	6910
0.01	fluc.	324	911	417	0.05	852	1290	2010	4.69	10000	7710
0.1	no fluc.	110	824	58	-	1116	1962	68	0.36	10000	9930
0.1	fluc.	337	962	72	0.01	1600	2200	77	1.21	10000	9920
1.0	no fluc.	360	845	6	-	1068	1690	297	1.37	1000	700
1.0	fluc.	487	950	82	0.04	1234	1710	492	3.49	1000	500

Table 2. The number of the nuclei captured due to the different scavenging mechanism and that of the hail particle formed by contact and immersion nucleation in 10 min.. The concentration are given in 1/kg.

r_a		Brownian	phoretic	gravitational	contact	immersion
0.01	no fluc.	3090	-	-	160	2860
0.01	fluc.	2200	90	-	60	1950
0.1	no fluc.	70	-	-	13	55
0.1	fluc.	50	30	-	7	70
1.0	no fluc.	≈ 0	-	300	296	1
1.0	fluc.	≈ 0	≈ 0	500	491	1

3. RESULTS

The brief summary of the results are given in the Table 1. and Table 2.. The number concentration of the hail particles depends on the nucleus size and changes three

order. The vapor fluctuation also effects it, but to a lesser degree. Comparing the number concentration of the captured nuclei and that of the hail particles it could be pointed

that of the hail particles it could be pointed out that the freeze of a supercooled drop was initiated only by one nucleus.

The average number of nuclei in a drop slightly increases by increasing of nuclei concentration. The effect of vapor content fluctuation depends on the nucleus size. While the largest nuclei were more efficiently captured, the number of smallest nuclei collected by water drops decreased by about one third when the vapor mixing ratio fluctuated randomly. The low number of collected nuclei of $0.1\mu\text{m}$ was hardly increased by the fluctuation. These different effects could be explained by the broadening of size distribution caused by vapor content fluctuation near to the saturation. The increasing probability of forming larger drops and the decreasing concentration result in decrease of the total surface of water drops. While the appearance of the larger drops increase the gravitational collection rate of largest nuclei, the decreasing total surface accounts for the less efficient scavenging of smaller nuclei. As it was expected only very small fractions of the medium-sized nuclei were captured by the water drops. It is interesting that appearance of the phoretic transport is almost balanced by decrease of the Brownian collection when vapor content fluctuates.

The first hail particles formed after the air temperature reached about -5°C . Using the above mentioned updraft profile this happened between 6. and 7. min.. The evolution of hail spectrum was quite different in the investigated cases. The smaller nuclei (0.01 and $0.1\mu\text{m}$) mostly act as immersion nuclei the role of contact nucleation was not so important. The largest nuclei initiate the freeze almost completely by contact nucleation. The change of number concentration of hail particles also depends on nuclei size. While in the case of the medium-sized nuclei the concentration of the hail particles practically did not change in the last three minutes, in the other cases it increased more dramatically. The fluctuation results in larger hail size

independently of the nuclei size, because the appearance of the bigger water drops increases the coagulation growth rate.

4. REFERENCES

- Beard, K.V. and S. N. Grover, 1974: Numerical collision efficiencies for small raindrops colliding with micron size particles. *J. Atmos. Sci.*, **31**, 543-550.
- Beard, K. V., 1976: Terminal velocity and shape of cloud and precipitation drops aloft. *J. Atmos. Sci.*, **33**, 851-864.
- Brazier-Smith, P. R., S. G. Jennings and J. Latham, 1973: Raindrop interactions and rainfall rates within clouds. *Quart. J. Roy. Meteor. Soc.*, **99**, 260-272.
- DeMott, P. J., 1995: Quantitative description of ice formation mechanism of silver iodide-type aerosols. *J. Atmos. Res.*, **38**, 63-99.
- Deshler, T. and G. Vali, 1992: Atmospheric concentrations of submicron contact-freezing nuclei. *J. Atmos. Sci.*, **49**, 773-784.
- Gorbunov, B. Z., N. A. Kakutkina and K. P. Koutzenogii, 1980: Studies of silver iodide ice-forming activity: verification of theory. *J. Appl. Meteor.*, **19**, 71-77.
- Hall, W. D., 1980: A detailed microphysical model within a two-dimensional framework: model description and preliminary results. *J. Atmos. Sci.*, **37**, 2486-2507.
- Kovetz, A. and B. Olund, 1969: The effect of coalescence and condensation on rain formation in a cloud of finite vertical extent. *J. Atmos. Sci.*, **26**, 1060-1065.
- Rasmussen, R. M. and A. J. Heymsfield, 1987: Melting and shedding of graupel and hail. Part I: Model Physics. *J. Atmos. Sci.*, **44**, 2754-2763.
- Young, K. C., 1973: The role of contact nucleation in ice phase initiation in clouds. *J. Atmos. Sci.*, **31**, 768-776.
- Acknowledgment*. The research was supported by the Hungarian Scientific Research Fund (number: T 017118).

MICROPHYSICAL PROCESS OF OROGRAPHIC SNOWFALL

Toshio Harimaya and Yasumi Nakai

Division of Earth and Planetary Sciences, Hokkaido Univ., Sapporo, 060 JAPAN

1. INTRODUCTION

There are two characteristic types of heavy snowfall patterns in coastal and orographic areas, respectively, in areas toward the Japan Sea, Japan. Orographic snowfall occurs during northwesterly winter monsoons under a west-high and east-low pressure pattern. However, the microphysical process of snowfall formation in orographic areas has not yet been elucidated.

A conceptual model of the mechanism of orographic rain was proposed by Bergeron (1965), according to which cloud droplets in a low-level orographic "feeder cloud" located mainly below the 0°C level are washed out by raindrops falling from a pre-existing "seeder cloud". Many observational investigations and numerical simulations have since been carried out, but direct evidence supporting the conceptual model has not yet been presented. The problem is that a raindrop which has fallen on the ground can not be separated into cloud droplets and a raindrop. If orographic snowfall is formed by the same mechanism, a rimed snowflake could be separated into cloud droplets and snow crystals.

Harimaya and Sato (1989) developed a quantitative measuring method to determine the amount of rime in snowflakes as the riming proportion(%). Using this method, Harimaya and Sato (1992) showed that the deposition process did not contribute to strong snowfall intensity, being controlled instead by the riming process over coastal areas. Later, Harimaya and Kanemura (1995) showed that the riming process

plays an important role in the growth of snow particles in coastal areas, but not in inland areas. This difference was explained by differences in meteorological conditions. Mosimann et al. (1994) then proposed methods similar to that of Harimaya and Sato (1989).

The contribution of feeder clouds in orographic snowfall formation can be shown by the above method, and observations were carried out using radar and a microwave radiometer to clarify the microphysical process of orographic snowfall. The observational results are presented here.

2. OBSERVATIONS

The mountains selected for observation are located in the center of the main island of Japan and intersect at right angles against the direction of northwesterly winter monsoons. Observation was carried out at the Sagurigawa-dam in the mountain side of the mountains. The observation site is located about 50km from the coastline in the direction of the prevailing winter monsoon wind, as can be seen in Fig.1. The observation variables were snowfall intensity measured over one minute, riming proportion every ten minutes, liquid water path by the microwave radiometer, and general meteorological conditions such as temperature and wind speed. The structure of snow clouds over the area were observed by the radars of the Japan Meteorological Agency and the Ministry of Construction. Riming proportion, which is the important variable in this study, is

the ratio of rime to total mass, and was measured by the method of Harimaya and Sato (1989).

3. RESULTS

3.1 Radar analyses

Cumulus clouds or cumulus clusters which form over the Japan Sea generally move from the Japan Sea toward land, parallel to the wind direction, during a northwesterly winter monsoon. They bring snowfall to coastal areas and then finish their whole life, whereas long-lived snow clouds move further inland where they dissipate gradually. The behavior of snow clouds is explained next.

Figure 2 shows the time change in the vertical section of radar echoes and the vertical section of the topography from north-northwest to south-southeast through the Sagurigawa-dam. In this figure, snow clouds move from left to right. The radar echo cluster seen in the left part at 1745 JST moved in a south-southeasterly direction at the same speed as the wind, and gradually dissipated until 1750 JST. However, when the cluster reached the side of the mountains, it developed again as seen in the vertical section at 1755 JST. The cluster then moved the leeward, and continued to develop. It appeared to have stopped moving. As the mountains intersect at right angles against the northwesterly direction, topographic updraft gliding on the slope occurs on the side of the mountains during a winter monsoon. As a result, dissipating snow clouds develop again. Near the top of the mountains, snow clouds are forming always by the topographic updraft, causing heavy snowfall in the orographic areas.

3.2 Microphysical analyses

Next, we investigated how snow particles are formed through the microphysical process. The

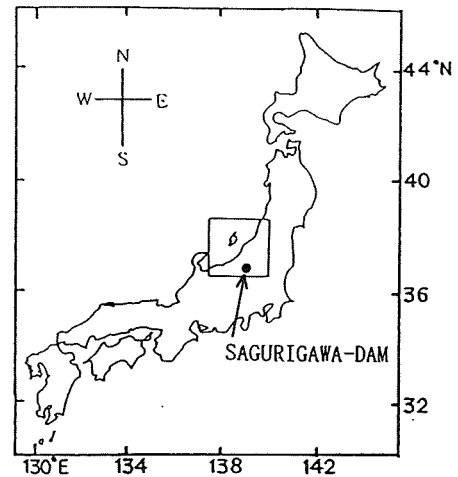


Fig.1 Map showing the observation area.

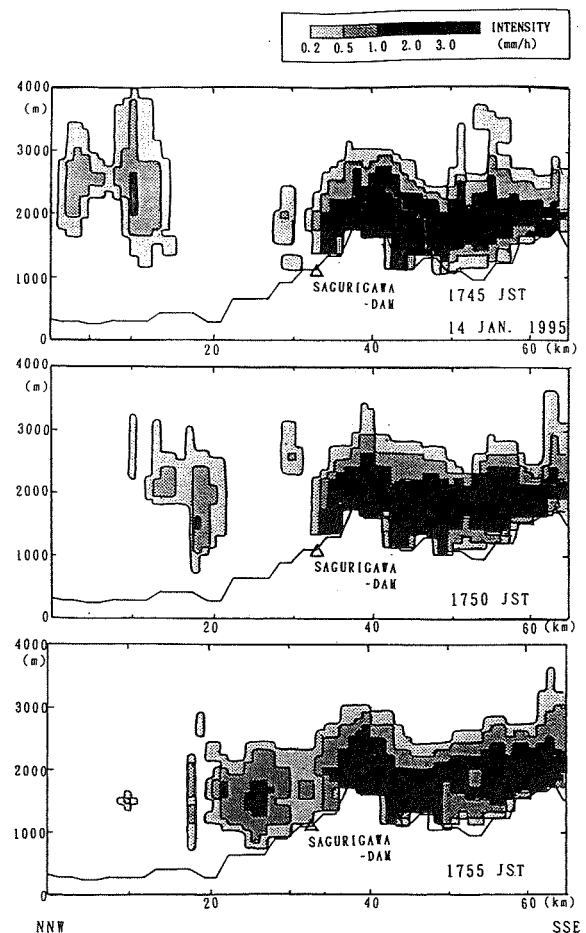


Fig.2 Time change in the vertical section of radar echoes.

relationship between snowfall intensity and the riming proportion, which represents the contribution of the riming growth process, is shown in Fig.3 in order to study what kinds of processes contribute to the growth of snow particles. The lower limit of the riming proportion tends to increase and the blank space without solid points tends to expand with an increase in snowfall intensity. Therefore, stronger snowfall does not occur when there is a low riming proportion, i.e., no contribution of the riming growth process. Snow particles with a rime mass of over 50% of the total mass increased such as 30, 50, 55, 69, 67 and 77% as the snowfall intensity increased. This shows that the riming growth process is important in the formation of orographic snowfall.

The riming proportion is determined by the ratio between the amount of ice crystals and the amount of rime. Figure 4 shows how the ratio of rime amount to snowfall intensity is determined with a constant ratio of ice crystal amount. Solid points and open points indicate cases under conditions of strong wind and weak wind, respectively. The upper limits of the solid points and open points are indicated by a solid line and broken line, respectively. The riming proportion was higher in the case of a strong wind under the condition of a constant ice crystal amount. This means that the cloud droplet amount in a snow cloud is higher in the case of a strong wind. The cloud droplet amount is determined as the sum of pre-existing cloud droplets in snow clouds and newly formed cloud droplets in the orographic areas. It is thought that in the case of stronger wind, many snow clouds in the developing stage reach the orographic areas and newly formed cloud droplets in the orographic areas increase due to topographic updraft. This can explain the observations described above.

Next, we study how much the pure increase in the cloud droplet amount contributes to the riming proportion of snowfall on the ground in the case of snow clouds which have developed

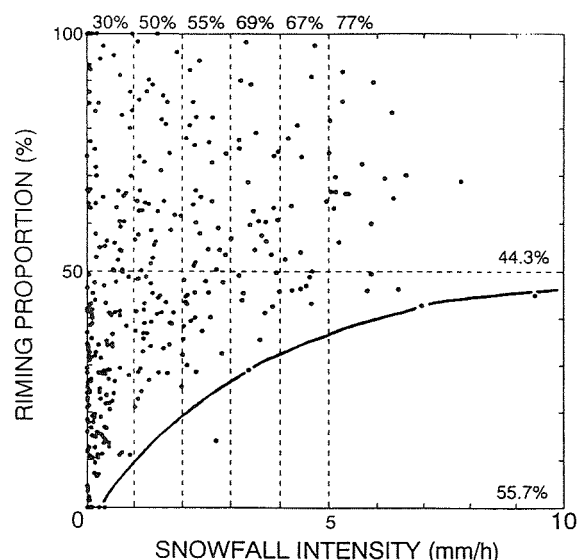


Fig.3 Relationship between snow intensity and riming proportion.

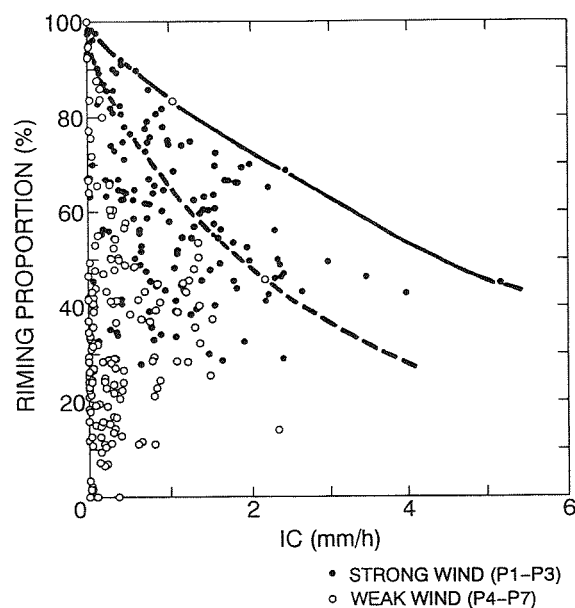


Fig.4 Relationship between ice crystal amount and riming proportion.

again and formed by topographic updraft. The results are shown in Fig.5, in which the abscissa corresponds to the wind speed on the ground and the ordinate to the riming proportion. In this figure, the lower limit of the riming proportion tends to increase, i.e., the blank space without solid points tends to expand as the wind speed

increases. It is thought that the lower indicates the extent to which cloud droplets newly formed by the topographic updraft contribute to the riming proportion. There are two reasons why the riming proportion varies widely according to wind speed. One reason is due to the amount of pre-existing cloud droplets in the snow cloud, and the other reason is due to the case where the ice crystal amount is relatively less than the cloud droplet amount. Figures 4 and 5 show that the topographic updraft increases and cloud droplets are formed proportionately as the wind speed increases. The ice crystals can wash out a lot of cloud droplets by falling in cloud droplets increased. As a result, the snowfall changes to that with a high riming proportion and to that with a high intensity.

4. CONCLUSIONS

Heavy snowfall occurs every year in orographic areas near the Japan Sea, Japan. The formation mechanism was studied by radar and microphysical analyses. The snow clouds which form over the Japan Sea move from the sea toward the land, parallel to the wind direction. The snow clouds change from the developing to mature stage, and then to the dissipating stage as they move inland. If the clouds reach an orographic areas, they develop again due to topographic updraft. From the microphysical viewpoint, many supercooled cloud droplets are newly formed when the snow cloud develops again. The ice crystals can wash out many cloud droplets by falling in cloud droplets increased. As a result, the snowfall changes to that with a high riming proportion and to that with a high intensity. Therefore, the riming growth process contributes significantly to the formation of orographic snowfall. As the topographic updraft causes snow clouds to develop again, this effect is considered to be greater as the wind speed increases. This was shown by observational results. If a snow cloud in the developing stage reaches an orographic area and many cloud

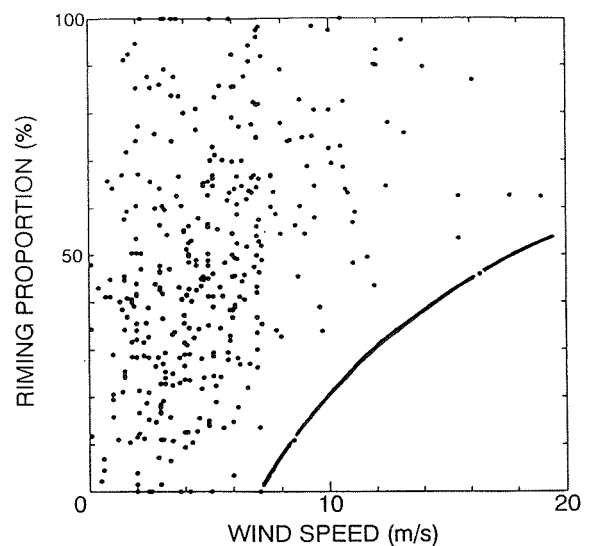


Fig.5 Relationship between wind speed and riming proportion.

droplets are formed by the topographic updraft under the condition of a strong wind, observations showed that this case has highest potential for artificial seeding experiments.

5. REFERENCES

- Bergeron, T., 1965 : On the low-level redistribution of atmospheric water caused by orography. *Suppl. Proc. Int. Conf. Cloud Phys.*, Tokyo, May 1965, 96–100.
- Harimaya, T. and N. Kanemura, 1995 : Comparison of the riming growth of snow particles between coastal and inland areas. *J. Meteor. Soc. Japan*, **73**, 25–36.
- Harimaya, T. and M. Sato, 1989 : Measurement of the riming amount on snowflakes. *J. Fac. Sci., Hokkaido Univ., Ser.VII (Geophysics)*, **8**, 355–366.
- Harimaya, T. and M. Sato, 1992 : The riming proportion in snow particles falling on coastal areas. *J. Meteor. Soc. Japan*, **70**, 57–65.
- Mosimann, L., E. Weingartner and A. Waldvogel, 1994 : An analysis of accreted drop sizes and mass on rimed snow crystals. *J. Atmos. Sci.*, **51**, 1548–1558.

SELF-ORGANIZATION EFFECTS IN A MODEL WITH PARAMETERIZED CLOUD MICROPHYSICS

Ulrike Wacker

Institut für Meteorologie und Geophysik der Universität Frankfurt a.M.
60054 Frankfurt a.M., Germany

1. INTRODUCTION

Coagulation of condensate particles is an important cloud physical process. Its course as well as its effect on the content of cloud water, rain, graupel etc. are influenced by the attributes of the particles involved. In this study, we investigate coagulation processes among cloud droplets and precipitation particles of different kinds. The ensembles of the precipitation particle types influence each other e.g. by consuming the supply of cloud water common to all during coagulation with cloud drops. Such a competitive situation is comparable with the one well known in population dynamics, where several predatory species rival for the same prey.

The objective of this basic study is to investigate the dynamic structure and the long-term evolution patterns of the cloud system. As a cloud volume interacts with its environment and as coagulation processes are mathematically represented by nonlinear relationships, a cloud system constitutes an open nonlinear system in the sense of the theory of self-organization (outlined e.g. by Nicolis and Prigogine (1977), Ebeling et al. (1990)), and this theory provides the methods to study qualitatively the dynamics also of the cloud system. To this end, number and type of attractors and bifurcation points will be determined in dependency on the parameters, which control internal cloud physical interactions and exchanges with the environment. Starting point is a conceptual model of the relevant cloud physical processes with few degrees of freedom, which is compatible with commonly used descriptions of cloud physical processes. For further information see Wacker (1995).

2. MODEL DESCRIPTION

The qualitative analysis of the cloud physical system is carried out for a horizontally homogenous cloud layer. The system contains cloud droplets (index c) and precipitation particles of several kinds of habit types ('species'; index k with $k = 1, \dots, N$), e.g. rain drops, graupel or snow. The cloud microphysical processes accretion, riming, and sedimentation are parameterized using a scheme of the Kessler

(1969) type. Prognostic variables are the mass mixing ratios of cloud water C and of the N species of precipitation particles P_k for $k = 1, \dots, N$. These variables satisfy the following evolution equations:

$$\begin{aligned} \frac{dC}{dt} &= \Phi_c - \sum_{k=1}^N b_k C P_k^{\beta_k} \\ \frac{dP_k}{dt} &= \Phi_k + b_k C P_k^{\beta_k} - d_k P_k^{\delta_k} + B_k \end{aligned} \quad \begin{array}{ccc} I & II & III \end{array} \quad (1)$$

The terms on the right hand side stand for I: external source rates, II: accretion/riming rate, which is an *autocatalytic nonlinear* transformation rate, III: divergence of sedimentation flux, discretized for a cloud layer. The external source rates Φ_c and Φ_k stand for all processes that are not considered in the other terms; in the following, the source B_k caused by the sedimentation flux entering the layer from above, will be included in Φ_k . $\Phi_c = \text{const.} > 0$ and $\Phi_k = \text{const.} \geq 0$ are assumed. To calculate b_k , d_k , β_k , δ_k , relationships between fall speeds, particle masses and maximum diameters as given by Locatelli and Hobbs (1974) for ice particles and by Kessler (1969) for rain drops have been used. Details of the derivation of Eqs.(1) are given in Wacker (1992).

The coefficients b_k , d_k and exponents β_k , δ_k depend on the type of precipitation particles and are assumed constant during the evolution. Via b_k , d_k , β_k , δ_k any chosen type of particle species accordingly plays the same rôle for the dynamic structure as other system parameters, and the whole of Φ_c , Φ_k , b_k , d_k , β_k , δ_k constitute the set of control parameters.

3. CASE STUDY: FLAT PRECIPITATION PARTICLES

In a first case study we consider a model system with four categories of condensate particles, namely cloud droplets and 3 species of flat precipitation ice particles with $\beta_k > \delta_k$ for $k = 1, 2, 3$ (Table 1). We assume $\Phi_k = \Phi_K$ for all k , however, the principle findings hold also for different Φ_k -values.

For these model conditions the number of steady states varies between 1 and 7, depending on the ex-

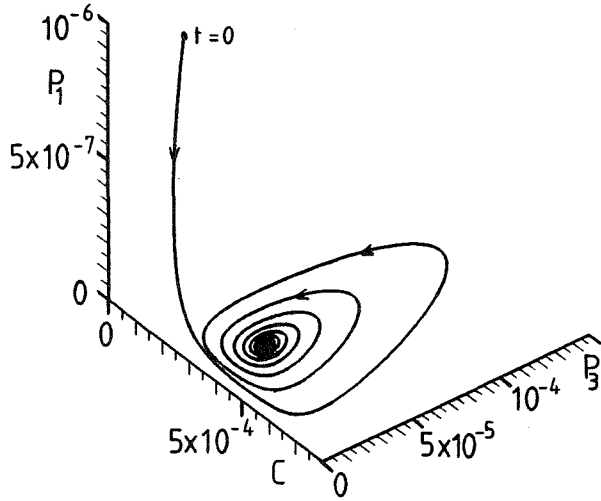


Figure 1: Trajectory in phase subspace spanned by mass mixing ratios of cloud water (C) and precipitation species 1 (P_1) and 3 (P_3). Source rates: $\Phi_c = 3.5 \times 10^{-7} \text{ s}^{-1}$, $\Phi_K = 2 \times 10^{-10} \text{ s}^{-1}$. Initial conditions: $C(t=0) = 1.5 \times 10^{-4}$, $P_1(t=0) = 10^{-6}$, $P_2(t=0) = 10^{-7}$, $P_3(t=0) = 2 \times 10^{-5}$.

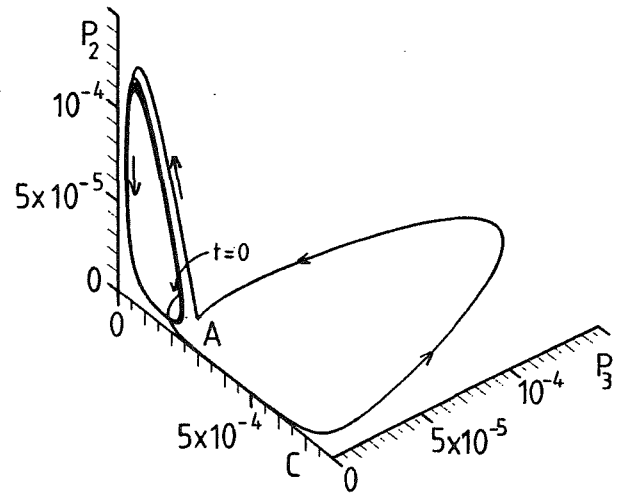


Figure 2: Trajectory in phase subspace spanned by mass mixing ratios of cloud water (C) and precipitation species 2 (P_2) and 3 (P_3). Model conditions as in Fig.1 except $C(t=0) = 10^{-4}$.

ternal source rates. Figs. 1 and 2 show evolution patterns by means of the trajectory in the 3d subspace of the 4d phase space. For the selected external source rates 7 steady states exist; one of them is stable, all other are unstable in view of small disturbances. Nevertheless, the long-term behaviour is not uniquely determined by the parameters. Although the initial conditions for Figs. 1 and 2 deviate only slightly in the C -values, the evolution is completely different with respect to the prevailing species as well as to the temporal structure.

Species 3 dominates in the long-term under the initial conditions used for Fig.1, while this holds for species 2 for Fig.2. The prevalence of a single species is caused by the competition of precipitation species

for cloud water. The dominant species is provided by the best combination of a favourable gain – (riming) to – loss (sedimentation) ratio on the one hand and suitable initial conditions on the other hand. Though the concentrations of the other species are low in the long-term, they do not vanish completely at $\Phi_K > 0$, and in case of a parameter variation – whatever the cause – they may gain higher concentrations again.

In Fig.1 the trajectory oscillates around the steady state with a period of approximately 30min and ends up in the point attractor. In Fig.2, the trajectory first performs an extensive excursion in phase space. In this initial phase the evolution is determined by species 3, however this part passes over to species 2 as soon as its concentration exceeds a certain threshold (point A in Fig.2 at $t \approx 2500\text{s}$). Later on the trajectory runs into a closed loop (limit cycle), which represents the periodic attractor of the system. Amplitude and period ($\approx 20\text{min}$, a reasonable time scale in cloud physics) depend only on the prescribed control parameters.

In both cases the model dynamics gives rise to oscillations, which can be interpreted as showers. They are caused by the nonlinear interactions between cloud drops and precipitation particles by coagulation. A maximum in precipitation content is always preceded by a maximum in cloud water content. Similar temporal patterns have been observed by e.g. Rauber et al. (1986). The shower character either ceases (Fig.1) or holds on without damping (Fig.2). Note that for other external source rates, the concentrations may reach their final values without periodic oscillations.

Table 1: Types of precipitation particles used in the case studies in Sections 3 and 4.

k	β_k	δ_k	type
1	1.406	1.085	Aggregates of unrimed radiating assemblages of dendrites or dendrites
2	1.426	1.105	Aggregates of unrimed side planes
3, i	1.146	1.107	Aggregates of densely rimed radiating assemblages of dendrites or dendrites
r	0.875	1.125	rain drops

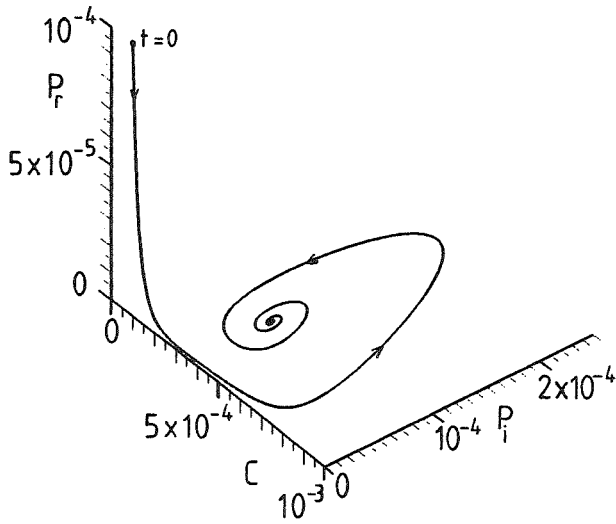


Figure 3: Trajectory in phase space spanned by mass mixing ratios of cloud water C , rain water P_r and ice particles P_i . Source rates: $\Phi_c = 10^{-6} \text{s}^{-1}$, $\Phi_K = 10^{-8} \text{s}^{-1}$. Initial conditions: $C(t=0) = 10^{-4}$, $P_r(t=0) = 10^{-4}$, $P_i(t=0) = 0$.

4. CASE STUDY: RAIN DROPS AND RIMED ICE PARTICLES

In this section the competitive situation is investigated for a common combination of precipitation particles in clouds, rain drops (index $k = r$) and rimed ice particles (index $k = i$). A type of flat ice particles is chosen with $\beta_i > \delta_i$, while for rain drops $\beta_r < \delta_r$ holds (see Table 1). Again, equal external source rates $\Phi_k = \Phi_K$ for $k = i, r$ are assumed. For this model system, multiple steady states are possible only in case of $\Phi_K = 0$; for $\Phi_K > 0$ rain drops and ice particles always coexist. Depending on the chosen external source rates, the long-term behaviour is characterized by a point or periodic attractor.

The evolution pattern is shown in Fig.3 for a special case. Despite equal external source rates and an ice-free initial state, the ice particle species dominates in the long-term; rain water concentration falls below 10^{-6} already after 200s and is unimportant thereafter. The trajectory spirals around the steady state with a period of approximately 1000s and approaches the point attractor.

The result of the dominance of the ice particles is in agreement with observations that show hardly any precipitation sized drops in supercooled mixed-phase clouds (see e.g. Rauber et al., 1986).

5. DISCUSSION

The qualitative analysis elucidates the decisive impact of the habits of the precipitation species on the dynamical structure of the model system. The main results are summarized as follows (see also Wacker, 1992, 1995). If the particles of all species have an

(approximately) spherical shape with $\beta < \delta$, such as rain drops or graupel, then the evolution ends up in a unique point attractor with all species present. Such a system is always structurally stable.

If on the other hand, one or more species of flat particles with $\beta_k > \delta_k$ are present, the dynamics may become structurally unstable in two ways: (i) The number of steady states of Eqs.(1) changes depending on the parameter values via a so-called tangent-bifurcation. (ii) A stable steady state may become unstable via a so-called Hopf-bifurcation; beyond the critical parameter value a self-excited oscillation (limit cycle) emerges around the unstable steady state. A slight change of a parameter near its critical value causes a qualitative change in the long-term evolution. The crucial process is the autocatalytic nonlinear transformation accretion/riming of precipitation particles with cloud drops.

The oscillation is not caused by an external effect ($\Phi_c, \Phi_k = \text{const.}$), but this temporal structure is formed spontaneously by cooperation of the system elements by way of nonlinear interactions in an open system far from equilibrium. Thus the periodic attractor in form of a limit cycle is an example for self-organization in time.

More than one of the steady states can be coupled with an attractor for the same parameter values (multistability). Each stable steady state defines a point attractor, and some of the unstable steady states can be connected with a periodic attractor. In case of multistability, the long-term evolution is also sensitive to the initial conditions. Types of long-term behaviour show up, which are qualitatively different with respect to the prevalence and suppression of precipitation species in the competitive situation (see Figs. 1 and 2). The selected precipitation species is distinguished by making the best use of the available cloud water in the presence of a concentration-dependent sink in combination with an initial advantage. Different initial conditions may be interpreted as natural fluctuations. Accordingly, fluctuations can drive the system into the attracting basin of a different attractor and cause a change in the predominant precipitation particle type. As such a system is unstable with respect to the occurrence of a species with suitable parameters and initial conditions, it is capable of self-organization.

For vanishing external sources $\Phi_k = 0$, the competition between the precipitation particles by coagulation gives rise to a selection mechanism for species with $\beta_k \geq \delta_k$. The attractor is characterized by the presence of only a single species i , and for $\beta_k \geq \delta_k$, it depends on the initial conditions, which one is left. In the limiting case $\beta_k = \delta_k = \beta = \delta$ for all k , the steady state is stable, if species i is distinguished by the maximum selection value, i.e. $b_i/d_i > b_k/d_k$ for all $k \neq i$. This finding conforms with the famous

predator-prey model in population dynamics with $\beta = \delta = 1$ ('survival of the fittest'). As the system is unstable with respect to the occurrence of a new species $N + 1$ with $b_{N+1}/d_{N+1} > b_i/d_i$, this system is capable of self-organization as well. For $\Phi_k > 0$, no species can of course vanish completely from the system; its concentration, however, may be kept low.

In all cases considered, the (dissipative) self-organization effects demand interactions of the open system with its environment, here in form of an external forcing by mass supply Φ_c, Φ_k .

As to comparison between the model results and observations, both the similarities and differences must be carefully interpreted in the context of the simplified conceptual model. A proof cannot be given, that a special mechanism evolving from the model, is responsible for an observed effect. However, the main dynamic evolution patterns, as dominance of ice particles and suppression of rain in precipitation from a mixed phase cloud or oscillations in the condensate concentrations, are also found in observations; yet it remains open, whether the physical origins of the similarities are the same.

These studies give an example of a structurally unstable system in cloud physics and make clear the decisive rôle of the particle types for the dynamic structure. As any parameterization of microphysical processes requires the assignment of particle types, these studies also elucidate the influence of parameterization assumptions on the long-term behaviour of the nonlinear system 'cloud'.

6. REFERENCES

- Ebeling, W., A. Engel, and R. Feistel, 1990: *Physik der Evolutionsprozesse*. Akademie-Verlag Berlin, 371pp.
- Kessler, E., 1969: *On the Distribution and Continuity of Water Substance in Atmospheric Circulations*. Meteorol.Monogr., No.32, Amer.Meteor.Soc., 94pp.
- Locatelli, J.D. and P.V. Hobbs, 1974: Fall speed and masses of solid precipitation particles. *J.Geophys.Res.* 79, 2185-2197.
- Nicolis, G. and I. Prigogine, 1977: *Self-Organization in Non-Equilibrium Systems*. J.Wiley & Sons, 491pp.
- Rauber, R.M., L.O. Grant, D. Feng, and J.B. Snider, 1986: The characteristics and distribution of cloud water over the mountains of northern Colorado during wintertime storms. *J.Climate Appl.Meteorol.*, 25, 469-488.
- Wacker, U., 1992: Structural stability in cloud physics using parametrized microphysics. *Beitr.Phys.Atmosph.*, 65, 231-242.
- Wacker, U., 1995: Competition of precipitation particles in a model with parameterized cloud microphysics. *J.Atmos.Sci.*, 52, 2577-2589.

SOME NUMERICAL RESULTS OF FORMATION OF HAIL CLOUD MICROSTRUCTURE

B.A. Ashabokov, L.M. Fedchenko, A.V. Shapovalov

High – Mountain Geophysical Institute, Nalchik, Lenin 2, 360030, RUSSIA

1. INTRODUCTION

The interactions of the different type processes play the main role in the formation of the microstructural characteristics of the convective clouds. They have very complicated nonlinear nature, so their detailed investigation is very difficult problem.

The interaction between the dynamical and thermodynamical processes is the most studied one. It represents itself in deformation of the fields of thermodynamical parameters under the effect of vertical airflows.

It's worth to note that though the interaction nature of pointed processes between each other is known, the interaction role in the formation of the hail cloud microstructure is not studied enough. Some results of the numerical simulation of the formation and growth of hail particles in clouds of different types and the role of deformation of thermodynamical – parameter fields as a result of the interaction with vertical airflows are given in this paper.

2. CALCULATIONAL RESULTS

The two – dimensional model of micro – physical processes in hail clouds on the background of specified thermohydrodynamics was used in our study. It was described in detail in Ashabokov, et al. (1994). We want only to note that the coordination between dynamical and microphysical characteristics of cloud was established by the sources of drops and crystals. The empirical models of the airflow structures in clouds of different types and measurement data were used for construction of the airflow dynamics. The two types of hail clouds were considered: symmetric and asymmetric.

In the case of asymmetric clouds in the front and central parts there is the wide region of updrafts with maximum velocity of 35 m/s and in the low half of rear part of cloud there is the downdraft. Such structure of airflows agrees with the vertical section of the severe hail cloud along the movement direction on

the stage of quasi – stationary state (Browning, Foote, 1975).

During the temperature field construction it was taken into account that due to the heat transfer by vertical airflows and heat release during the phase transition of water the field undergoes the deformation in vertical plane in relation to the temperature field in the ambient atmosphere (Mazin, Shmeter, 1983, Shmeter, 1987).

The maximum deviation of temperature in the cloud from its value out of cloud at the same level was assumed to be equal to 13 – 14 °C. In the rear part of the cloud, where the downdrafts occurred the magnitude ΔT is negative and maximum $|\Delta T|$ equals to 4 – 5 °C.

During the calculations the regions of the crystal localization were traced from the formation moment up to the fallout of the hailstones from the cloud.

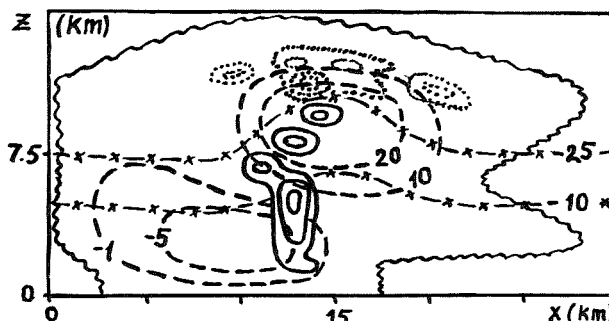


Fig.1 Isolines of parameters of asymmetric cloud at 18th min.

- isolines of concentration of large hailstones ($d \geq 1$ cm);
- isolines of concentration of crystals with $d = 2 - 5$ mm;
- - - - - isolines of velocity of vertical flows;
- *-*-*-*-* isolines of temperature.

Fig. 1 shows the isolines limiting the zones of crystal localization with sizes of $r = 2 - 5$ mm and $r > 1$ cm at the time of $t = 18$ min. According to the calculation the appearance of hail particles occurred first in the local region placed in the upper part of the zone with the maximum values of updraft velocity in the

temperature interval of $-10...-30^{\circ}\text{C}$. The generated hailstones, due to the interaction with airflows, drift into the region with lower values of updraft velocities to the boundary with downdrafts at the same temperature interval. Meanwhile the sizes and concentrations of hailstones increased.

So some part of hail embryos has the opportunity to stay long enough in the zone favourable for growth ($-10...-30^{\circ}\text{C}$). The finite sizes of hailstones will depend on the formation place of embryos in this zone and time of their existence in it. The formation of different layers on hailstones can be explained by the change of growth regime during the movement in pointed temperature interval but not by the multiple ascent and descent in the updraft as it is considered in some other hypotheses of hail formation.

The achieved results are in good agreement with experimental data of different authors (Bailey et al., 1969; Jouzel et al., 1975; Khorguani, 1984). Besides, the calculations show that the time from the formation moment of large hailstones up to the moment of their fallout is of the order of 6–8 min. That also agrees with the observational data.

The achieved results indicate that the cloud separation in vertical or horizontal section into different zones as in some papers (Abshaev, 1982) is very conventional and does not reflect the real picture.

The picture of formation and growth of hailstone in symmetrical clouds is differ from asymmetrical one. To study this problem the field of velocity and temperature of airflows were constructed taking into account their interactions. The maximum value of updraft velocity was $20\text{ m}\cdot\text{s}^{-1}$ and the temperature deviation in the cloud from the value in the ambient atmosphere was 10°C .

Such picture of dynamical and thermodynamical characteristics corresponds to the maximum development of the symmetrical clouds (before fallout of precipitation). We want to note that in the calculations in the case of symmetrical clouds on the base of the used model we faced to a problem. It consists in the nonstationary state of cloud parameters. This feature limits the duration of the simulating interval of time of cloud evolution but with a certain degree of assumption. The qualitative picture of the formation and growth of hailstones can be achieved in this case.

Fig.2 gives the isolines of the concentration of crystals and hailstones with $d=2-5\text{ mm}$ and $d \geq 1\text{ cm}$, respectively, as well as the isolines of velocity of vertical airflows at 18 min.

The hail particles form firstly in the upper

part of the region of the maximum values of vertical flow velocities in the temperature interval of $-10...-30^{\circ}\text{C}$. Then at the same temperature interval they drift to the edges of this region.

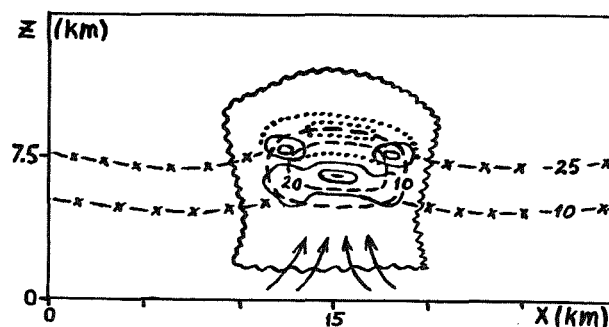


Fig.2. Isolines of parameters of symmetric cloud at 18th min. The symbols are as in Fig.1.

3. CONCLUSIONS

The results of this work confirm the important role of the interaction of dynamical and thermodynamical processes in the formation of the hail cloud microstructure. It is shown that in the result of this interaction in the cloud the wide zone, in which the movement and growth of hail particles are observed, generates.

REFERENCES

- Abshaev M.T., 1982: Structure and development dynamics of hail and thunderstorms on North Caucasus, Proc. VGI, 53 (in Russian).
- Ashabokov B.A., Fedchenko L.M., Shapovalov A.V., Shoranov R.A., 1994: Numerical simulation of formation and growth of hail at natural development of cloud and seeding. Meteorology & Hydrology, 1, 41–48 (in Russian).
- Bailey J.H., Helstone J.R., Maklin W.G., Steward J.R., 1969: On the isotopic composition of hailstones. J. Atm. Sci., 26, 4.
- Browning K.A., Foote G.B., 1975: Airflow and hail growth in supercell storms and some implications for hail suppression. Nat. Hail Exper., 75/1.
- Jouzel I., Merlivat L., Roth E., 1975: Isotopic study of hail. J. Geophys. Res., 80, 36.
- Khorguani V.G. 1984: Microphysics of generation and growth of hail. M., Gidrometeoizdat. (in Russian).
- Mazin I.P., Shmeter S.I., 1983: Clouds: structure and physics of formation. L. Gidrometeoizdat.
- Shmeter S.I., 1987: Thermodynamics and physics of convective clouds. L., Gidrometeoizdat.

ON TEMPERATURE AND MECHANISM OF HAIL EMBRYO FORMATION

V.G. Khorguani¹, Z.V. Khvedelidze²

¹Geophysics Institute, M.Alexidze, 1, Tbilisi, GEORGIA, 380093

²Tbilisi State University, Chavchavadze, 3, Tbilisi, GEORGIA, 380028

The scientific researches showed that the generation of the hail particles occurs heterogeneously on the active particles of ice formation (Tlisov, Berezinski, 1984; Khorguani, 1984). The ice-forming nuclei of different sizes and different physical properties can represent themselves and lead to the formation of hail embryos in different ways. The ice-forming activity of the atmospheric aerosols depends on the supercooling, supersaturation and the dimensions of the aerosol particles (Khorguani, 1990).

$$\frac{N_i}{N} = K \Delta S d^\alpha e^{\beta \Delta T} \quad (1)$$

where N_i and N are the numbers of ice embryos and aerosol particles, ΔS is ice supersaturation, d is the diameter of the particle, ΔT is the supercooling and the coefficients $K=1.1 \text{ cm}^{-\alpha}$, $\alpha=1.5$, $\beta=0.4 \text{ grad}^{-1}$. At the relatively high temperature ($-6...-10^\circ\text{C}$) the ice-forming embryos mainly are the gigantic and the super gigantic particles but at -20°C all the particles of the atmospheric aerosol with size of $100 \mu\text{m}$ are the ice-forming ones. For clearing up the role of the ice-forming embryos in the hail formation first of all the coefficients of the hailstones with ice-forming embryos must be compared. The Fig.1 shows the concentrations of the hailstones as a function of their mean cubic diameter, $N=AD^{-\alpha}$, achieved by the ground measurements (Khorguani, 1984) (curve 2) and the concentrations of the ice embryos as a function of the temperature (curve 1).

The comparison of curves shows that the concentration of the ice embryos in atmosphere is by a factor of 10^2 larger than the concentration of the hailstones. Their concentration are comparable only at the temperatures above -10°C .

It is difficult to carry out the direct measurements of the microphysical characteristics of hail clouds, so the important in-

formation may be received from the analysis of hailstone embryos.

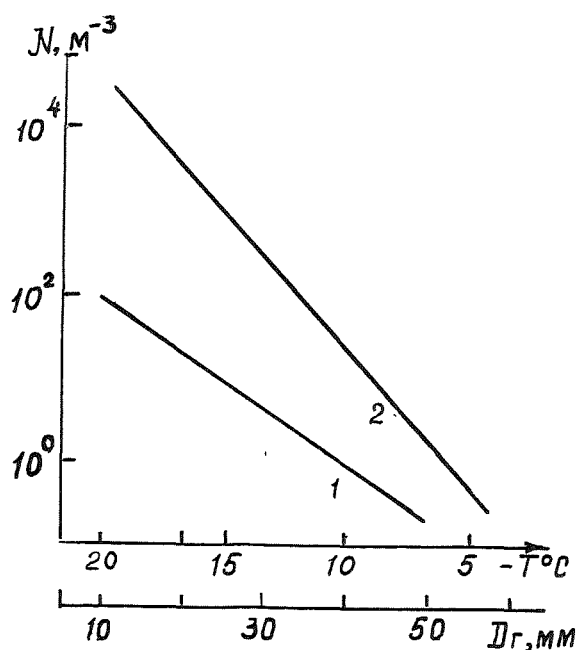


Fig.1. Concentration of ice-forming embryos in atmosphere (1) and the concentration of hailstones in clouds (2) as a function of temperature and mean-cubic diameter of hailstones.

The research of the aerosol structure of hail embryos, large drops and grauples, which were well identified, was made. Their sizes changed from 3 to 7 mm. The embryo was cut out from the hailstone, placed on the special substrate in the cold chamber and evaporated overpassing the liquid phase. Then the sample of the aerosol deposition of embryo was developed in the thermo-diffusional cold chamber "Grad-3" at the water saturation (Khorguani, 1984). The development of the samples began at -1°C , then repeated after every degree: -2°C , -3°C and so on until the first crystal appeared. After the appearance of the first crystal, the development of the sample stopped,

Appearance temperature of first crystal and size of aerosol particles—ice nuclei (IN) in embryos of hailstones of different types.

Table

Hailstone diameter D_h , mm		Embryo diameter d_e , mm		Appearance temperature of first crystal $-T$, °C		Size of IN particles d , μm	
Droplet embryo	Grauple embryo	Drop	Grauple	Droplet embryo	Grauple embryo	Droplet embryo	Grauple embryo
23	18	5	5	4	10	60	50
15	16	6	4	3	11	70	35
18	28	4	7	7	12	65	40
14	30	5	8	10	15	45	25
21	16	7	3	2	13	50	20
26	18	5	4	2	12	110	45
11	24	3	6	8	8	80	20
28	28	4	5	6	10	35	25
24	14	5	4	7	7	45	30
16	18	4	6	4	9	55	40
$\bar{D}_h = 19.6$	21.0	$\bar{d}_e = 4.8$	$\bar{d}_e = 5.2$	$\bar{T} = -5.3$	$\bar{T} = -10.7$	$\bar{d} = 61$	$\bar{d} = 33$

crystal evaporated and the size of the aerosol particle was determined, i.e. the size of the ice-forming embryo, on which the crystal arised, was determined. The Table contains the temperature of the first crystal appearance and the size of the aerosol particle of the ice-forming embryo on which the crystal for the grauple and droplet embryo was formed. It is clear that all the droplets were formed in the temperature interval from -2°C to -10°C on the supergiant particles. Meanwhile the average temperature was $T = -5.3^\circ\text{C}$ and the average size of the embryo was $d = 61\ \mu\text{m}$. The layer in the cloud of about 1.6 km corresponds to the abovementioned temperature interval. The possible mechanisms of the droplet embryo generation are either the immersional freezing or the collision of the large drop with the ice crystal, formed on the supergiant embryo.

The time of the collision of crystal with the supercooled large droplet in the gravitational field can be determined from

$$t = \frac{1}{ESVN} \quad (2)$$

where E is the coefficient of the collection, S , V are the effective section and the velocity of the falling drop, respectively, N is the crystal concentration, $S = \pi D^2/4$, $V = (4\rho g D/3\rho_a C_x)^{1/2}$, where D is the diameter of the supercooled droplet, ρ , ρ_a is the density of the droplet and air, C_x is the coefficient of motion drag, g is the acceleration of gravity.

If we take into account that $E \approx 1$, $\rho = 1\text{g}\cdot\text{cm}^{-3}$, $\rho_a = 1.2\cdot 10^{-3}\text{g}\cdot\text{cm}^{-3}$, $C_x = 0.42$, $g = 980\text{cm}\cdot\text{s}^{-2}$ from (2) it will turn out that:

$$t = \frac{1}{1.3 \cdot 10^3 D^{5/2} N} \quad (3)$$

In the temperature interval of $-2 \dots -10^\circ\text{C}$ the concentration of the ice-forming aerosols equals to $N \approx 10^{-1} \dots 10\text{m}^{-3}$. Then for the droplet with $D = 4\text{mm}$ from (3) we'll get that the quantity t changes from $7.7 \cdot 10^4$ to $7.7 \cdot 10^2\text{s}$. If we take into consideration that the concentration of large drops is so small (Waldvogel, 1987), it is scarcely probable that this mechanism of formation of droplet embryos takes place. Besides it is difficult to assume that the supergiant aerosol particle in hail cloud rises up to the temperature intervals showed in the Table without the coagulation with the cloud droplets or a large embryo drop didn't appear on it. So the droplet embryos of the hailstones are the result of the immersional freezing.

The temperature of the first ice crystal appearance and the size of the aerosol particles of ice-forming nuclei for the grauple embryos are given in the Table as well. The comparison of Table data shows that the temperature of the first crystals for the grauple embryos is lower and the average value is -10.7°C .

The size of the aerosol particle—nuclei is

smaller as well and equals to $d=33\text{ }\mu\text{m}$. The grauple embryos grow on these nuclei as a result of sublimation and coagulation with the supercooled cloud droplets. On the whole the hail formation takes place in the temperature interval from $-2\text{ }^{\circ}\text{C}$ to $-15\text{ }^{\circ}\text{C}$. So, the formation of hail embryos of different kinds is divided in the cloud along the vertical that is in good agreement with the results of the isotopic analysis that was received earlier (Tlisov, Khorguani, 1988).

It is possible that the formation of the different types of embryos is divided in time as well. The special study is to be carried out for this purpose.

REFERENCES

- Khorguani V.G., 1984: Microphysics of hailstone generation and growth. Gidrometeoizdat, Moscow, 184 (in Russian).
- Khorguani V.G., 1990: Ice-forming activity of atmospheric aerosols. *Aerosols, Science, Industry. Proc.3-d Int. Aeros. Conf., Japan, II*, 1016–1019.
- Tlisov M.I., Berezinski N.A., 1984: Spectrum of sizes and ice-forming characteristics of aerosol particles contained in hailstones. *Meteorology, and Hydrology*, 3, 50–55 (in Russian).
- Tlisov M.I., Khorguani V.G., 1988: Microphysical concept of hail formation. *Proc. 10-th Int. Cloud Phys. Conf., Bad Homburg, II*, 554–556.
- Waldvogel A., Klein L., Musil D., Smith P., 1987: Characteristics of radar-identified big drop zones in Swiss hailstorms. *J. Clim. Appl. Met.*, 26, 8, 861–877.

ON THE ROLE OF ARTIFICIAL ICEFORMING REAGENTS AND
RADIOACTIVE INTERMIXTURES IN THE VARIATION OF CONVECTIVE CLOUDS
THUNDERSTORM AND HAIL ACTIVITY

A.G. Amiranashvili,¹ T.G. Gzirishvili,² Z.A. Chumburidze³

¹Geophysics Institute, M.Aleksidze 1, Tbilisi, Georgia

²Main Adm. of Hydrometeorology, D.Agmashenebeli 150, Tbilisi, Georgia

³Tbilisi State University, I.Chavchavadze 1, Tbilisi, Georgia

The problem of artificial regulation of the convective clouds thunderstorm and hail activity has been a subject to scientists' attention over a long period of time. One of the most widespread means of influence on these clouds is seeding them with iceforming reagents. In addition, the success of the influence should significantly depend on a presence of an iceforming nuclei natural background in the atmosphere. One should also take into account that inactive under regular conditions atmospheric aerosol can, for a number of reasons, become active in a sense of iceforming within a cloud [1].

In this aspect a special role can be played by radioactive aerosols of natural and artificial origin. So, in the work [2] it was shown that the freezing temperature of radioactive water droplets is by several degrees higher than of distilled water droplets of the same size. Besides, radioactive aerosols ionize the space around them and getting gathered in clouds are able to change their electric state. This, for example, was noticed by Israelsson et. al. [3] in the summer of 1986 after Chernobyl accident, when in some regions of Sweden together with high radioactive precipitation an increase in the frequency of lightnings was detected. So, radionuclides decay in clouds can initialize electric discharges, which, in turn, will be more intensively ionizing the environment, generating ultraviolet radiation, ozone, nitrogen oxides, etc. As a result of this the

conditions for inactive aerosols modification, cloud droplets chemical content change, condensation nuclei formation are created, which should lead to a rebuilding of the electric state of clouds and their microphysical structure [1,4]. In the end one should expect the phenomena of 'selfseeding' with natural iceforming nuclei of clouds to occur leading to a significant change in their thunderstorm and hail activity.

Taking into account the abovementioned considerations an analysis of the data of multiennial observations over the season variations (April to September) of convective clouds thunderstorm and hail activity in Kakheti region of Eastern Georgia under influence of massive impacts by antihail rockets with allowance to beta - radioactive sedimentations on the territory of Georgia has been carried out. Radioactive background measurements were carried out by Georgian Hydrometeorological Service in 10 various points by means of registering the β - radiation of the radioactive dust, which had been sedimented on boards during the day. The data on thunderstorm and hail processes were acquired by Hydrometeo Service and Antihail Service of Georgia. Analysed were the data of 1967 - 1984, when hail prevention activities were carried out using an invariable method. For Telavi region (a region under influence), Dusheti region was selected as a background for annual thunderstorm duration. The value of the correlation coefficient

between the thunderstorm durations in these two points in the years without influence (1946 - 1960) on hail processes is about + 0.60.

During the investigated period the level of daily radioactive sedimentation for the whole territory of Georgia, from April to September, in various years changed at the average from 1.2 to 15.4 Bq/m². Out of 18 years during 10 seasons average radioactive background R_p was > 3.0 Bq/m².day, whereas in the others less than the mentioned value. It must be noted that the mentioned meanseason variations of R_p are not considerable. For example in the period of nuclear weapon testing the value of R_p in 1963 in Tbilisi was 746 Bq/m².day [5], whereas after Chernobyl accident at the average for Georgia R_p reached 1760 Bq/m².day. Nevertheless the annual thunderstorm duration in Dusheti (a region without influence) is in a direct correlation with the values of R_p (correlation coefficient is +0.45). A comparison of the data on the number of lightning discharges in Dusheti in May - September 1971 - 1973 [6] with the average level of β - radioactive sediments for the same period of time showed that the intensity of lightning discharges increases with a radioactive background increase (Tab. 1).

Table 1

Ratio between thunderstorm activity in Dusheti and average level of β - radioactive sedimentations on the territory of Georgia in May - September 1971 - 1973

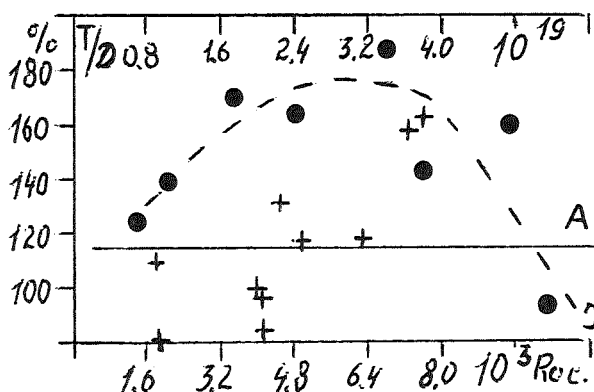
Year	Lightning discharge intensity		R_p Bq/m ² .day
	Dayly average	Minute average	
1971	187	1.16	16.2
1972	129	0.91	10.4
1973	93	0.82	2.1

Thus, the radioactive background (at least in the indicated range of meanseason variations) influences the electric state of clouds. It is shown below how this influence evinces itself in the reaction of convective clouds to carrying into them artificial iceforming nuclei.

Fig.1 and Tab.2 represent the data on the variation of some clouds thunderstorm activity parameters in Telavi and Dusheti at various levels of radioactive sedimentations and scales of impact on them. Thus, according to Fig.1, at meanseason beta - radioactive background levels (3.0 Bq/m².day the impact on clouds in Telavi region led to an increase in the annual duration of thunderstorms, excluding one season, when by means of 10300 rockets the maximum quantity of crystallization nuclei (more than $5 \cdot 10^{19}$) was carried into clouds.

Figure 1

Dependence of ratio of annual thunderstorm durations in Telavi and Dusheti (T/D) on quantity of carried into clouds crystallization nuclei (rockets). '-' - $R_p < 3.0$ Bq/m².day; '+' - $R_p > 3.0$ Bq/m².day; line A - average value of T/D in years without influence (1946 - 1960) $A = (115 \pm 12)\%$



The dependence of the annual duration of thunderstorms on the intensity of the impact is a non - linear one. Carrying into clouds from 1400 to 6800 rockets per season conducted an increase in the thunderstorm duration, more than 6800 rockets per season - a decrease in the thunderstorm duration. On the other hand, at $R_p > 3.0$ Bq/m².day the

Table 2

Characteristics of thunderstorm activity in Telavi and Dusheti.

P_L - number of thunderstorm days per year; T_L - thunderstorm duration per year;
 T_d - thunderstorm day duration; T/D - ratio between mentioned parameters in
 Telavi and Dusheti

Radioactive background $R_p, \text{Bq/m}^2 \cdot \text{day}$	Telavi(T)			Dusheti(D)			ratio T/D (%)		
	P_L	T_L, h	T_d, h	P_L	T_L, h	T_d, h	P_L	T_L	T_d
I. Years with influence (1967-1984)	45	119	2.65	43	95	2.2	105	125	120
including:									
at $R_p < 3.0$ ($\bar{R}_p = 2.0 \pm 0.3$)	47	115	2.45	38	81	2.1	124	142	115
at $R_p > 3.0$									
1. for all years, sign '+' on Fig.1	44	123	2.8	47	107	2.3	94	115	122
2. years below line A, Fig.1, sign '+' ($\bar{R}_p = 11.4 \pm 1.7$)	41	107	2.6	49	113	2.3	84	94	113
3. years above line A, Fig.1, sign '+' ($\bar{R}_p = 5.9 \pm 1.6$)	46	139	3.0	45	101	2.25	102	137	133
II. Years without influence (1946 - 1960)	42	90	2.1	37	78	2.1	115	115	100

dependence of the thunderstorm duration variation on the number of rockets carried into clouds is near to linear (correlation coefficient between the values of T/D and I is $+0.80$). Besides, carrying of additional crystalization nuclei up to the value $2.1 \cdot 10^{19}$ per season (4200 rockets) led to a decrease in the annual thunderstorm duration, while above this value - to an increase in the thunderstorm duration.

In the years with influence (1967-1984) the number of thunderstorm days P in Telavi in comparison to Dusheti decreased to a certain extent on average (Tab.2). However at $R_p < 3.0 \text{ Bq/m}^2 \cdot \text{day}$ an increase in the values of P_L was detected (124% vs 115% in the years without influence), whereas at $R_p > 3.0 \text{ Bq/m}^2 \cdot \text{day}$, on average, a decrease in the number of thunderstorm days in Telavi, in comparison with Dusheti, to 94% was observed. The minimum value of the ratio T/D for P_L takes place at $\bar{R}_p = 11.4 \text{ Bq/m}^2 \cdot \text{day}$ and equals to 84%. The ratio T/D for T_L varies from 94% at $\bar{R}_p = 11.4 \text{ Bq/m}^2 \cdot \text{day}$ to 142% at $\bar{R}_p = 2.0 \text{ Bq/m}^2 \cdot \text{day}$ at the average value, in the years without influence, 115%. Finally, the ratio T/D for T_d varies from 113% at $R_p = 11.4 \text{ Bq/m}^2 \cdot \text{day}$ to 133% at $\bar{R}_p = 5.9 \text{ Bq/m}^2 \cdot \text{day}$ at the

average value, in the years without influence, 100%. Thus, unlike the number of thunderstorm days and annual thunderstorm duration, as a result of the influence, an increase in the average duration of a thunderstorm day was observed for all values of R_p .

Tables 3 and 4 represent the data on some parameters of hail processes in Kakheti at various levels of radioactive background and the ratio between these parameters and R_p . According to these tables, with an increase in R_p a decrease in the number of clouds subject to the influence, a decrease in the expected and actual number of hails and also in the share of the hail - damaged territory by 100%, an increase in the efficiency of the influence on hail processes is detected. The biggest effect of the influence on hail processes was observed in the years with $\bar{R}_p = 11.4 \text{ Bq/m}^2 \cdot \text{day}$ (the years below line A Fig.1). In these years the least values of the parameters $y_1 \dots y_4$ were detected. I.e. a decrease in the thunderstorm activity was accompanied by a decrease in the hail activity of clouds. However, an interesting fact is noteworthy here. The decrease of the hail activity evinces itself in a decrease in the number of hails, whereas the potential

Table 3
Some parameters of hail processes in Kakheti at various levels of
radioactive sedimentations

Radioactive background R_p Bq/m ² .day	Parameters of hail processes on area 10 ⁴ Hectares per year					
	Number of clouds subject to influence	Number of hails		Share of haildamaged territory per 100%	Efficiency of influence on hail clouds (%)	Share of haildamaged territory per 100%, per number of hails (%)
		Expected	Actual			
$R_p < 3.0$	10	2.2	0.3	0.4	81	1.33
$R_p > 3.0$						
1. for all years	8	1.9	0.19	0.32	84	1.68
2. years below line A, Fig.1	6.2	1.6	0.11	0.27	87	2.45
3. years above line A, Fig.1	9.7	2.2	0.27	0.38	80	1.41

Table 4
Correlation coefficients and regression equations between some parameters of hail processes in Kakheti region and mean season radioactive background on territory of Georgia at $R_p > 3.0$ Bq/m².day.

Hail-thunderstorm process parameters (normalized on area 10 ⁴ Hect. per year)	Correlation coefficient	Regression equation
y_1 - number of hail clouds subject to influence	- 0.55	$y_1 = -0.31R_p + 10.6$
y_2 - expected number of hails (radiolocator data)	- 0.61	$y_2 = -0.096R_p + 2.7$
y_3 - actual number of hails	- 0.63	$y_3 = -0.016R_p + 0.33$
y_4 - share of protected territory, hail - damaged per 100%	- 0.51	$y_4 = -0.016R_p + 0.46$

of clouds to damage the protected territory increases by 100%.

REFERENCES

1. Amiranashvili A.G., Gzirishvili T.G. Aerosoli i ledianie kristalli v atmosphere, "Metsniereba", Tb., 1991, p. 1 - 113.
2. Rosinski J. et al, Radionuclides as ice - forming nuclei, J.R. Atmos., v 6,4, 1972, p.p. 693 - 696
3. Israelsson S. et al - Effect of radioactive fallout on lightning frequency, Proc. VIII Int. conf. on Atmospheric electricity, June 11-19 1988, Uppsala, Sweden, pp. 416 - 419.
4. Muraleedharan T.S., Subba Ramu M.C., Vahra K.G. Experimental studies of

the formation of Aitken nuclei in the atmosphere. 11th In. Con. on atm. aerosols, condensation and ice nuclei, 3-8 Sept. 1984 Budapest, Hungary, Pre-print, vol. 1, p. 52-57.

5. Gavasheli Sh.G. Radioaktivnoie zagriaznenie vozdukh v g. Tbilisi i ego zavisimost ot atmosfernih osadkov. Tr. Mezhd. simp. "Meteor. asp. radioakt. zagriazn. atmosfery", g. Tbilisi, 15-20 October 1973, L. Gidrometeoizdat, 1975, p. 166-177.
6. Dvali E.R., Kalaidjeva L.L. Resultati instrumentalnikh nabliudenii grozovoi aktivnosti v Dusheti i Radionovke. Tr. Zak. NIGMI, L., Gidrometeoizdat, N 54 (60) p. 137 - 139.

THREE DIMENSIONAL FINE STRUCTURES OF BULLET TYPE SNOW CRYSTALS SHOWN BY STERO-PHOTOMICROGRAPHS

Kunimoto Iwai

Faculty of education, Shinshu University, Nagano, Japan

1. Introduction

Snow or ice crystals of bullet type are scarcely observed at the surface in temperate region such as Japan, but they are the most popular one in the Antarctic atmosphere (Iwai, 1986; Ueda and Kikuchi, 1979) and in cirrus or cirrostratus clouds (Heymsfield and Knollenberg, 1972).

Morphological features of combination of bullet type snow crystals were discussed from the observations using their stereo-micrographs by Iwai (1986). However, their samples were not real crystals but replicas made on 1977 at Syowa Station, Antarctica.

Though their replicas were not deformed, their fine structures were lost during the process of replication.

It is hoped to take photomicrographs directly using real crystals. I took many stereo-photomicrographs of bullet snow crystals during my second time stay at Syowa Station from February to November 1992.

2. Examples of stereo-photomicrographs of bullet type snow crystals

Photo.1 shows a typical example of tuzumi (japanese tonitomo) type snow crystal. It consists of two bullets, both the c- and a-axes are in common with two bullets, that is, this bullet crystal is a single crystal. Transparent parts A, A' are the thin prism plane. Fig.1 shows schematic representation of this crystal viewed along the c-axis.

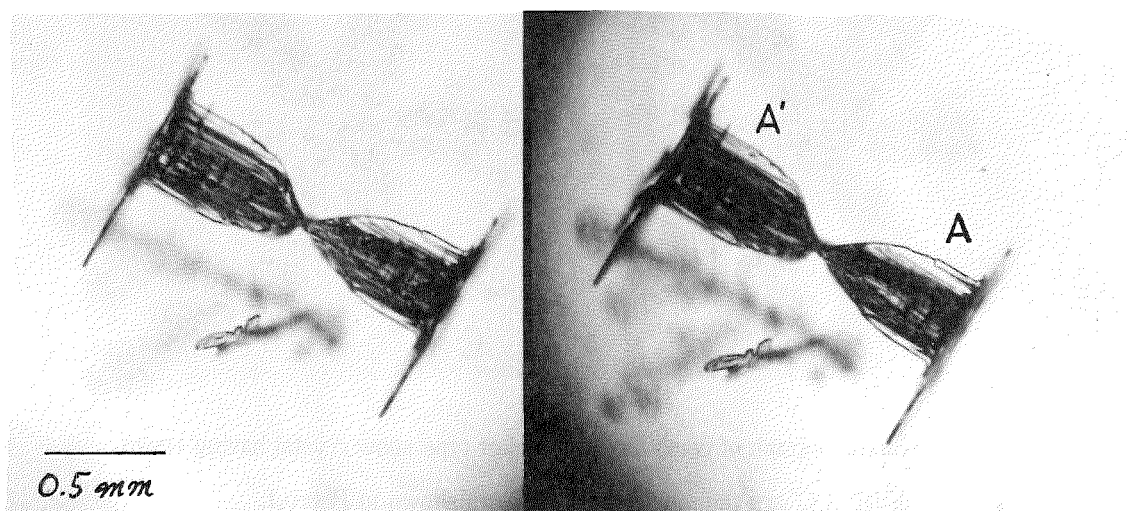


Photo.1: Stereo-photomicrograph of a typical tuzumi (japanese tonitomo). Transparent parts A, A' show the inside prism plane named by Yamashita (1971).

Ordinary prism plane shown by thin broken line do not appear but inside planes named by Yamashita(1971) appear.

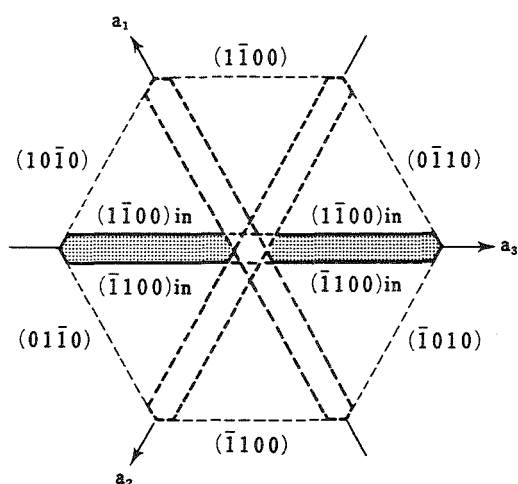
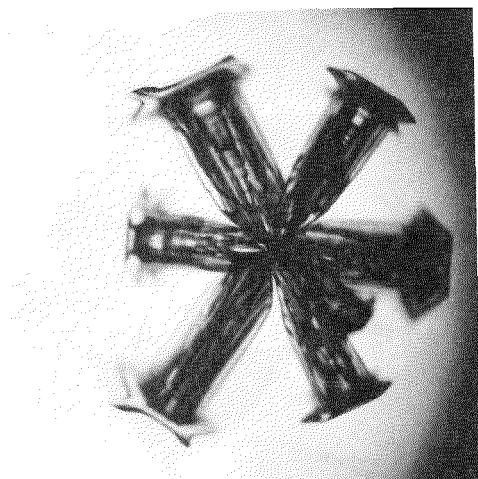


Fig.1: Schematic representation of a crystal shown in Photo.1 along the c-axis. (from Yamashita, 1971).

Photo.2 shows a stereo-photomicrographs of combination of bullet having seven components. From stereo-scopic viewing, we can discern that this crystal consists of three pairs of a single crystal AA', BB', CC' and a small one D.



The inside prism plane also developed in this crystal.

Photo.3a shows a stereo pair of combination of bullet crystal having two components. Photo.3b shows an enlarged photograph of the same crystal. Two crystals were connected by a short ice fiber of diameter $10 \mu\text{m}$. This combination of bullet crystal is considered to be just before separation and could become to two single bullets. Up to the present, artificial single bullet crystals have not been made freely. Kikuchi(1968) assumed that single bullet crystals were produced by disintegration of combination of bullet during their descent based on the statistical treatment of their size distributions. Bullet crystal shown in Photo.3 directly shows evidence that single bullet crystals result from the separation of combination of bullet crystals.

In this extended abstract, only three examples are shown. Many stereo-photomicrographs will be shown at the Poster Session in the conference.

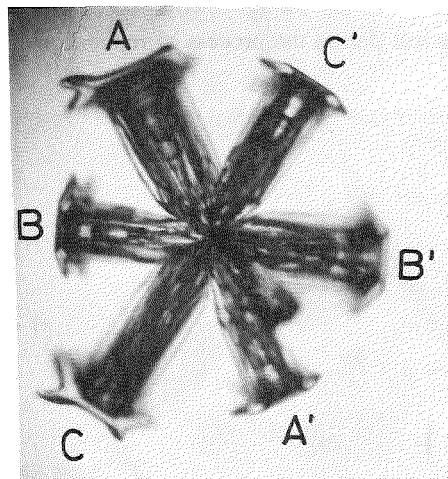


Photo.2: Stereo-photomicrograph of combination of bullet type snow crystal having seven components. AA', BB', CC' are the single crystal like as shown in Photo.1.

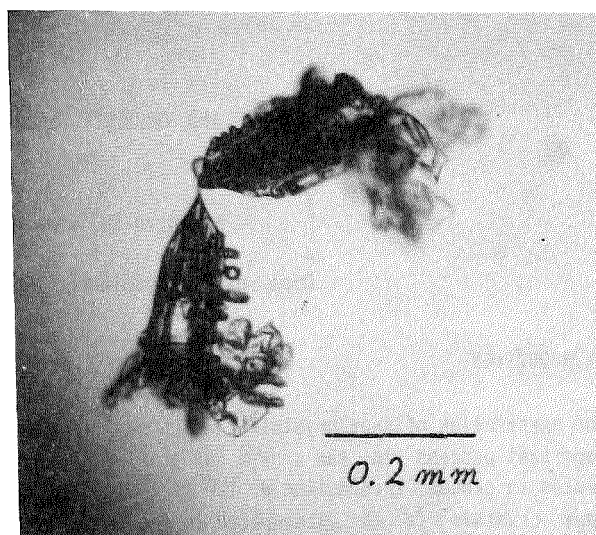
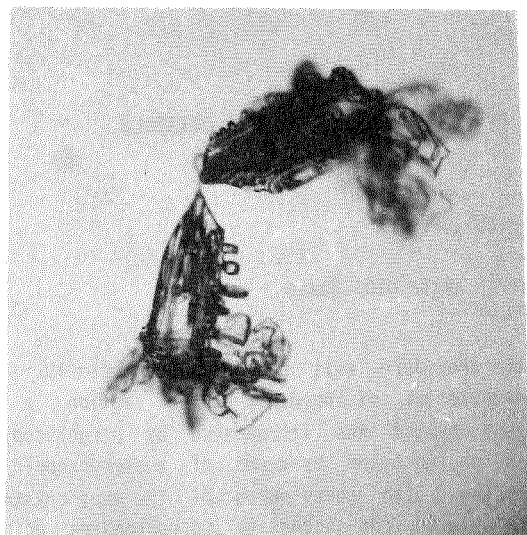


Photo.3a:Stereo— photomicrograph of combination of bullet crystal having two components connected by a short ice fiber of diameter $10\ \mu\text{m}$.

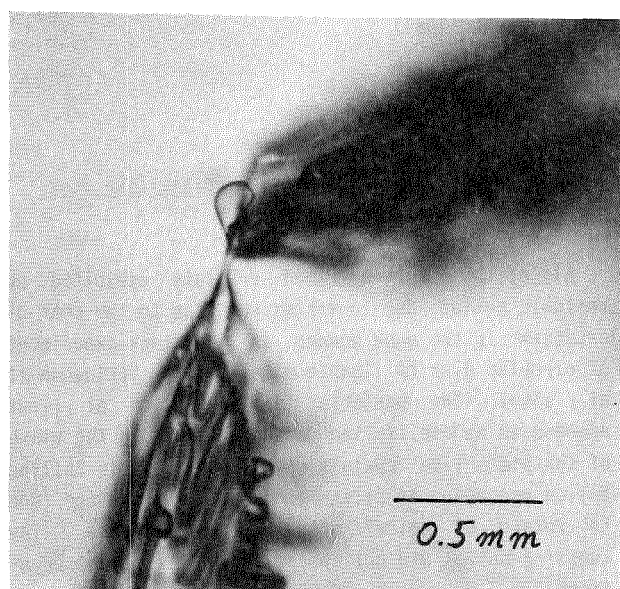


Photo.3b:An enlarged photographs of the same crystal.

References

- Heymsfields, A.J. and Knollenberg, R.G., 1972: Properties of cirrus of cirrus generating cells J. Atmos. Sci., 29, 1358-1366.
- Iwai, K., 1986: Morphological features of combination of bullet-type snow crystals observed at Syowa Station, Antarctica., Mem. Natl. Inst. Polar Res., Special Issue No.45, 38-46.
- Kikuchi, K., 1968: On snow crystals of bullet type. J. Met. Soc. Japan, 46, 128-132
- Uyeda, H. and K. Kikuchi, 1979: Observations of the three dimensional configuration of snow crystals of combination of bullet type., Ibid. 57, 488-492.
- Yamashita, A., 1971: Skeleton ice crystals of non-hexagonal shape grown in free fall., Ibid. 49, 215-231.

FREE-FALL PATTERNS AND VELOCITY VARIATIONS OF RIMED PLATE-LIKE SNOW CRYSTALS

Masahiro Kajikawa and Kyoichi Okuhara

Dept. of Earth Science, Akita Univ., Akita 010, Japan

1. INTRODUCTION

The aggregation of snow crystals to form snowflakes is important process in the growth of precipitation particles in clouds. Information on the falling motion of snow crystals in the atmosphere is required to investigate the aggregation process, as pointed out by Sasyo (1972) and Rogers (1974).


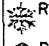

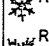
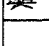
The falling motion of snow crystals is attended with the horizontal motion and both vertical and horizontal velocity variations (Zikmunda and Vali, 1972; Kajikawa, 1992). Those velocity variations and horizontal motion are responsible for an increase in the collision efficiency of snow crystals.

In a previous paper (Kajikawa, 1992), the free-fall pattern and velocity variation of unrimed plate-like snow crystals in still air were analyzed. In this paper the correlations between falling motion and features of rimed plate-like snow crystals will be analyzed and discussed using the data obtained at the Mt. Teine Observatory (1024 m altitude) of Hokkaido University and the Mt. Hachimantai Observatory (1200 m altitude) of Akita University.

2. METHOD OF OBSERVATION

Since the method of measurement of falling motion is the same as in the previous paper (Kajikawa, 1992),

Table 1. The four types of unstable fall patterns of rimed plate-like snow crystals and the observed number of each type. The classification of the crystals follows the manner of Magono and Lee (1966).

Type Crystal Shape	Nonrotation	Swing	Rotation	Spiral
 R1c: Rimmed plate or sector	0	4	5	1
 R1d: Rimmed stellar crystal	5	26	32	7
 R2a: Densely rimmed plate or sector	7	4	6	1
 R2b: Densely rimmed stellar crystal	4	21	19	7
 R3a: Graupellike snow of hexagonal type	11	2	1	0
Total Number (Rate, %)	27 (16.6)	57 (35.0)	63 (38.7)	16 (9.8)
Unrimed Plate-Like Crystals (Rate, %)	15 (27.8)	23 (42.6)	13 (24.1)	3 (5.6)

the procedure will be described briefly. For the measurement of three-dimensional motion, a falling snow crystal was illuminated by stroboscopic light and photographed by means of a stereoscopic camera system. The coordinates of the snow crystal were calculated from successive corresponding points (the center of images) on the pair of photographs. The fallen snow crystals were caught in a laboratory dish filled with silicon oil and were microphotographed for determining shape, size, and mass. The fall velocity \bar{V}_z (the mean vertical velocity) of individual snow crystals was previously described as a function of the size d or mass M (Kajikawa, 1975; Heymsfield and Kajikawa, 1987).

3. RESULTS

3.1 The free-fall pattern of rimed plate-like snow crystals

All of the observed rimed crystals exhibited an unstable motion due to vortex shedding to the rear of crystals, in the same manner as the tank experiment of circular disk (Willmarth et al., 1964; Stringham et al., 1969). The unstable falling motion at first appears as an oscillation about the axis in the plane of the plate-like crystals. Next, the unstable falling motion proceeds to swing from side to side and then to rotate or spiral about the vertical axis. The tumbling motion did not appear in the present observations.

According to the horizontal movement of crystals, unstable fall patterns were classified into four types in the same way as the unrimed crystals (Kajikawa, 1992), as follows:

1) The nonrotation type which exhibits falling motion without rotation about the vertical axis, but with horizontal movement roughly of a straight line.

2) The swing type having falling motion without rotation about the vertical axis, but with horizontal movement of a zigzag line.

3) The rotation type where the falling motion has rotation about the vertical axis, with the horizontal movement traced as a part of an ellipse.

4) The spiral type where the falling motion shows rotation about the vertical axis, with horizontal movement of a spiral.

It is assumed that the rotation type approaches the spiral type with large amplitudes or long periods, if the observation of the falling motion is performed over a longer distance. The classified unstable fall patterns along with their observed number for each type are summarized in Table 1, including the data of unrimed crystals (Kajikawa, 1992) for the purpose of comparison. From this table it can be seen that the rate of the rotation type is more, and in turn, the rate of the swing and nonrotation types are smaller than that of the unrimed crystals. The reason for this may be found in the difference in degree of asymmetry. Namely, it appears likely that rimed crystals become more asymmetrical as they capture a large amount of cloud droplets than the unrimed crystals.

3.2 Characteristics of the unstable fall pattern

Analogous to the results of tank experiments for disk (Willmarth et al., 1964), it appears that over the range of unstable falling motion as the values of Reynolds number $Re (= \bar{V}_z d / \nu)$ and the nondimensional moment of inertia $I^* (= Ia / \rho d^5, \text{stability number})$ of crystals increase, the more developed the unstable patterns become. Here, ν is the kinematic viscosity of air, $Ia = M d^2 / 16$ the moment of inertia about the a -axis of crystals and ρ the density of air.

Thus, the unstable pattern can be approximately divided by the combination of Re and I^* , considering the riming proportion R , as shown in Figs. 1 and 2. In those figures, only rimed stellar crystals (Rld) and densely rimed stellar crystals (R2b) are shown since their observed numbers are relatively abundant, as shown in Table 1. R is defined as the ratio of riming amount $(M - M_0)$ to M , according to Harimaya and Sato (1989). Here, M_0 is the mean value of the mass of unrimed dendritic crystals (Heymsfield and Kajikawa, 1987). The solid lines in those figures indicate the

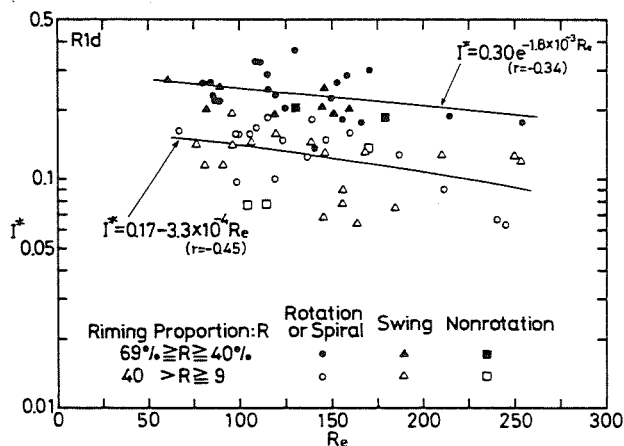


Fig. 1. The relationship between the stability number I^* and the Reynolds number Re , considering the riming proportion R for the rimed stellar crystals (Rld). The solid lines are the empirical equations with the correlation coefficient r for the two groups divided by the riming amount of crystals.

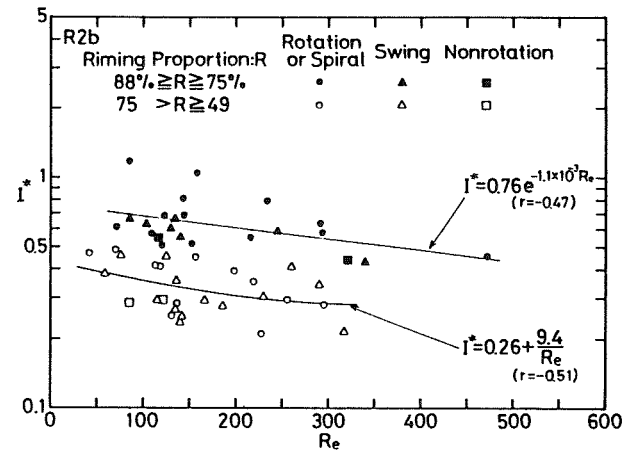


Fig. 2. The relationship between the stability number I^* and the Reynolds number Re for the densely rimed stellar crystals (R2b). The symbols are similar to Fig. 1 except the ranges of riming amount.

empirical equations with the correlation coefficient r obtained by a least-squares technique, for two groups divided by the ranges of riming proportion. It can be seen in the individual group that the rate of rotation or spiral type increases with an increase in I^* .

Fig. 3 shows the relationship between the nondimensional frequency $n' (= n d / \bar{V}_z)$ of the swing and rotation or spiral types and the size d for Pld. Here, n is the frequency of the swing and the rotation or spiral about the vertical axis. The solid and broken line represent the empirical equations of n' as a function of d for the rotation or spiral and the swing type, respectively. It is evident that n' increases with an increase in d . The value of n' for the swing type is greater than that of the rotation or spiral type when holding d constant, although the large amount of scatter appear in n' .

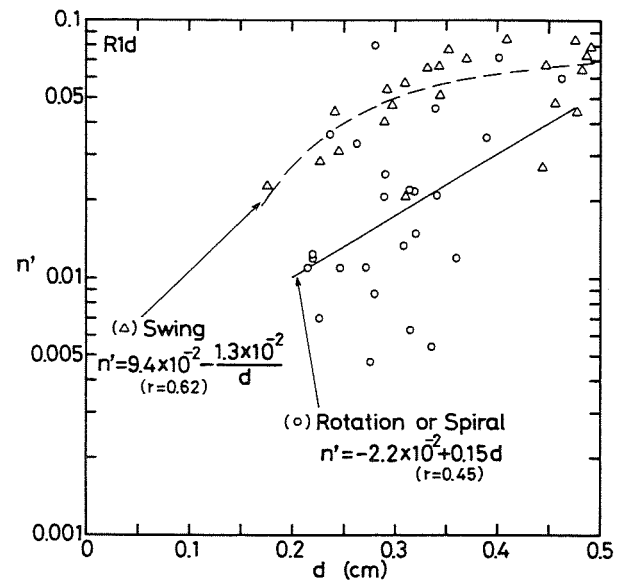


Fig. 3. The relationship between the nondimensional frequency n' and the size d of Rld for the rotation or spiral and swing type.

The relationship between n' and Re is shown in Fig. 4 for the swing type of rimed crystals (R1d and R2b). It can be seen that n' exists in the extended range of the results of tank experiment for circular disk (Willmarth et al., 1964; Stringham et al., 1969).

Fig. 5 shows the relationship between the nondimensional amplitude $a' (=a/d)$ and n' of the swing and the rotation or spiral type for R2b. Here, a is the amplitude of the types. As with the unrimed dendritic crystals (Kajikawa, 1992), a' is inversely proportion to n' .

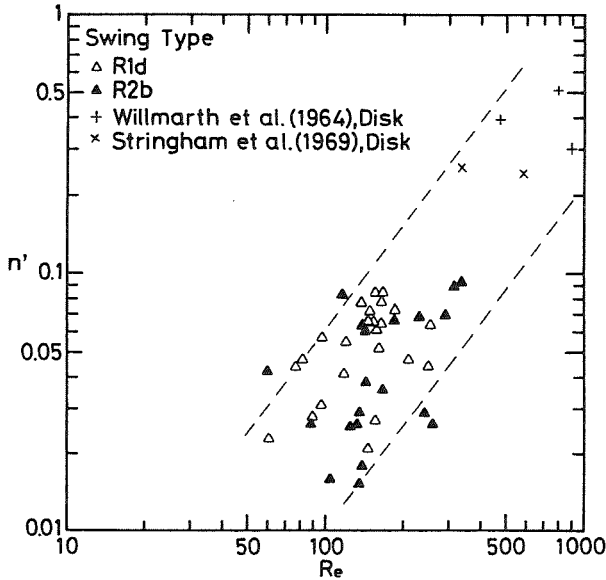


Fig. 4. The relationship between n' and Re for the swing type including the results of tank experiments.

3.3 Velocity variations of rimed snow crystals

The degree of the velocity variation of rimed snow crystals can be expressed by the standard deviation of the velocity distribution for individual stereophotographs, using the same method that was applied to the early snowflakes by Kajikawa (1989). The standard deviation σ_z of the vertical velocity V_z is shown in Fig. 6 for R2b. Although σ_z exhibits a slight increase with \bar{V}_z , the values are usually smaller than $3.5 \text{ cm} \cdot \text{s}^{-1}$ (approximately 1 to 3 % of \bar{V}_z). The broken line in this figure represents an empirical equation for the swing type having a relatively good correlation coefficient ($r=0.38$). In the case of rotation or spiral type, the empirical equation selected when r is large is shown in Table 2, involving the case of various factors of unstable fall patterns.

Fig. 7 shows the relationship between the standard deviation σ_H of V_H and \bar{V}_H for R1d. It can be seen that σ_H increases as \bar{V}_H increases and has a slight dependence on the type of unstable pattern. The values of σ_H amount to approximately 50% of \bar{V}_H or 4 to 15% of \bar{V}_z , and are considerably larger than σ_z .

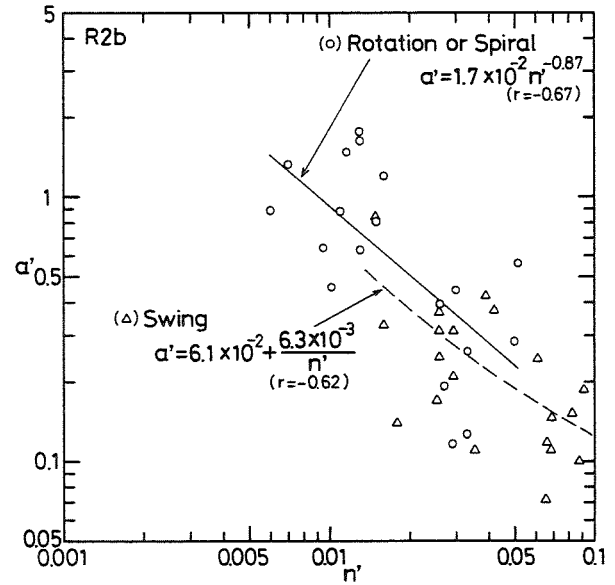


Fig. 5. The relationship between the nondimensional amplitude a' and n' for R2b. The symbols are similar to Fig. 3.

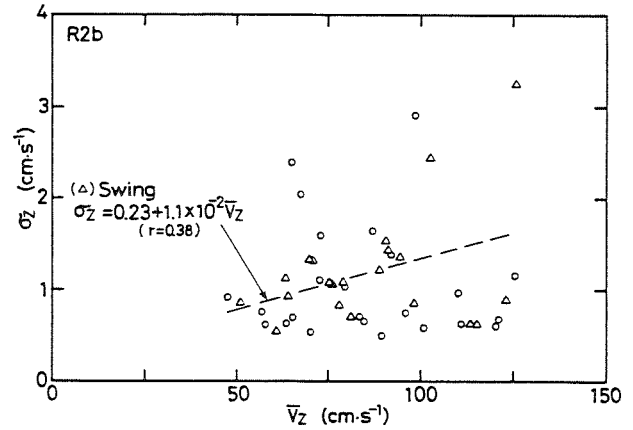


Fig. 6. The relationship for R2b between the fall velocity \bar{V}_z (mean vertical velocity) and the standard deviation σ_z of variation in vertical velocity. The symbols are similar to Fig. 3.

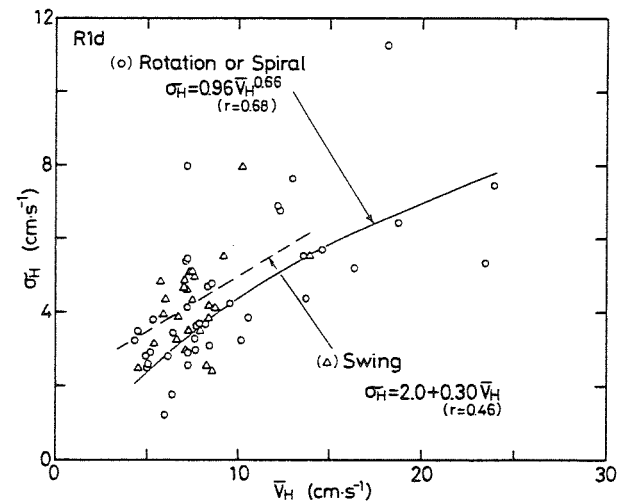


Fig. 7. The relationship for R1d between the mean horizontal velocity \bar{V}_H and the standard deviation σ_H of variation in horizontal velocity. The symbols are similar to Fig. 3.

Table 2. Summary of the empirical equations for rimed plate-like snow crystals. See text for the definitions of n' , a' , and l' . Mass M is given in grams; size d in centimeters; fall velocity \bar{V}_Z in centimeters per second; N is the number of crystals, and r the correlation coefficient.

Crystal shape	R1d:Rimmed stellar crystal		R2b:Densely rimed stellar crystal	
	Swing	Rotation or spiral	Swing	Rotation or spiral
Nondimensional frequency n'	$n' = 9.4 \times 10^{-2} - \frac{1.3 \times 10^{-2}}{d}$ $N=23, r=0.62$	$n' = -2.2 \times 10^{-2} + 0.15d$ $N=25, r=0.45$	$n' = 1.5 \times 10^{-2} + 1.8 \times 10^{-4} Re$ $N=20, r=0.55$	$n' = 1.0 \times 10^{-2} e^{0.0031 Re}$ $N=19, r=0.50$
Nondimensional amplitude a'	$a' = 9.8 \times 10^{-2} + \frac{1.3 \times 10^{-2}}{l'^2}$ $N=23, r=-0.38$	$a' = 4.8 \times 10^{-2} n'^{-0.66}$ $N=25, r=-0.72$	$a' = 6.1 \times 10^{-2} + \frac{6.3 \times 10^{-3}}{n'}$ $N=20, r=-0.62$	$a' = 1.7 \times 10^{-2} n'^{-0.87}$ $N=19, r=-0.67$
Mean horizontal velocity \bar{V}_H (cm.s ⁻¹)	$\bar{V}_H = 5.7 - 1.3 \ln a'$ $N=23, r=-0.32$	$\bar{V}_H = 7.0 + 3.1a'$ $N=25, r=0.42$	$\bar{V}_H = 8.7 \times 10^2 M^{0.51}$ $N=20, r=0.63$	$\bar{V}_H = 1.5 Re^{0.41}$ $N=25, r=0.48$
Standard deviation in vertical velocity σ_z (cm.s ⁻¹)	$\sigma_z = 1.2 - \frac{1.4 \times 10^{-5}}{M}$ $N=25, r=0.27$	$\sigma_z = 1.5 - \frac{52}{Re}$ $N=39, r=0.28$	$\sigma_z = 0.23 + 1.1 \times 10^{-2} \bar{V}_Z$ $N=20, r=0.38$	$\sigma_z = 0.71 e^{0.35 a'}$ $N=18, r=0.37$
Standard deviation in horizontal velocity σ_H (cm.s ⁻¹)	$\sigma_H = 2.0 + 0.30 \bar{V}_H$ $N=25, r=0.46$	$\sigma_H = 0.96 \bar{V}_H^{0.66}$ $N=39, r=0.68$	$\sigma_H = -4.2 + 4.5 \ln \bar{V}_H$ $N=20, r=0.88$	$\sigma_H = 2.7 e^{0.056 \bar{V}_H}$ $N=25, r=0.66$

From the results described above, it seems likely that in particular the variation of the horizontal velocity plays an important role in random aggregation process of snow crystals.

4. CONCLUDING REMARKS

The falling motion in still air of rimed plate-like snow crystals was analyzed by means of a stereo-photogrammetry. Difference in types of the unstable fall patterns depends on the riming proportion, the nondimensional moment of inertia (stability number), and Reynolds number with respect to the fall velocity (mean vertical velocity) of the crystals, as shown in Figs. 1 and 2.

The standard deviation of variation in vertical velocity is less than 3% of the fall velocity. On the other hand, the standard deviation of variation in horizontal velocity is considerably large (4 to 15% of the fall velocity). Accordingly, it seems likely that in particular the variation of horizontal velocity plays important role in random aggregation of rimed plate-like snow crystals having almost the same shape and size. The standard deviations of the velocities can be empirically estimated as functions of various factors (e.g., the fall velocity, size, mass, and non-dimensional moment of inertia of rimed crystals), as shown in Table 2.

5. ACKNOWLEDGEMENTS

The authors are very grateful to Prof. K. Kikuchi, Hokkaido University for the Mt. Teine Observatory available for this study. Partial funding for this study was provided by the Scientific Research Branch of the Ministry of Education and Culture of Japan.

6. REFERENCES

- Harimaya, T., and M. Sato, 1989: Measurement of the riming amount on snowflakes. *J. Fac. Sci., Hokkaido Univ., Ser. VII*, 8, 355-366.
- Heymsfield, A. J., and M. Kajikawa, 1987: An improved approach to calculating terminal velocities of plate-like crystals and graupel. *J. Atmos. Sci.*, 44, 1088-1099.
- Kajikawa, M., 1975: Experimental formula of falling velocity of snow crystals. *J. Meteor. Soc. Japan*, 53, 267-275.
- _____, 1989: Observation of the falling motion of early snowflakes. Part II: On the variation of falling velocity. *J. Meteor. Soc. Japan*, 67, 731-738.
- _____, 1992: Observations of the falling motion of plate-like snow crystals. Part I: The free-fall patterns and velocity variations of unrimed crystals. *J. Meteor. Soc. Japan*, 70, 1-9.
- Magono, C., and C. W. Lee, 1966: Meteorological classification of natural snow crystals. *J. Fac. Sci., Hokkaido Univ., Ser. VII*, 2, 321-335.
- Rogers, D. C., 1974: The aggregation of natural ice crystals. Rep. No. AR 110, Dept. Atmos. Resources, Univ. of Wyoming, 35 pp.
- Sasyo, Y., 1972: Study of the formation of precipitation by the aggregation of snow particles and the accretion of cloud droplets on snowflakes. *Pap. Meteor. Geophys.*, 22, 69-142.
- Stringham, G. E., D. B. Simons and H. P. Guy, 1969: The behavior of large particles falling in quiescent liquids. Geol. Survey Prof. Paper, 562-C, Washington, D. C., Government Printing Office, 36 pp.
- Willmarth, W. W., N. E. Hawk and R. L. Harvey, 1964: Steady and unsteady motions and wakes of freely falling disks. *Phys. Fluids*, 7, 197-208.
- Zikmunda, J. and G. Vali, 1972: Fall patterns and fall velocities of rimed ice crystals. *J. Atmos. Sci.*, 29, 1334-1347.

A POSSIBLE RELATIONSHIP BETWEEN LIGHTNING DISCHARGE IN CLOUD AND GUSHES OF RAIN

Zlatko R. Vukovic¹ and Mladjen Curic²

¹ Toronto, Canada

² University of Belgrade, Yugoslavia

1. INTRODUCTION

Abrupt heavy gushes of rain have frequently been observed shortly after a lightning flash. Moore and Vonnegut (1977) showed that 75% of summertime precipitation that had fallen on one mountain top station has done so within 5 minutes of nearby lightning discharge. Similar results have been showed by many other authors (Piepgrass *et al.*, 1982; Curic and Vukovic, 1991, etc.)

Radar measurements also show that after the first thunder occurrence the radar echo becomes suddenly stronger by few tens of dB in a minute (Moore *et al.*, 1964, Szymanski *et al.*, 1980, etc.). The investigation of lightning channels with Doppler radar (Zrnica *et al.*, 1982, Williams and Lhermitte, 1983), have indicate that the spectral peaks associated with precipitation and lightning are often distinct in the Doppler velocity spectrum.

Although the close association between lightning and precipitation is evident, there is still no general agreement about the mechanism operating in real clouds. Two main different mechanisms have been proposed to explain how lightning might cause the formation of a rain gush: one is acoustic and the other is electric.

There are several versions of the electrical explanation. According to one view, such as expressed by Schonland (1950) and Levin and Ziv (1974), the electric field, which retains in some way the precipitation particles, is weakened by lightning flash and therefore allows the particles to be released. According to another view, (Vonnegut and Moore, 1960) lightning introduces electric charges that accelerate the coagulation of cloud droplets.

Several authors have suggested that acoustic forces associated with thunderclaps, influence gushes of rain. Goyer (1965a,b) reported experiments carried out on Old Faithful Geyser, where rapidly moving rain gushed some time after detonating cords were exploded near the Geyser plume. He explained his findings as the result of increased rate of coalescence between water droplets due to radial wind produced by the detonation. Studies of the influence of explosion (gunshots) on precipitation (Hung *et al.* 1981) conclude that gunshots can produce precipitation from cumulus congestus clouds in which precipitation had not appeared before gunshots. Additionally, the intensity of precipitation quickly increased within six minutes after the gunshots. The results of the numerical model (Curic and Vukovic, 1991, 1992) indicate that the acoustic wave generated by electrical discharges can shift droplet spectra toward larger size.

In this study we will analyze the influence of acoustic waves on rain gushes as well as the effects of the rearrangement charge deposited along the lightning channel on coagulation of droplets. The purpose of this paper is to

demonstrate that the droplet motion and electrical effects produced by lightning strikes within clouds may cause a rapid and effective droplet coalescence process. Since this process is much shorter than coagulation under gravity, its real effects are not expected to show significant shifting of the droplet size spectrum. The evolution of the droplet spectra under the impact of the acoustic wave of thunder tends to produce larger drops which then enhance gravitational coagulation. This means that, if a certain "critical droplet size spectrum" is not reached in a cloud, the acoustic coagulation can overcome this stage by shifting the droplet spectrum to the "critical one". This might be one of the mechanisms that causes gushes of rain after lightning.

2. DESCRIPTION OF THE MODEL

2.1. Qualitative description

In this study, the slab-symmetric, time-dependent numerical cloud model of Curic and Vukovic (1991) is modified into an one-dimensional axisymmetric type cloud model and developed further to take into account droplet charged electrical effects. Consider the acoustic shock wave produced by lightning discharge. Immediately after lightning in a negatively charged cloud we assume that droplets are negatively charged and there are only positive ions around the lightning channel (Moore *et al.*, 1964). Those ions, carried by the shock wave front, will be moved away from the channel and collected by negative droplets. The ions may first neutralize the negative cloud droplets and because of the high space density of the ions, then give them a very large positive charge. According to this picture we will have mostly positive charged droplets near the channel and more negative ions with increased distance from it. The final result is that air motion caused by the acoustic wave suddenly increases the velocity of differently charged droplets. Faster drops come across the slower ones, and create conditions for coagulative growth. Since the droplets are charged, the electrostatic forces cause increased intensity of coagulation. This growth is called "acoustic-electrostatic coagulation" (AEC).

2.2 Model assumptions

- The model is one-dimensional (x) slab-symmetrical and time-dependent.
- The cloud is composed of water drops.
- The cloud characteristics are axial-symmetrical around the lightning channel.
- Only the acoustic field and the electrostatic field exist around charged droplets.

- The system is closed and only the laws of energy and mass conservation exist.

2.3 Basic discretion equations

Cloud droplets are assumed to fit a *Marshall-Palmer* (*Sekhon and Srivastava*, 1970) type distribution for raindrops.

Initially concentration of positive (+) charged droplets in each radius droplet class (i) exponentially decrease with distance ($x_k = k\Delta x$) while negative (-) droplets increase:

$$N_{i,+}^k = N_i e^{-\lambda(x_k - x_1)}, \quad N_{i,-}^k = N_i (1 - e^{-\lambda(x_k - x_1)})$$

where parameter λ control the range inside initial positive charged droplets. In the model it takes values between 5m and 20 m.

The charge-size relationship is still an open question. Relatively few in situ measurements exist of charge carried by thunderstorm cloud and precipitation particles, especially before the storm's first lightning flash (see *Weinheimer et al.* 1991). In our investigation, we analyzed two options about the charge-size relationship.

The first option ($|Q| < |Q_{\max}|$) is that the initial intensity of negative charged droplets is given by *Taquisi* empirical relation and for positive charged droplets is given by *Rayleigh* theoretical equation (*Pruppacher and Klett*, 1978):

$$Q_{i,-} = -8000r_i^2, \quad Q_{i,+} = 10^3 \sqrt{16\pi\sigma r_i^3}$$

Radius of droplet is given in metric and electricity in esu; σ is surface tension of water-air.

And second option ($|Q| = |Q_{\max}|$) is that positive and negative charged droplets have a maximum theoretical charge given by the *Rayleigh* equation.

Immediately after lightning and depending on distance from the channel, the initially velocity of droplets and that of air, are given by equations described in *Curic and Vukovic's* paper (1991):

$$V_i^{t=0,k} = \frac{\Phi \Omega^k}{r_i},$$

$$U^{t=0,k} = \frac{2}{\rho_a} \sqrt{\frac{\alpha_a E_0}{2\pi x_k \exp[x_k(\alpha_c + \alpha_a)]}}$$

Where Φ and Ω^k are given with:

$$\Phi = \sqrt{\frac{B^4}{(8\pi A \rho_w)}}, \quad B = \frac{3}{R_{av}}, \quad A = \frac{145L_{wc}}{\rho_w R_{av}}$$

$$\Omega^k = \sqrt{\frac{\alpha_c E_0}{\pi x_k \exp[x_k(\alpha_c + \alpha_a)]}}$$

Here L_{wc} is the liquid water content (kgm^{-3}), R_{av} is the mean radius (m); ρ_w is density of cloud drop (kgm^{-3}); E_0 is initially front energy (Jm^{-2}/m); α_c and α_a are attenuation coefficients of drops and gaseous.

After passing the acoustic front, further movement is determined by the following equations:

$$m_i \frac{\Delta V_i^{t,k}}{\Delta t} = -6\pi\eta_i [1 + \Psi(N_{Re})](U^{t,k} - V_i^{t,k})$$

$$U^{t,k} = U^{t=0,k} \exp(-t/\tau),$$

where $\Psi(N_{Re})$ is parameterization function of *Reynolds* number given in *Wang and Pruppacher's* paper (1977); τ is empirical parameter which represents the typical time duration of the air motion caused by thunder clap (*Zrnica et al.*, 1982).

To describe the cloud growth we used the modified equation of stochastic growth (*Berry*, 1967 and *Scott and Levin*, 1975):

$$\frac{\Delta N_i^{t,k}}{\Delta t} = \frac{1}{2} \sum_{j=1}^{\text{imx}} \sum_{l=1}^{\text{imx}} N_j^{t,k} N_l^{t,k} K_{jli} - N_i^{t,k} \sum_j N_j^{t,k} K_{ji},$$

where K_{ji} is the acoustic-electrostatic coagulation kernel:

$$K_{ji} = \pi(r_i + r_j)^2 E_{ij} (V_i - V_j)$$

and K_{jli} is the redistribution kernel which has similar meaning as formulated in *Kovetz and Olund* papers (1969). The E_{ij} is acoustic-electrostatic collection efficiency (*Curic and Vukovic*, 1991) except that it is modified by taking the *Atkinson and Paluch* (1968) approximation of numerically determined collision efficiency E_c of charged droplets with the high relative velocity.

$$E_c = \begin{cases} 1 + 1.4Z, & \text{for } Z \leq 5 \\ 1.6Z, & \text{for } Z > 5 \end{cases}$$

$$Z = \frac{E_{el}}{E_{ki}},$$

where E_{ki} is the kinetic energy of the relative motion and E_{el} is the electrical energy that occurs as the particles move from infinite to minimal separation.

2.4 Numerical computation technique

Numerical experiments were carried out in a cylindrical domain. The grid interval used was $\Delta x = 5\text{m}$. The time increment used at the each step was determined in according with the condition that it must be smaller than the characteristic time of the fastest droplet. For all the time-dependent partial differential equations a forward time differences scheme was used.

Values of concentration, velocity and electricity of each of droplets are averaged before each time step at every grid point. During the time period of one time step, the fastest droplets leave the elementary volume and go to right grid volume. At the same time, some of fastest droplets from left neighboring volume come into this elementary volume. The incoming and outgoing fluxes of droplets result in averaged concentration of droplets for that time. Consequently we have averaged values of velocity and averaged value of charged droplets.

As well, inside each time step, new droplet electricity in each radius class is calculated as average values of new and existing electricity. The charge on droplets of average size is not allowed to exceed the *Rayleigh* limit.

3. NUMERICAL EXPERIMENT

Several experiments have been carried out and classified according to the following parameters: the liquid water content L_{wc} , the average spectra radius R_{av} , the initially acoustic front energy E_0 ; the maximum values of droplet charge (0 means no charge, $< Q_{\max}$ empirical relation

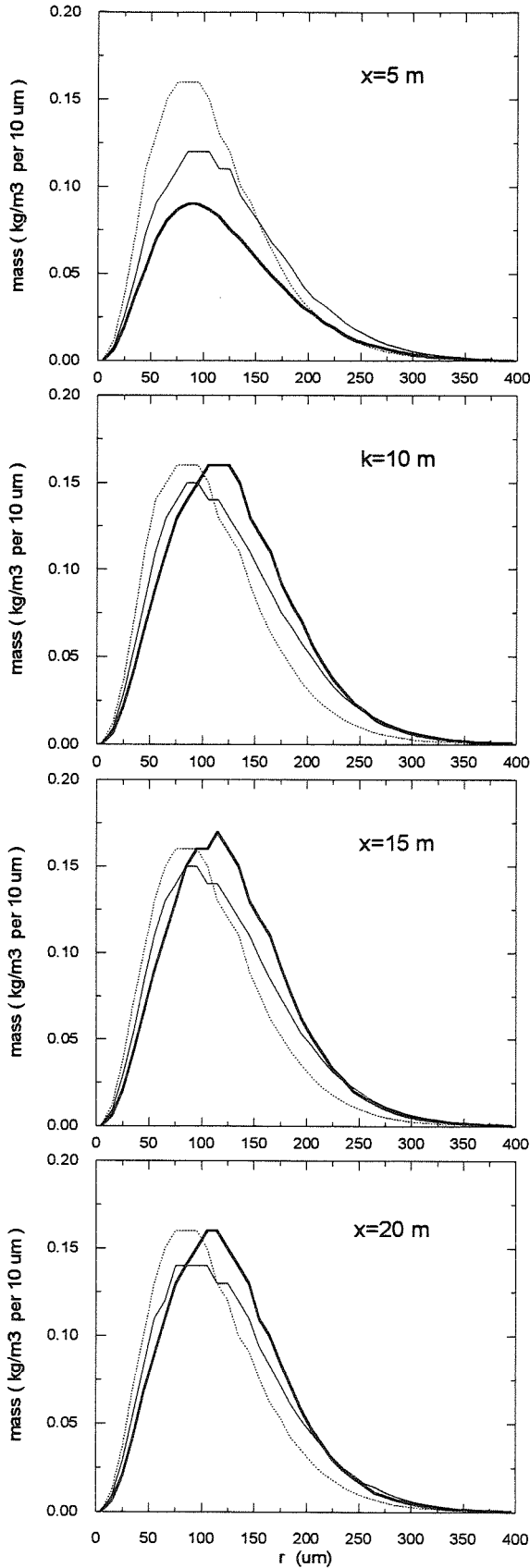


Fig. 1. Evolution of the initial spectrum (dashed line) due to acoustic-electrostatic coagulation for initial conditions shown in case 3 (full line) and case 4 (bold line) for four different distance from lightning channel ($x=5, 10, 15, 20$ m).

between droplet size and charge and $= Q_{mx}$ Rayleigh limit charge) and the radius of positively charged droplets area λ . The differences among the cases are given in Table 1 where dR_{mv} and dZ are relative rates of mean volume radius and radar reflectivity as a consequence of AEK influence.

TABLE 1. Experimental parameters and dR_{mv} , dZ values.

Case	L_{wc} [gm^{-3}]	R_{av} [μm]	E_o [$Jm^{-2}m^{-1}$]	Q	λ [m]	dR_{mv} [%]	dZ [dBZ]
1	1	100	10^5	$< Q_{mx}$	15	7	1.5
2	3	100	10^5	$< Q_{mx}$	15	13	2.0
3	2	100	10^5	$< Q_{mx}$	15	10	1.8
4	2	100	10^5	$= Q_{mx}$	15	23	1.5
5	2	100	10^5	0	15	9	2.0
6	2	100	10^4	$< Q_{mx}$	15	7	1.3
7	2	100	10^6	$< Q_{mx}$	15	10	2.5
8	2	50	10^5	$< Q_{mx}$	15	12	2.0
9	2	50	10^5	$= Q_{mx}$	15	28	3.0
10	2	150	10^5	$< Q_{mx}$	15	9	1.5
11	3	150	10^6	0	15	10	1.8
12	3	150	10^6	$< Q_{mx}$	15	11	2.0
13	3	150	10^6	$= Q_{mx}$	15	22	2.0
14	2	100	10^5	$< Q_{mx}$	5	9	1.8
15	2	100	10^5	$< Q_{mx}$	25	9	1.8

In above case studies we used radial domain of 25m and always assume that drop and gaseous attenuation coefficients are 10^{-3} [m^{-1}] and 10^{-2} [m^{-1}] and $\tau=0.5$ sec.

For given cases the model shows a typical increase of volume average radius for about 10% for $Q=0$ or $|Q| < |Q_{mx}|$ and about 20% for $|Q| = |Q_{mx}|$. The average increase of radar reflectivity is about 2 dBZ. For all cases, the duration time of the AEK process is less than 0.1 sec.

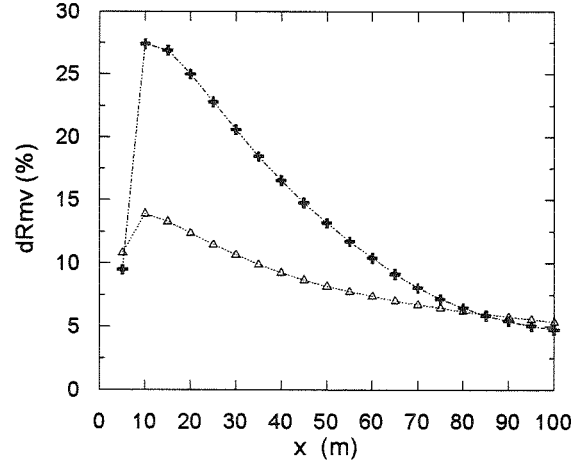


Fig 2. Variation of the relative rate of mean volume droplet radius with distance from the lightning channel for Taquashi (triangles) and Rayleigh (crosses) charge-size relations

An example of the evolution of the drop spectra under the AEK can be seen in Figure 1. The figure shows that in the closest grid volume ($k=1$, $x=5$ m) initial droplet concentration (dashed line) decreases while in the further grid points there are noticeable effects of AEK. That effect decreases in magnitude as the distance from the channel is

increased and they are more significant for higher charged droplets (bold line) than for less charged droplets (full line).

Usually, the maximum effects of AEK are found in the second grid point which depends on the initial condition (especially from the acoustic front energy). The Figures 2 and 3 show an example of the variation in relative rate of mean volume radius and radar reflectivity with distance from the lightning channel. Initial condition is the same as in the case 3, except 20 is used instead of 5 grid points, and the expected radius area of significant AEK influence is around 50 m.

Duration time of AEK process depends on initial condition and the typical value is a few tenth, of a second. For case 3, with 20 grid points instead of 5, we got results which are shown in Figure 4. Maximum charged droplets (crosses) need shorter time for AEK (~ 0.07 sec) than less charged droplets (triangles, ~ 0.08 sec).

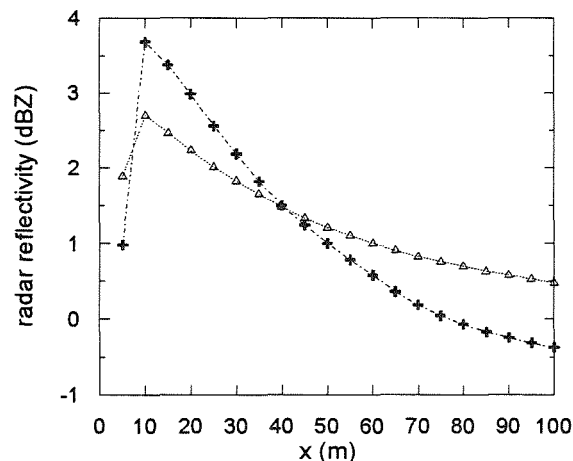


Fig 3. Variation of the radar reflectivity with distance from the lightning channel for Taquashi (triangles) and Rayleigh (crosses) charge-size relations.

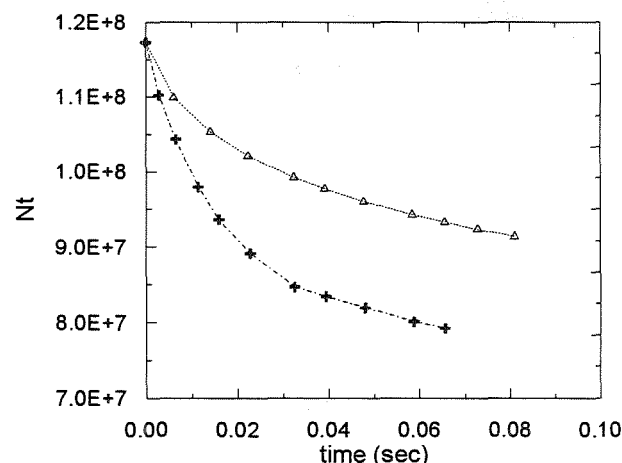


Fig 4. Time variation of the total number of droplets inside 20 grid volumes for Taquashi (triangles) and Rayleigh (crosses) charge-size relations.

DISCUSSION AND CONCLUSION

Using a relatively simple model, we were focusing only on the possible effects of AEK. Even though we didn't include the ice phase, which should exist in the dominant part of a

thunder cloud, we showed that AEK for less than one second can increase the mean volume radius of the initial spectra by 10 to 20 %. That increase of the droplet size could be important for further gravitational growth (see for example *Edwin and Morris*, 1972).

The predicted increase of radar reflectivity of a few dBZ gives us the possibility for verification of the model results, if we can get the appropriate radar measurements with regards to the location of lightning and cloud particles. A more sophisticated model including other relevant parameters such as external electric fields and the ice phase of droplets, should be developed. From that model, we can expect more realistic results which can be compared with observed measurements. Also, the output of that model can be useful as the input for larger cloud models with more microphysics and cloud dynamics.

Acknowledgments. The authors wish to thank Dr. George Isaac for his helpful suggestions and to Maria Latyszewskij for proof reading the paper.

REFERENCES

- Brazier-Smith R.P., 1971: Stability and Shape of Isolated and Pairs of Water Drops in an Electric Field. *The Physics of Fluids*, V14, No.1
- Berry, E.X., 1967: Cloud droplet growth by collection. *J. A. S.*, 34, 543-50
- Curic, M. and Z. R. Vukovic, 1992: Numerical Experiments on the Influence of Thunderstorm-Generated Acoustic Waves on Coagulation. *Proc. 11. ICCP*, Montreal, Canada.
- 1991: The influence of thunderstorm generated acoustic waves on coagulation. Part one: Mathematical formulation. *Z. Meteor.* 41, 164-9.
- 1988: Influence of Thunderstorm Generated Acoustic Wave on Coagulation. *Proc. 10. ICCP*, Bad Homburg, Germany.
- Huang Mei-yun et al. 1981: Studies of the influence of explosion upon the development processes of convective clouds. *J. W. Mod.* 13, 226-230.
- Kovetz, A. and B. Olund, 1969: The effect of coalescence and condensation on rain formation in a cloud of finite vertical extent. *J. Atm. Sci.* 26, 1060-1065.
- Moore, C. B., Vonnegut, B., Vrablik, E. A. and McCaig, A.D., 1964: Gushes of Rain and Hail After Lightning. *J. Atm. Sci.* V21, 646-665.
- Moore, C.B., and B. Vonnegut, 1977: The thunder cloud. In: *Lightning, Vol. 1., Physics of Lightning* (Ed. R.H. Golde) Ac. Prs, London 51-98.
- Piegras, V. M., Krider, E. P. and Moore B. C., 1982: Lightning and Surface Rainfall During Florida Thunderstorms. *J.G.R.* V87, No. C13, 11193-11201.
- Pruppacher, R. H. and J. D. Klett, 1978: Microphysics of Clouds and Precipitation. *D. Reidel Publishing Company*, Boston, USA.
- Sekhon and Srivastava, 1971: Doppler Radar Observations of Drop-Size Distributions in a Thunderstorm. *J. Atmos. Sci.* 28, 983-994.
- Schonland, B.F.J., 1950: The Flight of Thunderbolt. pp 150-151, Oxford, Oxford University Press, New York.
- Scott, D. W. and Z. Levin, 1975: A Comparison of Formulations of Stochastic Collection. *J. Atmos. Sci.* 32, 843-847.
- Szymanski, E.W., S.J. Szymanski, C.R. Holmes, and C.B. Moore, 1980: An Observation of a Precipitation Echo Intensification Associated With Lightning. *J.G.R.* V85, No. C4, 1951-1953.
- Goyer, G.G., 1965a: Effects of lightning on hydrometeors. *Nature*, 206, 12203-1209.
- 1965b: Mechanical effects of a simulated lightning discharge on the water droplets of 'Old Faithful' Geyser. *Nature*. 206, 1302-1304.
- Vonnegut b. and C.B. Moore, 1960: Possible effect of lightning discharge on precipitation formation process. *Geophys. Mon.* 5, 287-290.
- Williams, R.E. and M.R. Lhermitte, 1983: Radar Test of the Precipitation for Thunderstorm Electrification. *J.G.R.* V88, No. C15, 10984-10992
- Wang, P.K. and H.R. Pruppacher, 1977: Acceleration to terminal velocity of cloud and raindrops. *J. Appl. Met.* 16, 275-280.
- Weinheimer, A.J., et al. 1991: Simultaneous measurements of the charge, size, and shape of hydrometeors in an electrified cloud. *J.G.R.* 96, 20809-20829.
- Zrnic, S. D., W.D. Rust and W.L. Taylor 1982: Doppler Radar echoes of Lightning and Precipitation at Vertical Incidence. *J.G.R.* V87, No. C9 7179-7191.

FORMATION MECHANISMS OF MULTI-BRANCHED SNOW CRYSTALS

Katsuhiro Kikuchi and Hiroshi Uyeda

Graduate School of Science, Hokkaido University, Sapporo 060, Japan

1. INTRODUCTION

Twelve-branched snow crystals have been discussed in various reports. There have been few discussions, however, about the formation mechanisms of these snow crystals. Regarding the formation mechanisms of the crystals, Nakaya (1954) speculated that they consisted of two overlapping dendritic crystals, that is to say, a "snowflake theory" based on a macroscopic viewpoint alone, although he did not measure the angle between both crystals. In contrast, Kobayashi and Furukawa (1975) tried to explain the mechanisms using by a "rotation twinning theory" based on the concept of the "Coincidence-Site Lattices" from a microscopic viewpoint. Since the discovery of eighteen-branched snow crystals by Kikuchi (1987) at Inuvik, N.W.T. Canada, the study of the formation mechanisms of the multi-branched snow crystals including twelve- and eighteen-branched snow crystals has been carried out up to the present. Kikuchi and Uyeda (1987) proposed a "frozen cloud droplet theory" as one of formation mechanisms of eighteen-branched snow crystals based on laboratory experiments. In this paper, we will describe the three dimensional structure and the most probable formation mechanisms of multi-branched snow crystals, especially regarding the adequacy of the rotation twinning theory in the multi-branched snow crystals based on the observational results in Inuvik, Arctic Canada and Kautokeino, Northern Norway.

2. OBSERVATIONS AT INUVIK, CANADA

During the observation period in Inuvik ($68^{\circ}22'N$, $133^{\circ}42'W$), Arctic Canada from December 1985 to January 1986, as shown in Fig. 1

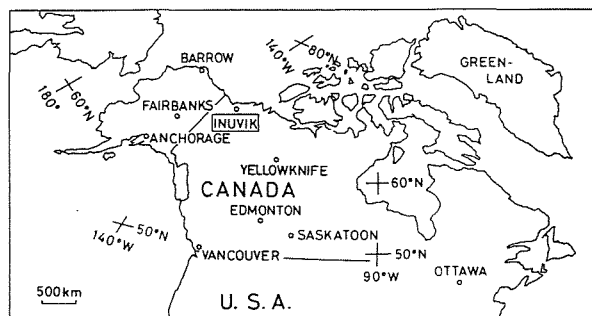


Fig. 1. Location of observation site in Arctic Canada.

a minimum temperature of $-47.5^{\circ}C$ was recorded. On January 8 and 11, 1986, however, under relative warm temperature conditions, the eighteen-branched snow crystals were observed

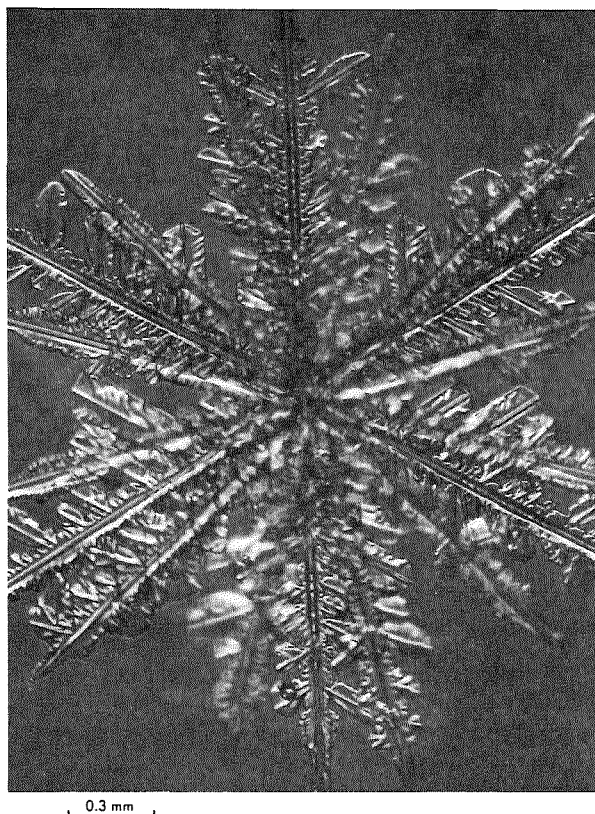


Fig. 2. An example of typical eighteen-branched snow crystals.

mingling with typical dendrites and twelve-branched snow crystals. A centered, symmetric, complete and beautiful eighteen-branched crystal as shown in Fig. 2 is the first of its kind discovered in the world. According to the sounding curves, there was a water saturation layer from 880 to 700 hPa level. The air temperatures of this layer are from -13 to -18°C . The temperature range coincides exactly with that of dendritic growth. The external dimensions of dendrites observed were relatively large and they were 3 mm or more approximately.

3. ANALYSES

Kobayashi and Furukawa (1975) have explained the formation mechanism of twelve-branched crystals using the rotation twinning theory based on the concept of coincidence-site lattices. Thus, the authors have attempted to test this theory in considering formation mechanisms of the eighteen-branched crystals. Figure 3 shows a schematic arrangement of the crystals. As a matter of convenience in this figure, the smaller

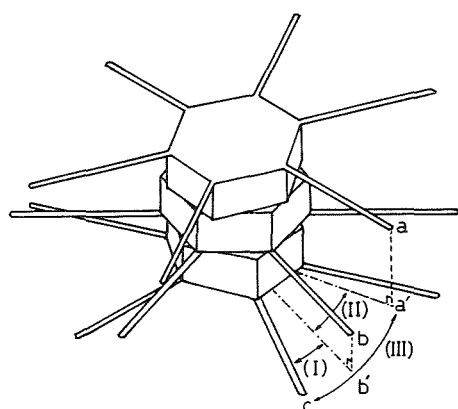


Fig. 3. Schematic arrangement of eighteen-branched snow crystals.

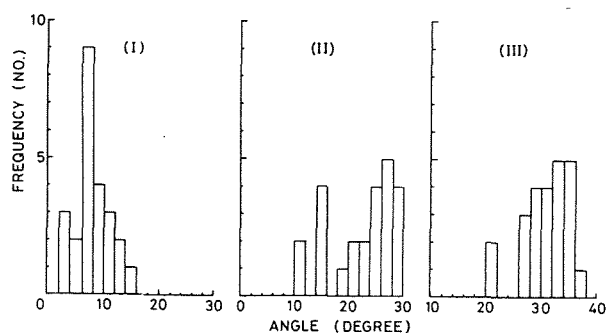


Fig. 4. Frequency distributions of angles (I), (II), and (III) of each crystal component.

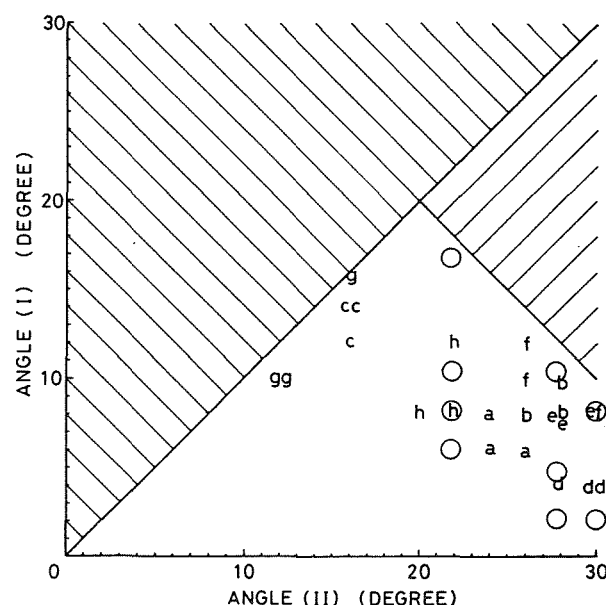


Fig. 5. Relationship between the angle (I) and (II).

angle ($b'-c$), the larger angle ($a'-b'$), and the total angle ($a'-c$) are named (I), (II) and (III), respectively. Frequency distributions of each angle are shown in Fig. 4. As the angle (III) is invariably smaller than 40° , the peak of angle (III) is found in a range between 33° and 36° . Further, it is recognized that the peaks of angles (I) and (II) are 7° to 8° and 27° to 28° , respectively. According to Table 1 of Kobayashi and Furukawa (1975), the rotation angles which are expected from relatively small multiplicity (Σ) which is a measure of the energy at the interfacial boundary are 22° , 28° and 30° . The results when these angles are applied to the upper (a), middle (b), and lower branches (c) are shown as open circles in the Fig. 5. As the angle (I) is smaller than 20° , and the angle (II) is larger than 10° , a relationship between the angles (I) and (II) is included on the outside of the shaded region. Alphabetical letters (a) to (h) represent each eighteen-branched crystal analyzed. As the same letter is seen in threes, the angles (I) and (II) are noted as three for each crystal. Therefore, the concentration of the same letter means the centered crystal. As seen in the Fig. 5, the crystals named (a) to (e) are centered and the crystals (f) to (h) are off-centered. As clearly seen, the positions which are measured in each crystal do not coincide with each other. Especially,

the relationship between the angles (I) and (II) of the typical crystal shown in Fig. 2 is shown as the letter (c) in Fig. 5, and the angles are far from those expected by the rotation twinning theory. Therefore, it is concluded that the formation mechanism of eighteen-branched snow crystals can not be explained in total by the rotation twinning theory. The maximum diameter of multi-branched crystal and dendrites is larger than 3 mm. Therefore, the ratio (d) will be $150 \mu\text{m}$. It can be concluded that it is difficult to explain a $150 \mu\text{m}$ difference between the two centers in each crystal component using the rotation twinning theory.

4. FURTHER OBSERVATIONS AT KAUTOKEINO, NORWAY

In order to understand the formation mechanisms of multi-branched crystals, the three-dimensional structure should be analyzed with photographs taken from the direction perpendicular to the c-axis (Uyeda and Kikuchi, 1990). No analysis of multi-branched crystals from the direction perpendicular to the c-axis has been carried out to date, though Iwai (1983) and Bruinjets et al. (1987) carried out the observations of the side views of crystals. During the

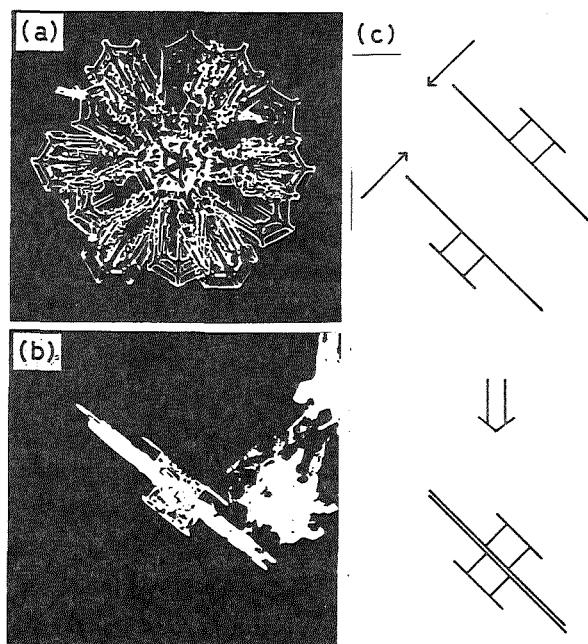


Fig. 6. An example of twelve-branched snow crystals. (a) Front view, (b) Side view, and (c) Schematic illustration of the attached double plates.

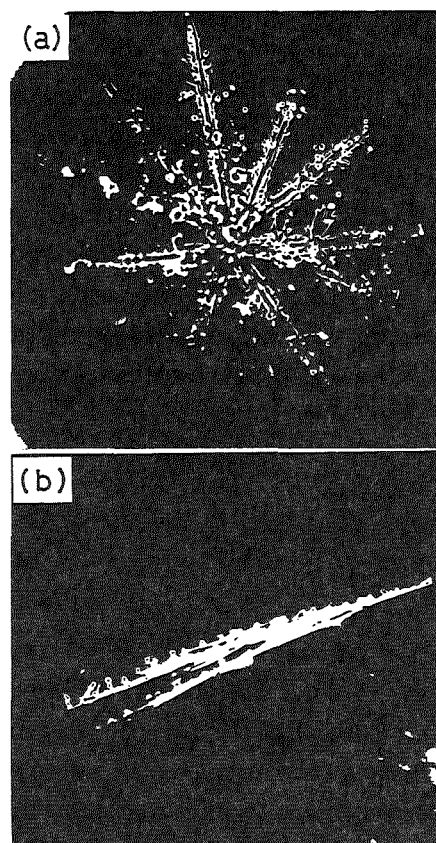


Fig. 7. Same as Fig. 6 except (c).

observations at Kautokeino ($69^\circ 01'N$, $23^\circ 03'E$) in Northern Norway, we tried to take micro-photographs from the direction perpendicular to the

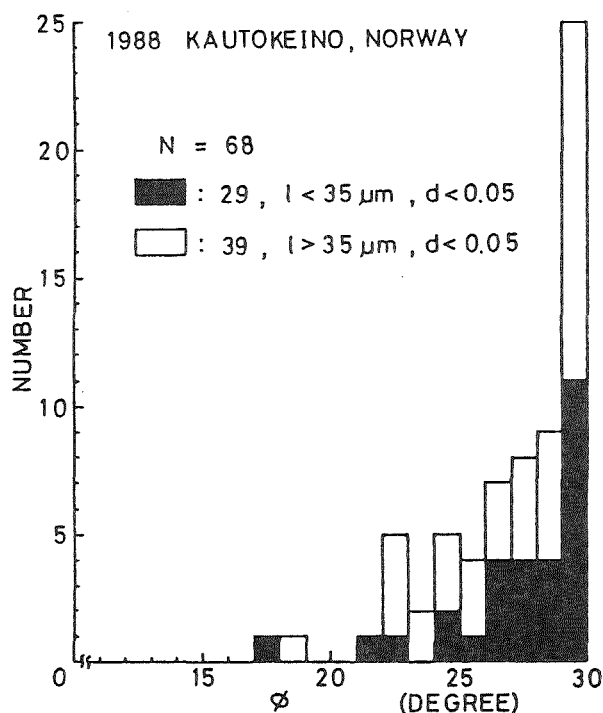


Fig. 8. A histogram of measured angle ϕ between branches of twelve-branched snow crystals. Solid column shows the crystal with a small value of $l < 35 \mu\text{m}$ and $d < 0.05$.

c-axis of multi-branched crystals. At Kautokeino, fortunately, 68 twelve-branched and a few eighteen-branched crystals were micro photo-graphed.

Figure 6 shows an example of twelve-branched crystals. In the figure, (a) and (b) are front and side views, respectively. This crystal is composed of two double plates which are attached to each other at the basal planes of larger sectors of two double plates as shown in Fig. 6 (c). This crystal can obviously be explained by the "snowflake theory." The snow crystal in Fig. 7 is also a snowflake, because the inclination of basal planes and the large spacing of two double plates suggests this.

In summation of all the centered twelve-branched crystals, the histogram of the angle ϕ between the branches is shown in Fig. 8. Predominant differences between the solid and open columns in the histogram are not identified. Further, the prominent peak around 27° suggested by Kobayashi and Furukawa (1975) is not identified.

5. CONCLUSIONS

Formation mechanisms for the multi-branched snow crystals were discussed based on the relationship between the angles (I) and (II) of each component crystal compared with the rotation twinning theory introduced by Kobayashi and Furukawa (1975). As a result, it was concluded that the mechanism of rotation twinning could not always be applied to the multi-branched snow crystals. Further, from the microphotographs of the side views of twelve-branched snow crystals, it was concluded that most of the crystals were composed of two double plates. From the measurement of the angle ϕ between branches, a peak at 27° was not predominant, but rather a peak approximately 30° only was predominant.

The most probable formation mechanism of multi-branched snow crystals is considered to be the "snowflake theory", though a slight possibility of their formation by "rotation twinning theory" (Kobayashi and Furukawa, 1975) and "frozen cloud droplet theory" (Kikuchi and Uyeda, 1987) was determined to exist.

ACKNOWLEDGMENTS

The expense of this research was supported by the Grant-in-Aid for Scientific Research (Overseas Scientific Survey) of the Ministry of Education, Science and Culture of Japan.

REFERENCES

- Bruinjets, R. T., A. J. Heymsfield and T. W. Krauss, 1987: An examination of double-plate ice crystals and the initiation of precipitation in continental cumulus clouds. *J. Atmos. Sci.*, **44**, 1331-1349.
- Iwai, K., 1983: Three-dimensional structure of plate-like snow crystals. *J. Meteor. Soc. Japan*, **61**, 746-755.
- Kikuchi, K., 1987: The discovery of eighteen-branched snow crystals. *J. Meteor. Soc. Japan*, **65**, 309-311.
- Kikuchi, K. and H. Uyeda, 1987: Formation mechanisms of eighteen-branched snow crystals. *J. Fac. Sci., Hokkaido Univ., Ser. VII*, **8**, 109-119.
- Kobayashi, T. and Y. Furukawa, 1975. On twelve-branched snow crystals. *J. Crystal Growth*, **28**, 21-28.
- Nakaya, U., 1954. *Snow Crystals, natural and artificial*. Harvard Univ. Press, Cambridge, 510 pp.
- Uyeda, H. and K. Kikuchi, 1990: Formation mechanisms of twelve-branched snow crystals. *J. Meteor. Soc. Japan*, **68**, 549-556.

MICROPHYSICAL PROCESS OF CLOUDS FORMED IN THE ARTIFICIAL CLOUD EXPERIMENTAL SYSTEM

Akira Sasaki and Toshio Harimaya

*Division of Earth and Planetary Sciences, Graduate School of Science,
Hokkaido University, Sapporo, 060, Japan*

1. INTRODUCTION

Research methods for cloud physics include experiments in a laboratory, observations of natural clouds, numerical simulations, etc.. Each of these methods, however, has some problems; the scale of experiments in a laboratory is too small, the repeatability of phenomena and data acquisition are difficult in observations of natural clouds, and numerical simulations have the problem of insufficient available data of natural clouds for comparison. Thus, we constructed the artificial cloud experimental system (ACES), using a long vertical mine shaft. The vertical mine shaft has a quasi-real scale of natural clouds and allows us to obtain data easily, and environmental conditions can be controlled.

This quasi-real scale experiment is the first attempt in the field of cloud physics. The ACES was constructed by using a long vertical exhaust shaft at a coal mine in Kamisunagawa-cho, Hokkaido, Japan. Artificial clouds can be formed under conditions of constant updrafts in the vertical shaft. Data for various environmental conditions and microphysical processes of cloud formation could be obtained using various observational instruments installed in the vertical shaft (Fujiyoshi et al., 1993; Yamada et al., 1993).

Cloud droplet spectra are the basic data which are necessary to obtain the reflectance of solar radiation by clouds and the formation rate of rain drops in the warm rain process. Thus, evaluation of the parameters that determine cloud droplet spectra is very important in cloud physics. This study aims to clarify the microphysical processes of clouds formed in the vertical shaft, and to quantitatively evaluate the relationship between CCN concentrations and cloud droplet spectra.

2. EXPERIMENTAL SYSTEM AND OBSERVATION METHOD

The vertical shaft has a depth of 710 m and inside diameter of 5.5 m. A fan was installed at the top of the shaft and it generated constant updrafts of about 2.0 m/s, and clouds were formed in the vertical shaft. Sprinklers were installed near the bottom of the shaft to increase the vapor quantity in air parcels which were introduced into the vertical shaft. Many variables related to the microphysical processes of cloud formation were measured by observational instruments installed in a gondola which moved up the vertical shaft from 0 m to 700 m in height, usually stopping for 5 minutes at every 50 m. However, only on the morning of 12 August, the gondola was stopped for a longer time at a few observation points in order to sample cloud water. The gondola was installed with instruments such as a thermometer, hygrometer, anemometer, cloud water sampler, cloud droplet spectrometer, etc.. Simultaneously, variables for air parcels introduced into the vertical shaft were observed by instruments such as an aerosol sampler, particle counter, etc. which were installed at the bottom of the shaft.

The following three kinds of data are mainly used in this study. Firstly, aerosols were collected by an aerosol sampler, and analyzed by an X-ray microanalyzer to determine their elemental components. Secondly, aerosol concentrations were measured by a particle counter, which recorded the concentrations in 5 ranges according to sizes from above 0.3 μm to above 5.0 μm . Thirdly, cloud droplets were collected on glass plates by a cloud droplet spectrometer, and recorded by a video camera system. The size distributions of cloud droplets were determined from the video images by a computer.

3. OBSERVATION RESULTS

Observations were carried out 2 times in the morning and afternoon of every day from 10 to 12 August, 1993. Each observation is sequentially numbered, for example, the observation in the

morning of August 10 is CASE1, and the observation in the afternoon of August 12 is CASE6.

The elemental components of aerosols were investigated in CASE1 and CASE4. Water was sprinkled in CASE4 but not in CASE1. A total of 180 aerosols were analyzed. Figure 1 shows the frequencies of elemental components of aerosols which are $0.5 - 2.0 \mu\text{m}$ in size. Na and Cl were frequently observed in the sprinkling case (black bar), but not in the non-sprinkling case (white bar). On the other hand, it was shown that the groundwater used for sprinkling contained a large amount of NaCl. Sprinkling not only increased the vapor quantity but also changed the elemental components of aerosols. It is thought that most of effective CCN contained NaCl originating from groundwater.

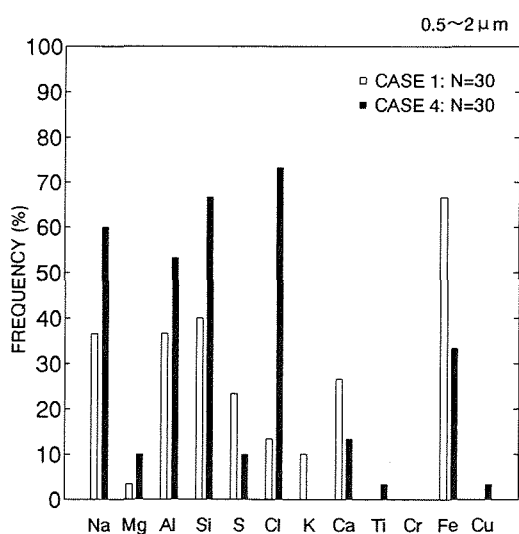


Fig.1. Frequencies of elemental components of aerosols in sprinkling case (CASE4) and non-sprinkling case (CASE1).

A particle counter was used to measure the concentrations of aerosols in air parcels introduced into the shaft. The concentrations of aerosols, which were larger than $0.3 \mu\text{m}$ in size, were $22 - 28 \text{ cm}^{-3}$ in the non-sprinkling case (CASE1). In sprinkling cases, the concentrations were $7 - 8 \text{ cm}^{-3}$ in CASE4, and $20 - 93 \text{ cm}^{-3}$ in CASE5. It is thought that partial aerosols were effective CCN and grew into cloud droplets when air parcels moved upward.

Figure 2 and 3 show the changes in observed cloud droplet spectra with changes in height. The cloud droplet spectrometer can not measure cloud droplets which are smaller than $4 \mu\text{m}$ in size due to limitations of resolution. In CASE1, most of cloud droplets were smaller than the minimum measurable size, and therefore, the obtained concentrations of cloud droplets were very low (figure is omitted). This is thought to be because most of the shaft was subsaturated and most of aerosols were soil particles

which are a little effective as CCN in the non-sprinkling case. On the one hand, in CASE4 (Fig.2), a low CCN concentration case, cloud droplets grew with the upward motion of air parcels. The mode diameter of cloud droplets was $10 - 15 \mu\text{m}$ at a height of 700 m , and they grew into larger sized droplets than those in the non-sprinkling case. This is thought to be because the vapor quantity increased and most of the aerosols contained NaCl due to the sprinkling. On the other hand, in CASE5 (Fig.3), a high CCN concentration case, the mode diameter of cloud droplets was $5 - 10 \mu\text{m}$, and they could not grow into the same sizes as under a low CCN condition. This is thought to be because generated cloud droplets were more numerous than those in a low CCN case, and cloud droplets could not grow into a large size due to competition for vapor. As the maximum size of cloud droplets observed in the experiments was less than $40 \mu\text{m}$, it is thought that contributory factors in the growth process of observed cloud droplets were not collision and coalescence, but condensation (Beard and Ochs, 1993).

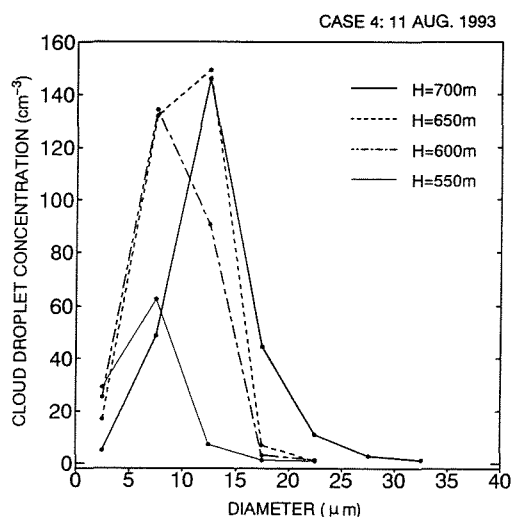


Fig.2. Changes in observed cloud droplet spectra with changes in height in CASE4.

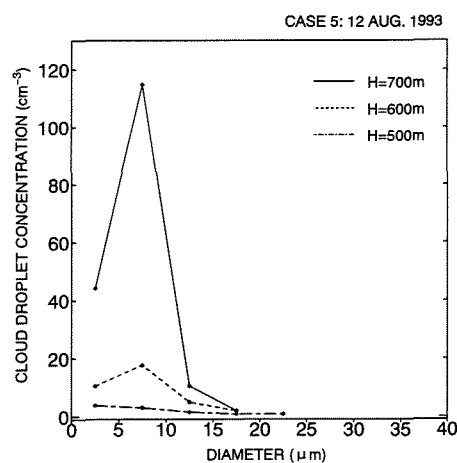


Fig.3. The same as Fig.2 except for CASE5.

These results show that a low CCN concentration generates a small number of large-sized cloud droplets, while a high CCN concentration generates a large number of small-sized cloud droplets. However, comparisons were not strictly carried out for cloud droplets smaller than the minimum measurable size under conditions of constant LWC. Thus, in order to discuss the details, numerical simulations were carried out for condensation growth of cloud droplets.

4. NUMERICAL SIMULATIONS

Numerical simulations were carried out under the conditions that air parcels move upward in the shaft, and CCN consists of NaCl and grow into cloud droplets by condensation. The height of air parcels can be replaced by the time of growth, because the vertical shaft can be regarded as a system of one dimension with constant updrafts. The condensation growth of cloud droplets is calculated by the equations shown in Takahashi (1976). Cloud droplets are divided into many classes according to sizes, and growth of cloud droplets in each class is calculated for one step, and they are redistributed into appropriate classes. For the initial conditions of CCN spectra, observed spectra were used in the observed size range and assumed Junge spectra were used in the smaller size range.

Tests of numerical model were carried out with various time steps and class numbers. The cloud droplet spectra calculations were found to be accurate, if the time step was 0.1 seconds and the class number was 150, and thus, these values were used. When the coefficients of Junge spectra were changed in the range from -2.0 to -3.5, LWC hardly changed, while cloud droplet spectra changed greatly. Thus, changes in the CCN concentration hardly affect LWC, but greatly affect cloud droplet sizes.

Some factors require consideration in order to reproduce the microphysical processes in the shaft. Firstly, the quantity of vapor condensed to the wall of the shaft has to be determined. This quantity can be evaluated indirectly from the observed thermal decreasing rate with height. The calculated thermal decreasing rate is different from the observed rate, due to the effects of "apparent heat" and "latent heat". The effect of "apparent heat" is a direct heat flux between air parcels and the wall of the shaft, and can be assumed by the difference between the dry adiabatic rate and the thermal decreasing rate in CASE1 when most of the shaft was subsaturated. Thus, the effect of "latent heat" which is a reduction of generated condensational heat caused by vapor condensation on the wall can be calculated by the

above values. Secondly, the exact values of humidity at the bottom of the shaft have to be determined. The hygrometer installed in the gondola had an error of about 3 - 5 %, and therefore, microphysical processes can not be reproduced in the shaft if observed values of humidity are used as initial values. Thus, the values of humidity at the bottom of the shaft were corrected under the condition that calculated and observed LWC at a height of 700 m were nearly consistent. Finally, we must obtain the appropriate coefficients of Junge spectra in order to obtain CCN spectra in a smaller size than the observed range. Thus, the coefficients were obtained under the condition that calculated and observed cloud droplet spectra at a height of 700 m were nearly consistent. The corrected values of humidity are still thought to be exact, because changes in the coefficients of Junge spectra hardly affect LWC.

5. CONSIDERATIONS

The determined CCN spectra are shown in Fig.4. In a small size range, CASE1 and CASE5 show high CCN concentrations, and CASE4 shows low CCN concentrations. There is an approximately one-order difference between high and low cases.

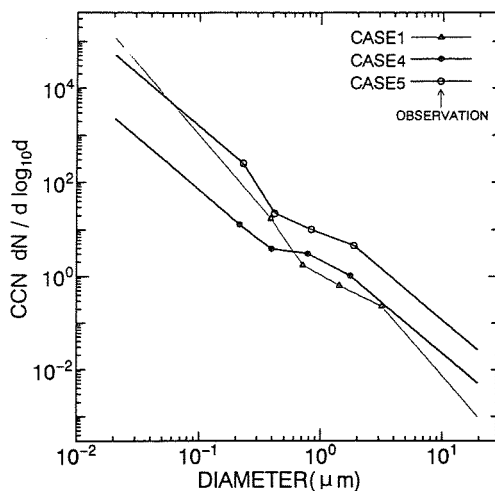


Fig.4. CCN spectra determined by numerical simulations.

Figure 5 shows the cloud droplet spectra at a height of 700 m reproduced by numerical simulations. In CASE1, the cloud droplet spectrum is not monomodal due to little growth. It is thought that the size difference between activated and non-activated cloud droplets were still small because the height from a saturated position was small. On the other hand, in CASE4 and CASE5, cloud droplet spectra were monomodal, due to growth by condensation. The mode diameter is about 13 μ m and the cloud droplet concentration is low in CASE4, while the mode is about 4 μ m and the concentration is high in

CASE5. As stated above, sequential cloud physical processes in the shaft were evaluated, and cloud droplet spectra were reproduced. However, the difference in reproduced cloud droplet spectra in each case is thought to be also affected by the difference of LWC.

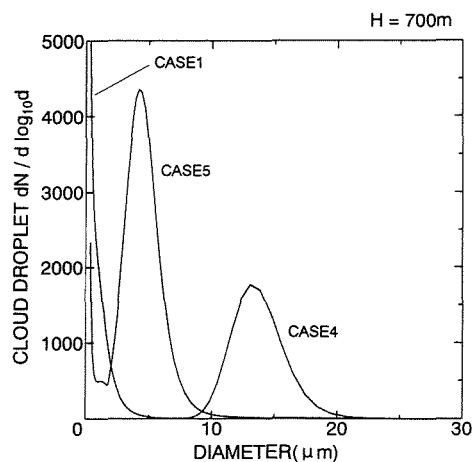


Fig.5. Cloud droplet spectra at a height of 700 m reproduced by numerical simulations.

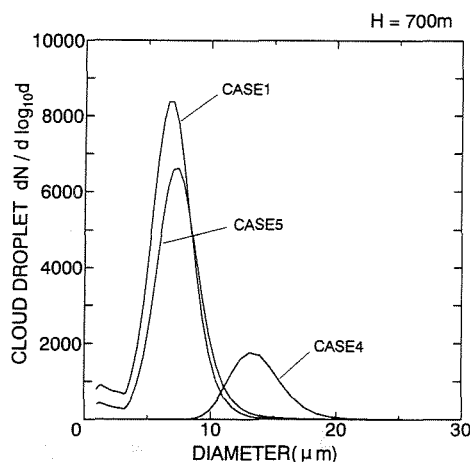


Fig.6. Cloud droplet spectra affected by the difference in CCN spectra.

Thus, the height of cloud bases was regulated to about 530 m in all cases by changing the initial values of humidity at the bottom of the shaft. Under these conditions, the differences in cloud droplet spectra were evaluated for each case. It is thought that they were affected only by the differences in CCN spectra. The calculated cloud droplet spectra at a height of 700m are shown in Fig.6. In CASE1 and CASE5, cloud droplet spectra are nearly equal, and the mode diameter is small at about 7 μm , and the cloud droplet concentration is high at about 1600 cm^{-3} in CASE5. On the other hand, in CASE4, the mode diameter is large at about 13 μm and the cloud droplet concentration is low at about 250 cm^{-3} . These results show that when CCN concentration increases approximately one order, the generated cloud droplet

concentration increases about 6 times and the mode diameter decreases by about half. Thus, the relationship between CCN concentrations and cloud droplet spectra has been quantitatively determined.

6. CONCLUSIONS

By comparing and considering the results of observations and calculations, we could clarify and evaluate the microphysical processes of clouds formed in the shaft. The CCN spectra in air parcels introduced into the shaft were obtained under each condition. These CCN grew only by condensation processes with the upward motion of air parcels. There was an approximately one-order difference in the CCN concentrations between high and low case. A comparison of cloud droplet spectra at a height of about 170m above cloud bases showed that cloud droplet concentrations in 1cm^3 were about 1600 and 250, and mode diameters were about 7 and 13 μm , respectively. Under conditions of constant LWC, it was quantitatively demonstrated that a large number of small-sized cloud droplets are generated in the case of a high CCN concentration, and a small number of large-sized cloud droplets are generated in the case of a low CCN concentration.

Acknowledgements. The authors would like to express their thanks to Dr. Yamada, Department of Civil Engineering, Chuo University, and Dr. Fujiyoshi, Institute of Hydrospheric-Atmospheric Sciences, Nagoya University, and Mr. Inage, Mitsui Construction Co. Ltd., for their joint studies. This study was supported by a Grant-in-Aid for Scientific Research from the Ministry of Education of Japan.

REFERENCES

- Beard, K. V., and H. T. Ochs, 1993: Warm-rain initiation: An overview of microphysical mechanisms. *J. Appl. Meteor.*, **32**, 608-625.
- Fujiyoshi, Y., T. Yamada, M. Inage, and T. Harimaya, 1993: Tentative results of artificial cloud experimental system (ACES). *Proceedings of IAMAP-IAHS (Yokohama)*, **J.4.3**, 19.
- Takahashi, T., 1976: Warm rain, giant nuclei and chemical balance - A numerical model. *J. Atmos. Sci.*, **33**, 269-286.
- Yamada, T., T. Hibino, G. Fukawa, M. Matsuura, Y. Fujiyoshi, T. Harimaya, and M. Inage, 1993: Quasi-prototype experiments of cloud physics using long shaft in the mine. *Proceedings of 25th International Association for Hydraulic Research*, 113-118.

MICROPHYSICAL CHARACTERISTICS OF THUNDERSTORMS AS RELATED TO STORM LIGHTNING ACTIVITY

Hartmut Höller and Ullrich Finke

Deutsche Forschungsanstalt für Luft- und Raumfahrt (DLR)
Institut für Physik der Atmosphäre, Oberpfaffenhofen, D-82234 Wessling, Germany

1. INTRODUCTION

Polarimetric radar measurements have turned out to be very useful for the discrimination of different kinds of hydrometeors in convective storms. Measurements of differential reflectivity Z_{DR} help to identify rain regions and to discriminate them from hail or graupel zones aloft (Seliga and Bringi 1976). Linear depolarization ratio LDR helps to identify graupel, snow and hail e.g. in the upper parts of a thunderstorm. Wet growth of hailstones or melting of ice causes the particles to be covered by liquid water resulting in typical polarimetric signatures of enhanced LDR values. Z_{DR} and LDR can also help to identify mixed phase regions in the cloud where e.g. raindrops and hailstones do co-exist (Höller et al 1994). Moreover, reflectivity Z can be used for quantitative determination of the water or ice contents (Höller, 1995).

In the present investigation the microphysical information obtained from radar observations is combined with measurements of the storms' lightning activity (Finke and Hauf 1996) as derived from an LPATS system (Lightning Position and Tracking System). The temporal and spatial distribution of lightning strokes is compared with the microphysical evolution obtained from the polarization measurements. Similar studies have been done recently by Lopez and Aubagnac (1995) and Carey and Rutledge (1995). In contrast to these investigations we use a different kind of hydrometeor classification and quantification. It is based on LDR rather than on differential phase as applied by these authors.

Doppler radar measurements as well as the observed evolution of the storm system in terms of cell types do complete the interpretation.

2. GENERAL STORM DEVELOPMENT

The storms discussed in the following were observed in southern Germany on 10 August 1994. In a west-south-westerly airflow aloft thunderstorms

developed ahead of an upper level trough in association with an approaching cold front. The low level winds were veering with height indicating the potential for cyclonic updraft rotation which was indeed observed for both of the major storm systems shown in Fig.1 (northern and southern storm track). The direction of propagation of the northern storm changed markedly at about 1900 LT (local time = UTC+2h) when it weakened and got incorporated into a larger scale convective system.

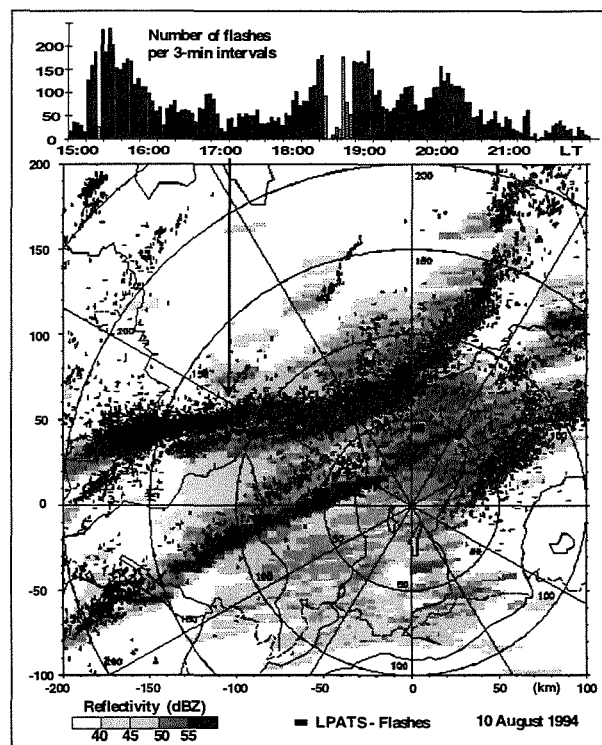


Fig. 1. Storm tracks as derived from Radar and LPATS network. Flash frequency of the northern storm is shown in the upper panel. The correspondence of time and location is indicated by the arrow.

The lightning activity of the two storms differed considerably. The northern storm was much more active than the southern one. Therefore the northern system is studied in more detail in the following.

3. LIGHTNING AND MICROPHYSICS

The lightning activity of the northern storm as observed by an LPATS network is shown in Fig. 1. The flash frequency exhibits distinct variations with time. Three periods of high activity can be noted: (i) from 1530 to 1600 LT, (ii) from 1830 to 1915 LT, and (iii) between 2000 and 2030 LT. Due to system thresholds of the LPATS system, some data are missing during the second maximum (ii).

The period from 1746 to 1949 is investigated in more detail in Fig. 2. The storm had moved closer to the radar and the polarimetric volume scans could be used for inferring microphysical information on the liquid and solid phase precipitation particles. Here we concentrate on the maximum hail amount as derived after Höller (1995). LDR, Z_{DR} , and Z are used for computing the hail content. For demonstrating the essential features, the maximum values above (AML) and below the melting level (BML) are shown in Fig. 2.

We start with an active phase of the cloud development. High hail concentrations have been generated by strong updrafts in the upper levels of the cloud. Maximum AML-values of hail content and LDR decrease until 1816 LT whereas maximum BML-values increase simultaneously. This illustrates the fallout of the hail to the ground. During this phase the flash rate starts to increase until about 1911 LT where hail aloft reaches a minimum. There is still some hail falling out to the ground. At 1922 LT all parameters start to decrease further indicating a general weakening of the storm system.

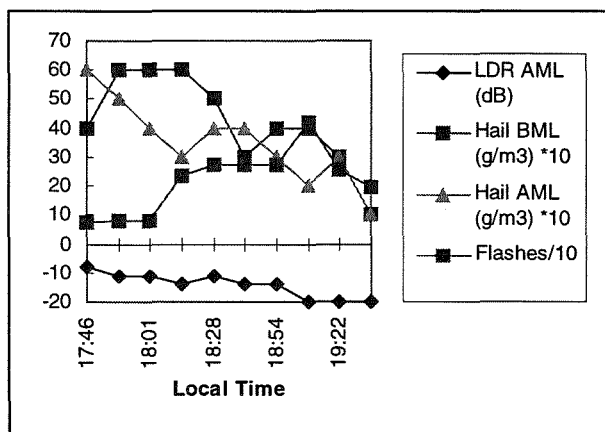


Fig. 2. Time series of flash frequency and different radar parameters (maximum values) for the northern storm system shown in Fig. 1. 'AML' and 'BML' indicate values above and below the melting level, respectively.

4. CONCLUSIONS

Based on polarimetric radar parameters, the results presented in the present study demonstrate that the

release of precipitation (hail) to the ground is accompanied by an increase of the storm's lightning activity. This type of dependency is in accordance with the findings of previous studies (Williams et al. 1989). In addition, more information on the types of precipitation particles as well as on their concentration is obtained by the polarimetric measurements.

5. ACKNOWLEDGEMENTS

The LPATS data were kindly provided by the Bayernwerk AG.

6. REFERENCES

- Carey, L. D., and S. A. Rutledge, 1995: Positive cloud to ground lightning in severe hailstorms: a multiparameter radar study. *27th Conference on Radar Meteorology*, Vail, CO, USA, 9-13 October 1995, 629-632.
- Finke, U., and T. Hauf, 1996: On the spatial and temporal distribution of thunderstorms in southern Germany. This preprint volume.
- Höller, H., V.N. Bringi, J. Hubbert, M. Hagen and P.F. Meischner, 1994: Life cycle and precipitation formation in a hybrid-type hailstorm revealed by polarimetric and Doppler radar measurements. *J. Atmos. Sci.*, **51**, 2500-2522.
- Höller, H., 1995: Radar-derived mass-concentrations of hydrometeors for cloud model retrievals. *27th Conference on Radar Meteorology*, Vail, CO, USA, 9-13 October 1995, 453-454.
- Lopez, R. E., and J. P. Aubagnac, 1995: The lightning activity of a hailstorm as a function of changes in its microphysical characteristics inferred from polarimetric radar observations. *27th Conference on Radar Meteorology*, Vail, CO, USA, 9-13 October 1995, 626-628.
- Seliga, T.A., and V.N. Bringi, 1976: Potential use of radar differential reflectivity measurements at orthogonal polarizations for measuring precipitation. *J. Appl. Meteor.*, **15**, 69-76.
- Williams, E.R., M. E. Weber, and R. E. Orville, 1989: The relationship between lightning type and convective state of thunderclouds. *J. Geophys. Res.*, **94**, 13213-13220.

THE HOMOGENEOUS NUCLEATION KINETICS OF WATER VAPOR NEAR A SMALL ICE BIT

Sergei P. Fisenko

A.V.Luikov HMTI, Minsk, 220072, Belarus, CIS

1. INTRODUCTION

It is well known, that during a quite long period of time large gradients of the temperature and the chemical potential of the water vapor can be observed in the mixture air- water vapor - ice bit. Therefore there is the big supersaturation of water vapor and nucleation takes place. The homogeneous nucleation of water vapor near ice bit is the important problem for microphysics of clouds. The classic theory of the nucleation kinetics can be applied for description nucleation kinetics only for spatially uniform systems. Hence more developed theory of the nucleation kinetics is necessary for the investigation of such effects, as the nucleation in a supersaturated vapor near ice bit.

The modern theory of the nucleation kinetics in gaseous system with big gradients of thermodynamic variables, which was developed by the author earlier. This theory is used to investigate the nucleation kinetics of water vapor near ice bit now. The mathematical model of such kinetics includes the two-fold kinetic equation for the cluster distribution function, equation for heat and mass transfer between the ice bit and the mixture of air - water vapor. The steady - state approximation are used here and some temporal estimates are made.

2. MATHEMATICAL MODEL

We will use the distribution function $f(g, x)$, where g is the number of molecules at the new phase cluster at x point. The kinetic equation for $f(g, x)$ was obtained by Fisenko(1990) using the methods of nonequilibrium statistical thermodynamics developed by Zubarev (1974). This equation can be written as

$$\begin{aligned} \partial_t f(g, x, t) = \partial_g \{ f(g, x, t) L_{11}(x) \\ \partial_g [\ln f(g, x, t) + \Delta\Phi(g, x)\beta(x)] \} + \\ + \nabla \{ f(g, x, t) [-v(g, x) + D\nabla(\ln f(g, x, t))] \} \end{aligned} \quad (1)$$

where $\Delta\Phi(g, x)\beta(x)$ is the dimensionless free energy cluster formation, nucleation coefficient L_{11} is weakly depending on x in contrast of classical nucleation theory

$$L_{11}(x) = n(x)kT(x)\Sigma(x) / \sqrt{2\pi mkT(x)}$$

$\beta(x)=1/kT(x)$, m is the mass of the water molecule, $\Sigma(x)$ is the surface area of critical cluster (Frenkel) at x point, $n(x)$ and $T(x)$ are, respectively, the water vapor density and the temperature of system at x point, k is the Boltzmann constant, v is the phoretic velocity of clusters, depending on the gradient of temperature, and D is the coefficient of brownian diffusion of clusters at physical space (Fuchs(1964)). For steady-state regime a similar equation was written by phenomenological way by Shi et al. (1990)

Also, the mathematical model includes the two equations, which are necessary to find distribution vapor density $n(x)$

$$\partial_t n(x, t) = D_w \nabla^2 n(x, t) \quad (2)$$

where D_w is the water vapor in air diffusivity coefficient, and the distribution temperature of the vapor-air mixture $T(x, t)$

$$\partial_t T(x, t) = a^2 \nabla^2 T(x, t) \quad (3)$$

where a^2 the air thermal diffusivity coefficient. The boundary conditions are the following:
at surface ice bit

$$\begin{aligned} f(g, x) &= 0 \\ n(x, t) &= n_s(T_1) \\ T(x, t) &= T_1 \end{aligned}$$

where $n_s(T_1)$ is the density of saturated water vapor at temperature T_1 .

Far from the ice bit the temperature of vapor-air mixture is equal to T_0 and the humidity of air is equal to ϕ , so the water vapor density is equal to $n_s(T_0)\phi$ and the value of distribution function $f(g, \infty)$ is equal 0.

If R is the characteristic spatial scale of the ice bit then the temporal scale of diffusion process τ_d can be estimated as

$$\tau_d \approx R^2 / D_w$$

and at the same manner the temporal scale of the thermal diffusion process τ_t can be estimated as

$$\tau_t \approx R^2 / a^2$$

If $R > 0.001m$, then $\tau_d \sim 0.1s$. So, this time much greater than characteristic temporal scale of nucleation τ_n which as the rule is about 10^{-7} s. On the basis of this estimates

we will use the steady-state solutions of the equation (2) and (3).

3. SPHERICAL- SYMMETRICALLY ICE BIT

Let us begin calculate the nucleation rate near the spherical-symmetrically ice bit with the radius R . At Fig.1 the supersaturation $S(r)$ is presented, where r is the distance from the center of the ice bit.

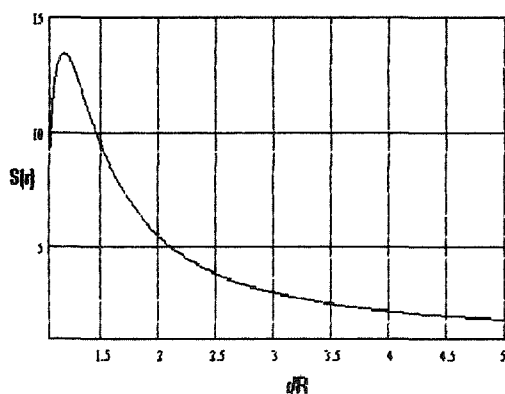


Figure 1. The dependence of supersaturation $S(r)$ versus dimensionless distance r/R . $T_1 = 273\text{K}$, $T_0 = 279\text{K}$ and the relative humidity $\phi = 0.9$

Note, that the coordinate of the supersaturation maximum is equal to $r/R = 1.19$ for mention above conditions near ice bit.

The dimensionless free energy formation cluster $\Delta\Phi(g, x)\beta(x)$ (Frenkel (1945)) has more complicated behavior. It was shown by our calculations that the surface of $\Delta\Phi(g, r)\beta(r)$ has the saddle point. The coordinates of the saddle point on the plane (g, r) are equal $g^* \approx 13$, $r^*/R \approx 1.18$ and $\Delta\Phi(g^*, r^*)\beta(r^*) = 17.8$. These parameters don't depend on the ice bit radius. The saddle point exists determine the nucleation kinetics near ice bit mainly. The boundary conditions for the equation (1) are the generalization of the usual boundary conditions used in the theory of nucleation kinetics.

Usually, the motion of nucleus of new phase at the cluster size space is the fastest process. Only the supercritical clusters move at physical space. Indeed, the characteristic nucleation time τ_n is about $\tau_n \approx g_c^2 / L_{11}$, where g^* is the number molecules at the critical cluster. The estimates have been shown that the kinetic equation can be split, and we can solve the modified Frenkel-Zeldovich equation (the first term at right side equation (1)) at neighborhood of the saddle point. The well-known Zeldovich solution (Frenkel) permit now to easy calculate, but only the density nucleation rate $I(r)$. The total nucleation rate for steady-state regime I is equal to the integral from $I(r)$ over r . At Fig.2 the density nucleation rate $I(r)$ is presented for the same conditions near ice sphere as Fig.1

The total nucleation rate I is equal to

$$I = 4\pi \int_R^\infty I(r) r^2 dr \quad (4)$$

The dependence I from radius R is obvious

$$I \sim R^3.$$

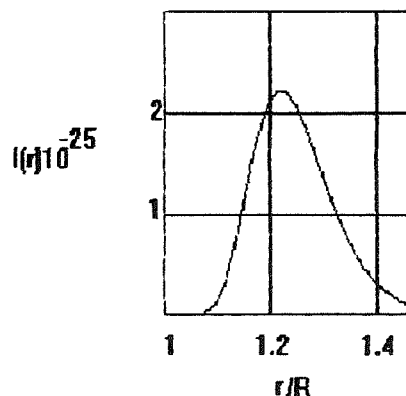


Figure 2. The dependence of the density nucleation rate $I(r)$ versus dimensionless distance r/R . $T_1 = 273\text{K}$, $T_0 = 279\text{K}$ and the relative humidity $\phi = 0.9$

4. DISCUSSION OF RESULTS

The temperature difference between the ice bit and air and relative humidity play the most important role in determine the value total nucleation rate I . As was shown by our numerical simulation there is minimal temperature difference for beginning of the homogeneous nucleation near ice bit. If $T_1 = 273\text{K}$, then the minimal temperature difference $(T_0 - T_1)$ is equal to 4K . The bigger the temperature difference the bigger total nucleation rate. The increasing the temperature difference on 1K enhanced the nucleation rate for the same humidity about 3 orders. At table 1 dependence I from relative humidity ϕ are presented ($R = 6 \cdot 10^{-3}\text{m}$, $T_1 = 273\text{K}$ and $T_0 = 279\text{K}$).

table 1

ϕ	0.6	0.8	1
$I(\text{s}^{-1} \text{m}^{-3})$	$5 \cdot 10^{15}$	$2 \cdot 10^{18}$	$9 \cdot 10^{19}$

The existence of small water clusters near ice bit strongly decrease the velocity of heating of ice bit because the release of the latent heat of the phase transition takes place out of surface. This effect can be refined for non steady-state conditions. The fast growth water clusters can drastically changed the vapor density near ice bit. This problem is under investigation now. The thermophoretic force (Fuchs) will move the clusters to the surface of ice bit during about 10^{-2}s , so its disappear. But due to brownian diffusion a division of clusters will enhanced the rate of phase transition.

The air flows near ice bit make the situation more complicated but much more realistic for microphysics of clouds.

5. REFERENCE

- Fisenko, S.P., 1995: Nucleation kinetics in spatially nonuniform gaseous systems. *Prague Workshop on Nucleation*
- Fuchs, N.A., 1964: *The Mechanics of Aerosols*. Pergamon Press, Oxford
- Frenkel, J.I., 1955: *Kinetic Theory of Fluids*, Dover, New York.
- Shi, G., Seinfeld, J.H. and Okuyama, K, 1990: Homogeneous nucleation in spatially inhomogeneous systems. *J. Appl. Phys.* 68, 4550-4555.
- Zubarev, D.N., 1974: *Nonequilibrium Statistical Thermodynamics*. Plenum, NY

MICROPHYSICAL AND ELECTRICAL PHENOMENA DURING FREEZING OF WATER DROPS AND HAILSTONE GROWTH

Anatoli Adzhiev

High – Mountain Geophysical Institute, Nalchik, RUSSIA

The formation of electrical structure of convective cloud is very complex and now there is no enough information on the electrification mechanisms of cloud particles.

The present paper describes the experimental study of some electrification processes coming into being in single-phase and multi-phase aerosol systems. The electrical charge separation was studied related to the following processes: drop freezing, hailstone growth, collision of ice crystals and super-cooled water drops with hailstones.

The effect of such different factors on the process of charge separation as the size of drops, hailstones and ice crystals, the environmental temperature, hailstone growth rate, humidity and so on was studied in the experiments. The achieved laboratory data were compared to the convective cloud investigations made by the active – passive radars.

In the most experiments, studied this phenomenon, the limit charge of the frozen drop was measured. But this method does not allow to make the accurate estimate of the total amount of the electrical charge separated during the drop freezing and hailstone growth. As it is known, the reason of the charge appearance is the mass separation during the drop freezing and hail growth and due to in what phase (solid, liquid or gaseous) and in what amount the particle separates from the drop the magnitude and the sign of the charge change. So the residual charge, as the sum of charges accumulated as the result of the multiple separations of mass during the drop freezing and hailstone growth, does not characterize this process to the full.

Some experimental results of the effect of the pointed factors on the electrical charge separation are given in this paper. The detection of the charge was based on the measurement of the electric current from the freezing drop. The source of the recorded electrical current was the charge appeared on the frozen drop which was caused by the mass separation at presence of the contact potential difference on the vapour – water – gas interface. The mass separation during the

water freezing takes place during 0.01...0.1s. That is why to study so quick processes of electric charge separation during drop crystallization the high – sensitive electrometer was used. It's current sensitivity is $1 \cdot 10^{-15}$ A at the input resistance of $5 \cdot 10^{11}$ ohm and input capacity of 20 pF.

In the tests the measurement error was 1.8 % and the accuracy of charge detection was 26 %. As a rule the crystallization in tests began on the drop surface or on the water coat of hailstone. At first, it covers the ice coat, then during crystallization the solid coat began curving, bulging and cracking due to the excess pressure inside the drop. The air bubbles, microparticles of water and ice came from the frozen drop or hailstone. Very often the explosion – like splitting of drops into frozen debris takes place. During the hailstone growth the ejection of the ice particles, water droplets and air bubbles takes place as well.

Usually during the covering of the drop by ice coat the small particles are observed on the plot (section BC, Fig.1). 99 % of the tests contains the positive pulses and 1 % – negative ones.

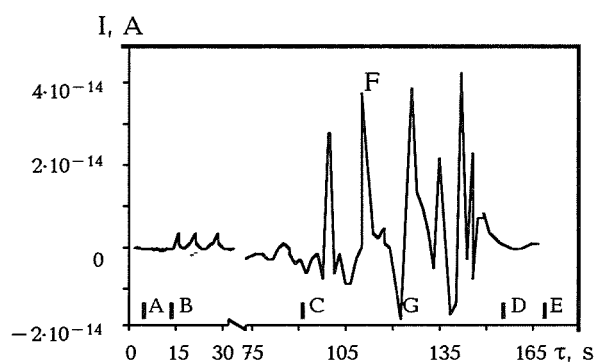


Fig.1. The record of the electric current from the frozen drop at -20°C with 2 mm diameter. AB, DE is the background current, B is coating moment of drop by ice coat, CD is the current during multiple ejection of particles, F is the current pulse at the ice particle ejection, G is current pulse at the ejection of liquid particle or air bubble.

The separation of the largest electrical charge is observed at the explosion-like splitting of the freezing drop. The crystallization of the supercooled water drops with the explosion-like splitting as a rule is observed at the temperature interval $-8...-16$ °C.

The probability of the explosion-like splitting is 10...12 % for the water drops with electrical conductivity of $2.4 \cdot 10^{-6}$ S/cm and pH=5.3.

At the peculiar conditions which are differ from the conditions observed in clouds (Takahashi, Yamashita, 1969) the freezing of drop fraction with explosion-like splitting can reach 40 %.

Our experimental results showed that the maximum charge, separating during the explosion-like splitting of drops can reach the value of 10^{-10} C. If after the splitting the crystallization of the residual continues the remained part of drop achieves the positive charge. If the explosion-like splitting occurs at the end of crystallization the charge sign can be any. The mean value of the separating electrical charge therewith is $3 \cdot 10^{-10}$ C per gram of freezed water.

Oscillographic measurements showed that the time of the charge separation at the explosion-like splitting equals to 0.01...0.1 s and the current growth speed is from 10^{-11} to 10^{-10} A/s at the mean value of $8 \cdot 10^{-11}$ A/s. In the range of 600 μ m to 2 mm we were failed to detect the relationship between the value and sign of charge on drop size.

At the absence of the visual explosion-like splitting the drop electrification is observed from the covering moment by ice coat up to the total freezing.

To detect the optimal temperature regimes with the more intensive mass separation a set of experiments on the waterdrop freezing at the interface of two not mixed and optically transparent media was conducted. The technical oils with different density were used the viscosity of which increased with temperature decrease, preventing the removal of the splitting microparticles from drop. The average size of the splitted microparticles and their amount increased with the drop diameter increase. From the freezing drop with millimetre size up to 30 particles were splitted, about 10 of which were qualified as solid

according to their form and colour. The largest amount of the ejections was observed in the temperature interval of -8 to -16 °C. The sizes of the splitted particles varied from 10 to 100 μ m with average value of 35 μ m. The value of maximum charge for distilled water was of $7 \cdot 10^{-12}$ C per gram of freezed water.

At the "calm" crystallization the pulsing separation of electric charge is observed (Fig.1, section CD) during the whole freezing process. In this case the charge separation was related to the intensive and multiple ejection of different debris from the surface of freezed drop. Meanwhile the water particles and air bubbles took away as a rule the positive charge but ice particles — the negative one. The number of the elemental events of charge separation in some tests reached up to 30. The charge separation is more intensive in temperature interval of $-5...-15$ °C.

So we can make the following conclusions:

1. The mass separation leads to the charge separation during the crystallization of waterdrops. The value and sign of the residual charge depend on in what phase (solid, liquid, gaseous) and in what amount the particle separates from the drop.

2. The largest effect of the electrification up to $3 \cdot 10^{-10}$ C per gram of water is observed during the explosion-like splitting of the freezed drops.

3. At the absence of the explosion-like splitting the air bubbles and microparticles of water and ice separate from the drop. Up to 30 particles flow away from the millimetre drop at the freezing in the temperature interval of $-8...-16$ °C. Among them 10 particles have the solid phase and average size of 35 μ m.

4. The every event of the microparticle ejection from the freezed drop leads to the separation up to 10^{-13} C of electric charge depending on the chemical content of water.

5. The largest separation effect takes place during the hailstone growth when the water droplets and ice crystals collide with the growing hailstone in the temperature interval of $-6...-12$ °C.

REFERENCES

Takahashi T., Yamashita A. 1969. Deformation and fragmentation of freezing water drops in free fall. J. Meteorol. Soc. Japan., 47, 6.

SUPERCOOLED CLOUD TUNNEL STUDIES ON THE RIMING GROWTH OF SNOW CRYSTALS

Tsuneya Takahashi¹ and Tatsuo Endoh²

¹Center for Educ. Res. & Develop, Hokkaido Univ. of Educ., Sapporo 002, JAPAN

²Inst. of Low Temp. Sci., Hokkaido Univ., Sapporo 060, JAPAN

1. INTRODUCTION

The riming of snow crystals or the capture of supercooled cloud droplets by snow crystals is one of the fundamental precipitation formation processes. The riming process has important effects on the evolution of a cloud, such as the water budget and the precipitation efficiency.

There have been many studies on the riming characteristics of snow crystals in natural clouds, such as the minimum snow crystal dimensions for the onset of riming and the size distribution of captured droplets. To study the riming growth of snow crystals quantitatively, however, experiments under clearly controlled conditions are necessary.

In this paper, we report the results of experiments on the riming growth of snow crystals.

2. EXPERIMENTS

The present study was carried out using a supercooled cloud tunnel, in which a snow crystal can be suspended freely and grown by applying aerodynamical mechanisms for horizontal stability, which are described in detail by Fukuta et al. (1982), Takahashi and Fukuta (1988b) and Takahashi et al. (1991).

Experiments were carried out at constant temperatures with a liquid water content of 1.5 to 2.5 g m⁻³. The liquid water content was calculated from the temperature in the cloud and the dew point of the cloud after evaporation which were continu-

ously monitored by a thermistor thermometer and a quartz dew point hygrometer, respectively. The distribution of droplets sizes in a supercooled cloud was measured by an impactor. The average diameter was 10.1 μ m. The average charge of a cloud droplet was below 10⁻⁷ esu, measured by an oscillation method using an electrical field of alternating current (Wells and Gerk, 1919). Theoretical studies by Schlamp et al. (1976) have indicated that electrostatic charges do not have a significant effect on the riming growth of snow crystals.

3. RESULTS AND DISCUSSION

3.1 Riming characteristics

Figure 1 shows examples of rimed crystals grown at about -5.5 and -14.5°C. The photographs shown for the same temperature are different crystals grown at the indicated periods of time. At both temperatures, few droplets were captured by crystals during the early growth stage. For a temperature of about -5.5°C, riming was striking, especially on the crystal edges, at growth time of 12 min. Crystal growth ceased because the crystal surfaces were filled with rime droplets. The shapes of rime droplets could not be recognized, which indicated that the water film, which was formed by cloud droplets captured on the crystal, was frozen.

For a temperature of about -15.5°C, riming was prominent at a growth time of 15 min, although

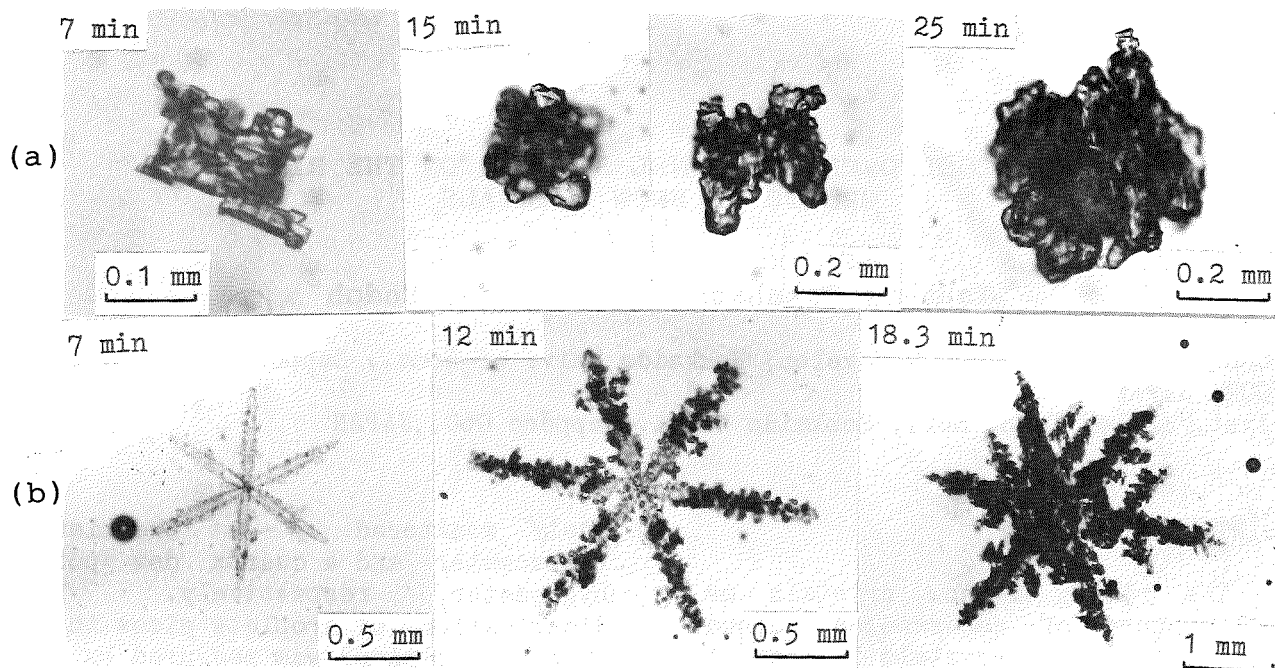


Fig. 1 Rimed crystals grown at about (a) -5.5°C and (b) -14.5°C under a liquid water content of 1.6 to 2.2 g m^{-3} . The growth time is shown in each photograph.

considerably fewer frozen droplets were captured within a circle of 0.2 mm radius from the dendritic crystal center. This annular riming pattern is common with naturally rimed planar snow crystals. This behavior may be explained by the viscous force which moves the droplets around the falling crystal (Pitter and Pruppacher, 1974). It was confirmed from the displacement of focus under a microscope that the rimed parts grew to windward. Figure 2 shows side views of rimed dendritic crystals. Few cloud droplets attached to the upward crystal surface. This is because shape-enhanced crystals hardly turned over due to the stability of attitude. The shapes of rimed droplets were maintained because cloud droplets were frozen immediately after they were captured on the crystals. In the natural atmosphere, the rimed parts seem to separate easily from the mother crystal by wind shear, and then become rimed particles, which have been classified by Magono and Lee (1966). The particles seem to develop into graupel. By carefully disassembling natural graupel particles under a stereomicroscope, Takahashi and Fukuta (1988a) showed that embryos were not clearly identifiable in

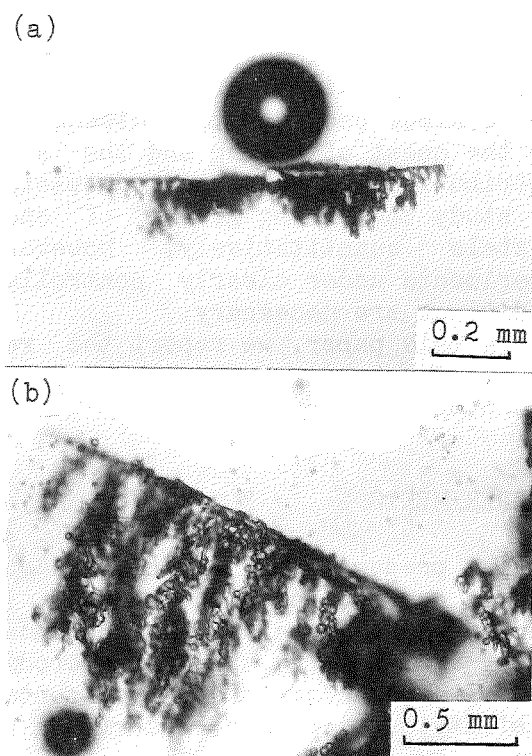


Fig. 2 Side views of (a) a rimed dendritic crystal and (b) a rimed dendritic branch. Experiments were carried out for growth times of 12 and 20 min, respectively, at about -14.5°C under a liquid water content of 1.5 g m^{-3} .

the majority of graupel particles, suggesting that embryos in graupel particles occur as a result of rime breakup.

3.2 Fall velocity and mass

Figure 3 shows the variation in fall velocity of a dendritic crystal (right-hand side of Fig. 1) with time. The variation to a growth time of 6 min overlapped with that of vapor diffusional growth reported by Takahashi et al. (1991). This was because the snow crystal grew only by vapor deposition during the early growth stage. Two sharp bends were seen at growth times of 6 and 16 minutes. These bends indicated the onset and the superiority of riming, respectively. The onset size of riming was 0.8 mm, calculated using the empirical relationship by Takahashi et al. (1991). The size was in agreement with that of ordinary dendritic crystals observed by Harimaya (1975).

Figure 4 shows the variation in crystal mass with time in the log-log scale at about -14.5°C . The variation was represented by a

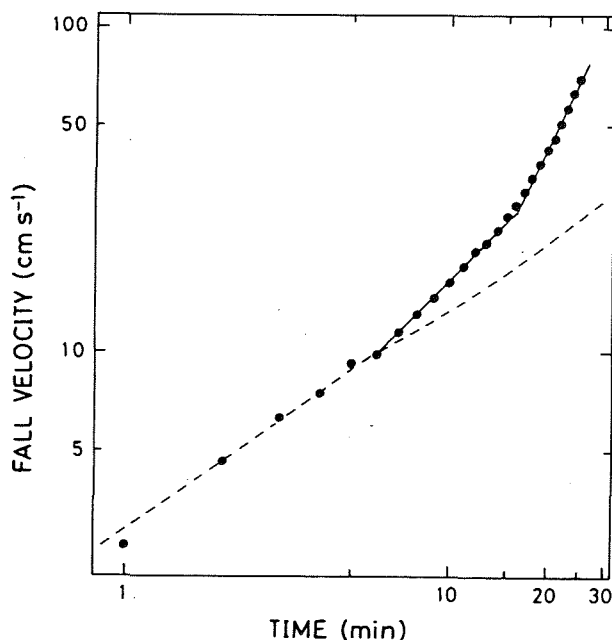


Fig. 3 Variation of fall velocity of a dendritic crystal with time, analyzed at 1-min intervals from the recorder chart. The dashed line shows the vapor diffusional growth case under water saturation (Takahashi et al., 1991).

straight line.

3.3 Collection efficiency

The collection efficiency (E) was calculated by the following equation:

$$E = \frac{(\text{dm}/\text{dt})_{\text{exp}} - (\text{dm}/\text{dt})_{\text{v}}}{w_{\text{L}} S V},$$

where $(\text{dm}/\text{dt})_{\text{exp}}$ is the mass growth rate obtained from Fig. 4 and $(\text{dm}/\text{dt})_{\text{v}}$ is the mass growth rate by vapor deposition. w_{L} , S and V are the liquid water content, the cross-sectional area of a crystal exposed to the flow and fall velocity of the crystal, respectively. $(\text{dm}/\text{dt})_{\text{v}}$ and S for dendritic crystals were calculated using the empirical relationship by Takahashi et al. (1991).

Figure 5 shows the relationship between the collection efficiency and the Stokes number of dendritic crystals. The collection efficiency of cloud droplets with a dendritic crystal was almost constant, i.e. 0.15 to 0.2, at the Stokes number ranging between 0.15 and 0.4.

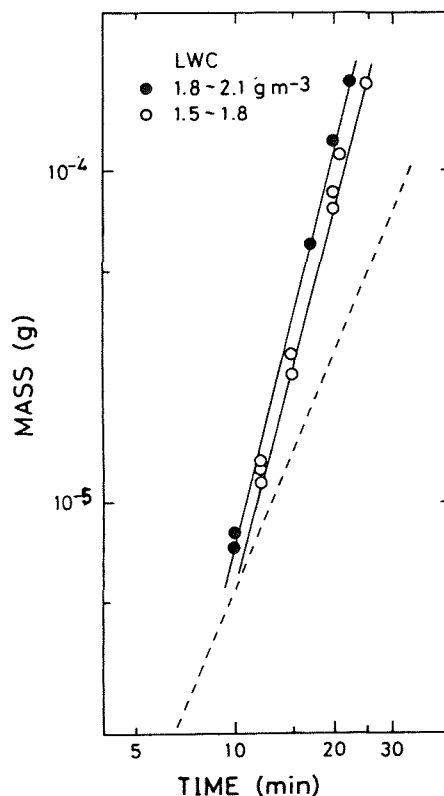


Fig. 4 Variation of crystal mass with time at -14.5°C . The dashed line shows the vapor diffusional growth case under water saturation (Takahashi et al., 1991).

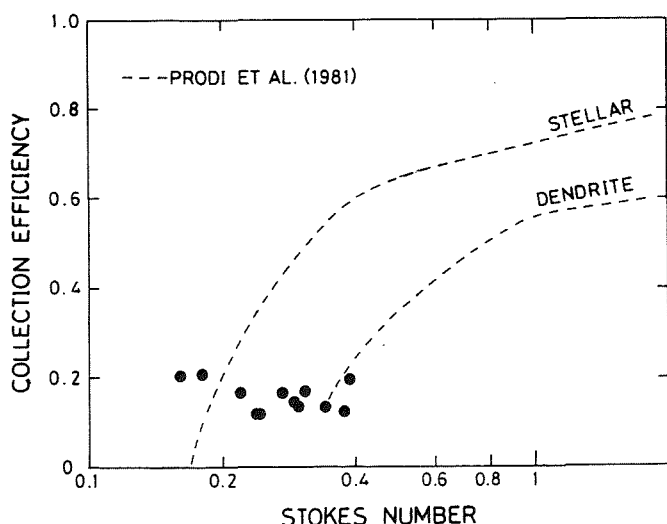


Fig. 5 Collection efficiency as a function of the Stokes number for dendritic crystals grown at about -14.5°C . Also shown are the experimental results for planar-shaped models by Prodi et al. (1981).

4. SUMMARY

Riming properties of snow crystals were studied under free suspension in a supercooled cloud tunnel.

Snow crystals captured very few cloud droplets during the early growth stage. In columnar crystals grown at about -5.5°C , there was marked riming at the crystal edge and all the crystal surfaces were filled with rime droplets. In a dendritic crystal grown at around -14.5°C , rime droplets accumulated only on the windward crystal surfaces. Few cloud droplets attached to the surface within a radius of 0.2 mm from the crystal center, which is a common pattern in a naturally rimed crystal. The riming structures were all delicate. The variation in fall velocity with time showed two bends, corresponding to the onset and the superiority of riming. The collection efficiency of cloud droplets with a dendritic crystal was almost constant, i.e. 0.15 to 0.2, at the Stokes number ranging between 0.15 and 0.4.

ACKNOWLEDGEMENTS. We gratefully acknowledge the financial support of the Sumitomo Foundation. This work was a joint research conducted at the

Inst. of Low Temp. Sci., Hokkaido Univ..

REFERENCES

- Fukuta, N., M. W. Kowa and N. H. Gong, 1982: Determination of ice crystal growth parameters in a new supercooled cloud tunnel. Proc. Conf. on Cloud Phys., Chicago 15-17 Nov. 1982, 325-328.
- Harimaya, T., 1975: The riming properties of snow crystals. J. Meteor. Soc. Japan, 53, 384-392.
- Magono, C. and C. W. Lee, 1966: Meteorological classification of natural snow crystals. J. Fac. Sci., Hokkaido Univ., Ser. VII, 2, 322-335.
- Pitter, P. L. and H. R. Pruppacher, 1974: A numerical investigation of collision efficiency of simple ice plates colliding with supercooled water drops. J. Atmos. Sci., 31, 551-559.
- Prodi, F., M. Caporloni, G. Santachiara and F. Tampieri, 1981: Inertial capture of particles by obstacles in form of disks and stellar crystals. Quart. J. R. Met. Soc., 107, 699-710.
- Schlamp, R. J., S. N. Grover, H. R. Pruppacher and A. E. Hamielec, 1976: A numerical investigation of the effect of electric charges and external electric fields on the collision efficiency of cloud drops. J. Atmos. Sci., 33, 1747-1755.
- Takahashi, T., T. Endoh, G. Wakahama and N. Fukuta, 1991: Vapor diffusional growth of free-falling snow crystals between -3 and -23°C . J. Meteor. Soc. Japan, 69, 15-30.
- Takahashi, T. and N. Fukuta, 1988a: Observation of the embryos of graupel. J. Atmos. Sci. 45, 3288-3297.
- Takahashi, T. and N. Fukuta, 1988b: Supercooled cloud tunnel studies on the growth of snow crystals between -4 and -20°C . J. Meteor. Soc. Japan, 66, 841-855.
- Wells, P. V. and R. H. Gerke, 1919: An oscillation method for measuring the size of ultramicroscopic particles. J. Amer. Chem. Soc., 41, 312-319.

Laboratory Experiments With Supercooled Water Drops In A Vertical Wind Tunnel

ROBERT R. CZYS* AND JEFFREY K LEW†

**Illinois State Water Survey
Office For Cloud and Precipitation Research
Champaign, Illinois*

*†University of California
Department of Atmospheric Sciences
Los Angeles, California*

1. Introduction

This paper reports a result from laboratory experiments with supercooled drops using the UCLA vertical wind tunnel. The experiments were conducted to learn more about the origin and evolution of ice in summer rain clouds.

2. Experiment Setup

The UCLA vertical wind tunnel was set-up to produce collisions between small, supercooled precipitation-size drops. The general characteristics of the wind tunnel have been described in numerous previous papers including Beard and Pruppacher (1969). Figure 1 shows a schematic diagram of the experiment setup and the relative configuration of the major system components.

Drops for experimentation were produced in the upper tunnel working section using a simple drop fountaining system. The system consisted of a 5 liter polyethylene bottle and heat exchanger that fed a curved hypodermic needle that was positioned in the vertical direction within the upper tunnel working section. The supply bottle, filled with distilled deionized water, was slightly pressurized to cause water to continuously flow from the needle tip. The liquid jet emanating from the needle would break-up into a spray of water drops that resembled a fountain. The drop fountain naturally produced a distribution of drops in the size range from about 500 to 1000 μm radius. The smallest drops in the spray were carried upward out of the upper working section. Larger drops fell down through the working section against the air flow in effect producing a light shower of supercooled rain.

Drops from the fountain were introduced at a temperature very near 0°C . This was accomplished by submerging the water supply and heat exchanger in an ice bath. A thermocouple was fastened to the tip of the hypodermic needle to obtain an estimate of the temperature of the water as it entered the tunnel. At times during a trial, it was not unusual for the measured temperature at the needle tip to be several degrees colder than 0°C because of additional cooling caused by the cold air flow. Another thermocouple was used to measure tunnel air temperature. All temperature measurements, as well as tunnel air velocity,

were recorded continuously during each trial using a PC-based data acquisition system (DAS).

A trial began when the fountain needle was inserted into the upper tunnel working section. Next, using a flow-controller-insert the system operator would catch a medium size drop from the shower and "float" it at a quasi-fixed position relative to the view of a macro video camera. Study drops were typically about 500 μm radius as indicated by the tunnel air velocity which was sufficient to float the drop.

Interaction between a subject drop and a drop in the supercooled rain shower was a rare event. Hence, some trials consisted of no drop interactions while other trials consisted of one or more interactions depending on how many subsequent subject drops could be floated. When an interaction occurred, the operator would attempt to adjust the air velocity to keep the result in camera view. It was not always possible to do this because the response of the drops to collision was often much faster than the ability of the operator to anticipate and respond.

Trials in which no interaction occurred served as a control to demonstrate that the subject drop could be reliably supercooled. However, the subject drop did spontaneously freeze on a few occasions. When this happened a reduction of tunnel velocity was required to compensate for the decrease in terminal velocity associated with the aerodynamic difference between a liquid and solid quasi-spherical particle of the same mass. Another feature

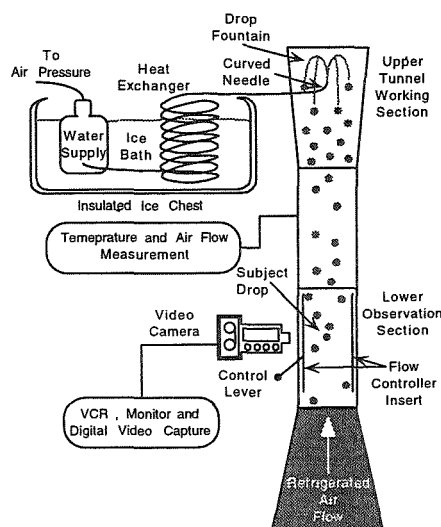


Figure 1. Schematic diagram showing experiment setup.

*Corresponding author's address: Dr. Robert R. Czys, Illinois State Water Survey, Office for Cloud and Precipitation Research, 2204 Griffith Drive, Champaign, IL 61820 - 7495. Tel: 217.333.8496; Telefax: 217.244.0220; e-mail: r-czys@uiuc.edu

exhibited by a frozen subject drop was a very regular orbiting motion around a quasi-stationary point within the flow-controller-insert.

A trial terminated when the build-up of water obscured vision into the tunnel and/or caused air flow instabilities so large that it made it impossible to control a subject drop. This usually occurred 10 to 15 minutes after the fountain needle was inserted into the tunnel. At termination, the fountain needle was removed, the refrigeration system was shut-down and the access ports of the tunnel opened to allow room temperature air to circulate through the tunnel and remove the water build-up.

3. Results

The experiments resulted in several important findings. However, here we limit reporting to one noteworthy result that may be of interest to those who analyze aircraft data and/or who are working on problems related to the evolution of precipitation. Figure 2 shows an extreme close-up of a dumbbell-shaped ice particle that was produced during one of the experimental trials. The figure was produced from a single frame of video imagery recorded several seconds after the particle was created. As indicated in the figure, some of the other larger circular images are out-of-focus water drops that had accumulated on the interior glass walls of the lower observation section.

The sequence of events that led to the ice particle began with spontaneous freezing of the subject drop. Upon freezing, the subject drop began to rise and then interacted with one of the larger supercooled drops in the shower. During this time the system operator made appropriate adjustments to stabilize the motion of the newly formed ice particle and bring it back into view of the video camera. As was seen during the event and recorded on video, the ice particle displayed a dumbbell-shape that obviously rotated around an axis. This movement contrasts with orbital motion associated with the freezing of a single drop.

4. Discussion and Conclusions

The production of a dumbbell-shaped ice particle in these experiments helps explain the presence of other dumbbell-shaped particles that have been identified in particle replicator and 2D Optical Array Probe (OAP) data. Alkezweeny (1969) reported the presence of what appeared to be two small precipitation-size drops that had frozen together on contact near the -10°C level in Arizona convective clouds and attributed this to freezing during the course of collision. Couplet sizes observed by Alkezweeny were 200 and 140 μm , and 120 and 60 μm diameter, respectively. Alkezweeny's report prompted Czys (1994) to examine 2D-OAP image records from 71 cloud penetrations made near the -10°C level of warm-based, Midwestern summer rain clouds. This examination revealed a total of 96

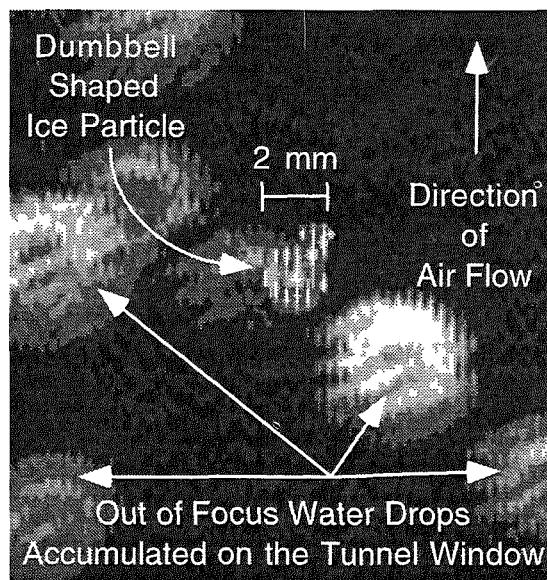


Figure 2. Extreme close-up of dumbbell-shaped ice particle.

dumbbell-shaped images; 21 in 2DP records and 75 in 2DC records. These numbers are too large to be accounted for by coincidence errors (Baumgardner 1985). Hence, the laboratory investigation suggests that double-images in replicator and 2D image data are not artifacts and need to be accounted for in deriving ice particle concentrations from aircraft measurements and in development of conceptual and numerical models about the evolution of precipitation involving ice.

Acknowledgments. This research was conducted with support from the National Science Foundation under grant NSF ATM 9320632.

5. References

- Alkezweeny, A.J., 1969: Freezing of supercooled water droplets due to collision. *J. Atmos. Sci.*, **8**, 994-995.
- Baumgardner, D., W. Strapp, J.E. Dye, 1985: Evaluation of the Forward Scattering Spectrometer Probe. Part II: Corrections for Coincidence and dead-time losses. *J. Atmos. Ocean. Technol.*, **2**, 626-632.
- Beard, K.V., and H.R. Pruppacher, 1969: A determination of the terminal velocity and drag of small water drops by means of a wind tunnel. *J. Atmos. Sci.*, **26**, 1066-1072.
- Czys, R.R., 1995: Preliminary observational evidence of a collision-freezing ice initiation mechanism. Proceedings of the AMS Conference on Cloud Physics, Dallas, Texas, 177-181.

OBSERVATIONAL INVESTIGATION OF CHARACTERISTICS OF HAILSTORM ECHO SHAPE IN PINGLIANG REGION

Zhang Hongfa , Gong Naihu and Wang Zhiju

Lanzhou Institute of Plateau Atmospheric Physics,
Chinese Academy of Science

1. INTRODUCTINO

Radar is the main tool in detecting and warning hailstorm damage, because it returns radar signal may supplied more intuition cloud signature ; such as echo shape and structure, echo intensity, echo height, motion and variation of hailstorms, these factor reflected formation, development, evolution and thermodynamic of severe thunderstorm, and studied to mechanism of it for our.

The recently ten yares radar observation in field, we found that the most hailstorm appeare echo shapes of cyclone pattern measured by radar for the local hail suppression experiment during summers of 1986–1995 in pingliang, following evolving into hook echo, exclusion of the common intensity > 40 dBZ, cloud height > 9.0 Km at $0 > \text{dBZ}$, intensed core thickness > 4.5 km at 40 dBZ . A few very strong hailstorm evolving chatracteristic was from anticyclonic swirling hook into cyclonic inwarding hook. Echo reflectivity maxmum at duration fivetime when hook echo formed and maintained a several minutes, after in this time, cloud height of hook position (intesed core) suddenly increased to 1–3 km and expanded echo area, the overhang separated its downward from the main cloud and whole cloud collapsing. To study the morphotogical structure of hailstorm of development stage, we reviewed a large number of history echo data mearsured by the same radar at the same region during summers of 1974–1985.

The purpose of this paper is to report on observation phenonena about morphogenesis of developing hailstorm in the cruial time, and in order study the relationship associated with evolving process and thermodynamic, enviornment and effects of topography, as well as applies in weather modification.

2. HAILSTORM AND TOPOGRPHY IN PINGLIANG

Pingliang is one of the region with the much hailfall in China, annula mean 18.2 date, it being in eastern of the northwestern plateau of the country. The topography in the region is that the west is higher than the east, in generally 1300–2300 SLH, the Liupan mountain passed through the certra from the north to the south (see Fig.1)

Early at 1972, our institute has been made observation and invesgation in the region, to find out the radar echo characteristic of the local severe thunderstorms, was supported by Chinese

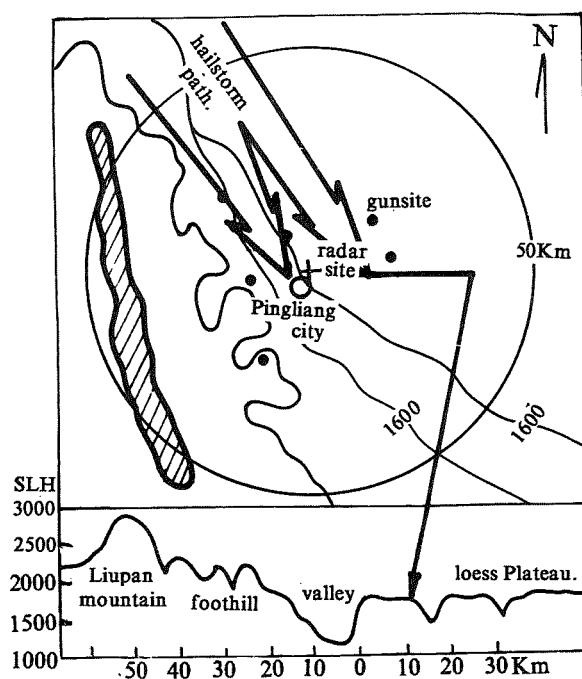


Fig1. The site of radar station, the motion paths of hailstorms and the topography in pingliang.

Academy of Science. So as to suggest a well indicator in identifying hailstorm for the local hail suppression, theoretical studies have been carried out by orographic effects on hailstorm formation mechanisms, active rules and wind fields around mountain.

Since 1986 beginning, we undertaked the local hail suppression that should be demanded by Gansu government, enhancement observation in investigated with X - band conventional weather radar and C - band dual linear polarization radar, the major range of radar measurements was limited 50 km, and the range was to collected hailfall area, hail damage and raindrop distribution data, were use to assess the radar, we have enhanced attention to the variation and discrimination of echo morphotogy structure feature of hailstorm and combine echo parameters and palarization feature echo.

3. CHARACTERISTICS OF ECHO SHAPE OF HAILSTORM

The echo shapes reexamined form 347 storms of developing stage and matureing stage during

1974-1995 as follows:

(1) The most hailstorm echo shape exhibited cyclone pattern in developing process, occupying all echo data 73%, these echo all producted hailfall belong to midrate to strong hailstorms, the reflectivity $> 40\text{dBZ}$, cloud height $> 9.0\text{ km}$. Occupying 45% exhibited distinite hook echo, these echo reflectivity $> 50\text{dBZ}$, cloud height $> 12\text{ km}$ (see Fig.2). Occupying about 10%, exhibited anticyclonic hook echo, these echo is very strong hailstorms (see Fig.3), and evolution characteristics was from anticyclonic hook into cyclonic hook echo.

(2) The hook position usually located in the main echo rear of hailstorm movement direction, the cyclonic hook appeared at the right rear flank of the reflectivity maximum, the anticyclonic hook at left rear flank. Hook part displayed like opening ring, diameter of ring is normally at $1 < 3\text{ km}$, and linking flank with the main echo appeared high reflectivity gradient. They were vertical profile (RHI) of all hook echo is consist of the overhang , the vault or weak echo region and echo wall.

(3) Forming hook echo from cyclone pattern

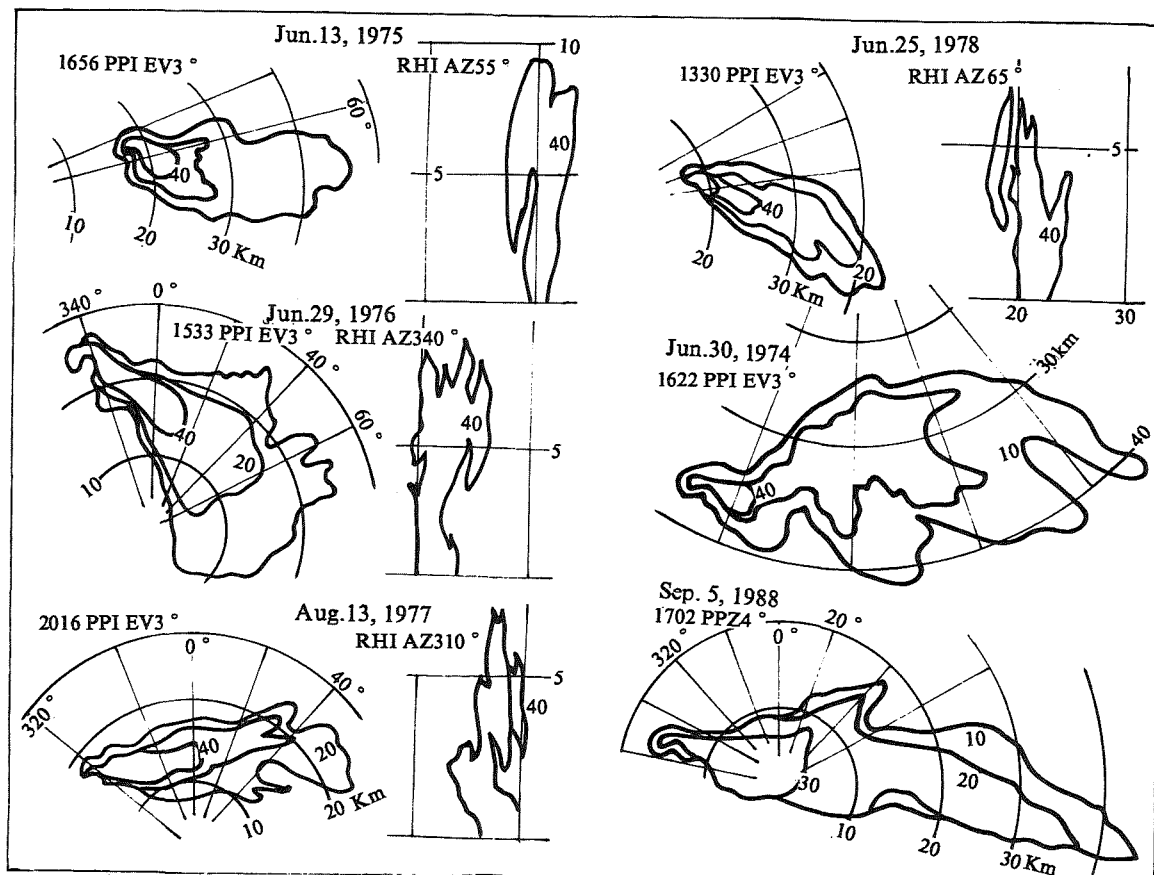


Fig2. The partly of hailstorm in pingliang appeared cyclonic houk echo(PPI)and vertical profile (RHI).

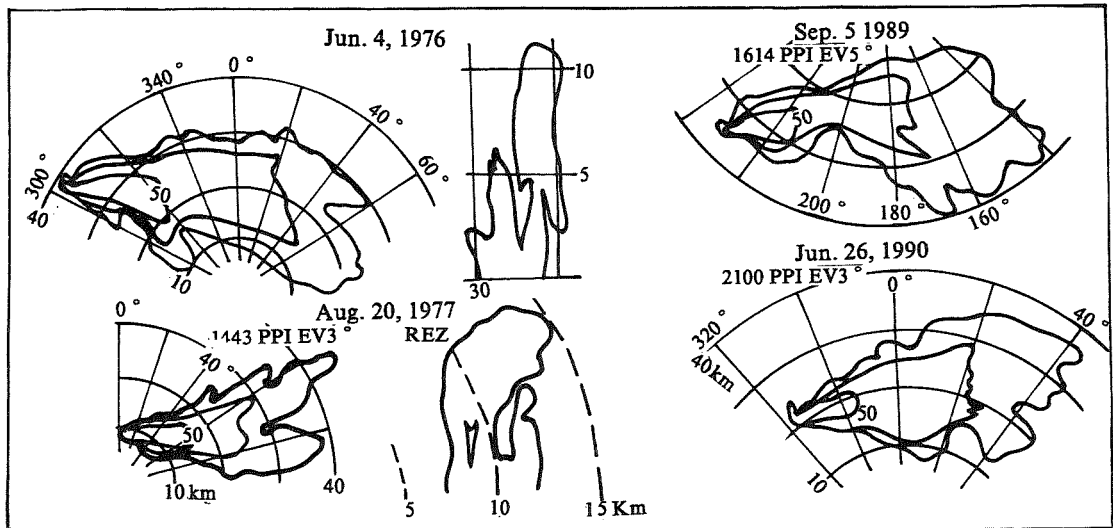


Fig3. The partly of hailstorm in pingliang appeared anticyclonic hook echo(PPI)and vertical profile (RHI, REI).

echo a general needed 3–5 min., then and maintained 5–8 min, the echo displayed motion slowly or not, at this time the echo intensity occurred the strongest stage at duration entire time. Secondly, the hook shrinked tend to disappear, and expanded echo area, then the cloud height of hook position in this time suddenly leaping uprised to 1–3 km (see Fig.4), the overhang separated it downward from the main cloud, soon after, occurring on the surface hail, A few hailstorm can lasting longtime about 30 min, they have reproduced from anticyclonic hook evolving into cyclonic hook.

(4) The hailstorm of exhibition hook echo moved the main direction from northwest to southeast along the east flank of the Liupan mountain, some time motion to favoured east, but the strong hailstorm moved direction from north to south, and trailing echo area is larger than echo area of other movement direction. The hailstorm motion direction associated with mid-latitude wind direction, hailstorm of hook echo in motion were deviated to right of the wind direction, normally is deflected 40–60° .

4. ANALYSIS TO TYPICAL HOOK ECHO AND LEAP INCREASING OF A HAILSTORM

In order to prove these characteristics about, we detailed the radar echo of a hailstorm, Fig.5

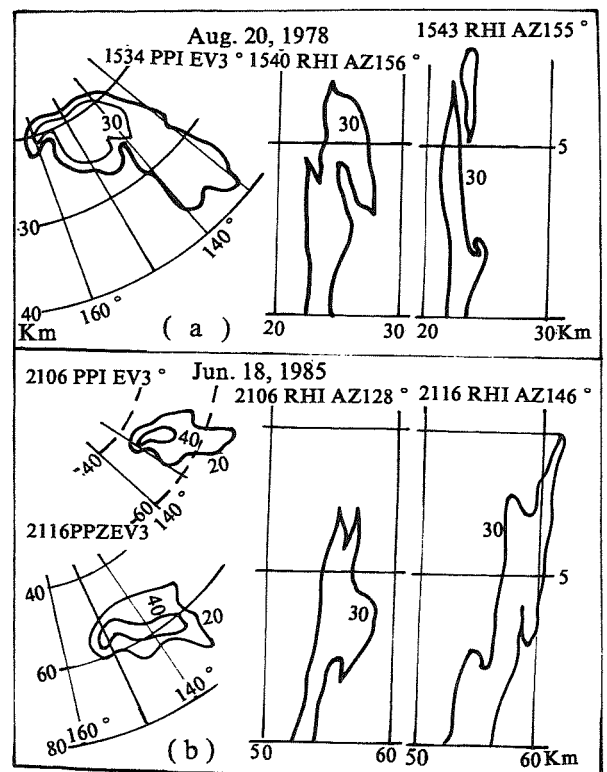


Fig4. The two events of ordinary hailstorm in pingliang exhibited the hook echo(PPI)and its profile (RHI)of leaping phenomena. (a) X-band radar measurements (b) C-band radar measurements.

displayed echo morphological structure of developing hailstorm that observed by radar in Jun. 4, 1976. PPI radar echo at 1917 BJT exhibited distincte anticyclonic spiralling hook echo, 4 min after, the hook part shirnked and disappeared, echo area expanded 2-3 times, this time RHI appeared obviously the vault and weak echo region, cloud height about 11.0km at 40 dBZ, vertical profile displayed up side large and the main body small. 1929 BJT, PPI echo decresed echo area agine, RHI exhibited cloud height leaping uprise 1.0km at 40dBZ and the overhang separated the main body downwead from it before high, acorrding to report on occurring the surface hail at this

time. To 1934 BJT, the strong hailstorm evolved the cyclonic hook echo, the hook echo lasting long time until 1959 disappeared, 1944 BJT, RHI displayed echo shape of vertical profile like look 1921(BJT) RHI, but cloud height is lower 1.0 km than it, about 6 min after, the overhang splited with the main echo and it downward, PPI hook echo was cyclonic spiralling in ward and increaded large area, soon after, reported to occurring the surface of severe hail.

This events in pinliang was every year, the midrate to stronger hailstorm occurred frequently, dut to space was limited, we were not illustration.

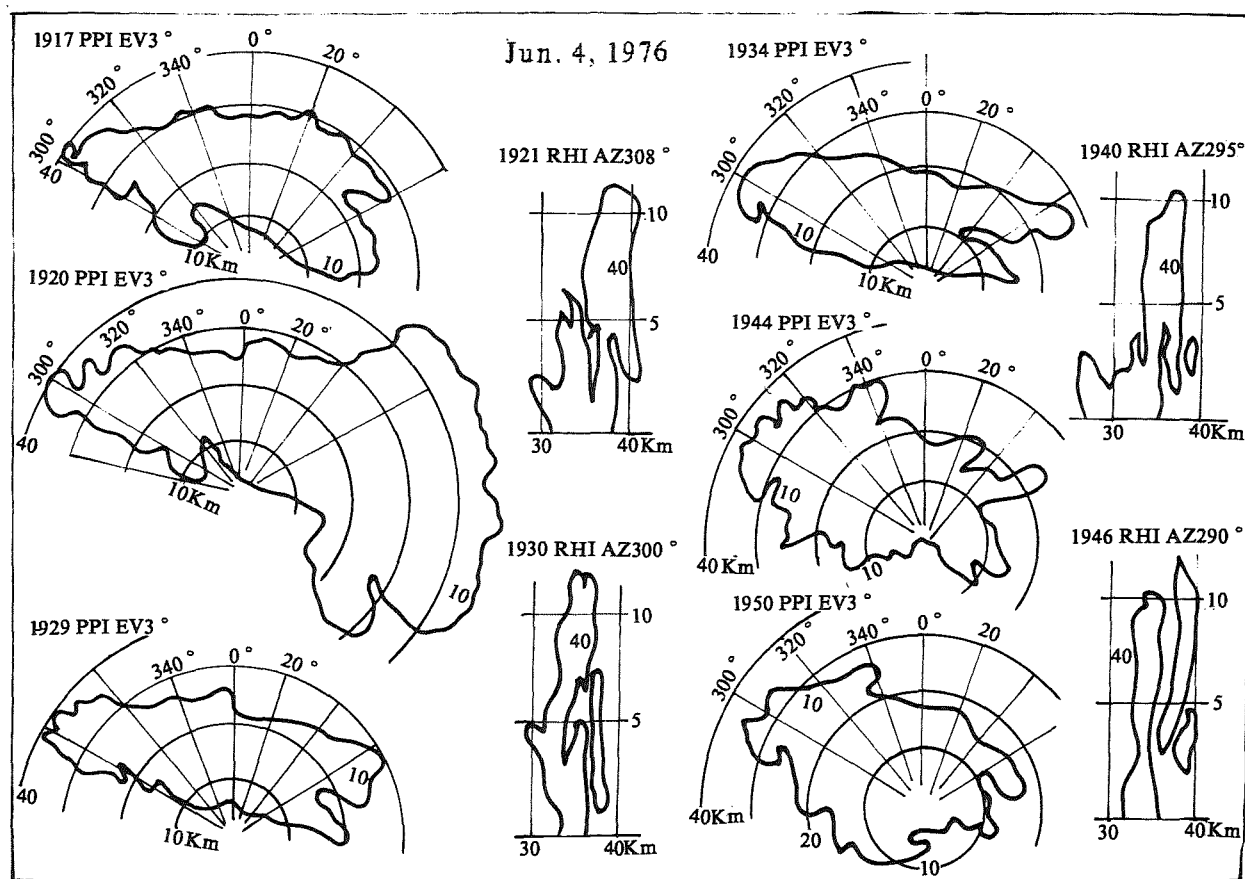


Fig5. A strong hailstorm in Pingliang was evolved Process from anticyclonic hook to cyclonic hook echo, Cloud height leap increased and occurred intermitly hailfall.

5. DISCUSSION AND CONCLVSION

By about observation the fact and the events brief analysis, showed the midrate or strong hailstorm in pingliang may appeared hook echoes. Hailstorm is one of severe thunderstorm, they developed model which have the structure of rotation flow and strong shear, so the most hailstorm can exhibited cyclone pattern echo, occurring hook echo demostrated hailstorm which have been mature and producted the sign of haifall. Note: we often made operating artificial modification with gun at appearing the hook echo, as well critertor for hail suppression. From the local environment and climate condition, showed hailstorm formation in pingliang associated with the mid-level jet of northwest wind located at 500 pha, the jet which have cold and dry oposited with the low-level average environment wind which have warn and moist, formed strong shear and rotation circular, therefore, the hook position of the radar echo often exhibited contrary with the mid-level wind direction. In addition, the climbing mountain flow and the blowing wind along valley from southeast to northwest at east flank where effected by the Liupan mountain barrier, it was importion role to forced lefting and tiggig hailstorm formation and development.

ACKNOWLE DGEMENTS

The authors express their hearty thanks to Mr. Cai Qiming, Mr. Yang SongXi in the paper use to their early observation radar data. This study was partly supported by Lanzhou Branch Academy of Chinese Science of Supericuity Foundation. The hail suppression work in pinliang was supported by GanSu Province Govenment of Reduce Discester Foundation.

REFERENCE

- Atals, D., 1990: radar in Meteorology, American Meteorological Society, Boston.
- Browning, K. A., 1977: structare and mechainsms of hailstorm, Meteor. Monogr., Vol. 16, No. 38, Amer. Meteor. Soc., 1-43.
- Fankhauser, J. c., 1976: structure of an evolving hailstorm, Part II: Thermodynamic structure and airflow in the near environment. Mon. Wea. Rev., 104, 576-587.
- Lomon, L. R., and C. A. dosuell III, 1979: severe thurelerstorm evolution and mesocyclone structure as related to torndogenesis, Mon. wea. Rev., 107, 1184-1197.
- Rotunno, R., 1981: On the evotution of thunderstorm rotation, Mon. Wea. Rev., 109, 171-180.
- Schmid, W., 1992: The predicting of hail. Part I: Radar quantities of hail intensity, Atmos. Res., 28, 49-69.

THE INTERACTION OF AEROSOLS WITH DEVELOPING MARITIME AND CONTINENTAL CUMULUS CLOUDS

Darrel Baumgardner, William A. Cooper, Lawrence F. Radke

National Center for Atmospheric Research, Boulder, CO, USA

1.0 INTRODUCTION

As it becomes increasingly apparent that anthropogenic aerosols have a significant role in global climate change the focus on aerosols and their interactions with clouds will naturally sharpen. However, cloud and aerosol interactions are all too frequently treated one-dimensionally, i.e., as seen from the aerosol perspective, clouds are viewed as the principal means of removing or vertically redistributing aerosols in the atmosphere. This simplistic view has been slowly transformed as experimental evidence has mounted that supports a far more complex role for clouds in their interactions with aerosols (Hobbs, 1993). Clouds are now seen to play a role with varying efficiencies as aerosol sink and source and modifier of aerosol properties. This increased complexity has obvious implications for current efforts to correctly place clouds and aerosols in their proper context within global climate models (GCM's).

Observations of clouds appearing to generate aerosols (e.g. CCN) date back at least to Radke and Hobbs (1969); however, in these early observations it was less than certain as to whether vertical transport of aerosols, cloud droplet modification of CCN size and chemistry, a sampling artifact, or a new particle formation was being observed. New attention was brought to the subject by the airborne measurements of Hegg et al.

(1990) who found aerosol production associated with the clear and cloudy air interface of marine stratocumulus. This gave impetus to a series of later experimental confirmations by Radke and Hobbs (1991), Hobbs and Radke (1992) and Perry and Hobbs (1994). As a result, an aerosol production mechanism at the cloudy interface is no longer in serious doubt. Interestingly, no entirely satisfactory explanations of this unexpected phenomena have been offered. Candidates range from the shattering of supersaturated solution droplets on final evaporation (Dessens, 1946), (Twomey and McMaster, 1955), (Radke and Hegg, 1972) to homogeneous-bimolecular nucleation of sulfuric acid droplets from H_2SO_4 vapor (Perry and Hobbs, 1994). In addition, it has become clear that some aircraft observations at the atmosphere's cloudy interface are complicated by apparent sampling artifacts which falsely lend themselves to a particle formation misinterpretation (Radke and Twomey, 1993). The remainder of this abstract offers new evidence for Near Cloud Aerosol Production (NeCAP) and will discount the possibility of sampling artifacts.

2. DATA SET AND OBSERVATIONS

In July, 1995, an international consortium of investigators began a study of the early stages of development of tropical cumulus clouds on the NE coast of Florida, the Small Cumulus Measurement Study (SCMS). The principle tools for this study were the NSF/NCAR CP-2 polarimetric radar and C-130 aircraft which was flying for the

first time as an extensively instrumented cloud physics and aerosol research platform. Operating close in to the radar, the early life cycle of cumulus along the shoreline was observed almost daily over a period of 25 days. The cloud and aerosol case studies presented here are from two out of the twenty flights and 60 hours of research flown.

The study area was particularly unique because of the dependency of aerosol origins on the wind direction: winds from the west/northwest produced clouds of continental origin while maritime clouds were formed when winds were predominately from the east or southeast. Flights 5 (R5) and 13 (R13) were evaluated as continental and maritime cases, respectively.

The aircraft aerosol sampling strategy was somewhat dictated by SCMS's desire to follow the early time history of tropical cumulus. Multiple cloud penetrations were made at constant altitude. The flight legs at 600 m (cloudbase) and 800 m were analyzed from R5 and R13 for this study.

Figures 1 - 4 show time traces of the aerosol and cloud particle concentrations measured with an FSSP-100 (2 - 47 μm), FSSP-300 (0.3 - 20 μm) and a modified TSI 3760 CN counter ($> .01 \mu\text{m}$). Note:: the CN concentrations have been divided by 10 to allow easier comparison of trends with the FSSP-100 and 300. The average clear air aerosols concentrations at cloud base measured with the CN and FSSP-300 are 2000 and 30 cm^{-3} for the continental case and 800 and 30 cm^{-3} for maritime conditions. The maximum cloud droplet concentrations for the continental and maritime cases were ≈ 1000 and 300 cm^{-3} respectively.

The measurements shown in these figures do not represent all the cloud penetrations at these levels and were selected in order to point out a number of

features of the aerosol population. Similar trends are seen in the majority of the other near-cloud distributions of aerosol populations. The near cloud base penetrations were made within approximately 30 minutes of visible cloud formation.

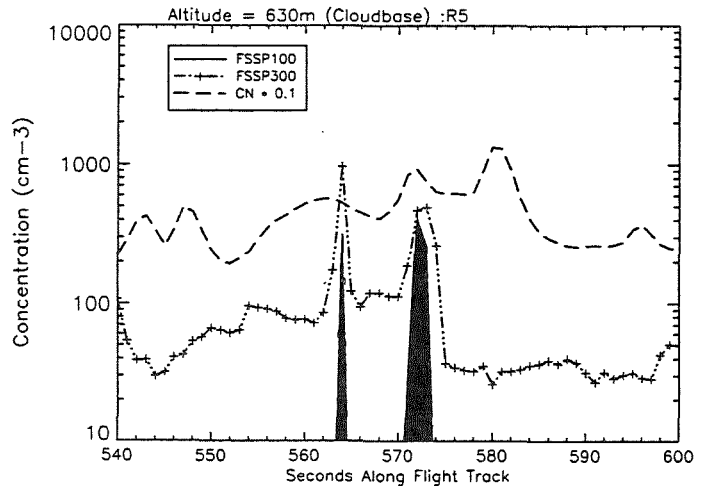


Fig.1 Time traces of CN, FSSP-300, and FSSP-100 particle concentrations at cloudbase (630 m) on a continental aerosol day.

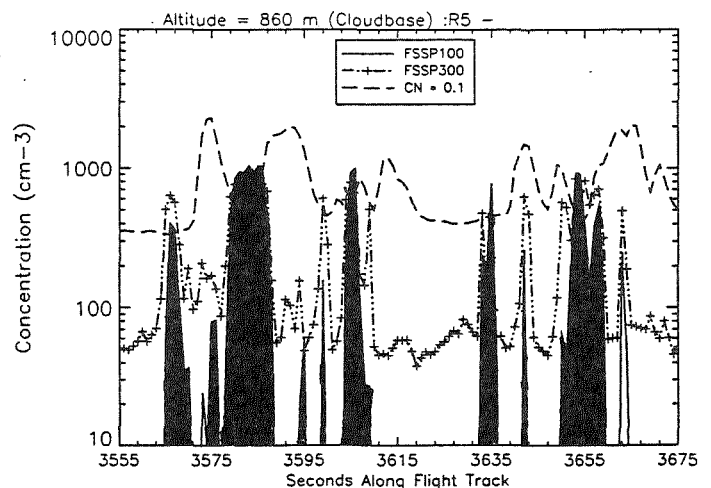


Fig. 2 Same as Fig. 1 but at 860 m.

In Fig. 1, measurements prior to cloud penetration were upwind, those afterwards

were downwind. There is a lot of variation in both CN and FSSP300 measurements but there is a clear increase in the FSSP-300 concentrations as the aircraft approaches the cloud and a significant drop and increased homogeneity downwind. Downwind of these very small clouds the CN concentration increases to a peak that is more than a factor of 5 larger than background. The flight leg at 860 m (Fig. 2) shows a similar trend in both the FSSP-300 and CN values with even larger increases in CN over the background values. It is also interesting to compare the FSSP-300 and 100 concentrations in Figs. 1 and 2. The FSSP-300 measurements mirror the FSSP-100, sometimes exceeding them by factors of 2 or more and other times almost equaling the FSSP-100. The CN measurements, on the other hand, are more often negatively correlated as not.

The maritime case shown in Figs. 3 and 4. is quite similar to the continental case except for the generally lower CN concentrations. The FSSP300 is also generally higher than the FSSP100 even in those cloud penetrations that appear adiabatic based upon the general "top-hat" structure and maximum concentrations. The near-cloud increase in CN concentrations between clouds is also larger than seen in the continental case.

3. DISCUSSION

Aircraft observations of NeCAP, where the actual aerosol measurements take place within the aircraft following ingestion by an external inlet, have been plagued by fears of artifact formation. The reasonable hypothesis offered is that lingering cloud droplets in the apparently clear air surrounding clouds will make high energy impacts on the leading edges of the intake and create a cascade of particles formed from the resulting evaporated ruptured cloud micro-droplets.

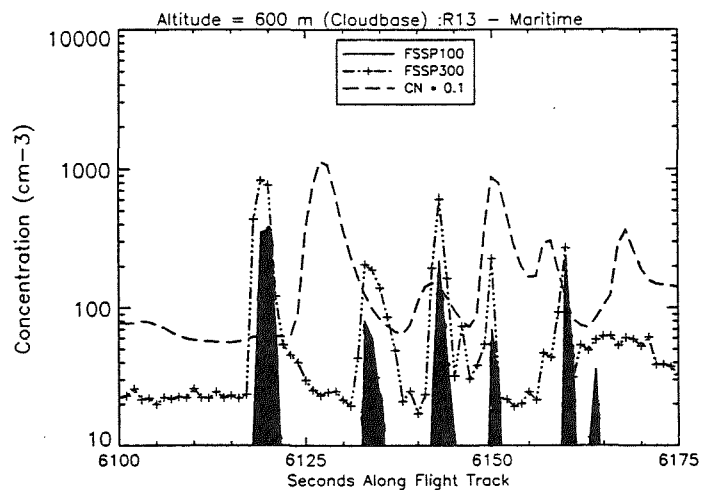


Fig. 3 Same as Fig. 1 but for maritime conditions.

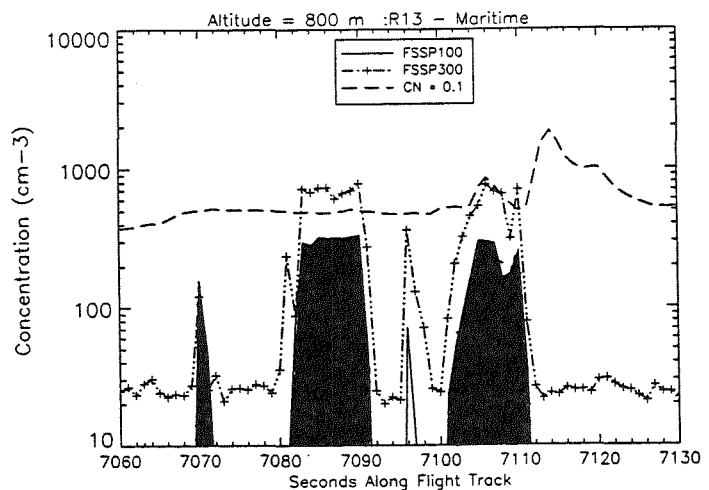


Fig. 4 Same as Fig. 2 but for maritime conditions.

The large CN increases in the present measurements, however, occur well outside cloud boundaries with no evidence of enhancements in clouds where shattering would be expected. This leaves us with one of three possible mechanisms for NeCAP:

- 1) Bimolecular nucleation in the aerosol surface area denuded air adjacent to the cloud,
- 2) Shattering of solution supersaturated cloud drops as they evaporate,

3)) Vertical transport of near surface aerosol which is redistributed by cloud wake motions.

The CN measurements at cloud base do not support the third mechanism which leaves either 1) or 2) as possibilities. If the second mechanism was dominate, one would expect a distribution of sizes, some that would be in the size range of the FSSP-300. The continental cases differ from the maritime ones in this respect. Figure 2 shows that the FSSP-300 concentrations do show modest increases in many of the same locations as the CN but the maritime cases shown in Fig. 3 almost appear anti-correlated. This does not rule out mechanism 2 in the maritime case but may indicate that the bimolecular nucleation is more predominate in maritime than in continental clouds. This would possibly be a result of less surface area in maritime cases leading to potentially higher supersaturation for gas to particle conversions.

The comparison of FSSP-300 with CN and FSSP-100 measurements is also a very useful indicator of the size of aerosols being activated for cloud droplet formation. The continental clouds indicate that at least all of the CN larger than 0.3 μm become activated as cloud droplets when the clouds have an adiabatic signature. In the case of the maritime clouds, however, there appear to be a much larger percentage of inactivated CN.

4. CONCLUSIONS

This data set which is only partially analyzed has the potential, when more completely considered, to greatly increase our knowledge of particle formation at the atmosphere's cloudy interface. The NeCAP mechanism might be very important in modifying cloud evolution in addition to providing a source for aerosols that impact the earth's radiation balance. These field observations of what could be

the NeCAP phenomena are, like others, suggestive but not wholly compelling. We may alter this view as the rest of the SCMS data is analyzed, but far from narrowing the choice of explanations, a variety of hypotheses for NeCAP measurements remain viable.

REFERENCES

- H. Dessens, 1946: Les noyaux de condensation de l'atmosphere. *C.R. Acad. Sci.*, 233, 915-7.
- D.A. Hegg, L.F. Radke, P.V. Hobbs, 1991: Measurements of Aitken Nuclei and Cloud Condensation Nuclei in the Marine Atmosphere and their Relation to the DMS-Cloud-Climate Hypothesis. *J. Geophys. Res.*, 96, 18,727-18,733.
- P.V. Hobbs: *Aerosol-Cloud=Climate Interactions*. Academic Press, Inc.
- Perry, K.D. and P.V. Hobbs, 1994: Further evidence for particle nucleation in clear air adjacent to marine cumulus clouds, *J. Geophys. Res.*, 99, 22,803-22,818.
- L.F. Radke, P.V. Hobbs, 1991: Humidity and particle Fields Around Some Small Cumulus Clouds. *J. Atmos. Sci.*, 48, 1190-1193.
- L.F. Radke, D.A. Hegg, 1972: The Shattering of Saline Droplets Upon Crystallization. *J. Rech. Atmos.*, 6, 447-455.
- J.W. Telford, P.B. Wagner, 1980: The dynamical and lliquid water structure of the small cumulus as determined from its environment. *Pure Appl. Geophys.*, 118, 935-952.
- S. Twomey, K.N. McMaster, 1955: The production of condensation nuclei by crystallizing salt particles. *Tellus*, 7, 458-61.

FIELD EXPERIMENTAL DETERMINATION OF COLLISION EFFICIENCIES AS A FUNCTION OF RAINDROP AND AEROSOL PARTICLE SIZE

Peter Ebert¹, Gerhard Frank², Matthias Kibler¹, Antje Mainka¹, Thomas Prokop¹, Birgit Tenberken¹, Jochen Tschiersch² and Knut Bächmann¹

¹Technische Hochschule Darmstadt; Fachbereich Chemie; Petersenstr. 18; D-64287 Darmstadt; Germany

²GSF-Forschungszentrum für Umwelt und Gesundheit GmbH; Institut für Strahlenschutz; Ingolstädter Landstr.1; D-85764 Oberschleißheim; Germany

1. EXPERIMENTAL

Monodisperse aerosol particles (produced with a Sinclair LaMer generator, MAGE, Palas, Karlsruhe, Germany; mean radius varying from 0.19 μm to 1.8 μm) tagged by a fluorescent dye tracer were released during several precipitation events (Fig.1). Raindrops which scavenge these particles are collected with the "Guttalgor" method described in detail elsewhere [Bächmann et al., 1993]. Analysis of the raindrops is carried out by Capillary Electrophoresis (CE) with Laser-Induced Fluorescence (LIF) detection.

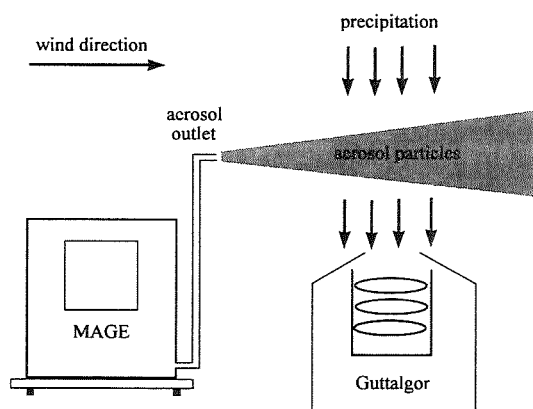


Fig.1: Experimental set-up of the field experiment

Collision efficiencies are calculated by formula (1):

$$\lambda_{D,i} = \frac{\Delta n * v}{Q * l * \tau} \quad (1)$$

with $\lambda_{D,i}$: collision coefficient [s^{-1}]
 Δn : number of scavenged particles
 v : wind velocity [m/s]
 Q : source strength of MAGE [s^{-1}]
 l : length of sampling basin [m]
 τ : sampling time [s]

2. RESULTS

2.1 c/r-Dependence

An interdependence between the tracer concentration and raindrop size was found (further abbr. as c/r-dependence). The c/r-dependencies obtained by the scavenging of aerosol particles smaller than 1.8 μm radius show a maximum concentration at a specific raindrop radius. The maximum concentration shifted to a drop radius of 0.35 mm with decreasing scavenged aerosol particle size (Fig.2). A continuous decrease in concentration with increasing drop radius was measured for the scavenging of large particles (r_{AP} : 1.8 μm).

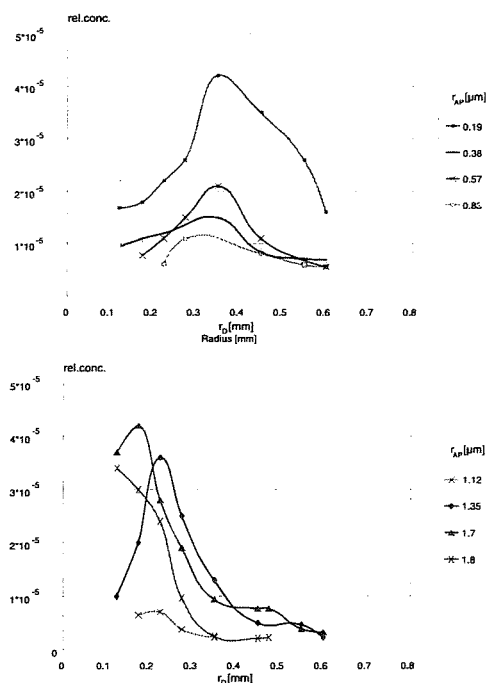


Fig.2: c/r-dependencies as a function of aerosol particle size (r_D : drop radius; r_{AP} : aerosol particle radius)

2.2 Collision Efficiencies E as a Function of Drop Radius

The collision efficiencies E range from 10^{-2} s^{-1} to 10^{-6} s^{-1} . An increase of the collision efficiency with increasing raindrop size showing a maximum collision efficiency at a drop radius of $550 \mu\text{m}$ was obtained (Fig.3). With increasing scavenged particle radius the slope of E to larger raindrops becomes flat and lower values for E were found.

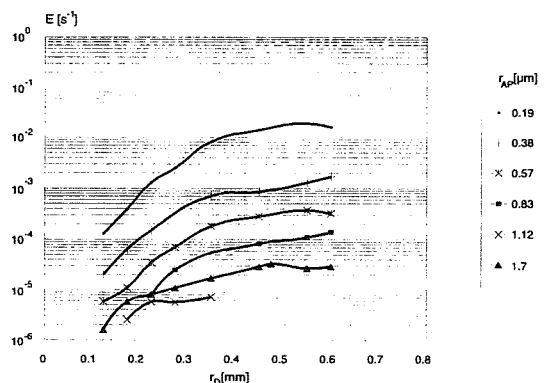
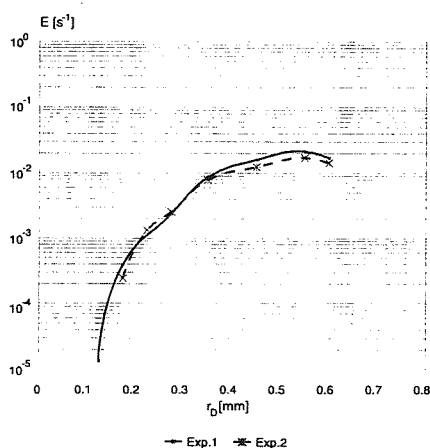


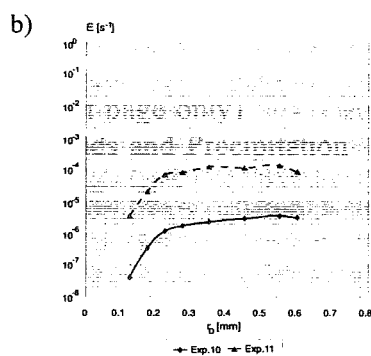
Fig.3: Collision efficiency as a function of drop size for different particle radii

In Fig.4 we show the obtained results of different tracer experiments for the same aerosol particle size. For aerosol particles with a radius of $0.19 \mu\text{m}$ the same collision efficiencies were measured at different rain events. For aerosol particles with a radius of $1.35 \mu\text{m}$ we found the same curve shape at both events but different absolute values for the collision efficiency. Below the figures we show meteorological parameters of the experiments.

a)



Nr.	T_0 [°C]	T_E [°C]	RH_0 [%]	RH_E [%]	p [mm/h]	clouds
1	24	22	72	87	1.1	1
2	22	-	87	-	1.7	1



Nr.	T_0 [°C]	T_E [°C]	RH_0 [%]	RH_E [%]	p [mm/h]	clouds
10	16.6	16.6	94	-	2.0	3
11	17.2	17.4	100	100	4.4	2

Fig.4: Results of different tracer experiments for the same particle radius: a) r_{AP} : $0.19 \mu\text{m}$; b) r_{AP} : $1.35 \mu\text{m}$; T: temperature; RH: relative humidity; p: rain intensity; index 0: start of experiment; index E: end of experiment; clouds: 1: cumulus; 2: incomplete cloud cover; 3: stratus

2.3 Collision Efficiency as a Function of AP Size

The collision efficiency λ shows a decrease with increasing aerosol particle size from a particle radius of $0.19 \mu\text{m}$ to $1.35 \mu\text{m}$ (Fig.5).

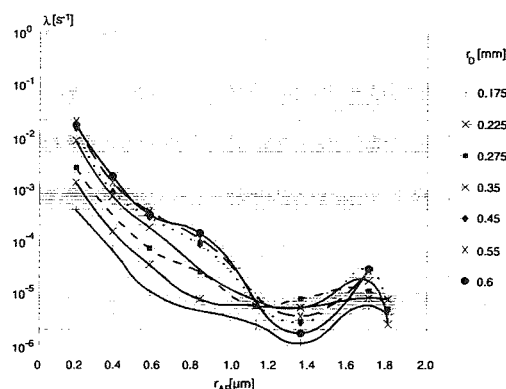


Fig.5: Collision efficiency (λ) as a function of aerosol particle size for different raindrop radii

For aerosol particles with a radius of $1.35 \mu\text{m}$ a minimum for the collision efficiency is seen for all raindrop sizes (only raindrops with 0.275 mm radius show a minimum scavenging efficiency at $1.12 \mu\text{m}$). For aerosol particles larger than $1.35 \mu\text{m}$ an increase for the scavenging efficiency was found up to a radius of $1.7 \mu\text{m}$ showing a local maximum. Larger aerosol particles show a decrease in the scavenging efficiency which becomes stronger the larger the raindrop radius is. At an aerosol particle radius of $0.8 \mu\text{m}$ a bend for the collision efficiency is seen for all drop sizes.

3. DISCUSSION AND INTERPRETATION

3.1 c/r -Dependence

As the "Guttalgor" method [Bächmann et al., 1993] enables us to collect raindrops according to their size we are able to calculate mean collision efficiencies taking all raindrops of one sieve into account. Therefore each value is based on more than 100 single raindrops and represents a high statistic reliability.

The measured c/r -dependencies are in agreement with c/r -dependencies of trace compounds in rain found in former field experiments [Bächmann et al., 1993]. The results show that diffusional effects become stronger for aerosol particles with a radius smaller than $0.4\text{ }\mu\text{m}$. Their curve shape is a consequence of diffusional effects by small scavenged aerosol particles.

3.2 Collision Efficiencies E as a Function of Drop Radius

In Fig.6 we present a comparison between our results, those of Wang and Pruppacher (1977) and Flossmann (1986).

In no case our results show an increase of E for drop sizes smaller than $230\text{ }\mu\text{m}$ which Flossmann (1986) and Wang and Pruppacher (1977) found. Taking into account that the concentration c is proportional to E and the inverse raindrop radius r_D it is not possible to calculate the obtained c/r -dependencies of this experiment by the calculated values of Flossmann (1986).

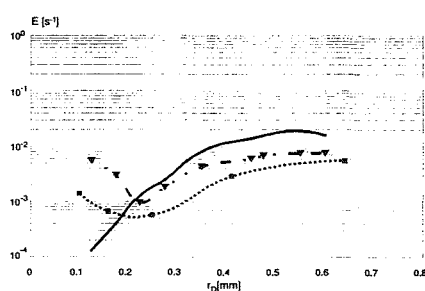


Fig.6: a) our results (r_{AP} : $0.19\text{ }\mu\text{m}$; RH: 85 %)
b) Wang and Pruppacher (1977) (r_{AP} : $0.25\text{ }\mu\text{m}$; RH: 23%)
c) Flossmann (1986) (r_{AP} : $0.16\text{ }\mu\text{m}$; RH: 75 %)

For small raindrops the increase of E calculated by theory leads always to an increase in concentration with decreasing drop radius as soon as the collision efficiency starts to increase for drop sizes smaller than $230\text{ }\mu\text{m}$. Therefore for small particle sizes a c/r -dependence with an increase in concentration for raindrops smaller than $230\text{ }\mu\text{m}$ should arise. Since our results show a concentration maximum and no increase

in concentration with decreasing drop radius the model calculations do not match with our results and previous measurements of c/r -dependencies of trace compounds in size classified raindrops [Bächmann et al., 1993]. Our results indicate that the minimum E must be at a drop radius smaller than $125\text{ }\mu\text{m}$. We conclude that certain parameters not yet taken into account by theory are responsible for this discrepancy between theory and field experimental determined collision efficiencies.

For larger aerosol particle sizes we obtain the same curve shapes as Flossmann (1986). Only differences in the mean values for the collision efficiency which get larger the larger the scavenged particle radius becomes were obtained. These discrepancies can be a consequence of the used aerosol particles. The particles consist of di-2-ethylhexy-sebacate (DES). Problems can occur during the scavenging of the particles by raindrops because the density of this oil is smaller than water. This may be the reason for the discrepancies between the results of Flossmann (1986) and ours. Since the influence of impaction scavenging becomes stronger the larger the aerosol particles are the discrepancies for the relative values between theory and our results become stronger the larger the aerosol particles are. For small aerosol particles diffusional or electrical effects dominate the scavenging process. Since we obtain the same curve shapes as theory and only differences in the mean values our above mentioned interpretation for small raindrops is not influenced by this effect.

3.3 Collision Efficiencies λ as a Function of Aerosol Particle Radius

The results for the collision efficiencies λ are in agreement with similar field experiments but do not match with theoretical predictions. We find the minimum λ at a larger aerosol particle radius than theory predicts. The local maximum of the collision efficiency was not reported by theoretical predictions but measured by Volken and Schumann (1993).

The large aerosol particle size showing the minimum λ can be a consequence of the smaller density of the used aerosol particles compared to water. As described in 3.2 our values are too low for larger aerosol particles. Therefore our minimum λ is found at larger aerosol particle sizes. Our results show a bend at a particle radius of $0.8\text{ }\mu\text{m}$. For this particle radius the minimum λ was measured by other authors.

3.4 Influence of Meteorological Parameters

It is obvious that our field experimental collision efficiencies are in contrast to theory. We find the local maximum at a constant particle size independent of

meteorological parameters as precipitation rate, temperature or relative humidity. Against that Schumann (1989) finds a local maximum scavenging efficiency at different particle sizes. Since both field experiments are done at different meteorological conditions we conclude that all these effects show no influence on the specific particle radius with the local maximum scavenging efficiency. There is only one difference our experiments and those of Schumann (1989). We used synthetic aerosol particles whereas Schumann (1989) measured the washout of atmospheric aerosol particles. Volken and Schumann (1993) concluded that particle shape may play an important role for the scavenging of aerosol particles. We conclude that phoretic forces of raindrops play an important role for below-cloud scavenging processes. Since our particles are uncharged and atmospheric particles may have an electric charge this should be the main difference between Schumann (1989) and our experiments. Electric effects are not negligible in the removal of particles as Schamberger et al. (1990) showed. They reported that for uncharged particles and a charged collector electrostatic torque's can lead to either increase or decrease in the collision efficiency, depending on the collector charge level. Since no in situ measurements of electrical charges of raindrops or aerosol particles have been performed their influence on particle scavenging in this study can not be excluded.

In Fig.4a we pointed out that the results obtained by our experiments with equal aerosol particle size are repeatable. It is obvious that for the equal particle radius the same collision efficiencies are obtained. An exception are the collision efficiencies measured for a particle radius of 1.35 μm radius (Fig.4b). Higher collision efficiencies are obtained for experiment Nr.11 compared to experiment Nr.10 but we found the same curve shapes in both cases. At experiment Nr.10 the rain arises out of stratus clouds. At all other experiments cumulus cloud or an incomplete cloud cover takes place. It seems that the raindrops creation process influences the scavenging processes.

Schumann (1989) pointed out that an increase of phoretic forces of raindrops and/or aerosol particles can be explained by the fact that in winter raindrops reaching the ground are melted a few hundred meters above the ground. These drops may not have reached the ambient temperature and may even be colder than the dewpoint temperature. In this case the thermophoretic forces increase considerably and at dewpoint temperature the diffusiophoretic forces exceed the thermophoretic force. As the rain in our case originates from "cold rain" process - i.e. cloud- droplets are passed through an ice phase stage - an electric charge of the raindrops is possible.

4. SUMMARY

It seems that for small raindrops some processes which have not been taken into account by theory have an important influence on below-cloud particle scavenging. The collision efficiency shows a strong dependence on several parameters which explains the different results of field experiments and theoretical calculations. At the moment these parameters are not totally taken into account by models and can not represent the observed effects of the interaction between aerosol particles and raindrops correctly. Therefore it is necessary to perform further field experiments to get a more detailed data base which allow reliable statistics for new theoretical models.

Acknowledgements - The authors acknowledge the financial support of the Deutsche Forschungsgemeinschaft (DFG) under Project SFB 233 ("Dynamik und Chemie der Hydrometeore") and the team of Prof. H.R. Pruppacher, Dept. Meteorology, Johannes-Gutenberg Universität Mainz, Germany for their helpful suggestions.

5. REFERENCES

- Bächmann, K., Haag, I. and Röder, A. (1993) A field study to determine the chemical content of individual raindrops as a function of their size, *Atmospheric Environment* 27A, 1951-1958.
- Flossmann, A. I. (1986) A theoretical investigation of the removal of atmospheric trace constituents by means of a dynamical model, Ph. D. Thesis, Dept. Meteorology, Johan.-Gutenberg-Universität Mainz, Germany.
- Schamberger, M. R., Peters, J. E. and Leong, K. H. (1990) Collection of prolate spheroidal aerosol particles by charged spherical collectors, *J. Aerosol. Sci.* 21, 539-554.
- Schumann, T. (1989) Large discrepancies between theoretical and field-determined scavenging coefficients, *J. Aerosol Sci.* 20, 1159-1162.
- Volken, M. and Schumann, T. (1993) A critical review of below-cloud aerosol-scavenging results on Mt. Rigi, *Water, Air, Soil Pollution* 68, 15-28.
- Wang, P.K. and Pruppacher, H.R. (1977) An experimental determination of the efficiency with which aerosol particles are collected by water drops in subsaturated air, *J. Atmos. Sci.* 34, 1664-1669.

SUB-CLOUD CONCENTRATIONS AND CLOUD DROPLET EVOLUTION IN WARM CUMULI. IS THERE AN OBSERVABLE LINK?

G. B. Raga¹ and P.R. Jonas²

¹Centro de Ciencias de la Atmosfera, UNAM, 04510 Mexico City, Mexico

²Physics Department, UMIST, Manchester M60 1QD, UK

1. INTRODUCTION

The presence of aerosol particles in the atmosphere has a direct effect on the Earth's energy balance. Aerosol concentrations, and more precisely, cloud condensation nucleus (CCN) concentrations determine, to first approximation, the number of cloud droplets that will initially form. The details of the droplet size distributions are crucial for the calculation of the single scattering properties of these clouds. In previous studies (Raga and Jonas, 1993a and b), we have determined the importance of the sub-cloud aerosol concentrations in determining the microphysical and radiative characteristics of small cumulus clouds over the sea. The analysis has shown a substantial reduction of the effective radius near cloud-top in clouds that had developed under heavily polluted conditions. As a consequence of this, the single scattering albedo was greatly enhanced, resulting in brighter clouds.

The link between background aerosols, cloud droplet distributions and derived radiative properties is one aspect of the influence of pollution on overall cloud characteristics and has important climatic implications. However, this is not the only aspect in which aerosols affect cloud properties. Increased aerosol concentrations also lead to the possible suppression of precipitation (as suggested by the evidence of ship tracks) and this, in turn, modifies the cloud lifetimes. The possibility of having longer-lived clouds when pollution levels are high, also has climatic implications (Albrecht, 1989), while a reduction of precipitation from such clouds would modify the hydrological balance.

In this study we present observations obtained in warm cumulus clouds that suggest that there is a direct link between sub-cloud aerosol

concentrations and precipitation development and evolution.

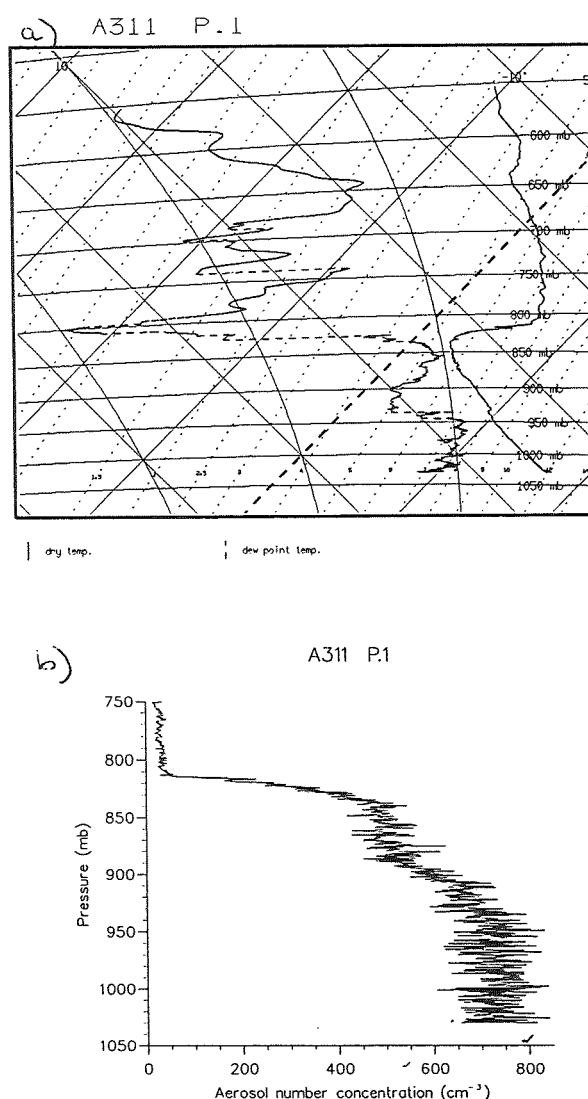


Figure 1. Thermodynamic diagram (a) and vertical profile of the aerosol size distribution (b) observed during aircraft descent for the period 13:13 to 13:33 UTC on January 25, 1994.

2. OBSERVATIONS

Two flights were made by the UK Meteorological Research Flight C-130 aircraft on consecutive days (25 and 26 January 1994, flights A311 and A312, respectively) through warm cumuli over the sub-tropical eastern Atlantic, in the vicinity of the Canary Islands. The low-level aerosol concentrations were considerably different on both days, providing an excellent opportunity to study the influence of aerosol particles on cloud microphysical properties. Sub-cloud aerosol concentrations ranged from 600 per cc on the first flight down to about 50 per cc on the second flight.

Both flights were made in the same approximate region (28N, 21W), under the influence of the semi-permanent high pressure system, and lasted over 6 hours. Back trajectories are needed to determine the difference in the observed low-level aerosol concentrations between the two days and will be computed in the near future. Seven individual clouds were sampled (3 on the first flight and 4 on the following one) at different levels, with typically three passes within the clouds. Two clear air soundings were also obtained, before and after cloud sampling had been completed. The skew-T diagrams show qualitatively the same features, with the main trade inversion located between 840 and 800 mb. Fields of cumuli were observed on both days, but showed a more 'clustered' pattern on the first flight; the cumuli were aligned in rows on the second flight. On the first flight, the wind at low levels was ENE (60°) and reached 10 m/s from the surface up to cloud base height (about 1 km) and then decreased uniformly to 5 m/s at the top of the boundary layer. On the following day, the low level wind was from 50° and reached 11 m/s at the surface but then decreased steadily to 7 m/s at cloud base. Both days showed decoupled boundary layers, as seen in the thermodynamic diagrams (Figs. 1a and 2a) and was also evident in the aerosol profiles (Figs. 1b and 2b).

The first flight had a fairly constant concentration up to cloudbase and then decreasing concentrations with height. In contrast, the second flight indicated very low concentrations below cloudbase, but showed a layer of higher concentrations at mid-level in the boundary layer. This could be linked to the vertical shear of the horizontal wind, which would suggest a different origin for the aerosol particles within that layer.

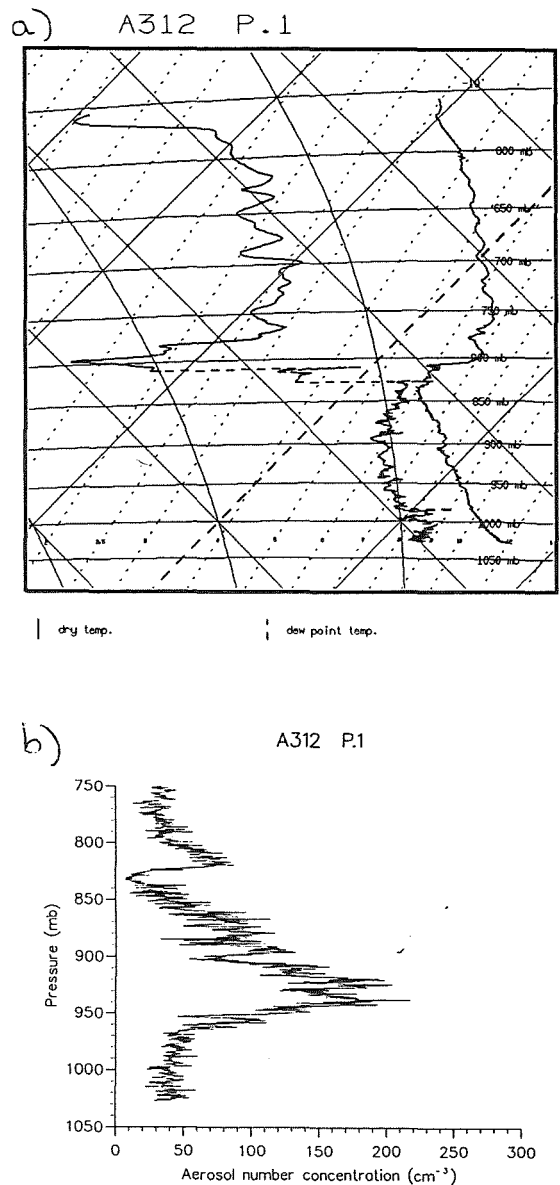


Figure 2. Thermodynamic diagram (a) and vertical profile of the aerosol size distribution (b) observed during aircraft descent for the period 13:21 to 13:43 UTC on January 26, 1994.

3. RESULTS

3.1 Case studies

We have selected one cloud from each flight (polluted vs. clean) to be presented here. The third cloud sampled on January 25th had cloud top height of about 2010 m and cloudbase height around 750 m, with a horizontal extent of about 1.4 km (aspect ratio ≈ 0.9). The cloud was penetrated at three different levels (1970, 1220 and 815 m) in the NW-SE direction. The wind shear between cloudbase and cloud top was not large and the shear vector

pointed in the WNW direction, such that the cloud was approximately sampled in the up/downshear direction. Figure 3 shows the time series of the near cloud top pass (at 1970m) for cloud droplet number concentration (N_{fssp} , in cm^{-3}), liquid water content (Q_l , in gm^{-3} , solid line), precipitation rate (R_{rate} , in ms^{-1} , dashed line), number concentration of precipitation droplets (N_{2D} , in l^{-1}), and the three velocity components (U, V and W, in ms^{-1}). Up to 160 droplets per cc were observed in this pass, while the number of precipitation droplets reached about 10 per liter.

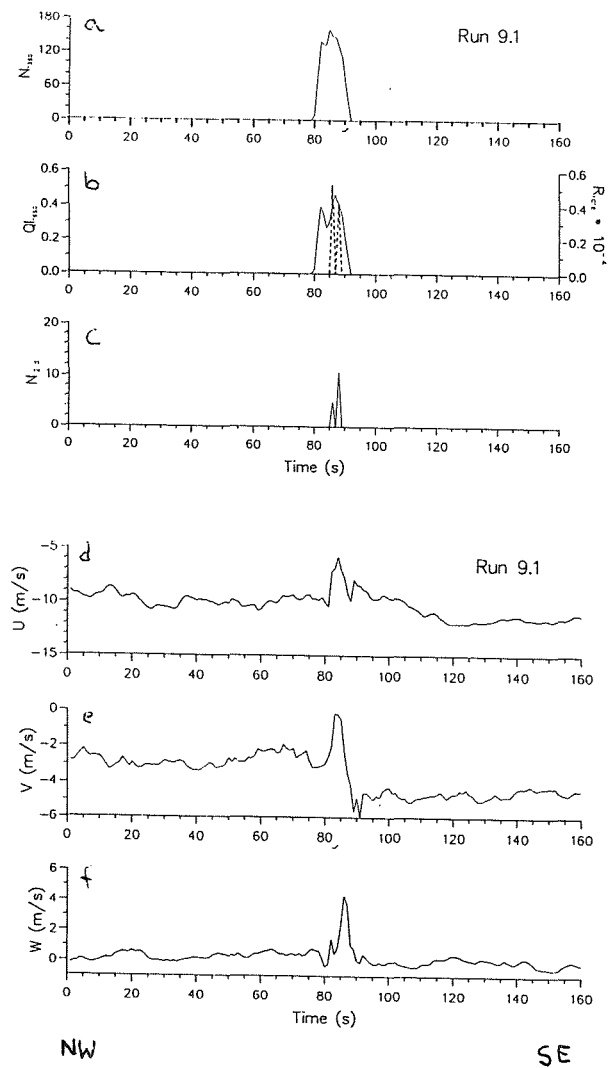


Figure 3. Time series of: a) cloud droplet number concentration; b) LWC (solid line) and precipitation rate (dashed line); c) number concentration of precipitation size droplets; d) E-W component of the horizontal velocity; e) N-S component of the horizontal velocity and f) vertical velocity, for the period 16:53 to 16:56 UTC on January 25, 1994.

The horizontal velocities show significant deflections as the cloud was encountered. Most of the incloud points during this pass were in an updraught region, with downdraughts observed at both sides of the turret, the downshear side one being larger in magnitude. The peak updraught was about 4 ms^{-1} , at 1220 m about cloudbase (where peak updraught was about 1 ms^{-1}). The peak precipitation droplet concentration almost coincided with the peak updraught near cloud top. In contrast, lower down in the cloud the highest concentrations were clearly located in the downdraught region.

The third cloud sampled during the clean day, was very similar to the one just described. Cloudbase was a little lower on this day (690m as opposed to 750 the previous day), but cloud top height was about the same (2010m). The main core of the cloud had a horizontal extent of about 1.1 km, so the aspect ratio was 1.2 in this case. The cloud was also sampled at three different levels (1980, 1770 and 1260 m). The shear between cloudbase and cloud top was stronger in this case than in the previous flight and the shear vector was directed almost towards the West. The cloud was penetrated in the NNE-SSW direction, which was almost perpendicular to the shear vector. The time series near cloud top (equivalent to Fig. 3, but not shown), showed a maximum cloud droplet concentration of about 50 per cc (as opposed to 160 the previous day), while the precipitation droplet concentration soared to about 200 per liter. The mean effective radius for this pass was $13 \mu\text{m}$, compared to only $9 \mu\text{m}$ on the polluted day. This indicates that the collision and coalescence process was responsible for increasing the size of the cloud droplets (given almost the same water vapor conditions on both days). The larger droplets resulted in decreased albedo of this cloud compared to the polluted one described above.

3.2 Radiative properties

The same methodology used in Raga and Jonas (1993a) was used here to analyze the in-cloud radiative properties. The mean effective radius near cloud top was about $9 \mu\text{m}$ on the polluted day and reached $13 \mu\text{m}$ on the clean day. Based on the empirical formulae obtained by Raga and Jonas (1993b), which account for sub-cloud aerosol concentrations, the mean effective radii calculated (8.1 and $12.6 \mu\text{m}$, respectively) compare well with the observed ones. Both the mean and effective radii

as a function of height were much larger in the clean cloud, in fact they were larger than all the other values presented in Raga and Jonas (1993a). The vertical profile of the single scattering co-albedo computed for these clouds was much less than those reported previously, while the asymmetry factor was somewhat larger on average.

4. CONCLUSIONS

The composite analysis of the individual clouds indicates a marked upshear/downshear pattern in vertical velocity, LWC, and the number concentrations of cloud and precipitation droplets, particularly in the near cloud top passes. Stronger downdraughts were observed in the downshear side of the cloud and higher LWCs were observed in the upshear side.

The number concentration of precipitation drops (in the 2D-C range from 25 to 800 μm) near cloud top, indicated an order of magnitude difference between the two days. The increased precipitation droplet concentration in the clean day can account for the somewhat lower LWC observed that day.

Large numbers of 2D-C range droplets were observed slightly offset from the main updraught near cloud top and clearly in the downdraught regions lower down in the clouds.

5. REFERENCES

Albrecht, BA, 1989: Aerosols, cloud microphysics and fractional cloudiness. *Science*, **245**, 1227-1230.

Raga, GB and PR Jonas, 1993a: Microphysical and radiative properties of small cumulus clouds over the sea. *Q. J. Roy. Meteorol. Soc.*, **119**, 1399-1417.

Raga, GB and PR Jonas, 1993b: On the link between cloud-top radiative properties and sub-cloud aerosol concentrations. *Q. J. Roy. Meteorol. Soc.*, **119**, 1419-1425.

6. ACKNOWLEDGEMENTS

The authors gratefully acknowledge the help from the crew and staff of the Meteorological Research Flight of the British Meteorological Office, who collected the data and helped with the post-flight analysis.

RELATIONS BETWEEN AEROSOL AND CLOUD PROPERTIES IN NORTH DAKOTA CUMULUS CLOUDS

Paul J. DeMott¹, Jeffrey L. Stith², Ryan J. Zerr² and David C. Rogers¹

¹Department of Atmospheric Science, Colorado State University, Fort Collins, CO, USA

²Department of Atmospheric Sciences, University of North Dakota, Grand Forks, ND, USA

1. INTRODUCTION

Understanding initial cloud droplet and ice formation is important to the understanding and modeling of precipitation formation in cumulus clouds. Relatively few historical observations exist for which measurements of aerosols active as CCN and/or ice nuclei (IN) were obtained at the same time as measurements of cloud particle populations. These data are necessary to evaluate the connections between aerosols and initial cloud properties.

Though few in number, studies which have compared CCN to cloud droplet measurements (e.g., Hindman et al., 1977; Fitzgerald, 1972) have found general agreement between CCN and initial cloud droplet concentrations formed in clouds. A number of studies have addressed ice initiation in cumulus clouds using aircraft observations (e.g., Blyth and Latham, 1993). Other studies have addressed IN populations in the general locale of the study performed in this paper (e.g., Bowdle et al., 1985). On only a few occasions (e.g., Heymsfield et al., 1979; Vali et al., 1982) have studies of IN and ice formation been conducted concurrently.

In the study presented in this paper, coincident measurements were made of populations of cloud-active aerosols in the summertime boundary layer and cloud microphysical properties in cumuli in North Dakota. Measurements of CCN and ice nucleus aerosols were made on both ground level air and air collected in special sampling bags from near cloud base. Thermodynamic, air motion and cloud particle measurements were made by the same aircraft which made aerosol collections and a second aircraft which penetrated clouds at a different level. This permitted an assessment of both CCN activation near cloud base and IN activation versus ice initiation in updrafts.

2. METHODS AND PROCEDURES

Measurements of cloud-active aerosols were made as part of the 1993 North Dakota Tracer Experiment

(NDTE). This experiment was focused on the formation and transport of aerosols and hydrometeors, particularly in relation to hailstorms and hailstorm suppression methods. Instrumentation used for this study were based at the NDTE operations center located on the grounds of the Bismarck, ND airport and on two aircraft; the University of North Dakota Citation and the South Dakota School of Mines and Technology T-28. Sampling at the surface laboratory was conducted during the daylight hours of an 18 day period from July 5 through July 23, 1994. The sample site was at the extreme southeast limit of the Bismarck area, such that airflows from about 10 through 240 degrees were typically representative of rural, agricultural influences.

At the ground-based laboratory, measurements were made of aerosol particle concentrations $> 0.01 \mu\text{m}$ in size (TSI Model 3010 condensation nucleus counter), CCN and IN. This paper focuses on the CCN and IN data. CCN were measured by the thermal gradient diffusion chamber technique. The instrument used was a Mee Industries Model 130 CCN counter, but the detection system was modified from the original white light source with calibrated photodetector to a CCD video-imaged Helium-Neon laser system. Ten representative sample views (each of volume of 0.0156 cm^3) were averaged at each supersaturation set point. Measurements were made at nominal supersaturation values of 0.5, 1.0 and 2.0%. One supersaturation spectra could be obtained in about a 10 min time period.

Ice nuclei were measured using the continuous flow ice-thermal diffusion (hereafter referred to as CFD) chamber described in detail by Rogers (1988; 1993). This diffusion chamber has vertically-oriented geometry and is capable of exposing aerosol samples to humidity conditions ranging from ice saturation to water supersaturation in laminar flow at supercooled temperatures. The sample occupies a range of temperatures and humidities because it spans a region with a temperature gradient. This range is typically 0.6°C and 1% RH. The size differential between ice crystals and solution droplets at the outlet of the

CFD, due to the high supersaturations experienced by ice crystals compared to liquid droplets, is the basis for discriminating ice crystals. This size differential is further enhanced by reducing the humidity to ice saturation in the outlet section. Sizes of ice particles were measured at the outlet of the CFD processing section by a Climet optical particle counter interfaced to a multichannel analyzer. Aerosols $>3\mu\text{m}$ diameter were impacted at the inlet region and a size threshold for counting particles exiting the CFD as ice was set at $4\mu\text{m}$ for this study. The ability of the CFD technique to distinguish IN from non-IN in this way has been physically and chemically validated by Rogers (1994) and Chen *et al.* (1996).

Both CFD temperature and humidity were varied in cycles on any day of sampling. If aircraft microphysical sampling was being conducted, CFD sample temperatures were focused around the cloud sampling temperatures. The temperature range covered by measurements was -8 to -18°C . Sampling periods were either 5 or 10 min with a sample flow rate of 1 to 2 L min^{-1} .

Airborne air samples were collected in 50 liter electrically-conductive bags on the Citation aircraft. Airborne samples were collected either below cloud base or outside mid-cloud levels where the Citation cloud penetrations were focused. Typically only 30 minutes transpired between aerosol collection and return to the laboratory. Measurements of CN on bag samples after their return to the laboratory were used to calculate aerosol decay rates and to correct measured values of CN, CCN, and IN for this factor. IN concentrations were usually measured at both below and above water saturation conditions in order to differentiate populations of IN active for these conditions. Aerosol concentrations in bag samples were also corrected for the compression of air in bringing it back to the surface.

Additional aerosol measurements were made on the Citation aircraft, including CN and aerosols in the size range 0.1 to $3\mu\text{m}$ made using a Particle Measuring Systems (PMS) Passive Cavity Aerosol Spectrometer (PCASP). The T-28 and Citation carried similar other instruments for making cloud microphysical measurements, including PMS probes (FSSP and 2DC), liquid water measuring devices (Johnson Williams, CSIRO probes), standard pressure, temperature, and wind measuring instruments.

The cumulus cloud data base used for this study has been described by Stith *et al.* (1996). Data from the two aircraft, typically flying at different cloud levels in the same storms, were combined and 5 s averaged cloud properties were determined for all flight segments defined as liquid or ice cloud penetrations. The lifting condensation level was also determined

from soundings and pilot reports, so that adiabatic liquid water fraction (ALWF) could be computed for each cloud record.

3. RESULTS

Cloud droplet concentration data are summarized in Fig. 1 for all flights during the sampling period (#?). The data are summarized as a cumulative frequency distribution for cloud regions within 100 mb of cloud base, and for penetrations containing ALWF exceeding 0.3 ($>30\%$ adiabatic). The CCN data collected at the surface site are shown on the same figure as cumulative frequency distributions of CCN concentration at the three values of water vapor supersaturation used. Aircraft profiles of the vertical distribution of CN and accumulation mode aerosols indicated that the convective boundary layer was typically well-mixed to an altitude of about 4 km. Therefore, CCN data were only corrected for expansion dilution above this level to the altitude of cloud sampling. The cumulative frequency of CCN concentrations measured in aircraft bag samples at 1% supersaturation are plotted in Fig. 1 as well. These show excellent agreement with the ground-based values, giving confidence to the representativeness of ground-based values and the procedure used to adjust them to the aircraft sampling level.

It is seen from Fig. 1 that the observed form of the droplet concentration frequency distribution agreed very well with the CCN data and suggest that cloud-base supersaturations typically exceeded 2% with respect to water during the project period. The project period CCN supersaturation spectrum could be summarized as $N_{\text{CCN}} = 300\text{ S}^{0.98}$. While clearly continental, this spectrum is less so than ones typically associated with continental areas. This may be reflective of the nature of the air masses present during the period of research and the fact that this was a period of greater than average precipitation, so scavenging processes may have greatly modified CCN populations.

Figure 2 shows a segment of IN data measured on aerosols collected in aircraft bag samples on two days. The processing temperature was equivalent for these samples, at $-13 \pm 0.3^\circ\text{C}$. This figure demonstrates the effort made on any day to process the samples to determine IN sensitivity to humidity and to isolate IN populations active by different nucleation mechanisms. It is noted that IN concentrations increase more sharply above water) saturation (condensation freezing or immersion freezing nuclei) than below water saturation (presumably deposition nuclei). The dependence of ice formation on humidity inside clouds is then possibly much stronger than the dependence on temperature alone.

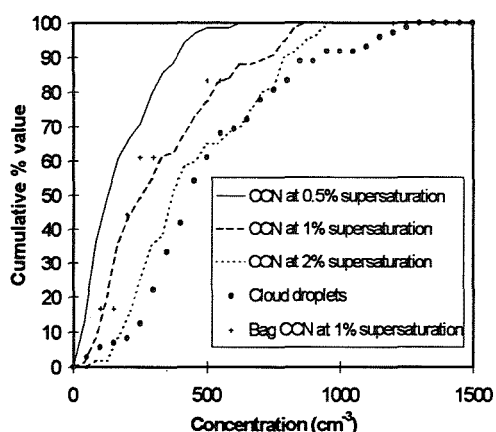


Figure 1. Cumulative frequency distributions of CCN and cloud droplet concentration data (processed as described in the text) during IN sampling period. CCN measured at the surface are given as lines at specific values of water vapor supersaturation. Cloud droplet concentrations and CCN concentrations (at 1% supersaturation) measured in aircraft-collected bag samples of air are indicated as data points.

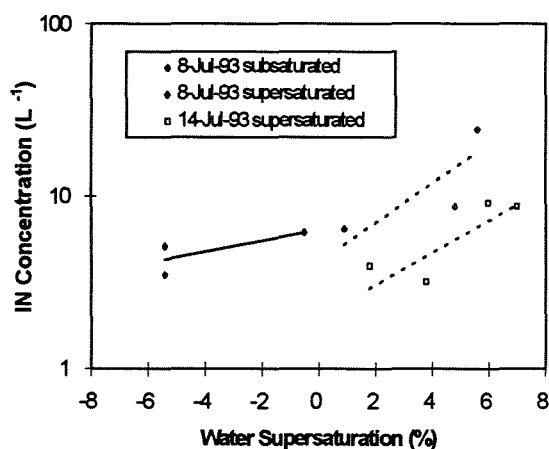


Figure 2. Ice nuclei concentrations measured in aircraft bag samples of air on two days. Each data point represents about 5 L of air. The solid and dashed lines highlight logarithmic fits to concentrations effective below and above water saturation, respectively. The strong sensitivity to water supersaturation is noted.

Ice crystal concentrations and IN concentrations are summarized together for the 15 day sample period in Fig. 3. Values given for ice crystal concentration are 2DC values with artifact rejection applied. An additional criteria applied was to limit comparisons to cloud passes with ALWF > 0.3, as done for cloud

droplet/CCN comparisons. This tends to focus on the more adiabatic portions of the clouds. The IN data represent a range of humidity conditions at the sample temperature. This, along with natural variability in concentrations, explains the wide range of concentrations measured. It is seen that the IN concentration range during the project period agrees with some proportion of ice crystal concentrations measured in more adiabatic portions of clouds. Nevertheless, there remain regions of higher ice crystal concentrations within precipitating storms which must result from secondary ice formation processes and/or mixing of ice from higher altitudes. As shown by Stith et al. (1996), shadow-or 2DC concentrations in excess of 100 L^{-1} were commonplace (approximately 30% of all observations) in NDTE clouds at temperatures between -5 and -15°C .

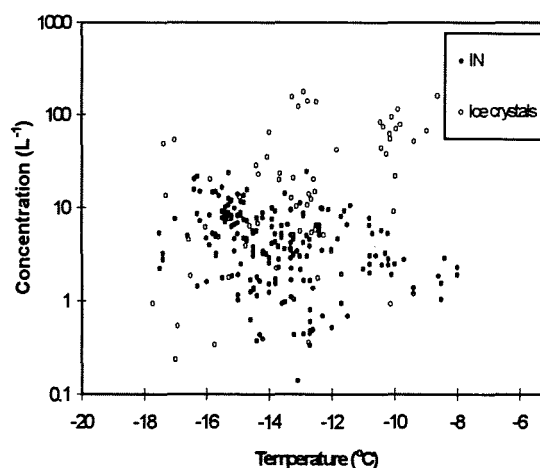


Figure 3. IN concentrations measured in surface air and from aircraft bag samples combined and plotted along with ice crystal concentrations on 5 flights during the 15 day IN sampling period. The ice crystal data are from the 2DC probe with rejection criteria applied. Additionally, ice crystal concentrations are only shown for cloud regions with adiabatic liquid water fraction > 0.3.

4. SUMMARY

The results of the study presented in this paper may be summarized as follows:

1. Initial cloud droplet concentrations showed excellent agreement with CCN data measured both at the surface and at cloud-base levels.
2. IN populations were highly variable and found to be quite sensitive to water vapor supersaturation. A typical concentration of 4 L^{-1} at -14°C is much higher than previously noted by other measurement techniques in this locale.

3. IN and ice crystal concentrations show fair agreement in more adiabatic cloud parcels, but occasional concentrations in excess of 100 L^{-1} cannot readily be explained by primary ice formation.

Some additional results have been presented by DeMott et al. (1995) and will be presented.

5. ACKNOWLEDGMENTS

This work was funded in part by cooperative agreement NA47RA0184 with the National Oceanic and Atmospheric Administration through the North Dakota Atmospheric Resource Board, State Water Commission. The views expressed herein are those of the authors, and do not necessarily reflect the views of NOAA or any of its subagencies. Additional support was provided by NSF Grant ATM-9311606.

6. REFERENCES

- Blyth, A.M. and Latham, J., 1993: Development of ice and precipitation in New Mexican summertime cumulus clouds. *Q.J.R. Meteor. Soc.*, **119**, 91-120.
- Bowdle, D.A., P.V. Hobbs, and L.F. Radke, 1985: Particles in the lower troposphere over the High Plains of the United States. Part III. Ice Nuclei. *J. Clim. Appl. Meteor.*, **24**, 1370-1376.
- Chen, Y., D.C. Rogers, S.K. Kreidenweis and P.J. DeMott, 1996: Isolating and identifying atmospheric ice nucleating aerosols - A new technique. Submitted for presentation at *14th International Conf. on Nucleation and Atmos. Aerosols*, Helsinki, Finland, 26-30 August.
- DeMott, P.J., J. L. Stith, and D.C. Rogers, 1995: Studies of cloud-active aerosols and ice initiation in North Dakota cumuli. Preprints, AMS Conf. on Cloud Physics, 15-20 January, Dallas, TX, 182-187.
- Fitzgerald, J.W., 1972: A study of the initial phase of cloud droplet growth by condensation: Comparison between theory and observation. *Univ. of Chicago Tech. Note 44*, 144 pp.
- Heymsfield, A.J., C.A. Knight, and J.E. Dye, 1979: Ice initiation in unmixed updraft cores in northeast Colorado cumulus congestus clouds. *J. Atmos. Sci.*, **36**, 2216-2229.
- Hindman, E.E., P.V. Hobbs, and L.F. Radke, 1977: Cloud condensation nucleus size distributions and their effects on cloud droplet distribution. *J. Atmos. Sci.*, **34**, 951-956.
- Rogers, D.C., 1988: Development of a continuous flow thermal gradient diffusion chamber for ice nucleation studies. *Atmospheric Research*, **22**, 149-181.
- Stith, J.L., R.J. Zerr, A.G. Detwiler, and P.L. Smith, 1996: A comparison of the microphysical characteristics of convective clouds during a wet summer and a dry summer. [This volume]
- Vali, G., D.C. Rogers and J.E. Dye, 1982: Aerosols, cloud nuclei and ice nuclei. Chapter 3 of *Hailstorms of the Central High Plains*, **1**, The National Hail Research Experiment (C.A. Knight and P. Squires, Eds.), 35-57.

OBSERVATION AND STUDIES OF AEROSOL PARTICLES IN THE LOWER ATMOSPHERE LAYER IN XINJIANG IN WINTER

Shi Wenquan Li Bin

(Xinjiang Weather Modification Office, Urumqi, Xinjiang, P.R. China)

1. INTRODUCTION

Xinjiang with a large area and sparse population is situated in the centre of the Asian continent. In cold winter, mountainous regions to northern 43° N and the north of Mt. Tianshan are universally covered with snow. It is exceptionally fine unless there are local pollution sources or strong inversion. In this paper, basing on the measurement of 13 flights in winter, we have analyzed the characteristics of aerosol particles' distributions with different regions, altitudes and weather conditions.

Based on the natural geographical conditions and sounding routes, the sounding areas can be divided into 5 regions: the Yili River Valley, the Zhunger Basin, the Tianshan mountainous, the northern hillside of Mt. Tianshan and the southern hillside of Mt. Tianshan.

For convenient comparison, the sounding weather standards are divided into 2 types: the clean atmosphere and the unclean atmosphere. The clean atmosphere is the clear air without the influence by local pollution sources. The regions without the influence by local pollution sources are far away cities or upwind of cities. Avoiding the influence of inversion, we chose the clear day without inversion or inversion just beginning after systematical weathers.

2. MEASURING INSTRUMENTS

The sounding aircraft with 80 mps speed were installed with PMS measuring instruments. Aerosol particles were chiefly measured by FSSP-100 whose measuring range is $0.5\text{--}47\mu\text{m}$. Because of small scales, the $0.5\text{--}8\mu\text{m}$ range

grade with $0.5\mu\text{m}$ pre space was used. The flight ways were horizontal, vertical and spiral flight.

3. ANALYSES

3.1 The characteristics of aerosol particles' distributions in the clean atmosphere

The observation indicates that the aerosol particles' concentrations and scales in the clean atmosphere are quite small, and relatively well-distributed with space and regions. The measurement of aerosol particles' concentrations, spectral distributions and scales in above-mentioned regions is given in Table 1. The mean measurement of particles' concentrations is $4.45\text{--}6.66\text{ cm}^{-3}$, the maximum is 16.03 cm^{-3} at the northern hillside of Mt. Tianshan, and the minimums are 1.13 cm^{-3} and 1.14 cm^{-3} at the Tianshan mountainous and the Yili River Valley. Except that it is $5.41\text{E-}6\text{ g.m}^{-3}$ at the southern hillside of Mt. Tianshan, the mean measurement of masses' concentrations is $1.08\text{E-}6\text{--}2.35\text{E-}6\text{ g.m}^{-3}$, the maximum is $43.96\text{E-}6\text{ g.m}^{-3}$ at the southern hillside of Mt. Tianshan, and the minimum is $0.36\text{E-}6\text{ g.m}^{-3}$ at the Yili River Valley. The mean diameter is $0.752\text{--}0.760\mu\text{m}$ except that it is $0.842\mu\text{m}$ at the southern hillside of Mt. Tianshan. The maximum spectral width is below $4\mu\text{m}$ except it is $0.5\text{--}8\mu\text{m}$ at the southern hillside of Mt. Tianshan, and it is only $2\mu\text{m}$ at the Tianshan mountainous.

The distributions of aerosol particles' concentrations with altitudes in several regions are given in Fig. 1. The figure shows that the aerosol particles' distributions with altitudes are well-distributed below 3000m at the Yili River Valley (Fig. 1a), slow decrease below 2500m and slight increase above 2500m

in Kuerla (the southern hillside of Mt. Tianshan) (Fig.1b) and Urumqi (the northern

hillside of Mt. Tianshan) (Fig.1c). The maximum is at the ground layer.

Table1. The measurement of aerosol particles' concentrations, diameters and spectral distributions in the clean atmosphere.

Sounding regions	Altitudes (m)	N(cm^{-3})			M(E-6 g.m^{-3})			Mean diameters (μm)	Spectral widths (μm)
		Means	Maximums	Minimums	Means	Maximums	Minimums		
The Yili River Valley	1233-3877	4.45	15.72	1.14	1.08	3.48	0.30	0.752	0.5-4
The Zhunger Basin	2588	6.66	11.29	3.57	2.35	9.51	1.28	0.760	0.5-4
The Tianshan mountainous	2888, 3388	5.75	14.82	1.13	1.32	3.27	0.46	0.752	0.5-2
The northern hillside of Mt. Tianshan	3039, 3147	6.49	16.93	2.67	1.83	6.60	0.69	0.752	0.5-4
The southern hillside of Mt. Tianshan	1595-3533	5.72	13.88	1.72	5.41	43.96	0.49	0.842	0.5-8

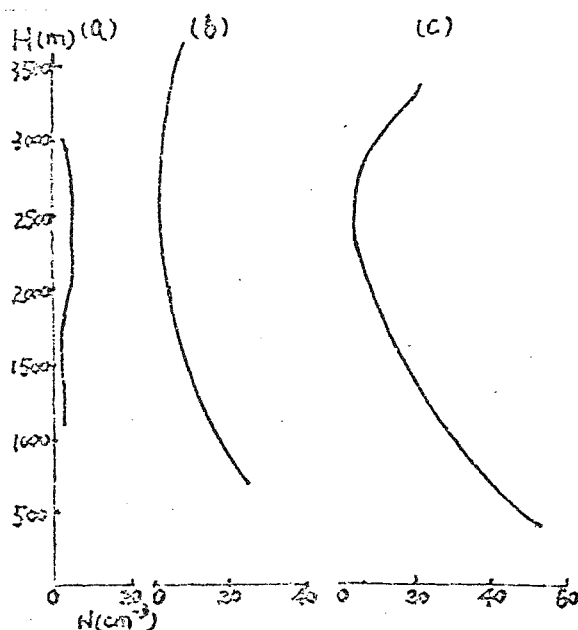


Fig.1. The aerosol particles' distributions with altitudes in the clean atmosphere in (a) Yili at 10:51-10:59, Jan. 8 1988, (b) Kuerla at 10:29-10:42, Dec. 28 1987, and (c) Urumqi at 15:58-16:15, Jan. 7 1988.

3.2 The characteristics of aerosol particles' distributions in the unclean atmosphere

The aerosol particles' concentrations and masses' concentrations in the unclean atmosphere are obviously higher than those in the clean atmosphere, and their distributions with space and regions are more different. The data of both the south and the north of Mt. Tianshan obtained by a flight, with moderate inversion, are given in Table2. It indicates that the mean particles' concentrations in the unclean atmosphere are 2-7 times higher than those in the clean atmosphere (Table1.), the maximums are 156.14 cm^{-3} and 111.14 cm^{-3} at the northern and southern hillsides of Mt.

Tianshan, and the minimums are 3.11 cm^{-3} and 4.18 cm^{-3} at the centre of the Zhunger Basin and the Tianshan mountainous. The table also shows that the masses' concentrations in the unclean atmosphere are 2-6 times higher than those in the clean atmosphere, the maximum is 117.51 E-6 g.m^{-3} at the southern hillside of Mt. Tianshan, and the minimum is 0.71 E-6 g.m^{-3} at the centre of the Zhunger Basin.

Table2. The measurement of aerosol particles' concentrations and masses' concentrations in the unclean atmosphere.

Sounding regions	Time	N(cm^{-3})			M(E-6 g.m^{-3})		
		Means	Max	Min	Means	Max	Min
The Zhunger Basin	12:38 ~12:59	29.36	79.18	3.11	4.68	17.51	0.71
The Tianshan mountainous	14:38 ~14:19	13.37	58.17	4.18	3.15	12.98	0.84
The northern hillside of Mt. Tianshan	13:28 ~13:49	43.74	156.14	5.79	9.88	35.84	1.28
The southern hillside of Mt. Tianshan	14:38 ~14:48	48.56	111.14	6.18	33.54	117.51	2.58

The distributions of particles' concentrations with altitudes over cities, with strong inversion, are given in Fig.2. The aerosol particles' concentrations increase with altitudes increasing below the inversion layer, and obviously meet the maximums near the top of the inversion layer (100-500 m from the top), and then decrease with altitudes increasing. The maximums near the top of the inversion layer are 1-3 times higher than the means, and the scales and spectral widths are the biggest here.

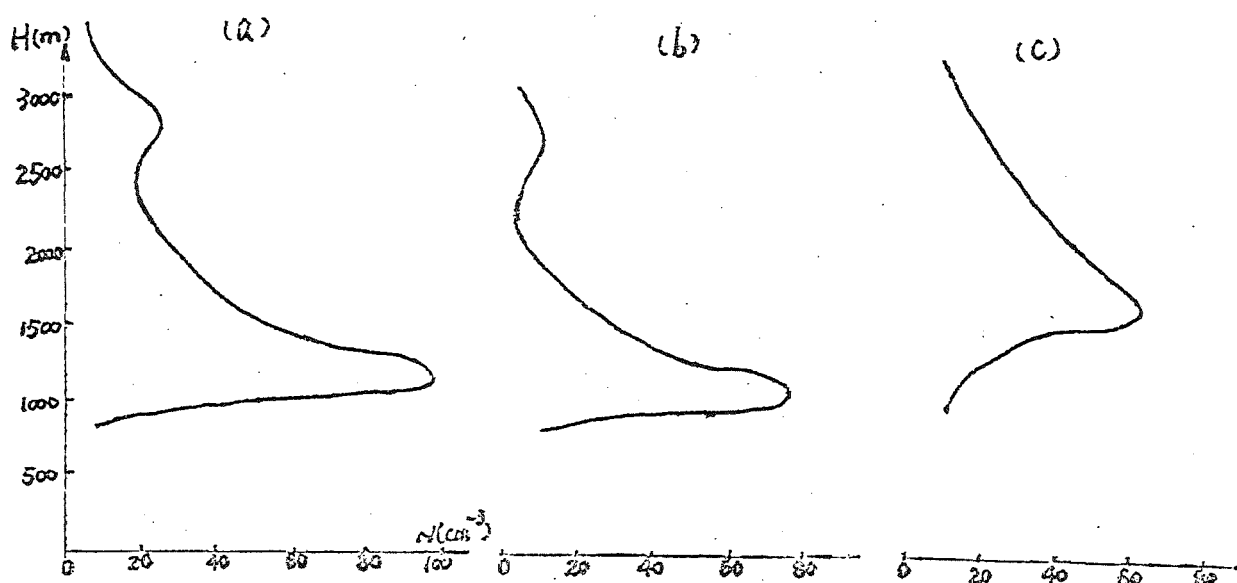


Fig.2 The distributions of aerosol particles' concentrations with altitudes in the unclean atmosphere in (a)Yili at 10:51-10:59,Jan.8 1988, (b) Kuerla at 10:29-10:42,Dec.28 1987,and (c) Urumqi at 15:58-16:15,Jan.7 1988.

3.3 The characteristics of aerosol particles' distributions over cities

The aerosol particles' concentrations, scales and spectral widths over cities are evidently bigger than those over villages, mountainous and desert regions. The means of particles' concentrations, diameters and masses' concentrations over 4 cities as Urumqi, Kelamayi, Kuerla and Yinin obtained with the vertical flight, with moderate strong inversion, are given in Table3. The table indicates that the aerosol particles' concentrations,scales are comparatively quite big with moderate strong inversion, and closely related to size of cities,dense populations and industrial production. For example, both the population and the industrial production scale in Urumqi are bigger than those in the other cities, so the aerosol particles' concentrations over Urumqi are higher than those over the other cities. The reason why the masses' concentration and diameter over Kuerla at the southern hillside of Mt.Tianshan are higher than those over the other cities, maybe is that the earth's surfaces were covered without snow.

Table3.The measurement of aerosolparticles' concentrations over cities withmoderate strong inversion.

Regions	Time	\bar{N} (cm ⁻³)	\bar{M} (g.m ⁻³)	\bar{D} (μm)
Urumqi	Dec,28,1987 11:47-11:56	62.971	22.865E-6	0.836
Kelamayi	Nov,30,1987 15:21-15:38	54.278	20.476E-6	—
Yinin	Jan,7,1988 18:00-18:09	31.756	9.255E-6	0.766
Kuerla	Dec,24,1987 14:38-14:47	46.899	54.778E-6	0.998

The observation also indicates that several maximums of aerosol particles' distributions over urban districts can appear because of inversion and not uniform distributions of populations and industries. The high values (>100 cm⁻³) of aerosol particles' concentrations can often be observed over fire-power stations, steel mills, cement factories and large chemical plants.

4.MAIN CONCLUSIONS

4.1 The characteristics of aerosol particles' geographical distributions in the lower atmosphere layer in Xinjiang in winter

(1). Because of the industrial and cities' pollution and the influence of topography and winters' inversion, the aerosol particles' concentrations at both sides of Mt. Tianshan are obviously higher than ones in the Zhunger Basin and the Tianshan mountainous.

(2). For the earth's surfaces at the southern side of Mt. Tianshan and Talimu Basin are dry and without snow, the masses' concentrations, scales and spectral widths of aerosol particles at the southern hillside of Mt. Tianshan are bigger than those at the Tianshan mountainous and the northern hillside of Mt. Tianshan, where the earth's surfaces are covered with snow. It is proved that the snow covering the earth's surfaces obviously holds back the pollution sources.

(3). Under the same inversion intensity condition, the aerosol particles' concentrations and masses' concentrations at the Tianshan mountainous and the Yili River Valley are evidently lower than those at both sides of Mt. Tianshan and the Zhunger Basin.

4.2 The characteristics of aerosol particles' vertical distributions in the lower atmosphere layer in Xinjiang in winter

(1). In the clean atmosphere, the maximums of aerosol particles' concentrations are at the ground layer, and then, with altitudes increasing, slowly decrease and slightly increase above 2500m.

In the unclean atmosphere or under the strong inversion stratification condition, the

aerosol particles' concentrations increase with altitudes increasing at first, and obviously meet the maximums near the top of the inversion layer, and then rapidly decrease with altitudes increasing.

(2). The aerosol particles' concentrations in afternoon are generally higher than those in morning. It is usual that the vertical distributions of aerosol particles' concentrations in morning are close to those in the clean atmosphere. But the maximum concentrations obviously appear near the top of the inversion layer in afternoon.

4.3 The characteristics of aerosol particles' distributions over cities in Xinjiang in winter

(1). The concentrations, scales and spectral widths of aerosol particles over urban districts, big cities and downwind of cities are bigger than those over suburbs, small cities and upwind of cities.

(2). Many maximums of aerosol particles' distributions over urban districts can appear with not uniform distributions of industries and populations.

(3). The aerosol particles' concentrations over cities obviously increase and decrease with time because of the stratification variation and the precipitations' washing out, and have a certain variation characteristic in a day.

(4). With the influence of the inversion layer, the cities' pollution sources can extend dozens miles or more toward downwind so that the downwind of cities are evidently polluted.

A MECHANISM OF FORMATION OF NONCONVECTIVE AEROSOL AND GASEOUS CLOUDS IN TURBULENT ATMOSPHERE

Tov Elperin¹, Nathan Kleeorin¹ and Igor Rogachevskii²

¹The Pearlstone Center for Aeronautical Engineering Studies,
Department of Mechanical Engineering, Ben-Gurion University,
POB 653, 84105 Beer-Sheva, Israel

²Racah Institute of Physics, Hebrew University of Jerusalem,
91904 Jerusalem, Israel

1. INTRODUCTION

Problem of formation of aerosol and gaseous clouds is of fundamental importance in many areas of environmental sciences, physics of the atmosphere and meteorology. Important mechanisms which determine formation and evolution of aerosol clouds is the preferential concentration of atmospheric particles. However, in turbulent atmosphere a mechanism of concentration of atmospheric particles in nonconvective clouds is still a subject of active research. It is well-known that turbulence results in decay of inhomogeneities of concentration due to turbulent diffusion, whereas the opposite process, e.g., the preferential concentration of particles in turbulent fluid flow still remains unexplained.

A new effect of turbulent thermal diffusion that results in the preferential concentration of particles in turbulent atmosphere is discussed (Elperin et al. 1995; 1996a,b). This phenomenon is related to the dynamics of small inertial particles in incompressible turbulent fluid flow. Physical mechanism of the effect of turbulent thermal diffusion is associated with correlation between velocity and temperature fluctuations in the presence of a nonzero mean temperature gradient. The latter results in additional non-diffusive flux of aerosols. At large Reynolds and Peclet numbers the turbulent thermal diffusion is much stronger than the molecular thermal diffusion. It is shown that turbulent thermal diffusion under certain conditions can cause a large-scale instability of spatial distribution of aerosols. Aerosols are concentrated in the vicinity of the minimum (or maximum) of the mean temperature of the surrounding fluid depending on the ratio of material particle density to that of the surrounding fluid.

2. MECHANISM OF PREFERENTIAL CONCENTRATION OF PARTICLES IN TURBULENT ATMOSPHERE

First let us discuss the mechanism of the instability. The inertia effect results in particles inside the turbulent eddy are carried out to the boundary regions between eddies by inertial force (this regions with decreased velocity of the turbulent fluid flow and maximum of pressure of the surrounding fluid). This means that in regions with maximum pressure of turbulent fluid there is accumulation of inertial particles. Similarly there is an outflow of inertial particles from regions with minimum pressure of fluid. In a homogeneous and isotropic turbulence without large-scale external gradients of temperature a drift from regions with increased (decreased) concentration of inertial particles by a turbulent flow of fluid is equiprobable in all directions. Location of these regions is not correlated with turbulent velocity field. Therefore they do not contribute in large-scale flow of inertial particles.

Situation is drastically changed when there is a large-scale inhomogeneity of the temperature of the turbulent flow. In this case the mean heat flux $\langle \tilde{u}\Theta \rangle \neq 0$. Therefore fluctuations of both, temperature Θ and velocity \tilde{u} of fluid, are correlated. Fluctuations of temperature cause fluctuations of pressure of fluid. The pressure fluctuations result in fluctuations of the concentration of inertial particles. Indeed, increase (decrease) of the pressure of surrounding fluid is accompanied by accumulation (outflow) of the particles. Therefore, direction of mean flux of particles coincides with that of heat flux, i.e. $\langle \tilde{u}n_p \rangle \propto \langle \tilde{u}\Theta \rangle \propto -\vec{\nabla}T$, where n_p is the number density of the particles, and T is the mean temperature of fluid. Therefore the mean flux of

the inertial particles is directed to the minimum of the mean temperature and the inertial particles are accumulated in this region. This effect is more pronounced when turbulent fluid flow is inhomogeneous in the direction of the mean temperature gradient.

Evolution of the number density $n_p(t, \mathbf{r})$ of small particles in a turbulent flow is determined by equation:

$$\frac{\partial n_p}{\partial t} + \vec{\nabla} \cdot (n_p \mathbf{v}_p) = D \Delta n_p, \quad (1)$$

where \mathbf{v}_p is a random velocity field of the particles which they acquire in a turbulent fluid velocity field, D is the coefficient of molecular diffusion. We consider the case of large Reynolds and Peclet numbers. The velocity of particles \mathbf{v}_p depends on the velocity of the surrounding fluid, and it can be determined from the equation of motion for a particle. This equation represents a balance of particle inertia with the fluid drag force produced by the motion of the particle relative to the surrounding fluid. Solution of the equation of motion for small particles with $\rho_p \gg \rho$ yields (Maxey, 1987):

$$\mathbf{v}_p = \mathbf{v} - \tau_p \left[\frac{\partial \mathbf{v}}{\partial t} + (\mathbf{v} \cdot \vec{\nabla}) \mathbf{v} \right] + O(\tau_p^2), \quad (2)$$

where \mathbf{v} is the velocity of the surrounding fluid, τ_p is the characteristic time of coupling between the particle and surrounding fluid (Stokes time), ρ_p is the material density of particles, ρ is the density of the fluid. For instance, for spherical particles of radius a_* the Stokes time is $\tau_p = m_p / (6\pi a_* \rho \nu)$, where ν is the kinematic viscosity of the surrounding fluid, and m_p is the particle mass. The second term in (2) describes the difference between the local fluid velocity and particle velocity arising due to the small but finite inertia of the particle.

In this study we consider incompressible turbulent flow $\vec{\nabla} \cdot \mathbf{v} = 0$. However, the velocity field of particles is assumed to be compressible, i. e. $\vec{\nabla} \cdot \mathbf{v}_p \neq 0$. Indeed, Eq. (2) for the velocity of particles and Navier-Stokes equation for the fluid yield $\vec{\nabla} \cdot \mathbf{v}_p = -\tau_p \vec{\nabla} \cdot (d\mathbf{v}/dt) = \tau_p \Delta P / \rho$, where P is the fluid pressure. We study the large-scale dynamics of small inertial particles and average Eq. (1) over an ensemble of random velocity fluctuations. For this purpose we use the stochastic calculus (Zeldovich et al., 1988; Kleeorin and Rogachevskii, 1994; Elperin et al., 1995). It

yields the equations for the mean number density of particles $N = \langle n_p \rangle$

$$\frac{\partial N}{\partial t} + \vec{\nabla} \cdot [N \mathbf{V}_{\text{eff}} - \hat{D} \vec{\nabla} N] = 0, \quad (3)$$

where $\hat{D} \equiv D_{pm} = D \delta_{pm} + \langle \tau u_p u_m \rangle$, $\mathbf{V}_{\text{eff}} = \mathbf{V} - \langle \tau \mathbf{u} (\vec{\nabla} \cdot \mathbf{u}) \rangle$, and $\mathbf{v}_p = \mathbf{V} + \mathbf{u}$, $\mathbf{V} = \langle \mathbf{v}_p \rangle$ is the mean velocity, \mathbf{u} is the random component of the velocity of particles, and τ is the momentum relaxation time of random velocity field \mathbf{u} , which depends on scale of turbulent motion.

Now we derive an equation for N^2 . Multiplication of Eq. (3) by N and simple manipulations yield

$$\frac{\partial N^2}{\partial t} + (\vec{\nabla} \cdot \mathbf{S}) = -N^2 (\vec{\nabla} \cdot \mathbf{V}_{\text{eff}}) - I_D,$$

where $\mathbf{S}_m = N^2 (\mathbf{V}_{\text{eff}})_m - D_{mp} \vec{\nabla}_p N^2$, $I_D = 2D_{mp} (\vec{\nabla}_m N) (\vec{\nabla}_p N)$. The latter equation implies that if $\vec{\nabla} \cdot \mathbf{V}_{\text{eff}} < 0$, a perturbation of the equilibrium distribution of inertial particles can grow in time, i. e., $(\partial/\partial t) \int N^2 d^3r > 0$. However, the total number of particles is conserved. Therefore the growth of N^2 when $\vec{\nabla} \cdot \mathbf{V}_{\text{eff}} < 0$ is accompanied by formation of an inhomogeneous spatial distribution of the inertial particles whereby regions with an increased concentration of particles coexist with regions depleted from particles.

Now we calculate the velocity \mathbf{V}_{eff} , using the equation of state $P = \kappa T_f \rho / m_\mu$, where m_μ is the mass of molecules of surrounding fluid and $T_f(t, \mathbf{r})$ is the temperature field with a characteristic value T_* . To obtain an equation for $\langle \tau \mathbf{u} (\vec{\nabla} \cdot \mathbf{u}) \rangle$, we take into account that the fluctuating component of the particle velocity \mathbf{u} can be expressed in terms of the turbulent velocity of fluid $\tilde{\mathbf{u}}$: $\mathbf{u} = \tilde{\mathbf{u}} - \tau_p d\tilde{\mathbf{u}}/dt$ [see Eq. (2)]. Note that $\vec{\nabla} \cdot \mathbf{u} \neq 0$, whereas $\vec{\nabla} \cdot \tilde{\mathbf{u}} = 0$. Therefore the velocity \mathbf{V}_{eff} is given by $\mathbf{V}_{\text{eff}} = \mathbf{V} - (\tau_p v_T^2 / T_*) \langle \tau \tilde{\mathbf{u}} \Delta \Theta \rangle$, where $v_T^2 = \kappa T_* / m_\mu$, and we neglect terms $\sim O(\tau_p^2)$. The latter formula shows that \mathbf{V}_{eff} depends on the mean turbulent heat flux $\langle \tilde{\mathbf{u}} \Theta \rangle$ that is determined by the well known equation $\langle \tilde{\mathbf{u}}(\mathbf{x}) \Theta(\mathbf{x}) \rangle = -\chi_T \vec{\nabla} T$ (see, e. g., McComb, 1990), where the total temperature is $T_f = T + \Theta$, $T = \langle T_f \rangle$ is the mean temperature field, $\chi_T \sim u_0 l_0 / 3$ is the coefficient of turbulent thermal conductivity. Note that herein we do not consider situation with very high gradients when gradient transport assumption is violated. The above formula for the mean turbulent

heat flux is written in the \mathbf{r} -space. The corresponding second moment in \mathbf{k} -space is given by $\langle \tilde{u}_m(\mathbf{k})\Theta(-\mathbf{k}) \rangle = -\tau(k)\langle \tilde{u}_m(\mathbf{k})\tilde{u}_n(-\mathbf{k}) \rangle (\partial T / \partial R_n)$, where \mathbf{R} is a large-scale variable, and a spectrum of the turbulent velocity field and correlation time $\tau(k)$ can be chosen as Kolmogorov's spectrum:

$$\langle \tilde{u}_m \tilde{u}_n \rangle = \frac{2}{3k_0} \left(\frac{\langle \tilde{u}^2 \rangle}{8\pi k^2} \right) \left(\frac{k}{k_0} \right)^{-\frac{5}{3}} \left(\delta_{mn} - \frac{k_m k_n}{k^2} \right),$$

$$\tau(k) = 2\tau_0 \left(\frac{k}{k_0} \right)^{-\frac{2}{3}},$$

where $k_0 < k < k_0 \text{Re}_*^{3/4}$ (see, e. g., McComb, 1990), $\text{Re}_* = \min\{\text{Re}, \text{Pe}_T\}$, $\text{Re} = l_0 u_0 / \nu$ is the Reynolds number, $\text{Pe}_T = l_0 u_0 / \chi$ is the thermal Peclet number, $l_0 = k_0^{-1}$ is the maximum scale of turbulent motions, u_0 is the characteristic velocity in this scale, χ is the coefficient of molecular thermal conductivity. Multiplying equation for $\langle \tilde{u}_m(\mathbf{k})\Theta(-\mathbf{k}) \rangle$ by $-k^2 \tau(k)$ and integrating in \mathbf{k} -space we obtain $\langle \tau \tilde{u}_m \Delta \Theta \rangle = \alpha \ln(\text{Re}_*) \nabla T$, where $\alpha = 2/3$. Finally we arrive for the following equation for velocity

$$\mathbf{V}_{\text{eff}} = \mathbf{V} - \frac{\alpha \tau_p v_T^2}{T_*} \ln(\text{Re}_*) \nabla T.$$

Equation (3) with this effective velocity \mathbf{V}_{eff} can be rewritten in the form

$$\frac{\partial N}{\partial t} + \nabla \cdot (N \mathbf{V}) = -\nabla \cdot (\mathbf{J}_T + \mathbf{J}_M), \quad (4)$$

where

$$\mathbf{J}_T = -D_T \left[\frac{k_T}{T} \nabla T + \nabla N \right], \quad (5)$$

$$k_T = N \frac{3\alpha}{\text{Pe}} \left(\frac{m_p}{m_\mu} \right) \left(\frac{T}{T_*} \right) \ln \text{Re}_*, \quad (6)$$

where $D_T = u_0 l_0 / 3$ is the coefficient of turbulent diffusion, k_T can be interpreted as turbulent thermal diffusion ratio, and $D_T k_T$ is the coefficient of turbulent thermal diffusion. We use here an identity

$$\frac{\tau_p v_T^2}{l_0 u_0} = \frac{1}{\text{Pe}} \left(\frac{m_p}{m_\mu} \right),$$

and $\text{Pe} = u_0 l_0 / D_*$ is the Peclet number and the molecular diffusion coefficient $D_* = \kappa T_* / (6\pi a_* \rho \nu)$. Note that for $\text{Re}_* \gg 1$ and $\text{Pe} \gg 1$ both turbulent diffusion coefficients are much larger than

the corresponding molecular coefficients (i.e., $D_T \gg D$ and $D_T k_T \gg D k_t$).

Now we will show that turbulent thermal diffusion results in large-scale pattern formation whereby initially spatial distribution of particles in a turbulent incompressible flow of fluid evolves under certain conditions into large-scale inhomogeneous distribution due to excitation of an instability. One of the most important conditions for the instability is inhomogeneous spatial distribution of mean temperature of surrounding fluid. In particular, the instability can be excited in the vicinity of the minimum in the mean temperature distribution. The growth rate of the instability in dimensionless form is given by

$$\gamma_0 = \eta_0 + \frac{3}{2} a_0 - \left[\eta_0^2 + \frac{9}{4} a_0^2 - a_0 k^2 \right]^{\frac{1}{2}} - k^2 \quad (7)$$

(see Elperin et al., 1996), where

$$\eta_0 = \frac{3\alpha}{\text{Pe}} \left(\frac{m_p}{m_\mu} \right) \left(\frac{\delta T}{T_*} \right) \ln \text{Re}_*,$$

$$a_0 = \frac{1}{2} \frac{d^2}{dZ^2} \ln \langle u^2 \rangle,$$

the axis Z is directed along mean temperature gradient, the wave vector \mathbf{k} is perpendicular to the axis Z , and Eq. (7) is written in dimensionless form, coordinate is measured in units Λ_T , time t is measured in units Λ_T^2 / D_T , wave number k is measured in units Λ_T^{-1} , the temperature T is measured in units of temperature difference δT in the scale Λ_T , and concentration N is measured in units N_* . Thus the initially spatial distribution of the concentration of the inertial particles evolves into a pattern containing regions with increased (decreased) concentration of particles. Characteristic vertical size of the inhomogeneity when $\eta_0 \geq a_0$ is of the order of

$$l_z \sim \Lambda_T \left[\frac{3\alpha}{\text{Pe}} \left(\frac{m_p}{m_\mu} \right) \left(\frac{\delta T}{T_*} \right) \ln \text{Re}_* \right]^{-\frac{1}{2}}.$$

Remarkably $l_z \rightarrow \infty$ when $\text{Pe} \rightarrow \infty$, i. e., this effect exists for large but finite Peclet numbers.

3. DISCUSSION

The effect of turbulent thermal diffusion is important in some atmospheric phenomena (e. g., atmospheric aerosols, cloud formation and

smog formation). Observations of the vertical distributions of aerosols in the atmosphere show that maximum concentrations can occur within temperature inversion layers. Using the characteristic parameters of the atmospheric turbulent boundary layer (Seinfeld, 1986; Jaenicke, 1987): maximum scale of turbulent flow $l_0 \sim 10^3 - 10^4$ cm; velocity in the scale l_0 : $u_0 \sim 30 - 100$ cm/s; Reynolds number $Re \sim 10^6$ and of the temperature inversion: scale $\Lambda_T \sim 3 \times 10^4$ cm and dimensionless mean spatial temperature variation $\delta T/T_0 \sim (1 - 3) \times 10^{-2}$, we obtain that the characteristic time of excitation of the instability of concentration distribution of aerosols with material density $\rho_p \sim 2$ g / cm³ and radius $a_* = 10 \mu\text{m}$ varies in the range from 0.3 to 3 hours. This value is in compliance with the characteristic time of growth of inhomogeneous structures in atmosphere. It is essential that this time strongly depends on the aerosol size, i.e., $\sim a_*^{-2}$.

Remarkably, similar phenomenon of preferential concentration in the vicinity of temperature inversion layers can occur during formation of gaseous clouds (Elperin et al. 1995; 1996b). The latter effect is caused by compressibility [$\text{div } \mathbf{u} \propto -(\mathbf{u} \cdot \nabla)\rho \propto (\mathbf{u} \cdot \nabla)T \neq 0$] of a turbulent carrying flow, where ρ is the density of surrounding fluid. Equation similar to Eq. (6) is valid also in a case of a gaseous passive scalar (for details see Elperin et al. 1995; 1996b). The difference is that in gases the turbulent thermal diffusion ratio $k_T = N$ and there exists also an additional flux caused by turbulent barodiffusion $\sim -D_T N(\vec{\nabla}P/P)$, i.e., the equation for turbulent flux \mathbf{J}_T in gases reads:

$$\mathbf{J}_T = -D_T N \left[\frac{\vec{\nabla}T}{T} - \frac{\vec{\nabla}P}{P} + \frac{\vec{\nabla}N}{N} \right].$$

This effect plays an important role in dynamics of gaseous pollutants in atmosphere.

The discussed effect of preferential concentration of particles and gaseous admixtures in turbulent atmosphere may play an important role in the process of precipitation formation which remains a classic problem in cloud physics. It is not well understood which processes cause the fast broadening of the drop size distribution in cumulus clouds. Also the formation of large drops in stratiform clouds remains a subject for research because the low values of the supersaturation observed in these clouds is insufficient

to explain the formation of large drops during a reasonable time. The effect of preferential concentration of small inertial particles and gaseous admixtures may exist in all types of clouds and can act as a universal mechanism which substantially increases the rate of the collection process, especially in the early stages of cloud development.

4. REFERENCES

- Elperin, T., Kleeorin N. and I. Rogachevskii, 1995: Dynamics of passive scalar in compressible turbulent flow: large-scale patterns and small-scale fluctuations, *Phys. Rev. E*, **52**, 2617-2634.
- Elperin, T., Kleeorin N. and I. Rogachevskii, 1996a: Turbulent thermal diffusion of small inertial particles, *Phys. Rev. Lett.*, **76**, 224-228.
- Elperin, T., Kleeorin N. and I. Rogachevskii, 1996b: Turbulent barodiffusion and thermal diffusion in gases. *Phys. Rev. E*, submitted.
- Jaenicke, R., 1987: *Aerosol Physics and Chemistry*. Springer, Berlin.
- Kleeorin N. and I. Rogachevskii, 1994: Nonlinear Theory of Magnetic Fluctuations in Random Flow: The Hall Effect. *Phys. Rev. E*, **50**, 493-501.
- Maxey, M. R., 1987: The gravitational settling of aerosol particles in homogeneous turbulence and random flow field. *J. Fluid Mech.*, **174**, 441-465.
- McComb, W. D., 1990: *The Physics of Fluid Turbulence*. Clarendon, Oxford, and references therein.
- Seinfeld, J. H., 1986: *Atmospheric Chemistry and Physics of Air Pollution*. John Wiley, New York.
- Zeldovich, Ya. B., Molchanov, S. A., Ruzmaikin, A. A. and D. D. Sokoloff, 1988: Intermittency, diffusion and generation in a nonstationary random medium. *Sov. Sci. Rev. C. Math Phys.*, **7**, 1-110, and references therein.

CHARGE DISTRIBUTION ON AEROSOLS CONSISTING OF PARTICLES OF DIFFERENT MATERIALS UNDER PHOTON IRRADIATION

Olga A. Mikhalkova and Pavel P. Poluektov.

A.A.Bochvar Scientific Research Institute of Inorganic Materials, 123060, Moscow, Russia.

Aerosol particles are known to accumulate electric charge as a result of photoemission of electrons. Emitted electrons significantly increase the number concentration in the atmosphere of negative ions which will attach particles due to the diffusion. Thus the problem of photoelectric charging proves to be self-consistent. The theoretical analysis of the problem is presented in the paper. We shall consider monodisperse aerosol system with a fixed number of particles of two materials in equal concentrations. The method for calculating the steady-state charge distribution was described in detail by Poluektov et al. (1991) and Kascheev et al. (1994). The analysis is based on the balance of electric charge flows among the charge states of aerosol particles. In the steady-state:

$$W_Z^- n(Z) = W_{Z-1}^+ n(Z-1), \quad (1)$$

where $n(Z)$ - the number of particles in the Z -th charge state (i.e. the number of particles with Z elementary charges); W_Z^\pm - the probability of single change in the Z -th charge state per unit time. The general result for all single-electron recharging processes can therefore be derived:

$$n(Z) = n(0) \prod_{i=1}^Z \frac{W_{i-1}^+}{W_i^-}, \quad Z > 0 \quad (2)$$

If aerosol particles are not subjected to any external factors leading to changes in their electric charges and the particles do not emit electrons or ions, then any change in particle charges will be caused by the charge flow to the particles from the atmosphere. The classical theory of ion diffusion gives the following expression for positive and negative charge flows:

$$\begin{aligned} W_Z^{(0)+} &= \frac{4\pi D_+ n_+ Z e^2}{k_B T [\exp(Ze^2/Rk_B T) - 1]}, \\ W_Z^{(0)-} &= \frac{4\pi D_- n_- Z e^2}{k_B T [1 - \exp(-Ze^2/Rk_B T)]} \end{aligned} \quad (3)$$

where D_\pm and n_\pm - diffusion coefficients and concentrations of positive and negative ions in the atmosphere; k_B - the Boltzmann's constant; T - temperature; R - particle radius. The above expression

is valid for particles with sizes greater than the mean free path of ions in the atmosphere. By substituting (3) into equation (2), we obtain the charge distribution (Clement and Harrison, 1992; Poluektov et al, 1991):

$$\begin{aligned} n(Z) &= \frac{C}{Z} \sinh\left(\frac{\alpha Z}{2}\right) \exp\left(-\frac{\alpha}{2}(Z - \langle Z \rangle)^2\right), \\ \alpha &= \frac{e^2}{Rk_B T}, \quad \langle Z \rangle = \alpha^{-1} \ln(D_+ n_+ / D_- n_-) \end{aligned} \quad (4)$$

where C is the normalizing constant. Under the influence of external irradiation particles with photoelectric work function below photon energy emit electrons and equation (1) takes the following form:

$$W_Z^- n(Z) = (W_{Z-1}^+ + W_{Z-1}^{ph}) n(Z-1) \quad (5)$$

Provided the irradiation is quite intensive, negative ions concentration will originate only from photoelectrons. The probability W_Z^{ph} - of the emission of an electron as a function of the photon energy $\hbar\omega$ and the threshold A is defined by the following law:

$$W_Z^{ph} = \frac{I\sigma_0}{\hbar\omega} \left(1 - \frac{A}{\hbar\omega}\right)^m \quad (6)$$

where: I - light intensity; σ_0 photoemission cross-section. The exponent equals $m = 2$ for metal (Burtscher, 1992). In a more suitable form equation (6):

$$W_Z^{ph} = \frac{\tilde{I}\sigma_0}{\hbar\omega} (Z - Z_0)^m, \quad (7)$$

where $Z_0 = R/e^2(\hbar\omega - A_0)$. Otherwise photoemission is probable for particles acquiring not more than Z_0 charges. Provided light intensity is high, the charging process will be governed by photoemission and diffusion charging term in (5) may be neglected. The charge balance equation (5) becomes:

$$n(Z+1) = \frac{\beta}{n_-} (Z - Z_0)^m \frac{e^{\alpha(Z+1)} - 1}{\alpha(Z+1)} n(Z) \quad (8)$$

where $\beta = \tilde{I}\sigma_0/4\pi R D_- \hbar\omega$. Supposing $\alpha Z \ll 1$, the charge distribution can be obtained:

$$n(Z) = C_1 \left(\frac{\beta}{n_-}\right)^Z \frac{1}{(Z - Z_0)!^m}, \quad Z \leq Z_0$$

$$n(Z) = 0, Z > Z_0 \quad (9)$$

The normalizing constant C_1 is defined by following:

$$N = \sum_{Z \leq Z_0} n(Z) \quad (10)$$

N - the number of aerosol particles in the unit volume. The set of equations (9-10) should be complemented by the electroneutrality condition:

$$n_- = \sum_{Z \leq Z_0} n(Z)Z \quad (11)$$

Using the function:

$$S_m(x) = \sum_{k=0}^{\infty} \frac{x^{-k}}{(k!)^m}, \quad x = \frac{\beta}{n_-} \quad (12)$$

the complete charge of aerosol particles can be obtained:

$$Q_{ph} = N \left(Z_0 + x \frac{S'_m(x)}{S_m(x)} \right) \quad (13)$$

In the limiting case of very intensive irradiation $N/\beta \ll 1$: $n_- \approx NZ_0$, i.e. all particles acquire equal charge Z_0 and monocharging occurs. When aerosol consists of equal amounts of particles of different materials, charge distributions for each material will differ from each other. For particles which can not be ionized by photon irradiation the equation (4) gives the charge distribution. For the photo-ionizable particles the charge distribution is (9). The resulting electroneutrality condition:

$$Q_{ph} + Q_0 - n_- = 0 \quad (14)$$

where Q_0 - the total charge of non-ionizable particles. The solution of this equation defines the negative ion concentration and charge distributions. The equation (15) have been solved numerically and results for different light intensities are shown at Fig. 1. It is to be pointed out that monocharging occurs under lower intensities compared to those for homogeneous aerosol consisting only of the same photo-ionizable particles. That is to say takes place stimulation of monocharging.

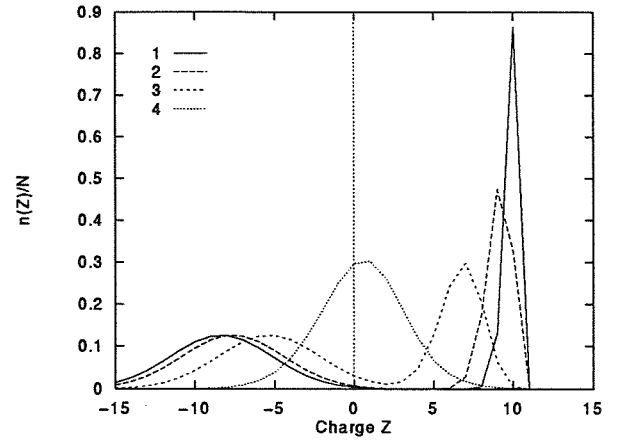


Figure 1: Charge distribution for different light intensities $I_1 > I_2 > I_3 > I_4$. The first peak corresponds to non-ionizable particles and the second to ionizable particles.

REFERENCES

- Burtsher H. (1992), Measurement and characteristics of combustion aerosol with special consideration of photoelectric charging and charging by flame ions. *J. Aerosol Sci.* **6**, 549-595.
- Clement, C.F. and Harrison, R.G. (1992) The charging of radioactive aerosols. *J. Aerosol Sci.* **23**, 481-504.
- Kascheev V.A., Mikhalkova O.A., Poluektov P.P. (1994) The statistics of β - radioactive aerosol electric charging. *Atomic energy.* **76**, 36-41.
- Poluektov P.P., Emets E.P., kashcheev V.A. (1991) On steady-state distribution of aerosol particles electric charges. *J. Aerosol Sci.* **22**, s237-s240.

THE RELATIVE IMPORTANCE OF NSS-SULPHATE AND SEA-SALT AEROSOL TO THE MARINE CCN POPULATION

Colin D. O'Dowd¹, Michael H. Smith¹, Andrew D. Kaye², and Jason. Lowe¹

¹Physics Department, UMIST, Manchester, M60 1QD, UK

²NERC, ARASF, Meteorological Research Flight, DRA Farnborough, GU14 6TD, UK

1. INTRODUCTION

Marine low-level stratiform clouds contribute significantly to the planetary albedo (Slingo 1990), and consequently, perturbations in their reflectance can potentially modify the Earth's radiative budget. Cloud optical properties are controlled by the mean effective radius of the cloud droplet distribution, which, in turn, is controlled by the availability of cloud condensation nuclei (CCN) for a given liquid water content (Twomey 1977). It is generally assumed that non-sea-salt (nss)- sulphate, both natural and anthropogenic, dominates the marine CCN population. Natural nss-sulphate is derived from the oxidation of SO₂, an oxidation product of Dimethyl sulphide (DMS) which is produced as a waste product of the marine biota. Anthropogenic sulphate in the marine environment results from long-range transport of SO₂ and sulphate aerosols.

Twomey *et al.*, (1984) suggested that an increase in pollution emissions, and thus, an increase in available sulphate CCN, would lead to a reduction in the effective radius of cloud droplets, and thus, to brighter clouds, thereby resulting in a planetary cooling. This cooling effect is thought to be of similar magnitude to the radiative forcing induced by greenhouse gases, but, opposite in sign. Charlson *et al.*, (1987) also postulated that a natural negative feedback mechanism may exist where global warming, resulting from increased CO₂ emissions, could be offset by an increase in biogenic nss-sulphate CCN over the oceans which may ensue from increased biological activity in warmer oceanic waters, and consequently, an increase in the emission rate of DMS.

Due to the potential effect of increased SO₂ and sulphate aerosol emissions, it is desirable to accurately know, and be able to predict, the radiative forcing induced by increased anthropogenic activity. Recent attempts to predict anthropogenic sulphate radiative forcing have resulted in an estimated cooling of between -0.5 and -1.5 W m⁻² (Jones *et al.*, 1994; Boucher and Lohmann, 1995). One possible source of error in these studies is, however, in assuming that nss-sulphate aerosol, particularly over the ocean, is the primary source of CCN. This assumption may lead to an over-estimation of the radiative forcing by sulphate

aerosol if there is a significant contribution to the CCN population from other sources. O'Dowd and Smith (1993) suggested that the general assumption of nss-sulphate aerosol being the only significant contributor to the marine CCN population is not entirely accurate, and, they suggested that sea-salt could, not only provide a significant source of CCN, but sometimes, could dominate the actual CCN population. Peak sea-salt concentrations were observed under conditions of high wind speeds and were observed to follow a power-law relationship dependent upon wind speed. The measurements of O'Dowd and Smith were, however, confined to surface based measurements and may not have been representative of aerosol composition and concentration at cloud base.

In this study, we present airborne measurements of accumulation mode aerosol (covering the size which provides the majority of CCN), inferred aerosol composition using a volatility technique, and, cloud droplet concentrations over the North East Atlantic and the North East Pacific. Flights were undertaken during conditions when different source strengths of nss-sulphate and sea-salt CCN were dominant.

2. INSTRUMENTATION

Accumulation mode aerosol (0.05 - 1.5 µm radius) measurements were taken using a PMS ASASP-X optical particle counter mounted inside the Meteorological Research Flight C-130 research aircraft. An airborne volatility system was deployed to infer aerosol composition and its variation with size. The scanning-temperature volatility system previously used by O'Dowd and Smith (1993) required one-hour scanning periods, and thus, was not suitable for airborne use. Instead, four heater tubes, each set at a specific temperature were used: 40°C to dry the ambient aerosol, 80°C to volatilise MSA, 150°C to volatilise sulphuric acid, and 350°C to volatilise ammonium sulphate. Aerosol remaining at 350°C was considered sea-salt aerosol. Supporting aerosol measurements were performed by a wing-mounted PCASP optical particle counter whilst cloud droplet and sea-spray concentrations and size were measured by using a PMS FSSP optical particle counter.

3. OBSERVATIONS

Measurements were taken under a variety of conditions and air mass types over the North Atlantic and East Pacific. The North Atlantic flights were undertaken on a seasonal basis from 1993-1995 whilst the East Pacific flights were undertaken during the Monterey Area Ship Tracks Experiment in June 1994. Observations under low winds and moderate sulphate loadings are presented from the Pacific Ocean whilst observations under both high winds, resulting in high sea-salt CCN fluxes, and, sulphate-rich conditions are presented from the North Atlantic.

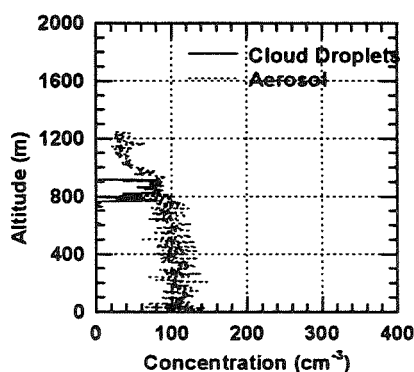


Figure 1: Vertical profile of aerosol and cloud droplet concentration for Pacific low-wind case.

3.1 Pacific maritime: low-wind:

Figure 1 displays the observed aerosol and cloud droplet concentration during a profile through the marine boundary layer approximately 500 km off the Californian coast. The boundary layer height was 900m in depth and was capped by a shallow stratocumulus cloud deck approximately 150 m deep. Sub-cloud aerosol concentrations were $\approx 90 \text{ cm}^{-3}$ whilst cloud droplet concentration were $\approx 80 \text{ cm}^{-3}$, indicating that nearly 90% of the aerosol were active as CCN. Using the volatility technique we were able to separate the nss-sulphate and sea-salt distribution and examine the relative contribution of each aerosol species to the CCN population.

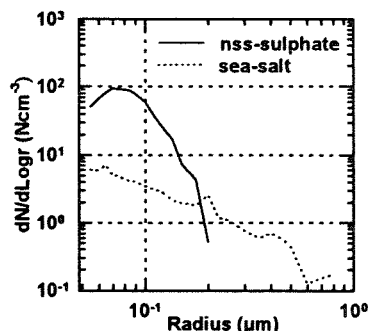


Figure 2: Nss-sulphate and sea-salt size distributions observed for low-wind Pacific aerosol.

Nss-sulphate and sea-salt size distributions, observed on the same flight but at a distance of 600 km off the coast are shown in Figure 2. The sulphate contribution to the total accumulation mode aerosol concentration ($N=71 \text{ cm}^{-3}$) was 90%, whilst the

remainder was attributed to sea-salt aerosol. The reduction in the aerosol concentration compared to the concentration at 500km is thought to be due to the increase in boundary layer height as one moves further off the coast. It is inferred that approximately 90% of the cloud droplets are formed on nss-sulphate nuclei. This is not surprising since no white-caps were observed during this flight, and thus, sea-salt CCN production was at a minimum. For most cases where wind speeds were 10 m s^{-1} or less, the majority of cloud droplets were formed upon sulphate nuclei.

3.2 Atlantic maritime - high wind

The highest wind speeds ($17-18 \text{ m s}^{-1}$) encountered during this series of flights were to the west of the Irish coast over the North East Atlantic. Air mass back trajectories indicated a tropical maritime history for this air mass. The maritime nature of this air mass was corroborated by observations of typically-maritime soot carbon mass loadings (20 ng m^{-3}) upwind, and in the same air mass, at the Mace Head background monitoring station on the Irish coast. The vertical distribution of aerosol and cloud droplets is shown in Figure 3. The boundary layer was decoupled with a surface layer 600 m in depth which contained a solid stratocumulus cloud deck approximately 300 m thick. The decoupled layer, extending from 600 m to 1500 m, possessed a very shallow dissipating cloud of about 50 m in thickness. We should note that the PCASP measurements in cloud are removed due to droplet shattering effects.

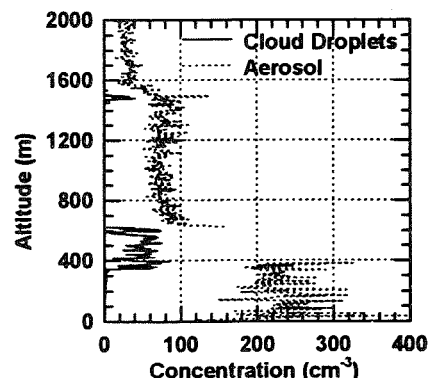


Figure 3: Vertical profiles of aerosol and cloud droplet concentration for Atlantic high-wind case.

In the surface layer, sub-cloud aerosol concentrations were well mixed from the surface to cloud base and averaged $\approx 250 \text{ cm}^{-3}$, however, the cloud droplet concentration observed was a very modest 50 cm^{-3} , and thus, the ratio of cloud droplets to sub-cloud aerosol was considerably less than that observed under low-to-moderate wind speed conditions.

Volatility analysis of the aerosol indicated that the contribution of nss-sulphate and sea-salt aerosol to the sub-cloud aerosol was 167 cm^{-3} and 72 cm^{-3} , respectively. It should be noted that both the nss-sulphate and sea-salt aerosol in the surface layer were well mixed up to cloud base. The nss-sulphate and

sea-salt size distributions taken just below cloud base are shown in Figure 4. Nss-sulphate aerosol possessed a mode radius of $0.078 \mu\text{m}$ and dominated the concentration at sizes smaller than $0.1 \mu\text{m}$ radius whilst sea-salt aerosol dominated the aerosol concentration at larger sizes.

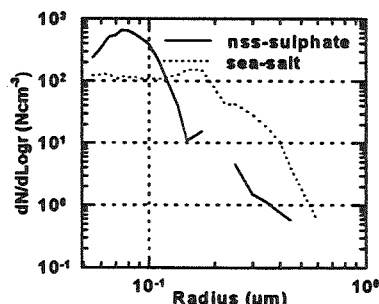


Figure 4: Nss-sulphate and sea-salt distributions observed for high wind Atlantic aerosol.

The larger sizes associated with sea-salt aerosol compared with that of nss-sulphate, combined with the lower activation threshold required to activate sea-salt nuclei of a similar size, suggests that the sea-salt nuclei would be activated first, and, in preference to nss-sulphate nuclei, during the early stages cloud formation (Pruppacher and Klett, 1978).

3.3 Cloud droplet - aerosol relationship

The relationship between sub-cloud aerosol and cloud droplet concentration for all flights is shown in Figure 5. It is readily seen that this relationship is non-linear, somewhat resembling a 1:1 relationship at low aerosol concentrations, but flattening off at higher sub-cloud concentrations. The equation of the curve which provided the best fit to the data is as follows: $CD = 197(1 - \exp(-6.13 \times 10^{-3} A))$ where $A \text{ cm}^{-3}$ is the sub-cloud aerosol concentration and $CD \text{ cm}^{-3}$ is the cloud droplet number concentration.

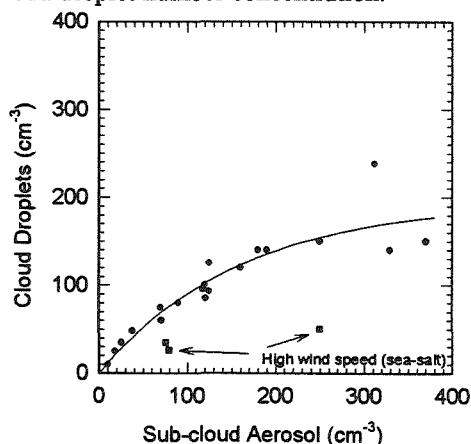


Figure 5: Observed relationship between sub-cloud aerosol concentration and cloud droplet concentration.

This curve provides excellent agreement with the fitted curve applied by Jones *et al.*, (1994) to the Martin *et al.*, (1994) data. There are, however, three cases for which this curve significantly over-predicts the observed cloud droplet concentration. These three cases correspond to moderate-to-high wind speed

conditions ($12\text{--}18 \text{ m s}^{-1}$). The observations suggest that the addition of additional sea-salt nuclei results in a lower cloud droplet concentration - contrary to the expectation that increasing the CCN population will lead to increased cloud droplet concentrations.

3.4 Influence of sea-salt on CCN activation

To examine the fraction of sea-salt nuclei activated into cloud droplets (for the high-wind Atlantic case) we can use a simple rising-parcel cloud model (Pruppacher and Klett, 1978) to predict, by inserting the observed aerosol distributions, the supersaturation reached in the cloud which will activate the observed cloud droplet concentration of 50 cm^{-3} . By inputting the separate sea-salt and nss-sulphate distributions, we can also infer the fraction of activated cloud droplets which were formed on sea-salt and sulphate nuclei. The nss-sulphate distribution was found to resemble a log-normal curve possessing the following parameters: $N_{\text{nss-s}} = 167 \text{ cm}^{-3}$; $r_g = 0.078 \mu\text{m}$; and $\sigma = 1.27$ where N is the concentration, r_g is the dry mode radius of the distribution, and σ is the standard deviation. The film-drop sea-salt aerosol distribution ($0.05\text{--}0.5 \mu\text{m}$ radius) observed using this optical particle counter is, however, affected by multiple-scattering optical response artefacts. Rather than applying a scattering response correction to overcome this effect, we can use the film-drop log-normal distributions reported in O'Dowd *et al.*, (1996) and scale this distribution to the concentration observed here. This approach results in a mode radius of $0.1 \mu\text{m}$, a σ of 1.9 , and a concentration of 72 cm^{-3} .

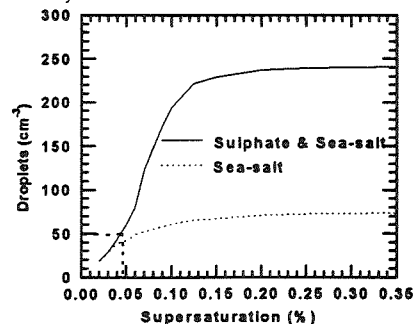


Figure 6: Calculated total and sea-salt supersaturation spectrum for Atlantic high-wind case.

The larger jet-drop sea-salt mode (O'Dowd *et al.*, 1996) must also be included in the calculations: the log-normal parameters for this mode, under these conditions, are $N = 3.5 \text{ cm}^{-3}$, $r_g = 1 \mu\text{m}$, and $\sigma = 1.9$. The supersaturation spectrum derived from the parcel model simulations is shown in Figure 6 which illustrates that 50 cm^{-3} droplets are activated at a supersaturation of $\approx 0.045\%$. At this supersaturation, $\approx 80\%$ of the cloud droplets are activated on sea-salt nuclei. Such a low supersaturation is brought about by the presence of the more active, and larger sized, sea-salt nuclei which are activated at supersaturations considerably lower than that required to activate nss-sulphate nuclei. The activation of these nuclei in the initial stages of cloud nucleation tends to consume water vapour at low supersaturations, and thus, suppress the peak supersaturation achieved within the

cloud. A more detailed analysis of this effect can be found in an associated manuscript (Smith *et al.*, 1996).

It is useful to illustrate what happens if no sea-salt was present, and thus, predict the cloud droplet concentration if nss-sulphate is the only source of CCN. The previous simulation was recreated using a similar range of updraft velocities to what was used in the previous case, but, only the observed nss-sulphate distribution was used as the potential CCN input. Figure 7 displays the constructed CCN supersaturation spectrum for these updrafts. The same updraft required to activate 50 cm^{-3} droplets in the previous example now results in a higher peak supersaturation of 0.121%, leading to an increase in the activated CCN from 50 cm^{-3} to 149 cm^{-3} droplets.

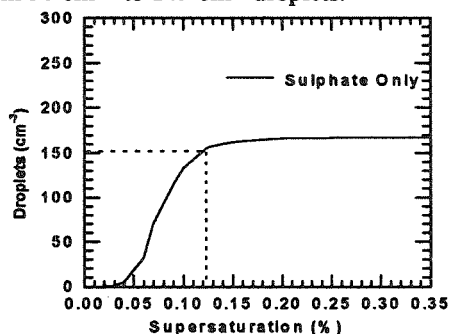


Figure 7: Calculated nss-sulphate CCN supersaturation spectrum for Atlantic high-wind case with sea-salt aerosol removed.

Thus, the addition of 72 cm^{-3} sea-salt nuclei to an existing sulphate CCN population of 169 cm^{-3} results in a decrease in the cloud droplet concentration from 149 cm^{-3} to 50 cm^{-3} . These results illustrate the importance of knowing CCN size and composition when considering the impact of increased CCN concentrations on cloud micro-physics. It is also suggested that, in order to predict accurately the effect that increased sulphate CCN will have on cloud micro-physics, and thus radiative forcing, the presence of other sources of CCN, such as sea-salt, must be taken into account. The reduction in the predicted anthropogenic radiative forcing by sulphate aerosol, once sea-salt CCN are taken into account, is examined by using a general circulation model in an associated manuscript (Smith *et al.*, 1996).

4. CONCLUSIONS

In clean maritime conditions and low wind speeds, nss-sulphate aerosol dominates the CCN population, and thus, is responsible for most of the activation of cloud droplets. The relationship between sub-cloud aerosol and cloud droplet concentration found to be non-linear, in agreement with other studies, and followed the form: $CD = 197(1 - \exp(-6.13 \times 10^{-3} A))$. In the presence of other CCN sources, such as sea-salt under moderate-to-high wind speed conditions, this relationship over predicted the observed droplet concentration by at least 100%.

Using the observed sea-salt and sulphate aerosol size distributions combined with a simple cloud model,

it is found that approximately 80% of the cloud droplets are formed upon sea-salt nuclei, even under sulphate-rich conditions. The reason the over-prediction of cloud droplets for a given sub-cloud aerosol concentration, under moderate-to-high wind speed conditions, is due to the presence of larger, more active, sea-salt nuclei which are activated in preference to the smaller, less active nss-sulphate nuclei, and, since sea-salt nuclei are activated at lower supersaturations compared with that required to activate nss-sulphate nuclei, the peak supersaturation reached in the cloud is suppressed.

5. ACKNOWLEDGEMENTS

This work was supported by the Natural Environment Research Council (NERC) under contracts GST/02/659 and GR3/9416. The authors would like to thank the aircrew of the C-130 and the support staff at MRF.

6. REFERENCES

- Boucher, O. and U. Lohmann, 1995: The sulphate-CCN-cloud albedo effect: A sensitivity study with two general circulation models. *Tellus*, **47B**, 81-300.
- Charlson R.J., J.E. Lovelock, M.O. Andreae, and S.G. Warren, 1987: Oceanic phytoplankton, atmospheric sulphur, cloud albedo and climate, *Nature*, **326**, 655-661.
- Jones, A., D.L. Roberts, and A. Slingo, 1994: A climate model study of indirect radiative forcing by anthropogenic sulphate aerosol, *Nature*, **370**, 450-454.
- Martin, G. M., D.W. Johnson, and A. Spice, 1994: The measurement and parametrisation of effective radius of droplets in warm stratocumulus clouds, *J. Atmos. Sci.*, **51**, 1823-1893.
- O'Dowd, C.D. and M.H. Smith, 1993: Physico-chemical properties of aerosols over the North Atlantic: Evidence for wind-speed related submicron sea-salt aerosol production. *J. Geophys. Res.*, **98**, 1137-1149.
- , M.H. Smith, I.E. Consterdine, and J.A. Lowe, 1996: Marine aerosol, sea-salt, and the marine sulphur cycle: A short review. *Atmos. Environ.* in press.
- Pruppacher, H.R., and J.D. Klett, 1978: *Microphysics of Clouds and Precipitation*. D. Reidel, Dordrecht.
- Slingo, A., 1990: Sensitivity of the Earth's radiation budget to changes in low clouds, *Nature*, **343**, 49-51.
- Smith, M.H., A. Jones, J.A. Lowe, and C.D. O'Dowd, 1996: The role of atmospheric aerosol in the indirect climate cooling mechanism, *this issue*.
- Twomey, S.A., 1974: Pollution and the Planetary albedo. *Atmos. Environ.*, **8**, 1251-1256.
- , S.A., M. Piepgrass, and T.L. Wolfe, 1984: An assessment of the impact of pollution on global cloud albedo, *Tellus*, **36B**, 356-366.

A LASER-OPTICAL DEVICE FOR MEASURING CLOUD DROPLET SIZE DISTRIBUTIONS

M. Löffler-Mang, T. Garbrecht, K.D. Beheng

Inst. f. Meteorologie und Klimaforschung, Forschungszentrum Karlsruhe / Universität Karlsruhe
D-76021 Karlsruhe, Germany

1. INTRODUCTION

The main concern of this study is to show the capability of the Malvern Particle Sizer (MPS) to reliably observe cloud droplet size distributions. The MPS has widely been used in the engineering field of investigations for more than fifteen years (Swithenbank et al. 1977; Leschonski 1984; Löffler-Mang and Leuckel 1992). Note that in an earlier investigation (Löffler-Mang et al. 1995) a comparison of raindrop size distributions measured by MPS as well as by a disdrometer (Joss and Waldvogel 1967) has already been presented. As will be shown in this paper the system is even more suitable for measuring size distributions of cloud droplets than size distributions of raindrops. That is due to the need of a high number concentration of drops for the MPS (the typical situation in clouds) and the maximum MPS measuring range reaching from 1 to 2000 μm .

2. MEASURING PRINCIPLE

The MPS is a laser diffraction system which is schematically sketched in Fig. 1: a helium-neon laser operates as a light source with an expanded beam of 9 mm in diameter. The light scattered by drops located in the beam is focused by a lens to a concentric diode array in the distance f (focal length) behind the lens.

The radial light intensity distribution detected by the diode array is a measure of the drop diameters in the ensemble within the laser beam.

In order to determine the actual drop size distribution the signals from the diode array are evaluated indirectly and iteratively: assuming a certain initial drop size distribution the resulting light intensity distribution is calculated with the help of 15 definite size classes. By systematically varying the 15 parameters of the assumed drop size distribution the difference between the calculated and the actually measured light intensity is minimized, finally resulting in the size distribution of drops present in the laser beam.

The number of sweeps, each being a snapshot, is a user defined variable. The signals of the individual sweeps are superposed and evaluated in the above mentioned manner. The chosen number of sweeps for this investigations was 3000, leading to a measuring time of approx. 1 min.

For adaption of the MPS to a wide range of applications specific lenses with different focal lengths can be mounted. The focal length of the configuration used for cloud investigations is $f=300$ mm, leading to a sizing range of diameters from 5 to approx. 600 μm .

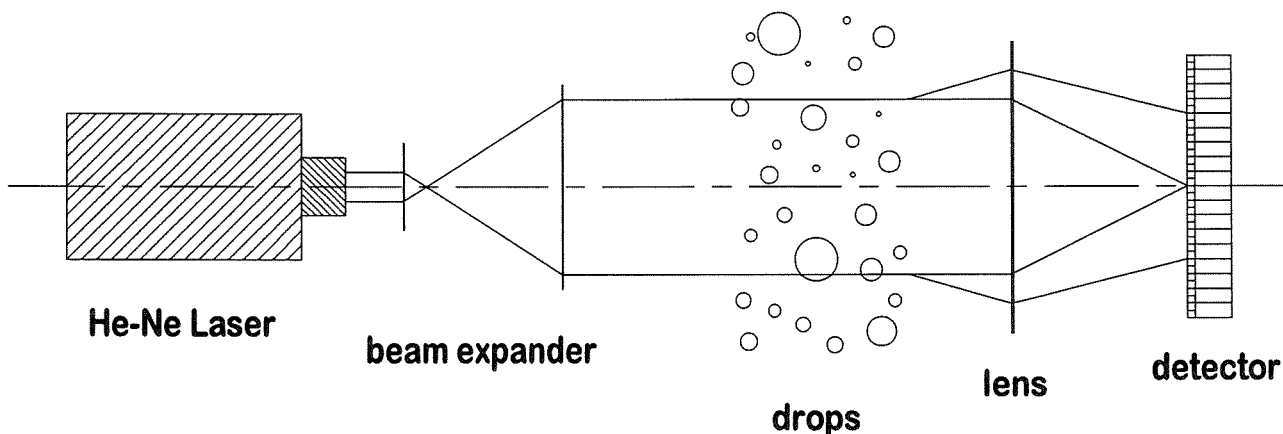


FIG. 1: Scheme of the Malvern Particle Sizer (MPS)

3. THE FIELD EXPERIMENT

The device has been used during FELDEX 95, the field campaign of the cap cloud experiment on top of Kl. Feldberg/Taunus near Frankfurt/Main, lasting from 30 October to 20 November 1995. A map of the investigation area in the North of Frankfurt is shown in Fig. 2.

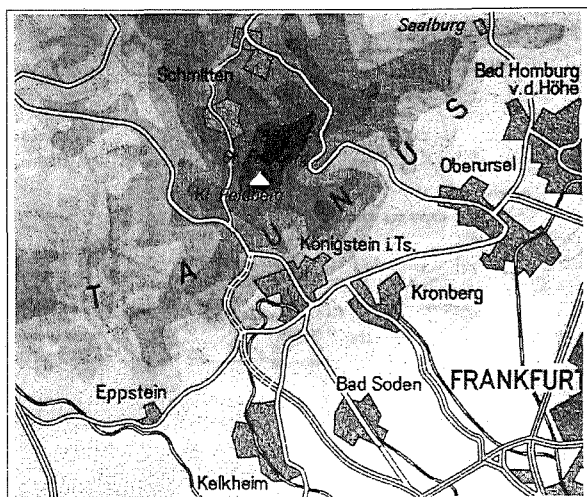


FIG. 2: FELDEX investigation area with Kl. Feldberg

A number of interesting phenomena occurring in ground based clouds could be observed, such as:

- variation of drop size distributions during the subsidence of clouds to the ground, during night and during dispersal of clouds/fog in the morning,
- multimodal size distributions near the cloud base with drizzle-size drops,
- broad size distributions within clouds of maritime origin.

Some examples will be presented in the next chapter.

4. RESULTS

The results of two periods of FELDEX are now discussed in detail (2-3 and 7-8 November).

The synoptical situation during the first period was mainly determined by a low-pressure system over Iceland. Polar air was transported from northwesterly directions to the Kl. Feldberg. During 2 November the low-pressure system moved towards the Baltic Sea and in the night to 3 November a warm front passed the investigation area.

On 2 November a cloud mass which subsided in the late afternoon reached the Kl. Feldberg. At the beginning of the measurements the city of Frankfurt still could be seen from the Kl. Feldberg (15 km distance), but in the evening the range of sight decreased to below 500 m.

A typical drop size distribution is shown in Fig. 3, measured with the MPS. The fraction of each size class on the total drop mass (bars with scale at the right hand axis) within the measuring volume is plotted as a function of the drop diameter for 21:55 UTC. The spectrum is rather narrow, the mean diameter amounts to about 10 μm indicating that the drops are mostly grown by condensation.

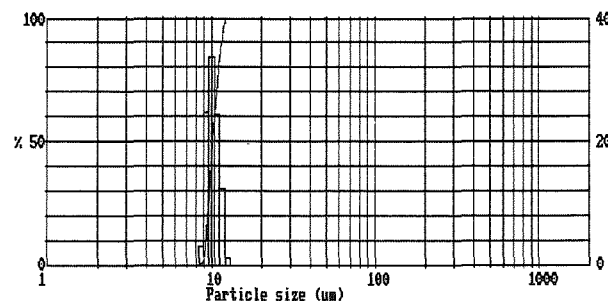


FIG. 3: Drop size distribution (volume density) on November 2, 1995, 21:55 UTC

Around midnight a slight drizzle occurred with increasing intensity after 1:00 UTC. The maximum rain rates reached up to 10 mm/h. In comparison to Fig. 3 in Fig. 4 measurements for 1:05 UTC are shown. The size of the cloud drops has increased a little bit. The drizzle-size drops have diameters ranging from 100 μm to about 600 μm . The sharp cut-off at 600 μm diameter is due to the upper limit of the optical configuration applied. The cumulative mass distribution (line, left hand axis) shows that approx. 50 % of the totally measured drop mass stem from cloud droplets and 50 % from raindrops.

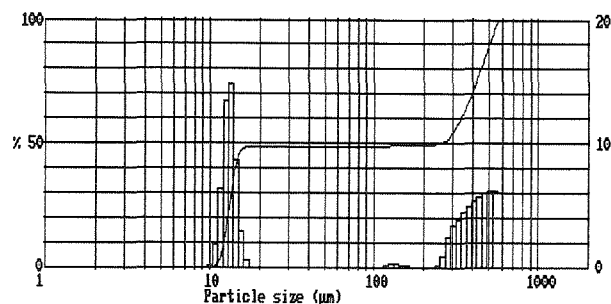


FIG. 4: Drop size distribution (volume density) on November 3, 1995, 1:05 UTC

The time development of the size distributions during the night is presented in Fig. 5 where drop diameter information is drawn as a function of time. The black squares represent the size class with highest drop mass in the cloud droplet range and the open squares the size class with highest drop mass in the raindrop range. The lines indicate the edges of the cloud spectrum. The above mentioned slight increase of cloud drop diameter and a weak broadening of the spectrum during the night can be seen as well as the

beginning rain around 1:00 UTC. Because only ground based measurements were available the growth mode responsible for this feature cannot unambiguously be determined.

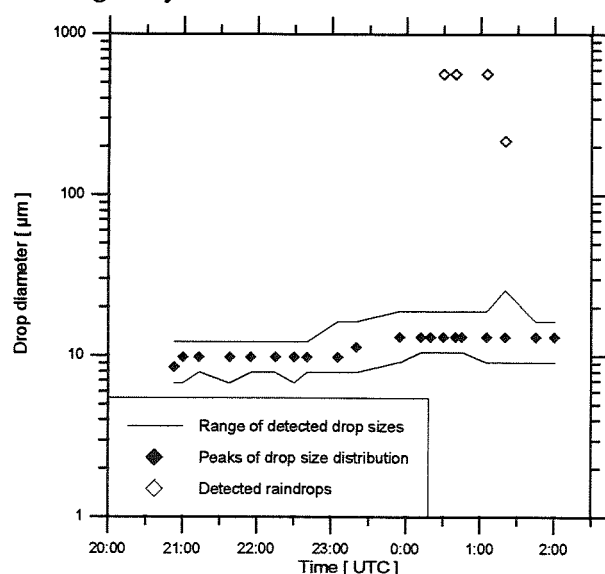


FIG. 5: Time series of cloud drop size spectra (black squares) and rain drop size (open squares)

The synoptical situation of the second period (7-8 November) was dominated by two high-pressure systems over Central Europe and over Scandinavia with a low-pressure system over Greenland. Maritime air masses linked to two frontal systems were advected to the Kl. Feldberg.

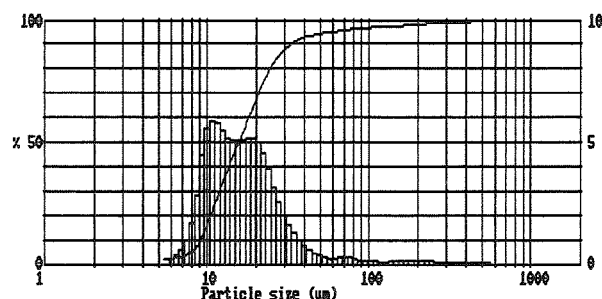


FIG. 6: Integrated drop size distribution (volume density) on November 7, 1995, 12:25 - 20:00 UTC

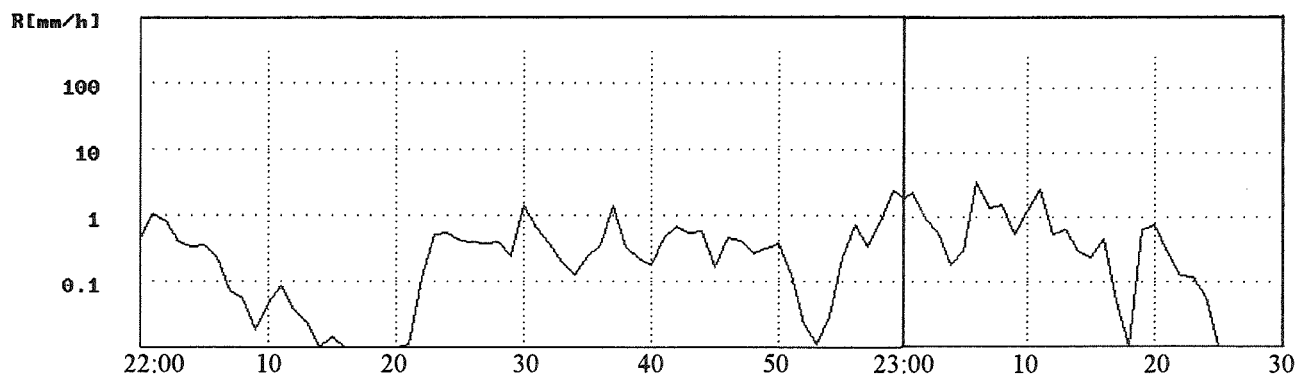


FIG. 7: Disdrometer time series of rain intensity on November 8, 1995, 22:00 - 23:30 UTC

The drop size distributions during 7 November were characteristically different compared to the distributions on 2 November. In Fig. 6 the integrated spectrum from noon until 20:00 UTC is shown. It is a rather broad distribution. This is not an effect of the integration since most single distributions are also fairly broad. It is not clear which mechanism leads to that broadening. One possible explanation may be that these drops developed from a specific aerosol size distribution. The aerosol spectra soon will be available from other groups participating in FELDEX and will be included in the future work of interpreting that case study.

After a clear sky in the morning hours of 8 November, clouds did not form again before the evening (range of sight below 100 m). Around 21:00 UTC it began to rain. In Fig. 7 disdrometer measurements in terms of rain intensity are shown for the time interval between 22:00 and 23:30 UTC. In the first hour of the plotted time series the maximum intensity reached 1 mm/h. Thereafter the intensity attained values of 3 mm/h and rain was also detected by the MPS.

This last event makes it possible to construct a combination of MPS and disdrometer data since drops registered by the MPS in the size range 5 - 600 μm are present as well as drops measured by the disdrometer in the size range 0.3 - 5 mm. The MPS spectrum originally looked similar to the spectrum shown in Fig. 4 with the cloud droplet part neglected.

For the combination aimed at it is necessary to transform the disdrometer spectrum into a concentration dependent volume distribution supplied by MPS. The reason for the transformation is that the disdrometer measures absolute flux-dependent values whereas the MPS data are at hand in normalized concentration units. The basic transformation procedure is explained in detail by Löffler-Mang et al. (1995) such that only the final relations are given here.

First the number density of the disdrometer size distribution is calculated via:

$$q_0(x_i) = \frac{1}{N_{\text{tot}}} \frac{\Delta N(x_i)}{\Delta x_i}$$

x_i : mean diameter of class i

Δx_i : width of class i

$\Delta N(x_i)$: number of drops in class i

N_{tot} : total number of drops

Then the results are converted from flux-dependent to concentration-dependent distributions according to:

$$q_0^c(x) = \frac{q_0^j(x)}{v^*(x)}$$

$v^*(x)$: normalized fall velocity

Finally the number distribution is transformed into a volume distribution yielding:

$$q_3^c(x) = \frac{x^3 q_0^c(x)}{\int_0^\infty x^3 q_0^c(x) dx}$$

For 8 November, 23:05 UTC in Fig. 8 the volume distribution is plotted as a function of the drop diameter, where the dashed line represents the MPS data, the solid line the disdrometer data. The combined spectrum shows a qualitative agreement in the overlapping region. Thus it is evident that both measuring devices supplement well each other.

A comparison of the MPS results (cloud droplet spectra) obtained during FELDEX 95 with measurements obtained by two FSSP-probes and by a holographic method is planned for future work.

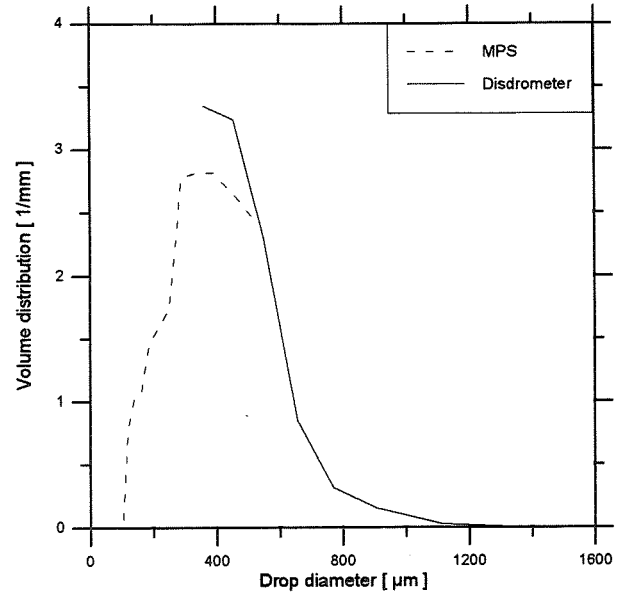


FIG. 8: Combined rain drop size distribution ($q_3^c(x)$, volume density) on November 8, 1995, 23:05 UTC

5. ACKNOWLEDGEMENT

The authors wish to express their gratitude to W. Leuckel from the Engler-Bunte-Institut (Bereich Feuerungstechnik) at the University of Karlsruhe, who made available the Malvern Particle Sizer for this measurements.

6. REFERENCES

- Joss, J., A. Waldvogel, 1967: Ein Spektrograph für Niederschlagstropfen mit automatischer Auswertung. *Pure Appl. Geophys.*, **68**, 240-246
- Leschonski, K., 1984: Representation and evaluation of particle size analysis data. *Part. Character.*, **1**, 89-96
- Löffler-Mang, M., W. Leuckel, 1992: A comparison of four drop sizing methods when applied to swirl pressure-jet atomizers. *ILASS-Europe, 8th Annual Conf. (Proceedings)*, Amsterdam, 247-255
- Löffler-Mang, M., K.D. Beheng, H. Gysi, 1995: Drop size distribution measurements in rain - a comparison of two sizing methods. Accepted for publication in *Meteorol. Z., N.F.*
- Swithenbank, J., J.M. Beer, D.S. Taylor, D. Abbot, C.G. Mc Greath, 1977: A laser diagnostic technique for the measurement of particle size distribution. *ALAA, Prog. in Astron. and Aeron.*, **53**, 421-447

PROGRESS ON A NON-WETTING TEMPERATURE PROBE FOR AIRBORNE RESEARCH

Alfred R. Rodi¹, John K. Chu², and R. Paul Lawson³

¹Dept. Atmospheric Science, University of Wyoming, Laramie, WY 82071 USA

²Physics Dept., Sheridan College, Sheridan WY 82801 USA

³SPEC, Inc., Boulder, CO 80301 USA

1. INTRODUCTION

Immersion sensor wetting in the measurement of static temperature from a research aircraft can be seen readily in the evaporative cooling that occurs on cloud exit into dry air, but the effects of wetting in clouds are more subtle (Lenschow and Pennell, 1974; Lawson and Cooper, 1990). Remote sensors such as the Ophir 4.25 μm radiometric thermometer offer hope for overcoming the problem of sensor wetting (Lawson and Cooper, 1990), but these are not yet widely available nor fully tested.

The goal of designing non-wetting immersion sensors using the method of inertial separation of droplets has remained elusive. The commonly used immersion thermometers—the Rosemount Model 102 total temperature probe and the reverse-flow thermometer (RFT) of the design of Rodi and Spyers-Duran (1972)—have been shown by Lawson and Cooper (1990) in comparisons with the Ophir radiometric thermometer to not be completely immune to wetting. Using a conductivity probe to sense wetting placed in the RFT housing, they showed in particular that the reverse-flow wetted in warm clouds, but the effects in supercooled clouds are not clear.

Haman (1992) described an immersion instrument being developed which uses with some success a thin rod to protect the sensing element from contact with cloud droplets. Lawson and Rodi (1992) described another attempt which was designed using particle trajectories around a simple shape. The design, shown conceptually in Fig. 1, was intended to be simple enough so that the flow and trajectories can be numerically simulated in contrast to the complicated flow through the RFT. The idea is that small droplets will be swept around the body causing the shadow region while large drops will collide with the leading edge and will run back in the narrow boundary layer in a "sheet" of water. Preliminary flight evidence is that the probe stays relatively dry in warm

clouds but shows wetting in the presence of drizzle-size drops.

It is the purpose of the present paper to interpret this result further using more sophisticated numerical modeling of the flow and particle trajectories than used by Lawson and Rodi.

2. NUMERICAL MODEL

2.1 Finite-element model

The simulations were done with an axisymmetric, steady-state model of the non-linear momentum and energy equations of turbulent, compressible flow based upon the finite-element method (FIDAP ver. 7.50, Fluid Dynamics International, Evanston, IL 60201 USA). Turbulence was modeled with a two-equation $k-\epsilon$ method and the laminar near-wall sub-layer effects are resolved using the special wall elements. Heat conduction between the air and the probe is neglected.

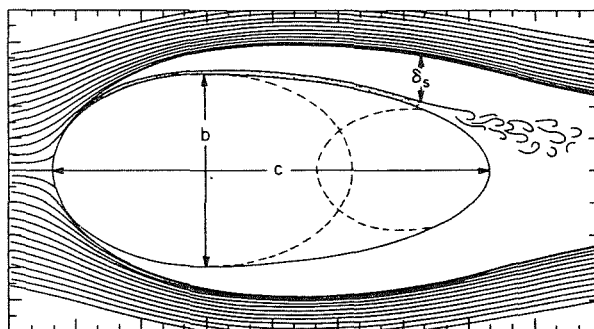


Fig. 1: Conceptual model cross section of the body shape used in the prototype where b is the thickness (~ 15 m) and c is the chord length (~ 30 m). The shadow-depth parameter δ_s is defined as the distance between the surface and the closest $5\text{-}\mu\text{m}$ drop trajectory at the point of boundary layer separation (from Lawson, 1988).

2.1 Particle trajectories

A Lagrangian approach to particle trajectories was used with no particle-particle interactions, no particle breakup or coalescence, and neglecting the particles' effect on the flow. An empirical polynomial model of drag coefficient versus Reynolds number was used, and tested to reproduce known terminal speeds in separate model runs. The stochastic model of Gosman and Loannides (1981) was used to simulate influence of turbulence on particle trajectories. The effect of gravity was not considered in these runs. Drops were injected at points on the inlet at various distances from the axis of symmetry.

3. RESULTS

3.1 Properties of the flow field and turbulence

Model profiles of flow properties at several locations along the probe body as shown in Fig. 2 are plotted in Fig. 3.

The pressure gradient (Fig. 3 c) in this region is "adverse" ($\partial p / \partial x > 0$, i.e. pressure increasing in the flow-wise direction), and there is a suggestion that a separation point is developing in this region. However, there is no evidence of a flow reversal, and the radial gradient of the velocity, however, is still positive. The depth of the turbulent boundary layer as measured by the

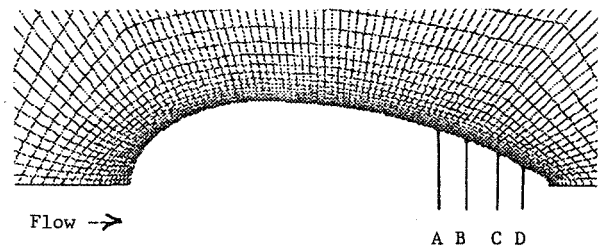
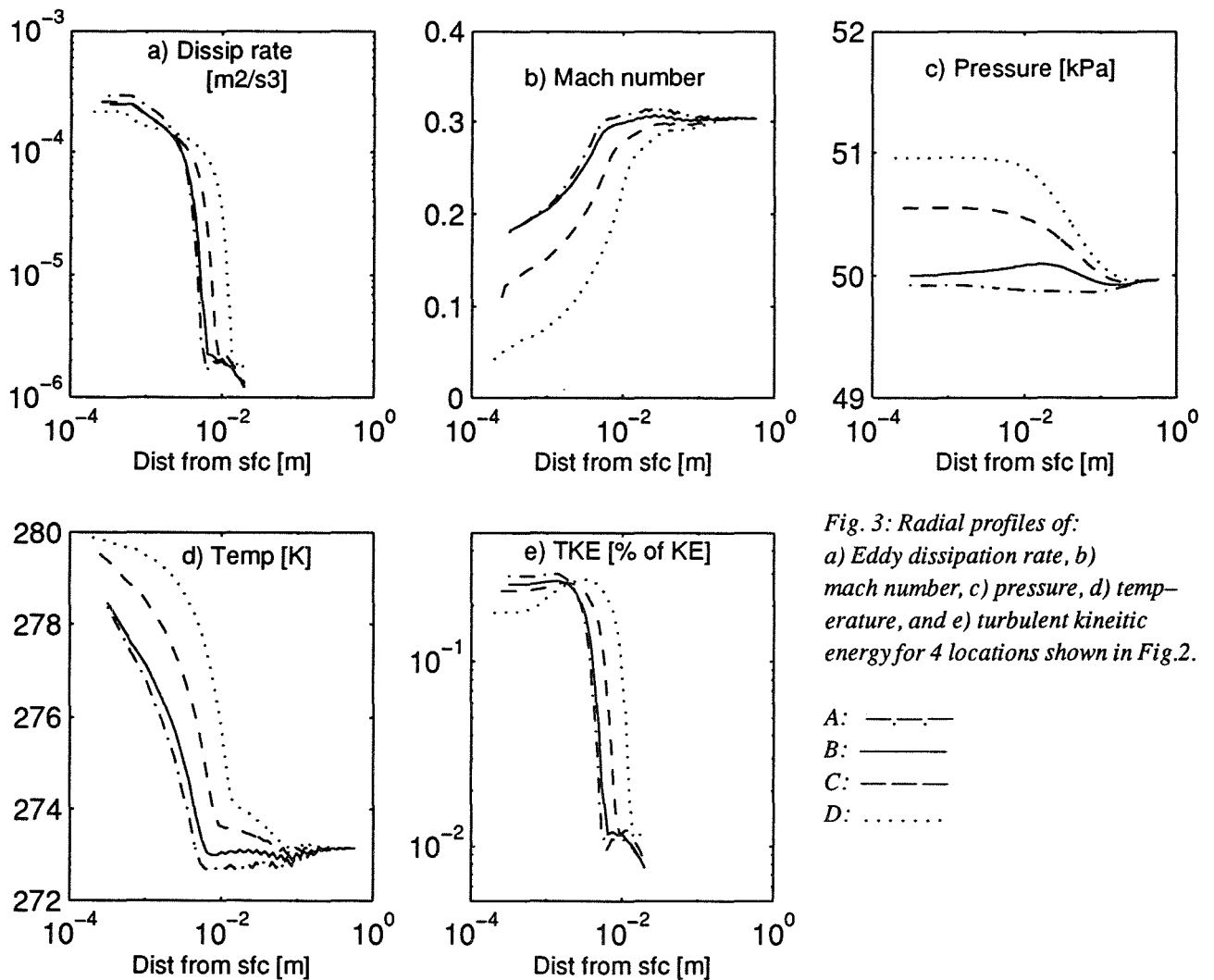


Fig. 2: Locations of profiles shown in Fig. 3



sharp decrease in the turbulent kinetic energy (TKE) or eddy dissipation rate appears to increase from about .05 m to .1 m along this .075 m distance from point A to D. This is the 'wake' region which contains eddies which may be to be a factor as discussed below in the capture of droplets in a manner which was not predicted by the potential flow results of Lawson (1988) and Lawson and Rodi (1992).

The prototype thermocouple placement has been placed at position B in Figs. 2 and 3 at a height of about .01 m from the surface in the field tests thus far. This at this distance from the surface, there are strong gradients of temperature and velocity (Fig. 3b and d) which may affect the ultimate accuracy of the technique assuming that location is indeed shadowed from drops.

3.2 Particle trajectories

The effect of flow turbulence on the droplet trajectories can be seen in Fig. 4(a-d) for 12.5-, 25-, and 40- μ m radius drops where the flow is from left to right. In the three smallest sizes shown, trajectories can be found which extend into the turbulent boundary layer suggesting wetting effects. Only at sizes >40- μ m radius, the blocking and shadowing effect occurs.

4. DISCUSSION

Data from a prototype this probe collected on the NCAR King Air in Florida in 1994 (project SPICE) and on the NCAR C-130 (project SCMS) suggest that it is the larger drop sizes which cause the wetting, contrary to these model results. The wetting seemed to be most evident when the PMS 2D-P (200- μ m resolution) sensed particles present.

The model does not include the possible effects of drop bouncing from the front surface, splashing of water from the surface sheet into the turbulent boundary layer, or other effects causing splashing and spray which were evident in our wind-tunnel work with this prototype. Work continues to determine the quantitative effects of the droplet and precipitation spectrum on wetting with both the SPICE and SCMS data sets.

Alternate shapes and configurations are being considered and tested with the model. One such modification to the prototype was to add a ring in front of the thermocouple to cause a separation in the flow with

gutters to relieve the damming effect near the surface. Simulations suggest that this forms a shadow zone more like the Lawson (1988) model.

The non-wetting immersion thermometer for airborne cloud physics continues to elude our grasp. However, our modeling shows promise for better understanding of the problems and this may lead to a suitable design at some point in the future.

5. REFERENCES

- Haman, K. E., 1992: A new thermometric instrument for airborne measurements in clouds. *J. Atmos. Oceanic Technol.*, **9**, 86-90.
- Gosman, A. D., and E. Loannides: Aspects of computer simulation of liquid fueled combustors. AIAA 19th Aerospace Science Mtg., Paper No. 81-0323, St. Louis, MO.
- Lawson, R. P., 1988: The measurement of temperature from an aircraft in cloud. Ph.D. dissertation. University of Wyoming, Laramie, WY, 336 pp. [Available as report AS-159].
- Lawson, R. P., and A. R. Rodi, 1992: A new airborne thermometer for atmospheric and cloud physics research. Part I: Design and preliminary flight tests. *J. Atmos. Sci.*, **9**, 556-574.
- Lawson, R. P., and W. A. Cooper, 1990: Performance of some airborne thermometers in cloud. *J. Atmos. Oceanic Technol.*, **7**, 480-494.
- Lenschow, D. H., and W. T. Pennell, 1974: On the measurement of in-cloud and wet-bulb temperatures from an aircraft. *Mon. Wea. Rev.*, **102**, 447-454.
- Rodi, A. R., and P. Spyers-Duran, 1972: Analysis of time response of airborne temperature sensors. *J. Appl. Meteor.*, **11**, 554-556.

6. ACKNOWLEDGEMENTS

This work was supported by NSF Grant ATM-8819676, the University of Wyoming Planetary and Space Science (PaSS) Center, NASA Grant #NGT 40050, and Pittsburgh Supercomputing Center Grant ATM950001P.

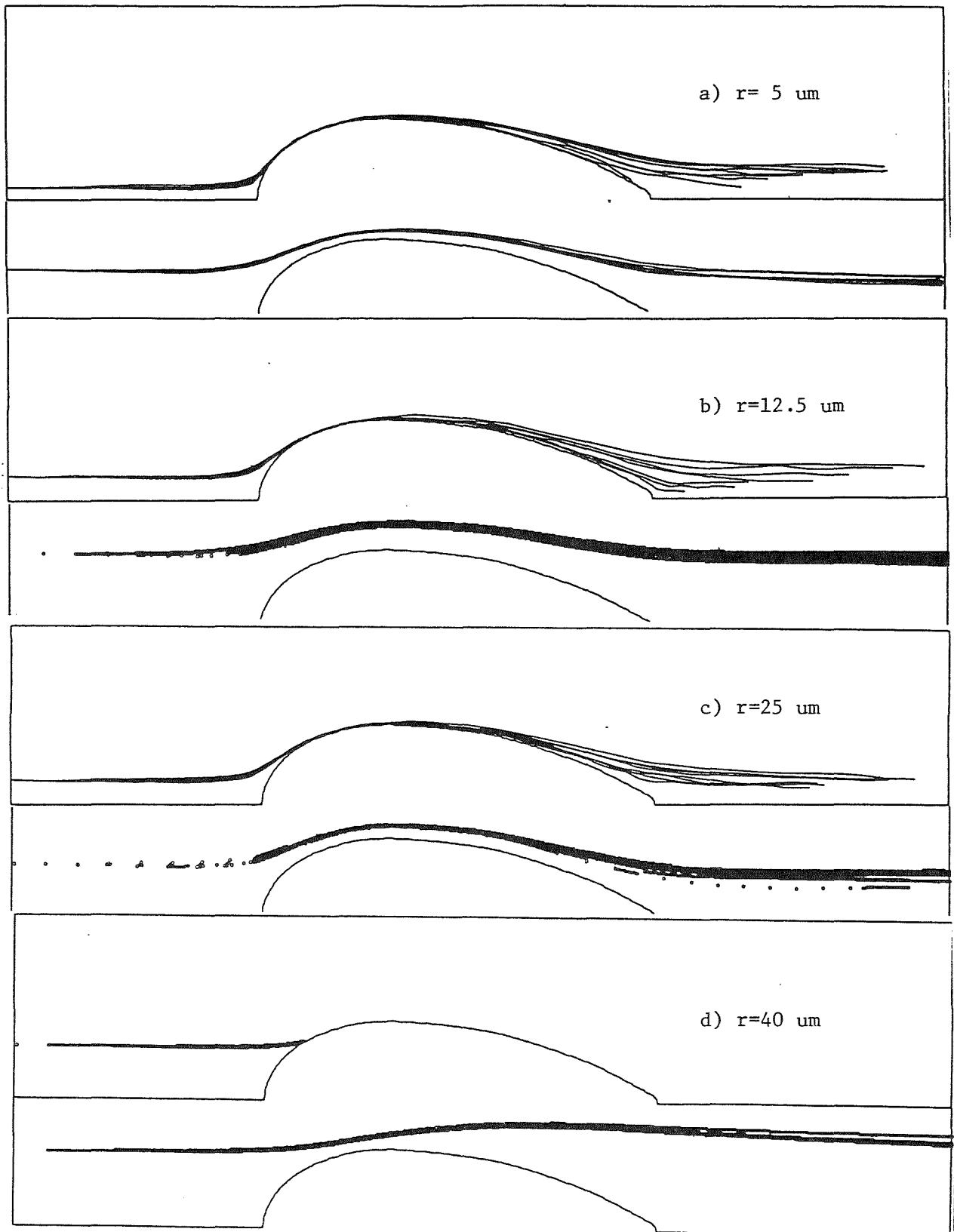


Fig. 4: Droplet trajectories for a) 12.5- μm , b) 12.5- μm , c) 25- μm -, and d) 40- μm radius droplets in flow around the temperature probe. In each panel, there are several droplets injected into the flow at two locations, and the stochastic effects of the turbulence produces the distribution of trajectories.

On the Accuracy of Nevzorov Airborne Hot Wire LWC/TWC Probe

Korolev A. V., J. W. Strapp,
Atmospheric Environment Service
Downsview, Ontario, Canada, M3H 5T4
and
A. N. Nevzorov
Central Aerological Observatory,
Dolgoprudny, 141700, Russia

1. Introduction

Cloud water content is one of the most fundamental of cloud physics measurements. Many research organisations currently use hot wire probes for airborne measurements of liquid water content (LWC). The most wide spread versions of hot wire probes are the Johnson-Williams, and the CSIRO and PMS King probes. The latter two probes are derived from the design described by King et al. (1978). Measurements of the total water content (TWC) have been accomplished mainly from interpretation of particle image data, or from prototype instruments which evaporate all hydrometeors and measure humidity changes.

The Nevzorov LWC/TWC probe is a constant temperature hot wire probe designed for aircraft measurements of the ice and liquid water content of clouds and fogs. The first version of this probe (originally named *Izmeritel Vodnosti Oblakov (IVO)* for Cloud Water Content Meter) was developed in the Cloud Physics Laboratory of the Russian Central Aerological Observatory in the mid 70s. The first version of this probe was designed to make measurements of total (ice plus liquid) water content (Nevzorov, 1980; 1983). A second version included a sensor designed for liquid only measurements, making it possible to separately measure both the ice and liquid components of clouds (Nevzorov and Shugaev, 1992).

The Nevzorov probe was installed by the Atmospheric Environment Service on the NRC Convair 580 in 1994, and has since been used in three Canadian field experiments. In this paper performance tests of the sensitivity of the probe are discussed, and examples of the unique phase separation capabilities are shown. Comparisons are made with other conventional instruments.

2. Technical description

2.1. The sensor configuration

Fig. 1 shows the basic configuration of TWC and LWC sensors. Each probe consists of two sensors, heated to the same temperature. The temperature is maintained constant with the help of a bridge feedback. The leading sensor, or collector, has the sampling surface exposed to the airflow and cloud particles. The reference sensor is aerodynamically protected from collision with particles and remains dry in clouds. Both collector and reference are ventilated by the same air flow, albeit with a different orientation to the flow. The reference sensor measurement is used to perform a precise removal of the dry air heat loss term.

The LWC and TWC sensors consist of close single-layer windings of nickel wire. For the TWC probe, the collector winding is cemented to the hollow cone at the end of a

textolite cylinder, and the reference sensor is wound within a shallow groove cut into the same cylinder (Fig. 1a). Both collector and reference sensors for the LWC probe are wound on solid copper rods and cemented to the opposite edges of a flat textolite plate (Fig 1b). The diameter of the sample area of the TWC collector is 8 mm; the cone angle is 90°. The dimensions of the cylindrical LWC collector are 1.8 mm diameter by 16 mm length.

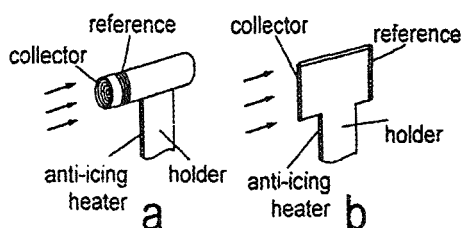


Fig. 1 Views of (a) TWC and (b) LWC sensor heads

The phase discriminating capability of the TWC and LWC collectors results from the difference in behaviour of liquid and solid particles impacting with their surfaces. Small liquid droplets after collision with LWC or TWC collector sensors are flattened into a thin surface film and completely evaporate. At the same time, ice particles tend to remain inside the conical hollow of the TWC collector (Fig. 1a) until they melt and evaporate. In contrast, ice particles are expected to instantly break away from the convex surface of the LWC collector (Fig. 1b) with negligible heat expended relative to that for complete ice evaporation.

The LWC and TWC sensors are mounted on the same flow sensitive vane plate, designed to remain parallel to the airstream during aircraft pitch changes. The pivoting vane stabilizes the flow characteristics of the sensors and further protects the reference sensors from particle impacts.

2.2. Electronic Circuitry

A simplified schematic of IVO control circuitry is presented on Fig. 2. The collector and reference windings form the temperature-dependent arms of two different bridges. The bridges are balanced to a set resistance which determines the temperature of the active sensor wire. The reference sensor forms the arm of a resistance bridge controlled by alternating current AC (A). This bridge consists of the AC amplifier of the imbalance (error) signal, phase-sensitive detector, amplitude modulator of the gain reinserted AC carrier, and power amplifier loaded by the bridge. Other control circuits are built in an analogous way to operate with AC error signals with no affect from the DC component. The collector bridge is balanced with both AC and DC in parallel, where the AC voltage is exactly proportional to that across the reference winding and is adjusted in the clear sky so that the DC is zero while adjusting the collector bridge with AC power only. Thus,

the DC circuit of the collector winding is inactive outside of cloud and operates as soon as cloud particles impact and cool the winding. The cloud water content signal is carried on the DC component voltage the collector winding, which is easily measured by across suppressing the AC voltage with a low pass filter. Thus the cooling caused by

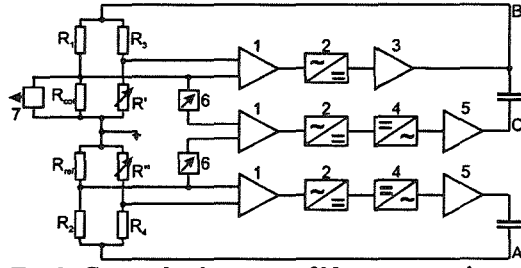


Fig.2 General schematic of Nevzorov probe

the dry air convective heat loss is compensated by the reference winding of the sensor such that the DC power measured from the collector winding is only that required to evaporate water and ice particles. The water content can then be directly derived from the measured DC power with the appropriate heat balance equation.

2.3. LWC/TWC calculation

Since the reference sensor does not impact with cloud particles, its heat losses are due primarily to convection. Thus, the reference sensor bridge is balanced by the power:

$$P_r = \frac{V_r^2}{R_r} = \alpha_r (T_r - T_a) \quad (1)$$

where V_r is the AC voltage across the reference sensor with resistance R_r , $\alpha_r = K g_r N u_r$ is the integral convective heat transfer coefficient; $N u_r$ is Nusselt number; K is the thermal conductivity of air, g_r is a sensor shape dependent coefficient; and T_a is the air temperature.

In cloud, heat losses of the collector sensor are result from wet and dry components:

$$P_c = \alpha_c (T_r - T_a) + W L^* S U \quad (2)$$

where $\alpha_c = K g_c N u_c$ is integral convective heat transfer coefficient for the collector sensor; S is collector sample area; L^* is the energy expended in heating and evaporating the water; U is the air speed; and W is measured water content.

The use of noncoherent currents (i.e. AC and DC) in the collector bridge provides a simple algebraic sum of the powers responsible for dry and wet collector heat losses, so that dry, wet and total heat losses may be expressed respectively as:

$$P_{c \text{ dry}} = \frac{V_{ca}^2}{R_c} = \alpha_c (T_c - T_a) \quad (3)$$

$$P_{c \text{ wet}} = \frac{V_{cd}^2}{R_c} = W L^* S U \quad (4)$$

$$P_{c \text{ tot}} = \frac{V_{ca}^2 + V_{cd}^2}{R_c} \quad (5)$$

where V_{ca} , V_{cd} are AC and DC voltages across the collector sensor with resistance R_c ; T_c is the collector sensor temperature that corresponds to resistance R_c .

From Eq.(4) we obtain the measured water content

$$W = \frac{V_{cd}^2}{S U L^* R_c} \quad (6)$$

For liquid water :

$$L^* = C(T_e - T_a) + L(T_e) \quad (7)$$

where C is the specific heat of water, $L(T_e)$ is the latent heat of evaporation of water at the evaporative temperature T_e . For simplicity it is possible to use the average value of $L^* = 2589$ J/g, which adds a $\pm 5\%$ error to the LWC in the temperature interval from -40°C to $+20^\circ\text{C}$.

For ice particles $L_i \approx 1.12 L_w$. In mixed clouds with the true values of $LWC = W_l$ and $IWC = W_i$, the measured values of LWC and TWC probes will be, respectively, as follows:

$$W_{TWC} = \epsilon_{il} W_l + 1.12 \epsilon_{il} W_i \quad (8)$$

$$W_{LWC} = \epsilon_{il} W_l + \beta W_i \quad (9)$$

where $\beta \ll 1$ is the factor for the residual effect of the ice on the LWC collector, ϵ_{il} , ϵ_{il} are liquid droplet collection efficiencies for LWC and TWC probes, respectively; ϵ_{il} is ice particle collection efficiency for TWC probe. In general $\epsilon_{il} \sim 1$, since in most cases IWC is mainly contributed by large particles.

3. Dry air drift tests

The ratio of the powers dissipated by the collector and reference sensors in cloud free air is:

$$P_{cdry}/P_{rdry} = \alpha_c (T_c - T_a) / \alpha_r (T_r - T_a)$$

Since the reference and collector sensors are maintained at the same temperature (i.e. $T_r = T_c$), this ratio reduces to:

$$P_{cdry}/P_{rdry} = \alpha_c / \alpha_r = k$$

Although α_c and α_r are dependent on temperature, pressure, airspeed, and sensor shape, the dry air removal scheme makes use of the empirical result that their ratio k is approximately constant. Removal of the dry air convective heat loss (zeroing) of the IVO probe is accomplished by adjusting of the coefficient k using the potentiometer 6 (Fig. 2) in cloud free air so that:

$$k P_{c \text{ dry}} - P_{r \text{ dry}} = 0 \quad (10)$$

In reality the dependent parameters affect the coefficient k to some degree. The resulting baseline LWC/TWC drifts not only affect the zero reading out of cloud, but also affect the accuracy and sensitivity of the measurements in cloud. Since the baseline drift can only be monitored when the probe is disbalanced towards an excess P_{cdry} due to electronics limitations, some occasional operator adjustment is required to ensure the most accurate results. The magnitude of baseline drift effects is examined in the following sections.

3.1 Drift with airspeed

Fig. 3 (a, b) demonstrates the baseline drift expressed as water content due to air speed changes in cloud free air. The measurements collected by the NRC Convair 580 aircraft are given for two altitudes. Fig. 3 indicates that the slope of curves at different altitudes are almost the same at approximately to $\partial W / \partial u \sim 2 \times 10^{-3} \text{ gm}^{-3} / 10 \text{ ms}^{-1}$ for the LWC sensor and $\partial W / \partial u \sim 3 \times 10^{-3} \text{ gm}^{-3} / 10 \text{ ms}^{-1}$ for TWC sensor.

3.2 Drift with air temperature

Tests of the baseline drift due to temperature changes were performed at the NRC High Speed Icing Wind Tunnel. At an air speed of 100ms^{-1} and $p=1000\text{mb}$, baseline was found to vary as $\partial W/\partial T \sim 0.5 \times 10^{-3} \text{gm}^{-3}/10^\circ\text{C}$ for both the LWC and TWC probes, in the temperature interval from -20°C to -5°C .

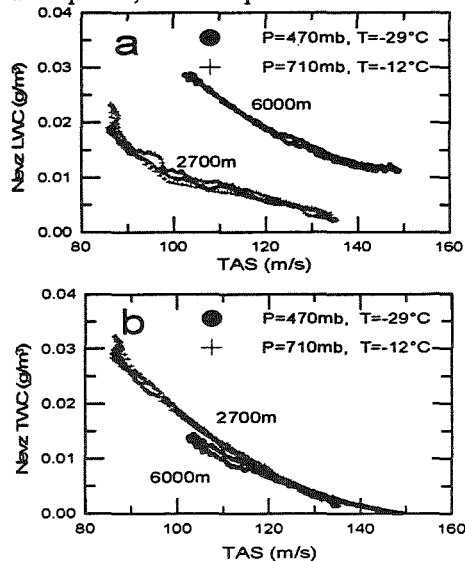


Fig. 3 Clear sky speed test at two different altitudes

3.3 In-flight altitude/temperature drift

Fig. 4 shows variations of measured water content during a constant airspeed ascent of the Convair 580 from 3 to 6 km. Temperature changed from -12°C to -29°C along the ascent. Baseline drift on both the TWC and LWC probes displayed the same dependence on altitude/temperature of $\partial W/\partial Z \sim 5 \times 10^{-3} \text{gm}^{-3}/\text{km}$.

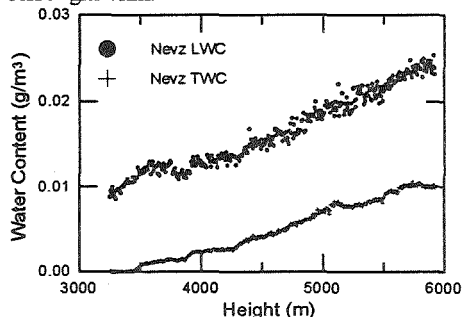


Fig. 4 Clear sky altitude test of Nevzorov probe

3.4. Random in-flight drift

Baseline drift in cloud free sky during normal level horizontal flight at constant air speed was measured on the Convair 580 under relatively low turbulence levels. During these tests, both the LWC and TWC probes were artificially disbalanced in order to observe fluctuations around an average positive value. Maximum deviations were found to be $\pm 0.002 \text{gm}^{-3}$ for both probes. It is expected that these deviations will increase with increasing turbulence. This drift normally appears as excursions with periods of several seconds.

4. Liquid cloud measurements

Intercomparisons between the Nevzorov probe, King probe, FSSP ($2\text{--}32\mu\text{m}$) and extended range FSSP ($5\text{--}96\mu\text{m}$) have been accomplished in liquid clouds during several projects with Convair 580. Fig. 5 shows variations of LWC in

stratiform clouds measured by Nevzorov and King probes during the Canadian Freezing Drizzle Experiment. The scatterplots shown in Fig. 6 demonstrate a good agreement between Nevzorov and King probes. Good agreement was also found in most cases with FSSP derived LWCs.

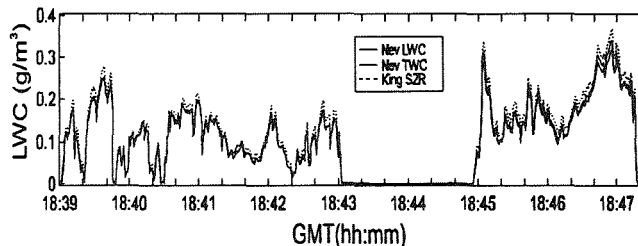


Fig. 5 Intercomparisons of Nevzorov LWC/TWC and King probes in liquid St clouds. 17-Mar-95, Newfoundland.

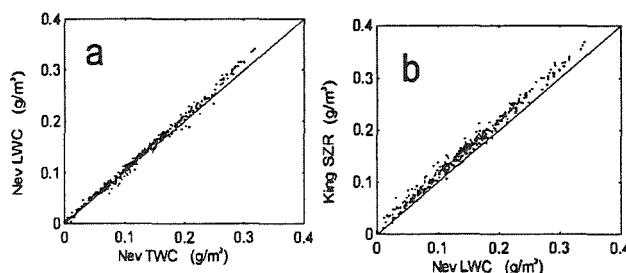


Fig. 6 Scatterplot of (a) Nevzorov LWC versus TWC and (b) King probe versus Nevzorov LWC. 17-Mar-95, 18:39-18:48.

Figure 7 displays a descent by the Convair 580 into a cloud which contained mostly small droplets at cloud top, and heavy drizzle lower in the cloud. The sample PMS 2D-C imagery displays drizzle drops up to approximately 300 microns, although droplets 600 microns were observed. Note that the TWC is approximately equal to the LWC at cloud top, but almost a factor of 2 higher in the area of heavy drizzle. Biter et al. (1987) has shown that the PMS King probe has a reduced efficiency for droplets in the drizzle size range. This case illustrates the unique capability of the TWC probe to make LWC measurements beyond the range of conventional hot wire devices due to its aerodynamic properties.

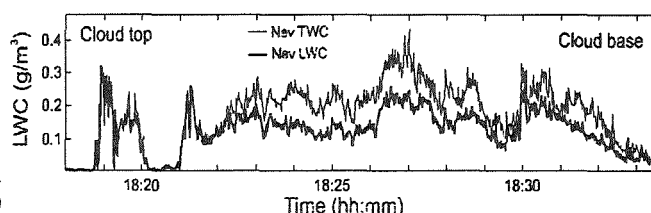


Fig. 7 N_s , $H=1500\text{m}$, $T=2^\circ\text{C}$, Newfoundland.

5. IWC measurements

5.1 Wind tunnel tests

The reaction of the LWC and TWC sensors to ice particles was tested in the NRC wind tunnel. While maintaining a relatively constant water spray, the temperature in the wind tunnel was decreased in a stepwise fashion, eventually producing a partial glaciation of the spray. Fig. 8 shows that the TWC stayed

approximately constant while LWC measured by the Nevzorov and King probes decreased with decreasing temperature. At the outset, the King probe signal was higher than the Nevzorov LWC and TWC because in this case it was situated in a different region of the spray plume. The residual signal at cold temperatures is explained by incomplete freezing of the spray. The presence of nonfrozen water was confirmed by ice buildup observed on the sensor holders.

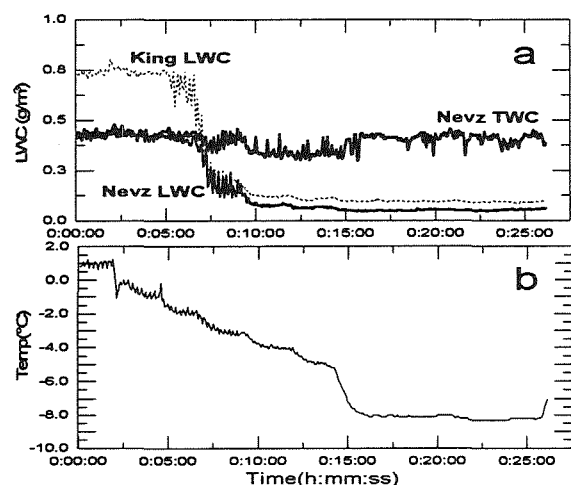


Fig. 8 Wind tunnel cold test of Nevzorov probe

5.2 Mixed phase cloud measurements

The Nevzorov probe exhibits the unique capability to separate ice and liquid zones in mixed clouds. The example presented in Fig. 9 illustrates a flight in mixed Ns. On the left and right portions of the graph, cells of nearly glaciated cloud are observed (TWC >> LWC). On the central are two cells of nearly all liquid cloud, where LWC and TWC measurements nearly coincide.

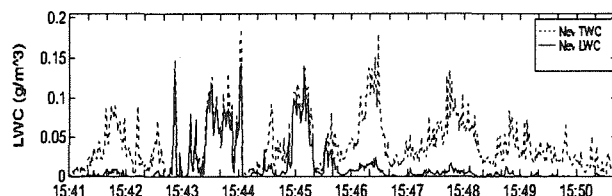


Fig. 9 Ns, H=3500m, T=-5°C, Newfoundland.

An additional example of measurements in mixed clouds is shown in Fig. 10a. The measurements were collected by the Convair 580 in the upper part of a cumulus congestus. The IWC for this case in some places reaches 1.5 g/m³. It is interesting to note that the ratio of LWC/TWC stayed approximately constant in cloud, and increased towards the cloud edges (Fig. 10b). This kind of observation may prove useful in understanding the factors affecting ice formation and distribution in cloud.

6. Conclusions

The Atmospheric Environment Service has collected a large data set with the Nevzorov LWC/TWC probe during several research experiments conducted on the NRC Convair 580 aircraft and at the NRC high speed icing wind tunnel since 1993. These tests show that the error in water content measurement due to baseline drift attributed to variations of temperature, pressure and air speed are of the order of $\partial W/\partial T \sim 0.5 \times 10^{-3} \text{ gm}^3/10^\circ\text{C}$, $\partial W/\partial Z \sim 5 \times 10^{-3} \text{ gm}^3/\text{km}$,

$\partial W/\partial u \sim 3 \times 10^{-3} \text{ gm}^3/10\text{ms}^{-1}$, respectively. Intercomparisons of the Nevzorov LWC/TWC and PMS King probes displays good agreement in liquid clouds (usually < 10% difference), although the Nevzorov probe shows distinct advantages in low LWC situations due to its superior baseline stability. Tests at the wind tunnel have provided some verification of the TWC measurement for small frozen droplets, but verification in snow has not yet been possible due to the absence of any accurate standards. The TWC measurement offers not only the possibility of direct measurements of ice content, but also improved liquid water contents in drizzle situations, and perhaps water content measurements in light rain situations.

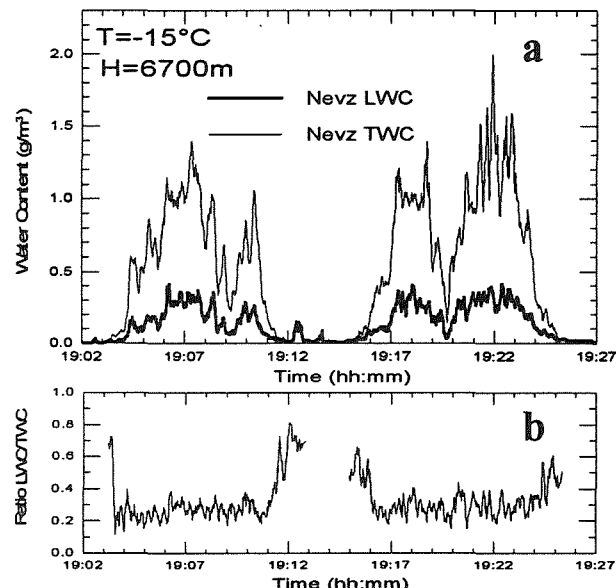


Fig. 10 Cu cong. 19-Aug-94, Ottawa.

7. ACKNOWLEDGMENTS

The authors acknowledge the contribution of the National Research Council in instrumentating and operating the Convair 580 research aircraft, and in the joint planning and execution of collaborative research projects. The Canadian Freezing Drizzle Experiment was funded in part by the Canadian Search and Rescue Secretariat and Transport Canada.

REFERENCES

- Biter C.J., J.E. Dye, D. Huffman, and W.D. King, 1987: The drop response of the CSIRO liquid water content. *J. Atmos. Oceanic Technol.*, 4, 359-367
- King, W.D., D.A. Parkin and R.J. Handsworth, 1978: A hot-wire water device having fully calculable response characteristics. *J. Appl. Meteor.*, 17, 1809-1813.
- Nevzorov, A. N., 1980: Aircraft cloud water content meter. *Comm. a la 8eme conf. int. sur la phys. des nuages, Clermont-Ferrand, France*, v. II, 701-703.
- Nevzorov, A. N., and V. F. Shugaev, 1992: Observations of the initial stage of ice phase evolution in supercooled clouds. *Soviet Meteorology and Hydrology*, No 1, 69-76

AN INSTRUMENT FOR THE REAL-TIME CLASSIFICATION OF PARTICLE SHAPE WITHIN CLOUDS AND AEROSOLS

Paul H Kaye, Edwin Hirst, Spencer J Saunders¹, and
Doug W Johnson, Martyn A Pickering²

¹ERDC, University of Hertfordshire, Hatfield AL10 9AB, UK.

²Meteorological Office, MRF, DRA Farnborough, Hampshire, GU14 6TD, UK.

1. INTRODUCTION

In investigations of the composition and dynamics of the particulate atmosphere, particle shape is an important parameter by which classification and possibly identification of particles may often be achieved. Spherical droplets, cuboidal crystals typical of marine aerosols, and the wide variety of morphologies assumed by ice crystals, are examples where the determination of shape may be used in combination with size spectra measurements to provide experimental data upon which theoretical models of macroscopic and microscopic physical behaviour of clouds and aerosols may be developed and tested. A specific example of this involves the study of ice microphysics and the behaviour of droplets and ice crystals which can occur simultaneously within clouds. The radiative properties of these mixed-phase clouds can be radically dependent upon the relative proportions and size spectra of the two phases, and a large proportion of precipitation that falls in mid-latitudes is governed by the processes that accompany the glaciation of clouds (Moss et al. 1993). To be able to understand the radiative transfer properties of ice and mixed phase clouds, a detailed knowledge of the particles' shapes and sizes is required, along with measurements of the number concentration of ice and super-cooled liquid water particles (Foot 1988; Arnott et al. 1994). In addition, measurement of the total ice crystal number is important to facilitate the testing of theories of the nucleation of ice crystals and their interaction with aerosol.

This paper describes progress of the development of a new aircraft mounted instrument for use in cloud and aerosol microphysical research where particle size and shape are important parameters, such as in the discrimination between super-cooled water droplets and ice crystals of 1-25 μm size within cirrus clouds, (virtually impossible to achieve with current instrumentation). The instrument will allow the automatic, real-time classification of cloud or aerosol particles into size and shape parameter distributions based on an analysis of the spatial laser light scattering

characteristics of individual particles. The instrument is designed to achieve particle classification at throughput rates of up to 10,000 particles per second for particles within the size range $\sim 1\mu\text{m}$ to $100\mu\text{m}$ (spherical equivalent) diameter.

2. BACKGROUND

The University of Hertfordshire has developed several ground-based instruments for the classification and identification of airborne particles by analysis of the manner in which individual particles spatially scatter incident laser illumination. (See for example Kaye et al 1991; Hirst et al. 1994). The new aircraft-mounted instrument is based in part upon the physical principles of an existing, commercially available, real-time aerosol monitoring system, the *Aerosol Shape Analyser*, or ASA, (Kaye et al. 1996). The ASA instrument, illustrated schematically in Figure 1, continuously classifies airborne particles drawn from an ambient environment into size and shape spectra.

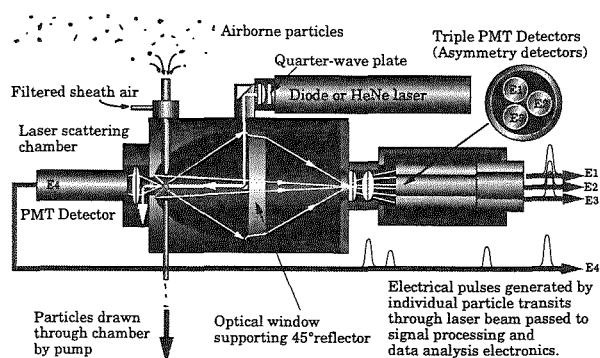


Figure 1: Original ASA particle monitoring system.

In brief, airborne particles are drawn from the ambient atmosphere by a suction pump, and are constrained by delivery tubes and aerodynamic focusing to pass through a laser beam. The beam has a flat elliptical cross-section of $120\mu\text{m}$ depth, and the intersection with the particle laden air defines a *scattering volume* of typically 1mm in diameter. Particle flow is such that statistically, particle

coincidences within the scattering volume are rare. Light pulses scattered by each particle passing through the scattering volume are reflected by an ellipsoidal reflector to three *asymmetry* detectors arranged symmetrically about the beam axis. These detectors, (E1 to E3) provide particle shape parameter data. A fourth detector (E4) in the forward scattering plane provides, in combination with the other three outputs, particle size data. The signal pulses from the four detectors are processed in real-time for throughput rates of up to 10,000 particles per second. These data are then displayed graphically (updated at 5 second intervals) to provide size and shape parameter spectra. Figures 2 and 3 below show such data from water droplet and salt crystal aerosols respectively.

The Centroid Plot on the left in Figures 2 and 3, presents particle data by a dot whose position within the triangle denotes the centroid of the three detector outputs E1, E2, and E3. Thus spherical particles which scatter equally to all three detectors (as is the case for droplet scattering) will result in dots at the centre of the triangle. Non-spherical particles will result in dots away from the centre, in the case of elongated particles towards apex E2 because of preferential orientation of such particles with the axis of flow (Hirst et al. 1994). The shade of the dot, normally colour but here rendered in grey-scale, represents the frequency of particle data at that pixel location. The Contour Plot on the right in the Figures, represents on a 20 by 20 matrix the spherical equivalent particle size computed from Mie theory (Bohren and Huffman 1983) using all four detector values) versus an empirical particle Asymmetry Factor, Af, based on the root-mean-squared sum of E1, E2, and E3 and defined in detail in Kaye et al. 1996. Af is computed such that for perfect spheres (such as the droplets in Figure 2) Af=0, and for elongated particles, Af=100.

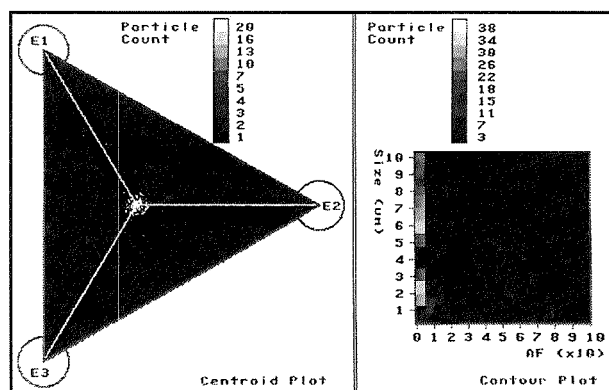


Figure 2: Real-time display output from the ASA instrument showing data recorded from a water droplet aerosol. Since the droplets are highly spherical they produce a tight peak at the centre of the Centroid Plot (left), whilst the Contour Plot (right) shows that the size distribution of the droplets, all appearing at the left-hand (spherical) end of the Af axis, ranges from 1µm to 10µm and beyond.

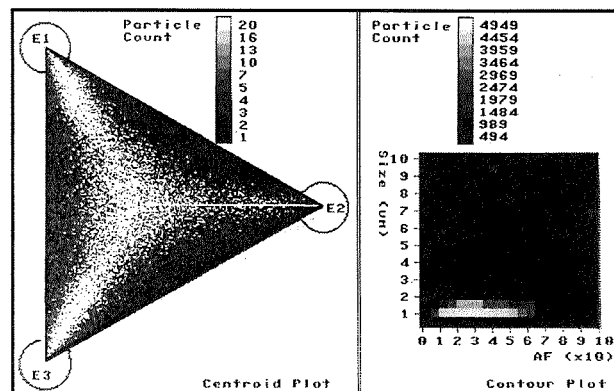


Figure 3: Real-time display output from the ASA instrument showing data recorded from a salt (NaCl) crystal aerosol. The micron sized cuboidal crystals result in the characteristic 'tri-corn' display in the Centroid Plot, and produce a mean Af of ~30.

The examples illustrate that the triple-detector arrangement can provide significant real-time discrimination between particle species on the basis of shape and optical scattering size. The same fundamental principles of operation are being employed in the development of the new cloud monitoring instrument.

3. INSTRUMENT DESIGN CONSIDERATIONS

The new instrument will be carried in a wing pod with communication to an inboard processor for real-time data display and data logging. It has to meet two specific performance criteria:

(i) As far as practically possible, it has to measure the cloud particles in their native state without affecting their phase or orientation. This precluded the type of particle delivery system used in the original ASA instrument of Figure 1 (which drew particles through the laser scattering chamber via narrow delivery tubes) since such a system would adversely affect particle orientation and could also cause partial melting of small ice crystals. It was necessary therefore to define a particle measurement space free from intrusion by any mechanical supporting structures.

(ii) The instrument has to cope with the very large dynamic range of scattered light intensities experienced with individual particle sizes from 1µm to 100µm in diameter. Mie scattering theory has been used to assess this range for scattering from spherical particles. For illustration, an optical detector subtending a cone of semi-angle 10° and placed at a scattering angle of 30° to the incident illumination direction would receive approximately 3,300 times more scattered radiation from a 100µm water droplet than a 1µm droplet. The situation is made more demanding by the fact that in order to assess the shape of the smallest particles, their scattering

signals must be determined with signal-to-noise ratios of at least 10:1 to allow accurate comparison between signals from the three asymmetry detectors. This results in an overall dynamic range requirement of $\sim 33,000:1$.

4. NEW INSTRUMENT DESIGN

Since there could be no mechanical constraint to force the particles to pass through a scattering volume as in the earlier ASA instrument, a *virtual* scattering volume, free from obstructions and close to the leading edge of the instrument, is created by the intersection of two laser beams of differing wavelengths, as shown in Figure 4. The primary beam ($633\mu\text{m}$ red HeNe laser), produces particle scattering from which size and shape information is derived. The secondary beam (612nm orange HeNe) is of smaller diameter and not only defines the extent of the scattering volume within the central, more uniform, section of the primary beam, but also is used to produce a validation signal for particles passing through that scattering volume. Radiation scattered by particles passing through the scattering volume is collected by an arrangement of eight discrete detector modules, as shown in Figure 4.

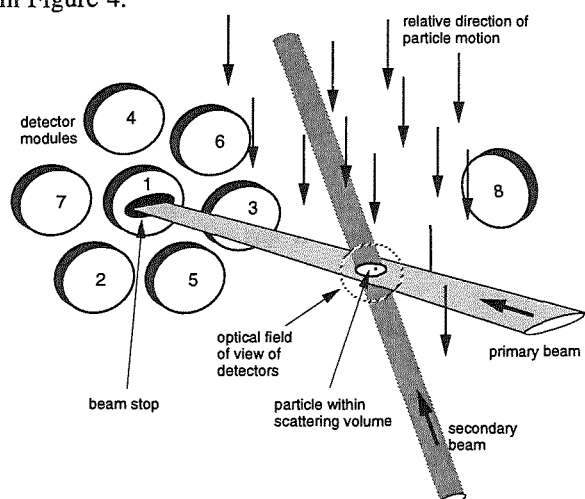


Figure 4: Schematic showing virtual scattering volume produced by two intersecting laser beams, and the arrangement of eight detector modules.

Particles may pass through any part of the cross-sectional area of the inlet pipe, this being $\sim 30\text{mm}$ in diameter. To ensure that only those particles passing through the scattering volume (1mm diameter) are measured, the scattered light pulses received by the detectors 1 and 8 must be coincident. (Optical filters restrict detectors 1 and 8 to detection of the primary and secondary beam wavelengths respectively). However, this alone is insufficient since coincidence could occur with particles passing simultaneously through both beams away from the scattering volume. The field of view of the eight detector modules is therefore limited to an area just sufficient to encompass the scattering

volume. Particles traversing the beams beyond this area cannot be detected.

The six detectors (labelled 2-7 in Figure 4) act as two parallel triple-sets, each similar to the ASA asymmetry detectors. They allow the large dynamic range to be essentially halved. The first set, numbered 2-4, incorporates miniature photomultiplier tubes capable of recording signals for particle sizes from 1 to $15\mu\text{m}$; the second set, numbered 5-7, incorporates photodiode detectors, capable of recording signals from particles throughout the range 15 to $100\mu\text{m}$.

In operation, if detectors 1 and 8 simultaneously register the presence of a particle within the scattering volume valid measurements may take place. The peak values of signals from the six other detectors are recorded, together with the peak value recorded by detector 1 (the latter used for sizing purposes as low angle scattering is less dependent upon particle shape). The processing electronics then determines which set of three asymmetry detectors provides appropriate in-range data, and from these three values a particle shape parameter is determined as in the original ASA instrument. Particle size and shape parameter values are recorded for particle throughputs up to $\sim 10,000$ particles per second, and cumulative data of size and shape spectra are sent to the inboard data logging and display computer at 100ms intervals. For a flight speed of 100m/s (used by the supporting Hercules C-130) the recorded spectra will therefore provide 10 metre spatial resolution of particle size and shape distributions within clouds. ($10,000$ particles s^{-1} would be realised with a cloud particulate concentration of $\sim 10^5 \text{ litre}^{-1}$).

Figure 5 overleaf shows the layout of the measurement head of the new instrument.

5. DATA DISPLAY

Logged data may be analysed post-flight using a display format similar to that in Figures 2 and 3. For in-flight data display in real-time, a simplified display format is required. Figure 6 illustrates the proposed format showing a continuously updated history of the spherical and non-spherical particle concentrations over the past 5 minutes of flight time.

6. DEVELOPMENT SCHEDULE

Ground-based wind-tunnel trials of the new instrument described in this paper are scheduled to commence by the end of 1996. Flight trials are scheduled for mid-1997. When fully commissioned, it is hoped the instrument will provide a valuable additional tool for the study of particulate component concentrations within clouds, and

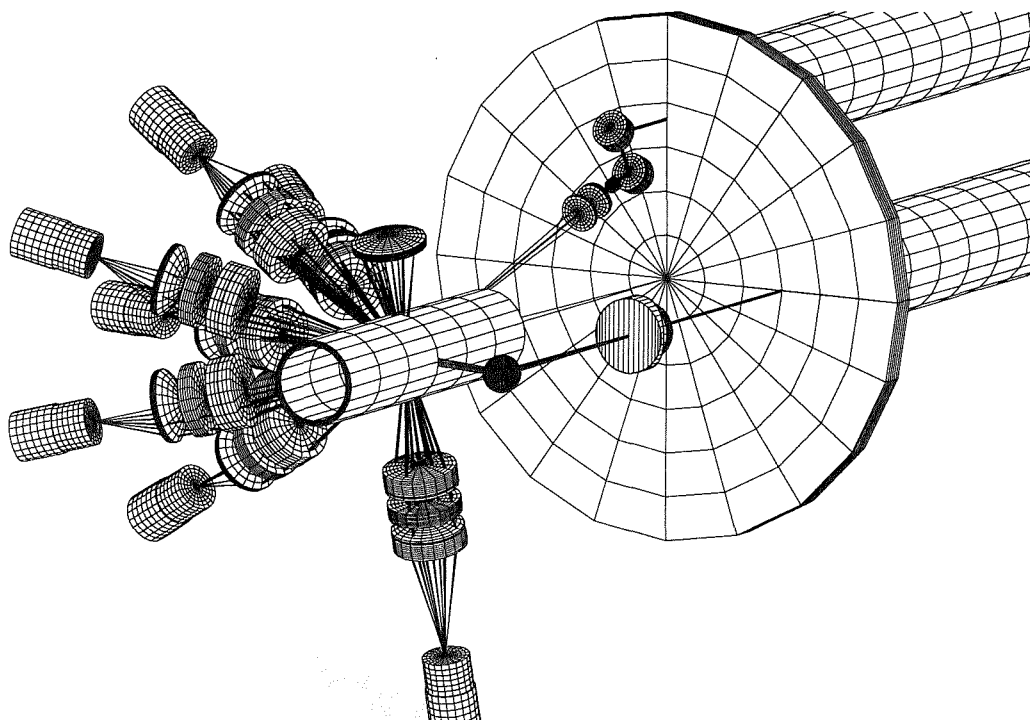


Figure 5: Layout of the measurement head of the new instrument. The laser tubes visible to the right are housed in a cylindrical PMS™ canister together with processing electronics. (For clarity, supporting structures and the aerodynamic shroud protecting the head have been omitted). Airflow is from left to right.

will allow detailed spatial and temporal variations of these concentrations to be investigated.

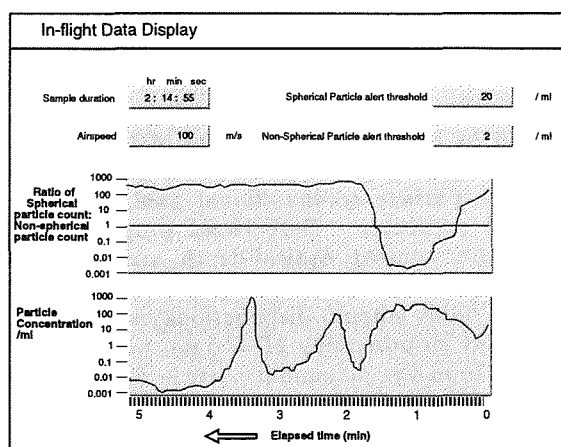


Figure 6: Hypothetical example of proposed in-flight data display providing real-time spherical/non-spherical particle concentrations within clouds.

7. ACKNOWLEDGEMENTS

The authors gratefully acknowledge the support of the UK Natural Environment Research Council (NERC) who have underwritten this research, and of the Meteorological Research Flight for the provision of aircraft facilities.

8. REFERENCES

- Arnott W. P., Dong Y. Y., and Hallett J. 1994: Role of Small Ice Crystals in Radiative properties of Cirrus: A Case Study, FIRE II, November 22 1991. *J. Geophysical Res.*, **99**, D1, 1371-1381,
- Bohren, C. F. and Huffman, D. R. 1983: Absorption and scattering of light by small particles. Wiley, New York.
- Foot J. S. 1988: Some Observations of the Optical Properties of Clouds. II: Cirrus". *Q. J. R. Meteorol. Soc.* **114**, 145-164.
- Hirst E, Kaye, P.H., Guppy, J.R. 1994: Light Scattering from Non-spherical Airborne Particles; Theoretical and Experimental Comparisons. *Applied Optics*, **33**, 30, 7180-7187.
- Kaye, P.H., Alexander-Buckley, K, Hirst, E, and Saunders S. 1996: A Real-time Monitoring System for Airborne Particle Shape and Size Analysis. *J. Geophysical Res.* (in press).
- Kaye, P.H., Eyles, N.A., Ludlow, I.K. and Clark, J.M. 1991: An Instrument for the Classification of Airborne Particles on the Basis of Size, Shape and Count Frequency. *Atmospheric Environment* **25A**, 3/4, 645-654.
- Moss S.J., Brown P.R.A., Johnson D.W., Lauchlan D.R., Martin G.M., Pickering M.A. and Spice A. 1993: Cloud Microphysics Measurements on the MRF C-130: Working Group Report. MRF Technical Note No.12. Meteorological Office.

A BALLOON-BORNE CLOUD PARTICLE REPLICATOR FOR MEASURING VERTICAL PROFILES OF CLOUD MICROPHYSICS: INSTRUMENT DESIGN AND PERFORMANCE

Larry M. Miloshevich and Andrew J. Heymsfield

National Center for Atmospheric Research
Boulder, Colorado, USA

1. INTRODUCTION

A balloon-borne formvar replicator was developed for measuring vertical profiles of cloud microphysics during the 1991 FIRE-II Cirrus experiment in Kansas, USA, and has been used in several subsequent experiments. A primary purpose for its development was to measure particle sizes smaller than the 50-100 μm detection threshold of the airborne Particle Measuring Systems (PMS) 2D-C probes. This paper investigates the accuracy of size distributions measured by the replicator for particles smaller than 100 μm , primarily by determining the instrument's Collection Efficiency and Detection Threshold. The design and operational characteristics of the replicator have been described in Miloshevich and Heymsfield (1995), and will only be summarized here.

2. REPLICATOR DESIGN, DEPLOYMENT, AND DATA CHARACTERISTICS

The replicator (Figure 1) has an aluminum frame with a continuous loop of transparent 35 mm film that is pre-coated with formvar (a plastic). A motor pulls the film past an exposure opening in the box that encloses the replicator. When solvent is released onto the film during ascent, softening the formvar, cloud particles that impact the film are enveloped in a viscous formvar solution. The solvent then evaporates and 3-D formvar replicas of the particles are preserved. A second opening for ventilation promotes airflow into the box.

The replicators are launched with a radiosonde and a transmitter beacon, then tracked and retrieved using radio direction-finding equipment. Electrical signals from reference positions cut in the replicator film produce a timestamp in the radiosonde signal, allowing the microphysical and radiosonde data to be correlated.

Cloud particles collected at a given point on the film represent an average of cloud properties over a vertical distance given by the width of the exposure opening, the ascent rate ($\approx 5 \text{ m s}^{-1}$), and the film speed ($\approx 0.1 \text{ cm s}^{-1}$). For typical exposure opening widths of 15 mm and 35 mm, the vertically-averaged distances are 75 m and 175 m respectively; corresponding sample volumes are 39 L (2.6 L s^{-1}) and 214 L (6.1 L s^{-1}).

The replicator film is imaged with a CCD videocamera mounted on a microscope, then pro-

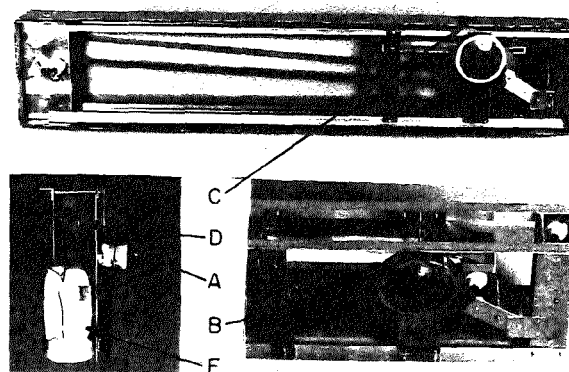


Figure 1. The ice crystal replicator. Labeled components are: drive motor (A), solvent container (B), exposure opening (C), pressure switch that activates the motor (D), and insulated battery (E). Dimensions of the instrument are 91x17x8 cm.

cessed using a software package called "Image," developed by the National Institute of Health. The software identifies, counts, and sizes particles, and measures particle cross-sectional area, aspect ratio, and perimeter. Bulk cloud properties such as ice-water content, optical depth, and equivalent radar reflectivity factor are derived from particle size and habit (shape) distributions using existing algorithms for processing 2D-C data, where habit is inferred from the maximum particle diameter and the cross-sectional area.

The qualitative characteristics of replicator ice crystal data are illustrated in Figure 2, from a study where detailed ice crystal properties characteristic of ice-subsaturated versus ice-supersaturated regions of a cirrus cloud were used to assess the accuracy of relative humidity measurements from a balloon-borne cryogenic hygrometer. Figure 2 also demonstrates the natural variability of cirrus microphysical properties in the vertical, and the importance of obtaining vertical profiles of cloud microphysics. An imaging resolution (pixel size) of 3.4 μm is typically used to image large ice crystals and a resolution of 1.4 μm is used to image droplets or small ice crystals (as compared to the 25-50 μm resolution of 2D-C data). The high resolution of replicator data may permit more accurate automated determinations of habit, from such quantities as the ratio of particle perimeter to maximum diameter or cross-sectional area.

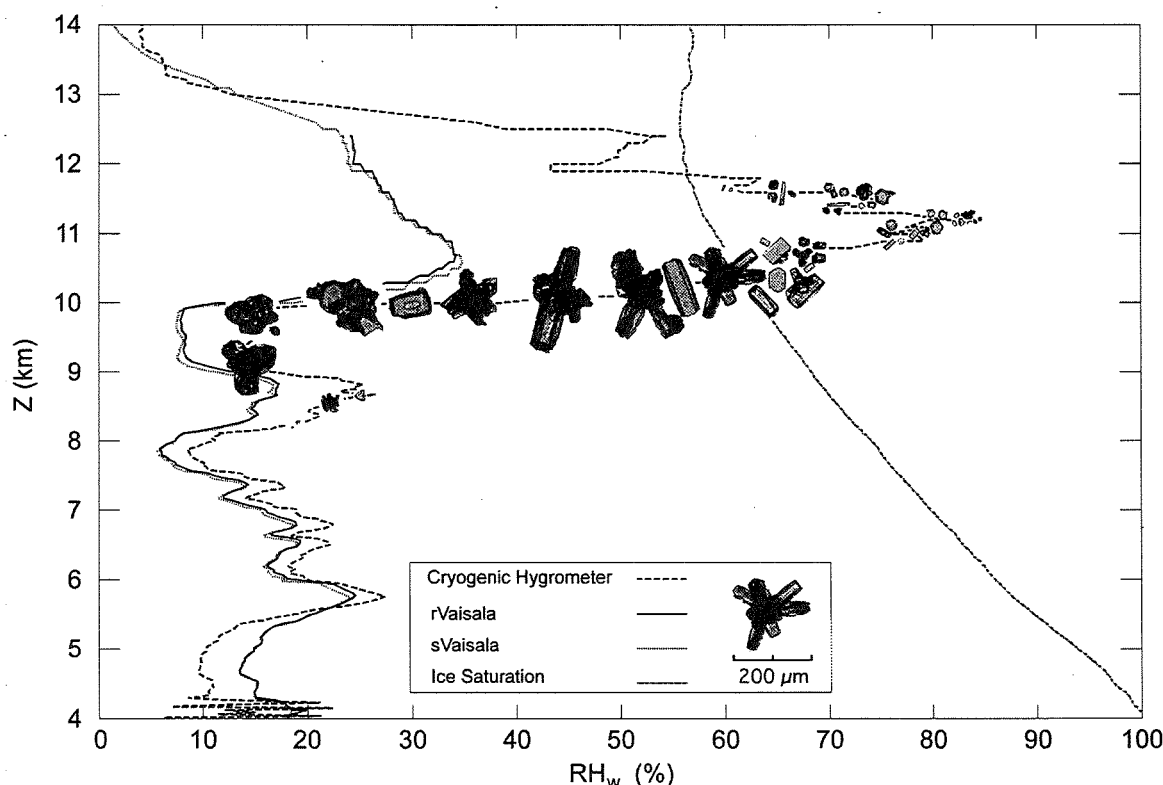


Figure 2. Simultaneous relative humidity profiles from two Vaisala RS-80 radiosondes and a balloon-borne cryogenic hygrometer, with example ice crystals measured simultaneously by the replicator. An ice-saturation curve is shown for reference. Cryogenic hygrometer data are courtesy of Sam Oltmans of NOAA.

3. COLLECTION EFFICIENCY ANALYSIS

The accuracy of size distributions determined from impactor-type particle collection devices depends on the Collection Efficiency (CE) — the size-dependent fraction of the upstream particle concentration that impacts on the collector rather than being carried around the collector by the airstream. The CE is the cross-sectional area far upstream within which particles will impact on the replicator film, divided by the area of the collecting surface. The CE depends primarily upon the size and density of the particles, the windspeed and air viscosity, and the geometry of the collector. If the CE is known, the “true” size distribution can be determined from the measured size distribution.

The theoretical calculations of CE available for simple collector shapes cannot be applied to the complicated replicator geometry and flowfield. This study uses a numerical fluid dynamics model called STAR-CD, developed by Computational Dynamics Ltd. and supported in the U.S. by Adapco Inc., to calculate the velocity and pressure fields and particle trajectories for a simulated replicator. STAR solves the Navier-Stokes equations, with a $k-\epsilon$ model of turbulence, for arbitrary geometries and computational meshes. The simulation models the replicator box with its exposure and ventilation openings, the 35 mm film, and the basic structure of the replicator frame. The specified model domain consists of 180,000 cubic cells with dimensions ranging from 3 cm in the free-stream flow to 0.125

cm near the exposure opening and film. A steady-state flowfield was calculated for a windspeed of 5 m s^{-1} , then droplets (density 1.0 g cm^{-3}) or small ice crystals (spheres with density 0.7 g cm^{-3}) were released far upstream and tracked until they struck a surface or exited the model domain.

The velocity field and trajectories of 30 μm droplets are shown in Figure 3. Analysis of many particle sizes shows that the motion of small particles is very sensitive to the local velocity perturbations that occur near the exposure opening and the film; larger particles, by virtue of their inertia, follow straighter trajectories. Substantial air motion parallel to the film tends to carry particles, particularly sizes $< 25 \text{ μm}$, beyond the “sample area” defined by the height of the exposure opening and width of the film. Particles that impact the film outside the sample area are not considered to be replicated and are not included in the CE calculations; “above” the exposure opening solvent has not yet been released, and “below” the exposure opening the formvar has most likely dried (although the temperature-dependent drying time of the formvar remains an unknown at this time).

The static pressure profile upstream of the center of the exposure opening from the model is compared in Figure 4 to the analogous pressure profile measured with a small pitot tube in the NCAR Atmospheric Technology Division windtunnel. The profiles are in good agreement and give confidence that the modeled flowfield and particle trajectories are realistic, especially given such sources of er-

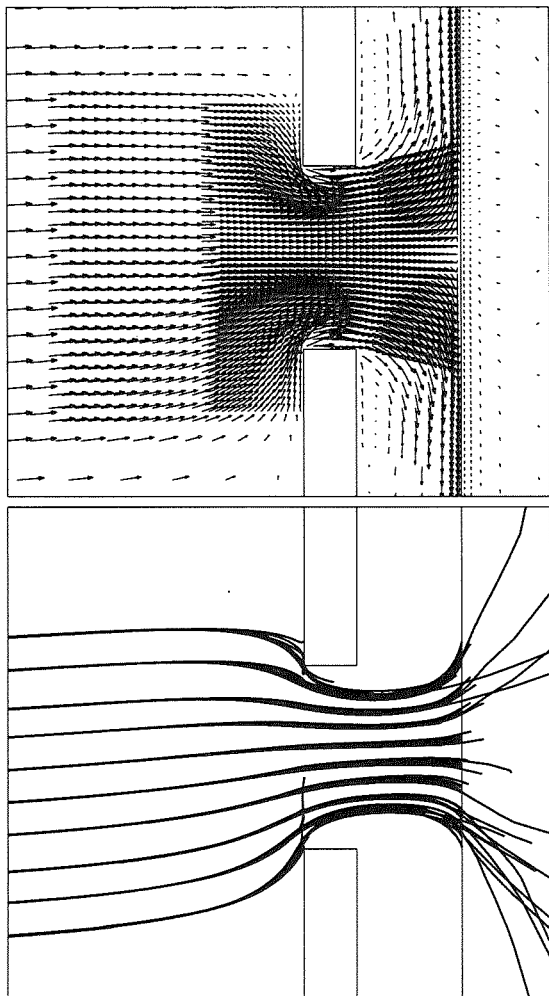


Figure 3. Numerical simulation of the velocity field and trajectories of $30\text{ }\mu\text{m}$ droplets incident on the replicator exposure opening and film. A 10×10 grid of droplets was started far upstream. The views are cross-sections through the center of the exposure opening parallel to the film.

ror as the $\pm 0.1\text{ m s}^{-1}$ fluctuations in windspeed in the windtunnel and the simplification of the replicator's detailed structure in the model. Figure 4 also shows that the replicator modifies the upstream flowfield on three length scales: 1) furthest upstream ($X < 0.47\text{ m}$) the air and particles sense only the 85 mm width of the box and not the exposure opening or film (as judged by the similarity to Fig. 4 of a pressure profile measured with the exposure opening sealed); 2) near the exposure opening the pressure decreases to a minimum ($0.47 < X < 0.50\text{ m}$), causing air and particles to be accelerated into the lower-pressure interior of the box by the "suction" effect seen in Fig. 3 (which likely results from the spacious interior and large ventilation opening to the low-pressure wake behind the box, at $X > 0.69\text{ m}$); and 3) near the film ($X = 0.53\text{ m}$) the pressure increases to a maximum as air and particles are forced either around the film or along the film.

The CE for droplets and small ice crystals was computed from model runs of 900 particles in a

30×30 grid started far upstream (Figure 5); the uncertainty in the cross-sectional area far upstream within which particles are collected, given by the particle spacing, corresponds to uncertainties in the CE of $\pm 7\%$. The CE increases slowly from 50% for $32\text{ }\mu\text{m}$ droplets ($40\text{ }\mu\text{m}$ ice crystals) to 60-65% for $100\text{ }\mu\text{m}$ particles and 75-85% for $200\text{ }\mu\text{m}$ particles (not shown). The CE decreases rapidly for particle sizes $< 40\text{ }\mu\text{m}$, to about 10% for $20\text{ }\mu\text{m}$ droplets ($24\text{ }\mu\text{m}$ ice crystals). Two collecting areas are considered in Figure 5 — one includes only particles collected on the typical "imaging area" of the film, the smooth area between the sprocket holes at the edges of 35 mm film; the second includes the entire width of the film. The collection of particle sizes $< 20\text{--}25\text{ }\mu\text{m}$ is enhanced at the edges of the film; the preferential collection of small ice crystals at the edges of the film has been observed in the replicator data. The Detection Threshold, where the CE drops to zero, is $< 10\text{ }\mu\text{m}$ for droplets and $< 15\text{ }\mu\text{m}$ for ice crystals, consistent with the smallest particle sizes observed in the data.

Droplet size distributions from the replicator and from a PMS Forward Scattering Spectrometer Probe (FSSP) provide a means of assessing the CE determined from the model (Figure 6). Although the replicator and FSSP measurements were made from different platforms about six hours apart, and spectra certainly cannot be compared directly, the FSSP measurements show the range of size distributions measured in this cloud; mean droplet diameters were nearly always in the range $7\text{--}20\text{ }\mu\text{m}$ and were usually in the range $8\text{--}15\text{ }\mu\text{m}$, which is typical of non-precipitating liquid water clouds. The replicator appears to collect only the large-droplet end of the spectrum, with a peak at $25\text{ }\mu\text{m}$ and a mean diameter of $23.7\text{ }\mu\text{m}$ (curve 1a); the rapid decrease in concentration below $25\text{ }\mu\text{m}$ (where FSSP measurements show the true peak is located), is consistent with the rapid decrease in CE at these

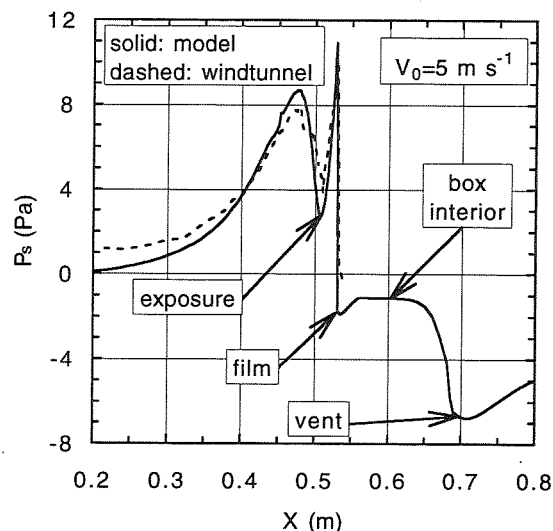


Figure 4. Static pressure (P_s) at the center of the replicator exposure opening vs position (X) measured along the wind direction, from the numerical model and from windtunnel measurements.

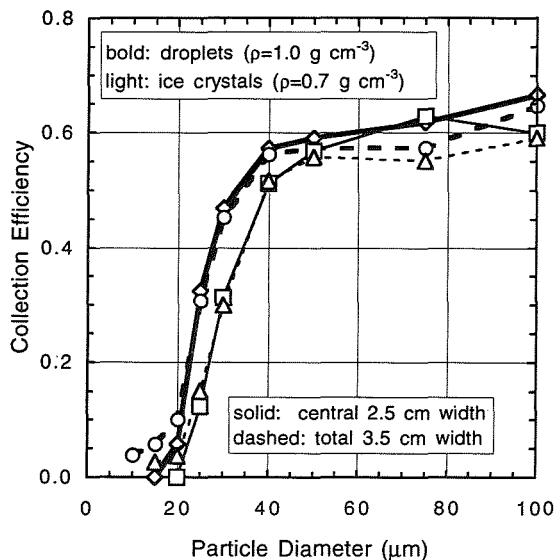


Figure 5. CE from the numerical model, for droplets (bold curves) and small ice crystals (light curves). The CE was computed considering either just the central 2.5 cm “imaging area” of the film (solid curves), or considering the total 3.5 cm width of the film (dashed curves).

sizes. The CE-corrected spectrum (1b) shows a slope reasonably consistent with the FSSP spectra for sizes down to 18 μm , where the CE is nearly zero and correction of spectra is no longer valid. [Note that replicator data were necessarily chosen from a region where total droplet concentrations were atypically low; when the total concentration exceeds about 1 cm^{-3} incident droplets strike and coalesce with droplets already on the film. The replicator is designed for use in lower-concentration cirrus clouds.]

4. CONCLUSIONS

The collection efficiency of the replicator as determined by numerical modeling seems sufficiently consistent with in-situ and windtunnel measurements to apply to measured size distributions, especially when the CE exceeds 10% ($>20\text{ }\mu\text{m}$ for droplets and $>24\text{ }\mu\text{m}$ for ice crystals). Additional model runs are needed to reduce uncertainty in the upstream area of particles collected, and to determine the dependence of the CE on bulk particle density, windspeed, air density, temperature, turbulence parameters, and film width.

This study also suggests several instrument design considerations applicable to the new, smaller, acrylic-framed replicator now being developed: 1) the box width should be minimized to decrease divergence of the upstream airflow; 2) an airflow guide that inhibits airflow parallel to the film would reduce particle impacts outside the sample area; 3) the replicator frame should minimally obstruct airflow perpendicular to the film; 4) the exposure opening should be located in the center of the box

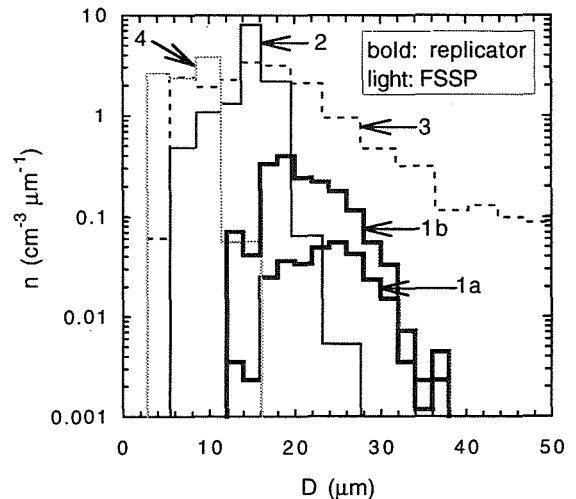


Figure 6. Droplet size distributions from the replicator (1a and 1b) and from an FSSP (2-4), measured in a stratocumulus cloud during FIRE-II on 22 Nov. 1991. Spectrum 1a contains 250 droplets and represents a sample volume of 430 cm^3 (counting statistics are poor for concentrations $<0.01\text{ cm}^{-3}\text{ }\mu\text{m}^{-1}$); spectrum 1b has had the CE correction applied. The FSSP spectra are 5-second averages, giving a sample volume similar to the replicator spectra. Total concentrations and mean diameters are: (1a) 0.58 cm^{-3} , $23.7\text{ }\mu\text{m}$; (1b) 3.39 cm^{-3} , $20.9\text{ }\mu\text{m}$; (2) 33.3 cm^{-3} , $14.3\text{ }\mu\text{m}$; (3) 59.7 cm^{-3} , $18.9\text{ }\mu\text{m}$; and (4) 25.3 cm^{-3} , $7.8\text{ }\mu\text{m}$. FSSP data are from the University of North Dakota Citation aircraft, courtesy of Prof. Michael Poellot.

to promote an even distribution of particles across the film; 5) a fan in the ventilation opening may enhance the natural “suction” effect that improves the collection of small particles; and 6) decreasing the film width to 16 mm would improve the collection of small particles.

5. ACKNOWLEDGEMENTS

We gratefully acknowledge Steve Aulenbach (NCAR) for developing the image processing techniques, Cindy Twohy (NCAR) and Mary Laucks (University of Washington) for assistance with the numerical model, Mike Poellot (University of North Dakota) for providing the FSSP data, and Sam Oltmans (NOAA) for providing the cryogenic hygrometer data. This work was primarily supported by NASA/FIRE-III grant no. L55549D.

6. REFERENCES

Miloshevich, L.M., and A.J. Heymsfield, 1995: Performance analysis of an ice crystal replicator sonde developed for cirrus microphysical measurements during FIRE-II. Preprints, *9th Symp. on Meteorological Observations and Instrumentation*, Charlotte, NC, 421-426.

A NEW CLOUD CONDENSATION NUCLEI COUNTER

Kleiton do Carmo Mendes¹, Carlos Jacinto de Oliveira², Murilo Pereira de Almeida³
and José Carlos Parente de Oliveira³

¹ Fundação Cearense de Meteorologia e Recursos Hídricos - FUNCEME

² Departamento de Física e Química, Universidade Estadual do Ceará - UECE

³ Laboratório de Física de Nuvens e Mesoescala, Departamento de Física, Universidade Federal do Ceará - UFC

1.. INTRODUCTION

The cloud droplet concentration is fundamentally important in determining the radiative properties of clouds and their precipitation evolution. Measurements of cloud condensation nuclei (CCN) have a parallel importance since there is a reasonably clear and simple link between them and droplet concentrations. For a recent review of cloud condensation nuclei observations we refer to Hudson (1993). Many aspects of CCN measurements are covered in the summary of the Third International Cloud Condensation Nuclei Workshop (July-December 1981 issue of the *Journal de Recherches Atmosphériques*, pp 177-370).

CCN measurements, which provide considerable predictive capability about cloud characteristics, can be obtained by direct activation of the nuclei in a chamber of controlled supersaturation. Direct CCN measurements can be performed by the static thermal-gradient diffusion chamber (SDC). This chamber is the main component of the Cloud Condensation Nuclei Counters (CCNC). The SDC devices are useful for measurements of the concentration of droplets in the supersaturation range 0.2% to 1.2%. Two approaches are used: direct counting of droplet images, or the measurement of light scattered by the droplets. The

indirect approach of measuring the light scattered by droplets leads to a convenient automation of the measurement, at the cost of introducing the additional uncertainty associated with the relationship of scattered light signal to droplet count in the chamber. A common problem is the fact that the scattered signal is proportional to the integral of droplet number times scattering cross-section, not just droplet number. As a consequence the CCNC calibration procedure is not a simple task (de Oliveira, J.C.P. and G. Vali, 1995). The direct counting is done on a photographic or video image. This method has the advantages of being independent of the sizes of the droplets. On the other hand, the counting would be laborious and time consuming if it is not automatic. The latter method can be very attractive if we use image analysis techniques.

In this paper we describe a new calibration method for the CCNC, which uses stochastic techniques of Digital Image Processing and can originate a completely new CCN counter.

2. DESCRIPTION OF THE EQUIPMENT

The image processing algorithm was designed to automate the calibration of the University of Wyoming cloud condensation nucleus counter

(UW-CCNC 1983). Inside this instrument controlled supersaturations are created in the chamber by cooling the bottom plate, while allowing the top plate to be at ambient temperature. Both plates carry water-soaked paper. The interior of the chamber is visible through three windows. One is used for illumination by a 5 mW He-Ne laser tube. One window allows visual inspection, or viewing by a video camera. For video recording this window has lenses which provide a two times magnification. A photodetector and lens arrangement is placed at the third window. The basic design of the chamber follows that of Lala (1981). The CCNC is controlled by a Motorola MC68010 microprocessor which provides digital temperature control, data manipulation, read-out.

3. THE CCNC ALGORITHM

The CCNC algorithm (Mendes et al., 1995) consists in determining the droplet concentration using the images captured by the video camera. Video data is recorded with a standard video tape recorder.

The images of the droplets developed in the SDC are digitalized. The algorithm reads the digitalized images, process them and generates idealized images. In each cycle of measurement of the counter the algorithm chooses the image with maximum number of droplets. Then the algorithm counts and classifies the droplets by comparing them with circles of varying radius. This procedure can well substitute the direct visual approach. The output produced by the algorithm is the real concentration of droplets inside the chamber. Also the algorithm categorizes the droplets by sizes. This algorithm is based on the modeling of the digital image by Markov Random Fields, and its implementation uses a Simulated Annealing scheme via Metropolis rule (Carnevali, et al., 1985, Metropolis, et al., 1953). It determines a configuration of circles that best fits the real image observed by the camera.

4. RESULTS

Our evaluation of the algorithm consists in comparing its result with the direct visual counting of droplets. For a random choice of 39 measurements (images) the correlation coefficient between the two counting methods was equal to 0.94. The Figure 1 shows the number of droplets counting by the algorithm versus the number of droplets determined by visual counting. The number of droplets inside the chamber is directly determined. As a consequence this method suppress the need of CCN counter calibration. In this case we have an "absolute" counter.

Furthermore, this new method besides counting droplets also classifies them by size. The new CCN counter does not need a photodetector since it is an imaging detector. The big advantage is the fact that we get the histogram of droplet distribution size.. In Figure 2 and 3 we present an observed and its respective processed image., for a measurement which 1% supersaturation.

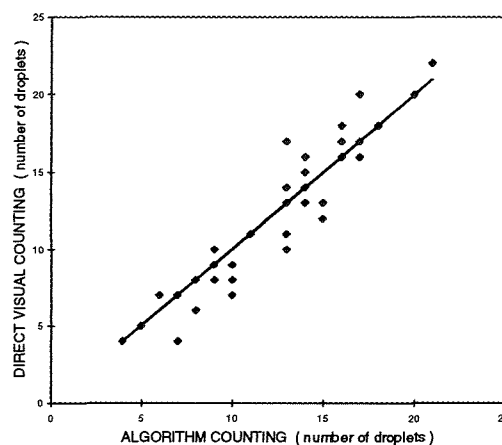


Figure 1. Number of droplets counted by the algorithm versus number of droplets counted by eye.

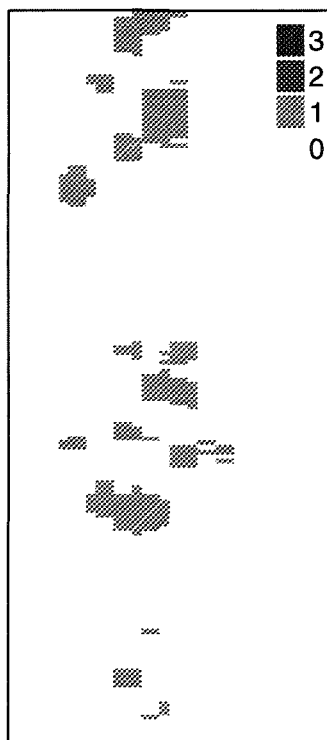


Figure 2. A digital image of droplets inside the chamber.

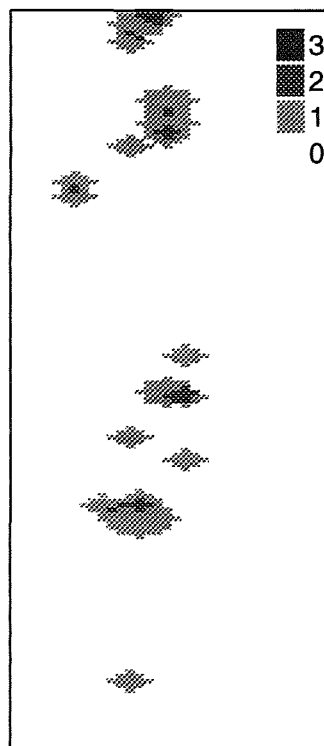


Figure 3. A processed image by the algorithm.

ACKNOWLEDGMENTS

The authors are indebted to the Department of Atmospheric Science of the University of Wyoming, especially to Dr. Gabor Vali, for the support in using the UW-CCNC. Partial funding for this work was provided by FUNCEME. The researchers C.J. de Oliveira, K.C. Mendes and J.C.P. de Oliveira were partially supported by CNPq (Conselho Nacional de Científico e Tecnológico).

REFERENCES

- Carnevali, P., L. Collet, and S. Patarnello, 1985: Image Processing by Simulated Annealing, IBM, *J. Rech. and Development*, **29**(6), 569-579.
- de Oliveira, J.C.P., and G. Vali, 1995: Calibration of a Photodetector Cloud Condensation Nuclei Counter, *Atmospheric Research*, **38**, 1-4
- Hudson, J.G., 1993: Cloud Condensation Nuclei, *J. Appl. Meteorol.*, **32**, 596-607.
- Lala, G. G., 1981: An Automatic Light Scattering CCN Counter. *J. Rech. Atmos.*, **15**, 259-262.
- Mendes, K.C., J.C.P. de Oliveira and M.P. de Almeida, 1995: Annealing Simulado para Contar Automaticamente Núcleos de Condensação de Nuvens. Anais do XVIII Congresso Nacional de Matemática Aplicada e Computacional, **2**, 503-506.
- Metropolis, N., A.W. Rosenbluth, A.H. Teller and E. Teller, 1953: Equations of State Calculations by Fast Computing Machines, *J. Chem. Phys.*, **21**, 1087-1091

MICROPHYSICAL SONDE

N.A.Berezinsky

Scientific and Production Geophysical Center, Stavropol, Russia

L.M.Fedchenko, M.I.Tlisov

High-Mountain Geophysical Institute, Nalchik, Russia

A radiotelemetric sonde is designed for the atmosphere parameters researching both inside of heavy thunder-and-hail clouds and at their vicinity. It is placed in the head part of an anti-hailing missile "Oblako" and is delivered in it to the measurements point being launched from a ground launcher or dropped from the outer suspension bracket of a laboratory-plane.

This sonde provides for the measurements in the real time scale of the following:

- the dimensions spectrum of drops and crystals, μm . from 100 to 5000;
- particles concentration, m^{-3} from 1 to 20000;
- liquid-water, g/m^3 from 0.3 to 10;
- temperature, $^{\circ}\text{C}$ from -50 to 30;
- relative humidity, % from 30 to 100;
- wind speed, m/s from 1 to 50.

Measurements are taken when the missile is descending by a braking parachute at the speed of 30-40 m/s . The main parachute gets opened at the altitude of 1500 m over the sea level and the landing speed makes 8-10 m/s .

A data-transmitter unit is mounted in the fore part of the sonde (Fig.1).

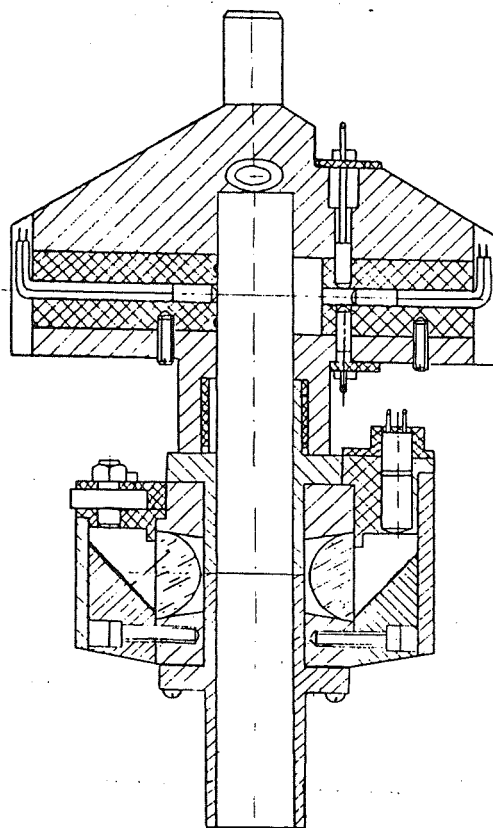


Fig.1. A data-transmitter unit.

The cloudy atmosphere is transmitted through it via a fluoroplastic airduct of 10 mm diameter, separated symmetrically into two streams and released out.

A specktometer for large cloud particles is schematically shown in Fig.2

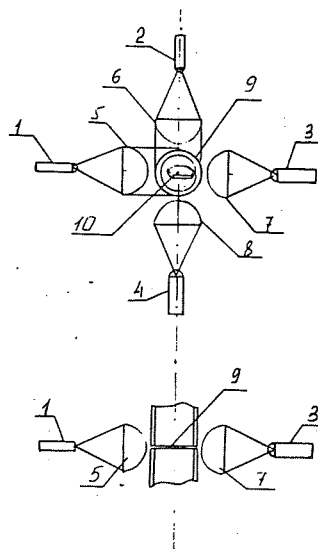


Fig. 2. A spectrometer for large drops and crystals.

- 1, 2 - a light-emitting diode;
- 3, 4 - a photodiode;
- 5, 6 - collimation lenses;
- 7, 8 - collecting lenses;
- 9 - read-out volume;
- 10 - cloud particle.

It comprises two identical optical channels with spectrally adjusted parameters, a light-emitting diode (1 and 2), a photodiode (3 and 4). The channels also comprise collimation (5 and 6) and collecting (7 and 8) lenses. One and the same read-out volume (9) formed by the air duct section and the width of slot in it is illuminated by two collimated beams of light. The flying by cloud particle (10) casts shadows onto the both photodetectors. The electronics compares the amplitudes of the signals got from the photodetectors. If the signals are identical the particle is referred to the drops category and is counted by one of its counters in accordance with the

dimensions. If the signals amplitudes differ more than 30% it is counted by a crystals registering spectrometer. The particles dimensions are determined by pulses duration above the noise level.

A bodyless silicon diode having a linear temperature characteristic from -60 to 100 C is a sensing element of the temperature-sensor. It is mounted in the recess of an intake branch pipe. The measuring circuit is conventional.

A volumetric meter of air relative moisture content (hygrometer) is used in this sonde (Fig. 3).

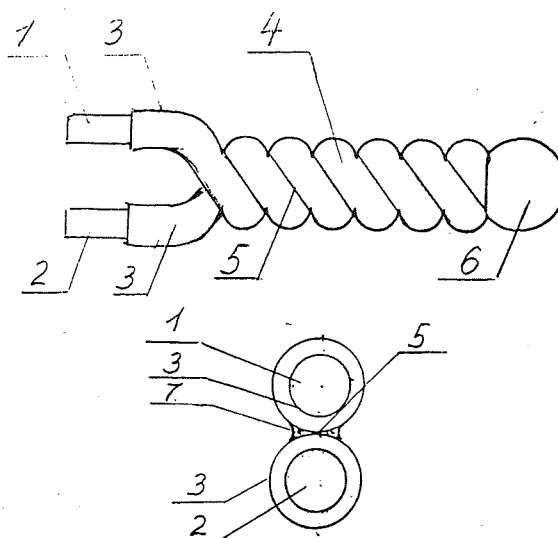


Fig. 3. 1, 2 - electrodes; 3 - enamel of insulation; 4 - twist of electrodes; 5 - capillary; 6 - larmisti insulation; 7 - meniscus.

A condensing sensor is made of two tightly twisted copper conductors insulated with enamel. A sensing element is a capillary tube formed

along the contact line of these conductors. The measurements are taken by a differential scheme making use of a supporting sensor filled in with moisture-proof varnish.

A liquid-water content sensor (Fig.4) is similar by the method of operation to the particles counter. The radiation flux passes from the light-emitting diode (LED) through the air-duct diameter and is perceived by the photodiode. Above the flux flow an inclined heated rod is mounted in such a manner that its projection coincides with the light guide-photodiode line. The cloud drops get trapped by the rod. An air stream blows off the accumulated water to the rod end and tears it down in separate drops. The photodiode signals being the result of shading by drops are integrated by the electronic device. Measurements are taken by the differential method.

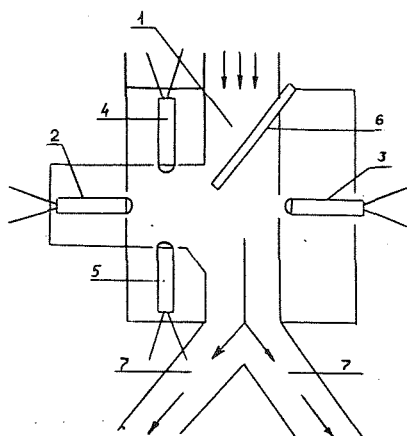


Fig.4. A liquid-water content sensor
 1 - airduct;
 2,4 - light-emitting diode;
 3,5 - photodiode; 6 - pivot;
 7 - airduct.

The compensational couple light-emitting diode- photodiode is mounted aside from the cloud particles stream.

The sensors-telemetry-matching unit effects the sensors electric signals amplification, frings them to one and the same level, encodes and transmits to the radiotelemetry unit.

The radiotelemetry unit is modification of the aerologis radiosonde telemetry system. It effects measurements data transmittance aground. The tracking radar simultaneously with recarding of the measured information also registers the sonde coordinates in the course of time by which air traffics parameters in the cloud are calculated.

The telemetry unit is mounted in the fore part of the sonde. A rod aeral is directed along the sonde axis and in the direction of its movement.

The sonde is power supplied from a dry cell or storag battery providing for stabilized voltages of 9V; +9.5V; 15V required for the sonde operation. The general view of the sonde is given in Fig.5.

The serviceability of all the sonde units and sensors was carried out from a helicopter. The sensors pulse signals oscillograms are shown in Fig.6.

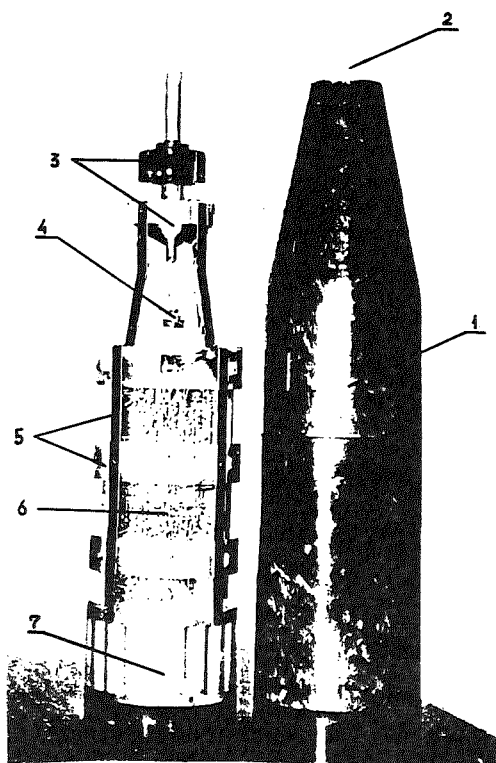


Fig. 5. Microphysical sonde 1 - head of rocket; 2 - nut; 3 - data-transmitter; 4 - radiotelemetry; 5 - framework, 6 - electronics, 7 - feed..

An aerologic radar resolutely tracked the helicopter with a sonde suspended under it. At the distance of 50 km (the limiting range of reception for the used radiostation) the signal power became twice less, i. e. the reception range margin was still enough for taking measurement information from sonde.

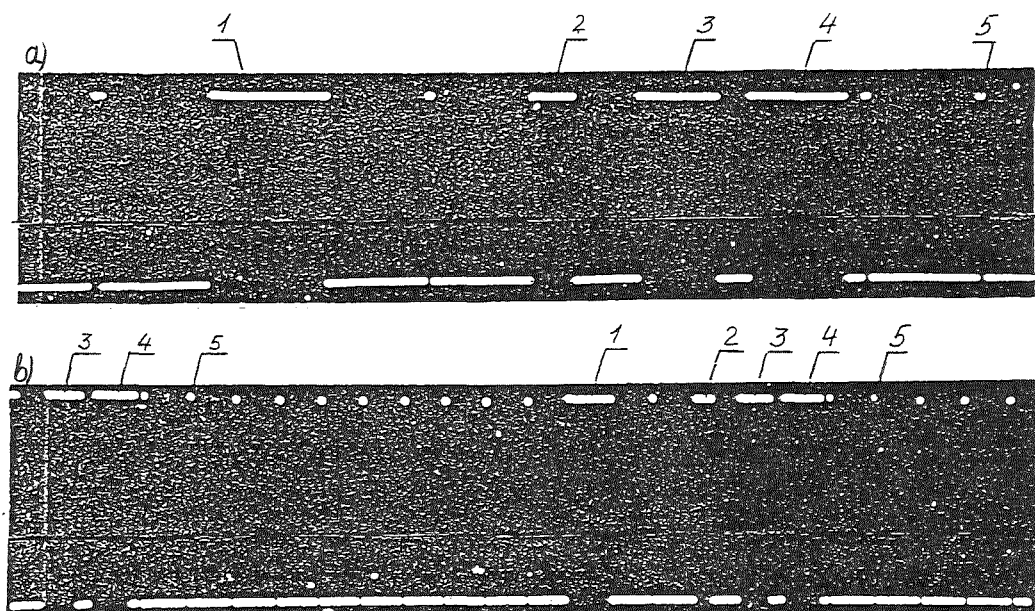


Fig.6. Pulse signal from the sonde. a-single sampling; b-continuous series of pulses; 1 - zero pulse; 2 - water content; 3 - temperature; 4 - humidity; 5 - hydrometeores.

IMPROVED AIRBORNE MEASUREMENTS OF THE DROP SIZE DISTRIBUTION IN FREEZING DRIZZLE

R. Paul. Lawson^{*}, A. V. Korolev[†], T. Huang^{*}, L. J. Angus^{*}, K. A. Weaver^{*},
J. W. Strapp[†], G. A. Isaac[†], S. G. Cober[†]

^{*} SPEC Incorporated, Boulder, CO, USA.

[†] Atmospheric Environment Service, Downsview, Ontario, Canada.

1. INTRODUCTION

There is a significant potential icing hazard to general aviation and commuter aircraft flying in freezing drizzle (Cooper et al. 1984; Politovich 1989; Politovich 1996; Ashenden et al. 1996). Following the crash of an American Eagle ATR-72 commuter aircraft enroute from Indianapolis to Chicago on 31 October 1994, awareness of this hazard has gained international attention (for example, see the *New York Times*, March 4, 1995).

The Canadian Freezing Drizzle Experiment (CFDE) field program conducted near St. Johns, Newfoundland in March 1995 focused on improving our understanding of the meteorology associated with freezing drizzle and making improved in situ observations (Isaac et al. 1996). A Convair 580 research aircraft operated by the National Research Council (NRC) and the Atmospheric Environment Service (AES) of Canada was extensively equipped with microphysical instrumentation. The instrumentation on the Convair 580 included a new optical imaging probe with 3.7 μm size resolution that makes digital images of particles from about 10 μm to 2 mm in diameter. The new probe uses digital holography to reconstruct in-focus images from in-line holograms (Lawson and Cormack 1995; Lawson 1995). Photographs of the Convair 580, the new digital holographic probe installed under the right wing tip and sample images are shown on the cover of this volume.

New data collected in freezing drizzle during the CFDE support theoretical calculations (Korolev et al. 1991, 1996) and recent laboratory work (Reuter and Bakan 1996) showing that size measurements of drops up to about 200 μm diameter using the PMS 2D-C imaging probe (Knollenberg 1981) can be overestimated by nearly a factor of two. A statistical correction applied to the 2D-C data (Korolev et al. 1996) can improve the measurements somewhat, but cannot correct for all of the measurement deficiencies of the older imaging probes. In this paper, we compare measurements in freezing drizzle using the new digital holographic probe to PMS 2D-C measurements with and without the Korolev et al. (1996) statistical corrections.

2. 2D-C MEASUREMENTS

Korolev et al. (1991) present theoretical arguments and laboratory measurements which suggest that the PMS 2D-C can overestimate by up to 80% the size of spherical objects up to about 200 μm in diameter. Recently, Korolev et al. (1996) and Reuter and Bakan (1996) have strengthened both the theoretical and laboratory results. Basically, the 2D-C measurement problems stem from two inadequacies: 1) the probe provides only a one-bit digitization of the shadow size, so particles that are from about $3 \rightarrow 8 \sqrt{r^2/\lambda}$ (where r is radius and λ is the wavelength of laser light) are mis-sized by about $20 \rightarrow 80\%$ and 2) at aircraft (100 m s^{-1}) speeds, the probe electronics detect only a fraction of the particles that are $< 150 \mu\text{m}$ in diameter.

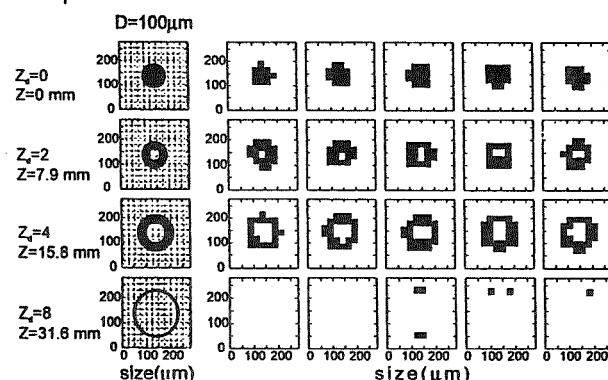


Figure 1. Korolev numerical simulations of Fresnel diffraction of a 100 μm spherical particle. Patterns on the left are for 1-bit shadow images with infinitely small pixels and on the right as seen by the PMS 2D-C with 25 μm pixels resolution. Moving down the figure, the patterns vary as a function of distance from the focal plane.

Figure 1 shows examples of numerical simulations of Fresnel diffraction of 100 μm diameter spherical particles seen by the PMS 2D-C probe as a function of distance ($Z_d = r^2/\lambda$) from the focal plane. The simulation on the left shows the diffraction pattern with infinite size resolution and on the right with 25 μm pixels. The numerical simulations show that the 100 μm particles are oversized as Z_d increases until about $Z_d = 8$ where they are missed all together or severely undersized. The patterns in Figure 1 only take into account the pixel size and thresholding

inadequacies of the 2D-C probe and not latency in the electronics. Recent laboratory tests at the GKSS in Geesthacht, Germany by two of the authors (AVK and JWS) suggest that the number of particles with diameters $< 150 \mu\text{m}$ that are missed or undersized increases dramatically with particle velocity.

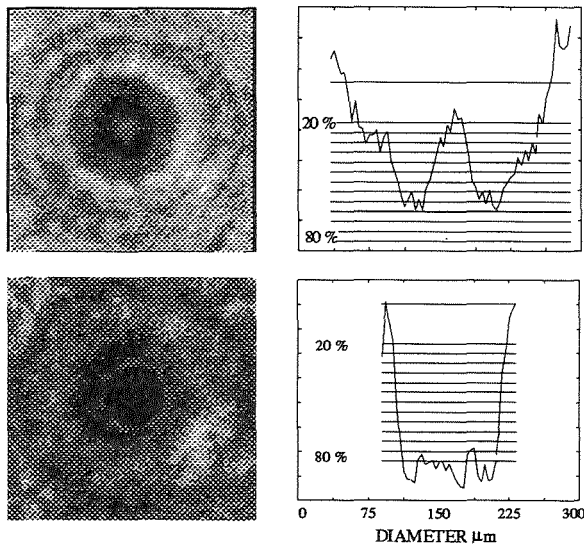


Figure 2. Example of (top) digital hologram of $100 \mu\text{m}$ bead taken at $Z_d=4$ and cross-section with shadow intensity labeled at 20% and 80%, and (bottom) image and shadow cross-section of bead after digital holographic processing.

3. DIGITAL HOLOGRAPHIC MEASUREMENTS

Lawson and Cormack (1995) describe the measurement technique of the digital holographic probe in detail. Here we give a brief overview of the instrument used in the CFDE. Interruption of the beam from an upstream laser diode triggers another laser diode which is pulsed for 30 ns to cast a Fresnel diffraction (shadow) pattern of the particle on a 512×512 solid state camera. The shadow pattern, actually an in-line (Gabor 1949) hologram, is computer-processed by numerically propagating the particle through the sample volume until the best in-focus image is obtained. An example of the numerical process is depicted in Figure 2. The first panel in the figure shows the 256 grey-level (8 bit) hologram and a cross section of shadow depth of a $100 \pm 1\sigma = 4.2 \mu\text{m}$ glass bead that is $Z=13.5 \text{ mm}$ ($Z_d=4 \text{ } r^2/\lambda$) from the focal plane. Casting the Fresnel equation in terms of Fourier transforms, the image was propagated through the sample volume in 0.5 mm steps until the best in-focus image was found. The second panel in Figure 2 shows the result of propagating the image and the cross section of the resulting shadow. The processed size of the drop, $103 \mu\text{m}$, is determined by thresholding the propagated image at the 65% (of full shadow) level.¹

The holographic sizing technique is compute intensive and requires some operator interaction to select and process the holograms. In order to increase processing speed, an alternative processing technique was developed which uses a software neural net to size spherical particles. A cross-section of the hologram with shadow widths at thirteen thresholds ranging from 20 \rightarrow 80% of shadow depth is feed into the neural net algorithm. The neural net was first trained using polystyrene beads and water drops generated by a TSI 3450 drop generator and then tested on another data set.

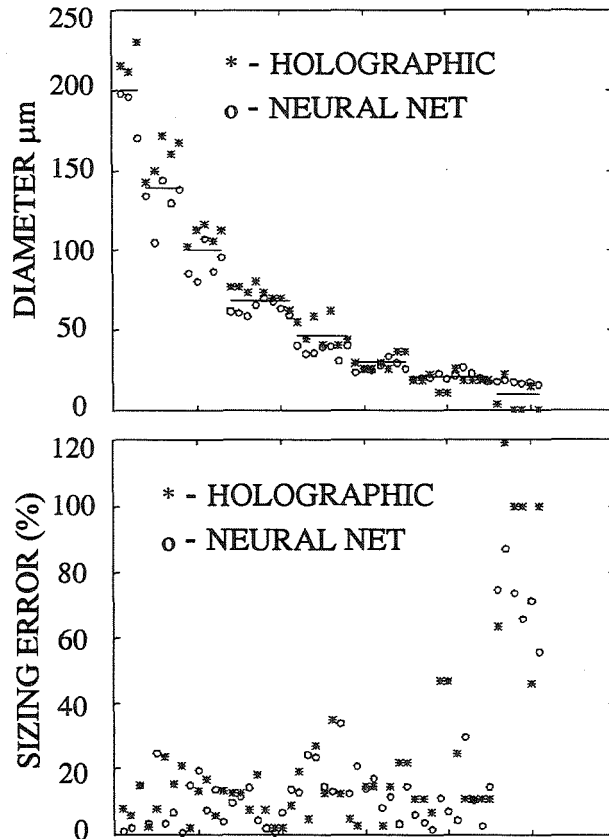


Figure 3. Top graph shows results of holographic (*) and neural net (o) sizing measurements where solid horizontal lines represent (from left) 200, 139, 100, 68, 30, 20, 10 μm beads and 45 μm diameter drops. Bottom graph plots sizing error on the vertical axis versus particle diameters which register with the horizontal lines on the top graph.

Figure 3 shows laboratory measurements using both the holographic technique and the neural net algorithm for various diameter polystyrene beads and 45 μm water drops produced by the TSI device. The manufacturers' standard deviations in diameters of the actual size distributions of the beads and drops differs for different sizes, but is on the order of 4%. Both the holographic and neural net algorithms produced good results; the RMS sizing errors over the range of diameters from 30 \rightarrow 200 μm is 11%

the shadow at the 50% level), the bead is measured to be 125 μm in diameter, which is in good agreement with the theoretical simulation shown in Figure 1.

¹ By thresholding the original hologram (the top left image in Figure 2) in a way analogous to the processing done in the PMS 2D-C probe (i.e., sizing the particle by measuring the width of

for the neural net algorithm and 12% for the holographic technique. The RMS error increases for both techniques to about 35% at diameters $< 30 \mu\text{m}$. The neural net approach takes less computer time and facilitates data processing.

The holographic data from the CFDE were processed using a hybrid approach. Holograms where the drops were noisy or far out of focus (say, $Z_d > 20 r^2/\lambda$) were flagged and processed using the full holographic algorithm while the bulk of the drops were processed using the neural net algorithm. Periodic comparisons between the holographic and neural net techniques provided a quality check. The measurement of particle concentration using the holographic probe involves corrections for probe activity and dead time. These corrections are currently being refined.

4. MEASUREMENTS IN FREEZING DRIZZLE

The numerical simulations of Fresnel diffraction for discretized pixels shown in Figure 1 were used as a basis to develop a technique to statistically correct the PMS 2D-C measurements. The details of the technique are given in Korolev et al. (1996). Figure 4 shows the theoretical results of the Korolev statistical corrections as a function of particle size, without the effects of particle speed, mentioned above, and instrument noise.

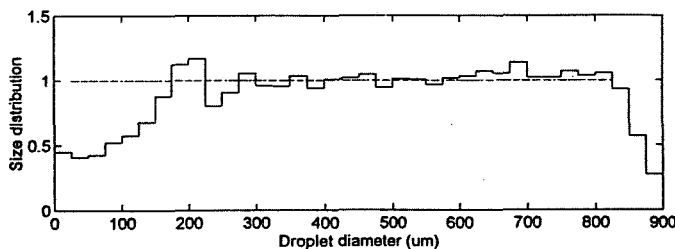


Figure 4. Theoretical results using the Korolev statistical correction scheme for the 2D-C probe. Size distribution on the vertical axis is the normalized number concentration of drops versus drop diameter. Dashed line is actual concentration.

Simultaneous measurements from the 2D-C and the new digital holographic probe were made in freezing drizzle during the CFDE. Both probes have a sample volume on the order of 4 l s^{-1} at 100 m s^{-1} . Figure 5 shows a comparison of drop size distributions from the two probes along with the Korolev theoretical correction. The measurements were made on 15 March 1995 near cloud top from 1943 - 1947 UTC in a region which appeared to form via the coalescence freezing drizzle process (Cober et al. 1995; Isaac et al. 1996). The 2D-C data suggest that drops with diameters out to $350 \mu\text{m}$ were observed, while the holographic probe measured drops only as large as $225 \mu\text{m}$. The median volume diameter (MVD), a quantity commonly used in icing studies, computed from the PMS size distribution is $136 \mu\text{m}$ while the MVD computed from the holographic measurements is $118 \mu\text{m}$. The large

“tail” of the drop size distribution is important for computing icing severity (Politovich 1989, 1996).

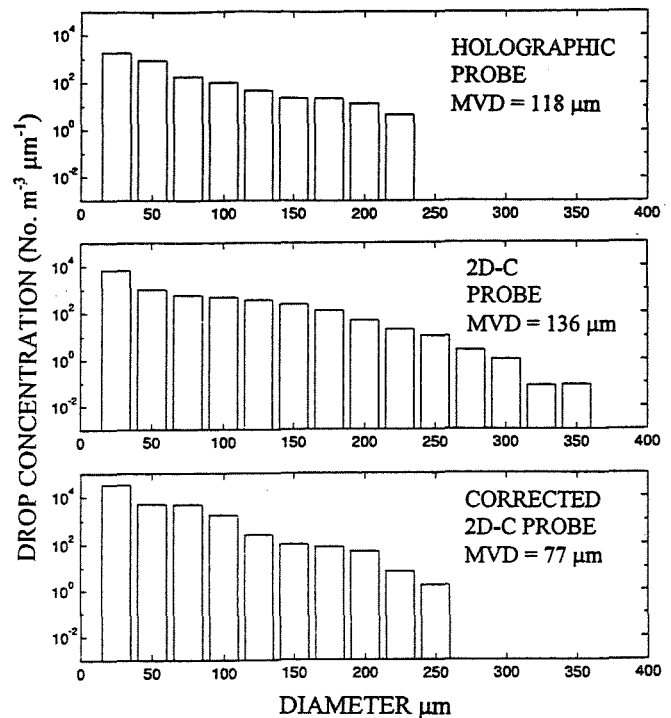


Figure 5. Comparison digital holographic, uncorrected and corrected 2D-C measurements collected in freezing drizzle from 1943-1947 UTC on 15 March 1995.

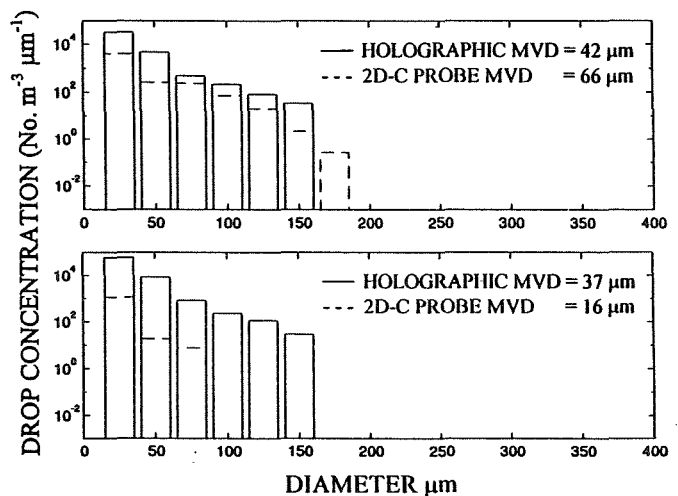


Figure 6. Comparison of 2D-C and digital holographic measurements collected in freezing drizzle from (top) 1939-1941 UTC and (bottom) 1938-1939 UTC on 15 March 1995.

The apparent oversizing in the $150 \rightarrow 350 \mu\text{m}$ range by the 2D-C is in general agreement with the Korolev theoretical correction, also shown in Figure 5. The agreement in the overall shape of the holographic and corrected 2D-C distributions is very good. The large (artificial) tail seen in the uncorrected 2D-C measurements is shifted to smaller sizes by the correction scheme. The MVD has been reduced from 136 to $77 \mu\text{m}$, which is $41 \mu\text{m}$ less than the holographic measurements. This is

mostly due to the shifting of all of the particles to smaller size bins, which may not be applicable at aircraft speeds.

As shown in Figure 4, the 2D-C is predicted to significantly undercount particles $<150\text{ }\mu\text{m}$, even without airspeed effects. Preliminary results of laboratory tests with a spinning disk rotating at aircraft speeds at the GKSS suggest that a substantial percentage of particles are undersized and missed all together in the $50 \rightarrow 150\text{ }\mu\text{m}$ size range. Figure 6 shows measurements taken in freezing drizzle on 15 March from 1938-1939 and 1939-1941 UTC. The MVD determined from the holographic probe is about $40\text{ }\mu\text{m}$ in both time periods, smaller than for 1943-1947. The size distributions measured by the 2D-C in Figure 6 are grossly different than the holographic measurements. These data suggest that when the (actual) MVD is on the order of $40\text{ }\mu\text{m}$, counting and sizing errors due to airspeed effects may render the 2D-C measurements statistically uncorrectable. More theoretical, laboratory and flight data are needed to verify this suggestion.

5. OBSERVATIONS OF ICE CRYSTALS

The cover of this volume shows examples of in-focus images of ice crystals observed during the CFDE. The $3.7\text{ }\mu\text{m}$ pixel size of the digital holographic probe provides excellent reproduction of in-focus ice crystals, showing growth habits and the effects of riming on the crystals. For example, a hex-plate center can be seen inside of a dendrite and frozen drops can be seen on some of the needles on the cover. Two of the needles observed at -6°C showed split ends typical of needles observed in melting conditions on the ground by Knight (1979). It is difficult to explain how melting could have occurred in these clouds at -6°C ; however, the crystals may have sublimated after being exposed to a region which was subsaturated with respect to ice.

6. DISCUSSION

Numerical simulations, laboratory and flight data strongly suggest that the PMS 2D-C probe can create an artificial "tail" in the drop size distribution of freezing drizzle. The new digital holographic probe does not create the artificial tail in the drop size distribution. Theoretical corrections applied to the 2D-C data can statistically correct for the artificial tail in the $150 \rightarrow 350\text{ }\mu\text{m}$ region; however, due to effects of airspeed and noisy data,

corrections to 2D-C measurements in the $25 \rightarrow 150\text{ }\mu\text{m}$ do not appear to be straightforward at this time.

Acknowledgments. This work was partially supported by NSF Grant No. DMI9322818, NASA Contract No. NAS1-19591 and funding from Transport Canada.

7. REFERENCES

- Ashenden, R., W. Lindberg, and J. Marwitz, 1996: Two-dimensional NACA 23012 airfoil performance degradation by super cooled cloud, drizzle, and rain drop icing. AIAA 96-0870. Presented at the 34th Aerospace Sciences Meeting and Exhibit, 15-18 Jan., 1996, Reno, Nevada.
- Cober, S. G., G. A. Isaac, and J. W. Strapp, 1995: Aircraft icing measurements in east coast winter storms. *J. Appl. Meteor.*, **34**, 88-100.
- Cooper, W.A., W.R. Sand, M.K. Politovich, and D.L. Veal, 1984: Effects of icing on performance of a research airplane. *J. Aircraft*, **21**, 708-715.
- Gabor, D., 1949: Microscopy by reconstructed wave-fronts. *Proc. Roy. Soc.*, **A197**, 454-487.
- Isaac, G. A., A. Korolev, J. W. Strapp, S. G. Cober, A. Tremblay, and R. A. Stuart, 1996: Freezing drizzle formation mechanisms. 12th International Conference on Clouds and Precipitation, 19-23 Aug., 1996, Zurich, Switzerland.
- Knight, C.A., 1979: Observations of the Morphology of Melting Snow. *J. Atmos. Sci.*, **36**, 1123-1130.
- Knollenberg, R. G., 1981. Techniques for probing cloud microstructure. In: Clouds, Their Formation Optical Properties and Effects. Eds: P. V. Hobbs and A. Deepak. Academic Press, New York. 15-92.
- Korolev, A. V., S. V. Kuznetsov, Y. E. Makarov, and V. S. Novikov, 1991: Evaluation of measurements of particle size and sample area from optical array probes. *J. Atmos. Oceanic Technol.*, **8**, 514-522.
- Korolev, A. V., J. W. Strapp, and G. A. Isaac, 1996: To be presented at the FAA International Conference on Aircraft Inflight Icing, 6-8 May, 1996, Springfield, Virginia.
- Lawson, R. P., 1995: Digital holographic measurements of cloud particles. Reprint from: AMS Conference on Cloud Physics, 15-20 Jan., 1995, Dallas, Texas.
- Lawson, R. P. and R. H. Cormack, 1995: Theoretical design and preliminary tests of two new particle spectrometers for cloud microphysics research. *Atmos. Res.*, **35**, 315-348.
- Politovich, M.K., 1989: Aircraft icing caused by large supercooled droplets. *J. Appl. Meteor.*, **28**, 856-868.
- Politovich, M.K., 1996: The effect of icing on a research aircraft and evaluation of severity indices. *J. Aircraft*, in press.
- Reuter, A. and S. Bakan, 1996: Improvements of cloud particle sizing with a 2D-grey probe. Submitted to: *J. Atmos. Oceanic Technol.*

A NEW INSTRUMENT FOR THE MEASUREMENT OF CLOUD DROPS

Thomas Hauf

Institut für Physik der Atmosphäre, DLR Oberpfaffenhofen, Germany

1. INTRODUCTION

There is a great need for small, light-weighted, and easy-to-handle instruments with sufficient accuracy for the airborne analysis of cloud drop size. Here a new system based on hot-film technique is presented, the Hf-probe, which tries to meet these requirements.

2. OPERATIONAL PRINCIPLE

The Hf-probe measures continuously the size of water drops in the range of 1 - 100 μm diameter and at 50 - 120 m/s relative flow speed. The system consists of (Fig.1): (i) the hotfilm probe of approximately 5 cm length with an heated area of 4 mm^2 ; (ii) a constant-temperature-anemometer bridge which keeps the hotfilm at a temperature of app. 120 $^{\circ}\text{C}$; (iii) data acquisition with 1 Mhz sampling rate; (iv) data processing with a special algorithm, (v) data display and storage.

The Hf-probe analyzes the signal of individual drops impinging on the hotfilm. It determines the electrical energy which is necessary to heat the drops to the boiling temperature and to evaporate them. On the base of a simple energy budget, the drop size is derived. No calibration is required and no further assumptions are made. Drop spectra can be calculated for any given time interval and displayed.

3. MEASUREMENTS

We generate in a wind tunnel water drops with a vibrating orifice and analyze the size spectra with the Hf-probe and the conventional FSSP and OAP probes. Figure 2 shows that the Hf-probe is able to detect drops in the size range of 3 - 100 μm . The expected maximum is at 43 μm and is reproduced remarkably well by both OAP and Hf-probe. The evaluation algorithm based on the energy budget yields a quite satisfying agreement between both systems.

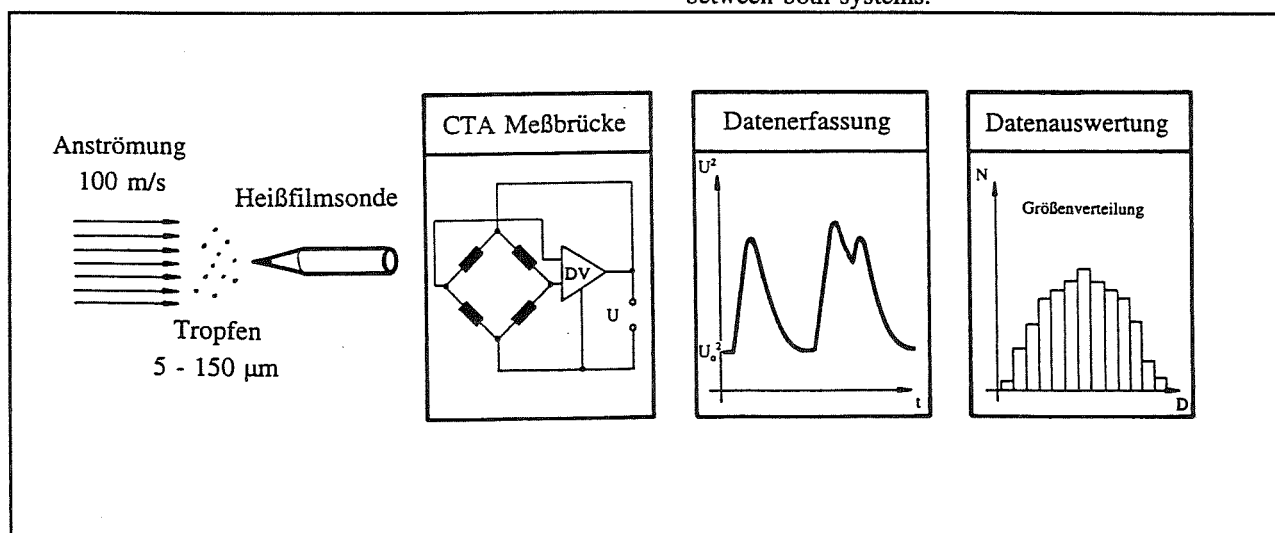


Fig. 1: Principal sketch. From left: Water drops suspended in an air stream impinge onto the hotfilm probe which is kept at a constant temperature by a CTA bridge. The signal is analyzed and the drop size distribution determined.

Detailed studies showed, however, that with increasing drop size a folding effect towards smaller drops becomes significant. The liquid water content derived from the spectra is, therefore, underestimated. Aircraft measurements in cumulus clouds revealed that the Hf-

probe gives about 40% of the LWC measured with a Johnson-Williams probe. This percentage is significant, but of the same order as what is reported for the FSSP and OAP probes. The in situ measurements in natural clouds showed a drop size spectra in the expected range

of 1 - 20 μm with a maximum at 11 μm . The smallest detectable drop diameter in natural clouds is 1 μm . In the wind tunnel due to the increased turbulence level its value is slightly higher. The maximum detectable drop is determined by the hotfilm area and the decay time of an individual drop signal. Its value ranges between 100 - 150 μm . The Hf-probe is further limited by the maximum allowable drop frequency. If too many drops hit the sensor simultaneously, their individual signals superimpose and cannot be resolved unambiguously. Thus the error increases with increasing drop concentration.

4. SUMMARY

It was shown that the new developed Hf-probe is capable of measuring the drop size of water drops suspended in an air flow in the size range 1 - 100 μm . It can be used either in a wind tunnel or for airborne cloud physics research. The Hf-probe can be mounted easily on an airplane.

Flow distortion is negligible. In principle the system allows an autonomous operation. It may be used whenever the use of the more complex optical devices such as FSSP or OAP cannot be afforded due to financial, weight or operational constraints, and, if the accuracy requirements are not too high. The wind tunnel intercomparisons with the optical probes give satisfying and encouraging results. A complete error analysis can be presented when in-cloud intercomparisons with FSSP and OAP have been performed. So far, data processing is only possible after a flight. Currently a new version is under development which allows an on-line evaluation. Weight and size of the complete system will also be minimized.

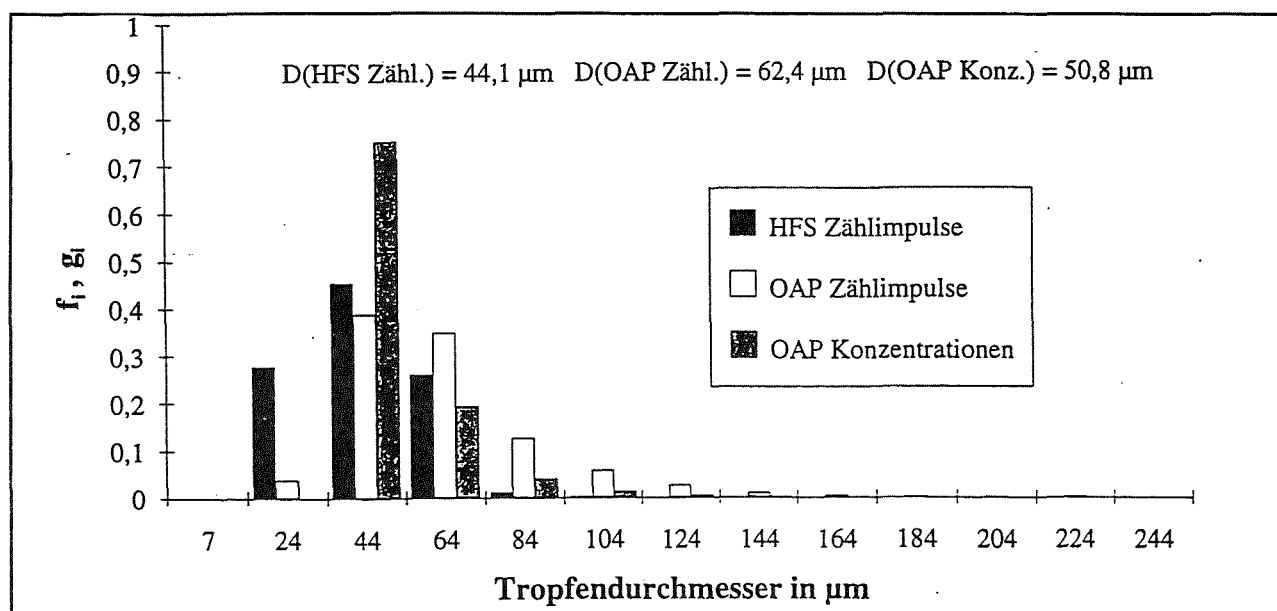


Fig. 2: Comparison of measured drop spectra. Normalized counts versus drop diameter. Hf-probe: closed column, OAP counts: open columns, OAP after correction: grey columns. $U=100$ m/s. Wind tunnel measurements.

CAO AIRCRAFT INSTRUMENTATION FOR CLOUD PHYSICS

Anatoly N. Nevzorov

Central Aerological Observatory
Dolgoprudny 141700, Russia

1. INTRODUCTION

Currently used widespread aircraft instrumentation for cloud microphysical studies, being highly perfect technically, unfortunately leaves uninvolved most important measurements applying to specifically ice and mixed, or ice-containing clouds (ICC). The major of these problems are:

- (i) High-sensitive identification of cloud phase composition;
- (ii) Measurement of total and separately ice and liquid water content over wide temperature range;
- (iii) Determination of individual concentrations and size spectra of liquid and ice particles;
- (iv) Direct measurement of extinction in ICC and determination of its phase components for the problems of cloud optics and radiation, etc.

Definite possibilities in some of listed measurements might be presented by impact and holographic techniques; however, the former is long since been abandoned and the latter is still out of wide use, both because of known inconveniences of their operation and data processing.

An aircraft cloud microphysical instrumental complex (ACMC) to be briefly described here is nowadays actually unique in providing an acceptable means for deeper penetration to the problem of experimental studies upon ICC microphysics. The instruments incorporated to the ACMC have been originally developed by the author and used for many years in Central Aerological Observatory (CAO). In the last years, the instrumentation

is not in routine use because of unfavourable current state of flight explorations in Russia.

2. GENERAL

The ACMC performs the following measurements:

- liquid and total (liquid plus ice) water content with the sensitivity of around 0.003 g m^{-3} ;
- cloud transparency (extinction);
- concentration, size spectra and phase state of particles of $>20 \mu\text{m}$ in size;
- concentration and size spectra of large ($>0.2 \text{ mm}$) particles.

The set of parameters to measure allows to determine by calculation some other cloud microphysical characteristics not embraced by the direct measurements, as well as to intercompare some measurements in ICC.

In creating the meters, we succeeded in avoiding those operating principles which require only experimental calibration, particularly under high-speed conditions. The devices except a light scattering particle spectrometer are based on "absolute" measurement methods admitting physically justified, wholly calculable calibration. When possible, in-flight comparisons were made to verify the reliability of measurements.

The in-flow sensor probes have been originally designed for leak-proof through-hole mounting on the fuselage side walls or on window blank flanges, which has simplified their design, electrical connections, and in

many ways in-flight servicing. Other design versions are in principle practicable. The probes are effectively protected against adverse effects of moistening, icing, and sweating of optics.

All the instruments have continuous outputs of analog or pulse-to-count types. The power supply required is 25 to 30 V DC.

3. CONSTITUENT INSTRUMENTS

3.1 Cloud water content measurement

Both liquid and total water content (LWC and TWC, respectively) meters are based on the same constant-temperature "hot wire" principle (Nevzorov, 1980) and differ only in sensor configuration (Nevzorov and Shugaev, 1992a; Korolev *et al.*, 1996). Both hot collectors are made as close single-layer wire windings. Their phase discriminating capability results from the difference in behaviour of ice particles impacting with the hollow-shaped collector of the TWC probe against the convex-surface LWC collector, while liquid droplets equally evaporate on both collectors.

Each probe also involves auxiliary reference ("dry") wire sensor to perform, using special circuitry, a continuous precise removal of the dry air heat loss term from the output signal. This results in unique sensitivity of the probes estimated as $<0.003 \text{ g m}^{-3}$ in horizontal flight. The upper measurement limit is about 4 g m^{-3} for LWC and 1 g m^{-3} (linear range) for TWC probe.

More detail description of the probes as well as of results of their recent tests is presented by Korolev *et al.* (1996).

3.2 Cloud extinction measurement

The aircraft cloud transparency meter (CTM) (Nevzorov and Shugaev, 1992a, 1992b) performs direct measurement of attenuation T of visible

light beam passing through the designed distance L in the medium to investigate, whence the extinction coefficient EC is determined from the Bouguer's law:

$$EC = (1/L) \log (1/T).$$

Unlike light scattering technique, this one needs no experimental calibration in terms of EC irrespective of cloud phase composition, though has more limited measurement range. Some dependence of measurements on sizes of particles contributing EC remains here due to forward light scattering into the receiving aperture, which requires a correction of metered EC up to twice for precipitation.

The device consists of optical unit for both projection and reception of the sounding light beam, three-mirror prism 180° reflector, and remote control unit.

The reflector is mounted on a plane in a unit affording a distance of 4 - 10 m from the optical unit, rigid enough position, and mechanical and thermal protection against moistening. The sounding light beam reflected exactly back returns to optical unit so that the optical base L is twice the distance apart the units. Aboard the IL-18 airplane, the optical unit was installed inside just ahead a light port, and the reflector on the end of the stabilizer 8 m distant.

An electronic circuitry uses an auxiliary reference flux formed inside the optical unit to produce the output precisely proportional to T value.

The E determination range corresponding to errors of $\leq 25\%$ is about from 1 km^{-1} to 200 km^{-1} depending on the optical base. The distortions caused by light scattering as above are analysable (Kosarev *et al.*, 1976) and can be corrected for by the use of combined measurement of LWC and EC in water clouds or particle size spectra in the general case (Nevzorov, 1993).

3.3 Particle size spectrometry

For the measurements of particle concentration and size spectra in clouds and precipitation, two instruments based on distinct photoelectric techniques are employed in the APMC. The analog conversion techniques used allow to arrange size count intervals so that they were as broadened as particle count falls with their sizes increasing. The use of halogen lamps with a collimating optics proves itself in their longevity, relative simplicity and compactness of probe design, and finally in measurement accuracy.

The large particle spectrometer (LPS) was in routine use in CAO since 60's (Borovikov *et al.*, 1968). In this probe, a collimated light passes sequentially two identical narrow (0.12 mm wide) slits and then is focused on a photodetector. The sample volume of 25 mm x 28 mm x 0.12 mm is formed by and spaced between the slits. This simplest optics admits also simplest calculation of the relation between the particle size to determine and a response pulse height if the size exceeds the slit width. The size measurement range is from 0.2 to 6 mm.

The reliability of drop measurement have been verified experimentally. The technique involves an automatic stabilization of the response characteristics. Pulse shapes allow to distinguish between particle phases. The long-standing operating experience has shown high reliability of the probe under any occurring field conditions.

Other instrument, particle phase/size analyzer (PPSA) (Nevzorov and Shugaev, 1992a, 1992b), operates as a light scattering detector of individual particles at 90° angle and integrates particle spectrometry with phase determination as described in the next section. As a spectrometer, it has different responses against drop and crystal sizes. The drop size response is established from experi-

mental calibration with monodisperse water drops. It has been shown by Kosarev *et al.* (1986) that the mean response of individual ice crystal is definitely related to its mean cross-section diameter irrespectively of its shape. The response characteristics in terms of so defined crystal size, derived in this paper, is used in our measurement practice.

The lower limits of size measurement ranges are 20 μm for ice crystals and 30 μm in diameter for water drops. The upper limits can be any reasonable, e. g. 200 μm and 300 μm , respectively. The sample volume is optically formed and has the dimensions of 4 mm x 4 mm (sampling area) x 1 mm, with a zone of falling-to-zero sensitivity of less than 20% of the sampling area.

3.4 Particle phase determination

The present version of the PPSA just described does not distinguish between crystals and drops in determining of their size spectra while such possibility conceptually exists. In the general case of mixed clouds, its output is an integral spectrum distorted with respect to both drop and crystal sizes because of the stated difference in their responses.

An additional means is applied in the probe for the objective detection of ice crystals in total particle population counted. For this purpose, the illuminating light is linearly polarized in the scatter plane and the cross-polarization detector is added to the receiving optics. The ice sensitivity of associated "crystal" counter is made the same as the lower spectrometric threshold, i. e. 20 μm in the given case. However, this counter proves to be sensitive to drops larger than 80 - 100 μm . To eliminate the drop term, the counter readings are merely subtracted from by the spectrometer count of drops >80 μm plus accordingly crystals >53 μm , thus providing the concentration of only crystals ranging between 20 μm and about 50 μm .

Numerous field measurements with the PPSA revealed that the referred spectral interval contains, as a rule, the overwhelming majority of cloud crystals of $>20 \mu\text{m}$ in size (Kosarev *et al.*, 1984, 1986). Consequently, the difference between the total measured concentration and the gained crystal concentration yields an approximation for the concentration of drops exceeding $30 \mu\text{m}$ in accordance with the PPSA calibration. Beyond expectation, the concentrations of these drops turned out to be comparable with those of crystals in most ice-containing clouds, as exemplified by Nevzorov (1993).

The PPSA and LWC/TWC measurements well complement each other in determination of cloud phase composition as well as in extracting more information of the microstructure of mixed clouds (Nevzorov and Shugaev, 1992a, 1992b; Nevzorov, 1992, 1993).

4. CONCLUSIONS

The instruments described above had active applications in diverse studies on cloud physics performed in Cloud Physics Laboratory, CAO. By now there are a number of published works devoted to statistics of various cloud microphysical parameters such as large particle and ice crystal concentration and size spectra, cloud extinction, water content, phase composition, etc. Radically new results have been obtained from the use of the instrumentation as a whole in physical studies of ice generation in supercooled clouds (Nevzorov, 1996) as well as of properties and nature of liquid phase in ice-containing clouds (Nevzorov, 1992, 1993).

Acknowledgements. The author is indebted to Prof. G. A. Isaac, Dr. J. W. Strapp and Dr. A. V. Korolev for recent organization and performing of careful tests of the cloud water con-

tent and extinction probes on the experimental base of AES, Canada.

REFERENCES

- Borovikov, A. M., I. P. Mazin, and A. N. Nevzorov, 1968: Large particles in clouds. *Int. Conf. on Cloud Phys., Toronto, Canada*, 356-363
- Korolev, A. V., J. W. Strapp, and A. N. Nevzorov, 1996: On the accuracy of Nevzorov airborne hot wire LWC/TWC probe. *Rep. pres. at this Conf.*
- Kosarev, A. L., A. N. Nevzorov, and V. F. Shugaev, 1984: On the microstructure and ice water content of high clouds. *9th Int. Cloud Phys. Conf., Tallinn, Estonia*, 1, 73-76
- , I. P. Mazin, A. N. Nevzorov, and V. F. Shugaev, 1976: Optical density of clouds. *Trudy CAO*, 124, 128 pp. (in Russian)
- , ----, ----, ----, 1986: Microstructure of cirrus clouds. *Some problems of cloud physics (collected papers)*, *Gidrometeoizdat, Leningrad*, 160-186 (in Russian)
- Nevzorov, A. N., 1980: Aircraft cloud water content meter. *VIII conf. int. sur la phys. des nuages, Clermont-Ferrand, France*, v. II, 701-703
- , 1992: Permanence, properties and nature of liquid phase in ice-containing clouds. *11th Int. Conf. on Clouds and Prec., Montreal, Canada*, 270-273
- , 1993: Studies into the physics of liquid phase in ice-containing clouds. *Russian Met. and Hydr.*, No 1, 47-59
- , and V. F. Shugaev, 1992a: Observation of the initial stage of ice phase evolution in supercooled clouds. *Soviet Met. and Hydr.*, No 1, 69-76
- , ----, 1992b: Experimental studies of the phase-disperse structure of stratiform clouds at negative temperatures. *Soviet Met. and Hydr.*, No 8, 41-51

IMPROVEMENT OF SIZE CORRECTION TECHNIQUE FOR PARTICLES WITH SIZES LESS THAN 100 μm IN DIAMETER FOR OAP-2D-GA2

H. Panskus and A. Reuter

Meteorological Institute, University of Hamburg, Germany; GKSS Research Institut, Geesthacht, Germany

1 Introduction

The determination of cloud droplet size distribution and concentration is essential for the study of precipitation growth and radiative properties of clouds. The two-dimensional (2D) optical array probes (OAP) from Particle Measuring Systems (PMS, Boulder, Colorado, USA) are airborne instruments for measuring cloud particles. The most advanced version is the 2D-Grey probe (OAP-2D-GA2) with a photodiode array of 64 elements and a zoom optics that enables a resolution of 10 to 20 microns. The instrument records two dimensional shadow images from the cloud particles yielding to information about the size and shape. Here we are only interested in the size determination of water droplets.

2 Principle of operation

We used the two-dimensional optical array probe with a zoom factor 20 thus a resolution of 10 microns along the photodiode array results. Between the probe tips the sampling area is given with 640 microns at maximum across the flight direction (Figure 1). Due to the maximum slice rate of 5 MHz resolutions of 10 to 20 microns in flight direction limits the true air speed to 50 to 100 m/s. The 2D-Grey probe enables the distinction between four shadow levels per photodiode element, according to thresholds at 100 (NONE), 75(MIN), 50(MID) and 25%(MAX) of the laser illumination intensity. The distinction is accomplished by three comparator steps that compare the actual array element illumination with the unshadowed value.

3 Development of a new size correction technique

For systematic investigation Reuter (1995) made laboratory measurements with a spinning glass disk. Korolev et al. (1991) argued that at

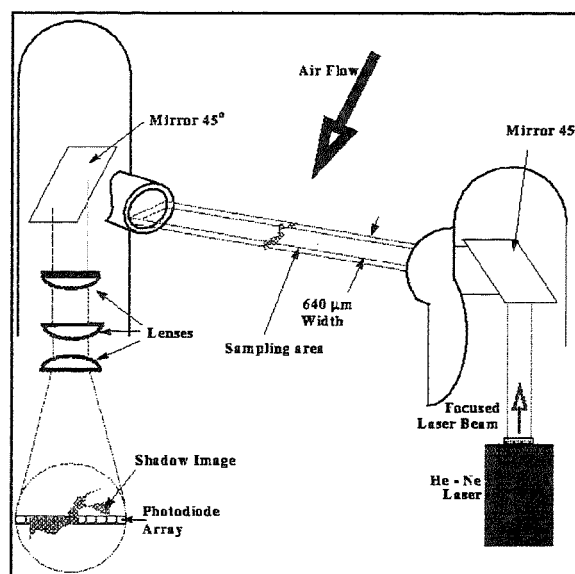


Figure 1: Schematic of the 2D-Grey probe distances larger than 10 droplet radii the shadow image of water spheres consists mostly of the diffraction pattern, which is identical to that of an opaque disk of equal radius. Using such a spinning glass disk with steamed up aluminium dots in various diameters the depth-of-field and the image diameter as a function of particle diameter was determined.

From measurements with the first OAPs the image diameter was found to be within 10% of the particle diameter for the entire depth-of-field when using a threshold of 50% of the undisturbed laser intensity for the 2D-C probe (Knollenberg, 1970). Knollenberg provided a formula for the depth-of-field

$$l_{\text{DOF}} = \frac{3}{2} \lambda d^2 \quad (\text{Eq. 1})$$

with d =particle diameter and λ =laser wavelength (632.8 nm). For the 2D-C and 2D-Grey probe the maximum depth-of-field is given by the distance between the probe tips and equals 61 mm. However for the 2D-Grey probe the situation is different. Generally, the image contains three different shadow levels and is in many cases also accompanied by refraction fringes. Due to the functional

principle only images of particles, passing through the focal plane, are focused exactly on the photodiode array. All other images are more or less blurred as the particle passes the optical plane but is out of focus. The most striking feature is the increase of the particle image diameter with distance from the focal plane, associated with a reduction of the number of completely shadowed (100%) pixels and an increase in barely shadowed (25%) image elements. At large distances from the focal plane even the shape of images does no longer resemble the spherical shape of the particle itself.

3.1 Measurements with the spinning glass disk

The variation of the image sizes with distance from the focal plane is representative for all sizes used and also for the other shadow levels. The **image diameter** increases to a maximum with an interruption at about half that distance. At this maximum position Reuter found that the image diameter is about 80% larger than the real diameter of the opaque disk, which is similar to the maximum increase in apparent size found by Korolev et al. (1991) for the 2D-C probe.

Reuter pointed out that the variability of the three shadow levels with distance from the focal plane turns out to behave systematic for each test spot size. Especially the ratio q_{MIN} of the number of MIN (=50 - 75% illumination intensity of unshadowed) pixels to the total number of shadowed pixels, increases systematically with distance from the focal plane. As this increase is different for different spot sizes he used the quantity q_{MIN} to characterize the true particle size (Figure 2).

Reuter (1995) showed that in a good approximation, the overall relation between image diameter and q_{MIN} can be considered linear throughout the observed parameter range (Figure 2). This results in a simple relation for a reliable estimation of true particle diameter from apparent diameter d_{25} and the fraction q_{MIN} of pixels at the lowest shadow level

$$d = \frac{d_{25} - D - F \cdot q_{\text{MIN}}}{E \cdot q_{\text{MIN}} + C} \quad (\text{Eq. 2})$$

The parameters are derived from the measurements to $C=0.9616$, $D=-10.3453\text{ mm}$, $E=1.4436$ and $F=7.0355\text{ mm}$.

Reuter argued that with this image size definition (Eq. 2) it is possible to define a unique depth-of-field. He used $q_{\text{MIN}}=0.98$ as a criteria for rea-

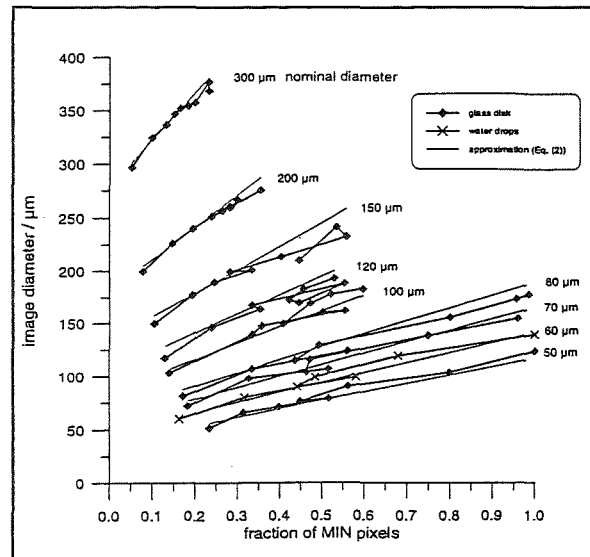


Figure 2: Apparent particle image diameter d_{25} versus fraction of pixels at the lowest shadow level q_{MIN} (Reuter, 1995)

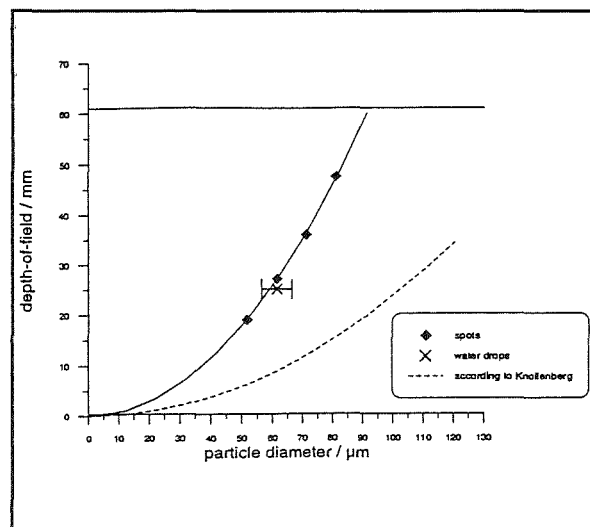


Figure 3: Depth-of-field of the 2D-Grey probe versus nominal spot size as showed by Reuter (1995)

ching the depth-of-field. That means a droplet is in the depth-of-field when only 2% of the image pixels are at the MID shadow level, while 98% are at the MIN level. Figure 3 shows the values found by this definition. Obvious is that the depth-of-field is a factor 3.02 times larger than that given by Knollengbergs formula (Eq. 1). This intriguing factor could not yet be explained by theoretical reasoning.

4 Further investigations

Reuter used a spinning glass disk with spot sizes of $50\mu\text{m}$ to $500\mu\text{m}$. For further investigation we used a „little“ glass disk with spot sizes of $10\mu\text{m}$ to $100\mu\text{m}$. For these measurements we found the same behaviour in the imaging as for the big-

ger spot sizes. Both measurements, that by Reuter and the actual one, are made at corresponding true air speeds of 20m/s to 25m/s. It is necessary to made supplementary measurements at realistic true air speeds in the order of 50m/s to 100m/s. We suppose that there are effects due to dead and/or reset times of the electronics. The effect is that especially for little drops the highest shadow level can't be reached any more even if the droplet crosses through the focal plane. The results of these measurements and further investigation of the electronics will be presented in our poster.

5 References

- Albers, F., 1989: Flugzeugmessungen der Eiskristallkonzentration und -größenverteilung mittels optisch abbildender Sonden in Cirrus-Wolken. Thesis, Univ. Köln
- Albrecht, B.A., 1989: Aerosols, cloud microphysics, and fractional cloudiness. *Science*, 245, 1227-1230
- Baumgardner, D., 1987: Corrections for the response times of particle measuring probes. In: *Proceedings of the Sixth Symposium on Meteorological Observations and Instrumentation*. AMS, Jan. 12-16, 1987, New Orleans, LA, 148-151
- Knollenberg, R. G., 1970: The Optical Array: An Alternative to Scattering or Extinction for Airborne Particle Size Determination. *J. Appl. Meteor.*, 9, 86-103
- Korolev, A. V., S. V. Kuznetsov, Yu E. Makarov and V. S. Novikov, 1991: Evaluation of Measurements of Particle Size and Sample Area from Optical Array Probes. *J. Atmos. Oceanic Technol.*, 8, 514-522
- Reuter, A., S. Bakan, 1995: Improvements of cloud particle sizing with a 2D-Grey probe. MPIfM Report No. 182, Max-Planck-Institut für Meteorologie, Hamburg.

FAST RESPONSE TURBULENCE MEASUREMENTS FROM AN INSTRUMENTED LIGHT AIRCRAFT

Robert Wood, Ian M Stromberg and Peter R Jonas

Physics Dept., UMIST, Manchester M60 1QD, UK

1. INTRODUCTION

A system has been developed for use on a light aircraft for the measurement of the turbulent wind vector components which does not rely on the use of either an inertial navigation system (INS) or doppler radar. The system described here uses a 5-hole probe to measure the wind vector relative to the aircraft. A three-axis accelerometer system is used to determine the aircraft velocity. Drift in the accelerometer signals are corrected in post-processing by combination with long term position references (pressure altitude and GPS) in a third order feedback system. Under conditions of straight and level flight the estimated rms errors are 0.3 ms^{-1} for the vertical wind component and 2 ms^{-1} for the horizontal components.

2. INSTRUMENTATION

2.1 Aircraft

The aircraft used is a propeller-driven single engine Cessna-182. The typical cruise speed is 55 ms^{-1} and the aircraft has a maximum ceiling of 4000 m, with an endurance of 5 hours.

2.2 Five-hole probe/accelerometer system

A 5-hole probe (see Fig. 1) is used to measure accurately the wind vector relative to the aircraft. This particular instrument is an in-house design with a pressure sensing boom similar to the Rosemount Type AJ 858 probe. The boom tip is hemispherical and 30mm in diameter with five pressure ports on its surface to measure the angles of attack and sideslip and the pitot pressure.

The static pressure port is located coaxially on the probe boom 280 mm to the rear of the probe tip and consists of a ring of ten 1.2 mm diameter holes which all connect to the static pressure transducer. This design of static pressure port is less affected by changes in airflow angle than conventional plate type ports.

The central port on the boom tip is used to measure the pitot-static pressure difference using a differential pressure transducer. The upper and lower ports are connected across another differential transducer to measure the attack angle. Similarly, the left and right ports measure the sideslip angle. All the pressure transducers are temperature compensated and the signals are amplified and digitised with 12 bit precision before being sampled by the aircraft's data logging system at a rate of 20 s^{-1} . The five-hole probe tip is located 960 mm ahead of the starboard wing of the aircraft

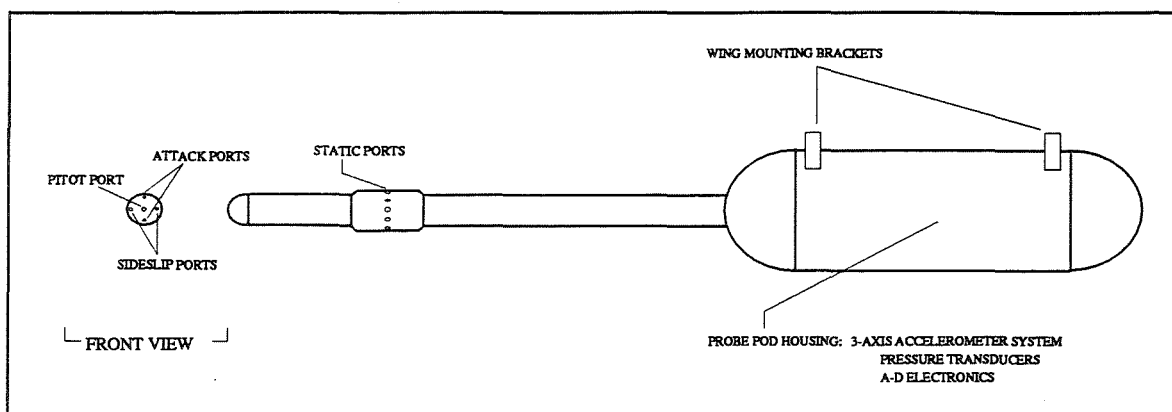


Figure 1: Schematic diagram of the five-hole probe on the UMIST Cessna-182.

immediately outboard of the wing strut. The pressure transducers were calibrated to 0.1 hPa. In-flight calibration of the attack and sideslip ports was necessary since distortion of the airflow around the probe and wing cannot be deduced from ground based measurements alone. A three-axis accelerometer system is housed in the main body of the probe to measure the three components of the aircraft acceleration at a rate of 20s^{-1} . Calibration of the accelerometers was achieved with an inclinometer system.

2.3 Pitch, roll and heading gyroscopes

Aircraft pitch and roll angles are measured using a King KVG 350 vertical gyroscope and are logged at 20s^{-1} . Tests indicate that the random error in the pitch and roll measurements is less than 0.02° , with a systematic offset of less than 0.1° . The systematic error introduces a maximum possible offset in the mean vertical wind of around 0.1 ms^{-1} . The gyroscope is mounted close to the centre of mass of the aircraft. A King KCS55A slaved gyro compass system is used to obtain compass heading information also logged at 20s^{-1} .

2.4 Navigation instrumentation

A Garmin GPS100 system provides latitude, longitude, track and ground speed information and is logged at 1 s^{-1} . Accuracy is typically 30 m. The GPS position information is used to correct for accelerometer drift in the computation of the horizontal winds.

2.5 Cloud physics instrumentation

Air temperature is measured using a Rosemount total temperature probe type 102 is mounted on the aircraft wing. The static air temperature is derived using a recovery factor of 0.91 determined from flight tests to compensate for true air speed. Dewpoint is measured using a Mitchell Type 2000 cooled-mirror hygrometer. All temperatures are currently logged at 1 s^{-1} . The aircraft has provision to house droplet and particle measuring devices under the port which provides a mounting for an FSSP or similar probe. Additional space inside the aircraft is available to house aerosol and trace gas instrumentation.

3. MEASUREMENT OF WIND COMPONENTS

The derived wind velocity \underline{V} is given by

$$\underline{V} = \underline{V}_p + \underline{V}_a$$

where \underline{V}_p is the aircraft velocity relative to the earth and \underline{V}_a the velocity of the air relative to the

aircraft (the airflow vector). Because the aircraft has freedom to rotate in pitch, roll and yaw a set of transformations is required to transform the wind velocity into the earth frame. See Axford (1968) for the full derivation of these equations. The simplified equations for the wind vector components are:

$$u = -V_a \sin(\varphi + \beta) + u_p$$

$$v = -V_a \cos(\varphi + \beta) + v_p$$

$$w = -V_a \cos(\theta - \alpha) + w_p$$

where u, v, w are the eastward, northward and vertical (w positive upwards) components of \underline{V} as measured in a local earth frame, u_p, v_p, w_p are the northward, eastward and vertical components of \underline{V}_p , θ and φ are the pitch and heading angles, α and β are the attack and sideslip angles, and V_a is the true air speed (the magnitude of the airflow vector).

The aircraft velocity is determined by using a combination of accelerometers and pitch^o and roll gyroscopes. Integration of the aircraft acceleration components gives the aircraft velocity. However, long-term drift in the accelerometer signals would cause errors to build up in the integrated aircraft velocity. This is avoided by combining the accelerations with a long term stable reference in a third-order feedback loop to compute accurately the aircraft velocity (Blanchard, 1971). The static pressure, which is stable but noisy in the short term is used as the vertical reference signal. Similarly, the GPS horizontal position information is used for the reference for the horizontal components of the aircraft velocity.

4. FLIGHT TESTS

4.1 Pitch oscillation manoeuvre

Flight manoeuvres are essential in the evaluation of an airborne wind-measuring platform. From flight manoeuvres documented by Lenschow (1986) and more recently Bogel and Baumann (1991), errors in many of the crucial parameters required to determine wind components can be identified, and corrected. These include constant offset errors, and response time (phase) errors which are difficult, if not impossible, to evaluate using ground-based tests. We have performed flight manoeuvres using the UMIST aircraft as documented below. From the results, modifications both to software and hardware have been made, with the final conclusion being that the absolute error in the vertical wind is less than 0.3 ms^{-1} .

Pitching oscillation tests described by Lenschow

(1986) were implemented to determine errors in some of the key parameters necessary for computation of vertical wind. The tests are carried out by the pilot inducing a sinusoidal pitching oscillation with an amplitude of between 4 and 8 degrees. We decided to perform the tests at two pitching frequencies: low frequency oscillations at $0.03\text{--}0.05\text{ s}^{-1}$; high frequency oscillations at $0.5\text{--}1\text{ s}^{-1}$. The modulation of the pitch angle modulates V_a , w_p , and to a smaller extent α , and any modulation in derived vertical wind is assumed to arise from the manoeuvre itself rather than from atmospheric motion, providing the test is carried out in smooth air. A considerable number of tests were performed, and the results from a high frequency test are shown in figure 2. The rms of w is over an order of magnitude less than the rms of w_p , demonstrating that to a great extent the effects of the aircraft velocity are accounted for. From the small residual oscillation in the derived vertical wind we discovered that the gyroscope pitch signal consistently lags behind the pressure and accelerometer signals by 0.25 s. Similar oscillation tests were performed in roll and again a lag of 0.25 s in the roll signal was determined.

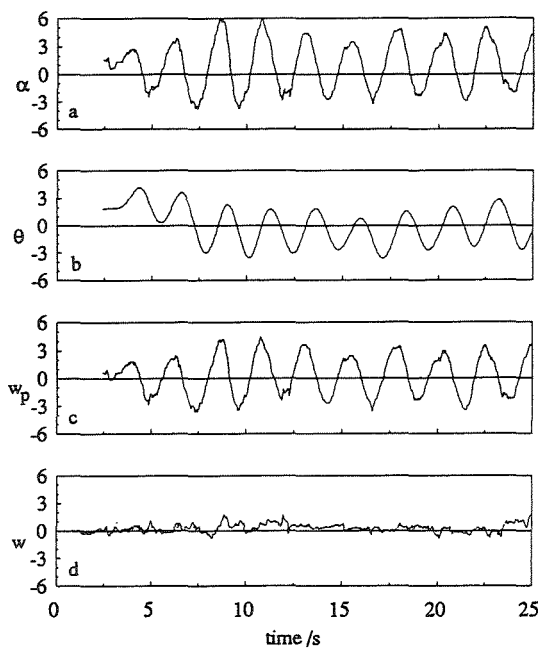


Figure 2: Time series of attack and pitch angles (units degrees), aircraft vertical speed and derived vertical wind (units ms^{-1}) during a high frequency pitch test.

4.2 Intercomparison runs with the M.R.F. C-130 aircraft

On 3rd June 1993, the Meteorological Office C-130 was available to make intercomparison runs in order to further test the validity of the Cessna-182 wind measuring system. Because of the difference in normal operating speeds between the two aircraft a side-by-side intercomparison (Nicholls et. al., 1983), was impossible. Instead, it was decided that runs of fixed track and altitude would be flown, with the Cessna

starting the runs at an earlier time than the C-130 so as to end the runs with the aircraft as close together as possible. GPS is used for horizontal position and to compute the distance of the aircraft along the fixed track. This allowed us to compare spatial series of vertical wind. The lateral separation of the aircraft tracks was less than 350m at all times on the runs, and the runs were flown in a well mixed boundary layer, with strong surface heating.

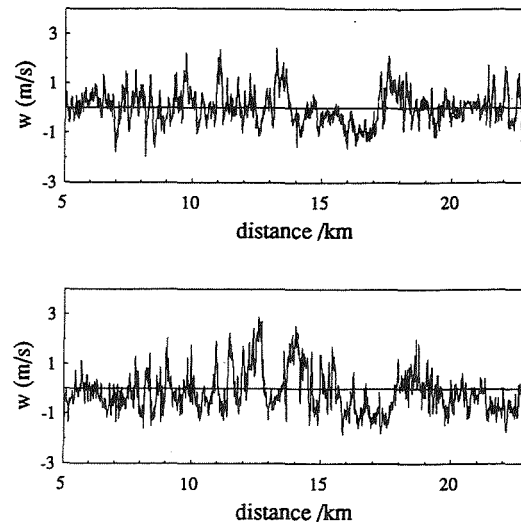


Figure 3: Spatial series of vertical velocity as measured by the Cessna (top) and C-130 (bottom).

Spatial series of w from one run (altitude:150m) is shown in Fig.3, and the respective power spectra in Fig. 4 (top), as a function of k the wavenumber. The spatial series show that many of the larger features are common to both the C-130 and the Cessna data, although there are inevitable differences due to the time difference in the sampling between the two aircraft on any run. Fig. 4 (bottom) shows the ratio of the C-130/Cessna power spectra. The power spectra show good agreement for wavenumbers up to around 0.05 m^{-1} . Deviations in the power spectra at higher wavenumbers are expected due to both the time and the spatial differences between the air velocity measurements from the two aircraft (the dissipation time scale for motion on the scale of 1 k was roughly 13 minutes). In addition, since the aircraft tracks were separated laterally by up to 350 metres, motions on this scale sampled by the Cessna may not have been sampled by the C-130. The C-130 power spectrum exhibits unexpected peaks at wavenumbers of 0.10 m^{-1} and 0.12 m^{-1} (Fig. 4), corresponding to frequencies of 10 Hz and 12 Hz respectively. The peaks are not present in the Cessna power spectra, and do not represent true atmospheric motions on these scales. One suggestion is that the peaks arise from resonances of the noseboom on the C-130, on the end of which are mounted the vanes for measurement of attack and sideslip angles.

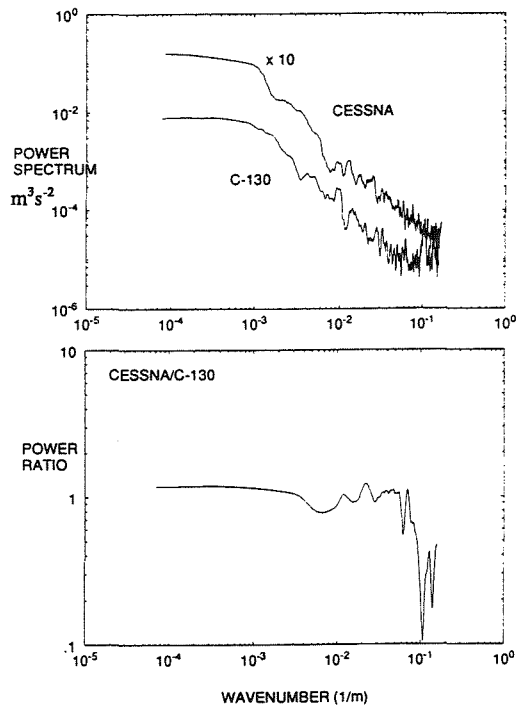


Figure 4: Power spectra (top) and ratio of spectra (bottom) from a Cessna/C-130 intercomparison run.

4.3 Reciprocal runs

To further check the accuracy of the vertical wind component reciprocal runs were flown. A straight and level run is flown and then the aircraft is turned through 180 degrees and a reciprocal leg is flown through the same air. The rms value of the vertical wind for both forward and reciprocal legs should be equal if the measurements are accurate. A total of 13 such runs of between 12 and 24 k were carried out on five flights. The values of σ_w measured on each leg are plotted against each other (Fig. 5). The results indicate that, assuming the conditions were homogeneous, the difference in σ_w calculated for the two runs is typically 0.1 ms^{-1} or less. Whilst the reciprocal runs indicate that the measurements of vertical wind using the Cessna are consistent, it is not possible to infer information on the absolute accuracy of the system using this technique.

5. HORIZONTAL WIND COMPONENTS

We have in this paper concentrated mainly on the measurement of vertical wind using the Cessna-182. Tests have been performed to assess the validity of the derived horizontal wind components from the Cessna-182, and the initial results are encouraging. It is beyond the scope of this paper to present a detailed analysis of the horizontal wind measurements and indeed the measurements are still undergoing development. It is hoped that these will be described in the literature at a later date.

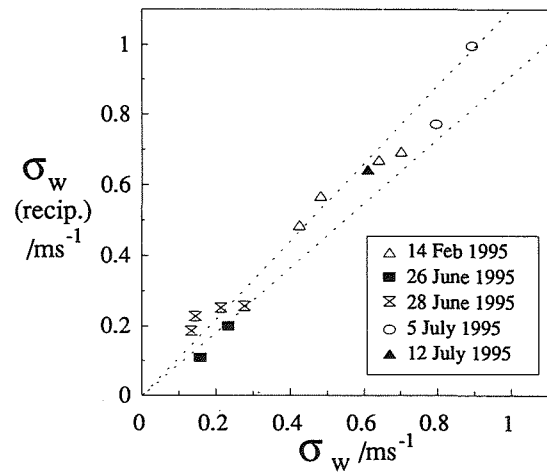


Figure 5: Standard deviations of vertical wind from the reciprocal run test. The dotted lines indicate 10% error.

6. DISCUSSION

It has been shown that a relatively low-cost system without an INS can be used to obtain accurate fast-response measurements of vertical velocity. Our concentration is currently focused on obtaining accurate horizontal wind measurements using GPS as a long-term position reference to correct for accelerometer drifts. With the current uncertainty surrounding the funding of larger and more costly wind-measuring platforms the opportunities for the development of cheaper systems are clear. Although the range and altitude of light aircraft are limited they will continue to be an invaluable tool in boundary layer research.

7. REFERENCES

- Axford, D. N., On the accuracy of wind measurements using an inertial platform in an aircraft, and an example of a measurement of the vertical mesoscale of the atmosphere. *J. Appl. Meteor.*, 7, 645-666.
- Blanchard, R.L., 1971: A new algorithm for computing inertial altitude and vertical velocity. *IEEE Trans. Aerosp. Electron. Syst.* AES 7, 1143-1146.
- Bogel, W., and R. Baumann, 1991: Test and Calibration of the DLR Falcon by Maneuvres. *J. Atmos. Oceanic Technol.*, 8, 5-18.
- Lenschow, D.H., 1986: Aircraft Measurements in the Boundary Layer. *Probing the Atmospheric Boundary Layer*, Lenschow, D.H., Ed. Amer. Meteor. Soc., 39-55.
- Nicholls, S., W. Shaw, and T. Hauf, 1983: An intercomparison of aircraft turbulence measurements made during JASIN. *J. Clim. App. Meteor.*, 22, 1637-1648.

SCATTERING AT 35.8 GHZ BY AXIALLY SYMMETRIC PARTICLES: MEASUREMENTS AND NUMERICAL CALCULATIONS.

Orazio Sturniolo¹, F. Prodi^{1,2} and A. Cola³

¹ Institute FISBAT-CNR, Clouds and Precipitation Group, Bologna, Italy

² Department of Physics, University of Ferrara, Italy

³ Diploma in Aerospace Engineering, University of Bologna in Forlì, Italy

1. INTRODUCTION

Millimeter-wavelength radars can detect small cloud and precipitation particles and therefore they may be more suitable for cloud microphysical studies. FISBAT's Cloud and Precipitation Group has developed a 35.8 GHz scatterometer for laboratory measurements (Prodi 1989, Montanari et al., 1993, Prodi et al., 1993 and 1996), which are needed to interpret the data from radars used in the field and, at the same time, the Group performs numerical computations in the same scattering conditions. Our measurements and computations have been performed on three different types of axially-symmetric ice particles : cylinders, Chebyshev (Wiscombe and Mugnai, 1986) and Wang shapes (Sturniolo et al., 1992 and 1995).

Moreover, calculations of scattering by populations of spheroidal particles randomly oriented using the Hansen & Travis size distribution have been computed (Mishchenko, 1993).

2. MEASUREMENT SYSTEM

The FISBAT's scatterometer is essentially a coherent dual circular-polarization, low-powered, continuous wave/pulsed radar with Doppler capability composed of two parts: an RF microwave system and a video processor. The experimental details, not reported here, are described in Prodi et al., 1996. Once the radar calibration constant A has been determined, the scatterometer can be used for measurements of backscattering cross section σ_{bs} like a function of backscattering electric field:

$$\sigma_{bs} = \frac{|E_{bs}|^2}{A}$$

The scatterometer measures the signal received in the same polarization of incident radiation. To perform the measurements, the scatterometer has been utilized in CW mode. The antenna's beam was emitted in a small anechoic chamber, i.e. a metal box

coated internally with "egg-carton" absorbing material glued to the walls. This material's factory-stated maximum reflectivity at 35 GHz is -40 dB of incident energy. The chamber size (61×61×121 cm) allows a minimum distance of 30 cm (about 35 wavelengths) between target and cell walls. However, reduced dimensions require particular care in positioning the samples and in processing the measurements to meet far-field conditions. The diameter of the antenna mouth permits application of the Fraunhofer approximation (far-field conditions) starting from a distance of about 25 cm. The targets in our environment were located 50 cm from the antenna. The theoretical radiation pattern of the antenna has a 15° principal lobe in amplitude (half-power beamwidth), thereby yielding an e.m. beam 50 cm from the antenna mouth of about 13 cm. We thus selected targets less than 13 cm in size (max. 3 cm in diameter). Two computer-controlled linear positioners (indexers) were used for precise positioning of the targets in the pattern radiation axis. These indexers enable precise and repeatable positioning of the target in a plane perpendicular to the antenna axis, both in the horizontal (X axis) and the vertical (Y axis).

Teflon's particles have been produced by means of a numerically controlled machine-tool. Teflon has been utilized as the complex refractive index m in the range 30 to 60 GHz of this plastic material is known and m is necessary to perform numerical computations.

The cylinders of ice have been produced using very small plastic tubes with different diameter and length in which distilled water is frozen at -14 °C. To produce Wang and Chebyshev particles of ice half-moulds in polymeric resin have been built, then filled with distilled water and frozen at -14 °C in a freezer. Finally, the two halves of ice were glued (with a layer of cold melt water) to obtain the particles. A thin nylon thread (completely invisible to millimeter radiation) was frozen between two halves to suspend the targets in the anechoic chamber during the measurements.

3. NUMERICAL COMPUTATIONS

Different computer codes based on the EBCM (\mathcal{T} -matrix method) have been used for numerical results. First of all the amplitude scattering matrix between 0 and 180 degrees at horizontal polarization for a horizontally polarized unit incident field was performed, then σ_{bs} , at circular polarization was computed following this equation (Bohren and Huffman, 1983) for axially symmetric particles (Chebyshev and Wang particles):

$$\sigma_{bs} = \frac{4\pi}{k^2} \left| \frac{S_1 + S_2}{2} \right|^2$$

where $k = 2\pi/\lambda$ (λ is the wavelength of the incident radiation), S_1 and S_2 are the amplitude scattering matrix elements. For the cylinders (Barber and Hill, 1990) we have performed the numerical calculations for a normally incident radiation to an infinite ($l/2a \geq 10$) cylinder: we have calculated the backscattering efficiency G at circular polarization using the elements of scattering matrix and then the backscattering cross section according to:

$$\sigma_{bs} = 2alG$$

where a is the radius and l the length of cylinder. For Wang particles calculations, the Maxwell-Garnett mixing rules have been utilized to compute the average complex refractive index of soft ice (with density equal to 0.6 g cm^{-3}) since the measurement conditions showed the presence of a thin liquid film due to fusion around the particle. Finally we have used a computer code extended by Mishchenko (1993), to calculate scattering by size-shape distributions of randomly oriented oblate and prolate polydisperse spheroids.

4. RESULTS AND DISCUSSION

Measurements and numerical results are shown in the following tables. Table 1 shows the results for different cylinders of ice with dry surface. The great differences (sometimes greater than 10) between measurements and calculations are essentially due to three factors:

- the numerical results are obtained using a computer code in which the cylinder are of infinite length and not all the cylinders are in the condition $l/2a \geq 10$;
- the sizes of cylinders are comparable with the constant zone of antenna;
- during the freezing it is not easy to verify the homogeneity of ice due to air bubbles being nucleated during freezing along the axis of the thin cylinders. Therefore, in the future, it would be convenient to have the ice grow around the thread.

Table 1. Measured and computed σ_{bs} for cylinders of ice with dry surface ($m = 1.78 - i0.0024$) with different length and radius, at $\lambda = 0.838 \text{ cm}$.

$l \text{ (cm)}$	$a \text{ (cm)}$	measured $\sigma_{bs} \text{ (cm}^2\text{)}$	computed $\sigma_{bs} \text{ (cm}^2\text{)}$
2	0.15	0.424	0.0599
2.1	0.11	0.667	0.0774
2.1	0.12	0.687	0.0549
2.3	0.15	0.290	0.0689
3	0.15	1.122	0.0899
3.3	0.13	1.458	0.0915

Table 2 shows the measured and computed values of σ_{bs} for two different Chebyshev particles of ice with dry surface and teflon. As can be seen all results are in good agreement but the computed values show not great differences in spite of being the particles of different shape. It's important to note that the ice particles have a σ_{bs} greater than teflon, since the refractive index of ice has a small absorption coefficient. For $n = 6$, σ_{bs} is very large due to the presence of surface concavity.

The results shown in table 3 for Wang particles are in very good agreement in both cases. Similarly to Chebyshev particles, σ_{bs} for Wang ice particles is greater than teflon. It's interesting to compare Chebyshev particle of ice for $n = 3$ and Wang; in fact these particles have an equivalent radius ≈ 1 and are very similar to each other: measured values of σ_{bs} are different while computed values are practically the same still with m different. This difference is due to the presence of a thin liquid film around the Wang particle during the measurements.

Table 2. Measured and computed σ_{bs} for Chebyshev particles of ice with dry surface and teflon ($m = 1.4666 - i0.042426$) for different values of Chebyshev polynomial order n , same deformation parameter ε and different radius of undeformed sphere r_0 , at $\lambda = 0.838 \text{ cm}$.

n	$r_0 \text{ (cm)}$	ε	measured $\sigma_{bs} \text{ (cm}^2\text{)}$	computed $\sigma_{bs} \text{ (cm}^2\text{)}$
3	0.9952	0.10	3.955	5.744
6	0.9979	0.10	7.574	6.373

n	$r_0 \text{ (cm)}$	ε	measured $\sigma_{bs} \text{ (cm}^2\text{)}$	computed $\sigma_{bs} \text{ (cm}^2\text{)}$
3	0.9952	0.10	2.287	1.931
6	0.9979	0.10	3.842	1.941

Table 3. Measured and computed σ_{bs} for Wang particles of soft ice (with density equal to 0.6 g cm^{-3} and $m = 1.522 - i0.0024$) and teflon for elongation parameter $b = 1.0$ and conicity parameter $\delta = 0.8$, at $\lambda = 0.838 \text{ cm}$.

WANG PARTICLE OF SOFT ICE			
b	δ	measured $\sigma_{bs} (\text{cm}^2)$	computed $\sigma_{bs} (\text{cm}^2)$
1.0	0.8	5.661	6.055

OF TEFLON			
1.0	0.8	1.104	0.99

The indication from reported data is that the comparison with numerical models are possible only for Chebyshev and Wang particles and therefore it is very important to have other moulds with different values of b and δ , r_0 and ϵ to better investigate the radar signal for particles that are very realistic in atmosphere. Besides, considering that it is very difficult to control the surface physical characteristics of particles, the next measurements should be made in a cold chamber.

Finally the scattering at 35.8 GHz, by size-shape distribution of Hansen & Travis has been computed for randomly oriented axially symmetric population of polydisperse ($0.1 \leq r \leq 1.0 \text{ cm}$) spheroidal particles of dry ice at $T = -5^\circ \text{C}$ ($m = 1.785 - i0.002426$) with different axis ratio a/b ($a/b = 0.5$ for prolate spheroids -- disk, and $a/b = 1.5$ for oblate spheroids -- column).

In Fig.1 the ratio S_{22}/S_{11} of the elements of scattering matrix versus scattering angle is shown; this ratio is equal 1 for spheres and therefore this ratio strongly depends on particle asphericity and deviate from unity. The ratio has a minimum for oblate spheroids near 120° . At 180° the backscattering for prolate spheroids is greater than oblate.

In table 4 the cross section for scattering C_{sca} , extinction C_{ext} , and absorption C_{abs} , single-scattering albedo w , and asymmetry parameter of phase function g are shown.

Table 4. Cross section for scattering C_{sca} , extinction C_{ext} , and absorption C_{abs} , single-scattering albedo w , and asymmetry parameter of phase function g for polydisperse size-shape distribution of spheroids, at $\lambda = 0.838 \text{ cm}$.

Particles	C_{sca}	C_{ext}	C_{abs}	w	g
Oblate	0.3593	0.3659	0.0066	0.9819	0.51
Prolate	0.3723	0.3790	0.0067	0.9823	0.56

The differences for moderately aspherical particles are not large.

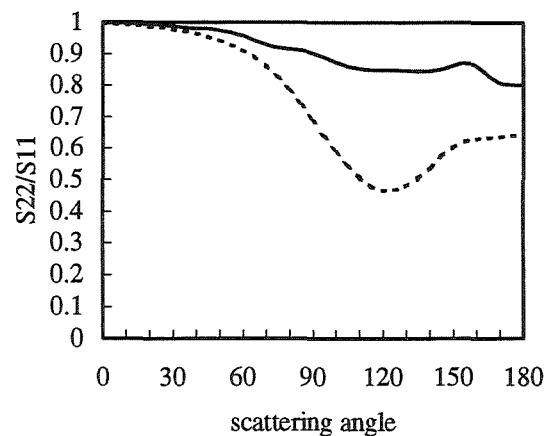


Figure 1. S_{22}/S_{11} versus scattering angle for randomly oriented polydisperse spheroidal particles with axis ratio $a/b = 0.5$ (prolate spheroids - solid curve) and $a/b = 1.5$ (oblate spheroids - dashed curve), and $0.1 \leq r \leq 1.0 \text{ cm}$ for a size-shape distribution of Hansen & Travis, at $\lambda = 0.838 \text{ cm}$.

In the future calculations of scattering by populations of Chebyshev and Wang particles randomly oriented of a given size distribution will be also performed to possible application to cloud/rain radar data interpretation.

5. ACKNOWLEDGMENTS

We wish to thank Prof. Peter Barber of the Atmospheric Sciences Center of the Desert Research in Reno, Nevada, USA, for providing us with his EBCM code for cylinder, and Prof. Michael I. Mishchenko of the NASA, Goddard Institute for Space Studies, New York, USA for computer code for randomly oriented population of scatterers, and Mr. Marcello Tercon of Institute FISBAT-CNR, Bologna, Italy for his technical assistance.

6. REFERENCES

- Barber, P.W., and S.C. Hill, 1990: *Light Scattering by Particles: Computational Methods*. World Sci. Publ. Co., 261 pp.
- Bohren, C.F., and D.R. Huffman, 1983: *Absorption and Scattering of Light by Small Particles*, Wiley, New York, 530 pp.
- Mishchenko, M.I., 1993: Light scattering by size-shape distributions of randomly oriented axially symmetric particles of a size comparable to a wavelength, *Applied Optics*, 32, 4652-4666.
- Montanari, M., F. Prodi, A. Tagliavini, and P. Bassi, 1993: Performance and testing of a 35 GHz scatterometer for laboratory measurements on hydrometeors, *Proceedings of the 26th International Conference on Radar*

- Meteorology*, Norman, Oklahoma, American Meteorological Society, 368-370.
- Prodi, F., 1989: A scatterometer for laboratory measurements of hydrometeor backscattering at millimeter wavelengths, *Proceedings of the Fifth WMO Sci. Conf. on Weather Modification and Applied Cloud Physics*, Beijing, China, WMO Tecu. Doc. No. 269, World Meteorological Organization, 117-118.
- Prodi, F., O. Sturniolo, A. Mugnai, and M. Montanari, 1993: Backscattering of ice hydrometeors at 35 GHz: Laboratory measurements and numerical computations, *Proceedings of the 26th International Conference on Radar Meteorology*, American Meteorological Society, pp. 126-128.
- Prodi, F., A. Moretti, and O. Sturniolo, 1996: Backscattering gain measurements of spherical ice hydrometeors at 35.8 GHz and comparison to numerical computations, *J. Atmos. Oceanic Technol.*, in the issue of April.
- Sturniolo, O., A. Mugnai, and F. Prodi, 1992: Hydrometeor backscattering at millimeter wavelengths, *Proceedings of the 11th International Conference on Clouds and Precipitation*, Elsevier Science Publ., pp. 1001-1004.
- Sturniolo, O., A. Mugnai, and F. Prodi, 1995: A numerical sensitivity study on the backscattering at 35.8 GHz from precipitation-sized hydrometeors, *Radio Science*, 4, 903-919.
- Wiscombe, W.J., and A. Mugnai, 1986: Single scattering from nonspherical Chebyshev particles: A compendium of calculations, *NASA Ref. Publ. 1157*, NASA/Goddard Space Flight Center, Greenbelt, MD, 284 pp.

ESTIMATION OF THE LIQUID WATER CONTENT BY MULTIPARAMETER RADAR MEASUREMENTS

Martin Hagen and Hartmut Höller

Institut für Physik der Atmosphäre, DLR Oberpfaffenhofen, Germany

1. INTRODUCTION

The estimation of the rainfall rate by weather radar is the challenge for radar meteorologists and hydrologists. In general it is practice to apply empirical Z - R relations to convert radar observations of the reflectivity (Z) to rain rates (R). However, it was found that different Z - R relations are necessary to cover the wide variety of natural rain events. Battan (1973) gives 69 relations for varying rain types, geographic locations, and wavelengths of the radar. It is the different dependence of the rain rate ($\sim D^{3.7}$) and the reflectivity ($\sim D^6$) from the drop size distribution which causes the deficiency in estimation the rain rate by the reflectivity measurements. For cloud-microphysical studies the mass of water or ice - the liquid water or ice content (LWC or IC) - is of more interest. Only a few empirical relations are available to relate Z to the mass of water (M). Sekhon and Srivastava (1971) give $M = 9.08 \cdot 10^{-4} Z^{0.70}$ (Z in $\text{mm}^6 \text{m}^{-3}$, M in g m^{-3}) for convective storms. It is evident that similar to Z - R relations various Z - M relations are needed for the large variety of rain. Further different Z - M relations are necessary for other kinds of precipitation like snow, graupel or hail. This makes it necessary to provide tools for the discrimination of the various hydrometeor types.

The introduction of linear polarized radar techniques made it possible to gain more insight in the nature of rain. Seliga and Bringi (1976) proposed a procedure to estimate parameters (intercept and slope) of the drop size distribution. This allows a flexible basis for the integration of the liquid water content or the rainfall rate. It is of disadvantage that this is limited to rain drop size distributions. On the other hand, polarimetric radar measurements have turned out to be very useful for the discrimination of different kinds of hydrometeors.

The presented study will be limited to the retrieval of the water content of rain. Due to the wave-length of the radar system (C-band) the water content of cloud droplets can only be considered to a certain degree. The term rain water content instead of liquid water content would be more appropriate to describe the retrieved parameter. In order to validate the procedure we will use other independent systems (Richter and Hagen, 1996). In addition we use a hydrometeor classification scheme

(Höller et al., 1994) to separate rain regions from regions with other hydrometeor types in a convective storm.

2. RETRIEVAL METHODS

2.1 Estimation of the drop size distribution

Rain drop size distributions can be represented by an exponential size distribution $N(D) = N_0 \exp(-3.67 D/D_0)$, where D is the diameter of the drops, N_0 the intercept and D_0 the median diameter. Also known is the slope $\Lambda = 3.67/D_0$. Natural rain drop size distributions have a wide range of the parameters N_0 and D_0 (Ulbrich, 1983). N_0 and D_0 are expected in the range of 2,000 to 20,000 $\text{mm}^{-1} \text{m}^{-3}$ and 0.5 to 2.5 mm, respectively.

The technique proposed by Seliga and Bringi (1976) will be used to retrieve N_0 and D_0 of an exponential drop size distribution. This technique is based on the fact that rain drops larger than about 1 mm in diameter are non-spherical and can be approximated by oblate spheroids. Therefore, it is necessary to consider relations between the shape and the size of raindrops. A large variety of experimental and theoretical studies on the shape of raindrops have been reported in literature (e.g. review by Tokay and Beard, 1993). Besides an equilibrium shape which can be determined from hydrostatic and aerodynamic laws, raindrops are observed to oscillate and rotate. This will cause considerable deviations from the equilibrium shape (Beard, 1984). For radar measurements the mean state of the raindrops in the pulse volume is of interest. Further, the scatter cross-section of a large-amplitude oscillating single drop could be affected considerably by Mie-resonances. This was shown for S-band by Beard (1984), the effect will be more pronounced at C-band.

Commonly used are the shapes determined by Pruppacher and Pitter (1971) which are based on theory and observations ($r = 1.03 - 0.062 D_{eq}$, $D > 1 \text{ mm}$). r is the ratio of the major to the minor axis of an ellipsoid. Radar observations of the differential reflectivity (Z_{DR}) showed that raindrops with $D < 2.5 \text{ mm}$ are less deformed than expected from theory (Goddard et al., 1982).

The differential reflectivity is defined as the ratio between the reflectivity at horizontal and vertical linear polarization, Z_H and Z_V , respectively:

Corresponding author adress: Martin Hagen, Institut für Physik der Atmosphäre, Deutsche Forschungsanstalt für Luft- und Raumfahrt (DLR), Oberpfaffenhofen, 82234 Weßling, Germany. E-mail: martin.hagen@dlr.de

$$Z_{DR} = 10 \log \left(\frac{\int_0^{D_{max}} D_{eq}^6 S_H \exp(-3.67 D_{eq}/D_0) dD_{eq}}{\int_0^{D_{max}} D_{eq}^6 S_V \exp(-3.67 D_{eq}/D_0) dD_{eq}} \right) dB$$

where D_{max} is the maximum expected rain drop diameter (e.g. 8 mm), D_{eq} the diameter of a spherical drop of volume equal to the volume of the actual drop, and S_H and S_V are shape factors (Seliga and Bringi, 1976) which are determined by the axis ratio r of an oblate raindrop. Evidently, Z_{DR} depends only on D_0 and is independent of N_0 . Once D_0 is known N_0 can be easily determined by the definition of Z_H :

$$Z_H = N_0 \int_0^{D_{max}} D_{eq}^6 S_H \exp(-3.67 D_{eq}/D_0) dD_{eq}$$

Seliga and Bringi (1976) showed that it is important to measure Z_{DR} precisely, i.e. within an error better than ± 0.2 dB.

2.2 Classification scheme

A radar derived classification scheme (Höller et al. 1994) discriminates between different hydrometeor types as well as mixtures between these particles: rain, snow, graupel, hail (dry or wet) and hail-rain mixtures can be identified. Differential reflectivity (Z_{DR}) and linear depolarization ratio (LDR) as determined from radar measurements are used for a primary particle classification (Fig. 1). Additional the height of the melting layer is used for the discrimination between rain and snow. Measurements of Z_{DR} help to identify rain regions (Seliga and Bringi 1976) and to discriminate them from hail or graupel zones aloft (Aydin et al. 1986). Positive Z_{DR} results from large oblate rain drops, whereas irregular shaped hailstones or graupel will give zero Z_{DR} at comparable reflectivity values. LDR helps to identify graupel, snow and hail e.g. in the upper parts of a thunderstorm (Bringi et al. 1986a,b). Linear horizontally polarized waves are depolarized by irregular shaped particles which are not oriented horizontally during falling. Wet growth or melting of ice causes the particles to be covered by liquid water. Due to the higher refractive index of water LDR reaches its highest values for melting ice particles. LDR is the preferred indicator for the melting layer, even in situations where the bright band is hardly visible in Z . Z_{DR} and LDR can also be used to identify mixed phase regions in the cloud where e.g. raindrops and hailstones do coexist.

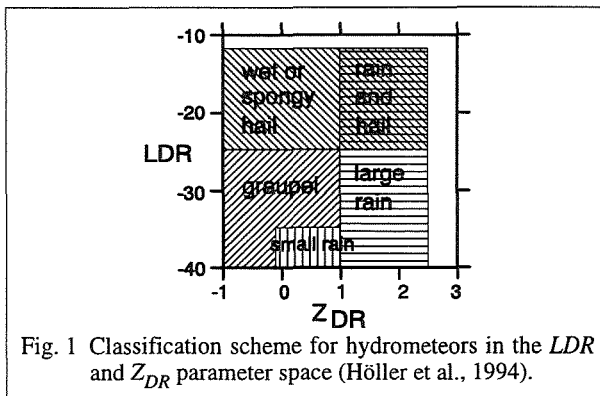


Fig. 1 Classification scheme for hydrometeors in the LDR and Z_{DR} parameter space (Höller et al., 1994).

3. MEASUREMENTS AND VALIDATION

During the CLEOPATRA (Meischner et al., 1993) field experiment in summer 1992 in Southern Germany several precipitation situations were observed. Measurements were taken with the DLR C-band polarimetric Doppler radar POLDIRAD (Schroth et al., 1988) located at Oberpfaffenhofen scanning in RHI and PPI mode, a disdrometer operated by the ETH Zürich and a vertical pointing L-band FM-CW Doppler radar and RASS system of the Universität Hamburg (Richter and Peters, 1994), both located at Penzing about 27 km west of Oberpfaffenhofen.

Figure 2 shows the derived drop size distribution parameters N_0 and D_0 and the resulting rain water content as they were estimated by the different systems during stratiform precipitation with embedded convection. The polarimetric radar and vertical Doppler radar measurements were done at 750 m above ground. Note that during the onset of the precipitation before 2020 the rain rate was below 1 mm/h and estimates are critical due to the low Z_{DR} . N_0 and D_0 from the vertical Doppler spectra were estimated by two methods: (a) an integral method used by Waldvogel (1974) and (b) an exponential regression within the drop size range 0.5 to 3.0 mm. The results show a high variability of the different systems, and also a dependency from the retrieval method.

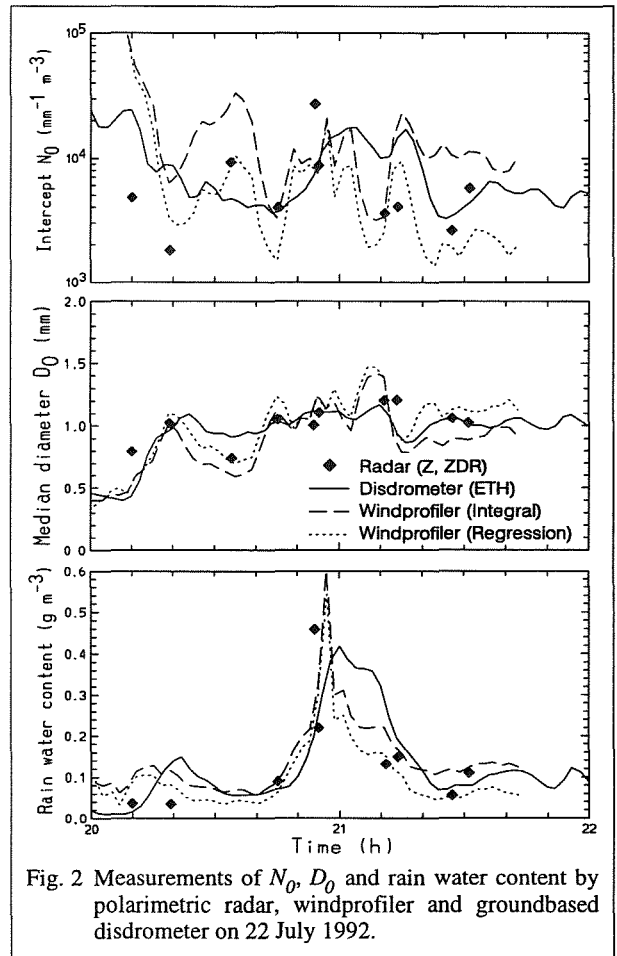


Fig. 2 Measurements of N_0 , D_0 and rain water content by polarimetric radar, windprofiler and groundbased disdrometer on 22 July 1992.

A direct validation of hydrometeor classification is critical, the classification relies on theoretical studies, scattering simulation and sparse observations. A validation of some partiel groups by aircraft observations is shown by Hagen et al. (1995).

4. RESULTS

The algorithm described above is applied to radar measurements during a squall line event in Switzerland and Southern Germany (Haase-Straub et al., 1994). For a preliminary result we will concentrate on a RHI which was observed when the squall line was about 40 km west of Oberpfaffenhofen.

Figure 3 shows the reflectivity (Z_H) and Fig. 4 the derived rain water content in the inflow region of the storm. The retrieval is limited to regions classified as rain, i.e. below the bright band. No retrieval was possible in regions with low reflectivity (< 24 dBZ) and where Z_{DR} was below 0.5 dB. Beyond the high reflectivity shaft (Fig. 3 at 50 km range) attenuation reduced Z_{DR} considerable and no confident retrieval was possible. The highest values of the rain water content at the right side ($M > 4$ g/m³) might also be contaminated by melting graupel. At heights below 1.7 km partial beam blockage caused a reduction of the reflectivity and also of the rain water content.

The highest values of the rain water content was observed in the region below the melting graupel. Here Z_{DR} indicates a zone of large drops which may include still an ice core. This is also the main downdraft region of the storm. It is interesting to note that there is a region (45-46 km from the radar) where rain is observed in heights well above 3.7 km. This is expected to be the updraft region. Raindrops are supercooled in this zone which is located well above the melting level.

5. CONCLUSIONS

The retrieval of the raindrop size distribution parameters N_0 and D_0 of an exponential distribution by polarimetric radar shows confidential results. According to sensitivity studies by Seliga and Bringi (1976) it is necessary to have high quality of radar measurements. Any offset in Z_{DR} will cause D_0 to be biased and consequently N_0 will be incorrectly estimated. If Z_{DR} is underestimated by 0.2 dB the resulting water content will be overestimated by 20%. The measurements show a high variability of N_0 and D_0 which can often be observed with disdrometers (e.g. Waldvogel, 1974). In contrast to groundbased measurements a scanning radar gives much more flexibility for studies of the microphysic and related dynamic.

Additional relations between polarimetric radar parameters and the ice content of graupel, snowflakes or hail have to be evaluated. In contrast to rain drops we have to consider a high variability of shapes and density for ice particles. This results in a larger number of unknown parameters for the retrieval process. Additional available radar parameters can be the specific differential phase (K_{DP}) and the correlation coefficient ($\rho_{HV}(0)$). Both can provide helpful informations for the parametrisation of the ice content as well as enabling the retrieval of water and ice content in mixtures of rain and hail. It has to be considered that only non-spherical particles can give a polarimetric signal, for small rain drops only classical Z - M relations are applicable.

At short wave-lengths attenuation effects have to be considered. This will be the case in heavy precipitation at C-band. Attenuation can cause further ambiguities in the estimation of Z_H and Z_{DR} . Correction procedures are only known for rain so far (Gorgucci et al., 1996). Phase measurements (not attenuated) can be used for correction procedures, however, the shape and the orientation of the particles has to be known.

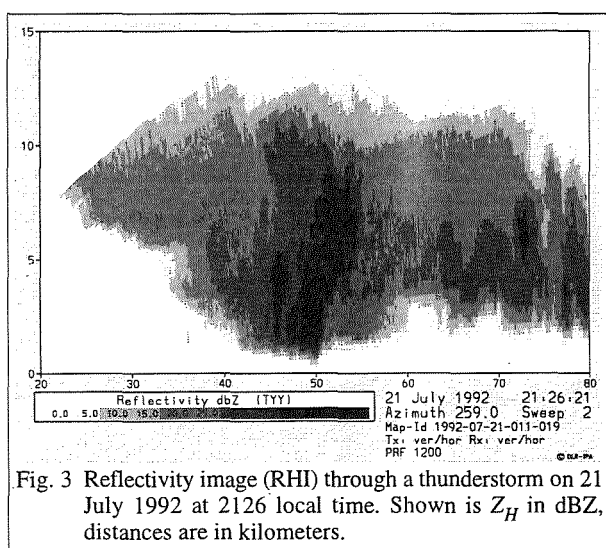


Fig. 3 Reflectivity image (RHI) through a thunderstorm on 21 July 1992 at 2126 local time. Shown is Z_H in dBZ, distances are in kilometers.

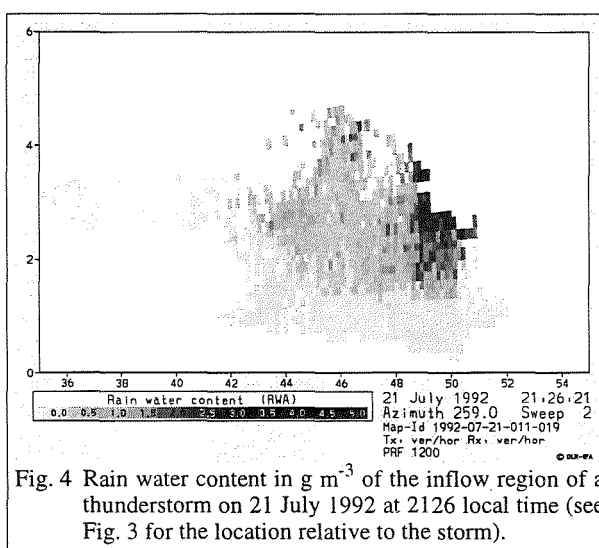


Fig. 4 Rain water content in g m⁻³ of the inflow region of a thunderstorm on 21 July 1992 at 2126 local time (see Fig. 3 for the location relative to the storm).

6. ACKNOWLEDGEMENT

C. Richter (formerly Universität Hamburg) and W. Henrich (ETH Zürich) provided the data for the intercomparison.

7. REFERENCES

- Aydin, K., T.A. Seliga, and V. Balaij, 1986: Remote sensing of hail with a dual linear polarization radar. *J. Climate Appl. Meteor.*, **25**, 1475-1484.
- Battan, L.J., 1973: *Radar observations of the atmosphere*. University Press of Chicago, 84-113.
- Beard, K.V., 1984: Oscillation models for predicting raindrop axis and backscatter ratios. *Radio Science*, **19**, 67-74.
- Gorgucci, E., G. Scarchilli, and V. Chandrasekar, 1996: Error structure of radar rainfall measurements at C-band frequencies with dual polarization algorithm for attenuation correction. Submitted to *J. Geophys. Res. - Atmosph.*
- Haase-Straub, S.P., D. Heimann, T. Hauf and R.K. Smith (eds.), 1994: The squall line of 21 July 1992 in Switzerland and southern Germany - a documentation. DLR Forschungsbericht 94-18, pp 226.
- Hagen, M., H. Höller und P. Meischner, 1995: Multiparameter radar characterization of precipitation particles with in situ measurements. COST 75 Intern. Seminar on Weather Radar Systems, Bruxelles, 519-526.
- Höller, H., V.N. Bringi, J. Hubbert, M. Hagen and P.F. Meischner, 1994: Life cycle and precipitation formation in a hybrid-type hailstorm revealed by polarimetric and Doppler radar measurements. *J. Atmos. Sci.*, **51**, 2500-2522.
- Meischner, P., M. Hagen, T. Hauf, D. Heimann, H. Höller, U. Schumann, W. Jaeschke, W. Mauser and H.R. Pruppacher, 1993: The field project CLEOPATRA, May-July 1992 in Southern Germany. *Bulletin of the Amer. Meteorol. Soc.*, **74**, 401-412.
- Pruppacher, H.R. and R.L. Pitter, 1971: A semi-empirical determination of the shape of cloud and raindrops. *J. Atmos. Sci.*, **28**, 86-94.
- Richter, C., and M. Hagen, 1996: Dropsizes distributions of raindrops by polarisation radar and simultaneous measurements with disdrometer, windprofiler and PMS-probes. Submitted to *Quart. J. Roy. Meteor. Soc.*
- Richter, C., and G. Peters, 1994: Deriving rainfall parameters by using a Doppler radar-RASS system at vertical incidence. Preprints 3rd Intern. Symposium Tropos. Profiling: Needs and Technologies, Hamburg, 453-455.
- Schroth, A.C., M.S. Chandra and P. Meischner, 1988: A C-Band coherent polarimetric radar for propagation and cloud physics research. *J. Atmos. Ocean. Technol.*, **5**, 803-822.
- Sehkon, R.S., and R.C. Srivastava, 1971: Doppler radar observations of drop-size distributions in a thunderstorm. *J. Atmos. Sci.*, **28**, 983-994.
- Seliga, T.A., and V.N. Bringi, 1976: Potential use of radar differential reflectivity measurements at orthogonal polarizations for measuring precipitation. *J. Appl. Meteor.*, **15**, 69-76.
- Tokay, A., and K.V. Beard, 1993: The influence of raindrop oscillations on dual-polarization radar measurements of precipitation. Preprints, 26th Conf. Radar Meteorol., Norman, Amer. Meteorol. Soc. Boston, 100-102.
- Ulbrich, C.W., 1983: Natural variations in the analytical form of the raindrop size distribution. *J. Appl. Meteor.*, **22**, 1764-1775.
- Waldvogel, A., 1974: The N0 jump of raindrop spectra. *J. Atmos. Sci.*, **31**, 1067-1078.

VALIDATION OF SATELLITE ESTIMATION OF PRECIPITATION USING SPARSE GROUND TRUTH DATASET IN TROPICAL AFRICA.

Isabelle JOBARD¹, Henri LAURENT², Ana MAIA² and Alexandru TOMA³

¹ Laboratoire de Météorologie Dynamique - CNRS, Palaiseau, France

² Laboratoire d'Hydrologie - ORSTOM, groupe PRAO, Montpellier, France

³ Centre d'Informatique Géologique - Ecole des Mines, Paris, France

1. INTRODUCTION

In continental tropical regions where raingauge networks are very sparse, satellite estimation of precipitation is essential for various purposes. Rainfall in these regions is mainly provided by large convective systems. It can be estimated from the satellite infrared images assuming that precipitation is related to the convective activity measured by the height (or the temperature) of the cloud top. This approach, based on a statistical relationship between thermal infra-red temperature and precipitation, is valid only for space and time averaged estimates.

This paper deals with the different issues encountered in the validation procedure of any rainfall estimation method, when the rainfall field which is estimated from satellite pixel data is to be compared to a rainfall field which is computed from point values provided by raingauges and considered as the "ground truth". These issues mainly concern :

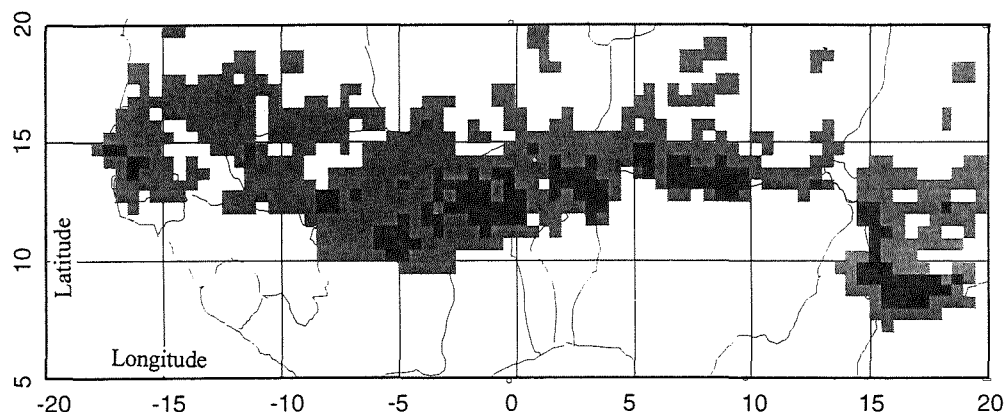
- the method for interpolating point values and producing areal values with acceptable uncertainties,
- the choice of the appropriate spatial scales and time integration periods,
- the requirement for a partition of the data sets according to various characteristics, such as rainfall classes, homogeneous climatic regions or periods,
- the criteria allowing performance assessment.

This is discussed in the section 2 and a case study is presented in section 3 where rainfall estimates from four different methods are compared with rainfall reference values using the ten-day rainfall records from the low density raingauge network of the Sahelian band in tropical Africa, during five rainy seasons.

2. METHODOLOGY

For the validation of a rainfall estimation method using satellite image pixel data, the reference values which are needed to be compared to the estimated values, must represent a spatial average rainfall value. As the ground rainfall measurements are obtained from a rain gauge network, it is necessary to use an interpolation algorithm to obtain areal rainfall values from point values. In the case of 10-day rainfall amounts, as the climatic gradient is not strong, a suitable method is the ordinary kriging method, since a non-stationary kriging method is needed only when there is a drift; for more details, see Toma (1996). The average uncertainty of the areal values depends on the local density of stations. The grid cells which have a minimum number of stations in their vicinity allowing an acceptable uncertainty for the areal rainfall values are considered as reliable; thus only these reliable cells must be taken into account as reference values. In the **Figure 1** representing our study area in western Africa, with a $0.5^\circ \times 0.5^\circ$ grid cell, the grey region shows the distribution of the cells which have at least 1 rain station, while the black region shows the cells with at least 5 rain stations. The minimum number of stations in the cell area, which is function of the grid cell size, must be high enough to give values with a low uncertainty but its choice is also guided by the necessity to have enough values for the validation and also to cover a large enough surface of the region. The **Figure 2** (top) shows the curves representing the number of grid cells in our study area for a minimum number of stations from 1 to 10, for different grid cell sizes ranging from 0.1° to 2.5° . The **Figure 2** (bottom)

Figure 1
(see text)



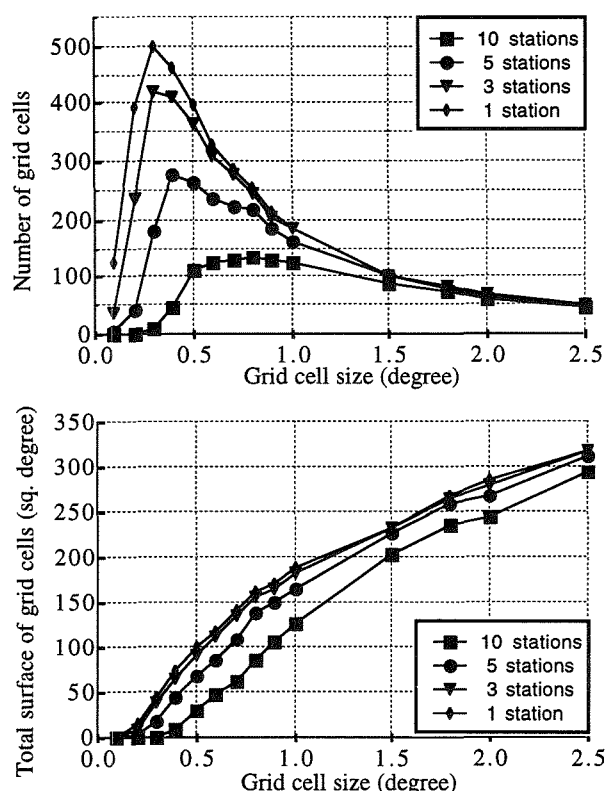


Figure 2 (see text)

shows the curves representing the corresponding total surface covered by the reliable cells. Taking also into account the results presented by Lebel and Le Barbé (1996) regarding the uncertainties, the compromise chosen for our study is 5 stations for any reliable cell and a $0.5^\circ \times 0.5^\circ$ grid cell.

The spatial resolution and time integration period of the reference values are to be chosen considering not only the characteristics of the available dataset but also the scales which are relevant for the type of application for which the rainfall is estimated, such as hydrology, agrometeorology, climatology, etc.. For our case study, the rainfall data were delivered by the AGRHYMET center in Niamey which is mainly interested in crop monitoring in the Sahelian countries and archives for that purpose, the 10-day rainfall amounts at about 580 stations in the Sahel. Thus, our choice for the time integration period was constraint to be at least 10-day.

As it is said before, the spatial resolution is constraint by the rain gauge density of the network. We chose a 0.5° resolution and considered also wider resolutions, up to 2.5° which is appropriate for climatic studies.

When the dataset corresponds to a large zone covering different climatic regions or to a long time period such as the whole rainy season, it may be necessary to define separate subsets of the reference data. The dataset is partitioned in order to validate the estimation method for each rainfall regimes and for homogeneous regions. For example, we delimited three geographical zones in our case study: the Sudan region south of 10°N latitude, the Sahel region and the Senegal region north of 10°N

latitude and respectively east and west of the 10°W longitude. The choice of this partition may be critical.

The last but not least issue is the choice of the relevant criteria allowing performance evaluation of the estimation methods. Various statistical parameters can be used to measure the strength of the statistical relationship between the estimated values and the reference values; the most commonly used criterion is the linear correlation coefficient (R). It is also interesting to consider other criteria which reflect different aspects of the performance such as the root mean square error (RMSE), the bias (b), the slope of the regression line (a) and a skill score index (I) such as the index defined in Murphy (1995) as : $I = 1 - \text{RMSE}/\text{sdev}$, where sdev is the standard deviation of the reference values. All these parameters depend more or less on each other as discussed in Murphy (1995) or Toma (1996). It is also important to add to these quantitative criteria, a visual and qualitative information given by the scatterplot which allows to identify some characteristics of the data distribution or defaults of the method that the statistical criteria do not show up.

3. CASE STUDY

The validation of four rainfall estimation methods was achieved in order to evaluate how the results of their performance assessment depend on the different choices or parameters involved in the procedure and discussed in the previous section.

Table 1 (see text)

[a] 1990 / 2056 values / 10-day / 0.5° / 5 stations

method	R	RMSE	bias	I
A	0.66	21	0	0.24
B	0.70	28	17	-0.03
C	0.69	21	0	0.25
D	0.79	17	-4	0.37

[b] 1990 / 514 values / 30-day / 0.5° / 5 stations

method	R	RMSE	bias	I
A	0.77	14	0	0.35
B	0.74	24	18	-0.13
C	0.64	17	1	0.20
D	0.83	12	-4	0.42

[c] 1990 / 1160 values / 10-day / 1.0° / 5 stations

method	R	RMSE	bias	I
A	0.73	18	1	0.30
B	0.73	28	19	-0.08
C	0.69	20	1	0.23
D	0.82	15	-1	0.42

[d] 1990 / 296 values / 30-day / 1.0° / 5 stations

method	R	RMSE	bias	I
A	0.82	13	2	0.43
B	0.79	20	20	-0.13
C	0.65	18	1	0.17
D	0.88	11	-1	0.51

[e] 1990 / 885 values / 10-day / 0.5° / 10 stations

method	R	RMSE	bias	I
A	0.64	21	0	0.22
B	0.69	29	17	-0.06
C	0.73	19	2	0.30
D	0.78	17	-4	0.36

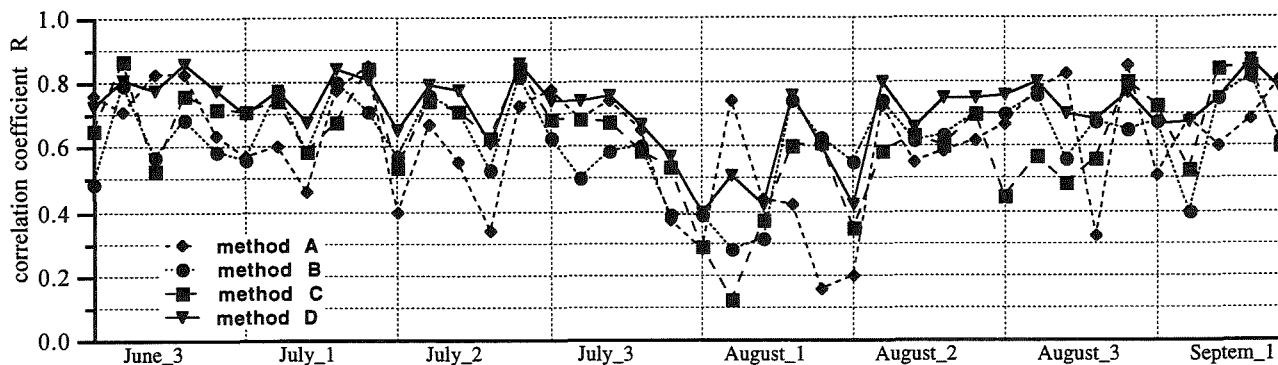


Figure 3 : Correlation coefficients for the methods A, B, C and D, obtained for each of the forty 10-day periods (from the third of June to the first of September) plotted for years 1989, 1990, 1991, 1992 and 1993.

Among the numerous algorithms for estimating rainfall from satellite data, we chose simple Infrared algorithms that are run in operational routines. They provide 10-day rainfall estimates for 5 rainy seasons from 1989 to 1993, for eight 10-day periods running from 21 June to 10 September of each year, over West Africa (Fig. 1) at the Meteosat pixel resolution (5 km). Estimates are then averaged over the $0.5^{\circ} \times 0.5^{\circ}$ grid cells defined for the reference data.

The four methods are:

- the method A which is a climatic rainfall value yielded by the mean rainfall during the period 1970-1990;
- the method B which is the GOES Precipitation Index (Arkin, 1979);
- the method C which is a multiple infrared threshold method developed at the Reading University (Dugdale et al., 1990);
- the method D, developed at ORSTOM-Lannion, which is an infrared method calibrated every 10 days with the synoptic stations data (Carn et al., 1989).

Due to the limited length of this paper, it is impossible to display all the results; only a few examples are shown for comments. The Tables 1 [a] to [e] give a sample of the statistical results for the four methods (correlation coefficient R, RMSE, bias and score skill index I), for the data subset of year 1990, at different time and space resolutions (Tables [a] to [d]); a minimum of 5 stations are used for the reference values while 10 stations are used for the results of Table [e]. Comparison between Tables [a] and [e] indicate that this parameter has a small effect on the coefficients. Increasing the grid cell size from 0.5° to 1.0° has a more important effect, and increasing the time integration period from 10 days to 30 days has the largest effect: the improvement of the coefficients is important especially for R and I. It is worth noticing that the method C does not behave like the others.

To test the effect of partitioning the dataset, we compared for the 4 methods, the correlation coefficient obtained with the whole dataset (given in Table 2), to the correlation coefficients obtained for each of the 40 10-day periods (8 10-day periods for each of the 5

years). These correlation coefficients are plotted on the Figure 3 and the mean value of the coefficients are given in Table 2. The large scatter of the values and the comparison of the coefficients in Table 2 indicate clearly that the correlation coefficient is highly dependent on the partitioning.

The Figures 4 display the scatterplots for the four methods A, B, C and D, for the 10-day periods of 1992 and the statistical coefficients. Though these coefficients are very similar for the methods A and C, the scatterplots are different and reveal that the method A does not produce neither low nor high rainfall. This is actually normal that climatic values (method A) cannot fit extreme precipitation. The typical default of the three satellite infrared methods, i.e. underestimating large rainfall amounts, can also be verified on the scatterplots.

Table 2 : Correlation coefficients R obtained for the whole dataset and for the same dataset partitioned into 40 subsets, the mean R of the R shown in Figure 3.

method	A	B	C	D
R (1 dataset)	0.61	0.66	0.54	0.78
mean R (40 subsets)	0.61	0.62	0.63	0.71

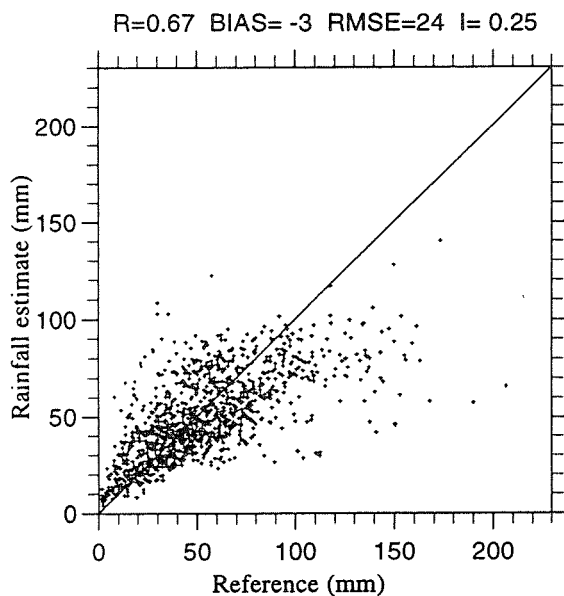
4. CONCLUSION

The analysis of the performance of four rainfall estimation methods, using the same reference dataset for their validation, shows that the results are dependent on the level of uncertainty required for the reference values, on the space scales and time integration periods and on the dataset partition. When several methods are intercompared, it is important to take that into account, therefore the validation for different scales and partitions must be tested. In our case study, it appears that the method D is doing better than the others, most of the time; then one can state that the method D is likely to produce better rainfall estimates. This method has in fact an advantage comparing to the others, since the estimates are calibrated with the synoptic rain gauge precipitation of the actual ten-day period.

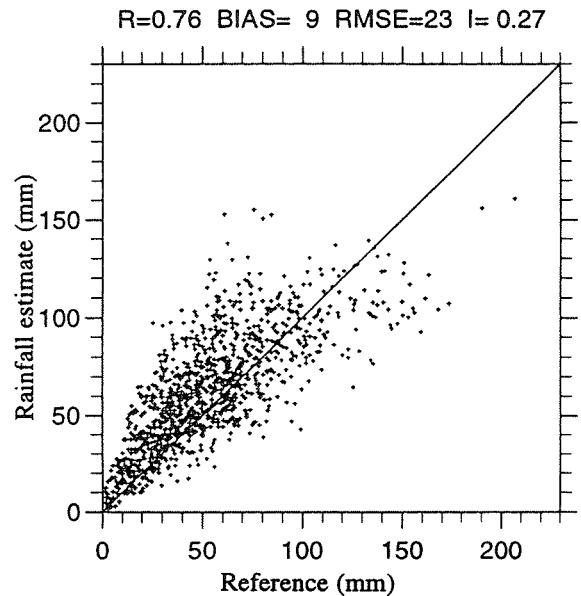
5. REFERENCES

- Arkin, P. A. (1979): The relationship between fractional coverage of high cloud rainfall and accumulations during GATE over the B-scale array. *Mon. Wea. Rev.*, 107, pp. 1382-1387.
- Carn M., J. P. Lahuec, D. Dagorne and B. Guillot, (1989): Rainfall estimation using TIR Meteosat imagery over the Western Sahel. 4th conf. on Satel. Meteor. and Oceanography., San Diego, AMS, pp. 126-129.
- Dugdale G., V. D. McDouglas and J.R. Milford, (1990): Potential and limitations of rainfall estimates for Africa derived from cold cloud statistics. 8th Meteosat scientific users' meeting, Norköpping, Sweden. Eumetsat Publ. EUM P08, pp. 211-220.
- Lebel, T. and L. Le Barbé, (1996): Rainfall monitoring during HAPEX-Sahel: 2. Point and areal estimation at the event and seasonal scales. *Journal of Hydrology* (to be published).
- Murphy, A. H., (1995): The Coefficients of Correlation and Determination as Measures of Performance in Forecast Verification. *Weather and Forecasting*, Vol.10, pp. 681-688.
- Toma, A. C., (1996): Variabilité spatio-temporelle des champs précipitatnts et application aux méthodes d'estimation. Thèse de doctorat de l'Ecole des Mines de Paris, 154 p.

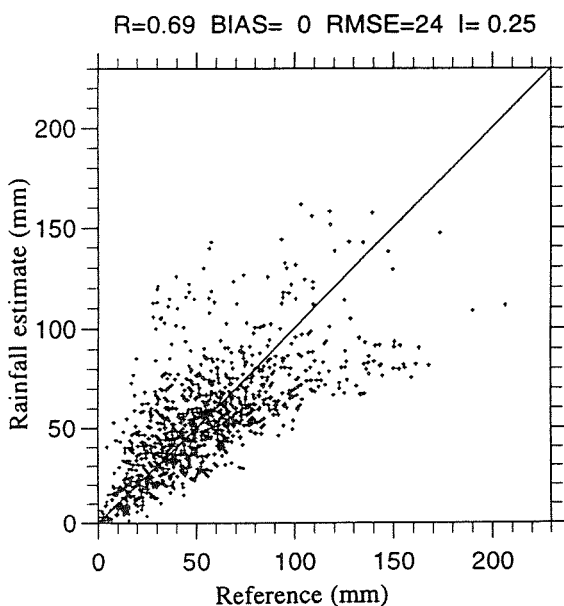
Method A



Method B



Method C



Method D

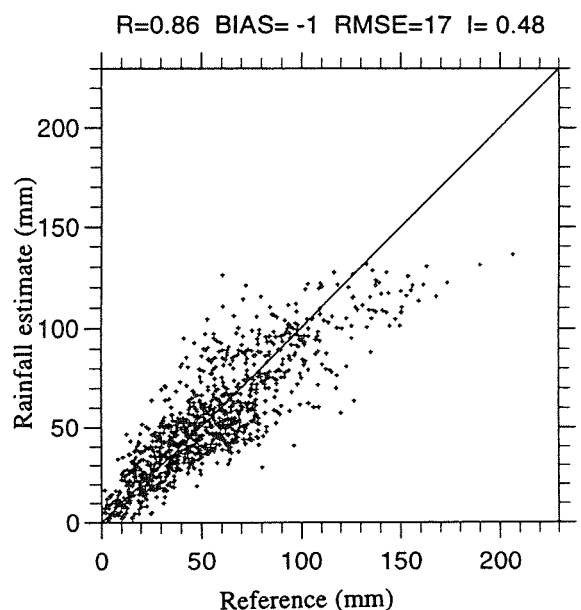


Figure 4 : Rainfall estimates for the methods A, B, C and D, for all the 10-day periods of 1992, and reference values, in mm. (1118 values)

EXPERIMENTAL RETRIEVAL OF CLOUD OPTICAL THICKNESS DURING EUCREX : COMPARISON OF THREE APPROACHES

Jacques Descloitres¹, Hanna Pawlowska², Jacques Pelon³, Jean-Louis Brenguier²,
Frédéric Parol¹, Jean-Claude Buriez¹, and Pierre Flamant⁴

¹ Laboratoire d'Optique Atmosphérique, Villeneuve d'Ascq, France

² Centre National de Recherches Météorologiques, Toulouse, France

³ Service d'Aéronomie, Paris, France

⁴ Laboratoire de Météorologie Dynamique, Palaiseau, France

1. INTRODUCTION

Because of their multiple interactions with radiation in the Earth surface-atmosphere system, clouds play an important role in the Earth radiation budget, and consequently have a strong impact on the climate. In order to characterize and estimate their influence, there is a clear need to establish a global climatology of cloud properties. The International Satellite Cloud Climatology Project (ISCCP ; Rossow and Schiffer, 1991) is the first initiative in this way.

One of the most significant parameters used to determine the cloud-radiation interactions is the cloud optical thickness, which is directly related to the drop size distribution and the liquid water path. On the one hand, such programs as ISCCP try to retrieve the cloud optical thickness from satellite measurements of visible radiances. On the other hand, general circulation models can forecast a liquid water content and then deduce radiative properties of clouds.

The aim of this paper is to compare various estimations of the optical thickness of a stratocumulus, derived from simultaneous measurements of the cloud reflectance, the lidar backscatter, and in situ microphysics.

2. INSTRUMENTS

2.1 POLDER : cloud reflectance

POLDER (POLarization and Directionality of the Earth's Reflectances) is a recent French instrument devoted to the global observation of polarization and directionality of solar radiation reflected by the Earth surface-atmosphere system (Deschamps et al., 1994). The instrument is composed of a CCD array detector, a rotating wheel which carries nine spectral and polarizing filters, and a wide field-of-view lens. An original feature

of POLDER is its ability to provide quasi-simultaneous multidirectional reflectance measurements of any scene, that means to observe a part of its BRDF (Bidirectional Reflectance Distribution Function). The instrument concept has been accepted on the Japanese ADEOS platform scheduled to be launched in August 1996. One of the scientific objectives of the satellite mission concerns the Earth radiation budget and the cloud characteristics : optical thickness, pressure, and phase. Here we used the airborne simulators of the instrument.

2.2 LEANDRE : lidar backscatter

LEANDRE 1 is a backscatter lidar dedicated to cloud and boundary layer studies at the mesoscale. It uses a Nd-Yag laser source and operates at 532 and 1064 nm. The backscattered signal is sampled with a vertical resolution of 15 m, and is recorded in the visible channel on a shot to shot basis, corresponding to a 10 m horizontal resolution. Further details on the system characteristics can be found in Pelon et al. (1990).

2.3 Fast FSSP : in situ microphysics

The Fast FSSP is a modified version of the PMS (Boulder-CO, USA) Forward Scattering Spectrometer Probe, an airborne optical spectrometer currently used for the measurements of the droplet size distributions. This modified version provides a much better accuracy for the measurements of the droplet size distribution than the standard instrument (Brenguier et al., 1996 ; Coelho et al., 1996 ; Pawlowska et al., 1996a, 1996b).

3. DATA

During the EUCREX (EUropean Cloud and Radiation Experiment) experiment in Brittany (France), the two airborne remote sensing instruments, POLDER and LEANDRE, were flown over extended low level clouds, while the Fast FSSP performed quasi-

simultaneous in situ measurements. During mission 206, 18 April 1994, a stationary stratocumulus has been sampled along a 110 km leg, perpendicularly to the low level flow, between point A ($49^{\circ}18' \text{ N}$, $5^{\circ}34' \text{ W}$) and point M ($48^{\circ}25' \text{ N}$, $4^{\circ}47' \text{ W}$). The cloud top altitude was varying from 0.8 km, with a cloud depth of 200 m, at the northern edge (point A), to 1.1 km, with a cloud depth of 200 m, at the southern edge (point M).

Despite the significant inhomogeneity of the stratocumulus at all scales, this continuous gradient of the cloud depth at the 100 km scale provides a unique data set for the comparison of the various estimations of the cloud optical depth.

3.1 POLDER data

Two airborne versions of the POLDER instrument were flown simultaneously. For both of them, the field-of-view extends up to $\pm 52^{\circ}$ in the along-track direction and $\pm 42^{\circ}$ in the cross-track direction. The first one was flown aboard the German Falcon of the DLR (Deutsche Forschungsanstalt für Luft und Raumfahrt), and the second one aboard the French Fokker-27 ARAT (Avion de Recherche Atmosphérique et de Télédétection). The respective dimensions of the CCD array were 288×242 detectors and 384×288 detectors. The altitude of the Falcon and the ARAT was 6.1 km and 4.5 km respectively, and the displacement of both aircrafts between two successive acquisitions of POLDER was around 0.9 km. In those conditions, each cloud target was observed under 14 different viewing angles from the Falcon and 9 viewing angles from the ARAT. Here it is made use of reflectance measurements without polarization at $0.86 \mu\text{m}$.

3.2 LEANDRE data

The airborne backscatter lidar LEANDRE 1 was operated from the ARAT both in zenith and nadir viewing. Results presented here have been obtained from upper altitude flights, during four legs between points M and A, using the polarized visible wavelength channel. To increase signal to noise ratio, 10 shot averages are performed. Reaching the stratocumulus layer, the backscattering increases very rapidly allowing to define precisely the altitude of the top of the cloud layer. Inside the cloud, the transmission is reduced and the detected signal is more or less rapidly decreasing, depending on the extinction coefficient. The cloud top height probability distribution function is a relevant parameter to address internal entrainment dynamics. As shown on Fig. 1, the altitude of the stratocumulus layer top is seen to decrease from 1.1 km close to the coast (point M), down to 0.8 km near the edge of the stratocumulus deck close to point A. In this region the cloud deck is breaking.

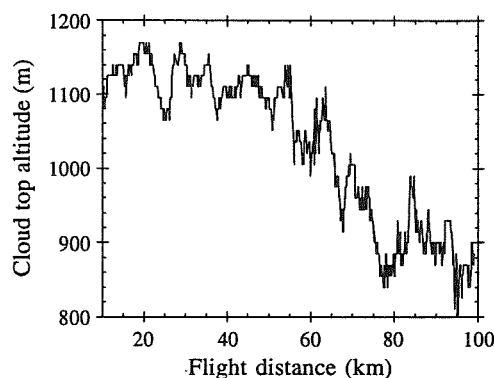


Fig. 1 : Cloud top altitude measured by LEANDRE, as a function of flight distance from point M

3.3 Fast FSSP data

The Fast FSSP was flown aboard the Météo-France instrumented aircraft, the Merlin-IV. Two procedures were used during this flight : horizontal legs just below cloud top for a statistical description of the microphysical parameters and vertical ascents and descents for the description of the vertical profiles. The sequence of these procedures for the whole flight is shown in Fig. 2. It must be noted that the aircraft is limited in its climbing or descending rate, so that a vertical profile corresponds in fact to a horizontal shift of about 5 to 10 km. Because the cells had a limited horizontal extension, it was unlikely to sample the whole depth of the cells during ascent or descent, mainly at the southern edge. On the contrary, the horizontal legs were flown close to the cloud top so that they provide information about the statistics of the values at the top of the vertical profiles. More information about the experimental strategy and the data processing can be found in Pawlowska and Brenguier (1996).

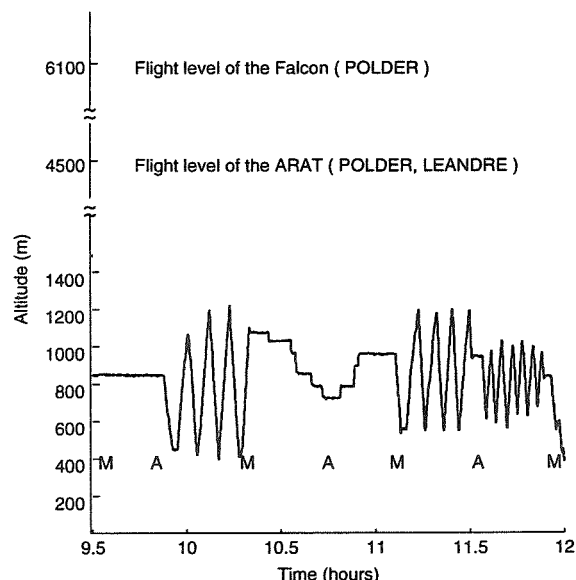


Fig. 2 : Flight pattern of the Merlin-IV along six successive legs between points M and A

4. RESULTS

For a given drop size distribution $n(r)$, where $n(r)$ is the density of droplets of radius r per unit of volume, Mie theory leads to the cloud extinction coefficient at wavelength λ

$$\sigma_{\text{ext}} = \int_0^\infty \pi r^2 Q_{\text{ext}} \left(\frac{2\pi r}{\lambda} \right) n(r) dr, \quad (1)$$

where Q_{ext} is the Mie extinction factor. We can define $\overline{Q_{\text{ext}}}$ so that

$$\sigma_{\text{ext}} = \overline{Q_{\text{ext}}} \int_0^\infty \pi r^2 n(r) dr. \quad (2)$$

Moreover, the expression of the liquid water content w is

$$w = \int_0^\infty \frac{4}{3} \pi r^3 \rho n(r) dr, \quad (3)$$

where ρ is the liquid water density ($\rho = 1000 \text{ kg.m}^{-3}$). If we introduce the mean effective radius r_e of the distribution (Hansen and Travis, 1974), σ_{ext} is related to w and r_e by

$$\sigma_{\text{ext}} = \frac{3 w \overline{Q_{\text{ext}}}}{4 r_e \rho}. \quad (4)$$

When integrating along a vertical profile, the cloud optical thickness is related to w and r_e by

$$\delta = \int_{\text{base}}^{\text{top}} \sigma_{\text{ext}}(z) dz = \int_{\text{base}}^{\text{top}} \frac{3 w(z) \overline{Q_{\text{ext}}(z)}}{4 r_e(z) \rho} dz. \quad (5)$$

The mean effective radius, as measured by the Fast FSSP, is around $6 \mu\text{m}$ (see Fig. 3a), which leads to a value of 2.2 for $\overline{Q_{\text{ext}}}$.

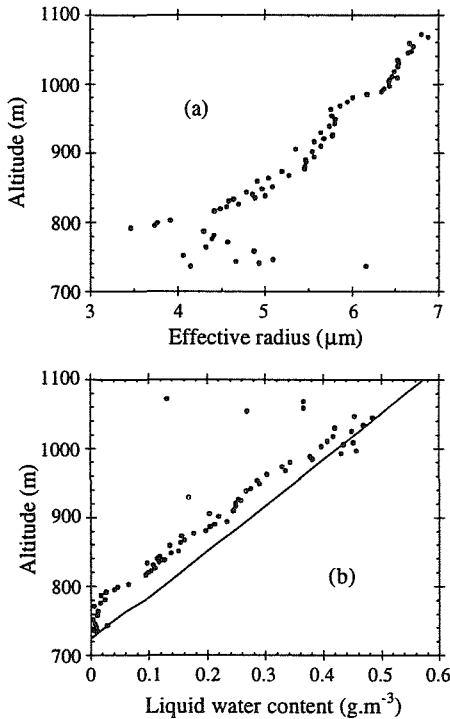


Fig. 3 : Typical profile of effective radius (a) and liquid water content (b) measured by the Fast FSSP ; the dots are measurements and the solid line corresponds to the adiabatic liquid water content

In a first step, the cloud optical thickness is calculated by integrating the $w(z)/r_e(z)$ ratio measured with the Fast FSSP along the vertical profiles. However, the number of profiles per leg is not sufficient for a significant description of the general trend of the cloud depth and the related optical thickness, but they suggest that w/r_e varies linearly with altitude and that the maximum value at the top corresponds to the adiabatic value. This empirical result is then used to estimate the cloud optical thickness from the values of w/r_e measured along the horizontal legs just below cloud top, assuming the profile is linear, even when the measured value is lower than the adiabatic value. The estimates derived from the data sampled along the horizontal legs have been plotted, and the envelope of the maximum values is represented in Fig. 4 by a solid line, with the estimates derived from integration along the vertical profiles (dots) (Pawlowska and Brenguier, 1996).

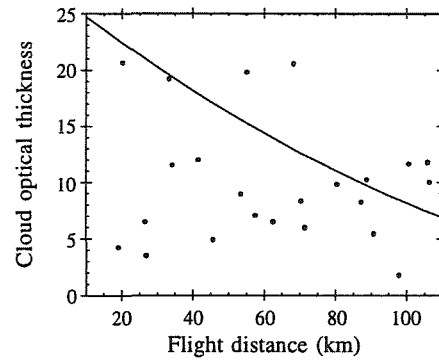


Fig. 4 : Cloud optical thickness retrieved from the Fast FSSP as a function of flight distance from point M ; the dots correspond to vertical profiles, while the solid line is the optical thickness derived from measurements at the top of the cloud during the horizontal legs

The cloud optical thickness is also estimated from the POLDER radiance measurements, assuming the plane-parallel approximation. For each cloud target, the reflectance set is compared to the plane-parallel model, using the discrete ordinate method (Stamnes et al., 1988). The cloud optical thickness is adjusted so that the mean reflectance over the different viewing angles equals the plane-parallel one (Descloîtres et al., 1995). For these computations, which are almost not dependent on the drop size, a fixed size distribution with $r_e = 6 \mu\text{m}$, very close to the Fast FSSP measurements, is assumed. The cloud optical thickness map of the $110 \text{ km} \times 11 \text{ km}$ scene, observed from the Falcon along one leg, is reported in Fig. 5, and the quasi-simultaneous location of the Merlin-IV as well.

In view of both the uncertainty on the location of the three aircrafts and the slight lag between the respective measurements, it is not possible to perform an instantaneous comparison between POLDER and the Fast FSSP measurements, according to the rather inhomogeneous aspect of the cloud. Therefore, the cloud

optical thickness retrieved from the two POLDER instruments is averaged over sections of 10 km along five legs, as shown in Fig. 6.

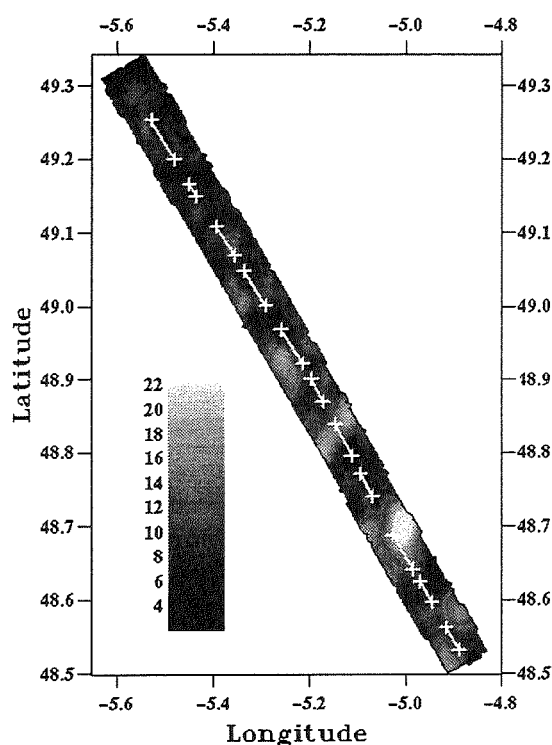


Fig. 5 : Cloud optical thickness map established from POLDER measurements and corresponding cloud sections sampled by the Fast FSSP along vertical profiles (white segments limited by crosses)

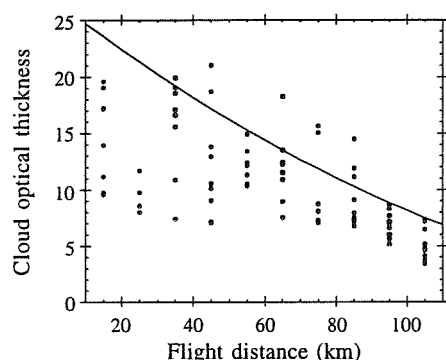


Fig. 6 : Cloud optical thickness retrieved from POLDER along five legs from both the ARAT and the Falcon (dots), and that established from the Fast FSSP measurements at the top of the cloud (solid line)

At last, the lidar measurements provide the cloud top altitude, from which we can derive the cloud optical thickness, assuming the liquid water content profile is adiabatic. In addition, the extinction coefficient of the very top of the cloud layer can be deduced directly from the attenuation of the backscatter signal. In the near future, those results will be compared to the values retrieved from both POLDER and the Fast FSSP.

5. CONCLUSION

Despite the heterogeneity of the observed cloud, and the strong horizontal variations of optical thickness, it is remarkable that both POLDER and the Fast FSSP give a comparable mean value (around 10) and the same extremes (values from 2 to 21). Furthermore, the general trend of the cloud optical thickness is retrieved from both instruments, and it follows the same trend as the top altitude measured by the lidar. Since the extinction coefficient profile derived from the Fast FSSP measurements is rather stationary, the optical thickness appears mainly related to the cloud depth. In the near future, a more advanced use of the lidar measurements will be helpful to perform more accurate comparisons.

6. ACKNOWLEDGMENTS

This research was supported by EEC (European Economic Community), CNES (Centre National d'Etudes Spatiales), Météo-France and INSU (Institut National des Sciences de l'Univers) under grant D13570. The authors are grateful to Pr. Y. Fouquart, and to all persons who also participated in EUCREX.

7. REFERENCES

- Brenguier, J. L., D. Trevarin, R. Peytavi, A. Coelho, P. Wechsler, and J. Isbert, 1996 : New electronics for the Forward Scattering Spectrometer Probe : The Fast FSSP. Accepted in *J. Atmos. Oceanic Technol.*
- Coelho, A., J. L. Brenguier, and T. Bourianne, 1996 : A model for the Fast FSSP operation. *Proceedings of the ICCP 1996*.
- Deschamps, P. Y., F. M. Bréon, M. Leroy, A. Podaire, A. Bricaud, J. C. Buriez, and G. Sèze, 1994 : The POLDER mission : instrument characteristics and scientific objectives. *IEEE Trans. Geosci. Remote Sensing*, **32**, 598-615.
- Descloutres, J., F. Parol, and J. C. Buriez, 1995 : On the validity of the plane-parallel approximation for cloud reflectances as measured from POLDER during ASTEX. *Ann. Geophysicae*, **13**, 108-110.
- Hansen, J. E., and L. D. Travis, 1974 : Light scattering in planetary atmospheres. *Space Sci. Rev.*, **16**, 527-610.
- Pawlowska, H., and J. L. Brenguier, 1996 : A study of the microphysical structure of stratocumulus clouds. *Proceedings of the ICCP 1996*.
- , —, and G. Salut, 1996a : Optimal non-linear estimation for particle measurements. Submitted to *J. Atmos. Oceanic Technol.*
- , —, —, 1996b : Optimal non-linear estimation for particle measurements. *Proceedings of the ICCP 1996*.
- Pelon, J., P. H. Flamant, M. Meissonnier, 1990 : The French airborne backscatter lidar LEANDRE I : Conception and operation. V. E. Zuev ed., 15th ILRC, Institute of Atmospheric Optics pub., Tomsk, USSR, p. 36.
- Rosow, W. B., and R. A. Schiffer, 1991 : ISCCP cloud data products. *Bull. Amer. Meteor. Soc.*, **72**, 2-20.
- Stamnes, K., S. C. Tsay, W. Wiscombe, and K. Jayaweera, 1988 : Numerically stable algorithm for discrete-ordinate-method radiative transfer in multiple scattering and emitting layered media. *Appl. Opt.*, **27**, 2502-2509.

PRECIPITATION RATE ESTIMATION IN TROPICAL MARITIME CLOUDS

Christian Asselin de Beauville and Constantin A. Pontikis

Université des Antilles et de la Guyane/METEO France, Faculté des Sciences, Laboratoire de Physique de l'Atmosphère Tropicale, 97159, Pointe à Pitre Cedex, Guadeloupe (F.W.I.), France.

1. Introduction

Numerous convective cloud rain rate estimation techniques based upon the use of satellite infrared imagery data relate given precipitation intensities R to the coldest cloud surfaces S (Negri et al., 1984; Adler and Negri, 1988; Arkin and Meissner, 1987; Richards and Arkin, 1981; Morissey and Greene, 1993). These surfaces are usually delimited by an upper temperature limit whose value varies between 225K and 253K, thus considering that the precipitation rates developed in clouds with cloud top heights lower than the 253K isotherm height are negligible. However, it is well known that tropical convective clouds are often capable of developing important precipitations even if cloud top heights are considerably lower than the 0°C isotherm height (Mason, 1971). Leopold and Halstead (1948) have indicated that "a majority of tropical convective showers comes from clouds which do not reach sub-freezing temperatures". More recently, Pruppacher and Klett (1978) have reported that "continental type clouds need to build considerably higher than maritime clouds, and must become considerably wider" before radar echos corresponding to precipitation appear and also, "the higher the cloud base, the higher the level in the cloud at which precipitation echos develop". The capability of tropical maritime warm clouds with low bases of developing precipitation attenuates the validity of the relations between the precipitation rate and the coldest cloud areas ($T < 253K$). As a consequence, the use of the above mentioned techniques in maritime tropical convective clouds could in some cases lead to underestimated rain rate values.

The main goals of this paper are to present the comparison between precipitation rates produced by warm and mixed phase cloud systems in the vicinity of the island of Guadeloupe (F.W.I.) and to present a rough algorithm that takes into account the contribution of the warm cloud regions. The precipitation rates have been calculated at ground level on a 24 hour base by using data obtained from the meteorological rain gauge network of the island.

2. Warm rain development and observations

Warm rain development starts when the cloud droplets have reached a critical radius of 20mm and are capable of initializing the collision-coalescence process. Clouds developing in continental air masses are characterized by high droplet concentration values ranging between 200cm^{-3} and 1000cm^{-3} . In such clouds, the water vapor condensed between cloud base and the 0°C isotherm height is not sufficient to lead to 20mm radius droplets and precipitation develops only when large ice crystals have been formed at higher altitudes (Bergeron process). In contrast, tropical maritime clouds are characterized by low droplet concentrations that range between 50cm^{-3} and 200cm^{-3} . Simple calculations reveal that in such clouds the droplets reach the critical 20mm radius as from 2000m above cloud base. Further, in such clouds vertical velocities are low (Jorgensen and Lemone, 1989), thus allowing droplets to coalesce before reaching the 0°C isotherm level. It appears that convective tropical maritime clouds are most probably capable of producing precipitation even if cloud top heights are still located in the positive temperature region. The partial inefficiency of the Bergeron process in such clouds is also attested by the quasi-absence of supercooled droplets above the -5°C isotherm level in mature hurricanes (Black and Hallett, 1986). This is also consistent with radar observations revealing very low large ice crystal concentrations in the mixed phase region of tropical maritime clouds. As a consequence, the precipitation issued from warm cloud systems that have developed in typically tropical maritime air masses should in some cases be comparable to the precipitation developed in cloud systems with cloud top heights largely exceeding the 0°C isotherm level.

The precipitation issued from 50 cloud systems that crossed the Carribean archipelago during 1994 has been studied in relation to the coldest cloud surface temperatures T_{\min} determined by using the IR METSAT 3 images. Tables 1 and 2 present T_{\min} for a given day as well as the corresponding mean and maximum rain-rates

observed at ground level on the flat (east) part of the island for some selected cases. They correspond to cloud systems with roughly similar horizontal extents that are active during comparable time periods over the island. It appears that in some cases the precipitation issued from warm cloud systems are non negligible when they are compared to the precipitation issued from systems with an important mixed phase region.

date	T _{min} (°C)	RE (mm/24h)	R _{max} (mm/24h)
June 23	-2.0	1.0	6.5
June 24	8.0	1.0	3.3
June 27	10.0	1.0	2.0
June 28	1.5	2.0	11.5
August 5	1.5	2.0	7.5

Table 1 : Examples of mean and maximum precipitation rates corresponding to ice-free cloud systems.

date	T _{min} (°C)	RE (mm/24h)	R _{max} (mm/24h)
May 17	-35.0	2.0	14.0
June 16	-27.0	3.0	9.1
Sept. 15	-68.0	8.0	31.0
Nov. 10	-52.0	1.0	18.0
Dec. 7	-52.0	9.0	25.0

Table 2 : Examples of mean and maximum precipitation rates corresponding to cloud systems with coldest temperatures lower than -20°C.

Since the rain-rates were available on a 24 hour base, cloud systems have been considered as warm only if the coldest cloud temperatures did not exceed -10°C during the corresponding 24 hours. As an example, Table 3 presents the evolution of the coldest cloud surface temperature between 0h and 24h local time for the cloud system observed on June 23.

time	02.00	10.00	15.00	20.00	22.00
T _{min} (°C)	13.0°	13.0°	12.5°	-2.0°	-1.0°

Table 3 : Evolution of the coldest cloud surface temperature (23 June 1994) as a function of time.

3. Relation between R_{max} and T_{min}

The maximum rain-rates observed over the flat part of the island of Guadeloupe have been related to the coldest cloud surface temperatures. As an example, Figure 1 presents R_{max} as a function of T_{min} for some cloud systems presenting similar horizontal extent characteristics. This figure shows that at ground level, for some cloud systems with T_{min}<0°C, the precipitation rates are comparable to the rates observed for warm cloud systems.

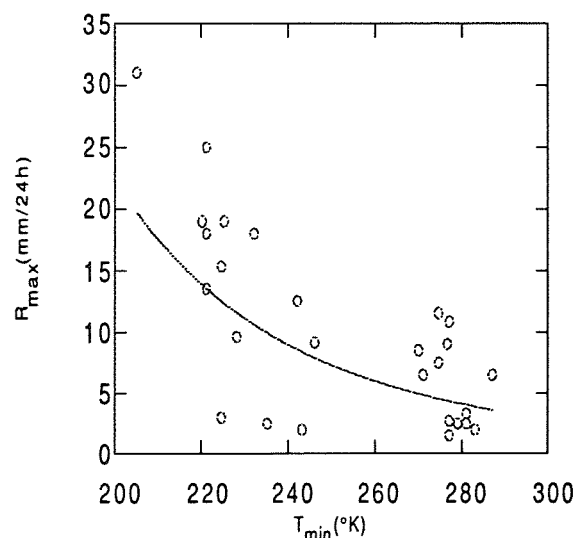


Figure 1 : Maximum 24 hour observed rain-rates as a function of the coldest cloud surface temperature.

Further, this figure suggests that for these cloud systems, the maximum rain-rate is proportional to a power of the coldest cloud surface temperature. The power regression best-fit line is also shown in this figure and is given by the equation :

$$R_{max} = 8.1247 \times 10^{-12} (T_{min})^{-5.0238} \quad (1)$$

whereby the correlation coefficient is equal to 0.77. The best-fit linear regression line for the (T_{min}, R_{max}) points corresponding to T_{min}<253 K is given by the equation :

$$R_{\max}(T < 253\text{K}) = 138.94 - 0.5478T_{\min} \quad (2)$$

This line is shown in Figure 2. The corresponding correlation coefficient is equal to 0.72. The regression line intersects the T_{\min} axis ($R_{\max}=0$) at $T=253.6$ K, thus suggesting that in these cloud systems the Bergeron process is the only mechanism of precipitation formation. Note that the air masses in which these cloud systems have developed were most probably not clearly maritime since they were mostly related to synoptic perturbations. In such cloud systems that are characterized by high droplet concentrations the Bergeron process is active, thus leading to an important contribution of the mixed phase in the development of precipitation.

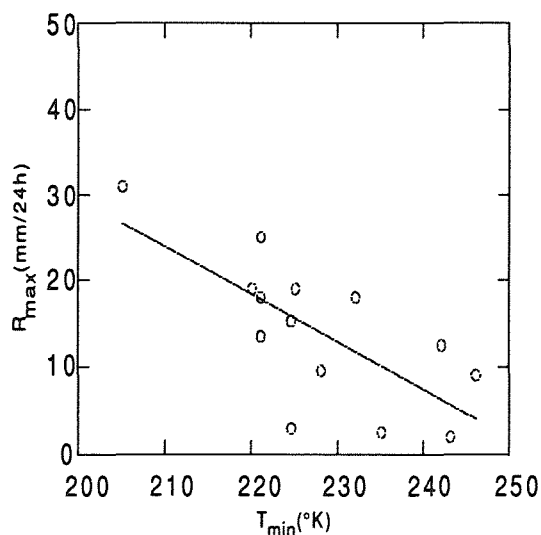


Figure 2 : R_{\max} for cloud systems with revealing surface temperatures colder than 253 K.

Further, a rough estimation of the maximum contribution of ice free clouds to the total 24 hour maximum precipitation leads to $R_{\max} \approx 12\text{mm}$. It is clear that cloud systems with important horizontal extents that last for a very long time over the island may produce very large precipitation amounts at ground level independently of the involved precipitation formation mechanisms, thus leading to very high rain-rates. As an example, the very large cloud

systems observed over the island on the 21 of October ($T_{\min} = -61^\circ\text{C}$) and on the 11 of November ($T_{\min} = -68^\circ\text{C}$) led respectively to $R_{\text{E}} = 33\text{mm}/24\text{h}$, $R_{\max} = 103.5\text{mm}/24\text{h}$ and $R_{\text{E}} = 12\text{mm}/24\text{h}$, $R_{\max} = 84\text{mm}/24\text{h}$.

4. R algorithm

In order to take into account the contribution of all cloud regions, the temperature scale (13°C , -75°C) has been divided into 6 intervals (13°C , 0°C), (0°C , -10°C), (-10°C , -20°C), (-20°C , -40°C), (-40°C , -60°C) and (-60°C , -75°C), hereafter represented by the indices 1, 2, 3, 4, 5, 6. The mean rain rate R may be obtained by using a multiple regression that relates R to the cloud system surface expressed in pixels P corresponding to each temperature interval :

$$R = -11.6048 + (1.6264P_1 + 14.6P_2 - 14.8P_3 + 6.2P_4 - 3.4357P_5 + 1.5P_6)10^{-2} \quad (3).$$

The corresponding correlation coefficient is equal to 0.75.

5. Conclusion

In this work, the combined analysis of the rain-rates observed on a 24 hour base at ground level on the flat part of the island of Guadeloupe and the IR determined coldest cloud surface temperatures leads to the conclusion that tropical convective maritime warm clouds may produce precipitation amounts that are similar to the precipitation amounts produced by mixed phase clouds in which the Bergeron process is exclusively operating.

An algorithm is presented that allows the estimation of the mean rain-rate observed at ground level. Since the statistical sample is small, further validation using a larger data set is necessary.

References

- Adler, R. F., and A. J. Negri, 1988 : A satellite infrared technique to estimate tropical convective and stratiform rainfall. *J. Clim. Appl. Meteor.*, 28, 30-51.
- Arkin, P. A., and B. N. Meissner, 1987 : The relationship between large-scale convective rainfall

- and cold cloud over the western hemisphere during 1982-84. *Mon. Wea. Rev.*, 115, 51-74.
- Black, R. A., and J. Hallett, 1986 : Observations of the distribution of ice in hurricanes. *J. Atmos. Sci.*, 43, 802-822.
- Jorgensen, D. P., and M. A. Lemone, 1989 : Vertical velocity characteristics of oceanic convection. *J. Atmos. Sci.*, 46, 621-640.
- Leopold, L. B. and Halstead, M. H., 1948 : First trials of the Shaefer-Langmuir dry ice cloud seeding technique in Hawaii. *Bull. Am. Met. Soc.*, 29, 525.
- Mason, B. J., 1971 : *The physics of clouds*. Clarendon Press, Oxford, p.p. 671.
- Morrissey, M. L., and Greene, 1993 : Comparison of two satellite-based rainfall algorithms using pacific atoll raingage data. *J. Appl. Meteor.*, 32, 410-425.
- Negri, A. J., R. F. Adler, and P. J. Wetzel, 1984 : Rain estimation from satellites : An examination of the Griffith-Woodley technique? *J. Clim. Appl. Meteor.*, 23, 102-116.
- Pruppacher, H. R. and J. D. Klett, 1978 : *Microphysics of clouds and precipitation*. D. Reidel publishing company, p.p. 714.
- Richards, F., and P. Arkin, 1981 : On the relationship between satellite-observed cloud cover and precipitation. *Mon. Wea. Rev.*, 109, 1081-109

MARINE BOUNDARY LAYER CLOUD FORMATION AND CHARACTERISTIC MEASUREMENTS MADE BY LIDAR DURING ACE-1

Bruce M. Morley¹, Darrel Baumgardner¹ and Craig Walther²

¹Research Aviation Facility, National Center for Atmospheric Research*, Boulder, CO, USA

²Remote Sensing Facility, National center for Atmospheric Research, Boulder, CO, USA

1. INTRODUCTION

The Atmospheric Technology Division (ATD) of NCAR has developed an aerosol lidar for use from the Research Aviation Facility (RAF) aircraft and from Surface and Sounding Systems Facility (SSSF) Integrated Sounding System (ISS). The Scanning Aerosol Backscatter Lidar (SABL) was deployed for the first time during the Aerosol Characterization Experiment-1 (ACE-1) in late 1995. SABL was used as a nadir- and zenith-looking lidar system during ACE-1 and is expected to evolve over time into a cross track scanning volume imager. During ACE-1, SABL was used to map the vertical aerosol structure and illuminate the complex mixing processes of the marine boundary layer and the free troposphere over the southern oceans. These backscatter maps were used as a real-time guide for *in situ* sampling of air masses that had different backscatter properties and possibly different origins. For the post-flight data analysis we have included measurements made with some of the aerosol probes that were in use when the lidar data were taken.

2. INSTRUMENTATION AND OPERATIONS

SABL is a two-wavelength Nd:YAG lidar system that ATD has developed with two main goals. The first was to develop an instrument that could be used in real-time by scientists to see the aerosol back-scatter structure of the atmosphere. This qualitative information could be used to help determine the next steps the investigator would take. One example of this would be to direct the aircraft to a layer where there is some unusually high or low backscatter indicated. The second objective was to be able to make quantitative measurements of aerosol properties. Extinction coefficients, scattering ratios and backscatter coefficients are some of the quantitative properties that we plan to determine in post-flight data

analysis. Table 1 is a summary of SABL specifications.

Wavelength/energy	1064 nm/75 mJ 532 nm/50 mJ
Pulse length	15 nsec
Pulse rate	Up to 60/second
Beam divergence	1 mrad to 4 mrad adjustable
Telescope diameter - speed	14 inch - f/5
Telescope field-of-view	1 mrad to 4 mrad adjustable
Background filter bandwidth	0.92nm @ 1064nm 0.16nm @ 532nm
Detectors	APD @ 1064nm PMT @ 532nm
Digitizer - 2 channel	12 bits up to 40MHz
Range gates / channel	Up to 2500
Recording media	Exabyte tapes
Transmitter/receiver size / weight	15 X 15 X 32 inches / 110 pounds
Computer / operating system	VMEBus/VxWorks for data acquisition Sun Sparc-5 for data display and system control

Table 1. SABL Specifications

Simple backscatter lidars have been used to profile the lower atmosphere almost since the laser arrived on the geosciences scene (Measures, 1984) and were used almost immediately on

*The National Center For Atmospheric Research is sponsored by the National Science Foundation.

aircraft (Uthe, 1980). Limitations with both transmitter and receiver stability together with calibration complexity have conspired to relegate airborne backscatter lidars to a descriptively very useful and largely qualitative role (McElroy, et al., 1981, Radke, et al., 1989 and Morley, et al., 1990).

However, a number of the technological advances which have provided the thermal and temporal stability necessary for airborne differential absorption techniques, Browell, et al., 1988 and Nielsen, et al., 1992, have been incorporated into SABL. The early results described here are extremely gratifying as we have begun to explore some of SABL's quantitative aspects.

The conceptual design for the SABL transmitter/receiver module was done at NCAR. The detailed optical/mechanical design and construction of SABL were done by Lentec Corporation of Albuquerque, NM. Some of our goals in the design of SABL were to maximize the signal-to-noise ratio and to build a stable instrument, one that would not require a lot of operator fine tuning to perform well. The critical components of the telescope are built of low expansion materials so that the optical performance will not change with large temperature changes.

The receiver is built on a rigid optical plate that also serves as the baseplate of the telescope. This was done to minimize the effect of vibration on system performance. To maximize the signal-to-noise ratio we have done several things in component selection. In the infrared channel we control the temperature of the silicon avalanche photodiode (APD) with a thermoelectric cooler. This does two things; it reduces the dark current noise of the detector and it keeps the gain of the detector stable. We also control the temperature of the photomultiplier tube (PMT) used to detect the green signal. The benefit of cooling the PMT is not in reduced dark current but in gain stability.

To reduce the background noise in the system we use narrow-band interference filters. We have filters of less than 1.0 nm at this time and will obtain filters of less than 0.2nm in the near future. The combination of cooled detectors and narrow filters will result in a system which is dark current limited except under high background light level conditions.

A two-channel 12-bit, 40-MHz digitizer is used in the receiver. Using these high dynamic

range digitizers enables us to record the signals from the detectors without using logarithmic amplifiers. Removing the logamps from the receiver has made the analysis for quantitative aerosol properties easier and more accurate. For the operator and scientist displays, we have the option of displaying either logarithmic/range corrected data or raw lidar data. Either the scientist or the lidar operator can save any interesting display image to a disk file by clicking on a button on the display screen. This image can be displayed or printed out at a later time to show colleagues. We plan to have an onboard printer working on the C-130 so that the scientist can walk off the aircraft after a flight with examples of lidar data.

3. DATA EXAMPLES AND ANALYSIS

Figures 1 and 2 are plots of the scattering ratio, total backscatter over Rayleigh backscatter at the green or 532nm (Figure 1.) and infrared or 1064nm (Figure 2.) wavelength of the laser. These measurements were taken during the Aerosol Characterization Experiment-1 (ACE-1) southwest of Tasmania. The time of the measurements was

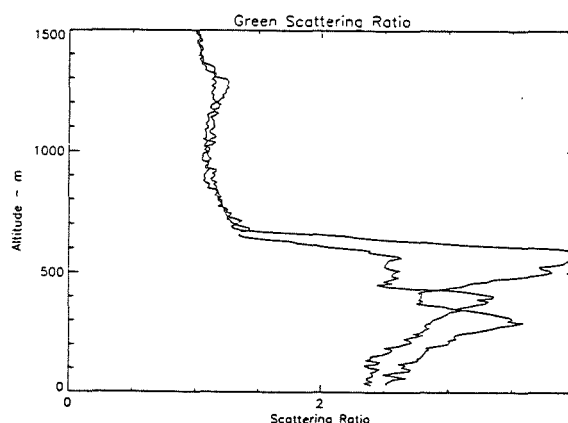


Figure 1. Green (0.532nm) Scattering Ratio of SABL lidar data, December 7, 1995, 2112-3 UTC.

December 7, 1995 at 2112-3 UTC. Over the Indian Ocean the meteorological conditions were clear with small cumulus clouds starting to form at the top of the marine boundary layer. Two backscatter profiles are shown in each figure and in neither case was there significant signal attenuation; in other words there were no optically thick clouds in the lidar path for either profile. There were however a significant differences between the return signals at different wavelengths and also at the same wavelengths at different times. The first return signal at both wavelengths had a high return signals at 600 meters above the surface with a second smaller

peak near 300 meters above the surface. In the infrared return signal the scattering ratio exceeds 100 in the first profile while it peaks at approximately 20 in the second return. The green return signal behaves in a similar manner but the differences are not as dramatic. The peak return signal from the first profile peaks at about 4.0 while the second backscatter profile peaks at about 3.3. There is no high level (600 meter) return signal peak in the second profile at either wavelength. The peak that occurs at 300 meters in the first profile has shifted to about 400 meters in the second profile. This is not unreasonable as the two profiles are separated in time by one minute and in distance by about 6 kilometers.

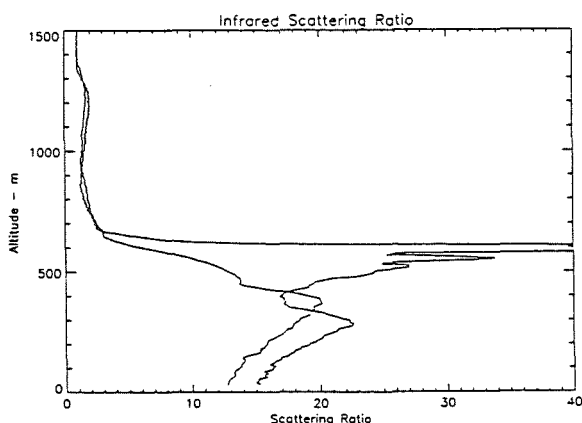


Figure 2. Infrared (1.064nm) Scattering Ratio of SABL lidar data, December 7, 1995, 2112-3 UTC.

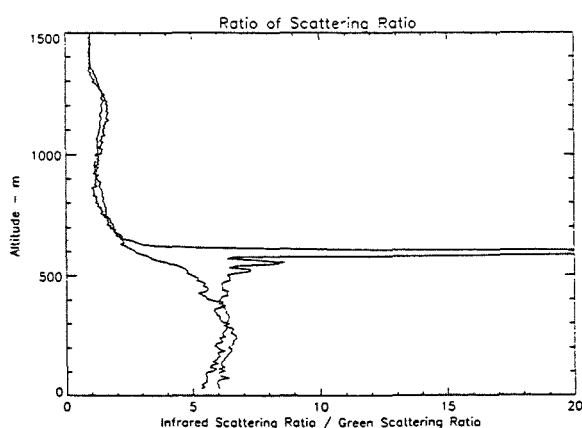


Figure 3. Ratio of Scattering Ratios, December 7, 1995, 2112-3 UTC.

Figure 3 is the ratio of scattering ratios (infrared scattering ratio / green scattering ratio). This ratio removes the effects of changes in number density from the profiles and leaves information about the size distribution. In Figure 3 this characteristic of little change in the ratio of scattering ratios is also true in the marine boundary layer. The only place where this does not hold is at the top of the boundary layer, where

the small cumulus clouds begin to form. The best explanation for this is that in the first backscatter profile there was some growth of the aerosols which changed the size distribution so that there were more large particles. This region is where cloud droplet are just beginning to form on active cloud condensation nuclei (CCN). The second lidar profile was taken where the CCN are not active.

Figure 4 is a ratio of scattering ratios plot from SABL data taken earlier in ACE-1 in the Kilauea volcano plume. There are three distinct air masses in this profile. There is a clean (nearly Rayleigh) atmosphere above 1700 meters. The volcano plume is between 600 and 1500 meters. The aerosols in this region are formed through gas phase chemistry and have a small size distribution. The lowest layer, from the surface to 600 meters, is the marine boundary layer which is characterized by aerosols with a large size distribution. It should be noted that the ratio plotted in Figure 4 does not change much inside any of the three distinct layers even though the number density can and does change inside the volcano plume and also the marine boundary layer.

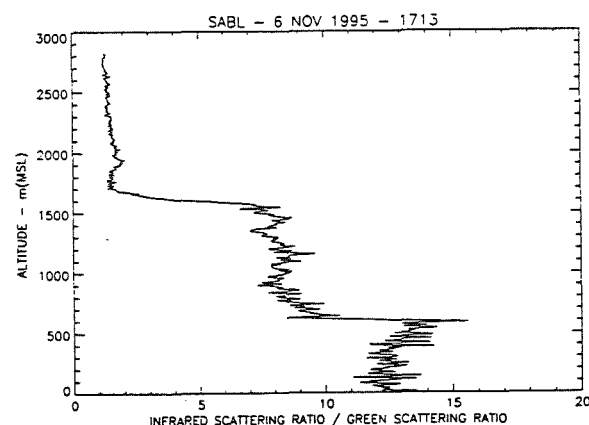


Figure 4. Ratio of Scattering ratios, November 6, 1995, 1713 UTC.

4. CONCLUSIONS

The SABL lidar has been shown to a useful tool for investigating both the quantitative optical properties atmospheric aerosols as well as providing scientists with a real-time qualitative image of aerosol structure and atmospheric mixing processes. The real-time information is useful to scientists because it can help direct the aircraft to atmospheric areas of interest that are revealed by either high or low backscatter. The quantitative data that is obtained in post-flight data processing

can be combined with *in situ* measurements to compute aerosol properties away from the aircraft and extend the range of the *in situ* measurements away from the aircraft. We also plan to try and compute atmospheric loading of aerosols and other *in situ* species measurements that are made from the aircraft.

5. ACKNOWLEDGMENTS

The development of SABL could not have occurred without the support of the National Science Foundation and the encouragement and support of Richard Carbone, David J. Carlson, Peter H. Hildebrand and Lawrence Radke. The coordinating efforts of the first Aerosol Characterization Experiment investigators, especially Barry Huebert, were also crucial. The display and control software was developed by Charlie Martin, NCAR/SSSF.

6. REFERENCES

- E.V. Browell, G.L. Gregory, R.C. Harriss, V.W.J.H. Kirchhoff, 1988: "Tropospheric ozone and aerosol distributions across the Amazon Basin." *J. Geophys. Res.*, 93, pp. 1431-1451.
- J.L. McElroy, J.A. Eckert, C.J. Hager, 1981: "Airborne downlooking lidar measurements during STATE 78." *Atmospheric Environment*, 15, pp. 2223-2230.
- R.M. Measures, 1984: *Laser Remote Sensing*. New York: Wiley.
- B.M. Morley, E.E. Uthe, W. Vizee, 1990: "Airborne lidar observations during AGASP-2," *Journal of Applied Meteorology*, vol. 29, pp.268-271.
- N.B. Nielsen, E.E. Uthe, J.M. Livingston, E.J. Scribner, 1992: "Compact airborne lidar mapping of lower atmospheric ozone distributions," In: *Lasers '91 Proceedings of the 14th International Conference on Lasers and Applications, San Diego, CA, Dec. 9-13, 1991*. McLean, VA, STS Press, pp. 332-339.
- L.F. Radke, C.A. Brock, J.H. Lyons, P.V. Hobbs, 1989: "Aerosol and Lidar Measurements of Hazes in Mid-Latitude and Polar Airmasses," *Atmospheric Environment*, Vol. 23, No. 11, pp. 2417-2430.
- E.E. Uthe, W.L. Jimison, N.B. Nielsen, 1980: SRI International Corp., Menlo Park, CA. Atmospheric Science Center, 45P., Report No. EPRI-EA-1538.

AUTOMATED RADAR SYSTEM MRL-INFO

Ekba Ya.A.

Atabiev M.D., Kapitannikov A.V., Kaplan L.G.

Scientific and Production Geophysical Center,
Stavropol, Russia

1. Introduction

The MRL-INFO system is designed to obtain, process, store and to transmit data on cloudiness, as well as for influence control and its results checking at precipitation artificial enhancement and hailing protection by an aircraft method. It can also solve the problem of storm warning, identification of the nature dangerous phenomena and of operation within the system of air traffic, etc.

An important feature of the System is that at the fulfilment of the afore - enumerated tasks, which are multi-factor ones, separate parts of the tasks are being solved simultaneously with various computers, what provides for much higher efficiency and flexibility of the MRL-INFO system as compared with other automated radiolocation systems of analogous purpose.

2. Equipment and software composition

Automated radar system MRL-INFO

includes a stock-produced meteoradar MRL-5 and the computerized data processing system developed at the Stavropol SPGC (Fig. 1).

The automated data processing and control system includes the following subsystems:

- radar MRL-5 control, its conditions check and data primary processing;
- data storage, analysis and presentation on users request;
- data exchange with laboratory -planes and communication with the users.

The automated data processing and control system comprises the following devices: a personal user's computer IBM PC AT 486 - 3 pcs; a check-and-control board for MRL-5; a board for video signals analog-to-digital conversion; a board for sound data input - output; a modem plate; a stream - line chromatic printer - plotter; a VHF radio station "Backlan" type; an uninterrupted power supply unit - 3 pcs; automated data processing and control system software components; an operating system MS DOS 6.2; a

programme for MRL-5 check and control input (BORLAND PASCAL 7.0); a communication driver; an operating system WINDOWS 3.1; an radar

information (data) analysing system (BPW); a telephone line servicing programme (COMM); radio channel servicing programme (COMMR).

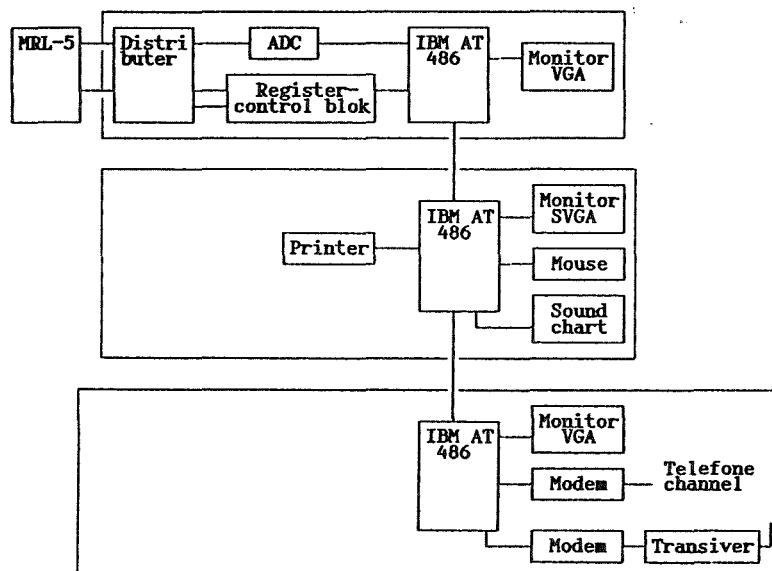


Fig.1. Automated radar system MRL-INFO

3. Solvable problems

This System enables to obtain full information on meteoroprocesses and the effected activity. The tasks of radiolocation data collection and primary processing, data secondary processing and representation as well as those of communication with planes and activity checking are solved with the appropriate computers separately at that. This makes it possible to solve several problems simultaneously and, thus, to reduce considerably the time required to take the decision on activity and to carry it out as well as to provide for the activity maximum efficiency at minimum time, efforts and means expenditures.

The System provides for the

following:

- radar data obtaining in the scanning hemisphere within the time period of not more than 3,5 min (17 revolutions) by two wave lengthes;
- general data representation on cloudiness presence, intensity, the direction and speed of its movement, as well as the development tendency within the range of up to 240 km;
- detailed data representation on cloudiness of high resolution at the distance of 120 km; including the altitudes of the upper and lower boundaries, radar reflectability representation with the gradation in 10 dB, the movement direction and speed, the presence of sheds and overhangs;
- generation and representation of specialized data on meteorphenomena, including clouds water content, rain

intensity, hail presence and intensity;

- measuring of precipitation summary quantity within the range of 120 km from the place of the radar location;

- generation of instructions on activity upon the processes in the clouds and transmission then aboard the planes;

- reception and representation of the transmitted from planes data on the atmosphere parameters, flight route and on the carried out effect;

- the activity results check in the real time scale and in the activity period as a whole;

Within the framework of the enumerated tasks the following subtasks are solved:

- automatic switching on and diagnostics of the MRL-5 equipment;

- automatic switching the radar equipment off when the survey is completed;

- automatic switching the equipment off when an emergency signal is received and audible warning to the attending personnel;

- automatic control of the antenna;

- automatic change of the switching on periodicity of the survey operating modes in accordance with the received meteodata;

- electromagnetic modes radiation, reception and amplification at two wave lengths (3.2 cm and 10 cm);

- digital spatial-and-temporal filtering of the two channels video signals;

- turbulent zones allocation;

- filtering of impulse noise and cluttering permanent echoes;

- calculation of the survey

integral characteristics;

- calculation of the cloud processes radiolocation characteristics;

- identification of meteophenomena, including especially dangerous in accordance with the given criteria;

- transmission of general data about meteophenomena and the equipment conditions by an audible signal through a telephone channel;

- definition of clouds suitable for indication in activity aimed at precipitation enhancement;

- indication of sites for activity at precipitation enhancement and hail-fighting in a semi-automatic regime;

- representation of tables and cloudiness characteristics plots in a separate representation window in colour gradations;

- data representation in conventional colours as horizontal and vertical sections;

- data representation as tables for the given point or area of the space;

- memorizing of all the space surveies in the archive file of radar characteristics;

- data extraction from the archive file on the operator's request;

- data communication (by a radio channel) on location and intensity of meteo-objects dangerous for aeroplanes flights;

- data communication (by radio channel) aboard of meteolaboratory planes on the chosen sites for activity aimed at precipitation enhancement and hail-fighting;

- data reception (by a radio channel) from meteolaboratory planes and data representation about the flight route and effected activity.

4. Technical characteristics of MRL-INFO system

Mode of operation - 24-hour.
Scanning interval, min.: full - 5, shortened - 3.5, short - 1. Accuracy of antenna positioning by azimuth and angle of elevation - 0.1° . Accuracy of antenna position measurement - 0.05° . Analogue-digital conversion of a video signal - 8 bits. Range quantization - 500 m. Azimuth quantization - 0.36° . Angle of elevation quantization - variable, 0.2° - 10° . Maximum range by cloudiness - 240 km. Maximum range by precipitation - 120 km. Automatic control of the MRL-5 equipment. Periodic switching on operation mode with periods of 1 h; 30 min, 15 min, 10 min, 5 min, and non-stop. Operation in a real time scale as new radar data arrive. Radar data analysis is carried out as new data arrive within a period of 1 s. Data representation on the operator's request - within a period of 10 s. Simultaneous screen scanning of several kinds of information. Data storing in an archive file at a 24 - hour operation mode is not less than 1 month (HDD 300 Mbytes). Data extraction from the archive file for scanning the period of 5-8 hours - during not more than 1 min. The possibility to choose the mode of automatic consecutive scanning of information (MULT regime) in order to determine the tendency of cloud processes development in time and space.

A dialogue with an operator is

effected in accordance with the standards adopted for the system of windows and dialogues in WINDOWS 3.1.

The choice of representation mode includes the choice of the information type which should be represented, the choice of additional information which is combined with the main one including the choice of a coordinate grid, representation of a laboratory-plane flight route, conditional diagram of the operations region, passages of aeroplanes approaching, the choice of an ordinal number or scanning time, scaling.

The mode of simultaneous scanning of the phenomena which are represented graphically is effected by means of creation of an additional position of the windows are given by the operation as per the rules adopted in the system WINDOWS. The radar characteristics obtained after each of the scanings are memorized in the archive file. When memorizing the characteristics at the level of the receivers sensibility are not taken into account. Memorizing of the phenomena chosen by the operator may be effected by his choice after the radar characteristics processing and analysing. Extraction of required for scanning data from the archive file is carried out on the operator's request in accordance with the given conditions of choosing. The procedure of the conditions choosing is effected in the dialogue mode in accordance with standards adopted for the dialogue windows of the firm BORLAND.

AIRCRAFT AUTOMATED COMPLEX

M.Yu. Pashkevich¹, Ya.A. Ekba¹, N.A. Berezinski¹, A.A. Sinkevich², A.A. Malkov³, A.A. Khorikov³

¹ Scientific—Production Geophysical Centre, RUSSIA, 355005, Stavropol, Abramova str., 2^a

² A.I. Voeikov Main Geophysical Observatory, RUSSIA, 194018, St. Petersburg, Karbyshev str., 7

³ High—mountain Geophysical Institute, RUSSIA, 360030, Nalchik, Lenin av., 2

1. INTRODUCTION

The investigations of cloud physics and seeding of hail clouds are connected to the improvement of aircraft measuring complexes for direct measurements. The particular and important trend in creation of the aircraft measuring systems is the development of the automated complex collecting, processing and operatively representing the information.

2. COMPLEX DUTY

The creation of the aircraft automated complex had the following aims:

- optimal control of data collection and cloud seeding to enhance the precipitation artificially from the ground—based complex;

- operatively making a decision about seeding in specified cloud volume by this or that seeding means according to direct and radar data;

- estimation of physical efficiency of seeding by comparison of measured cloud characteristics in one and the same cloud volume in different time moments;

- opportunity to analyze all cases of seeding in the frameworks of artificial enhancement of precipitation.

3. COMPOSITION OF COMPLEX AND WORK MODES

Aircraft automated complex includes two IBM/386 computers, multichannel analogue—to—digital processor, switching circuit with USW channels and GPS system for satellite navigation. The complex is able to connect up to 32 different airborne sensors. The period of complete survey of sensors is 0.2 s. The integral characteristics are set through the pass—by accumulator.

The complex has three main modes of work:

- recording, processing and display of

- information;

- exchange of information and instructions with ground—based radar control sites;

- examination of data and analysis of cloud seeding experience.

The availability of two computers allows to use all three modes of work simultaneously. The mode of processing and display of data makes:

- averaging over the specified volume of measured parameters of cloud;

- introducing the corrections into the indications of devices;

- calculation of microphysical characteristics of humidity, water content, ice content, expected intensity of rain;

- representation on the maps of the current microphysical, dynamical and electrical characteristics in the form of histogram and size distributions of cloud droplets and ice particles;

- recommendations on seeding according to a group of microphysical and dynamical parameters and determination of the expected effect of seeding;

- introduction and display of the information on the moment, amount and type of introduced agent on the flight trajectory of aircraft—laboratory;

- calculation and representation of the aircraft coordinates on the background of territory map or radar echo structure, received from the ground—based control radar site.

In automatic regime of information exchange from the aircraft to the radar site the data on the current coordinates of aircraft, the moment of injection, type and amount of crystallizing agent are transmitted. According to the choice of the leader of experiment the information on the microphysical, dynamical and electrical parameters of atmosphere came from the board of aircraft. From the ground to the board of aircraft—laboratory the control instructions as well as the radar echo structure with values of volumes and regions of seeding are transmitted.

In the mode of examination and analysis of data there are the following opportunities:

- examination of data from any moment of

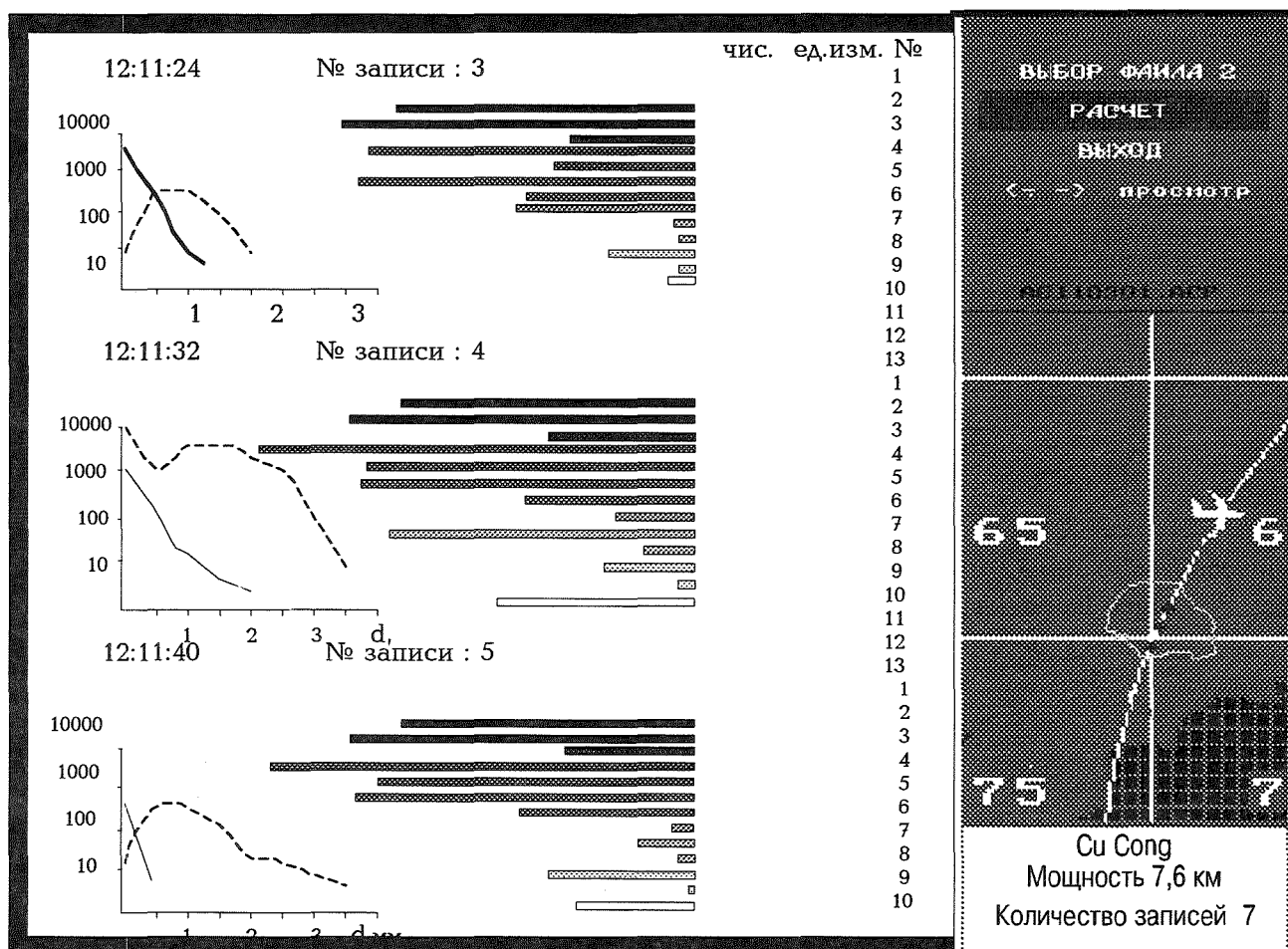


Fig.1. Operative information on the screen of display:

1—flight velocity; 2—sounding height; 3—temperature; 4—relative humidity; 5—overloading; 6—wind direction; 7—wind velocity; 8—concentration of large drops; 9—concentration of large crystals; 10—average diameter of drops; 11—average diameter of crystals; 12—liquid water content; 13—ice content.

time or any point of trajectory of aircraft flight;
comparison of data in one cloud volume before and after the seeding;

calculation of correlation coefficients and display of experimental data in dynamics.

For subsequent using the primary and calculated data are converted to the magnetic storage media. On the board of aircraft to conduct the seeding there are two types of devices for shooting of phyrotechnical shells of 26 calibre with 40 g of 2 % AgI and of shells of 50 calibre with 320—400 g of 2 % AgI.

Fig.1 shows the operative information on the screen of display as the illustration of the complex work. In the central part of figure the three fragments with measured microphysical parameters are given. The size distributions of droplet and ice particles are given as well as the histograms with measured and calculated characteristics related to three—cloud volumes. Their locations are shown on the right part of screen on the background of territory map and target area, transmitted from the control radar site. On the right upper part of screen the

modes of work, that can be used by operator, are given.

4. CONCLUSIONS

The given automated complex is realized on the board of aircraft—laboratory Yak—40. The detailed description of the used sensors is given in Berezinski et al. (1991) and Begalishvili et al. (1993). The aircraft automated complex was used for artificial enhancement of liquid precipitation in Stavropol region in summer season of 1995 and showed a high efficiency and reliability. Now

the improvement works of complex are in progress.

REFERENCES

Begalishvili N.A. et al., 1993: Aircraft—laboratory Yak—40. Meteorology & Hydrology, 4, 102—108 (in Russian).

Berezinski N.A. et al., 1991: Aircraft—laboratory Yak—40 and preliminary results of investigation of microstructure of severe cumulus. Seeding of hailstorms and outlook of the improvement of ice—forming agents for seeding. M. Gidrometeoizdat, 84—94 (in Russian).

IMPROVEMENT OF LIQUID WATER CONTENT MEASUREMENT WITH COMBINED RADAR-RADIOMETER SYSTEM

Jinli Liu, Ling Zhang and Hongbin Chen

Institute of Atmospheric Physics, CAS
Beijing, 100029, P.R. CHINA

1. INTRODUCTION

For investigating Cloud-radiation interaction, improving the decision making and validating weather modification, distribution of liquid water content (LWC) measurement in clouds are required. we have shown that remote sensing of LWC with a combined radar-radiometer system is better than that with only a single radar(Lu & Lin, 1980), we also have discussed that the limitation of the combined method (Liu & Zhang, 1992). In order to obtain more accurate results of LWC measurement, the improved method of LWC measurement with the combined radar-radiometer system is suggested in this paper. We use a 3-layer cloud model instead of the simple uniform structure which we used before. A brief description of the model and some comparative results are given below, the uncertainties of this method are discussed.

2. MODEL AND METHOD

From the field observation of North China it is indicated that

the stratified precipitating cloud usually have 3-layered structure, i.e. ice layer, mixed layer contained liquid water droplets and ice particles in varying proportion, and rain drop layer. Fig.1 is a schematic view of the model. We considered the top of second layer H_3 as the height of -10°C , and the bottom H_2 is chosen as 0.3 km below freezing level, they can be determined by radio sounding data; Cloud top H_4 and the bottom H_1 can be obtained by radar measurement. In the calculation we choose 9.364GHz (X-band) frequency which is commonly recognized as one of the suitable wavelength in precipitation measurement, and there is a combined

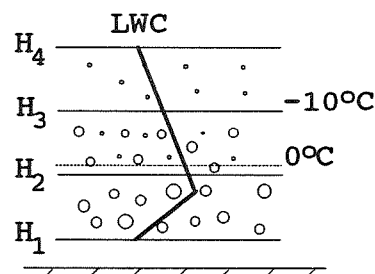


Fig.1 Schematic view of the model.

radar-radiometer system with this wavelength in our Institute.

For investigating the influence of the cloud structure on LWC measurement with combined radar-radiometer system, some numerical comparison study were made through forward and inverse procedure. Firstly, we calculated the radar reflectivity Z_e , attenuation coefficient σ_e and brightness temperature T_b corresponding to varying LWC value for different cloud models. Then we used the retrieval algorithm of combined radar-radiometer to obtain LWC distribution in corresponding cloud model. The main idea of retrieval algorithm of LWC distribution can be briefly described as follow: 1) from microwave radiometer brightness temperature of ray path by the radiometer we may derive the total attenuation (optical depth) τ_0 . 2) we may derive the distribution of attenuation coefficient $\sigma(r)$ from radar reflectivity along ray path with empirical regressive relation between radar reflectivity and attenuation coefficient for liquid and ice droplet respectively 3) with the constraint that the integration of $\sigma(r)$ along the path τ_c should be equal to τ_0 . The proportion of ice droplets and liquid cloud drop in the mixed layer should be given in advance from statistics of field observation. 4) through $\sigma-M$ empirical relation the LWC distribution along ray path $M(r)$ is obtained. The details of this retrieval method can be found in the paper written by Lin et al (1984).

3. RESULTS

In this model calculation, our main focus is on the influence of the cloud structure, comparative study were made on 3-layer (see Fig. 1) and 1-layer (contained same distribution of rain drop for whole cloud) structures. The variation range of average LWC is from 0.1 to 1.0 g/m^3 .

• Variations with different cloud structure

According to the field observations, the vertical profiles of LWC are different in different cloud type and evolution stage, the statistic results show that in mature stage the LWC profile mostly has the pattern indicated in Fig.1, the maximum value occurs in the middle of the cloud, and decrease toward the cloud top and cloud base. Here we only discuss this kind of LWC vertical profile. Four kind of cloud drop size distribution (DSD) are chosen here: 1. M-P DSD in all three layer; 2. Γ DSD for ice droplets and M-P for liquid drop; 3. BJS DSD for liquids drop derived from stratified precipitating clouds of Beijing, Γ DSD for ice droplets; 4. BJC same as BJS but derived from convective precipitating clouds. The regressive parameters of rain drop distribution of Beijing are listed by Group of Microwave Remote Sensing, IAP (1982).

When changing the average LWC from 0.1 to 1.0 g/m^3 and holding the same type of drop size distribution, and the same LWC proportion of ice and liquid drop (M_q/M_i) of

the mixed layer in the forward and inverse calculation, we may obtain the LWC vertical profiles for different cloud structure; Fig.2 shows one example of the results. For comparative study, the original LWC vertical profile which we used in forward procedure and the results of one-layer structure are also given in Fig.2. The relative deviation of root-mean-square(RMS) are given in Table 1. We also do the same calculation but using different type of DSD. From the calculation results it can be seen that the 3-layer model are much better than 1-layer structure for various size distributions, especially when the value of LWC is small.

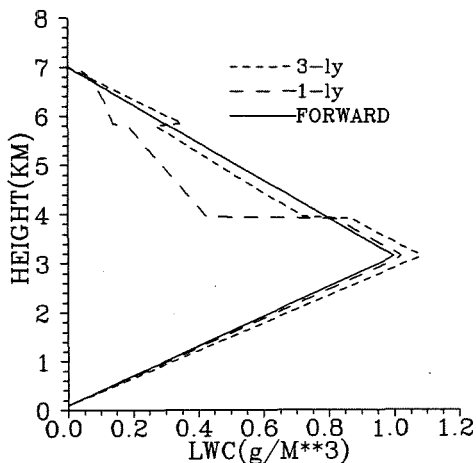


Fig.2 Vertical profile of LWC obtained by different cloud model, Γ distribution, $Mq/Mi=1/1$, $\overline{LWC}=0.5 \text{ g/m}^3$

Table 1. The relative deviation of RMS in LWC vertical profile calculation with different cloud model for different \overline{LWC} , Γ DSD, $Mq/Mi=1/1$

\overline{LWC}	0.1	0.2	0.4	0.6	0.8	1.0
1-ly	0.22	0.25	0.27	0.29	0.29	0.30
3-ly	0.06	0.07	0.09	0.13	0.17	0.21

Variation with drop size distribution

Different type of DSD are chosen between the forward and inverse calculations. One of the results is given in Table 2. It can be seen the relative deviation of RMS is larger than in Table 2, it means the influence of DSD is important; it also shows that the 3-layer model is still better than 1-layer structure.

Table 2. As Table 1 but M-P DSD in forward and Γ DSD in inverse

\overline{LWC}	0.1	0.2	0.4	0.6	0.8	1.0
1-ly	0.32	0.32	0.32	0.32	0.32	0.32
3-ly	0.28	0.21	0.19	0.21	0.23	0.26

Variation with the LWC proportion of ice and liquid drop in mixed layer

For investigating the influence of LWC proportion of ice and liquid drop in the mixed layer, we change the ratio of Mq/Mi from 5/1 to 1/5 and holding the same \overline{LWC} and the DSD type, the results are given in Table 3.

Table 3. As Tab.1 but for different ratio of Mq/Mi in Mixed layer, $\overline{LWC}=0.5 \text{ g/m}^3$

Mq/Mi	5.0	3.0	1.0	0.5	0.33	0.2
1-ly	0.16	0.19	0.32	0.41	0.47	0.51
3-ly	0.12	0.11	0.10	0.09	0.09	0.09

It can be seen that there is larger error in 1-layer structure than in 3-layer structure for various LWC proportion. When changing

the proportion of M_q and M_i in forward and inverse calculation, it was found that large deviation existed in retrieving LWC vertical profile, especially when overestimated M_i is in inverse calculation. For example, when $M_i/M_q=1$ is chosen in the forward calculation and $M_i/M_q>4$ in inverse calculation, it can be found that the deviations of 3-layer are larger than 1-layer structure. The reason is that, the retrieval method(inverse calculation) is based on both radar return and radiative absorption of cloud particles, the contribution of ice particles to radar reflectivity is larger than water drops for the same LWC while the contribution of ice particles is smaller to radiative absorption. When M_i overestimated, through constraint the total attenuation obtained by radiometer and radar reflectivity vertical distribution, it would result in larger overestimation of the retrieval LWC in the mixed layer, also in ice layer.

4. CONCLUSION AND DISCUSSION

From numerical study of different cloud model, the following can be deduced.

1. The cloud structure plays important role in 'observed' LWC with combined radar-radiometer system. 3-layer structure is better than 1-layer, in mostly conditions, the accuracy of retrieval LWC profile will increase about 10-20%.
2. It should be pointed out that the present model calculation still has some uncertainties, it is very

difficult to obtain reliable data on the structure of real cloud, especially the phase, the proportion of M_q and M_i in Mixed layer and the corresponding droplet size distribution etc. It seems helpful to have a complimentary observation data from meteorological polarization radar for identifying particle phase and distribution.

5. ACKNOWLEDGMENT

This work is sponsored by National Science Foundation of China.

6. REFERENCES

- Lin, Hai et al, 1984: Remote sensing of liquid water content in cloud and rainfall distribution by a combined radar-radiometer system, *Scientia Atmospherica Sinica*, Vol.8, No.3, 332-340.
- Liu, Jinli and Ling Zhang, 1994: Remote Sensing of Liquid Water Content with Combined Radar-Radiometer System, *ATMOSPHERIC RESEARCH*, 34, 145-152.
- Lu, Daren and Hai Lin, 1980: Comparison of radar and microwave radiometer in precipitation measurements and their use, *Scientia Atmospherica Sinica*, Vol.4, No.1, 30-39.
- Group of Microwave Remote Sensing, (IAP), 1981: Microwave propagation and radiation characteristics of clear and cloudy atmosphere over China, National Defense Industry Press, Beijing, 200pp.

ACCURACY OF EVALUATION OF THE WIND FIELD BY SINGLE DOPPLER RADAR

V.N. Efremov,

Central Asian Research Hydrometeorological Institute, Tashkent,
Republik of Uzbekistan

According to the existing method, proposed by Lhermitte and Atlas (1961) and worked out in details by Browning, Wexler (1968) and Caton (1963) the wind velocity can be determined using a single Doppler radar. The essence of this method is that the radial component is measured on along reserved circular outline with the fixed elevation angle and distance of signal strobing. In this case the value and distance of the wind velocity are considered to be the characteristics averaged by area; restricted by the outline of scanning and considered to be applied to the point of radar installation.

It is known, that when antenna of Doppler radar is rotating by azimuth the law of radial component of the wind velocity change in the horizontal surface U_{pr} can be expressed by the equation as:

$$U_{pr} = U_0 \cos(\alpha - \alpha_0) + C, \quad (1)$$

where α_0 and U_0 is a direction and module of the wind velocity horizontal component, C is a constant, proportional to the wind field divergency. The majority of problems on interpretation Doppler radar observations come to the definition of these three parameters by the values of U_{pr} .

Our method of approach based on the use of the equation (1) is considered below.

Algorithm of the solution of the inverse task of the wind field reconstruction by the values of radial component of the

wind velocity enables to measure the wind velocity vector in any point of space in the zone of radar scanning using only a single Doppler radar. In this case the special method of interpretation the input information about radial velocities is suggested. Moreover, the assumption that the wind field in the zone of vector measuring appears to be a linear one is introduced. The zone dimensions are considered to extend from kilometres to some dozens of kilometres length.

Let us assume that in the wind field measuring by method analogous to that one proposed by Lhermitte and Atlas the wind field is considered to be linear and homogeneous on the small segments of area and submitted to the law of change described by the equation (1). In this case it is enough to carry out 3 measurements of the radial component of the wind velocity on one of the segments of area with different azimuth angles in order to obtain the system of 3 equations:

$$\left. \begin{aligned} U_{pr1} &= U_0 \cos(\alpha_1 - \alpha_0) + C \\ U_{pr2} &= U_0 \cos(\alpha_2 - \alpha_0) + C \\ U_{pr3} &= U_0 \cos(\alpha_3 - \alpha_0) + C \end{aligned} \right\}, \quad (2)$$

which can be easily calculated. Here α_1 , α_2 , α_3 and U_{pr1} , U_{pr2} and U_{pr3} respectively are azimuth angles of the chosen arc and values of the wind velocity radial component measured on these angles. The obtained values U_0 , α_0 and C appear to be the averaged characteristics of the

wind field on the chosen arc section of the measurement outline and may be applied to a given point in space.

It is known that correlation radius of tangential and radial components of the wind velocity in boundary layer (the pulsations are meant) is approximately 300-400 m (Melnichuk 1973). Consequently, the wind velocity radial component measurements are preferably carried out with such a step along the length of area. In this case we will obtain n equations with 3 unknown quantities, i.e. overdetermined system. To solve such systems the method of least squares for n couples of values of U_{pr} and α_i is to be used.

Hence, from general propositions of the theory of least squares for multiparametrical equations the following formulae

for the calculation have been deduced (Efremov 1984).

To estimate the efficiency of the mentioned above algorithm of the wind field reconstruction on single Doppler radar data the following method has been suggested. Data of the actual wind observations obtained by the aircraft-laboratory have been used. Using them the values and directions have been calculated by approximation in the groups of the spatial grid (5×5 km). They were taken into account as the input ones. Subsequently the point of radar installation (x_0, y_0) has been chosen and the radial velocities field for this position has been calculated. Using described above algorithms the procedure of the wind field reconstruction on the radial field velocities has been carried out.

$$U = \sqrt{L^2 + K^2} \frac{n(L \sum_{i=1}^n U_{pri} \sin \alpha_i - K \sum_{i=1}^n \cos \alpha_i) - \sum_{i=1}^n U_{pri} \sum_{i=1}^n (L \sin \alpha_i - K \cos \alpha_i)}{(L \sum_{i=1}^n \sin \alpha_i - K \sum_{i=1}^n \cos \alpha_i)^2 - n \sum_{i=1}^n (L \sin \alpha_i - K \cos \alpha_i)^2} \quad (3)$$

$$C = \frac{(L \sum_{i=1}^n \sin \alpha_i - K \sum_{i=1}^n \cos \alpha_i)(L \sum_{i=1}^n U_{pri} \sin \alpha_i - K \sum_{i=1}^n U_{pri} \cos \alpha_i)}{(L \sum_{i=1}^n \sin \alpha_i - K \sum_{i=1}^n \cos \alpha_i)^2} \rightarrow$$

$$\rightarrow \frac{\sum_{i=1}^n U_{pri} \sum_{i=1}^n (L \sum_{i=1}^n \sin \alpha_i - K \sum_{i=1}^n \cos \alpha_i)^2}{-n \sum_{i=1}^n (L \sin \alpha_i - K \cos \alpha_i)^2} \quad (4)$$

$$\alpha_0 = \arctg \left(-\frac{L}{K} \right) \quad (5)$$

$$L = -n \sum_{i=1}^n U_{pri} \cos \alpha_i \sum_{i=1}^n \sin \alpha_i \cos \alpha_i + \sum_{i=1}^n U_{pri} \cos \alpha_i \sum_{i=1}^n \sin \alpha_i \sum_{i=1}^n \cos \alpha_i -$$

$$- \sum_{i=1}^n U_{pri} \sum_{i=1}^n \cos \alpha_i \sum_{i=1}^n \sin \alpha_i \cos \alpha_i - n \sum_{i=1}^n U_{pri} \sin \alpha_i \sum_{i=1}^n \cos^2 \alpha_i + \sum_{i=1}^n U_{pri} \sin \alpha_i \left(\sum_{i=1}^n \cos \alpha_i \right)^2 \quad (6)$$

$$K = n \sum_{i=1}^n U_{pri} \sin \alpha_i \sum_{i=1}^n \sin \alpha_i \cos \alpha_i - n \sum_{i=1}^n U_{pri} \cos \alpha_i \sum_{i=1}^n \sin^2 \alpha_i -$$

$$- \sum_{i=1}^n U_{pri} \sin \alpha_i \sum_{i=1}^n \sin \alpha_i \sum_{i=1}^n \cos \alpha_i + \sum_{i=1}^n U_{pri} \sum_{i=1}^n \sin^2 \alpha_i \sum_{i=1}^n \cos \alpha_i - \sum_{i=1}^n U_{pri} \sum_{i=1}^n \sin \alpha_i \times$$

$$\times \sum_{i=1}^n \sin \alpha_i \cos \alpha_i + \sum_{i=1}^n U_{pri} \cos \alpha_i \left(\sum_{i=1}^n \sin \alpha_i \right)^2 \quad (7)$$

Then it has been compared with the actual one. The figure 1 below shows the results of this comparison.

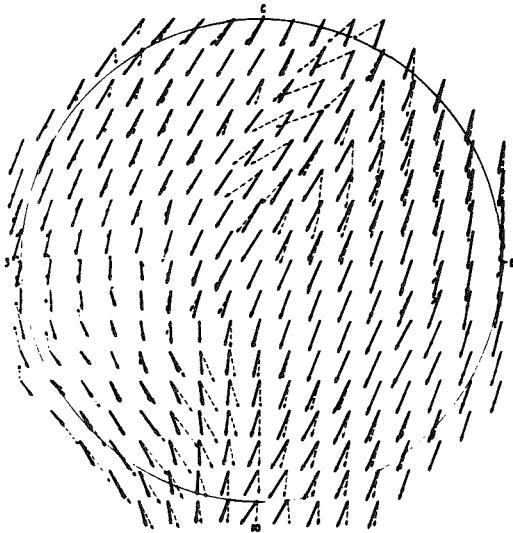


Fig.1. Wind field. 1 - actual, 2 - calculated

Having analyzed the figure it has been established that there is very close agreement between the calculated wind field and the actual one. However, there exist some sections which are essentially different. One of them is the field located in the sector $240 - 260^\circ$ with the range of 15-40 km. Here we observe the significant discrepancy between the actual field and the calculated one being calculated by direction and by velocity. Vectors are reduced sharply by module and change their direction to almost opposite one.

It could be explained by the assumption that the wind field in the zone is evidently nonlinear one. In this zone we observe the wind velocity vector change almost on 90° . However, assumption about the linearity of the wind field was put into the numerical model of this method of calculation. Therefore, it is quite natural that great discrepancies of the vector field should be expected in this zone.

Besides, we can observe another two zones with great discrepancies by direction and velocity. They are situated approximately on azimuths of $20 - 30^\circ$ and

$180 - 200^\circ$. Here the errors by direction are less than in the zone considered above. They equal $30 - 40^\circ$. As it concerns the velocities they differ on $2-3 \text{ ms}^{-1}$.

In the remaining part of the section the calculated vector field has very good agreement with the actual one.

The actual wind field measured by the aircraft-laboratory in the considered section comprised both zones close to homogeneous linear flow and ones with essential change of the wind vector. Above mentioned analysis has shown that the errors in the zones of wind nonlinearity when interpreting the actual wind field by linear equations for the concrete chosen variant are about 4 ms^{-1} by amplitude and 176° by direction of velocity vector. They appear to be so small in the zones of linear wind change that they can be neglected.

The author wishes to express his sincere appreciation to colleagues from the Central Aerological Observatory (Moscow) for data of wind observations by aircraft-laboratory.

REFERENCES

- Browning K.A., Wexler R. A determination of kinematic properties of a wind field using Doppler radar// J. Appl. Meteorol.-1968.-V. 7.- N 1 P. 105-113.
- Caton P.A.F. Wind measurement by Doppler radar// Meteorol. Mag.-1963.-V. 92.- N 1092.- P. 213-222.
- Efremov V.N. Interpretation techniques of radar observation data// Proc. SANIGMI. - 1984. - V. 100 (181).- P. 9-14.
- Lhermitte R. M., Atlas D. Precipitation motion by pulse Doppler radar// Proc. 9th Weather Radar Conf.- 1961.- P. 218-223.
- Melnichuk Yu.V., Chernicov A.A. Radar observations of the wind field divergence and vertical flow in the atmosphere// Proc. CAO.- 1973.- N 110.- P.36-46.

COORDINATE METHOD OF THE WIND PROFILE EVALUATION BY DOPPLER RADAR

V.N. Efremov, K.N. Kim, E.I. Sophiev

Central Asian Research Hydrometeorological Institute, Tashkent,
Republik of Uzbekistan

Nowadays pulse Doppler radar technique potentialities and advantages for measuring the dynamic characteristics of atmosphere appear to be extensively known. These potentialities are not restricted by use of the single Doppler effect only. For example, this technique is supplied with auto follow tracking regime.

Such regime enables to follow the local object, without man interfering into the process of antenna operating. In this case the information about elevation angle, azimuth and distance is represented on corresponding indicators of circle scanning and automatic registration. The accuracy of the following characteristics measurement is as follows: that of angle 0, 15° and distance of the order of 15 m. All this enables to estimate the observation object in polar coordinates.

It is not difficult to show that if a balloon in the moment of time t_1 and t_2 has the following coordinates on the elevation angle β_1 and β_2 , azimuth α_1 and α_2 , distance R_1 and R_2 its horizontal velocity will be calculated by the equation as:

$$V = \sqrt{\frac{R_1^2 \cos^2 \beta_1 - 2R_1 R_2 \cos \beta_2 \cos \beta_1 \cos(\alpha_1 - \alpha_2) + R_2^2 \cos^2 \beta_2}{\Delta t}}, \quad (1)$$

where $\Delta t = t_2 - t_1$

The direction of the balloon transport can be defined using the following expression:

$$\alpha_0 = \arctg \left(\frac{R_2 \cos \beta_2 \sin \alpha_2 - R_1 \cos \beta_1 \sin \alpha_1}{R_2 \cos \beta_2 \cos \alpha_2 - R_1 \cos \beta_1 \cos \alpha_1} \right). \quad (2)$$

Thus, carrying out the series of successive determinations of the balloon displacement in space the wind profile in this region can be obtained. In this case a middle part of the layer is taken for the height (H), where the wind velocity and direction may be calculated by the equation:

$$H = \frac{R_1 \sin \beta_1 + R_2 \sin \beta_2}{2}. \quad (3)$$

The error theory of this method considered in (Efremov 1992) has shown that in 70% of cases the wind velocity and direction at the distance of the order of 20 km can be determined not worse than 2 ms^{-1} and 6° respectively. In 90% of cases they are not worse than 2,4 ms^{-1} and 10°.

However, the theoretical estimations of wind measurement should be confirmed by experimental data, i.e. that they should be evaluated by an independent method, which errors are well investigated. The results of a comparison between Doppler radar wind observations and the basic theodolite balloon observation technique, which is characterized by very high accuracy, are represented below. The latter one has been chosen because of its errors being well investigated both theoretically and in experimental way. In particular, errors have been studied from two bases following one and the same balloon (Kurbatkin, 1973).

The essence of this technique is to register the balloon angular coordinates by optical theodolite with accuracy of $0,01^\circ$ in the fixed moment of time. Theodolites are located at two ends of the base several kilometers long. It is known that in many cases an important source of errors of wind parameters arises from the variability of factors, such as: a base length, a balloon transport, a time interval between measurements, a number of other factors and besides, a qualification of an observer. Probable errors are close to $0,2-0,5 \text{ ms}^{-1}$ for the velocity and $1-3^\circ$ for the wind direction by measurements at the heights up to 10 km and layer thickness about 100-200 m. It seemed to be evident that basic balloon observation technique excelled other ones in accuracy of measurement in free atmosphere. Such observations might be assumed as standard ones. In our case they were used for a comparison with Doppler radar wind observations.

The experiment on the comparison described in this paper was performed in the following way. Balloons being operationally launched by ground station have been observed by three theodolites and one Doppler radar. The time interval between measurements has been established of the order of 20 s. To synchronize the measur-

ings quartz spot-watches have been used. Discrepancy between recordings for the observation time interval (1 hour) was not more than 0,1-0,2 s. The observation points have been situated in the apexes of triangles with sides dimensions of 1780, 2389 and 3773 m. Taking into account such arrangement of theodolites location and also the special techniques of the combined treatment of obtained results it has been expected that the accuracy of the wind velocity and direction up to the heights of 8-9 km would not be worse than $0,2 \text{ ms}^{-1}$ and 15° respectively. (Kurbatkin 1973, Kurbatkin 1984). Doppler radar has been situated at 50 m direction from the point where balloons have been launched.

The comparison has been made by the results of 12 balloons launchings. As an example, in order to compare the results of the wind field and direction estimations by two methods Fig.1 has been constructed. Fig.1 shows that there exists satisfactory agreement between data obtained by theodolite and radar techniques. Definite points with the sharp wind intensification and weakening

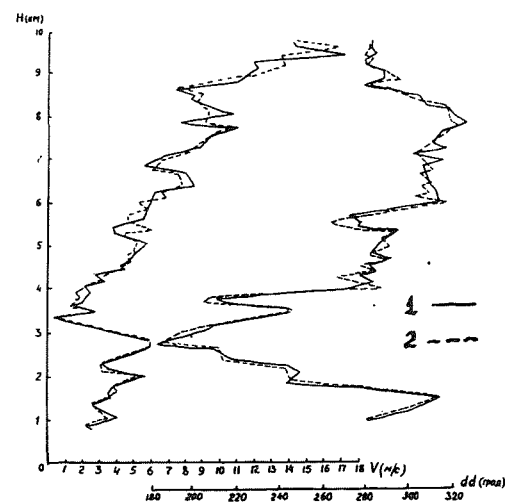


Fig.1. Wind velocity and direction profiles obtained by both methods
1- Doppler radar observations; 2- theodolite observations

and also the change of its direction are evidently observed by both methods.

Analysis of all measurements showed that discrepancies in wind profiles obtained by basic observations and Doppler radar ones appeared to be not so high as it might be expected. Thus, coefficient of correlation between velocities equaled to 0,94, between directions it was as large as 0,98. Mean square deviations were respectively equal to $1,3 \text{ ms}^{-1}$ and 8° .

Statistical researches showed that in 70% of cases discrepancies in velocity did not exceed $1,5 \text{ ms}^{-1}$, in 90% they were as large as 3 ms^{-1} .

Wind direction discrepancies up to 3° have been observed almost in 70% of cases. In 90% of cases they reached 6° . At the same time separate extreme discrepancies reached $4,5 \text{ ms}^{-1}$ and 19° .

Fig.2 illustrates an idea about errors in spatial coordinates determination by both methods.

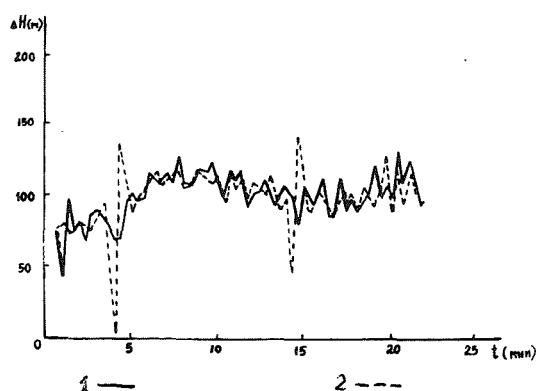


Fig.2. Profiles of balloon altitude increment change

1- Doppler radar observations; 2- theodolite observations

In this figure increments of sound altitude are given on ordinate axis and time

intervals from the beginning of launching are marked on absciss axis. Fluctuations of the curves are partially caused by natural fluctuations of balloon ascension velocity and at the same time by errors of observers. Improbably great peaks on the curve portrayed by theodolite observations show their most striking effect in Fig.2. Dispersion of radar observations is 10,8 m, while by theodolite technique it reaches 17,7 m. If 4 peaks caused by mentioned above errors are rejected, then the dispersion of theodolite observations will reduce to 8,6 m. Thus, when balloon observation by theodolite technique is carried out, in order to avoid the rough errors the selection of the obtained data should be done. In our experiment about 8% average have been considered to be unfitting recordings. There was no need to do such selection by radar observations since evident errors have not been revealed in this case.

On the basis of all observations, with the selection of the obtained data being taken into account, theodolite technique gave dispersion of vertical coordinate increment equal to 22,1 m and by radar technique data it was meaningful to 23,8 m.

Thus, experimental estimation of the errors of Doppler radar techniques shows insignificant deviation from those ones of balloon observation method by theodolite. All this mentioned above makes Doppler radar technique observations to be a proper method for wind inhomogeneities measurements with the scale of 100 m towards the balloon transport at the direction of 15-20 km. Such high accuracy with comparatively low angular coordinate value ($0,15^\circ$) can be explained by small errors in inclined distance determination (15 m). Having practically the same accuracy Doppler radar technique observation possesses an advantage over theodolite one for the first enables to carry out wind velocity measurements in clouds.

REFERENCES

- Efremov V.N., Kim K.N., Sophiev E.I.
Coordinate method errors by radar
observations/ Proc. SANIGMI. -
1992. - 144 (225).- P. 111-120.
- Kurbatkin V.P., Sophiev E.I.
Wind structure balloon observations
with the use of a computer// Proc.
SARNIGMI.- 1973.- 6(27).- 58 pp.
- Kurbatkin V.P. Empirical model of
troposphere structure in mountain-
ous regions// Proc. SANIL.- 1984.-
100(181).- P. 25-34.

OBSERVATIONS OF CLOUD STRUCTURE WITH A 3.2 MM-WAVE RADAR

Markus Quante¹, Olaf Danne¹, Ehrhard Raschke¹, Ivan Popstefanija² and Andrew Pazmany²

¹GKSS Research Center, Institute of Atmospheric Physics, D-21502 Geesthacht, Germany

²Microwave Remote Sensing Laboratory, University of Massachusetts, Amherst, MA, USA

1. INTRODUCTION

Clouds play a dominant and complex role within the climate system. They modulate the radiation and energy budget and are an important component of the hydrological cycle. Currently the representation of clouds in GCMs appears to be rather poor (Cess et al. 1990). An improved knowledge of the three-dimensional large scale distribution as well as of the cloud structure on the mesoscale is of great importance for the improvement of parameterization schemes for global and regional models.

In recent years, improvements in microwave technology have allowed the development of radars operating at millimeter wavelength (Lhermitte, 1987, 1988). These radars have proven to be invaluable for studying i.e. stratiform clouds and their internal structure (i.e. Pazmany et al., 1994; Clothiaux et al., 1995; Syrett et al., 1995, Danne et al., 1996). They are sensitive to small cloud particles and are able to penetrate multilayered cloud systems and therefore well suited for cloud boundary studies (Uttal et al., 1995). Bluestein et al., 1995, have also demonstrated that mm-wave radars can contribute to studies of severe convective storms. An overview of the state of the art concerning mm-wave radars for remote sensing of clouds is provided by Mead et al., 1994.

2. DESCRIPTION OF THE GKSS CLOUD RADAR

Recently a 95-GHz (3.2 mm) polarimetric cloud radar has been taken into operation by the GKSS Research Center, Geesthacht. The main cloud radar specifications are listed in Table 1. Pulse repetition frequency, the number and location of range gates and pulse width are software selectable and allow for a range resolution between 15 m and 300 m. The beamwidth of the antenna leads to a range cell diameter of about 30 m at an altitude of 10 km. The real-time data products include polarimetric quantities (ZDR, LDR, ρ), the first three moments of the Doppler spectrum (total power, mean velocity, velocity variance) as results of the pulse pair

algorithm and 64 point FFT spectrum analysis. The minimum sensitivity at an altitude of 10 km is about -30 dBZ.

TABLE 1: Characteristics of the GKSS 3.2-mm wave radar.

Frequency	95 GHz
Peak power (EIA)	1.7 kW
Duty Cycle	1.2 % max
Pulse repetition frequency	50 Hz - 80 kHz
Pulse width	50 - 2000 ns
Beamwidth	0.17°
Antenna diameter	1.2 m
Antenna gain	60 dB
Transmit Polarization	H or V
Receive Polarisation	H and V
Cross-polarization isolation	> 25 dB
Dynamic range	> 70 dB
Bandwidth	20, 10, 2 MHz
Output channels	$\log(h ^2)$, $\log(v ^2)$, I_h , Q_h , I_v , Q_v *

* $|v|^2$ and $|h|^2$ are received power in the vertical and horizontal receiver channel; I and Q are in-phase and quadrature components of the signal phase.

The cloud radar system was designed and built by Quadrant Engineering Inc., Amherst, MA, USA. The main part of the system is an extended interaction amplifier from CPI, Georgetown, Canada. The center-fed Cassegrain antenna was manufactured by Millitech Corporation, South Deerfield, MA, USA. The radar control and data handling is based on a VXI data acquisition and processing system. The system is designed for groundbased measurements and is installed in a transportable container. It will be integrated in an azimuth-elevation scanning system. Plans have been made for an optional installation on an aircraft. The GKSS-radar is currently used for a variety of studies related to the structure of layer clouds. Its high temporal and spatial resolution allows detailed observations of cloud boundaries as well as of the internal structure of the clouds. Examples of first measurements are presented in the next chapter.

3. MEASUREMENTS AND RESULTS

The capability of this radar to investigate the internal structure of stratiform clouds as well as the occurrence of multiple cloud layers is highly illustrated by a cloud event which was observed on December 7th, 1995, during the first measurements at GKSS. Fig. 1 shows a height-time cross section of the radar reflectivity obtained from the received copolarized signal (hh) with vertical beam for a time period of about 18 minutes. The vertical resolution was 30 m, the temporal resolution about 0.2 seconds. The observed cloud field can be divided into three, partly even into four different layers, obviously including stratus/stratocumulus (below about 2 km) and cirrus/cirrostratus/altostratus with internal structures and fallstreaks above 3.5 km. The collection of a large amount of this kind of datasets will be helpful to investigate the occurrence of multiple cloud layers as well as typical heights of cloud upper and lower boundaries in a statistical manner in order to establish climatologies of these parameters.

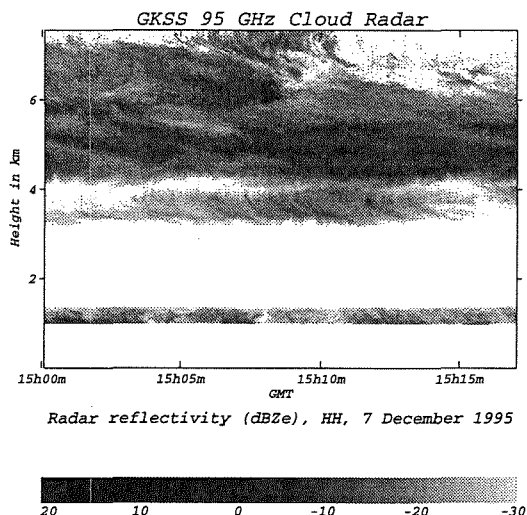


Figure 1: Height-time cross-section of the reflectivity obtained with the vertical pointing radar on 7.12.95.

Another example which shows especially the capability to resolve meso- and microscale internal structures of stratiform clouds is given by a cloud event which was observed on December 6th, 1995. Fig. 2 shows the height-time cross section of the radar reflectivity obtained from the received copolarized signal (vv) for a time period of about 6 minutes. The vertical and temporal resolution was the same as in Fig. 1. The reflectivity pattern looks very stratiform below about 4 km, while significant structures on several scales together with fallstreaks between 4 and 4.5 km and an inhomogeneous cloud top can be seen further above. The corresponding Doppler velocities (Fig. 3) show similar features. In regions below 4 km we have relatively uniform velocities of less than 1 m/s downward. In the upper cloud regions the

fluctuations on small timescales are larger, and even regions with upward motion can be identified. These observations lead to the assumption of an unstable layer between 4.5 and 5 km, resulting in convection and enhanced turbulence activity.

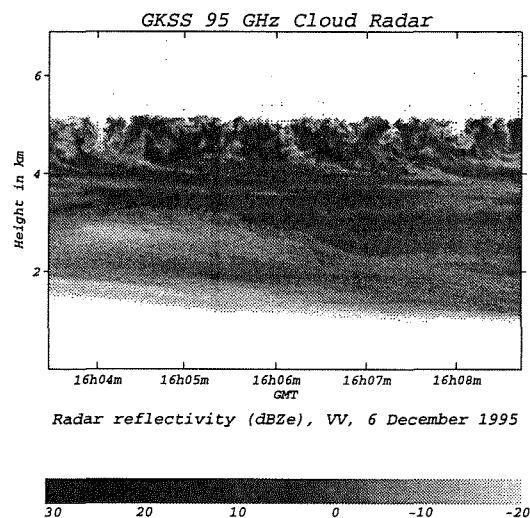


Figure 2: Reflectivities (vv) from the vertical pointing cloud radar on 6.12.95.

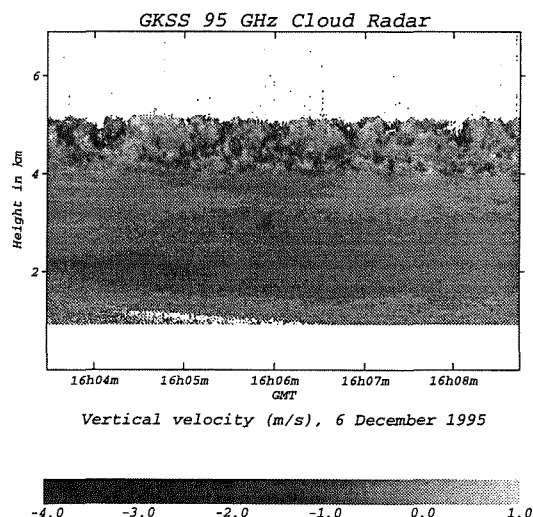


Figure 3: Doppler velocities in for the time segment shown in figure 2 (positive values denote movements away from the radar).

To confirm this assumption, the corresponding atmospheric conditions were investigated. Several radiosonde ascents in the surrounding area were considered. With regard to the synoptical situation with a stable south-easterly flow throughout most parts of the troposphere, the radiosonde data from Lindenberg at 1200 GMT, although about 280 km southeast of Geesthacht, seems to be most representative for the flow field approaching the radar site in the late afternoon. Fig. 4 shows the profiles of the potential temperature and the relative humidity. A slightly unstable and saturated layer can be seen between about 4.5 and 4.8 km, which could partly

explain the observed cloud features about 4 hours later and 280 km downstream. However, with the large temporal and spatial distance, this can only be regarded as a hint for generally less stable conditions in this height region compared to the layers below and above.

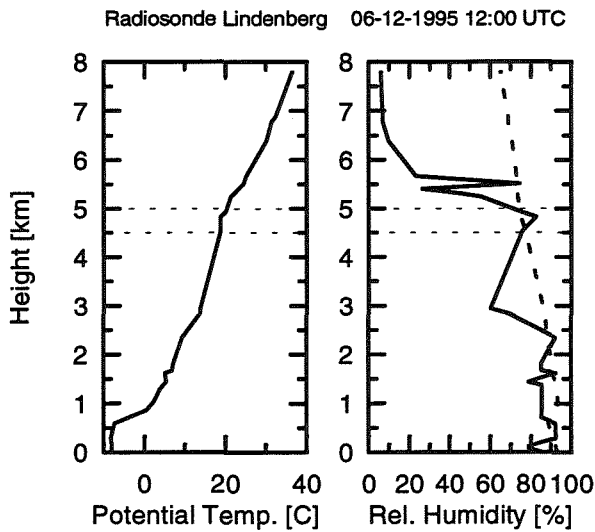


Figure 4: Radiosonde soundings of potential temperature and relative humidity (dashed profile gives ice saturation). Horizontal lines mark the convective height band in the observed clouds.

Another important parameter for the description of cloud microphysical processes in models is the phase (liquid or ice) of the hydrometeors. Since backscattering from irregular shaped ice particles leads to an enhanced depolarization of the transmitted polarized signal, the received cross-polarized signal (e.g., a received horizontal polarized signal from a transmitted vertical polarized signal) can be used for a first qualitative location of regions containing ice particles within stratiform clouds.

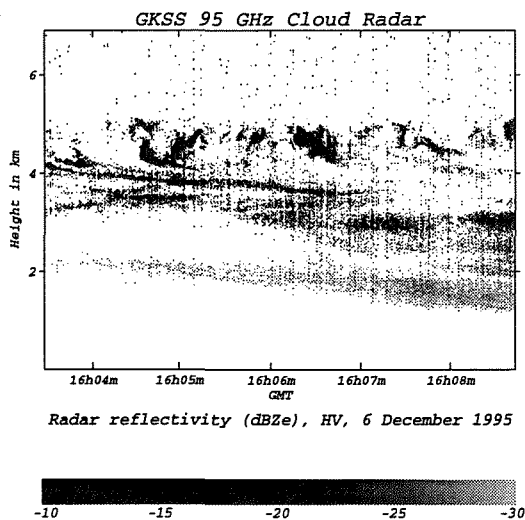


Figure 5: Cross-polarisation reflectivities (hv) for the time segment shown in figure 2.

Fig. 5 shows the reflectivity obtained from the cross-polarized (hv) signal. The highest values were observed in the turbulent layer above 4.5 km, however, regions with high hv signal and very low hv signal are located close to each other, indicating that there are changes in the amount and/or shape of ice particles on small temporal or spatial scales. Again, further similar datasets are needed for more quantitative investigations.

The cloud structure (reflectivity and Doppler velocity) was investigated in more detail for the convective cloud layer compared to the stratiform layer. This was carried out by spectral analysis of reflectivity and velocity time series for certain height ranges. Fig. 6 shows power spectra of reflectivity and Doppler velocity time series for two selected height regions (3300-3600m and 4500-4800m). To improve statistical significance of the spectral estimates, for both regions spectra of 11 single time series for consecutive range gates were averaged.

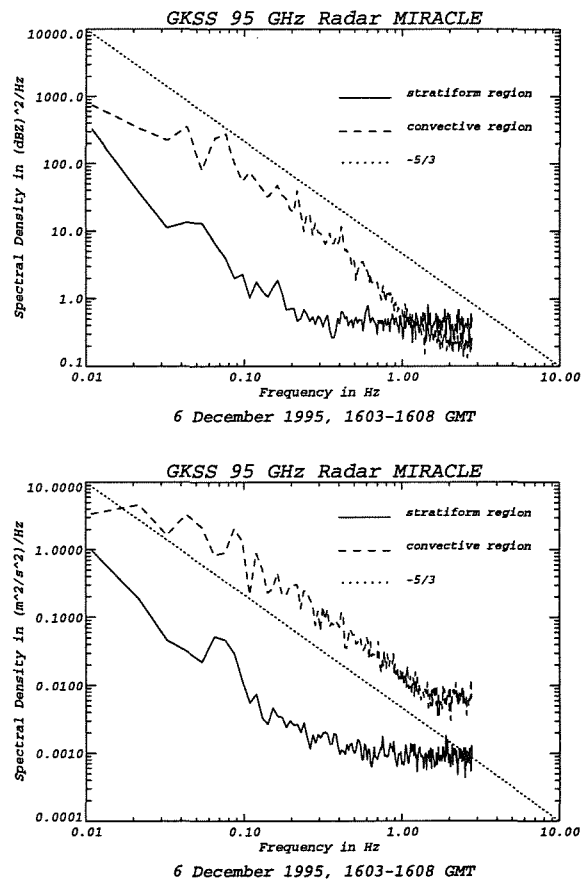


Figure 6: Power spectral densities of reflectivity (upper graph) and Doppler velocity (lower graph) for selected height bands in the convective and stratiform region of the cloud shown in figure 2.

For frequencies below 1 Hz, the reflectivity as well as the velocity spectrum show higher spectral amplitudes for the convective region. Especially the velocity spectrum for the convective region shows

microscale turbulence processes give a significant contribution to the observed Doppler velocities. Statistical significant peaks (although indications can be seen), corresponding with dominant periods (wavelengths) of internal structures, are not visible in the spectra of the convective region, whereas the velocity spectrum for the stratiform region shows a distinct peak near 0.07 Hz. With an advective wind speed of 16 m/s, estimated from the Lindenberg radiosonde ascent, this peak corresponds with a wavelength of 230 m. The origin of this peak could be a gravity wave within the stable layer but also a pattern caused by fallstreaks. Here it is difficult to identify the processes without additional information.

With regard to cloud dynamics, the correlation between reflectivity and Doppler velocity is of interest to estimate the contribution of wind components as well as of particle fallspeeds in the observed velocities. Scatter plots of reflectivity-velocity pairs (not shown here) for the height regions of the spectra in Fig. 6 have been analysed. It was clearly visible that there is a well-defined relationship with increasing Doppler velocities for increasing reflectivities in the stratiform region, whereas in the convective region there is almost no correlation between the two variables, again indicating that in this region turbulence is the dominating factor for the particle motions. Empirical relations between reflectivity and Doppler velocity can be one step to improve estimates of the corresponding particle size distributions which are generally unknown, when no additional information from other remote sensing instruments using a different wavelength is available.

4. CONCLUSIONS

The given examples show some of the capabilities of a millimeter wavelength cloud radar. The ability to provide information about the location and structure of clouds is an obvious strength of this instrument. The possibilities for the analysis of cloud structures will be improved by adding scanning capability to the radar in near future, which will allow quasi-three-dimensional measurements to obtain also information on lifecycles of cloud fields and internal structures. The analysis of full Doppler spectra, which will help to improve the knowledge about the relationship between cloud structure and microphysics, has been started. Future plans include simultaneous measurements of the radar and a backscatter lidar, which will improve the knowledge of particle size distributions. This combination of instruments is also planned to be deployed on an aircraft, not only to obtain the chance to cover large horizontal areas, but also as an important step towards a planned satellite-borne combination of these instruments to obtain relevant cloud parameters on a global scale (IGPO, 1994).

5. ACKNOWLEDGEMENTS

The authors wish to thank D. Milferstädt, J. Oldag and A. Weiss from GKSS for their help during the set-up of the radar system and their assistance during measurements and data evaluation.

6. REFERENCES

- Bluestein, H.B., A.L. Pazmany, J.C. Galloway, and R.E. McIntosh, 1995: Studies of the substructure of severe convective storms using a mobile 3-mm-wavelength Doppler radar. *Bull. Amer. Meteor. Soc.*, **76**, 2155-2169.
- Cess, R.D. et al., 1990: Intercomparison and interpretation of climate feedback processes in nineteen atmospheric general circulation models. *J. Geophys. Res.*, **95**, No. D10, 16601-16615.
- Clothiaux, E.E., M.A. Miller, B.A. Albrecht, T.P. Ackerman, J. Verlinde, D.M. Babb, R.M. Peters, and W.J. Syrett, 1995: An Evaluation of a 94-GHz Radar for Remote Sensing of Cloud Properties. *J. Atmos. Oceanic Technol.*, **12**, 201-229.
- Danne, O., G.G. Mace, E.E. Clothiaux, X. Dong, T.P. Ackerman, and M. Quante, 1996: Observing structures and vertical motions within stratiform clouds using a vertical pointing 94-GHz cloud radar. *Contr. Atmos. Phys.*, in press.
- IGPO, 1994: Utility and feasibility of a cloud profiling radar: Report of the GEWEX topical workshop. IGPO Publication Series No. 10, 46pp.
- Lhermitte, R., 1987: A 94-GHz Doppler radar for cloud observations. *J. Atmos. Oceanic Technol.*, **4**, 36-48.
- Lhermitte, R., 1988: Cloud and precipitation remote sensing at 94-GHz. *IEEE Trans. Geosci. Remote Sens.*, **26**(3), 207-216.
- Mead, J.B., A.L. Pazmany, S.M. Sekelsky, and R.E. McIntosh, 1994: Millimeter-wave radars for remotely sensing clouds and precipitation. *Proceedings of the IEEE*, **82**, 1891-1906.
- Pazmany, A.J., J. Mead, R. McIntosh, M. Hervig, R. Kelly, and G. Vali, 1994: 95-GHz polarimetric radar measurements of orographic cap clouds. *J. Atmos. Oceanic Technol.*, **11**, 140-153.
- Syrett, W.J., B.A. Albrecht, and E.E. Clothiaux, 1995: Vertical structure in a midlatitude cyclone from a 94-GHz Radar. *Mon. Wea. Rev.*, **123**, 3393-3407.
- Uttal, T., E.E. Clothiaux, T.P. Ackerman, J.M. Intrieri, and W.L. Eberhard, 1995: Cloud boundary statistics during FIRE II. *J. Atmos. Sci.*, **52**, 4276-4284.

COMBINED TRIPLE-CHANNEL GROUND-BASED MICROWAVE RADIOMETER FOR MEASURING ATMOSPHERIC WATER PARAMETERS IN RAINY DAYS

Wei Chong

Institute of atmospheric Physics, CAS, Beijing 100029

I. INTRODUCTION

A dual-channel radiometer can give fairly high accuracy in probing the precipitable water vapor Q and vertically path-integrated cloud liquid water content L . However, with precipitation underway, it has no ability to obtain the accurate amount of total vapor and cloud liquid water, let alone the differentiation between the quantities of cloud- and rain- water, and in that case a rain measuring channel or other tools for rainfall measurement are required.

A physically iterative scheme is proposed in the present work for retrieving the parameters, including the atmospheric precipitable water vapor Q in a rainy period, path-integrated cloud liquid water L and the vertical rain parameter (RP) in terms of the combined radiometers, one being dual-channel of 0.86, 1.35 cm and the other single of 3.2 cm.

II. DETECTION PRINCIPLES AND RETRIEVAL CONSIDERATIONS

In non-precipitation cloudy weather, microwave attenuation optic thickness (MWAOT) τ_c has a good linear relation to the precipitable water vapor Q and path-integrated cloud liquid water content L , respectively. With subscripts 1,2 and 3 denoting the wavelength of 0.86, 1.35 and 3.2 cm (thereafter), we have the relation

$$\tau_{c3} = a_3 + b_3 \cdot Q + c_3 \cdot L \quad (1)$$

where a_3 , b_3 and c_3 are empirical regression constants.

For a rainy day, the total along-path MWAOT τ represents the sum of the background MWAOT τ_c of rainy atmosphere, which is the rainy atmospheric MWAOT after removing rain particles (equivalent to the path MWAOT under a non-precipitation cloudy sky), and the along-path rain particle MWAOT τ_r . Thus we find,

$$\begin{aligned} \tau_1 &= \tau_{c1} + \tau_{r1} \\ \tau_2 &= \tau_{c2} + \tau_{r2} \\ \tau_3 &= \tau_{c3} + \tau_{r3} \end{aligned} \quad (2)$$

where the rain path MWAOT $\tau_{r1,2,3}$ comes from the path integration of its attenuation coefficient α_r . The results in our previous work (Lin et al. 1981) show

$$\alpha_r = A \cdot R^B \quad (3)$$

where R is rain intensity, A , B are constants depending on spectrum form, wavelength and temperature.

Now our problem comes down to the following : with τ_1 , τ_2 and τ_3 known, how can we differentiate τ_{r3} , τ_{c1} and τ_{c2} correctly in the virtue of Equations (1) and (2) and other auxiliary relations. On this basis, the related Q and L can be acquired from τ_{c1} and τ_{c2} by use of the retrieval method suitable for non-precipitation cloudy weather and the associated rain parameters will be found through τ_{r3} .

Based on the analysis of microwave radiation characteristic of rain, two aspects of the rain-caused MWAOT are of note: i) some nonlinear relationship exists between the rain MWAOTs for different wavelengths, that is,

$$\begin{aligned}\frac{\tau_{r1}}{\tau_{r3}} &= f(\tau_{r3}) \\ \frac{\tau_{r2}}{\tau_{r3}} &= g(\tau_{r3})\end{aligned}\quad (4)$$

where f and g are some forms of function. We have known from the results of the Section IV that under the assumption of M-P droplet spectrum their particular manner are the functions decreasing logarithmically as τ_{r3} increasing; ii) for a non-precipitation cloudy sky, the 3.2 cm wavelength MWAOT τ_{c3} changes little as a function of Q and L . Therefore, if the initial value of τ_{r3} is to be found from the total MWAOT τ_3 using the third relation of Equations (2), we will take τ_{c3} to be the climatic constant τ_{c30} , which is then removed.

Based on the foregoing analysis, an iterative scheme is presented as follows:

1) The initial values $\tau_{r3}^{(0)}$ of 3.2 cm wavelength rain MWAOT is obtained by removing τ_{c30} from the measurement τ_3 ;

2) The initial values of the other two channel's MWAOT are found with the aid of equation (4), viz.,

$$\tau_{r1}^{(0)} = f(\tau_{r3}^{(0)}) \cdot \tau_{r3}^{(0)}$$

and

$$\tau_{r2}^{(0)} = g(\tau_{r3}^{(0)}) \cdot \tau_{r3}^{(0)}$$

3) The initial value of a non-precipitation cloudy sky MWAOT is found from Equation (2) for 0.86 and 1.35 cm wavelengths, separately

$$\tau_{c1}^{(0)} = \tau_1 - \tau_{r1}^{(0)}$$

$$\tau_{c2}^{(0)} = \tau_2 - \tau_{r2}^{(0)}$$

4) In the light of the given scheme, the initial values of precipitable water vapor $Q^{(0)}$ and of the path-integrated cloud liquid water content $L^{(0)}$ are retrieved from $\tau_{c1}^{(0)}$ and $\tau_{c2}^{(0)}$, respectively.

5) With the help of the Equation (1) and the third relation of Equations (2), the reduced 3.2 cm wavelength rain MWAOT is found as

$$\tau_{r3}^{(1)} = \tau_3 - a_3 - b_3 \cdot Q^{(0)} - c_3 \cdot L^{(0)}$$

6) $(\tau_{r3}^{(1)} - \tau_{r3}^{(0)}) / \tau_{r3}^{(0)} \leq \varepsilon$ (with ε assumed to be 0.01 for calculation) is used as the criterion. If it is not satisfied, then $\gamma = \tau_{r3}^{(0)} / \tau_{r3}^{(1)}$ is set, and with $\tau_{r3}^{(0)} \cdot \gamma$ in lieu of $\tau_{r3}^{(0)}$ steps from (2) through (6) are repeated for iteration till the criterion is met. And the $\tau_{r3}^{(n)}$, $Q^{(n)}$ and $L^{(n)}$ thus obtained are the retrieved parameters of rain, water vapor and cloud liquid water, respectively.

III. ATMOSPHERIC CLOUD/RAIN MODEL

In order to put the scheme presented in the last section into effect and make numerical test of the results, it is necessary to compute related quantities of a statistically representative sample in the framework of a cloud/rain genesis model.

Decker et al. (1978) proposed a scheme for constructing a cloud model based on soundings which was employed as a geometric and physical framework for calculating non-precipitable cloudy radiation transfer. And in the context of this cloud model, with vertical path-integrated cloud liquid water content L as a criterion, rain occurrence is determined for L greater than a given critical value L_0 . The rain layer spans from ground to 0 °C level and shows the same rain droplet spectrum everywhere; for the same case of a cloudy sky, rainfall intensity can be put into an variable range, depending on L_0 . That is to say, clouds with a small or smaller amount of cloud liquid water L will produce light or light to moderate rain

whereas those of great L can generate both light and heavy to torrential rain.

IV. REGRESSION SAMPLES AND RELATIONS

80 sets of summer soundings were selected from the Yap Island ($9^{\circ} 39'N$, $138^{\circ} 05' E$) in the western Pacific tropical waters. These sets were dealt with by the technique described in the last section to produce 112 sets of atmospheric cloud/rain samples. With these resulting sets and the M-P rain spectrum assumption, the related quantities of each of these samples were calculated, leading to regression relations and coefficients relative to retrieval mentioned in section II and III.

V. TEST SAMPLES OF RETRIEVAL RESULTS

100 sets of winter soundings in Yap were chosen that were in strong contrast to the samples used above for the regression on a seasonal basis, and formed 134 sets of cloud/rain atmospheric test samples. The verified samples are separated, according to R , into the categories as $0.05 < R < 3$, $3 < R < 20$ and $20 < R < 50$ mm/h for statistical purpose. Statistics of errors from the comparison of the retrieved to the simulated true values is prepared.

VI. RESULTS AND CONCLUSION

From the foregoing analysis the following are of note:

1) Test against 134 independent samples shows that the retrieved Q , L and rain parameters in a rainy atmosphere have relative error of 4, 18 and 13%, respectively, from comparison of their retrieved to the simulated true values. For $R > 20$ mm/h, the iteration proposed in this work is of no use on account of the "saturation" of 0.86 and 1.35 cm wavelength measurements. In that case, high accuracy rain parameters can be obtained by the proposed removal scheme with no iteration to be done and so can the acceptable accuracy Q and L .

2) For small rainfall intensity, the vertical measurement by a mere 3.2 cm radiometer yields

poor accuracy with relative error in excess of 600%. However, the combination of the two radiometers can dramatically raise the measurement accuracy, keeping relative error inside 13%, and for $R < 20$ mm/h the retrieved rainfall accuracy is more than doubled from the measurements of the combined set as compared to that from the 3.2 cm wavelength device only. For higher R , both techniques produce comparable accuracy.

3) This article investigates problems under the assumption of M-P rain droplet spectrum. For a practical rain spectrum, the form of Eq.(4), mode of selecting γ in step (6) of Section II and all coefficients in relation to retrieval performance are perhaps subjected to a proper adjustment, following the characteristics of a statistically typical spectrum. Nevertheless, the retrieval considerations presented in Section II remains of use. Since the M-P spectrum is marked by wider representativeness, the combination technique is expected to be of practical use to a considerable extent. This work demonstrates that all-weather atmospheric water measurement by the combined radiometers are of great promise.

ACKNOWLEDGEMENT

The study is supported by the National Science Foundation of China.

REFERENCES

- Decker, M. T., et al., 1978, Experimental evaluation of ground-based microwave radiometric sensing of atmospheric temperature and water vapor profiles, *J. Appl. Meteor.*, 17, 1788-1795.
- Lin Hai, Wei Chong and Lu Daren, 1981, Microwave radiation features of raindrops, *Chinese Journal of Atmospheric sciences*, 5(2), 188-197.

STUDY OF SPACIAL DISTRIBUTION OF PHASE AND SIZE OF HYDROMETEORS BY DUAL LINEAR POLARIZATION RADAR

Liu Liping and Wang Zhijun

Lanzhou Institute of Plateau atmospheric Physics, Chinese Academy of Sciences,
Lanzhou, Gansu, 730000, China

1. INTRODUCTION

Radar can provide an important means to study the cloud physics and precipitation. Development of advanced theory and new detecting facilities is one of the subject in radar meteorology. Since Seliga and Bringi (1976) proposed a dual linear polarization radar theory to improve the accuracy of rainfall measurement, more and more meteorologists have been attracted in this field. Most of researchers indicated that the dual linear polarization radar may provide direct evidences for identification of hailshaft and research on crystals and snowflakes.

The C band dual linear polarization radar at Lanzhou Institute of Plateau Atmospheric Physics, Chinese Academy of Science has been used to observed the several storms since 1987. In this paper, we presented the observational results of stratiform and convective clouds by the C band dual linear polarization radar.

2. THE RADAR SYSTEM

The dual linera polarization radar was located in Pingliang Radar Station ($106^{\circ}40'$

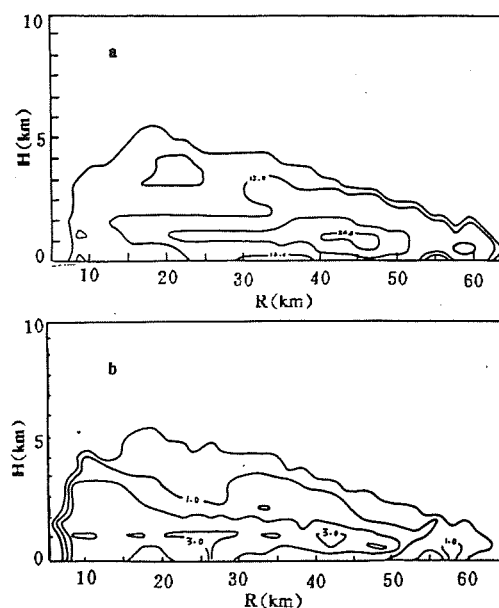


Fig1. Z_H (a) and Z_{DR} (b) at the vertical cross sections of the stratiform cloud along 163° azimuth on June 6, 1995.

$E, 35^{\circ}36'N$), Gansu Province, China, which work in model of transmitting and receiving horizontally and vertically polarized microwave alternately on pulse to pulse (Xu et al. 1991). Its Pulse Repetition Frequency (PRF) is 500Hz, the standard deviation of Z_H and Z_{DR} are less than 1. 0dB and 0. 2dB respectively. During summer of 1987 — 1995, we operated the radar system for collection of data .

3. OBSERVATIONAL RESULTS

3.1 Stratiform Cloud

Fig. 1 illustrates the stratiform cloud vertical cross section of June 6, 1995, along the azimuth of 163° . The Z_H and Z_{DR} increase significantly above the altitude of 1.5km, and decrease below this altitude as the altitude decrease. Five local maximums in Z_{DR} (>3.0 dB) accompanied by Z_H of over 20dBZ is at altitude of 1.2km. There is a pronounced bright band at all range. The changes of Z_H and Z_{DR} with altitude might explain melting processes of ice particles below 0°C isotherm. The ice phase particles above 0°C isotherm, such as crystals and snowflakes, in form of plate which fall with their larger dimension horizontally aligned fall to the 0°C isotherm, begin melt and form big raindrops, which have larger Z_H and Z_{DR} . Then particles complete their melting process, as even raindrops breakup, which make Z_H and Z_{DR} decrease again.

3.2 Convective Cloud

The Fig. 2 show a typical convective cloud vertical cross section of July 6, 1994 through the most intense section of the cloud. The top of echo is at 11.5km, The region of high positive Z_{DR} (>3.0 dB) extended to altitude of 5.5km, accompanied by Z_H of over 30dBZ. The maximum in Z_H of 40dBZ and Z_{DR} of 4.0dBZ is at 1.5km. We shall offer an explanation assuming that there are larger wet ice particles or supercooled raindrops in the upper parts of cloud where the Z_{DR} is over 3.0dBZ. The region of negative Z_{DR} at 44km range behind the intensive Z_H area is due to the microwave attenuation through the huge rain area.

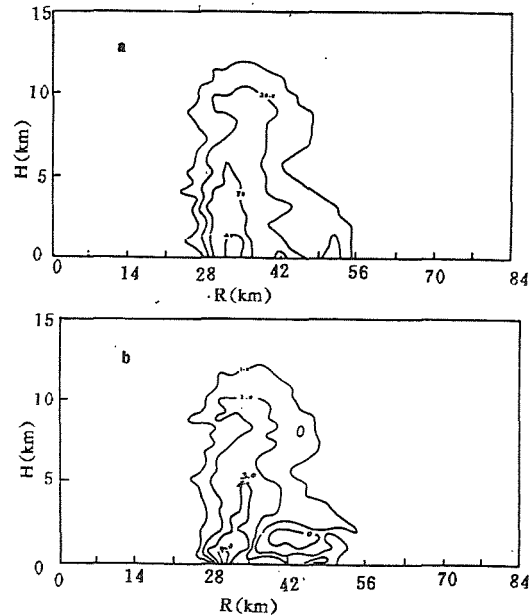


Fig2. Z_H (a) and Z_{DR} (b) at the vertical cross sections of the convective cloud along 151° azimuth on July 6, 1994.

3.3 Hail Storm

The supercell of August 9, 1990 is good case to show the Z_H and Z_{DR} vertical structures of hail storm (Fig. 3). The maximum of Z_H is 55dBZ, two regions where Z_{DR} is larger than 3.0dB are over 4.0km. The Z_{DR} vertical cross section show a positive Z_{DR} in upper part and negative Z_{DR} in lower part within the intensive echo, where exited the hailstones. The changes of shape, phase and size of hailstone due to the melting process below 0°C isotherm is the reason that Z_{DR} decreases with decrease of altitude. The calculations of scattering properties of oblate hailstone with C band radar wave demonstrated that the Z_{DR} of big hailstone ($D > 2.0\text{cm}$) changes with the size of dimension of hailstone, for example, the Z_{DR} of oblate hailstone with $D = 2.0\text{cm}$ and $D = 2.4\text{cm}$ are positive and negative respectively.

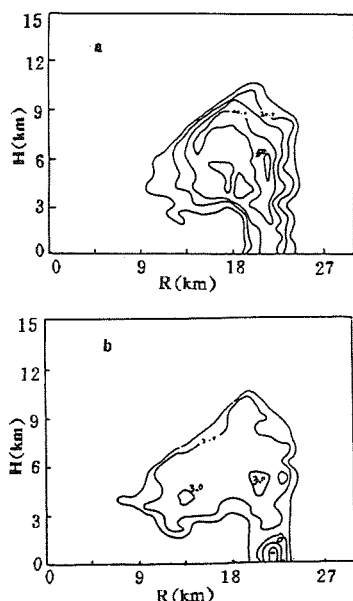


Fig. 3 Z_H (a) and Z_{DR} (b) at the vertical cross sections of the hail storm along 339° azimuth on Aug. 9, 1990.

In this paper, we have analyzed systemly the vertical cross section of Z_H and Z_{DR} in stratiform and convective clouds. The regions of high positive Z_{DR} subsequently extended to 5.0 km altitude in convective cloud, where there is possibly larger supercooled raindrops and ice particles. These particles may effect the development of cloud. The change of Z_{DR} with altitude due to the melting process below 0°C isotherm is explained.

4. REFERENCES

Seliga, T. A., and V. N. Bringi, 1976: Potentail use of radar differential reflectivity measurements at orthogonal polarizations for measuring precipitation. J. Appl. Meteor., 15, 69—76.

Xu Baoxiang, Wang Zhijun, Cai Qiming, and Liu Liping et al., 1991: Study on applications of C — band dual linear polarization radar in meteorology. ACTC Meteor. Sinica, 5, 285—292.

DETERMINATION OF EFFECTIVE RADIUS OF DROPS IN WATER CLOUDS FROM SPACE: A NEW APPROACH

Alexander A. Kokhanovsky ¹, Eleonora P. Zege ²

¹EORC/NASDA, 1-9-9 Roppongi, Minato-ku, Tokyo 106, Japan

²Institute of Physics, 70 Skarina Avenue, Minsk 220072, Belarus

1. INTRODUCTION

The investigation of microphysical properties of water clouds from space is an important source of information about cloud media in the global scale. There has been an increasing number of studies pertaining to the retrieval theories and methods for obtaining cloud optical thickness and particle size from multispectral radiometers on satellites (Curran and Wu, 1982; Arking and Childs, 1985; Patnick and Twomey, 1994; Han et al., 1994; Nakajima and Nakajima, 1996). All of them are based on numerical solutions of the radiative transfer equation for plane parallel media.

The task of this contribution is to introduce a simple method of the particle size determination from the reflection function measurements. It is based on the asymptotical radiative transfer equation solutions for thick weak absorbing layers and the geometrical optics approximation for the local optical characteristics of water clouds.

2. REFLECTION FUNCTION OF WATER CLOUD

In the visible and the near infrared regions of the spectrum water clouds can be considered as thick weakly absorbing light scattering media. The reflection function $R(\mu_0, \mu)$ of such media can be represented in the following form (Zege et al., 1991; Kokhanovsky & Zege, 1996):

$$R(\mu_0, \mu) = R_\infty(\mu_0, \mu) \exp(-Fy) - \Pi g(\mu_0) g(\mu) \exp(-y[1+z]) + A \Pi g(\mu_0) g(\mu) / (1 - Ar), \quad (1)$$

where

$$R_\infty(\mu_0, \mu) = \frac{1 + 4\mu\mu_0}{2(\mu + \mu_0)}, \quad (2)$$

$$g(\mu) = \frac{3}{7}(1 + 2\mu), \quad \Pi = \frac{\sinh(y)}{\sinh(y[1+z])}, \quad (3)$$

$$F = \frac{g(\mu_0)g(\mu)}{R_\infty(\mu_0, \mu)}, \quad (4)$$

$$r = e^{-y} - \Pi e^{-y(1+z)}, \quad (5)$$

$$y = 4 \sqrt{\frac{\sigma_{abs}}{3\sigma_{ext}(1 - \langle \cos \theta \rangle)}}, \quad (6)$$

$$z = 0.75(1 - \langle \cos \theta \rangle) \sigma_{ext} L. \quad (7)$$

Here A is the albedo of the Lambertian underlying surface, $\langle \cos \theta \rangle$ is the asymmetry parameter, σ_{ext} and σ_{abs} are the extinction and absorption coefficients of cloud media, L is the geometrical thickness of cloud, μ_0 and μ are the cosines of the sun and the observation angles. The solutions (1)-(7) can be used for small observation angles, because they do not account for the azimuth dependence of reflection functions of water clouds.

The values of $\sigma_{ext}, \sigma_{abs}, \langle \cos \theta \rangle$ depend on the effective radius of particles $a = \frac{\langle a^3 \rangle}{\langle a^2 \rangle}$, where brackets mean the averaging on the particle size distribution.

They can be calculated within the framework of the Mie theory or the geometrical optics approximation. In the last case one can use the following solutions (Kokhanovsky & Zege, 1995):

$$\sigma_{ext} = \frac{1.5C_v}{a} \left\{ 1 + \frac{1.1}{(ka)^{2/3}} \right\}, \quad (8)$$

$$\sigma_{abs} = 1.2\alpha C_v (1+s)(1-\alpha a), \quad (9)$$

$$1 - \langle \cos \theta \rangle = 0.118 + \frac{0.5 + 0.2c}{(ka)^{2/3}} \quad (10)$$

$$-0.75c \left\{ 0.1 + \frac{1}{2(ka)^{2/3}} \right\},$$

where

$$\alpha = 4\pi\chi/\lambda, c = 2\alpha a,$$

$$s = 0.34(1 - \exp(-8\lambda/a)),$$

$k = 2\pi/\lambda$, C_v is the volumetric concentration of particles, λ is the wavelength, χ is the imaginary part of the refractive index of drops.

The relative error of Eqs. (8) - (10) is less than 10 percent for $\lambda < 2.2\mu\text{m}$, $a = 4 \div 20\mu\text{m}$.

From Eqs. (6) - (10) it follows:

$$y = G\sqrt{\alpha a}, \quad z = \frac{Dw}{a\rho}, \quad (11)$$

where $w = C_v \rho L$ is the liquid water path, ρ is the density of water and

$$G = 6 \sqrt{\frac{(1+s)(1-\alpha a)}{1+5(ka)^{-2/3}}},$$

$$D = 0.7(0.2 + (ka)^{-2/3}) - 0.17\alpha a.$$

The accuracy of solutions (1) - (5), (11) was investigated by Kokhanovsky & Zege(1996). It was found, e. g., that the relative error of calculation of the reflection function is less than 15 percent at sun angles less than 50° , nadir observations and the optical thickness $\tau > 13$, $\lambda < 2.2\mu\text{m}$, $a = 4 \div 12\mu\text{m}$.

So, simple solutions (1) -(5), (11) can be used to investigate the dependence of the reflection function of water clouds from their microstructure parameters. They simplify the inverse problem solution as well.

3. RETRIEVAL ALGORITHM

Eqs. (1) - (5), (11) can be used to retrieve the effective radius and the liquid water path of water clouds. To do so one should measure the reflection function at two wavelengths (in the visible and the near-infrared regions of the spectrum). In the visible band water clouds almost do not absorb solar radiation and $y=0$ (see Eq. (6)). In this case it follows from Eq. (1):

$$z(\lambda = \lambda_1) = \frac{g(\mu_0)g(\mu)}{R_\infty - R(\lambda = \lambda_1)} - \frac{1}{1-A}. \quad (12)$$

Here $R(\lambda = \lambda_1)$ is the measured reflection function at $\lambda = \lambda_1$ and $z(\lambda = \lambda_1)$ is the value of z at $\lambda = \lambda_1$.

In the near infrared region of spectrum one should solve the following equation to find the value of the effective radius (see Eq. (1)) :

$$\begin{aligned} &R(\mu_0, \mu, \lambda = \lambda_2) - R_\infty(\mu_0, \mu) \exp(-Fy(\lambda = \lambda_2)) \\ &+ \Pi g(\mu_0)g(\mu) \exp(-y(\lambda = \lambda_2)[1 + z(\lambda = \lambda_2)]) \\ &- A \Pi g(\mu_0)g(\mu)/(1 - Ar) = 0. \end{aligned} \quad (13)$$

Note, that the value of

$$z(\lambda = \lambda_2) = \frac{D(\lambda = \lambda_2)}{D(\lambda = \lambda_1)} z(\lambda = \lambda_1), \quad (14)$$

in Eq. (13) depends on the effective radius of particles and the value of $z(\lambda = \lambda_1)$. The value of $y(\lambda = \lambda_2)$ depends only on the value of the effective radius of particles .

So it is possible to find the value of a from Eq. (13) even one can not have information on the liquid water path of water cloud. After that the liquid water path can be determined from Eq. (11).

To determine the error of the retrieval of the value of the effective radius within the framework of this approach, the calculations of reflection functions $R(\lambda = \lambda_1), R(\lambda = \lambda_2)$ of water clouds of different microstructure were performed with the doubling method of the radiative transfer equation solution. The Mie theory was used to calculate the extinction and absorption coefficients as well as the phase function of cloud media at $\lambda_1 = 0.659 \mu\text{m}$, $\lambda_2 = 2.13 \mu\text{m}$. After that the effective radius of drops was retrieved with Eqs. (12) - (14). It was found that the error of the effective radius determination is less than 15 percent for sun angles, ranged from 30 to 45 degrees at the nadir observation. The maximum error (around 30 percent) is located at glory and rainbow scattering angles, where the geometrical optics approximation is characterized by small accuracy.

4. CONCLUSION

A new simple technique to retrieve the effective radius of water drops from satellite measurements of reflection functions of water clouds is proposed. It is based on the asymptotical solutions of the radiative transfer theory for thick weak absorbing layers and the geometrical optics approximation for local optical properties of water clouds.

5. Acknowledgments

The authors wish to thank I. L. Katsev and A. S. Prikhach for helpful discussions.

6. REFERENCES

Arking, A., and J. D. Childs, 1985: Retrieval of clouds cover parameters from satellite images. *J. Appl. Meteor.*, **24**, 322-333.

Curran, R. J., and M. L. C. Wu, 1982: Skylab near infrared observations of clouds indicating supercooled liquid water droplets. *J. Atmos. Sci.*, **39**, 635-647.

Han, Q., et al., 1994: Near-global survey of effective droplet radii in liquid water clouds using ISCCP data. *J. Climate*, **7**, 465-497.

Kokhanovsky, A. A., and E. P. Zege, 1995: Local optical properties of spherical polydispersions: simple approximations. *Appl. Optics*, **34**, 5513-5519.

Kokhanovsky, A. A., and Zege E. P., 1996: The determination of the effective radius of drops and liquid water path of water cloud from satellite measurements. *Space Res.*, 1996, in press.

Nakajima, T., T. Nakajima, 1996: Wide-area determination of cloud microphysical properties from NOAA AVHRR measurements for FIRE and ASTEX regions. *J. of Atmos. Sci.*, **52**, 1-22.

Platnick, S., and S. Twomey, 1994: Determining the susceptibility of cloud albedo to changes in droplet concentration with the Advanced Very High Resolution Radiometer. *J. Appl. Meteor.*, **33**, 334-347.

Zege, E. P., et al., 1991: *Image transfer through scattering media*. Berlin: Springer Verlag, 247p.

INVESTIGATION OF CLOUDS FROM A DUAL BEAM 95 GHz RADAR

Anne GUYOT and Jacques TESTUD

Centre d'études des Environnements Terrestres et Planétaires
Issy-les-Moulineaux, France

1. INTRODUCTION

Clouds strongly influence the radiative budget of the meteorological atmosphere. So they play an important role in the dynamics of the atmosphere and in the control of the climate. Presently they are only crudely represented in the weather forecast models, partly because of an imperfect knowledge of their physical processes. RALI (airborne RADar and LIdar) plans to associate a dual beam 95 GHz cloud Doppler radar and a backscattering lidar on a same airborne platform, in order to document the microphysical and dynamical properties of non precipitating clouds.

In the case of optically thin clouds, data from both instruments are available and can be combined to retrieve the microphysical characteristics of the cloud particles size distribution. But in dense clouds, the lidar is extinguished over a few tenth of meters, only the radar provides attenuated reflectivities from the two viewing angles. Correcting reflectivity for along path attenuation, at 95 GHz, is a major problem in warm clouds, as the linear attenuation at this frequency is about 4 dB km^{-1} for a 1 g m^{-3} liquid water content (W). This is why we have chosen to use the dual beam methodology (which was successfully tested with the CaPE and TOGA-COARE experiments data; see Kabèche and Testud, 1994), and to evaluate its performance in the retrieval of the "true" reflectivity Z and specific attenuation K fields. Thus, our work is focused on the scientific exploitation of the dual beam cloud radar following the stereoradar analysis.

We have first simulated the sampling of the attenuated reflectivity field by the cloud radar along the two beams, one pointing at nadir and the other at 40 degrees fore. Then we have applied the stereoradar methodology to these "data" which provided us the attenuation and true reflectivity fields.

In the second part of the paper, we perform Mie scattering calculation at 95 GHz for cloud and rain particle spectra, in order to determine the corresponding integrated parameters Z and K . It is shown that cloud drop and rain drop spectra produce quite different Z - K relationships. Thus the ability of the dual beam technique to provide simultaneously estimate of Z and K provides a mean to discriminate cloud from rain.

2. CUMULUS SIMULATION

We consider an axisymmetric cumulus cloud in which the vertical profile of liquid water content along

the cloud axis $W_{\max}(h)$ follows the wet adiabatic curve between the cloud base (assumed to be at 1.2 km altitude and at 20°C wet bulb potential temperature, typical values for Florida summer cumuli), and the level 2.7 km, and then decreases rapidly due to entrainment between 2.7 km and 3.2 km, the assumed cloud top. $W_{\max}(h)$ is illustrated in Fig.1. To determine the corresponding radar reflectivity profile $Z_{\max}(h)$, we apply a Z - W relationship determined by Atlas (1994) for cumulus:

$$Z (\text{mm}^6\text{m}^{-3}) = 9.64 \cdot 10^{-2} W (\text{g}\cdot\text{m}^{-3})$$

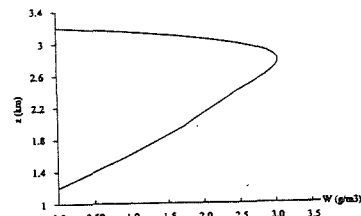


Fig.1: Cumulus vertical liquid water content profile.

The full three-dimensional reflectivity model is obtained assuming a gaussian shape in the horizontal plane, whose expression in dBZ will be:

$$Z(x,y,h) = Z_{\max}(h) - 3 \cdot (x^2 + y^2) / r_0^2$$

[x, y in km; Z, Z_{\max} in dBZ]

where r_0 is the "3 dB cloud radius".

The X-band radar observations from Knight and Miller (1993) suggest a value for r_0 of 0.28 km. Fig.2 illustrates a vertical section of the reflectivity field model obtained with this value of r_0 . The corresponding field of specific attenuation K (in dB km^{-1}) is derived from the relation $K = 4 W$ given by Meneghini and Kozu (1990) valid for a temperature of 15°C .

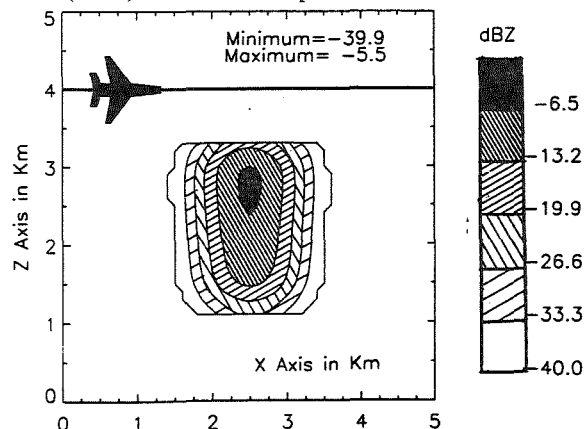


Fig.2: Vertical section of the cumulus reflectivity field model.

3. RALI SIMULATION AND DUAL BEAM ANALYSIS

At an attenuated frequency as 95 GHz, the radar does not measure the "true" reflectivity Z but an "apparent" reflectivity Z_a subject to the two-way path attenuation. Z_a is related to Z through:

$$Z_a = Z - 2 \int_0^r K dr \quad [Z, Z_a \text{ in dBZ}] \quad (1)$$

The principle of the dual beam methodology consists of operating at two incidence angles, namely, in the RALI project, at nadir and at 40° fore (from nadir). Denoting r_1 and r_2 the radial distance along the fore and nadir look, respectively, we obtain by differentiation of (1) with respect to r :

$$\frac{dZ_{af}}{dr_1} = \frac{dZ}{dr_1} - 2K \quad \text{and} \quad \frac{dZ_{an}}{dr_2} = \frac{dZ}{dr_2} - 2K \quad (2)$$

where subscripts n and f stand for nadir and 40°fore incidence, respectively.

Eliminating K by subtraction of Eqs. (2), and expressing the differential as a function of the partial derivatives, we get the "stereoradar equation" as:

$$\sin \theta \frac{\partial Z}{\partial X} + (1 - \cos \theta) \frac{\partial Z}{\partial h} = \frac{dZ_{af}}{dr_1} - \frac{dZ_{an}}{dr_2} \quad (3)$$

[Z in dBZ]

Eq. (3) is a partial derivative equation that may be solved for Z with the appropriate boundary condition $Z = Z_{af}$ (or $Z = Z_{an}$) at the cloud edge in direct sight from the radar¹. Once Z is retrieved, K may be subsequently determined using (2). Thus the stereoradar analysis, without making any assumption about the phase of hydrometeors, provides independently two parameters: Z and K . For details about the implementation of this technique, see Kabèche and Testud (1995).

The cloud radar is assumed to sample alternately the nadir and fore looks, with the following characteristics:

Antenna beam width:	0.8°
Range resolution:	30 m
Detectivity at 0dB SNR:	-18 dBZ at 3 km
Integration time:	0.2 s
Aircraft velocity:	80 m/s
Along track resolution:	32 m
Nb of indep. samples:	2000

Table 1: Sampling characteristics

The subsequent noise in the Z_a data is simulated following the scheme described in Testud et al. (1996). When the SNR gets below -13.5 dB, the data is rejected from the analysis. This threshold is determined from the consideration that a Z_a data cannot be exploited when the radiometric resolution exceeds 2 dB.

¹In a stratiform cloud, $\partial Z / \partial x = 0$. The Eq. (3) should be integrated downward with the boundary condition $z = z_{af}$ (or $z = z_{an}$) at cloud top.

Fig. 3 illustrates the apparent reflectivity fields observed along the fore and nadir looks. The aircraft is assumed to fly at 4 km altitude. Note the significant effect of attenuation when referring to the original Z field.

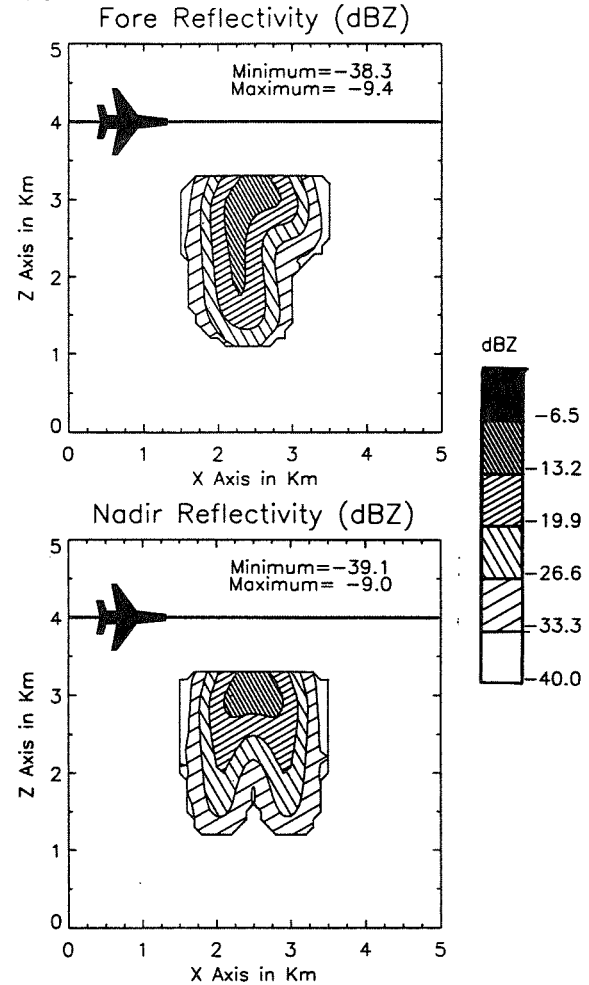


Fig.3: Apparent reflectivity fields simulation along fore and nadir beams.

The application of the stereoradar analysis is illustrated in Figs. 4. Fig. 4a displays the domain where a boundary condition $Z = Z_{af}$ or $Z = Z_{an}$ is available. Fig. 4b displays the retrieved reflectivity Z and specific attenuation K , respectively.

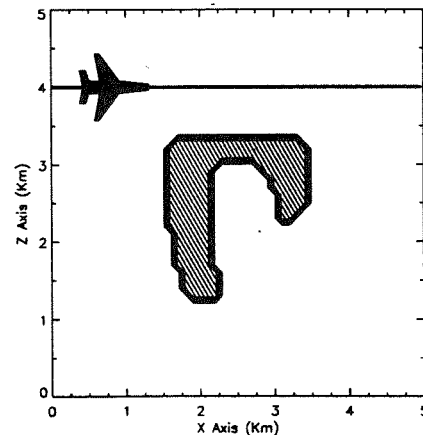


Fig.4a: Boundary conditions domain.

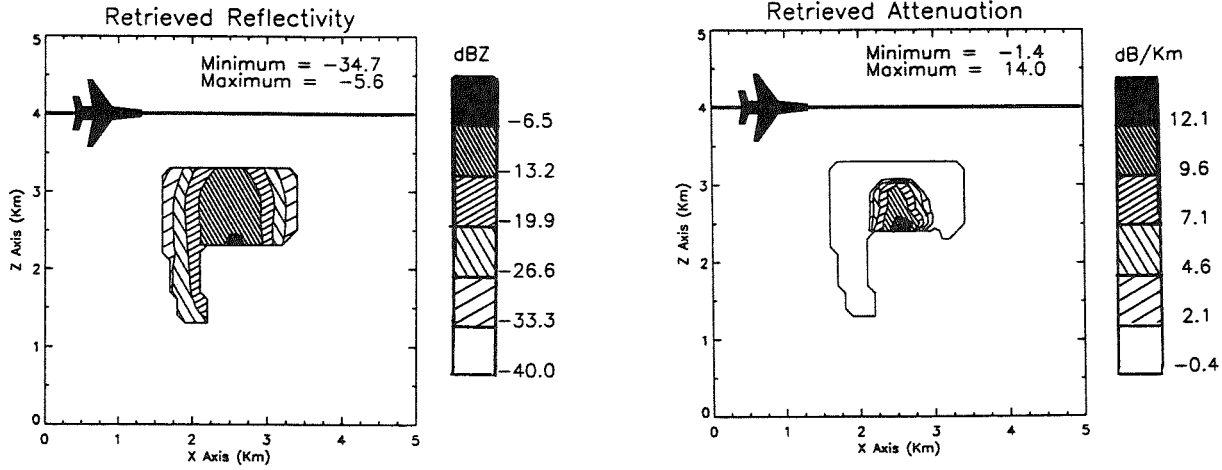


Fig. 4b: Stereoradar analysis results: retrieved reflectivity Z and specific attenuation K fields.

Fig. 5 representing the scatter plot K against Z, allows to evaluate the quality of the retrieval. The fit by a powerlaw of the "data points" provides a relation which is very close to the original, which means that the bias of the retrieval is quite moderate. As for the fluctuation of the K estimate, it seems of the order of 1 dB/km.

$$\text{FIT: } K = 3.9963e+01 \cdot Z^{0.929} \quad R = 0.987$$

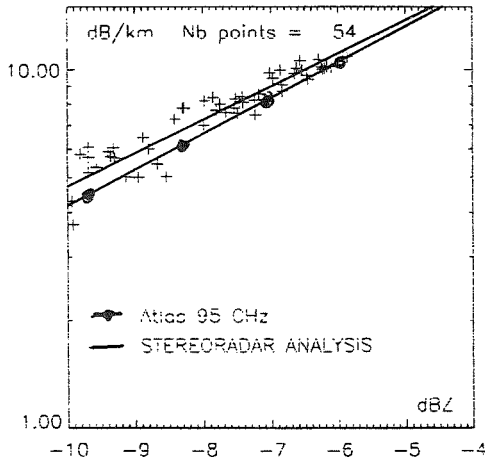


Fig. 5: K-Z scatter plot, original relation and fitted relation.

4. MIE SCATTERING CALCULATIONS

In order to exploit the potential of the stereoradar analysis (which lays in its ability to simultaneously retrieve the Z and K fields), we have performed some calculations of Z and K for various types of raindrop and cloud drop spectra, using the Mie scattering theory. As a matter of fact rain and cloud are known to have quite different scattering and attenuating properties.

For rain, we have considered the standard exponential rain drop size distribution (DSD) (Marshall and Palmer, 1948) $N(D) = 8 \cdot 10^6 e^{-\Lambda D} \text{ m}^{-4}$ where $\Lambda = 41R^{-0.21} \text{ cm}^{-1}$. By means of a Mie scattering calculation, we then calculate the reflectivity Z, the

attenuation K and the rain rate R, defined respectively as:

$$Z = \frac{\lambda^4 10^{18}}{0.93 \cdot \pi^5} \int N(D) \sigma_b(D) dD \quad (\text{mm}^6 \text{m}^{-3})$$

$$K = \frac{10^4}{\ln 10} \int N(D) \sigma_a(D) dD \quad (\text{dB} \cdot \text{km}^{-1})$$

$$R = 3.6 \cdot 10^6 \frac{\pi}{6} \int N(D) v(D) D^3 dD \quad (\text{mm} / \text{h})$$

Our calculation covered the range of rainfall rate 1 to 100 mm/h.

In the case of clouds, we have chosen gamma drop size distributions (Shettle, 1990) as $N(R) = N_0 R^\mu e^{-\Lambda R}$ for three different sorts of clouds: cumulus, strato-cumulus and stratus:

$$N_c(R) = 2.604 \cdot 10^{30} R^3 e^{-0.5 \cdot 10^6 R} \text{ m}^{-4}$$

$$N_{sc}(R) = 52.734 \cdot 10^{24} R^2 e^{-0.75 \cdot 10^6 R} \text{ m}^{-4}$$

$$N_s(R) = 27 \cdot 10^{24} R^2 e^{-0.6 \cdot 10^6 R} \text{ m}^{-4}$$

At 95 GHz, for $D_{\max} = 100 \mu\text{m}$, we always have $D < 0.07\lambda$, so we are in the Rayleigh scattering approximation. The reflectivity calculation is then $Z = \int N(D) D^6 dD \quad (\text{mm}^6 \text{m}^{-3})$, the liquid water content

formula is $W = \frac{\pi}{6} \cdot 10^6 \int N(D) D^3 dD \quad (\text{g} / \text{m}^3)$. The attenuation is still calculated by needs of the Mie scattering cross sections computation, which is more general.

These calculations permit us to plot K versus Z and K versus W for the three different types of cloud spectra, and for the Marshall-Palmer rain, for a temperature of 10°C (Fig. 6 and 7). We have also performed power law fits of the data pertaining to each type of spectra, and for two other temperatures, 0°C and 20°C . Table 2 displays the obtained K-Z relationships and Table 3 the K-W ones.

From Figure 6 it clearly appears that rain and clouds can be distinguished from the domain they occupy in the K-Z plane. The dependence of the various K-Z relationships as a function of the temperature is quite moderate from Table 2.

Particles	0°C	10°C	20°C
Rain	$K=0.018Z^{1.182}$ $\rho=0.99$	$K=0.015Z^{1.184}$ $\rho=0.99$	$K=0.013Z^{1.186}$ $\rho=0.99$
Cu	$K=33.91Z^{0.701}$ $\rho=0.99$	$K=30.82Z^{0.701}$ $\rho=0.99$	$K=27.11Z^{0.701}$ $\rho=0.99$
StCu	$K=48.09Z^{0.667}$ $\rho=1.00$	$K=43.69Z^{0.667}$ $\rho=1.00$	$K=38.40Z^{0.667}$ $\rho=1.00$
St	$K=38.50Z^{0.667}$ $\rho=1.00$	$K=34.99Z^{0.667}$ $\rho=1.00$	$K=30.76Z^{0.667}$ $\rho=1.00$

Table 2: K-Z relations and linear correlation coefficient ρ for different types of particles and three temperatures.

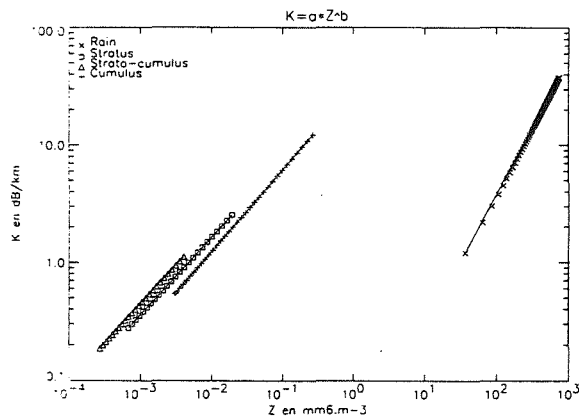


Fig. 6: K-Z scatter plots for different particle types, and their fit at 10°C

Figure 7 displays also a clear difference between rain and clouds. Table 3 shows that the K-W relationships in clouds are linear at any temperature. K is an excellent W estimator if ever we know particles are cloud or rain particles.

Particles	0°C	10°C	20°C
Rain	$K=11.98W^{0.845}$ $\rho=0.99$	$K=12.05W^{0.840}$ $\rho=0.99$	$K=12.01W^{0.837}$ $\rho=0.99$
Cu	$K=4.803W^{1.001}$ $\rho=1.00$	$K=4.364W^{1.001}$ $\rho=1.00$	$K=3.837W^{1.001}$ $\rho=0.99$
StCu	$K=4.797W^{1.000}$ $\rho=1.00$	$K=4.358W^{1.000}$ $\rho=1.00$	$K=3.829W^{1.000}$ $\rho=1.00$
St	$K=4.800W^{1.000}$ $\rho=1.00$	$K=4.360W^{1.001}$ $\rho=1.00$	$K=3.832W^{1.001}$ $\rho=1.00$

Table 3: K-W relations and their linear correlation coefficient ρ for different particles types and three temperatures.

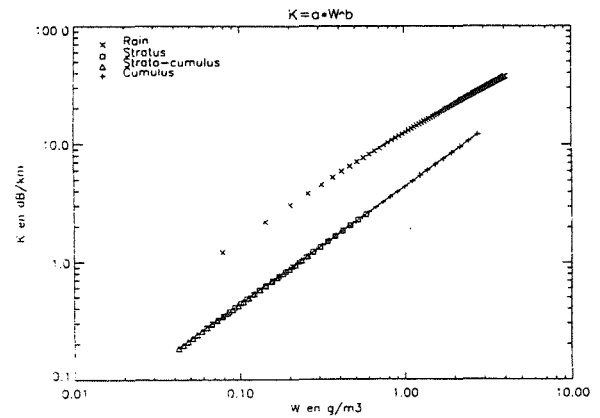


Fig. 7: K-W scatter plots for different particle types, and their fit at 10°C

5. CONCLUSION

Using an axisymmetric cloud model representative of a tropical cumulus, we have simulated the data from the dual beam 95 GHz radar of the RALI project. The simulation takes account of along path attenuation, and realistic noise in the data generation. We have then applied the stereoradar analysis to these data to retrieve the "true" reflectivity and attenuation fields. We have seen that the K retrieval could be operated with a quite moderate bias, and with a random fluctuation of ± 1 dB/km.

On the other hand we have performed Mie scattering calculation at 95 GHz for various particle spectra (in rain and clouds) and have obtained a set of K-Z and K-W relationships pertinent for each type of spectra and for various temperatures.

The results we have obtained in this paper will help us to interpret real 95 GHz radar data. We have seen that the stereoradar analysis provides satisfactory results at this frequency, so we may hope to be able to retrieve the true reflectivity and attenuation fields. Once we know Z and K, we will be able to determine the nature of particles: rain or cloud, and further to estimate the liquid water content W.

6. REFERENCES

- Atlas, D., 1994: Multiparameter relations for clouds. *WCRP-84*, B39-B41.
- Kabèche, A., and J. Testud, 1994: Stereoradar Meteorology: a new unified approach to process data from airborne or ground-based meteorological radars. *J. Atmos. Oceanic Technol.*, **6**, 89-108.
- Knight, C. A., and L. J. Miller, 1993: First radar echoes from cumulus clouds. *Bull. Amer. Meteor. Soc.*, **74**, 179-188.
- Marshall, J. S., and W. M. K. Palmer, 1948: The distribution of raindrops with size. *J. Meteor.*, **5**, 165-166.
- Meneghini, R., and T. Kozu, 1990: Spaceborne weather radar. *Artech House*, pp 199.
- Shettle, E. P., 1990: Models of aerosols, clouds and precipitation for atmospheric propagation studies. *Proc. 454 AGARD Conf.*, **15**.

GROUND BASED MICROWAVE MEASUREMENTS OF INTEGRAL LIQUID WATER CONTENT OF ARCTIC CLOUDS DURING BASE

A. Koldaev,¹ A. Troitsky,¹ J.W. Strapp² and B. Sheppard,²

1. Central Aerological Observatory, Moscow

2. Atmospheric Environment Service, Downsview, Canada

1. INTRODUCTION.

The importance of the liquid and ice phase in arctic cloud formation and evolution has not been thoroughly studied, and relatively few observations of the properties of arctic cloud have been presented to date. Liquid cloud droplets also play a key role in atmospheric radiation exchange. As more attention is paid over the next few years to arctic exchange processes in a number of major research projects, interest in the role of arctic clouds in these processes will intensify.

This study reports on arctic cloud integral LWC data obtained during the Beaufort and Arctic Storms Experiment (BASE), conducted by the Atmospheric Environment Service of Environment Canada in Inuvik, Northwest Territories in the fall 1994 (31 Aug-10 Oct. 1994).

2. INSTRUMENTATION

During the experiment a variety of platforms provided measurements throughout a 2 month period, including a research aircraft, two 3 cm Doppler radars, enhanced radiosondes, special surface precipitation monitors, and ground based microwave radiometers.

The research aircraft was a Convair-580 twin engine turboprop, owned and operated by the National Research Council of Canada, and instrumented by the AES and NRC with a set of equipment for storm research.

Measurement of integral LWC and other parameters using ground based microwave radiometry were supported by Central Aerological Observatory (Hydrometeoservice, Russia), using 3 mm, 5 mm, and 8 mm microwave radiometers produced by Atmospheric Technology Ltd. "ATTEX" (Russia).

The two microwave radiometers were installed on the roof of the meteorological station, situated ~ 2 km of the Inuvik airport. The radiometers were used to make continuous zenith-direction measurements of the brightness temperature of clouds. All radiometers are of the Dicke-type, with a sampling rate of 1KHz. The specifications of the cloud detecting ground-based microwave system are contained in Table 1.

3. DATA PROCESSING TECHNIQUES

Research aircraft data routinely documented the vertical distribution of the liquid water in clouds from ground level to 3000-5000 m during take-off and landing at Inuvik.

N	Parameter	Value	
		3mm	8mm
1	Central frequency	94GHz	37GHz
2	Sensitivity	0.1K	0.15K
3	Bandwidth	2GHz	2GHz
4	Stability	1K	1.5K
5	Modulation rate	1KHZ	1KHZ
6	Integration time	1s	1s
7	Recording rate	10s	10s
8	Power supply (27V)	40W	40W
9	Weight	3Kg	3Kg

Table 1. Radiometers system parameters.

airport. Vertical profiles of the temperature, dew-pond, LWC, and Ice Water Content (IWC) were constructed for each case. An estimate of the temperature range where LWC layers were encountered was made using aircraft microphysical probes (LWC, FSSP).

Remote microwave integral LWC data were obtained continuously.

Attenuation for each wavelength (3mm and 8mm) were calculated according to the following equation:

$$\tau_{3,8} = -\ln\left(1 - \frac{T_b}{T_a}\right) \quad (1)$$

where T_a is the mean radiating temperature of the atmosphere (usually 10K less than the simultaneous ground temperature).

Individual scatter plots in $T_b \times T_a$ were constructed for each LWC zone, identified manually from a time series of both 3 mm and 8 mm T_b s.

As it is well known the attenuation of the 3mm and 8mm wavelength radiation is the sum of absorption by clouds

liquid water- $\beta \cdot W$, atmospheric water vapour oxygen- $c \cdot Q$. The total absorption for each wavelength is thus given by the following equation:

$$\tau_{3,8} = b_{3,8} \cdot W + c_{3,8} \cdot Q + \tau_a \quad (2)$$

where W is integral LWC, Q is integral water vapour content, and b and c are coefficients .

The absorption by oxygen is assumed to be constant for both wavelengths, because the variation in its concentration is negligible. The absorption by water vapour outside the resonance absorbing lines (as for 3mm and 8mm) is due mainly to the total column water vapour. The total water vapour is then assumed to be constant within the chosen individual time periods (LWC zones). With this assumption, the angle of the best fit line for the scatter plot in can be shown to be simply the ratio of the absorption coefficients of each wavelength in liquid water. Haikin and Koldaev (1994) have shown that this ratio has a linear dependence on the temperature of liquid water. This fact has been used to compute an estimate of the average temperature of each liquid water layer, by calculating the slope of the best fit line in the scatter plot for each LWC zone.

This method of simultaneous determination of the average liquid water layer temperature and the integral LWC has been described in detail by Koldaev (1983).

4. STATISTICAL RESULTS AND COMPARISONS OF REMOTE AND IN-SITU DATA.

During the BASE project, significant supercooled LWC was observed in radiometric records about 16% of the total

time. In order to provide reliable identification of LWC zones, an LWC event was defined only when integral LWC values exceeded 0.05 kg/m^2 , and thus our estimates are lower limits to actual values due to the absence of cases $< 0.05 \text{ kgm}/^2$. By examining the total fraction of time when sky was cloud-covered, an upper limit of the probability of LWC is estimated as 29%.

A frequency distribution of the average integral LWC based on the entire period of measurements is given in fig. 2. The average integral LWC in this figure is defined as the zone average LWC value. The total number of LWC zones identified and summarized in this figure was 97.

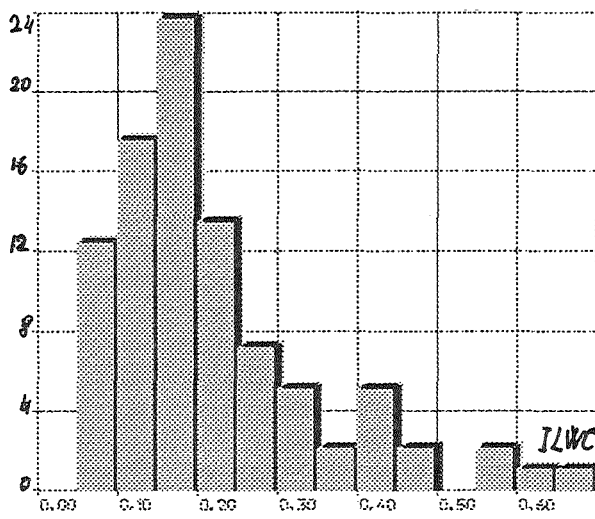


Fig 2: Frequency distribution of the average integral LWC for 97 separate liquid water zones observed in BASE arctic clouds.

Another very important parameter describing supercooled LWC zones is horizontal dimension. Using ground based radiometer measurements, since we do not know the velocity of clouds, it is more reasonable to estimate this parameter as

time duration of observation of each separate LWC zone. The frequency distribution of this parameter is presented in fig 3.

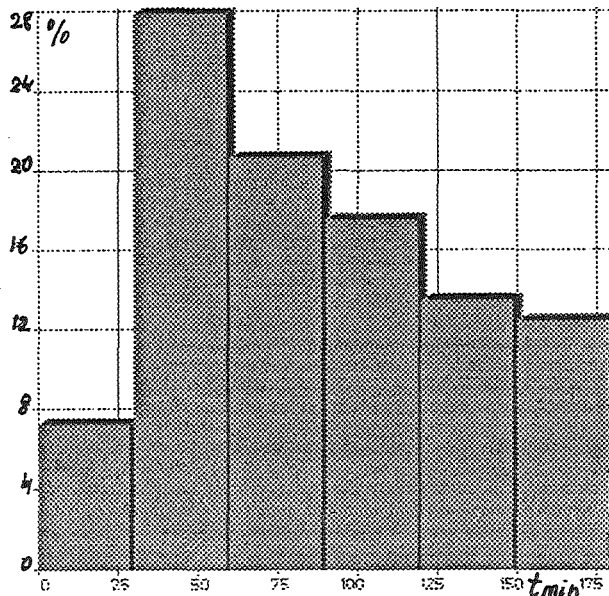


Fig 3: Frequency distribution of the duration of the LWC zones passing over ground based microwave radiometers.

Unlike the distribution of the integral LWC, the time duration of these zones has very wide range of values. More than 28% of the zones have a duration about 1 hour, reduced in frequency by about a factor of two for LWC zones of 3 hours.

On the basis of the two wavelength method described above, the mean temperature of each LWC zone was retrieved. The frequency distribution of these cloud temperatures is shown in fig. 4, and since the temperature profile is known or can be estimated from radiosonde data, this distribution can also be reinterpreted in terms of a distribution of LWC zones with height.

The accuracy of remote measurement of integral LWC in the clouds has been established in previous studies (Westwater, 1980). However, no ve-

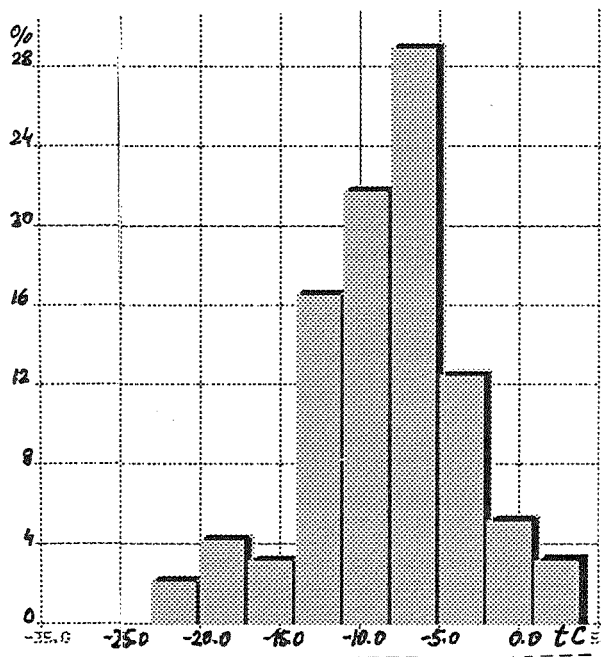


Fig 4: Distribution of the average temperatures of liquid water layers.

rification of the estimate of remote retrievals of temperature the liquid water zones has yet been achieved. In this study, the authors attempted to perform these comparisons by using aircraft simultaneous microwave radiometers data

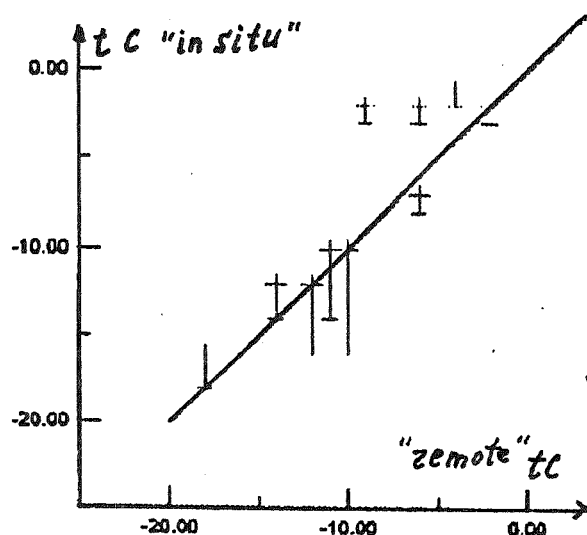


Fig 5: Comparisons of in-situ and the remote estimation of average temperature of liquid water zones.

5. DISCUSSION

The climatology of fall arctic clouds in the area of Inuvik, NWT reveals a fairly narrow distribution of cloud integral LWCs, with median values near 0.15 Kg/m^2 and maximum values below 0.30 Kg/m^2 . Estimates of the horizontal scales of LWC zones were between 40 and 130 Km. Roughly 35% of the LWC zones were colder than -5°C .

The results of this study are preliminary, but do reveal the kinds of climatological information that can be derived from continuous ground microwave radiometer systems. This study also provides the first positive indication of the possibility of the remote detection of the average temperature of cloud LWC zones.

6. ACKNOWLEDGEMENTS

Dr, Ron Stewart, Dr. George Isaac, and Prof. Albert Chernikov are thanked for their help in organizing of the experimental work described in this article, and for their continued interest to the results of this work. The BASE experiment was partially funded by the Panel of Energy and Resource Development.

7. REFERENCES

Haikin M.N., Koldaev A.V., 1994: Remote sensing of aircraft icing zones parameters. *TECO-94 WMO/TD-No 588 Report No 57*, 413-417.

Koldaev A.V., 1983: Remote sensing of liquid water content of precipitable clouds (in Russian). *Ph.D Report, Moscow, VINITI*, 1-130.

Westwater E.R., Guirand F.O., 1980: Ground-based microwave radiometric retrieval of precipitable water vapour in the presence of clouds with high liquid content. *Rad.Sci, V15, No 5*, 947-957.

DIFFERENTIATION OF FREEZING DRIZZLE FROM ICE HYDROMETEORS WITH POLARIZATION RADAR

Roger F. Reinking,¹ Sergey Y. Matrosov,² Brooks E. Martner,¹ and Robert A. Kropfli¹

¹NOAA/Environmental Technology Laboratory, Boulder, Colorado

²CIRES, University of Colorado/NOAA, Boulder, Colorado

1. INTRODUCTION AND CONCLUSIONS

Current evidence indicates that drops the size of freezing drizzle are a primary aircraft icing hazard (Cooper et al. 1984; Politovich 1996). Some means is needed to detect freezing drizzle that may occur below cloud base or in cloud between layers containing ice. Depolarization ratio (DR) measurements were made to distinguish (freezing) drizzle from ice crystals of various growth habits, crystal aggregates, and graupel during the Federal Aviation Administration's (FAA) Winter Icing and Storms Project (WISP; Rasmussen et al. 1992). The K_a -band (8.66 mm) dual-polarization radar from the NOAA Environmental Technology Laboratory (ETL) was used (Kropfli et al. 1995). Measurements of the elliptical depolarization ratio (EDR) and linear depolarization ratio (LDR) backed by scattering calculations and hydrometeor samples indicate that drizzle should be detectable and distinguishable from the other hydrometeor types. The addition of a temperature sounding will establish if the drizzle is freezing or warm. These results suggest a practical procedure for identifying and monitoring this aviation hazard. NEXRAD has the potential to add dual-linear polarization, so given that (freezing) drizzle is detectable in LDR, technology transfer to NEXRAD should be possible without a major capital investment.

2. BACKGROUND

The ETL K_a -band radar has an agile polarization capability provided by a phase-retarding plate (PRP) that resolves the beam into two components, retards the phase of one relative to the other, and then recombines them for transmission (Shurcliff 1962). A 90°-phase-shift PRP produces circular polarization from incident horizontal polarization when its "slow" axis is rotated 45° from horizontal ($\alpha = 45^\circ$). If its phase shift differs from 90°, all the polarizations produced by the PRP will be elliptical except where rotation angle $\alpha = 0^\circ$ and multiples of 90°, for which the polarization will remain linear horizontal. The most nearly circular polarization state possible is then produced at PRP rotations to $\alpha = 45^\circ \pm n90^\circ$, where n is an integer. In WISP, a 79.5°-phase-shift PRP was used. Measurements of EDR were made with fixed, nearly circular polarization during range-height indicator (RHI) scans. A second observing mode was to rotate the PRP at

constant speed with the radar set at a fixed elevation angle (β) to cycle the transmitted polarization through the available continuum of states between linear horizontal and near-circular elliptical. This was repeated at two or three fixed elevation angles (e.g., $\beta = 7.5^\circ$, 45° , and 90°); from this, the limiting depolarization values, LDR and EDR, were used to determine hydrometeor type. With either scanning strategy, data from any specific altitude can be selected for examination.

Ice crystals, drizzle, and rain scatter microwaves according to their aspect ratio (shape), bulk density, orientation, and the polarization state of the incident radiation. Drizzle should not measurably depolarize the incident radiation if it is circular or linear because the scatterers are nearly spherical. Rain is nonspherical and will depolarize the signal. Theoretical calculations to differentiate the depolarizations caused by the various ice crystal types and drizzle were made by Matrosov (1991), and expanded and verified with measurements with the ETL K_a -band radar by Matrosov et al. (1996) and Reinking et al. (1996). The calculated EDR- β relationships for the 79.5° PRP are shown in Fig. 1a, and the LDR- β relationships are shown in Fig. 1b (the details of how these measurements are made make it convenient to reverse the sign of DR from Fig. 1a to Fig. 1b; the sign of LDR is opposite the conventional definition).

The EDR for planar crystals (hexagonal plates, dendrites) is predicted to decrease by about 9 ± 2 dB as β is increased from 0° to 90° . The pattern is the same but the magnitude of change with β is much less for the columnar crystal types. The EDR for the crystals is offset from the -14.8 dB signature for drizzle by 2–10 dB at the lowest β . Drizzle should show no variation of DR with elevation angle. An LDR of about +35 dB is expected for drizzle; the value is determined by the cross-talk limit between the polarization channels of this radar. In LDR, the offset of drizzle from depolarizations caused by the planar ice crystals is of the same order as that in EDR, and likewise large (8 ± 2 dB) at the low radar elevation angles. The DR- β curve slopes are opposite for columnar and planar crystals in LDR (Fig. 1b) but the same in EDR for a 79.5° PRP (Fig. 1a). When LDR is measured, columnar crystal depolarizations *increase* with increasing β ; the predicted maximum offset from drizzle is much larger (11–19 dB) than for EDR and occurs toward zenith rather than toward low β .

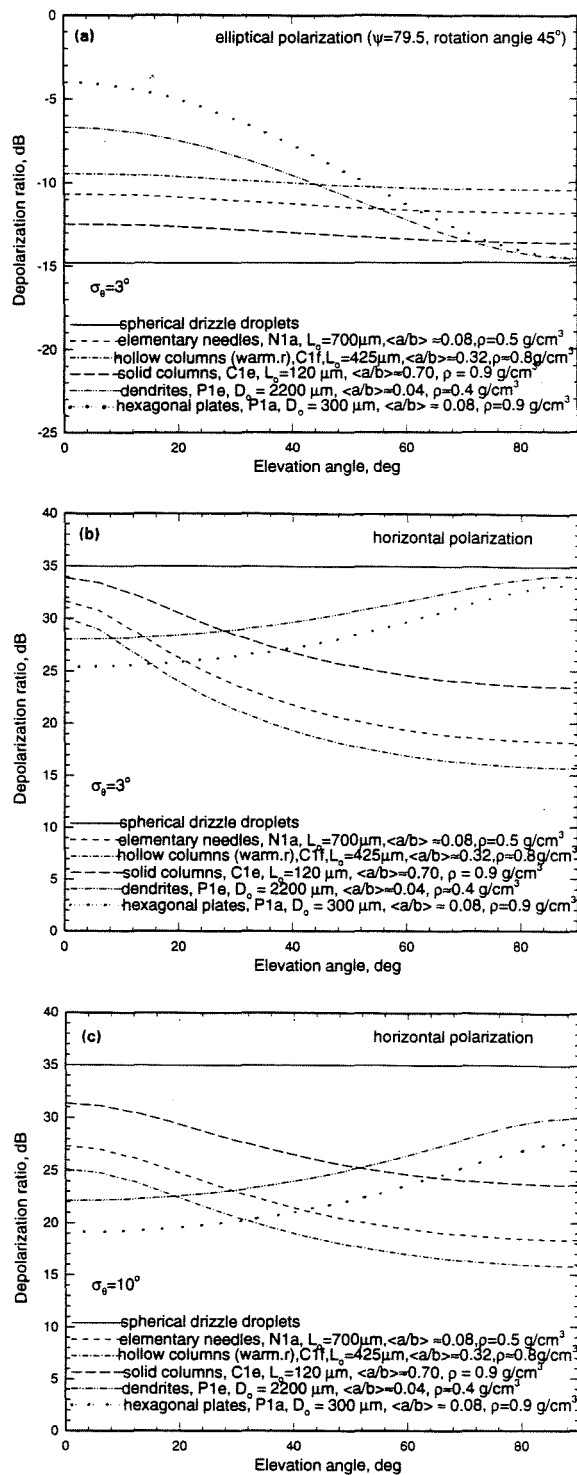


Fig. 1. Calculations of depolarization ratio, DR (dB), as a function of radar elevation angle, $\beta(^{\circ})$: (a) EDR, $\sigma_{\theta} = 3^{\circ}$; (b) LDF, $\sigma_{\theta} = 3^{\circ}$; (c) LDR, $\sigma_{\theta} = 10^{\circ}$. Depolarization increases as the absolute value of DR decreases toward zero.

These plots show that radar measurements of EDR or LDR as a function of β should differentiate columnar from planar crystal types, and these from drizzle. This differentiation might be easiest in LDR, due to the larger differences in DR among particle types and the opposite slopes of the DR- β curves for columnar versus planar crystals,

were it not for the effect of the randomness of crystal orientation (or standard deviation, σ_{θ}) relative to horizontal settling. The determination of ice particle type is degraded minimally by randomness in crystal orientation when a true circular depolarization ratio (CDR) is measured, and only slightly more using near-circular EDR, but substantially using LDR (Matrosov 1991). The theory in Figs. 1a,b is based on $\sigma_{\theta} = 3^{\circ}$; at least this much randomness is expected. Figure 1c shows the effect on LDR of a more random orientation with $\sigma_{\theta} = 10^{\circ}$. The effect is to cluster the LDR- β curves for columnar crystals with those for planar crystals, such that practical differentiation decreases significantly. Measurements confirm that the columnar and planar types are easily differentiated using EDR but more difficult to differentiate using LDR, evidently because of the orientation effect (Reinking et al. 1996). However, the model results in Fig. 1c also predicts that the separability in LDR of both columnar and planar habits from drizzle (+35 dB) will *increase* measurably, by 3–5 dB, with an increase in σ_{θ} from 3° to 10° .

To summarize, the scattering calculations show that EDR should provide a very good capability to distinguish among crystals of the various habits and to distinguish these from drizzle, and CDR should be the best. However, if the objective is limited to distinguishing (freezing) drizzle from ice hydrometeors, LDR should offer the better alternative that may be applicable to NEXRAD, which transmits and receives horizontal polarization.

3. MEASUREMENTS

Radar measurements have verified many of the calculations in Figs. 1a–c. The measured EDR from planar crystals provide excellent fits to the theory (Fig. 2), and the differentiation from drizzle is lucid (Figs. 2 and 3). Graupel (Fig. 3) is a type of ice hydrometeor that is most similar in shape to drizzle. Although graupel and freezing drizzle are expected to occur in atmospheres with mutually exclusive temperature soundings, a capability to differentiate them would establish considerable confidence for distinguishing drizzle from other ice hydrometeors. The measurements of EDR in Fig. 3 demonstrate that graupel particles depolarize the signal 1–2 dB more than drizzle for the PRP used in WISP. A PRP at 90° (i.e., circular) would provide greater differences.

During WISP, EDR and LDR were measured concurrently as the extreme values from PRP rotations. For drizzle (Fig. 4a), LDR = $+34.6 \pm 0.9$ dB and EDR = -14.7 ± 0.5 dB; these compare well with calculated values of +35 dB and -14.8 dB, respectively. This PRP rotation was at $\beta = 30^{\circ}$, but the measured values were independent of elevation angle as expected for drizzle. In contrast, for dendrites, Fig. 4b shows that LDR = $+24 \pm 3$ dB and EDR = -8.6 ± 0.3 dB at $\beta = 30^{\circ}$, and the depolarizations depended on elevation angle, as in Fig. 2. This is a definitive, theoretically verifiable differentiation from drizzle.

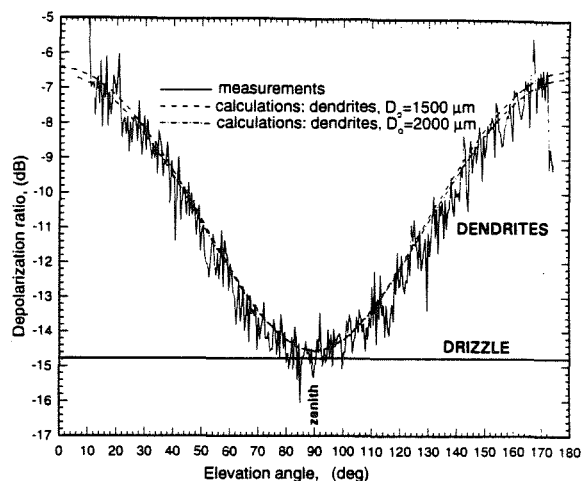


Fig. 2. Over-the-top RHI of EDR (dB) from dendrites (2057 UTC 11 March 1993) and theoretical curves for dendrites and drizzle.

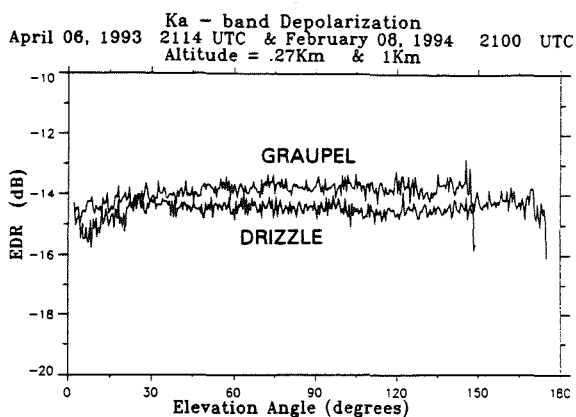


Fig. 3. Over-the-top RHIs of EDR (dB) for drizzle (2114 UTC 6 April 1993) and graupel (2100 UTC 8 February 1994).

No scattering calculations have been made for graupel. However, in PRP rotations, graupel (Fig. 4c) showed similar EDR values irrespective of elevation angle, and the consistent departure from the EDR for drizzle was similar to that in Fig. 3. However, with $LDR = +32.1 \pm 4.6$ dB and $EDR = -13.8 \pm 0.3$ dB, the average departure from drizzle values was significantly larger in LDR (albeit more variable). Since graupel is expected to be one of the most difficult hydrometeors to distinguish from freezing drizzle, these results are very encouraging for the general application of the depolarization measurements to identify the drizzle.

4. A HYPOTHESIZED PROCEDURE FOR ROUTINE DETECTION OF FREEZING DRIZZLE

The scattering calculations and initial measurements described above suggest that measurements of depolarization versus altitude combined with measurements of depolarization as a function of radar elevation angle can be used to identify cloud layers containing freezing drizzle.

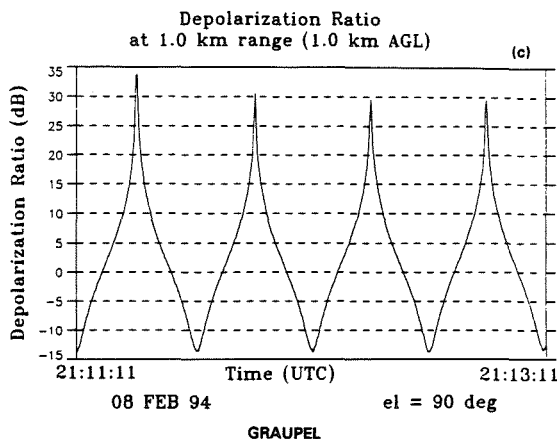
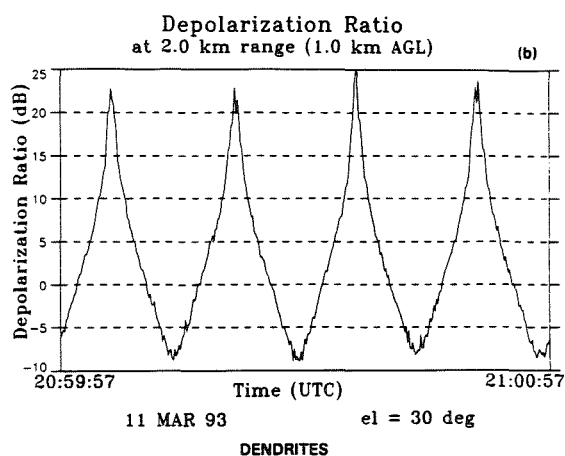
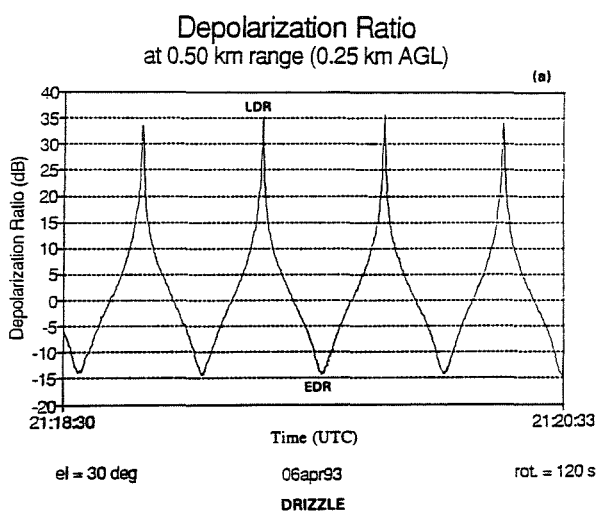


Fig. 4. DR vs. time from a PRP rotation. Positive maxima are LDR; negative minima are the limiting EDR (peak to peak = 90° rotation). (a) In drizzle, $\beta = 30^\circ$, 6 April 1993; (b) in planar crystals (dendrites), $\beta = 30^\circ$, 11 March 1993; (c) in graupel, $\beta = 90^\circ$, 8 February 1994.

In practice, the radar scanning procedure could be refined significantly with the addition of (1) microwave radiometer measurements to establish the absence or presence of liquid (but not the form—drizzle, small cloud drops, or rain—the drizzle being the greater aviation hazard when subcooled), and (2) a temperature sounding to differentiate freezing drizzle from warm drizzle. Radar reflectivity measurements will simply determine cloud boundaries and therefore restrict the altitudes that have any possibility of producing freezing drizzle. The presence of a melting level, easily found in the depolarization signatures, will indicate rain or drizzle below it; however, freezing drizzle can form by drop coalescence rather than melting ice that subsequently subcools, so it is not necessarily accompanied by a melting level. In the cloud layers, the measurements of either LDR or EDR can be obtained from RHI scans or PRP rotations, and either type of measurement should be applicable to achieve the desired drizzle detection. The best separation of the various individual hydrometeor types might be achieved by measuring CDR instead of a near-circular EDR; this is possible with another phase-retarding plate. LDR is expected to be less well behaved in distinguishing among the ice hydrometeor types but is predicted to do well in distinguishing drizzle from the ice hydrometeors. This hypothesis and the envisioned procedure need to be tested with further measurements.

5. ACKNOWLEDGEMENTS

This work was funded by WISP, a project of the FAA's Weather Development Program, through a subcontract with the National Center for Atmospheric Research. The views expressed are those of the authors and do not necessarily represent the official position of the U.S. Government.

6. REFERENCES

- Cooper, W. A., W. R. Sand, M. K. Politovich, and D. L. Veal, 1984: Effects of icing on performance of a research airplane. *J. Aircraft*, **21**, 708–715.
- Kropfli, R. A., S. Y. Matrosov, T. Uttal, B. W. Orr, A. S. Frisch, K. A. Clark, B. W. Bartram, R. F. Reinking, J. B. Snider, and B. E. Martner, 1995: Cloud physics studies with 8-mm-wavelength radar. *Atmos. Res.*, **35**, 299–313.
- Matrosov, S. Y., 1991: Theoretical study of radar polarization parameters obtained from cirrus clouds. *J. Atmos. Sci.*, **48**, 1062–1070.
- Matrosov, S. Y., R. F. Reinking, R. A. Kropfli, and B. W. Bartram, 1996: Estimation of ice hydrometeor types and shapes from radar polarization measurements. *J. Atmos. Ocean. Technol.*, **13**, 85–96.
- Politovich, M., 1996: Response of a research aircraft to icing and evaluation of severity indices. *J. Aircraft*, **33** (in press).
- Rasmussen, R., M. Politovich, J. Marwitz, W. Sand, J. McGinley, J. Smart, R. Pielke, S. Rutledge, D. Wesley, G. Stossmeister, B. Benstein, K. Elmore, N. Powell, E. Westwater, B. B. Stankov, and D. Burrows, 1992: Winter Icing and Storms Project (WISP). *Bull. Amer. Meteor. Soc.*, **73**, 951–974.
- Reinking, R. F., S. Y. Matrosov, R. T. Brientjes, and B. E. Martner, 1996: Identification of hydrometeors with elliptical and linear polarization K_a -band radar. *J. Appl. Meteor.* (submitted).
- Shurcliff, W. A., 1962: *Polarized Light*. Harvard Univ. Press, 208 pp.

Measurement of Kinematics and Precipitation of Stratiform Rainfall with Airborne Multiparameter Rain Radar

Nobuhiro Takahashi¹, Hiroshi Hanado¹ and Shinsuke Satoh²

¹Kashima Space Research Center, Communications Research Laboratory, Kashima, Ibaraki 314, Japan

²Global Environment Division, Communications Research Laboratory, Koganei, Tokyo 184, Japan

1. INTRODUCTION

The Communications Research Laboratory (CRL), Japan developed a new airborne multiparameter precipitation radar (CAMPR) in 1994 (Takahashi, et al., 1995; Kumagai et al., 1996). The major objective of this radar was to validate the Precipitation Radar (PR) onboard the TRMM satellite that is scheduled to be launched in 1997 (Simpson et al., 1988). Before the TRMM launch, the CAMPR will be used to collect data supporting algorithm development for the TRMM-PR.

Recently, airborne multiparameter radars have been actively utilized to allow kinematic fields and cloud physical characteristics such as the ELDORA of NCAR (Testud et al., 1995), the ARMAR of NASA/JPL (Durden et al., 1994) and the EDOP of NASA/GSFC (Heymsfield et al., 1995) to be studied. One of the advantages of airborne radar is that the radar can

directly measure the vertical motion of raindrops.

In this study, we will show the analyzed results of stratiform precipitating clouds which were observed on September 23, 1995. As will be mentioned later, because CAMPR can obtain horizontally (H) and vertically (V) polarized data and Doppler velocity data in cross-track scanning, we were able to calculate kinematic fields and cloud physical parameters such as ZDR and LDR within the clouds. We will first explain the radar system and analysis method, and after that the results of analysis will be shown.

2. RADAR SYSTEM AND ANALYSIS METHOD

The radar specifications are shown in Table 1. The frequency is 13.8 GHz. As this radar enables dual polarization observation using two plates of slot array antennas; it is possible to receive co-polarization and cross-polarization data simultaneously. The antennas are housed in a radome which hangs below the fuselage, and scans mechanically in a cross track direction between -55° and 88° centered at the nadir. Very high polarization isolation higher than 40 dB is available by the use of separate plane antennas. The radar transmitter uses a pulsed TWTA with a peak power higher than 2 kW. Pulse width is changeable from 0.5 to 1.0 to 2 μ sec. and pulse repetition frequency is also changeable from 2 to 4 to 8 kHz.

The data system has the capability to collect data in two modes: the first is the collection of all raw I, Q data for full polarimetric analysis, and the second is the collection of integrated data of reflectivity for both polarizations, Doppler velocity and its spectrum width.

Before the analysis of Doppler velocity, the effect of airplane motion which contains Doppler velocity data should be removed. The procedure is that the pitch, roll, and drift angles which have been obtained from gyros and GPS are calibrated by referring to sea surface Doppler velocity as zero. The kinematic field in the stratiform clouds is estimated from the Doppler velocity averaged over a plane of cross-track scanning. If we assume uniform rainfall over the plane of scanning, Doppler velocity field can be expressed as

Table 1. Specifications for CAMPR

frequency	13.8 GHz
antenna	slotted waveguide antenna array, H and V, each
beam width	1.9 x 4.5°
polarization	H and V
antenna scan	cross track direction, -55° to 90° centered nadir
transmitter	TWTA
maximum power	2 kW
pulse width	0.5, 1.0, 2.0 μ sec (75 m, 150 m, 300 m)
pulse repetition frequency	2.4, and 8 kHz
receiver	two channels for simultaneous reception
noise figure	8 dB
data recording	all pulse hit data of both polarization signals (I, Q data)
	integrated data (ZHH, ZHV, ZVV, ZVH, V, σ)

$$v = u * \sin(\theta) + (w + Vt) * \cos(\theta) .$$

where v is observed Doppler velocity, u is the horizontal wind component in the scanning plane, w is vertical wind, Vt is the falling velocity of raindrops, and θ is the scan angle from nadir minus airplane roll angle. The vertical profiles of u and $w + Vt$ have been estimated by fitting a sinusoidal curve to the observed Doppler velocity field for each height in each scan data by using the least square method. Smaller scale wind field were calculated within a small sector by the same procedure.

From Doviak and Zrnic (1992), ZDR is expressed as,

$$ZDR = 10 \log \left(\frac{|shh|^2}{|svv|^2} \right)$$

where shh and svv are the backscattering coefficients of horizontal and vertical polarization respectively which can be expressed as,

$$shh = k_0^2 \left[(p_v - p_h) \sin^2 \delta \sin^2 \psi + p_h \right]$$

$$svv = k_0^2 \left[(p_v - p_h) \cos^2 \delta \cos^2 \psi + p_h \right]$$

where,

$$p_{h,v} = \frac{ab^2}{3} \left\{ \frac{m^2 - 1}{A_{h,v}(m^2 - 1) + 1} \right\}$$

$$A_v = \frac{1}{e^2} \left\{ 1 - \left(\frac{1 - e^2}{e^2} \right)^{\frac{1}{2}} \sin^{-1}(e) \right\} = 1 - 2A_h$$

$$e = \left\{ 1 - (a/b)^2 \right\}^{\frac{1}{2}} .$$

This is where m is the refractive index, δ is the angle between the propagation direction of the incident field and the symmetry axis, ψ is the canting angle, and a and b are the lengths of the short and long axes of a raindrop approximated as an ellipsoidal shape. For practical calculations of the ZDR value, these equations should be express by the elevation angle of the radar ($\theta + \pi/2$), the canting angle (ψ'), and the canting direction (ϕ) (e.g. relative to direction of airplane motion). The relationship between (ψ, δ) and (θ, ψ', ϕ) is

$$\cos \delta = -\sin \psi' \sin \theta \cos \phi + \cos \psi' \cos \theta$$

and

$$\cos^2 \psi = \frac{1}{\left(\frac{\sin^2 \psi'}{\cos^2 \psi'} \sin^2 \phi + 1 \right)} .$$

Therefore, if we know the drop size distribution and canting angle of raindrops, ZDR variation as a function of antenna angle (cross-track angle from nadir) can be determined in a unique way. Figure 1 shows the relationship between ZDR and scan angle for several canting angles for cases where $\phi = 0$, and 90° , and assuming an exponential distribution

($N = N_0 \exp(-3.67D / D_0)$) with $N_0 = 8000$ and $D_0 = 1$ mm. Assuming uniform rainfall and given drop size distribution, we can estimate both the rainfall rate and canting angle of raindrops, simultaneously by fitting the theoretical ZDR curve to the observed one.

The objective of analysis using ZDR is to estimate the ZDR value equivalent to a ZDR with a 0 degree elevation angle and canting angle on average within the scan plane at each height; that is, to estimate average rainfall intensity and the average canting angle at each height. Since ZDR with a 0 degree elevation angle generally varies between -1 to 3 dB, a precision for ZDR of about 0.1 dB is needed. In particular, precise calibration is needed to estimate ψ' and ϕ . Calibration between H and V reflectivities were performed using data of nadir angle. Therefore, in this study, we tried to estimate the ψ' value assuming that $\phi = 0$ (estimate canting angle relative to scan plane). In practical calculation, we integrated several scan data in estimating ZDR to reduce the data fluctuation of quantum error and because we need to accumulate a large amount of data sufficient to gain precision.

Cross-polarization data (LDR) has been utilized to determine the bright band.

3. RESULTS

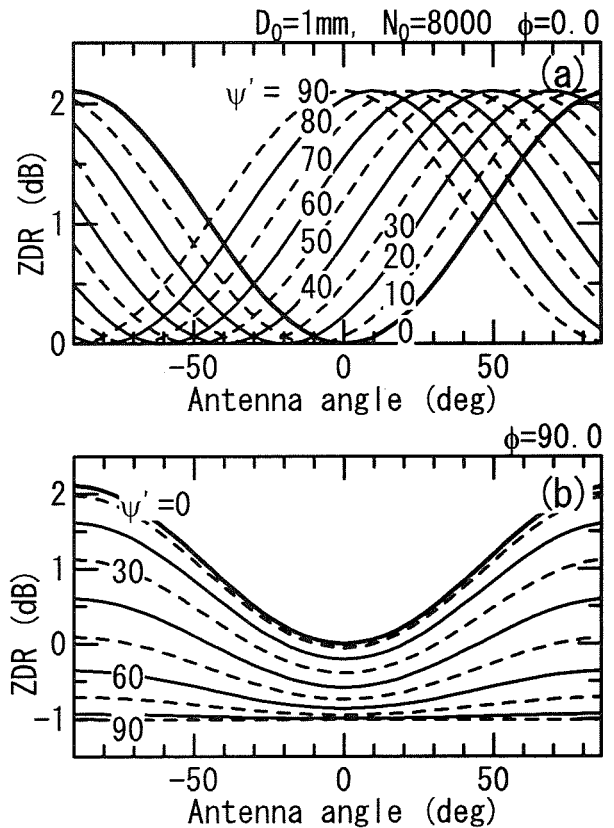


Fig. 1. Relationship between ZDR and antenna angle for canting angles between 0 degree and 90 degrees, with canting directions of 0 degree and 90 degrees.

We analyzed stratiform precipitating clouds on September 23, 1995 over the Japan Sea. Figure 2 shows the flight path of this study. Data along paths 923_07 and 923_08 have been utilized to analyze the east-west structure of the cloud. Both paths are almost a straight flight but in the opposite direction. Figure 3 shows a GMS IR image at the time of flight. Large stratiform cloud extended over the western part of Japan which was stimulated by a typhoon located in the south of Japan.

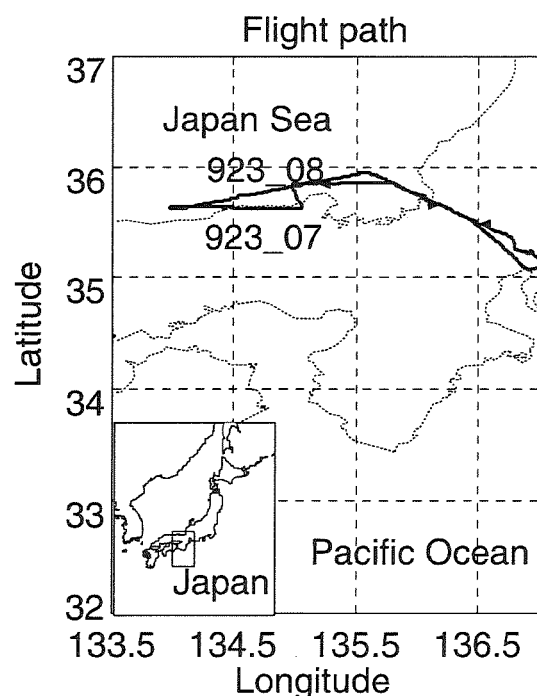


Fig. 2. Flight path of CAMPR observation on September 23, 1995.

Figure 4 shows a cross section of the horizontal wind component and vertical component along the path 923_07. In this figure, the horizontal distance is about 100 km. The horizontal wind component almost expresses the southerly wind component in this case, and the vertical component expresses the summation of vertical air motion and particle fall velocity. In the figure for the horizontal wind component, faster wind speed appeared at 1 km in the western part of the figure. Its height changed higher to the east. This shows that the southerly wind affected by the typhoon change its height with the distance from the typhoon center. Stronger reflectivity appeared in the western part. The vertical component shows a more fluctuating pattern than the horizontal wind component. This is partly explained by the difference in fall velocities of precipitation particles which were well-correlated with the reflectivity and the inhomogeneous distribution of the vertical wind component: this is, however, thought to be small. The vertical component, however, clearly shows acceleration at around 4 km. This is because

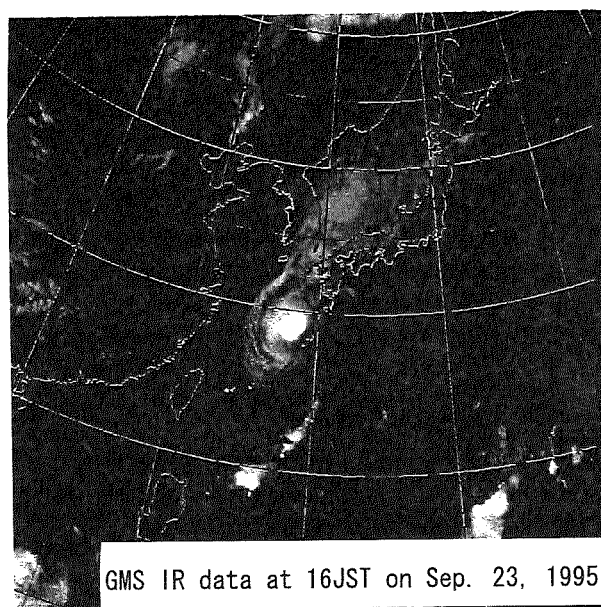


Fig. 3. GMS IR image at 16JST (JST = UTC + 9 hours) on September 23, 1995.

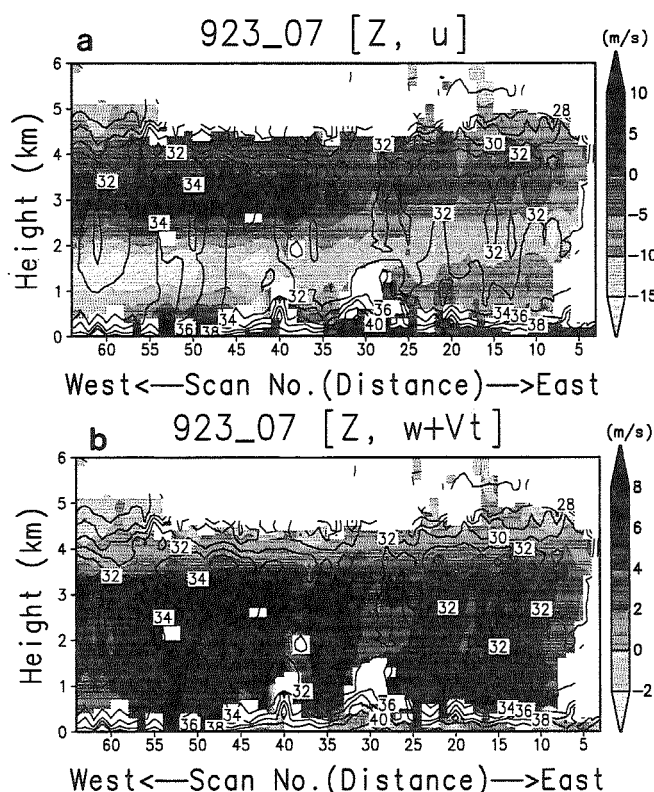


Fig. 4. Vertical cross section along the path 923_07 of (a) horizontal wind and reflectivity and (b) vertical velocity and reflectivity.

the bright band existed at a height of 4 km. Figure 5 shows the distribution of $(u, Vt+w)$ within the scan plane of the 923_07 flight path. As mentioned above, the vertical wind component was very small above the bright band (speed of falling snow). This figure also shows the smaller velocity structure of the stratiform

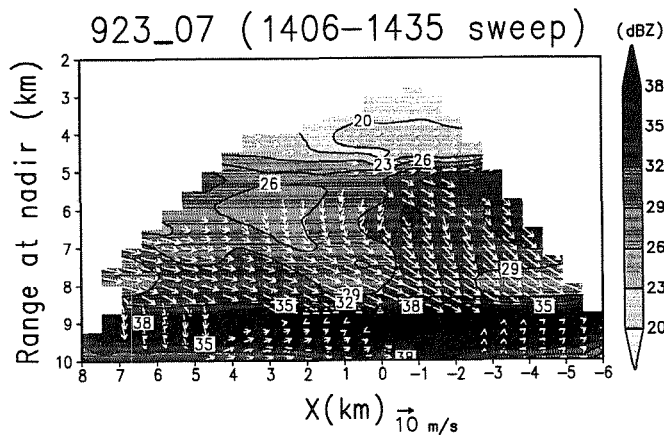


Fig. 5. Velocity vectors within a scan plane. Contour lines express the reflectivity

rain cloud.

Figure 6 shows the vertical profiles of ZDR integrated from scan 30 to 45 and from 45 to 60 of path 923_07 (Fig. 4). The average ZDR ranged 1 to 1.5 dB, suggesting about a 3 to 10 mm/h rainfall intensity. This figure also shows the different profiles between two profiles. These results were doubtful, because, these values contain relatively large RMS error, resulting from quantum error, the small integration number (small pulse hit number for integration) and the horizontal change of ZDR.

4. CONCLUDING REMARKS

In this study, we analyzed the kinematic and cloud physical structure of a stratiform precipitating cloud

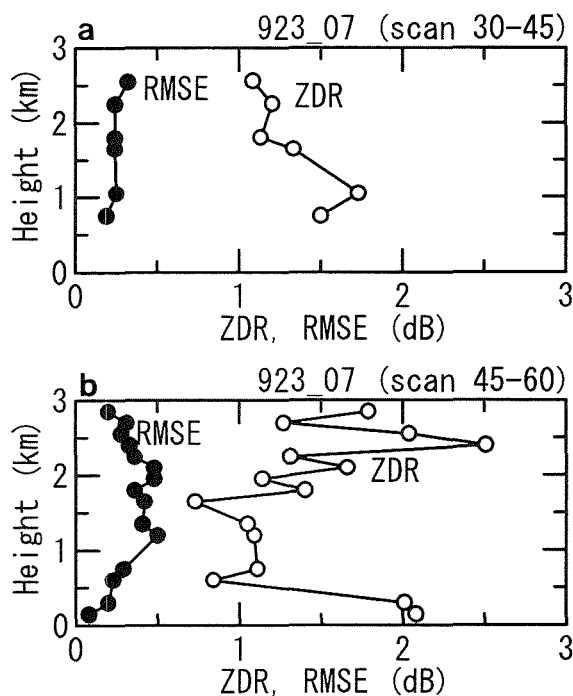


Fig. 6. Vertical profile of ZDR and RMS error for (a) from scan 30 to 45 and (b) 45 to 60 of 923_07 flight path.

with CAMPR. The analysis methods to estimate the kinematic field is and ZDR from the scan data of CAMPR are calculated by assuming the uniform precipitation. The results of this analysis suggest that this methods are useful for airborne radar to estimate vertical and horizontal wind component and that the advantages of airborne measurements is to estimate vertical wind component directly. The analysis using ZDR data had some difficulty in this analysis, however, it suggested the possibility to estimate not only rainfall intensity but also canting angles with this procedure.

ACKNOWLEDGMENT

The CAMPR experiments are being conducted in collaboration between CRL and NASDA. Observation was performed using a Beachcraft B200 provided by Nakanihon Airlines.

REFERENCES

- Doviak, R. J. and D. S. Zrnic', 1992: Doppler radar and weather observations. 2nd Ed. Academic Press, 562pp.
- Durden, S. L., E. Im, F. K. Li, W. Ricketts, A. Tanner, and W. Wilson, 1994: ARMAR: An airborne rain-mapping radar. *J. Atmos. and Oceanic Technol.*, **11**, 727-737.
- Heymsfield, G. M., I. J. Caylor, S. W. Bidwell, S. Amen, and J. Scala, 1995: Structure of vertical velocities in a rapidly advancing Gulf coast squall line observed by EDOP. *Proc. 27th Radar Meteor. Conf.*, Vail, Amer. Meteor. Soc., 556-558.
- Kumagai, H., K. Nakamura, H. Hanado, K. Okamoto, N. Hosaka, N. Takahashi, T. Iguchi, H. Miyauchi, and T. Moriyama, 1996: CRL airborne multiparameter radar (CAMPR): System description and preliminary results. *IEICE Trans. Commun.* (in print).
- Simpson, J., R. Adler, and G. North, 1988: A proposed tropical rainfall measuring mission (TRMM) satellite. *Bull. Amer. Meteor. Soc.*, **69**, 278-295.
- Takahashi, N., H. Kumagai, H. Hanado, T. Kozu, and K. Okamoto, 1995: The CRL airborne multiparameter precipitation radar (CAMPR) and the first observation results, *Proc. 27th Radar Meteor. Conf.*, Vail, Amer. Meteor. Soc., 83-85.
- Testud, J., P. H. Hidebrand and W.-C. Lee, 1995: A technique to correct airborne Doppler data for coordinate transformations errors using surface clutter. *J. Atmos. and Oceanic Technol.*, **12**, 800-820.

OPTIMAL NON-LINEAR ESTIMATION FOR PARTICLE MEASUREMENTS

Hanna Pawlowska^{1,2}, Jean-Louis Brenguier¹ and Gerard Salut³

¹ METEO-FRANCE (CNRM/GMEI), Toulouse, France

² on leave from Institute of Geophysics, University of Warsaw, Poland

³ LAAS (CNRS), Toulouse, France

1. INTRODUCTION

Particle concentration is a key parameter in atmospheric physics. It is generally measured with an airborne particle counter and derived from measurements by cumulating particle counts over a given sampling period and dividing this particle number N by the corresponding sampled volume V .

The accuracy of this measurement is strongly affected by the fact that, no matter what is the physical process that drives particle concentration, the occurrence of particles in the counter is a random process. If particles are independently distributed in space, which is generally the case in the atmosphere, arrivals of particles into the counter are independent events and the counting is a Poisson process, for a given local concentration. The sampling period must be chosen to be long enough for the number of counted particles to be a good statistical estimator of the concentration. However, if the sampling period is too long, information about variation in the local concentration is lost. The same problem occurs when looking at low concentration regions, as for example at the interface between a cloud and the surrounding clear air. Measurements at the finest scale through such transitions are crucial for understanding the mixing process, but the relative error in the evaluation of low values of the concentration is so high that it is impossible to decide whether the observed variations are physically significant or if they reflect only the randomness of the counting.

The Poisson process is characterized by the expected counting rate through the counter, λ , also called the intensity of the process. For a homogeneous Poisson process, the intensity λ can be defined as the expectancy of the number of particles N counted during the sampling period T , divided by T :

$$\lambda = E[N/T]. \quad (1)$$

When only one realization of the process is available, N/T for this realization provides a good estimate of its expectancy if N is large. In the atmosphere the particle concentration (and λ as well) is not constant so that N/T is an estimate of the mean droplet rate over T . The usual estimation of this intensity, as N/T , is thus equivalent to linear smooth-

ing with a rectangular window of a fixed sampling period, which corresponds to a low-pass filter. If the sampling period is extended, the accuracy of intensity estimation is improved, but information on variations at scales smaller than T is lost. If, on the contrary, the sampling period is shortened for resolving smaller scales, variations of the measured concentration that are due only to the randomness of the counting interfere with physically significant time variations of the mean rate. Figure 1 illustrates the difficulty of selecting a good compromise for removing the noise intrinsic to random counting yet preserving the detection of sharp variations in particle concentration. For the example shown in figure 1, the reference intensity has been set to a constant value of $50,000s^{-1}$ (a value typical of airborne droplet measurements), except for a short interval of $1ms$, during which the intensity has been doubled ($100,000s^{-1}$). One series of particle arrival times has been produced using a Poisson process generator. The estimated rate has been calculated as the ratio of the number of arrivals to a given sampling period T (equal respectively to $1ms$ in (a) and $2ms$ in (b)).

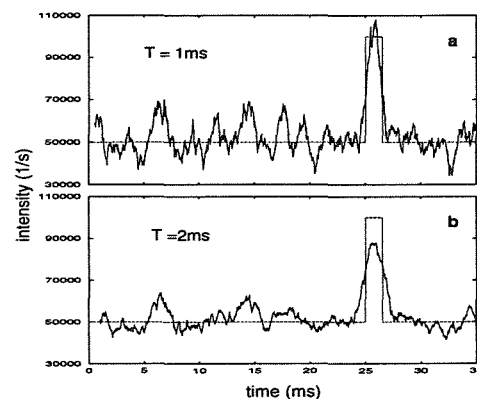


Fig. 1 Results of the moving average procedure (solid line) for sampling periods of $1ms$ (a) and $2ms$ (b) for a simulated time series of Poisson distributed particle arrivals, conditionally to the function represented by the dashed line.

If a large number of independent realizations of the same process were available, it would be possible to estimate the expected particle rate λ at any time

t , with any time resolution δt . Accuracy and time resolution would only depend on the number of realizations. When a single realization is available, i.e. a unique series of interarrival times between particles in the counter, such a procedure is meaningless. All information, in these conditions, is contained in the conditional probability distribution of λ with respect to i) the available measurements, ii) the available *a priori* assumptions on the λ statistics. This calls for a Bayesian approach, which proceeds as follows: we consider an inhomogeneous Poisson process whose time-varying intensity is itself governed by a process, called the underlying process (the Poisson process is said to be conditional to the underlying process). It is important to mention that additional *a priori* information about this (possibly random) underlying process must be provided. The Bayesian approach allows a clear and coherent mathematical model of the *a priori* assumptions that are used to define optimal estimation of the intensity of an inhomogeneous Poisson process. Estimation is termed optimal whenever it relies upon the conditional probability measure of the variable of interest with respect to the observations which are considered. An extensive study of the subject is given in the book *Random Point Processes* by Snyder (1975). The next section briefly describes the application to the specific problem of particle concentration measurements in the atmosphere.

2. OPTIMAL ESTIMATION OF THE PARTICLE RATE

There are two types of estimation of the particle rates: filtering and smoothing. In Bayesian filtering, the estimation is determined only by the data preceding the current location, which is a constraint for real-time processing. In Bayesian smoothing the estimation is determined by preceding data as well as any desired section of forthcoming data. Smoothing is more complex and more accurate than filtering but only suits off-time processing.

2.1 The optimal non-linear filtering equation

The filtering problem associated with a Poisson process is described as follows: let $\{N_t; t \geq t_0\}$ be a stochastic Poisson process conditional to its intensity $\{\lambda_t; t \geq t_0\}$. We assume that $\{N\}$ is observed on the interval $[t_0, t]$ and that the entire counting path $\{N_\sigma; t_0 \leq \sigma < t\}$ is available. The endpoint time t corresponds to a real-time parameter which increases from t_0 as additional data are accumulated. The objective is to evaluate the conditional probability density function (PDF) of λ_t with respect to the observed measurements of N up to time t . It obviously evolves in time as i) λ_t is a *a priori* time-varying, ii) new data become available. In the filtering process,

only the current value λ_t of λ is to be estimated. Past values are not specifically updated after new data has been obtained, as opposed to smoothing which will be described later on.

As mentioned before, one has to assume a possible type of randomness for λ_t as a stochastic process. In the absence of any information, the obvious choice is to assume a random drift with independent increments (random walk). In continuous time, one has only two possibilities: a Poisson process if the drift is made of jumps or Brownian motion if the drift has no discontinuities. In both cases, these are Markov processes represented by a linear evolution operator (L) on their *a priori* PDF $p_t(\lambda)$ (Chamon et al, 1994).

The conditional distribution $p_t \equiv p(\lambda_t | \{N_\sigma; t_0 \leq \sigma \leq t\})$ with respect to the observed measurements $\{N\}$ obeys the following filtering equation (Snyder, Chap.6, Eq.6.142), whose main feature is its forcing term (second term on the right hand side):

$$dp_t(\lambda) = L \cdot p_t(\lambda)dt + p_t(\lambda) \frac{(\lambda - \hat{\lambda}_t)}{\hat{\lambda}_t} (dN_t - \hat{\lambda}_t dt) \quad (2)$$

where $\hat{\lambda}_t = \int_{\lambda_{min}}^{\lambda_{max}} \lambda p_t(\lambda) d\lambda$ is the conditional mean of λ , dN_t is the stochastic increment of N in the sense of jump differentials ($dN_t = 1$, if there is a new particle at t , $dN = 0$, otherwise). Note that the filtering equation is non-linear in p_t , due to the presence of $\hat{\lambda}_t$ as well as p_t in the forcing term.

If the *a priori* random changes of λ are themselves parameterized as a Poisson process, the operator L has the following form:

$$L \cdot p_t(\lambda) = \Lambda \left(\int_{\lambda_{min}}^{\lambda_{max}} f(\lambda - v) p_t(v) dv - p_t(\lambda) \right), \quad (3-a)$$

where Λ is the *a priori* mean rate of jumps of the intensity process, and f is the probability distribution of the amplitude of these jumps. λ_{min} and λ_{max} are the limits of all possible values of λ .

If no information is available concerning the underlying process, one can only admit *a priori* that all jumps are equally probable. Eq. 3-a then takes the form:

$$L \cdot p_t(\lambda) = \Lambda \left(\frac{1}{\lambda_{max} - \lambda_{min}} - p_t(\lambda) \right) \quad (3-b)$$

Computations in this paper are mainly based on this simplified form, that corresponds to the simplest *a priori* hypothesis for droplet measurements in clouds.

The form of the operator L for Brownian motion, as well as many other details about filtering can be found in Pawlowska et al (1996).

2.2 Optimal non-linear smoothing

Filtering is the way to process data in real time, as it is by definition non-anticipatory of the future. Since the method described here aims at post-processing one should use information from the entire data series. Such a procedure is called *smoothing*. As the local intensity mainly correlates with its immediate future (as well as past), only a short section of the data following the current location must be used for updating the estimation derived after filtering. This numerical scheme is called *fixed lag smoothing* and it provides $p_t(\lambda | \{N_\sigma; t_0 \leq t \leq t_1\})$, at time t in an observation interval $[t_0, t_1]$, where t_1 increases with t as additional data are taken. The precise equations and algorithm for smoothing can be found in Pawlowska et al (1996).

3. APPLICATION TO SIMULATED DATA

The estimator presented in this paper has been especially developed to process airborne droplet measurements. In-situ observations have shown that the occurrence of a change can happen at any time. This leads to the choice of a Poisson process for describing the statistics of the intensity changes. The following step is to identify the probability density function of the amplitude of the changes. Here again, in-situ observations are valuable. Inside cloud cells, the droplet concentration is often continuously varying but examples of a sharp jump are also common. Brenguier (1993) documented an interface where the counted droplet rate increases from 0 to its maximum value (about $200,000 \text{ s}^{-1}$ in this case) in less than 0.1 ms . It has thus been assumed in a first step that all values of sudden variations from 0 to the maximum intensity are *a priori* equiprobable and the linear operator that describes the statistics of the intensity changes has taken the simplified form (3-b).

The method of optimal estimation cannot be directly evaluated with experimental data since the required intensity (particle concentration in the atmosphere) is unknown and not measurable. Tests are thus performed with simulated data using a Poisson process generator.

The first example describes the filtering of a simulated series of arrival times for an intensity of $150,000 \text{ s}^{-1}$ that falls suddenly to a value of $50,000 \text{ s}^{-1}$. Figure 2-a shows the time evolution of the λ PDF $p_t(\lambda)$. Fig. 2-b shows the true value of the intensity (dashed line), and the estimates represented by the value at the peak of the distribution or most probable value λ_m . The values λ_- and λ_+ on either side of λ_m delimit the interval containing 80 % of the probability (the 80 % confidence interval). They provide information about the flattening of the probability density distribution in the region of the peak. The calculating procedure assumes that λ_- and λ_+ are symmetric with respect to λ_m . Fig. 2-

c represents the probability at the peak $p_t(\lambda_m) \times \Delta\lambda$. After 0.6 ms of filtering, a mode appears and the estimates are stable around the true value.

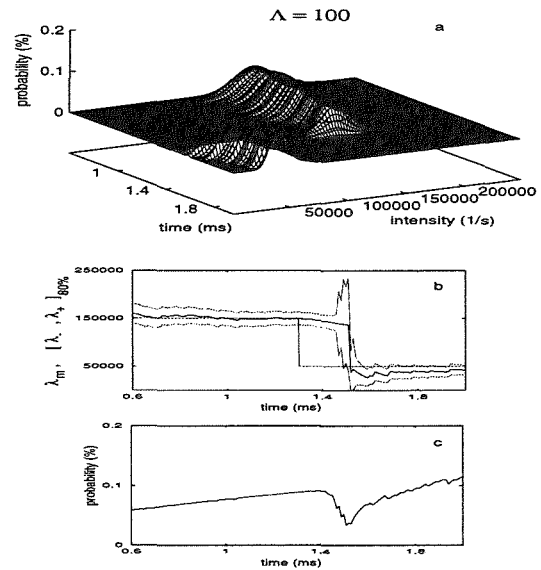


Fig. 2 Results of the filtering of a simulated series of arrivals times for an intensity changing as a step function. (a) - time evolution of λ PDF. (b) - the most likely value of intensity λ_m (solid line), the values (λ_-, λ_+) giving the 80% confidence interval (dotted lines) and the true intensity value (dashed line). (c) - the value of the λ PDF at the peak.

The probability at the peak increases progressively showing that the longer the intensity is constant, the higher is the likelihood of the estimate. Less than 0.1 ms after the intensity has fallen to a smaller value, a second mode appears in the λ PDF; the density at the mode decreases until the second mode at $50,000 \text{ s}^{-1}$ becomes higher than the previous one. About 0.2 ms after the jump, the estimates have moved to the new mode and the corresponding density is rapidly increasing. This figure shows that only 10 events, arriving three times less often than previously are enough for a significant detection of the change in the intensity of the process. Fig.2 -a shows clearly the non-linear behaviour of the equation. The mode is not sliding slowly from $150,000$ to $50,000 \text{ s}^{-1}$, but on the contrary, it almost jumps from the previous value to the new one.

The non-linear estimator is much more effective than the usual method for distinguishing between randomness of the counting and physically significant variations of the intensity. This is illustrated in Fig. 3, which shows the true value of the intensity (dashed line), the most probable value and the 80 % confidence interval after smoothing, for a simulation similar to Fig. 1, with two widths of the jump: 1 ms (Fig.3-a) and 0.65 ms (Fig. 3-b). In this example, Λ has been set to 300 s^{-1} . The comparison of Fig. 3-a with Fig. 1, for the same width of the jump (1 ms), shows that, in the region of constant

intensity, the fluctuations due to the counting have been completely smoothed, while the estimator remain capable of detecting precisely the amplitude of the jump and its sharpness. When compared to Fig. 2-b, this example shows how smoothing eliminates the lag in the detection of sharp changes. When the width of the jump becomes so small (Fig. 3-b) that it contains less than 65 events on average, the mode of the λ PDF stays at the value $50,000 \text{ s}^{-1}$, but the sudden broadening of the 80 % confidence interval suggests that some fluctuation occurred in the intensity (precise information can be obtained by examining the probability density distribution).

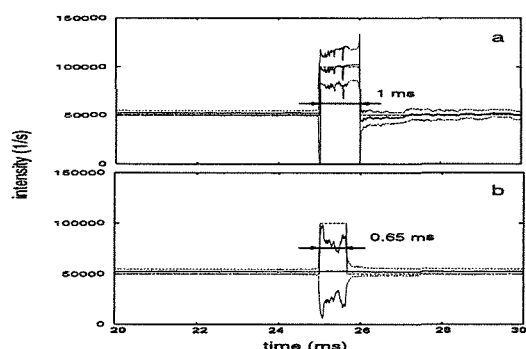


Fig. 3 Results of the smoothing for the simulated series of arrivals times for intensities in the form of a jump function with jump widths 1ms (a) and 0.65ms (b). Solid lines represent the most likely value of intensity, dotted lines the 80% confidence interval and dashed lines the true value of the intensity.

4. CONCLUSIONS

From the statistical point of view, each cloud sample is a unique realization of a random inhomogeneous Poisson process, whose intensity (the droplet rate through the counter) is an unknown process which is not directly measurable. The problem is thus to derive from this unique realization an optimal estimation of the intensity, viewed as an *a priori* random process, which leads to a Bayesian approach. It has been shown in this paper that cumulating the particle counts over a given sampling period is a crude procedure which is never optimal. The optimal solution consists in calculating the probability density function of the possible values of the intensity as a function of time. Of course, this Bayesian approach is more expensive in term of computation time but it provides an estimate of the most probable value and its likelihood. Interpretation of the data is thus more objective. *A priori* information about the dynamical statistics of the intensity process is a crucial step in the optimal estimation. If nothing is known, optimal tracking of a time-varying intensity is meaningless. Defining an optimal estimation implies that some assumptions have been made upon these statistics.

Tests performed with simulated series have shown that this non-linear Bayesian approach efficiently removes the noise due to the counting, whilst preserving the detection of sharp variations in the intensity. The conclusion of the paper is that non-linear estimation is far superior to usual linear windowing for detecting microstructures in clouds. Indeed, non-linear estimation behaves in that case as a permanent jump detection of a state variable (λ), when a suitable *a priori* model is provided from a probabilistic point of view.

The most important feature of the method is its potential for improvements. Results shown in Pawlowska et al (1996) and Pawlowska and Brenguier (1996) for actual measurements have been obtained with very little *a priori* information about the jump amplitude statistics of the droplet concentration, namely that it is subject to random changes and that any amplitude of change is equiprobable. It is also necessary to fix the value of the parameter Λ corresponding to the expected rate of change of the intensity. For very high values of Λ , the estimator detects small scale fluctuations but their likelihood is low. For very low values of Λ , the estimator misses significant changes in the intensity and the likelihood is also low. As Λ approaches its optimal value the likelihood of the estimated value of intensity is increased. When the probability density function of the jumps is known, the likelihood of the estimated value is improved. It follows that, as our knowledge of the microphysical processes increases, the performance of the estimator is progressively improved. Finally, if the particle concentration is itself modelled as a parametric function, the estimator can be extended to a parametric estimation that can retrieve from the particle counts, the conditional distribution of the parameters.

5. ACKNOWLEDGEMENTS

This research was supported by Météo-France and INSU under drant D13570.

5. REFERENCES

- Brenguier, J.L., 1993: Observations of cloud microstructure at the centimeter scale. *J.Appl.Met.*, **32**, 783-793.
- Chamon, M., A. Monin, and G. Salut, 1994: Estimation/detection non-linéaire. Theorie, algorithmes et applications. Rapport LAAS no.94.507 [Available from G. Salut, 7 Av du Colonel Roche, 31077 Toulouse Cedex, France.]
- Pawlowska, H., J.L. Brenguier, and G. Salut, 1996: Optimal non-linear estimation for particle measurements. Submitted to *J. Atmos. Oceanic Technol.*
- Pawlowska, H., and J.L. Brenguier, 1996: A study of the microphysical structure of stratocumulus clouds. Proceedings of ICCP 1996.
- Snyder, D.L., 1975: Random point processes. Wiley & Sons, 495pp.

A MODEL FOR THE FAST FSSP OPERATION

Afranio de Araujo Coelho¹, Jean-Louis Brenguier^{2,3} and Thierry Bourrienne²

¹ Cloud Physics Lab.; University Federal of Ceara (Brazil), visiting scholar at CNRM/GMEI

² METEO-FRANCE (CNRM/GMEI), Toulouse, France

³ Affiliate Scientist at NCAR/ATD+MMM

1. INTRODUCTION

Airborne measurements of the droplet size distribution are currently performed with optical spectrometers such as the Forward Scattering Spectrometer Probe (FSSP), manufactured by Particle Measuring Systems (Boulder-CO, USA). This kind of instrument is referred to as a single particle counter, because droplets are counted and sized one after another along the aircraft trajectory. The estimation of the droplet size distribution from the sampled series of counts is calculated according to the following equation:

$$C_{(\phi_1, \phi_2)}(\vec{x}(t)) = \lambda_{(\phi_1, \phi_2)}(t) / (S \times v_a(t)) \quad (1)$$

where $C_{(\phi_1, \phi_2)}(\vec{x}(t))$ is the concentration of droplets with sizes between ϕ_1 and ϕ_2 , at the location $\vec{x}(t)$ along the aircraft trajectory; S is the probe sampling section and $v_a(t)$ is the air speed through the probe sampling section at time t . $\lambda_{(\phi_1, \phi_2)}(t)$ is the rate of droplets with sizes between ϕ_1 and ϕ_2 passing through the probe sampling section at time t .

When (ϕ_1, ϕ_2) corresponds to the whole diameter range of the probe, C is referred to as the total droplet concentration; when (ϕ_1, ϕ_2) represents a size class of the instrument, the mean droplet density in the class is derived as $C/(\phi_2 - \phi_1)$ and it is directly comparable to the conventional size distribution $f(\phi)d\phi$.

Such a measurement is affected by various uncertainties in the estimation of λ , ϕ , S and v_a . A modified version of the FSSP-100 has been designed at Météo-France, the Fast FSSP, for improving the accuracy of the measurements. In addition, a new processing method has been developed that allows optimal processing of these data. Finally, a numerical model of the probe operation has been completed in order to simulate the sources of uncertainty and develop correction procedures. After a brief description of the Fast FSSP characteristics, and of the model of operation, the sources of uncertainty are discussed in order to demonstrate how the accuracy of the measurements is improved with these new tools.

2. THE MAIN CHARACTERISTICS OF THE FAST FSSP

In the FSSP, a thin laser beam is exposed to the air flow. The direct beam is masked by a dump spot. When a droplet crosses the beam, the forward scattered light is collected around the dump spot (between 3 and 12 deg) and analyzed by detection diodes. The main diode (*signal*) is used for the determination of the droplet size (the amplitude of the pulse is almost proportional to the square of the diameter). The second diode (*annulus* in the standard probe, *slit* in the Fast FSSP) provides information about the location of the droplet trajectory across the laser beam.

In the standard probe, the *annulus* diode allows selection of a cylindrical portion of the beam, called the depth of field or DOF, at the middle of the sampling tube and centered at the focal point of the beam, where the intensity of the laser is maximum. Both *signal* and *annulus* pulses are then processed by analog electronics. After DOF selection, by comparing the amplitude of these two pulses, an additional selection is needed in order to reject particles crossing the beam inside the DOF, but at the beam edge (velocity rejection). The probe sends a strobe to the acquisition system each time a detection is valid with respect to the DOF and beam edge selections. For each strobe, the acquisition system uses the droplet size information, that is coded on 4 bits (15 size classes), for a diameter range between 2 and 45 microns. In addition, the probe provides a count for all particles valid in DOF (total strobe) and for all the detections (total reset). More detailed information about the FSSP can be found in Dye and Baumgardner, 1984; Baumgardner et al, 1985; Brenguier, 1989; Baumgardner and Spowart, 1990.

In the Fast FSSP, the *slit* diode (similar to the system used in the FSSP-300), allows us to select a limited portion of the beam located at the focal point and along the beam axis so that the beam edge selection is no longer needed. Both *signal* and *slit* pulses are then converted from analog to digital at a 16 Mhz rate on 8 bits (255 size classes). For each detection, the probe provides the acquisition system with: a strobe, the amplitude of the pulse on 8 bits,

its duration on 8 bits, the interarrival time between the detections (14 bits) and the validation flag for DOF.

The amount of data produced by the FFSSP and its acquisition system (500 kbytes/s), which records these parameters for each detected droplet, is of course much larger than for the FSSP with a standard acquisition system. However, it will be demonstrated throughout this paper that all these data are extremely useful for optimal processing. For example, three values are recorded for the DOF validation depending on if the droplet crossed the laser beam inside the DOF, outside, or at the edge of the DOF. Fig. 1 shows a droplet spectrum measured with the Fast FSSP. The solid line corresponds to detections validated in DOF, the dashed line to all of them and the dot-dashed line to detections that have been validated at the edge of the DOF. The difference between the distribution in the DOF and the distribution without selection shows that the new optics are very efficient at rejecting particles crossing the beam outside of the DOF. The question is then to guarantee that the DOF is well centered on the beam axis and corresponds to a region where the intensity of the incident light is very uniform. Otherwise, the measured distributions are artificially broadened. The similarity between the distributions obtained with DOF validated particles (solid line) and with particles categorized at the edge of the DOF (dot-dashed line) proves that the spectrum broadening by the instrument is considerably reduced.

This preliminary discussion illustrates briefly the complexity of droplet measurements from an aircraft. In order to improve the accuracy of the measurements and possibly develop correction procedures, it is crucial to understand clearly the various sources of artifacts in the instrument and an efficient solution is to develop a numerical model of the probe operation.

3. THE MODEL OF THE PROBE OPERATION

3.1 Description of the model

The model combines the various steps that relate the crossing of a droplet through the laser beam to the measured pulse amplitude and duration. The values of these parameters depend on the droplet diameter, ϕ , and on the location of the droplet trajectory through the beam. This location is described by the co-ordinates X along the laser beam and Z perpendicular to X and to the air flow (Y axis). The position of the droplet along its trajectory is related to time by: $dy = v_d(t) dt$.

As a first step, Mie theory is used for the calculation of the probability P_{ϕ,A_0} for a droplet of diameter ϕ to be measured with an amplitude A_0 , when it is crossing the center of the beam.

The second step consists of the calculation of the voltage measured by the detection module when a droplet, that would scatter an intensity I_{0d} and would be measured with the amplitude A_0 when

crossing the center of the beam, passes the location (x, y, z) . The intensity of the incident light in the laser beam has been measured with a camera and its ratio to the nominal intensity at the beam center has been parameterized by the function i_{xyz} . The active area of the detection diodes is limited and only a fraction ϵ_{xyz} of the diffused light is collected. When the droplet crosses the beam close to its center, the image of the droplet is fully inside the active area, and $\epsilon_{xyz} = 1$. When the droplet crosses the beam out of the DOF, the image of the dump spot covers the active area and the fraction tends to 0. The collected intensity is thus expressed as: $I_c = I_{0d} i_{xyz} \epsilon_{xyz}$.

The measured voltage after amplification is directly proportional to the collected intensity: $V(x, y, z) = V_0 + g I_c(x, y, z)$,

and its maximum value is obtained when a particle passes the beam center: $A_0 = V_0 + g I_{0d}$. It follows that the measured voltage can be expressed as: $V(x, y, z) = V_0 + (A_0 - V_0) i_{xyz} \epsilon_{xyz}$

Finally, the measured amplitude can be calculated for any trajectory (characterized by its coordinate (x, z) when the droplet crosses the median plane of the beam ($y=0$)), as $A = V(x, 0, z)$ and the pulse width l is given by the section $[z_- - z_+]$ such that $V(x, y, z) > V_s$, where V_s is the detection threshold of the electronics.

The probability for a droplet, that would produce an amplitude A_0 when crossing the beam center, to be counted with the amplitude A and the pulse width l , $P_{A_0,A,l}$ has been calculated by integration over the whole beam section, assuming all the trajectories are equi-probable.

The conditional probability for a droplet with a diameter ϕ to be counted with the amplitude A and the pulse width l is then given by:

$$P_{\phi,A,l} = \sum_{A_0} P_{\phi,A_0} P_{A_0,A,l} \quad (2)$$

This calculation can be done for all the detections or only the detections validated in DOF.

3.2 The applications of the model

The model is currently used in the laboratory for understanding observations that are difficult to interpret. For example, the adjustment of the DOF is an important step in the preparation of the instrument for a field campaign. By changing the amplification ratio between the *signal* and the *slit* lines, it is possible to adjust the area of the DOF. For a very small DOF, the incident light intensity is very uniform and instrumental broadening is reduced, but the measured droplet rate is reduced too and the statistical significance of the data is poor. The DOF area can be adjusted from 0 to the whole detection beam. In fact, the simulation of the *signal* to *slit* comparison with the model has shown that the DOF cannot be made too small or too large without increasing significantly the uncertainty in the measurements. The

model has also been very useful for testing hardware modifications of the probe and estimating the optimal characteristics of the components.

The model has contributed to the development of a new calibration method. The probes are currently calibrated at the ground by using glass beads, droplet generators or optical pin-holes. The method used for the Fast FSSP, based on the actual data collected during the flight, is briefly described here. Because of the oscillations of the Mie response curve, a flat spectrum (uniform size distribution) will be measured with spurious peaks corresponding to the flat parts of the Mie curve (in this size ranges, the probability of measuring a given amplitude is greater than the average). The measured spectra are thus smoothed and the peaks are identified by the difference between the raw spectrum and the smoothed one. Some of those peaks reflect actual structures of the distribution and some are instrumental artifacts. By averaging over many spectra taken at various altitudes (various positions of the mode), the contribution from actual peaks is smoothed while artifacts are enhanced. By comparing the positions of the measured peaks, in the amplitude scale, with the values simulated by the model for a zero offset and a unity gain, it is possible to derive the actual values of the offset, V_0 , and the gain, g that characterize the probe calibration. During the SCMS experiment in 1995, the ground calibrations have shown that the sensitivity of the probe decreased during the experiment. The diameter range of the probe changed from $[3,35\mu\text{m}]$ at the beginning of the campaign to $[3,45\mu\text{m}]$ at the end. With the new calibration method it has been possible to estimate the calibration coefficients for every flight and detect when a loss in performance occurred.

Another objective of the model was the development of a correction procedure for the instrumental broadening based on a method similar to the transfer matrix method developed by Cooper (1988). In fact, with the improvement of the DOF validation, the measured spectra are not significantly broadened and the correction procedure is no longer needed, except for the effects of the optical coincidences. When the droplet concentration is higher than 500 cm^{-3} , the deformation of the measured size distributions becomes significant, but their simulation by the model is complex and it has not yet been solved.

4. DISCUSSION

In this section, the various sources of uncertainties are discussed in order to evaluate the progress in the measurement of the droplet size distribution and the scope for further improvement.

4.1 The air speed: $v_a(t)$

It has been shown that the air speed in the sampling tube of the FSSP is not identical to the air speed measured onboard the aircraft (Drummond and MacPherson, 1985; Norment, 1988). This difference affects the calculation of the sampled volume

and consequently the estimation of the concentration. A detailed study of the particle speed in the sampling tube is needed in order to characterize these effects. It has not yet been made but it can be noted that the measurement of the pulse duration for every detection will be very useful for such a study.

4.2 The sampling section: S

The sampling section is poorly defined in the FSSP. It corresponds to a percentage of the DOF section after rejection of beam edge counts. It has been shown that this percentage is dependent on the particle sizes and that it is affected by the coincidences (Brennguier, 1989). The resulting uncertainty in the sampling section is of the order of 15 to 25 % depending on how carefully the probe optics have been aligned. In the Fast FSSP, the whole DOF selection is made by the optical module and the calibration with a pin hole provides an estimation of the DOF section with an accuracy better than 10 % (Coelho, 1996).

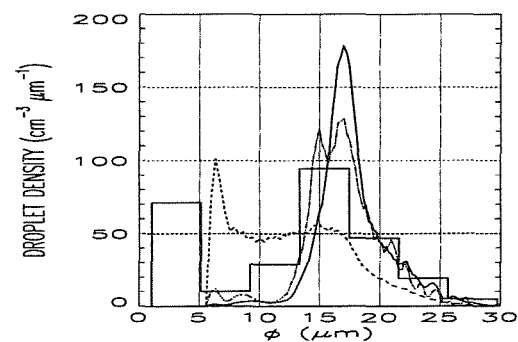


Fig.1 Droplet spectrum measured in a cumulus during SCMS-95. For the Fast FSSP, the solid line shows the size distribution of the droplets selected in the DOF, the dashed line, the distribution for all the detections and the dot-dashed line, the distribution of the droplets selected at the edge of the DOF. The histogramme shows the same spectrum measured with a standard FSSP.

4.3 The size classes $[\phi_1, \phi_2]$

With 255 size classes, the Fast FSSP provides a much better measurement of the size distribution than the FSSP, especially for narrow spectra. In Fig.1, the histogramme represents the spectrum measured with a FSSP. The concentration in the first class is overestimated because this probe was used with the delay mode (Dye and Baumgardner, 1984). Two additional instruments were also mounted for this intercalibration flight (NCAR and Univ. of Wyoming FSSP's). They were running without the delay mode and they are not showing this artefact in the first class. The two instruments showed similar estimations of the droplet concentration and of the LWC, respectively 766 cm^{-3} and 2.73 g m^{-3} for the Fast FSSP, 842 cm^{-3} 2.41 g m^{-3} for the FSSP after rejection of the first class. However, it is obvious from this figure, that the spectrum shape cannot

be correctly described with only 15 classes, even if the range of the FSSP is reduced for a better size resolution of $2\text{ }\mu\text{m}$ instead of $4\text{ }\mu\text{m}$ (a range from 3 to $60\text{ }\mu\text{m}$), as it was selected for the Météo-France FSSP during this experiment.

With respect to the accuracy of the size determination, the new calibration method based on the peaks of the Mie curve provides a much better absolute accuracy than any other indirect method of calibration at the laboratory. The method is not fully operational because the present analog to digital converter is not linear enough and it introduces additional artifacts in the measured distributions that interfere with the Mie peaks. A new detection module is currently tested, where this default of linearity is negligible.

4.4 The estimation of the droplet rate $\lambda(t)$

Two cases must be distinguished in the estimation of the droplet rate. When the sampling duration is long enough for the number of counted particles to be statistically significant, the droplet rate can be estimated directly as the ratio of the counted number to the sampling period. However, if the concentration is higher than 300 cm^{-3} the coincidence and dead-time losses must be corrected. In the Fast FSSP, there are no dead-time losses as in the standard probe and the correction procedures are much more accurate because the activity (sum of the pulse durations) is measured with a 16 MHz clock and because the measurement of the inter-arrival times between particles allow calculation of a redundant estimate of the actual rate (Baumgardner et al, 1993; Brenguier et al, 1994). Brenguier (1993) has shown that the resulting accuracy in the estimation of the droplet rate is better than 5 % even at very high concentrations (more than 1500 cm^{-3} in Brenguier, 1993) instead of 20 % or more with the standard probe.

When the number of particles is too low, as for the biggest particles in a spectrum, the optimal estimator developed by Pawlowska et al (1996-a and -b) is an efficient method that improves considerably the statistical significance of the estimation.

5. CONCLUSION

The performances of the FSSP have been significantly improved by hardware modifications of the probe and a new acquisition system that records crucial parameters for every detected droplet. A new method has been developed for optimal processing of the available data. Finally, a numerical model of the probe operation has been completed for improving the optical and electronical adjustments of the instrument, for designing a new calibration method and for the development of efficient correction procedures. The potential for further improvements has not been fully utilized and some are currently in progress at the laboratory. However, the present

performances are already remarkable and the probe has produced unique observations of the condensation process.

6. ACKNOWLEDGEMENTS

The authors are grateful to R. Peytavi for his contribution to the Fast FSSP development and to the team of the Centre d'Aviation Météorologique for their active collaboration during the flights. This research was supported by Météo-France and INSU under grant D13570.

7. REFERENCES

- Baumgardner, D., D.W. Strapp, and J.E. Dye, 1985: Evaluation of the Forward Scattering Spectrometer Probe. Part II: Correction for coincidence and dead-time losses. *J. Atmos. Oceanic Technol.*, **2**, 626-632.
- Baumgardner, D., and M. Spowart, 1990: Evaluation of the Forward Scattering Spectrometer Probe. Part III: Time response and laser inhomogeneity limitations. *J. Atmos. Oceanic Technol.*, **7**, 666-672.
- Baumgardner, D., B. Baker, and K. Weaver, 1993: A technique for the measurement of cloud structure on centimeter scales. *J. Atmos. Oceanic Technol.*, **10**, 557-565.
- Brenguier, J.L., 1989: Coincidence and dead-time corrections for particle counters. Part II: Height concentration measurements with an FSSP. *J. Atmos. Oceanic Technol.*, **6**, 585-598.
- Brenguier, J.L., 1993: Observations of cloud microstructure at the centimeter scale. *J. Appl. Meteor.*, **32**, 783-793.
- Brenguier, J.L., D. Baumgardner, and B. Baker, 1994: A review and discussion of processing algorithms for FSSP concentration measurements. *J. Atmos. Oceanic Technol.*, **11**, 1409-1414.
- Coelho, A., 1996: Mesure aéroportée de la distribution dimensionnelle des gouttelettes d'eau en nuage. PhD dissertation, Université Paul Sabatier, Toulouse, France, 151pp.
- Cooper, W., 1988: Effects of coincidence on measurements with Forward Scattering Spectrometer Probe. *J. Atmos. Oceanic Technol.*, **5**, 823-832.
- Drummond, A.M., and J.I. MacPherson, 1985: Aircraft flow effects on cloud drop images and concentrations measured by the NAE Twin Otter. *J. Atmos. Oceanic Technol.*, **2**, 633-643.
- Dye, J.E., and D. Baumgardner, 1984: Evaluation of the Forward Scattering Spectrometer Probe. Part I: Electronic and Optical Studies. *J. Atmos. Oceanic Technol.*, **1**, 329-344.
- Norment, H.G., 1988: Three-dimensional trajectory analysis of two drop sizing instruments: PMS OAP and PMS FSSP. *J. Atmos. Oceanic Technol.*, **5**, 743-756.
- Pawlowska H., J.L. Brenguier, and G. Salut, 1996: Optimal non-linear estimation for particle measurements. Submitted to *J. Atmos. Oceanic Technol.*
- Pawlowska, H., and J.L. Brenguier, and G. Salut, 1996: Optimal non-linear estimation for particle measurements. Proceedings of the ICCP 1996.

DEEP CONVECTIVE CLOUD DETECTION IN A REDUCED RESOLUTION DATA SET

Inés Velasco and Patricia Rodaro

Depto. Cs. de la Atmósfera, Universidad de Buenos Aires, Argentina

1. INTRODUCTION

The first successful attempt to extract cloud amounts from satellite imagery was carried out by Arking (1964). A parallel effort, but utilizing manual processing, was done by Clapp (1964). In 1972, the polar orbiting operational meteorological satellites began providing on a daily basis a near-complete mosaic of the Earth, once every 12 hours, in the visible and thermal infrared wavelengths. Rossow et al. (1983) used those data to derive cloud amount, optical thickness and cloud top temperature in a pilot program to derive a cloud climatology based on visible and thermal infrared satellite imagery.

With the growing interest in developing a cloud climatology, there are now a number of techniques for extracting cloud cover parameters from satellite measurements. They can be generally divided in two classes: 1) those using radiative transfer calculations combined with a threshold test to detect cloudy pixels and 2) those based upon identification of clusters in the multidimensional radiance space formed by one or more channels.

Before satellite images were available accurate information concerning cloud distribution was severely lacking. Weather observations estimate cloudiness as scattered (1/8 to 4/8 coverage), broken (5/8 to 7/8 coverage) or overcast. Accuracy in an observation site was therefore not better than 25 - 30 %. The spacing of the observation sites results in a still lower accuracy. By contrast a 446 km square satellite image with a degraded resolution of 8 by 8 km relates to 3111 individual locations. Images over Argentina, with this degraded resolution, were routinely collected at the National Weather Service (NWS) for several years. These data also are limited to two bands, near-infrared (0.70 - 1.10 μm) and infrared (10.3 - 11.3 μm). It is the purpose of this research to use these images to make a preliminary study of the deep convective cloud coverage in Argentina over three areas with different topographies.

2. THE STUDY AREAS

The method was applied to arrays segmented according to the availability of upper air stations which

are in three different topographic areas. Figure 1 shows the study areas. One station (Resistencia, SIS) is located in Chaco province, in northeastern Argentina. This area is crossed by the Bermejo and Parana rivers and composes the Gran Chaco. A second one (Cordoba, CBA) is located in Cordoba province in central Argentina. The area extends from Sierra Grande in the west, which rises to 2,884 m and slopes eastward to the great Pampa grasslands, being drained by several rivers, with extended lake Mar Chiquita. The third one (Ezeiza, EZE) is in Buenos Aires province, eastern Argentina, lying south of Parana river and southeast of the wide *de la Plata* river (which forms the border with Uruguay) and extending westward from the Atlantic Ocean to include part of the humid Argentina Pampa, a grass cover plain with small lakes scattered across the area. These features offer an opportunity to examine relationships between terrain variations and cloudiness.

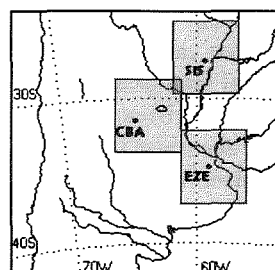


Figure 1. Geographical area considered in the study. The shading areas are the three different topographic areas for developing the scheme. SIS, CBA and EZE identify the upper air stations available in each area

3. DATA SET

In the present study, the imagery data set was obtained from the NWS of Argentina operational data bases. The images were collected from NOAA-11 at the NWS Satellite Station for December 1992 and January and February 1993 close to 1930 UTC. This data set is a reduced satellite data set generated from the 1x1 km high resolution data to 8x8 km resolution and mapped into a gnomonic projection. The spatial resolution was reduced by simple arithmetic averaging of the satellite pixel counts. The area mapped is bounded by the 40° and 80°W meridians and 20° and 60°S latitudes. From this area three subareas were selected (see Figure 1). The study used a total of 31

images, about 10 for each month. Although the data supplied were georeferenced, it was decided to group pixels into boxes containing 61 scan lines (north-south direction) by 51 elements (west-east direction) for each of the three selected subareas. These boxes were about 5° of latitude/longitude square.

Cloud coverage was obtained over the areas of analysis using this degraded data set, however, for comparison, this data set has a 20 time higher linear resolution than the average distance between ground stations in any of the three subareas selected for the study and only a 13% or less of the total area is covered by the surface observations (see Figure 2). An image from a near cloudless day provided a base image. The digital data available has 256 possible brightness values for near-infrared (NIR) and infrared (IR) data. The IDRISI system used in this study depicts images using 16 levels of brightness. There is a capability of masking that portion of any image which is brighter (or darker) than some threshold value.

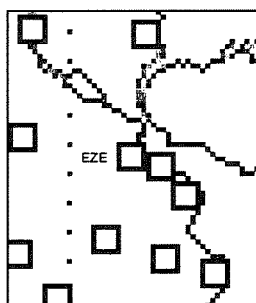


Figure 2. The ground stations nearby Ezeiza. Each square is about 48 by 48 km.

4. CLOUD DETECTION TECHNIQUE

Clouds formed by strong convection have high, cold tops. Additionally, these cumulonimbus clouds reflect considerable light and are, therefore, bright in the visible spectrum. By way of contrast, clouds formed by weak convection, though they may be bright, have warm cloud top temperatures. Additionally, cirrus anvil clouds, though they may have cold tops, reflect less light compared to an overshooting cumulonimbus top. Using these two characteristics, convective cloudiness is determined by using a combination of brightness of the near-infrared image and the cloud-top temperature as indicated by the brightness of the infrared image.

Over land the shorter wavelengths are more useful as land surface has a much lower reflectance making the contrast between land and cloud much greater and hence detection of cloud easier (Saunders, 1986). However, most cloud types have a high reflectance at visible and near-infrared wavelengths when compared with the low reflectance of the land and water surface. This allows a NIR threshold to be applied where all reflected radiances which are above a certain level are

identified as cloud contaminated. (NIR wavelength is the only short wave available in our data set).

The first step consisted in estimating a NIR threshold count value (representing albedo) to separate cloud cover from land and water cover for each of the three regions. A "background" image was constructed for each month. These images represent the cloud free brightness count detected by the satellite in the near infrared band. Because variations in surface compositions and topography produce changes in the background brightness (Mimis and Harrison, 1984) a different background image was constructed for each of the three areas and for each month. Figure 3a is a background NIR image at 2010 UTC for 24 February 1993, representing the cloud free scene for that specific month in the area located in the vicinity of Ezeiza. Over land and over *de la Plata* river two cloud-free peaks can be identified in the reflectance histograms of 51 x 61 pixels arrays as shown in Figure 3b. A reflectance threshold with an 80 count value was determined for discriminating clouded of unclouded pixels. This threshold was checked by the inspection of all the histograms of the NIR count values (ranging from 0 to 255) for the pixels that formed each "box" at the time of the overpass of the satellite. It was verified for the three areas and for the data of December 1992, and January and February 1993, and it does not seem to depend of the geographical location or month. Hereafter all pixels with reflectance lower than this threshold were considered unclouded.

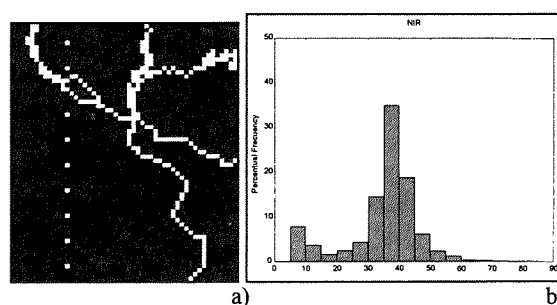


Figure 3. a) Example of NIR reflected radiance, b) The histogram with cloud-free peaks.

In a second step, using this brightness count, a graphic overlay was made within the computer for each NIR image, which masks all but the clouded pixels. This graphic was then placed over the infrared image for the same time and date. An image was then made that consider only the infrared data within the unmasked area. This image outlined areas where the cloud top temperature was -30°C or colder. At this temperature, cloud tops are approximately 9000 m high (Velasco and Necco, 1980). Hereafter, convection that results in cloud top temperatures of -30°C or colder will be considered deep convection. Cloud covered areas were assigned a brightness value of 255 and non cloudy areas a value of zero. Using these two values of brightness, a cloud-no cloud image was made for each NIR image collected for the period of study, which has

count values higher than the prefixed threshold. Figure 4 shows the IR image and the classification results at 2002 UTC, for 8 February 1993.

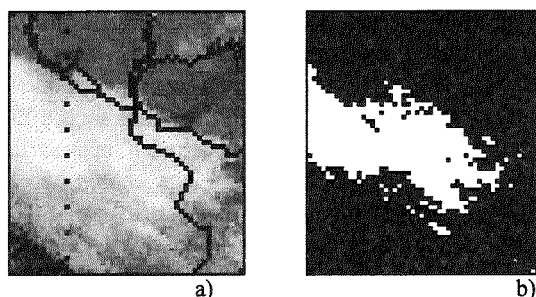


Figure 4. a) IR image. b) Deep convective cloud (white)/other cloud or non cloud (black), 2002 UTC, 8 February 1993

5. INTERCOMPARISON WITH SURFACE BASED OBSERVATIONS

The search for an objective verification procedure of any kind of classification from satellite data is a rather difficult task (Tsonis, 1984). In this study the images constructed from the scheme were compared with ground based cloud observations. Data from over 11 surface stations were obtained from the Argentine NWS for the area nearby Ezeiza (EZE) (see Figure 2). The occurrence of cloud from surface observations close to the time of the satellite overpasses (between 1930 and 2030 UTC), was determined by assigning a cloud/no cloud value for a specific hour of each day. If a station reported 5/8 or more of deep convective clouds, it was considered cloudy and so all the pixels in the area of 48 km square around the geographic location of the surface observation site. This area was selected to approximate the surface observer's "sky dome" which is the imaginary hemisphere of 50 km diameter that the observer report obscured by cloud (Reinke et al., 1992).

The validation has been restricted to the total deep convective cloud cover, which is among the parameters derived from the procedure the easiest to verify. If a station reported less than 3/8 of clouds all the pixels within the box of 6x6 pixels were considered unclouded. If a station reported 4/8 of clouds, 50% of the pixels in the box were considered clouded and the scene was considered partly clouded. The observed clouds were considered deep convective clouds when the station reported according to the WMO code, clouds of vertical development of type 3 or 9. When middle clouds of type 2 or 7 and rain is reported it was considered that *Nimbostratus* were present. Since *Nimbostratus* typically extends from a base at 4 km level or lower to tops near the tropopause (Houze, 1993) and they are associated primarily with the wide spread continuous cloud of the mesoscale convective systems, it could be very difficult to separate *Nimbostratus* from deep convective towers using the developed scheme.

6. VERIFICATION OF THE SCHEME

The verification was done over the Ezeiza area because at the moment of this study these were the only ground station reports available. A summary of the estimated and observed deep convective cloud cover is presented in Table 1. The information contained in this table could be combined to obtain a number of interesting verification statistics to evaluate the method to estimate areas with deep convection. Clearly, no single measurement of estimating success can give a complete picture and it is desirable to include at least four statistics in any summary of verification. For further discussion about the use of contingency tables see, e. g., Panofsky and Brier (1968); Doswell et al. (1990) and Collier and Lilley (1994).

Probability of cloud detection: $POD = CC / (CC + NC)$

False alarm ratio: $FAR = 1 - [CC / (CN + CC)]$

Percent error: $PE = [(NC + CN) / (NN + NC + CN + CC)]$

Critical success index: $CSI = CC / (CC + NC + CN)$

Skill score: $SS = (CC + NN - E) / (CC + NN + NC + CN - E)$

where: NN: number of stations correctly classified as non-clouded; NC: number of stations incorrectly classified as non-clouded; CN: number of stations incorrectly classified as clouded; CC: number of stations correctly classified as clouded and E is the expected number of stations correctly classified due purely to chance and it is expressed by

$$E = [(CC + CN)(CC + NC) + (NN + CN)(NN + NC)] / (CC + NN + NC + CN)$$

POD shows the ability of the scheme to detect the points (pixels) where it is cloudy, 1 is a perfect value. FAR gives the possibility of indicating cloudy where there is not clouds and has a perfect value of 0. PE shows the error in detecting pixels with clouds. CSI is the most-severe score because it gives no credit for correct detection of the non occurrence of convective clouds (Collier and Lilley, 1994). SS is giving credit for correct detection of the non occurrence but in a reasonably controlled way (Doswell et al., 1990).

Table 1. Contingency Table for estimated versus observed convective cloud cover

Observed	Estimated		Total
	N	C	
N	228	44	272
C	18	51	69
Total	246	95	341

POD=0.739, EP=0.181, FAR=0.463, CSI=0.451, SS = 0.506.

A second NIR threshold was estimated using the average and the standard deviation calculated for the pixels in the NIR images which also have $T \leq -30^{\circ}C$ in the IR images. Using these values a new threshold of 85 count value was set up. A second summary of the estimated and observed deep convective cloud cover is

presented in Table 2. With the second threshold an improvement of about 5% is observed in the FAR and SS statistics due to the decrease in the CN value.

Table 2. As Table 1 for a threshold count of 85

Observed	Estimated		Total
	N	C	
N	241	34	275
C	18	48	66
Total	259	82	341

POD=0.727, PE=0.152, FAR=0.414, CSI=0.480, SS = 0.552.

7. COMPOSITES OF SATELLITE CLASSIFIED IMAGERY

Composites images were constructed by simply adding together several images which have been biaspectrally classified. The classified composites represent a kind of convective frequencies. Figure 5 shows the variation of convective cloud frequency in each area (white pixels have the highest frequencies). A comparison of these figures shows that the cloudiness in the vicinity of Ezeiza and Cordoba is largely associated to the frequent pass of the fronts over these areas, oriented NW-SE. Instead around Resistencia it is possible to observe a more random distribution of deep convection, probably associated to the frequent occurrence of mesoscale convective systems in this area (see e.g., Velasco and Fritsch, 1987). In the sample available, examining the month to month variations of convective cloud frequency it is observed that January registered the highest frequency of days with deep convective cloudiness.

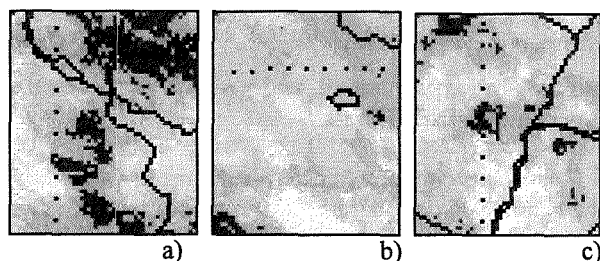


Figure 5. Frequency of convective cloud tops to -30°C or colder, a) EZE, b) CBA and c) SIS, January 1993.

8. SUMMARY AND CONCLUSIONS

Based on the spectral characteristics of the NIR and IR images a scheme has been developed which identifies deep convective clouded pixels. The scheme has been developed using images recorded over Argentina by the AVHRR on NOAA-11. The scheme has been verified using records from ground synoptic stations. Some deficiencies have been noted along the way, particularly concerning the discrimination among *Altostratus*, *Alto cumulus* or *Nimbostratus*. The accuracy of the scheme resulting from all days of the sample is about 73%.

Even though this work is a first step in an objective classification from a satellite imagery over Argentina, it has been demonstrated that a satisfactory identification of deep convective clouds can be achieved. Such analysis of the satellite images provided useful information that can be automatically extracted and presented. This information would be very important to cloud climatology, synoptic applications and the like.

In the opinion of the authors, further analysis employing better resolution images and considering different IR thresholds will improve the scheme to be applied to distinguish other type of convective clouds. Also climatological relationships between deep convective frequencies and vertical wind shear and atmospheric stability should be examined.

9. ACKNOWLEDGEMENTS

To the NWS for supplying us with the data. This work was supported by UBA-Grant EX-174.

10. REFERENCES

- Arking, A., 1964: Latitudinal distribution of cloud cover from TIROS III photographs. *Science*, 143, 569-572.
- Clapp, P. F., 1964: Global cloud cover for seasons using TIROS nephel analyses, *Mon. Wea. Rev.*, 92, 495-572.
- Collier, C. G. and R. B. E. Lilley, 1994: Forecasting thunderstorm initiation in north-west Europe using thermodynamic indices, satellite and radar data, *Met. Apps.*, 1, 75-84.
- Doswell, C. A. III, R. Davies-Jones and D. L. Keller, 1990: On summary measures of skill in rare event forecasting based on contingency tables. *Wea. Forecasting*, 5, 576-585.
- Houze, R. A. Jr., 1993: *Cloud dynamics*, Academic Press, N. Y., 573pp.
- Minnis, P. and E. F. Harrison, 1984: Diurnal variability of regional cloud and clear-sky radiative parameters derived from GOES data. Part I: Analysis Method. *J. of Climate and Appl. Met.*, 23, 993-1011.
- Panofsky, H. A. and G. W. Brier, 1968: *Some Applications of Statistics to Meteorology*, PSU, Pennsylvania, USA, 224 pp.
- Reinke, D. L., C. L. Combs, S. Q. Kidder and T. H. Vonder Haar, 1992: Satellite cloud composite climatologies: a new high-resolution tool in atmospheric research and forecasting. *Bull. Amer. Meteor. Soc.*, 73, 278-285.
- Rosow, W. B. E. Kinsella and L. Garder, 1983: Seasonal and global cloud variations deduced from polar orbiting satellite radiance measurements. *Proc. Fifth Conf. on Atmospheric Radiation*, Baltimore, AMS, 195-198.
- Saunders, R. W., 1986: An automated scheme for the removal of cloud contamination for AVHRR radiances over the western Europe. *Int. J. Rem. Sens.*, 7, 867-886.
- Tsonis, A. A., 1984: On the separability of various classes from the GOES visible and infrared data. *J. of Clim. and Appl. Met.*, 23, 1393-1410.
- Velasco, I. and G. V. Necco, 1980: *Upper air statistics for Argentina stations (original in Spanish)*. 275 pp. Available at Dept. of Atmos. Scs., Univer. de Bs. As., 1428 Bs. As., Argentina.
- Velasco, I. and J. M. Fritsch, 1987: Mesoscale Convective Complexes in the Americas. *J. of Geophys. Res.*, 92, 9591-9613.

ASPIRATION DISTORTIONS OF AEROSOLS: INVESTIGATION BY PHOTON CORRELATION SPECTROSCOPY

Vladimir I Jakimchuk and Nikolay Kh Kopyt

Odessa State University, Res. Lab. for Aerosols, 2 Petra Velikogo Str., Odessa, Ukraine

1. INTRODUCTION

Optical non-destructive methods nowadays are frequently used for investigations of aerosol systems. But contact methods with aspiration sampling are still widely applied for measurements of particles concentration, their analysis by electron microscopy, investigation of their chemical activity in problems of aerosols, clouds physics, environment and ecology, etc. The sampling-based measurements disturb the aerosol systems, so much attention is paid to possible sources of errors inherent in this technique (Dunnett (1992), and references cited therein). Actual problems here are aerosol flow behaviour, particles concentration and size distribution under aspiration. In the present report application of photon correlation spectroscopy in homodyne regime, and the laser Doppler anemometry (LDA) to these problems is considered.

2. EXPERIMENTAL

2.1 Cumulant description of scattering spectra

In the photon correlation spectroscopy (Berne and Pecora (1975)) and in LDA technique (Durst et al. (1976)), parameters of the investigated aerosol and its flow are obtained from the analysis of the scattering spectrum and its Doppler-shifted component. They can be described by moments of the distribution or, preferably, in terms of cumulants. The general theory of the latter was given, for example, by Cramér (1975). Their application to correlation spectroscopy was considered by Koppel (1972), Ostrowsky and Sornette (1983).

If moments m_p of order $p = 0, 1, 2, \dots$ are known, the cumulants α_p can be determined from the relations

$$\begin{aligned}\alpha_1 &= m_1, \quad \alpha_2 = \sigma^2 = m_2 - m_1^2, \\ \alpha_3 &= m_3 - 3m_1m_2 + 2m_1^3, \\ \alpha_4 &= m_4 - 3m_2^2 - 4m_1m_3 + 12m_1^2m_2 - 6m_1^4, \\ \alpha_5 &= m_5 - 5m_1m_4 - 10m_2m_3 + 20m_1^2m_3 + \\ &\quad + 30m_1m_2^2 - 60m_1^3m_2 + 24m_1^5, \quad \dots\end{aligned}\quad (1)$$

The convenience of the cumulant description can be summarised as follows. In many cases, first-order cumulants are sufficient for a description of the distribution,

whereas in a moments description, all moments must be known. The example is the Gaussian function

$$w_G(t) = (2\pi)^{-1/2} \exp(-t^2/2), \quad (2)$$

where $t = (\alpha - m_1)/\sigma$, and α is a current value. For a description of this function, only α_1 and α_2 are needed, all higher order cumulants are zero.

According to Cramér (1975), an arbitrary probability density function $w(t)$ can be approximated by the Edgeworth power series of the derivatives of $w_G(t)$. Taking into account only the first five cumulants, this approximation is

$$\begin{aligned}w(t) &= w_G(t) - \frac{\gamma_3}{3!} w_G^{(3)}(t) + \frac{\gamma_4}{4!} w_G^{(4)}(t) - \\ &\quad - \frac{\gamma_5}{5!} w_G^{(5)}(t) + \frac{10\gamma_3^2}{6!} w_G^{(6)}(t) - \\ &\quad - \frac{35}{7!} \gamma_3 \gamma_4 w_G^{(7)}(t) - \frac{280}{9!} \gamma_3^3 w_G^{(9)}(t) + \dots\end{aligned}\quad (3)$$

where, $w_G^{(p)}(t) = (-1)^p H_p(t) w_G(t)$, $H_p(t)$ is an Hermitian p -order polynomial, and $\gamma_p = \alpha_p/\sigma^p$ are normalised cumulant coefficients.

The first order cumulant α_1 is the mean value. For the symmetric distribution, α_1 coincides with the abscissa of the maximum, the mode; in LDA measurements it determines the mean frequency shift $\langle f_D \rangle$ and, thereby, the mean flow velocity $\langle v \rangle$ of the scatterers. For the asymmetric distributions the mode can be determined from the Pierson relation

$$f_0 = \alpha_1 - \gamma_3(\gamma_4 + 6)\sigma / 2(5\gamma_4^2 - 6\gamma_3^2 + 6). \quad (4)$$

Cumulant α_2 characterises the width of the spectrum; σ is the standard deviation; γ_3 describes the spectrum symmetry with respect to the mean value. In flow investigations, this coefficient is connected with the velocity gradient within the measuring volume. γ_4 is the excess coefficient characterising the flatness of the peak, the kurtosis. In the polydispersity analysis γ_3 and γ_4 characterise the symmetry and the kurtosis of the size distribution, respectively.

Cumulants of statistically independent ensembles are additive. If a distribution is a sum of s statistically independent distributions with their own sets of

α_p , the resulting distribution cumulants are their sum

$$\alpha_p = \alpha_p^{(1)} + \alpha_p^{(2)} + \dots + \alpha_p^{(s)} \quad (5)$$

regardless of the distributions of the ensembles.

To obtain moments and cumulants of the measured spectrum or a Doppler component, its frequency range is divided into a finite number of intervals; the frequency shifts in these points f_j and their corresponding amplitudes A_j , $j=1, 2, 3, \dots n$, are determined. Then using formula proposed by Marenkov (1984),

$$\mu_p = \frac{1}{2(p+1)} \sum_{j=2}^n (A_{j-1} + A_j) (f_j^{p+1} - f_{j-1}^{p+1}), \quad (6)$$

moments $m_p = \mu_p / \mu_0$ and cumulants (1) are calculated. Formula (6) is valid for unimodal distributions only; its error depends on the number n . For $n=50$, the error for m_1 was 0.5% and for α_p , 5%.

2.2 The set-up and measurement procedure

In the present report distortions of flow under aspiration sampling and aerosol size distribution functions are investigated by methods of photon correlation spectroscopy: LDA with difference optical scheme and forward scattering, and by homodyne technique. In both cases power spectra $S(q, f)$ of the photocurrent were investigated in the ranges 10 Hz - 60 kHz, and 10 kHz - 110 MHz. with $\pm 1\%$ accuracy

The scheme of the set-up with LDA control of the flow is shown in Figure 1.

The particles were water aerosol, oil one, soot particles, and Lycopodium spores, the concentration was 10^4 particles/cm³. The aerosol was sampled from a) calm conditions, and b) from laminar flow with $v_0 = 0.22 \pm 0.01$ m/s, flat velocities profile was formed

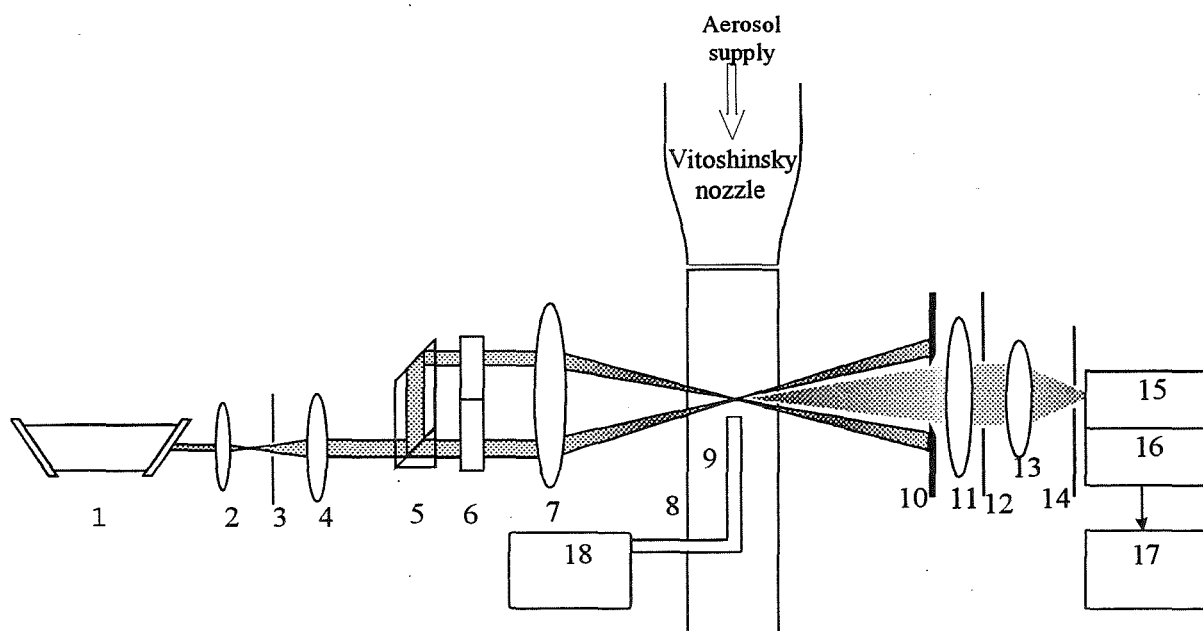


Fig. 1. Schematic illustrations of the set-up: He-Ne laser (1), spatial filter and beam expander (2, 4 lenses, 3 pinhole), beam splitter (5), Pockels cell (6), transmitting lens (7), investigated fluid flow (8), thin-walled sampler (9), receiving spatial filter (10, 12 apertures, 11, 13, lenses, 14 slit), photomultiplier (15), wide range amplifier (16), spectrum analyser (17), a reservoir with sampled aerosol (18).

by Vitoshinsky nozzle. Mean sampling velocities through thin-walled sampler with internal diameter $d=2.0$ mm were varied in the range $\langle u \rangle = 1$ cm/s - 10 m/s.

The investigated volume with aerosol and its flows was mounted on a three-coordinate stage, and could be scanned in all coordinates with a position accuracy of ± 20 μ m.

The broadening of the measured Doppler-shifted

component results from the following factors:

- instrumental broadening σ_{opt} due to the finite size of the scattering volume, the finite transit time of the particles, the parameters of the receiving optics, and broadening caused by the finite filter pass band Δf in the spectrum analyser, σ_f ,
- velocity gradients within the scattering volume, σ_T ,
- fluctuations of particle velocities, σ_v ,
- Brownian motion of the particles, σ_B .

Regarding these factors as statistically independent and taking into account (5), the resulting measured

broadening can be written as

$$\sigma_m^2 = \sigma_{opt}^2 + \sigma_f^2 + \sigma_T^2 + \sigma_v^2 + \sigma_B^2. \quad (7)$$

In Doppler-difference scheme with Gaussian beams $\sigma_{opt}/f_D = b/(2^{1/2}a)$, where b is the radius of the laser beams in the plane of the focusing objective at e^{-2} level, and $2a$ is a distance between the beams. Broadening due to the filter pass band is $\sigma_f = 2\pi\Delta f/2.36$ and can be minimised by appropriate selection of Δf . Direct estimation shows that σ_B is essential only at flow velocities $v < 0.5$ m/s.

Excluding $\sigma_{instr}^2 = \sigma_{opt}^2 + \sigma_f^2$ from measured σ_m^2 values one can obtain $\sigma_{flow}^2 = \sigma_T^2 + \sigma_v^2$ and related flow parameters.

In photon correlation spectroscopy particles size analysis is of special interest. For submicron and ultrafine electrically neutral particles in Brownian motion their effective radii r are obtained from Brownian diffusion coefficient $D(r)$ measured either from the power spectrum or from its time-Fourier transform, the time-correlation function

$$g^{(2)} = \langle I(q,r,t) I(q,r,t) \rangle / \langle I \rangle^2 = \exp(-2D(r)q^2t), \quad (8)$$

where $I(q,r,t)$ is intensity of laser light scattered at $|q| = (4\pi/\lambda)\sin(\vartheta/2)$, λ is laser light wavelength in the medium, and ϑ is the scattering angle. For the polydisperse system with radii distribution function $N(r)dr$

$$g^{(2)}(q,t) = \frac{\int N(r) \exp(-2D(r)q^2t) I(q,t,r) dr}{\int N(r) I(q,t,r) dr}, \quad (9)$$

and a variety of methods has been worked out for processing these complicated spectra and correlation functions. One of them (Koppel (1972)) is fitting of $g^{(2)}(q,t)$ in semilogarithmic scale by cumulants:

$$\ln g^{(2)}(t) = -\langle Dq^2 \rangle t + \frac{1}{2!} \alpha_2 t^2 - \frac{1}{3!} \alpha_3 t^3 + \frac{1}{4!} \alpha_4 t^4 + \dots$$

(brackets denote mean value), and determination of α_p for size distribution.

Recent advances in this subject and homodyne technique one can find in the works of Schweiger (1993), Weber *et al.* (1993), Weber and Schweiger (1995).

At micron size particles when sedimentation is essential the polydispersity can be analysed in the following way. Particle relaxation time $\tau_r = 4r^2\rho_p/18\mu$ and stationary sedimentation velocity $v = \tau_r g$, depend on r as second power, here g is gravity, μ is dynamic viscosity of the medium, ρ_p particle substance density. At the sedimentation in calm air the polydispersity leads to correspondent velocities distribution and separations of different particles fractions in different planes of the flow cross-section with density function $W(x)$, where x is a coordinate in the flow. Each frac-

tion has its own Doppler-shifted peak, that neglecting (7) can be written as delta-function $s(\omega,x) = \delta[\omega - q \cdot v(x)]$, where ω is angular frequency shift at scattering, and $v(x)$ is a velocity of the fraction. If no multiply scattering occurs, the registered Doppler-shifted component of the spectrum scattered by particles in the layer from x_1 to x_2 covered by scattering volume is

$$S(\omega,q) \propto \int_{x_1}^{x_2} W(x) s(\omega,x) dx \quad (10)$$

and one can obtain information on the polydispersity within layer, covered by this scattering volume. At charged particles their distribution across the flow can be emphasised by an external field. Semenov and Kononenko (1987) used this approach for the analysis of particles concentration in a chromatographic column.

3. RESULTS AND DISCUSSIONS

Measuring longitudinal and transversal components of velocity in the vicinity of the sampler with a step of 0.25 mm at various ratios of u/v_0 velocity vectors and their spatial distribution in the investigated flows have been obtained. One of the results is shown in Figure 2.

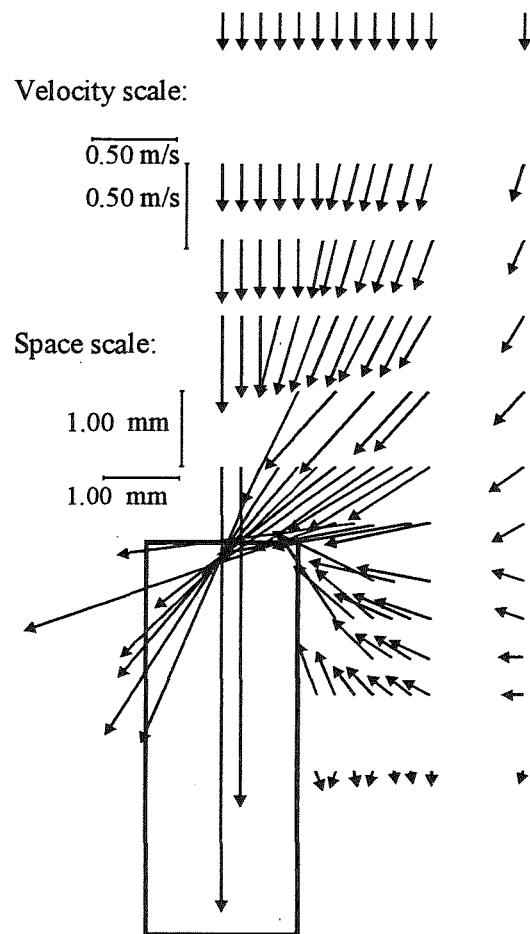


Fig. 2. Measured flow pattern at $\langle u \rangle / v_0 = 14.0$

The oncoming laminar flow with $\sigma_{flow}/\langle f_D \rangle = 0.005$ under the aspiration turned to turbulent one, $\sigma_{flow}/\langle f_D \rangle$ was found to vary in the range 0.05-0.32. The spatial area of flow disturbance at the ratio $\langle u \rangle/v_0 = 14$ can extend to distance $l = 4d$ countered from the centre of the nozzle orifice, spatial and temporal flow instability appeared.

Determining cumulants from measurements, taking into account broadening factors (7), relations (5), (10) and approximating measured spectra by the power series (3) particles diameters distribution density functions have been determined for the investigated aerosol before aspiration and for the sampled one. One of the results is shown in Figure 3.

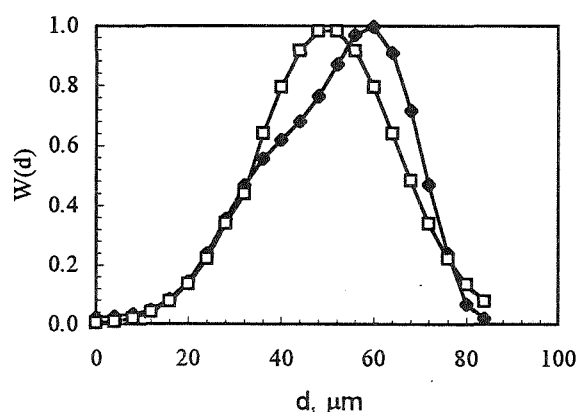


Fig. 3. Distribution density function $W(d)$ for soot particles: (□) before sampling: $m_1 = f_0 = 50 \mu\text{m}$, $\sigma/m_1 = 0.01$, $\gamma_3 = \gamma_4 = 0$; (◆) sampled aerosol: $m_1 = 50 \mu\text{m}$, $f_0 = 58 \mu\text{m}$, $\sigma/m_1 = 0.3$, $\gamma_3 = -1.1$, $\gamma_4 = 0.3$, $\langle u \rangle/v_0 = 14$.

The sampling affects particles size distributions, their crushings at interactions with the sampler were registered, the polydispersity could increase up to 300 % of the initial value. Symmetric size distribution function as a result of the sampling turned to asymmetric one, the asymmetry coefficient could reach value -1.7, and the kurtosis 0.8.

At submicron particles their Brownian motion was investigated in homodyne regime under calm conditions and compared with measurements in the volume the aerosol was aspirated into. Similar results have been obtained.

Using *Mathcad 5.0 for Windows* software computer modelling of polydispersity, velocities gradients, and turbulence influences on LDA spectra were performed. Obtained results will be reported elsewhere.

4. CONCLUSIONS

Our experiments show that aerosol distortions under aspiration are minimal at $\langle u \rangle/v_0 = 1.0$ in a good agreement with investigations of Dunnett (1992).

Application of LDA technique makes possible simultaneous measurements of aerosol flow parameters, particles size distribution functions and correct unambiguous interpretation of the results.

5. ACKNOWLEDGEMENTS

Dipl.-Ing. R. Weber (Ruhr-Universität Bochum, Germany) is acknowledged for the reprints of original papers on particles analysis by photon correlation spectroscopy.

6. REFERENCES

- Berne B.J., Pecora R. (1975) Dynamic light scattering with applications to chemistry, biology and physics. J. Wiley @ Sons, New York, 376 p.
- Cramér, H. (1975) Mathematical methods of statistics, Mir Publishers, Moscow, 648 p., (In Russian).
- Dunnett, S.J. (1992) A mathematical investigation into the effects of the position of the sampling inlet upon the aspiration of a thin-walled sampler. *J. Aerosol Sci.*, Vol.23, Suppl. 1, pp.S579-S582.
- Durst, F., Melling, A. and Whitelaw, J.M. (1976) Principles and practice of laser-Doppler anemometry. Acad. Press, London, 401 pp.
- Koppel, D.E. (1972) Analysis of macromolecular polydispersity in intensity correlation spectroscopy: the method of cumulants. *J.Chem.Phys.*, Vol.57, No 11, pp. 4814-4820.
- Marenkov, V.I. (1984) Thermal ionisation in low-temperature plasma with condensed dispersed phase. Thesis, Odessa Univ., 187p., (in Russian).
- Ostrowsky, N. and Sornette D. (1983) Data reduction in polydisperse studies. In: E.O. Schulz-DuBois (Editor), Photon correlation technique in fluid mechanics. Springer-Verlag, Berlin, pp.286-297.
- Schweiger, G. (1993) Application of photon correlation techniques to ultrafine particle analysis. In: Synthesis and measurement of ultrafine particles. (Eds.: Marijnissen, J.C.M., and Pratsinis, S.), pp.155-170, Delft University Press, Delft.
- Semenov, S.N. and Kononenko, V.L. (1987) Integral Doppler anemometry in a flow and transversal focusing force field. *Journ. Phys. Chem. (Moscow)* Vol. LXI, Issue 7, 1947-1949, (in Russian).
- Weber, R., Rambau, R., Schweiger, G. and Lucas K. (1993) Analysis of a flowing aerosol by correlation spectroscopy: concentration, aperture, velocity and particle size effects. *J. Aerosol Sci.*, Vol.24, No. 4, pp. 485-499.
- Weber, R., Schweiger, G. (1995) Determination of particle size distribution in flowing aerosols by photon correlation spectroscopy *J. Aerosol Sci.*, Vol.26, Suppl 1, pp. S29-S30.

SNOWFALL RATE DETERMINED BY IMAGE PROCESSING DATA

Ken-ichiro Muramoto¹, Toshio Harimaya² and Toru Shiina³

¹Faculty of Engineering, Kanazawa University, Kanazawa 920, Japan

²Graduate School of Science, Hokkaido University, Sapporo 060, Japan

³Toyama National College of Technology, Toyama 939, Japan

1. INTRODUCTION

Radar measurements of precipitation are based on the relation between the radar reflectivity factor Z and precipitation rate R (Boucher and Wieler, 1985; Carlson and Marshall, 1972; Gunn and Marshall, 1958; Sekhon and Srivastava, 1970). In order to determine Z - R relationship for snowfall, Z and R have to be measured independently with high accuracy at short time interval. However, few systems have been developed for measurement of snowfall rate with high degree of time interval and accuracy (Boucher and Wieler, 1985; Carlson and Marshall, 1972; Fujiyoshi et al. 1990). The purpose of this paper is to propose the measurement system for snowfall rate only by image processing data in real time. One of the advantages of using the image processing data is that snowfall rate could be measured at short time interval for a long time automatically.

In this paper, a new system to measure physical snowfall parameters is proposed. To make such determinations every minute, snowflake weight in a bucket is automatically recorded with an electric balance and computer system. This system is synchronized with a TV camera by which of snowflake images are taken. The diameter and velocity of snowflake are computed from the images. Snowfall rates calculated from the image data are compared with values directly obtained.

2. PRECIPITATION MEASUREMENT

To measure the snowfall rate in a short period, snowfall weight in a bucket is automatically recorded with an electric balance and computer system. This weighing gauge measures the amount of snowfall directly without delay or error due to melting or evaporation. The minimum

detectable snowfall rate by this gauge is 0.062 mm/h using a bucket of 35 cm in diameter with a balance weight sensitivity is 0.1 g. The data are stored on a disk in 1 min intervals. The efficiency of snowfall collection was almost unity in compared to other points near the gauge.

3. SNOWFLAKE PARAMETER DETERMINED BY IMAGE PROCESSING

3.1 Size and velocity

Since the system which measures the size and fall velocity of snowflakes has been reported (Muramoto et al., 1993), a brief explanation will be provided. A side view of falling snowflakes into a photographing space in a vertical tunnel was taken by a TV camera 6 m distance from the tunnel shown Fig. 1. The images of snowflakes

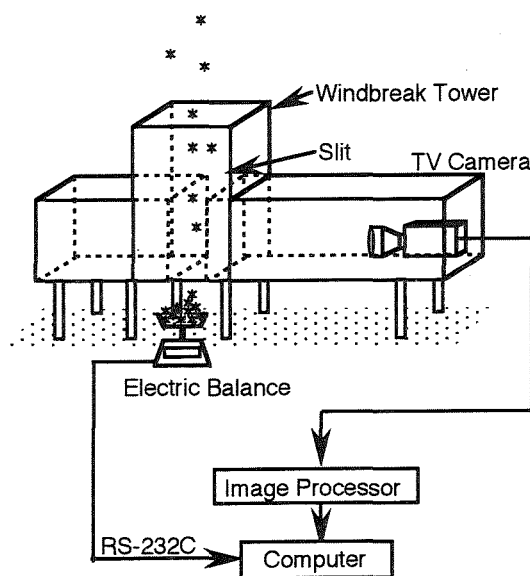


Fig.1 System for measuring the physical parameters of snowflakes and snowfall rate.

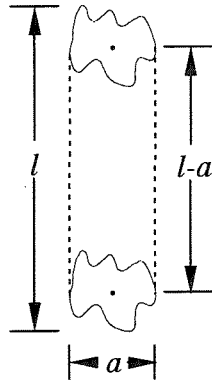


Fig.2 Model of typical photographed image of snowflake.

were inputted in an image processing unit continuously every 5 s. The shutter speed of the TV camera used for this observation was adjusted at 1/60 s. The images of snowflakes were divided into binary image in order to separate the snowflakes from background. The model of the binary images of snowflake was shown in Fig. 2. Since the shape of snowflakes is almost spherical, diameter is obtained by width a . Fall velocity is calculated by $(l-a) / (1/60)$ from fall distance $(l-a)$ during 1/60 s. The number concentration per unit space was computed from the observed data on the number of snowflakes in the photographing space.

3.2 Snowflake density

In the case of raindrops, density has a constant value with 1.0 (g/cm³). But the density of falling snowflakes changes every moment, therefore a method for calculating the density has been proposed (Muramoto et al., 1996). We shall outline here only briefly the method. The density of snowflakes can be determined using two values: the total volume V (cm/s) of falling snowflakes passing the unit space in unit time determined by image processing and the total weight M (g/(cm² s)) of falling snowflakes deposited in unit area per unit time can be directly measured with an electric balance. Therefore, the density of falling snowflakes ρ is calculated by following equation.

$$\rho = \frac{M_s}{V_s} \quad [g/cm^3] \quad (1)$$

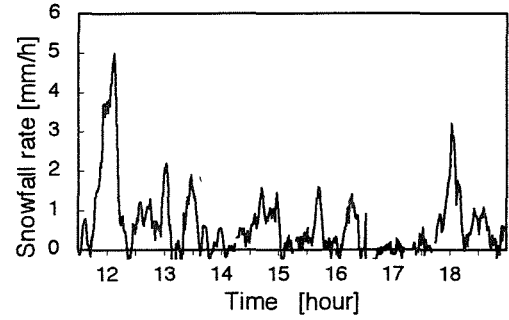


Fig.3 Time series of snowfall rate measured by an electric balance from 1130 to 1900 in January 9, 1996.

3.3 Experimental results and characteristics of snowfall

Fig. 3 shows the time series of the snowfall rate measured by an electric balance from 1130 to 1900 in January 9, 1996. Fig. 4a shows the size distribution of all snowflakes in the observation period. Fig. 4b expresses the relation between diameter and fall velocity of all snowflakes within observation period by using mean value and standard deviation of diameter.

Size distribution of snowflakes $N(D)$ can be expressed from diameter as following equation (e.g., Gunn and Marshall, 1958), where N_0 and λ are constant.

$$N(D) = N_0 \exp(-\lambda D) \quad (2)$$

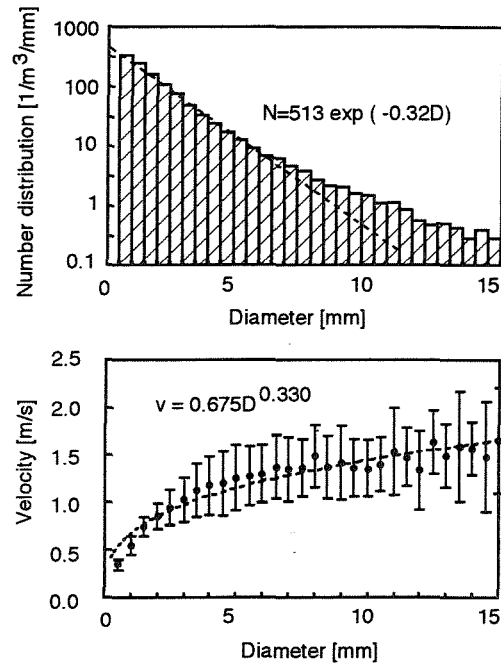


Fig.4 (a) Size distributions of snowflakes. (b) Fall velocity versus diameter of snowflakes.

And the fall velocity $v(D)$ can be expressed as follows (e.g., Langleben, 1954), where κ and ε are constant.

$$V(D) = \kappa D^\varepsilon. \quad (3)$$

With respect to snowflakes observed from 1130 to 1900 on January 9, 1996, the relation between Eqs. (2) and (3) were examined. In the case of Fig. 4a, if $N_0 = 513$ and $\lambda = 0.32$, then the characteristic of Eq. (2) was fitted well the data. Dotted lines shown in the graphs are characteristic equation. In the case of Fig. 4b, when $\kappa = 0.512$ and $\varepsilon = 0.406$ were used, the characteristic of Eq. (3) agreed well with the relation between diameter and fall velocity.

The relation between the diameter and velocity, and between diameter and density at each time were plotted using the values of mean diameter of all the snowflakes every 1 min are shown in Figs. 5a and b. Fitting curve can be approximated by using ε of Eq. (3).

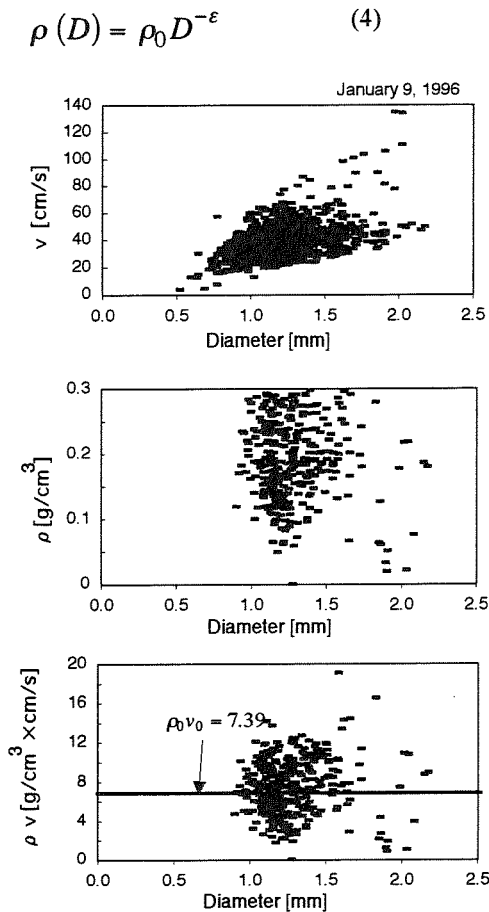


Fig.5 Each parameter versus diameter of snowflakes
(a) Fall velocity. (b) Density. (c) $\rho \cdot v$.

Fig. 5c shows the relation between the diameter and product of ρ and v has almost constant with respect to diameter.

3.4 Snowfall rate

3.4.1 Calculation of snowfall rate from image processing data

A method of determining the snowfall rate without using an electric balance will be described below. In the case of raindrops, since the constant value of $1.0 \text{ [g/cm}^3\text{]}$ can be used as density, rainfall rate will be calculated from diameter and fall velocity. In the case of snowfall, however, as the density is not constant, approximating equations for calculating the density from image processing data must be derived. If the diameter of snowflakes is D , and the fall velocity, number and density with diameter are respectively $v(D)$, $N(D)$ and $\rho(D)$, then the snowfall rate R can be derived from

$$R = \int \frac{4}{3}\pi \left(\frac{D}{2}\right)^3 \rho(D) v(D) N(D) dD$$

$$= \frac{\pi}{6} \int D^3 \rho(D) v(D) N(D) dD. \quad (5)$$

By substituting the Eqs. (2) - (4) to Eq. (5),

$$R = \frac{\pi}{6} \int D^3 \rho_0 \kappa N_0 \exp(-\lambda D) dD.$$

$$\doteq \frac{\pi}{\lambda^4} \rho_0 \kappa N_0 \quad (6)$$

Therefore, the snowfall rate can be determined from the characteristic values of N_0 , λ , κ and ρ_0 obtained from the image processing data without using the density of snowflakes.

3.4.2 Snowfall rate determined from image processing data

Figs. 6a, b and c show the calculated values of N_0 , λ and κ at every minute from 1130 to 1900 on January 9. The snowfall rate could be determined every minute by

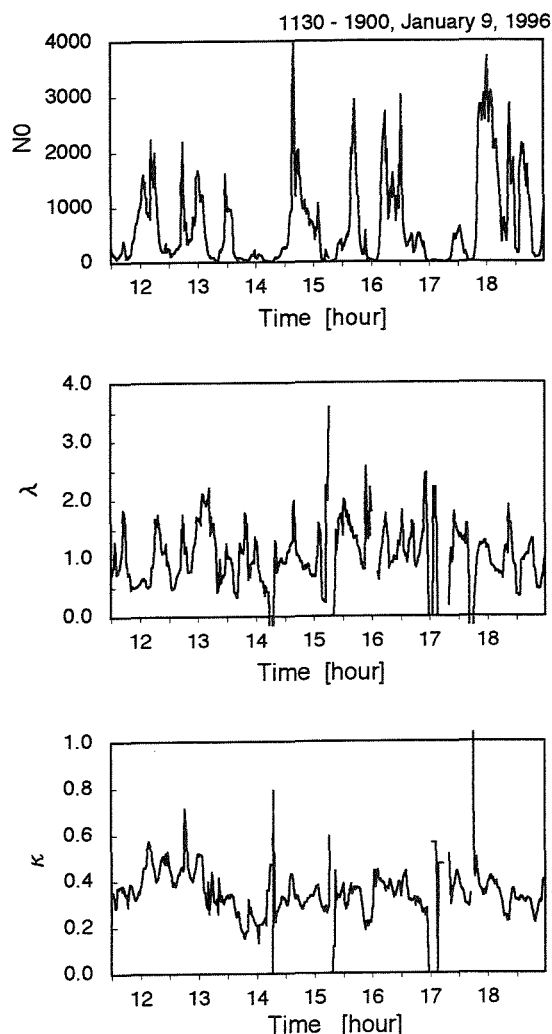


Fig.6 Time series of the characteristics of each parameter. (a) N_0 (b) λ (c) κ

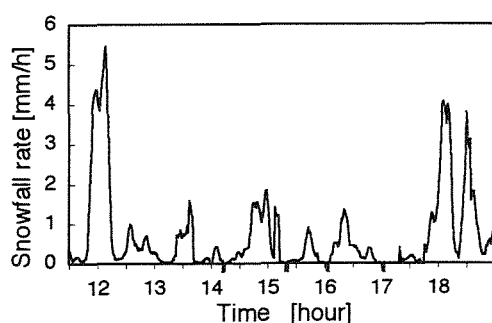


Fig.7 Time series of snowfall rate calculated by image processing data.

substituting these values into Eq. (6). Fig. 7 shows the snowfall rate accumulated during 60 s using Eq. (6).

Comparing with the measured value of Fig. 3, they agree fairly well each other and therefore the proposed method is considered to be valid and effective.

4. CONCLUSION

A new system for the simultaneous measurement of velocity of falling snowflakes using image processing system over a long period was developed. Snowfall rate determined from diameter and velocity agreed with the results of direct measurement.

5. REFERENCES

- Boucher, R.J., and J.G. Wieler, 1958: Radar determination of snowfall rate and accumulation. *J.Climate Appl. Meteor.*, **24**, 68-73.
- Carlson, R.E., and J.S. Marshall, 1972: Measurement of snowfall by radar. *J. Appl. Meteor.*, **11**, 494-500.
- Fujiyoshi, Y., T. Endoh, T. Yamada, K. Tsuboki, Y. Tachibana and G. Wakahama, 1990: Determination of a Z-R relationship for snowfall using a radar and high sensitive snow gauges. *J.Appl.Meteor.*, **29**, 147-152.
- Gunn, K.L.S., and J.S. Marshall, 1958: The distribution with size of aggregate snow particles. *J.Meteor.*, **16**, 452-461.
- Langleben M.P., 1954: The terminal velocity of snowflakes. *Quart.Roy.Meteor.Soc.*, **80**, 174-181.
- Muramoto, K., K. Matsuura, T. Harimaya and T. Endoh, 1993: A computer database for falling snow particles. *Ann.Glaciol.*, **18**, 11-16.
- Muramoto, K., K. Matsuura and T. Shiina, 1996: Measurement of density of snow particles and snowfall rate. *Sys. Computer Japan* (in print).
- Sekhon, R.S., and R.C. Srivastava, 1970: Snow size spectra and radar reflectivity. *J.Atmos. Sci.*, **27**, 299-307.

Observations of Divergence and Vorticity during ACE-1

Steven T. Siems¹, Donald H. Lenschow², Paul B. Krummel¹, Ashley J. Bainbridge¹

¹ Centre for Dynamical Meteorology and Oceanography, Monash University, Australia

² National Center for Atmospheric Research, Boulder, USA

correspondence: s.siems@sci.monash.edu.au

1. Introduction

In working towards understanding the role that marine stratocumulus play in the global energy balance, one immediate aim is to be able to better represent these clouds, and their evolution, in the context of a GCM. Such a numerical representation, however, must be made at an extremely coarse resolution compared with the actual dynamics of these boundary layer clouds. As such, it is essential to develop more advanced two and three dimensional models to guide the coarse parameterizations.

More sophisticated models of stratocumulus naturally require a more detailed understanding of the natural forcings and their interactions. Numerous research efforts have focussed on such processes as radiative exchange, drizzle and cloud microphysics. Research includes both field observations such as FIRE (First ISCCP Regional Experiment) and ASTEX (Atlantic Stratocumulus Transition Experiment), as well as modelling efforts in two-dimensional cumulus ensemble models (Krueger et al, 1995) and three dimensional large eddy simulations (eg., Moeng et al, 1995).

One process which remains poorly understood is the entrainment of the overlying air into the stratocumulus cloud deck. This involves the interaction of radiative transfer, cloud microphysics and turbulent mixing at a buoyancy stratification. Rather crude parameterizations exist but are not robust when compared with observations (Turton and Nicholls, 1987). Moreover, these poorly understood physics must be parameterized on the scale of tens of meters, much larger than the actual physics dictate. Numerical investigations have indicated that even small changes in this rate, well within the margin of observational error, can lead to unrealistic cloud thickening or cloud break-up.

As a consequence of this, more detailed field observations are needed to guide the numerical investigations. Indeed, at a workshop on modeling and large-eddy simulation of the boundary-layer clouds (NCAR/GCSS Workshop on Boundary Layer Clouds, 16-18 August 1994, Boulder USA, reported in Moeng et al, 1996) the participants agreed that the entrainment rate was the single most important variable that needed observational confirmation.

2. Measuring entrainment

There are numerous means of measuring the entrainment rate. Bretherton et al (1995) compared three different approaches on a series of flights during ASTEX. They estimated errors in their entrainment rates of 0.3 cm s^{-1} . This is inadequate for state-of-the-art numerical models. Moreover, two of the three means of measuring the entrainment rate used variables at time and length scales inappropriate for the numerical models. Large-eddy simulations typically simulate three or four hours of real time. Only the derivation of entrainment through turbulent ozone flux calculations,

$$w_e = -(\overline{w'O^{3'}})/\Delta O^3, \quad (1)$$

is on this scale. Here ΔO^3 is the jump in the mean value of ozone across the inversion and $\overline{w'O^{3'}}$ is the turbulent flux of ozone at cloud-top. This was found to be the most sensitive technique for entrainment rate. Ozone, being produced mostly in the lower stratosphere, can be highly variable in the stably-stratified air overlying the stratocumulus, making it less than ideal as a tracer.

Another means of locally measuring entrainment at the time scale of large-eddy simulations is

$$w_e = d(z_i)/dt - w_s, \quad (2)$$

where w_s is the mean subsidence velocity at z_i , and $d(z_i)/dt$ is the time rate of change of the boundary-layer height. Conceptually, this is a very straightforward calculation. It is possible to obtain $d(z_i)/dt$ by observation of z_i over the several hours of a typical research flight. At present, however, it is not possible to directly measure w_s due to instrument limitations. w_s may be expressed in terms of the large-scale mean divergence, D , as $w_s = -D \cdot z_i$.

Equation (2) was one of the three techniques of calculating entrainment used by Bretherton et al (1995). Measurements of the large-scale divergence, however, came from ECMWF analysis. As noted, these data are often noisy and are unsuitable unless some kind of time averaging is taken. Moreover the large spatial scales of a GCM may make D inappropriate to use with the scale of observations considered here, and thus it is not feasible to compare airplane estimates from equation (1) with ECMWF estimates from equation (2). A new means of calculating D , and therefore w_s , is needed.

Accurate measurements of D are not only important for use in equation (2) but also directly for simulations. Schubert et al (1979) discuss the response of a one-dimensional model to divergence rates varying from $1.0\text{E-}06$ to $6.0\text{E-}06 \text{ s}^{-1}$. Siems et al (1993) numerically examined the response of the air overlying the inversion and found it to be sensitive to the large-scale subsidence. This sensitivity gives rise to a number of questions.

Do equations (1) and (2) give consistent measurements of entrainment rate?

Is divergence uniform throughout the boundary layer?

Is divergence uniform across the inversion?

Does divergence experience a diurnal cycle?

In this paper we describe a technique for directly examining the divergence using the same flight pattern as is used to estimate entrainment by equation (1).

3. Measurement technique

The vertical velocity at any level can be estimated by integrating the horizontal divergence through the boundary layer:

$$\partial(\bar{w})/\partial z = -1/A \int v_n \cdot dl, \quad (3)$$

where A is the area of the surface defined by the closed integral, v_n is the velocity normal to the line of integration, dl is the incremental change in the integration path. This integral can be easily made with an aircraft. Similarly, the vorticity, ζ may be calculated as

$$\zeta = 1/A \int v_t \cdot dl, \quad (4)$$

where v_t is the tangential velocity.

Relatively large circular flight tracks (figure 1) are optimal for these calculations as they maximize the area A for a given flight time and do not require sharp turns. Equation (4) then reduces to

$$\partial(\bar{w})/\partial z = -2 \cdot \bar{v}_n / R, \quad (5)$$

where R is the radius and \bar{v}_n is the average normal velocity. Here the absolute accuracy of the measurement depends inversely on R . For most of the data presented here the circles were flown

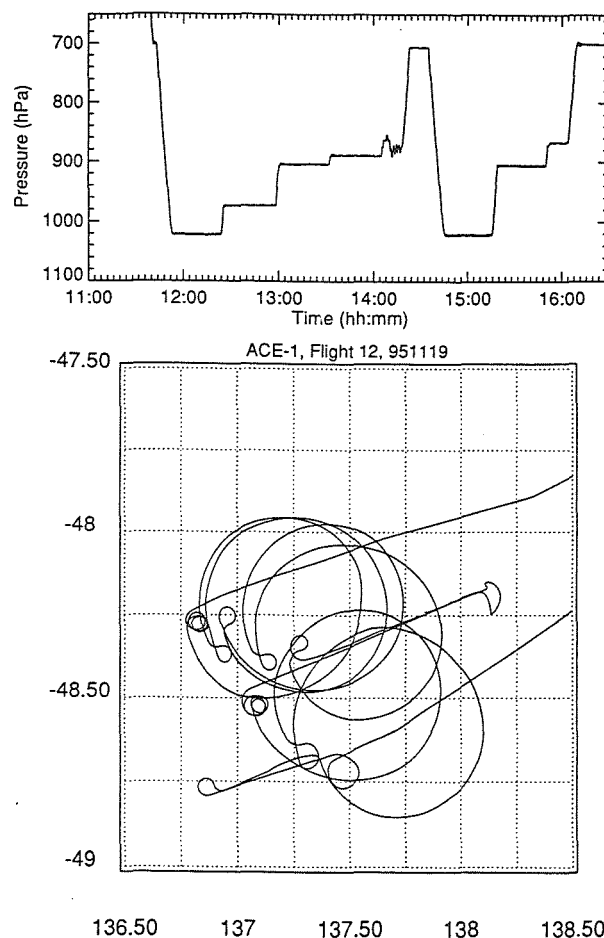


Fig. 1 Flight track for flight 12 (local time).

in 24 minutes yielding a radius of approximately 23 km. We can approximate the absolute accuracy that this provides if we assume that the divergence is constant through the boundary layer. In such a case, $\partial \bar{w} / \partial z = D = w_s / z$, and thus $w_s = -2\bar{v}_n \cdot z / R$. If $z = 1000$ meters and $\bar{v}_n = 30 \cdot w_s$, then the absolute accuracy on w_s is 0.0024 ms^{-1} . Larger circles would have given proportionately better accuracy, but this was not feasible here because of other mission objectives.

4. Data analysis

These circular flight maneuvers were conducted regularly throughout the Aerosol Characterization Experiment (ACE-1, Nov-Dec 1995). One of the principal scientific objectives of this field experiment was to characterize the evolution of the marine aerosols in an unpolluted environment.

Missions were flown aboard the NCAR C-130 Hercules over the Southern Ocean. The Southern Ocean is noted for having a regular progression of weather systems which allowed us the opportunity to examine boundary-layer divergence under a wide variety of meteorological conditions. We report here on the divergence and vorticity estimates from five flights. The results reported here used the uncorrected data collected in the field. The processed data were not available at the time of this writing, but we anticipate using the corrected data for the conference presentation.

Flight 12 is a classic stratocumulus flight in which boundary layer clouds formed under a high pressure ridge. Flight 21, similarly was flown under conditions of extreme subsidence. Here, however, the mesoscale conditions were more inter-

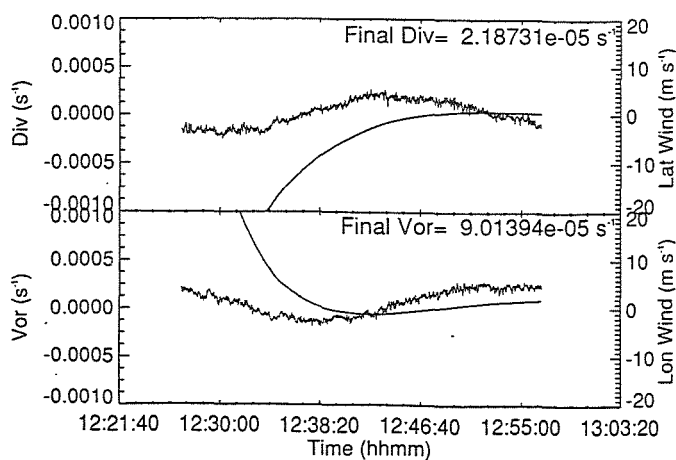


Fig. 2 Cumulative divergence and vorticity for a single circular flight tract (local time).

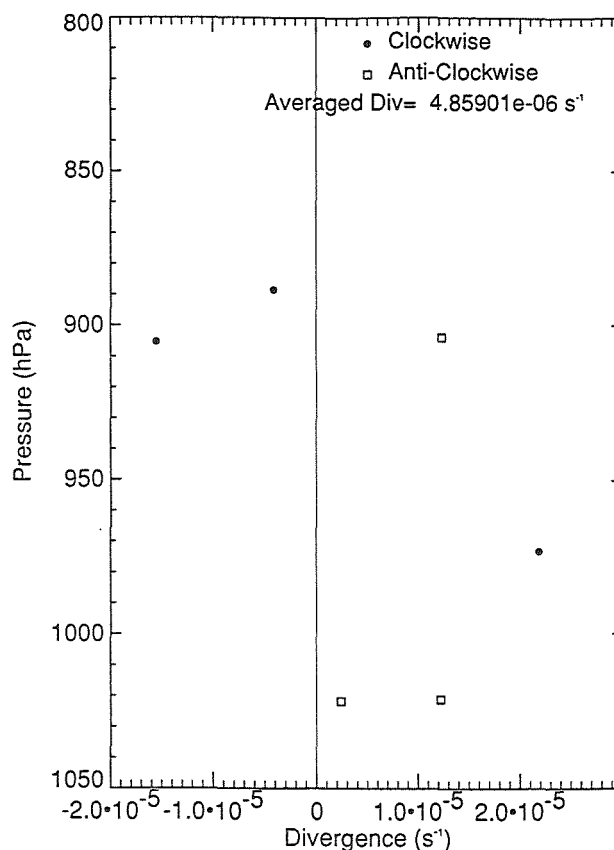


Fig. 3 Composite of all divergences from flight 12.

esting as a gravity wave was moving through the flight region. The C-130 observed that the boundary layer grew from roughly 700 meters to 1400 meters in three hours.

The final three missions (flights 24, 25 & 26) were flown as part of a Lagrangian experiment, in which an air parcel was tagged with a balloon and followed for a period of 30 hours. Again synoptic conditions were characterized by subsidence.

Figure 1 shows the flight track of flight 12. Circular loops were flown at various altitudes through the boundary layer and above it. After each loop, the plane reversed direction to allow for the bias in the measurement to be assessed. For one single loop we present a time series of the normal and tangential winds, along with the cumulative divergence and vorticity (figure 2) computed using uncorrected winds.

For each loop flown within the boundary layer of flight 12, the divergence and vorticity are diagrammed in figures 3 and 4, respectively. We note that the vorticity measurements are very consistent through the depth of the boundary layer given the direction of the circle. This would

suggest that the boundary layer is uniform. The divergence, however, does not appear to be as consistent. Still, the average measurement is well within the range found for marine stratocumulus.

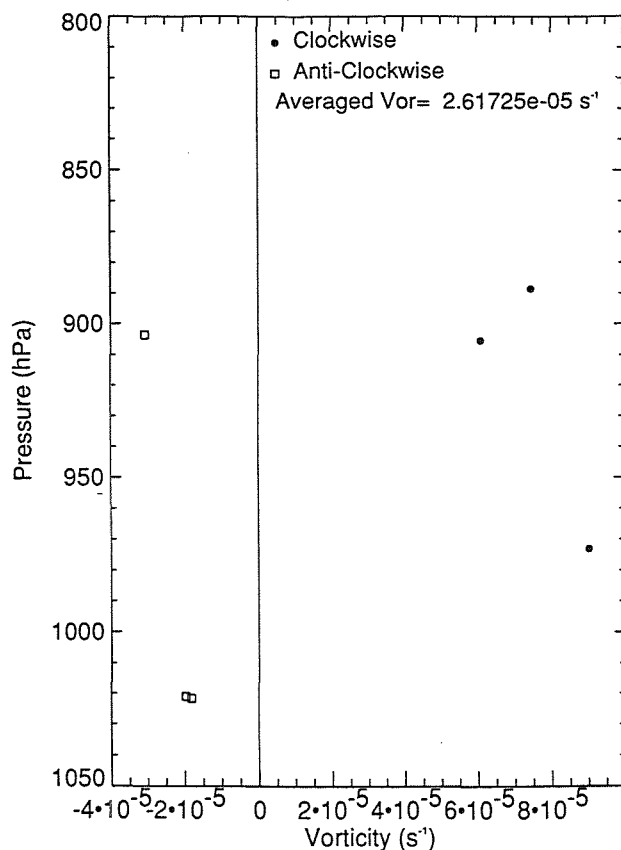


Fig. 4 Composite of all vorticities from flight 12.

Table 1 provides the flight averages for the five different missions. We note that the divergence estimates from the uncorrected data are rather large, but within the proper realm. In analyzing data from the Bureau of Meteorology GCM (GASP) we found that without some type of smoothing the values were not consistent.

Flight	D (10^{-6})	$\zeta(10^{-6})$
12	4.86	26.6
21	8.40	24.8
24	26.4	43.6
25	25.0	28.1
26	9.29	-6.7

Table 1 Summary of uncorrected divergence and vorticity measurements.

References

- Bretherton, C.S., et al, 1995: Cloudiness and marine boundary layer dynamics in the ASTEX Lagrangian experiments. Part II: cloudiness, drizzle, surface fluxes, and entrainment. *J. Atmos. Sci.*, **52**, 2724-2735.
- Krueger, S.K., et al, 1995: Numerical simulations of the stratus-to-cumulus transition in the subtropical marine boundary layer. Part I: boundary layer structure. *J. Atmos. Sci.*, **52**, 2839-2850.
- Moeng, C.-H., et al, 1996: Numerical investigations of the roles of radiative and evaporative feedbacks in stratocumulus entrainment and cloud breakup. *J. Atmos. Sci.*, **52**, 2869-2883.
- Moeng, C.-H. et al, 1996: Simulation of a stratocumulus-topped PBL: intercomparison among different numerical codes. *Bull. Amer. Meteor. Soc.*, in press.
- Schubert, W.H., et al, 1979: Marine stratocumulus convection. Part I: governing equations and horizontally homogeneous solutions. *J. Atmos. Sci.*, **36**, 1286-1307.
- Siems, et al 1993: A numerical study of the interaction between stratocumulus and the air overlying it. *J. Atmos. Sci.*, **50**, 3663-3676.
- Turton, J.D., and S. Nicholls, 1987: A study of the diurnal variation of stratocumulus using a multiple mixed layer model. *Q. J. Roy. Meteor. Soc.*, **113**, 969-1009.

TRANSITION OF A STRATOCUMULUS INTO A CUMULUS TOPPED-BOUNDARY LAYER AS OBSERVED DURING THE FIRST LAGRANGIAN OF ASTEX: MEAN STATE AND TURBULENCE.

Stephan R. de Roode and Peter G. Duynkerke

IMAU, Utrecht University, Princetonplein 5, 3584 CC Utrecht, The Netherlands

E-mail: roode@fys.ruu.nl

1. INTRODUCTION

Stratocumulus-topped boundary layers (BL) are currently under great interest in many fields of meteorology. Due to its large horizontal extent, persistence and high albedo stratocumulus influences the Earth's energy balance and climate and is therefore an important consideration for Global Climate Models. In order to understand the dynamics of such a cloud deck aircraft observations are used to interpret boundary layer properties like mean state and turbulence. In all previous papers in which aircraft measurements were described one primarily studied the relationship between the local structure and the local mean conditions rather than investigating the evolution of the cloudy BL with time. The Atlantic Stratocumulus Transition EXperiment (ASTEX) was set up in order to characterise the evolution and vertical structure of a marine boundary layer (Albrecht et al., 1994). In ASTEX a very successful experiment was carried out during the "First Lagrangian", in which an air mass was followed for two days between 12 and 14 June 1992. The air mass was advected by the mean wind over a nearly linearly with time increasing sea surface temperature (from 16.8 to 21.1 °C). As a result, a solid stratocumulus deck gradually dissipated into thin and broken patches which were penetrated from below by cumulus clouds (de Roode and Duynkerke, 1996). Mean wind velocities were moderate and occasional showers were observed. The mean state, subsidence and entrainment during the First Lagrangian are described in detail by Bretherton and Pincus (1995) and Bretherton et al. (1995). In this study we are presenting the mean state, turbulence, and cloud-top structure from NCAR Electra (RF05, RF06 and RF07) and UK-MRF (A209 and A210) aircraft flights. The instrumentation on board the aircraft and data analysis techniques are described in Duynkerke et al. (1995) and de Roode and Duynkerke (1996).

Flight	Day / type Time Start-End	z_{top} z_{base} (m)	θ_e $\Delta\theta_e$ (K)	q_t Δq_t (g·kg ⁻¹)
RF05	12 / (Sc)	740	315.9	10.6
Flight 1	1719-2133	250	-3.04	-2.89
A209	13 / (Sc)	755	313.7	10.0
Flight 2	0032-0426	240	2.32	-1.16
RF06	13 / (Sc)	770	315.0	10.3
Flight 3	0451-1013	280	-0.64	-2.26
RF07	13 / (Sc)	1070	317.7	10.3
Flight 4	1627-2109	610	-6.15	-4.37
A210	14/ (Cu/Sc)	1600	317.3	9.5
Flight 5	1111-1302	500	-6.60	-4.45

Table 1. Details of cases studied: day of flight (June 1992), start and end time (GMT), cloud base (z_{base}) and height (z_{top}), the mean BL equivalent potential temperature (θ_e) and total water content (q_t) and their jumps across the inversion (Δ symbol) The cloud type is denoted between brackets as 'Sc' for stratocumulus while 'Cu/Sc' means cumulus penetrating thin and broken stratocumulus above.

2. MEAN STATE

During Flight 1 the surface layer was stably stratified due to a relatively cold sea surface temperature. The cloud showed a complicated two-layered structure and was very inhomogeneous, since the cloud fraction derived from the horizontal legs was found less than one on many levels. From Figure 1 it is clear that the BL cooled between Flight 1 and 2, while from Flight 2 onwards the BL gradually warmed and the BL height increased. Remarkably, it seems that the virtual potential temperature in the free atmosphere is approximately stationary, which suggests that warming due to subsidence is in balance with radiative cooling. Although not visible from Fig.1, it was suggested from pilot observations and vertical profiles of the virtual potential temperature that the BL was decoupled during Flight 4 and 5, probably as a

result of solar radiative warming of the cloud layer.

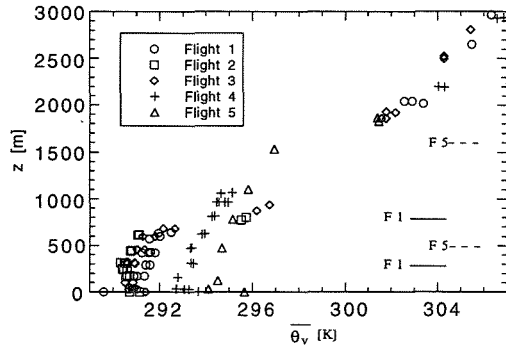


Figure 1. The virtual potential temperature as a function of height. The cloud base and top for Flight 1 (F1) and Flight 5 (F5) are schematically indicated with the solid and broken lines, respectively. Flight symbols are according to the legend.

3. TURBULENCE

3.1 Virtual potential temperature flux

We calculated the virtual potential temperature flux $\overline{w'\theta'_v}$ as follows:

$$\overline{w'\theta'_v} = \overline{w'\theta'} + \bar{\theta} (0.61\overline{w'q'_v} - \overline{w'q'_l}) \quad (3.1)$$

where $\overline{w'q'_v}$ and $\overline{w'q'_l}$ are the water vapour and liquid water flux, respectively. During the time of the First Lagrangian the buoyancy flux at the surface increased from a slightly negative value of -0.002 to a positive flux of about 0.015 Km/s from Flight 2 onwards (see Figs. 2). All flights in stratocumulus show a maximum buoyancy flux near the cloud top, which can be explained by negatively buoyant downdrafts which are formed by longwave radiative loss. However, during Flight 4 the fluxes near the cloud top maximum are about a factor 3 or 4 higher compared to the previous flights.

We can express the buoyancy flux in a cloud (Nicholls, 1984):

$$\overline{w'\theta'_v} = \beta \overline{w'\theta'_e} - \bar{\theta} \overline{w'q'_t} \quad (3.2)$$

where β is function of the temperature and is typically about 0.6. Using Eq. (3.2) and Lilly's (1968) relationship for the entrainment velocity w_e ,

$$w_e = - \frac{\overline{w'x'_H}}{\Delta x} \quad (3.3)$$

with $\overline{w'x'_H}$ the flux of a conserved variable at the boundary layer top H, the virtual potential temperature flux at H can be written as:

$$(\overline{w'\theta'_v})_H = w_e [-\beta \Delta \bar{\theta}_e + \bar{\theta} \Delta \bar{q}_t] \quad (3.4)$$

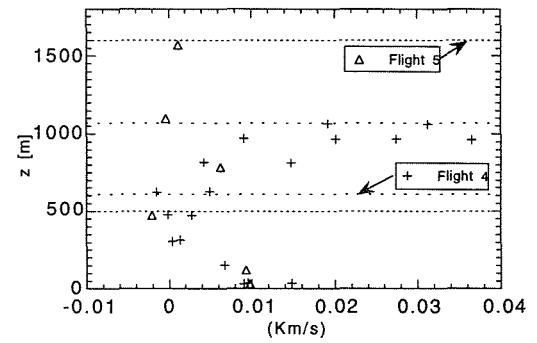
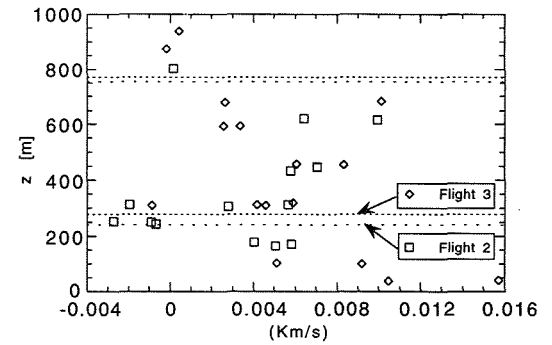
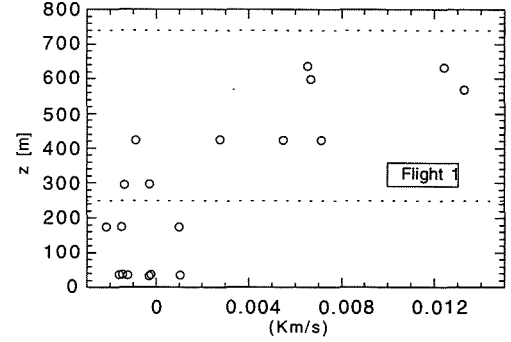


Figure 2: The virtual potential temperature flux for Flight 1 (upper), Flight 2 and 3 (middle) and Flight 4 and 5 (upper). The cloud base and top are indicated with the dashed and solid lines.

Using the jumps given in Table 1 we evaluated the term within square brackets of Eq. (3.4) and found values of 1, -1.7, -0.3 and 2.4 for Flight 1 till 4, respectively. This means that entrainment ($w_e > 0$) will cause a positive

buoyancy flux at the top of the cloud for Flight 1 and 4. In other words, when air from above the inversion is entrained, potential energy will be released which will be converted into TKE. It also means that the cloud-top entrainment instability criterion of Randall (1980) and Deardorff (1980) is satisfied, according to:

$$\Delta\bar{\theta}_e < K (L/c_p) \Delta\bar{q}_T \quad (3.5)$$

where $\Delta\bar{\theta}_e$ and $\Delta\bar{q}_T$ represent the jumps in equivalent potential temperature and total water content across the inversion, respectively, and the constant K has a value of about 0.23. L and c_p are the latent heat of condensation and the specific heat of dry air. Probably, this mechanism is causing the increased virtual potential temperature fluxes in the cloud layer as observed during Flight 4. During Flight 1, however, the fluxes are of the same order of magnitude as on Flight 2 and 3. Possibly, this is because the cloud was very inhomogeneous on Flight 1.

3.2 Vertical velocity variance

During Flight 1 the vertical velocity variance is rather weak in the subcloud layer (Fig. 4), since turbulent fluctuations are damped by the stable surface stratification. In the cloud layer there is a large scatter of the results, which is possibly due to a complicated two layer structure of the stratocumulus cloud.

A similarity curve for the vertical velocity variances derived from measurements in the free convective boundary layer over land was proposed by Lenschow et al. (1980):

$$\overline{w'^2} = 1.8 \frac{z^{2/3}}{H} \left(1 - 0.8 \frac{z}{H} \right)^2 w_*^2 \quad (3.6)$$

During Flight 2 and 3 the vertical velocity variance profiles are very similar to this curve. For both flights the buoyancy flux near the surface is of the same order of magnitude as at the cloud top. Thus, the convection driven from the surface and cloud top are nearly as important. For Flight 1 we scaled the curve upside down for the cloud layer assuming the turbulence is mainly driven by longwave radiative loss from the cloud top. In spite of the inhomogeneity of cloud layer the measured maximum value of the vertical velocity variance is of the same order of magnitude as the maximum from the curve for Flight 1. Furthermore, it is of the same order of magnitude as the maximum measured during Flight 2 and 3.

The vertical velocity variances during Flight 5 are much weaker on average than during Flight 4 because in the last flight the turbulence was mainly dominated by broken cumulus clouds, and in between these clouds the boundary layer was nearly laminar. However, for both cases there are two maxima found in the subcloud and cloud layer, suggesting these two layers are decoupled. In the upper part of the cloud layer during Flight 4 the vertical velocity variance is larger relatively to the other flights, which is in line with the increased buoyancy fluxes and the consideration that entrainment would generate TKE for this case.

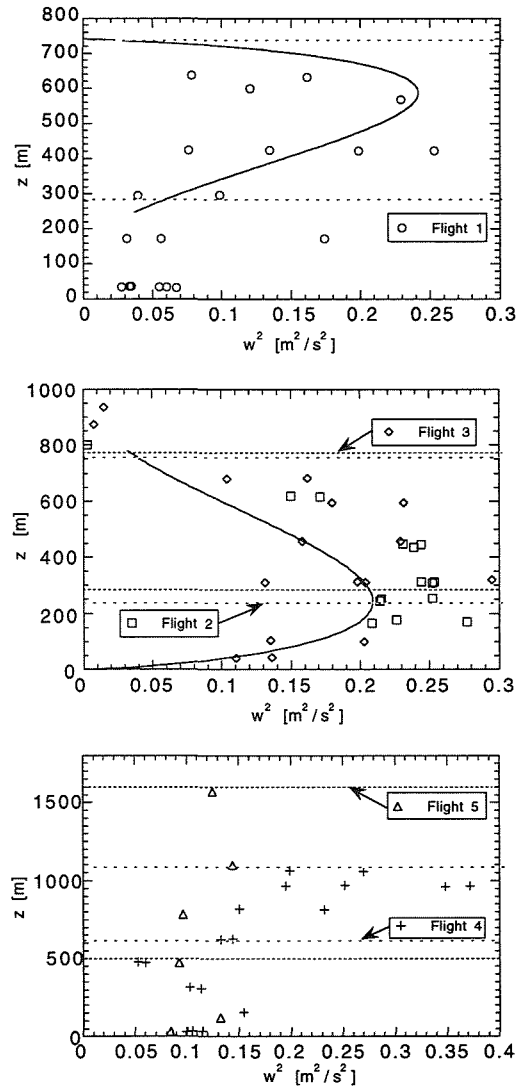


Figure 3: The vertical velocity variance. Flights, symbols and lines as in Figure 2.

4. CONCLUSION

Aircraft observations were used to analyze the mean and turbulence structure of the transition of a stratocumulus to a cumulus-topped boundary layer. During Flight 1, 2 and 3 the boundary layer height did grow very slowly. During daytime between Flight 3 and 4 the BL height increased about 300 m and was found decoupled possibly due to the absorption of solar radiation. As a result, the cloud-top stability had decreased. According to the cloud-top stability criteria of Randall (1980) and Deardorff (1980) Flight 1 and 4 are unstable. In the cloud layer during Flight 4 an increased buoyancy flux and vertical velocity variance were found. We showed from the jumps across the inversion of the equivalent potential temperature and total water content that the enhanced turbulence might be caused by a positive buoyancy flux at the top of the cloud due to entrainment. We did not find increased turbulence for Flight 1, but in that case the cloud showed a very complicated two-layered structure and was very inhomogeneous. Because stratocumulus break-up was observed between Flight 4 and 5 it is therefore likely that cloud-top entrainment instability is an important mechanism in the transition of stratocumulus into cumulus.

5. ACKNOWLEDGEMENTS

The investigations were in part supported by the Netherlands Geosciences Foundation (GOA) with financial aid (grant 750.295.03A) from the Netherlands Organization for Scientific Research (NWO). The aircraft data were kindly provided by Dr. Doug Johnson and Dr. Gill Martin of the UK Meteorological Research Flight and Dr. D. Lenschow of NCAR.

6. REFERENCES

Albrecht, B. A., C. S. Bretherton, D. W. Johnson, W. H. Schubert, and A. S. Frisch, 1994: The Atlantic Stratocumulus Transition Experiment - ASTEX. *Bull. Amer. Meteor. Soc.*, **76**, 889-904.

Bretherton, C. S., P. Austin and S. T. Siems, 1995: Cloudiness and Marine Boundary Layer Dynamics in the ASTEX Lagrangian Experiments. Part II: Cloudiness, Drizzle, Surface Fluxes, and Entrainment. *J. Atmos. Sci.*, **52**, 2724-2735.

Bretherton, C. S. and R. Pincus, 1995: Cloudiness and Marine Boundary Layer Dynamics in the ASTEX Lagrangian Experiments. Part I: Synoptic Setting and Vertical Structure. *J. Atmos. Sci.*, **52**, 2707-2723.

Deardorff, J. W., 1980: Cloud-top entrainment instability. *J. Atmos. Sci.*, **37**, 131-147.

Duykerke, P. G., H. Q. Zhang and P. J. Jonker, 1995: Microphysical and Turbulent Structure of Nocturnal Stratocumulus as Observed during ASTEX. *J. Atmos. Sci.*, **52**, 2763-2777.

Lenschow, D. H., J. C. Wyngaard, and W. T. Pennell, 1980: Mean-field and second-moment budgets in a baroclinic, convective boundary layer. *J. Atmos. Sci.*, **37**, 1313-1326.

Lilly, D. K., 1968: Models of cloud-topped mixed layers under a strong inversion. *Quart. J. Roy. Meteor. Soc.*, **94**, 292-309.

Nicholls, S., 1984: The dynamics of stratocumulus: Aircraft observations and comparisons with a mixed layer model. *Quart. J. Roy. Meteor. Soc.*, **110**, 783-820.

Randall, D. A., 1980: Conditional Instability of the first kind upside down. *J. Atmos. Sci.*, **37**, 125-130.

de Roode, S. R. and P. G. Duykerke: Dynamics of cumulus rising into stratocumulus as observed during the first "Lagrangian" experiment of ASTEX. Accepted in the *Quart. J. Roy. Meteor. Soc.*

THE INTERACTION BETWEEN CUMULUS AND STRATOCUMULUS CLOUDS IN THE MARINE BOUNDARY LAYER

G.M. Martin¹, P.R. Jonas² and D.W. Johnson¹

¹Meteorological Research Flight, Y46 Building, DERA Farnborough, GU14 6TD, UK

²Physics Department, UMIST, Manchester M60 1QD, UK

1. INTRODUCTION

Decoupling of the marine boundary layer beneath stratocumulus clouds, and the formation of cumulus clouds at the top of a surface-based mixed layer (SML) have frequently been observed and modelled (e.g. Nicholls 1984, Martin *et al.* 1995). When such cumulus clouds penetrate the overlying stratocumulus layer, they directly affect the microphysics and hence radiative properties of the cloud locally. However, the details of the microphysical interaction between the two cloud types can differ substantially between boundary layers with different vertical structures and airmass characteristics. Observations of cumulus - stratocumulus interaction made by the Meteorological Research Flight C-130 aircraft in different regions of the world and in different airmass types are used here to illustrate how the stratocumulus microphysical properties are altered by the occurrence of penetrating cumulus clouds, and a simple model study of the interaction is described.

2. OBSERVATIONS

Many observations of cumulus-stratocumulus interaction were made during the Atlantic Stratocumulus Transition Experiment (ASTEX) in the Azores in June 1992. Figure 1 shows profiles of total water content (q_t), equivalent potential temperature (θ_e) and aerosol concentration (for particles in the diameter range 0.1 - 3.0 μm) measured during an ascent through the boundary layer on 19th June, at 37N 22W. The boundary layer is clearly not well-mixed vertically; high values of θ_e and q_t are seen in the SML and the cloud layer, and there is a transition layer between the SML and a drier, lower θ_e and q_t subcloud layer below the stratocumulus. The profile of particle concentration shows that although the experimental region was several hundred kilometres from Europe, the boundary layer was polluted, with particle concentrations of 2000 cm^{-3} in the SML and 1000 cm^{-3} in the subcloud layer.

Figure 2 shows measurements of q_t , θ_e , droplet concentration (N), liquid water content, droplet effective radius, liquid water content and vertical velocity, measured during a hori-

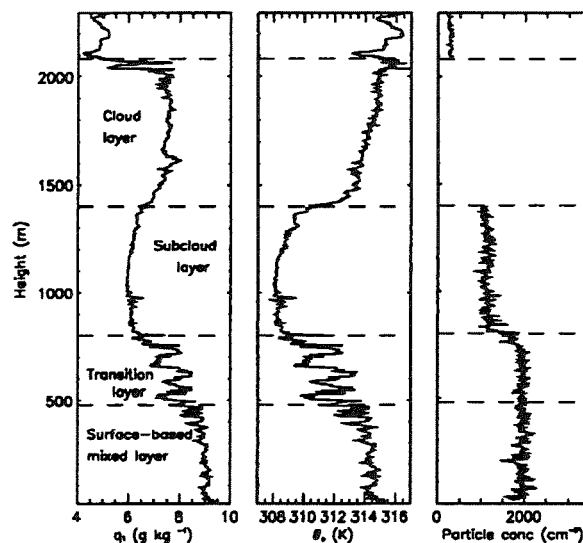


Figure 1: Profiles of q_t , θ_e and particle concentration measured in the boundary layer on 19th June 1992.

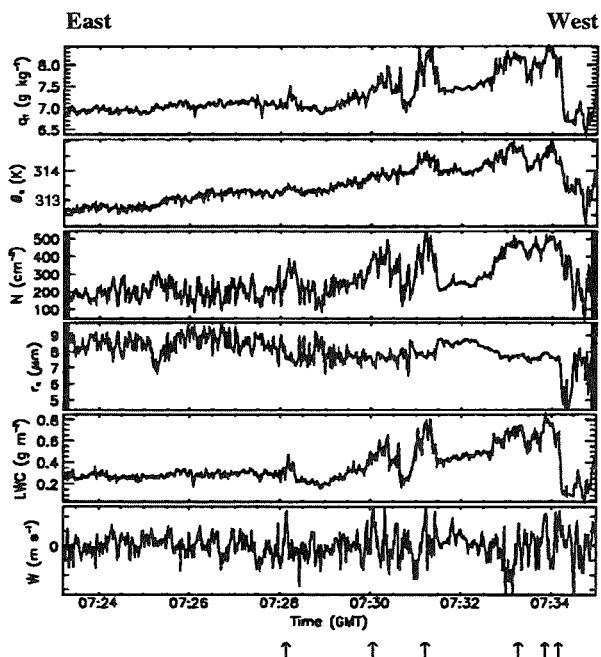


Figure 2: Time series of q_t , θ_e , droplet concentration (N), liquid water content (LWC), effective radius (r_e) and vertical velocity (W) measured during a horizontal run through stratocumulus in ASTEX on 19th June 1992.

zontal run through the stratocumulus layer on 19th June 1992. The arrows highlight where spikes in the vertical velocity indicate the presence of penetrating cumulus clouds, and corresponding increases in θ_e and q_t are seen. Comparison with Figure 1 reveals that these higher values are characteristic of the SML air, which suggests that the cumulus clouds were transporting SML air into the stratocumulus layer.

In regions where stratocumulus and cumulus clouds interact, the resulting droplet size spectrum should be a combination of that in each of the two cloud types. It can be seen from Figure 2 that where cumulus clouds are penetrating the stratocumulus the liquid water content and droplet concentration are larger but the effective radius is smaller. The increase in liquid water content will be a result of both the greater vertical extent of the cumulus clouds and the larger q_t in the SML. Since the cumulus clouds form on particles in the SML, where the particle concentration is much greater than in the subcloud layer (see Figure 1), it is likely that the increases in droplet concentration and the decreases in droplet effective radius which are observed in the regions of cumulus penetration are a direct result of the difference in particle concentration between the SML and subcloud layer.

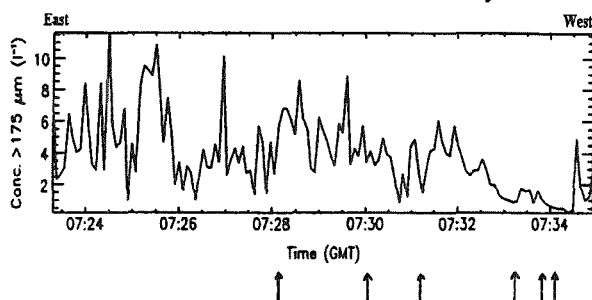


Figure 3: Concentration of drops $>175\mu\text{m}$ diameter measured with a 2DC probe during the run in Figure 2.

Figure 3 shows a time series of the concentration (number per litre) of drops larger than $175\mu\text{m}$ diameter, measured during the run in Figure 2. The concentrations of these drizzle-sized drops are small, and are less within the region of penetrating cumulus clouds than in the surrounding stratocumulus, with the smallest concentrations occurring in the most active updraughts (indicated by arrows).

The results from the ASTEX flight in a polluted air mass as described above can be compared with measurements made in a clean air mass over the North Sea to the east of the UK. Figure 4 shows profiles of q_t , θ_e and aerosol concentration (0.1 - $3.0\mu\text{m}$ diameter) measured on 18th May 1990 at 53.75N 2.5E . Once again, the profiles indicate that the boundary layer is not well-mixed vertically, and, during the flight, many cumulus clouds were observed to form with their bases at the top of the SML and to rise through the subcloud layer into the stratocumulus. One such cloud was penetrated by the aircraft during the slanted profile, as

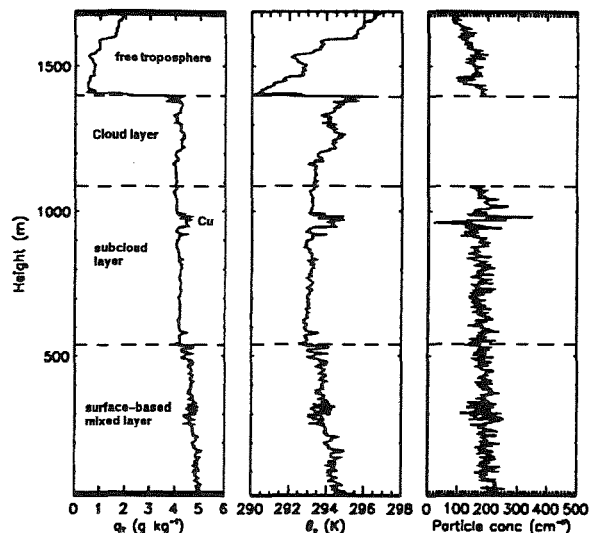


Figure 4: Profiles of q_t , θ_e and particle concentration measured over the North Sea on 18th May 1990.

indicated in Figure 4. The profile of aerosol concentration illustrates that this air mass was relatively clean, with particle concentrations of around 180 cm^{-3} .

Figure 5 shows measurements of θ_e , q_t , droplet concentration, droplet effective radius, liquid water content and vertical velocity made during a horizontal run through the stratocumulus layer on 18th May 1990. A region of penetrating cumulus clouds was identified during a run below the stratocumulus and is indicated on Figure 5. It is apparent that the penetrating cumuli are associated with distinct increases in q_t and θ_e to values which are similar to those in the SML (see Figure 4), suggesting that the cumulus clouds are transporting air from the SML into the stratocumulus. Sharp increases in droplet effective radius and liquid water content are also seen in the region of

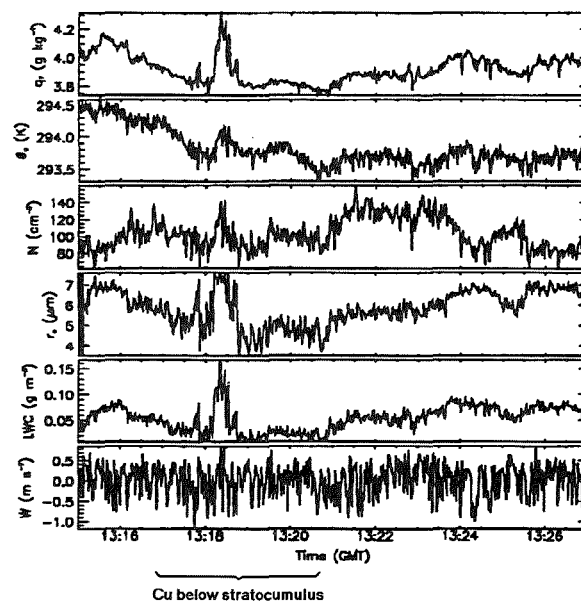


Figure 5: Time series of q_t , θ_e , N , LWC , r_e and W measured during a level run through the stratocumulus on 18 May 1990.

cumulus cloud penetration, and a smaller but noticeable increase in droplet concentration.

The contrast between the microphysical changes seen in these measurements with those in the polluted airmass over the Azores is thought to be a result of the lower particle concentrations in the boundary layer in the cleaner airmass, the similarity between the concentrations in the SML and subcloud layer, and the fact that the vertical extent of the cumulus clouds (850m) relative to the stratocumulus thickness (300m) was significantly greater than in the ASTEX case (cumulus thickness 1350m, stratocumulus thickness 700m). The relative cloud thickness will influence both the liquid water content and the droplet size at the level at which the cumulus cloud penetrates the stratocumulus. In the polluted airmass case from ASTEX, although the vertical extent of the cumulus clouds was significantly larger than that of the stratocumulus, the large particle concentrations in the SML compared with those in the subcloud layer was sufficient to decrease the droplet effective radius below that in the surrounding stratocumulus at the level at which the measurements were made. In the cleaner airmass over the North Sea, the small particle concentration and large vertical extent of the cumulus clouds compared with that of the stratocumulus combined such that the droplet effective radius was increased in the region of cumulus cloud penetration. This suggests that the microphysical interaction between cumulus and stratocumulus clouds in a decoupled marine boundary layer may be very sensitive both to the airmass in which the clouds form and to the vertical structure of the boundary layer in which the interaction occurs.

Observations made during horizontal runs within and below the stratocumulus layer on 19th June 1992 showed that the cloud layer varied in thickness laterally from around 460m thick where no penetrating cumulus clouds occurred to over 700m thick in the region of cumulus cloud penetration. This is illustrated in Figure 6, which shows a time series of cloud liquid water path measured with a microwave radiometer during a run below the stratocumulus (but above the cumulus cloud bases). The liquid water path more than doubles along the run as the region of penetrating cumulus clouds (at the western end of the run) is ap-

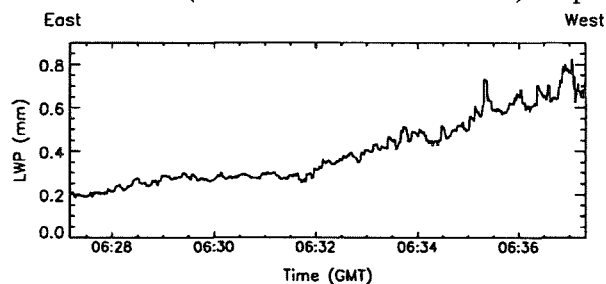


Figure 6: Time series of liquid water path measured remotely using a microwave radiometer during a run below the stratocumulus layer shown in Figure 5.

proached. This is thought to be a result of detrainment of the cumulus clouds into the surrounding stratocumulus. Such observations indicate that cumulus-stratocumulus interaction may be associated with changes in both the microphysical and geometrical structure of the stratocumulus. Both of these aspects of the interaction will affect the radiative properties of the cloud, and may therefore have implications for the global radiation budget.

3. SIMPLE MODEL STUDY

3.1 Entraining parcel model

The main limitation of aircraft observations in determining and understanding the processes involved in the cumulus-stratocumulus interaction is that most of the observations are made after the interaction has begun, at different, randomly-sampled, stages of the interaction, and usually when the stratocumulus has already been modified to some extent. Therefore, an attempt has been made to simulate the interaction using a one-dimensional entraining parcel model. Although there are several limitations associated with the use of such a simple model (see Blyth 1993), it is thought that at least some insight can be gained as to the relative contributions of different processes and initial boundary layer conditions, as suggested by the observations, to the outcome of the cumulus-stratocumulus interaction.

The model environment for the parcel model is based on a profile of temperature and humidity measured with the MRF C-130 aircraft during ASTEX. The parcel is initialised at the small temperature inversion which marks the top of the SML, close to saturation and with a positive vertical velocity. As it rises through the subcloud layer the parcel entrains aerosol particles, and when the environment is saturated the parcel entrains cloud droplets as well as unactivated nuclei. The stratocumulus "cloud" is created using an approximately neutrally-buoyant adiabatic parcel. Although both the cumulus and the stratocumulus droplet spectra simulated by the model are considerably narrower than those which are generally observed in either cloud type, the basic difference in spectral shape (namely, that the cumulus cloud droplet spectra are broader than those in the stratocumulus) is, at least, reproduced by the model.

The effects of altering the relative particle concentration in the SML and subcloud layer on the difference in droplet size between the cumulus and stratocumulus at the stratocumulus top are compared with the effects of altering the relative thickness of the two clouds by the same fraction, in both a clean and a polluted airmass. The results are shown in Table 1. It is apparent that although the decrease in stratocumulus cloud thickness results in a decrease in droplet size,

N_{SML} (cm^{-3})	N_{SL} (cm^{-3})	Sc_T (m)	Cu_T (m)	S_m/C_m	$\Delta(S_m/C_m)$
710	464	287	500	1.194	-
710	319	287	500	1.323	0.129
710	464	201	500	1.065	-0.129
237	155	287	500	1.046	-
237	108	287	500	1.186	0.14
237	155	201	500	0.907	-0.139

Table 1: Results of model study of cumulus-stratocumulus interaction. N_{SML} : particle conc in SML; N_{SL} : particle conc in subcloud layer; Sc_T : stratocumulus thickness; Cu_T : cumulus thickness; S_m/C_m : stratocumulus mode drop radius / cumulus mode drop radius.

whereas a decrease in the subcloud layer particle concentration (and consequently the stratocumulus droplet concentration) causes an increase in the droplet size at the cloud top, in both the clean and the polluted cases, the absolute change in the ratio of the stratocumulus mode droplet radius to the cumulus mode droplet radius (S_m/C_m) is approximately the same in each case. This suggests that the relative cloud thickness and the relative particle concentration may be of similar importance in determining the relative droplet sizes in the cumulus and stratocumulus clouds at the stratocumulus top.

It is also possible to investigate how the growth of those stratocumulus droplets which are entrained into the cumulus parcel at different levels differs from that of the droplets in the original stratocumulus cloud. Figure 7 shows that, for most of the depth of the stratocumulus, the maximum radius of the entrained droplets is smaller at each height than the surrounding stratocumulus droplets at the same level, implying that the growth of the entrained droplets is suppressed. This is because the entrained droplets only experience the higher supersaturations in the cumulus cloud for a short time, because of the higher vertical velocity.

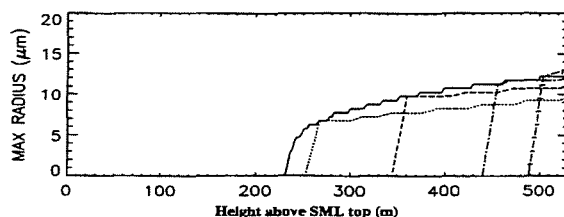


Figure 7: The development of the maximum droplet radius in spectra from the stratocumulus (solid line) compared with that of drops entrained into the cumulus parcel at different heights.

3.2 Drizzle calculation

Even if the cumulus cloud droplets are smaller than those in the stratocumulus (such that the droplet effective radius and concentration of large drops decrease locally), the broadening of the spectrum which occurs when the two clouds mix, combined with the thickening of the stratocumulus layer as the cumulus clouds detrain into it, may increase the potential for growth of drizzle drops during the subsequent evolu-

tion of the cloud. This can be investigated with the use of a simple calculation of stochastic coalescence. Figure 8 compares the development of a measured droplet spectrum from a stratocumulus cloud in a region where there were no penetrating cumulus clouds with the development of a mixed spectrum formed by averaging the spectrum from an actively penetrating cumulus cloud with that from the stratocumulus. The measurements were made in a relatively clean airmass (particle concentrations of about $80 cm^{-3}$) off the coast of Monterey. It is apparent that the rate of development of drizzle drops in the mixed spectrum greatly exceeds that in the stratocumulus spectrum alone. Although the timescales shown in Figure 8 are very long in comparison with the lifetime of a typical cumulus cloud (~30 minutes), and it is assumed that conditions within the affected stratocumulus remain the same throughout the development of the precipitation, which is unlikely to be the case, the results suggest that the interaction between cumulus and stratocumulus could help to enhance drizzle formation in the stratocumulus. However, further modelling studies, using more sophisticated dynamical and microphysical models, are required in order to investigate this fully.

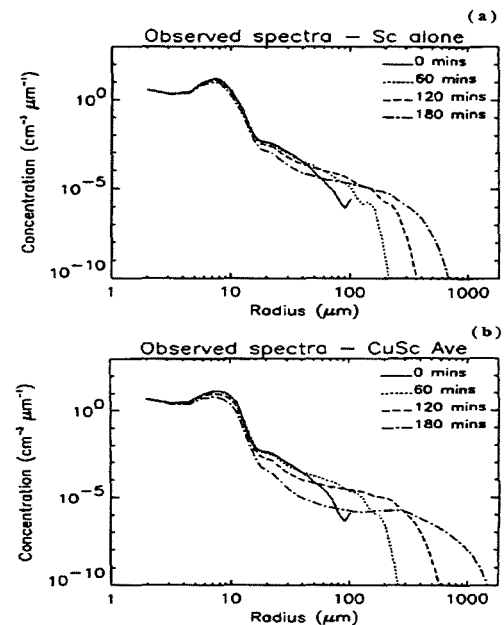


Figure 8: Development of spectra from (a) stratocumulus alone, and (b) mixed Cu-Sc, by coalescence

4. REFERENCES

- Blyth, A.M. 1993. Entrainment in cumulus clouds. *J. Appl. Meteor.*, **32**, 626-641
- Martin, G.M., D.W. Johnson, D.P. Rogers, P. Minnis and D.A. Hegg 1995. Observations of the interaction between cumulus and stratocumulus in the marine boundary layer during ASTEX. *J. Atmos. Sci.*, **52**, 2902-2922
- Nicholls, S. 1984. The dynamics of stratocumulus: aircraft observations and comparisons with a mixed layer model. *Quart. J. Roy. Meteor. Soc.*, **110**, 783-820

ON THE DIURNAL CHARACTERISTICS OF CLOUD STRUCTURE IN THE MARINE STRATOCUMULUS TRANSITION REGIME

Mark A. Miller

Brookhaven National Laboratory, Upton, NY 11933, USA

1. Introduction

It is known that stratus-topped marine boundary layers in the mid-latitudes are subject to significant diurnal changes in structure caused by solar heating (Nicholls, 1984, Hignett, 1991). One characteristic of the transition cloud regime that has not been thoroughly explored is its diurnal variability. Although this variability has been previously discussed by Miller and Albrecht (1995) and Rogers et al. (1995), in both of these studies the size of the database used was restrictive: 24 hours in former case and only 1 hour in the latter case. Thus, it is of importance to examine the diurnal characteristics of transition cloud structure in a larger data sample to validate the conclusions of these previous studies and to enhance our understanding of the effects of this diurnal variability on the climatology of the transition itself.

The Atlantic Stratocumulus Transition Experiment (ASTEX; Albrecht et al., 1995) was designed to help understand transition clouds by making comprehensive measurements of their structure over a one-month period. Data collected using a suite of *in-situ* and surface-based remote sensors deployed on the island of Santa Maria (37° N, 25 °W) during this experiment are analyzed below. These sensors were used to sample the clouds from a Eulerian perspective and quantify the cloud, precipitation, and thermodynamic structure in a column above the surface site, while at the same monitoring the effects of this structure on the surface radiative fluxes. While such a data set cannot

serve as a proxy for obtaining a global climatology of transition clouds from satellites, it can be used to validate satellite radiance-based retrieval algorithms and to study cloud properties that may not be adequately deduced from satellite measurements.

Diurnal changes in stratus cloud structure are caused by radiation-induced changes in mixing processes. In extreme cases, the marine boundary layer may separate into multiple mixed layers that do not interact, the uppermost layer being the only one capable of supporting mixing clouds. This separation into non-interacting sublayers is termed decoupling. In general, however, the sublayers interact sporadically through cumulus convection that is initiated by the accumulation of moisture in the sublayer adjacent the ocean surface. In this situation, the state of the marine boundary layer can be described as intermittently decoupled.

The thermodynamic structure of an intermittently decoupled marine boundary layer is shown schematically in Figure 1 and described using terminology suggested by Miller and Albrecht (1995). In daytime soundings from the ASTEX, a shallow stratum is found above the surface layer in which the vertical gradients of θ and θ_v are nearly zero. This stratum has a higher mixing ratio than the layers above and is termed the *surface moist layer* and its upper boundary is called the *transition level*. From the transition level to the base of the trade inversion, the vertical

gradients of θ and θ_v become positive. Because a layer of stratus is often found beneath the inversion in this upper stratum, it is termed the *stratus layer*. Note that stratus may not occupy the full depth of the stratus layer and that the transition level represents the lower boundary of a weak inversion.

The thermodynamic profile shown in Figure 1 can support both mixing and convective clouds and, as a result, it is necessary to define two additional sublayers to account for this possibility. Cumulus clouds with bases at z_{LCL} can potentially rise to the base of the trade inversion, so the *cumulus* and *subcloud* layers are defined accordingly. Cumulus elements can form in a decoupled environment because the surface moist layer moistens with time. A rough measure of the buoyancy experienced by a parcel that is lifted from the subcloud layer to the surface lifting condensation level, z_{LCL} , is $\theta_e(\text{SML}) - \theta_{es}(\text{SL})$, where θ_e is the equivalent potential temperature, the subscript s denotes saturation, and the acronyms SML and SL indicate the surface moist layer and the stratus layer, respectively. A dotted line has been placed on the diagram to help illustrate this condition. It can be demonstrated that the minimum possible depth of the subcloud layer is the depth of the surface moist layer and it should be noted that the stratus and cumulus layers overlap.

The location of z_{LCL} is a critical variable in this thermodynamic system, because latent heat release associated with condensation provides additional energy that can be used to overcome the negative buoyancy experienced by parcels as they penetrate the weak inversion just above the transition level. Under some conditions, cumulus clouds associated with parcels that have low enough z_{LCL} 's may form at the base of the cumulus layer, but have insufficient energy to develop vertically and reach the stratus beneath the inversion. Thus, this thermodynamic structure can easily support two nearly decoupled cloud layers. Strictly

speaking, these two cloud layers are not completely decoupled because the penetrating cumulus elements detrain moisture into the stratus layer. If parcels from the surface moist layer can overcome the weak inversion above the transition level, they will reach their level of free convection shortly thereafter, and rise into the stratus that may occupy the upper portion of the stratus layer. Hence, this vertical structure not only allows for decoupled cloud layers to exist, but it may permit rising cumulus to interact with the stratus above.

2. Data Collection and Processing

The instrument package deployed by Penn State University to measure cloud and boundary layer structure during ASTEX included standard surface sensors, radiosondes, a Väisälä laser ceilometer (model CT 12K), a 4-channel microwave radiometer, and a 94 GHz radar. These sensors were deployed on northwestern coast of the island of Santa Maria in the Azores and operated for 27 days during the experiment. The specifications of this suite of sensors can be found in Miller and Albrecht (1995).

Half-hour averages of the cloud fraction, cloud thickness, integrated cloud liquid water content, and surface rainfall rate are used to describe the state of the cloud structure in this paper. The characteristics of this cloud field are sampled during a period

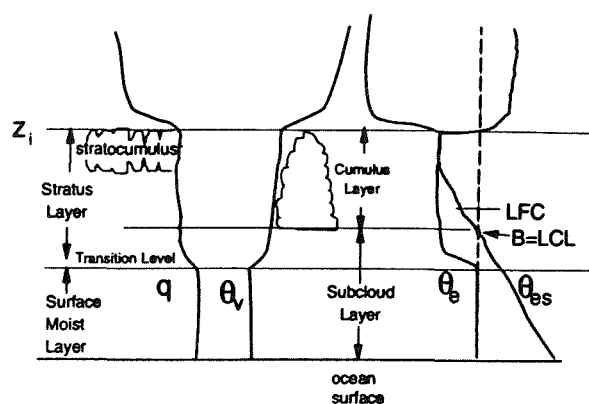


Figure 1. Schematic diagram of the thermodynamic structure of an intermittently decoupled marine boundary layer.

Δt_n by narrow-beam, zenith-pointing instruments and these samples are averaged over a period Δt_a . In this study, $\Delta t_n = 30$ seconds and $\Delta t_a = 0.5$ hours and the cloud fractional coverage is given by $f = \Delta t_c \Delta t_a^{-1}$, where Δt_c is the time period during which cloud echoes are detected. Because f is frequently less than unity, it is necessary to divide the half-hour averages of cloud top height, cloud base height, cloud thickness, cloud liquid water, and precipitation rate by f . This normalization technique is used to compute all of the averages presented below.

To satisfy the needs of the current study, the surface air temperature in the marine boundary layer is assumed to be constant. The bulk of the data analyzed below was collected during mid-June when the air temperature measured by a nearby ship was $\sim 18^\circ\text{C}$, which is the surface temperature used to compute

z_{LCL} .

To ensure that the boundary layer cloud statistics computed from the measurements taken on Santa Maria are representative of the stratus cloud system over open ocean, a stringent conditional sampling strategy was developed to minimize potential island effects. Out of a possible 648 hours of available data, 218 hours (33.6%) were found not to be island-influenced, but only 176 hours (27%) had a northeasterly wind component representative of the climatological mean flow in the region. Accordingly, these 176 hours (~ 7.3 days) are analyzed below.

3. Results

The diurnal cycle of the marine boundary layer inversion height, z_i , cloud boundaries, cloud thickness, z_c , and surface LCL is shown in Figure 2, along with fifth-order polynomial fits to highlight trends in these data. This fit must be viewed with some caution near the boundaries of the plot (~ 0000 UT), as is the case with all polynomial fits. Despite this shortcoming, the figure illustrates a steady decrease in the cloud base, cloud top, and surface lifting condensation level after

sunrise at ~ 0630 UT and a strong, rapid increase in the same three variables after ~ 1600 UT until sunset at ~ 2100 UT. Despite some variability in the observed cloud and thermodynamic structure during the nighttime, no well-defined trend is evident. Interestingly, the cloud thickness remains relatively constant through the diurnal cycle (recall that this is the thickness of individual cloud elements since the data have been normalized by cloud fraction), although Figure 3 shows that the cloud fraction decreases in response to solar heating.

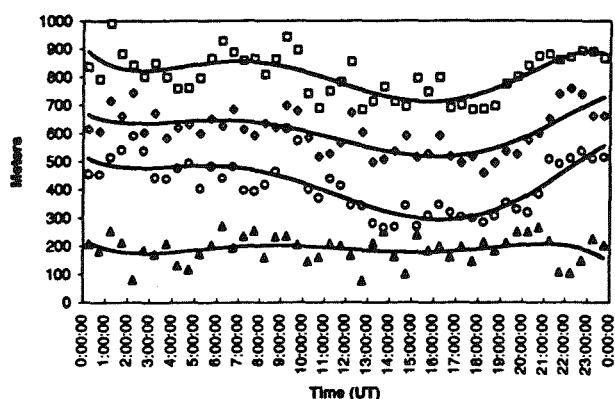


Figure 2. Composite half-hour averages of cloud top height (squares), cloud base height (diamonds), lifting condensation level (circles), and cloud thickness (triangles) for the 7.3-day sample. The solid lines are 5th order polynomial fits to the data.

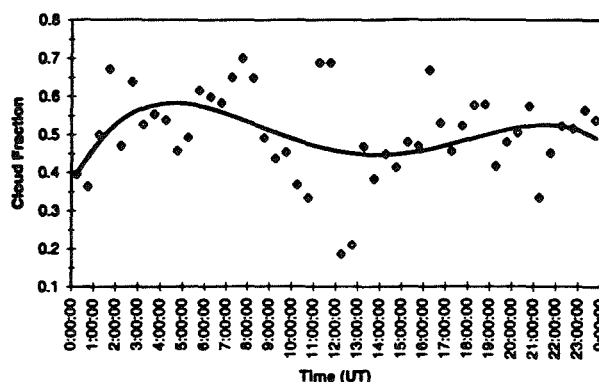


Figure 3. Composite half-hour averages of cloud fraction (diamonds) for the 7.3-day sample. The solid line is a 5th order polynomial fit to the data.

The observed decrease in the cloud base height during the daytime is accompanied by a similar decrease in the lifting condensation level due to the accumulation of water vapor in the intermittently decoupled surface moist layer. The evolution of the surface mixing ratio is shown in Figure 4. Although water vapor is being transported out of the surface moist layer through cumulus convection, the water vapor flux due to the convective elements is inadequate to offset the moisture being added to the layer through the surface water vapor flux and evaporating drizzle.

Another interesting component of the diurnal cycle in the transition region is the presence of morning and evening maxima in

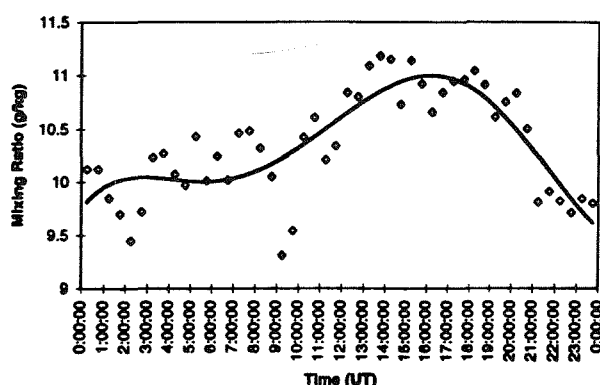


Figure 4. Composite half-hour averages of the surface mixing ratio (diamonds) for the 7.3 day sample. The solid line is a 5th order polynomial fit to the data.

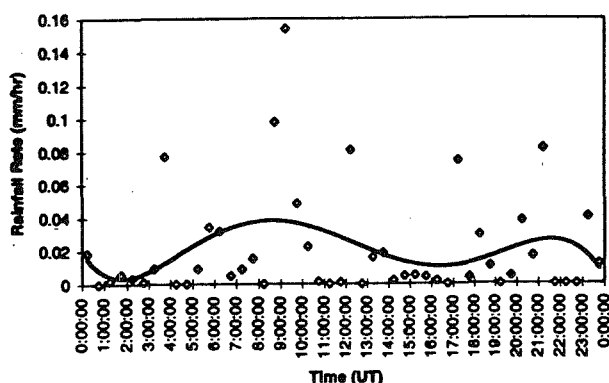


Figure 5. Composite half-hour averages of the surface rainfall rate (diamonds) for the 7.3 day sample. The solid line is a 5th order polynomial fit to the data.

the surface drizzle rate as shown in Figure 5. Both of these peaks in the surface drizzle rate correspond to periods of transition within the marine boundary layer as evidenced in Figure 2. The morning peak is the most prominent and suggests drizzle rates that are approximately twice as large as those observed during the late afternoon and at night.

4. Conclusions

It can be concluded from these data that the marine boundary layer in the transition region shows a well-defined response to solar heating, and that this response is a gradual decrease in cloud top height, cloud base height, z_{LCL} , and cloud fraction. The decrease in z_{LCL} is caused by an increase in the mixing ratio of the surface moist layer. In addition, the surface drizzle rate exhibits diurnal variability in the form of morning and late afternoon maxima. In contrast to all of the other variables examined in this study, the normalized cloud thickness showed little diurnal variability.

5. References

- Albrecht, B.A., C.S. Bretherton, D. Johnson, W.H. Schubert, A.S. Frisch, 1995: The Atlantic Stratocumulus Transition Experiment -- ASTEX. *Bull. Am. Meteor. Soc.*, **76**, 889-903.
- Hignett, P., 1991: Observations of the diurnal variation in a cloud-topped marine boundary layer. *J. Atmos. Sci.*, **48**, 1474-1482.
- Miller, M.A. and B.A. Albrecht, 1995: Surface-based observations of mesoscale cumulus-stratocumulus interaction during ASTEX. *J. Atmos. Sci.*, **52**, 2809-2826.
- Nicholls, S., 1984: The dynamics of stratocumulus: aircraft observations and comparisons with a mixed-layer model. *Quart. J. Roy. Met. Soc.*, **110**, 783-820.
- Rogers, D.P., X. Yang, P.M. Norris, D.W. Johnson, G.M. Martin, C.A. Friehe, and B.W. Berger, 1995: Diurnal evolution of the cloud-topped marine boundary layer. Part I: nocturnal stratocumulus development. *J. Atmos. Sci.*, **52**, 2953-2966.

LIDAR OBSERVATION OF FAIR-WEATHER CLOUDS

Ivan N. Kolev, Orlin P. Parvanov

Institute of Electronics, Bulgarian Academy of Sciences, Sofia, Bulgaria

1. INTRODUCTION

The clouds play a significant role in the atmosphere particularly in the determination of the radiant balance. Since their type, structure and height considerable influence the transmission, absorption and re-radiation of the IR radiation they are of great importance for the local meteorology and the global climatology. In small spatial scales (micro- and meso- ones) the clouds considerable change in space and time. Therefore certain difficulties exist the parameters characterizing them or should be introduced in the models for analyses and prediction of various atmospheric processes to be determined.

The ECLIPS program in which we also take part is well described (WMO/TD-No251, 1988). The main purpose is a ground-based lidar observation of the clouds to be performed simultaneously with NOAA 10 NOAA 11 meteorological satellites over-passing the same areas.

Essential lidar data are the recorded profiles from which the information about the clouds height, optical depth and vertical extinction can be derived.

2. METHODS AND APPARATUS

The presented experiment was conducted using triple-beam aerosol meteorological lidar (Fig. 1) developed at

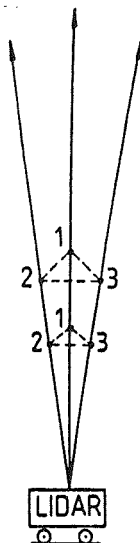


Fig. 1. The general scheme of sounding.

Standard commercial Q-switched doubled-frequency Nd-YAG laser of about 10-20 mJ (wavelength $\lambda = 532$ nm) at a repetition rate up to 50 Hz is used as transmitter.

The receiving antennae and electronics are based on three 150 mm in dia. Cassegrain type telescopes (equivalent focal length 2250 mm) aligned with model FEU 84 (made in USSR) photomultipliers. The interference filters at the working wavelength with bandwidths of 1 nm and a transmission of about 50 per cent are incorporated in order the day-time optical background to be rejected.

The data acquisition and processing system is constituted basically by a 10 bits 20 MHz waveform recorder model HP5180A and a PC "Pravetz 16" (fully 8 MHz IBM PC-XT compatible).

The listed main characteristics of the lidar determine adjustable time and spatial resolutions as high as 0.02 seconds and 7.5 meters respectively.

The investigation of the clouds is essential for us in three aspects connected with the applied meteorology, namely, the clouds physics, aviation meteorology and the ecological problems of the industrial center (which the city of Sofia represents) situated in a valley near the Vitosha mountain.

Trough the strong backscattered signal the clouds are the first investigation objects for the most of the lidar groups. Due to the reliable lidar return we used different algorithms to determine the clouds base height, namely, the signal maximum, the slope change of the derivative and based on the statistical characteristics of the time series recorded at close volumes (strokes) along the sounding paths, the first two of which are well known. The third one is based on the mode structure of the lidar returns' amplitude distributions at each distance (stroke). Trough the typical mode shapes from a "clear atmosphere" (normal) and from a cloud (normal-logarithmic) the amplitude level of the signal from the cloud (if presents) for a certain stroke can be determined (Fig. 2c). Further, obtaining such values for each stroke the time change of the cloud base height is rendered. We

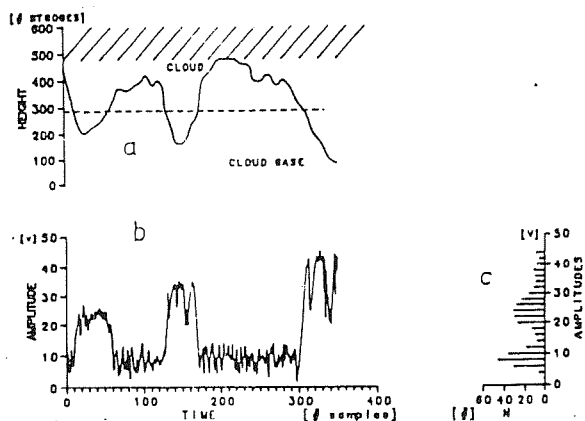


Fig. 2. (a) – the shape and the base height time behaviour of a cloud, (b) – the corresponding time series recorded from one of the strobes, (c) – its histogram (Kolev, I et al., 1987).

shall not go in more details, but every algorithm can be used in dependence of the specific conditions (Kolev I. et al., 1987). It should be noted that we are interested basically in low clouds St and Sc on account of already mentioned three aspects. A part of these studies are directed to serve forecasting purposes (Kolev S. et al., 1988). The lidar is in close vicinity to the Institute of Hydrology and Meteorology and we can use their surface measurements of the temperature, wind velocity, pressure and humidity as well as the data from the standard radio-soundings carried out at 08:00 am, 02:00 and 08:00 p.m. SLT. Soon a satellite photographs receiving system will be put into operation.

3. EXPERIMENTAL RESULTS

These measurements were performed within the ECLIPS Phase II (WMO/TD – No 251, 1988). A near-vertical sounding along three paths was conducted and the clouds' development during the NOAA 10 and NOAA 11 overpasses as well as the twenty-four hours changes of the aerosol stratification in the whole PBL were observed.

For more proper study of the observed processes two types of data have been acquired during the campaign:

1. Time series (12.5 minutes) of 2058 points with a discretization of $\Delta t = 0.3$ s along the three paths from 8 heights.

2. The profiles of lidar returns containing from 200 to 500 points with a spatial resolution of 7.5 meters and a time averaging of about 32 seconds.

The experimental data required for the ECLIPS Phase II measurements were recorded during the period from 21 May to 09 July 1991 at 30 observations by 3 hours each, i.e. 1 hour before and 1 hour after the NOAA 10

and NOAA 11 satellites overpasses. The lidar data are completed with the mentioned above meteorological information obtained by the conventional means.

On Fig.3 the cloud base height distribution obtained from 54 measurements during the ECLIPS session is summarized. Two cloud groups are mainly observed: one at 700–1200 m and another at 2000–2600 m. The great bulk is concentrated at the lower height.

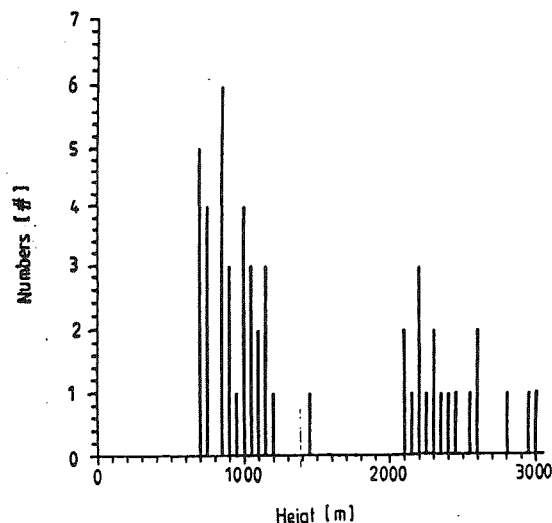


Fig. 3. The Cloud Base Height Distribution.

Shown on Fig.4a are typically observed (during this season) the temperature (T) and the dew point (td) height profiles obtained from the sounding at 9:03 a.m. An approaching of the curves reveals an approaching to the air saturation with water vapors, while a moving of the

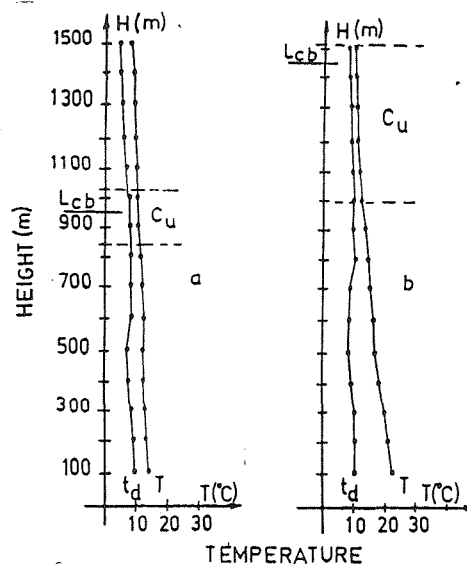


Fig. 4. The Meteorological Measurements

two curves at a distance indicates a moving apart from the saturation condition i.e. a decreasing of the humidity at the certain height (Petersen, 1956). So the probability (C_u) of clouds appearance at certain heights can be

determined. The lidar measured clouds base height (L_{cb}) is also marked.

4. DISCUSSION

The case of the morning observations connected with the ECLIPS '91 gave a good opportunity the formation and the development of the CBL over an urban area at similar conditions in the mountain valley to be traced. Such observations are interesting also in an ecological aspect since at complete development of the CBL the space of the aerosol pollution spreading can be determined. From the lidar data the height of the mixing layer and the depth of the interaction layer can be determined as well (Donev, 1992).

A typical aerosol stratification over the region caused by a multilayer temperature inversion was observed. Systematic lidar investigation of the PBL over the region of Sofia city confirm a presence of aerosol layers at heights of 50–70 m, 200–400 m and 600–800 m, which stratification remains several hours after the sunrise. After the beginning of the CBL formation, at these heights a periodically increasing of the lidar return is observed owing to an increasing of the humidity. The vertical speed determined from our data is in the limits of 0.3 to 1.5 m/s similar to that obtained in (Crum et al., 1987).

The formation of the CBL completes about 2 p.m. local time. Fair-weather clouds are observed above 1200 m, usually in the limits of 1400–2000 meters (Fig.5).

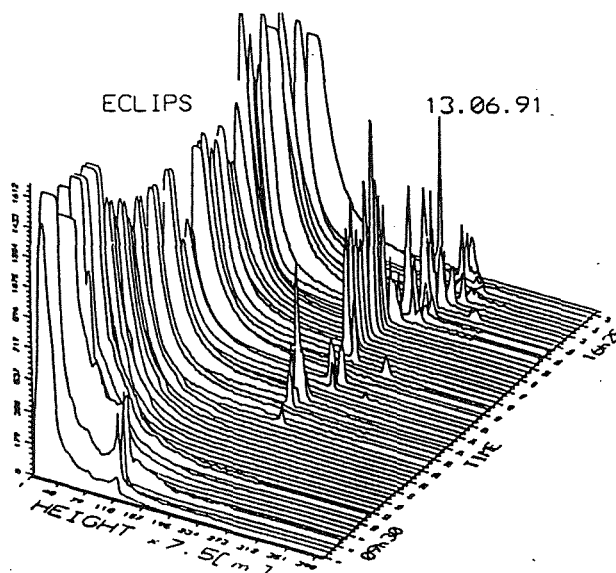


Fig. 5. Time series of LIDAR returns.

The clouds at 700–1200 m also form in the aerosol layers zone but not at the height of the first elevated inversion (as in the case of the winter observation), they form at one of the higher located inversions i.e. where

proper conditions exist. In Fig.4b the temperature (T) and the dew point (t_d) height profiles obtained from the sounding at 02:30 p.m. are shown. The zone of the cloud formation probability (1000–1500 m) with a depth of about $\Delta H = 500$ m is marked. On the same graph the determined from the lidar data clouds base height at $H=1440$ m is also marked.

A comparison between the data obtained employing the different methods definitely show that the presented one can be used for a determination of the cloud base height regardless of the optical characteristics variations in the cloud base area. For a determination of the clouds motion velocity, the rendered time behaviour of the cloud base along three near-vertical paths can be used. Further, the space spectra and the amount of the clouds can be also determined.

On the grounds of a field experiment conducted during the ECLIPS '91 (Sofia) it is concluded that the cloud base heights reported by the operational weather services based on the lifting condensation levels (LCL) are inaccurate for the fair-weather cumulus clouds (Stull et al., 1985). LCLs also vary with a diurnal cycle, starting low in the morning and reaching a peak at about three hours before the local sunset.

5. CONCLUSION

The investigation of the humidity motion and transformation in the atmospheric planetary boundary layer is of a separate significance since these processes not always correlate with the thermal changes.

In the other case (in summer) due to the development of the convective boundary layer a decreasing of the humidity in the ground boundary layer occurs owing to the evaporation processes and the turbulence which transport the humidity to the higher layers bordering upon the free atmosphere. Under proper conditions, this transportation leads to fair-weather clouds formation.

6. REFERENCES

- WMO/TD No 251, 1988. Report of the WCR/CSIRO Workshop on Cloud Base Measurement.
- Kolev, I., Parvanov, O., Kaprielov, B., Kolev, S., 1989. "Lidar Observation of Time and Spatial Variations of Backscattering Coefficient Near the Stratiform Cloud Base". *Atmospheric Research*, **24**, 13-32.
- Peterssen S., 1956. *Weather Analysis and Forecasting*, McGraw-Hill Book Company, New York.
- Donev, E., Ivanov, D., Kolev, I., Kaprielov, B., Parvanov, O., Zeller, K., 1992. "Some Relations Between Lidar Measured Aerosol Layer Heights and Surface Turbulent Heat Fluxes". *Bulg. J. of Meteorology & Hydrology*, **3** (2), 101-106.

- Kolev, I., Parvanov, O., Kaprielov, B., Naboko, V., 1987. "Lidar Measurements of Cloud Base Height". Proc. of 2nd Int. Conf. "Optika '87", Varna; 366-369.
- Crum T., Stull, R., Eloranta, E., 1987. J. Climate Appl. Meteor., **26**; 774-788.
- Stull R., 1985. "A Fair-Weather Cumulus Cloud Classification Scheme for Mixed-Layer Studies", J. Climate and Appl. Meteor., **24** (1); 49-56.
- Kolev S., Parvanov O., Kostadinov L. Kolev I., 1988. Use of Lidar Data in Short-term Forecast of Stratiform Cloudiness Base Height. Proc. 10th Int. Cloud Physics Conf., Bad Homburg, 515-517.

ON THE FORCING OF WINDWARD ISLAND RAINFALL IN HAWAII

R. E. Carbone, J. Tuttle, W-C Lee, W. A. Cooper, V. Grubišić

NCAR *, Boulder, Colorado, USA 80307

1. INTRODUCTION

The windward sides of islands in the trades are among the rainiest places on earth. Often such rains exceed regional oceanic precipitation by several-fold, and sometimes by an order of magnitude or more. This study examines the morphology of tradewind rainfall as observed over the ocean and land during a 45 day field program called the Hawaiian Rainband Project (HaRP). HaRP was conducted on the island of Hawaii during the summer of 1990 in the vicinity of Hilo (located at -5,0 in Fig. 1). Three hundred hours of Doppler radar data, 100 hrs of research aircraft data, and a 50 station surface meso-network allowed relatively complete documentation of tradewind rainfall patterns and related circulations at the mesoscale. The main purpose of our study is to determine the distribution of rainfall during normal tradewind conditions and to quantify the dependence of its amount and distribution on the large scale environment.

Hawaiian rainfall has been studied for decades including investigations by Leopold (1949), Lavoie (1967), Blanchard (1953), and Takahashi (1977, 1986). These investigators and others examined various phenomena on the island including sea and land breezes, orographic rainfall, windward ocean rainbands, mountain-valley effects, and the evolution of warm rain drop-size distributions. For the most part, these studies emphasized diurnal thermal forcing effects that seemingly control rainfall, wind direction, and temperature near Hilo.

Smolarkeiwicz, Rasmussen and Clark (1988) (hereinafter SRC), based on a series of numerical simulations, advanced the argument that island blocking of the mean flow is principally responsible for windward island rainbands. They argued that this dynamical effect, in a low Froude number (Fr) regime, is dominant over thermal forcing. The results of these simulations represented a new paradigm for scientific thought on the forcing of rainfall over tropical islands with topography.

Rainfall over the island during HaRP was first examined by Chen and Nash (1994), hereinafter C-N. Their analyses revealed considerable variation in rainfall with respect to topography, the relationship between location and phase of the diurnal cycle, windspeed, static stability, and other factors. Among other findings, their

analyses (C-N Fig.13) revealed a steady nocturnal progression of rainfall from the slopes west of Hilo eastward to the coast through the evening hours. C-N also confirmed the development of a well-known westerly downslope flow that occurs in the nocturnal hours and typically extends to the shoreline by local midnight. Carbone et al (1995) have clarified the forcing of this flow reversal and quantified the thermodynamic properties of the evolving westerly flow.

HaRP investigators focused most of their efforts on banded precipitation, typically 10-15 km offshore, that occurred with highest frequency in the hours near sunrise. As will be evident from the data presented herein, most rainbands propagated toward shore and some of these rained on shore, typically in an advanced stage dissipation. Some rainbands exhibited a quasi-stationary behavior that produced heavy local rains. This study does not focus on rainbands per se but rather the accumulation of rainfall of all types in the windward island domain when conditions fit the description of an undisturbed tradewind regime.

2. DATA AND CALCULATIONS

To determine the distribution of rainfall and to quantify any dependence of its amount and distribution on the environment requires a rainfall estimation procedure that is similarly applicable over land and sea as well as a definition of "environment" that is not heavily influenced by the island itself. Defining the environment was satisfied by aircraft soundings that were taken by the NCAR Electra approximately 100 km upstream of Hawaii. Rainfall was estimated in a *relative* sense from 5 cm radar (NCAR CP-4) reflectivity data, thus enabling us to estimate the island amplification effect over oceanic background. These relative rainfall estimates were subsequently "calibrated" by boundary conditions such as raingauge measurements, analyses thereof, and climatologies that are applicable both to the island and the nearby eastern North Pacific.

2.1 UPSTREAM SOUNDING DATA

Numerous quantities, often associated with the convective organization, were calculated from twenty upstream soundings. These included convective available

* NCAR is sponsored by the National Science Foundation

potential energy (CAPE), convective inhibition (CIN), tradewind layer depth, horizontal vorticity, gradient Richardson Number (Ri), island-blocking Froude number (Fr), level of free convection (LFC), differential saturation mixing ratio between the lifted condensation level and tradewind inversion (Dm_{∞}), and a condensate production rate index, $Dm_{\infty} CAPE^{0.5}$. Based upon our preliminary analyses, most of these quantities are either uncorrelated, inconsistently correlated, or not independently correlated with rainfall production. Section 3 focuses on Fr aspects of these data.

2.2 RAINFALL ESTIMATES

Radar scans at approximately 15 min intervals were used to estimate rainfall in the 40x100 km computational domain illustrated in Fig. 1. This domain is oriented along the nominal tradewind direction and allows us to examine rainfall as a function of distance from the eastern shore. An ordinary morning rainband pattern from 3 August 1990 is also shown in Fig. 1. Battan (1973) reviews relationships between equivalent reflectivity, Z_e (mm^6/m^3), and rainfall rate, R (mm/hr), of the form $Z = aR^b$ for warm rain showers. It is evident that $b=1.4-1.7$ with a preponderance of values around 1.5. A transfer function with exponent 1.5 was applied to the data together with an arbitrary coefficient, a . *Relative* rainfall amounts were accumulated in each 5 by 40 km slab illustrated in Fig. 1.

To obtain an approximation of total rainfall, the data were normalized in four independent ways. Data in the coastal slab were matched to Hilo airport climatology for the July-August period and to the rainfall analysis of C-N for the 45-day HaRP period. Both of these normalizations yielded an inferred coefficient, $a = 45$. The third and perhaps most definitive normalization matched data from the four mesonet raingauges (NCAR PAM system) located within the coastal slab. These gauges were arithmetically averaged for the 20 days actually used in this study and yielded the coefficient, $a = 50$. Using either transformation, when accumulations for the most distant slab, 70 km upstream, were compared to maps of eastern Pacific rainfall (e.g. Trewartha, 1954), there is favorable agreement with oceanic climatology, 45-60 cm per annum. Consequently, the coefficient 50 is used for all figures depicting rainfall in this paper, as it maintains good consistency with observed rainfall near Hilo and oceanic climatology. The radar literature supports coefficients from 17 to 125, with 31 (Blanchard, 1953) being the best documented value in the vicinity of Hilo.

3. RESULTS

To investigate the location and propagation of rainfall, Hovmöller-type diagrams of slab-averaged rainfall rates were calculated for the entire dataset. These depict rainfall activity as a function of time and distance from the windward shore in the computational domain.

3.1 3 AUGUST 1990, AN EXAMPLE

The signatures of travelling rainbands and other precipitation are evident in Fig. 2, a Hovmöller summary of rainfall for 3 August 1990. Slab-average rates typically range from 0.5 to 3 mm/hr. Finescale coherent structures exhibit a slope that defines westward propagation approximately at the mean tradewind speed, 7 m/s. An opposing eastward propagation of the broad forcing zone is evident from 0500 UTC (1900 LT) to 1700 (0700), during which rainfall gradually shifts from the mountainside west of Hilo to the ocean, 10-40 km offshore. This is followed by a sudden transition of the forcing zone at 2100 (1100) back to a mountainside location, where orographic rains often persist. Based upon the numerous studies previously cited, we attribute the diurnal component of the rainfall forcing zone movement to thermally driven circulations. We note that on 3 August the maximum precipitation occurs offshore in the morning rainband regime. More generally, maximum rainfall may occur at any point in the diurnal cycle.

3.2 COMPOSITE RAINFALL PATTERNS

Data composited from all days are shown in Fig. 3 to follow a forcing pattern similar to that exhibited on 3 August. On average, the forcing zone propagates eastward beginning one hour after sunset, through the coastal zone near local midnight, to a quasi-steady condition roughly 20 km offshore beginning near sunrise. In late morning a sudden transition from the offshore regime to orographic rainfall occurs and this condition persists for many hours. The later stages of orographic rain seem to coexist with dissipation of evening coastal showers and rainbands. From Fig. 3 it appears that the highest average rainfall rates occur in the transition from orographic rain to the offshore regime, along the coastline near midnight. This is not the region of maximum cumulative rainfall, however, as the forcing period is relatively short compared to the orographic region. A significant feature in Fig. 3 is the nocturnal occurrence of coherent rainfall structures having their origin in the upstream oceanic region. This may be related to factors described by Austin et al (1996).

Froude number approximates the ratio of kinetic energy in the mean flow to the potential energy required for ascent over an obstacle. It was defined by SRC as U/Nh where U is the upstream tradewind speed, N is the Brunt-Vaisala frequency, and h is the characteristic height of the island. Owing to the considerable body of literature on the low Fr flow regime and its relationship to rainbands, the data herein were stratified to discern and clarify this dependence. Fig. 4 represents a composite of 14 days having "ordinary" Fr between 0.19 and 0.28, with a group mean of 0.24. Qualitatively it is similar to Fig. 3. We note there is somewhat less rainfall and a much shorter duration of rainfall in the orographic region.

There were five days with elevated Fr from 0.32 to 0.42 (0.37 mean) and the composite of these is depicted in Fig. 5. A markedly different pattern is apparent, most

notably a pattern of much heavier rainfall and the absence of a quasi-steady offshore regime in the hours near sunrise. A brief transition to forcing offshore occurs around local midnight (1000), but strong forcing stays within 10 km of shore. Rainfall quickly returns to the orographic zone beginning at sunrise. Qualitatively, this pattern is in substantial agreement with the expectations of SRC.

3.3 CUMULATIVE RAINFALL

A more quantitative assessment of the response to data stratification by Fr may be obtained from time integrals of domain rainfall (Fig. 6) where amounts are expressed as annual rates. Several significant features emerge from the general pattern. First, the island influence on cumulative precipitation is not felt beyond 45 km, independent of Fr. This suggests that island-oriented rainbands beyond 45 km are a consequence of deformation in the flow field, but not divergence. Second, the flow between 20 and 40 km, while mostly deformative, does experience significant divergence and, nominally, a doubling of rainfall. Third, offshore rainfall sharply increases within 20 km of shore and a bimodality is introduced to the rainfall distribution when Fr is in the "ordinary" range. The eastern mode is the result of morning rainbands located offshore. Fourth, a strong maximum of rainfall exists over land, the position of which is essentially independent of Fr. The amplitude of this maximum is four to ten times oceanic background over the range of Fr observed. Furthermore, the rainfall response to elevated Fr appears to be marginally greater (about 40%) than a linear response.

4. CONCLUSIONS

Rainfall near the windward shore of Hawaii is very sensitive to mean flow speed, lower tropospheric stability, and diurnal thermal forcing. Each of these factors plays an important role in the amount and distribution of rainfall. Given a tradewind layer of moderate depth with small conditional instability, the total domain rainfall is most strongly a function of the island Fr as defined by SRC. The location of rainfall and its relative apportionment is heavily influenced by thermal forcing when Fr is appreciably below 0.35, as is often the case. When Fr exceeds 0.40, the zone of rainfall forcing is ten times stronger than oceanic background.

Two quasi-steady conditions arise at opposite phases of the diurnal cycle. Orographic rainfall persists from late morning through sunset and offshore rainbands continually develop in the hours around sunrise. An asymmetry is introduced during the transition periods. The evening transition from orographic rain to offshore bands is a slow and rainy one over the coastal zone near midnight. Conversely, the morning transition from offshore bands to orographic rain is sudden and relatively dry in the coastal zone. The evening transition is thought to be governed by gravity current dynamics (Carbone et al, 1995).

High rainfall rates occur most often in the coastal zone during evening transition, but these may occur at any time and at any place within about 15-20 km from shore. The cumulative rainfall maximum is in the orographic zone, owing to much longer periods of gentle rain.

5. ACKNOWLEDGEMENTS

The dedicated efforts of numerous staff from the Atmospheric Technology Division of NCAR are gratefully acknowledged for the collection of data. T. Schroeder and D. Johnson were especially helpful in providing guidance to HaRP generally and in carrying out the operations. Y.L. Chen graciously provided edited rainfall data for the surface stations used in this study. Linda Morris-Gonzales assisted in the preparation of this manuscript.

6. REFERENCES

- Austin, G.R., Rauber, R.M., Ochs, H.T., Miller, L.J., 1996: Tradewind cloud and Hawaiian Rainbands, *Mon. Wea. Rev.*, **123**, submitted.
- Battan, L. J., 1973: *Radar Observations of the Atmosphere*, Univ. of Chicago Press, Chicago, 324 pp.
- Blanchard, D.C., 1953: Raindrop size distributions in Hawaiian rains. *J. Meteor.*, **10**, 457-473.
- Carbone, R. E., W. A. Cooper, W.C. Lee, 1995: Forcing of flow reversal along the windward slopes of Hawaii. *Mon. Wea. Rev.*, **123**, 3466-3480.
- Chen, Y.L. and A.J. Nash, 1994: Diurnal variations of surface airflow and rainfall frequencies on the island of Hawaii. *Mon. Wea. Rev.*, **122**, 34-56.
- Lavoie, R.L., 1967: Air motions over the windward coast of the island of Hawaii. *Tellus*, **19**, 354-358.
- Leopold, L.B., 1949: The interaction of tradewind and seabreeze, Hawaii. *J. Meteor. Sci.*, **6**, 312-320.
- Rasmussen, R.M., P.K. Smolarkiewicz, and J. Warner, 1989: On the dynamics of Hawaiian cloud bands: Comparison of model results with observations and island climatology. *J. Atmos. Sci.*, **46**, 1589-1608.
- Smolarkiewicz, P.K., R.M. Rasmussen, T.L. Clark, 1988: On the dynamics of Hawaiian cloud bands: Island forcing. *J. Atmos. Sci.*, **45**, 1872-1905.
- Takahashi, T., 1977: Rainfall at Hilo, Hawaii. *J. Meteor. Soc. Japan*, **55**, 121-129.
- _____, 1986: Wind shear effects on water accumulation and rain duration in Hawaii warm clouds. *J. Meteor. Soc. Japan*, **64**, 575-584.
- Trewartha, G.T., 1954: *An Introduction to Climate*, McGraw Hill Inc., New York..

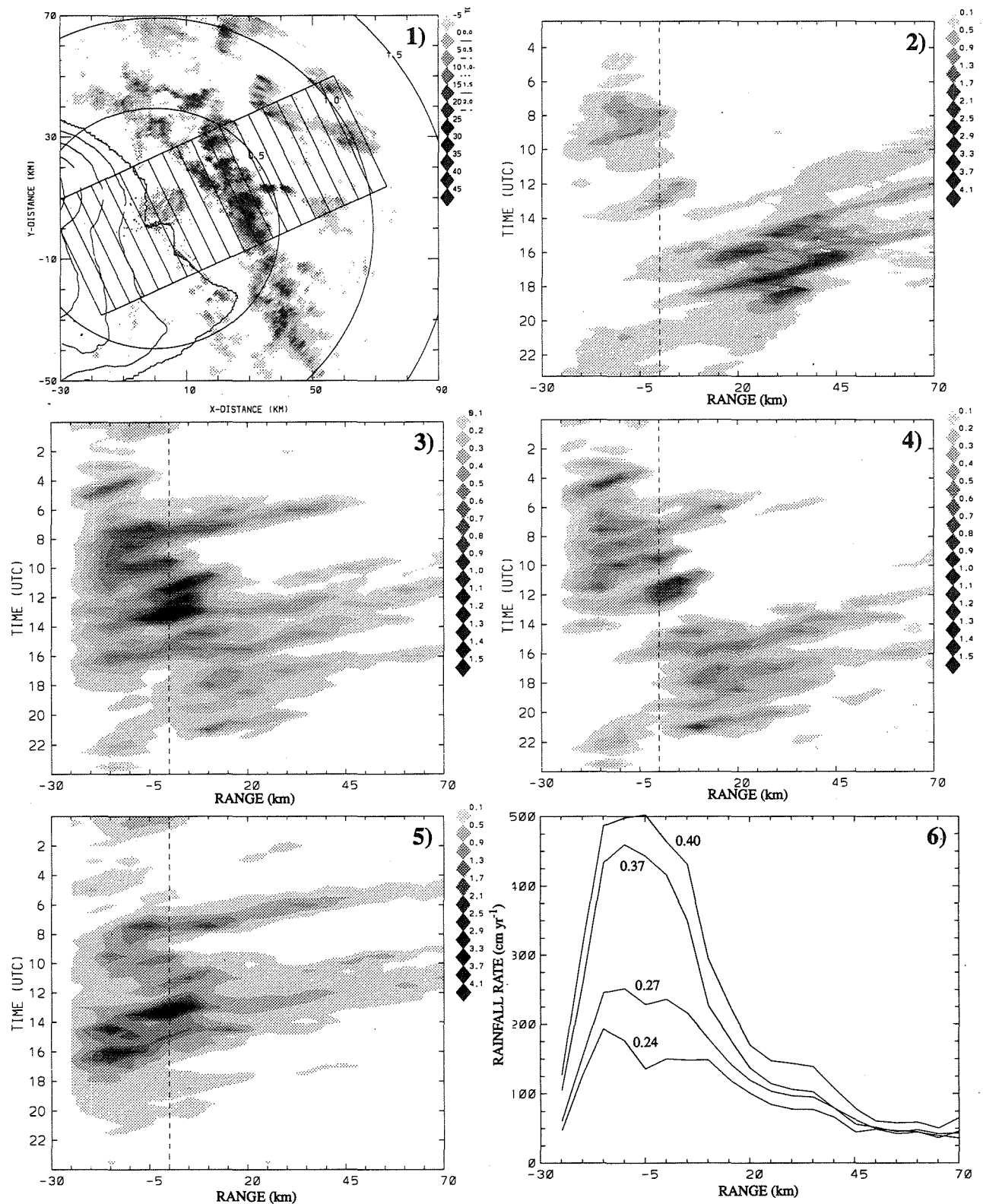


Fig. 1 Morning rainband radar echoes on 3 August 1990 (dBZe) together with island topography (0, 1, 2 km) and the Hovmoller computational domain oriented along a nominal stagnation streamline (065) from -25 to +70 km upstream.

Fig. 2 Areal rainfall rates (mm/hr) as a function of time (UTC) and distance upstream (km) for 3 August 1990. Sunset is at 0400 and sunrise is at 1600.

Figs. 3, 4, 5 As in Fig. 2 for: all days (0.27), ordinary Fr days (0.24), and elevated Fr days (0.37), respectively.

Fig. 6 Time-integrated rainfall rates (cm/yr) as a function of average Fr (0.40, 0.37, 0.27, 0.24) and distance upstream (km).

CONTINENTAL STRATUS CHARACTERISTICS FROM SURFACE-BASED REMOTE SENSING SYSTEMS

Bruce A. Albrecht¹, Gerald G. Mace², William J. Syrett², Daniel Thomas²,
Christopher Ruf³ and Justin Bobak³

¹MPO/RSMAS, University of Miami, Miami, FL 33149 USA

²Meteorology Dept., Penn State, University Park, PA 16802 USA

³Electrical Eng. Dept., Penn State, University Park, PA 16802 USA

1. INTRODUCTION

Stratocumulus clouds are frequently observed over the eastern United States during much of the year. Like their marine counterpart, these clouds reflect shortwave radiation back to space, but have little effect on the emission of longwave radiation at the top of the atmosphere. More importantly, they have a substantial impact on the surface energy budget, and thus are important in regulating surface temperatures. Despite the importance of these clouds for climate, weather forecasting, and aviation concerns a description of even the most basic characteristics of these clouds is lacking. To address this shortcoming, an extensive set of observations was obtained from a site in central Pennsylvania using a 94 GHz Doppler (cloud) radar in concert with other remote and *in situ* measurements. A laser ceilometer monitored cloud-base heights and a surface-based microwave radiometer provided estimates of cloud water content. Rawinsondes were used to the characterize boundary layer structure associated with selected stratocumulus events. Descriptions of the instrumentation used for these observations are given in Albrecht et al. (1991), Peters et al., (1993), and Ackerman et al., (1993), Miller and Albrecht (1995), Syrett et al. (1995). A complete description of the 94 GHz cloud radar is given in Clothiaux et al., (1995).

The measurements were made during two Intensive Observing Periods (IOPs). The first was 15 October to 15 December 1994 and the second was from 15 March to 15 April 1995 (Syrett, 1995). During the second IOP *in situ* cloud observations were made with the University of Wyoming King Air. In addition, researchers from the University of Massachusetts operated a dual-frequency (35 and 94 GHz) cloud radar. This paper gives an overview of the observations made during the two IOPs with an emphasis on the use of the 94 GHz radar to develop extensive statistics on continental stratus and stratocumulus. During the same observational period, returns from the radar were also used to provide

statistics on cirrus clouds that were present over the site (Mace et al., 1995). In addition, we discuss some new techniques that are being developed to better characterize cloud properties using the cloud radar.

2. CLOUD CHARACTERISTICS

During the first IOP, low-level stratus clouds were observed approximately 35% of the time by the ceilometer. Over 1000 hours of data were collected with the cloud radar and a wide range of cloud conditions was sampled. These data are being used to define mean characteristics of the clouds including cloud thickness, height, and liquid water content. Stratus clouds ranging in depth from about 100 m to 2 km were observed. Several multiple layer systems were sampled. Like their marine counterparts, the single layer systems are often associated with well-mixed boundary layers.

The radar returns from the fall IOP were examined subjectively to identify well-defined stratus clouds with tops below 3 km and with no evidence for clouds above. This resulted in a total of 246 hours of observations where radar, ceilometer, and microwave radiometer data were available to provide cloud top height, cloud base height, and liquid water content. Cloud top height was obtained from the radar reflectivity by applying the masking technique described by Clothiaux et al., (1995). The 246 hours of data were further classified by the synoptic conditions associated with the observed clouds. Although the sampling interval for each of the sensors varied from 5-30 seconds, hourly averages are used for the statistical analysis shown here.

The hourly averaged cloud thickness for the observed stratus events by synoptic classification are shown in Figure 1. Most of the clouds observed were associated with mid-latitude cyclones that affected the area during the IOP. Clouds typically varied from

100m to 1 km in depth. Work is in progress to define detailed statistics on the properties of the clouds.

The cloud thickness was used to calculate the adiabatic liquid water content using the technique described in Albrecht et al., 1990. Cloud temperatures needed for the adiabatic calculation were crudely estimated from surface observations made at the site with the assumption that the subcloud layer was dry adiabatic and the cloud layer was moist adiabatic. The adiabatic liquid water path and the observed liquid water path are shown in Fig. 2. Although the observed liquid water paths show substantial scatter, they are close to adiabatic for clouds 500 m or less in thickness. The observed liquid water path, however, is clearly less than the adiabatic for clouds thicker than 500 meters. At this point we have not examined each case to try to explain the relatively high observed liquid water path obtained for some of the very thin clouds.

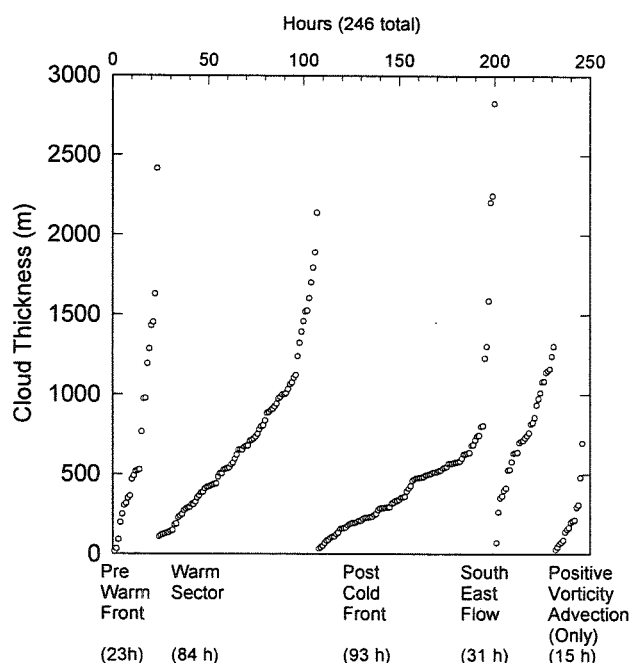


Figure 1. Cloud base height for the individual hours of data that were used in this study. Observations were sorted by cloud depth within each synoptic category.

The ratio of the observed liquid water path to the adiabatic path was calculated for the hourly averages. Averages of this ratio were made using the hourly observations available in 200 m increments of cloud thickness starting at 300 m. For thin clouds this ratio was sometimes much greater than one since the adiabatic liquid water content is relatively small. Any errors in the thickness or the observed liquid water path can give very unrealistic ratios. Consequently ratios that exceed 1.5 are not included in the average

ratio for 200 m layers shown in Fig. 3. For clouds with thicknesses greater than 500 m, the ratio of the observed liquid water path to the adiabatic path decreases nearly linearly with cloud depth to about 0.5 at 1 km. Work is in progress to further quantify this relationship and to examine how it varies with synoptic forcing and other characteristics of the cloud.

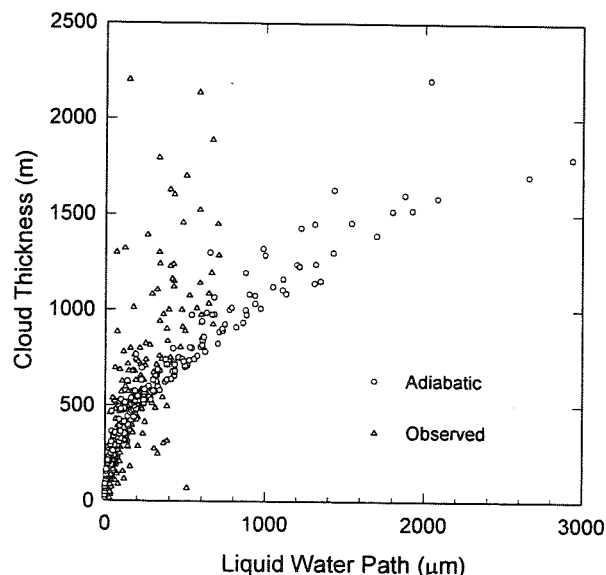


Figure 2. Hourly averaged adiabatic and liquid water path as a function of cloud thickness.

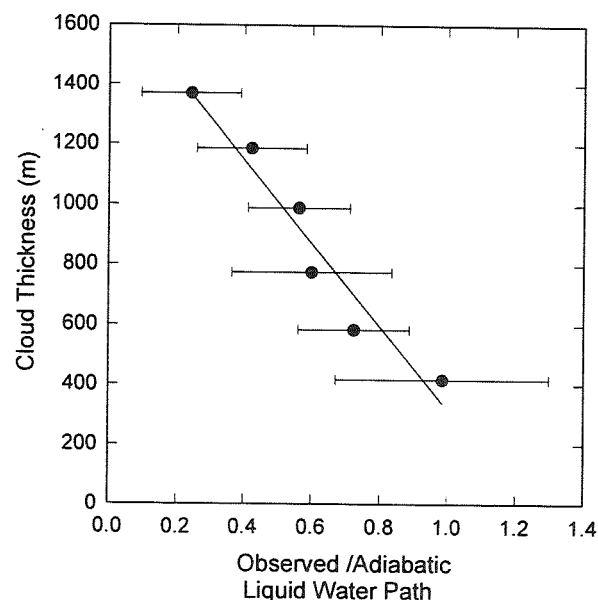


Figure 3. Ratio of observed liquid water path to adiabatic liquid water path calculated from hourly averaged values shown in Fig. 2. Averages and standard deviations are for hourly values calculated for 200 m increments of cloud thickness.

Numerous drizzle events were observed during the fall IOP and for approximately 80% of the stratus clouds observed radar echoes extended below the cloud base defined from the laser ceilometer. These cases will be examined in detail to characterize the reflectivity and the fall velocities associated with drizzle events observed during the period. In addition, the reflectivity gradient at cloud top is being used to characterize the depth of the entrainment mixing zone near cloud top. Illustrations of these techniques will be presented at the meeting.

3. NEW TECHNIQUES

Although low-level clouds were less extensive during the second (spring) IOP than during the first due to below-normal storm activity, there were ample opportunities for comparisons among the radars and the aircraft. These intercomparisons were a major focus of the second IOP. A substantial number of mixed-phase clouds were observed during the IOP. A total of eleven flights were made with the King Air. During this time we were able to perform some initial tests of a real-time full spectral processor (Peters et al., 1995) designed for the 94 GHz radar. An initial analysis of spectra from the 94 GHz radar and *in situ* measurements of cloud properties from the Wyoming King Air are presented by Babb et al, (1995). An example of spectra obtained during a drizzle event associated with a shallow cloud is shown in Fig. 1. The spectral peaks at about 2100 m show a clear separation between the drizzle and the cloud motions. An updraft of about 0.25 ms^{-1} is tracked by the cloud droplets while the drizzle has a fall velocity of about 0.75 ms^{-1} at this level. Furthermore, this technique allows us to define cloud base (about 2 km in this case) in clouds that generate drizzle. If the real-time spectral processor is applied to 10 gates within the cloud, we can calculate and store spectra every 2-4 seconds. Using this technique, variations in the peak of the reflectivity associated with returns from the cloud droplets can be used to define vertical velocity fluctuations in the cloud interior while simultaneously monitoring the characteristics of the larger droplets. Aircraft observations from the Wyoming King Air and a detailed model for simulating spectra for a wide range of cloud and precipitation conditions are being used to fully develop the spectral technique. From these initial tests it is apparent that the real-time spectral processor will be a powerful tool for studying drizzle and entrainment processes in continental stratus.

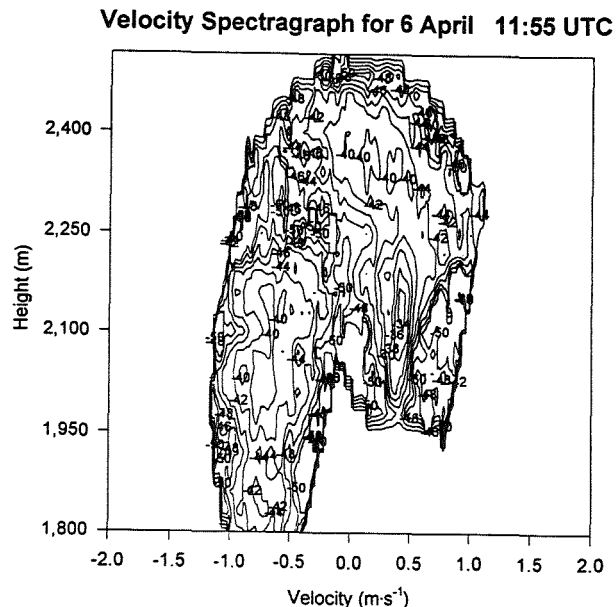


Figure 4. Spectrograph of reflectivities from 94 GHz radar for shallow cloud with drizzle observed on 6 April 1995. Isopleths are dBZ.

4. CONCLUSIONS

The initial focus of this work was to provide a physical description of continental stratus clouds using surface-based remote sensing systems. The eventual goal is to include this description into a meteorological context and to develop and test simple approaches for parameterizing these clouds in climate and forecast models. The ratio of the observed liquid water path to the adiabatic path as function of cloud thickness that we have derived in this study is a example of what this data set has to offer to the modeling community.

The use of the full spectra for radar cloud retrievals appears to offer great potential for investigating cloud and precipitation processes. As routine measurements of cloud top, height, and base become available at the DOE Atmospheric Radiation Measurements (ARM) sites, we hope to apply methods similar to those described here for long-term monitoring of cloud properties.

Although our analyses are still in the preliminary phase, it is already clear that this study will provide an unprecedented description of continental stratus. In addition, the data sets that we have obtained contain a wealth of data on the fine structure of stratus clouds that is waiting to be explored.

5. ACKNOWLEDGMENTS

This research was supported by the National Science Foundation (ATM-9317371) and the Department of Energy (DE-F602-90ER61071).

6. REFERENCES

- Ackerman, T.P., B.A. Albrecht, M.A. Miller, E. Clothiaux, R.M. Peters and W. Syrett, 1993. Remote Sensing of Cloud Properties Using a 94 GHz Radar. Topical Proceedings, Symposium on Combined Optical-Microwave Earth and Atmosphere Sensing, Albuquerque, NM, 22-25 March, IEEE, 211-214.
- Albrecht, B.A., C.W. Fairall, D.W. Thomson, A.B. White, J.B. Snider and W.H. Schubert, 1990. Surface-based remote sensing of the observed and the adiabatic liquid water content of stratocumulus clouds. *Geophys. Res. Lett.*, **17**(1), 89-92.
- Albrecht, B.A., T.P. Ackerman, G.G. Mace, D.W. Thomson, M.A. Miller and R.M. Peters, 1991. A Surface Based Cloud Observing System. Preprint vol., 7th Conference on Meteorological Observations and Instrumentation, New Orleans, January 14-18, American Meteorological Society, 580-582.
- Babb, D.M. and B.A. Albrecht, 1995. Comparing 94 GHz Radar Cloud and Precipitation Drop Spectra Measurements with Aircraft Observations, etc. Preprint vol., 27th Conference on Radar Meteorology, Vail, CO, 9-13 October, American Meteorological Society,
- Clothiaux, E.E., M.A. Miller, B.A. Albrecht, T.P. Ackerman, J. Verlinde, D.M. Babb, R.M. Peters and W. Syrett, 1995. An evaluation of a 94 GHz radar for remote sensing of cloud properties. *J. Atmos. Oceanic Tech.*, **12**, 201-229.
- Mace, G.G., T.P. Ackerman, B.A. Albrecht, D.M. Babb and R.M. Peters, 1995. An Examination of Cirrus Cloud Characteristics Observed by a 94 GHz Doppler Cloud Radar. Preprint vol., 27th Conference on Radar Meteorology, Vail, CO, 9-13 October, American Meteorological Society.
- Miller, M.A. and B.A. Albrecht, 1995. Surface-based observations of mesoscale cumulus-stratocumulus interaction during ASTEX. *J. Atmos. Sci.*, **52**(16), 2809-2826.
- Peters, R.M. B.A. Albrecht and M.A. Miller, 1993. Marine Boundary Layer Profiling with a 94 GHz radar. Preprint vol., 8th Symposium on Meteorological Observations and Instrumentation, Anaheim, CA, 17-22 January, American Meteorological Society, 205-208.
- Peters, R.M., B.A. Albrecht, G. Mace, T. Ackerman and D. Babb, 1995. Real-time Spectral Measurements of Cloud Microphysical Characteristics Using 94 GHz Radar. Preprints, 27th Conference on Radar Meteorology, Vail, CO, 9-13 October, 577-579.
- Syrett, W.J., 1995. Continental Stratus: Intensive Field Observations-Phases I & II, 15 Oct.-15 Dec. 1994 and 15 Mar.-15 Apr. 1995, Department of Meteorology, Penn State University. pp. 103 & 82.
- Syrett, W.J., B.A. Albrecht and E.E. Clothiaux, 1995. Vertical cloud structure in a midlatitude cyclone from a 94-GHz radar. *Mon. Wea. Rev.*, **123**, 3393-3407.

COASTAL STRATUS OBSERVATIONS WITH AN AIRBORNE RADAR

G. Vali, R.D. Kelly, S. Haimov, D. Leon and J. French
Department of Atmospheric Science, University of Wyoming
Laramie, WY, 82071, USA

1. INTRODUCTION

Progress in cloud and precipitation studies, and in the many applied disciplines related to these fields, continues to depend on a combination of field observations, laboratory experimentation and theoretical developments. The search for new observational methods is an integral part of this process and was, in large part, the motivation for the work here described. We have already given some reports on the development, in collaboration with the University of Massachusetts, of a 95 GHz radar (3 mm wavelength) with polarimetric and Doppler capabilities (Pazmany et al., 1994). The radar is installed in the University of Wyoming King Air research aircraft. Observations with the radar/aircraft system in a shallow stratus situations were described by Vali et al. (1995). The main strengths of these airborne radar observations are high spatial resolution, mobility to cloud areas of interest, and direct vertical observations at all points (important for velocity and polarimetry). There are great benefits from having these radar observations in close correlation with the *in situ* measurements from the aircraft-mounted instruments.

The other impulse for the coastal stratus studies was the importance of these clouds – as of all low-level maritime clouds – in the global radiation balance, and in the climates of coastal zones. The area selected for the field project was the Pacific coast of the NW U.S., specifically the central coast of the State of Oregon. Flights were made during late August and early September of 1995.

Upwelling of cold ocean water near the Oregon coast generates strong gradients in surface temperatures. Combined with the influence of the coast, and of the coastal mountain range, local circulations superpose mesoscale cloud features on the synoptic patterns. The semi-permanent California stratus frequently develops a narrow extension toward the north along this coast.

2. RADAR AND AIRCRAFT

The University of Wyoming King Air aircraft is equipped with instruments for measurements of state pa-

rameters, air motion and hydrometeor characterization. The 95 GHz radar is fitted with an antenna that provides a 0.7° beam. The beam can be directed either upward or sideways, normal to the flight path; in either case, data are collected in a plane extending from the flight path. Usual integration time is 0.05 s, which yields a resolution of about 5 m along the flight direction. In these studies a 15 m range gate spacing was employed and the maximum range was set at 1.5 km. Doppler velocities were obtained from real-time pulse-pair processing. Measured velocities were transformed to ground-relative velocities by subtraction of the component of the aircraft motion in the beam direction. Aircraft motion parameters were determined from the laser inertial navigation system.

Flights were launched from Corvallis, OR and took place between 44°N and 46°N latitudes and 124°W and 125°W longitudes. Each flight concentrated on a region of 100...200 km extent and lasted 1.5...2.5 hours. The flights were made during daylight hours, and with few exceptions had no significant cloud amounts at higher altitudes.

3. CLOUD CHARACTERISTICS

Over the 20 days of the study, stratus of a wide variety were observed on a total of 11 days. Cloud depth varied from 100 to 550 m with the tops of clouds at 250...900 m above the ocean surface. Inversions at cloud top ranged from 1 to 12°C . Temperatures at cloud base were $12\text{...}15^\circ\text{C}$. Within the cloud layers vertical gradients of the equivalent potential temperature ranged within ± 0.3 K per 100 m. Winds changed greatly from day to day both in direction and magnitude, producing a variety of advection and shear patterns within the cloud layers. As expected, vertical air velocities measured by the aircraft, on wavelengths of tens of meters and larger, were $< 10.5\text{ m s}^{-1}$, and small-scale turbulent intensities were characterized by eddy dissipation rates of $< 5\text{ cm}^{-2}\text{ s}^{-3}$.

Most of the stratus encountered during this experiment formed continuous layers with only small-scale perturbations discernible at cloud top. Flight locations were selected to be in the visually most homogeneous

cloud regions. Cloud droplet concentrations also varied from day to day, ranging from 150 to 800 cm⁻³ with no apparent relationship to wind direction. Within the cloud layer and over the region of the flight, droplet concentrations were quite uniform in comparison with the day to day variations. Droplet sizes increased upward, the average diameter reaching values of 10...22 μ m just below cloud top. Liquid water contents (LWC) were up to 0.8 g m⁻³ for the deeper clouds; in all cases the LWC increased upward, with a typical variation between 80% to full adiabatic values at all heights.

The LWC was much less variable at a given level in the cloud than the droplet concentration. This resulted in strong negative correlations between the concentration and the mean size in a manner similar to that reported by Hudson and Svensson (1995). Concentrations and drop sizes fluctuated by factors as large as 2 and 1.3 respectively. Correlation coefficients as strong as -0.76 were found over distances of 5...10 km. Local vertical air velocity and droplet concentration also show evident correlations over limited cloud regions; we have not yet examined the character of this relationship in detail.

Drizzle formed in the majority of clouds in rough proportion to cloud depth, but with several exceptions. Drizzle drops ≥ 100 μ m diameter reached concentrations of $[O]10$ L⁻¹, and precipitation rates ranged to 0.2 mm h⁻¹.

4. RADAR SIGNATURES

Even in cases that appeared most homogeneous, from visual observations and from the parameters monitored by the *in situ* probes, the radar reflectivity patterns were clearly cellular. To a first approximation, characteristic dimensions of the cells were similar to the boundary layer depth, as also found by Paluch and Lenschow (1991). Cloud top boundaries were uniform in all cases. At the bases, precipitation streaks were frequent, quite sheared in some cases. On a broad scale, Doppler velocities were dominated by particle fall velocities, hence they increased toward the base of the clouds. For the light drizzle encountered, the fall velocities reached maxima slightly above 1 m s⁻¹.

Data from one flight (September 14, 1995) will be used here to demonstrate typical cloud characteristics revealed by the radar data. The sample chosen is a case of intermediate cloud depth. In spite of some unusual features, the majority of characteristics to be discussed reflect well what has been seen with other cases examined so far. The most unusual feature of the case is that a stable layer with $\Delta\theta/\Delta z = 12$ K/km extended from the ocean surface to 300 m and the cloud formed in air above that. There was also a wind shear of 20 m s⁻¹ /km from the

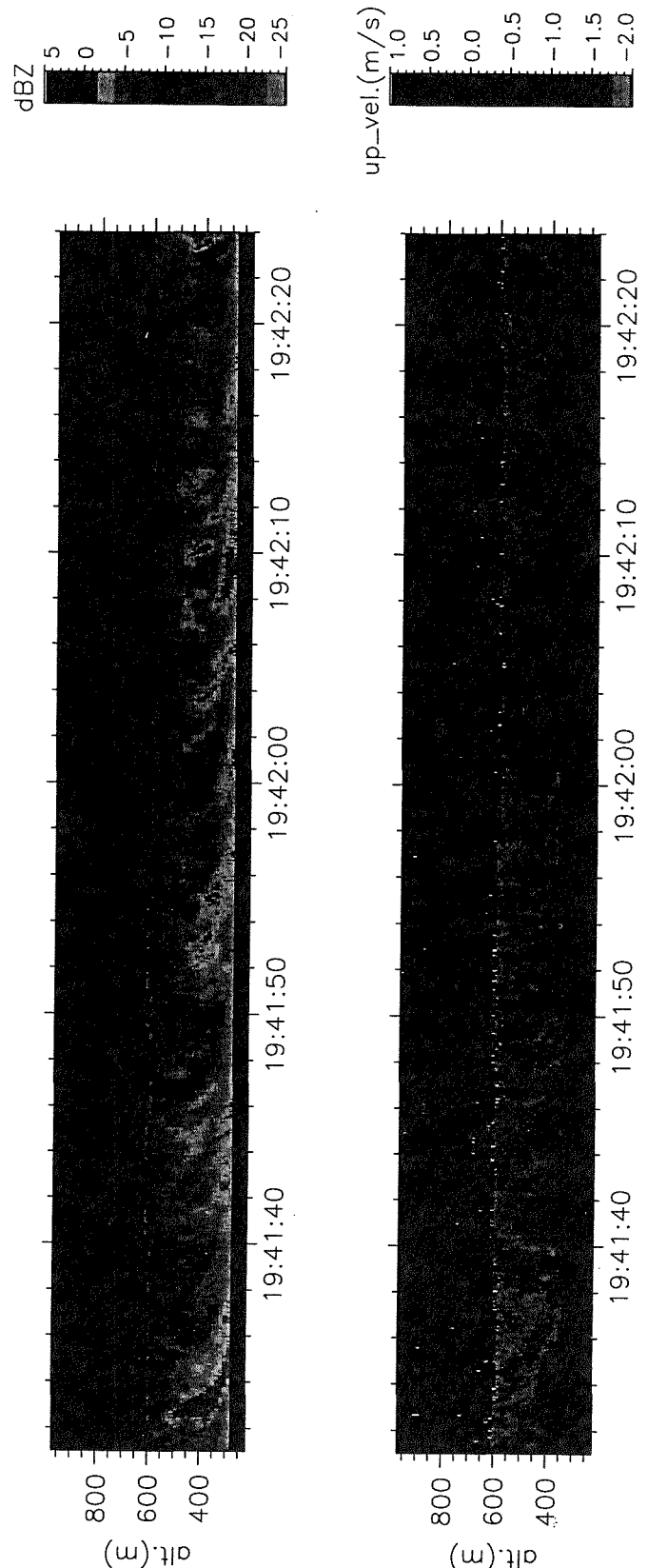


Figure 1. Reflectivity and velocity images for a 1-min flight segment. Horizontal and vertical scales are equal.

surface to near cloud top. The implications of these features haven't been explored yet. During the flight period the off-shore cloud field boundaries extended several hundred kilometers to the west and about 150 km to the north of location of the flight which itself was 30 km west of the coastline. Satellite images show that the cloud field was quite homogeneous in the area. The stratus field started to build at least a day prior to the flight period and with gradually increasing depth persisted at least for another 2 days beyond the time of the flight. In fact, flight data are available from the entire sequence of four days.

Figure 1 shows vertical sections of reflectivity and velocity (positive upwards) for a 1-min flight segment. The images in Fig. 1 cover about 5.5 km in the horizontal. As can be seen, cloud top was near 600 m. The lower edges of the images indicate the closest range from which data were accepted. The aircraft was flying at 155 m above the ocean surface during this period. Drizzle extended to the flight level. The cumulative spectrum of drop sizes, obtained from 1D and 2D imaging probes on the aircraft, had a slope of -5.4 , with a concentration of 10^{-4} L^{-1} at 800 μm diameter. The cellular structure of the reflectivity, with some shear, is clearly evident in the cloud layer (300...600 m). Below 300 m the streaks are more strongly sheared. The velocity image reflects somewhat the same pattern. (Full appreciation of the images requires that they be seen in color.)

A statistical summary of the data shown in Fig. 1 is given in Fig. 2 in terms of vertical profiles. In the panels for reflectivity and velocity, heavy lines indicate the average values of these parameters for given levels. The outermost bands around these lines are the boundaries which contain 90% of the data values. Inbetween, the lines indicate the ranges covered by \pm one standard deviation and the limits for 80% of the values. The right-hand panel shows the correlation coefficients between reflectivity and velocity for each level. This figure illustrates the patterns generally observed: both the reflectivity and the magnitude of the velocity increase from cloud top toward cloud base. There is more variation in the shapes of the upper percentile bands; in this case there is a notably broad region near 400 m altitude. Other data segments for the same day confirm that this isn't just a transient phenomenon. On the other hand, the spread of velocity values is quite small for these data, and for this day in general.

The pattern shown by the correlation coefficients for this case is typical of the other cases as well. Negative correlations at low altitudes indicate that stronger-than-average reflectivity regions have larger-than-average downward velocities. The correlation then decreases with altitude, changes sign and reaches the highest positive values near cloud top. Positive correlations indicate regions where lower-than-average reflectivities have smaller-than-average upward velocities. The variation

of the correlation with altitude is quite regular and has remarkably little scatter; this is also a general finding.

The scales of horizontal variability also changed systematically with altitude. This is demonstrated in Fig. 3. Frequency spectra were generated for the reflectivity, velocity and cross-correlation fields; the diagram depicts the magnitudes of the spectral densities as functions of frequency and altitude. A frequency of 1 Hz corresponds to a wavelength of 84 m and 0.1 Hz to 840 m. The dominant scales in the reflectivity variation are near 800 m for altitudes below 400 m and then changes to shorter scales. A mixture of two scales is present near the 400-m level. The change occurs at the level where the reflectivity field becomes dominated by 'cells'. Below that level 'streaks' dominate the visual appearance of the reflectivity field. The scales of variability in velocity and in cross-correlation resemble those of the reflectivity field. The change in sign in the cross-correlation accompanies the change in scale.

5. SUMMARY

The combination of *in situ* measurements from the aircraft and the near-environment remote sensing by the 95 GHz radar provide new possibilities for the description of cloud structure. Both hydrometeor distributions and motions are better described than with either system alone.

In the stratus cases here described, the radar data clearly show a cellular cloud structure not readily detectable, if at all, in the data from the *in situ* probes. Also, with the low drizzle drop concentrations of shallow stratus the imaging probes suffer from inadequate sampling.

More complete interpretations of the observed structure, of the change in dominant scales with altitude and the smaller-scale patterns observed in the data will require further work. At this stage features that appear to apply to most cases are the increase in average reflectivity from cloud top toward the base, the corresponding increase in the magnitude of the velocity and the smooth change from negative to positive correlations between reflectivity and velocity. The first two of these characteristics are in broad agreement with picturing the development of drizzle by coalescence in the absence of significant vertical air motions. However, the reversal in correlation indicates the weakness of that simple model and must be interpreted as a sign of descending air motions accompanied by partial evaporation of cloud. Whether these motions are driven by turbulence or entrainment is not resolved by the analyses we have done so far. The relative constancy of LWC places important additional limits on the quantitative aspects of the process.

For the specific case study presented, interesting questions arise with respect to how the cloud was maintained in spite of the underlying stable layer, which would have limited vapor transport from the ocean surface. A rough model of the situation may be constructed on the basis of cooling within the cloud layer due to mixing with the sub-cloud air and internal circulations in the cloud layer being driven principally by cooling associated with entrainment at the cloud top.

Acknowledgements: This work was funded by the Office of Naval Research. Acquisition of the radar was funded in part by the ONR and in part by the National Science Foundation, Division of Atmospheric Sciences. We thank the tremendous support of this work by the Department of Atmospheric Science staff and by A. Pazmany.

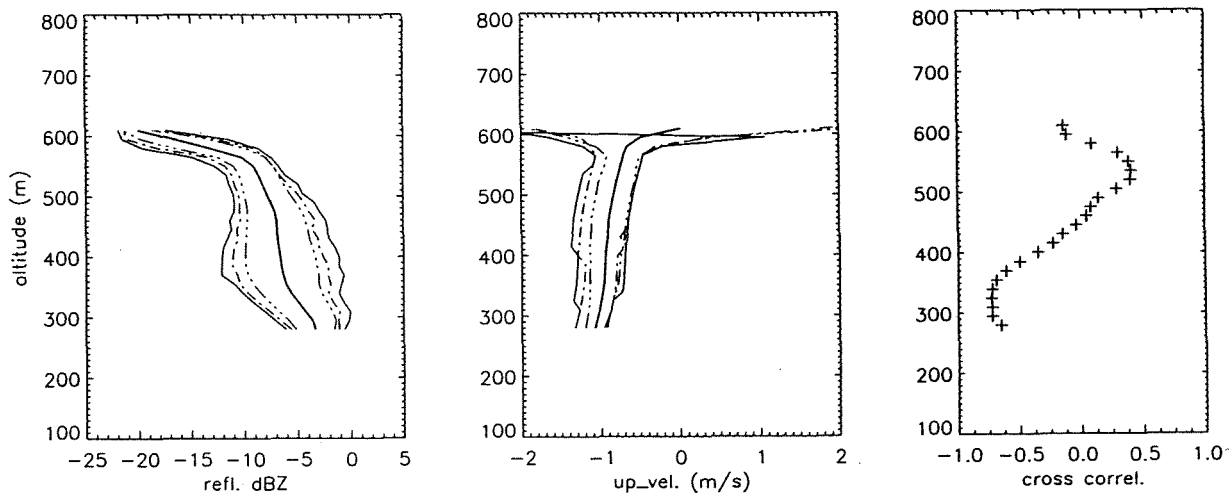


Fig. 2. Vertical profiles of radar reflectivity, Doppler velocity and reflectivity/velocity correlation coefficient.

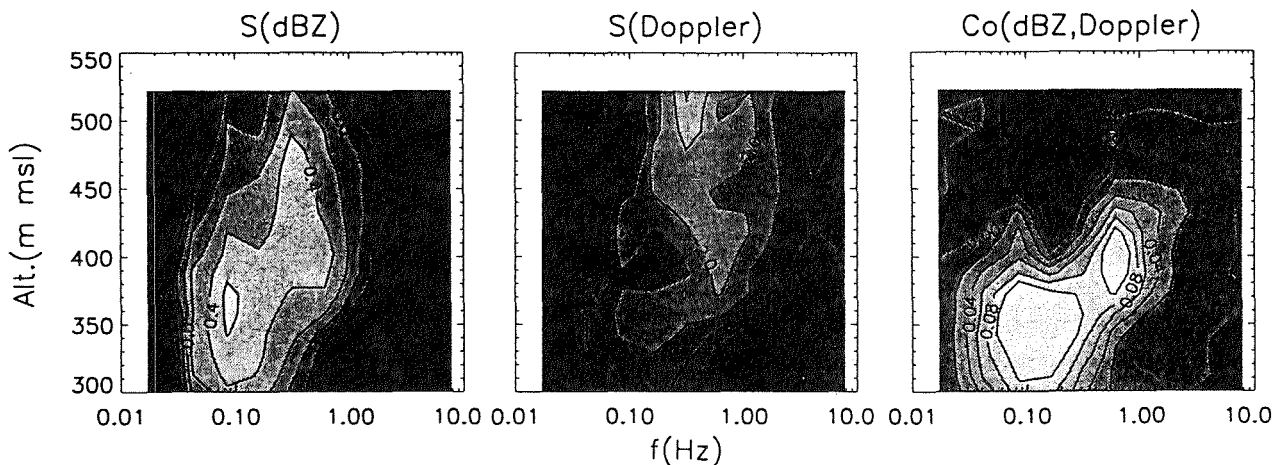


Fig. 3. Spectral density for reflectivity, velocity and cross-correlation as functions of altitude.

6. REFERENCES

- Hudson, J.G. and G. Svensson, 1995: Cloud microphysical relationships in California marine stratus. *J. Appl. Meteor.*, **34**, 2655–2666.
- Paluch, I.R. and D.H. Lenschow, 1991: Stratiform cloud formation in the marine boundary layer. *J. Atmos. Sci.*, **48**, 2141–2158.
- Pazmany, A.L., R.E. McIntosh, R.D. Kelly and Gabor Vali, 1994: An airborne 95 GHz dual-polarized radar for cloud studies. *IEEE Trans. Geosci. Remote Sens.*, **32**, 731–739.
- Vali, G., R.D. Kelly, A. Pazmany and R.E. McIntosh, 1995: Airborne radar and in-situ observations of a shallow stratus with drizzle. *Atmos. Res.*, **38**, 361–380.

SMALL-SCALE STRUCTURES OF ARCTIC STRATUS CLOUDS DURING SUMMERTIME

Andreas Reuter and Frank Albers

GKSS Research Center, Institute for Atmospheric Physics, 21502 Geesthacht, FRG

1. INTRODUCTION

During summertime, persisting decks of clouds can be found in the Arctic. While the majority of scientists working on this issue some decades ago fostered the idea that these clouds are mainly single layered stratus, there is recently a shift towards the concept of multi-layer decks in the planetary boundary layer during the arctic summer. These clouds significantly modify the earth's radiation budget as well as the vertical fluxes of heat, moisture and momentum and therefore influence the melting rate of the underlying pack ice (Curry, 1986).

2. THE EXPERIMENT REFLEX III

To study the interactions between the sea ice covered ocean and the atmospheric boundary layer, a series of experiments called REFLEX (for Radiation and Eddy Flux Experiment) was started in 1991 by AWI (Alfred Wegener Institute for Polar and Marine Research, Bremerhaven, FRG). REFLEX III took place on Svalbard (Spitzbergen) from June 15th to August 2nd, 1995 and for the first time also included the measurement of aerosol and cloud particles in cooperation between GKSS and AWI. During 19 flights, the conditions in the atmosphere north of Svalbard up to latitudes of 82 °N had been investigated.

3. INSTRUMENTATION

During REFLEX III, the Polar 4 aircraft which is a Dornier DO 228 type owned by AWI, was equipped to operate four PMS probes for in situ measurements. The standard configuration is given in table 1. The 2D-GA2 (2D-Greyprobe) was provided by the University of Hamburg where the other probes are owned by GKSS. The data was recorded by a SEA (Science Engineering Associates, Willington, CT, USA) Model 200 data acquisition system. This combination was chosen

to cover the entire particle sizerange between 0.1 and 800 μm thus enabling the analysis of aerosols and ice crystals beside the detection of cloud droplets. Additional data including temperature, humidity and short- and longwave radiation fluxes had also been recorded onboard the aircraft and have been mainly analyzed by AWI.

In this work, only data from the FSSP-100 which covers the sizerange of the cloud droplets is presented. FSSP data was recorded at 50 Hz.

Name	Size Range / μm	Channels
PCASP-100X	0.1 - 3.0	15 unequally spaced
FSSP-100	2 - 32	15
OAP-2D2-C	25 - 800	32 ^(*)
OAP-2D-GA2	10 - 620	64 ^(*)

TABLE 1: Summary of the PMS probes, used during REFLEX III onboard the POLAR 4 aircraft.

4. MULTI-LAYER SYSTEMS

Frequently, multi-layer cloud systems had been encountered during REFLEX III. One of the striking features for many of these cloud decks was the presence of even large ice crystals up to 1.5 mm in the upper decks at temperatures between 0 and -5° C. Figure 1 shows examples of large ice particles recorded with the 2D-Greyprobe at a temperature of -2.8 °C. Compared to former experiments in the polar regions, the occurrence of these large crystals at relative warm environmental temperatures is unusual (J. Curry, private communication, 1995).

^(*) For Optical Array Probes, the number of photodiodes is usually used as an equivalent for the number of channels, as it is done here.

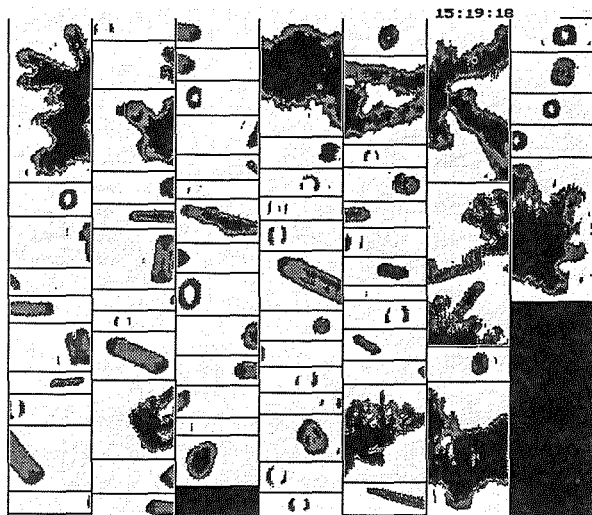


FIGURE 1: Example of large ice crystals, found in the upper layer of a multi-layer system on July 28th, 1995 at 15:19:18 UTC (2D-Greyprobe data). The temperature was -2.8°C .

The morphology of one of the multi-layered decks is illustrated in Fig. 2. A cross section of the liquid water content along the flight track was generated for this reason. By doing so, the influence of the

general air motion which was perpendicular to the flight track had to be neglected. Therefore, Figure 2 gives no authentic cross section but can only be treated with the mentioned limitations. Nevertheless, this procedure seems to be valuable to demonstrate the complex morphology of this multi-layer cloud deck. Between 7500 and 9000 m distance from point B (82°N , 7°E), there is a zone where precipitation is falling from the upper layer into the layer below. The microphysical situation in this regions needs further investigation which is one of the major tasks for future data analysis. Regarding the interactions between microphysics and radiation, this example suggests to apply radiation transfer models which account for the complex morphology of multi-layer cloud systems.

5. SINGLE-LAYER SYSTEMS

On July 24th, 1995 the stratus was a single-layered one. Average values for number density, diameter and liquid water content agree well with literature. The usual linear increase of diameter and liquid water content with height could be proved (see Fig.

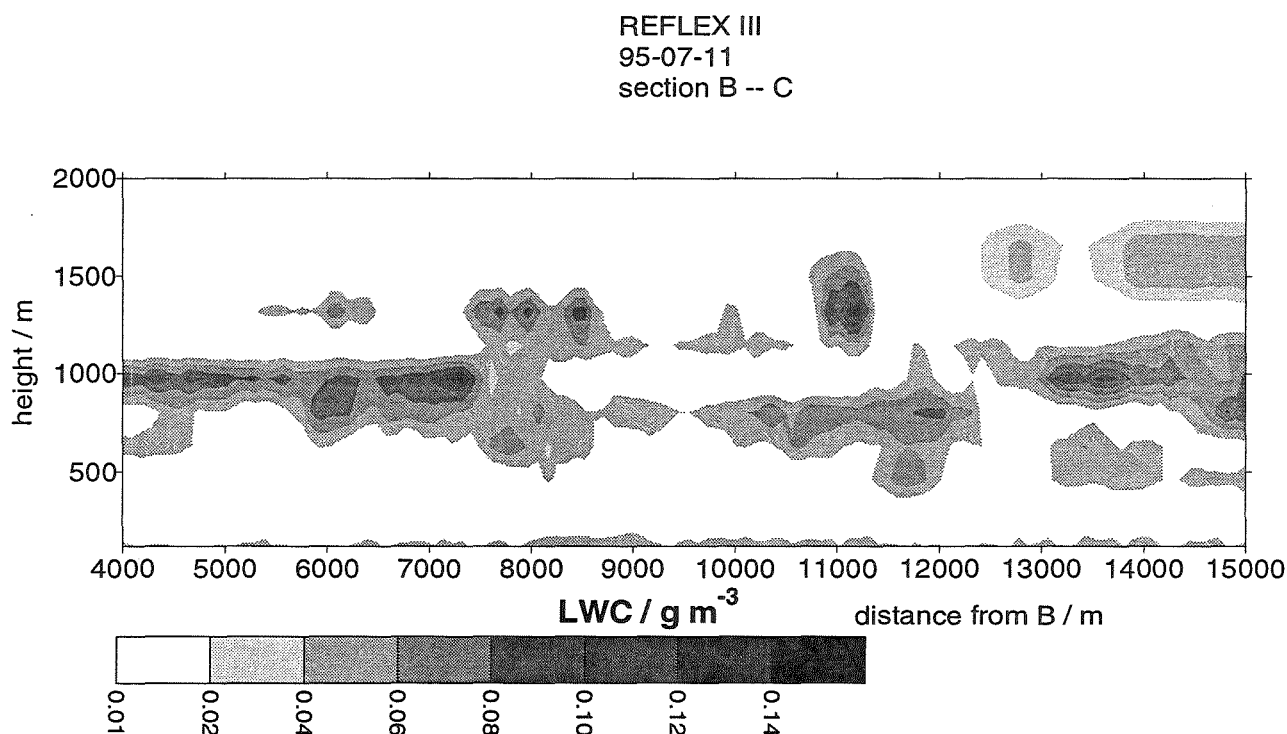


FIGURE 2: Cross-section of a multi-layered stratus along the flighttrack between points B \leftrightarrow C ($B = 82^{\circ}\text{N}$, 7°E ; $C = 82^{\circ}\text{N}$, 9°E). Between 7500 and 9000 m there is a zone where precipitation is falling from the upper layer into the layer below.

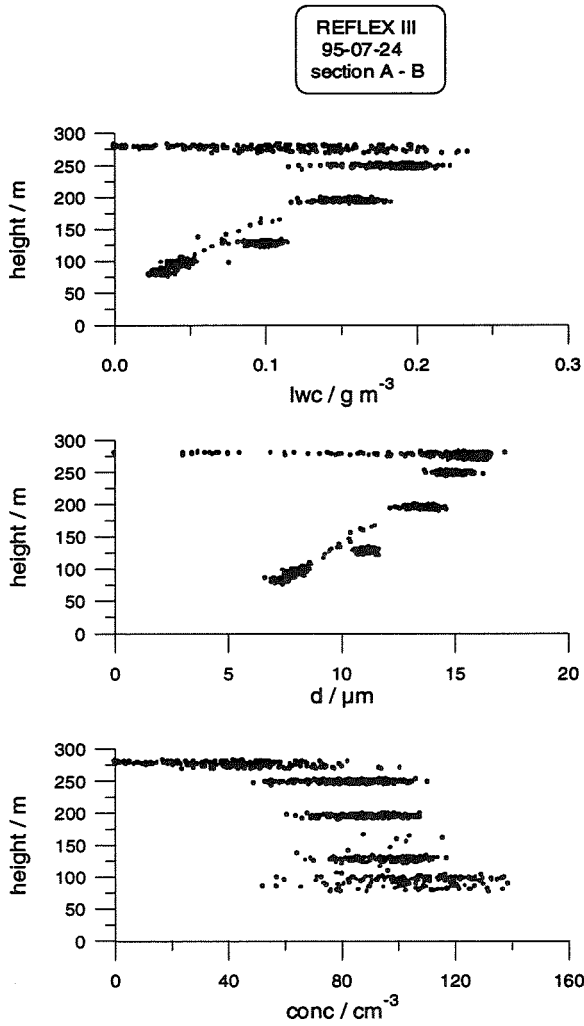


FIGURE 3: Number density, average diameter and liquid water content vs. height for a single-layered stratus. The values agree well with literature. The linear increase of the average diameter and liquid water content with height is typical for pure water stratus clouds.

3). Near cloud top, the variations along the horizontal flight leg show large variations, indicating inhomogeneous structures. Individual vertical profiles taken along a distance of 15 km (Fig. 4) yet differ significantly and show remarkable deviations from the horizontally averaged values. The maximum liquid water content of the profiles differs by a factor of about 3 and the height of the zone containing the maximum LWC differs from the lower third of the stratus (at 9920 m distance from point D) to the upper third of the cloud (at 1260 m distance from D). The effect of inhomogeneity was further investigated by creating a cross section of the stratus along the

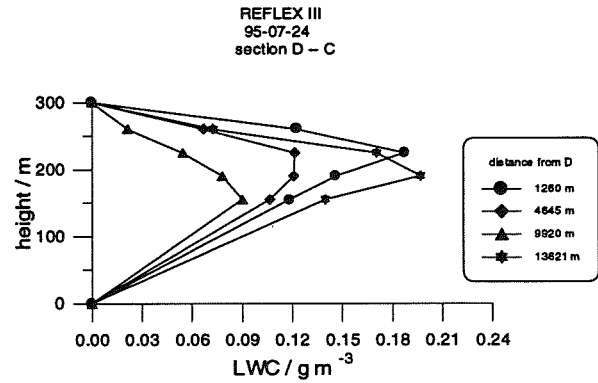


FIGURE 4: Individual profiles of the liquid water content along a horizontal distance of 15 km at different distances from point D (80.83 °N, 10.87 °E).

flight leg (Fig. 5). It shows that the maximum liquid water content is not distributed well-balanced at a certain altitude but generates cells in the upper half of the cloud. This corresponds to the presence of cloud droplets with the maximum diameter.

6. CONCLUSIONS AND OUTLOOK

The presented case of July, 24th can be seen as a classical one. It is a single-layered stratus cloud consisting only of water droplets. It was selected as a first starting point for the analysis. The average values for the liquid water content, diameter and number concentration agree well with literature (e.g. Curry, 1986). Also the intensity of small-scale inhomogeneity given by the parameter P (Baker et al., 1982) is comparable to published results of other scientists (Fig. 6). P is the percentage of drop concentrations which satisfy one of the conditions:

$$N > \bar{N} + 2\sqrt{\bar{N}}$$

or

$$N < \bar{N} - 2\sqrt{\bar{N}}$$

But even under these conditions the individual liquid water profiles taken along a distance of less than 15 km differ significantly. Therefore, it is questionable whether this cloud deck can be treated as homogeneous when e.g. investigating the interactions between microphysics and radiation. Frequently, one-dimensional radiation transfer models are used to calculate heating and cooling rates for stratus clouds. These models are not capable of accounting for any horizontal structures of the cloud.

In the future, the microphysics of arctic stratus will be analyzed on a higher spatial resolution (2-5 m), taking full advantage of the 50 Hz sampling rate of the FSSP-100. In addition, multi-layer cloud decks will be investigated to study seeding processes of ice crystals, settling from the glaciated upper layers into the lower, pure water layers. Another focus will be set on the interactions between cloud microphysics and radiation to achieve better parameterizations for the exchanges between the sea ice and the cloud topped boundary layer above.

7. REFERENCES

- Baker, M. B. and Collaborators, 1982: Field studies of the effect of entrainment upon the structure of clouds at Great Dun Fell. *Quart. J. Roy. Meteor. Soc.*, **108**, 899-916.
- Curry, J. A., 1986: Interactions among Turbulence and Microphysics in Arctic Stratus Clouds, *J. Atmos. Sci.*, **43**, 90-106.

Kottmeier, C., J. Hartmann, C. Wamser, A. Bochert, C. Lüpkes, D. Freese and W. Cohrs, 1994: Radiation and Eddy Flux Experiment 1991 (REFLEX I). *Berichte zur Polarforschung*, **133**.

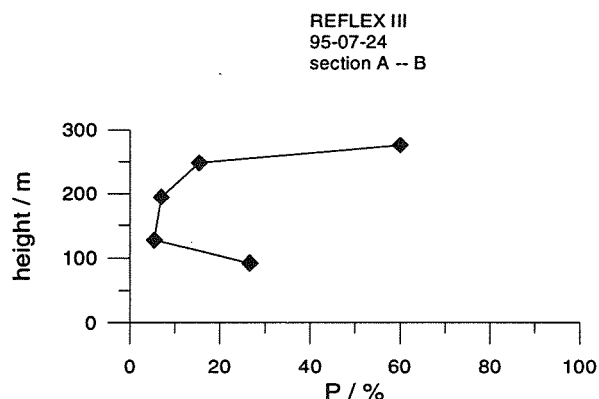


FIGURE 6: The parameter P (Baker et al., 1982) indicating small-scale inhomogeneities for the cross-section A \leftrightarrow B of July, 24th (see. Fig. 5). Large values for P refer to legs with strong small-scale inhomogeneities, which occur mostly near cloud top and cloud base.

REFLEX III
95-07-24
section A -- B

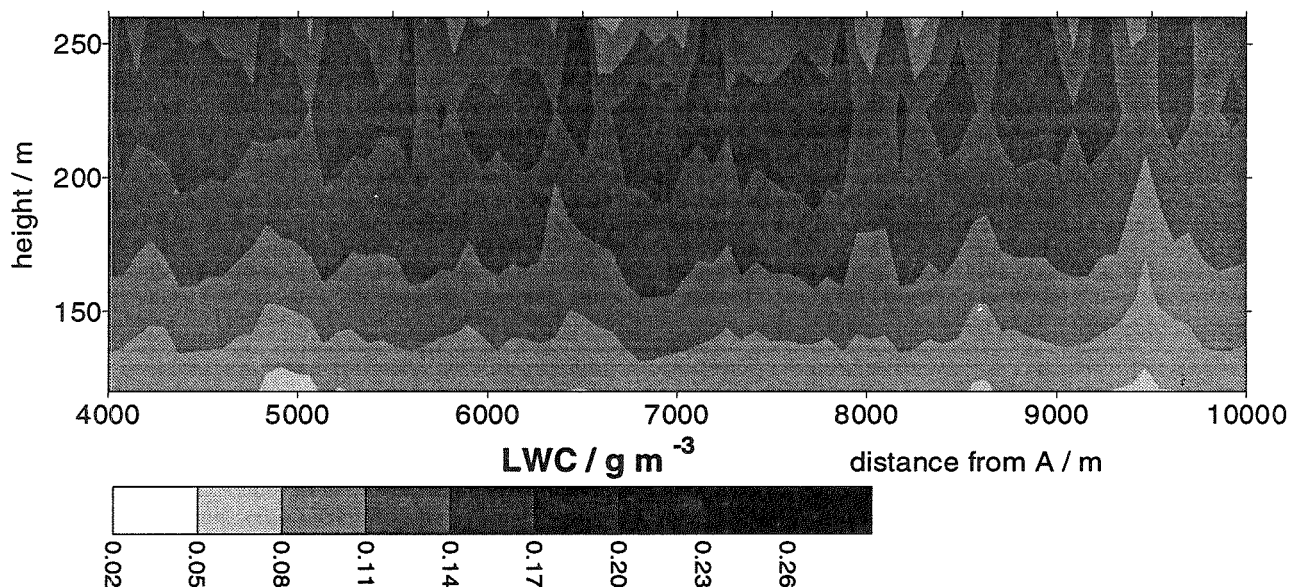


FIGURE 5: Cross-section of the stratus along the flight track between points A \leftrightarrow B (A = 80.83 °N, 10 °E; B = 80.97 °N, 10 °E). The zones containing the maximum liquid water content generate cells, located in the upper half of the stratus

STRUCTURE OF A TEMPERATURE FIELD IN SMALL CUMULI ON A CENTIMETER SCALE

Krzysztof E. Haman and Szymon P. Malinowski
Institute of Geophysics, University of Warsaw, Poland.

1. INTRODUCTION

It is known already for several years that small scale features in Cumulus clouds, resulting from inhomogeneous entrainment and mixing, play an essential role in determining microphysical and radiative properties of clouds (see e.g. Jensen and Baker 1989). The fact that mixing is not instantaneous, but consists of a cascade of steps with different time scales may be important not only for evolution of droplet spectra but - as shown recently by Haman and Pawlowska (1995) - for bulk dynamics of the cloud as well. Increasing interest in the small scale structure of clouds resulted in a number of theoretical and empirical studies devoted to this subject and further efforts in this direction are being continued.

The present paper deals with first measurements of temperature in clouds with resolution going down to centimeters i.e. two orders of magnitude better than any earlier results. They are performed with a new thermometric unit named UFT (for Ultra-Fast Thermometer) developed at University of Warsaw (Poland) in cooperation with DLR (Germany). Technical details on this instrument are given in the paper by Haman et al. (1996). Its sensor is made of $2.5\mu\text{m}$ thick, platinum-coated tungsten wire protected against impact of cloud droplets in a way which creates only negligible disturbances in the air temperature. Empirically determined time constant of this thermometer is about 2×10^{-4} s. The instrument is still under development and its prototype versions have yet some drawbacks, like high frequency aerodynamic noise (which becomes a problem at speeds over 40m/s), or drift of the record towards higher temperatures (happening sometimes due to certain manufacturing faults). Thus until now, the UFT was used for measuring temperature fluctuations rather than its absolute values, with possibly frequent recalibration against another thermometer.

Preliminary results of measurements made with use of UFT in Cumulus mediocris clouds in summer 1994 were presented at AMS Cloud Physics Conference in Dallas, January 1995, and in more detailed form in a paper by Haman and Malinowski (1996). In these measurements the UFT was installed on a motor glider flying with airspeed of about 27m/s - 30 m/s. Because

of relatively poor recorder (12 bit, 0.04K/bit resolution, 1kHz sampling rate with 300Hz low-pass filter) the advantage of fast response of UFT could not be fully taken. Nevertheless a number of interesting and sometimes surprising centimeter-scale features were detected.

In August 1995 an UFT unit has been installed on the French Merlin IV research aircraft, participating in Small Cumulus Microphysics Study (SCMS) in Florida. In September 1995 a new recorder with 16 bit (about 0.002K/bit) resolution and 10kHz sampling rate with 5kHz low-pass filter became available on the motor glider in Warsaw, yielding essential improvement in measurement quality. Unfortunately, poor weather conditions permitted only one flight. Some preliminary results from these measurements are presented below.

2. SCMS FLIGHTS

On the Merlin IV the UFT sensor has been mounted on the one FSSP container on the right side of the fuselage, about 2m from the Rosemount thermometer which could be used for comparisons. The sampling rate of the Merlin IV recording system was only 200Hz with 80Hz low-pass filter. This limited spatial resolution of measurements to 50 cm at 100m/s airspeed (typical for the Merlin's research flights), but on the other hand it filtered the aerodynamic noise, reducing its range to tolerable $\pm 0.2\text{K}$.

As an example of results collected during this experiment some data from a selected fragment of flight No 6 (August 5, 1996, 13:25 EDT= GMT-4) are presented in Fig. 1. These data were collected in upper parts of a maritime Cu med cloud in area of Kennedy Space Center (Cape Canaveral) at 755hPa level with $\pm 2\text{hPa}$ variations. Regretfully, an aerological sounding representative for this flight was unavailable to the authors at the time this paper was written. Figs 1a and 1b present the temperature records from UFT and Rosemount probe for the whole selected fragment of Flight 6. Fig. 1c gives the distribution of LWC on this fragment from Johnson-Williams (J-W) probe (recorded with 25Hz sampling frequency). Figs. 1d and

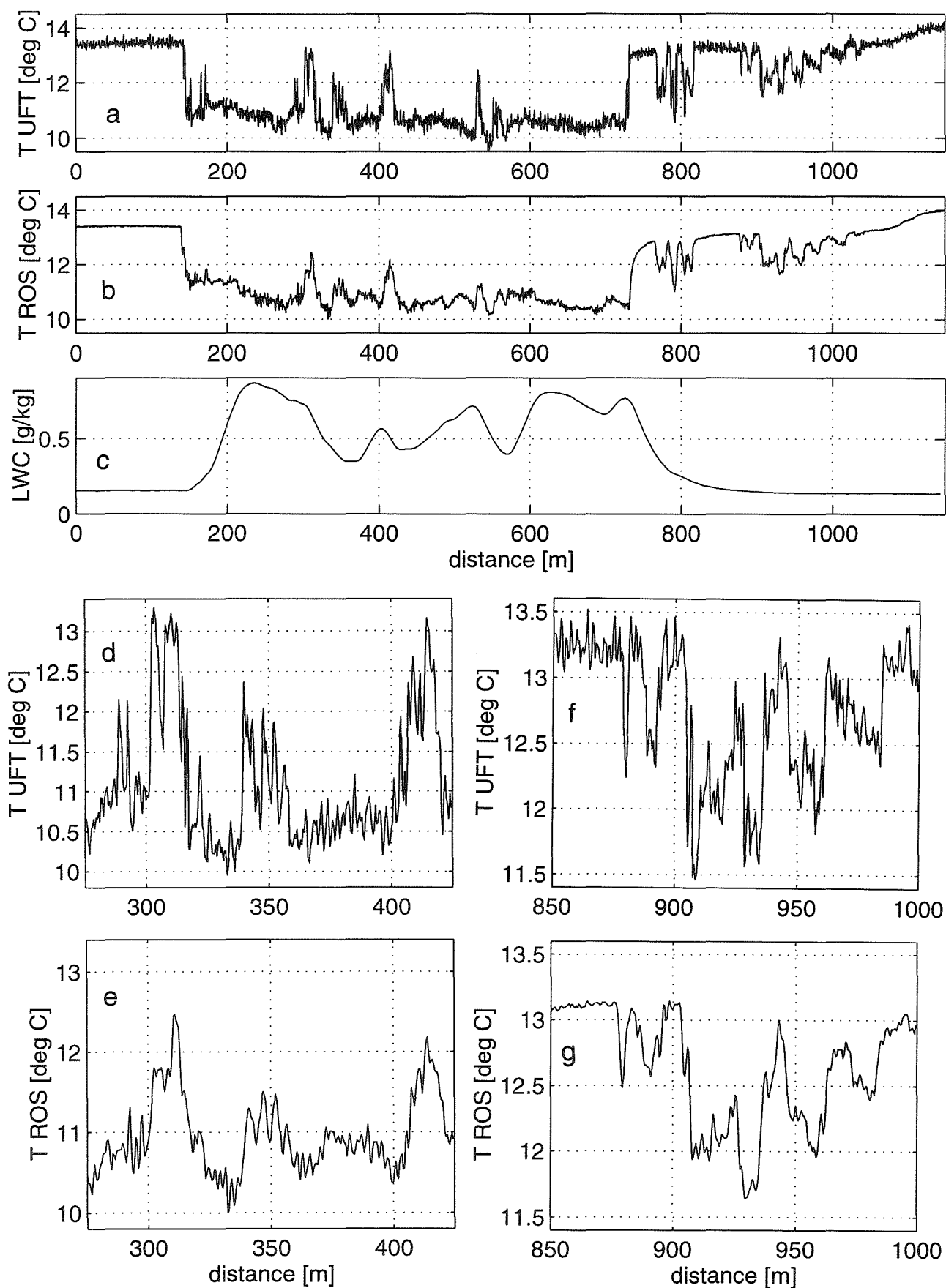


Fig. 1. Temperature and liquid water content (LWC) records from a selected fragment of SCME Merlin IV Flight No 6 in function of the flight path length in meters. This length is conventionally determined as a product of the recording time by 100m/s (approximate airspeed of the aircraft) and counted from an arbitrarily chosen beginning, the same for all subfigures. See text for other details.

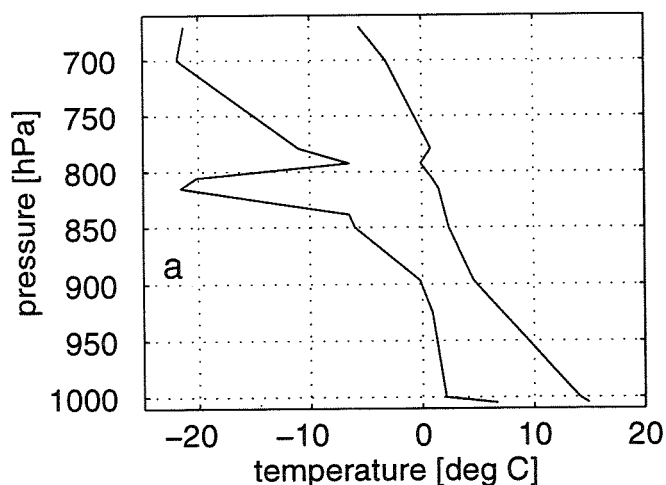
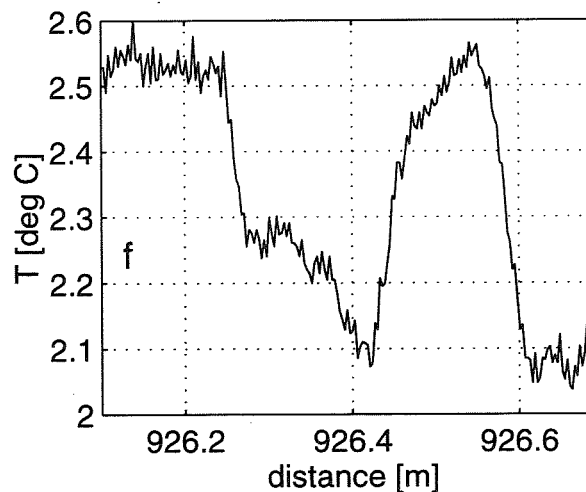
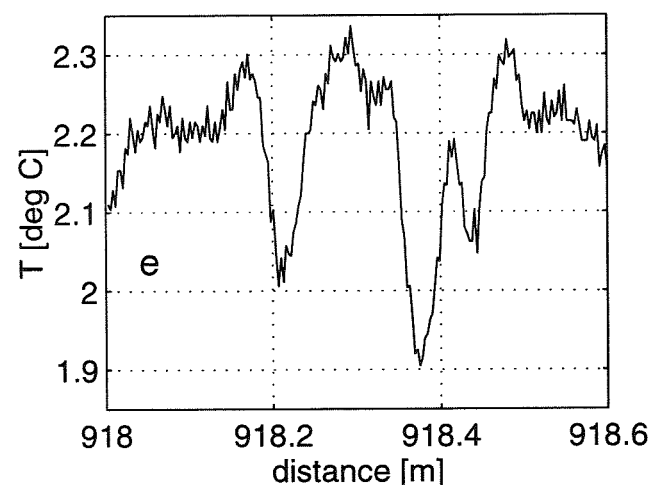
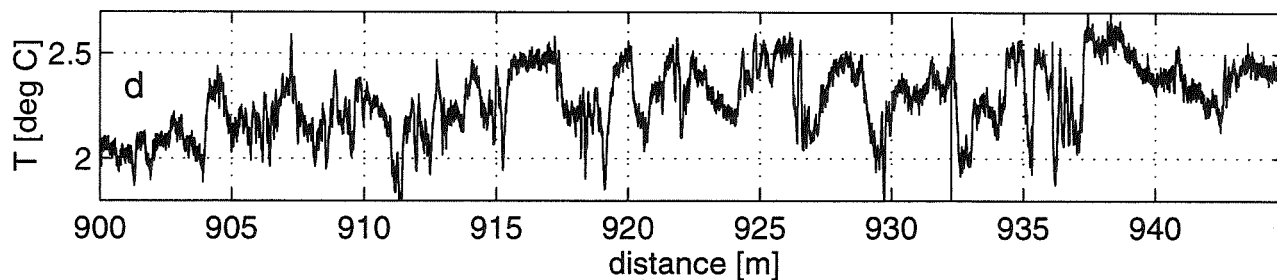
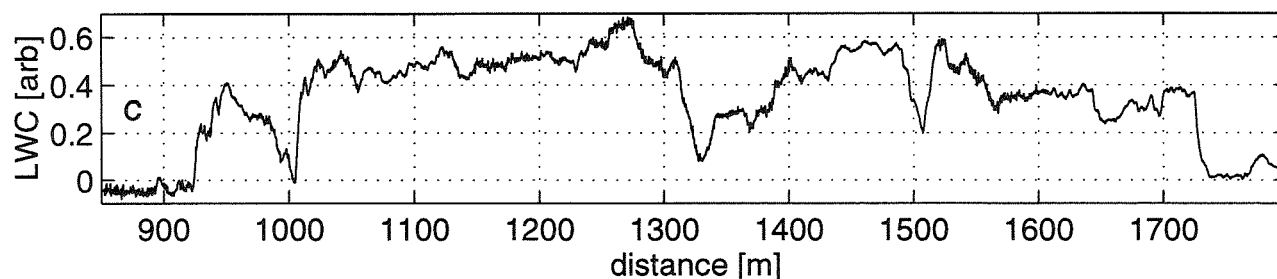


Fig. 2.a Temperature (right) and dew-point (left) 22 September 1996, 12 GMT aerological sounding from WMO 12374 station Legionowo, about 20 km from the operation area of "Ogar".

Figs 2b – e. Temperature from UFT and liquid water content (2c) records for penetration No 4 of the 22 September 1996 flight, in function of the flight path length. This length is conventionally determined as a product of the recording time by 30 m/s (approximate speed of the aircraft) and counted from an arbitrarily chosen beginning, the same for all subfigures. See text for other details.



1e show segments of Figs 1a and 1b respectively, expanded in order to present the full available spatial resolution (about 0.5m per sample) of the temperature field in presumable mixing region inside the cloud (as follows from the J-W record). Figs 1f and 1g are analogous to 1d and 1e but for a mixing region outside the cloud. Notice intermittent structures only few samples thick with temperature differences of 2-3K, visible on the UFT record even after damping by the 80 Hz low-pass filter, as well as thin transition layers (not more than 1 sample = 0.5m thick) between regions of extremely different temperatures. Since the UFT record is not corrected for dynamic heating, some low-frequency 0.2 - 0.3K differences between it and Rosemount record might be attributed to variations of air-speed, but certain others evidently suggest wetting effects on Rosemount sensor. Loss of some essential details due to slower response of the latter is also evident.

3. FLIGHT 22 SEPTEMBER 1996

This flight was made from the Warsaw-Babice airport on motor-glider Ogar, at 14:32-15:35 LT (GMT + 2). The sensor was placed on a one meter long nose boom (Ogar has pushing propeller). The records were taken during penetrations made through small Cu med clouds along straight lines at altitudes 1400m-1500m a.g.l. (860hPa - 850hPa), 250m-350m above the cloud base and about 100m -150m below the top. Height variations were not exceeding ± 20 m in each penetration. The sampling frequency was 10kHz after conditioning the signal with the 5kHz second order Butterworth low-pass filter, permitting spatial resolution of 3mm at 30 m/s. Unfortunately, the thermocouple thermometer serving usually as a reference failed in this flight, so calibration of the UFT is only approximate; the magnitudes of temperature fluctuations given in Fig.2 are accurate within about 5%.

Selected results from this flight are shown on Fig.2. Fig.2a gives the aerological sounding representative for the time of the flight. Fig.2b gives a general view of the temperature record taken during the penetration No 4 made through an upper part of Cu med cloud about 150m below the top. Fig. 2c gives the same for liquid water content as shown by an uncalibrated experimental LWC-meter. Figs 2d shows an expanded segment of the record from Fig.2b, while Figs 2e and 2f present more expanded subsegments of Fig. 2d, exposing full available spatial resolution of the UFT with the new recorder.

As in earlier flights, intermittent slices with sharp temperature differences are visible in the mixing region of the cloud. The lower limit of thickness of such slices found in this flight was about 10cm but transition layers between neighboring ones thinner than about 3cm were

not detected. It is worth of noticing that similar numbers were found in 1994, but then they could be attributed to poorer resolution of the recorder. One may hypothesize that 3cm is a sort of critical scale separating different regimes of mixing in Cumulus clouds. Let us notice that a very similar conclusion follows from certain laboratory experiments on mixing in clouds presented in an another paper in this issue (Banat and Malinowski, 1996). If confirmed, this would be an important statement, but the present set of data is too small for making it sure. Thus further measurements of such sort are planned.

4. ACKNOWLEDGMENTS

Cooperation of Centre National de Recherches Météorologiques, Toulouse, France and the team of the French research aircraft Merlin IV, F-GMTO, as well as the National Center for Atmospheric Research, Boulder, Co, USA is highly appreciated. The work was supported by the Grant #6P04D00908 of the Polish State Committee of Scientific Research.

5. REFERENCES

- Banat, P., and S. P. Malinowski, 1996: Anisotropy in turbulent mixing of clouds with clear air in small scales. *In this issue*.
- Jensen, J. B., and M. B. Baker, 1989: A simple model for droplet spectral evolution during turbulent mixing. *J. Atmos. Sci.*, **46**, 2812-2829.
- Haman, K. E., and H. Pawłowska, 1995: On the dynamics of non-active parts of convective clouds. *J. Atmos. Sci.*, **52**, 519-531.
- Haman, K. E., and S. P. Malinowski, 1996: Temperature measurements in clouds on a centimeter scale - preliminary results. *Atmos. Research*, in press.
- Haman, K.E., A. M. Makulski, S.P. Malinowski, and R. Busen, 1996: A new ultra-fast thermometer for airborne measurements in clouds. *J. Atmos. Oceanic Technol.*, in press.

Summary of Some Cloud Transport and Dispersion Experiments Using a Gaseous Tracer and Radar Chaff

Paul L. Smith, Trace A. Bowen, Andrew G. Detwiler¹, Jeffrey L. Stith², Brooks E. Martner and Roger F. Reinking³

¹Institute of Atmospheric Sciences, South Dakota School of Mines and Technology, Rapid City, South Dakota, USA

²Center for Aerospace Sciences, University of North Dakota, Grand Forks, North Dakota, USA

³Environmental Technology Laboratories, NOAA, Boulder, Colorado, USA

1. INTRODUCTION

Many lines of argument suggest that the development of hail begins in clouds (often called feeder clouds) flanking a mature storm cell that produces most of the precipitation. Considerations of particle residence times and growth rates in the strong updrafts of the mature cell suggest that development of hailstone embryos outside of the main updraft is necessary. Several numerical modeling studies of particle growth trajectories (e.g., Heymsfield 1982; Knight and Knupp 1986; Miller *et al.*, 1990) have indicated that embryos initiated in the feeder clouds can be carried into the favorable growth environment around the mature-cell updraft. The hail-suppression seeding procedures used by the North Dakota Cloud Modification Project (Boe 1992) and in other similar projects rely on this concept and introduce glaciogenic seeding agents into the feeder clouds with the objective of reducing the eventual hail production in the mature cell.

Direct confirmation of this particle transfer process has been lacking. The trajectory-modeling studies generally treat only individual particles in somewhat idealized environments, and take no account of possible interactions among precipitation-sized hydrometeors. Even with the storm wind fields derived from Doppler radar data, an element of uncertainty remains regarding actual particle trajectories.

About a decade ago tracer experiments were initiated in North Dakota to study transport and dispersion processes in convective clouds and storms. The primary focus has been on the transport and dispersion of seeding agents in the clouds, as the initial link in the chain of events leading to hypothesized modification of the precipitation produced. Examples of the early work are reported in Stith *et al.* (1990) and Huston *et al.* (1991). Building on this work, the 1989 North Dakota Thunderstorm Project (Boe *et al.*, 1992) and the 1993 North Dakota Tracer Experiment (Boe *et al.*, 1994) involved a series of tracer experiments focusing on hypothesized processes of transport and dispersion in clouds. Two types of these experiments concen-

trated on feeder cloud-mature cell systems. One type involved tracer releases at the bases of the feeder clouds (e.g. Stith *et al.*, 1996; Reinking and Martner 1996), which is a common mode of seeding in the NDCMP operations. The other involved releases at mid levels in the feeder clouds, designed to facilitate investigation of the transport between feeder cloud and mature cell. This paper provides an initial summary of the results from the latter category of experiments.

2. EXPERIMENT DESIGN AND PROCEDURES

Figure 1 illustrates the basic experimental design. The tracer release aircraft (a Duke) dispensed the tracer material(s) into the feeder cloud during a pass through the cloud between the 0°C and -5°C levels. The tracer could be either SF₆ or radar chaff, or both; on some occasions a seeding agent was also released at the same time. Research aircraft then penetrated the clouds at higher levels to search for the SF₆ tracer. The South Dakota School of Mines and Technology armored T-28 penetrated at about the -8°C level and could fly through the feeder cloud and on into the mature cell along the suspected transport paths. The University of North Dakota Citation searched for the SF₆ at higher levels in the feeder cloud. Meanwhile, a National Oceanic and Atmospheric Administration X-band radar with circular-polarization capability, useful in discriminating between chaff and precipitation echoes via the TRACIR technique (Martner *et al.* 1992), scanned the storm system to collect data on movement of the chaff. Other C-band Doppler radars also scanned the storm to determine the basic reflectivity structure and wind fields.

Flight tracks determined from Loran or GPS navigation systems and telemetered to the Operations Center, where they could be related to the radar echo structure, facilitated conduct of the experiments. Penetrations of the storm system were then guided by directions radioed from the radar site. In addition, the Citation used a Lagrangian pointer system that could be set in its airborne computer to facilitate returning to the same point in the cloud on succeeding penetrations.

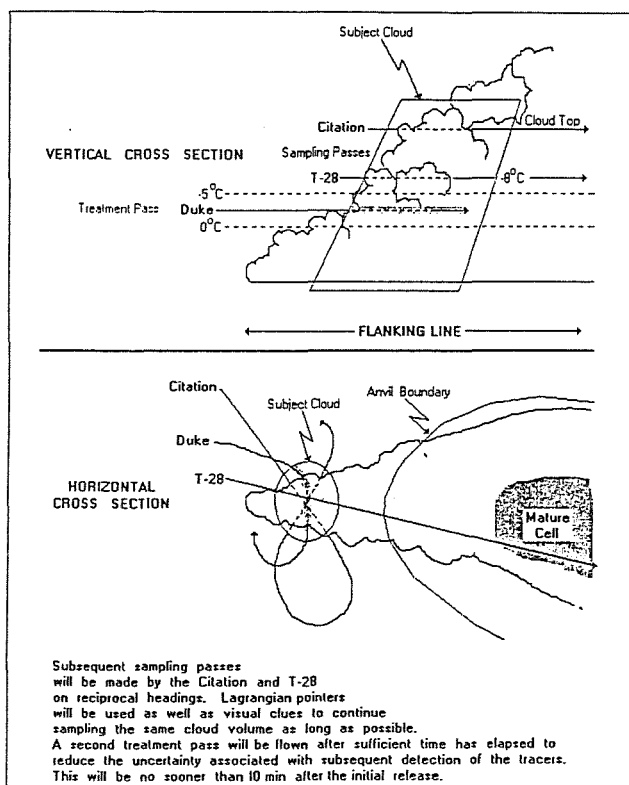


Figure 1: Flight plans for experiment involving mid-cloud treatment of feeder clouds in a flanking line adjacent to a mature cell.

3. SUMMARY OF EXPERIMENTS

A total of 22 mid-cloud feeder-cell experiments were conducted during the NDTP and NDTE. Some of the early NDTP experiments were conducted in marginal clouds in order to test and refine the experimental procedures. All cases involved SF₆ and about half of them involved concurrent chaff releases. In 1989 the chaff and SF₆ were dispensed from separate aircraft, and the focus was on the SF₆ tracer. The 1993 cases in which chaff was not released were generally clouds too far from the circularly-polarized radar for effective resolution of the chaff distributions.

The tracers used in these experiments have small (chaff) or negligible (SF₆) sedimentation rates, and so tend to follow air-parcel rather than embryo trajectories. The settling of embryos could displace them from the air parcels by distances of the order of 1 km, or even more, over the duration of a typical tracer experiment. Nevertheless, the tracers provide some indication of potential embryo transport paths.

In many of the experiments the SF₆ was observed at levels above the release level in the feeder cloud, indicating that it had been carried up in the feeder-cloud updrafts. In some of the observations it had dis-

persed through the upper part of the cloud. In the cases with chaff similar observations were obtained with the circularly-polarized radar. In only a few cases was there evidence of transport toward or into the mature cell. This might be due to experimental difficulties, for example, if such transport occurred above the level of the T-28 penetrations and in zones where the Citation could not fly, or in the case of the radar if the discrimination between chaff and precipitation echo was insufficient to establish when the chaff entered the stronger echoes in the mature cells. However, in the context of Foote's (1985) characterization of "closed" versus "open" cells it could also indicate that such transport between cells is not a consistent feature of the North Dakota thunderstorms.

4. EXAMPLE DATA

We present here an example of the data from an experiment of this type, conducted on 15 July 1993 during the NDTE. Hjelmfelt *et al.* (1995) give an overview of the storms on this day. Figure 2 shows the radar structure of the storm at the time of the first SF₆ interception by the Citation. The SF₆ and chaff were dispensed beginning at about 1832 CDT at 4.9 km MSL (the chaff in a continuous ring and the SF₆ in two in-cloud bursts of a minute or more duration, about four minutes apart), in the approximate location indicated in the figure. Updrafts at the release level were as strong as 10 m s⁻¹. The Citation encountered the SF₆ twice, at 6.7 km (1.8 km above the release level, at about -15°C) in the feeder cloud. The first encounter, 5 min after the release began, involved a narrow plume

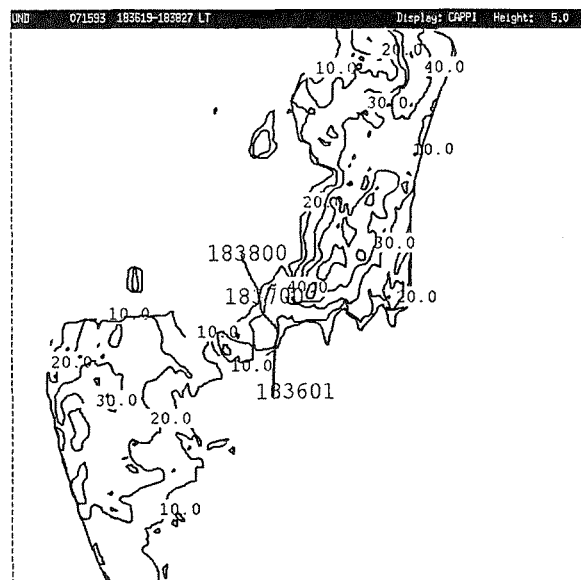


Figure 2: Radar structure of storm at time of first Citation SF₆ encounter on 15 July 1993. Track of Citation sampling penetration is superimposed.

with high SF_6 concentration associated with a weak updraft (Fig. 3). The second encounter, about 12 min later, exhibited a broader plume with lower SF_6 concentration. The T-28, penetrating about 1 km above the release level (at about -10°C) but beginning about 15 min after the release started, did not find the SF_6 tracer in any of its five penetrations into the periphery of the mature cell.

The circularly-polarized radar was able to observe the chaff being carried up in the feeder-cloud updraft (Figure 4). It was observed to reach at least 6.4 km (21,000 ft) height, about the same height as the Citation SF_6 encounters, by some 7-8 min after the release began as the feeder cloud was merging into the mature cell. The chaff echo subsequently became obscured by precipitation echo (even in the depolarization channel) in the mature cell.

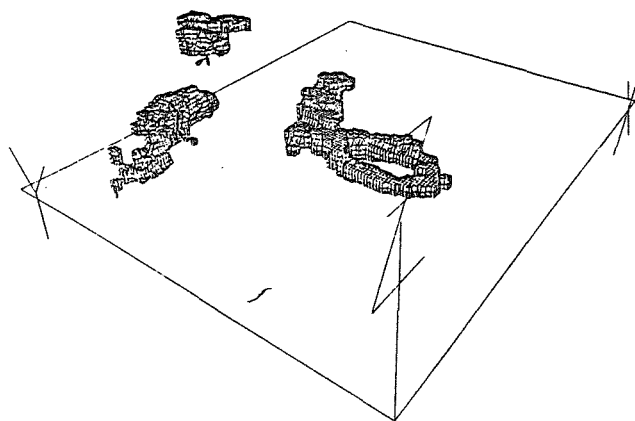


Figure 4: Perspective view from above, looking toward the northeast, of chaff distribution (indicated by Circular Depolarization Ratios > -2 dB) about 7-8 minutes after release began. The ring indicates the release area; echoes north and northwest of chaff zone are from mature cell, possibly from hail. Grid size 50 x 50 x 10 km.

5. SUMMARY

These experiments to explore the transport of material from feeder cloud to adjacent mature cell have revealed limited evidence of this process. With the relatively small sample available it is not easy to ascertain whether this is primarily due to experimental difficulties or to infrequent occurrence of the "open cell" transport process. The experiments are difficult to execute, but they provide direct evidence of the transport of air within and between cells. They constitute a new approach to help understand the origins of hail embryos and the role of feeder clouds in the development of hail. A clearer conceptual model of the transport process would be very useful in identifying the sources of hail embryos as well as in planning and conducting any future experiments of this type.

Acknowledgments. This work is funded by the National Science Foundation under Grant No. ATM-9221528 and Cooperative Agreement No. ATM-9401117 and by Cooperative Agreement NA47RA0184 with the National Oceanic and Atmospheric Administration through the North Dakota Atmospheric Resource Board, State Water Commission. Preparation of this paper was supported under sub-contract ARB-IAS-95-1. The views expressed herein are those of the authors and do not necessarily reflect the views of NOAA or any of its sub-agencies.

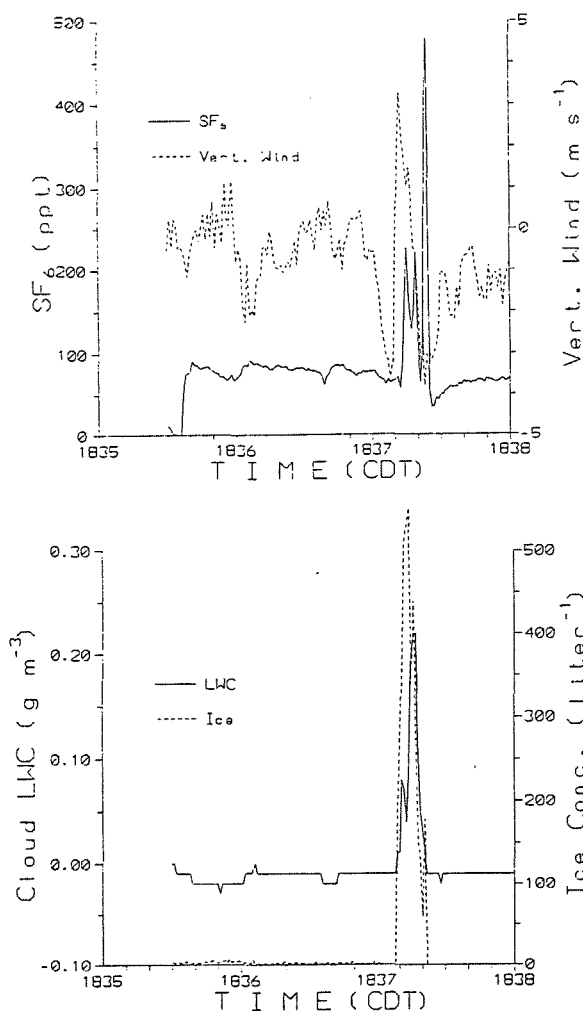


Figure 3: Plots of Citation data for first SF_6 encounter on 15 July 1993. Top: SF_6 concentration and vertical wind. Bottom: Concentrations of cloud liquid water (LWC) and ice particles.

6. REFERENCES

- Boe, B. A., 1992: Hail suppression in North Dakota. Preprints, *Symposium on Planned and Inadvertent Weather Modification*, Atlanta, GA, Amer. Meteor. Soc., 58-62.
- Boe, A. B., P. L. Smith and R. E. Rinehart, 1994: The North Dakota Tracer Experiment: Studies of transport, dispersion and hydrometeor development in cumuliform clouds. 6th WMO Scientific Conference on Weather Modification, WMO/TD-No. 596, 263-266.
- Boe, B. A., J. L. Stith, P. L. Smith, J. H. Hirsch, J. H. Helsdon, A. G. Detwiler, H. D. Orville, B. E. Martner, R. F. Reinking, R. J. Meitin and R. A. Brown, 1992: The North Dakota Thunderstorm Project—A cooperative study of High Plains thunderstorms. *Bull. Amer. Meteor. Soc.*, **73**, 145-160.
- Footc, G. B., 1985: Aspects of cumulonimbus classification relevant to the hail problem. *J. Rech. Atmos.*, **19**, 61-74.
- Heymfield, A. J., 1982: A comparative study of the rates of development of potential graupel and hail embryos in High Plains storms. *J. Atmos. Sci.*, **39**, 2867-2897.
- Hjclmfelt, M.R., L.R. Johnson, A.G. Detwiler, D.L. Priegnitz, P.L. Smith, B.A. Boe and R.F. Reinking, 1995: Radar analysis of the 15 July 1993 North Dakota record rainstorm. Preprints, *27th Conf. Radar Meteor.*, Vail, CO, Amer. Meteor. Soc. 571-573.
- Huston, M. W., A. G. Detwiler, F. J. Kopp and J. L. Stith, 1991: Observations and model simulations of transport and precipitation development in a seeded cumulus congestus cloud. *J. Appl. Meteor.*, **30**, 1389-1406.
- Knight, C. A., and K. Knupp, 1986: Precipitation growth trajectories in CCOPE. *J. Atmos. Sci.*, **43**, 1057-1073.
- Martner, B. E., J. D. Marwitz and R. A. Kropfli, 1992: Radar observations of transport and diffusion in clouds and precipitation using TRACIR. *J. Atmos. Oceanic Tech.*, **9**, 226-241.
- Miller, L. J., J. D. Tuttle and G. B. Footc, 1990: Precipitation production in a large Montana hailstorm: Airflow and particle growth trajectories. *J. Atmos. Sci.*, **47**, 1619-1646.
- Reinking, R. F. and B. E. Martner, 1996: Feeder-cell ingestion of seeding aerosol from cloud base determined by tracking radar chaff. *J. Appl. Meteor.*, **35** (in press).
- Stith, J. L., J. Scala, R. F. Reinking and B. E. Martner, 1996: Combined use of three techniques for studying transport and dispersion in cumuli. *J. Appl. Meteor.*, **35**, (in press).
- Stith, J. L., A. G. Detwiler, R. F. Reinking, and P. L. Smith, 1990: Investigating transport, mixing, and the formation of ice in cumuli with gaseous tracer techniques. *Atmos. Res.*, **25**, 195-216.

BOUNDARY LAYER ROLLS AND CLOUD BANDS: AIRCRAFT OBSERVATIONS AND MODELLING RESULTS

Ian M. Brooks¹, David P. Rogers¹, and John W. Glendening²

¹Scripps Institution of Oceanography, La Jolla, CA 92093-0230

²Naval Research Laboratory, Monterey, CA 93943-5502

1. INTRODUCTION

Large scale secondary circulations in the form of horizontal rolls are a frequent and widespread phenomenon, forming readily whenever conditions are favourable (Etling and Brown, 1993). They are often made manifest by the organisation of clouds into bands, or streets, along the updraught regions of the rolls. Observational and modelling studies have shown that roll circulations can be responsible for a significant fraction of the total turbulent transport of heat, moisture, and momentum across the boundary layer (BL), and there is evidence to suggest that rolls may enhance transport above the values that might otherwise be expected (Chou, 1993). In order to include the effects of rolls in large scale models it will be necessary to accurately diagnose their presence from bulk parameters, and to properly parameterize their influence on turbulent transport.

This study presents observations made by the UK Meteorological Office's C-130 Hercules aircraft off the coast of central California during June 1994. Most observational studies of BL rolls have taken place during cold air outbreaks, where highly convective conditions maintain strong, well defined rolls over large areas, which approximate the idealised 2D rolls of many theoretical studies. The current observations took place in conditions of much weaker convection, and the organisation of the circulations differs significantly from that of classic rolls in that they are not strictly periodic laterally (across wind), and they are of relatively limited longitudinal (along wind) extent. The satellite image in figure 1. shows cloud bands in a region of rolls; there is clearly an organisation into linear features approximately parallel to the mean wind ($\approx 330^\circ$), but individual bands are seen to meander, merge with adjacent bands, or simply peter out, and their spacing is irregular. In an attempt to identify rolls from bulk parameters we calculate stability parameters for a total of 13 cases, both with and without rolls. The contribution of the rolls to total turbulent transport is assessed by partitioning the fluxes into small scale and roll scale components. The results are compared with those from a Large Eddy Simulation (LES) model under similar conditions.

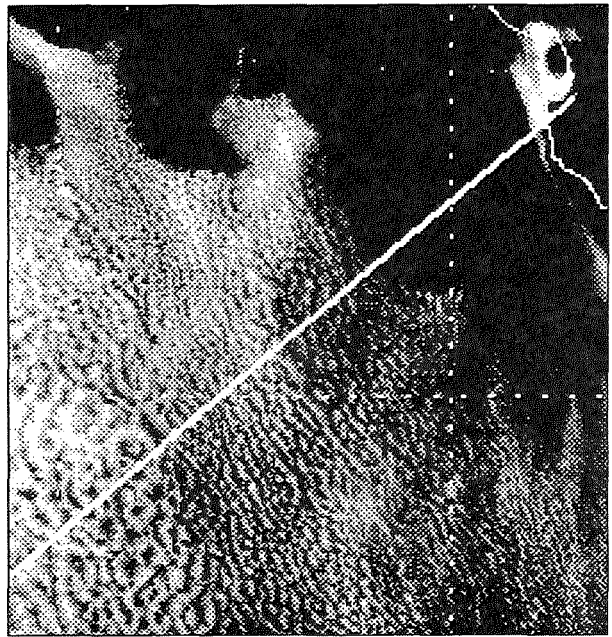


Figure 1. Satellite image showing a cloud bands formed over BL rolls (June 22). The solid white line indicates the aircraft track as it carried out a series of profiles from Monterey (top right), across the roll region and into a region of open cellular organisation in the deeper BL to the South West. Image is approximately 143 km wide by 149 km long.

2. AIRCRAFT OBSERVATIONS

2.1 Mean conditions

Synoptic conditions throughout most of June were typical of those for the region during the summer months. Winds were northerly, and averaged between 12 and 16 m s⁻¹ throughout the BL; large shears were frequently observed at the inversion as well as near the surface. Extensive, although often broken, sheets of stratocumulus were observed off the coast on a more or less daily basis. The inversion was generally low near to the coast, typically about 500 m, increasing to the west, but varied widely from day to day, ranging from 300 to 1600 m. The BL was typically only slightly unstable ($z_i/L \approx -1$), with low buoyancy fluxes, turbulence being predominately shear driven. Figure 2.

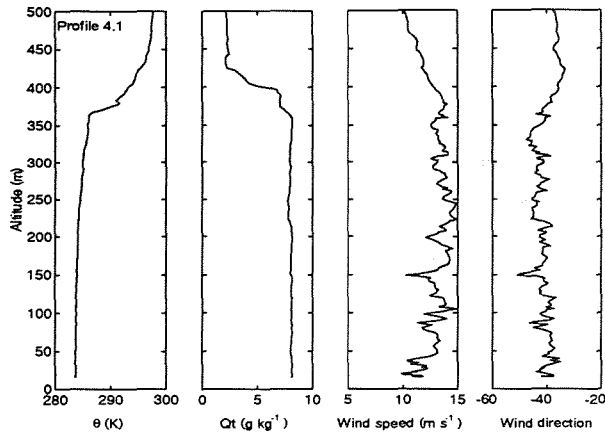


Figure 2. Mean profiles of potential temperature, θ , total water content, and wind speed and direction, on June 21.

shows typical profiles of temperature, humidity and wind speed.

2.2 Turbulence properties

Turbulence measurements were made by stacks of 60 km runs oriented across the mean wind; altitudes were chosen with reference to the mean BL structure, but usually included a near surface run at 30 m. The presence of roll circulations is evident in much of the turbulence data; figure 3. shows the cospectral density, and its running integral, or ogive curve, for the sensible heat flux near mid-BL on June 21. The rolls are responsible for the broad peak in the cospectrum with wavelengths between about 1.5 and 2.5 km, and contribute over 50% of the total flux.

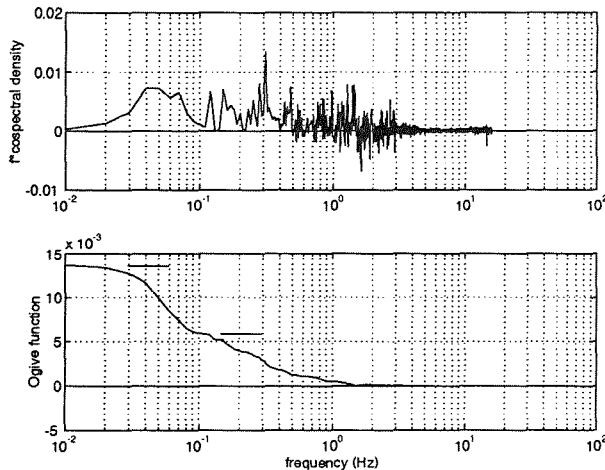


Figure 3. Example of frequency weighted cospectral density and ogive for sensible heat flux. The horizontal bars indicate the values of the small scale and total (small + roll scale) fluxes. A nominal airspeed of 100 m s^{-1} allows spatial scales to be determined from the frequency scale, so that $10^{-1} \text{ Hz} = 1 \text{ km}$, $10^{-2} \text{ Hz} = 10 \text{ km}$ etc.

Detailed turbulence measurements were made in four of the roll cases, and the fluxes and velocity variances partitioned into small scale and roll scale contributions. Figure 4. shows a composite of the

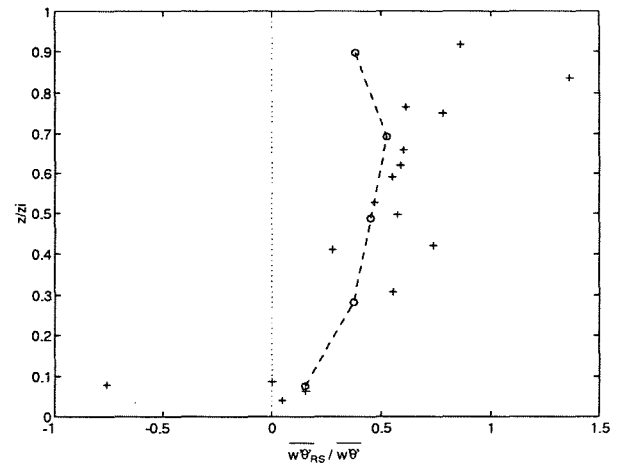


Figure 4. Fractional roll scale contributions to the sensible heat flux from 4 flights (+). Also shown are results from the LES model, averaged over the entire horizontal domain (o)

fractional roll scale contributions to the sensible heat flux from all four cases. The roll contribution clearly increases with altitude, accounting for most of the heat flux in the upper BL. Fractions in excess of unity, or less than zero, arise where the roll and small scale fluxes are in opposite directions, and depend on the relative magnitudes of the two contributions. Roll wavelengths were estimated from the separation of cloud bands, as indicated by the cloud droplet concentration. Table 1. lists the mean values and ranges of wavelengths and aspect ratios; considerable variability is evident.

TABLE 1. Roll wavelengths and aspect ratios (mean and range) from four flights, and the LES model. H is cloud top height or z_i .

DATE	H	λ (km)	λ/H
09 : P1	350	1.4 (0.5-2.7)	4.0 (1.4-7.7)
16 : P1	740	1.7 (0.7-2.7)	2.3 (0.9-3.6)
21 : P3.2	460	1.7 (0.9-3.1)	3.7 (1.9-6.7)
21 : P4.1	370	1.0 (0.5-1.5)	1.9 (1.3-4.0)
model	624	2.3 (1.1-4.9)	3.6 (1.8-7.8)

2.3 Stability parameters

The stability of the BL with respect to rolls is often related to the stability parameter z_i/L , where z_i is the BL depth and L is the Monin-Obukhov length. The wide range of the criteria quoted in the literature for both upper and lower limits ($z_i/L > -9.3$ (Sykes and Henn, 1988), $-4 > z_i/L > -11$ (Chou and Ferguson, 1991), $z_i/L < -1.5$ (Moeng and Sullivan, 1994)) suggest however, that this is an inadequate indicator - not surprisingly perhaps, since it relies on surface forcing and takes no account of the rest of the BL. An alternative indicator is the Richardson number, Ri . This is usually defined for idealised conditions, and it is not obvious how it should best be defined for a real BL; a number of different definitions have been used by various researchers (LeMone, 1973; Kelly, 1984;

Brümmer, 1985), but not all are generally applicable, and none have been tested on a range of cases both with and without rolls.

We define a bulk Richardson number

$$Ri_b = \frac{g}{\theta_v} \frac{\Delta\theta_v H}{u_g^2}$$

where g is gravity, H , cloud top altitude (usually equal to z_i), u_g , the geostrophic wind speed, taken to be equal to the mean wind speed just above the inversion, and θ_v , the virtual potential temperature; the jump $\Delta\theta_v$ is between the bottom of the aircraft profile at 14 m, and the level H . Ri_b was calculated for each of 13 profiles, drawn from 9 separate flights, where there was either a coincident turbulence stack, or the presence or absence of rolls was otherwise known with a high degree of confidence from visual observations during the flight. The results, along with the corresponding values of z_i/L , are given in table 2. It is seen that in the cases with BL rolls Ri_b is less than the critical value of 0.25, while for cases without rolls it is greater than critical. z_i/L is rather less successful at indicating rolls; for example, the June 28 case has no rolls, but z_i/L lies between the values on June 16 and 17 when there are rolls. On June 8, the turbulence data was inconclusive, and we found it impossible to confidently decide whether or not rolls were present. The Richardson number of 0.15 suggests that rolls should exist, and an examination of the flight records revealed that the measurements had been made in a region of transition between rolls and cellular convection. Other cases where the rolls were difficult to pick out in the turbulence data (June 17, 21(P4.1)), also have $Ri_b > 0.1$, thus the exact value Ri_b appears to give some indication of the strength of the circulations.

TABLE 2. Occurrence of rolls and the associated stability parameters. A dash indicates data unavailable.

DATE	ROLLS ?	z_i/L	Ri_b
08 : P2	?	-0.6	0.15
09 : P1	✓	-0.5	0.03
11 : P1	✗	—	0.3
16 : P1	✓	-2.3	0.04
17 : P1	✓	-0.16	0.13
21 : P3.2	✓	-0.9	0.05
21 : P4.1	✓	-0.06	0.17
22 : P2	✓	—	<0.1
22 : P3	✓	—	0.08
22 : P4	✓	—	0.08
22 : P5	✗	—	0.27
27 : P2	✗	0.3	0.3
28 : P2	✗	-1.6	0.5

3. MODELLING RESULTS

An LES model has been used to simulate BL rolls under conditions similar to those observed ($z_i/L \sim -2.5$). A distinctive feature of the modelling study, is the large horizontal domain (25×36 km), which allows a

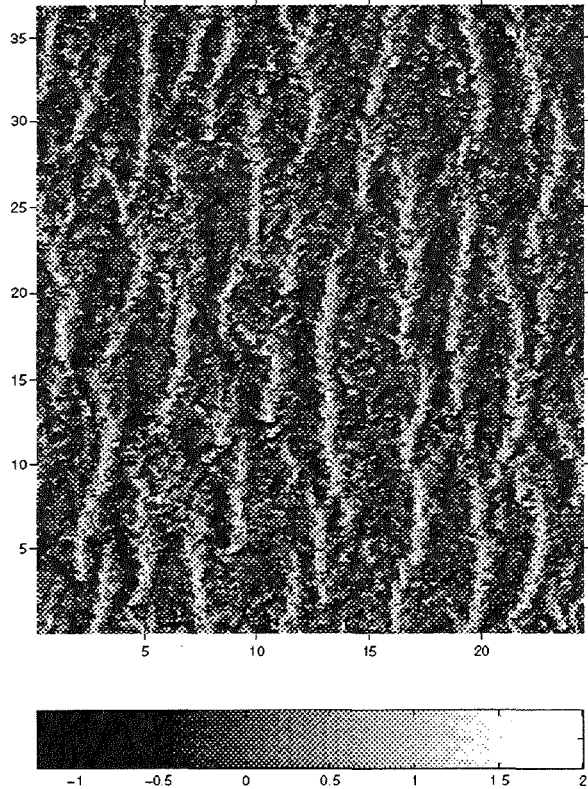


Figure 5. Vertical velocity field at $z/z_i = 0.49$. Axis scales are in km, grey-scale in $m s^{-1}$. Mean wind approximately parallels the y-axis from bottom to top of image.

greater number and variety of roll realisations, along roll variations, and reduced quantization errors. A detailed description of the model and results from earlier runs can be found in Glendening (1996). Figure 5. shows the vertical velocity field near mid-BL. The updraught regions clearly show the general lineal organisation, and have an appearance similar to that of the cloud streets in figure 1. It is evident that the secondary circulations have a limited along wind extent, and that the roll spacing and orientation varies considerably; the range of roll wavelengths, estimated from the spacing of updraught centres in a similar, is given in table 1. Fractional roll contributions to the fluxes were determined in a similar manner to those from the aircraft data, by scale partitioning the cospectral densities calculated in the cross-wind direction; the contributions to the heat flux are compared with the observations in figure 4 (the lowest level value is likely to be overestimated by 10 to 20% since subgrid scale fluxes have been neglected; at higher levels they contribute much less). Ri_b calculated between the lowest model level and z_i is 0.03.

4. SUMMARY

Bulk Richardson numbers calculated over the depth of the BL provide an accurate indication of the presence of BL scale secondary circulations or rolls, at least under conditions of high shear and low buoyancy

forcing. The contribution of the rolls to the total fluxes was found to be similar to that found by earlier studies, generally increasing with altitude. The spacing and orientation of individual rolls, as indicated by cloud bands in satellite imagery, is variable, and they are of limited along-wind extent; aircraft runs through the cloud bands show the roll aspect ratio to vary between about 1 and 8. An LES model with similar mean conditions, produces secondary circulations with a comparable structure to those observed. The modelled fluxes exhibit a similar scale partitioning to the observed fluxes, except near the inversion, where the modelled roll contribution decreases, possibly due to the weaker inversion and much greater degree of entrainment in the model. Modelled roll spacings are highly variable, with a similar range to the observations.

ACKNOWLEDGEMENTS – This work was supported by ONR through grants N00014-93-1-0972 and N00014-95-1-0857 (IMB & DPR), and program element 0601153N (JWG). Computing support was provided the Arctic Region Supercomputing Centre. Thanks to Doug Johnson of the Meteorological Research Flight for providing the aircraft data, and to the C-130 aircrew.

REFERENCES

- Brümmer, B., 1985: Structure, dynamics and energetics of boundary layer rolls from KonTur aircraft observations. *Beitr. Phys. Atmos.*, **58**, 237-254.
- Chou, S-H., 1993: A comparison of airborne eddy correlation and bulk aerodynamic methods for ocean-air turbulent fluxes during cold air outbreaks. *Boundary-Layer Meteorol.*, **64**, 75-100.
- , and M. P. Ferguson, 1991: Heat fluxes and roll circulations over the western gulf stream during an intense cold-air outbreak. *Boundary-Layer Meteorol.*, **55**, 255-281.
- Etling, D., and R. A. Brown, 1993: Roll vortices in the planetary boundary layer; a review. *Boundary-Layer Meteorol.*, **65**, 215-248.
- Glendening, J. W., 1996: Lineal eddy features under strong shear conditions. *J. Atmos. Sci.*, Accepted for publication.
- Kelly, R. D., 1984: Horizontal roll and boundary-layer interrelationships observed over Lake Michigan. *J. Atmos. Sci.*, **41**, 1816-1826.
- LeMone, M. A., 1973: The structure and dynamics of horizontal roll vortices in the planetary boundary layer. *J. Atmos. Sci.*, **30**, 1077-1091.
- Moeng, C-H., and P. P. Sullivan, 1994: A comparison of shear- and buoyancy-driven planetary boundary layer flows. *J. Atmos. Sci.*, **51**, 999-1022.
- Sykes R. L., and D. S. Henn, 1988: Large-eddy simulation of turbulent sheared convection. *J. Atmos. Sci.*, **46**, 1106-1118.

LIDAR FOR POLARIZATION STUDIES OF CLOUDS IN THE LOW ATMOSPHERE

Ivan N. Kolev, Boyan I. Tatarov, Boiko K. Kaprielov

Institute of Electronics, Bulgarian Academy of Sciences, Sofia, Bulgaria

1. INTRODUCTION

The lidar studies of the polarization characteristics of natural and anthropogenic atmospheric objects (Sassen et al., 1992; Werner et al., 1988) have been actively pursued in recent years both in their experimental (Werner et al., 1988) and theoretical (Oppel, 1989; Flesia et al., 1994) aspects for the needs of the applied meteorology and ecology. Such studies basically follow two directions:

- using the polarization characteristics to determine the microphysical properties of the aerosol, including the phase content of clouds of various types and heights (from the ground layer (Platt et al., 1994) up to cirrus clouds (Stefanutti et al., 1992));

- exploring the processes of multiple scattering (Sassen et al., 1992; Oppel, 1989). The international "MUSCLE" Workshop (Kolev, et al., 1992), coordinates the activities in this area.

On the other hand, tracking the temporal variation of the above parameters (Kolev, et al., 1994; Toshiyuki, 1994) can yield information on various processes which proceed in the atmosphere.

The present work describes the first Bulgarian polarization lidar for systematic investigations in the atmospheric planetary boundary layer; it also presents some results of pilot measurements in different meteorological situations.

2. EQUIPMENT AND EXPERIMENT

The lidar for polarization studies was constructed on the basis of an existing aerosol lidar (Kolev, et al., 1992). The polarization measurements were made possible by a polarization attachment fitted in between the receiving telescope and the photodetectors. The main functional units of the polarization lidar are:

- transmitter - a standard Q-switched frequency-doubled Nd:YAG laser (pulse energy 5–15 mJ, pulse duration 15–20 ns, wavelength 532 nm, pulse repetition rate 12.5 Hz);

- receiver - a 150 mm Cassegrainian telescope (equivalent focal length 2250 mm); polarization attachment (developed at the Institute of Electronics, Bulgarian Academy of Sciences); photodetectors - two photomultipliers (FEU-84 type) with interference filters ($\Delta\lambda=1$ nm) for the optical background suppression.

- data acquisition and processing system – an analog-to-digital converter (ADC, mod. HP5180A) and a personal computer (PC-AT/386).

The polarization attachment divides optically the lidar response (the backscattered by the atmospheric aerosol part of the sounding laser radiation) into two cross-polarized components – P_p and P_c (the polarization of P_p is parallel to the priority one of the transmitter). The separating element is a Wollaston prism, chosen because of the symmetry and relatively large angle of separation (11.2°). Two lenses form a Keplerian telescope, where a shift between the foci is introduced. This optical assembly serves for matching the diameter and divergence of the received beam with the parameters (requirements) of the separating element, the interference filters and the photodetectors. The right-angle prism directs the P_p and P_c components to the respective photodetectors.

The electric signals produced by the photomultipliers are digitized by the ADC and stored in the computer.

In this manner, the lidar registers the profiles (the intensity as a function of the distance) of signals with polarizations parallel and perpendicular to the priority one of the sounding radiation. Thus, besides the information usually obtained from the lidar data, one is enabled to determine the depolarization ratio (Van der Hulst, 1961) $\delta=I_c/I_p$ (I_c and I_p are the intensities of the P_c and P_p , respectively) and its profile as well.

To test the capabilities of the polarization lidar, we carried out a series of pilot observations in various meteorological situations. The profiles recorded were averaged for 32 measurements (sounding pulses) taking for 6–7 s. The depolarization ratio was calculated for each point of the lidar profiles, so the depolarization profiles were constructed for the entire sounding paths.

3. EXPERIMENTAL RESULTS

The experiments were performed during the period 1–15 June, 1995, in different meteorological situations - "clear" atmosphere, rain, and fog. (In the figures below, U_p and U_c present the natural P_p and P_c profiles recorded, respectively.)

A typical profiles obtained when sounding a "clear" atmosphere are shown in Fig. 1. The data are taken after

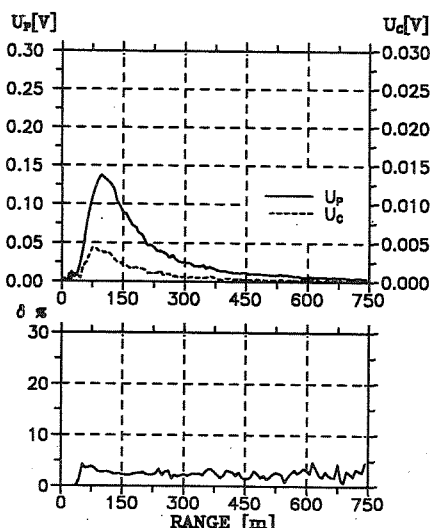


Fig. 1. Lidar (U_p , U_c) and depolarization ratio (δ) profiles obtained in "clear" atmosphere after a rain fall.

22:00 on June 3 along a horizontal path after a rain shower. The meteorological visibility was >20 km. The P_c -signal is weak and, therefore, the degree of depolarization is small ($\delta \approx 3\%$).

Fig. 2 shows signal profiles recorded in the morning

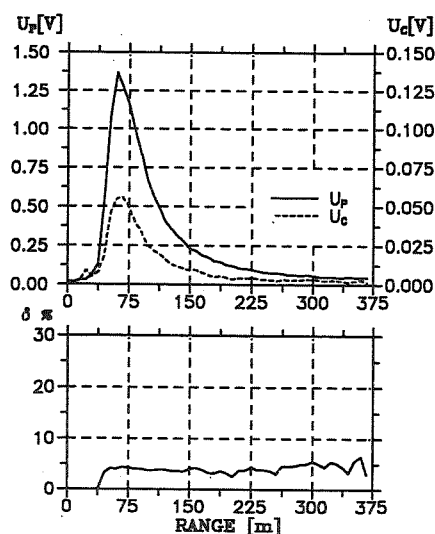


Fig. 2. Lidar (U_p , U_c) and depolarization ratio (δ) profiles obtained in "clear" atmosphere.

(after 10:00) of June 9 along a slanted path. The weather

was sunny ("clear" atmosphere), without previous rain showers. The profile of δ are also flat, although its average value is greater ($\delta \approx 5\%$).

Fig. 3 presents a typical profile taken during a rainfall (June 14). Both signal components have relatively small

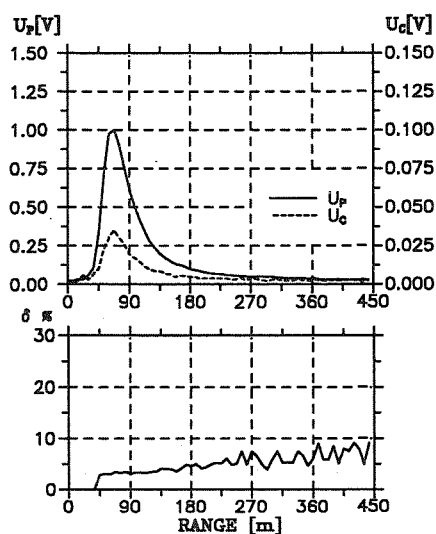


Fig. 3. Lidar (U_p , U_c) and depolarization ratio (δ) profiles obtained during a rain fall.

amplitudes and decrease rather quickly. The ratio δ has a relatively low value (3-4%) in the beginning, gradually increasing to 7-9% at comparatively small distances from the lidar.

Fig. 4 gives a signal profile obtained along a horizontal path in foggy quiet weather on June 15. In the beginning

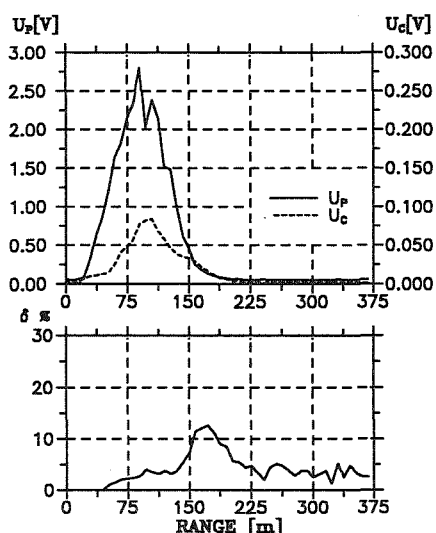


Fig. 4. Lidar (U_p , U_c) and depolarization ratio (δ) profiles obtained in fog.

of the observation the meteorological visibility was about 100 m. The profiles of the two components are similar, with the P_c maximum somewhat delayed with respect to that of P_p . The signals shape is definitely different from that of a "clear" atmosphere (which has a well expressed

quadratic behaviour). The depolarization profile exhibits a clear maximum delayed with respect to those of the lidar responses.

From the next profiles (Fig.5) (taken at 30–40 minutes

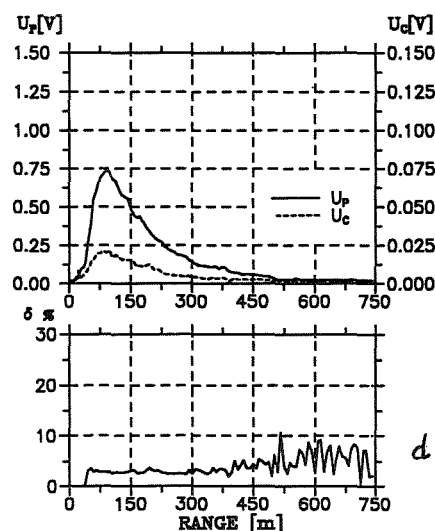
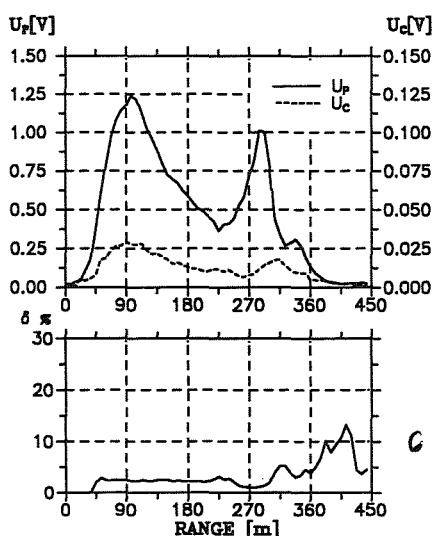
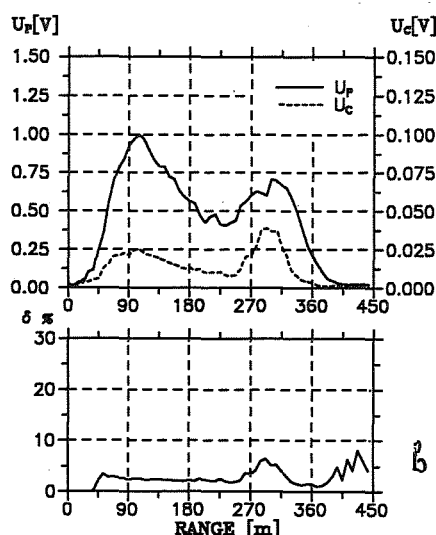
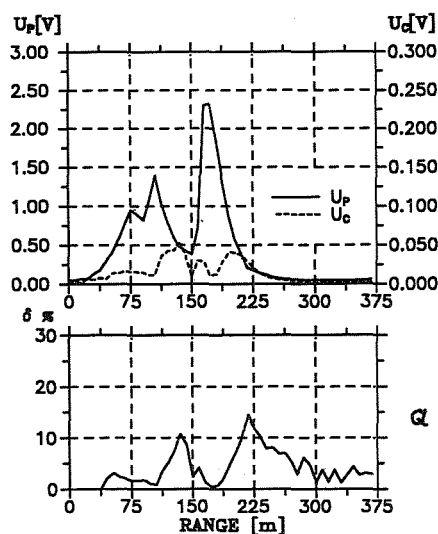


Fig. 5. Lidar (U_p , U_c) and depolarization ratio (δ) profiles obtained during the clearing up of the fog.

intervals during the clearing up of the fog under the same experimental conditions as the one in Fig.4) the temporal behaviour of the process can be followed.

4. DISCUSSION

The experiments reported aimed to evaluate the potentials of the polarization lidar. The experimental data presented demonstrate that using such a lidar makes it possible to register variations in the aerosol microphysical characteristics which vary depending either on the meteorological conditions or on the processes occurring in the studied object.

In a "clear" atmosphere (after a rain shower), the concentration of aerosol particles decreases and laser light scattering is weak (Fig.1). The degree of depolarization is negligible which is indicative of spherically-shaped scattering centers (watered aerosol).

The higher degree of depolarization, obtained during the morning observation (Fig.2), has likely to be related with the presence (along the sounding path) of particles with larger size and near-spherical shape (such as water droplets with relatively low concentration, or scattering centers formed through condensation on aerosol particles of moisture evaporated off the ground), which increase the multiple-scattering contribution.

The gradual rise of the depolarization degree in the case of observation during a rain shower is most probably due to the large number of rain drops which are gradually increasing the contribution of the multiple scattering along the sounding path.

During the sounding in a dense fog (Figs.4, 5a) the obtained signals shape (essentially non-quadratic owing

to the substantial change of the scattering and extinction coefficients) and the presence of a delay of the cross-polarized component's and the depolarization's maxima indicate that an optically dense object is being sounded - the multiple scattering affects considerably the lidar returns.

The profiles in Fig.5a point to the appearance of a structure in the fog. Two sharp maxima are clearly seen in the return curves along with the corresponding delayed depolarization maxima. The development of such a structure can be caused by radiative processes, by local motion of the air masses, or by the influence of the underlying surface.

The profiles in Fig.5b were taken during increasing solar influence. The depolarization behaviour allows us to conclude that the scattering medium in the near zone is relatively homogeneous; its aerosol content includes most probably small spherical droplets. The presence of the denser object farther away has to be related with the specific underlying surface - a park area in the near zone (up to about 200 m) followed by a residential district, where the radiative processes are presumably slower.

Later on the fog began to rarefy - the corresponding profiles are shown in Fig.5c. Two maxima, with the first one resembling that of a "clear" atmosphere are seen. Furthermore, in the beginning the degree of depolarization has low values and relatively flat behavior, followed by a maximum related most probably to multiple scattering.

After the fog has cleared the components' shape (Fig.5d) became close to that of a "clear" atmosphere. The clearing of the fog is a proof that a few hours after sunrise the radiative processes begin to predominate, which is further confirmed by the absence of wind during the measurements.

5. CONCLUSIONS

Based on the analysis of the experimental data, one can conclude that the polarization lidar can be readily used for obtaining additional information on the microphysical characteristics of the atmospheric aerosol during the formation of the atmospheric planetary boundary layer, e.g. in the study of the transformation of the aerosol shape, dense aerosol formations (clouds, rain, fog) which is of paramount importance to the applied meteorology (including air navigation) and for

ecological purposes. The "clear" atmosphere observations demonstrate that the polarization lidar detects differences in the aerosol concentration; what is more, it is evident that the degree of polarization can be used for qualitative estimates in the investigations of the atmospheric aerosol.

The authors wish to thank R. Nenchev for his contribution to the acquisition and processing of the data, and L. Hristov for his help in assembling the experimental set-up.

6. REFERENCES

- Sassen, K., Hongjie, Z., Dodd, G., 1992. Simulated Polarization Diversity Lidar Returns From Water and Precipitating Mixed Phase Clouds. *Appl. Opt.*, 31 (15); 2914-2923.
- Werner, Ch., Herrmann, A., Streicher, J., 1988. Cirrus-Experiment ICE-1987, Microlidar-Measurements. Oberpfaffenhofen, DFVLR-Mitteilung 88-17; 38 pgs.
- Oppel, U., 1989. Reconstructions of Scattering Distribution From Double Scattering Lidar Return Signals. *Proc. 4th Int. Workshop MUSCLE 3*, Germany; 34-49.
- Flesia C., Starkov, A., 1994. Analytical Inversion Method for the Lidar Equation: Sensitivity to Multiple Scattering and Particle Shape. *Proc. 17th Int. Laser Radar Conf.*, Sendai; 81-84.
- Platt, C.M.R., Kolev, I., Kaprielov, B., et al., 1994. The Experimental Cloud Lidar Pilot Study (ECLIPS) for Cloud Radiation Research. *Bulletin of American Meteor. Soc.*, 79 (8); 635-655.
- Stefanutti, L., et al., 1992. Four Wavelength Depolarization Backscattering Lidar for Polar Stratospheric Cloud Monitoring. *Appl. Phys. B*, 55, 13-17.
- Kolev, I., Parvanov, O., Kaprielov, B., 1992. Lidar Observation of Optically Dense Formations in Mountain Valleys. *Proc. 5th Int. Workshop MUSCLE 5*, Philadelphia; 28-31.
- Kolev, I., Parvanov, O., Kaprielov, B., 1994. Lidar Polarization Measurement Necessity in Two Cases of Study of Processes in the Atmospheric Planetary Boundary Layer. *Proc. 17th Int. Laser Radar Conf.*, Sendai; 129-130.
- Toshiyuki M., 1994. Lidar Observation of the Troposphere in Tokyo. *Proc. 17th Int. Laser Radar Conf.*, Sendai; 66-67.
- Van der Hulst, 1961. *Light Scattering by Small Particles*. M., Foreign Literature Publ.; 536 pgs.

ANISOTROPY IN TURBULENT MIXING OF CLOUDS WITH CLEAR AIR IN SMALL SCALES

Piotr Banat and Szymon P. Malinowski
Institute of Geophysics, University of Warsaw.

1. INTRODUCTION

In recent years a couple of papers about adopting fractal and multifractal formalism to the description of turbulent flows and turbulent mixing appeared (see the review by Sreenivasan, 1991). There were also some efforts to describe properties of cloud-clear air interface in terms of fractal dimension (Lovejoy, 1982, Cahalan and Joseph, 1989, Malinowski and Zawadzki 1993, Malinowski et. al. 1994). In these studies assumption of isotropy of fractal properties of cloud-clear interface played an essential role. However, due to buoyancy and gravity effects this assumption, at least for clouds, is questionable.

In the experiment described by Malinowski et. al., 1995, aimed at investigating turbulent mixing of cloud with dry air in small scales, the box-counting method was used to define a fractal dimension of an interface between a cloud and a clear air. This interface has been determined on the base of two-dimensional sections through small cloud undergoing mixing with the environmental air, observed in a specially designed laboratory chamber. The vertical direction is naturally favored in analyzed pictures due to effects of gravity and buoyancy. This means that also in small scales the interface may be anisotropic. Quantitative description of this anisotropy in terms characteristic for fractais is the main goal of the paper.

2. MEASURES OF ANISOTROPY

Problem of defining anisotropy is not new and various methods of approaching this issue are in use, depending on the way the primordial problem is formulated. In atmospheric physics the so-called General Scale Invariance formalism (Lovejoy et. al., 1992) introducing concept of elliptical dimension, was introduced. Below we propose another, much simpler approach, aimed at investigating scale-dependent anisotropy. It is based on the modified box-counting approach.

Let us define a function $\text{box}_S(x,y)$, given for a specified set S in a specified coordinate system:

$\text{box}_S(x,y)$:= Number of boxes of the sides x and y ,
needed to cover set S . (2.1)

In the case $x=y$ and existing self-similarity in of the set S , a function $\text{box}_S(x,y)$ can be used to determine box-counting dimension D :

$$\log(\text{box}_S(x,x)) = -D \log(x) + \text{const}, \quad (2.2)$$

Domain Σ of a function $\text{box}_S(x,y)$ in the logarithmic scale can be interpreted as in Fig.1.

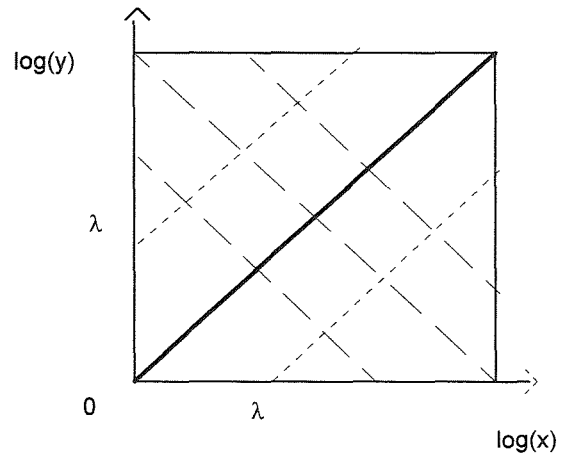


Fig. 1 Domain of the function $\text{box}_S(x,y)$ may be interpreted in the following manner:

- interior of the square – possible dimensions of boxes;
- thick solid line – square boxes;
- dotted line – boxes of constant proportion $(x, \lambda x)$ and $(\lambda y, y)$;
- dashed line – boxes of constant surface $(xy = \text{const})$;
- axis x – boxes of size $(x, 1)$.
- axis y – boxes of size $(1, y)$.

Now we may define isotropy:

$$\begin{aligned} &\text{The set } S \text{ is isotropic if for every } (x,y) \in \Sigma: \\ &\text{box}_S(x,y) - \text{box}_S(y,x) = 0. \end{aligned} \quad (2.3)$$

This gives a definition of anisotropy function:

$$an_S(x,y) := \log(\text{box}_S(x,y)) - \log(\text{box}_S(y,x)) \quad (2.4)$$

The above implies that $an_s(x,y)$ is symmetric with respect to $y=x$. $an_s(x,y)$ may be also scale-dependent.

The advantage of the above definition is that anisotropy does not depend directly on the value of the function $box_s(x,y)$. The disadvantage is the dependence of $an_s(x,y)$ on a choice of coordinate system for analyzed picture. If $an_s(x,y)=0$, the set S is isotropic. Non-zero values of $an_s(x,y)$ indicate anisotropy of importance growing with increase of $an_s(x,y)$.

Scale independent constant distortion λ (see Fig.1.), named here a *geometrical anisotropy*, may be computed finding minimum value of the expression:

$$box_s(\lambda x, y) - box_s(y, x\lambda). \quad (2.5)$$

It should be pointed out that not every anisotropic set can be characterized by constant λ . In the other words, not every set can be linearly extended so that condition of isotropy (2.3) is fulfilled. A simple example of such a set may be a fractal S with a self-similarity dimension D , which fulfills an additional condition:

$$box_s(x,y) \sim x^{-D_1} y^{-D_2}, \quad (2.6)$$

where quantities D_1 and D_2 determine (in analogy to the box-counting dimension) dependence of a function $box_s(x,y)$ on a change of size of boxes in directions x and y . For $x=y=\delta$ the equation (2.2) is obtained when:

$$D = D_1 + D_2. \quad (2.7)$$

D_1 and D_2 may be then computed fitting a plane on a logarithmic plot of to function $box_s(x,y)$. In a case $D_1 \neq D_2$, the set is anisotropic and no constant λ can be found. λ then is a function of x and y . This may be shown by inserting the expression (2.6) into (2.3):

$$(\lambda x)^{-D_1} y^{-D_2} = y^{-D_1} (\lambda x)^{-D_2}. \quad (2.8)$$

This implies:

$$\lambda^{-D_1} box_s(x,y) = \lambda^{-D_2} box_s(y,x), \quad (2.9)$$

what allows to compute λ :

$$\lambda(x,y) = \left(\frac{box_s(y,x)}{box_s(x,y)} \right)^{\frac{1}{D_2-D_1}}. \quad (2.10)$$

It may be easily shown that λ defined by equations (2.5) and (2.6) does not depend on sizes of boxes only when $D_2=D_1$.

When condition (2.6) is fulfilled there exists a specific kind of anisotropy, which properties are determined by D_1 and D_2 . In the following this will be called the *anisotropy of dimension*.

3. APPLICATION OF THE FORMALISM TO THE ARTIFICIALLY GENERATED FRACTAL

In order to facilitate the above approach the anisotropy function for a modified random quadratic Sierpinski carpet (Fig.2) was investigated. $an_s(x,y)$ obtained from 30 independent realizations of random Sierpinski carpets after 9 iterations is given in Fig. 3.

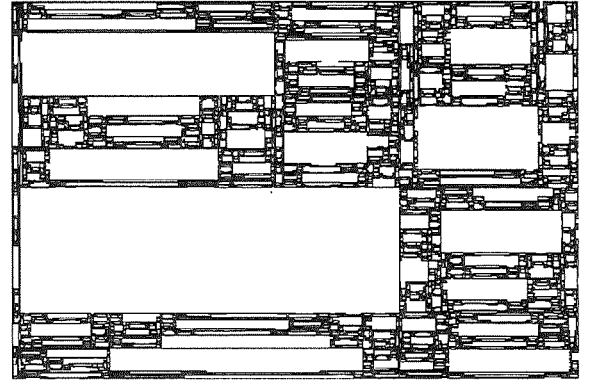


Fig. 2 Randomly generated modified anisotropic Sierpinski carpet.

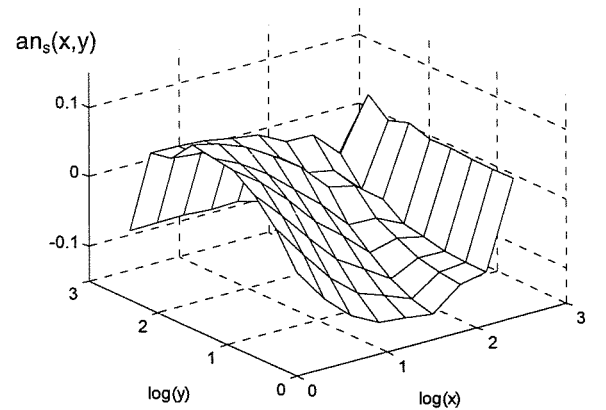


Fig. 3 The anisotropy function $an_s(x,y)$ averaged over 30 realizations of the set in Fig. 2 (1024x683 pixels, 9 iterations).

Due to the symmetry of $an_s(x,y)$ we analyze only $y \geq x$ half of the plot. For boxes of sizes $< 16 \times 16$ pixels ($\log(x) < 1.2$, $\log(y) < 1.2$) the plot of $an_s(x,y)$ is an inclined plane. This means that in small scales a well-established anisotropy appears and increases with a scale. For larger boxes $an_s(x,y)$ has a global maximum for $x=1$, $y=32$ pixels ($\log(x)=0$, $\log(y)=1.51$). For the largest boxes ($x=512$ or $y=512$ pixels) the value of $an_s(x,y)$ is a result of a non-square outline of the carpet

itself (sizes of boxes are comparable to the size of the carpet - "edge effects").

The anisotropy of dimension computed on the base of (2.6) for small scales of Sierpinski carpet is: $D_1=0.89$, $D_2=0.96$, respectively (correlation $r=0.998$). In this case $D_1+D_2=1.85$, and computed with a standard box-counting method dimension is: $D=1.83$. The difference between computed values of D_1+D_2 and D may be explained as a result of errors of fitting plane and line (errors in D_1 , D_2 , D) and of a fact that for investigated set expressions (2.2) and (2.6) are acceptable only in approximation.

Knowing D_1 , D_2 and $\text{box}_S(x,y)$ a function $\lambda(x,y)$ may be computed with help of (2.10). The result is shown in Fig.4. However, λ computed here has substantial errors. Even small error in D_1 and D_2 estimates has a considerable influence on λ .

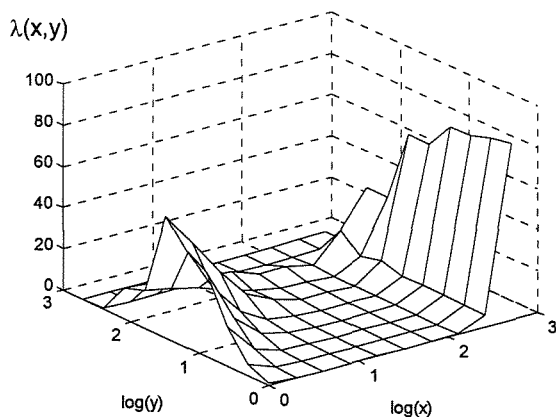


Fig. 4 The function $\lambda(x,y)$ averaged over 30 different realization of the set in Fig.2 (1024x683 pixels, 9 iterations) calculated for $D_1=0.89$, $D_2=0.96$.

Analysis of the geometrical properties of the investigated set based on the plot of $\lambda(x,y)$ is difficult but possible. In Fig.4 we observe the maximum of λ in the same place as maximum of $\text{an}_S(x,y)$. This is because anisotropic Sierpinski carpet contains many elongated (anisotropic) rectangles in small scales. In practice, when data from an experiment are analyzed, finding (x,y) for which the "considerable" increase of λ appears, may be problematic.

4. APPLICATION OF THE APPROACH TO THE EXPERIMENTAL DATA.

In the experimental part of this study we investigate an interface between cloud and clear air in the process of turbulent mixing (the experiment is described by Malinowski et. al., 1995). Mixing is nonconservative (cloud droplets may evaporate in the unsaturated air) and may be anisotropic due to the gravity (droplet fall with respect to surrounding air, non-negligible buoy-

ancy effects). This is a substantially different process than often investigated mixing of passive scalars in turbulent flows.

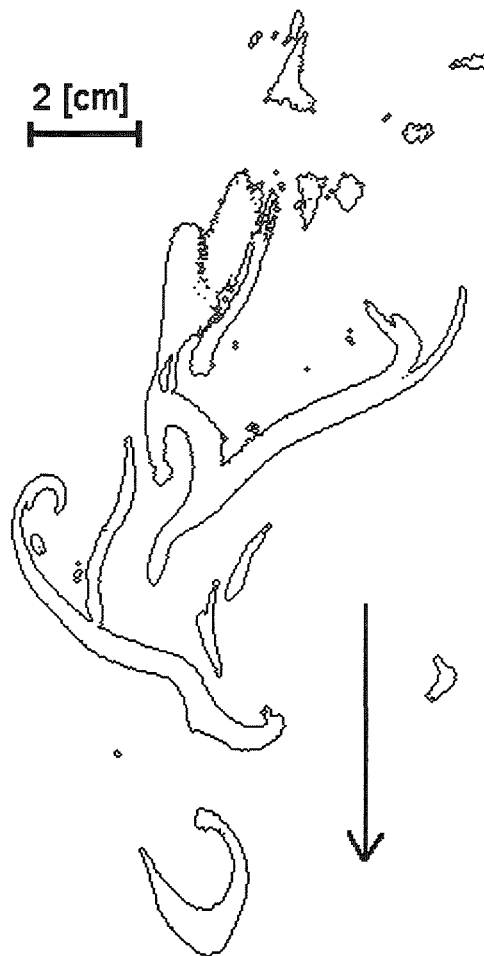


Fig. 5 A cut through the interface between a cloud and clear air. Arrow indicates the direction of gravity.

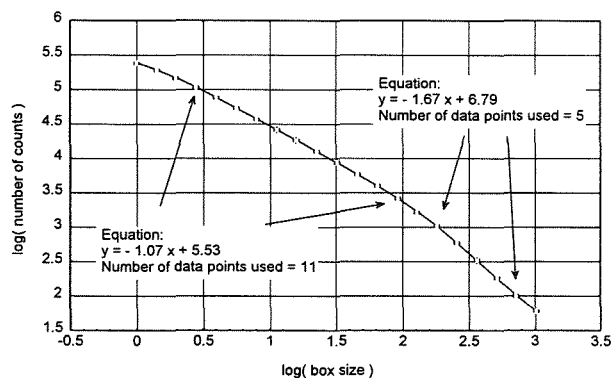


Fig. 6 Box-counting on cloud-clear air interface from the experimental data. Sum for 11 independent scenes. 100 pixels $\approx 1.5 \cdot 10^{-2}$ [m]. For the large scales, i.e. for boxes exceeding 124 pixels ($1.9 \cdot 10^{-2}$ [m]) the obtained anisotropy of dimension is respectively: $D_1=0.86$, $D_2=0.77$ (the correlation $r = 0.999$) or $D_1=0.90$, $D_2=0.77$ (the correlation $r=0.999$) depending on a range of scales adopted for fitting ($128 \leq x, y \leq 1024$ [pixels] in the first or $256 \leq x, y \leq 1024$ [pixels] in the second case).

In Fig.5 there is an example of a part of a vertical cut through an interface between cloud and clear air. Many such images were obtained by processing photographs collected during visualization of cloud-clear air mixing in cloud chamber. Resolution of each image was 1536x1024 pixels, with pixel size corresponding to about $1.5 \cdot 10^{-4}$ m.

From a group of scenes obtained in the same conditions the best 11 were chosen for investigation of anisotropy. The results of standard box counting (box(x,x)), presented in Fig.6, indicate a sharp change of the box dimension D from about 1 at scales below 1.9cm to about 5/3 in scales above 1.9cm

Assuming that the following expression for the cloud-clear air interface in three dimensions is valid:

$$\begin{aligned} &\text{the number of occupied boxes of sizes } (x,y,z) \\ &\sim x^{-D_1} y^{-D_2} z^{-D_3}, \end{aligned} \quad (4.1)$$

and assuming that anisotropy appears in vertical ($D_2=D_3$), the dimension D of the cloud - clear air interface may be estimated as:

$$D = D_1 + 2 D_2. \quad (4.2)$$

For the obtained values of D_1 and D_2 we get $D=2.41$ or $D=2.43$, respectively (see the description to Fig.6).

For scales smaller than $1.9 \cdot 10^{-2}$ m the geometrical anisotropy is observed. The estimated value of λ is $\lambda=1.6 \pm 0.1$.

5. SUMMARY AND CONCLUSIONS

- 1) The defined anisotropy function may be used to test the occurrence of scale-dependent anisotropy in the investigated direction.
- 2) In small scales the similarity between anisotropy characteristics obtained from the randomly generated square Sierpinski carpets (Fig. 3) and the experimental data (Fig. 7) exists.
- 3) For the cloud-clear interface observed on vertical cuts through the cloud generated in the laboratory conditions the anisotropy of dimension exists ($D_1 \approx 0.87$, $D_2 \approx 0.77$) for the range of scales from $1.9 \cdot 10^{-2}$ [m] to 10^{-1} m. Box-counting dimension of a of a this interface computed with the assumption (4.1) is $D=2.42 \pm 0.1$. The approximate value of geometrical anisotropy in scales less then $1.9 \cdot 10^{-2}$ [m] is $\lambda=1.6 \pm 0.1$.
- 4) For the cloud-clear air interface observed in the laboratory the preferred scale around 1.9 cm exists. In this scale the standard box counting dimension changes

from $D \approx 1$ (geometrical interface) in smaller scales to about $D \approx 5/3$ (fractal interface) in larger scales. In this scale there exist also change of anisotropy: from geometrical one to the anisotropy of dimension. The coefficient of geometrical anisotropy in small scales $\lambda=1.6$. This means, that in average structures in these scales are 1.6 times longer in vertical than in horizontal.

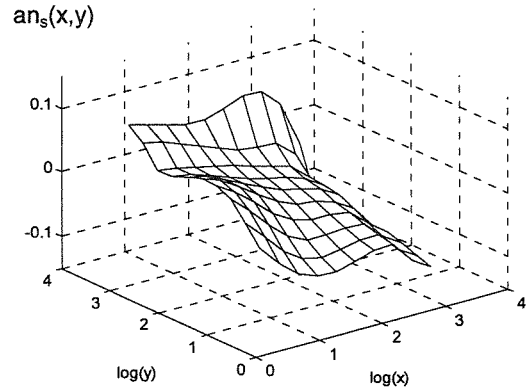


Fig. 7 The anisotropy function $an_s(x,y)$ averaged over 11 different images from the experiment (x and y in pixels). For boxes of sizes around 124 pixels the plot is almost flat and $an_s(x,y) \approx 0$ what is in agreement with the isotropy condition (2.3). 100 pixels $\approx 1.5 \cdot 10^{-2}$ [m].

6. ACKNOWLEDGMENTS

This research was supported by the grant No 6 P201 055 05 of the Polish Committee For Scientific Research.

7. REFERENCES

- Cahalan, R. F., and J. H. Joseph, 1989: Fractal statistics of cloud fields. *Mon. Wea. Rev.*, **117**, 261-272.
- Lovejoy, S., 1982: Area - perimeter relation for rain and cloud areas. *Science*, **216**, 185-187.
- Lovejoy, S., D. Schertzer, and K. Pflug, 1992: Generalized Scale Invariance and differential rotation in cloud radiances. *Physica A*, **185**, 121-128.
- Malinowski, S. P., and I. Zawadzki, 1993: On the surface of clouds. *J. Atmos. Sci.*, **50**, 5-13.
- Malinowski, S. P., M. Y. Leclerc, and D. G. Baumgardner, 1994: Fractal analyses of high-resolution cloud droplet measurements. *J. Atmos. Sci.*, **51**, 397-413.
- Malinowski, S. P., I. Zawadzki, and P. Banat, 1995: Laboratory observations of cloud clear air mixing in small scales. *Preprints of the AMS Conference on Cloud Physics, January 15-20, Dallas, Texas, USA*, 102-105. also submitted to *J. Atmos. Oceanic Technol.*
- Sreenivasan, K. R., 1991: Fractals and multifractals in fluid turbulence. *Annu. Rev. Fluid Mech.*, **23**, 539-600.

CALCULATION OF PARAMETERS OF A CUMULONIMBUS CLOUD TAKING INVOLVEMENT INTO ACCOUNT

Ya.A. Ekba,

M.R. Vatiashvili, R.G. Zakinyan

Scientific - and - Production Geophysical Center,
Stavropol, Russia

M.K. Zhekamoukhov

Kabardian - Balkar University, Nalchik, Russia

A nonadiabatic one - dimensional model of a cumulonimbus cloud (Cb) which makes it possible to calculate an involvement coefficient and with its help - the distribution in height of some parameters by the actual data of atmosphere sounding taken closely to the moment of convection maximum development - is proposed. The mentioned parameters: the speed of the cloudy air ascending currents (V), this air temperature (T), specific and absolute water content (W).

Equations of motion, heat balance, moisture balance and absolute water content are assumed as a basis of calculations.

The law of change in mass is represented as:

$$\frac{1}{m} \frac{dm}{dz} = K \frac{dE}{dz},$$

where E - the adiabatic energy of

unstability of the air unit mass determined by an aerological diagram, cm^2s^{-2} ; K - the value of a dynamic involvement coefficient conditioned by turbulent stirring, ordered inflow, etc., cm^{-2}s^2 .

Up to the convection level, i.e. to the level of a moist adiabat point of intersection with the curve of atmosphere stratification, ($T_b = T$) value $K = \text{const}$, and above this level up to the cloud upper boundary $K \approx 0$.

For calculation of W, T, q, Q and K we've got 5 equations. They were calculated taking into account the following assumptions: heat - and moisture exchange; weight of the water and crystallization effect; heat - and moisture exchange and the water weight; heat - and moisture exchange.

The following results have been obtained.

The involvement coefficient is strongly dependent on the synoptical situation and physico - geographic characteristic features of the North Caucasus region. On the well expressed in temperature and pressure cold fronts in Kabarda - Balkaria and in the South of the Stavropol region $K = 1.1 \cdot 10^{-7} \text{cm}^{-2} \text{s}^2$, in North

Ossetiya $K = 3,6 \cdot 10^{-7} \text{cm}^{-2} \text{s}^2$, in the Krasnodar region $K = 5.2 \cdot 10^{-7} \text{cm}^{-2} \text{s}^2$. On the poorly expressed cold fronts these values equal accordingly to $4.5 \cdot 10^{-7}$, $6 \cdot 10^{-7}$ and $6.3 \cdot 10^{-7} \text{cm}^{-2} \text{s}^2$; at the air - mass processes - to $4.4 \cdot 10^{-6}$, $1.3 \cdot 10^{-6}$ and $1.1 \cdot 10^{-6} \text{cm}^{-2} \text{s}^2$.

Table

Distribution in height of the Cb parameters

Parameter	Height, km									
	1	2	3	4	5	6	7	8	9	10
W (m/s)	7.5	17.2	19.5	23.1	23.5	27.1	30.2	31.6	24.0	4.0
(W _a -W)/W _a (%)	37.1	22.9	36.4	38.7	45.2	43.5	42.8	42.5	56.4	91.5
q 10^{-3} (g·g ⁻¹)	1.9	3.4	4.2	4.8	5.6	5.6	5.9	6.1	6.2	6.2
(q _a -q)/q _a (%)	36.4	16.0	23.6	30.6	33.7	36.8	38.8	39.6	39.4	39.4
Q (g·m ⁻³)	1.9	3.1	3.5	3.7	3.8	3.4	3.0	2.7	2.2	1.7
(Q _a -Q)/Q _a (%)	9.2	16.0	23.6	30.6	33.7	36.8	38.8	39.6	39.6	39.4

Buoyancy improvement of the cloud air at crystallization is balanced out by the buoyancy decrease due to the weight of the accumulated water. The values of parameters Cb calculated for the general case are, on the average, 20 - 30 % less than the similar ones obtained with the help of an adiabatic model. Calculated taking into account heat - and moisture exchange, water weight and crystallization at

$K = 1.1 \cdot 10^{-7} \text{cm}^{-2} \text{s}^2$ and comparison them with the adiabatic ones (a), is presented in the Table.

The obtained results made it possible to solve an inverse problem: to calculate parameters W, T, q, Q by the known synoptical situation and corresponded to it value of K; the said parameters are used in some methods of forecasting dangerous convective weather phenomena.

TURBULENT ENTRAINMENT INTO CUMULUS CLOUDS

Peter R. Jonas, Jacques R M Pasquier and Samantha A Smith

Physics Department, UMIST, Manchester M60 1QD, UK

1. INTRODUCTION

Turbulent transport within the cumulus-capped boundary layer is an important mechanism coupling the boundary-layer to the free troposphere transporting heat and water from the surface, as well as pollutants. In cloud systems, there are a variety of possible sources of turbulent kinetic energy, including differential radiative heating, latent heating and shear production. The importance of the different sources and the associated turbulent transports have been established for stratocumulus clouds (eg Nicholls, 1984) but few data exist for cumulus cloud fields in which there is considerable variation between the turbulence characteristics within and between the clouds (Kitchen and Caughey, 1981, 1982). In this paper we briefly summarize observations of the turbulent fluxes in maritime cumulus clouds penetrating the capping inversion. We demonstrate that a Large Eddy Simulation of such clouds produces turbulent kinetic energy profiles in reasonable agreement with the observations. We then use the simulations to identify the sources of the turbulent kinetic energy which are compared with those in stratocumulus layers. Air parcel trajectories derived from the model are used to highlight the effects of clouds on the exchange of air across the capping inversion at the top of the boundary-layer.

2. OBSERVATIONS

Smith and Jonas (1995) describe observations of the turbulent kinetic energy profiles in a number of cases of warm, non-precipitating, maritime cumulus clouds with a maximum depth of 3 km. They point out that in cases where the clouds penetrated the capping inversion, the maximum turbulent kinetic energy was found towards the top of the cloud, while in cases which did not penetrate the

inversion, the maximum was rather lower in the cloud. It was suggested that a major source of turbulent kinetic energy in the more vigorous clouds was through the formation of negatively buoyant downdraughts as a result of entrainment and evaporative cooling at cloud top. This conclusion was supported by the fact that the observations suggested the cloud tops were unstable to cloud-top entrainment instability (MacVean and Mason, 1990). The observations also showed that downdraughts contained a significant fraction of air originating from above the inversion, while the updraughts were composed largely of air from below cloud base.

3. LARGE EDDY SIMULATIONS

The large eddy model (Mason, 1989) with bulk parametrized microphysics was run with initial conditions based on one of the observed cases reported by Smith and Jonas (1995). For these three-dimensional simulations, the horizontal grid length was 200 m, the vertical grid length around 25 m and the domain was 10 x 10 x 4.7 km deep. Cyclic lateral boundary conditions were used with a damping layer in the top 900 m of the domain. The lower boundary was a stress-free rigid boundary with specified heat and moisture fluxes. The convection was initiated with a localized temperature perturbation. The initial profile was based on that observed and the prescribed, constant, surface fluxes were derived using the bulk aerodynamic formulae with observed air and sea temperatures.

The model was run for 6 h. During the latter 3 h of the run, a quasi-steady state was set up in which the average turbulent kinetic energy through the domain oscillated about a stationary mean as successive cumulus clouds grew and decayed with a period of about 40 min. There were typically one

or two clouds in the domain at this time, consistent with the observations of cloud size and spacing. The values of the cloud top water content and maximum updraught in the simulated clouds (1.5 g kg^{-1} and 5 m s^{-1}) were consistent with observed values, as were the cloud base (1 km) and typical values of the cloud top height (2.4 km). Analysis of the flow field through the simulated clouds revealed the 'P' shaped circulation observed by Kitchen and Caughey (1981, 1982) in small cumulus clouds.

4. RESULTS

4.1 Turbulent kinetic energy

From the simulated fields, a profile of the in-cloud turbulent kinetic energy was derived, averaged over three overlapping 10 min intervals. A typical averaged profile is shown in Figure 1, on which are also shown the observations of Smith and Jonas (1995) for their case A119. To facilitate the intercomparison, heights have been normalized using the distance between cloud base and the inversion ($z = 0$ corresponding to cloud base, and $z = 1$ to the average cloud top). The model correctly simulates the strong maximum in the turbulent kinetic energy towards cloud top, as well as giving reasonable quantitative agreement with the observations.

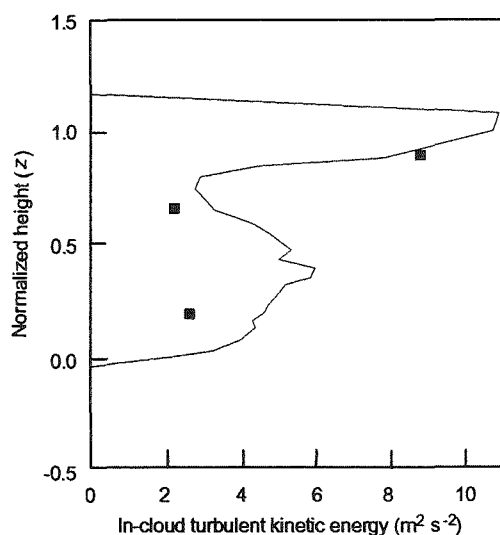


Figure 1. In-cloud profile of the turbulent kinetic energy derived from the simulation. Observations from Smith and Jonas (1995) are denoted by ■.

The contribution of different source and sink terms in the turbulent kinetic energy budget in the cloudy regions is shown in Figure 2. These calculations allow for transport through cloud boundaries. It is apparent that buoyancy production is the largest source of turbulent kinetic energy in these weakly sheared clouds, with a maximum production due to latent heating just below the mid-level in the cloud. There is also a small, but significant, buoyancy source of turbulent kinetic energy near to cloud top, resulting from entrainment and evaporative cooling in this part of the clouds. Most of the turbulent kinetic energy dissipation also occurs near cloud top, implying a large vertical transport of turbulent kinetic energy, as was observed.

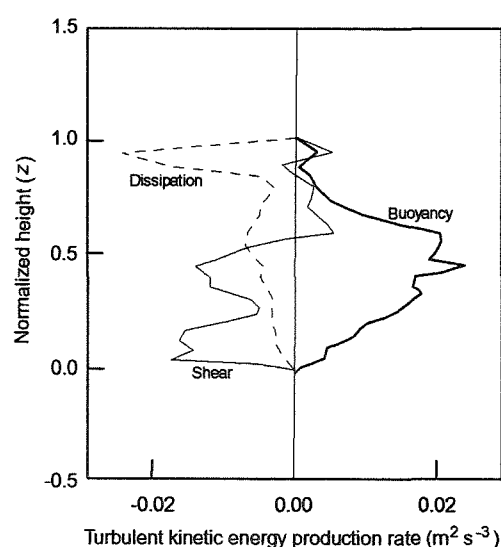


Figure 2. Profiles of sources of turbulent kinetic energy within the simulated cumulus clouds by buoyancy and shear stresses, together with the diagnosed turbulent dissipation.

The turbulent kinetic energy profile averaged horizontally through the domain is shown in Figure 3. In the cloud layer, the shape of the profile is similar to that in the cloud, reflecting the small contribution from the relatively quiescent clear air regions between the clouds. Much of the noise in the profile is associated with variations in the cloudy area at each level, varying between 0.04 and 0.11, with an overall cloud cover of 0.15. The fact that the maximum is at a higher level than that within cloud reflects the greater cloud cover at this level. The large values of the turbulent kinetic energy below cloud base, approaching the average values in the cloud layer, are a consequence of the strong surface heating.

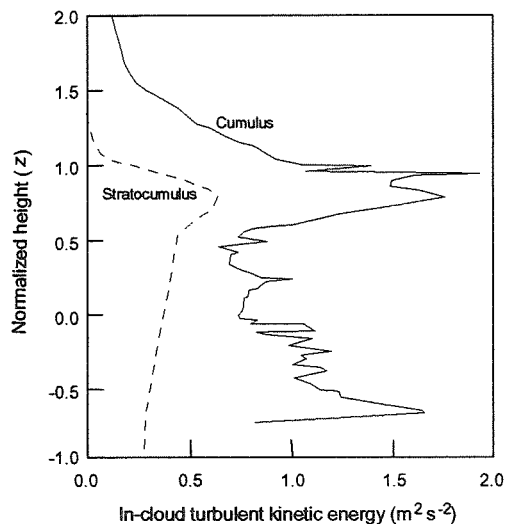


Figure 3. Profiles of turbulent kinetic energy averaged horizontally through the domains from simulations of cumulus and stratocumulus.

Also shown in Figure 3 is the horizontally averaged turbulent kinetic energy profile from a simulation of a nocturnal, ie radiatively cooled, stratocumulus layer obtained from a model run with reduced domain and increased resolution. The case, which formed the basis of the recent model intercomparison workshop, is described by Moeng *et al* (1996). The cloud base was at 480 m and cloud top at 740 m, with almost 100% cloud cover. The turbulent kinetic energy profile again has a maximum in the upper part of the cloud layer, but decreases below cloud base as there was little surface heating in this case.

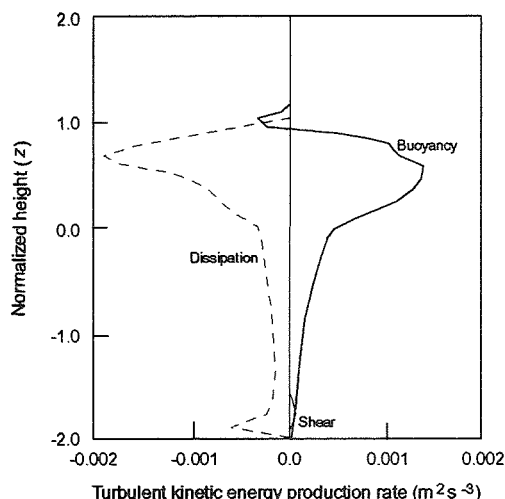


Figure 4. As Figure 2, except for the stratocumulus layer, averaged through the domain. The in-cloud profiles are almost identical due to the almost complete cloud cover.

The sources of the turbulent kinetic energy are shown in Figure 4. In this stratocumulus case, generation by the shear is negligible and, as in the cumulus case, there is a strong buoyancy source at mid-level in the cloud. However, there is a sink of turbulent kinetic energy near cloud top, despite the strong radiative cooling. In both cases most of the dissipation of turbulent kinetic energy occurs near cloud top, implying large vertical transports of turbulent kinetic energy.

The results show that although there are similarities in the mean profiles of turbulent kinetic energy in the two cloud systems, a cumulus-capped layer driven by strong surface heating and a radiatively cooled stratocumulus cloud layer, there are significant differences in the balance of the energy-producing processes and these have an impact on the mean profiles and on the turbulent transports within the clouds.

4.2 Exchange of air through the inversion

In order to investigate the role of the cumulus clouds on the exchange of air through the capping inversion, trajectories of representative air parcels were obtained from the time-series of wind fields from the simulation. (Pasquier and Jonas (1996) describe the technique and calculate microphysical development along these trajectories.) The results show that air from below cloud base, even from close to the surface, may be carried in the cloud updraught regions to the inversion. However, there is little evidence that this air is detrained above the capping inversion. There is also evidence that air is entrained into the clouds, both laterally and through cloud top. In the latter case, air from above the inversion may be brought down in penetrative downdraughts and detrained into the sub-cloud layer. Therefore, the clouds promote the entrainment of air into the boundary-layer, although there is little evidence that they result in air being transported from the boundary-layer into the free troposphere.

5. CONCLUSIONS

The results demonstrate that Large Eddy Simulation models can yield turbulent kinetic energy profiles in reasonable agreement with observations and hence may be used to diagnose transport and generation processes in broken cloud

layers. They also demonstrate that while the average turbulent kinetic energy profiles may resemble those in more uniform stratocumulus cloud layers, the mechanisms are very different. Trajectory analyses suggest that while cumulus clouds may locally increase the entrainment of air from above the capping inversion into the boundary-layer, there is little evidence that these small cumulus clouds result in significant venting of the boundary-layer air into the free troposphere.

6. REFERENCES

- Kitchen, M., and S. J. Caughey, 1981: Tethered-balloon observations of the structure of small cumulus clouds. *Quart. J. Roy. Meteorol. Soc.*, **107**, 853-874.
- Kitchen, M., and S. J. Caughey, 1982: Corrigendum to Kitchen and Caughey (1981). *Quart. J. Roy. Meteorol. Soc.*, **108**, 470-471.
- MacVean, M. K., and P. J. Mason, 1990: Cloud-top entrainment instability through small-scale mixing and its parameterization in numerical models. *J. Atmos. Sci.*, **47**, 1012-1030.
- Mason, P. J., 1989: Large-eddy simulation of the convective atmospheric boundary layer. *J. Atmos. Sci.*, **46**, 1492-1516.
- Moeng, C.-H., W. R. Cotton, C. Bretherton, A. Chlond, M. Khairoutdinov, S. Krueger, W. S. Lewellen, M. K. MacVean, J. R. M. Pasquier, H. A. Rand, A. P. Siebesma, R. I. Sykes, and B. Stevens, 1996: Simulation of a stratocumulus-topped PBL: Intercomparison among different numerical codes. *Bull. Amer. Meteorol. Soc.*, (in press).
- Nicholls, S., 1984: The dynamics of stratocumulus: aircraft observations and comparisons with a mixed layer model. *Quart. J. Roy. Meteorol. Soc.*, **110**, 783-820.
- Pasquier, J. R. M. and P. R. Jonas, 1996: Three-dimensional dynamics in a one-dimensional condensational growth model of cumulus clouds. *Proc. 12th Int. Conf. on Clouds and Precip.*, Zurich, 19-23 August 1996.
- Smith, S. A., and P. R. Jonas, 1995: Observations of the turbulent fluxes in fields of cumulus clouds. *Quart. J. Roy. Meteorol. Soc.*, **121**, 1185-1208.

AN ANALYSES FOR THE PRECIPITATION STRUCTURE OF THE STRATIFORM CLOUD SYSTEM IN NORTH CHINA

Duan Ying Wu Zhihui Shi Lixin

Hebei Province Weather Modification Office

11 Tiyu Zhong Street, Shijiazhuang, 050021, P. R. China

1. INTRODUCTION

Hebei Province is located in the North China Plain where the average annual precipitation is 540 millimetres, and the crops are always damaged by the drought. The operations of artificial precipitation enhancement have been carried out in the past thirty years in this area, and research projects have been progressed in past five years (1990-1994), some results reports were reported by You Jinyan et al(1994). In this paper, an case analysis on the cloud structure, precipitation characteristics and cloud seeding conditions of the precipitating stratiform cloud system in North China during 26-28 June 1993 is given.

2. MEASUREMENTS AND DATA

In North China area the stratiform cloud system are important rainfall processes in spring and

summer. In this case a weather process moved from west. and affected Hebei province area was in night of 26 June 1993. A cloud belt appeared from east to west on satellite infrared images over Hebei at 20:00 (BST) 27 June. The rainfall began in the night of 26 June.

In order to study the structure of cloud system, the characteristics of natural precipitation and cloud seeding conditions, the systematic observations were performed for this weather process. An aircraft equipped with the PMS probes had done the measurements three times through for cloud over Hebei province during 26-27 June 1993. The radio-sondage was released from surface at four hours interval. At the same time, the integrated liquid water content and vapour content in atmosphere were remote continuously by the dual frequency microwave radiometer on ground. And the radar echo data, meteorological satellite images and rainfall intensity were collected simultaneously.

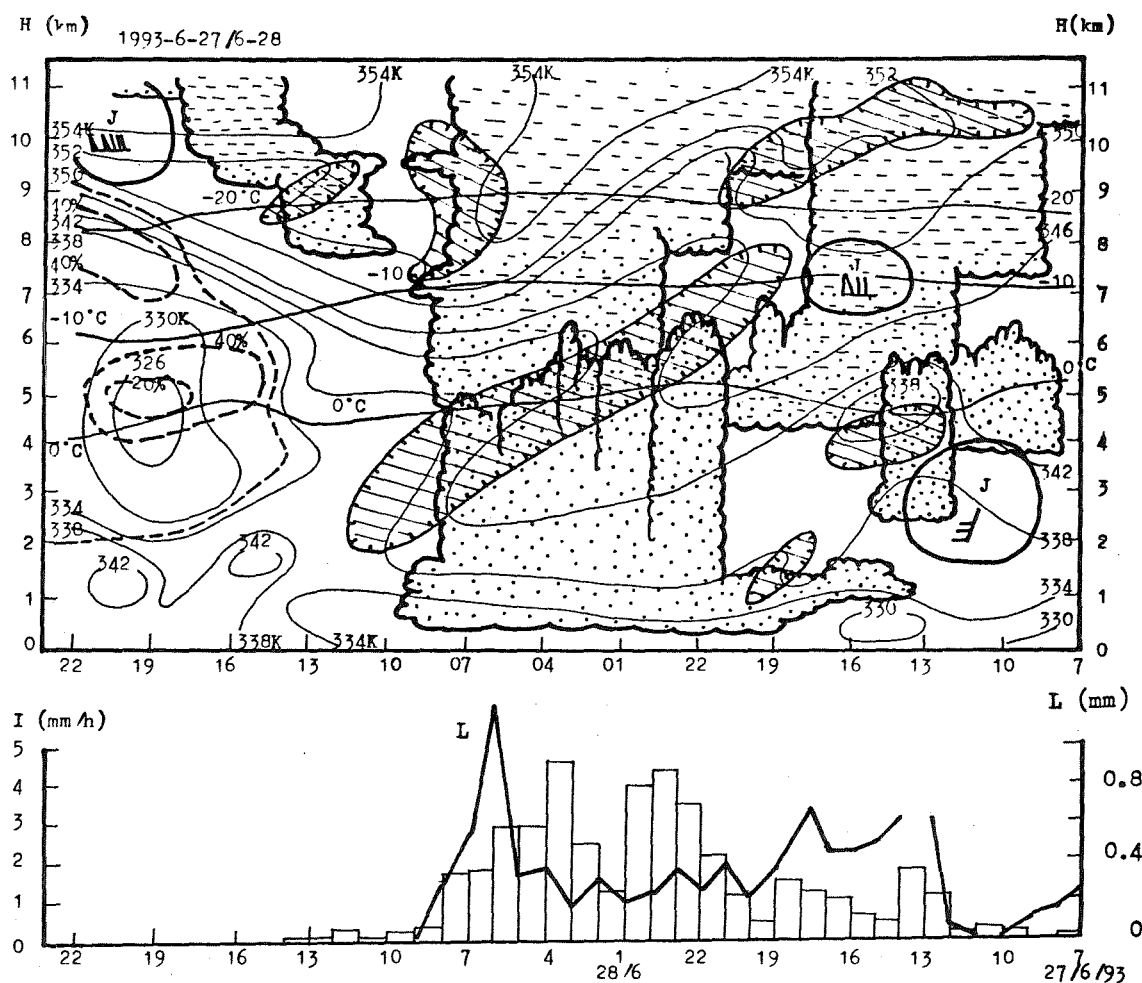


Figure 1 The time height cross-section of radiosonde data at Xingtai (37°N , 115°E). The horizontal coordinates is time, the vertical coordinates is the altitude above sea level, the under figure is the variation of rainfall intensity with time. The dot area is the cloud region with water droplet in lower level, and the short line area indicate the ice crystal region in the upper. J is region of bigger wind velocity in the figure. The wind arrow in the figure shows that the warmer wet air flowed from southwest direction of lower level into the cloud system.

3. RESULTS AND ANALYSIS

Figure 1 is the time height cross-section of radiosonde data at Xingtai (37°N, 115°E). The horizontal coordinates is time, the vertical coordinates is the altitude above sea level, the under figure is the variation of rainfall intensity with time. The isolines of temperature, potential pseudo-equivalent temperature and relative humidity are given in the figure. The dot area is the cloud region with water droplet in lower level, and the short line area indicate the ice crystal region in the upper. J is region of bigger wind velocity in the figure. The wind arrow in the figure shows that the warmer wet air flowed from southwest direction of lower level into the cloud system. Therefore the structure of air flow field is favourable for the cloud development. Based on the weather radar and cloud images data, there are weak convective cell cluster in the cloud system. The altitude of 0°C level is 4-5 km above sea level. The vertical thickness of cloud system is nearly 8 km, the maximum cloud top height is 10 km. Thus the cloud system is deeper. It is obvious that the cloud system is well developed and the conditions of natural precipitation is very favourable.

On the other hand, based on the

data of FSSP probe equipped at the aircraft (the figure is omitted), the maximum value of the supercooled liquid water content (SLW) is 0.1156 g m⁻³ in the middle-upper level of cloud system, and the maximum value of LWC is 0.1014 g m⁻³ in middle-lower level (under the 0°C level). The data of 2D-C probe show that the distribution of ice crystal concentration and liquid water content are obviously inhomogeneous in the stratiform cloud system.

The precipitation is formed when the cloud liquid water integrated amount value of L measured by the microwave radiometer is nearly 0.3 millimetre, and the rainfall intensity increased with the L value. The maximum value of L is 1.2 mm in the precipitation process. Therefore, it can be seen that there is the condition of cloud seeding at some area in this cloud system.

4. CONCLUSION

This case analysis results show that the natural precipitation conditions is relatively complete in the cloud system. The rainfall appears while the liquid water integrated amount value measured by a dual frequency microwave radiometer is nearly 0.3 millimetre over the surface. It has been found

that the condition of cloud seeding is existing at the region of SLW (supercooled liquid water content) more than 0.1 g m^{-3} and ice crystal concentration less than 10 l^{-1} in the cloud area.

5. Acknowledge

This study is supported by the Natural Sciences Foundation of Hebei Province, China.

REFERENCES

Duan Ying et al, 1992: Observational research on seeding cloud

conditions of aircraft artificial precipitation operation, WMP Report No.19, WMO workshop on cloud microphysical and applications to global change, 10-14, August, 1992, Toronto, Canada, Wmo/TD No 537, pp, 235-240.

Duan Ying et al, 1994: The study of stratiform cloud microstructure and the conditions of cloud seeding in different season over Hebei province area, WMO sixth scientific conference on weather modification, 30 May-4 June, Peastum, Italy, WMP/TD. No.22.

You Jinyan et al, 1994: The study of technology on precipitation physics and weather modification, Meteorology Press, China.

THE NORTHEAST OF BRAZIL CUMULUS CLOUD: AN OBSERVATIONAL AND THEORETICAL STUDY

Antônio José C. Sampaio¹, Carlos Jacinto de Oliveira², Alexandre A. Costa³ and José Carlos P. de Oliveira¹

¹Physics Dept., Universidade Federal do Ceará (UFC)

²Physics and Chemistry Dept., Universidade Estadual do Ceará (UECE)

³Meteorology Dept., Fundação Cearense de Meteorologia e Recursos Hídricos (FUNCEME)

1. INTRODUCTION

The evolution of an isolated cumulus cloud in June 22, 1994 (CC940622) over northeast region of Brazil (NEB) was monitored using the FUNCEME's instrumented aircraft (ALPA), described by de Almeida et al. (1992). ALPA is capable of furnishing 1 Hz measurements of temperature, dew point temperature, liquid water content(LWC), pressure, CCN concentration and concentration and mean diameter of drops on ranges of 30–450 μ m and 0.3–4.5 mm. It also furnishes 10 Hz measurements of droplet spectra with a PMS Forward Scattering Spectrometer Probe (FSSP). The data set obtained was analyzed (with distinction to FSSP measurements) and used to initialize two simple cloud models developed in the Cloud Physics and Mesoscale Laboratory of UFC.

2. THE MEASUREMENTS

In June, large precipitating systems are not common in the north portion of NEB and, on the afternoon of June 22, 1994, only isolated cumuli were observed over the coastal region of NEB, exhibiting small wind shear effects.

From 1438LST¹ to 1451LST, five passes in CC940622 were performed, from the cloud base (~900m) to its top (~3000m). Visually, it was observed that this cloud remained stable, producing small precipitation during this time.

Fig. 1 shows the corrected concentration and mean diameter obtained by the FSSP, the air temperature and height for the second(a) and the fourth(b) passes. The increase of the maximum value of the mean diameter from 12 μ m to 18 μ m was evident, according to a standard behavior of growth of the droplets with height.

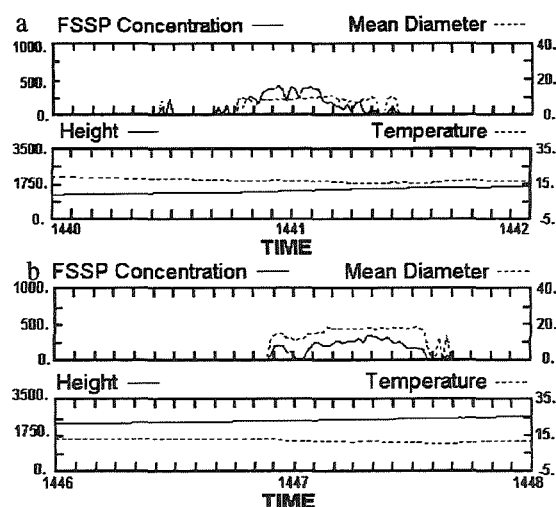


Fig. 1 - FSSP concentration, mean diameter, height and temperature for 2nd(a) and 4th(b) passes

The growth of the mean diameter is intrinsically related to the broadening of the spectrum. Fig. 2 shows that CC940622 exhibits narrow spectra at cloud base with small values for the mean diameter(a) and broad spectra near the top(b). Bimodal spectra are also observed, in the last sequence, showing that significant entrainment and turbulent mixing appear at cloud top(c).

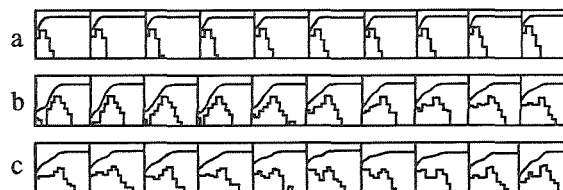


Fig. 2 - FSSP spectrum at each 0.1s, for the first pass (a)(t = 14:38:21) and the last pass (b)(t = 14:50:28) and (c)(t = 14:50:41)

In Fig. 3 it can be seen that CC940622 LWC clearly increases with height (from 0.1 g/m³ at cloud base to 1.1 g/m³ near its top).

¹ Local Standard Time is UTC minus 3h

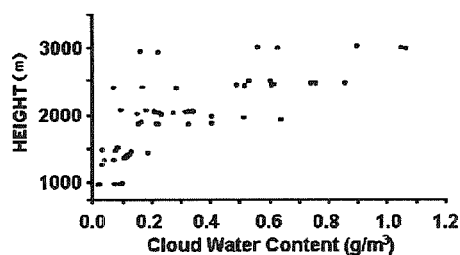


Fig. 3 - Cloud water content with height

3. NUMERICAL SIMULATIONS

Numerical simulations were performed with two simple models: an One-and-half dimensional model, with detailed microphysics (Lobato, 1994) and a Two-dimensional model, with parameterized microphysics (Costa, 1995). The initialization of both models were made defining a basic state, obtained through a smoothing of the ALPA data for pressure, temperature and relative humidity. Fig. 4 shows the vertical profile of temperature and relative humidity for the environment and this additional parcel.

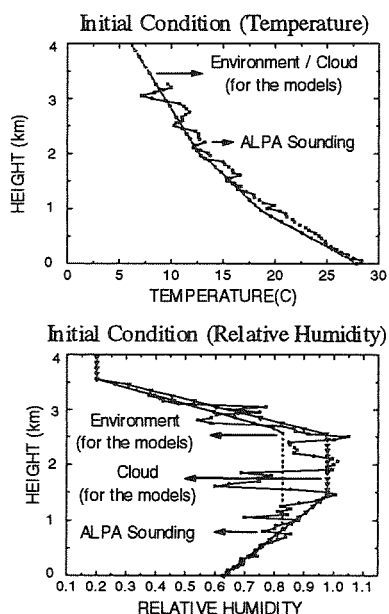


Fig. 4 - Vertical profiles (measured and adjusted) of temperature and relative humidity

3.1 One-and-half dimensional model

The present model has a simple dynamics, similar to that proposed by Asai and Kasahara (1967). Prognostic equations for vertical velocity, temperature, water vapor mixing ratio and distribution functions of droplets and CCN are solved. Radial velocity is calculated diagnostically, according to the anelastic approximation for continuity equation. The microphysical scheme includes

nucleation, condensation-evaporation, coalescence and break-up processes. Advection is evaluated using a semi-lagrangian procedure with a cubic spline interpolation (Purnell, 1976). An adequate treatment of the CCN distribution leads to reasonable values of supersaturation (maximum of 2.6% at this simulation), in contrast to other models that, when evaluating stochastic coalescence, produce unrealistically high values for the supersaturation.

Figs. 5, 6 and 7 depicts, respectively, the time evolution of vertical velocity, cloud water content and rain water content as predicted by this model. A maximum updraft of 5.1 m/s occurs at 34 min of simulation. Significant downdrafts, related to the evaporation process, are present at cloud top region.

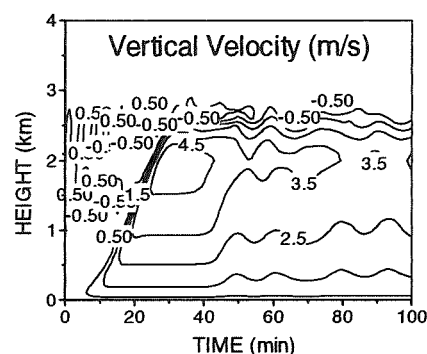


Fig. 5 - Time evolution of the vertical velocity (one-and-half dimensional model)

Fig. 6 shows that the time evolution of the cloud water content is strongly associated with the vertical velocity field, reaching a maximum value of 2.1 g/m^3 at 34 min.

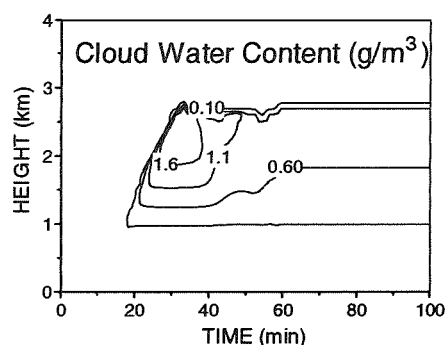


Fig. 6 - Time evolution of the cloud water content (one-and-half dimensional model)

Fig. 7 shows that the maximum value of rain water content of 3.8 g/m^3 occurs at 49 min, after the maximum cloud water was reached. Precipitation comes to the ground level at 41 min of simulation, and a maximum rain water content at ground level (0.9 g/m^3) occurs at 79 min.

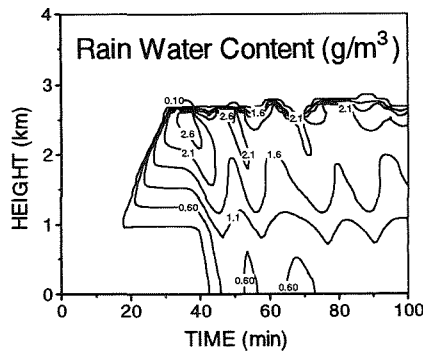


Fig. 7 - Time evolution of the rain water content (one-and-half dimensional model)

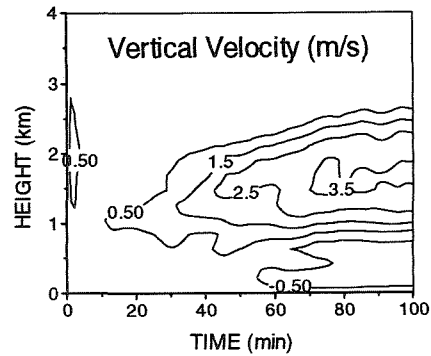


Fig. 8 - Time evolution of the vertical velocity (two dimensional model)

3.2 Two-dimensional model

The Two-dimensional model is similar to that proposed by Soong and Ogura (1973). Mass continuity is represented by the continuity equation for deep convection (anelastic assumption). The equations of motion are combined to result in a prognostic equation for vorticity. The wind components are calculated from a streamfunction, that is related to the vorticity through a diagnostic equation. The energy conservation is represented by an equation for the potential temperature. Three equations are related to the water conservation, evaluating water vapor, cloud water and rain water mixing ratios. Advection is solved using a semi-lagrangian procedure with a cubic spline interpolation and a first-order closure scheme is adopted to calculate turbulent diffusion. The streamfunction diagnostic equation is solved using an iterative scheme (Stone, 1968). Condensation and evaporation are evaluated according to the saturation technique. Kessler's parameterization is used to represent warm microphysical processes.

Figs. 8, 9 and 10 show the time evolution of the same parameters of the Figs. 5-7, but for the central axis of the two-dimensional cloud.

In Fig. 8 it can be seen that the maximum updraft (3.7 m/s) occurs at 76 min of simulation and that significant downdrafts do not occur in the cloud top region. However, notable downdrafts are present below the cloud base, associated to the precipitation process.

Fig. 9 shows that the correlation between ascending motion and condensation with release of latent heat is also represented by the two-dimensional model. A maximum cloud water content of 2.4 g/m³ occurs at 59 min of simulation.

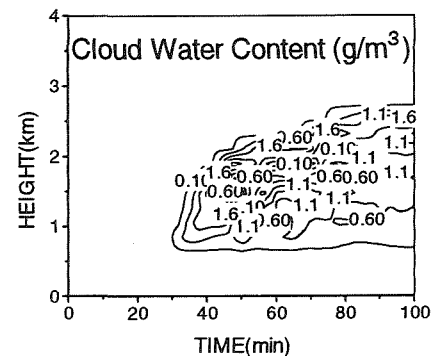


Fig. 9 - Time evolution of the cloud water content (two dimensional model)

Fig. 10 depicts the time evolution of rain water content. A significant amount of rain water is produced just after 42 min of simulation, when conversion processes become important. A maximum value of 2.2 g/m³ occurs at 85 min. Precipitation reaches the ground at 50 min, with a maximum of 2.0 g/m³ at 80 min.

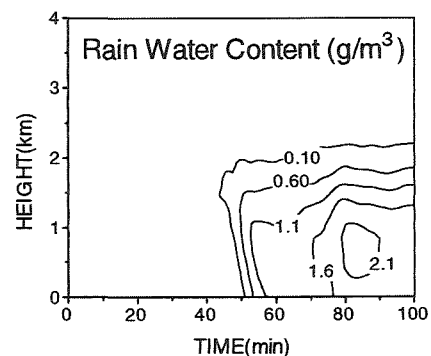


Fig. 10 - Time evolution of the rain water content (two dimensional model)

Fig. 11 shows the spatial distribution of cloud water content for the 80th min of simulation, when the simulated cloud exhibits maximum development. It can be seen that the simulated cloud reaches a

maximum horizontal extension of 5.0 km, with a cloud base at 700m and a cloud top at 2500m.

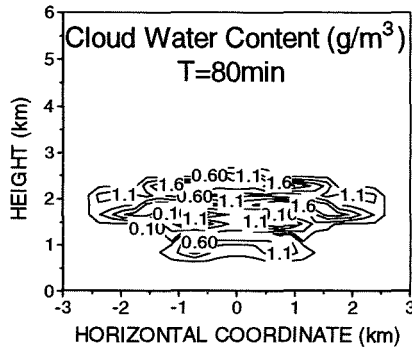


Fig. 11 - Spatial distribution of the cloud water content after 80 min of simulation (two dimensional model)

4. CONCLUSIONS

An experiment with an instrumented aircraft was realized on NEB on June 22, 1994, investigating an isolated precipitating cumulus cloud (CC940622). The micro and macrostructure of CC940622 were analyzed and the experimental data were used to validate the two cloud models described above.

The widening of the droplet spectra and the increase of the cloud water content with height was monitored with FSSP. It is also showed that turbulent mixing is very strong near the top of the cloud, producing bimodal spectra in this region. According to Paluch (1971), turbulent mixing and entrainment are some of the most important factors that influence the cloud evolution, because they permit the interaction between air parcels of different origins.

Parameter	Observed	One-and-half dimensional model	Two dimensional model
Maximum cloud water content	1.1 g/m ³	2.1 g/m ³	2.4 g/m ³
Maximum rain water content	—	3.8 g/m ³	2.2 g/m ³
Cloud base	950m	1050m	700m
Cloud top	3100m	2750m	2500m
Horizontal extension	4500m	—	5000m
Vertical velocity	—	5.1 m/s	3.7 m/s

Table 1 - Observed and simulated parameters of CC940622 cloud

Several important aspects of the real cloud life cycle were reproduced by the simulations, with acceptable values of LWC, height of cloud base and top, vertical velocity, etc. Table 1 compares the observed data and the model results for some significant parameters. It can be seen that reasonable agreement is obtained. The models are capable of simulating qualitatively well the main aspects of the life cycle of a real cloud.

ACKNOWLEDGMENTS

The authors wish to thank to the Department of Atmospheric Science of the University of Wyoming for the permission to use the aircraft data processing programs, Mr. Glenn W. Munroe for his help in the computational task and Dr. Isaka (Université Blaise Pascal) for the permission to use his microphysics routines.

REFERENCES

- Asai, T. and A. Kasahara, 1967: A theoretical study of the compensating downward motions associated with cumulus cloud, *J. Atmos. Sci.*, **24**, 487-496.
- Costa, A. A., 1995: Desenvolvimento de modelo bidimensional axi-simétrico de nuvem com microfísica parametrizada. Master's dissertation, Physics Department, UFC.
- de Almeida, F.C., G. W. Munroe, C. A. R. Morales, M. C. Pereira, F. A. Barros, A. J. C. Sampaio e J. C. P. de Oliveira, 1992: An instrumented aircraft for tropical precipitation physics research: description and opportunity. WMP report, **19**, 145-150.
- Lobato, R. M. F., 1994: Simulação unidimensional completa de uma nuvem quente. Master's dissertation, Physics Department, UFC.
- Paluch, I. R. , 1971: A model for cloud droplet growth by condensation in an inhomogeneous medium. *J. Atmos. Sci.*, **28**, 629-639.
- Soong, S. T. and Y. Ogura, 1973: A comparison between axisymmetric and slab-symmetric cumulus cloud models. *J. Atmos. Sci.*, **30**, 879-893.
- Stone, H. L., 1968: Iterative solution of implicit approximation of multidimensional partial differential equations. *S.I.A.M.J. Numer. Anal.*, **5**, 530-558.

INITIATION OF DEEP CONVECTION BY SHORT GRAVITY WAVES

Ulli Finke and Thomas Hauf

Institut für Physik der Atmosphäre, DLR Oberpfaffenhofen, Germany

1. INTRODUCTION

Tropospheric gravity waves are closely related to deep convection. Storms, for instance, may generate gravity waves by several mechanisms. In the lower troposphere the main wave generation process is the cold air outflow from a thunderstorm downdraft. If the boundary layer is stable stratified the generated gravity waves may propagate over large distances preserving their high amplitudes.

Gravity waves modulate or even initiate the convective activity. The interaction of *mesoscale* gravity waves with oscillation periods larger than 40 minutes is well documented (Koch et al. 1988). It was suggested and demonstrated in numerical studies (Balaji and Clark 1988) that also *small-scale* gravity waves may trigger the development of deep convection due to the wave-induced lifting. Though these short-period gravity waves are frequently present under conditions of shallow convection, their interaction with deep convection is still less understood. The small wave amplitudes cause severe observational difficulties. Here a case study is presented where the initiation of deep convection by small-scale gravity waves is studied. A network of microbarographs, radar, and aircraft observations are used together with linear model calculations.

2. GRAVITY WAVE OBSERVATION

Gravity waves were observed by a microbarograph network located in southern Germany. This network consists of an array of 4 pressure sensors with an average separation of about 1 km. The sensors have a high sensitive capacitor microphone which measures the differential pressure between the ambient air and an internal reservoir. Pressure variations of period ranging from 2 s to approximately 30 minutes can be resolved with a resolution of 3 μ bars.

Short period gravity waves appear mostly as wave packets of only a few oscillations. For isolating these events in time and frequency space a special wavelet-filter technique is applied. A cross-correlation method determines propagation speed and direction of the wave packet. Details of the network parameters and the data processing are given by Hauf et al. 1996.

3. CASE STUDY

On 25 July, 1992, during the CLEOPATRA cloud physics experiment, strong wave activity was observed by the microbarograph array. Fig. 1 depicts the time series of pressure variations from all 4 sensor stations. Below the curves the derived propagation velocity vectors are shown.

Oscillation periods of the waves range between 10-15 minutes with amplitudes reaching 60 μ bar. The waves appeared in short wave trains from slightly varying directions. This points to an unstationary generation process. During daytime, and in the presence of shallow convection, gravity waves are hard to detect at the ground. Due to the low stability of the convectively mixed atmosphere, the short waves are evanescent in the boundary layer and do not propagate downward from their elevated generation levels. Waves with strong amplitudes observed at the ground for the considered day, therefore, indicate extraordinary large amplitudes at greater altitudes and an effective generation mechanism. The likely source of the waves was the interaction of shallow convection with the sheared flow above the convective boundary layer. Aircraft measurements at altitudes between 3 and 10 km revealed gravity waves with wave lengths 10-15 km which then suggest the gravity waves being of the type "convection waves" (Hauf 1993). In the late afternoon thunderstorms developed in the observational area and were observed with the DLR Doppler and polarization radar.

Conventional analysis of the soundings revealed that the atmospheric stratification conditions did not favour the development of deep convection. Two layers with enhanced stability inhibited the initiation of deep convection.

It was a reasonable assumption that additional lifting supplied by the gravity waves might significantly support the development of deep convection. The amount of wave-induced lifting in the overlying inversion was estimated with a linear and stationary model. It was found that the waves with the observed oscillation periods and phase velocity were unstable eigenmodes for the given stratification of the atmosphere. These modes were trapped in wave-guide structure which explained the large wave amplitudes at the ground.

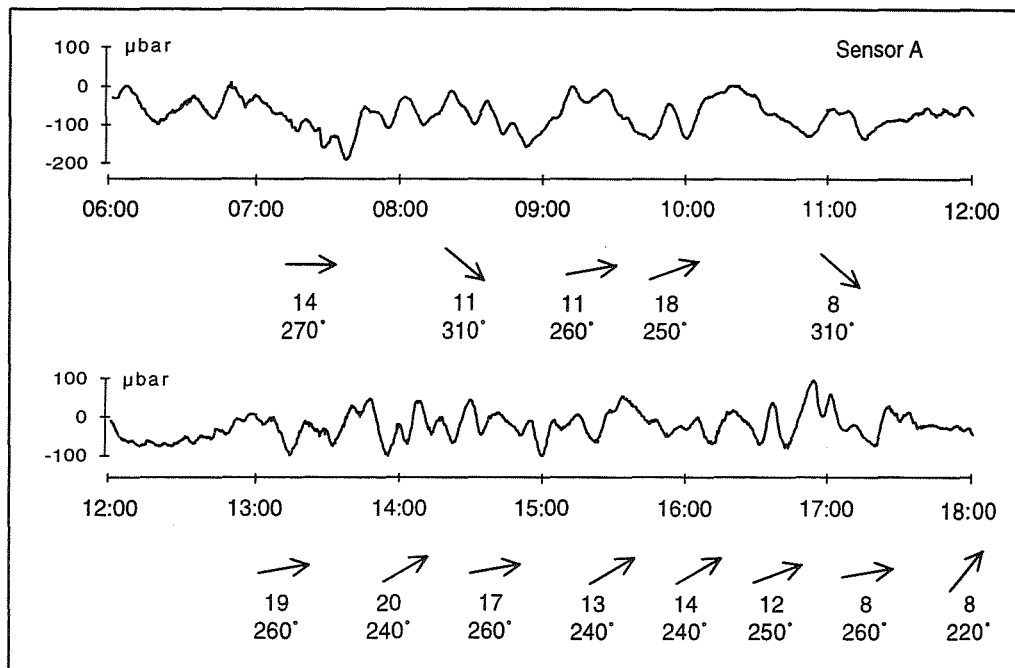


Fig. 1: Time series of pressure variations. The arrows and numbers below the graph indicate the calculated propagation velocity vector.

For the amplitudes observed at the ground, the lifting amplitudes were calculated to be 150-300m over a large height range. Observed wave-amplitudes aloft agree with this value and also agree with the observed surface-pressure fluctuations. This additional lifting, therefore, was sufficient for the initiation of deep convection.

This confirms results from numerical simulations by Balaji and Clark (1988). Thus, an initiation mechanism for deep convection is proposed where shallow convection in the presence of shear initiates gravity waves, the convection waves, which then fill the whole troposphere and also may provide the required lift for deep convection. The wave-induced triggering can be seen as a further candidate for thunderstorm initiation, in addition to the well known ones of orographic forcing, thermal instability and boundary-layer convergence.

5. REFERENCES

Balaji, V., T. L. Clark, 1988: Scale Selection in Locally Forced Convective Fields and the Initiation of Deep Cumulus. *J. Atmos. Sci.*, **45**, 3188 - 3211.

Hauf, T., 1993: Aircraft observation of convection waves over Southern Germany - A case study, *Mon. Wea. Rev.*, **121**, 3280-3290.

Hauf, T., U. Finke, J. Neisser, G. Bull, J.-G. Stangenberg, 1996: A ground based network for atmospheric pressure fluctuations, *J. Atmos. Oceanic Technol.* (accepted)

S. E. Koch, R. E. Golus, P. B. Dorian, 1988: A Mesoscale Gravity Wave Event Observed during CCOPE. Part II: Interactions between Mesoscale Convective Systems and the Antecedent Waves. *Mon. Wea. Rev.*, **116**, 2545 - 2569.

CHARACTERISTICS OF CLOUDS, CLOUD CLUSTERS AND A SUPERCLUSTER OBSERVED ON NOVEMBER 11-12, 1992 DURING THE TOGA-COARE IOP

Md. Nazrul Islam*, Hiroshi Uyeda, Osamu Kikuchi and Katsuhiro Kikuchi

Meteorological Laboratory, Division of Earth and Planetary Sciences, Hokkaido Univ., Sapporo 060, Japan

1. INTRODUCTION

One of the important scientific objectives of the TOGA-COARE(Tropical Ocean Global-Atmosphere program, Coupled Ocean-Atmosphere Response Experiment) is to describe and better understand the cloud-climate interaction and to study the large-scale cloud cluster in order to understand the impact of clouds on the climate. Prompt analyses of cloud clusters during the TOGA-COARE IOP (Intensive Observation Period) have been reported in several works.

For a better understanding of the water budget and to estimate the amount of imported moisture over the warm pool, it is necessary to separate the stages of the tropical cloud objectively. It is also necessary to divide the convective and stratiform cloud components into both radar and satellite images. In this analysis, the Convective Stratiform Technique(CST) algorithm was chosen because it was tested for the analyses of Florida convection (Adler and Negri, 1988), the Winter Monsoon Experiment (WMONEX) cloud clusters (Goldenberg et al., 1990) and TOGA-COARE cloud clusters (Kikuchi and Uyeda, 1996; Islam, 1996).

2. DATA AND METHODS

The research vessel "Keifu Maru" which was anchored in the TOGA-COARE IFA(Intensive Flux Array), carried a C-band (wavelength: 5 cm) conventional weather radar covering 250 km in radius (Fig. 1). The ship track of the Keifu Maru on the TOGA-COARE cruise is described in Mori (1995). Reflectivity data digitized over a 2.5 km mesh. 7.5 minute interval PPI($\text{el.}=0.0^\circ$) data from November 3-12, 1992 was utilized. The GMS-4 T_{BB} data (0.1° mesh on CD-ROM) provided by Dr. Nakazawa, Meteorological Research

Institute, Japan Meteorological Agency (JMA) were utilized. The JMA global analysis dataset (GANAL) with the 1.875° grid was also utilized.

The radar echoes($\geq 20\text{dBZ}$) were derived from the Keifu Maru PPI scan data. In order to calculate rain rate from reflectivity, this analysis adopted the standard Z-R relationship given by

$$Z=BR^\beta \quad (1)$$

where Z is the radar reflectivity, R is rain rate, and B and β are positive numbers. The most popular values of 200 and 1.6 for B and β respectively, determined by Marshall and Palmer (1948), were adopted in this analysis. The modified CST that is adapted for the TOGA-COARE (Islam, 1996) was used to analyze GMS-IR data, because this CST is uniquely able to provide information when clouds are out of radar range.

3. RESULTS

3.1 Squall line-like nonisolated radar echo (November 11-12 in IFA region)

Figure 2 represents the detailed structure and evolution of a squall line-like(SLL) nonisolated echo. Four echo cells a1, a2, a3, and b1 were identified at 2104GMT on November 11 at different locations. Their locations were traced in 30 minutes intervals. All of the echo cells moved to the ENE. Two cells, named a1 and a2, combined at 2204GMT. This combined echo of a1 and a2 is called the main echo. A new cell b2 was born at 2234GMT in the NE flank of the main echo. The combination of b1 and b2 joined with the main echo at 0004GMT on November 12 and started to form a line echo. Another new echo a4 was identified in the SW flank of the main echo at 2304GMT on November 11, and thus the chain continued. The maximum horizontal dimension of the SLL echo was about 340 km in length at 0204GMT on November 12. As the echo traversed, a few of the fragments (fs) separated from the main echo at different times. A large fragment f1(~ 60 km in length) and the main echo were out of radar range after 0245GMT and 0345GMT respectively. However, through examination of hourly GMS-IR data, this SLL echo was found to last approximately 13 hours and traverse a distance nearly 350 km in its lifetime (not shown). Similarly, the organization and life history of a quasicircular isolated radar echo was analyzed (not shown). This echo consisted of seven individual small echo cells and four fragments. The first echo cell was identified at 2122GMT on November 11. This quasicircular isolated echo traversed a distance of about 155 km in its lifetime (~ 5 hours).

To clarify the significant behavior of the SLL echo, its area and rain rate are shown in Fig. 3. The first peak appeared at the early developing stage, related to the warm rain; the second peak appeared when the area reached

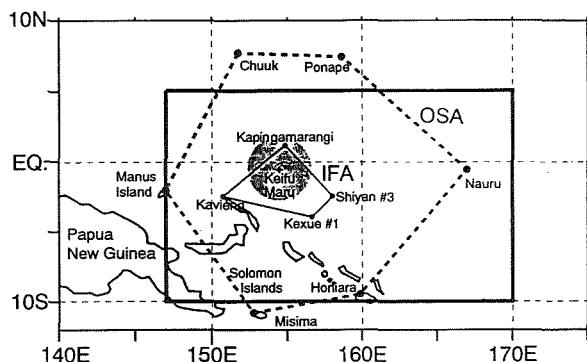


Fig. 1. Location of Keifu Maru(+ mark). The analysis area is out lined by the heavy line.

* On leave from the Department of Physics, BUET, Dhaka, Bangladesh.

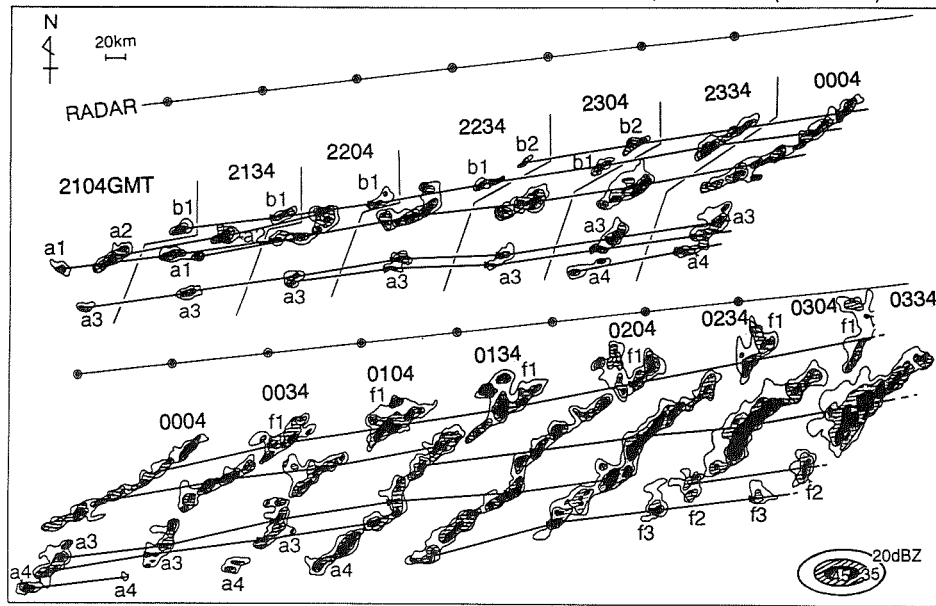


Fig. 2. Echo patterns and evolution of a nonisolated radar echo.

maximum, related to the cold rain. During the transition period, the rain rate was inversely proportional to the area due to the merging effect which was related to the formation of the SLL echo. The time duration of the strong rain rate in the developing stage (up to 2325GMT) was nearly one-third of the total lifetime of the SLL echo. The same length (1/3) of the time duration was also found by Young et al.(1995) using ship observation data. Therefore, it may be concluded that the time duration of the developing stage having a strong rain rate will be one-third of the total lifetime of the echo.

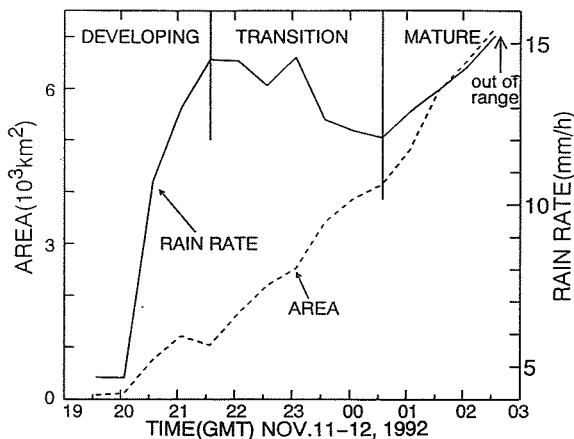


Fig. 3. Area and rain rate for nonisolated radar echo.

3.2 Classification of rain regimes in an objective way

Figure 4 shows the distributions of echo area, calculated from 10 days reflectivity data in a 500km x 500km domain, divided into three length ranges viz; formative: $L < 100$ km; mature: $100 < L < 330$ km; and dissipating: $L > 330$ km. The echo length(L) represented by the circumference of an equivalent area circle, $L = 2\pi r$ was used. At the formative stage, only the convective component(>40 dBZ) was dominated by small L , and a strong rain rate(R) confirmed the warm rain (Takahashi and Uyeda, 1995). The warm rain

was associated with the individual, shallow, convective clouds which lay below freezing level, and have a liquid phase, with no ice phase expected. In the mature stage, both convective and stratiform components were almost equally dominant. This stage appeared to be a mixture of convective and stratiform(≤ 40 dBZ) components, so the liquid and ice phases were almost equal. In the dissipating stage, large L and weak R were analyzed. These implied the production of anvil clouds which brought a large amount of rain associated with the cold rain process. In this stage most of the rain is expected to have an ice phase. One may easily estimate the echo areas in the formative, mature and dissipating stages from their respective L . Calculation showed that the maximum echo area ($L^2/4\pi$) at different stages were, formative: ~ 800 km², mature: ~ 8600 km², and dissipating: ~ 174300 km², respectively.

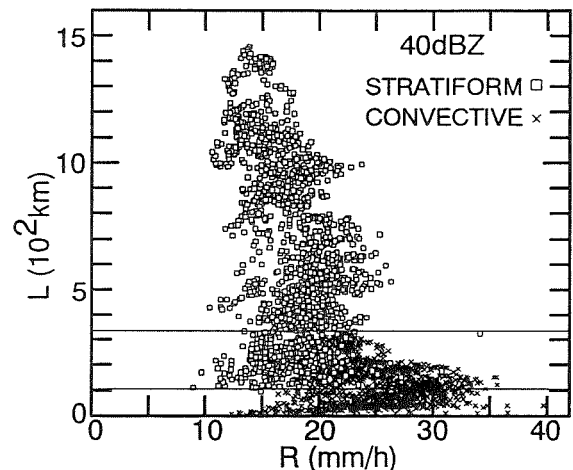


Fig. 4. Echo length(L) plotted against rain rate(R).

3.3 Analysis of a westward moving supercluster

During the analysis period, a significant supercluster was analyzed on November 11-12, 1992. As shown in Fig. 5, at 1500GMT on November 10, a large cloud area represented by the contour of $T_{BB} = 220$ K was observed just before

making a cloud burst(Mori, 1995) at its center(EQ., 165E). The internal structure is shown by superimposing convective and stratiform components for both radar and CST analyses. A few of the fragments moved westward and passed over the radar observation area named Area KM. At this time there were many developing echoes observed in Area KM which were moving E/ENE. In Area KM, the CST identified area was a few and small because the clouds were growing. The fragments dissipated and new clouds were successively developed and organized to form a westward moving uncommon supercluster at approximately 1200GMT on November 11. The whole system disappeared after 0900GMT on November 12 (not shown).

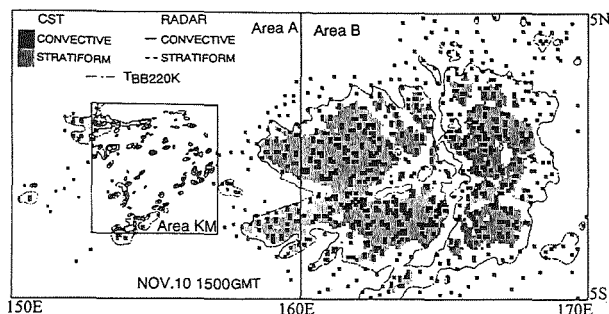


Fig. 5. Radar and CST identified regions with cloud boundary determined by T_{BB220K} .

The shape, size, propagation and organization mechanism of the studied supercluster was analyzed by consecutive T_{BB} area as shown in Fig. 6. By the conventional definitions, this large cloud cluster was undoubtedly a supercluster because its area of very low T_{BB} ($<210K$) was $\sim 40 \times 10^4 \text{ km}^2$ and the horizontal dimension was $\sim 2000 \text{ km}$. This supercluster consisted of a number of gregarious convections. A few of the cloud clusters were identified and named C1, C2, C3, and C4. The E/ESE movement ($\sim 9 \text{ m/s}$) of each cloud cluster labeled by C1, C2, C3, and C4 is clearly shown in Fig. 6. These cloud clusters (C1-C4) were ultimately indistinguishable from each other below $230K$ of T_{BB} . This represents cloud clusters (C1-C4) which were devoted to the supercluster. New cloud clusters successively developed in the western side of the system, and moved to E/ENE and merged with the system (i. e., cluster M). This reflects the westward movement of the supercluster even though it was actually stationary due to the effect of the westward propagating interio-gravity wave and eastward moving ambient air.

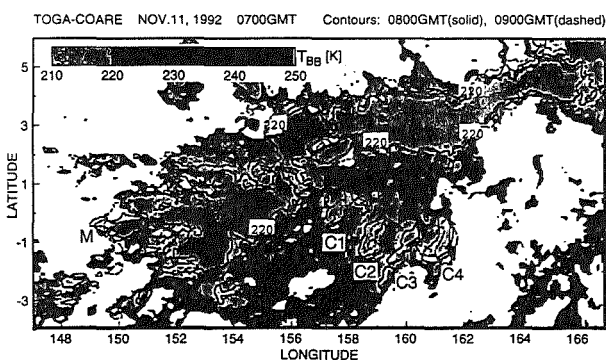


Fig. 6. Shape, size and movement of the supercluster.

While the supercluster itself was stationary, its speed was measured when a new cluster merged with it in the western edge. The analyzed supercluster propagated westward with a speed of about 6 m/s while Nakazawa (1988) reported a speed of $10\text{--}15 \text{ m/s}$ and Hashiguchi et al.(1995) reported a speed of 4 m/s for different superclusters. Using Fig. 5, one may calculate the speed of the westward moving cloud envelope which is about 17 m/s (Mori, 1995). As previously mentioned, after careful inspection of hourly T_{BB} data, the speed in this analysis was measured when a new cluster merged with the older cluster, and the western edge expanded with time even though the large part of the older cluster was stationary. This type of gregarious convection which is connected by an enclosed boundary of $T_{BB} < 230K$, and has a large-scale westward motion is a rare supercluster case among superclusters analyzed over the tropical ocean by hourly T_{BB} data. This uncommon characteristic was not reported by Nakazawa (1988), Mapes and Houze (1993) and Hashiguchi et al.(1995). If we analyze the long time-interval data i.e., 12 hours or 6 hours, or at minimum 3 hours, it is difficult to identify the E/ESE movement of each cluster and the formation of new clusters in the western side of the large older cluster. This is why hourly T_{BB} data was used to for clear detection, and a focus on only the supercluster, not on the envelop of the system.

A possible explanation of the formation mechanism and movement direction of this studied supercluster is as follows. The low-level environmental wind blew from both NW and SW to converge in the west side of the large cloud cluster(Fig. 7). The ambient temperature was relatively high in the east side of the large cluster and the low temperature was positioned in the convergence zone. This environmental condition may cause a situation suitable for the formation of new clouds which move E/ESE. New clouds successively developed, interacted between themselves, and organized to form cloud clusters. These cloud clusters merged with the older large cluster to take part in the maintenance of the supercluster. The equatorial wave forced the supercluster to move westward while ambient air pushed it eastward. So,

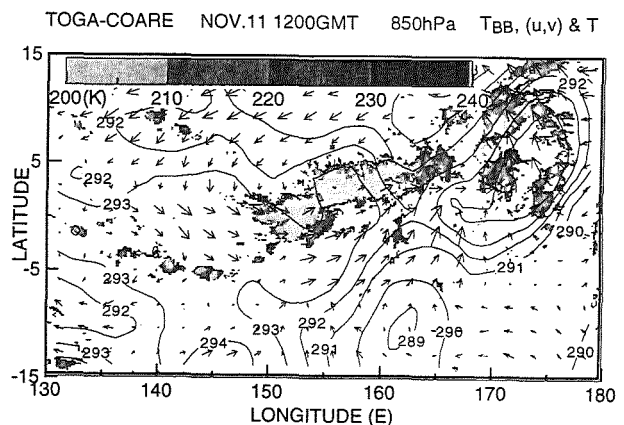


Fig. 7. The supercluster is superimposed with temperature (contours in unit of K) and wind field at 850 hPa . Maximum length of wind vector is 16 m/s .

the formation of a new cluster in the west side and the merge of this cluster with the old large cluster affected the movement direction of this supercluster.

The analyzed uncommon supercluster revealed some new

characteristics which are as follows: (1) a supercluster having horizontal length ~ 2000 km, lifetime of more than 2 days and very low $T_{BB}(<210K)$ cloud area of about 40×10^4 km², moved westward with a speed of ~ 6 m/s; (2) a large part of the old cluster remained stationary with time and expanded slowly in area; (3) a new cloud successively formed in the western side of the older, large cluster and organized to merge with the older one; (4) an individual cluster moved E/ESE with the speed of ~ 9 m/s; (5) interaction occurred between small-scale and large-scale cloud clusters. Furthermore, common features for all kinds of superclusters which were revealed as follows: (1) movement of the supercluster and cloud clusters will be in opposite directions; (2) the supercluster is composed of a number of cloud clusters; (3) new clusters will be formed in the convergence zone of the low-level wind field; (4) propagation speed and the direction of the supercluster will be followed by the formation of new cluster; (5) superclusters develop during a large-scale cloud disturbance.

4. SUMMARY AND CONCLUSIONS

Some basic characteristics such as size, shape, propagation, lifetime, and traversed path of the nonisolated and isolated echoes were revealed. The nonisolated echo was found to last ~ 13 hours and the isolated echo lasted ~ 5 hours. Inspection revealed that the developing stage of the echo lasted almost one-third of the total lifetime. These time durations are important to the model parameterization. The rainfall regimes were objectively separated to understand the size of the clouds at different stages. It was found that, the echo length(L) ranges were formative: $L < 100$ km; mature: $100 < L < 330$ km; and dissipating: $L > 330$ km.

The supercluster was composed of several cloud clusters. The westward moving uncommon supercluster was analyzed while each cloud cluster moved E/ESE and radar echo moved E/ENE. The description of common and uncommon features in section 3.3 of this study are able to improve to some degree the knowledge of the direction of movement and the organization mechanism of superclusters. We found that the formation-location of the new cluster leads to the movement direction and plays an important role in the organization mechanism of superclusters. The CST was able to reveal the internal structure of the cloud clusters and supercluster by identifying convective and stratiform components. In the GMS imageries, the low T_{BB} core seemed to be a convective one, but actually it was partially convective and surrounded by stratiform part as determined by the CST.

Finally, it is concluded that the merging of clouds and cloud clusters which are lasted several hours, identified by hourly T_{BB} , organized to form the supercluster.

5. ACKNOWLEDGMENTS

The authors would like to express their thanks to the

JMA for providing radar data. Special thanks to Dr. N. Takahashi, Dr. R. Oki and Mr. M. Katsumata for help in data reading. Thanks are extended to Dr. Y. Takayabu for providing GANAL data. We would also like to express our thanks to the TCIPPO(TOGA-COARE International Project Office) for providing sounding data.

6. REFERENCES

- Adler, R.F. and A.J. Negri, 1988: A satellite infrared technique to estimate tropical convective and stratiform rainfall. *J. Appl. Meteor.*, **27**, 30-51.
- Goldenberg, S.B., R.A. Houze, Jr. and D.D. Churchill, 1990: Convective and stratiform components of a winter monsoon cloud cluster determined from geosynchronous infrared satellite data. *J. Meteor. Soc. Japan*, **68**, 37-63.
- Hashiguchi, H., S. Fukao, M. D. Yamanaka, T. Tsuda, S. W. B. Harijono and H. Wiryosumarto, 1995: Boundary layer radar observation of the passage of the convective center over Serpong, Indonesia (60S, 1070E) during the TOGA COARE intensive observation period. *J. Meteor. Soc. Japan*, **73**, 535-548.
- Islam, M. N., 1996: Characteristics of the tropical clouds and cloud clusters and radar adjusted satellite rainfall estimation during the TOGA-COARE IOP. Doctorate Thesis, 1-153p, *Graduate School of Sci.*, Hokkaido Univ., Japan.
- Kikuchi, O. and H. Uyeda, 1996: Doppler radar observations on the structure and characteristics of tropical clouds during TOGA-COARE IOP in Manus, Papua New Guinea: Characteristics of cloud clusters analyzed with Doppler radar and GMS-IR data. *J. Fac. Sci. Hokkaido Univ.*, Ser. (Geophysics), **10**, 107-133.
- Mapes, B. E. and R. A. Houze, Jr., 1993: Cloud clusters and superclusters over the Oceanic warm pool. *Mon. Wea. Rev.*, **121**, 1398-1415.
- Marshall, J. S. and W. M. Palmer, 1948: The distribution of raindrops with size. *Jour. Meteor.*, **5**, 16-18.
- Mori, K., 1995: Equatorial convection observed by research vessel Keifu Maru during the TOGA-COARE IOP, November 1992. *J. Meteor. Soc. Japan*, **73**, 491-508.
- Nakazawa, T., 1988: Tropical super clusters within interseasonal variations over the western Pacific. *J. Meteor. Soc. Japan*, **66**, 823-839.
- Takahashi, N. and H. Uyeda, 1995: Doppler radar observation of the structure and characteristics of tropical clouds during the TOGA-COARE IOP in Manus, Papua New Guinea: -Three case studies on November 23 and December 16, 1992-. *J. Meteor. Soc. Japan*, **73**, 427-442.
- Young, G. S., S. M. Perugini and C. W. Fairall, 1995: Convective wakes in the equatorial western Pacific during TOGA. *Mon. Wea. Rev.*, **123**, 110-123.

RETRIEVED THERMODYNAMIC STRUCTURES OF MESOSCALE CONVECTIVE SYSTEMS OBSERVED IN THE WESTERN TROPICAL PACIFIC

Shinsuke Satoh¹, Daisuke Abe², Masayuki Kawashima³,
Tomoki Ushiyama² and Kensuke Takeuchi²

¹ Communications Research Laboratory, Tokyo 184, Japan

² Institute of Low Temperature Science, Hokkaido University, Sapporo 060, Japan

³ Ocean Research Institute, University of Tokyo, Tokyo 164, Japan

1. INTRODUCTION

Tropical rainfall is the primary driver of global atmospheric circulation, as a heat source. In spite of its important role, there are few measurements of rainfall over oceans in the tropics. Mesoscale convective systems (MCSs), composing a cloud cluster in the tropics, play an important role in conveying actual heat. During the TOGA-COARE IOP from November 1992 to February 1993, a lot of valuable data was obtained through the cooperation of several countries.

In the past, most studies focused on squall lines with well-defined structure and fast propagation, despite fewer occurrences than other MCSs. Many researchers preferred to study squall lines with a two-dimensional structure because they were easily understood. Satoh *et al.* (1995) investigated the kinematic structure of MCSs from dual-Doppler measurement. The first MCS moved faster than environmental wind, and is thus referred to as a fast-moving convective system (FMCS). The FMCS had several characteristics similar to a squall line, despite its three-dimensional structure, like a storm splitting. The second system was a stratiform echo system marked by an obvious bright band at melting level, which was developed independently of the first MCS. Although most stratiform flow appeared beneath the bright band, some remarkable vertical circulations were found above the bright band. These two systems associated with a cloud cluster were observed on January 18-19, 1993 on Manus Island (2° S, 147° E), Papua New Guinea, during the TOGA-COARE IOP.

Although Doppler radar data are useful in revealing the kinematic structure of MCSs, the thermodynamic structure and microphysical field cannot be measured directly. Gal-Chen (1978) first proposed dynamic retrieval techniques using the equations of motion, and Roux (1985, 1988) proposed a method for the retrieval of three-dimensional pressure and temperature fields. Furthermore, Hause and Amayenc (1986) retrieved water content fields by adding a water equation.

In this paper, the thermodynamic structures retrieved from the result of dual-Doppler analysis by Satoh *et al.* (1995), and the maintenance mechanisms of the two different types of MCSs are investigated.

2. METHODOLOGY

Dual-Doppler analysis was undertaken by Satoh *et al.* (1995) with correcting of rain attenuation using the k - Z_e relationship. After the interpolation of wind fields on the non-echo region using area-mean horizontal wind on each layer, variational integral constraint was applied to satisfy the anelastic continuity equation under the given lower and upper boundary conditions, based on Ray *et al.* (1980). The thermodynamic retrieval method used for the present analysis closely followed that of Roux (1988) and Kawashima *et al.* (1995). In this method, "virtual-cloud" potential temperature perturbation (θ_{c1}) and pressure perturbation (π_1) were deduced from three-dimensional wind fields and reflectivity. The micropysical retrieval method followed that of Hause and Amayenc (1986). Although the non-ice process was adopted for the first case (FMCS), the ice phase above the melting level was used for the stratiform case. For both cases, the environment conditions obtained by one-point sonde data few hours before were used.

3. KINEMATIC AND THERMODYNAMIC STRUCTURE

3.1. *Fast-moving convective system*

The horizontal cross section of a fast-moving convective system (FMCS) is shown in Fig. 1. The horizontal velocity field shows that the front inflow had two branching sub-flows ahead of an arc-shaped convective cell. Behind the cell, outflow from a downdraft also branched out in opposite directions. The branching inflow and outflow led to symmetrically-arranged strong updrafts (Fig. 1b). These distribution patterns were present at all levels below a height of 4 km,

2000 LST 18 JAN 93 HT= 3.0 km

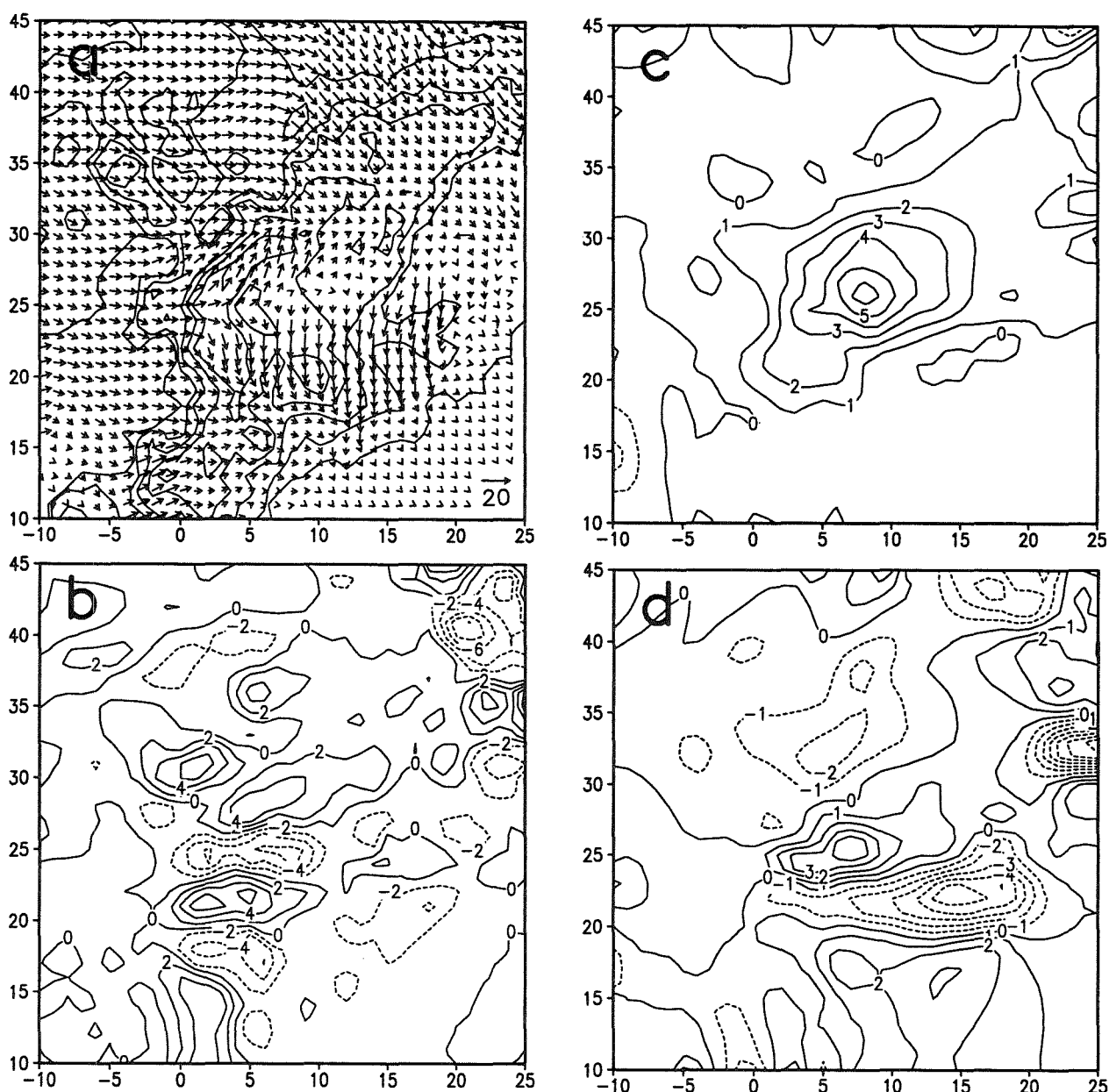


Fig. 1 Horizontal cross sections of the FMCS at a height of 3 km. (a) Storm-relative wind vectors and reflectivity contours (every 5 dB beginning at 15 dBZ). (b) Vertical velocity (ms^{-1}). (c) Retrieved temperature perturbations (K). (d) Retrieved pressure perturbations.

and were maintained for more than 30 minutes. Figures 1c and 1d show retrieved temperature perturbation (θ_{c1}) and pressure perturbation (π_1), respectively. The center of warm air, where the maximum temperature perturbation was more than 6 K, coincided with the downdraft core. This warm air may be transported from the upper layer by the downdraft. Although the alternate patterns of pressure perturbation were similar to those of vertical velocity, pressure perturbation broadened at the rear. This may be explained by flow around

an obstacle in a rainfall core with strong downdraft. The horizontal pressure gradient crossing to storm motion of the FMCS was very large, causing branching outflow.

Figure 2 shows a vertical cross section with an updraft region along storm motion. A storm-relative inflow appeared in the convective region with strong updraft having a maximum velocity of about 15 ms^{-1} at a height of 6 km. Although a small anvil echo extends behind the convective cell at the leading edge, rear inflow was not clear.

2000 LST 18 JAN 93

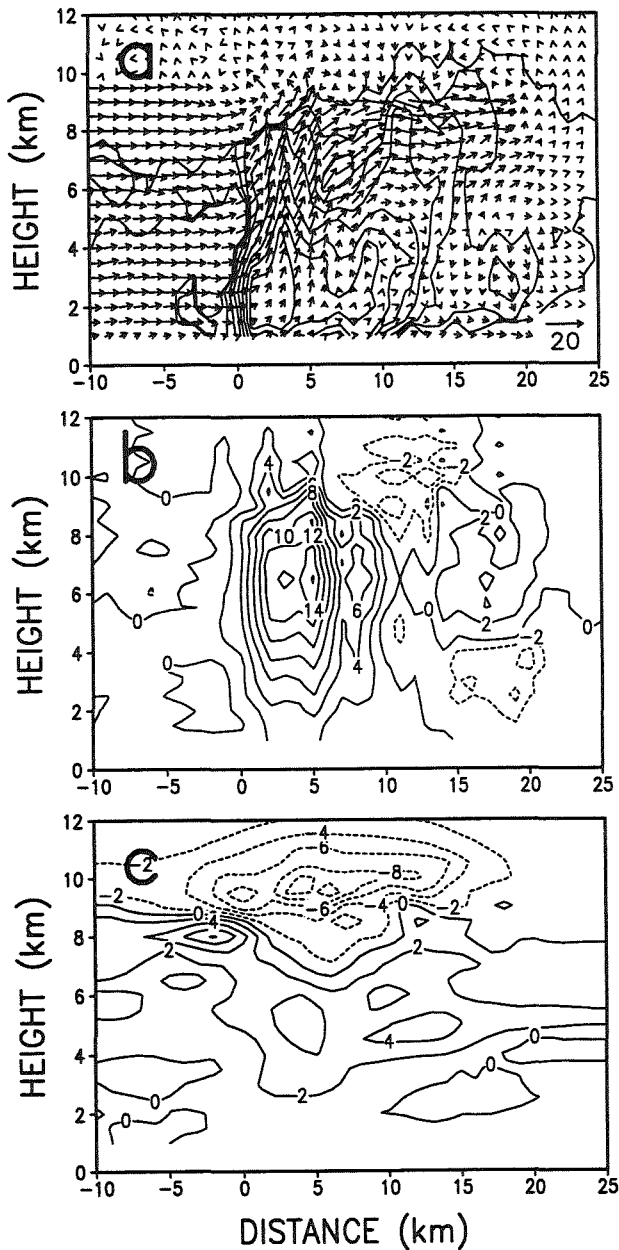


Fig. 2 Vertical cross sections along FMCS motion ($Y = 22$ km in Fig. 1). (a) Storm-relative wind vectors and reflectivity contours (every 3 dB beginning at 15 dBZ). (b) Vertical velocity (ms^{-1}). (c) Retrieved temperature perturbations (K).

The retrieved temperature perturbation (θ_{c1}) is shown in Fig. 2c. Significant warm air ($>2\text{K}$) extended from about 3 km up to nearly 7 km, caused mainly by the release of latent heat. Although cold perturbation appeared between 9 km and 11 km, there was an indistinct cold pool at low levels. This seemed to be caused by limited evaporation in the wet environment.

3.2. Stratiform echo system

Figure 3 shows the vertical cross section of the stratiform echo system. The reflectivity field (Fig. 3a) shows a bright band indicating melting level, at a height of 4.5 km. Although most stratiform flow appeared beneath the bright band, some remarkable vertical circulations were found above the bright band as shown in Fig. 3b. The retrieved temperature perturbation (θ_{c1}) is shown in Fig. 3c. Around the melting level, there were negative temperature perturbation regions. Above the melting level, alternate temperature perturbation indicated the release and absorption of latent heat, corresponding to both updraft and downdraft. Figure 3d shows the production rate of precipitation (F_{qr}), which is calculated from the three-dimensional wind velocity, rainwater mixing ratio and terminal fall velocity, based on Kawashima *et al.* (1995). While the negative F_{qr} just below the bright band indicated rain evaporation in subsaturated air, the positive F_{qr} above the bright band indicated generating precipitation from clouds in saturated air. Only the distribution of evaporation and cooling were close to the bright band.

4. CONCLUSION

The thermodynamic structures retrieved from dual-Doppler radar observation of two different types of MCSs were investigated. The first system (FMCS) had several characteristics similar to a squall line with a three-dimensional structure. The front inflow had two branching sub-flows in front of the convective cell with a strong downdraft. The lower level outflow from the downdraft also branched out into opposite directions. The retrieved pressure perturbation corresponded to the symmetrically-arranged updrafts and the downdraft between them, and was also affected by the branching subflows broadening behind the convective cell. It is thought that the force of the horizontal pressure gradient maintained the convection. The retrieved temperature perturbation showed that significant warm air extended to middle levels, corresponding to latent heat release, and an indistinct cold pool collected at lower levels. It seems that the indistinct cold pool caused the lack of rear inflow. On the other hand, in the stratiform echo system, the remarkable vertical circulations above melting level seemed to be maintained by the thermal buoyancy derived from the retrieved temperature perturbation. This buoyancy may be due to the release of latent heat above the melting level, while only evaporation cooling occurred close to the melting layer.

0230 LST 19 JAN 1993

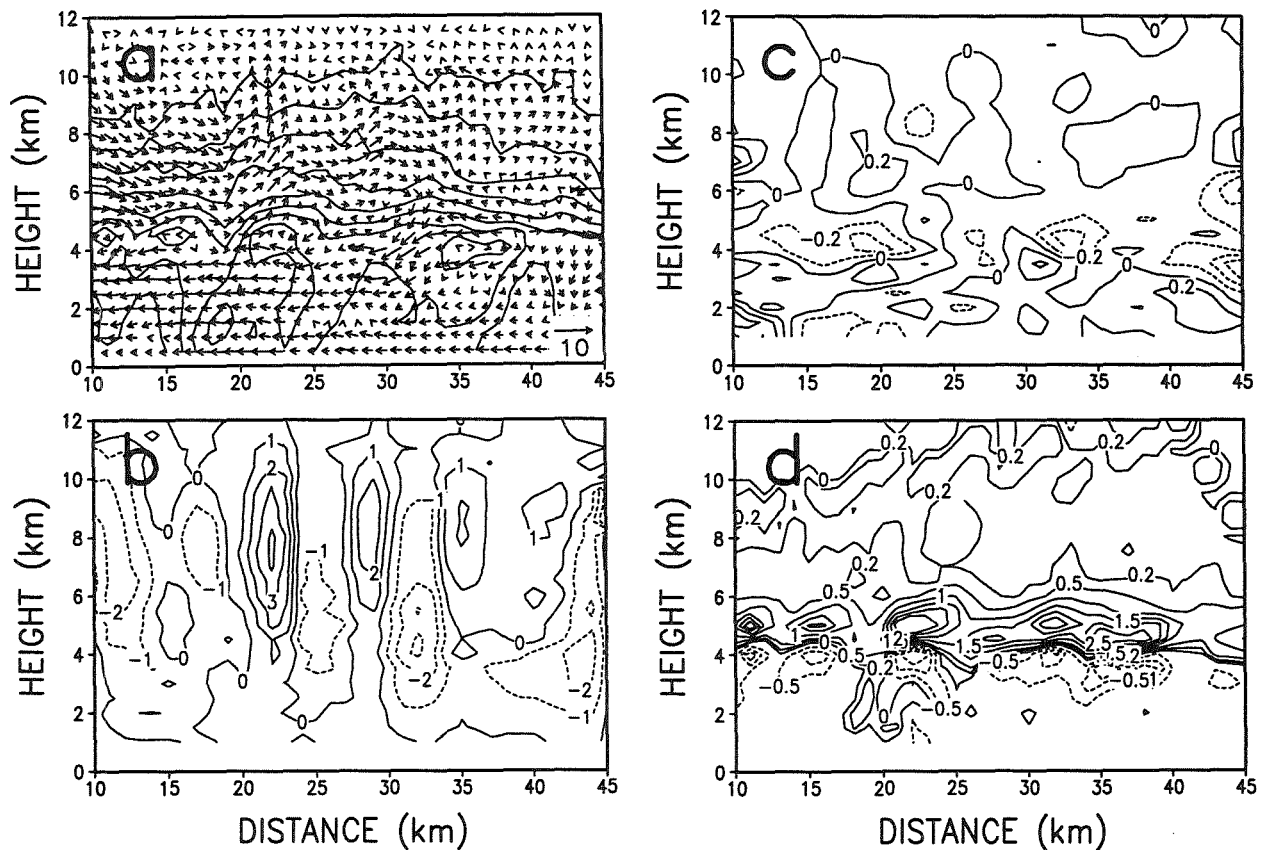


Fig. 3 Vertical cross sections of the stratiform echo system. (a) Ground-relative wind vectors and reflectivity contours (every 3 dB beginning at 15 dBZ). (b) Vertical velocity (ms^{-1}). (c) Retrieved temperature perturbations (K). (d) Production rate of precipitation ($\text{g kg}^{-1} \text{hr}^{-1}$).

ACKNOWLEDGMENTS

The authors wish to thank Dr. M. Yoshizaki and Mr. H. Seko of MRI for their valuable discussions. Thanks are also extended to Dr. K. Tsuboki of the Ocean Research Institute and Dr. T. Kozu of CRL for their valuable comments.

REFERENCES

- Gal-Chen, T., 1978: A method for the initialization of the anelastic equations: Implications for matching model with observations. *Mon. Wea. Rev.*, **106**, 587-606.
- Hauser, D. and P. Amayenc, 1986: Retrieval of cloud water and water vapor contents from Doppler radar data in a tropical squall line. *J. Atmos. Sci.*, **43**, 823-838.
- Kawashima, M., K. Tsuboki and T. Asai, 1995: Maintain mechanism and thermodynamic structure of a Baiu frontal rainband retrieved from dual Doppler radar observations. *J. Meteor. Soc. Japan*, **73**, 717-735.
- Ray, P. S., C. L. Ziegler, W. C. Bumgarner, and R. J. Serafin, 1980: Single and multiple Doppler radar observations of tornadic storms. *Mon. Wea. Rev.*, **108**, 1607-1625.
- Roux, F., 1985: Retrieval of thermodynamic fields from multiple-Doppler radar data using the equations of motion and the thermodynamic equation. *Mon. Wea. Rev.*, **113**, 2142-2157.
- Roux, F., 1988: The west African squall line observed on 23 June 1981 during COPT 81: kinematics and thermodynamics of the convective region. *J. Atmos. Sci.*, **45**, 406-426.
- Satoh, S., A. Kinoshita and Uyeda, H., 1995: Doppler radar observations on the structure and characteristics of tropical clouds during TOGA - COARE IOP in Manus, Papua New Guinea: Dual-Doppler Analysis of Mesoscale Convective Systems Composing a Cloud Cluster. *J. Meteor. Soc. Japan*, **73**, 443-459.

LIQUID WATER IN STORM-EMBEDDED OROGRAPHIC GRAVITY WAVES

Roger F. Reinking,¹ Jack B. Snider,¹ Roelof T. Buijntjes,² Janice Coen,² Terry Clark,² and William D. Hall²

¹NOAA/Environmental Technology Laboratory, Boulder, Colorado

²NCAR, MMM Division, Boulder, Colorado

1. INTRODUCTION

A numerical mesoscale-cloud-scale model and field observations with multiple remote sensors confirm that storm-embedded gravity waves can persistently have a strong influence on orographic cloud liquid water (CLW) and precipitation. Wave cloud water that is converted to ice will seed and convert to precipitation the water formed in underlying orographic clouds. Examples of measurements of wave-induced CLW and associated liquid content of rain (RLW) from a 4–6 March 1995 storm are presented. The LW is related to cloud structure, dynamics, and ice microphysics and intercompared with general predictions from the model. The data were collected during the 1995 Arizona Program (Buijntjes et al. 1994; Reinking 1995). The modeling results are discussed in more detail by Coen et al. (1996).

2. BACKGROUND

The topography of the project area is shown in Fig. 1. The main concern was precipitation falling on the Mogollon Rim, a key watershed. Winds during storm periods were normally from directions between south and west, with a major component perpendicular to the Black Hills. The main remote-sensing site was in the intervening Verde Valley at Cottonwood, Arizona (CTW). The data for this study were from a scanning microwave radiometer (Hogg et al. 1983) and a cloud-sensing K_a -band dual-polarization Doppler radar (Kropfli et al. 1995) from the NOAA Environmental Technology Laboratory (ETL). The radiometer separately measures the path-integrated water vapor and LW; range-height-indicator (RHI) scans were made to map the LW across the gravity waves. Corresponding radar RHIs mapped the cloud reflectivity (Z_e), radial velocity (V_r), and elliptical depolarization ratio (EDR). The latter parameter is used to identify hydrometeor types and distinguish ice from liquid, as detailed by Matrosov et al. (1995, 1996) and Reinking et al. (1996a,b). A 95° phase shift was applied to the transmitted signal to obtain the polarization measurements during the Arizona Program. Radar velocity-azimuth-display (VAD) scans were added to obtain wind profiles in the clouds.

This study used the anelastic, nonhydrostatic Clark numerical model (Clark 1977; Clark and Hall 1991). This application exploited the model's interactive grid-nesting

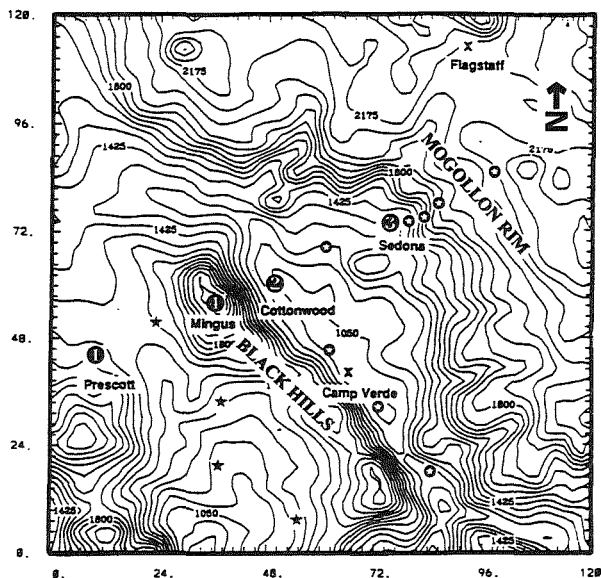


Fig. 1. Topographic map of the project area in northern Arizona, USA (m MSL, 120 km sq). Remote-sensing site (CTW) was at point 2.

capability, coarse grain parallelization, terrain-following coordinates, and stretched vertical grid. The model was initialized and the boundary conditions updated every 3 h with the Mesoscale Analyses and Prediction System (MAPS; Benjamin et al. 1991) data. Three levels of nesting were used for these preliminary simulations. The large-scale flow in the region was simulated with a domain 1157 km square with 24.1-km horizontal grid spacing; the innermost domain nested down to 2.7-km horizontal grid spacing focused on the Black Hills, Verde Valley, and the Mogollon Rim. Two large-scale domains were initialized at 0000 UTC 5 March. The fine-scale domain began at 0000 UTC 6 March, and the simulation continued until 1600 UTC 6 March.

3. OBSERVATIONS

Orographic wave clouds aloft and orographic clouds on the mountain slopes had developed over the area and were producing variable light precipitation in flow from 260° by 0000 UTC 4 March 1995. An example of the wave structure approximately along the wind is shown in the radar RHI in Figs. 2a,b. The cloud wavelength at this time was about 24 km. The path-integrated LW from two corresponding radiometer RHIs is shown in Fig. 2c.

Descending flow was indicated in the lee of the Black Hills below elevation angle $\beta \approx 40^\circ$, and ascending motion downstream of that ($\beta \geq 40^\circ$) as zenith was approached. The LW was that of the wave cloud; it was not influenced by precipitation at this time. This CLW was depleted to a minimal quantity in the downslope flow; here, EDR ≈ -15 dB confirms a presence of liquid-consuming ice particles (EDR ≈ -21 dB for spherical droplets or drizzle). The LW gradually increased in the wave updraft to about 0.5 mm near zenith, despite the ice influx from upstream. Downstream, CLW of 0.3–0.5 mm was maintained against the presence of transformed ice (EDR ≈ -16 to -18 dB, likely graupel). Persistent CLW of just 0.1 or 0.2 mm is significant to winter orographic precipitation, so 0.5 mm is a large quantity. The wave did produce rain (below the melting layer in Fig. 2b) on the windward slopes of the Mogollon rim. A more detailed account of this is given by Reinking et al. (1996a).

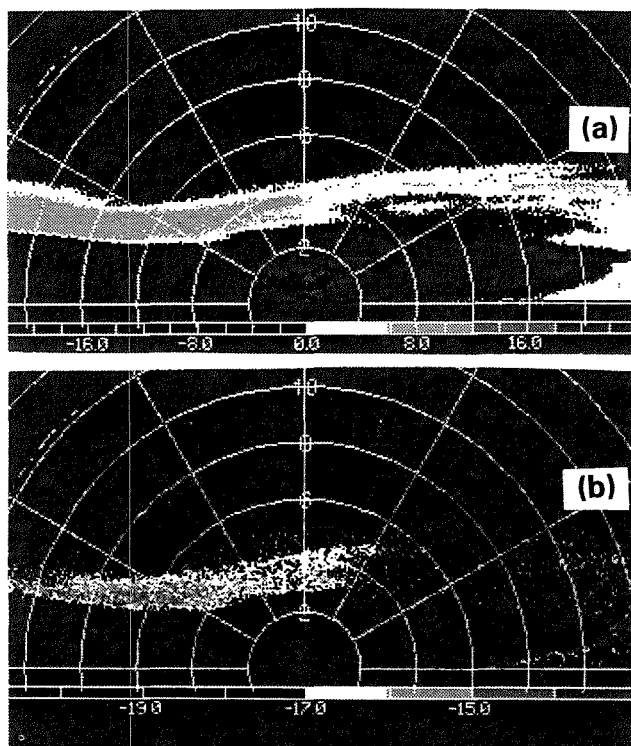


Fig. 2. Over-the-top radar RHI at 0430 UTC 4 March 1995 for (a) Z_e and (b) EDR; azimuth 70° is to the right, 2-km range rings. (c) LW from two microwave radiometer RHIs along the same azimuth, 0419–0430 UTC. Wind blew left to right.

Figure 3a shows a 5 March example of CLW reaching ~ 1.0 mm when a radar RHI indicated a wave updraft of ~ 2 m s^{-1} in the general absence of ice and precipitation. Consistently, the wave CLW was minimal (~ 0.1 mm) in the foehn gap toward the Black Hills (at antenna elevation angles nearest 180°). Two hours later, CLW was diminishing in air descending across the valley at ~ 2 m s^{-1} (Fig. 3b). From 21.5 h of radiometer observations during the 4–6 March 1995 period, wave-generated CLW was indicated to be persistent for 16 h, intermittent for 3.5 h, and absent for only 2 h. Thus, the wave activity and its production of CLW were persistent.

On the Mogollon Rim, the most intense and steady precipitation (~ 0.6 cm h^{-1}) occurred between 0030 and 1000 UTC 6 March. As much as 5 cm fell as rain on snowpack on the Rim and induced flash floods in the valley. In the middle of this period (0535 UTC), the half-wavelength of the wave cloud from the trough upstream to the crest downstream of CTW zenith was ~ 8 km (Fig. 4a). Cloud depth was ~ 6 km in the 2–3 m s^{-1} updraft of the wave. The pattern of ice in the cloud (not shown) was similar to that in Fig. 2b. It generated drizzle or light rain which fell from the air descending from the Black Hills and across the radar site, and again 20+ km downstream over the rising terrain toward the Rim. Surface measurements show that the precipitation rate increased dramatically farther downwind. The precipitation (RLW) is indicated by the flat part of the radiometer RHI in Fig. 4b; it accounted for 0.2–0.5 mm across the valley at this time. The CLW in the wave formed downwind of zenith and is clearly superimposed between the 80° and

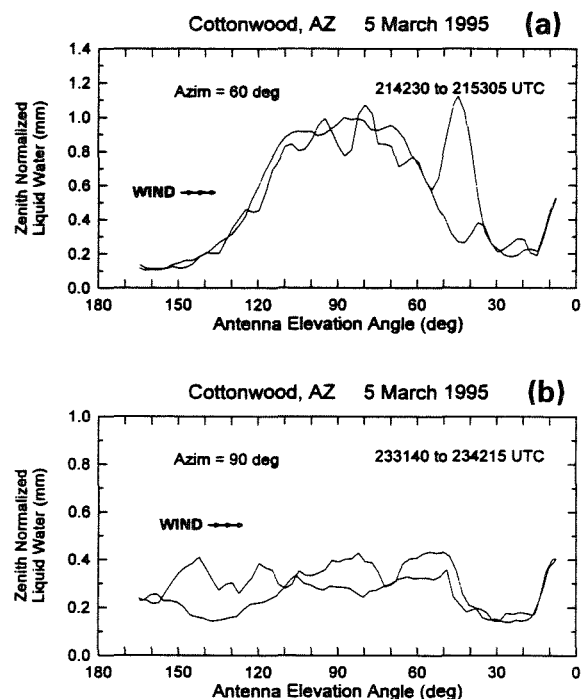


Fig. 3. (a) CLW in layered wave clouds with crest near zenith; (b) subsequent diminishing CLW in descending motion without wave structure.

20° elevation angles in Fig. 4b; it accounted for an additional 0.8–1.1 mm. The wave component increased to the 1.4–1.9 mm range by 0605 UTC. After that, the rain component toward the Rim increased and became difficult to separate from the CLW. A period of wave degeneration with rainout at approximately 1100 UTC produced 3–7 mm of LW (i.e., CLW + RLW) over the slopes of the rim (near 10° antenna elevation).

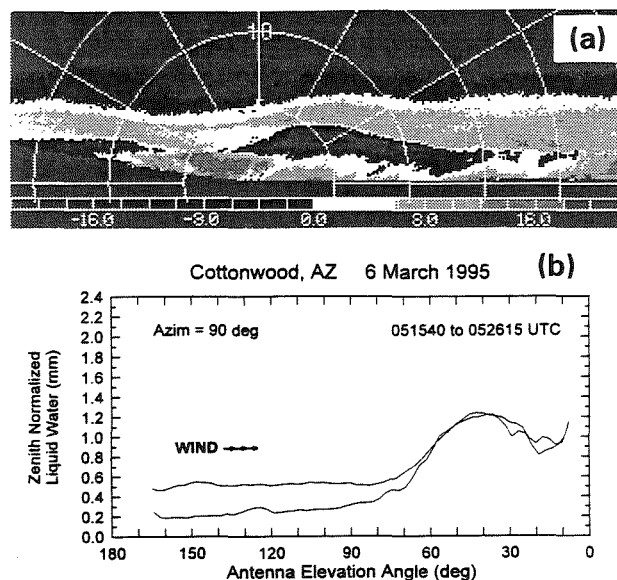


Fig. 4. (a) Over-the-top radar RHI at 0535 UTC 6 March 1995 for Z_e ; azimuth 60° is to the right, 5-km range rings. (b) LW from two microwave radiometer RHIs to azimuth 90°, 0515–0526 UTC. Azimuth 90° is to the right; wind blew left to right.

4. COMPARISONS WITH MODEL

General features of preliminary modeling results and observations can be compared. Calculations for 0655 UTC 6 March 1995 are used here, although model events seemed to lag actual events because MAPS did not initially do well in defining the associated front. The simulated wave cloud as indicated by CLW over CTW extended from about 3 to 6 km AGL (Fig. 5a); the ice cloud was deeper (more than 4 km over CTW; Fig. 5b). These are in generally the same volume as the observed cloud of liquid plus ice (2.0–8.5 km AGL). For 0530 UTC, the simulated CLW and ice clouds over CTW were much shallower (~2 km), whereas the depth of those observed varied little during this period. In the clouds, simulated updrafts over CTW were 1–4 m s⁻¹; updrafts of the order of 2–3 m s⁻¹ were measured (both depend, of course, on the position of the wave). In the lee of the Black Hills, in the 3–6 km AGL core of the observed wave cloud, the computed updraft and downdraft cores occurred about 12 km apart; the observed wave trough to crest was about 8 km along the same transect (~60° azimuth). The computed wave and associated CLW seem to be offset ~10 km upwind of the actual wave (Fig. 5a vs Figs. 4a,b). Smoothing at 2.7-km resolution and the need for nesting the model to the 1-km domain are indicated.

A time history of simulated CLW and ice mass concentration (Fig. 5b) shows a pulsation in both parameters, with ice properly lagging CLW. After the cloud was established, the simulation maintained some CLW against some ice throughout the period of activity. In general, the observations show this.

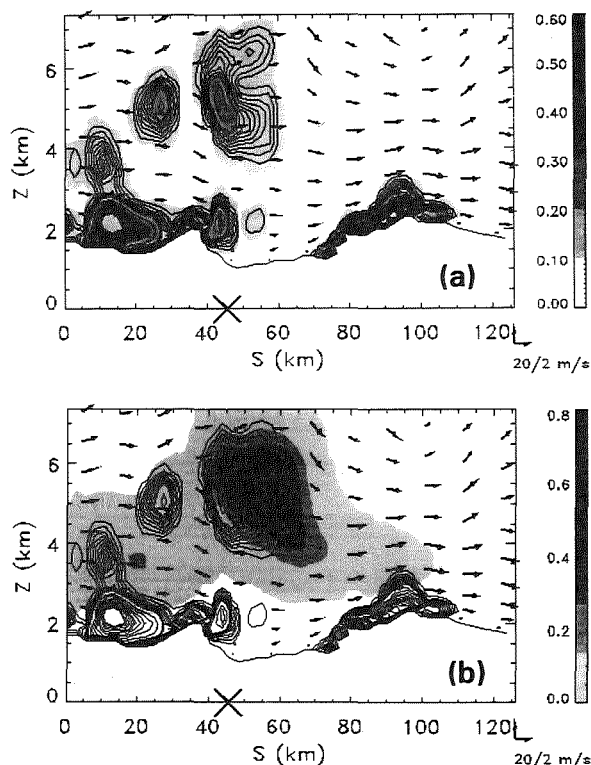


Fig. 5. Simulations of orographic wave and upslope clouds at 2.7-km resolution for 6 March 1995: (a) 0655 UTC QC (= CLW) contoured at 0.01–1 g kg⁻¹ and 0.05 g kg⁻¹ thereafter; (b) QC and ice mass concentration, QIA, vs time; (c) 0655 UTC QC, contoured, and QIA, shaded, in grams per kilogram. X marks position of the CTW remote-sensing site; azimuth ~60° is to the right.

At the four peaks in Fig. 5b, CLW reached 0.35–0.7 g kg⁻¹. These CLW contents equate to maximum estimates of 0.6–1.1 mm in a modeled cloud 2.5 km deep (these estimates exaggerate the peak values at cloud core by integration through cloud depth). At 0655 UTC model time (Fig. 5a), CLW was less than ~0.2 g kg⁻¹ through ~3 km deep; this equates to 0.36 mm, when according to Fig. 5b, CLW was about half the first simulated peak of 0.6 mm. Measured peak CLW values that could be attributed to the wave were about 2.0–2.5 mm in a cloud about 5 km deep. In all, the preliminary simulation appears to be dryer than the observations of the gravity wave, most probably because of insufficient horizontal resolution. Additional nesting to 1-km resolution is currently being added to the model.

The ice developed in the simulated wave precipitated to seed the greater quantities of orographic CLW formed in direct upslope flow (Fig. 5c). Only the near reaches of the upslope cloud on the slopes of the Rim were observed by the radar set at a 25-km range limit, but the observations

confirm that the wave ice generated snow and rain that would have seeded any upslope cloud beyond the field of view (Figs. 2a and 4a).

5. CONCLUSIONS

The data confirm that deep wave clouds are induced by the terrain, do develop significant cloud liquid water in their updrafts even against the presence of ice, and do generate ice-phase precipitation that commonly falls to the ground as rain in the Arizona study area. The wave activity and its effects were very persistent during periods of observation that totaled 21.5 h during a 3-day period. Observations and first-draft model calculations compared well on broad features. However, the scale of and position of wave motion and quantity of wave-induced liquid water need to be more accurately simulated. Scaling down from the 2.7-km resolution presented here to the model's 1.0-km model resolution is in progress. The value of using interactive modeling and observations is very evident.

6. ACKNOWLEDGMENTS

This work was funded by the Arizona component of the NOAA Atmospheric Modification Program. Eric Betteron directed the field operations. Dennis Sundie managed the Arizona Program.

7. REFERENCES

- Benjamin, S. G., K. A. Brewster, R. Brummer, B. F. Jewett, and T. W. Schlatter, 1991: An isentropic three-hourly data assimilation system using ACARS aircraft observations. *Mon. Wea. Rev.*, **119**, 888–906.
- Bruintjes, R., T. Clark, and W. Hall, 1994: Interaction between topographic airflow and cloud and precipitation development during the passage of a winter storm in Arizona. *J. Atmos. Sci.*, **51**, 48–67.
- Clark, T. L., 1977: A small-scale numerical model using a terrain following coordinate transformation. *J. Comput. Phys.*, **24**, 186–215.
- Clark, T. L., and W. D. Hall, 1991: Multi-domain simulations of the time-dependent Navier-Stokes equation: Benchmark error analyses of nesting procedures. *J. Comput. Phys.*, **92**, 456–481.
- Coen, J. L., R. T. Bruintjes, W. D. Hall, T. L. Clark, and R. F. Reinking, 1996: Numerical simulation of winter-time precipitation development in gravity-wave and upslope flow in Arizona's Verde Valley. Proc., 12th Int'l. Conf. on Clouds and Precipitation, 19–23 August 1996, Zurich, Switzerland. ICCP (this volume).
- Hogg, D. C., F. O. Guiraud, J. B. Snider, M. T. Decker, and E. R. Westwater, 1983: A steerable dual-channel microwave radiometer for measurements of water vapor and liquid in the troposphere. *J. Climate Appl. Meteor.*, **22**, 789–806.
- Kropfli, R. A., and colleagues, 1995: Cloud physics studies with 8-mm-wavelength radar. *Atmos. Res.*, **35**, 299–313.
- Matrosov, S. Y., R. F. Reinking, R. A. Kropfli, and B. W. Bartram, 1995: Identification of ice hydrometeor types from elliptical polarization radar measurements. *Preprints, 27th Conf. Radar Meteor.*, Vail, Colorado. Amer. Meteor. Soc., Boston, 539–541.
- Matrosov, S. Y., R. F. Reinking, R. A. Kropfli, and B. W. Bartram, 1996: Estimation of ice hydrometeor types and shapes from radar polarization measurements. *J. Atmos. Ocean. Technol.*, **13**, 85–96.
- Reinking, R. F., 1995: An approach to remote sensing and numerical modeling of orographic clouds and precipitation for climatic water resources assessment. *Atmos. Res.*, **35**, 349–367.
- Reinking, R. F., S. Y. Matrosov, and R. T. Bruintjes, 1996a: Hydrometeor identification with elliptical polarization radar: Applications to glaciogenic cloud seeding. *J. Wea. Mod.*, **28** (in press).
- Reinking, R. F., S. Y. Matrosov, R. T. Bruintjes, and B. E. Martner, 1996b: Identification of hydrometeors with elliptical and linear polarization K_a -band radar. *J. Appl. Meteor.* (submitted).

A MULTI-SCALE SIMULATION OF A CASE OF OUTBREAK OF SEVERE CONVECTION OVER THE ALBERTA FOOTHILLS

M.K. Yau and C. Li

Department of Atmospheric and Oceanic Sciences, McGill University, Montreal H3A 2K6, CANADA

1. INTRODUCTION

Central Alberta is a region highly susceptible to severe summertime convection. Climatological statistics show that the area is affected by hail on an average of 61 days each summer and between 10 to 20 tornadoes are reported annually. Although most of the hail comes from relatively weak single and multicell storms, highly organized multi or supercell storms develop three to five times a summer and produce widespread, large hail and/or tornadoes.

On days with severe convection in central Alberta, the morning soundings generally show a low-level tropospheric inversion or capping lid which initially inhibits the formation of deep convection. Towering cumulus clouds first form over the foothills region in the early afternoon. Under suitable conditions, they intensify rapidly into cumulonimbi which move eastward.

To investigate the essential synoptic-physical processes that distinguish severe convective events, Smith and Yau (1993a,b; hereafter SY93a,b) carried out a detailed analysis of a high resolution data set collected in a mesoscale experiment over Alberta (Limestone Mountain EXperiment 1985; LIMEX-85). In particular, they compared a severe convective event which occurred on 11 July 1985 with other case days with lesser or little convection. Their primary conclusions are:

- 1) Under generally clear sky conditions, cumulus convection begins over the Alberta foothills, where the capping lid is quickly eroded by strong surface heating.
- 2) Most severe convective outbreaks appear to occur when cooling aloft, associated with an approaching synoptic-scale, upper-level trough is in phase with strong surface heating over the foothills. The surface synoptic pressure gradient provides for east-northeasterly winds over the plains which transport moist plains air towards the foothills and into the lower-branch of the mountain-plain circulation. Such a configuration brings about localized, deep destabilization which gives rise to strong upslope moisture transport.
- 3) The mountain-plain circulation is ineffective in

initiating severe convection when subsidence warming associated with an upstream ridge inhibits its growth, and the surface synoptic pressure gradient provides for northwesterly, westerly or southwesterly winds over the plains. Under these conditions, the plains moisture is advected away from the foothills, so that by the time the thermally-induced upslope flow has developed, its moisture content has been depleted to the point of being unable to support severe convection.

Because of the limitation of the dataset, there were several outstanding questions left unanswered. One of which is what is the principle moisture source for convection in Alberta? Does it come from a tongue of modified maritime tropical air which enters the Prairie provinces in southern Manitoba and extends westward into east-central Alberta, or does an important fraction of the low-level moisture originate from evapotranspiration? Another question is what causes the formation of the capping lid in Alberta? Could the lid be the results of a subsidence inversion enhanced locally near the foothills by orography or does the lid arises partly due to advection of an elevated mixed layer (see Carlson et al. 1983) into central Alberta. There is also evidence in the LIMEX-85 data that lid formation in Alberta may be partly the result of radiative cooling at the surface. What are the relative contribution of all these factors?

The purpose of this paper is to validate the conclusion of Smith and Yau by simulations using a high resolution numerical model. Specifically, we will carry out a 30 h simulation of the 11 July 1985 case and compare the results with the analysis given in Smith and Yau. Another goal is to investigate the importance of topography, surface evapotranspiration, and long and short wave radiation through sensitivity experiments.

2. THE NUMERICAL MODEL

The model used is version 3.2 of the Mesoscale Compressible Community Model (MC2) originally developed by Tanguay et al. (1990). We have incorporated an explicit warm rain microphysical scheme by adding two prognostic equations, one for cloud water content and the other for rain water

content. These two new variables are advected by the fully three-dimensional semi-Lagrangian scheme. The microphysical processes include condensation, autoconversion, accretion, raindrop evaporation and sedimentation of precipitation particles.

To cover both the synoptic and mesoscale circulation, we used a one-way nesting strategy. Runs are conducted with 100 km, 50 km, 25 km, and 10 km resolution with the coarser resolution runs furnishing initial an conditions to the finer resolution runs. The initial analysis for the 100 km run is taken from the CMC (Canadian Meteorological Center) analysis. For the 100 km and 50 km runs, the Kuo cumulus parameterization and the Sundqvist scheme were used. For the 25 km and 10 km runs, the explicit microphysical scheme was employed. All runs were made with a vertical resolution of 49 levels. There are 23 levels below 1 km and the grid length below 200 m is about 20 m. The model is initiated at 18 LDT (00 UTC) 11 July. The time steps used for the 100 km, 50 km, 25 km, and 10 km runs are 10 min, 5 min, 1 min, and 30 s respectively.

3. RESULTS

3.1 Comparison with radar and satellite observations

According to SY93a, this day was marked by well-organized multicell storms which began moving out of the foothills around 16 LDT(22 UTC). Radar reflectivities between 60 and 70 dBz were present over the course of several hours. A total of 228 hail reports were reported and eight of these were for hail of golfball size.

At 06 LDT (12 UTC) the satellite imagery (not shown) indicated clear sky conditions prevailed over the foothills of Alberta while cloudy conditions were depicted over the northern half of the province. Fig. 1 shows the relative humidity at 600 mb at the same time. The relative humidity over the southern half of the province was less than 70%. A line of TCu started to form along the foothills around 1530 LDT (2130 UTC) as depicted in infrared satellite image in Fig. 11 of SY93a. Similarly the simulated 600 mb relative humidity indicated the presence of a cloud band near the same location at 14 LDT (20 UTC).

A sequence of radar observations taken by the Red Deer radar from 16 LDT (22 UTC) to 20 LDT (02 UTC 12 July) is given in Fig. 12 in SY93a. The first radar echo appeared at 300° at a range of 160 km. Two hours later, a large cell, with its maximum reflectivities reaching 60 dBz, can be found southwest of Edmonton. The storm continued to propagate eastward and two large echoes can be clearly identified at 20 LDT. The model generated radar reflectivities at the same times are depicted in Fig. 2. The qualitative features and locations of the echoes are in good agreement with the observations. The model maximum reflectivities were about 10 dBz

lower.

3.2 The larger scale environment

The 24 h forecast valid at 18 LDT (00 UTC) 12 July is shown in Fig. 3. The presence of a 500 mb trough upstream of central Alberta and a ridge downstream indicated favorable conditions for large-scale ascent over the region. The overall flow pattern agrees closely the operational analysis (Fig. 5 in SY93a). The southeastward displacement with time of the 558 decameter 1000-500 mb thickness line (not shown) is consistent with a net cooling over central Alberta associated with the passage of the upper-level trough from July 10-12.

At the surface, a trough of low pressure over southeastern Alberta and a high ridge toward the northwest dominated the MSL pressure field from 8 to 18 LDT (Fig. 4). During the day, the trough deepened while the ridge pushed southeastward. The resultant northerly and northeasterly flow channelled the moist plains air to the west of the foothills.

3.3 Cross-section of anomalous fields

The moisture transported to the west of the foothills feeds into the lower branch of the mountain-plain circulation to effect the outbreak of convection. To illustrate this point more clearly, we display cross sections of anomalous fields in a direction normal to the mountains in southern Alberta. If S is a scalar field, the anomaly field (S_A) is defined as $S_A = S - [S]$, where $[S]$ is the time-averaged field for the period from 8 to 16 LDT.

Vertical sections of anomalous equivalent potential temperature and anomalous u-component of the wind from LMW (Limestone Mountain) to AQF (Red Deer) are plotted in Fig. 5. The upslope transport of anomalously high θ_e air beneath the capping lid is well illustrated at 12 and 16 LDT when high θ_e air from the moist, capped boundary layer is transported by anomalous easterly winds to the narrow band of deepening convection over LMW. Upward transport of low-level easterly momentum by the ascending branch of the solenoidal circulation over the foothills is made evident by the negative anomalies above LMW at 16 LDT.

4. SENSITIVITY TESTS

The following experiments were performed:

<u>Expt</u>	<u>Remarks</u>
NGE	Surface evapotranspiration turned off over land
LRT	Lower resolution topography at 200 km resolution
FLAT	Flat topography
NLW	Longwave radiation turned off
NSW	Shortwave radiation turned off

The results (to be presented) indicated that

a) Local surface evapotranspiration is an important

source of moisture for severe convective outbreak. Without this source, not enough moisture is available for transport to the foothills regions to feed the convection. As a result, the mountain-plain circulation became ineffective in initiating severe convection.

b) An often observed condition for severe convection, the presence of a strong capping lid, was found to be formed from two processes. One factor is the presence of radiative cooling at the surface. Another factor is the advection from the downslope flow and the accompanying adiabatic warming. Strong surface heating is essential in eroding the lid over the foothills.

5. CONCLUSION

A fully compressible mesoscale model has been used to simulate a case of severe convection over the foothills of Alberta. The results confirm the finding of Smith and Yau that the 11 July 1985 severe convective outbreak arises from an interaction of the upper-level trough, low-level moisture transport from the synoptic scale flow, and surface heating leading to the erosion of the capping lid and the formation of the mountain plain circulation. Local evapotranspiration has been found to be an important source of moisture. Radiative cooling and adiabatic warming from the downslope flow contribute significantly to the formation of the capping lid.

Acknowledgement

This research is supported by the Natural Science and Engineering Research Council and the Atmospheric Environment Service of Canada.

REFERENCES

Carlson, T.N., S.G. Benjamin, G.S. Forbes, and Y.-F. Li, 1983: Elevated mixed layers in the regional severe storm environment: Conceptual model and case studies. *Mon. Wea. Rev.*, **111**, 1453-1473.

Smith, S., and M.K. Yau, 1993a: The causes of severe convective outbreaks in Alberta. Part I: A comparison of a severe outbreak with two nonsevere events. *Mon. Wea. Rev.*, **121**, 1099-1125.

Smith, S., and M.K. Yau, 1993b: The causes of severe convective outbreaks in Alberta. Part II: Conceptual model and statistical analysis. *Mon. Wea. Rev.*, **121**, 1099-1125.

Tanguay, M., A. Robert, and R. Laprise, 1990: A semi-implicit semi-Lagrangian fully compressible regional forecast model. *Mon. Wea. Rev.*, **118**, 1970-1980.

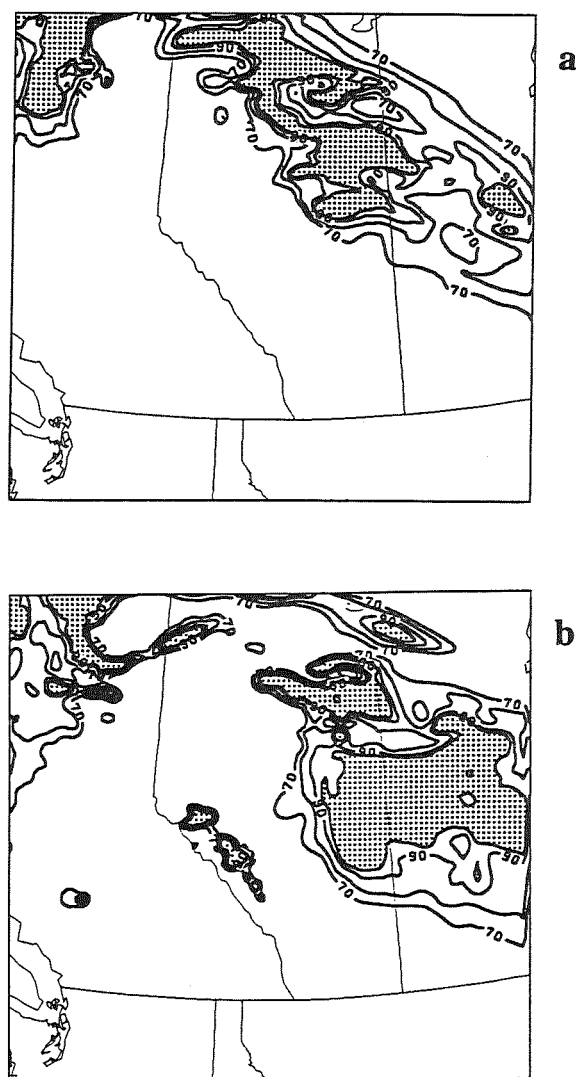
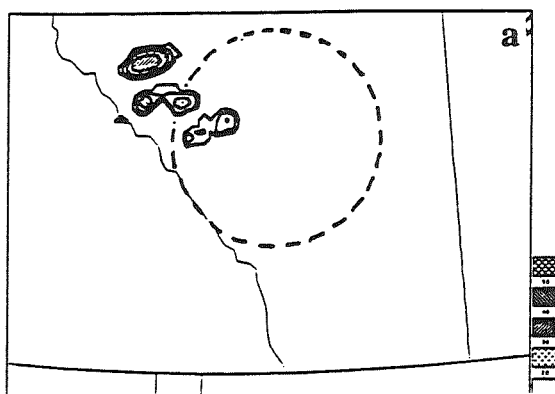


Fig. 1 Model predicted 600 mb relative humidity at a) 06 LDT (12 UTC) and b) 14 LDT (20 UTC) 11 July 1985 from the 10 km control run. Contours are 70%, 80%, 90% and 95%. Shaded areas > 95%.



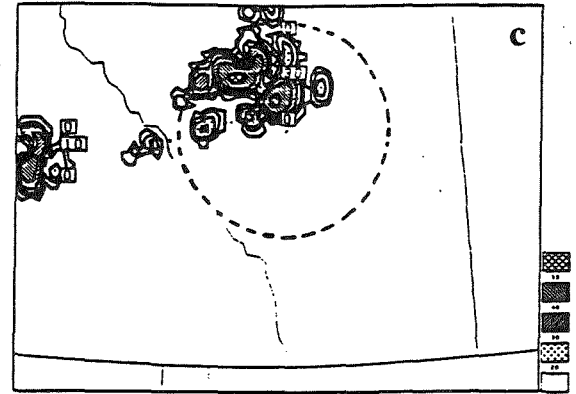
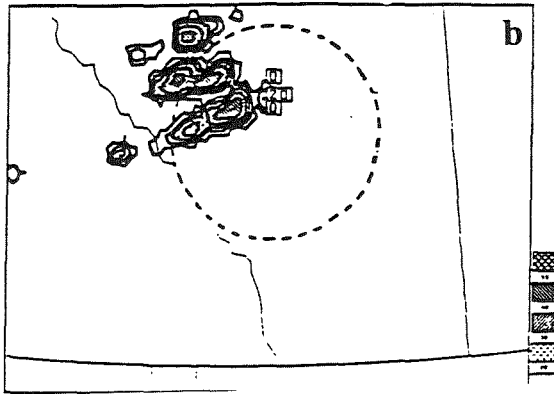


Fig. 2. Model predicted radar reflectivity at 600 mb at a) 16 LDT (22 UTC) 11 July, b) 18 LDT (00 UTC) 12 July, and c) 20 LDT (02 UTC) 12 July) from 10 km control. Contour interval every 10 dBz with minimum at 20 dBz. Dashed circle denotes 120 km range marker centered at Red Deer.

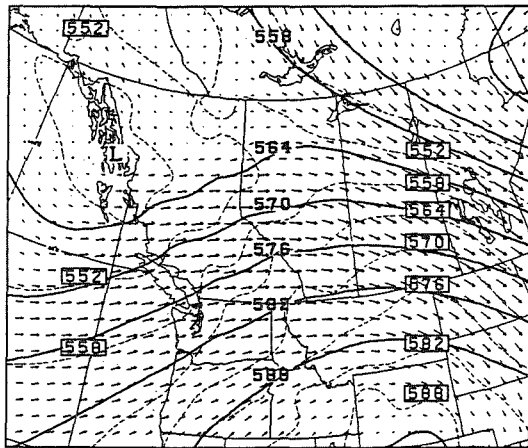


Fig. 3 Model predicted 500 mb height (solid) and 500-1000 mb thickness (dashed) at 12 LDT (18 UTC) 11 July from 100 km run.

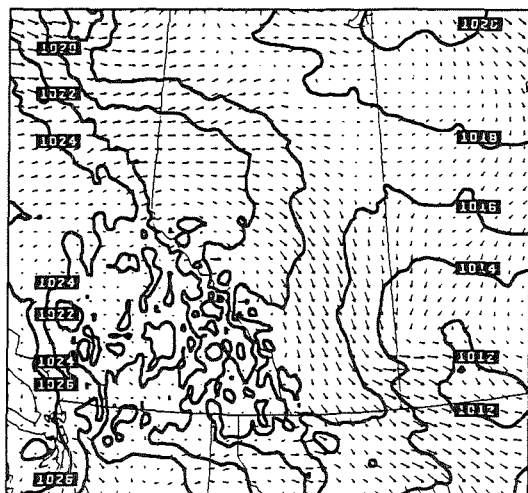


Fig. 4 Model predicted MSL pressure and surface wind at 12 LDT (18 UTC) 11 July from 10 km run. Contour interval is 2 mb. The largest wind vector is 8 m/s.

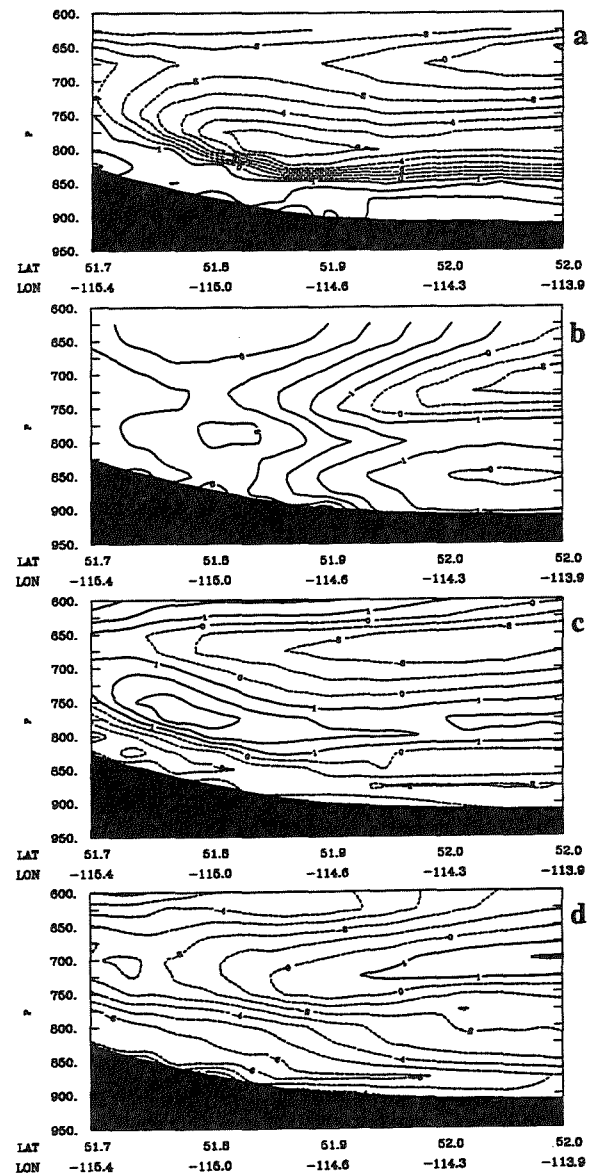


Fig. 5 Vertical cross section of anomalous equivalent potential temperature at a) 12 LDT and b) 16 LDT. Anomalous u-component of the wind at c) 12 LDT and d) 16 LDT 11 July from 10 km run. The contour intervals for temperature and wind are 1 K and 1 m/s respectively. Dashed contours are negative values. The section is from Limestone Mountain (left) to Red Deer (right).

MESOSCALE AND MICROSCALE STRUCTURES OF SHALLOW SNOW BANDS OVER THE SEA OF JAPAN

Masataka Murakami*, Yoshinori Yamada*, Takayo Matuso**, Koyuru Iwanami***
John D. Marwitz**** and Glenn Gordon****

* Meteorological Research Institute, Tsukuba, Ibaraki, Japan

** Japan Meteorological Agency, Tokyo, Japan

*** Nagaoka Institute of Snow and Ice Studies, Nagaoka, Niigata, Japan

**** University of Wyoming, Laramie, WY 82071, USA

1. INTRODUCTION

Snow clouds organize on mesoscale over the Sea of Japan during cold air mass outbreaks and take on various forms. Typical forms of snow clouds are longitudinal-mode (L-mode) snow bands, transverse-mode (T-mode) snow bands, and convergent snow bands.

From a linear theory for dry convections, Asai (1972) pointed out that roll convections with their orientation parallel to the wind shear vector within cloud layer are of a preferred mode. Yagi (1986), based on analyses of satellite images, radar data and aerological data, reported that the relationship pointed out by Asai (1972) held for most of L-mode and T-mode snow bands over the Sea of Japan.

However, it is considered that convections in snow bands are not merely accounted for by dry convections but are affected by latent heat release due to the phase change of water substances and loading of hydrometeors.

To understand the formation mechanism of such a L-mode snow band and subsequent precipitation processes, both microphysical and dynamical structures of the snow bands should be investigated simultaneously. However, such studies have not been made so far.

In the present paper, microphysical and dynamical structures of shallow snow bands are described on the basis of an instrumented aircraft and dual-Doppler radar observations.

2. OBSERVATIONAL FACILITIES

In the 1993 field campaign, which was the fifth season of the five-year project (Murakami et al., 1994), we deployed an instrumented aircraft (Wyoming King Air) and dual-Doppler radars.

3. ATMOSPHERIC CONDITIONS

Surface weather map at 0900 JST on 29 Jan. 1993, 2 to 3 hours prior to the aircraft observation, is shown in Fig. 1. A well-developed synoptic low with the deepest center of 970 hPa was located at ~44°N/145°E and contours over the observation area were packed and aligned in the direction of NW-SE.

Satellite images show that snow clouds started to form ~300 km offshore the continent over the Sea of

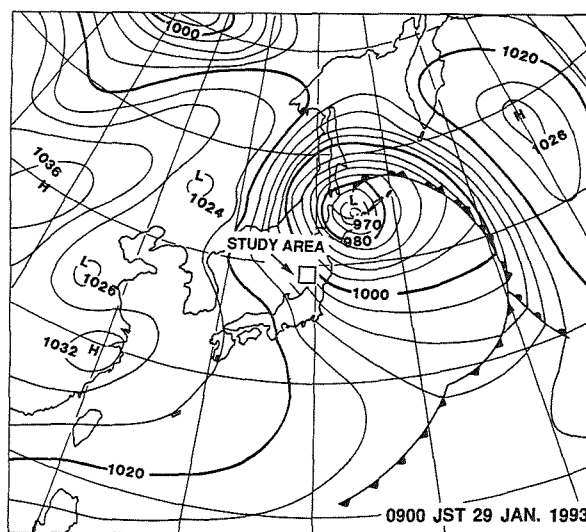


Fig.1 Surface weather map at 0900 JST on 29 Jan. 1993.

Japan, and their band-like structures were not distinct even near the Japanese Islands.

Thermodynamic structures of atmosphere is characterized by the strong temperature inversion at ~770 hPa level, below which convections are confined to. Above this level, air is very dry due to anticyclonic subsidence. From vertical profiles of temperature and dew point temperature, cloud top height (temperature) and cloud base height (temperature) are estimated to be ~2.5 km (-15°C) and ~1.0 km (-7°C), respectively. Vertical profile of equivalent potential temperature shows a convectively unstable layer at lower levels. West-northwest wind prevailed within the entire cloud layer although wind speed slightly decreased with increasing height. Wind shear vector within cloud layer directed NW with small magnitude.

4. OBSERVATIONAL RESULTS

During the period of 1100-1300 JST on 29 Jan., three snow bands were examined with the instrumented aircraft and dual-Doppler radars. PPIs of radar reflectivity in Fig.2 show that these snow bands consisted of

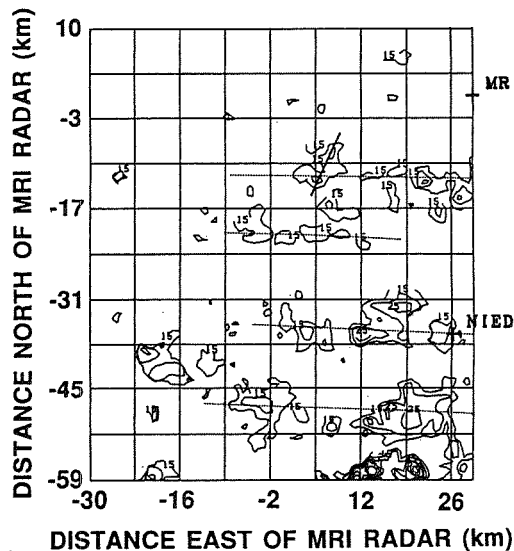
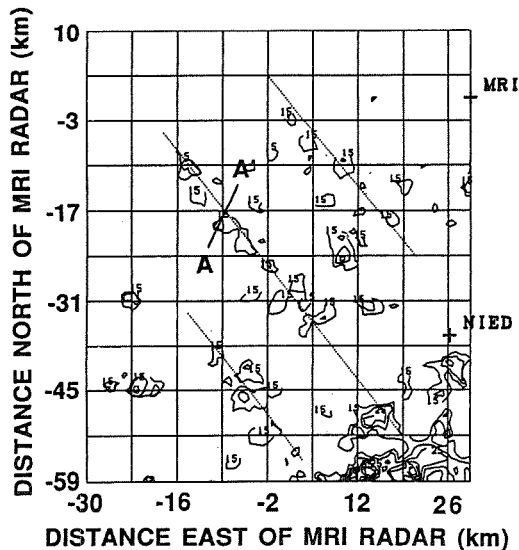


Fig.2 PPIs of radar reflectivity for snow bands of type A (upper) and type B (lower).

individual convective cells and are loosely organized in bands. The snow bands of type A (the primary mode) had their orientation deviating from the mean wind direction by 30 to 40 degrees to the right and snow bands of type B (the secondary mode) oriented parallel to the mean wind direction.

4.1 Snow Band of Type A

Figure 3 shows radar reflectivities and system relative wind, derived from dual-Doppler radar observation, in a vertical cross section perpendicular to the band orientation. The radar echo with maximum reflectivity of 20 dBZ stood almost elect and its top reached the 1.8 km level. Updraft region was located in the center of precipitation echo and has the maximum velocity of 1 ms^{-1} . Airflow in the vertical cross section was symmetric except for the inflow from the left at the

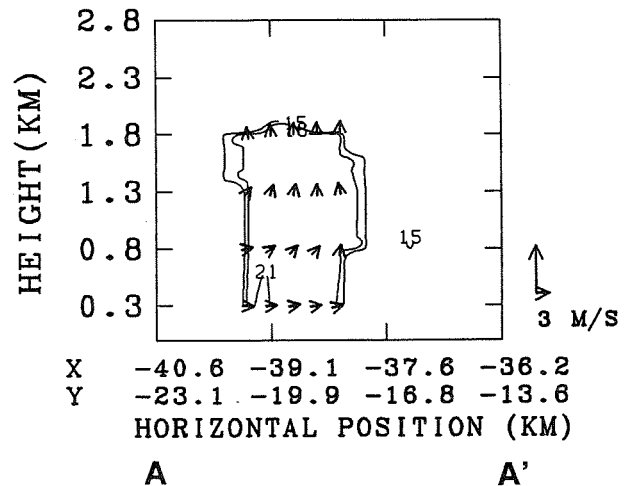


Fig.3 VW component of system relative wind and radar reflectivity in the vertical cross section along AA' in Fig.2a.

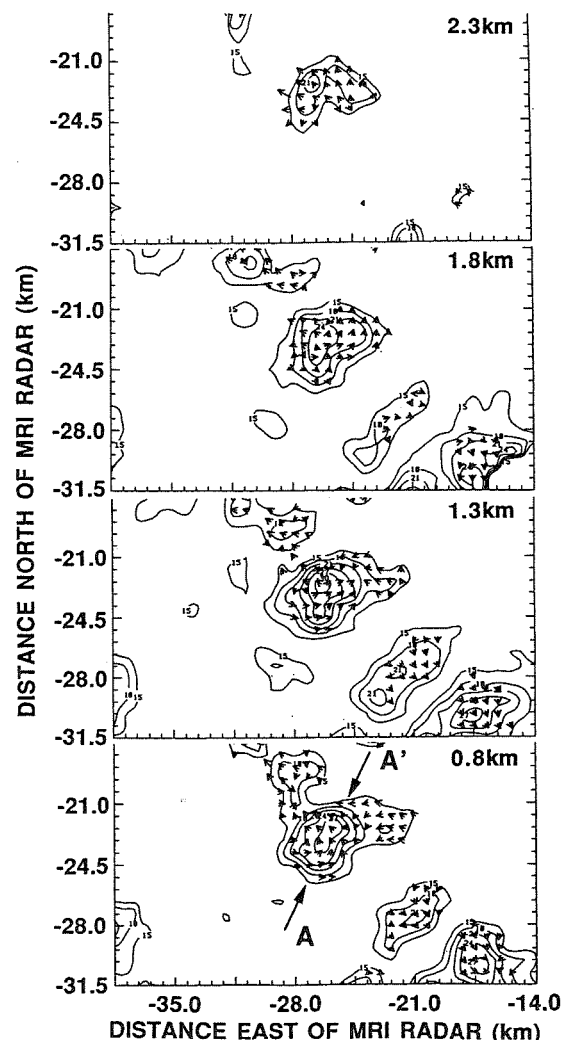


Fig.4 CAPPIs of radar reflectivities and system relative winds at 0.8, 1.3, 1.8, and 2.3 km levels at 1224.

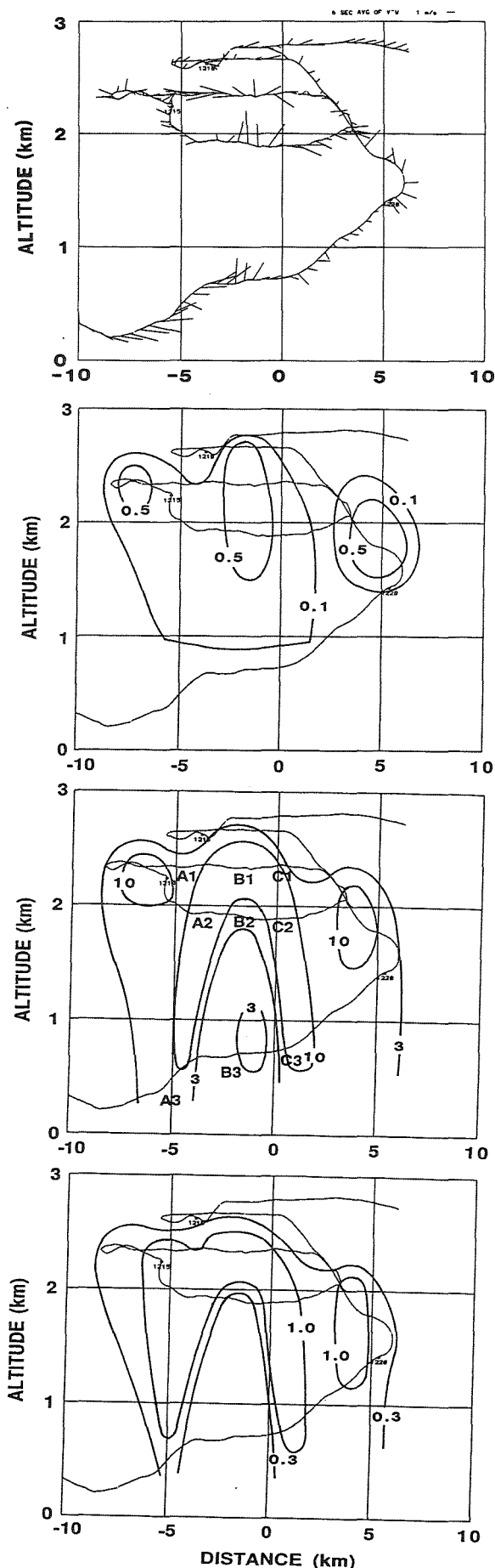


Fig.5 VW component of system relative wind (a), cloud water content (b), ice crystal concentration (c), and precipitation particle concentration (d) in the vertical cross section along AA' in Fig. 4.

lowest level. Horizontal convergence was found below the 1.3 km level whereas horizontal divergence was dominant above the level.

CAPPIs of radar reflectivities and horizontal wind relative to the system motion at 0.8, 1.3, 1.8, and 2.3 km at 1224 are shown in Fig. 4. At lower levels, air flow converges toward the center of echo cell while airflow diverges from the center to all the directions above the 1.8 km level. Thus the CAPPIs showed an axisymmetric structures of airflow in convective cell embedded in the snow bands except for the lowest layer.

The vw component of system relative wind, cloud water content (measured with King's probe), ice crystal concentration (measured with 2D-C probe), and snow particle concentration (measured with 2D-P probe) in the vertical cross section along AA' in Fig. 4. This vertical cross sections are based upon the aircraft sounding during the period 1208-1224. Figure 5a reveals an symmetric airflow structure except for at lower levels where the inflow stream came from the left. Updraft has the maximum velocity of $3 \sim 4 \text{ ms}^{-1}$ at $\sim 2 \text{ km}$ level and it turned to divergent outflows above this level. Weak downdraft existed on both sides of the main updraft region and on the right most and left most sides of the panel, weak updraft regions were found. Cloud water regions are distributed corresponding to the updraft regions. In the main cloud water region, the maximum cloud water content of $0.7 \sim 0.8 \text{ gm}^{-3}$ was found. High concentrations of ice crystals existed above and both sides of the main updraft region while in the updraft core ice crystal concentrations were generally very low. Note, however, that relatively high concentration of ice crystals were sometimes found in updraft core below cloud base, suggesting the importance of recirculation of snow particles in producing large graupel particles. Spatial distributions of snow particles were almost collocated with those of ice crystals.

Snow particle images (2D-P images) taken in the center and both sides of the updraft core at three different levels (see in Fig. 5c) are shown in Fig. 6. Inside the updraft core, snow particles with low number concentrations but large sizes up to $5 \sim 6 \text{ mm}$ existed, being consistent with the observational results of dual-Doppler radars that the precipitation core and updraft core are almost collocated.

4.2 Snow Band of Type B

A snow band with its orientation parallel to the mean wind direction was observed during the period 1230-1249. The observation showed a similar dynamical and microphysical structure to that in the snow band of type A. Major difference was an asymmetric inflow stream at lower levels that was found in type A but not in type B.

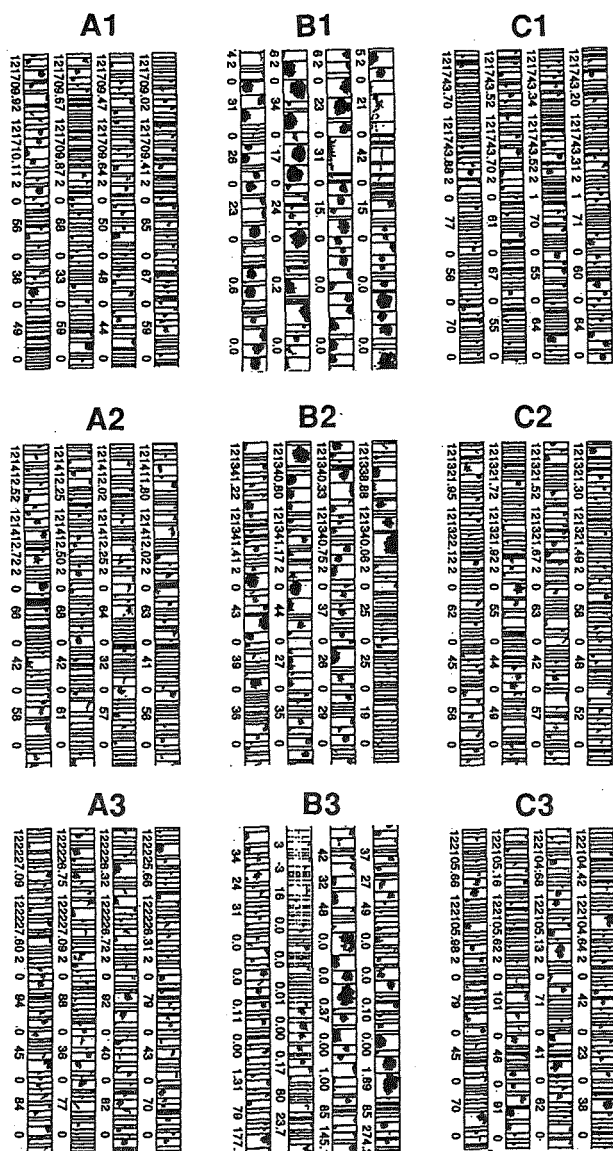


Fig.6 2D-P images in the center and on both sides of the updraft core at three different levels.

5. CONCLUSION

Shallow snow bands were examined over the Sea of Japan with an instrumented aircraft and dual-Doppler radars. During the aircraft observation period, two types of snow bands occurred. One is the snow bands with their orientation deviating from the mean

wind direction by 30 to 40 degrees to the right (primary mode). The other type of snow bands oriented parallel to the mean wind direction (secondary mode). Both types of snow bands consisted of convective clouds with top height of ~ 2.5 km and horizontal dimension of 5-10 km, and loosely organized in bands.

For the snow bands of primary mode, structures of system relative wind in the vertical cross section perpendicular to band orientation was symmetrical except for the air flow from the southwest at lower levels. By comparison, for the secondary mode, the air flow structure was symmetrical at all levels.

For both types of snow bands, maximum updraft velocity in convective cells was $3-4 \text{ ms}^{-1}$ and existed at around the 2 km level. Above this level, updraft velocity weakened and horizontal divergent flow became prominent.

In updraft cores, number concentrations of ice crystals and precipitation particles were low. But a considerable number of large graupel particles were found. This is consistent with the results of dual-Doppler radar observations that updraft cores were almost collocated with precipitation cores.

In updraft cores near cloud base levels, many graupel particles with their fall velocities smaller than updraft velocities were found. This fact suggests that recirculation of precipitation particles played an important role in producing large graupel particles (5-6 mm) in shallow convective snow clouds.

REFERENCES

- Asai, T., 1972: Thermal instability of a shear flow turning the direction with height. *J. Meteor. Soc. Japan*, 50, 525-532.
- Murakami, M., T. Matsuo, H. Mizuno, and Y. Yamada, 1994: Mesoscale and microscale structures of snow clouds over the Sea of Japan. Part I. *J. Meteor. Soc. Japan*, 72, 671-694.

Yagi, S., 1985: Large scale snow clouds with roll axes roughly perpendicular to the direction of winter monsoon burst. *Tenki*, 32, 175-187.

TURBULENCE PARAMETERS AND VERTICAL DRAFTS IN TROPICAL CONVECTIVE CLOUDS OVER CAMAGUEY, CUBA

Daniel Martínez Castro

Institute of Meteorology, Habana 17, Ap.17032, Cuba.

1. INTRODUCTION

The knowledge of the dimensions, velocities and buoyancy of vertical drafts in convective clouds, as well as turbulence, is of the greatest importance for establishing conceptual and numerical models of the cloud evolution, and particularly, to characterize the precipitation process in convective clouds. Some aspects of the dynamic characteristics of Cuban convective clouds have been discussed in several papers, as Beliaev et al. (1989), Martínez et al. (1989 and 1995), and Pérez et al. (1992), on the basis of measurements made during different phases of the Cuban Project for Artificial Weather Modification (PCMAT) in the Camaguey Meteorological Area (CMA). The objective of this paper is to give a more complete characterization of dynamics and turbulence in Cuban convective clouds, based on the analysis of data from the most informative seasons of the experiment.

2. INSTRUMENTATION, MEASUREMENTS AND DATA

The experimental period extended from June to September, corresponding to the Cuban rainy season, for the years 1986, 1987 and 1990. Measurements were made from 13:00 to 18:00 LST. The CMA is located in the central-eastern part of Cuba, and is limited by a circumference of 80 km radius, centered in the city of Camaguey (21°25'N and 77°10'W) and by the northern and southern coasts. In the experimental period, synoptic conditions were nearly typical for the time of the year, but with more than usual anticyclonic situations, mainly in 1986 and most of the 1987 season, which caused a low relative humidity in the layer from the surface to 3 km, and low rainfall.

Two instrumented aircraft were used, an IL-14, and an AN-26. The instrument set included mainly equipment developed at the Central Aerological Observatory of Moscow, and consisted on an aircraft load complex, for the measurement of vertical velocity, a low inertial resistance thermometer, liquid and total water content probes, from which ice content was estimated, and a precipitation drop spectrometer, from which rain water content was estimated (This was only installed in the IL-14). Standard navigation equipment was also used. Velocity and temperature fluctuation data were sampled at 4 Hz, and water content at 1 Hz. Measurement and error ranges for these instruments and references for a complete description may be found in Mazin and Shmeter, (1977) and Pérez et al. (1992).

The sample consisted on data from 337 penetrations into convective clouds or below their bases. In most in-cloud cases, the flight altitudes were near to 3 km for the IL-14 (8 to 11 °C), and to 6 km for the AN-26 (-10 to -5 °C). Data were stratified using altitude as one of the main parameters. The other parameters chosen for stratification were cloud depth, and the sign of mean vertical velocity (\bar{w}), as a cloud

development index (DI). Cloud base height ranged from 1 to 1.5 km, corresponding to temperatures from 18 to 25 °C; cloud horizontal extension ranged from 0.4 to 11 km, and cloud top height ranged from 2.5 to 12.5 km, corresponding to temperatures from 15 to -60°C. The measured clouds were individual towers that, in some cases were isolated and in others, united by their bases with other clouds of the same mesoscale band. These bands form frequently over Cuba, parallel to the coasts and are due to the combined action of the sea breeze and the easterlies (Beliaev et al., 1989). Repeated penetrations of the same cloud were made in some cases, but they are not analyzed separately in this paper.

3. RESULTS AND DISCUSSION

3.1. Spectra and cospectra

Vertical velocity and temperature fluctuation spectra were calculated for clouds which horizontal extension was greater than 3 km. Fig. 1 shows averaged vertical velocity energetic spectra, temperature dispersion spectra and w-T cospectra for 1987 and 1990 data. Although the form of individual spectra is very variable, averaged spectra for clouds with $\bar{w} > 0$ (DI=1) show a "large scale" maximum at scales from 0.8 to 1.5 km. These peaks are not evident in all cases, because of the limitation in the maximum calculated scale. The similar form of the vertical velocity and temperature fluctuation spectra suggests the predominantly thermic origin of vertical motions in these clouds. The maxima are related with the energy input in the spectrum due to condensation processes. The spectra for the DI=0 ($\bar{w} \leq 0$) groups is different, so that the main peak, either is absent, or has a similar intensity to that of secondary peaks. Regrettably, there were not enough penetrations of clouds with DI=0 for the warm layer, as to calculate a meaningful average, but the individual spectra are similar to the averaged ones for the cold layer (Martínez et al., 1995). The obtained vertical velocity spectra, if taken to log S-log k plots, follow approximately the well known -5/3 law, except for wave numbers near or lower than those of the peaks. These results are qualitatively coincident with those obtained by Warner (1970), Mazin and Shmeter (1977) and Murty et al. (1985). The scale of the main peak for the CMA clouds is greater, because of their greater dimensions.

Averaged w-T cospectra were positive for almost the whole k range for every group of the warm layer in 1987, implying that the mean heat flux is upwards for all scales. As kinetic energy, heat flux is concentrated in the larger scales. For the cold layer, instead, the averaged cospectra obtained for 1987 and 1990, were different. The first took low, or even negative values for all the k range, and the second was positive and similar to the one obtained for the warm layer in 1987. This different behavior of the cold part of the clouds for both years may be related with the difference in meteorological conditions, which is reflected

also in the values of other dynamic parameters (Tab. 1,2). Averaged cospectra for clouds with DI=0 were negative and showed moderate values.

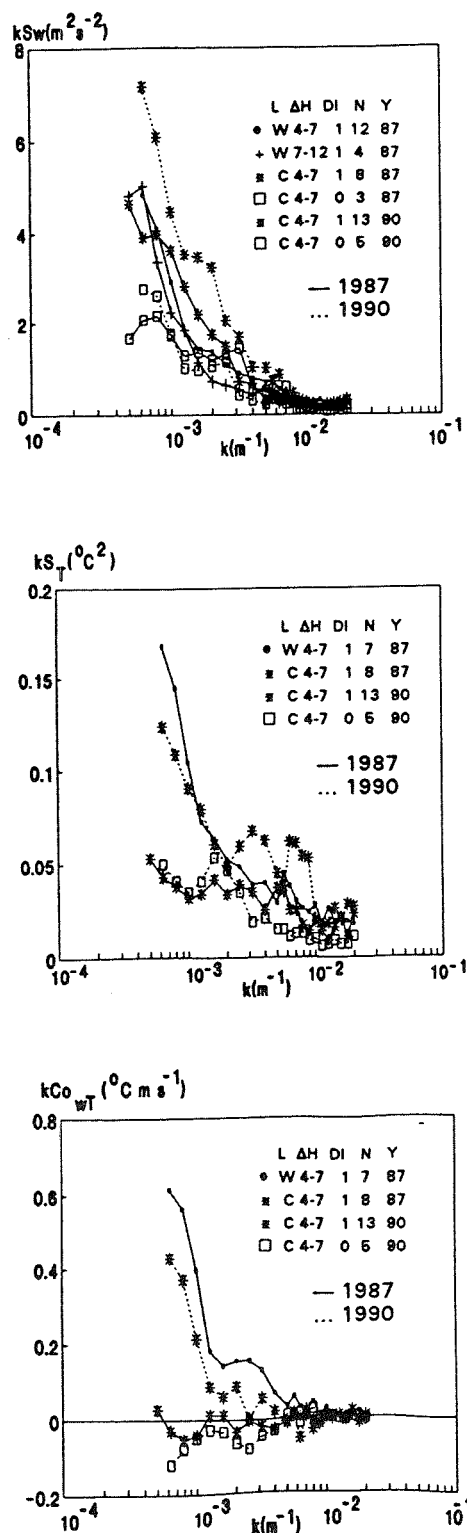


Fig. 1. Averaged energetic spectra, kS_w , temperature dispersion spectra, kS_T , and cospectra, kCo_{wT} .
L = layer
 ΔH = cloud vertical depth
DI = 1 ($\bar{w} > 0$) DI = 0 ($\bar{w} < 0$)
N = number of cases Y = year

Table 1. Some dynamic and turbulence related parameters for the Camaguey convective clouds, averaged for the different groups of cases.

ΔH (km)	DI	L	\bar{w}_+ ms^{-1}	\bar{w}_- ms^{-1}	σ_w ms^{-1}	σ_u ms^{-1}	ϵ $cm^2 s^{-3}$	K	N
1986									
1- 4	1	W	7.6	3.4	2.6	2.2	1180	100	21
4- 7	1	W	8.6	4.7	3.1	2.4	1550	120	41
7-12	1	W	9.9	6.3	3.4	2.7	1200	100	10
1- 4	0	W	3.6	5.3	2.3	1.7	1620	110	14
4- 7	0	W	4.6	6.2	2.5	2.0	800	100	9
7-12	0	W	5.9	6.8	3.2	2.7	860	90	8
1987									
1- 4	1	U	2.2	0.2	0.6	0.9	---	---	3
1- 4	1	W	5.7	2.6	2.1	1.8	400	80	25
4- 7	1	U	2.9	0.8	0.8	1.2	50	40	7
4- 7	1	W	8.2	3.6	2.8	2.6	960	100	49
4- 7	1	C	7.3	1.7	2.7	3.2	390	70	26
7-12	1	U	4.9	3.3	1.4	2.1	80	50	5
7-12	1	W	8.1	4.4	3.1	2.9	1030	100	9
2- 4	0	W	1.5	3.1	1.2	1.4	---	---	6
4- 7	0	W	3.1	4.4	1.6	2.2	650	90	7
4- 7	0	C	3.0	5.3	1.9	2.2	530	80	13
7-12	0	W	5.9	6.8	3.2	2.7	240	70	8
1990									
4- 7	1	C	9.6	3.7	3.3	2.9	1580	110	37
4- 7	0	C	3.5	6.2	2.4	2.2	480	80	30

ΔH = Cloud depth
DI=1 mean vertical velocity upwards.
DI=0 mean vertical velocity downwards.
W = warm layer C = cold layer
U = under base
+/- = maximum upwards/downwards
"---" = group average
N = number of cases for each group

3.2. Other turbulence parameters

Turbulent energy dissipation rate and turbulent viscosity coefficient were calculated from the Kolmogorov and Richardson-Obujov formulae (Mazin and Khirgian, 1989). Turbulence intensity for vertical and horizontal velocity fluctuations were estimated from the root mean square values of these quantities. Table 1 shows the averaged values of these parameters and of maximum vertical velocity for each group in the three seasons. In the warm layer (measured in 1986 and 1987), the greatest values of vertical velocity and turbulence intensity are obtained for the Cb clouds ($\Delta H \geq 7km$), and deep Cu cong ($4 \leq \Delta H < 7km$). For all the groups, except Cb, the parameters for DI=1 were greater than for DI=0. The values of \bar{w}_+ and σ_w obtained for the cold layer in 1987 were the least of the sample.

3.3. Drafts and cores

To study the characteristics of convective drafts, these were identified as individual units, following partially the methodology developed by LeMone and Zipser (1980). It was defined as a "draft", the part of the cloud register where vertical velocity w keeps its sign for more than 100 m and reaches, at least once, the value of $0.5 ms^{-1}$. A "core" is defined as the part of a draft where $w > 1 ms^{-1}$ for more than 100 m. This

threshold value differs from the one used in LeMone and Zipser (1980), but suits better to the PCMAT sample. So, it must be taken into account that the definitions, though analogous, do not have the same physical meaning. The "diameters" D of drafts and cores were estimated from their horizontal extensions in the direction of flight. It can be noticed (Table 2) that the number of updraft cores (upcores) is greater than the number of downdraft cores (downcores) for the warm layer, but they are nearly equal for the cold layer. It may be explained by the existence of penetrative downcores near cloud top and by the erosive action of entrainment against upcores. Empirical distributions of the values of diameter, mean and maximum vertical velocity and mass flux were obtained for each group of cases and in most cases follow log-normal distributions. The histogram of the D distribution for deep Cu cong measured in 1987 is shown in Fig. 2, as an example. It can be seen from these distributions that, for drafts greater than 500 m, corresponding to mesoscalar motions, there are more updrafts than downdrafts, and their diameters and vertical velocities are also greater. The greatest measured core had a diameter of more than 2 km, and the maximum values of vertical velocity were 21 ms^{-1} for updrafts, and 14 ms^{-1} for downdrafts, both measured in 1990, in the cold layer. For the great majority of the updrafts, mean vertical velocity lies between 2 and 8 ms^{-1} . Thus, the vertical velocity "seeding window" holds for most of the clouds. Liquid water and ice contents are also within the limits recommended for seedable clouds. (Czys et al., 1993).

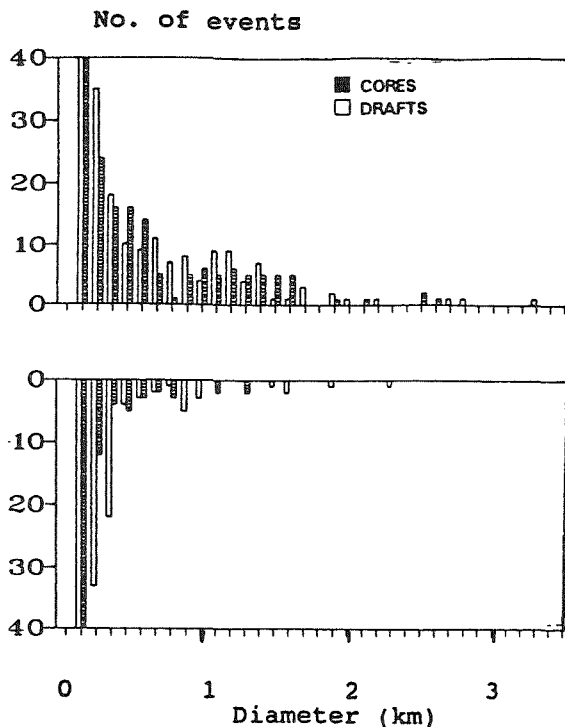


Fig. 2. Histograms of the diameters of drafts and cores for 1987 clouds. (Warm layer, $\Delta H=4-7 \text{ km}$). Upward bars refer to upward motions and downward bars to downward motions.

The analysis of the mass transport distributions showed that most of the air mass is carried up by drafts with $D > 1 \text{ km}$ and $w > 6 \text{ ms}^{-1}$. For Cb, some downdrafts with great values of mass flux were found.

Generally, cloud water is preferentially concentrated in upcores, and rain water (measured only in the warm

layer), in downcores. Ice content (measured only in 1990) was similarly distributed between upcores and

Table 2. Averaged and maximum dynamic parameters for convective drafts and cores.

ΔH km	L	w ms^{-1}	w_m ms^{-1}	q gm^{-3}	r gm^{-3}	ΔT_v $^{\circ}\text{C}$	ΔT_o $^{\circ}\text{C}$	ΔT_{ef} $^{\circ}\text{C}$	N
UPDRAFTS (1986)									
1-4 W	2.6	4.4	.72	.10	---	---	---	---	93
4-7 W	2.7	4.9	.87	1.4	---	---	---	---	180
> 7 W	2.4	4.5	.64	1.4	---	---	---	---	82
UPDRAFTS (1987)									
1-4 W	2.4	4.1	.61	---	---	---	---	---	48
4-7 W	2.9	4.9	.64	.61	.91	.45	.46	.162	162
4-7 C	2.5	4.4	.57	---	1.2	.24	.97	.82	82
> 7 W	2.4	4.1	.64	.97	1.4	.54	.85	.37	37
UPDRAFTS (1990)									
4-7 C	3.0	5.7	.64	.10	.44	.31	.12	.112	112
DOWNDRAFTS (1986)									
1-4 W	1.5	2.9	.31	.13	---	---	---	---	108
4-7 W	1.7	3.2	.46	1.6	---	---	---	---	189
> 7 W	1.8	3.5	.64	3.4	---	---	---	---	83
DOWNDRAFTS (1987)									
1-4 W	1.5	2.4	.23	---	---	---	---	---	42
4-7 W	1.3	2.6	.35	1.5	.55	.60	-.37	.171	171
4-7 C	1.7	3.3	.37	---	.97	.15	.66	.90	90
> 7 W	1.4	2.7	.51	1.3	1.3	.58	-.02	.44	44
DOWNDRAFTS (1990)									
4-7 C	2.0	4.0	.36	.07	.53	.17	.55	.114	114
UPCORES (1986)									
1-4 W	3.4	5.3	.74	.11	---	---	---	---	75
4-7 W	3.8	5.9	.94	1.3	---	---	---	---	147
> 7 W	3.3	5.1	1.2	2.6	---	---	---	---	78
UPCORES (1987)									
1-4 W	2.9	4.4	.63	---	---	---	---	---	46
4-7 W	3.7	5.7	.81	.47	.66	.47	.19	.144	144
4-7 C	3.4	5.2	.55	---	.72	.23	.49	.67	67
> 7 W	3.1	4.9	.82	.31	1.3	.34	.91	.33	33
UPCORES (1990)									
4-7 C	3.8	6.4	.72	.10	.53	.30	.23	.108	108
DOWNCORES (1986)									
1-4 W	2.9	4.0	.25	.09	---	---	---	---	63
4-7 W	2.8	4.2	.48	1.9	---	---	---	---	121
> 7 W	2.9	4.4	.57	3.5	---	---	---	---	63
DOWNCORES (1987)									
1-4 W	2.9	4.1	.10	---	---	---	---	---	23
4-7 W	2.6	3.8	.39	1.3	.19	.55	-.37	.73	73
4-7 C	2.7	3.9	.36	---	.81	.15	.66	.70	70
> 7 W	2.6	3.7	.53	1.4	.59	.60	-.02	.29	29
DOWNCORES (1990)									
4-7 C	2.6	4.3	.32	.08	.71	.17	.55	.109	109

ΔH = Cloud depth

W= warm layer C = cold layer

q= cloud water content

m= maximum

r= rain water content (for warm layer)

r= ice content (for cold layer)

"—" group average

ΔT_v = virtual temperature excess

ΔT_o = water load correction

ΔT_{ef} = effective temperature excess

N= number of cases (drafts or cores)

downdrafts (Table 2.) Averaged mean virtual temperature excess in upcores was generally higher than in downcores for the warm layer, but it was positive for many of the downcores. After introducing the water load correction (ΔT_o in Table 2), to obtain the effective buoyancy (ΔT_{ef}), the difference becomes more evident, but anyway, many updrafts remain with negative

buoyancy, which means that they ascend by inertia, and many downdrafts remain with positive buoyancy, which means that they are compensating downward motions, heated by compression. It must be considered, also, that the virtual correction has been included relative to the environmental humidity, that not always correspond to the immediate neighborhood of the downdrafts. The high positive buoyancy value obtained for cold layer downdrafts is a consequence of the lack of the rain water share of the water load correction, that is apparently important also for this level.

A comparison of the results obtained in this paper with the measurements of purely oceanic clouds in GATE, TAMEX and EMEX (LeMone and Zipser, 1980; Jorgensen and LeMone, 1989; Lucas et al., 1994) shows that, despite of the lower dimensions of the measured CMA clouds and their drafts and cores, their vertical velocities are similar and sometimes greater than those measured in tropical oceanic clouds, approaching the values measured over continental land (Byers and Braham, 1949; Czys, 1991). The general objectives of PCMAT and the limitations imposed by flight security for the type of aircraft used, prevented the penetration of supercell or hybrid Cb that were frequently present in the area, which, very likely may have had cores with much greater vertical velocities than the ones included in the sample.

The existence of relatively strong vertical drafts, even for cores less than 1 km wide, may be related with the high convective available potential energy (CAPE) of PCMAT soundings, which attained values of 2000-4000 J kg⁻¹ in most afternoon soundings, together with adiabatic maximum virtual temperature excesses of 10-15 °C. These CAPE values are comparable with those reported by Williams and Renó (1993) for Australia, and are a consequence of the CMA geographical situation, allowing at the same time high surface moisture, due to the proximity of the sea, and high surface temperature, resulting in high wet bulb temperature and CAPE. This allows to consider the PCMAT clouds nearer to continental than to purely oceanic clouds, by its dynamic characteristics, as was previously assessed in Pérez et al. (1992).

4. SUMMARY AND CONCLUSIONS

Aircraft data for 337 convective cloud penetrations over Camaguey, Cuba, have been analyzed. Dynamic and turbulence parameters have been obtained for the clouds, and have been averaged for different groups of cases, taking into account their vertical depth, penetration height and mean vertical velocity.

Turbulence intensity and maximum vertical velocity were found to be greater for deep developing Cu cong and Cb clouds, and attained values comparable with those measured in continental clouds. No general significant difference was found between measured parameters of the warm and the cold level.

Vertical velocity energetic spectra show peaks at scales from 0.8 to 1.5 km, associated to the energy inflow due to the condensation process. Cospectra of w and T show preferent upward heat flux for scales near to the kinetic energy peaks at the warm level. For the cold level, the form of cospectra was different for 1987 than for 1990 clouds, revealing dependence on meteorological conditions of cloud development.

Dynamic parameters were obtained for 1637 in-cloud drafts and 1249 cores, defined on the basis of a 100 m diameter threshold. Approximately lognormal distributions were found for diameter, mean and

maximum vertical velocities. These parameters showed dependence on cloud depth and were greater for upward than for downward drafts and cores. Positive average buoyancy was found in upcores for all the groups of cases. For the warm layer, downcores were generally negatively buoyant, but for the cold layer, their average buoyancy was positive.

The values obtained for turbulence parameters and for updraft velocities are nearer to those measured in continental clouds than in tropical oceanic clouds.

Acknowledgements

I am grateful to V.P. Beliaev, S.M. Shmeter and G.N. Shur for their valuable advices and remarks, and to C.A. Pérez, V.V. Petrov, V.V. Volkov, A.G. Rabelo, C. Fornés and R. Aroche, who participated in different stages of data processing and analysis. I also thank the scientific and piloting crews of the IL-14 and AN-26 for aiding in data collection. The experiments were supported by the Governments of Cuba and the former USSR. The preparation of the paper was supported by the ICTP Programme for Training and Research in Italian Laboratories, Trieste and the Institute of Atmospheric Physics, Rome.

REFERENCES

- Beliaev V., M. Valdés, D. Martínez and V. Petrov, 1989: An airborne investigation of cloud bands observed over the CMA (In Russian) *Trudy TsAO*, 172, 11-16.
- Byers H.R. and R.R. Braham, 1949: *Thunderstorm*, Wash. 247 pp.
- Czys R.R., 1991: A preliminary appraisal of the natural structure and seedability of updrafts in midwestern cumulus at the -10° C level. *J. Weath. Mod.*, 23.
- Czys R.R., S.A. Changnon, N.E. Westcott, R.W. Scott and M.S. Petersen, 1995: Responses of warm-based, Midwestern cumulus congestus to dynamic seeding trials. *J. Appl. Meteor.*, 34, 1194-1214.
- Jorgensen D.P. and M.A. LeMone, 1989: Vertical velocity characteristics of oceanic convection. *J. Atmos. Sci.*, 46, 5, 621-640.
- LeMone M.A. and E.J. Zipser, 1980: Cumulonimbus vertical velocity events in GATE. Part I: Diameter, Intensity and Mass Flux. *J. Atm. Sci.*, 37, 2444-2457.
- Lucas C., E.J. Zipser and M.A. LeMone, 1994: Vertical velocity in oceanic convection off tropical Australia. *J. Atmos. Sci.*, 51, 3183-3193.
- Martínez D., Pérez C., Aroche R., Beliaev V. and Petrov V., 1995: Espectros de potencia de la velocidad del viento en las nubes convectivas tropicales sobre Cuba. *Atmósfera*, 8, 65-80.
- Mazin I. P. and Shmeter S. M. (eds.), 1977: The clouds and the deformation of meteorological field. (In Russian) *Trudy TsAO*, 134, 280 pp.
- Mazin I.P. and A.J. Khirgian (eds.), 1989: *The clouds and the cloudy atmosphere. A Handbook*. (In Russian). L. Gidrometeoizdat. 648pp.
- Murty A.S.R., A.M. Selvam, S.S. Parasnis, Bh. Ramana Murty, 1985: Warm cloud dynamical responses to salt seeding. *Papers presented at the fourth WMO Scien. Conf. on Weather Modification*, 489-492.
- Pérez C., Martínez D., and Petrov V.V. 1992: Microstructure, mixing and turbulence in cumulus clouds over Cuba and the Caribbean Sea. *Proc. WMO Workshop on Cloud Microphysics and Appl. to Global Change*. WMO/TD No.537, 245-256.
- Warner J., 1970: The microstructure of cumulus clouds. Pt.3 The nature of updraft. *J. Atmos. Sci.*, 27, 682-688.
- Williams E. and N.O. Renó, 1993: An analysis of the conditional instability of the tropical atmosphere. *Mon. Wea. Rev.*, 121, 21-36.

STRUCTURE AND FORMATION MECHANISM OF A TERRAIN TRAPPED RAIN STORM

Yasushi Fujiyoshi, Biao Geng, Naohiro Yoshimoto, Sachie Kanada and Takao Takeda

Institute for Hydrospheric-Atmospheric Sciences, Nagoya Univ., Nagoya 464-01, Japan

1. INTRODUCTION

We made dual-Doppler radar (X-band) observations of orographic rain clouds at Kii Peninsula in Japan from May to October, 1993 (Fig. 1). This area is one of the heavy rainfall areas in Japan.

On 3 September, 1993, a multi-cell type of

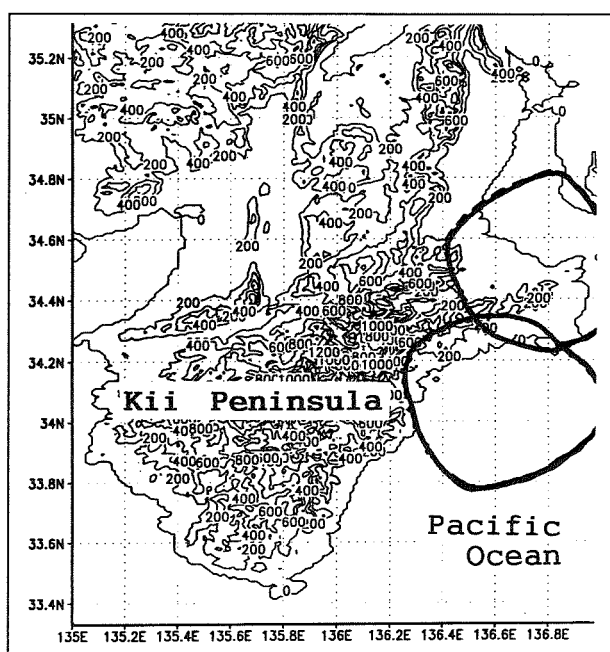


Figure 1: The topography of Kii Peninsula in Japan and the coverage area of dual-Doppler radar system of IHAS.

rain storm developed and lasted more than one hour. The storm did not move as a phase. This case was found to be quite interesting from the following reasons: (1) The rain storm did not develop on the slope of mountains, but off the sea coast. (2) We were able to observe the environmental 3-D wind fields 'before' the storm developed, since it had been raining from middle-level clouds before the development of the storm. (3) A terrain trapped low-level CW (clockwise) vortex had been existing near the region where the storm developed. (4) When a mid-level CW vortex had approached to the storm, the storm developed rapidly.

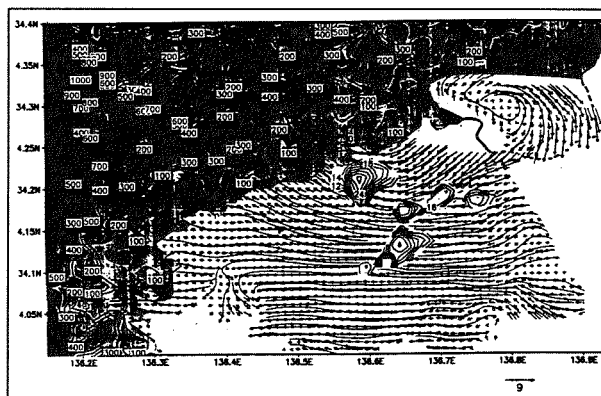


Figure 2: Topography, CAPPI ($H = 0.5$ km), wind vectors and stream lines at 0004 JST on 3 September, 1993.

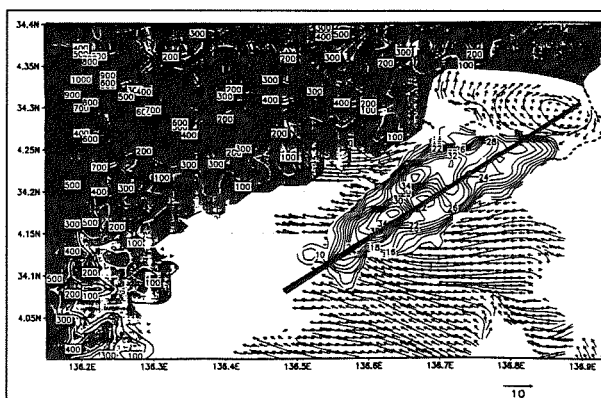


Figure 3: Same with Fig. 2 except at 0053 JST on 3 September, 1993.

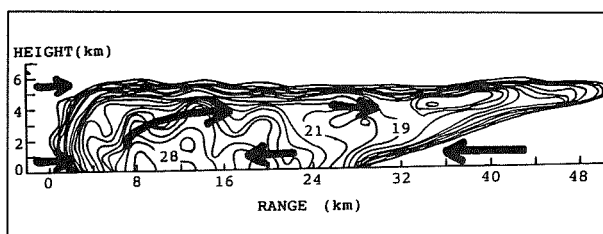


Figure 4: The vertical cross section of time averaged radar echo intensity along the line shown in Fig. 3. Contours are drawn every 1 dBZ above 10 dBZ. Thick arrows illustrate actual airflows.

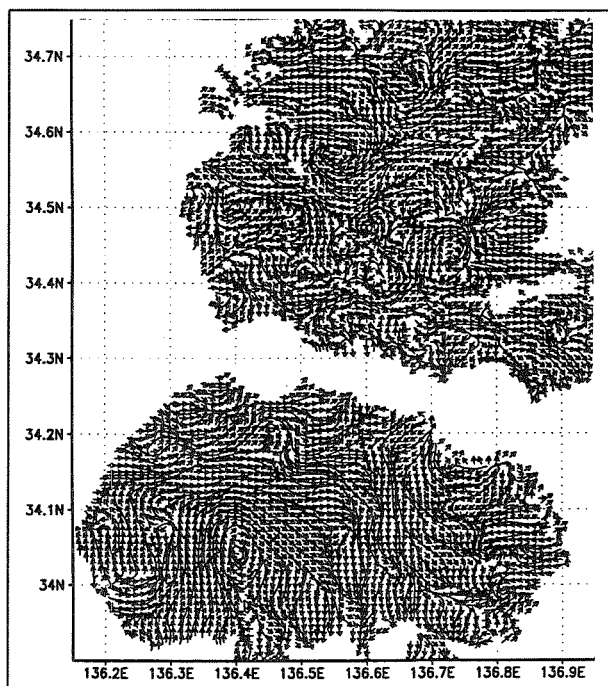


Figure 5: Wind vectors and stream lines at an altitude of 4.5 km at 2336 on 2 Sep., 1993. The wind vectors indicate the difference in wind field from that of the time of reference (2325 JST on 2 Sep.)

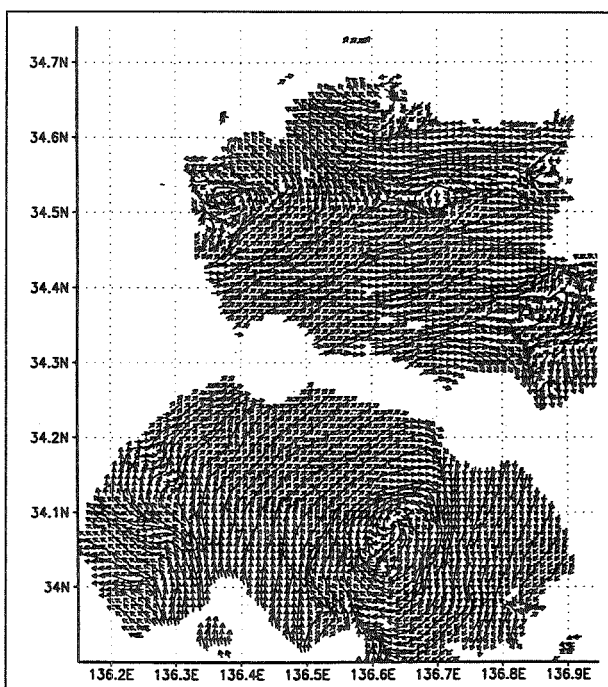


Figure 6: Same with Fig. 5 except at 0004 on 3 Sep., 1993.

2. MULTI-CELL STRUCTURE OF THE STORM

The multi-cell storm began to develop at 0004 JST (Japan Standard Time) and dissipated at 0142 JST on 3 September 1993. Convective cells composing the storm successively developed at almost the same place and moved to downshear side, that is, towards NE. Figures 2 and 3 show CAPPs ($H = 0.5$ km) of the storm at 0004 (developing stage) and 0053 JST (mature stage). The maximum horizontal scale of the storm was ~ 50 km in length and ~ 10 km in width. More than five convective cells were embedded in the storm. Wind vectors and stream lines are also shown in Figs. 2 and 3. The low-level wind blew from east to west, which is almost perpendicular to the slope of mountains. However, the storm did not develop on the slope of the mountains, but over the sea.

Figure 4 shows the vertical cross section of time averaged (from 0004 to 0142 JST) echo intensity along the line shown in Fig. 3. The height of echo top is ~ 6 km. The freezing level was ~ 4.4 km. This figure clearly shows the life cycle of each convective cell. Each convective cell developed at $X = \sim 4$ km, and attained its mature stage at $X = \sim 12$ km. It formed an anvil-like radar echo in its dissipation stage ($X \geq 32$ km). The actual airflows, not system-relative flows, are schematically shown in Fig. 4. Strong convergence between airflows with opposite direction is seen at the lower left flank. It is apparent that the maintenance of the low-level convergence is a reason why the multi-cell storm did not move as a phase.

3. LOW-LEVEL VORTEX

A terrain-trapped low level CW vortex, ~ 20 km in diameter and ~ 1.5 km in depth, had been existing in the northwest region of the storm. The center of the vortex slowly moved ($\sim 2 \text{ m s}^{-1}$) to the west. The NE-ly winds near the center of the vortex correspond with the airflow which blew from right to left in Fig. 4. Although the convergence between the NE-ly and E-ly winds seems to have occurred at the place where the storm developed, its magnitude was very small ($\leq 2 \times 10^{-4}$) 'before' the development of the storm.

Several convective cells formed in this area 'before' the storm developed. Different from the multi-cell storm, however, they did not develop large and had a short life. 'After' the development of the storm, the strong convergence zone corresponded well with the strong radar echo region. Its magnitude attained up to $\sim 2 \times 10^{-3}$ (0032 JST). The maximum size of the convergence zone was ~ 15 km in length and ~ 6 km in width. Wind vectors shifted to the storm and wind speeds increased near the storm. These facts indicate

that the existence of the low-level vortex (and associated NE-ly winds) was a necessary but not a sufficient condition to form the storm.

4. MID-LEVEL VORTEX

The SW-ly wind blew at altitudes above 3 km. Figures 5 and 6 show wind vectors and stream lines at an altitude of 4.5 km. Here the wind vectors indicate the difference in wind field from that of the time of reference (2325 JST on 2 Sep.). It is clearly shown that a mid-level CW vortex, ~ 60 km in diameter, had been moving towards ENE. Its speed was $\sim 13 \text{ m s}^{-1}$. The vortex was apparent between the altitudes of 4.0 and 5.5 km. There were small vortices and the wind fields were not organized in the northern part of Fig. 5 before the mid-level vortex approached. On the contrary, the wind field was organized and another CCW mid-level vortex formed in the northwest of the CW mid-level vortex (Fig. 6).

Just when the mid-level vortex passed above the storm (0004 JST, Fig. 6), the storm began to develop. During the passage of the mid-level vortex over the storm, the storm continued to develop. The storm dissipated after the vortex had moved further. The change in wind fields associated with the mid-level vortex was observed not only at middle levels but also at lower levels. That is, accompanied by the mid-level vortex, the air with strong S-ly wind component approached to the place where the storm developed. Therefore, the mid-level vortex closely related to the development of the storm.

5. FORMATION MECHANISM OF THE STORM

The formation mechanism of the storm is illustrated in Fig. 7. Small convective clouds develop and decay in the weak convergence zone before the mid-level vortex approaches to the place. This convergence is mainly caused by the low-level vortex (upper panel). The mid-level vortex is accompanied by the low-level strong wind. Therefore, the low-level convergence increases with approaching the mid-level vortex to the convergence zone. Since the airflow in the mid-level vortex is divergent, the updraft in a convective cloud would increase during the mid-level vortex passes over the cloud. The enhanced updraft causes strong low-level convergence. In addition the vorticity of the low-level vortex increases due to the acceleration of low-level wind. As the convective cloud moves to the downshear side, it forms an anvil. Precipitation particles would evaporate and melt below the anvil, and thus cool the lower level air. This process would enhance the temperature difference between low-level airflows and intensify the updraft velocity at the lea-

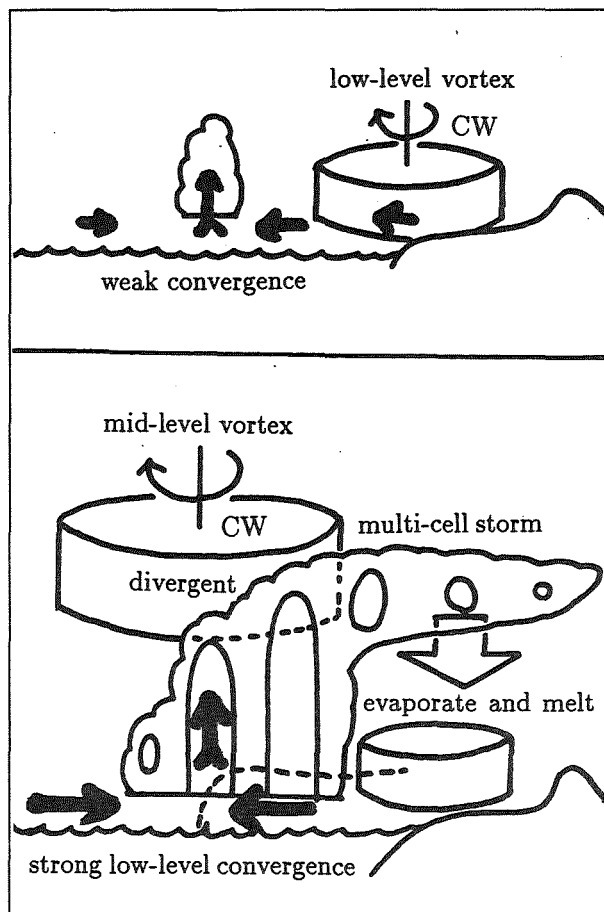


Figure 7: An illustration of the formation process of the storm

ding edge of the colder air.

6. CONCLUDING REMARKS

It is difficult to forecast when and where a meso-scale cloud system will develop. This case clearly shows that the low-level vortex is an important factor to forecast where the multi-cell storm will develop, and the mid-level vortex is important to forecast when and whether it will develop or not. Therefore, we must take into account the dynamics of the middle-level clouds to study the orographic rain in addition to low-level airflows over complex terrains and such microphysical processes as the seeder-feeder process.

INTERNAL STRUCTURE OF CLOUD BANDS OFF THE WEST COAST OF HOKKAIDO ISLAND, JAPAN, ANALYZED WITH SSM/I AND RADAR DATA

Masaki Katsumata, Hiroshi Uyeda and Katsuhiko Kikuchi

*Meteorological Laboratory, Division of Earth and Planetary Sciences,
Graduate School of Science, Hokkaido University, Sapporo 060 JAPAN.*

1. Introduction

During an outbreak of the winter monsoon from the Eurasian Continent, a broad cloud band (hereafter CB) extending from north to south is sometimes formed off the west coast of Hokkaido Island, Japan. A typical CB has a scale of several hundred kilometers in length and several tens of kilometers in width, is maintained for 1-2 days, and brings heavy snowfalls when it lands.

Many studies have been done about CB, using radar or infrared radiometer on satellites (Tsuboki *et al.*, 1989; Kobayashi, 1991; *etc.*). However, there are few studies on the internal structure of the entire area of CB. Among the satellite-borne sensors which can observe wide-spreading clouds, microwave radiometers detect the radiation affected strongly by cloud particles and precipitation particles. Therefore, we attempted to investigate the internal structure of CB by combining data from SSM/I, a satellite-borne microwave radiometer, and radars.

2. Data and Method

The CB event from January 26 to 28, 1991, was analyzed. The brightness temperature (hereafter TB) of SSM/I on DMSP-F10 satellite by Wentz(1991) was used for these analyses. We selected the 85.5GHz vertical and horizontal polarized channel (hereafter 85V and 85H, respectively) for the snow clouds in this study, because of its high spatial resolution and sensitivity on the scattering.

The data was utilized as two values, TB on 85V (hereafter TB(85V)) and the polarization ratio of these channels, $P(85) = TB(85H) / TB(85V)$. The addition of a non-polarized emission by the cloud water to the polarized emission from the sea surface make $P(85)$ higher, closer to one. We can detect the cloud water from this value. On the other hand, the depression of TB(85V) among the high $P(85)$ area is recognized as a snowing area, or an excess area of cloud ice, because of the scattering by these particles is large especially at the frequency (Spencer *et al.*, 1989). The detail was described in Katsumata *et al.*(1996).

The VISSR/GMS infrared channel data was also utilized. The TB (hereafter TB(IR)) was recognized as the cloud top temperature, because most of CB is a cumulus cloud system.

The position or area of the ground-based observational data is shown in Fig.1. Two radar data-sets were utilized.

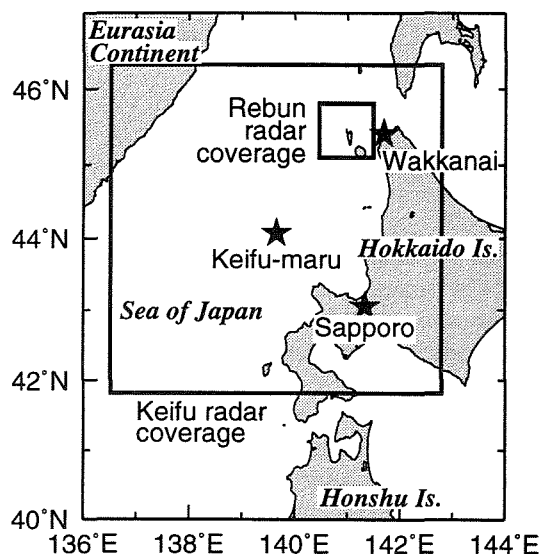


Fig.1: Map for observation area or position for each data.

The HUML (Hokkaido Univ., Meteor. Lab.) X-band Doppler radar was in observation at Rebun Island during the event (Uyeda *et al.*, 1992). Reflectivity and Doppler velocity at every 15 minutes was utilized. The other was on Keifu-maru, research vessel of JMA (Japan Meteorological Agency). Keifu-maru was in operation around 44N, 140E during the first half of the period of the event. The reflectivity data was available from the area of 500km x 500km. Aerological data was also available at every 6 hours. Aerological data at Wakkanai and Sapporo at every 12 hours were also utilized.

3. Results

Figure 2 shows the temporal change of CB. The scale was 400km in length and 50km in width. At 00GMT on Jan.27, the "bulged" part was recognized in the southern part (43N to 44N). After that, the northern part (44N to 46N) moved to the west, and the southern end moved to the south. From 16GMT on Jan.27, the westerly bulged part was suppressed rapidly by CB along 141E from the north.

Two scenes of SSM/I were available during the event. One was at 2320GMT on Jan.26 (Scene A), and the other was at 2250GMT on Jan.27 (Scene B). We will describe the result of the analyses of these two scenes in the following.

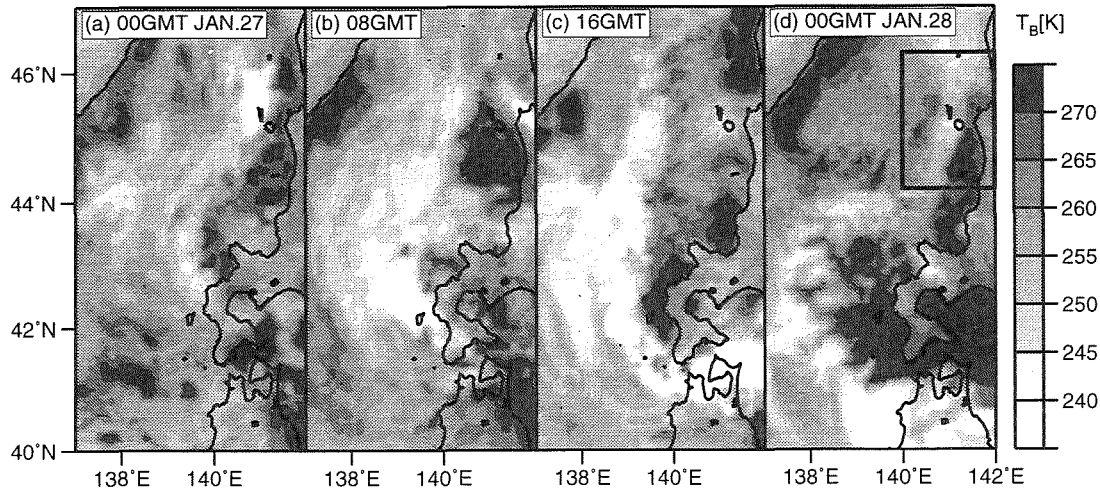


Fig.2: TB(IR) time series at every 8 hours during the event. The box in (d) represents the area of Fig.7.

3.1 Scene A

In the Fig.3(a), two band-shaped low-TB(85V) ($<230\text{K}$) areas existed north and south of 44°N . These were recognized as two different band clouds (hereafter BC): Both were high P(85) (>0.84) and low TB(IR) ($<250\text{K}$) areas, in Fig.3(b) and Fig.2(a), respectively. The northern BC (hereafter BC1, as denoted in figures) included a few streaks of the radar echo, which were observed by both Keifu-maru radar (Fig.4) and HUML radar. The echo cell moved to the southwest, parallel to the orientation of BC1.

The wind profile from Keifu-maru, located just east of BC1, at 00GMT, Jan.27 is shown in Fig.5. The wind is northeasterly below 700hPa, and westerly above. The height corresponds to the height of the cloud top detected by TB(IR) image. This shows that BC1 exists within the northeasterly layer. In addition to this, the wind profile at Wakkanai shows that the north-northeasterly or northerly layer is in the layer below 850hPa. This implies the development of mixing layer along BC1, with southwestward movement of the echoes.

These results suggest that BC1 has a structure similar to streak clouds, which usually appear under the winter

monsoon outbreak. However, BC1 was larger in width than streak clouds. It is known that CB is formed on the convergence line between northwesterly or westerly from the Eurasia Continent and northeasterly from the direction of Hokkaido Island. It is likely that BC1 consists of streak clouds organized to meso- α scale by the convergence field.

On the other hand, the southern BC (hereafter BC2) included a few lower peaks on TB(85V). These peaks lined BC2 with an interval of 30 to 50km. Corresponding to these features, we found the higher peaks on P(85), the stronger peak of Keifu-maru radar reflectivity and the lower peak of TB(IR).

The time series of Keifu-maru radar reflectivity (not shown) shows that the echoes had band-like shapes and were parallel to the orientation of northeast to southwest. This is different from the orientation of BC2, north to south or north-northwest to south-southwest, and similar to the wind direction to the east of CB, as shown in the wind profiles at Wakkanai and Sapporo. This suggests that BC2 is comprised of the meso- β scale band-shape convection with a different orientation from BC.

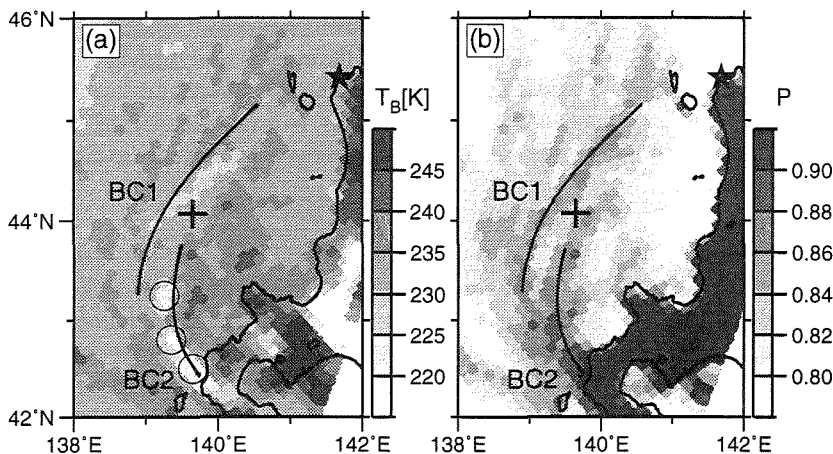


Fig.3: (a)TB(85V) and (b) P(85) image at Scene A. The cross denotes the position of Keifu-maru, and the star denotes the upper air station at Wakkanai.

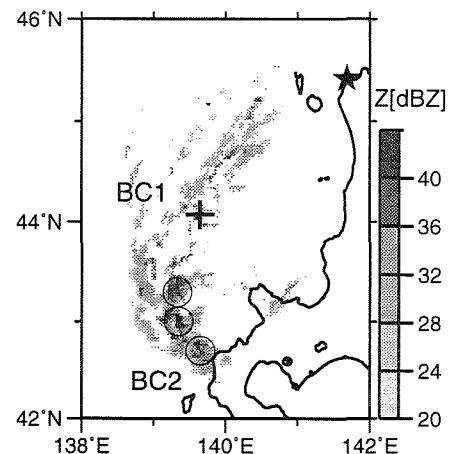


Fig.4: keifu-maru radar reflectivity image at Scene A. Symbols are the same as Fig.3.

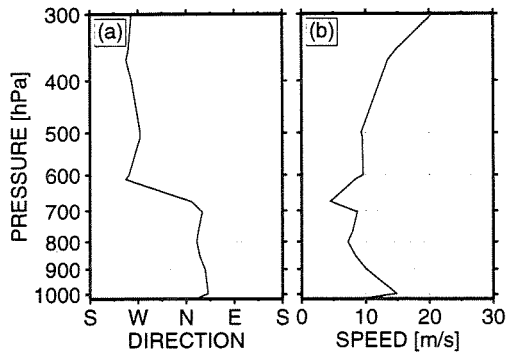


Fig.5: Wind profile observed at Keifu-maru in Scene A; (a) wind direction, and (b) wind speed.

3.2 Scene B

About 24 hours after Scene A, CB was comprised of two different parts, the northern part and southern part, with a border at 44°N. The former oriented north to south along 141°E, and the latter was arc-shaped and bulged to the west (Fig.2(d)). The northern part was in the range of the HUML radar. The reflectivity image at 30 minutes before and after SSM/I observation time showed a few echo streaks (Fig.6). The echo moved south at 60 to 80 km/h keeping the streak-pattern for 5 hours. However, the orientation of the streaks was different between Fig.6(a) and (b): north-northeast to south-southwest in (a), while north to south in (b). The difference was also seen in echo extent: larger in (a) than (b).

The southward-movement of the echoes resulted in the system in Fig.6(a) and (b) located in the south and the north of the radar site in the snapshot. In the images of TB(85V) and P(85) (Fig.7), we find the relative low TB(85V) area which extends 80km south-southwest from the radar site (broken line in Fig.7), and the relative high P(85) area which extends 80km to north (dotted line in Fig.7). The former correspond to the echo in Fig.6(a), while the latter to Fig.6(b).

This change of echo pattern was quasi-cyclic with about 1 hour intervals, until the dissipation of CB. This shows that the meso- β scale systems also exist in the streak-like system in CB.

In contrast, the parts of the significant low TB(85V) and high P(85) were only in the southern arc-shaped part of CB (not shown). The band-shaped features oriented differently from the axis of CB. The interval of each feature was about 50km, which is almost the same as BC2 in Scene A.

4. Discussion

As shown in the previous section, the structure of the convection in CB was different between the southern part and the northern part. The southern part was comprised of the band-shape features in the scale of tens of kilometers, i.e. meso- β scale. Because these features are similar to those of the "precipitation core" in NCFR (narrow cold frontal band) in the front of extratropical cyclones (James and Browning, 1979; Hobbs and Biswas, 1979), we will call them "cores" hereafter.

The "cores" were also oriented northeast-southwest, the

same as the echo streaks in the northern part of CB in both Scene A and B. The orientation of both were the same as the wind direction to the east of CB. It is possible that the wind to the east of CB partially effected the orientation of the meso- β scale convection. Nevertheless, the orientation of the southern part of CB was different from the wind to the east of CB. The northern part was also comprised of the echo streaks with a 60 to 80km scale structure within CB. It seems reasonable to suppose that the meso- α structure of the convergence determined how the meso- β feature organized to CB: streak cloud type or "core" type.

This organization of the meso- β scale features that are like "cores" resembles a cold front with extratropical cyclones. In addition to that, the wind parallel to CB seems to correspond to the low-level jet on a synoptic cold front. The synoptic situation suggests the existence of meso- α low around the southern part of CB: The wind below 700hPa at 00GMT, Jan.27 was northeasterly at Wakkanai, easterly at Sapporo, and northwesterly at Akita (39.72°N, 140.10°E, not shown in figures). The cold advection was also analyzed at 500hPa. It is likely that CB was the cold front of the meso- α scale cyclone.

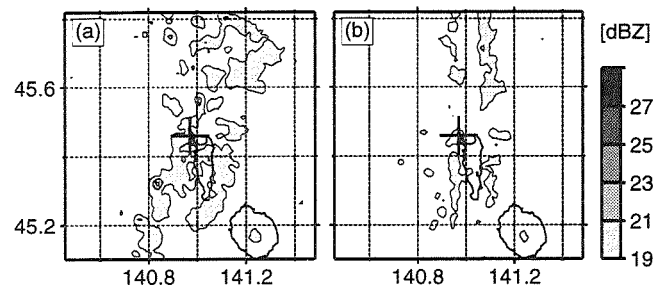


Fig.6: HUML radar reflectivity image at 30 minutes (a) before and (b) after the SSM/I observation in Scene B.

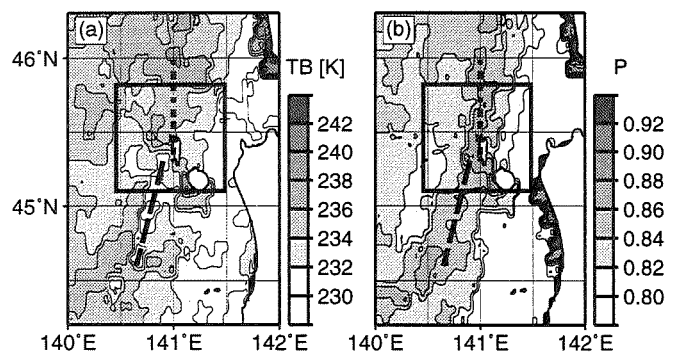


Fig.7: (a) TB(85V) and (b) P(85) image in Scene B. The box in each image represents the area of Fig.6. The lines are explained in the article.

5. Conclusion

The structure of a meso- α scale cloud band formed off Hokkaido Island (the Cloud Band) was investigated with SSM/I and radar data. The analysis revealed the existence of two different band clouds within the Cloud Band system. The northern band cloud which has a structure similar to that of the streak clouds, usually appears under the winter monsoon outbreak. On the other hand, the features like those of the "precipitation core" in NCFR were observed in the southern band cloud. These similar scale features were also observed in the northern part of the Cloud Band. In addition to these, the parallel wind to the Cloud Band in the northern part was similar to the low level jet in a synoptic cold front. These features imply that the Cloud Band could be recognized as the front accompanying to the meso- α low.

< Acknowledgment >

The authors wish to thank the Meteorological Satellite Center of Japan Meteorological Agency for the provision of VISSR/GMS data and the Division of Oceanic Meteorology of Japan Meteorological Agency for the provision of Keifumaru radar data.

This work is partly supported by Grant-in-Aid for Scientific Research of the Ministry of Education, Science and Culture of Japan (Grant Nos. 02201102, 03201104 and 04201102).

< References >

- Hobbs, P. V. and K. R. Biswas, 1979: The cellular structure of narrow cold-frontal rainbands. *Quart. J. Roy. Meteor. Soc.*, **105**, 723-727.
- James, P. K. and K. A. Browning, 1979: Mesoscale structure of line convection at surface cold fronts. *Quart. J. Roy. Meteor. Soc.*, **105**, 371-382.
- Katsumata, M., H. Uyeda, and K. Kikuchi, 1996: Characteristics of a Cloud Band off the west coast of Hokkaido Island analyzed with AVHRR/NOAA and SSM/I data. *J. Meteor. Soc. Japan*, submitted.
- Kobayashi, F., 1991: Observational and analytical studies on the Convergence Band Clouds occurring along the west coast of Hokkaido, Japan. Ph.D. Dissertation, Department of Science, Hokkaido Univ., 131pp.
- Spencer, R., H. Goodman and R. Hood, 1989: Precipitation retrieval over land and ocean with the SSM/I: Identification and characteristics of the scattering signal. *J. Atmos. Oceanic Technol.*, **6**, 254-273.
- Tsuboki, K., Y. Fujiyoshi and G. Wakahama, 1989: Doppler radar observation of Convergence Band Cloud formed on the west coast of Hokkaido Island. II: Cold frontal type. *J. Meteor. Soc. Japan*, **67**, 985-999.
- Uyeda, H., A. Takemoto, N. Osaki and K. Kikuchi, 1992: Structures of convective snow bands at formation stage in northwest coast of Hokkaido, Japan. *Proceedings of 11th ICCP*, 624-627.

A tornadic thunderstorm in Switzerland exhibiting a radar-detectable low-level vortex

Wolfgang Linder and Willi Schmid

Atmospheric Science ETH, CH-8093 Zurich, Switzerland

1. INTRODUCTION

Tornadoes in Europe are rare, but like their North-American counterparts they can cause considerable damage. The purpose of this paper is to present a case study of a tornadic thunderstorm on 22 July 1995. Evidence for a tornado came from an eyewitness at Oberhofen in Northern Switzerland. To this end, we first give an overview of the synoptic and mesoscale situation. Then we examine a mid-level vortex in the southern part of the storm, and a second vortex that is directly associated with the tornado. Finally we try to understand the formation of the tornado from existing conceptual models of tornadogenesis.

2. SYNOPTIC AND MESOSCALE SITUATION

Here, we give a summary on the meteorological environment, whereas a more detailed discussion of the mesoscale thermodynamic field can be found in Linder et al. (1996).

The synoptic situation on 22 July 95, 00 UTC was characterized by a fairly strong 500 hPa south-westerly flow over central Europe between a ridge over eastern Europe and a trough over western France. A NE-SW oriented surface cold front was moving southeastward over Germany and France, ending a period of sunny and very hot weather with temperatures of more than 30°C, and causing severe thunderstorms and a temperature drop of more than 10°C along its way. At 00 UTC Switzerland was still situated in the warm air with light surface winds.

In the following hours the front continuously moved southeastward and reached the Jura mountains in the afternoon, causing severe thunderstorms. The storm considered here developed explosively between 1350 and 1400 UTC in the Jura mountains, ahead of a line of frontal thunderstorms. The storm reached 50 dBZ within ten minutes. This rapid development was partly caused by lifting through the outflow of the frontal thunderstorms. Then the storm merged with part of the frontal storms and moved

east-northeast along the Jura mountains. At 1520 UTC the storm showed a clearly identifiable bow echo. This is also the most probable time for the occurrence of the tornado. A detailed analysis of the life cycle of the storm can be found in Schiesser et al. (1996).

The pre-storm conditions were inferred from a research radiosounding at Merenschwand, released at 14 UTC about 30 km south of the location where the tornado occurred. The sounding data were combined with VVP (velocity volume processing) measurements of the ETH radar. The VVP method calculates wind profiles from clear air and precipitation echoes ahead of approaching storms (see Siggia 1991).

The environment was characterized by high instability (Showalter-Index: -7.4), a CAPE of 1480 J kg⁻¹ (a fairly high value for Swiss storms) and a Bulk Richardson number (BRN) of 45, which, according to Weisman and Klemp (1984), allows formation of both multicell and supercell storms. For definition of CAPE and BRN see Weisman and Klemp (1984). Storm-relative helicity (Droegemeier et al., 1993) for the storm motion just prior to tornado formation was 179 m² s⁻², which lies in the range of supercell formation in Switzerland (Schmid et al. 1994).

3. VORTEX A: A MIDDLELEVEL VORTEX

In the following the term "vortex" (seen with volume-scan radar data) refers to what Schmid et al. (1996) called a meso(anti)cyclonic vortex signature (MVS). A MVS is defined as "a pair of a local maximum and minimum in Doppler velocity, both located at the same distance from the radar." A vortex should be distinguished from shear lines, which are "characterized by large azimuthal gradients in Doppler velocity, without showing, however, the couplet of extremes in Doppler velocity." A MVS fulfils the following conditions: the difference in velocity exceeds 32 m s⁻¹, or the azimuthal shear exceeds 0.005 s⁻¹ which corresponds with a velocity difference of 25 m s⁻¹ over a distance of 5 km.

The location of the updrafts was deduced using high level divergence signatures and high level reflectivity, especially the height of the 45 dBZ contour (see Brown et al. 1994).

Vortex A was located in the southern part of the storm. The vortex was cyclonic and was collocated with an updraft which already existed at 1441 UTC (at the beginning of the volume-scan radar measurements, approximately one hour after the storm developed). The updraft formed on the right side of a previous updraft and became dominant at 1453 UTC, before it died at 1708 UTC. The vertical extent of vortex A versus time is shown in Figure 1.

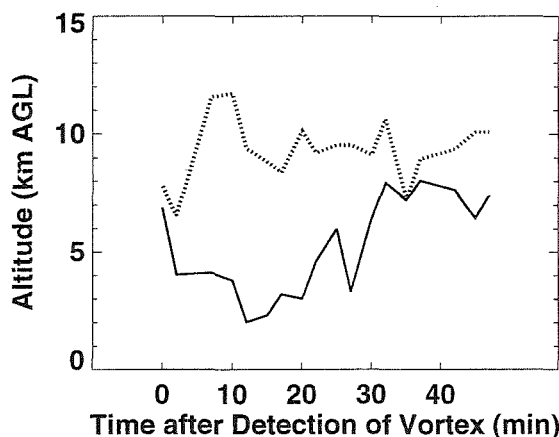


Figure 1: Time-height diagram of vortex A, 22 July 1995. Detection time of the vortex is 1441 UTC. The continuous line shows the lower boundary, the dotted line the upper boundary.

The vortex existed for about 45 minutes. For a period of 15 min (between 7 and 22 min) the vertical extent was between 5 and 7 km and was centered at midlevels (around 6 km altitude). At 25 min the lower part of the vortex disappeared, and the vortex only existed above 6 km. At 27 min the lower boundary descended down to 3 km again, but after 30 min the vortex only existed in upper midlevels, with a vertical extent of less than 3 km.

4. VORTEX B: A LOW LEVEL VORTEX

The time-height evolution of vortex B is shown in Figure 2. Vortex B was cyclonic and first detected at 1443 UTC between 2 and 3 km altitude. The vortex formed at the northern end of a convergence line which was identified on Doppler radar and reached from the ground up to 5 km (not shown). This convergence line was interpreted as a gust front. First the vortex increased in vertical extent at around 1450 UTC, then continued to exist more or less between 2 and 4 km until 1503 UTC. After 1506 UTC the vortex could be observed in the lowest radar level, which was about 400 m above ground. At this time

it is probably justified to extrapolate the lower boundary of the vortex to ground levels. At 1513 UTC the difference in Doppler velocity at 400 m altitude reached 38 m s^{-1} over a horizontal distance of about 1 km, corresponding to an azimuthal shear of 0.038 s^{-1} . It is quite possible that the shear was even larger but limited by the resolution of the radar.

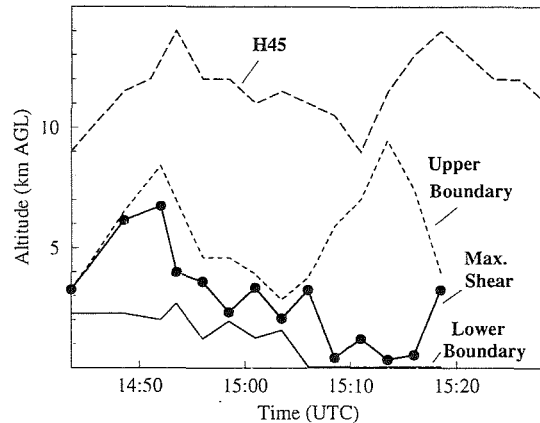


Figure 2: Time-height diagram of vortex B, 22 July 1995. The H45 curve marks the highest level of the 45 dBZ contour.

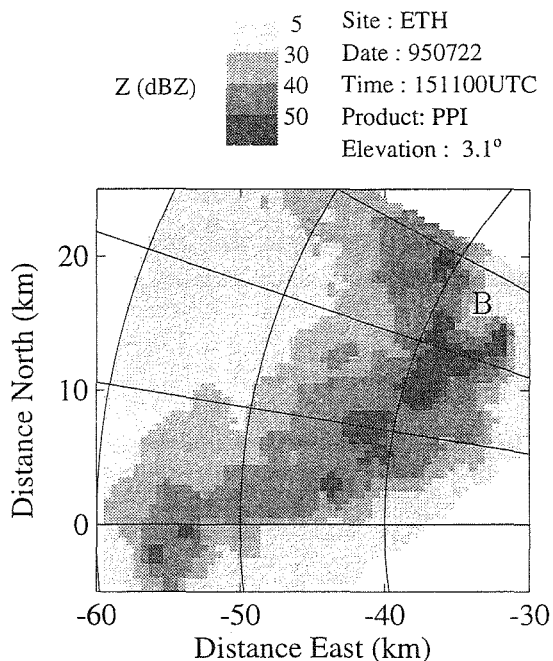


Figure 3: Contours of radar reflectivity at 1511 UTC, 22 July 1995. B marks the approximate position of vortex B.

Simultaneously with the downward motion the vortex also expanded upwards, increasing from 4 to 9 km between 1506 UTC and 1513 UTC. Looking at the 45 dBZ curve, it can be seen that the upward development of the vortex is accompanied by a marked increase in the 45 dBZ height. By this time the vortex is collocated with a developing updraft. This can be clearly seen in a three-dimensional visualisa-

tion of the storm (Schmid and Bresch 1996).

The same conclusion can be drawn from Figure 3 which shows the position of vortex B in relation to the reflectivity field at about 2.5 km for 1511 UTC, at the time of the strong upward development of the vortex. The figure shows in that region a hook-like echo pattern. The vortex is located in a region of weak reflectivity, surrounded by strong echoes on three sides. This configuration resembles the one described by Browning (1977), which exhibits a vigorous updraft in the weak echo region and is characteristic for supercell storms.

The hook-like echo configuration indicates the preferred location for the occurrence of tornadoes. Indeed, a tornado was observed at Oberhofen, -28.5 km east, 16 km north of the radar. The position of the tornado coincided with the weak echo region at 1516 UTC and, as shown in Figure 4, with the track of the vortex in the lowest levels as well as at 3 km.

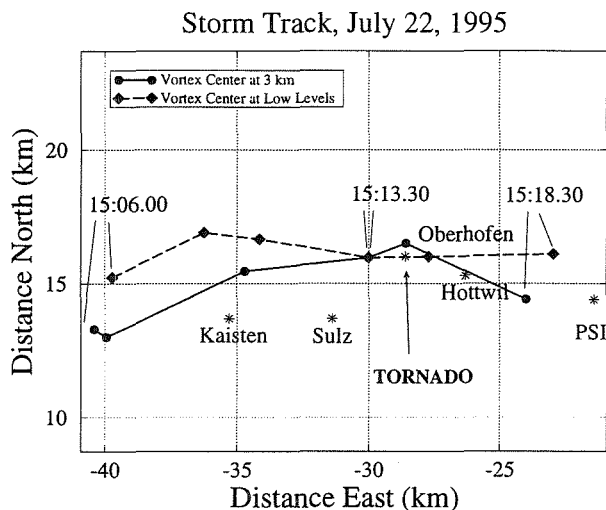


Figure 4: Track of vortex B at low levels and at 3 km AGL on 22 July 1995. The communities appearing on the map reported wind damage. At Oberhofen a tornado was observed. The location of the tornado corresponds to -28.5 km east, 16 km north in radar coordinates.

Figure 4 also shows that the vortex was first tilted to the southwest with height between 0 and 3 km. At 1513 UTC, just before the tornado was observed, the vortex became vertical, and later it was tilted to the southwest again. The communities marked in Figure 4 all reported wind damages. With the exception of Oberhofen, where the tornado was reported, they are situated south of the low-level vortex track. This is plausible since the highest wind speeds are expected at the southern side of a cyclonic vortex. The damages caused by the storm are discussed in detail by Furger et al. (1995).

5. DISCUSSION

The storm of 22 July 1995 caused severe damages in Northern Switzerland, mainly by strong winds. Schmid et al. (1996) noted that "the most severe hailstorms in Northern Switzerland have supercellular characteristics". Therefore, we try to investigate whether the storm could be classified as a supercell using their definition of a supercell storm: "Supercells are identified when a MVS (here called a vortex)

1. has a vertical extent of at least 4 km for at least 20 min.
2. is associated with a signature of large divergence near cloud top."

The midlevel vortex discussed in Chapter 3 was associated with a divergence signature near cloud top (not shown). However, it had a vertical extent of 4 km for only 15 min (from 7 to 22 min after formation) instead of the required 20 min. Therefore the storm did not quite meet the criteria for a Swiss supercell. Also, the storm did not exhibit one long-lasting updraft, but instead several updrafts, following each other within tens of minutes. The first one existed before the volume-scan radar measurements were started, the other two are related to the peaks in the H45 curve in Figure 2. Therefore the storm might rather be classified as multicellular. However, evidence exists that some of the updrafts were temporarily rotating.

In Chapter 4 we saw that the tornado was located below a vortex which developed at around 3 km altitude on the northern edge of a gust front and then descended to the ground. The tornado formed at a time when the vortex rapidly expanded upward as a new updraft developed. This situation is somewhat similar to the non-supercell tornado type described by Wakimoto and Wilson (1989), where tornadoes form below developing updrafts over pre-existing small scale vortices at low level shear lines. In their study vortex stretching seems to be the main reason for tornado formation. However, in their study the tornadoes occur with developing storms, often in the absence of strong radar echoes, whereas on 22 July 1995 the storm had existed for more than an hour and showed a well-defined hook echo. Nevertheless, it can be assumed that vortex stretching in a developing updraft played a role in forming the tornado. The hook echo does have some resemblance to the shearing instabilities at a severe prefrontal rainband described by Carbone (1982).

CONCLUSIONS

The storm of 22 July 1995 was the first radar-

observed storm in Switzerland which exhibited a low level vortex. The storm was multicellular, showing a succession of updrafts, some of which were rotating. A tornado formed below the low level vortex in a weak echo region of the storm, at the time when a new updraft developed explosively.

This storm was captured by a series of specific measuring systems:

1. A micronet of ground stations (mesh size about 5 km) was operated by the PSI (Paul Scherrer Institute) in the area where the wind damages occurred (see Furger et al. 1995).
2. Volume scan measurements were made with the ETH-radar and are discussed in this contribution.
3. Specific radiosoundings were made by the ETH in close vicinity of the storm.
4. The data from the operational systems of the Swiss Met. Institute are also available (ground mesonet, routine soundings at Payerne, operational weather radars and numerical model output).

This unique combination of different data sources allows us to study various aspects and scales of the storm event. Further investigations are planned for the near future.

ACKNOWLEDGEMENTS

The authors would like to thank M. Furger, D. Bresch, R. A. Houze, Jr., B. Smull and H.H. Schiesser for their important contributions to this study.

REFERENCES

- Brown, R. A., and R. J. Meitin, 1994: Evolution and morphology of two splitting thunderstorms with dominant left-moving members. *Mon. Wea. Rev.*, **122**, 2052-2067.
- Browning, K. A., 1977: The structure and mechanisms of hailstorms. *Meteor. Monographs*, Vol. **16**, 16-43.
- Carbone, R. E., 1982: A severe frontal rainband. Part I: Stormwide hydrodynamic structure. *J. Atmos. Sci.*, **39**, 258-279.
- Droegemeier, K. K., S. M. Lazarus, and R. Davies-Jones, 1993: The Influence of Helicity on Numerically Simulated Convective Storms. *Mon. Wea. Rev.*, **121**, 2005-2029.
- Furger, M., and W. Schmid, 1995: Meso-gamma-scale observations of a severe local storm in the vicinity of PSI. PSI (Paul Scherrer Institute). Annual Report 1995, Annex V General Energy Technology, 4pp.
- Schmid, W., and H. Huntrieser, 1994: The wind environment of supercell storms in Switzerland. *Annalen der Meteorologie*, **30**, DWD Offenbach, 13-16.
- Schmid, W., S. Hümbeli, B. Messmer, and W. Linder, 1996: On the Formation of Supercell Storms. 18th Conf. on Severe Local Storms, San Francisco, USA, 451-454.
- Schmid, W., and D. Bresch, 1996: 3d-Animations of a tornado-producing multicellular hailcloud. Preprints, 12th Int. Conf. on Clouds and Precipitation, Zurich, ICCP and WMO, this volume.
- Siggia, A., 1991: One pass unfolding for VVP analysis. Preprints, 25th Conf. on Radar Meteor., Paris, France, Amer. Meteor. Soc., 882-888.
- Wakimoto, R. M., and J. W. Wilson, 1989: Non-supercell Tornadoes. *Mon. Wea. Rev.*, **117**, 1113-1140.
- Weisman, M. L., and J. B. Klemp, 1984: The structure and classification of numerically simulated convective storms in directionally varying wind shears. *Mon. Wea. Rev.*, **112**, 2479-2498.

REGULATION OF CONVECTIVE ACTIVITY BY MID-TROPOSPHERIC RELATIVE HUMIDITY: INTERACTIONS BETWEEN TURBULENCE, MICROPHYSICS, AND LARGER-SCALE CONVECTIVE DYNAMICS

Nenad M Aleksic, Robert A Iacovazzi Jr., Chris J Walcek and Bosko T Telenta

State University of New York, Albany, New York, 12205, U. S.

1. INTRODUCTION

In this study, we try to understand how convection is regulated in tropical areas. Numerous measurements of tropical convection show that the mean thermal structure of the tropical atmosphere remains approximately constant, while periods of relatively intense convective activity alternate with more quiescent periods of little convection.

A high-resolution model of convective dynamics and microphysics is used to explicitly simulate convective clouds, and several sensitivity studies are performed demonstrating that the depth and intensity of convection are strongly regulated by the relative humidity of the atmospheric layer into which convective plumes penetrate. We show that Convective Available Potential Energy (CAPE) is a poor indicator of actual or potential convective activity, while upper tropospheric relative humidity is strongly correlated with convective activity.

2. MODEL DESCRIPTION

A fully compressible, non-hydrostatic, time dependent cloud model is used to study convective processes in unstable areas. Dynamic equations and associated numerical methods are based on Klemp and Wilhelmson (1978), while thermodynamics and microphysical processes follow Orville and Kopp (1977) and Lin et al. (1983). The current version of the model has ten prognostic variables: horizontal and vertical momentum, turbulent kinetic energy, nonhydrostatic pressure perturbation, potential temperature, four categories of water substance, and a passive tracer used for various diagnostic studies.

Simulations presented in this paper are obtained using a two-dimensional slab domain 16 km deep and 120 km long. A 200 m grid size is used in both the horizontal and vertical, and time steps of 2 s and 0.4 s are used to integrate large and small-scale processes.

For all simulations, a horizontally-uniform initial atmospheric state is taken from observations during a convective period in the tropical Atlantic atmosphere on 18 Sept. 1974 (Julian day 261 of GATE Phase III field measurement program).

Convection is initiated with a single ellipsoidal thermal bubble 13 km wide and 2 km deep, initially

centered 800 m above sea level. The maximum temperature perturbation is 1.1°C at the bubble center, and decreases toward zero at the bubble edges.

3. SIMULATIONS - BASE CASE

The left two panels of Fig. 1 show the development of an individual convective element for the conditions measured during GATE day 261. The convective bubble rises and grows, developing a tilt in the direction of the increasing wind speed with altitude. The original convective turret decays into an anvil-like feature in the upper troposphere during the period 1 - 2 hours after initiation, and secondary convective elements are initiated during this period.

The reference run qualitatively reproduces many features of the observed convection. According to Warner *et al.* (1980) observed clouds tended to be strongly slanted, with vertically rising protuberances at approximately regular intervals. Cloud bases were eroding upward with time from about 0.5 km to as high as 8 km; while the cloud tops occurred at about 13 km for cumulonimbi and between 5 and 8 km for cumulus congestus. The generation of the secondary medium-sized cumuli were found to be on the upshear side of existing clouds. Other clouds observed in the domain were cirrus, altostratus, altocumulus, and stratocumulus, which our simulation suggests could be the product of aged convective elements.

4. SENSITIVITY STUDIES- Rh

During the 3-week GATE phase III intensive observation period, the mean thermal structure of the tropical atmosphere remained approximately constant, while several periods of relatively intense convection propagated through the observation area. CAPE fluctuated by $\pm 20\%$ about the mean of 1300 Joules kg^{-1} , while convective precipitation fluctuated $\pm 80\%$ about the mean precipitation rate of slightly under 10 mm day^{-1} . There was a negligible or slightly negative correlation between convective precipitation rates and CAPE.

One of the motivations of this study is to identify the environmental factors regulating convective activity. We hypothesize that the mean Relative Humidity (Rh) of the middle and upper troposphere is an important factor regulating the intensity of convection. During GATE, Rh below 850 mb remains approximately constant, while the

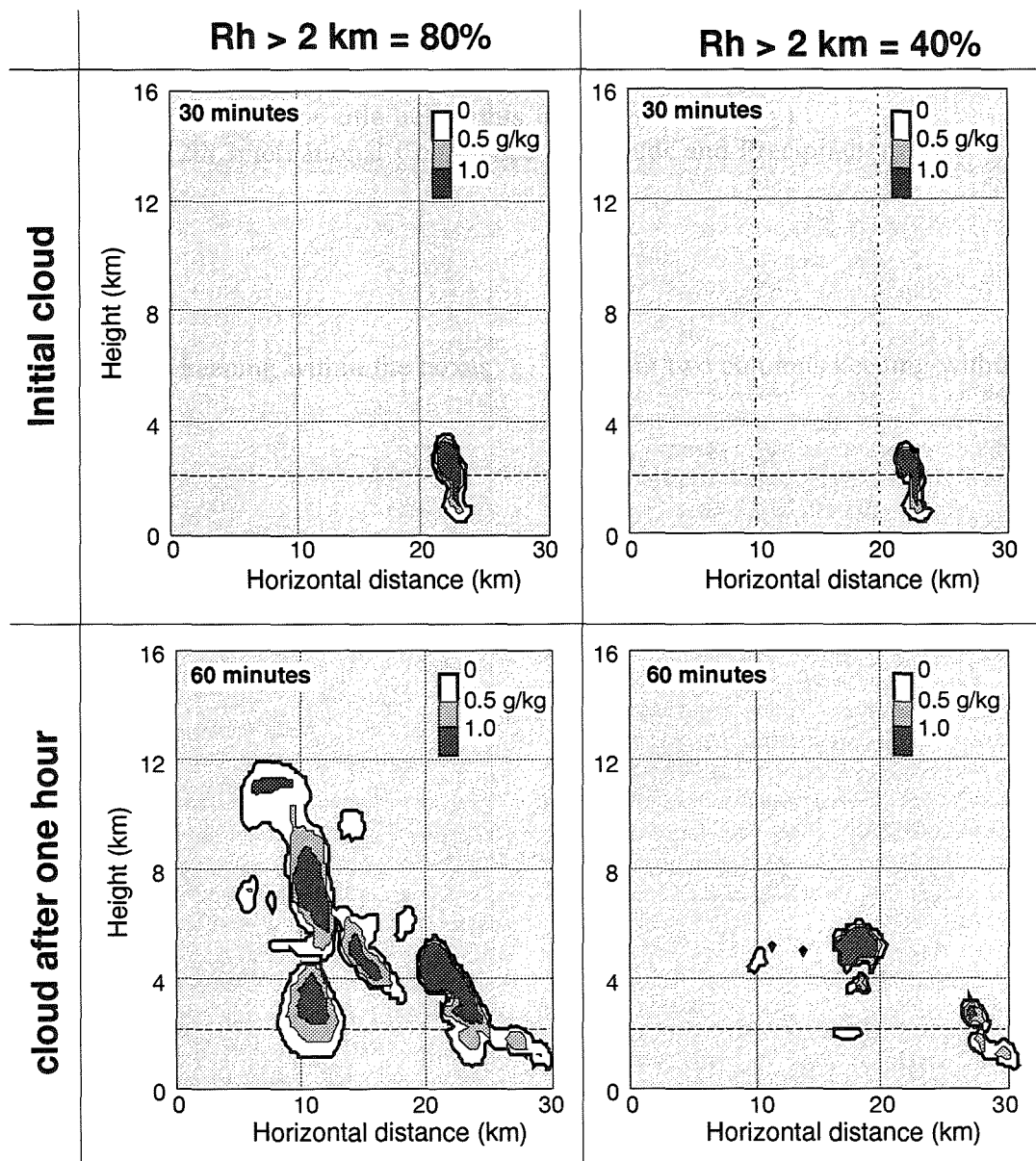


Figure 1. Contours of condensed water mixing ratio 30 and 60 min. after initiation within a convective bubble for the cloud growing into a moist atmosphere (left panels), and an atmosphere where the relative humidity in the upper troposphere has been reduced to half its observed value.

Rh in the layer 850-300 mb shows wide fluctuations that correlate with convective precipitation rates. In this study, we try to quantify the mechanism by which upper tropospheric relative humidity regulates convection.

A series of sensitivity studies are performed where all factors are the same, except the initial water vapor mixing ratios above 2 km are reduced by factors of 0.9 - 0.5 in increments of 0.1. This range of upper tropospheric Rh is approximately the same range observed during GATE. In the driest atmosphere, Rh above 2 km was 40-50%, while the base case sounding has a mean Rh of 84% in the same layer.

The right panels of Fig. 1 show the same cumulus tower depicted in the base case, except the cloud is growing into a drier atmosphere. The convective cloud's dynamic development is significantly suppressed, and

never develops appreciable depths or convective intensities.

One measure of convective intensity is the mean kinetic energy induced by the convective clouds. During these simulations, the cloud-induced kinetic energy grows exponentially during the first 50-60 min. as the initial bubble accelerates up through the conditionally unstable atmosphere, then decays for the next 30 minutes as the initial cloud dissipates. Secondary convective elements then form and grow, typically with less intensity than the initial rising bubble. Cloud volumes follow similar temporal trends. Fig. 2 shows the maximum mean cloud-induced kinetic energy and maximum cloud volume in the model domain achieved during the initial bubble lifetime as a function of the middle troposphere Rh.

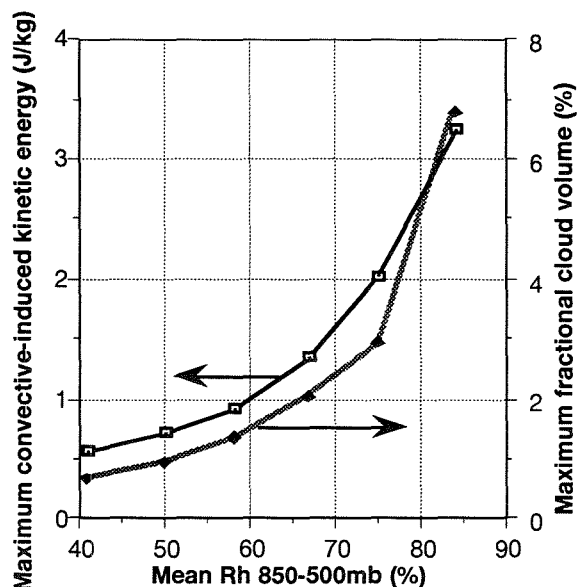


Figure 2. Maximum convective kinetic energy and cloud volume (both averaged over entire 120 x 16 km domain) of the convective bubble during its lifetime vs. the environmental relative humidity in the mid-troposphere.

It is readily apparent from Fig. 2 that convective activity is strongly influenced by relative humidity in the middle and upper troposphere. A 10% reduction of Rh (which approximately equals the measurement uncertainty for Rh) in the moistest atmospheres produces a 40% reduction in the mean cloud kinetic energy, and a nearly 60% reduction in cloud volume.

Fig. 3 shows results of a tracer experiment where air in the initial convective bubble is "tagged" with a passive tracer of concentration 10g/kg. Fig. 3 shows the change in the horizontally-averaged cloud-tracer concentration before and after the initial bubble grows and decays in the atmosphere. This numerical tracer thus tracks the integrated dynamics of the cloud lifetime, and shows where air is redistributed by an individual convective element. In both environments, air initially in the lower troposphere is removed from that layer and redistributed throughout the depth of the cloudy layer, but the cloud growing into the relatively dry atmosphere only penetrates to an altitude of 5-6 km, while in the moist atmosphere, the cloud grows to 12 km.

Fig. 4 shows the change in the mean altitude of the cloudy air before and after its growth and decay in the unstable column. In the moist atmosphere, air in the initial convective bubble is lifted on average to a height 5 km above its initial altitude, while in the dry atmosphere, this displacement is only about 2 km.

5. ENTRAINMENT AND DYNAMICS

The suppression of convective development by dry environmental conditions described above can be explained by the generation of negatively-buoyant air as moist plumes of warm cloud updraft air turbulently mix

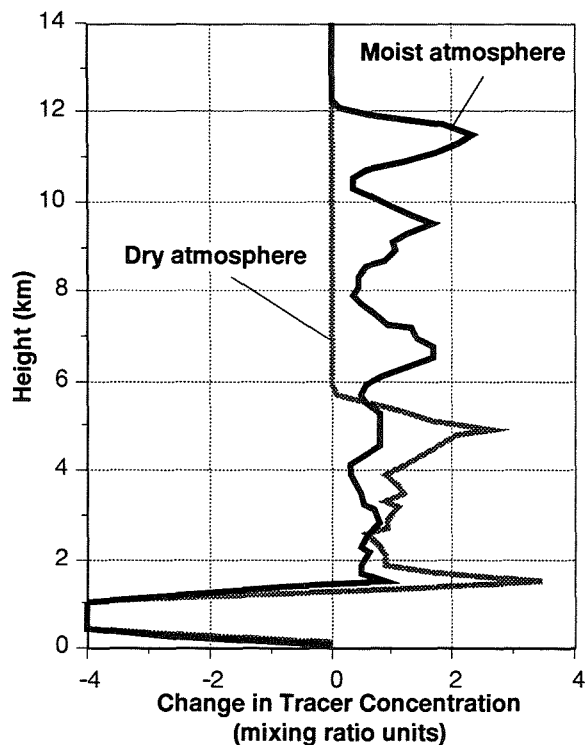


Figure 3. Change in the concentration of an inert tracer of air contained in the initial convective bubble before and after its convective life-cycle. convective cloud grows into a moist (solid curve) or dry (gray curve) atmosphere.

with the surrounding drier environment. In a low-Rh environment, significant evaporation of cloudwater occurs, suppressing precipitation formation while generating evaporatively-cooled, negatively-buoyant air which cannot rise in the atmosphere. In contrast, the same turbulent mixing of convective updraft air in a high-Rh environment produces little evaporation, and most mixtures remain positively buoyant. Therefore convective towers grow more rapidly and penetrate more easily into and through moist atmospheric layers.

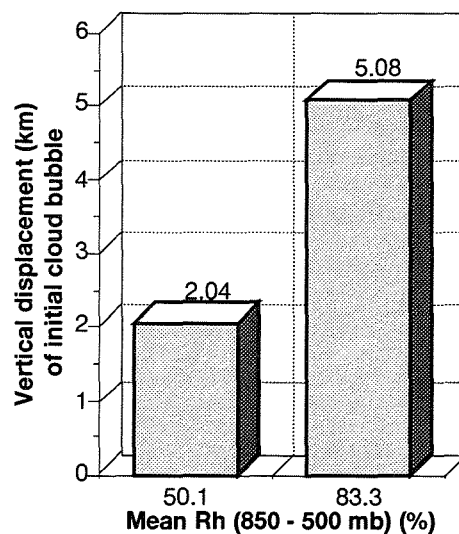


Figure 4. Change of the altitude of the mean height of the initial convective bubble before and after its lifetime in the conditionally unstable GATE day 261 atmosphere for two different environmental relative humidities.

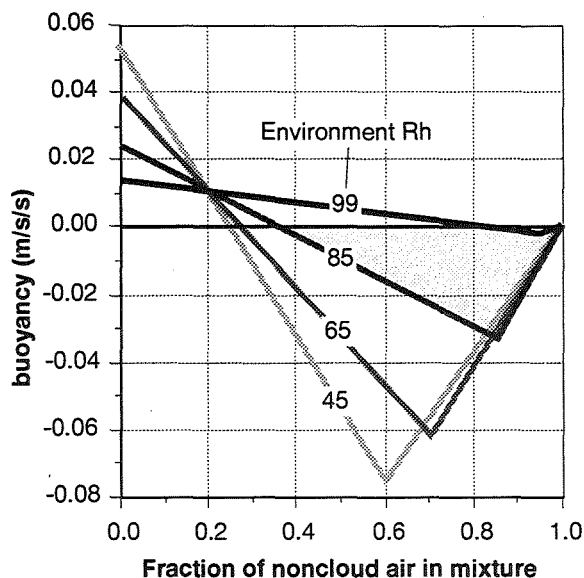


Figure 5. Buoyancy of mixtures of surface air lifted adiabatically to 800 mb and mixed with environmental air at 800mb at several specified environmental Rh. GATE day 261 environmental conditions. Gray area denotes mixtures of negatively buoyant air.

Fig. 5 shows the buoyancy of mixtures of surface air lifted adiabatically to 800 mb and mixed with environmental air at 800 mb as a function of the non-cloud mixing fraction in the mixture. Buoyancy calculations are done at several specified environmental relative humidities for the conditions of our cloud model simulations. A range of buoyancies are produced as cloudy air mixes with its environment, and many of these mixtures are more dense (colder) than either the cloud or the environment due to evaporation of cloudwater.

Fig. 6 shows the fraction of mixtures that are negatively buoyant for surface air lifted adiabatically to 800 mb and mixed with a uniform distribution of mixing fractions of environmental air at that level. There is a very dramatic increase in the amount of negatively buoyant air that can potentially form as a cloud mixes with its environment as the environmental air becomes drier. This negative buoyant air will rapidly detrain from any cloud updrafts, significantly reducing upward convective mass fluxes and cloud development.

6. SUMMARY & DISCUSSIONS

Using a fully compressible 2-dimensional cloud resolving model applied to simulate tropical oceanic convection, we demonstrate that the overall intensity and vertical development of convection can be controlled by the relative humidity of the middle and upper troposphere. When the environment is close to saturation throughout the troposphere, convective thermals originating in the boundary layer efficiently grow and penetrate to the tropopause, generating appreciable amounts of precipitation and kinetic energy. In contrast, when Rh in the middle and upper troposphere is below about 50%, the vertical growth and intensity of

convective thermals are reduced by a factor of 2-10. Thus environments with approximately identical CAPE produce strikingly different convective intensities: in the drier environment, only relatively shallow convective clouds form, while in higher Rh environments, deeper convective clouds develop.

These results suggest that convective parameterizations that do not allow environmental Rh to explicitly regulate convective intensities may incorrectly specify the interactions between convection and larger-scale dynamics under some relative humidity environments.

Acknowledgments. The authors are grateful to the U. S. Air Force Office of Scientific Research, the U. S. Department of Energy and the U. S. National Science Foundation for supporting this research.

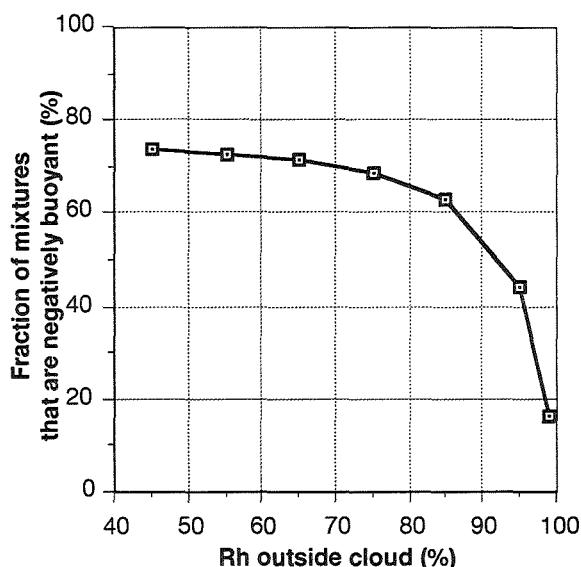


Figure 6. Fraction of mixtures that are negatively buoyant for surface air lifted adiabatically to 800 mb and mixed with uniform distribution of mixing fractions of environmental air at that level. GATE day 261 environmental conditions.

REFERENCES

- Klemp, J. B. and R. B. Wilhelmson, 1978: The simulation of three-dimensional convective storm dynamics. *J. Atmos. Sci.*, **35**, 1070-1096.
- Lin, Y.-L., R. D. Farley and H. D. Orville, 1983: Bulk parameterization of the snow field in a cloud model. *J. Climate Appl. Meteor.*, **22**, 1065-1092.
- Orville, H. D. and F. J. Kopp, 1977: Numerical simulation of the history of a hailstorm. *J. Atmos. Sci.*, **34**, 1596-1618.
- Warner, C., J. Simpson, G. Van Helvoirt, D.W. Martin, D. Suchman and G. L. Austin, 1980: Deep Convection on Day 261 of GATE. *Mon. Wea. Rev.*, **108**, 169-194.

MESO- γ SCALE CHARACTERISTICS OF VORTICES IN SNOW CLOUDS ANALYZED USING DOPPLER RADAR DATA

Hiroshi Uyeda, Keisuke Ueno, Yoshio Asuma and Katsuhiro Kikuchi

Graduate School of Science, Hokkaido University, Sapporo 060 JAPAN

1. INTRODUCTION

During the winter monsoon season, broad cloud bands (hereafter called Cloud Band, after Nagata, 1993) occasionally form off the west coast of Hokkaido, in northern Japan. A typical Cloud Band, with its horizontal scale of a few hundred kilometers in length (north-south direction) and several tens of kilometers in width, brings heavy snowfall. Most of the Cloud Bands seem to have vortex signatures at their southern tip, as identified from satellite images (Kobayashi et al., 1987). Meso- γ scale characteristics of the vortices must be studied in order to understand of the development and enhancement of the Cloud Band over Ishikari Bay, Hokkaido in relation to the development of snow clouds near the coast line of Ishikari Bay. The development of snow clouds near the coastline is closely related to snowfall in Sapporo, one of the largest cities on the west coast of Japan.

The experiment called "Studies on the Prediction of Heavy Snowfall Disasters in the Urban Areas and its Reduction and Protection" (Kikuchi, 1993) around Ishikari Bay revealed information about the fine structures of the vortices using Doppler radar observation data.

2. METHOD

During the experiment, observations with four Doppler radars (all were X-band, and one at the SHINKO site

had a dual-polarization function) were carried out from 17 January to 8 February, 1992, around Ishikari Bay, on the west coast of Hokkaido (Fig.1). At the SHINKO site, single Doppler radar observations were conducted from 14 December 1991 to 8 February 1992. The low-elevation-angle PPI (plan position indicator) scans were performed continuously every 10 minutes.

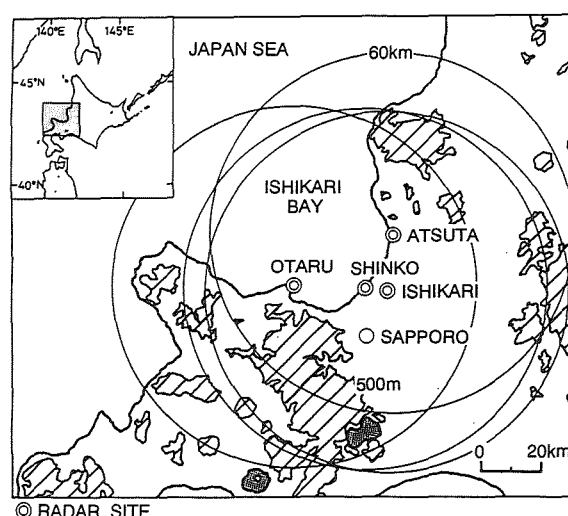


Fig. 1 Observation ranges of four Doppler radars.

A cyclonic vortex signature with a diameter more than 10 km over Ishikari Bay was identified with single Doppler radar data from a pair of the maximum Doppler velocities in opposite directions assuming the Rankine vortex. The method used to identify the vortex was similar to that used with tornados (Doviak and Zrnica, 1984). Dual Doppler radar data was utilized

for the three-dimensional analyses of the vortex structure.

Available data from a conventional weather radar on board the research vessel Keifu-Marui, JMA (Japan Meteorological Agency), as well as data from radio sonde, GMS/IR, NOAA/AVHRR, and surface weather stations were utilized for the analyses.

3. RESULTS

During the observation period, eleven cyclonic vortices (more than 10 km in diameter) were identified from the velocity fields of a single Doppler radar, as shown in Table 1. The location, size and moving direction of the vortices are shown in Fig. 2. The numbers in the figure correspond to those in Table 1. Most of the vortices were formed over Ishikari Bay at the southern end of the Cloud Bands. Estimated vorticity was on the order of $1 \times 10^{-3} \text{ s}^{-1}$ and the motion was southeastward (the same as the winter monsoon surge) with a speed of 6-18 m/s. The lifetime of the vortex was from 30 minutes to two hours. A snow cloud (radar echo) developed significantly at the southeastern front of the vortex and dissipated after arriving over land. The largest reflectivity was

Table 1 Characteristics of vortices observed by a single Doppler radar (at SHINKO) from 12 December 1991 to 8 February 1992. Cold flow from land identified by the single Doppler radar is shown by the symbols (○: significant, △: partly identified, -: not identified).

NO	PERIOD	DIAMETER (km)	VORTICITY ($\times 10^{-3} \text{ s}^{-1}$)	MOTION (deg), (m/s)	MAX. SPEED (m/s)	TYPE	LAND BREEZE
1	2235-0025 JST 26 DEC. 1991	11	10 (10)	305, 7.7 (350), (3.9)	11 (8)	CB	○
2	1243-1333 JST 13 JAN. 1992	14	9	310, 6.3	13	CB	-
3	2302-2333 JST 13 JAN. 1992	11	8	305, 4.8	6	CB	○
4	2302-2333 JST 13 JAN. 1992	13	7	300, 5.7	7	CB	-
5	0141-0212 JST 14 JAN. 1992	21	6	330, 6.7	11	CB	-
6	0201-0251 JST 14 JAN. 1992	12-18	12-10	335, 4.2	13	CB	△
7	1102-1202 JST 23 JAN. 1992	27	6	285, 10.3	14	CB	-
8	1830-1910 JST 23 JAN. 1992	23	3	300, 9.0	16	CB	-
9	0231-0429 JST 24 JAN. 1992	21 (13)	7 (11)	320, 13.2 (300), (14.0)	18 (16)	CB	-
10	0220-0340 JST 31 JAN. 1992	30	5	330, 4.7	11	CB	○
11	0301-0340 JST 4 FEB. 1992	13	12	325, 9.2	13	CB	-

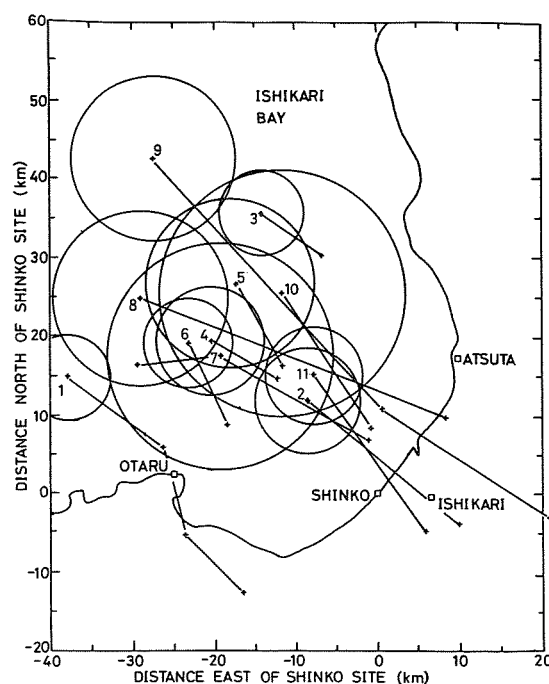


Fig. 2 Moving directions of detected vortices. Circles indicate the diameter of the vortices (distance between positive and negative peaks of Doppler velocities) at the first identification. Numbers at the center of the circles shown with (+) mark correspond to those in Table 1.

observed at the head and the right side of the vorticity movement.

An example of dual Doppler analyses of the most significant vortex at around 0330JST (JST = 9 hours + UTC) of 24 January 1992 is shown in Figs. 3 and 4. As shown in Fig. 3, large convergences are along the line echoes, and the largest reflectivity is at the merging of two line echoes extending west-east and northwest-southeast. The vortex center is ahead of the merging of the two echoes. Vertical cross sections (Fig. 4), along the lines in Fig. 3 show that large updraft and the rapid development of the cloud are at the fringe of the vortex center and in particular at the location of the echo merging (Fig. 4 (C)). Time variation of the vertical profile of a mean vortex in an area of 14 km x 14 km (Fig. 5) indicates that the vortex increased from the low altitude before arriving over land.

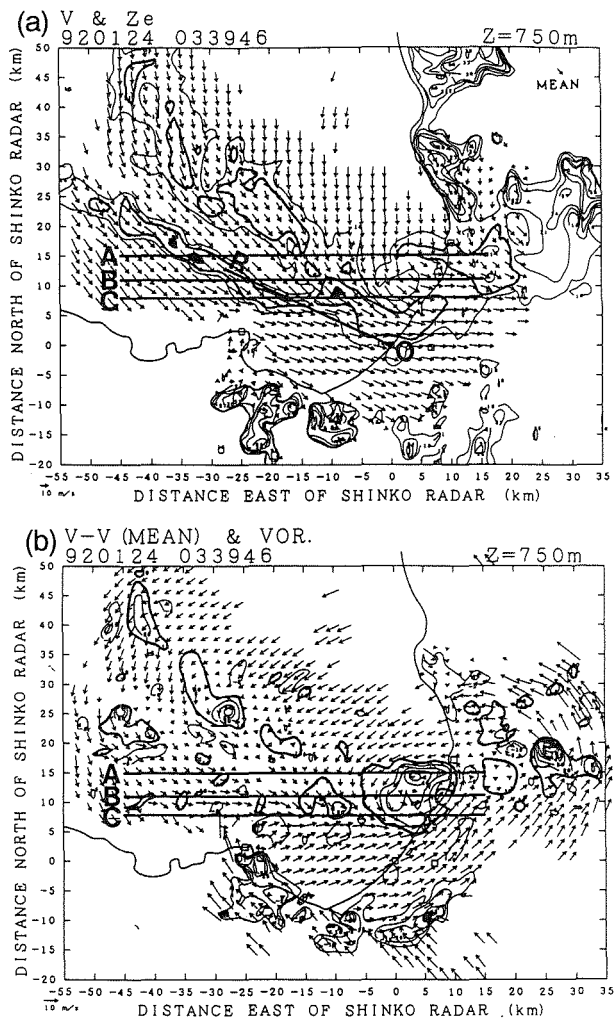


Fig. 3 Reflectivity, wind and vorticity field at 0339JST (JST = 9 hours + UTC) 24 January 1992 at the altitude of 750 m. a) Reflectivity and ground relative wind fields. Reflectivity contours are 18 dBZe (thin line), 21 dBZe (thick line) and > 24 dBZe (dark shaded). Large reflectivities on the land are ground clutters. b) Vorticity and storm relative wind fields. Cyclonic vorticity contours are every $1 \times 10^{-3} \text{ s}^{-1}$ from $1 \times 10^{-3} \text{ s}^{-1}$ (starting from thick line) and anticyclonic vorticity of $1 \times 10^{-3} \text{ s}^{-1}$ is shown by thin line. The location of O denote the radar site. The RHI scan of dual-polarization mode was made on the line OR. Lines A, B and C are the locations of vertical cross sections shown in Fig. 4.

Differential reflectivity factor Z_{DR} (not shown) on the vertical cross section along the line OR in Fig. 2 was mostly near 0 dB (from -0.5 to 0.5 dB), indicating that sphere particles are predominant in the snow cloud. Only in the high altitude above 3 km, relatively large differential

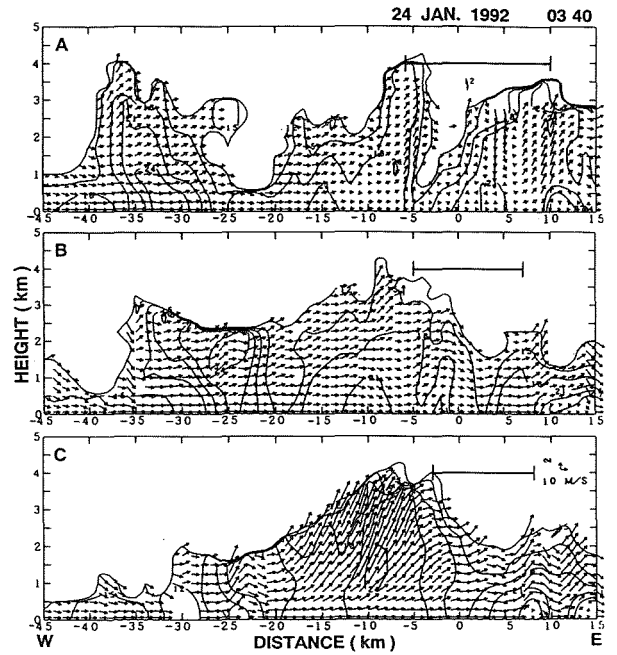


Fig. 4 Reflectivity and wind fields on the planes of cross section along the lines A, B and C in Fig. 3. A bar at the top-right of each frame represents the area of vorticity more than $1 \times 10^{-3} \text{ s}^{-1}$ at the altitude of 750 m.

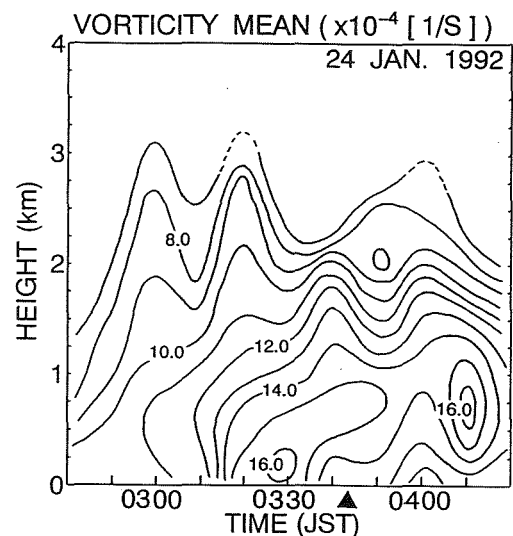


Fig. 5 Time height cross section of averaged vorticity in the area of 14 km x 14 km around vorticity center. Solid triangle denotes the arriving time of the vorticity center over land.

reflectivity factor more than 1 dB was recognized, which indicates the area of snowflakes. This characteristics implies that the portion of large reflectivity in the southern flank of the vortex is composed of small soft hail, considering relatively small reflectivity as a convective snow cloud.

A plausible explanation of the formation and development of the meso- γ scale vortex over Ishikari Bay is as follows. 1) Vorticity formed along the convergence of northwesterly winter monsoon and colder northerly from the land of Hokkaido. Analyses of sounding data of this case is reported by Katsumata et al. (1996). 2) The cyclonic vorticity is enhanced by the strengthening of northwesterly induced by the blockage of northerly component of the wind along the mountain (height about 1,000 m) at the southwestern edge of Ishikari Bay. This deformation of wind fields reflects the meso- β scale structure of wind fields around Ishikari Bay. 3) During the development of the vorticity, south and southwestern flank of the vorticity increased the convergence to form convective snow clouds. 4) Tilting of the axis of the vertical vortex caused the weakening of the vortex. Similar explanations are considered to be possible for another cases.

4. CONCLUDING REMARKS

Meso- γ scale characteristics of vortices associated with Cloud Bands were analyzed using Doppler radar data. The relation between the development of vortices and snow clouds is revealed. Detailed dual-Doppler analyses were performed on a few significant cases. Development of a snow cloud with a strong updraft and an echo top height of 4.5 km, much larger than ordinary snow clouds in the target area, was analyzed on the circumference of the vortex.

We conclude that the meso- γ scale vortex of snow clouds plays a role in the significant development of snow clouds at the head and right side of the vorticity movement, and also in the long endurance of the snow cloud formation. Detailed analyses revealed the possibility to improve short term forecasts of snowfall, although rotation of the snowfall area on the circumference of the vortex makes this difficult.

ACKNOWLEDGMENT

The authors express their thanks to all of the participants in the observation for obtaining data. They thank Prof. T. Takeda and Dr. Y. Fuiyoshi for making multi-Doppler observations realistic around Ishikari Bay. The authors extend their thanks to Japan Meteorological Agency for providing the Keifu-Maruru radar data, sounding data and another weather data. This study is supported by Grant-in-Aid for Scientific Research of the Ministry of Education, Science and Culture of Japan (Grant Nos. 02201102, 03201104 and 04201102)

REFERENCES

- Doviak, R. J. and D. S. Zrnic', 1984: Doppler radar and weather observations. *Academic Press*, 458pp.
- Katsumata, M., H. Uyeda and K. Kikuchi, 1996: Characteristics of a Cloud Band off the west coast of Hokkaido Island analyzed with AVHRR/NOAA and SSM/I data. (*Submitted to J. Meteor. Soc. Japan*)
- Kikuchi, K. (chief investigator), 1993: Studies on the prediction of heavy snowfall disasters in the urban areas and its reduction and protection. *Final report on the "MONBUSYOU-JUUTENROUIKI KENKYUU Predictability and preventability of natural disaster"*, 609pp (in Japanese with English abstract)
- Kobayashi, F., K. Kikuchi and T. Motoki, 1987: Studies on the convergence band clouds formed in the mid-winter seasons on the west coast of Hokkaido Island, Japan(I). *Geophys. Bull. Hokkaido Univ.*, **49**, 341-357. (in Japanese with English abstract)
- Nagata, M., 1993: Meso- β -scale vortices developing along the Japan-sea polar-airmass convergence zone (JPCZ) Cloud Band: Numerical simulation. *J. Meteor. Soc. Japan.*, **71**, 43-57.

RETRIEVED DYNAMIC AND THERMODYNAMIC STRUCTURE OF TROPICAL CONVECTIVE SYSTEM IN WEAK WIND PHASE IN TOGA-COARE IOP

Tomoki Ushiyama¹, Daisuke Abe², Shinsuke Satoh³ and Kensuke Takeuchi¹

¹ Institute of Low Temp. Sci. Hokkaido Univ. Sapporo, Japan, 060

² Weather News Cooperation, Makuhari, Chiba, Japan, 261

³ Communications Research Laboratory, Koganei, Tokyo, Japan, 184

1. INTRODUCTION

To study mesoscale convective systems, dynamic and thermodynamic retrieval techniques have been developed in recent 20 years. The technique was applied for several kinds of mesoscale systems and was proved as valid technique to derive dynamic and thermodynamic variable in the storms. However, while applying this technique, time dependent variables must vanish. So, applying to rapidly developing system makes substantial error. Our analyzing case is a tropical convective system observed in TOGA-COARE IOP (Tropical Ocean and Global Atmosphere Coupled Ocean Atmosphere Response Experiment Intensive Observation Phase), which is rapidly developed. However, considering the applicability of retrieval technique to any kind of convective systems, this study was attempted.

2. DATA

The analyzed convective system was observed on 13 Jan. 1993 by two Doppler radars settled in Manus island, Papua New Guinea (2 S, 147 E) (figure 1.). Both radars are x-band radars whose ranges are 60 km (Uyeda et.al. 1995). Sounding data of ISS (Intensive Sounding System) launched at Manus island distributed by TCIPPO (TOGA-COARE International Project Office) were used. To describe large scale wind oscillation, GANAL data (global objective analysis by Japan Meteorological Agency) were also utilized.

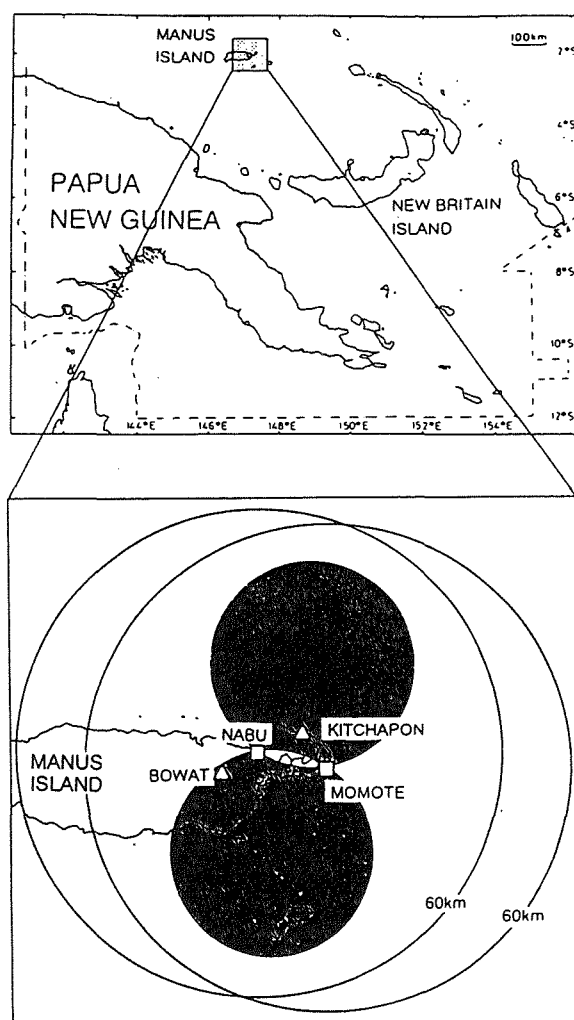


Fig.1 Map of Papua New Guinea (upper panel) and Manus island (lower panel). The lower panel shows the locations of the two Doppler radars, located at Momote and at Nabu, with a 60 km observational range. The shaded area indicates the domain of the dual Doppler analysis.

3.METHOD

Three-dimensional wind fields were synthesized from two Doppler radars by downward integration, and then variational adjustment was applied to satisfy continuity equation and to remove errors. After that, thermodynamic retrieval technique after Roux and Ju (1990) was applied to obtain pressure and temperature and other variable fields. Since the convective system was small horizontal extent especially in developing stage, winds around the radar echo were interpolated or extrapolated using synthesized wind data.

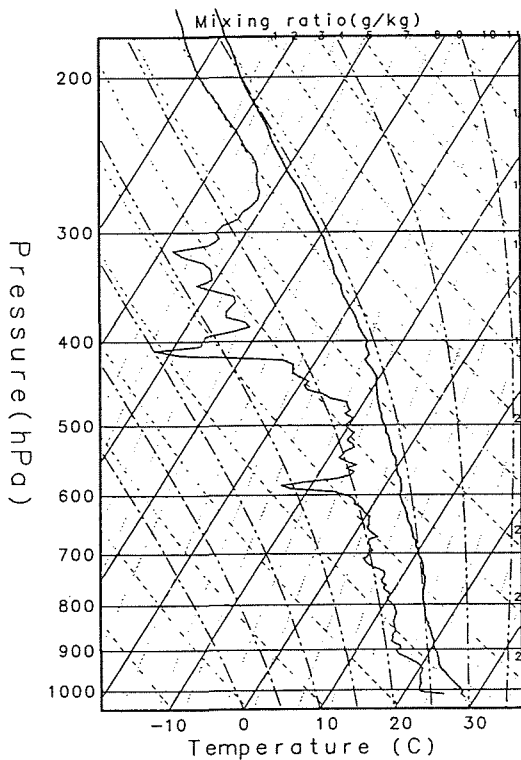


Fig.2. Skew-emagram at 20:18, 12 Jan. Two solid curve lines indicate the temperature (right) and the dew point (left).

4.RESULTS

This convective system appeared from 0:00 to 4:00 LST (hereafter times are shown in LST) on 13 Jan.1993 around the Manus island. This period is in a weak wind phase in 30-60 day oscillations, so the lower layer wind and the vertical shear on the environment were weak. The sounding data showed wet condition through the troposphere, but above 470 hPa (6.3 km) dry layer exited (Figure 2), and

CAPE was 748 (J/kg) at 2:43,13. The lower layer environmental wind was 3 m/s easterly, which was same as the system movement. Although these were not favorite condition for cloud systems to develop, this system alive four hours, and extended about 70 km horizontally.

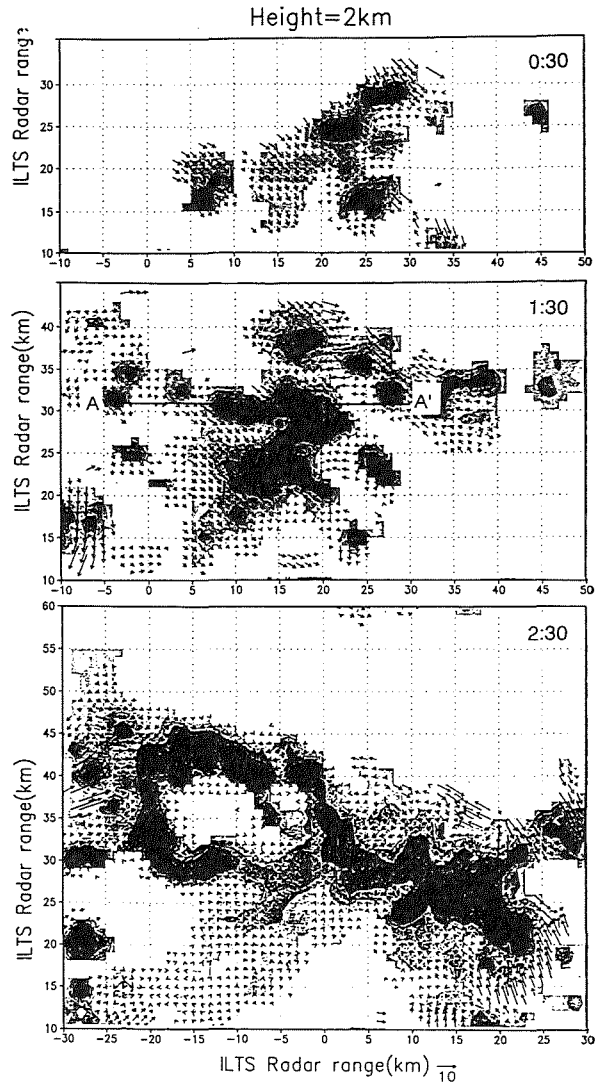


Fig.3. Horizontal section of cloud system at 2 km height. The shading indicates reflectivity from 10 dBZ, in 5 dBZ interval. The arrows show system-relative velocities. The times are indicated in right upper corner of each panels. Ordinate and abscissa indicate distance from ILTS radar (Momote). In the middle panel, a horizontal line and marks of A,A' shows intersection of vertical plane in Fig.5.

Figure 3 shows the system development in 2 km height CAPPI. In its developing stage at 0:30, the system was about 20 km horizontal extent. Small cells are generated successively. In the mature stage, from 1:30 to 2:30, several new cells were generated in the west of the system, and the system extended its

area westward. After 2:00, another system was generated in the west 20 km apart from the first system. In the dissipating stage, till 3:30, the first system dissipated, and till 4:00, the second system dissipated.

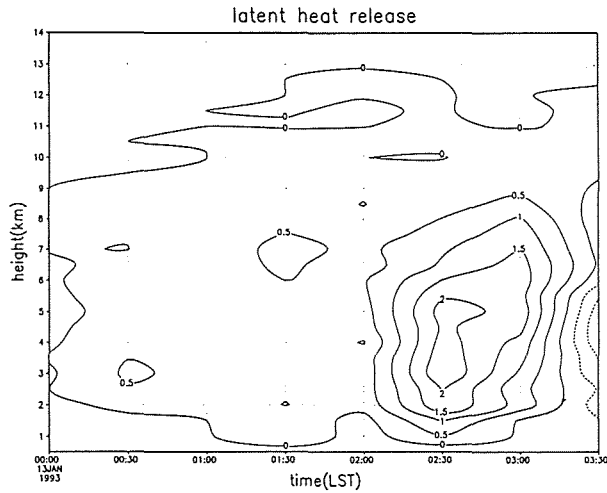


Fig.4. Time-height cross section of latent heat release. The unit is Joule. The latent head release in the mature stage (2:30-3:00) dominates other stages.

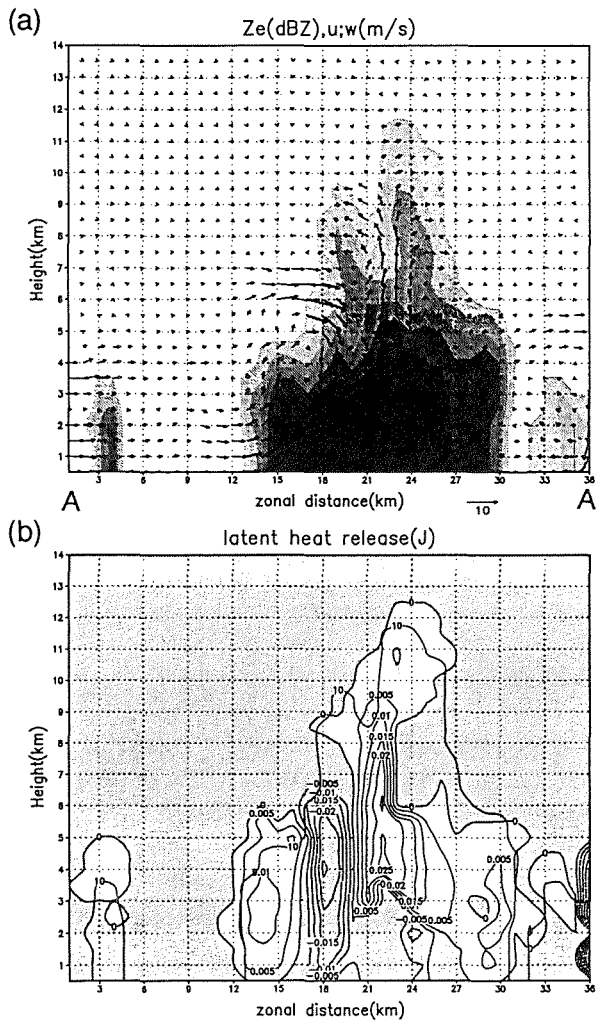


Figure 4 shows the time-height cross section of the summation of the latent heat release for each height. This figure clearly shows that in the mature stage of this system, almost latent head was released to the atmosphere, and in the dissipating stage, the heat release turns to negative. However, in the developing stage (until 2:00), the amounts were negligible small compare than the mature stage.

Figure 5 shows the vertical cross section of retrieved fields at 1:30 in the developing stage. The intersecting line was shown in the middle panel of figure 3. In Fig.5(a), a strong updraft was seen in the center of developing cells. This updraft was supported dominantly by buoyancy force around the updraft (Fig.5(c)), and near the ground pressure gradient force lifted the air above the LCL (Fig.5(d)). On the other hand, in the west of the updraft, strong downdraft appeared that was supported by negative

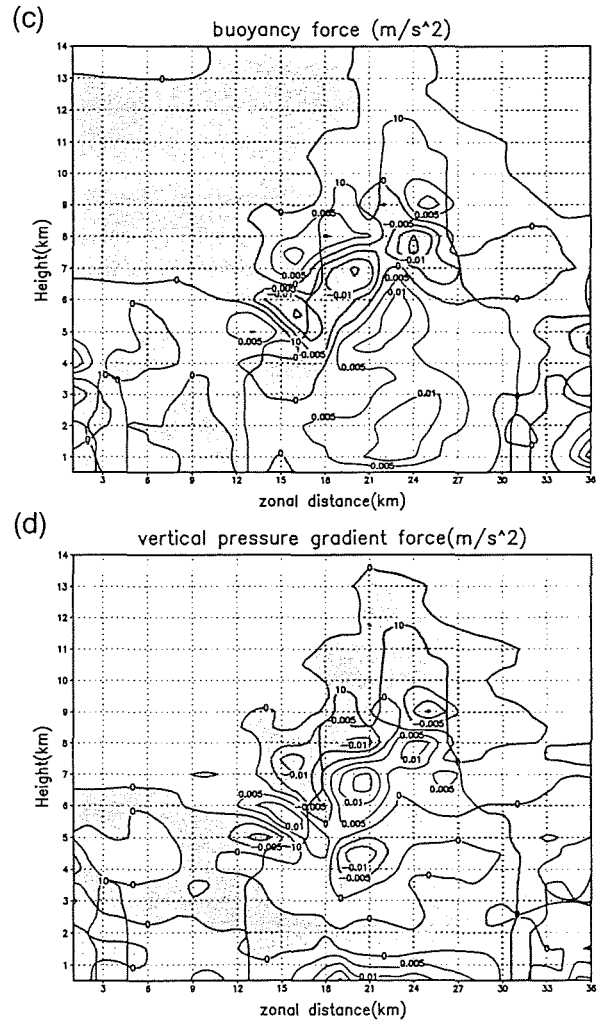


Fig.5. Vertical plane of the retrieved fields of the cloud system. Intersection was indicated in middle panel of Fig.3 by a horizontal line and the marks A,A'. Under the panel (a), the marks A and A' shows as same points in Fig.3. (a): Radar reflectivity and wind field. The wind vectors outside of the echos were interpolated or extrapolated using synthesized winds. (b): Latent heat release. Shaded area shows negative value. The outline of the echo area is shown by solid lines. (c): Same as (b) but buoyancy force. (d): Same as (b) but vertical pressure gradient force.

buoyancy. This negative buoyancy was a consequence of evaporation caused from incoming dry air above 6 km heights (Fig.5(b)). However, no cold pool was recognized in the virtual cloud potential temperature field in this case. That was considered as the result of oceanic wet atmospheric profile. For this case the 'momentum check' in Gal-Chen and Hane (1981) showed poor accuracy about vertical component of the temperature fields. However the acceleration terms were consistent with that derived from vertical winds.

5.REFERENCE

Gal-Chen,T. and C.E.Hane,1981:Retrieving buoyancy and pressure fluctuations from Doppler radar observations. A status report.,*Atmos.*

Technol., **13**, 98-104

F.Roux and S.Ju,1990:Single-Doppler observation of a west African squall line on 27-28 May 1981 during COPT 81: Kinematics, Thermodynamics and water budget, *Mon. Wea. Rev.*, **118**, 1826-1854.

Uyeda,H. et.al.,1995:Doppler radar observations on the structure and characteristics of tropical clouds during TOGA- COARE IOP in Manus, Papua New Guinea: -Outline of the observation-. *J. Meteor. Sci. Japan*, **73**, 415-426

6.ACKNOWLEDGEMENTS

This work was performed under the TOGA-COARE, and radar observation was performed by J-COARE at Manus island. The authors would like to much thank TCIPPO and P.N.G. national weather service for their great effort to providing this experiment. The authors would like to special thank Mr. Kawashima at Tokyo Univ. for his helpful advices and comments and providing his computational programs.

AEROSYNOPTICAL AND THERMODYNAMICAL CONDITIONS FOR HAIL-PROCESS FORMATION WITH SIMILAR RADAR STRUCTURE AND DEVELOPMENT DYNAMICS

M.V.Barekova¹, Z.A.Gazaeva², V.S.Makitov², A.I.Taumurzaev²

¹High-Mountain Geophysical Institute, 360000, Nalchik, av.Lenin 2, RUSSIA

²Hail Suppression Centre "Antigrad", 360000, Nalchik, av.Lenin 2, RUSSIA

The development of hail suppression activities on hail processes makes a strict demand on the hail forecast methods, their detalization and practice trend. The most actual method, to our mind, was developed in Goral and Barekova (1975), Goral (1984), Goral et al. (1984) allowing to forecast the type, intensity and mesoregion of hailstorm development with high degree of justification. For the North Caucasus region, where hail suppression activities were carried out during many years, the forecast of the mesoregion of supercell hail process development is of peculiar meaning. It is generally realized that the one of the main properties of such processes is their quasi-stationary state during enough long time of existence, due to this, stable extended trajectory of cloud displacement and the almost discontinuous streak of falling hail (hail streak) on the ground are observed. The mesoregion forecast of hail process development in this case is oriented on the identification of the most possible areas where the hail streaks of this process can be realized.

On the other hand, the radar investigations of the structure and dynamics of hail process development of different types conducted in the pointed region during many years allowed to identify a set of patterns in the formation of hail

precipitation fields. These patterns may essentially improve and broaden the possibilities of present forecast methods. Thus it was shown in Gazaeva et al. (1989) that three types of supercell hailstorms can be identified on the North Caucasus according to the movement direction of cells in the stage of quasi-stationary state. However, the more detailed consideration of the different cases shows that in every identified type of trajectories there are such that coincide with high degree of accuracy. In other words the energy realization of atmosphere instability in the frameworks of specific aerosynoptical and thermodynamical conditions occurs according to the similar scenarios forming the supercell-"twins". The similarity in radar structure in this case is supplemented by the process movement according to almost one and the same trajectories. There is an interesting opportunity to identify the most informative features or complex of parameters defining not only the fallout mesoregion but this or that trajectory of hailstorm movement. Hence, in this paper the attempt of the complex analysis of the aerosynoptical conditions on the North Caucasus of the development of the supercell hailstorms having the identical trajectories of movement is made.

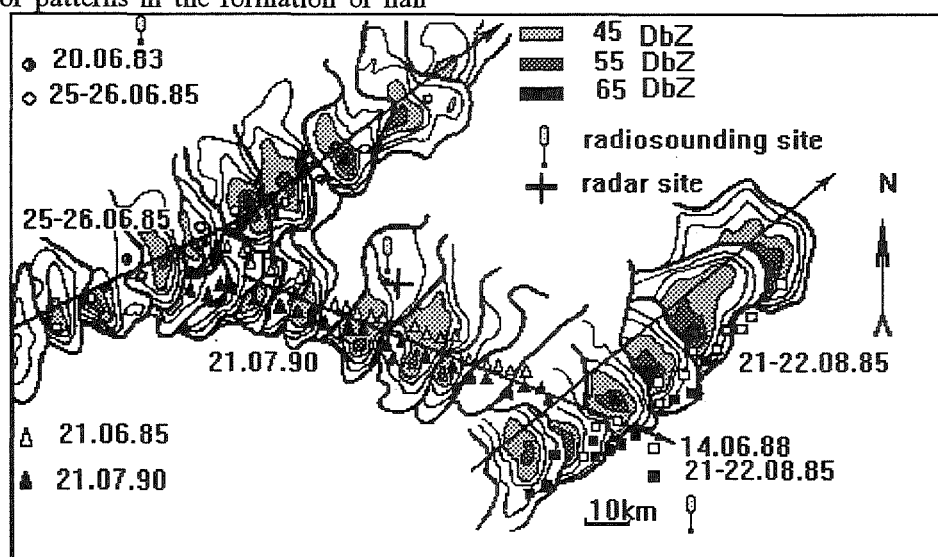


Fig.1 Movement trajectories of three pairs of supercell hailstorms. Trajectories are given as the successive horizontal cross-sections of radar echo at wavelength of $\lambda_2=10$ cm. The points of maximum values of radar reflectivity are shown.

As an example of such supercell storms Fig.1 shows the movement trajectories of six cells characterizing three most typical trajectories of hailstorm movement pointed in Gazaeva et al.(1989). For visualization the minimum number of cells was chosen in order not to make the drawing loaded. Three of them are presented as the successive horizontal cross-sections of radar echo at minimum angles of scanning in the form of isolines of radar reflectivity at wavelength of $\lambda = 10$ cm. Here you can see the trajectories of points of radar reflectivity maxima $\eta_{10\max}$ for all 6 cells which demonstrate the space proximity of hail streaks. To analyze the atmospheric condition in days with supercell storm development shown in Fig. 1 the maps of surface analysis and baric topography for European part of Russia and maps of surface analysis of large scale for North Caucasus region for all available periods were used as well as the

radiosounding data at the sites situated on the territory with 400 km extent from the west to the east in the premountain zone of the Great Caucasus.

The dependence of the intensive and disastrous hailstorms in Caucasus on such synoptical factors of different scales as the character of macroscale circulation, thermal characteristics and cyclone intensity in circumpolar zone and near the North Caucasian region was found in paper of Goral and Barekova (1985). The thermodynamical characteristics of tropospheric potential instability as well as the near-surface distribution of wet-bulb temperature as the factors, defining the mesoregion of hailstorm were considered in Goral (1984), Goral et al. (1984). So, Table 1 gives the set of macro- and mesoscale factors of atmospheric circulation was detected allowing to define the intensity of hailstorm development.

Macro-and mesoscale factors of atmospheric circulation, characterizing hailstorm intensity

Table 1.

Process intensity	Type of circulation	Mesoscale characteristics, map AT500	Characteristics of cyclones, forming "hail-dangerous" zones, map AT500	Characteristics of "hail-dangerous" zones, map AT500, 400, 300
Dangerous	Meridional type or type with disturbed zonality C, W _c	Arctic minimum. A number of closed isohypses, $n \geq 4$, $t \leq -30^\circ\text{C}$	Main or southern cyclone near target area, $t_{\text{main}} \leq -20^\circ\text{C}$ $t_{\text{south}} \leq -16^\circ\text{C}$	Overlapping of three hail-dangerous zones
Intensive	Meridional type, C Zonal type, W	Arctic minimum, $n \geq 2$ $t \leq -25^\circ\text{C}$	Main cyclone $t_{\text{main}} \leq -20^\circ\text{C}$	Frontal part of macro-trough or thermal meso-trough. Overlapping of 2 hail-dangerous zones.
Average	Zonal type, W Meridional type, C	Absence of arctic minimum Arctic minimum, $n \geq 2$ $-25^\circ\text{C} < t \leq -20^\circ\text{C}$	Main cyclone in any stage Main cyclone after mature stage	Front part of thermal meso-trough or cyclone over region
Weak	Zonal type, W	Absence of arctic minimum	Main cyclone out of target area or surface cyclone	Existence of cold region at heights. Surface front.

As shown in table the meridional type of macroscale circulation C corresponded to the disastrous processes. This type is represented by the well developed deep trough, the front part of which passed through the Caucasian region. For I and III pairs the trough was formed by active (3-7 closed isohypses) and cold arctic minimum ($-27^\circ\text{C} \leq t \leq -36^\circ\text{C}$). The cyclone in "dangerous" zone at these conditions had 1-2 closed isohypses and the average temperature of -19°C . For the II pair the absence of arctic minimum partially was compensated by the availability of cold cyclone in "dangerous" zone near the Caucasian region but this circumstance promotes the development of only intensive but not disastrous hailstorm. It is worth to note the similarity of the macroscale structure of

thermobaric field of mean triposphere for every pair of hailstorms, apparently, it provides for the analogous wind distribution in troposphere and the similarity of the spatial structure of the considered hailstorms (Fig.1). As for the quantitative values of the characteristics of potential atmospheric instability for each pair they differed insignificantly. Moreover, the characteristic feature of the diurnal run was the increase of parameters up to the optimal values as the beginning of the storm approached. At the nocturnal storms (25 - 26.06.85 and 21 - 22.08.85) the indices of the resolution of the accumulated potential instability are the data on tropospheric radiosounding carried out the day after the storm: there is a considerable decrease of

the vertical potential instability or atmosphere achieved a steady state.

If the macroscale synoptical characteristics of troposphere are responsible for the structure and intensity of the developing hailstorm such mesoscale characteristic of surface layer of troposphere as the gradient of the wet-bulb temperature calculated along the direction of the leading flow is responsible for mesoregion development (Goral 1984).

Near-surface distribution of wet-bulb temperature t_{wb} was characterized by minimum values in mountains (t_{wb} varied from 6 °C to 14 °C) and maximum values on the plane ($t_{wb \max} \geq 22$ °C).

The gradient regions $\Delta t_{wb} / \Delta x$ formed in the morning according to data of surface analysis maps, their location do not change during the whole

day but in some cases especially at the hailstorms at nights the formation of new lines of the surface potential instability of atmosphere occurred in later time (21-22.08.85 and 25-26.06.85).

Fig.2 gives $\Delta t_{wb} / \Delta x$ gradient regions. In all cases the gradient values of $\Delta t_{wb} / \Delta x$ were more than 2 °C per 100 km during the day in premountain zone and the hailstorm development was observed in the regions with $\Delta t_{wb} / \Delta x$ gradients from 3°C to 9 °C per 100 km. In certain extent the propagation direction of gradient regions depends on the leading flow (air-mass invasion direction) in troposphere.

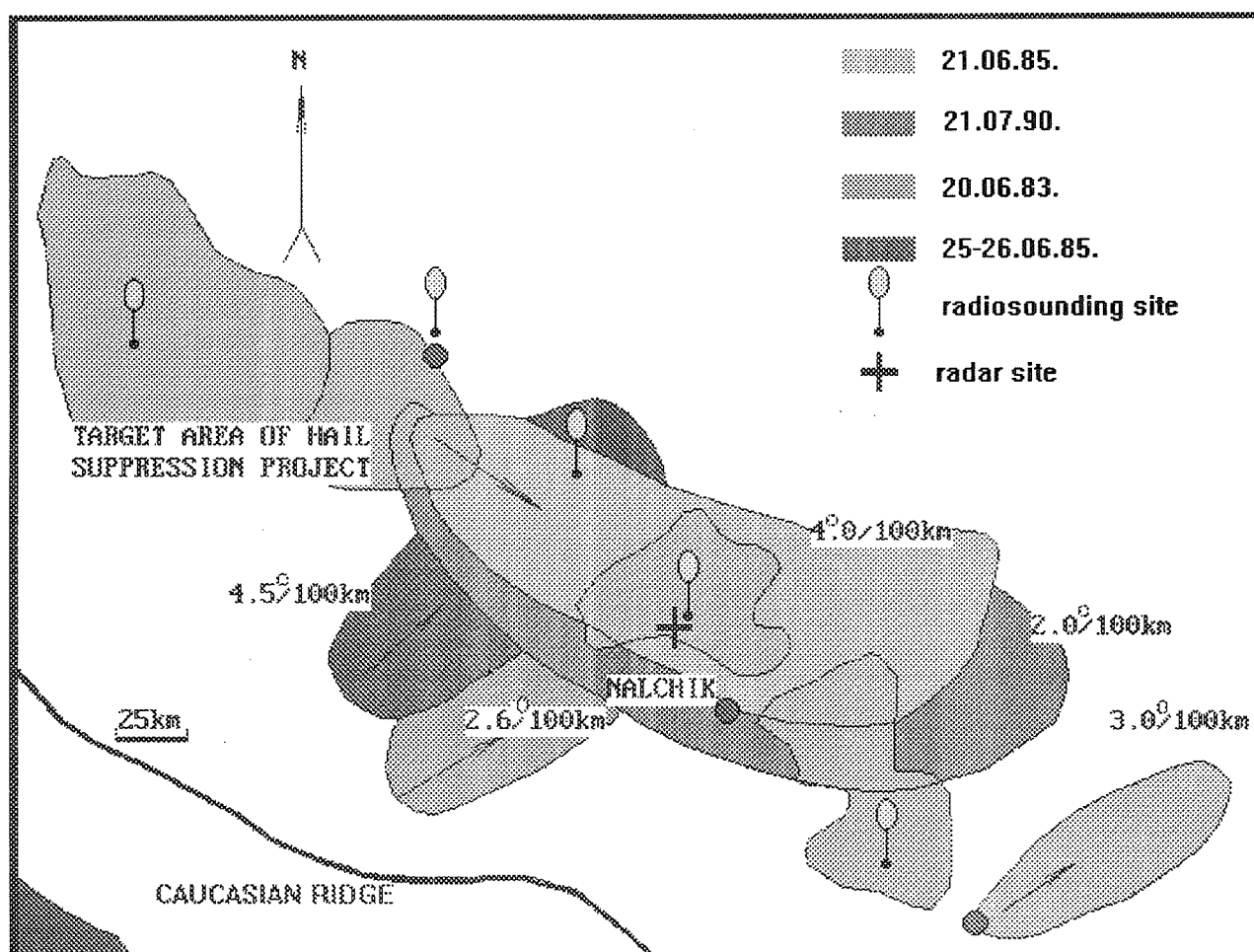


Fig.2. The regions of near-surface potential instability of atmosphere during the development of two pairs of supercell hailstorms given in Fig.1.

Finally, the orientation of the potential instability zones with $\Delta t_{wb} / \Delta x \geq 2$ °C per 100 km gradients can serve as the criterion to pinpoint the type of supercell trajectory at the quasi-stationary state. As Fig.2 shows in the days with southern-western direction of hail cell movement (20.06.83 - 25.26.06.85) the zones of surface instability are located along the main ravines of Main Caucasian Ridge and all are near the hail streaks. The attempt

to divide these trajectories into western and eastern according to this parameter was failed. Apparently there is the very rare type of atmospheric circulation at which the simultaneous existence of supercells, moving along these trajectories, is possible. For the whole observational period since 1976 to 1994 such process was observed only once. At the northern-western movement of the supercells in mountain and premountain regions (21.06.85 and

21.07.90) the latitude orientation of zones of surface potential instability is observed or the orientation of these zones shifts to the high-mountain region.

So the analysis of six disastrous hail processes on the North Caucasus showed that for their development in troposphere the optimal macro- and mesocyclonic regime, responsible for the intensity as well as the structure, was formed and the regions of surface potential unstability were responsible for the mesoregion of hailstorm development.

The development of the intensive and disastrous supercell hailstorms with closed movement trajectories takes place at the presence of similar cyclonic processes as macro-and mesoscale. The forecasting separation of hailstorms into the main groups of trajectories in the limits of the identified mesoregion of development is possible according to zone orientation of surface potential instability of atmosphere.

On the basis of the achieved results the automatic method of forecasting of the localization and orientation of hail streaks was developed. The software of this method was calculated for IBM PC and made in the Borland C++ medium. From the databank for processes with known hail streak trajectories according to the complex of aerosynoptical and thermodynamical parameters of atmosphere the "process analogue" was identified and the degree of its assumed similarity with forecasted process was calculated in percents. All the considered parameters were divided into 10 ranks in the order of increasing from the values characterizing the processes of weak intensity to the disastrous hailfalls. Among these parameters are the expert estimate of aerosynoptic situation, the energy content of the active layer of cloud formation, the minimum calculated velocity of updrafts, the

temperature of maximum-velocity level, the temperature of condensation level, the maximum pseudo-potential temperature of wet bulb thermometer, corresponding to the cloud adiabat, the temperature gradient of wet bulb thermometer near the ground in the direction of the air mass intrusion, the characteristics of wind sounding of troposphere and so on.

As the illustration of the method sensitivity the calculations of the similarity degree for one pair of storms are given in Fig.1. So, in the frameworks of the described system the processes on 21.06.85 and 27.07.90 were developed in the situations similar by 69 %. The further improvement of the given method assumes the increasing of the databank, the covering of the maximum number of aerosynoptical situations and using of the most informative parameters of atmosphere.

REFERENCES

- Goral G.G., Barekova M.V., 1975 :
Characteristic of cyclones, responsible for the development of intensive hailstorms. Pap. VGI, 69, 37-48 (in Russian).
Goral G.G., 1984: Thermodynamical state of surface air and localization of hailstorms. Pap. VGI, 61, 26-32 (in Russian).
Goral G.G., Gorokhova V.L., Chepovskaya O.I., 1984: Detection of mesoregion of severe hailstorm development on the North Caucasus. Pap. VGI, 55, 72-80 (in Russian).
Gazaeva Z. A., Dinaeva L. M., Makitov V. S., 1989: Characteristic trajectories of supercell hail clouds on the North Caucasus. Pap. VGI, 74, 99-109 (in Russian).

PRECIPITATION CAUSED BY CONVERGENCE AND CONVECTION AT THE MIDDLE LEVEL IN STRATIFORM REGION OF TROPICAL CLOUD CLUSTER

¹Shuji Shimizu, ²Hiroshi Uyeda, ³Warner L. Ecklund and ⁴Kenneth S. Gage

¹EORC, NASDA, Tokyo 106, Japan and Research Development Corporation of Japan, Kawaguchi 336 Japan

²Graduate School of Science, Hokkaido Univ., Sapporo 060 Japan

³CIRES, Univ. of Colorado, Boulder, CO USA

⁴NOAA/ERL Aeronomy Laboratory, Boulder, CO USA

1. INTRODUCTION

There have been many studies about tropical cloud clusters, and convective and stratiform clouds packed in a cloud cluster. In the Global Atmosphere Research Program's Tropical Experiment (GATE), the differences of characteristics between the stratiform and convective regions were pointed out. Zipser (1977), Houze (1977) and others made conceptual images of long-lived tropical squall line system with trailing stratiform precipitation. However, there were fewer detailed analyses of stratiform clouds than convective clouds. Since stratiform clouds which last a long time bring a large amount of precipitation, information on stratiform clouds is quite important to clarify the structures and characteristics of the tropical cloud cluster. For this purpose, the stratiform clouds are observed by two X-band Doppler radars and a wind profiler of the Integrated Sounding System (ISS) on Manus Island, Papua New Guinea during the Tropical Ocean and Global Atmosphere (TOGA) - Coupled Ocean Atmosphere and Response Experiment (COARE) Intensive Observation Period (IOP) (Uyeda et al., 1995). In this study we focus our analysis on wind fields and the temporal change in the stratiform region of a cloud cluster. These methods will be reported in Section 2 and the results in Section 3. We will discuss the detailed structure of the convection within the stratiform region in Section 4.

2. METHODS

In order to reveal meso- β and meso- γ scale structures and characteristics of tropical cloud clusters, we utilized two X-band Doppler radars and a wind profiler of an ISS. One X-band radar, belonging to the Hokkaido University Meteorological Laboratory (HUML), was established at Nabu. The other X-band radar, belonging to Institute of Low Temperature Science (ILTS), and the ISS, belonging to the National Ocean Atmospheric Administration (NOAA), were established at Momote (Fig. 1). The frequency of the wind profiler was 915 MHz. The time resolution was about 15 minutes, and the range resolution in the beam direction was 250 meters. The profiler can directly measure horizontal and vertical

winds above the radar site. We adopt the velocity azimuth display (VAD) method for X-band Doppler radar using the PPI velocity data at elevation angles of 20° or 21° in order to evaluate the horizontal wind profiles above the radar site. The winds were compared with the wind data of the ISS. We also used the simplified extended VAD (EVAD) method to evaluate horizontal divergence profiles. For the EVAD analysis, the data from elevation angles of 20° (or 21°) and 12° (or 13°) are used. We collected the radar data at 15-minute intervals for a volume scan. Rawinsondes launched every 6 hours from the Momote site were available for analysis. The hourly brightness temperature data (0.1°x0.1° mesh data) of Geostationary Meteorological Satellite - Infrared (GMS/IR) are also utilized. In addition, horizontal wind fields were analyzed with dual-Doppler radar data.

3. RESULTS

In this chapter, we will describe a case study from 2200 LST 14 December to 0600 LST 15 December in 1992 in detail. We use the local standard time (LST=UT+10) of Papua New Guinea as time designations hereafter. Rainfall was recorded between

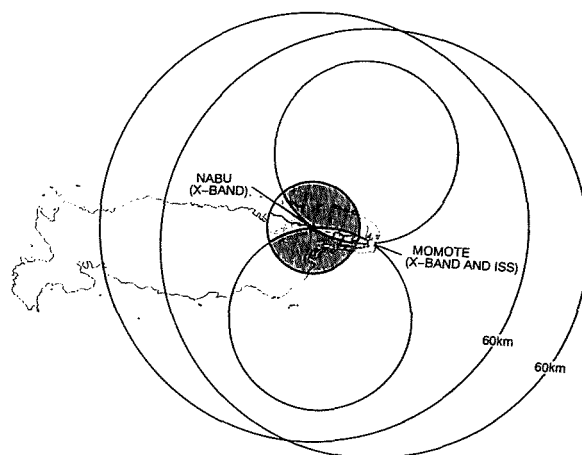


Fig. 1. Locations of the ISS, two X-band Doppler radars and two rain gauges. The area analyzed by dual-Doppler radar is hatched lightly. VAD and EVAD analysis range at an altitude of 5km is shown by dark circle.

2200 LST 14 December and 0300 LST 15 December. Figure 2 shows the brightness temperature (T_{BB}) of a GMS for every two hours from 2200 LST to 0200 LST. A cloud cluster existed on the east of Manus Island at 2200 LST. It broadened out to the west and covered the whole Manus Island at 0000 LST and 0200 LST. However, the low T_{BB} (less than 220°K) area gradually became smaller. Figure 3 shows reflectivity images from the X-band Doppler radar at Nabu at the same time of Fig. 2. A weak, stratiform echo appeared to the northeast of Manus Island at 2200 LST. It approached, and covered Nabu at 0000 LST, then suddenly diminished at 0200 LST.

Figure 4a shows the time-height cross section between 2200 LST 14 December and 0600 LST 15 December 1992 measured at Nabu by the VAD method; Figure 4b shows it measured at Momote by using the wind profiler. The time resolution for both is 15 minutes. The northerly winds in the upper layer and the northwesterly winds in the lower layer are seen through this period. The boundaries between them are shown by a solid line, as vertical shear lines of horizontal wind. The

line of the two layers descended to 1.5km. Dashed lines mean that the shear was weak. The two shear lines of the figures are similar, though they have a time lag. The peak time of the shear level and the time of the rapid descending of the shear line at Momote were delayed by about 45 minutes from the times at Nabu. Figure 5 shows the time-height cross section of the vertical profiles of divergence in the analysis area of the Nabu X-band radar by the EVAD method. When the shear line was ascending, the convergence strengthened more than 2×10^{-4} s between 2km to 4km around 0015 LST 15 December, and there was a divergence layer above the convergence layer. After 0215 a divergence dominated below 3km and there was a convergence above the divergence.

Figure 6 shows the reflectivity of the X-band radar (ILTS) at Momote and the horizontal winds from the dual Doppler radar analysis at 0000 and 0030 LST 15 December. A radar echo exceeding 10 dBZ covered this analysis area of both times. A linear and strong echo packed in it on the north of the radar sites and moved southward. The length was about 50km and the direction

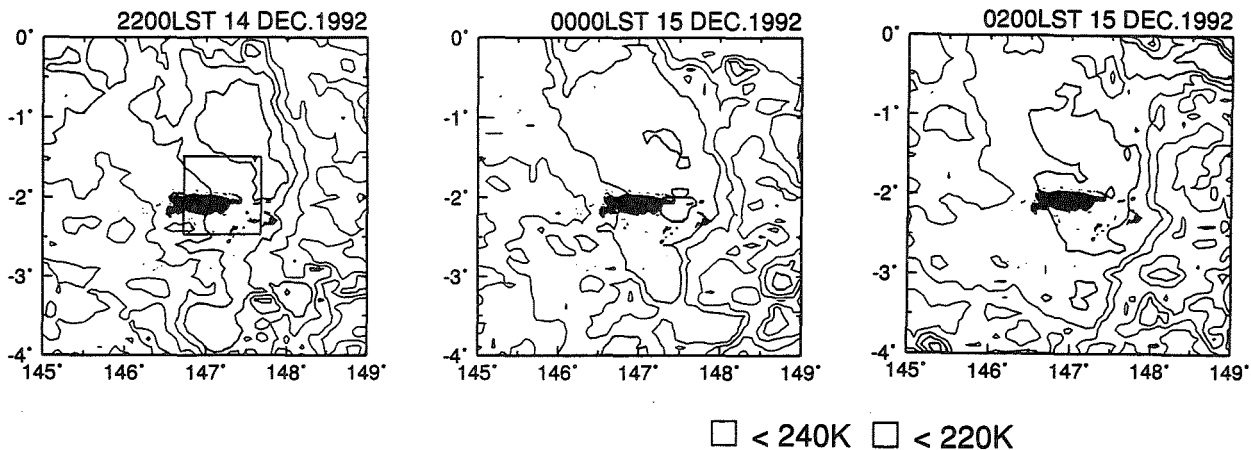


Fig. 2. The brightness temperature of the GMS-IR (at intervals of 20°K) from 2200 LST 14 December to 0200 LST 15 December 1992. The black area shows Manus Island and the shaded areas show less than 240°K . The rectangle represents the area in the X-band radar analysis of Fig. 3.

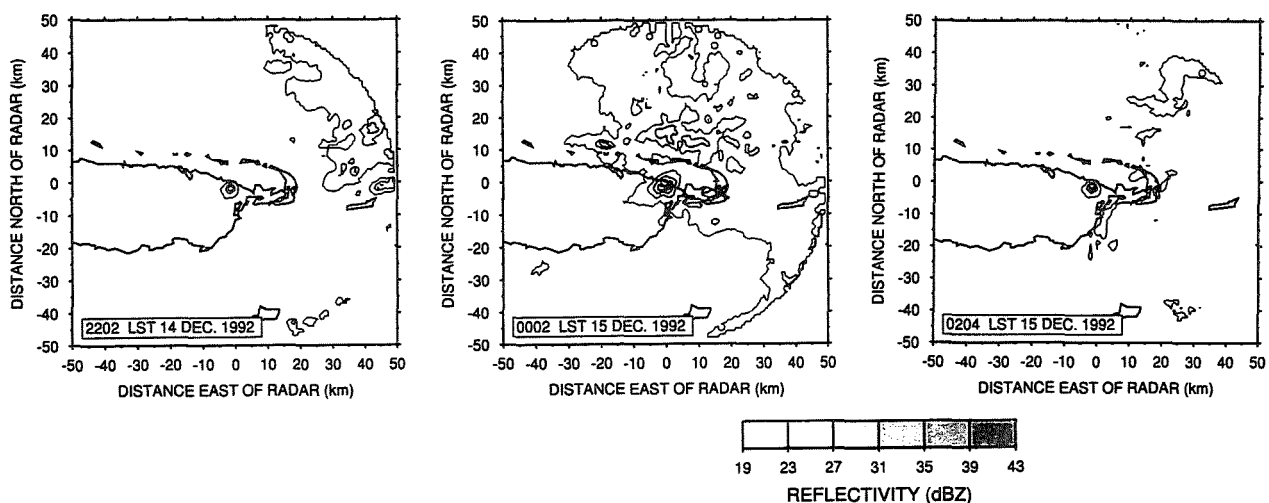


Fig. 3. Reflectivity displays of the PPI scan (with an elevation angle of 4°) of the X-band radar at Nabu every 2 hours from 2200 LST 14 December to 0200 LST 15 December 1992. The reflectivity contour interval is 4 dBZ beginning from 19 dBZ.

was from west-southwest to east-north east. At 0000 LST northwesterly winds dominated at 1.0 km. Northerly winds generally dominated at 3.0 km, and the wind field fluctuated on the linear echo. This indicated the existence of a convective part in a stratiform echo. At 0030 LST northwesterly winds existed on the north of the linear echo at 3.0 km. These wind fields corresponded to the profiles of the ISS wind profiler (Fig. 4).

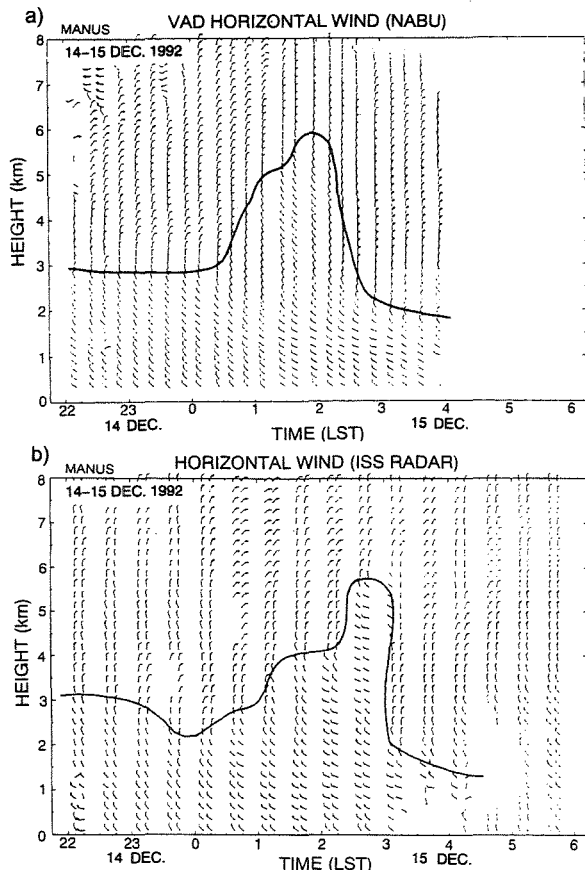


Fig. 4. The time-height cross sections of the horizontal wind profiles of (a) X-band Doppler radar at Nabu and (b) ISS radar at Momote from 2200 LST 14 December to 0600 LST 15 December 1992. The flag and barbs are the same as in Fig. 5. The solid lines show a large wind shear.

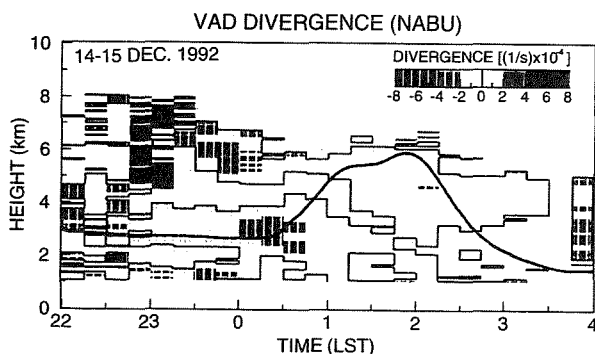


Fig. 5. The time-height cross section of the divergence profiles of the X-band Doppler radar at Nabu analyzed with the EVAD method from 2200 LST 14 December to 0400 LST 15 December 1992. The solid line shows a large wind shear which was the same as Fig. 4(a).

Figure 7 shows north-south cross section of reflectivity using the volume scan data of the ILTS radar at Momote every 20 minutes from 0000 LST to 0100 LST 15 December. At 0000, a strong and narrow echo existed at 15km north from Nabu. This part corresponded to the linear echo band in Fig. 6. The strongest reflectivity existed above 3.0 km. It propagated southward to 15 km south from Nabu at 0100. This corresponded to the linear echo that passed over Nabu from north to south (not shown).

4. DISCUSSIONS

We discuss the structure of the rainfall system that brought precipitation over Manus Island from the change of wind fields and convergence field within the analysis area of the radars. The stratiform echo gradually weakened because the cloud cluster over Manus Island and broadened out southwestward. Northwesterly wind in the lower layer and northerly wind in the upper layer dominated in this analysis area, and a strong vertical shear of horizontal wind existed between them. The northwesterly wind layer thickened in the northwest of the Manus Island after 0000 LST 15 December. Therefore horizontal shear entered the VAD analysis area. Convection and precipitation occurred from the middle level because of the middle level convergence in the area (Fig. 5). The southward propagating southwesterly wind and horizontal shear line accounted for the time lag of the vertical profiles of winds between Nabu and Momote. After 0215 LST, the southwesterly wind layer suddenly became thin and divergence dominated in the middle level. The strong echo then disappeared from the VAD analysis area in the stratiform echo. It seemed that this temporal change of the vertical profiles of horizontal wind was caused by a southward passage of a wave in the boundary between the northwesterly and northerly wind layers. The wave length of the wave was 60km and the height was 3.5km. Convergence and convection in the middle level developed in the front of the wave and divergence developed in the rear of the wave.

5. CONCLUDING REMARKS

We attempted to investigate the structure of a stratiform region of a tropical cloud cluster on Manus Island during the TOGA-COARE IOP. The convective part was found above 2.0 km in this stratiform cloud and had a length of about 50 km within the radar observation range. The linear convective was caused by large convergence more than 2×10^{-4} s around 3.0 km in height with a horizontal wind shear line. This convection contributed to initiating precipitation (10 mm/h) over the Manus Island in the dissipating cloud cluster. We believe that the dissipation process of the stratiform part of cloud clusters and convection from the middle level in the stratiform clouds are important for understanding tropical cloud clusters.

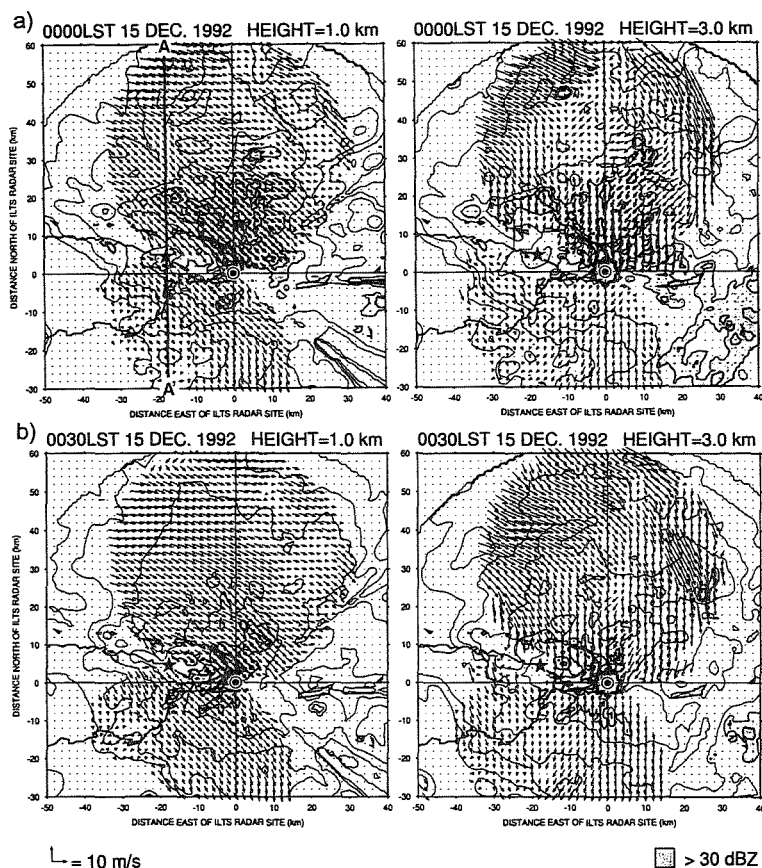


Fig. 6. The reflectivity of the X-band radar at Momote and the horizontal wind from the dual-Doppler radar analysis at (a) 0000 LST and (b) 0030 LST 15 December 1992. The horizontal cross sections at 1.0 km (left) and 3.0 km (right) are shown. The reflectivity contour interval is 5 dBZ from 10 to 45 dBZ. The hatched area is greater than 30 dBZ. The double circle indicates Momote; the black star, Nabu.

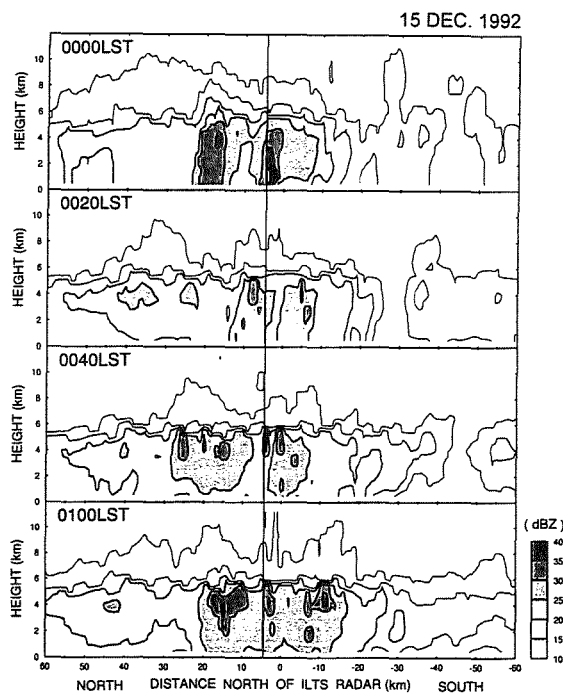


Fig. 7. Vertical cross sections of the reflectivity displays of X-band radar at Momote every 20 minutes from 0000 to 0100 LST 15 December 1992. The reflectivity contour interval is 5 dBZ beginning at 15 dBZ. Locations of these sections are indicated by the line A-A' in Fig. 6.

ACKNOWLEDGMENTS

We express our thanks to Prof. Katsuhiko Kikuchi and Dr. Yoshio Asuma, Hokkaido University, for their encouragement throughout our studies. We thank Mr. Yoshiaki Sato and Mr. Hiroyuki Yamada, Hokkaido University, for their assistance in making some of the figures. We are also thankful to the members of Manus radar observation group (Uyeda et al., 1995). The ISS at Manus Island is supported by the US TOGA Project Office. The GMS CD-ROM data was provided by Dr. Tetsuo Nakazawa, Meteorological Research Institute. This study is supported by a Grant-in-Aid (No. 06np021) of the Ministry of Education, Science and Culture of Japan.

REFERENCES

- Houze, R. A., Jr., 1977: Structure and dynamics of a tropical squall-line system. *Mon. Wea. Rev.*, **105**, 1540-1567.
- Srivastava, R. C., T. J. Matejka and T. J. Lorello, 1986: Doppler radar study of the trailing anvil region associated with a squall line. *J. Atmos. Sci.*, **43**, 356-377.
- Tsuboki, K. and G. Wakahama, 1988: Single Doppler radar measurements of a kinematic wind field: VAD analysis based on a least-squares-fitting method. *Low Temperature Science, Ser. A*, **47**, 73-88 (in Japanese).
- Uyeda, H., Y. Asuma, N. Takahashi, S. Shimizu, O. Kikuchi, A. Kinoshita, S. Matsuoka, K. Takeuchi, M. Ohi, S. Satoh, Y. Fujiyoshi, R. Shirooka, N. Nishi, T. Tomita, H. Uyeda, T. Sueda and A. Sumi, 1995: Doppler radar observations on the structure and characteristics of tropical clouds during TOGA-COARE IOP in Manus, Papua New Guinea: Outline of the Observation. *J. Meteor. Soc. Japan*, **73**, 415-426.
- Zipser, E. J., 1977: Mesoscale and convective-scale downdrafts as distinct components of squall-line structure. *Mon. Wea. Rev.*, **105**, 1568-1589.

ON THE SPATIAL AND TEMPORAL DISTRIBUTION OF THUNDERSTORMS IN SOUTHERN GERMANY

Ulli Finke and Thomas Hauf

Institut für Physik der Atmosphäre, DLR Oberpfaffenhofen, Germany

1. INTRODUCTION

Since 1992 lightning data from a Lightning Position And Tracking System (LPATS) is available for the southern half of Germany. It is operated by the two power supply companies Bayernwerk AG, München and Badenwerk AG, Karlsruhe. The system consists of an array with 6 receiving stations distributed over southern Germany with an average separation of 200 km. Cloud-to-ground lightning strokes are detected with an overall efficiency of 70%. The LPATS allows to monitor the thunderstorm activity. A statistical analysis of lightning for southern Germany is given in a recent paper by Finke and Hauf (1996).

2. TEMPORAL DISTRIBUTION

Within the analyzed area of $500 \text{ km} \times 430 \text{ km}$ a mean number of about 634,000 lightning strokes per year was detected. This gives a mean lightning frequency of 1.2 per minute. If only the period from May to August is considered, when most of the thunderstorms occur, the frequency increases to 3.6 per minute.

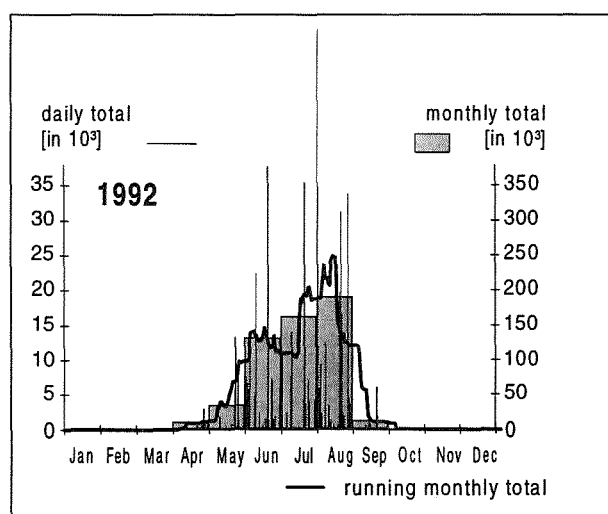


Fig.1: Daily and monthly total lightning sums for the 1992 year.

Only on 28% of all thunderstorm days more than 15,000 lightning events are detected. These few days, however, contribute with 60% to the total lightning. This clustering of lightning in few days is also reflected in the great spatial and temporal variability of lightning sums.

To characterize the *annual cycle*, the daily and monthly total numbers of lightning strokes for the 1992 year were calculated (Fig. 1).

As expected, a well-expressed annual cycle is found. About 95% of all lightning events were observed in the 4 summer months May to August. The lightning number increases from April to July and reaches its maximum between the end of July and the first weeks of August. Typically a minimum during June is observed which is caused by high pressure weather systems with suppressed thunderstorm activity. A steep decrease in lightning number in September marks the end of the thunderstorm period which is due to abrupt changes in synoptic weather conditions.

Thunderstorm activity exhibits a strong year-to-year variability. This goes parallel with the variability of synoptic flow conditions favourable for the development of thunderstorms. As, generally, synoptic conditions change on a time scale of 3-5 days, we find days with high thunderstorm activity clustered in groups of a few days while during the remaining days much less or no storms are found.

A comparison of the number of thunderstorm days as reported by synoptic stations illustrates the nature of this variability. Large differences in thunderstorm day numbers are mostly caused by the existence or absence of one or two period with high thunderstorm activity. For instance, the large difference of 11 more thunderdays observed in 1993 compared with 1992 was produced mainly by an abnormal low thunderstorm activity in May 1992 with 8 thunderdays less than in May 1993. For the other months the number of thunderdays for the two years was almost the same.

The *diurnal cycle* follows the well-known one of convective activity. It rises at about 11 local time and peaks at about 16 local time. The initiation of deep convection requires a well-mixed state of the full boundary layer which usually appears at about 1100 in the morning. While this storm initiation time is more or

less the same for all locations in space, later storm evolution including the dissipation shows considerable scatter of time scales.

One special and significant feature is the secondary maximum between 2000 and 2400, which is observed in the years 1992 and 1993. We found that long-lasting storms which propagate from their south-westerly source areas in predominantly easterly to north-easterly directions cause the secondary maximum. For single years only 2-3 intense storms, mostly in the southern part of the considered region, may generate already the secondary maximum. This small required number of strong storms explains also the observed great interannual and regional variability.

3. SPATIAL DISTRIBUTION

The common measure of thunderstorm activity is the number of thunderstorm days per year. By definition a day is called a thunderstorm day when an observer heard thunder. We compared this data with that of the lightning location systems. For that purpose, the lightning-based thunderstorm day is defined as a day when at least one lightning stroke was detected inside an 'audibility' range of about 20 km.

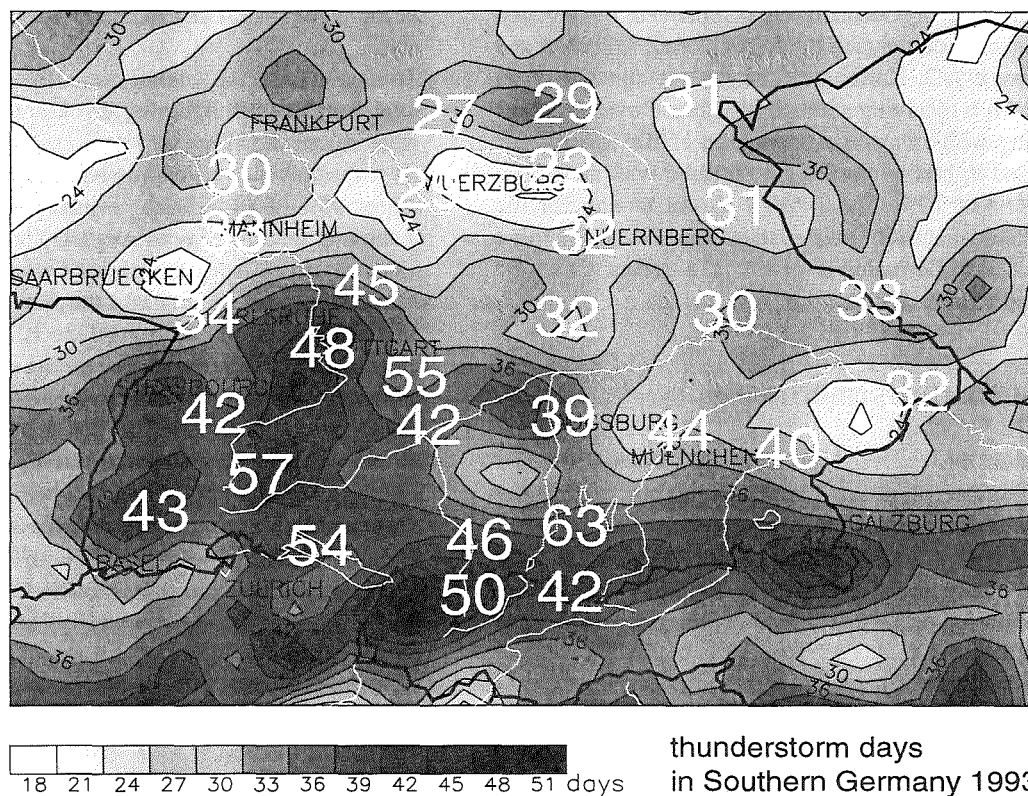


Fig. 2: Thunderstorm days as derived from lightning data (contours) compared with synoptic observations (numbers) for the 1993 year.

In Fig.2 we plotted the contours of equal number of thunderstorm days for the year 1993 as derived from the lightning data together with the number of thunderstorm days counted at selected synoptic stations. The latter data was taken from synoptic weather reports. The mean annual number of thunderstorm days is 29 with an increase of about 10 days from North to South. Maximum values are at about 50 and minimum values about 15. We note that the spatial pattern of thunderstorm days resembles the spatial distribution of lightning. Black Forest, the Prealpine region and some

other mountainous areas can be identified as regions with enhanced thunderstorm frequency. The comparison of the number of thunderdays obtained from lightning data with the synoptic observations demonstrate a satisfying agreement in the spatial structure. Minimum numbers agree better than maximum numbers, as some stations report significantly more thunderstorm days than indicated by the lightning data. This points to an enhanced audible range which is typical for mountain sites, such as the Hohenpeißenberg. On the other hand, observation stations located in cities

frequently report less thunderstorms due to high urban noise. These problems are well known and indicate the superiority of lightning positioning systems for defining thunderstorm days. However, lightning positioning systems also have their limitations: due to the limited detection efficiency, particularly for intracloud lightning, thunderstorms with low lightning activity may remain undetected by the lightning network.

4. STORM TRACKS

The loci of lightning strokes produced by a moving storm define an elongated pattern and indicates the area where the storm passed over. The lightning patterns can be classified into three types:

1. Small circular lightning clusters, which appear almost simultaneously over a large area. Their lifetime is generally shorter than 2 hours, and their spatial extension varies between 10 km and 20 km. These lightning patterns are most likely caused by single-cell storms. They were observed on 37% of all thunderstorm days.
2. Elongated lightning patterns of up to 500 km with only 30 km lateral extension (on 57% of all thunderstorm days). They are related to long-living and propagating storms.

3. Broad lightning fronts caused by fronts or squall lines with a propagation direction normal to the front (6%). A statistical analysis revealed that on over 50% of the thunderstorm days, storm tracks with lengths exceeding 150 km are observed. Quite surprisingly in 15 % of all cases tracks are longer than 400 km. Their dominant propagation direction was found to be from SW to NE with a mean propagation speed of 15 km/h.

ACKNOWLEDGEMENTS

We gratefully acknowledge the provision of the LPATS data by the Bayernwerk AG. This work is supported by the Bayerisches Staatsministerium für Landesentwicklung und Umweltfragen and is part of the Bavarian climate research program BayFORKLIM.

5. REFERENCES

- Finke, U., T. Hauf, 1996: The characteristics of lightning occurrence in southern Germany. *Contr. Atmosph. Phys.* (submitted), available as Report Nr. 49 Inst. f. Physik der Atmosphäre.

THE RESEARCH OF THE POSSIBILITY OF INVERSION LAYERS PIERCING THROUGH BY THE GROWING CONVECTIVE CLOUDS

Y.A.Ekba,

M.D.Atabiyev, R.G.Zakinian

Scientific and Production Geophysical Center, Stavropol, Russia

This work seeks to obtain an analytical expression for the criterion of barrier layers breaking - through. Let's consider the main equation of heat balance

$$dT_i/dz = -\gamma_a - \mathcal{L}(T_i - T) - L/c_p [dQ_i/dz + \mathcal{L}(Q_i - q)] \quad (1)$$

where \mathcal{L} - the involvement coefficient, Q_i and q - steam fractions of total mass in the cloud and ambient air. The rest of the designated symbols are the agreed - upon ones. Assume $\mathcal{L} = \text{const}$ and

$$T(z) = T_c - \gamma(z - z_c), \quad (2)$$

$$q(z) = q_c e^{-b(z-z_c)}, \quad (3)$$

$$Q_i(z) = Q_{ic} e^{-b_i(z-z_c)}. \quad (4)$$

Substituting (2) - (4) into (1) we shall get a solution of the main equation (1)

$$\begin{aligned} T_i(z) - T(z) &= (T_{ic} - T_c) e^{-\mathcal{L}(z-z_c)} - \\ &- (\gamma_a - \gamma)/\mathcal{L} [1 - e^{-\mathcal{L}(z-z_c)}] - \\ &- (L/c_p) Q_{ic} [e^{-b_i(z-z_c)} - e^{-\mathcal{L}(z-z_c)}] + \\ &+ (L/c_p) q_c \frac{\mathcal{L}}{\mathcal{L} - b} [e^{-b(z-z_c)} - e^{-\mathcal{L}(z-z_c)}] \end{aligned} \quad (5)$$

Let's write down (5) for a function of overheating $\Delta T(z) = T_i(z) - T(z)$. Further on we'll consider a particular case $b_i = b$.

Then

$$\begin{aligned} \Delta T(z) &= \Delta_c T e^{-\mathcal{L}(z-z_c)} - \\ &- (\gamma_a - \gamma)/\mathcal{L} [1 - e^{-\mathcal{L}(z-z_c)}] + \\ &+ \Delta_c^* [e^{-b(z-z_c)} - e^{-\mathcal{L}(z-z_c)}] \end{aligned} \quad (6)$$

where there were introduced the designations $\Delta_c T = T_{lc} - T_c$ and

$$\Delta_c^* = L/c_p [q_{\mathcal{L}}/(\mathcal{L} - b) - Q_{ic}]. \quad (7)$$

Let's write down (6) in more convenient form

$$\Delta T(z) = \Delta_c e^{-\mathcal{L}(z-z_c)} + \Delta_c^* e^{-b(z-z_c)} - \Delta_c', \quad (8)$$

where

$$\begin{aligned} \Delta_c' &= (\gamma_a - \gamma)/\mathcal{L}; \\ \Delta_c &= \Delta_c T + \Delta_c' - \Delta_c^*. \end{aligned} \quad (9)$$

Assume slightly elevated inversion

$$T(z) = \begin{cases} T_c - \gamma(z-z_c), & z_c \leq z \leq z_1, \\ T_1 - \Gamma(z-z_1), & z_1 < z < z_2, \\ T_2 - \gamma_1(z-z_2), & z > z_2 \end{cases} \quad (10)$$

Further on, following (Andreyev V. 1975) we write down a function of overheating for all the layers:

$$\Delta T(z) = \Delta_c e^{-\mathcal{L}(z-z_c)} + \Delta_c^* e^{-b(z-z_c)} - \Delta_c',$$

$$z_c < z < z_1, \quad (11)$$

$$\Delta T(z) = \Delta_1 e^{-\mathcal{L}(z-z_1)} + \Delta_1^* e^{-b(z-z_1)} - \Delta_1',$$

$$z_1 < z < z_2, \quad (12)$$

$$\Delta T(z) = \Delta_2 e^{-\mathcal{L}(z-z_2)} + \Delta_2^* e^{-b(z-z_2)} - \Delta_2', \quad z > z_2, \quad (13)$$

where

$$\Delta_1' = \frac{\gamma_a - \Gamma}{\mathcal{L}}; \Delta_1 = \Delta_1 T + \Delta_1' - \Delta_1^*;$$

$$\Delta_1^* = \frac{L}{c_p} [q_1 \frac{\mathcal{L}}{\mathcal{L} - b} - Q_{i1}], \quad (14)$$

$$\Delta_2' = \frac{\gamma_a - \gamma_1}{\mathcal{L}}; \Delta_2 = \Delta_2 T + \Delta_2' - \Delta_2^*;$$

$$\Delta_2^* = \frac{L}{c_p} [q_2 \frac{\mathcal{L}}{\mathcal{L} - b} - Q_{i2}], \quad (15)$$

The level z_T of temperatures equalization is to be found assuming the condition $T_L(z_T) = T(z_T)$ (or $\Delta T(z_T) = 0$)

In order to find the criterion of the inversion layer breaking - through we consider three cases:

1. To have $z_T < z$ it's nesesity to have $\Delta_c T > 0$, and $\Delta_1 T < 0$. From (11) we shall find a critical value of the overheating function needed to breaking-through the low boundary of the inversion layer

$$\begin{aligned} (\Delta_1 T)_{cr1} &= \Delta_c' [e^{\mathcal{L}(z_1-z_c)} - 1] - \\ &- \Delta_c^* [e^{(\mathcal{L}-b)(z_1-z_c)} - 1], \end{aligned} \quad (16)$$

i.e. to have the inversion layer low boundary broken through one should have $\Delta_c T > (\Delta_c T)_{cr1}$.

2. To have $z_1 < z_T < z_2$ it's necessary to have $\Delta_c T > 0$, $\Delta_1 T > 0$, and $\Delta_2 T < 0$. From (12) we shall find the necessary for breaking-through critical value of the overheating function on the low boundary of the inversion layer

$$(\Delta_1 T)_{cr} = \Delta_1' [e^{-\mathcal{L}(z_2 - z_1)} - 1] - \Delta_1^* [e^{(\mathcal{L}-b)(z_2 - z_1)} - 1], \quad (17)$$

i.e. to have the inversion layer upper boundary broken through one should have $\Delta_1 T > (\Delta_1 T)_{cr}$. Or, from (11) and (12) we shall get the broken through criterium for the condensation level

$$\begin{aligned} (\Delta_c T)_{cr2} = & \Delta_{c1} e^{\mathcal{L}(z_1 - z_c)} + \\ & + \Delta_1 e^{\mathcal{L}(z_2 - z_c)} - \\ & - \frac{\mathcal{L}(z_2 - z_c) - b(z_2 - z_1)}{e} - \\ & - \Delta_c^* e^{(\mathcal{L}-b)(z_1 - z_c)} + \Delta_c'', \quad (18) \end{aligned}$$

where

$$\Delta_{c1} = (\Gamma - \gamma) \mathcal{L}^{-1} + \Delta_1^*,$$

$$\Delta_c'' = \Delta_c - \Delta_c' \quad (19)$$

i.e. to have the inversion layer upper boundary broken through one should have the overheating at the condensation level being greater than

the critical one $\Delta_c T > (\Delta_c T)_{cr2}$. In view of $\Delta_c T$ being included into coefficient Δ_c as per (8), one can write down a criterion for a random level z_s . So, to have the inversion layer broken through one should have the overheating at the random level z_s being greater than the critical one

$$\begin{aligned} (\Delta_s T)_{cr} = & (\Delta_c)_{cr} e^{-\mathcal{L}(z_s - z_c)} + \\ & + \Delta_c^* e^{-b(z_s - z_c)} - \Delta_c' \quad (20) \end{aligned}$$

The formula (20) makes it possible to estimate, whether at the result of the artificially initiated crystallization processes (A.I.C.P) then cloud will break through the barrier layer or not. Really, if prior to the A.I.C.P. at the level z_s was $\Delta_s T < (\Delta_s T)_{cr}$, then at the result of A.I.C.P. the cloud is heated by the value of $(\Delta_s T)_{AI}$. In this case the necessary condition for the cloud breaking through the barrier layer is as follows:

$$\Delta_s T + (\Delta_s T)_{AI} > (\Delta_s T)_{cr}, \quad (21)$$

As the thickness and depth of the barrier layer gets increasing the breaking - through probability is getting decreased. Though at the stable stratification ($\Gamma > 0$) and little thickness of the barrier layer the criterion decrease is observed when the ΔH thickness is getting increased, i.e. a barrier layer may "favour breaking-through" (the breaking-through probability is increased).

In the practice of convection parameters forecasting by aerological diagrams overheating at the condensation level is assumed to be equal to $\Delta_c T = 0$. In this case, if $(\Delta_c T)_{cr} > 0$, breaking through the barrier layers is impossible; if $(\Delta_c T)_{cr} < 0$, breaking through the barrier layers is possible. The higher is a cloud at that, the easier is a barrier layer broken through. Thus for example, a cloud of 2 km thickness breaks through an isothermic layer of 400 m

thickness, and a cloud of 3 km thickness breaks a layer of 700 m thickness.

steam fraction of total mass $Q_i(z)$ the criteria of the inversion levels breaking - through were found.

The same results were obtained.

Reference

- Andreyev V., Panchev S. 1975, **Dynamics of atmospheric thermics.** Leningrad, Hydrometeoizdat, 152.

PECULIARITIES OF CONVECTIVE CLOUDINESS ORIGIN IN THE EASTERN DROUGHTY AREAS OF THE STAVROPOL REGION

Ya.A.Ekba,

L.I.Khachaturova

Scientific and Production Geophysical Center, Stavropol, Russia

The eastern areas of the Stavropol region are subject to frequent atmospheric droughts and hot dry winds. Thick cumulonimbus clouds, heavy showers, thunder-storms, hailing are seldom here, although unsteady stratification of the atmosphere is repeated frequently enough. Of 347 synoptical conditions considered in the spring-summer periods of 1989-1994 84 cases fall to the share of intramass instability. However, the probability of precipitation fall-out on these days is little and makes 56 % only (Table 1).

To eliminate the appearing uncertainties it is necessary to find additional individual signs conditioning the development of convective cloudiness at the region under consideration. Originally four types of synoptical processes favourable for thick cumulonimbus cloudiness appearance were marked out (Khachaturova L., Ekba Ya., 1993).

It was ascertained that the main precipitation share is connected with the fronts passing by when their probability gets increased up to 85-96 %. From Table 1 one can also

see that the most frequently the eastern areas of the Stavropol region fall under the influence of the fifth type of a synoptical processes at which ascending convective moves development is out of the question. This type corresponds to anticyclonic circulation and becomes apparent in 88 cases in the period under consideration, i.e. it is a predominant type. Fair with some clouds, dry weather in these periods is determined by the influence of the south-westerly periphery of a low-mobile anticyclone with a centre over Kazakhstan, or by separate closed zones of high pressure (the Azores maximum influence). In the close-to-surface layer south-easterly wind often blows for a long time, barrier layers of isothermy and inversion are formed and the air becomes dried up. At anticyclone stationing for a long period of time atmospheric droughts and hot dry winds emerge.

The analysis of the radiosonding daily data obtained in spring-and-summer periods during five years at the village of Divnoye (a droughty region) proved that frequent dryness of the air near the ground

surface and at various altitudes is a characteristic feature of that area.

As per the data for many years collected in the Region as a whole the air relative humidity maximum falls on a winter period (80-90 %). A gradual but stable abatement is observed by summer: from 70-60 % to 50-45 %. A new elevation of the relative humidity takes place by September end and October (Agriclimatic reference book, 1958).

As for the village of Divnoye, the average 10-days air relative humidity taken by 13-hours term varies from 51 to 38 %, and the monthly average number of days when atmosphere drought and dry hot wind are registered varies from 13 in may and September to 25 in July.

It becomes evident that the air natural dryness considerably hampers cloudiness forming not only under the conditions of anticyclonic circulation, but, evidently, in other synoptical situations as well. During the period under consideration rather often there were observed cases of cloudiness absence at the unsteady stratification when the known critical parameters were on hand (Glazova. O.P., 1968). For the first time the significance of the ambient air humidification factor by the altitudes in the local elevation point was formulated by us as the presence or absence of a moisture carrying layer. On an aerologic diagram the deficit of 1 - 3 °C corresponds to a moisture carrying layer. The further statistically significant relation of convective

precipitation creating cloudiness and the values of meteorologic parameters have been obtained in this work. This relation is represented as charts (dispersion diagrams) plotted based on the three years data collected in v. Divnoye. Use was made of the daily radiosonding during 15-hours observation. The zones where the correlation of precipitation fall out or their absence from the moisture carrying layer is seen especially distinctly turned out to be interesting on fig. 1. Zone A corresponds to the moisture carrying layer thickness of more than 2 km situated at the altitude of up to 5 km from the ground surface. Zone A is supplied with precipitation 93 %. The

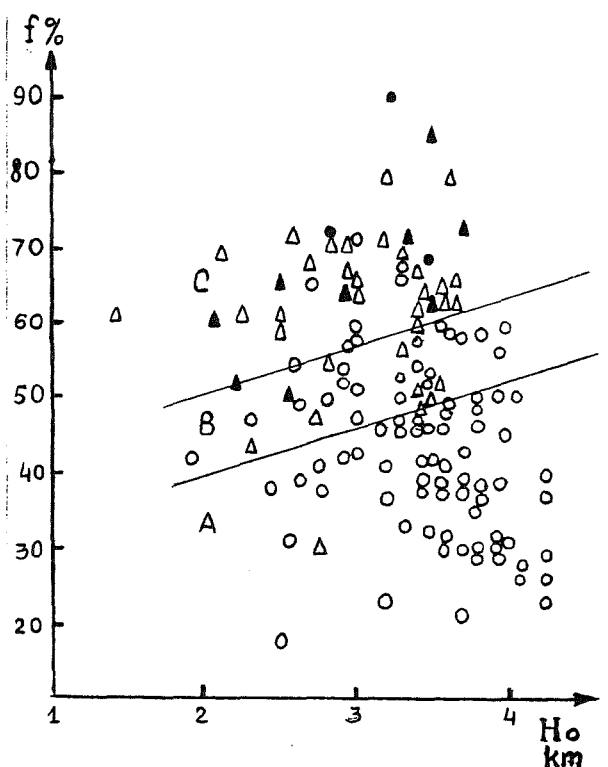


Fig 1. The probability of precipitation fall out depending on the thickness of the moisture carrying layer and on the height of the zero isotherm

most favourable location of the from 2.4 km to 3.5 km. The probability of precipitation absence is rather high under the conditions when a moisture carrying layer is not seen on the aerologic diagram; it makes 82 %. A compound zone C with corresponding thickness of a moisture carrying layer of less than 2 km is singled out; the probability of precipitation fall out here is 61.2 %. As a basis of the further selection assumed the experimental points fetched up at zone C. The value of average relative humidity (f_0) on the isobaric surfaces 850 - 700 - 600 - 500 - 400 hPa and the isotherm height 0°C (H) were taken as predictors fig.2. On the fig.2 there were single out three zones. Zone A corresponds to the situation when the air is so dry that precipitation forming cloudiness is not being created at all. But while f is getting increased the initial probability of inconsiderable precipitation of 1 mm and less appears (zone B). One can surely say about the presence of thick precipitation-forming cloudiness in zone C. Here the probability of precipitation fall out gets increased up to 90 %, and by intensity it may exceed 10 mm.

For the region under consideration there were noted 52 cases with certain characteristics of convection parameters: the condensation level - 2.2 km and less; the convection level - 5.5 km and more; average relative humidity at 850 - 700 - 600 - 500 - 400 hPa - 60 % and more. In 88 % of the cases precipitation fall out took place.

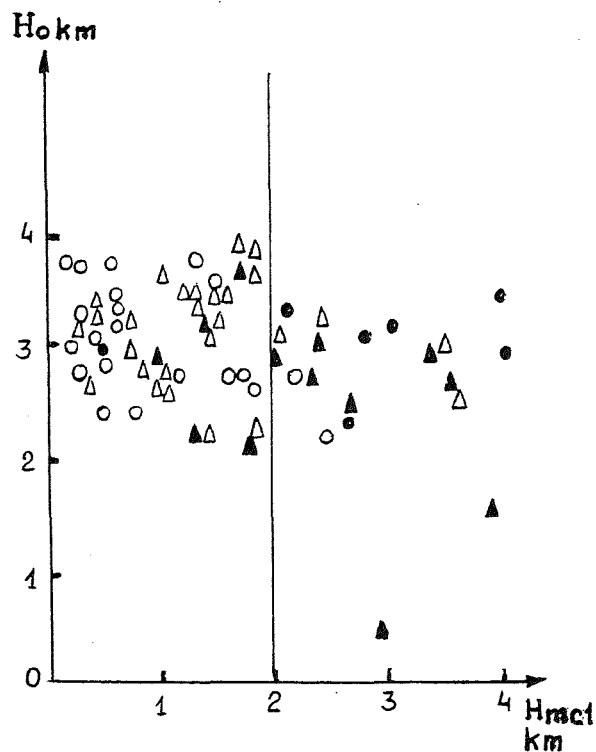


Fig 2. The probability of precipitation fall out depending on the humidity in the middle and low atmosphere and on the height of the zero isotherm

With the mentioned circumstances in view one may conclude that in the droughty areas of the Stavropol region the interrelationship of precipitation - forming cloudiness development and maximum humidification of the ambient air in some local point of elevation is positively certain. Fig. 1 and fig. 2 may be used as weather forecasting ones. The figured parameters can be easily read off from an aerologic diagram. The results are based on the analysis of statistical correlation between the fact of precipitation fall out and the parameter of humidity distribution in the power layer taken as a basis. The conclusions we've come to imbue us

Probability (P) of precipitation fall out at various types of synoptical processes

Type	1989		1990		1991		1992		1993		1994		T	p	no p	P
	p	no p	p	no p	p	no p	p	no p	p	no p	p	no p		processes		%
I	2		3		4		2		11	1	6		29	28	1	96.5
I ^I	3	1	7		5	3	1		17		5	2	44	38	6	86.3
II	2		4	1			4	1	3		4		19	17	2	89.1
II ^I	2		1						3		6	1	13	12	1	92.3
III	12	2	8	1	11	4	9		5	1	7	1	61	52	9	85.2
IV			3	1	1		4						9	8	1	89
V		8		14	1	13		10	1	22		19	88	2	86	3
I.I	4		8	10	10	2	10	6	9	7	6	12	84	47	37	56

no p - without precipitation, p - precipitation, T - Total amount

Type I - front from the west; I^I -subtype - secondary fronts; Type II - front from the north; II^I -subtype - secondary fronts; Type III - front from the south; Type IV - front is related with the Caspian cyclone; Type V - anticyclone; I.I - Intramass Instability.

with certain belief, but nevertheless there are no grounds to neglect such an important thing as an instability factor. The observed peculiarities of thick cumulonimbus cloudiness formation providing for considerable precipitation in the eastern droughty areas of the Stavropol region prove the fact of interrelation between powerful ascending movements and sufficient humidification of the ambient air.

REFERENCES

Agriclimatic reference book on the Stavropol region. 1958 Stavropol, 230.

Khachatourova L.I., Ekba Ya.A., 1993: Synoptical forecasting of the vertically developing clouds at the territory of the Stavropol region. Trudy SF VGI, No 1, 33-40.

SOME INVESTIGATION RESULTS OF AIRFLOW STRUCTURE IN HAILSTORMS

M.Yu. Pashkevich,¹ O.S. Bogomolov,² N.A. Kharakhonova³

¹ Scientific—Production Geophysical Center, Russia, 355005, Stavropol, Abramova str., 2^a

² A.I. Voeikov Main Geophysical Observatory, RUSSIA, 194018, St. Petersburg, Karbysheva str, 7

³ High—Mountain Geophysical Institute, Russia, 360030, Nalchik, Lenin av., 2

During the hail suppression activities on severe convective clouds there appears the necessity to identify the seeded zones and trajectories of dispersion of crystallizing agents in clouds.

In our investigations the special passive radar reflectors (PRR) "Uglen" were used. They are ecologically pure materials and have very slow speed of descend (0.6–0.8 m/s). Such passive impurities do not disturb the air medium and are entrained by air currents very well.

The main difficulty of this work is a problem of selection of radar signal from PRR group on the background of different weather—radar echo. To solve this problem the special polarized method and equipment (Pashkevich et al., 1989) were developed. The method is based on the structure analysis of the real Muller matrix of radar signal. In the papers of Huynen (1970), Kanareikin et al. (1966) the main theoretical bases of given method are given.

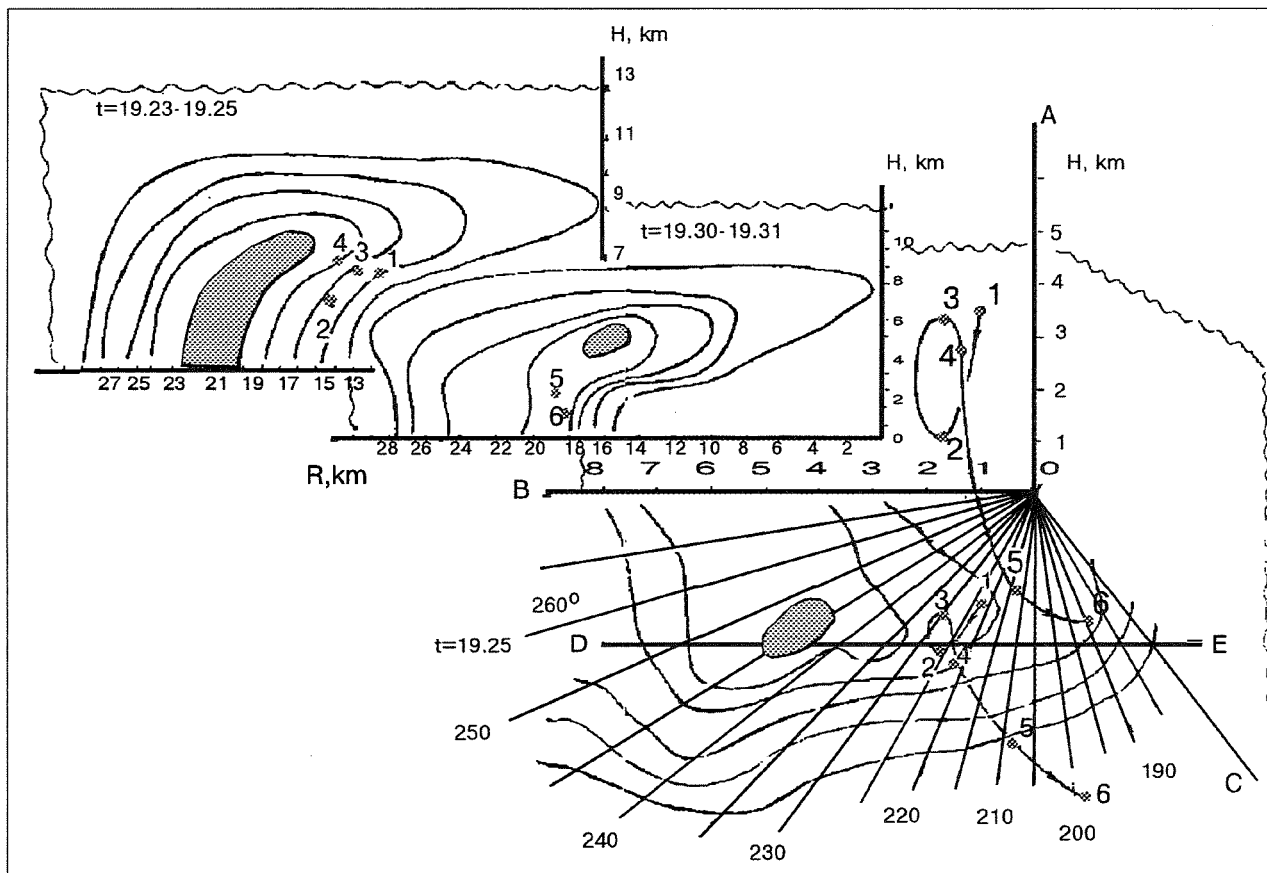


Fig.1. PRR trajectory, constructed in axonometry and on the background of different cross—sections of weather—radar echo.

Besides, during our investigations the main attention was paid to the achievement of the polarized parameters of different types of PRR and hydrometeors as well as their peculiarities. For this the tests were conducted on the dispersion of PRR in free atmosphere. On the basis of many observations of polarized parameters of PRR the relationships typical for these types of chaff were achieved. The values of these relationships approached to the theoretical plots, constructed on the basis of the corresponded Muller matrix. So, the problem of PRR selection on the background of different types of weather-radar echo was reduced to polarization analysis of Muller matrix structures for different chaff.

The anti-hail rockets delivered the chaff into the specified part of cloud. During the experiment 17 successful ejections of chaff were made in different parts of hail cloud with following them by radar polarimetric complex. Five of them were ejected into the near-cloud space, six — into the overhang region, one — into upper part of cloud, four — into reflectivity maximum of weather-radar echo.

Fig.1 shows the chaff trajectory in hail cloud. The main trajectory of chaff is constructed in axonometry. On BOC plane the horizontal structure of weather radar echo for 19.25 LT is shown. On its background the horizontal projection of chaff trajectory is

given. On two vertical cross-sections of weather-radar echo the coordinates of selected volumes of chaff are given in different time moments. The trace of vertical cross-section on the horizontal plane is shown as the straight line DE.

This example points to the complicated cyclic rotation of airflows in the region of overhang (1, 2, 3, 4 points) and during the chaff ejection in the zone of precipitation (5, 6 points) to the right side of cloud movement.

The velocities and trajectories of airflows depend not only on the hailstorm type but also on the stage of cloud development. For the successful cloud seeding it is necessary to follow the agent movement along the chaff trajectory during the seeding.

REFERENCES

Pashkevich M.Yu., Bogomolov O.S., Kapitannikov A.V., Shmagin D.A., 1989: Automated radar complex with changeable polarization of antenna on the basis of radar MRL—5. Pap. VGI., 74, 85—92 (in Russian).

Huynen J.R., 1970: Phenomenological theory of radar targets. Rotterdam, Drukkerij Bronderoffset, N.V., 190.

Kanareikin D.B., Pavlov N.F., Patekhin V.A., 1966: Polarization of radar signals. M., Sov. radio. 439.

3D-ANIMATIONS OF A TORNADO-PRODUCING MULTICELLULAR HAILCLOUD

Willi Schmid and David Bresch

Atmospheric Science ETH, CH-8093 Zurich, Switzerland

1. INTRODUCTION

The most commonly used displays of radar data are two-dimensional. Examples are the PPI (plan position indicator) or the RHI (range-height indicator), see e.g., Rinehart (1992). The computational effort for such displays is certainly smaller than for three-dimensional animations of volume-scan radar data. 3D-animations, however, are an excellent tool to visualize the complex dynamics of cloud systems. One of the first impressive animations of convective clouds was presented by Mohr and Vaughan (1978) at the 18th Conference on Radar Meteorology. After that, continuous progress in the computational speed of computers and in software development led to further advances in the 3D-display and animation of radar data. Maki et al. (1993), for instance, presented coloured displays of radar-measured snowbands, considering radar reflectivity, Doppler velocity and Doppler spectral width. Combined 3D-displays of radar data with terrain have been shown by Doick and Holt (1995). Operational applications of 3D-displays are possible with a software developed by Purcell and Parker (1996) for use with the WSR-88D radar systems.

Good data are required for successful use of 3D-displays and animations. When studying, for instance, the morphology and evolution of severe convective clouds, one needs volume-scan radar data with a time resolution of typically 2-3 min. To obtain such data is not easy. It's even more difficult to obtain volume-scan radar measurements of storms that cause severe damaging events (hail, floods, severe winds, tornadoes) at the ground. Such an opportunity happened on 22 July 1995 in northern Switzerland. On that day an intense convective storm spawned severe hail, damaging wind gusts, and a tornado. The wind damages are discussed by Furger and Schmid (1996). Damaged buildings and aisles of broken trees were reported within a strip of roughly 15 km in length and 1 km in width. One eyewitness observation of a tornado coincided with the location of an intense radar vortex seen at low levels. The storm was in an ideal distance from the radar (30-60 km), and volume-scan measurements were started about 30 min in advance of the damaging wind gusts. Details on the storm evolution in the mesoscale are given by Schiesser et al. (1996), and the evolution of radar vortices is analyzed in Linder and Schmid (1996, this volume).

In this contribution we intend to visualize the evolution of the storm with 3D-animations of radar reflectivity, combined with Doppler vortices and with orography. Several techniques are used, e.g., animation of shaded radar volumes, 3D-stereographic projection, and simulation of an aircraft flying around the hailcloud. The main purpose is to highlight the potential of 3D-animations in the direct recognition of the dynamical processes leading to the formation of the tornadic vortex tube.

2. DATA, HARDWARE AND SOFTWARE

The volume-scan data stem from a C-band Doppler weather radar, located at the ETH in Zurich, Switzerland. The volume scans were repeated in steps of 2.5 min. The data were converted to a cartesian grid with a mesh size of 1 km horizontally and vertically. Radar reflectivity and Doppler velocity are available. More details on the radar and the data processing can be found in Li et al. (1995).

The 3D loops were calculated on a network of SUN-workstations (Sparc 20) using the IDL graphics software package. The volume-rendering of the data is performed by IDL-routines. The terrain is reproduced by a combination of a high-resolution satellite picture with a digital map of the orography (100 m resolution). A graphical user-interface allows the interactive definition of a virtual flight path around the hailcloud. A spline-smoothed path is then used to calculate the images of the loops and to store the images as GIF, TIFF, PICT or EPS-files on disk. The files can then be transferred to various platforms (SUN, MAC, PC) and animated with suitable software (e.g., Quick-time or MPEG). It is also possible to calculate loops to be viewed with *anaglyphic red/green glasses* to fully enjoy the stereographic effect.

3. THE TORNADIC CELL

The number of sector-volume scans is 18, covering the period from 1445 UTC to 1530 UTC on 22 July 1995. Two intense cells (cells 1 and 2 hereafter) were scanned during this time period. The wind damages and the eyewitness observation of the tornado are associated with the growing cell 2. Fig. 1 shows four out of 18 radar

volumes, for 1508, 1511, 1513 and 1516 UTC. The terrain has been blended out in these representations. The shaded radar volume > 45 dBZ is combined with Doppler-identified vortex signatures (circles). Each circle represents the location and size of a vortex signature. Only those signatures are drawn that fulfil the following thresholding criteria: the difference between the neighboring minimum and maximum of Doppler velocity should be larger than 26 m s^{-1} , and the azimuthal shear between the extremes in Doppler velocity should be larger than 0.005 s^{-1} . The viewing angle of the virtual observer is from NE, and the storm propagated towards the virtual observer. The vertical line marks the location of the tornado touchdown (1 eyewitness observer).

The sequence shows the decaying cell 1 at the southern end of the storm system (left of the vertical line), and the growing cell 2 (right of the vertical line). The growth of cell 2 is explosive, and reaches about 1 km/min . Cell 2 is closely associated with the vortex signatures, implying that the updraft is collocated with vertical vorticity. The vortex tube lies within the "weak echo region" (e.g., Browning 1977) at low altitudes, just ahead of the convex-shaped precipitation curtain, but coincides with the overhanging high-intensity echo aloft. Another interesting point is the systematic decrease of the vortex diameter at low altitudes between 1508 and 1513 UTC (compare the mean size of the lowest three circles in Fig. 1a-c). The explanation is a combination of convergence and vortex stretching below the growing cell 2. Such effects are important in the formation of "non-supercell" tornadoes, see e.g. Wakimoto and Wilson (1989). A decrease of the vortex diameter means an increase of vertical vorticity within the vortex, finally leading to the visually observed tornado funnel. The low-level vortex tube probably decreases further in size after 1513 UTC and becomes partly undetectable with the radar at 1516 UTC due to the angular resolution of the radar beam. An extremely small vortex signature is still visible very close to the position of the eyewitness observer (Fig. 1d). It is probable that the tornado passed the location of the observer at that time.

4. CONCLUSIONS

Three-dimensional animations of a hail- and tornadic windstorm are presented. The animations impressively reveal the apparent connection between the explosively growing cell and the evolving vortex tube. Vortex stretching led to a subsequent decrease of the diameter of the vortex at low altitudes, finally culminating in the release of a short-lived tornado.

The advantage of 3D-animations lies in the fact that complex and highly variable dynamic interactions can be explored directly and without the need to analyse and combine a large number of heterogeneous 2D-diagrams. Further work, however, is required to fully utilize the po-

tential of 3D-animations. First, the user interface should allow to use all options of the software in a simple manner and without the need to modify the code of the programs. Second, it is planned to incorporate the display of additional data, such as meteorological data of mesonet-networks, larger-scale radar data, or satellite data. Additional flexibility in the program (e.g., a zoom-in/out function) would then allow to investigate various scales in the same cloud system.

ACKNOWLEDGEMENTS

The authors would like to thank M. Furger, R.A. Houze, Jr., W. Linder, and H.H. Schiesser for their important contributions to this study.

REFERENCES

- Browning, K.A., 1977: The structure and mechanisms of hailstorms. *Meteor. Monogr.*, **16**, Amer. Meteor. Soc., 1-43.
- Doick, J.J., and A.R. Holt, 1995: Combined three dimensional displays of weather radar data with terrain. Preprints, 27th Conf. Radar Meteor., Vail, Amer. Meteor. Soc., 371-372.
- Furger, M., and W. Schmid, 1996: Meso-gamma-scale observations of a severe local storm in the vicinity of PSI. PSI (Paul Scherrer Institute). Annual Report 1995, Annex V General Energy Technology, 4 pp.
- Li, L., W. Schmid, and J. Joss, 1995: Nowcasting of motion and growth of precipitation with radar over a complex orography. *J. Appl. Meteor.*, **34**, 1286-1300.
- Linder, W., and W. Schmid, 1996: A tornadic thunderstorm in Switzerland exhibiting a radar-detectable low-level vortex. Preprints, 12th Int. Conf. on Clouds and Precipitation, Zurich, ICCP and WMO, this volume.
- Maki, M., H. Ohkura, and H. Miyachi, 1993: Analysis of Doppler radar data by three-dimensional computer graphics. Preprints, 26th Conf. Radar Meteor., Norman, Amer. Meteor. Soc., 350a-350c.
- Mohr, C.G. and R.L. Vaughan, 1978: An economical technique for cartesian interpolation and display of reflectivity factor data in three-dimensional space. Preprints, 18th Conf. Radar Meteor., Atlanta, Amer. Meteor. Soc., 490-496.
- Purcell, D.W., and S.S. Parker, 1995: 4D visualisation of WSR-88D data: training and research applications. 27th Conf. Radar Meteor., Vail, Amer. Meteor. Soc., 64-66.
- Rinehart, R.E., 1992: *Radar for Meteorologists*. P.O. Box 6124, Grand Forks, ND 58206-6124, U.S.A., 334.
- Schiesser, H.H., W. Schmid, R.A. Houze, and B. Bauer, 1996: The life cycle of a tornado-producing mesoscale convective system in Northern Switzerland. Preprints, 7th Conf. on Mesoscale processes, Reading, U.K., Amer. Meteor. Soc., to be published.
- Wakimoto, R.M., and J.W. Wilson, 1989: Non-supercell tornadoes. *Mon. Wea. Rev.*, **117**, 1113-1140.

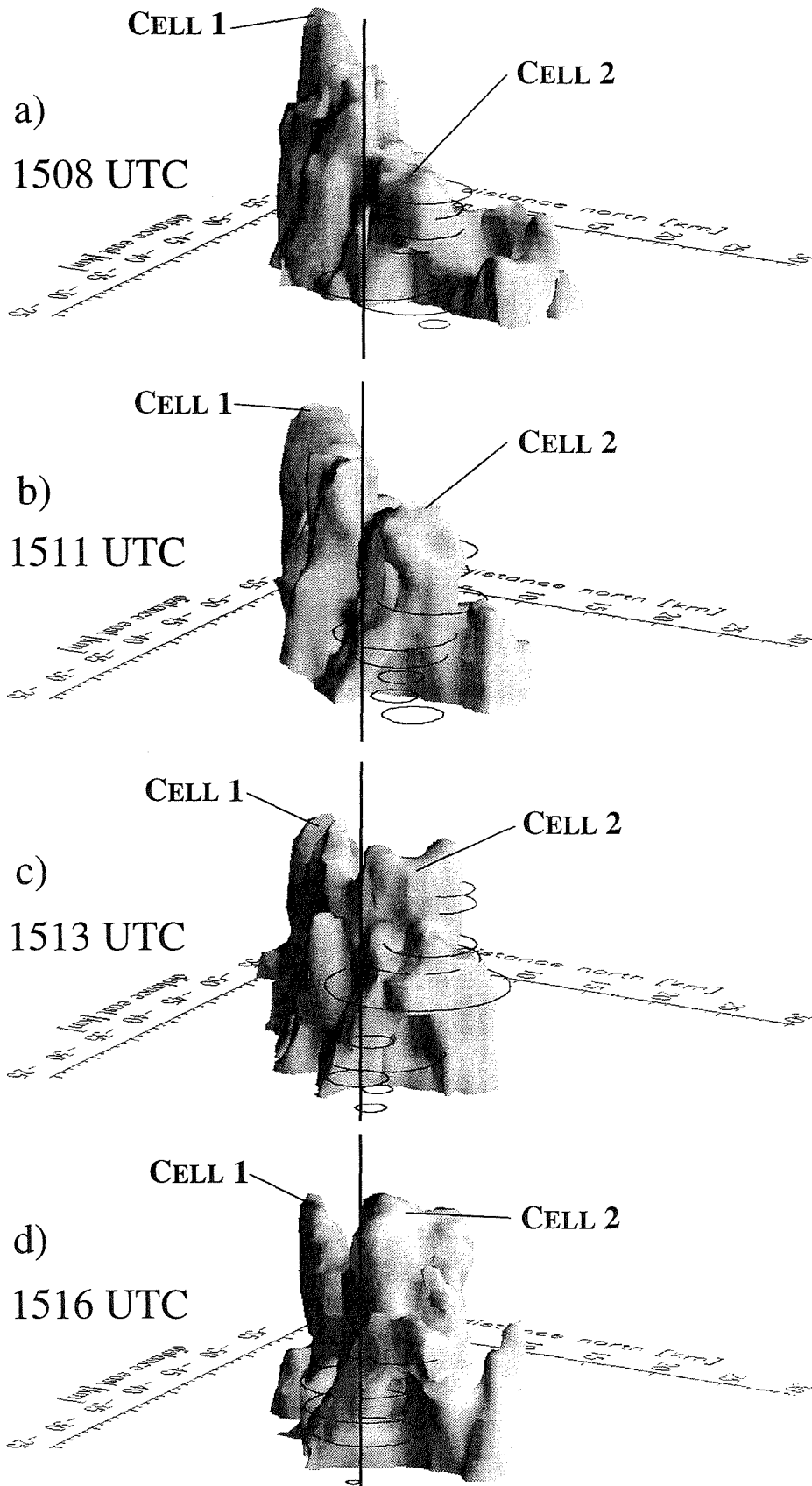


Fig. 1: Shaded radar volumes (45 dBZ) and vortex signatures (circles), for a severe hail- and windstorm from 22 July 1995, at 1508 (a), 1511 (b), 1513 (c), and 1516 UTC (d), respectively. The vertical line marks the location of an eye-witness observer of a tornado. See text for further details.

THE RESULTS OF INVESTIGATING THE CONVECTIVE CLOUD THERMAL REGIME WITH INFRARED THERMOMETER

A. A. Sinkevich

Main Geophysical Observatory, Karbyshev Str. 7, St. Petersburg,
Russia, 194018

1. INTRODUCTION

The measurements of in-cloud air temperature in most investigations are made with immersion type thermometers. Having a lot of advantages such as simplicity and reliability, they also have serious shortcomings owing to water droplets impinging temperature element. When the moistening of temperature element takes place, the measured temperature depends on latent heat effects. It decreases in warm clouds and grows when icing takes place. The errors are rather great and this method of measurement is limited to above freezing temperatures.

A radiometric measurement of in-cloud temperature eliminates many difficulties connected with direct immersion of the thermometer in the airflow, since it does not disturb the air volume being sampled. The IR-radiometers, operating in atmospheric absorption bands (centered at 4.3μ and 14.8μ), were designed during recent years (Albrecht B.A., Cox S.R., Schubert W.H., 1979; Atkinson N.S. et al, 1984; Combs A.C. et al, 1965; Nicholls S. et al, 1988; Lawson R.P. and Rodi A.R., 1992). The aim of the experiments was to investigate the operation of IR-radiometers as compared to immersion type thermometers in order to evaluate the work of these devices in clouds with different water content and concentration of droplets. The results of these investigations show that wetting effect of immersion type thermometers may be rather strong and lead to errors in measurements up to several degrees.

The IR-radiometer which operates in the absorption band of water vapour centered

at 6.3μ was designed by A.A. Sinkevich (Sinkevich A.A., 1979; Sinkevich A.A., 1981). The detailed analysis of IR-radiometer operation was made. The numerous aircraft temperature measurements in intact and seeded clouds which were developing in the north-west of Russia were made (Dovgalyuk Yu.A. et al, 1988; Sinkevich A.A., 1984; Vorobjov B.M. et al, 1984).

2. METHOD AND INSTRUMENTATION

It is known that air temperature can be determined by measurement of radiation emitted from isothermal surface which is practically a horizontal path. The water vapour absorption band centered at 6.3μ was chosen, because it provides great radiation contrast $dr(l,T)/dT$ value at little temperature difference ($r(l,T)$ is the Planks relationship) and also due to small values of cloud and clear-air sample volumes L forming black body radiation. The L values were calculated using published data on atmospheric spectral transmission and on microphysic cloud structure and visible radiance transmission coefficients of clouds. The L values - averaged temperature path - were calculated using the following assumption: the measured radiation equals 99% of black body radiation, consequently the atmospheric transmittance coefficient equals 0.01. Using this assumption, one can determine L values for cloudless atmosphere and clouds. Calculations and experiments show that the effective air path, forming emission measured by radiometer, is as long as several hundred meters to several kilometers (it is a function of humidity and height) for

cloudless atmosphere. The effective air path L for Cu cong varies from 30 to 100m (usually smaller L corresponds to thicker clouds), and from 70 to 170m for Cu hum (Rudneva L.B., Sinkevich A.A., 1981). Radiometer is the optic-electronic device. The optical part of it includes an input window, a chopper, a lens, a band pass filter and an energy receiver. The electronic part includes an alternative current amplifier, a synchronized detector and a direct current amplifier. Periodical calibration of the device is carried out with the help of black body imitator. The method allowing to use cloudless paths of atmosphere as a black body reference has been developed. Radiometer has the following main technical characteristics:

- a) measured temperature range -40-20 C;
 - b) resolved temperature variations are less than 0.1 C;
 - c) angular field of view-2°;
 - d) time response of the device-0.5 sec.
- One of the main methodological problems arising during temperature measurements in clouds, is the problem of divergency of data, obtained with the widely used immersion thermometers and IR-radiometer. To solve this problem, we have carried out experiments on simultaneous temperature measurement in convective clouds with the help of immersion type thermometer, IR-radiometer and ultrasonic thermometer. The analyzed data include 342 simultaneous measurements in clouds without icing and 513 measurements when icing takes place. The results has shown that immersion thermometer "underestimates" the cloud temperature on the average by 2.1 C in comparison with radiometer (aircraft speed was 240km/h). The temperature difference between radiometer

and ultrasonic thermometer equals 0.4 C. When severe icing takes place, the ultrasonic and immersion type thermometers give unreliable results (Zvonarev V.V., Sinkevich A.A., 1991).

3. RESULTS

The analyzed data include the results of aircraft measurements carried out in the north-west of Russia in warm seasons during 1977-1987. More than 1000 clouds were studied.

Synoptic-meteorological conditions were typical for convective clouds development. Most of the experiments (more than 70%) were carried out on the peripheral parts of cyclones with cold fronts and occluded fronts. Thickness of investigated convective clouds usually was less than 4-5 km. Main results of convective clouds thermal characteristics measurements are presented in Table 1.

Table 1. The averaged overheating \overline{DT} of convective clouds, and the maximum measured

positive T and negative T cloud temperature values in respect to the temperature of the ambient cloudless air.

Cloud type	Height over cloud base, km	Living stage	\overline{DT} C	T^+ C	T^- C
Cu hum-	-	develop.	0.4	2.9	-1.2
Cu med	-	stab.	0.3	0.9	-1.6
	-	dissip.	0.0	0.6	-1.2
Cu cong	0<h<1	develop.	0.2	2.7	-1.3
		stab.	0.1	2.1	-1.7
		dissip.	-0.1	4.1	-1.7
	1<h<2	develop.	0.5	2.5	-1.1
		stab.	0.3	3.0	-2.7
		dissip.	-0.1	1.6	-1.9
	2<h<3	develop.	0.7	4.1	-0.9
		stab.	0.4	4.0	-3.7
		dissip.	0.2	1.9	-1.5
	3<h<4	develop.	0.7	2.8	-0.3
Cb	upper half	develop.	0.9	2.6	-0.5
		stab.	0.3	1.2	-0.8
		dissip.	0.2	2.7	-1.1

The comparison of small vertical thickness convective clouds (Cu-hum-Cu med) average overheating shows that the maximum

value of \overline{DT} is observed in developing clouds

(0.4 C) and the minimum (0.0 C) - in dissipating clouds. The maximum temperature differences between cloud and ambient air are rather great and constitute on the average

1.0 C in Cu hum-Cu med in developing stage.

More than 50% of T lies within the limits 0.4-1.5 C. The maximum values exceed 2 C. In

dissipating stage T decreases in comparison with developing and stabilization stages. The

T values do not exceed 0.6 C in more than 80% of cases. The negative temperature differences between cloud and ambient air increase and reach on the average -0.5 C. The recurrence of negative DT is equal to 50%.

The value of averaged overheating DT and

T for developing Cu cong depends on the height over the cloud base and reaches maximum in our experiments on the height of 2-3 km over cloud base

($DT=0.7$ C, $T=1.5$ C). Considerable overheating is observed there; for example, in more than

10% of cases T exceeds 2.0 C. The maximum exceeding of cloud temperature in comparison with the ambient air was registered there.

$T=4.1$ C. 80% of cloud length has the temperature greater than the average temperature of ambient air. There is no

increase of DT and T at the height of 3-4 km over the cloud base. It can be explained by the fact, that measurements were made in most cases in the upper parts of Cu cong, while the development of the latter were limited by intercepting layers. The minimum average

values of T were observed in the lower part

of the cloud ($T=-0.5$) at the height 0-1 km over the cloud base.

Cumulonimbus clouds, being in developing or stabilization stages, have $DT>0$ in more than 85% of cases (only the upper part of cloud was examined). The developing clouds practically have no zones where temperature is lower than that of the ambient air. The maximum temperature excesses are great.

$T>1.0$ C in 45% of cases. The cloud

overheating DT depends on cloud living stage and decreases during the clouds transition from developing to dissipating stage

($DT=0.9$ C for developing clouds and $DT=0.2$ C for dissipating clouds). One can observe the

decrease of DT and T by the factor of 2-3 in stabilization stage in comparison with developing. Positive overheating values

($DT=0.2$ C) for dissipating clouds may be the result of crystallization processes going on in cloud.

The structure of convective clouds is rather inhomogeneous. The analysis of Cu cong temperature fluctuations shows that the average length of thermal fluctuations is 0.1-0.4 km. The closest relationship is observed between temperature fluctuations and vertical movement velocities. One can observe temperature increase in updrafts in comparison with neighboring parts of the cloud. Practically, there is no correlation between temperature and liquid-water content fluctuations.

4. CONCLUSIONS

1. The airborne IR-radiometer, which operates in the absorption band of water vapour centered at 6.3μ and provides temperature measurements without direct contact with airflow, was developed in Main Geophysical Observatory.

2. The comparison of temperature measured in convective clouds with IR-radiometer and immersion type thermometer shows, that the latter "underestimates" the cloud temperature

on the average by 2.1 C.

3. When severe icing takes place only IR-radiometer guarantees reliable results.

4. Convective clouds, developing in the north-western part of Russia, have the greater temperature than the ambient air at the same height. The maximum overheating is observed in Cb and equals on the average

0.9 C. One can observe the temperature decrease in decaying clouds.

5. The range of temperature differences between clouds and ambient air is rather great. The maximum temperature excess may

often reach 2-4 °C in developing convective clouds, while in decaying clouds the temperature decrease may be 1-3 °C.

5. REFERENCES

1. Albrecht B.A., Cox S.R., Schubert W.H., 1979: Radiometric Measurements of in Cloud Temperature Fluctuations. J. Appl. Met. 18, N6, 1066-1071.
2. Atkinson N.C. et al., 1984: A Radiation Thermometer for Cloud Temperature Measurement from Aircraft. Proceedings 9 International Cloud Physics Conference. Tallinn, VI, 811-813.
3. Combs A.C. et al., 1965: Application of Infrared Radiometers to Meteorology. J. Appl. Met. V4, N2, 253-262.
4. Dovgaljuk J.A. et al., 1988: Comprehensive Research of Convective Cloud Dynamics from the Data of Aircraft and Numerical Experiments. 10 International Cloud Physics Conference, Homburg, V2, 618-620.
5. Lawson, R.P. and Rodi, A.R., 1992: A new airborne thermometer for atmospheric and cloud physics research. Part 1: Design and preliminary flight tests. J. of Atm. and Oceanic echnology, 9, N6, 556-574.
6. Nicholls S. et al., 1988: A Comparison of Radiometric and Immersion Temperature Measurements in Water Clouds. 10 International Cloud Physics Conference, VI, 322-324.
7. Rudneva L.B., Sinkevich A.A., 1981: Estimation of Geometrical Path, Forming Black Body Emission in Different Types of Clouds. Trudy MGO, N448, 76-85.
8. Sinkevich A.A., 1984: Investigation of Cu Clouds Thermal Characteristics with IR-Radiometer. Meteorology and Climatology. N1, 40-46.
9. Sinkevich A.A., 1979: The Using of IR-Radiometer for Thermal Cloud Characteristics Measuring. Trudy MGO, N420, 105-112.
10. Sinkevich A.A., 1981: On the Analysis of IR-Radiometer Operation in Measuring Temperature of Cloudless and Cloud Atmosphere. Trudy MGO, N439, 93-102.
11. Vorobjov B.M. et al., 1984: Experimental and Theoretical Studies of the Dynamics and Microphysics of Convective Clouds. Proceedings of the 9 International Cloud Physics Conference. Tallinn, 1984, V2, 477-479.
12. Zvonarev V.V., Sinkevich A.A., 1991: Aircraft Methods of Temperature Measuring in Clouds. Trudy MGO, N534, 24-33.

Structures of Meandering Band Clouds Observed by Dual-Polarization Doppler Radar during the BASE Period in Canada

Yoshio Asuma¹, Katsuhiro Kikuchi¹, Hiroshi Uyeda¹, Taisuke Shimamura¹, Soshi Iwata¹, Ryuji Kimura², Kazuhisa Tsuboki², Ronald E. Stewart³, David R. Hudak⁴, Ed Hudson⁵ and G.W. Kent Moore⁶

¹Graduate School of Sciences, Hokkaido University, Sapporo 060, Japan

²Ocean Research Institute, University of Tokyo, Tokyo 164, Japan

³Atmospheric Environment Service, Downsview, Ont. M3H 5T4, Canada

⁴Atmospheric Environment Service, King City, Ont. L7B 1A3, Canada

⁵Environment Canada, Edmonton, Alb. T6B 2X3, Canada

⁶University of Toronto, Ont. M5S 1A7, Canada

1. Introduction

The BASE (Beaufort and Arctic Storms Experiment) Project was carried out over the southern Beaufort Sea and Mackenzie Delta in Northwest Territories (N.W.T.), Canada, during the fall of 1994. The purpose for the BASE project was to better understand the weather systems in the region and the climate impact of these weather systems. The synoptic features for this area and period were summarized by Hudak et al. (1995). The BASE project was mainly organized by the Atmospheric Environment Service (AES) in Canada and the University of Toronto. Additionally, Hokkaido University in Japan, the National Center for Atmospheric Research (NCAR) in USA and the Central Aerological Observatory in Russia also joined this project.

X-band dual-polarization Doppler radar observations were conducted by Hokkaido University, Japan, at Tuktoyaktuk, N.W.T., Canada. Meandering band clouds were observed several times over the Beaufort Sea by the radar. A Convair 580 research aircraft of National Research Council, Canada, observed

synchronously with radar for one of cases.

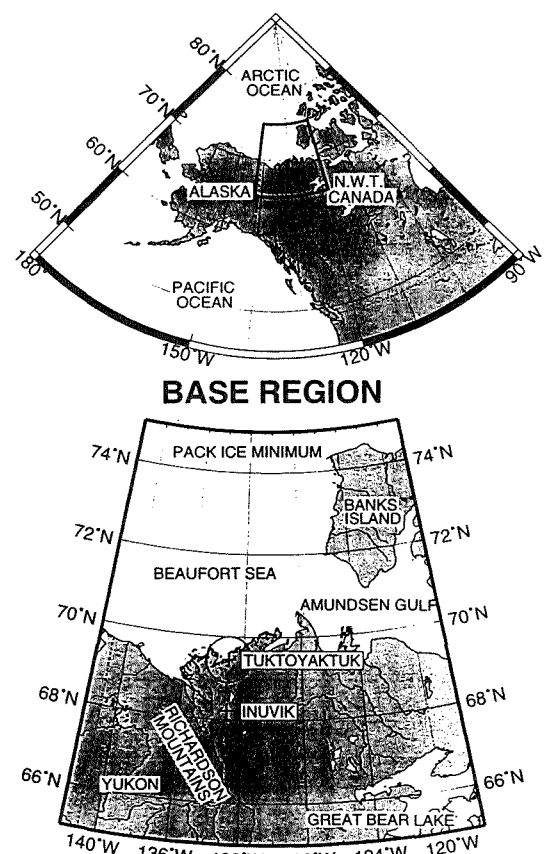


Fig. 1 Maps of BASE area. Dual-polarization Doppler radar was installed at Tuktoyaktuk. The range of the radar (60km) is indicated with a circle.

2. Data

The maps of the BASE area were shown in Fig. 1. The town of Tuktoyaktuk, installed the radar, is located on the north end of Mackenzie Delta. The radar system was set up at the seashore of Beaufort Sea. The radar specifications are listed in Table 1. The upper air soundings were conducted at Tuktoyaktuk and Inuvik.

3. Results

Figure 2 shows the schematic sketch of NOAA channel 2 of 18:11UTC on Sep. 26, 1994. Zonally extended open sea was observed along the northern coastline of Alaska. Cold air outbreaks from the inland of Alaska and the sea ice field in the Arctic Sea dominated. The convergence zone which originated between both outbreaks was recognized over the open sea. The band clouds in the convergence zone were organized over the open sea.

Table 1 Specifications of the dual-polarization Doppler radar.

Specifications	Dual-Polarization Mode	Doppler Mode
Frequency	9410 MHz	9410 MHz
Peak Power	40 kW	40 kW
Antenna Diameter	1.2 m	1.2 m
Antenna Rotation	4 r.p.m.	1 r.p.m.
Beam Width	2.0°	2.0°
Gain	38 dB	38 dB
Sidelobe Level	21 dB	21 dB
P.R.F.	750 p.p.s.	1500 p.p.s.
Pulse Width	0.8 μ m	0.4 μ m
Maximum Range	30 km	60 km

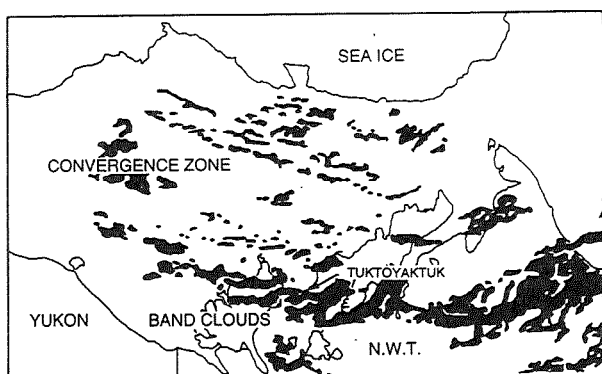


Fig. 2 Schematic illustration of NOAA channel 2 of 18:11UTC on Sep. 26, 1994.

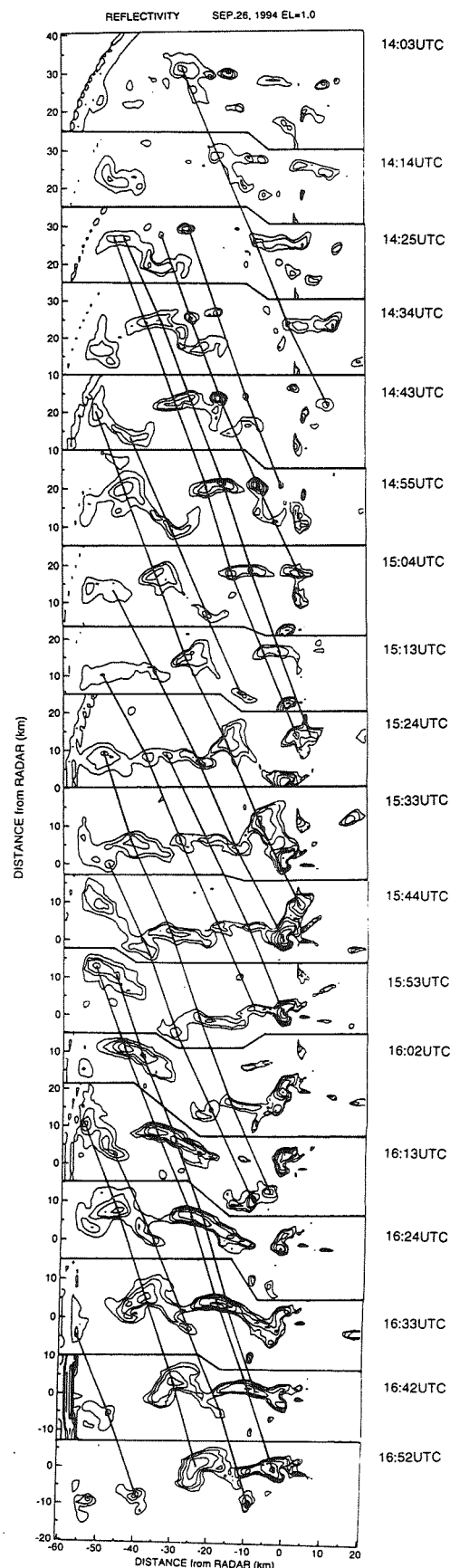


Fig. 3 Time variation of radar echoes at about 10 minute intervals from 14:03 to 16:52 on Sep. 26, 1994. The contour lines are drawn from 20dBZ at 2dBZ intervals.

Band shaped echoes appeared one after another at about three hour intervals in the radar observations. These band shaped echoes showed a meandering pattern with the strong precipitation cores (cells). The time variation of meandering radar echoes is shown in Fig. 3 at about 10 minute intervals. The corresponding precipitation cores are linked with lines in the figure. The meandering pattern and the precipitation cores maintained almost constant speeds from east to west and the speed of the precipitation cores was almost the same as that of the meandering pattern.

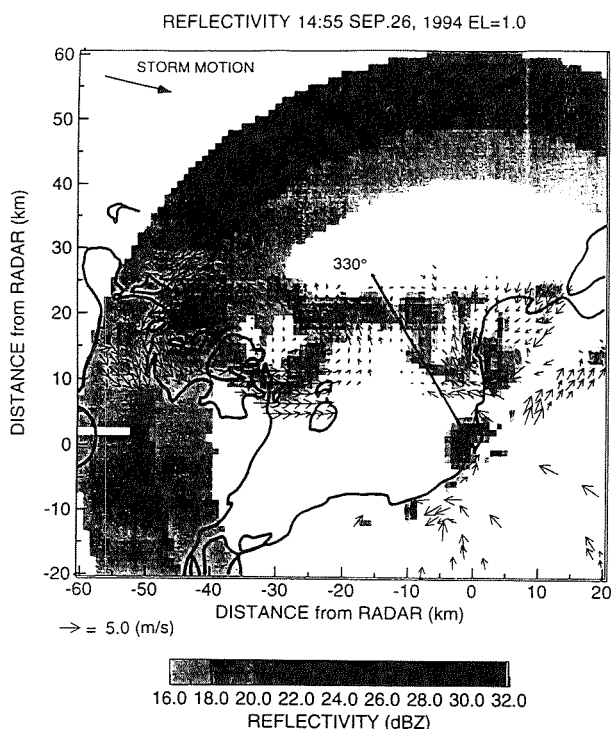
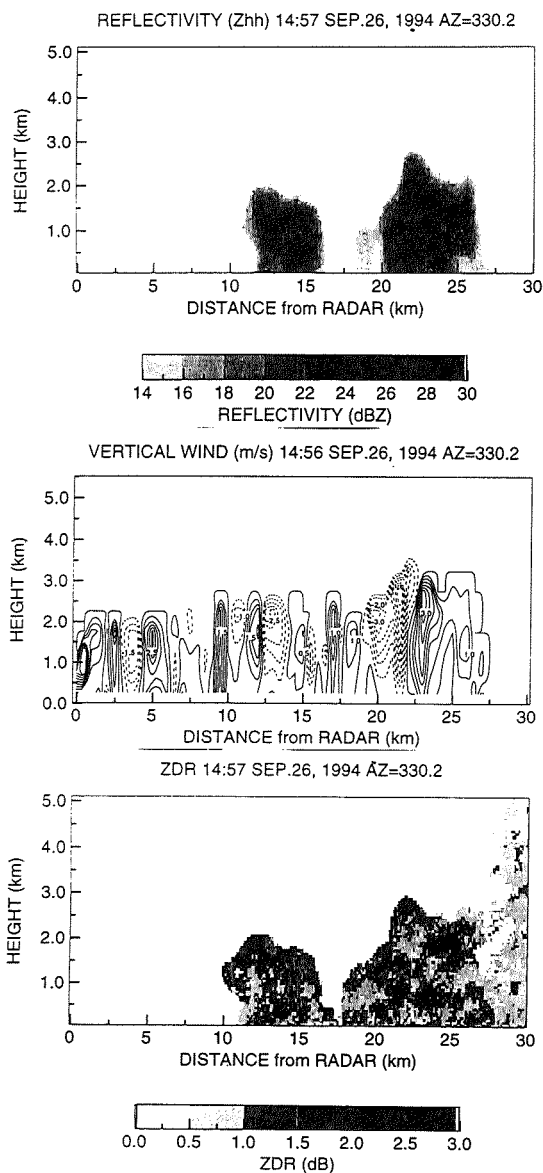


Fig. 4 PPI display of the radar reflectivity and storm relative horizontal wind speed calculated by TVAD. The line from radar site indicates the azimuth direction of Fig. 5.

Fig. 5 RHI displays of the radar reflectivity, vertical wind calculated from the two dimensional continuity and ZDR of 330.2 ° in azimuth of Fig. 4 at 14:57 on Sep. 26, 1994

When the echoes moved over the radar site, drastic changes of wind and temperature were recorded at the surface. An example of PPI radar echo, which is superimposed with storm relative horizontal wind speed calculated by TVAD (Tangential Velocity Assumed Display: Takahashi et al., 1991), is shown in Fig. 4. A strong horizontal wind shear was identified in the band cloud. Rotational components were also identified with the meandering structure. It was surmised, therefore, that the meandering band clouds were formed by the strong horizontal wind shear front associated with the cold air outbreaks over the open sea.



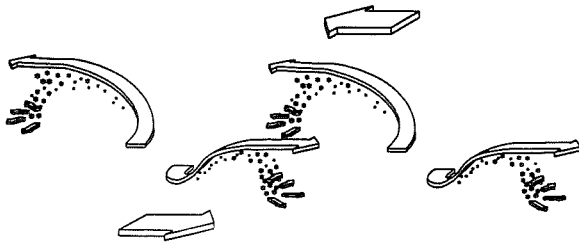


Fig. 6 Schematic illustration of the structure of the meandering band clouds.

The RHI displays of radar reflectivity, vertical velocity and ZDR are shown in Fig. 5. The azimuth direction is indicated by a line in Fig. 4. Strong radar reflectivity tilted outward and corresponded to the updraft. And the value of ZDR indicated around 1dB. It was inferred, therefore, that the stronger reflectivities are composed of larger snowflakes. This was confirmed by video camera ground observations for the precipitation particles.

Based on the observational results, the meandering band cloud is illustrated schematically in Fig. 6. The meandering band cloud transports the momentum flux horizontally across the shear front and transports the heat flux vertically from the open sea surface.

4. Conclusions

An X-band dual-polarization Doppler radar observations were carried out at Tuktoyaktuk, N.W.T., Canada, during the BASE period. Characteristic meandering band clouds were observed by the radar. These band clouds formed at the horizontal wind shear front under the cold air outbreaks between the inland of Alaska and the sea ice field in the Arctic Sea. These meandering band clouds transports the momentum flux horizontally across the shear front and the heat flux vertically from the open sea surface.

References

- Hudak, D.R., R.E. Stewart, G.W.K. Moore and E.T. Hudson, 1995: Synoptic Considerations of Storms in the Southern Beaufort Sea. - Expectations for BASE. Proc. 4th Conf. Polar Meteor. Oceanogr., Dallas, 234-237.
- Takahashi, N., H. Uyeda and K. Kikuchi, 1991: A method to describe the fluctuation and discontinuity of horizontal wind field by single Doppler radar. Proc. 25th Int'l Conf. Radar Meteor., Paris, 642-645.

APPLICATION OF NUMERICAL MODELS FOR TO STUDY THE CLOUD DYNAMICS AND STRUCTURE OF THE WINTER FRONTAL RAINBANDS

Anne M. Pirnach, UHRI, Kiev, Ukraine

1. INTRODUCTION

This work continues investigation of winter cloud systems that have been subject to measurement and observation in the steppe part of Ukraine. The two- and three-dimensional diagnostic and prognostic models of the real fronts and their clouds were used for simulation.

Two occluded frontal cloud systems will be considered below. They passed over Meteorological Proving Ground of Ukrainian Hydrometeorological Institute (MPG) on December 7, 1988 (named Case 1) and February 21, 1989 (named Case 2).

2. NUMERICAL SIMULATION OF OCCLUDED FRONTAL SYSTEMS

Two- and three-dimensional models were constructed to study the evolution of frontal rainbands and interaction between the dynamics and cloud microphysics evolution features (see Pirnach, 1984, 1987, Pirnach and Krakovskaya, 1994).

Two-dimensional models with nested (or stretched) grids were constructed to simulate large and small meso-scale structure of atmospheric fronts, condition of cloud and precipitation formation, their natural and artificially modified development (Pirnach, 1984, Krakovskaya, Pirnach and Suhinsky 1994).

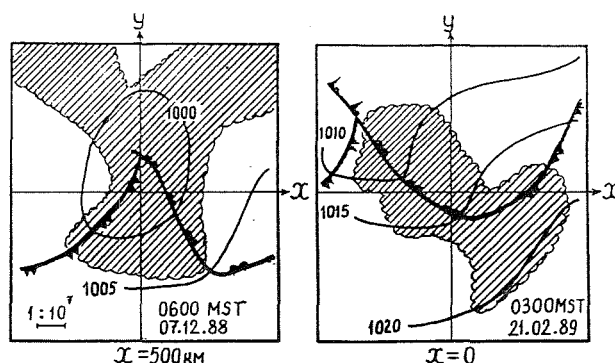


Fig.1. Schematic illustration of the surface pressure and rainbands into frontal systems.

2.1. Synoptic situations and initial conditions

The serial rawinsondes and air flight data were used to construct the diagnostic and prognostic models of above pointed systems. These models were used to construct the initial data fields for the below considered prognostic models. Some results of diagnostic modeling were cited in Krakovskaya, Pirnach and Suhinsky, 1994.

The constructed diagnostic models exhibited intricate and inhomogeneous structure. Every simulated frontal system included a few hyperbaroclinic zones, convective cells, broad moist-labile zones indicating on presence of embedded convection. Both frontal cloud systems, especially in Case 2, were in mature to decaying stage.

From synoptic maps cyclones were moving over Ukraine southeastward on December 7, 1988 and northeastward on February 21, 1989. The systems all warm, cold and occluded fronts accompanied it.

Fig.1 shows the pressure and rainbands situation in frontal systems. There is x-axis directed in a moving frontal system direction. The central point is MPG. The initial coordinate point was located in MPG in Case 2. In Case 1 it was replaced to $x = 500$ km. In Case 1 frontal systems moving with azimuth of 230, in Case 2 it was 300. Its velocities were 12 cm/s. The simulated frontal systems had different stages of development. In Case 2 it was more in decaying stage. In Case 1 an occluding of cyclone was just beginning and rainband existed during next 12 h yet.

2.2. Numerical simulation of the rainband evolution. Case 1.

The real rainband was situated (see Fig.1) in initial time between cold and warm fronts. The simulation is found that next 6h over MPG the cold and warm branch of occluded front coincided. Ahead the occluded front new cold hyper-baroclinic zones (HBZ) appeared. The nearest to occluded front cold HBZ likely presented the primary cold front. The next 6 h (see $t = 12$ h, Fig.2) the surge of cold front has appeared in occlusion and a new HBZ has formed.

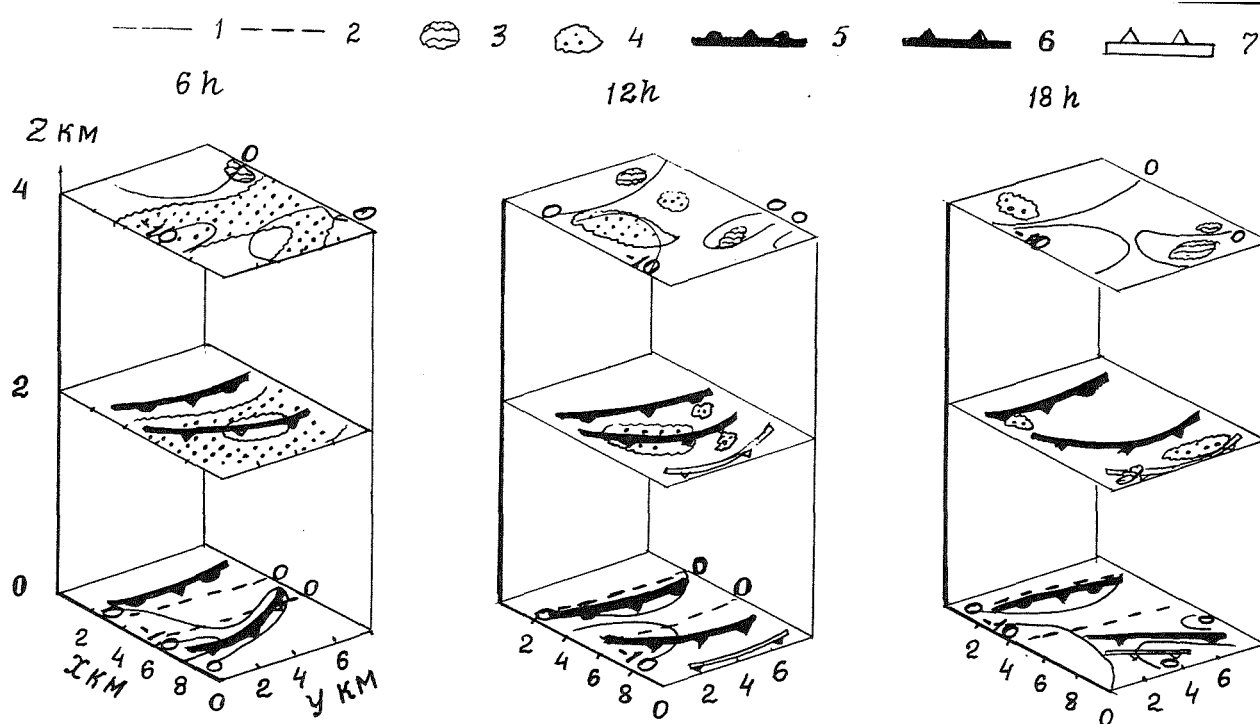


Fig.2. Horizontal sections through simulated frontal systems at different t . Case 1.

1) Pressure, P -1000 mb at $z=0$ and P -600 mb at $z=4$ km; 2) temperature, T ($^{\circ}\text{C}$); 3) $Ri < 1$; 4) clouds; 5) occluded front; 6) cold front; 7) HBZ.

The rainband replaced to warm front and narrowed. At $t = 6\text{h}$ it was located ahead occluded front and connected with the nearest HBZ (primary cold front). During next time the rainband continued narrowed and decayed after $t = 12\text{h}$.

The means of Richardson number, Ri , shows that likely mechanism of forming and existence such rainbands is the baroclinic effects. The zones of $Ri < 1$ were identified into separate areas of rainbands at their decaying. There is symmetric and other types of instability could to exist (after Shakina, 1990). They likely forced forming to embedded convective cells and convective rainbands.

In this run the space steps x_s and y_s were 50 and 100 km, respectively. They let to indicate the spread rainband only. It consisted of several rainbands of different size and structure (e.g., Houze and Hobbs 1982, Hobbs 1981). Investigation of these rainbands forced to construct the model with nested and stretched grids. It was more necessary for such modeling in Case 2. There have been indicated more dramatic synoptic conditions.

2.3. Numerical simulation of the embedded convective cell. Case 2

The Fig.1 shows the occluded frontal systems at 0300 MST (Moscow Standard Time) on February 21, 1989 (Case 2). Its front line has a wavelike structure on the ground. Its rainband was lined along a warm branch

of frontal line and was located in pressure trough. The cumulus cells appeared in it frequently and heavy rainfall is often caused by hugely developed cumulus clouds such as cumulonimbus or its ensemble.

Two-dimensional diagnostic model of frontal clouds, their prognostic micro-physical model with nested and stretched grids, three-dimensional diagnostic and

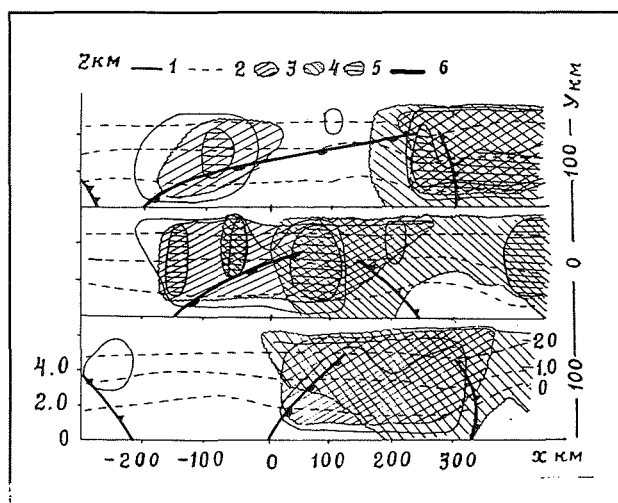


Fig.3. Vertical cross-section through simulated occluded front at $t = 2\text{h}$ and different y . Case 2. 1) Updraft motion, $w = 1\text{ cm/s}$; 2) temperature, T ($^{\circ}\text{C}$); 3) $q_w > 0.01\text{ g/kg}$; 4) $q_i > 0.01\text{ g/kg}$; 5) $w > 10\text{ cm/s}$; 6) front surface sections.

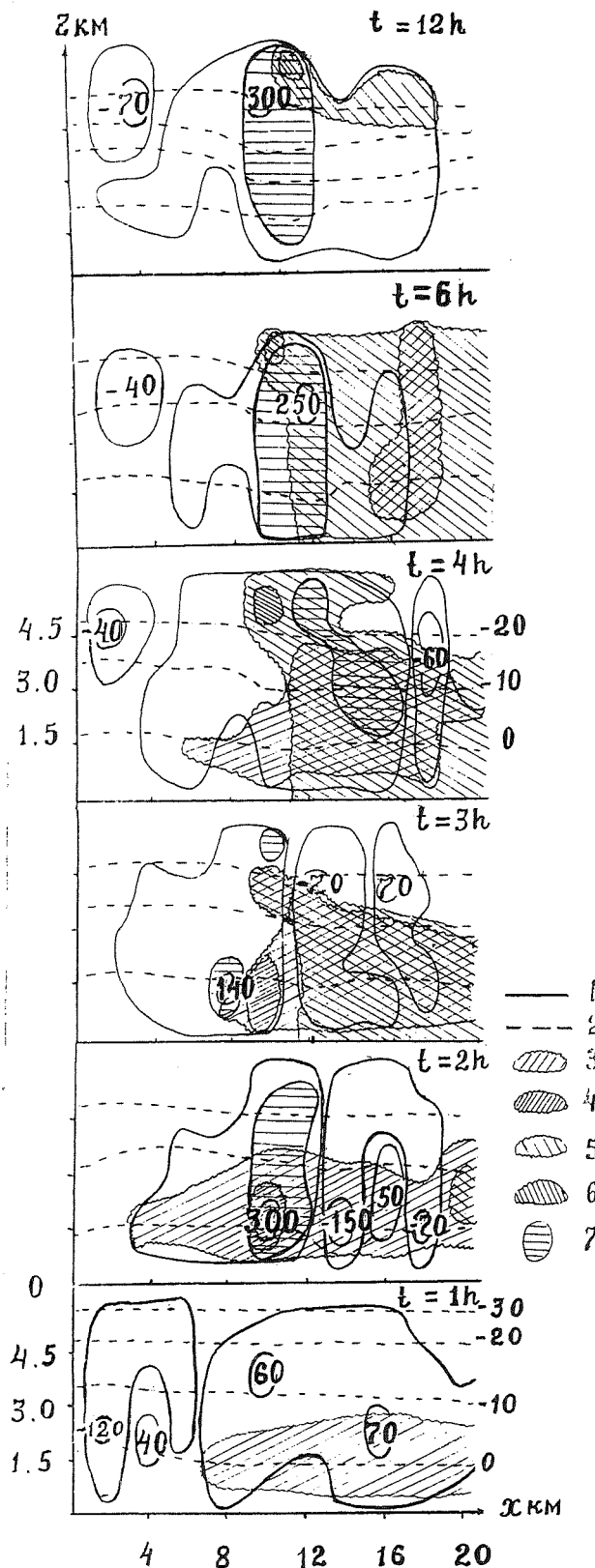


Fig.4. Vertical sections of convective cell at various t . 1) Vertical velocity, $w = 10$ cm/s; 2) temperature, $T(^{\circ}\text{C})$; 3) $q_w > 0.01$ g/kg; 4) $q_w > 1$ g/kg; 5) $q_i > 0.01$ g/kg; 6) $q_i > 1$ g/kg; 7) $w > 1$ m/s.

prognostic models were used to study of the meso- and microstructure of atmospheric fronts, condition of cloud and precipitation formation and embedded convective cell evolution. Space step in nested grid was $x_s = 2$ km and in stretched grid it was 100 km. Three-dimensional modeling was carried out with $x_s = 50$ km, $y_s = 50$ km. The dynamical and microphysical framework of a convective cell used in this study is based on the two-dimensional cloud model developed in Pirnach, 1984.

The vertical cross-sections in normal to a main wind direction were presented in Fig. 3. It was computed with aid 3-D model (Pirnach, 1987). The initial data for this run were computed by 3-D diagnostic model (Palamarchuk and Pirnach, 1992). The simulated rainbands at $t = 2$ h very like to rainbands presented in Fig.1. The mesoscale models smoothed several inhomogenities such as convective cells and small cloudiness bands, but the cores of highest updrafts and heavy mixed clouds indicate on their presence. In Fig. 3 at $y=0$ was found three such cores. The biggest one was found at $x>0$. The updraft reached of 30 cm/s in it.

The using of the nested grids have helped to identify the convective cell in the core at $10 < x < 12$ km. This cell was one strong updraft of 4 km dimension (see Fig.4). In next time it developed in convective cell. Especially dramatic situation was found at $t = 2$ h, $10 < x < 14$, $1 < z < 2$ km. In this time the updrafts have reached 3.3 m/s. Ahead updraft region has appeared downdraft branch. The peak of downdraft was -1.7 m/s. The highest updrafts, downdrafts and their horizontal gradients and vertical wind shear of > 5 m/s/km could to force the vortex features. Appearing the small ice concentration (less 1/g) in the highest liquid water

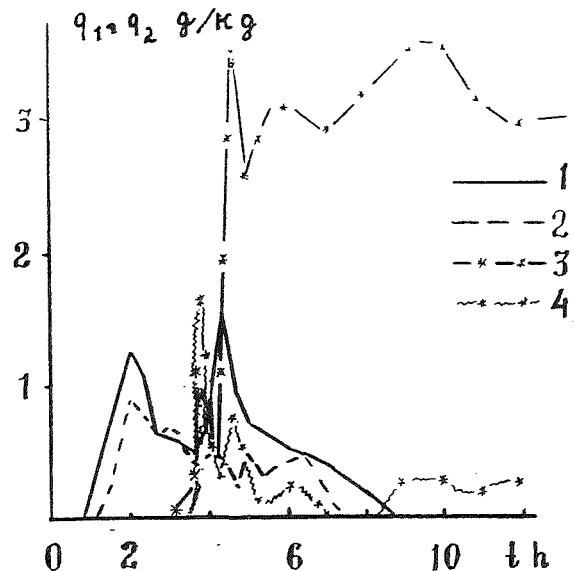


Fig.5. The cloud microphysics evolution in convective cell. 1) the z -highest liquid water content means at $x = 10$ km; 2) the same at $x = 12$ km; 3) the z -highest ice water content means at $x = 10$ km; 4) the same at $x = 12$ km.

content zones with water content, q_w , reaching 1.3 g/kg could to force the falling of hail, etc.

Modeling indicated the highest water content, $q_w > 1.6$ g/kg at $t = 4h20'$ over 1.5 km and highest ice content $q_i > 3.5$ g/kg at $t = 4h40'$ over 5 km (see Figs. 4 and 5). The ice concentration in this region indicated of >10 l/g. In this time the highest precipitation rate was computed. It was of 1.8 mm/h. In environment it was one degree less.

At $t=6$ h highest updraft replaced in the cloud top. The cloud crystallized, mixing layers disappeared and precipitation stopped. The ice concentration reached 10^4 /g. There was typical seeder zone but absence of feeder zones has discontinued development of convective cloud and precipitation.

3. CONCLUSION

Two- and three-dimension diagnostic and prognostic numerical models of two occluded winter frontal systems passing over Ukraine were constructed. Two-dimension model with nested and stretched grids was used to simulate of convective cell embedded in stratiform cloudiness. The some results of study are as follows:

The structure of simulated atmospheric fronts in occluded cyclones exhibited many features described earlier for other regions and other authors in midlatitudes and apparently has a common character: hyperbaroclinic zones of different mesoscale, small and large mesoscale rainbands, embedded convective cells, wave-like features of cloud and precipitation evolution, etc.

The qualitative estimations of instability in frontal zones imply that large rainbands can apparently be generated in large baroclinic zones with stable stratification. In unstable zones mainly small mesoscale rainbands with embedded convective cell formed.

The convective cells in separate moments of their evolutions exhibited the crucial cloud dynamics and microphysics features.

4. REFERENCES

- Hobbs, P.V., 1981. Mesoscale structure in midlatitude frontal systems. Proc. JAMAP symposium, Hamburg, August 1981: 1-8.
- Houze, R.A. and Hobbs, P.V., 1982. Organization and structure of precipitation clouds systems. Adv. Geophys., 24: 225- 315.
- Krakovskaya, S.V., Pirnach, A.M. Suhinsky, A.N., 1994. Simulation of seeded frontal clouds over Ukraine. Proc.6-th WMO/TD- No.596, 1994, v.2: 499-502.
- Palamarchuk, L.V. and Pirnach, A.M., 1992. Study a internal structure of frontal zone with help of three-dimensional numerical models. Tr. UHRI, 243: 107-124 (in Russian).
- Pirnach, A.M., 1984. Numerical simulation for interaction between dynamical and microphysical processes into winter frontal cloud systems. Tr.UHRI.199:48-57(in Russian)
- Pirnach, A.M., 1987. Numerical simulation of frontal cloud system with account for dynamic and microphysical processes (three-dimensional model). Trudy UHRI, 221: 71-83 (in Russian).
- Pirnach, A.M. and Krakovskaya S.V., 1994. Numerical studies of dynamics and cloud microphysics of the frontal rainbands. J. Atmos. Res., 33: 333-365.
- Shakina, N.P., 1990. Hydrodynamical instability in the atmosphere. Hydrometeoisd. Leningrad. 309pp.

THE ANALYSIS OF THE PRECIPITATION
RESOURCES IN NORTH CHINA
BY A DUAL FREQUENCY
MICROWAVE RADIOMETER

Wu Zhihui Duan Ying Shi Lixin
Hebei Province Weather Modification Office
11 Tiyu Zhong Street, Shijiazhuang, 050021, P.R.China

Wang Xiaobin
Chinese Academy of Meteorological Science
Baishiqiao Road 46, Beijing 100081, P.R.China

1. INTRODUCTION

The vapour and the cloud liquid water content (CLWC) are important parameters to understand the cloud and precipitation development in the weather system. The precipitation resources in North China is the focus in the research of artificial precipitation enhancement. During the period of the artificial precipitation in Hebei Province from 1993 to 1996, a dual frequency microwave radiometer was used to observed the vapour and the cloud liquid water content integrated over the surface (CLWC). In this paper the evolution of CLWC with time, the precipitation transform efficiency (E) and the potential resources for cloud seeding were analyzed with the data collected in 1993 and 1994.

2. THE OBSERVATIONAL DEVICE AND THE ACQUIRED DATA

The dual frequency microwave radiometer was made by Peking University. The working frequency are 22.235 GHz and 35.300 GHz. The device was located with vertical point at Shijiazhuang. The observing data were recorded continuously when the cloud system covered the observing station from April to June in 1993 and 1994, the total of observation time is about 400 hours. Table 1 is the sample number under different weather condition.

Table 1 The sample number under the different weather condition.

weather condition	part cloudy	cloud days	rain days
sample number	5407	14360	2664

3. THE ANALYSES OF DATA

3.1 The Frequency Distribution of the Total Vapour Content

Figure 1 is the cumulative frequency distribution of the total vapour content under the different weather condition during April to June (1993, 1994). V (mm) is the equivalent water depth for vapour total content in vertical air column. All of the V values are less than 35 mm and have a medium value of 16 mm in part cloudy days. The V are from 15 to 45 mm and with a medium value is 30 mm for cloud days. The V are from 30 to 100 mm in rain day, and its medium value is 50 mm.

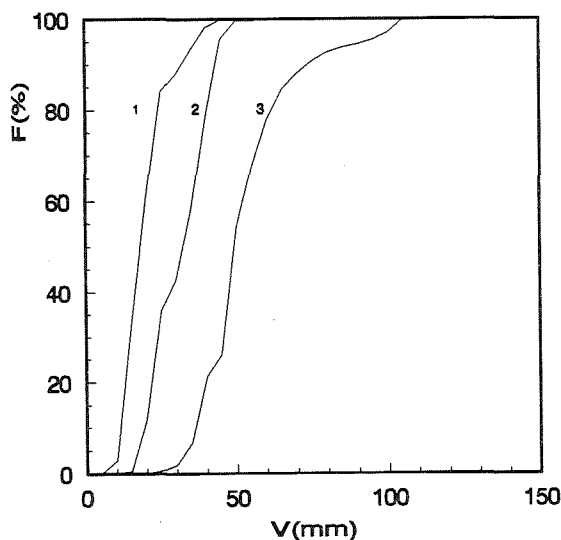


Figure 1 The cumulative frequency distribution of the total vapour content under different weather condition. 1 - part cloudy days; 2 - cloud days; 3 - rain days.

3.2 The Frequency Distribution of the Total Liquid Water Content

Figure 2 shows the frequency distribution of the total liquid water content with the different weather condition during April to June (1993, 1994). L (mm) is the equivalent water depth for total liquid water content of the vertical air column. All of the values of L are less than 0.2 mm in cloud day, the medium value is only 0.05 mm. The L are more than 0.3 mm in rain day, the maximum value of L is 1.51 mm and the medium value is 0.6 mm. The L value increase when the heavy precipitation appeared.

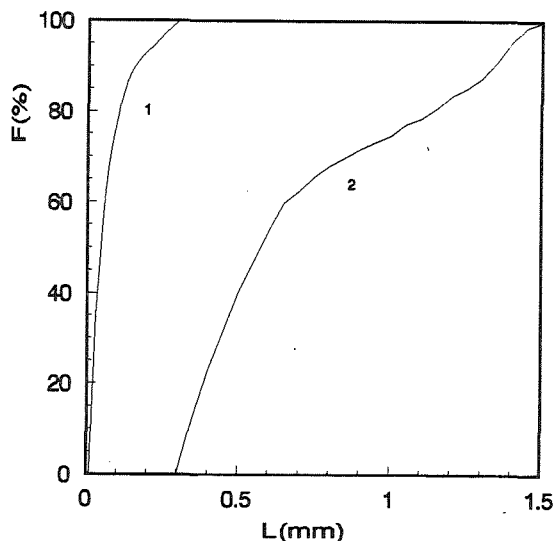


Figure 2 The frequency distribution of the total liquid water content under the different weather conditions: 1 - cloud days; 2 - rain days.

3.3 The Frequency Distribution of the Ratio V/L

The frequency distribution of the ratio V/L with the different weather condition during April to June

(1993,1994) is given in figure 3. V/L is 100 to 4000 in cloud days, the medium value is 750. V/L are from 50 to 150 in rain day and the medium value is 80.

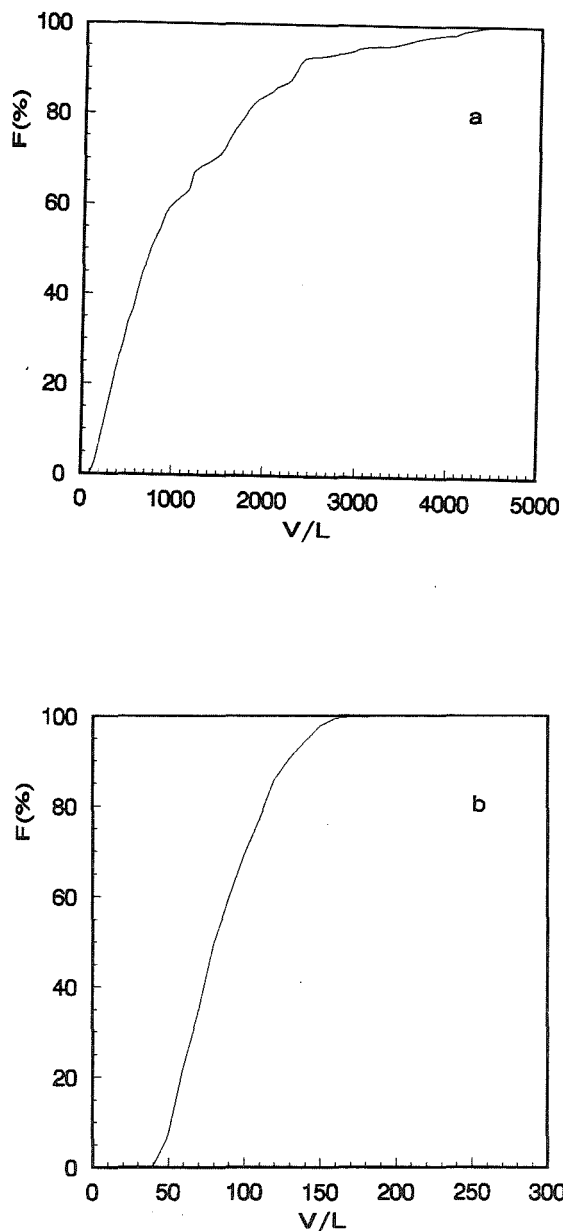


Figure 3 The cumulative frequency distribution of the ratio V/L with the different weather condition. 3a - cloud days; 3b - rain days.

3.4 The precipitation transform efficiency (E)

Based on the rainfall intensity I on ground, the rain water content W is calculated by the relation: $W(\text{mg m}^{-3}) = 70 I^{0.85} (\text{mm h}^{-1})$, and assuming that the rain water content is linearly increasing with the decreasing height, the cumulative rain water content (L_1) in the vertical air column can be estimated. The precipitation translating efficiency (E) is the ratio of L_1/L , and the potential resources for seeding is $1-E$ as follows. $1-E = 0.8482 \text{ Exp } (-0.079I)$, and the correlation coefficient r is -0.807207 . This expression suitable for I less than 5 mm.

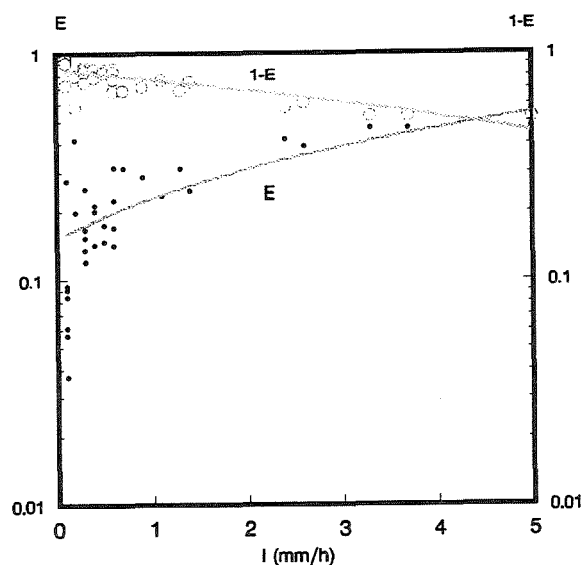


Figure 4 The relation of $(1-E)$ to I

4. Acknowledge

This study is supported by the Natural Sciences Foundation of Hebei Province, China.

REFERENCES

Mason, B. T., 1971: The physics of clouds. Oxford Press.
You, L. et al, 1994: Study of cloud

water content with a Dual-Band Microwave Radiometer in Beijing. WMO/TD-No.596, 383-386.

OBSERVATIONS OF TURBULENCE IN CIRRUS CLOUDS

Samantha A Smith¹ and Peter R Jonas

Physics Dept., UMIST, Manchester M60 1QD, UK

¹Present affiliation: Columbia University and NASA Goddard Institute for Space Studies

1 INTRODUCTION

Cirrus clouds play a major role in the earth's radiation budget as they can cover extensive areas, and so their representation must be improved in general circulation models. Small scale turbulence has an important influence on the cloud structure and life cycles of the clouds through internal mixing and entrainment processes, and therefore on the spatial distribution of the optical properties. Aircraft observations were made through thick frontal daytime cirrus clouds during September and October 1993 in the region of Scotland using the UK Met Office's Hercules aircraft, as part of the EUCREX campaign. The instrumentation has been described in Nicholls (1978), Nicholls et al (1983) and Slingo et al (1982). Straight horizontal runs were flown at various heights in and below the cirrus, and profiles up to 9000 metres were made. The aircraft never reached the cloud tops.

2 ANALYSIS

Two techniques were used to analyse the turbulence data - Fourier analysis and wavelet analysis. Fourier analysis can be viewed as a rotation in function space from the time (or space) domain to the frequency domain, which contains sines and cosines as basis functions. These are infinite in space, and so a local oscillation will contribute something to the average Fourier transform but its location will be lost as well as its amplitude. Power spectra were obtained for the variations in all 3 wind components (u , v and w) and in the Rosemount temperatures (T). The best fit straight line was removed from each time series and 10% of the data was tapered at both ends using the split cosine bell to reduce leakage

to neighbouring frequency bins.

In the case of wavelet analysis the basis functions are wavelets, a set of self-similar functions which are localized in both frequency and space. The wavelets are generated from the 'mother wavelet' by discrete dilations which are spaced in octaves, and translations which depend on scale (so at smaller scales the resolution in Fourier space decreases due to the uncertainty principle). These wavelets effectively provide a varying window size: higher frequency wavelets are shorter. A discrete wavelet transform was performed on the vertical velocity (w) timeseries containing $N=2^{13}$ datapoints at 32 Hz (37 km). Daubechies wavelets with 20 coefficients were used as they are smoother and therefore better localized in frequency space than those with fewer coefficients (Daubechies, 1988). To avoid problems with the non-periodic boundaries of data segments, a flat-topped window was applied to the timeseries with $N/2$ datapoints added to each end, as described by Meneveau (1991). The wavelet amplitudes are displayed as mean-square maps.

3 RESULTS

It was observed that the occurrence of turbulence within cirrus clouds is patchy and weak. It is also on the whole rather 2 dimensional, with more turbulent energy possessed by the horizontal wind components, but the more turbulent regions (more TKE in the vertical component) were associated with a more 3-dimensional isotropic flow field. Turbulent kinetic energy (TKE) can be produced in cirrus clouds either by shear instabilities or by buoyancy effects.

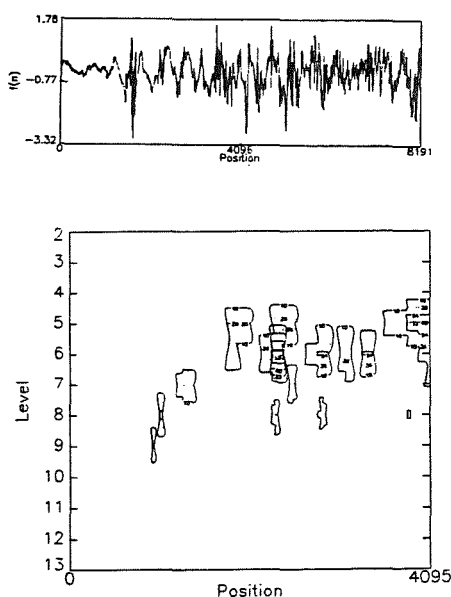


Figure 1: (a) Timeseries of w from run 1 at a height of 8.9 km from flight A283, containing 8192 datapoints at 32 Hz. (b) Mean square map of the wavelet amplitudes obtained from the timeseries shown in figure 1a. Scale increases down the y-axis from (for non-zeroed levels) $j=4$ (5 km) to $j=13$ (10 m).

3.1 Buoyant Production of TKE

Convective cells were observed only during flight A283, for which σ_T was largest. Large local ice water contents (and number concentrations) were observed in updraughts due to new crystal nucleations. The upper region of the cirrus cloud on this day was optically thick enough for the infrared cooling to be concentrated at cloud top, thus producing convection. Figure 1 shows a 37 km timeseries of w from run 1 in the upper part of the cloud observed during flight A283, with the mean-square map of the wavelet amplitudes. Figure 2 shows the corresponding Fourier transform, while figure 3 shows w , u , v , Q_T and T spectra for a 100 second section of this timeseries. Spectral peaks were observed in the vertical velocity power spectra at scales of 2 km, and also in the temperature spectra. Peak wavelet amplitudes are found at $j = 5$ to 6, or scales of 2.5 to 1.25 km, thus agreeing quite well with the Fourier analysis.

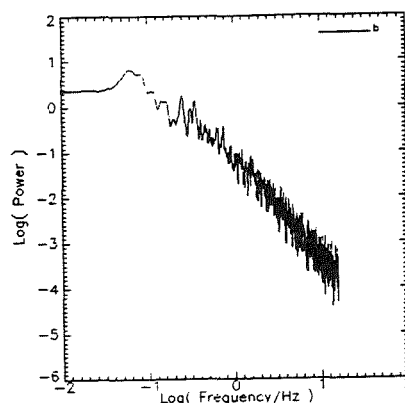


Figure 2: Fourier spectrum of the w timeseries analysed in figure 1.

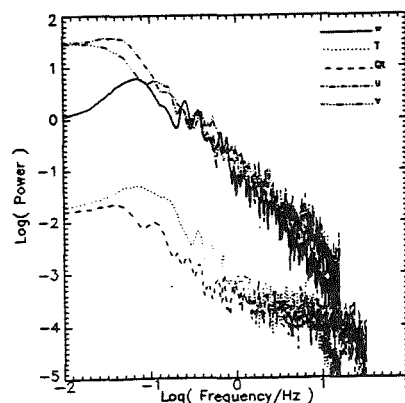


Figure 3: Spectra of w , T , Q_T , u and v from a 100 second section of the timeseries analysed in figure 1.

The cirrus clouds sampled during the other two flights did not seem to have much cellular convection occurring, possibly because ice water contents were small at high levels so that the radiative cooling was distributed vertically through the cloud.

3.2 Shear Generation of TKE

Kelvin-Helmholtz waves can form in a layer with a stable lapse rate and a vertical wind shear. If the Richardson number, Ri , is below its critical value of 0.25 (the strength of the shear is large enough to overcome the damping effect of the stable density stratification) within a layer

of thickness h , then these waves will break and become turbulent. The 'most unstable' wavelength is defined as that which becomes unstable first as Ri falls below 0.25, and it varies between $(6.3 \times h)$ and $(7.5 \times h)$ depending on the variation of the density and velocity profiles (Turner 1973).

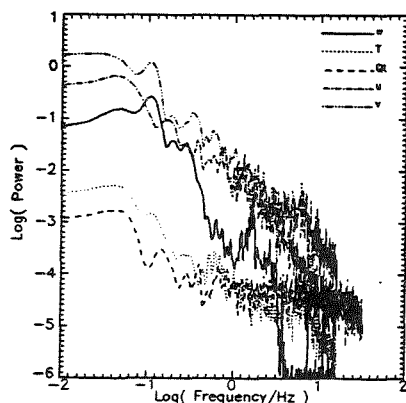


Figure 4: Spectra of w , T , Q_T , u and v for a 100 second section of run 1 (9150 metres) from flight A290.

From the profiles of the Richardson number calculated over 15 metre deep layers during the profile ascent at the start of each flight, this appears to occur within shallow layers of the cirrus in all three flights investigated. The observed peaks for flights A290 and A288 were on the whole at scales between 50 and 100 metres. An example from run 1 of flight A290 is given in figure 4. The energy in w is much less than in u and v , except at the peaks in the w spectral density. However, these very small scale peaks are not resolved by the wavelet transform due to the low frequency resolution at smaller scales. In contrast, small-scale peaks were observed for flight A283 at scales up to 600 metres in the spectrum from the shorter timeseries. (They are hidden in the longer timeseries spectrum). The wavelet transform shows small scale peaks at level $j=8$ or scales of 312 metres.

3.3 Gravity Waves

Only gravity waves with frequencies lower than $N/2\pi$ can propagate through the atmosphere with a Brunt-Vaisala frequency N . For flight A283 gravity waves with frequencies lower than 0.03 Hz were able to propagate through the cirrus. This corresponds to wavelengths on the scale of a few kilometres assuming that the phase speed is of similar magnitude to the observed wind speeds. For flights A290 and A288 gravity waves with wavelengths of the order of 10 km or more would have been able to propagate. The presence of turbulence means that finding the coherence and phase between w and θ does not produce much convincing evidence for the presence of gravity waves.

If a gravity wave propagates through a stable atmosphere it alters the local value of Ri . This may cause Ri to fall below the critical value in localized regions due to the enhancement of shear by the wave within certain phases of the wave cycle. Patches of turbulence are widely believed to be produced in this manner in stable environments with depths ranging from 10's to 100's of metres as determined by the vertical wavelength, and which are elongated in the horizontal due to the horizontal wavelength usually being longer than the vertical wavelength. The depth of the layer determines the size of the largest eddies produced.

4 ACKNOWLEDGEMENTS

The authors are indebted to the aircrew and scientists of the Meteorological Research Flight for their dedication in making the measurements and for their assistance in the post-flight analysis of the data. Support for this work from the CEC and the NERC is gratefully acknowledged.

5 REFERENCES

- Daubechies, I., Orthonormal bases of compactly supported wavelets., *Commun. on Pure and Applied Math.*, 41: 901-996, 1988.
- Meneveau, C., Analysis of Turbulence in the Orthonormal Wavelet Representation. *J. Fluid Mech.*, 232: 469-520, 1991.
- Nicholls, S., 1978. Measurements of turbulence by an instrumented aircraft in a convective atmospheric boundary layer over the sea., *Quart. J. R. Meteorol. Soc.*, 104: 653-676.
- Nicholls, S. Shaw, W. T. and Hauf, T., 1983. An intercomparison of aircraft turbulence measurements during JASIN. *J. Clim. Appl. Meteorol.*, 22: 1637-1648.
- Slingo, A., Nicholls, S. and Schmetz, J., 1982. Aircraft observations of marine stratocumulus during JASIN. *Quart. J. R. Meteorol. Soc.*, 108: 833-856.
- Smith, S. A. and Jonas, P. R., Observations of Turbulence in Cirrus Clouds., *Atmospheric Research*,. In press, 1996.

PRELIMINARY RESULTS OF THE VERTICAL STRUCTURE OF TROPICAL (20°S–20°N) SUBVISUAL CLOUDS FROM SAGE II OBSERVATIONS

Pi-Huan Wang,¹ M. Patrick McCormick,² Patrick Minnis,²
Geoffrey S. Kent,¹ Glenn K. Yue,² and Kristi M. Skeens¹

1. Science and Technology Corporation, Hampton, Virginia

2. Atmospheric Sciences Division, NASA Langley Research Center, Hampton, Virginia

1. INTRODUCTION

This study examines the vertical distributions of the tropical subvisual clouds based on measurements from the Stratospheric Aerosol and Gas Experiment (SAGE) II. The main emphasis is on the thickness and multilayer structures of the subvisual clouds (SVC). Subvisual clouds are relatively transparent to shortwave radiation but are somewhat opaque to longwave radiation. In terms of their radiative property, therefore, SVCs are similar to greenhouse gases. Recently much attention has been drawn to understanding the behavior of tropical SVCs. Because clouds redistribute radiative energy, their vertical structures may have profound influence on tropical circulation systems [Hobgood, 1986; Roecker and le Treut, 1996]. Recent studies further indicate that the development of tropical high-altitude clouds has important implication in the tropical stratosphere-troposphere exchange and dehydration processes essential to the dryness of the stratosphere [Newell and Gould-Steward, 1981; Danielsen, 1993; Reid and Gage, 1993; Russell et al., 1993; Newell et al., 1996].

In this study the SVCs are defined as clouds with extinction coefficients less than about $2\text{--}3 \times 10^{-2}$ (km^{-1}), corresponding to the optical depth of 0.02–0.03 for a 1-km-thick layer cloud. With a small field of view of the sensor, the limb-viewing geometry of the solar occultation technique allows SAGE II to measure the atmospheric structure with a 0.5-km vertical resolution. The SAGE II data have been used in the development of a global cloud climatology in which the vertical distributions of the frequency of clouds observed by the SAGE II instrument are discussed [Wang et al., 1996]. In the derived climatology, if a cloud occupies more than one 1-km-thick layer, it is counted as one occurrence in each of these layers. For this reason the derived climatology does not reflect information on cloud thickness. This is also the case when multilayer clouds are present.

2. RELEVANT SAGE II FEATURES

Several existing articles have described the cloud measurement feature of the SAGE II instrument [e.g., Wang et al., 1994]. Briefly, the slant path transmission measurements from the seven-channel SAGE II instruments, centered at 0.385-, 0.448-, 0.453-, 0.525-, 0.600-, 0.940-, and 1.02- μm wavelengths, are used to retrieve the profile of the stratospheric ozone, nitrogen dioxide, water vapor, and particulate extinction coefficients at four wavelengths (0.385, 0.453, 0.525, 10.2 μm) [Mauldin et al., 1985; McCormick, 1987; Chu et al., 1989]. Under cloud-free and nonvolcanic conditions the SAGE II channels at the four longer wavelengths also provide measurements in the troposphere. Due to the inherent instrumental features and the data processing procedures, the SAGE II data products represent smoothed measurements practically over a sampling volume of 1 km in the vertical, by 2.5 km in the horizontal normal to the line of sight, and by a 200-km path length along the line of sight. This sampling volume constrains the cloud measurements of the SAGE II instrument [Wang et al., 1994].

The upper extinction-coefficient measurement limit of the SAGE II 1- μm channel is about 0.02 to 0.03 (km^{-1}). Therefore, in the presence of optically thicker clouds (referred to as opaque clouds), the SAGE II profile is terminated at an altitude corresponding to this limit. According to the cloud classification of Sassen and Cho [1992], the SAGE II measurable clouds are generally SVCs [Wang et al., 1994; 1996]. Because of the limb-viewing geometry of the solar occultation technique, the SAGE II instrument is more sensitive to the presence of optically thin, layered clouds than other satellite instruments using the nadir-viewing method.

3. DATA AND ANALYSIS

The data used in the present study consist of SAGE II measurements obtained from December 1984 to May 1990 (the pre-Pinatubo eruption period) in the

tropics (20°S–20°N). Here the SAGE II cloud data identification is made by use of the two-wavelength method of *Kent et al.* [1993]. By using the SAGE II extinction coefficient measurements at 0.525 and 1.02 μm , the two-wavelength method, in principle, separates cloud data from aerosol measurements according to particle size. Because the measurements from the 0.525- μm channel are limited to altitudes above 6.5 km, the analysis is made for SVCs occurring above that altitude.

The SVCs are formed generally near the tropopause. We first examine the relative position between the tropopause and the SVCs, followed by an analysis of cloud thickness and multilayer clouds. In this study, we have used the tropopause-height data included in the associated meteorological information of the SAGE II measurements provided by the National Meteorological Center.

4. RESULTS AND DISCUSSION

Data on the position of the SVCs relative to the tropopause height are given in Table 1. The results indicate that over half of the SVCs never reach the tropopause. Only about 3% of the clouds appear above the tropopause. About 40% of the clouds reside at the tropopause. These clouds will be referred to as tropopause clouds. As shown in Table 2 the mean thickness of the tropopause clouds is about 3.6 km, with a standard deviation of 1.7 km. On average, over one-third of the body of the tropopause clouds (1.1 km) penetrate into the stratosphere, and about two-thirds (2.6 km) remain in the upper troposphere. Following

their development, the SVCs may engage in precipitation or evaporation processes. These processes have been confirmed in recent observations [e.g., *Danielsen*, 1993; *Vömel et al.*, 1993], and in simulation studies [*Wang et al.*, 1995].

TABLE 1. Occurrence of SVC

Subvisual Cloud	Frequency (%)
Above tropopause	3
Residing at tropopause	37
Below tropopause	60

TABLE 2. Configuration of Tropopause SVC

Mean thickness (SD)	3.65 (1.74) km
Mean thickness above tropopause (SD)	1.1 (0.65) km
Mean thickness beneath tropopause (SD)	2.6 (1.82) km

SD: Standard deviation.

In the course of examining cloud thickness, the vertical extent of the SVCs is determined for cloud top at each of the SAGE II levels, from 12.5 km to 17.5 km. The results of the analysis are presented in Figure 1. The distribution of the cloud occurrence frequency as a function of cloud thickness exhibits interesting patterns. First, at altitudes of 12.5 and 13.5 km, the frequency

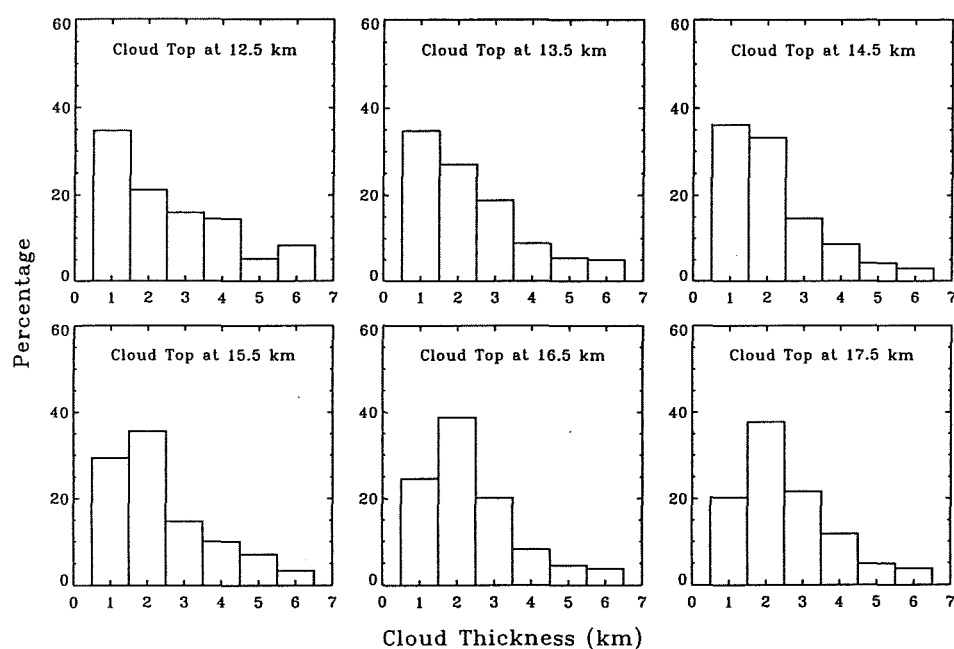


Figure 1. Subvisual cloud thickness.

distribution reveals a generally monotonically decreasing behavior as the cloud thickness increases. As the cloud top height increases, the frequency of the 1-km-thick clouds gradually diminishes, but the frequency of thicker clouds increases, particularly the 2-km-thick clouds. The transition of the dominant frequency from the case of 1-km-thick clouds to the one of 2-km-thick clouds occurs at an altitude of about 15 km. This feature is likely associated with the cold temperature in the tropopause region. The occurrence of SVCs several kilometers thick is very interesting. More studies are needed to understand the condition that favors their development.

The structure of SAGE II multilayer SVCs can be grouped into three different categories: (A) subvisual layer cloud(s) with no opaque cloud (above 6.5 km); (B) subvisual cloud(s) with detached opaque cloud (above 6.5 km); and (C) subvisual cloud(s) with attached opaque cloud. The frequency statistics of these three types of layer clouds are displayed in Table 3. The results indicate that most of the vertical structures are manifested as a single layer SVC with attached opaque cloud, which is followed by the case of single-layer and two-layer SVCs with no presence of opaque cloud above 6.5 km. The case of SVCs with detached opaque cloud (above 6.5 km) occurs relatively less frequently. The SVCs with attached opaque cloud are likely associated with tropical convective activities. The presence of isolated SVC layers could result from *in situ* formation or as part of the outflow of intense deep convective cloud systems.

TABLE 3. Tropical Multilayer Cloud

Case	Number of layers		
	1 (%)	2 (%)	3 (%)
A	17.4	8.3	1.0
B	4.6	0.7	0.0
C	63.5	4.5	0.1

Case A: SVCs with no opaque clouds (above 6.5 km).

Case B: SVCs with detached opaque cloud (above 6.5 km).

Case C: SVCs with attached opaque cloud.

5. ACKNOWLEDGEMENTS

P.-H. Wang, G. S. Kent, and K.M. Skeens are supported by NASA contract NAS1-19976.

6. REFERENCES

- Chu, W. P., M. P. McCormick, J. Lenoble, C. Brogniez and P. Pruvost, 1989: SAGE II inversion algorithm. *J. Geophys. Res.*, **94**, 8339–8351.
- Danielsen, E. F., 1993: *In situ* evidence of rapid, vertical, irreversible transport of lower tropospheric air into the lower tropical stratosphere by convective cloud turrets and by large-scale upwelling in tropical cyclones. *J. Geophys. Res.*, **98**, 8665–8681.
- Hobgood, J. S., 1986: A possible mechanism for the diurnal oscillation of tropical cyclones. *J. Atmos. Sci.*, **43**, 2901–2922.
- Kent G. S., D. M. Winker, M. T. Osborn, M. P. McCormick and K. M. Skeens, 1993: A model for the separation of cloud and aerosol in SAGE II occultation data. *J. Geophys. Res.*, **98**, 20725–20735.
- Mauldin, L. E., III, N. H. Zaun, M. P. McCormick, J. H. Guy and W. R. Vaughn, 1985: Stratospheric Aerosol and Gas Experiment II instrument: A functional description. *Opt. Eng.*, **24**, 307–312.
- McCormick, M. P., 1987: SAGE II: An overview. *Adv. Space Res.*, **7**, 319–326.
- Newell, R. E., and S. Gould-Stewart, 1981: A stratospheric fountain. *J. Atmos. Sci.*, **38**, 2789–2796.
- _____, Y. Zhu, E. V. Browell, W. G. Read and J. W. Waters, 1996: Walker circulation and tropical upper tropospheric water vapor. *J. Geophys. Res.*, **101**, 1961–1974.
- Reid, G. C., and K. S. Gage, 1993: Troposphere-stratosphere coupling in the tropics: The role of El Niño and the QBO. *The Role of the Stratosphere in Global Change*, M.-L. Chanin, Ed., NATO ASI Ser., Springer-Verlag, 245–266.
- Roeker, E., and H. le Treut, 1996: GCM studies and parameterization. *Clouds, Chemistry and Climate*, P. J. Crutzen and V. Ramanathan, Eds., NATO ASI Ser., Springer-Verlag, 109–133.
- Russell P. B., L. Pfister and H. B. Selkirk, 1993: The tropical experiment of the Stratosphere-Troposphere Exchange Project (STEP): Science objectives, operations, and summary findings. *J. Geophys. Res.*, **98**, 8563–8589.
- Sassen, K., and B. S. Cho, 1992: Subvisual-thin cirrus lidar dataset for satellite verification and climatological research. *J. Appl. Meteor.*, **31**, 1275–1285.
- Vömel, H. W., S. J. Oltmans, D. Kley, P. J. Crutzen and H. Nguyen, 1993: Balloon-borne observations of stratospheric and upper tropospheric water vapor in the tropics during CEPEX. *Eos Trans. AGU* **74** (43), 116.

- Wang, C., P. J. Crutzen and V. Ramanathan, 1995: The role of a deep convective storm over the tropical Pacific Ocean in the redistribution of atmospheric chemical species. *J. Geophys. Res.*, **100**, 11509–11516.
- Wang, P.-H., M. P. McCormick, L. R. Poole, W. P. Chu, G. K. Yue, G. S. Kent and K. M. Skeens, 1994: Tropical high cloud characteristics derived from SAGE II extinction measurements. *Atmos. Res.*, **34**, 53–83.
- _____, M. P. McCormick, P. Minnis, G. S. Kent and K. M. Skeens, 1996: A 6-year climatology of cloud occurrence frequency from SAGE II observations (1985–1990). *J. Geophys. Res.*, submitted.

Study of Cirrus Multi-scale Structure

Yangang Liu W. Patrick Amott John Hallett

Desert Research Institute, Atmospheric Sciences Center, Reno, NV 89506, USA

1. INTRODUCTION

Cirrus exhibits multiscale structure on wide range of scales, both coherent and chaotic, that interplay one another (Gultepe and Starr 1995; Gultepe et al., 1995). Knowledge of multiscale structure is essential for understanding cirrus clouds and their climate effects. Fractal and multifractal scaling have been found in turbulence and the atmospheric boundary layer (Mandelbrot 1983; Yee et al. 1996). Lovejoy (1982), and Collmer et al. (1995) investigated multiscale structures of clouds. Liu (1995) discussed the relationship between scaling particle size distributions and a hierarchy of atmospheric eddies. Multiscale structures of cirrus clouds, however, are not well understood. We explore cirrus multiscale structures using different techniques (Fourier analysis, wavelet analysis and fractal / multifractal analysis).

2. MULTISCALE TECHNIQUES

A number of multiscale methods have been proposed based on finding a relation between a measure (M) and scale (L): $M = f(L, x)$ where x is a position. The traditional approaches (Fourier analysis and structure function method) are for stationary series (Stull 1988). Power-laws between energy and frequency have been determined for homogeneous turbulence (e.g. the famous $-5/3$ law) and mesoscale dynamics (VanZandt 1982; Nastrom and Gage 1985). The fractal approach has found applications in characterizing multiscale properties (Mandelbrot 1983; Sreenivasan 1991). The three methods are essentially collective methods because they average position information. Recent research focuses on local methods for non-stationary series: wavelet and multifractal analysis. Wavelet analyses have been used in studying the atmosphere (Mahart 1991; Gao and Li 1993; Weng and Lau 1994). Gollmer et al. (1995) applied wavelet analysis to stratocumulus cloud inhomogeneity. Two advantages over the Fourier analysis are: (1) provide both frequency and position localization; (2) provide statistics even for stationary series (Meneveau 1991; Yee et al. 1996). A good discussion of the multifractal

method was given in Sreenivasan (1991). Table 1 is a summary of these methods.

Table 1. Multi-scale Approaches

	Methods in Fourier space	Methods in physical space
Collective methods	Fourier analysis	Structure function, fractal
Local methods	Windowed Fourier, Wavelet	Multifractal

3. CASE STUDY OF 5 DEC. 1991

3.1. Aircraft Measurements

Data were collected over Coffeyville on 5 December, 1991 during the First International Satellite Cloud Climatology Project (ISCCP) Regional Experiment (FIRE). Measurements were obtained from instruments mounted on UND Citation, including ice crystal spectra by PMS-2D probes, temperature, wind and vertical velocity. We analyzed data for three horizontal legs.

3.2. Fourier Analysis

Previous Fourier analyses have concentrated on quantities like temperature, wind speed and vertical velocity (Gultepe and Starr 1995). We add analysis of crystal concentration fluctuations considering its importance in studying cirrus clouds and their influence on radiation transfer. The results are shown in Fig.1.

As shown in the figures, (1) concentration fluctuations are consistent with the fluctuation of vertical velocity; (2) except leg 3 the power spectra of vertical velocity, wind speed, temperature, and particle concentrations tend to have similar slopes, $p \propto f^{-1.8}$, suggesting that coherent structures may exist in this cloud (Gultepe et al. 1995). The causes of different spectra of temperature and wind speed in leg 3 is unknown at this time.

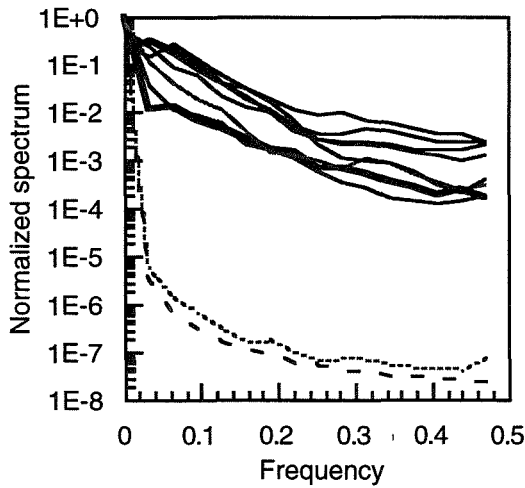


Fig.1a. Fourier spectra for leg2: $H = 11.512$ km. Vertical velocity is the thick solid line, crystal concentrations thin solid lines, temperature dashed line, and wind speed dotted line.

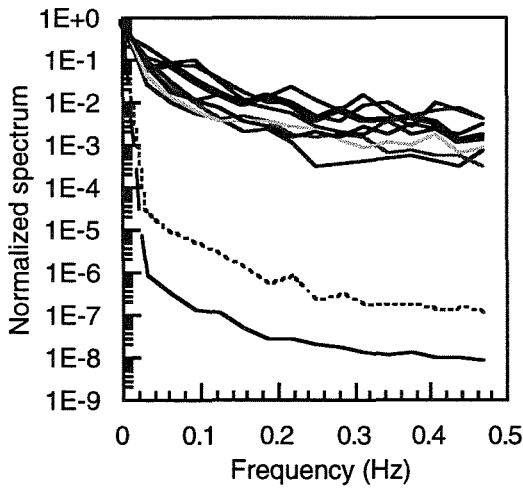


Fig.1b. Same as (a) except for leg3: $H = 10.890$ km.

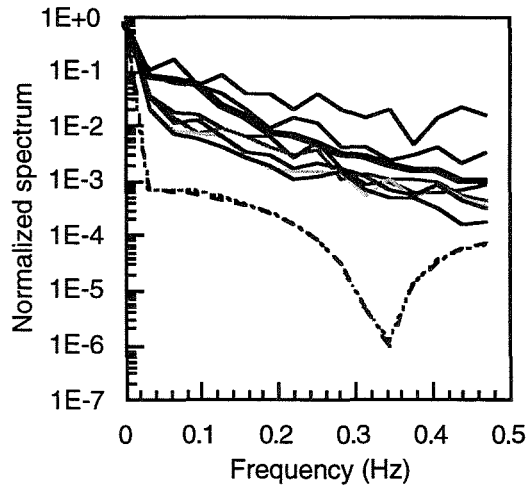


Fig.1c. Same as (a) except for leg4: $H = 10.270$ km.

3.3. Wavelet Analysis

We use the Haar wavelet analysis to demonstrate the two advantages of wavelet analysis. The wavelet analysis of a discrete series gives wavelet coefficients $\{W_{j,k}\}$ that represents the contribution from the frequency $f_j = 2^j(N\Delta)^{-1}$ at k -th position (N is the number of samples, Δ the time interval). The wavelet spectrum is $p(f_j) = \langle W_{j,k}^2 \rangle_k \Delta (\ln 2)^{-1}$ where $\langle \rangle_k$ denotes average over all positions. The wavelet spectrum is similar to the Fourier spectrum (Meneveau 1991; Yee et al. 1996). Figure 2 compares the Fourier spectra to the Haar wavelet spectra of the fluctuations of vertical velocity in leg 2.

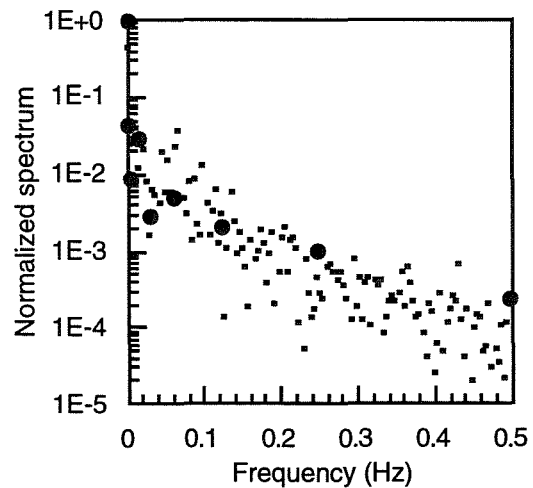


Fig. 2. Normalized Fourier (squares) and Haar wavelet (dot) power spectra.

Wavelet analysis readily provides us with other statistics such as standard deviation of the wavelet spectrum. Relevant definitions and formulas can be found in Meneveau (1991) and Yee et al. (1996). As an example, Figure 3 shows intensity variation with frequency (intensity of fluctuation is defined as standard deviation divided by mean).

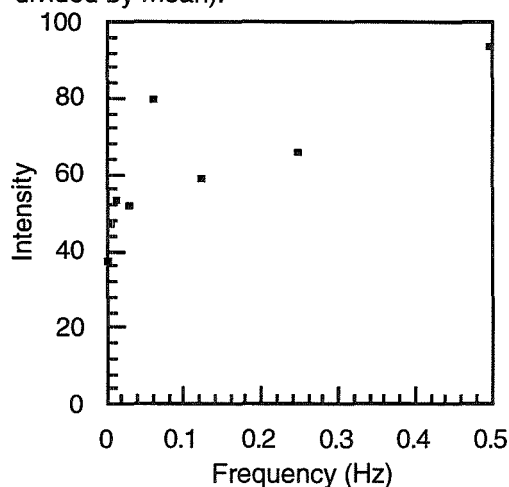


Fig.3. Intensity variation with frequency

Wavelet has the ability to localize both frequency and position, and hence to study non-stationary series. This is demonstrated by comparing the wavelet analysis of the vertical velocity (Fig.4) to the concentration fluctuations of crystals with $\sim 82 \mu\text{m}$ maximum diameter (Fig.5) in leg 2. Although their power spectra are similar, the detailed differences can be clearly seen in these plots. Cloud structures are shown to change with positions. Whether the patchy structures correspond to real cloud patches deserves considerable study.

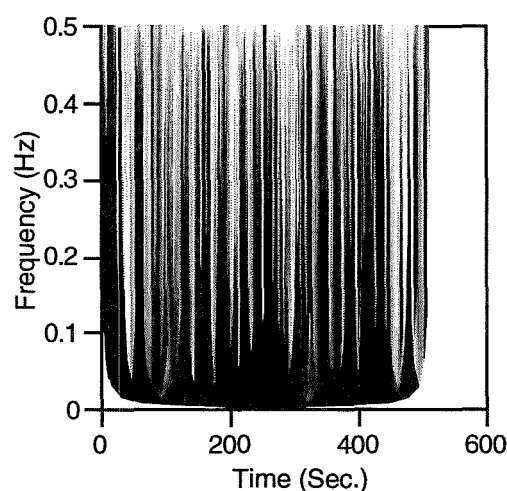


Fig.4. Wavelet transform for vertical velocity. Spectral energy variation with time is obvious, decreasing from dark to white.

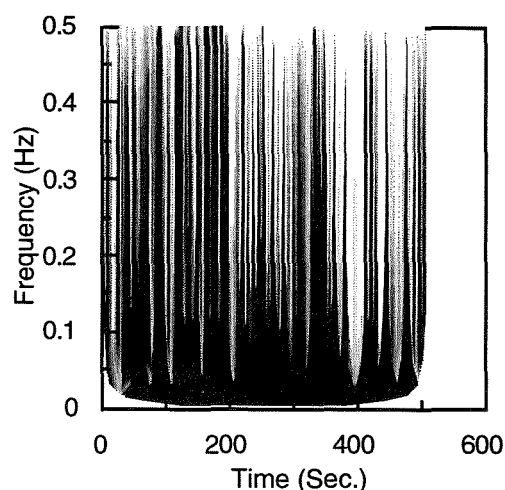


Fig.5. Same as Fig.4. except for the concentration fluctuation of crystals with $82 \mu\text{m}$ maximum diameter.

4. CONCLUDING REMARKS

We have studied multiscale structures of Dec. 5 cirrus for three legs. The preliminary results show that average multiscale structures follow self-similar scaling over scales roughly from 100 m and 10 km (aircraft speed is about 100 m/s), with spectral power-law slope about 1.8, and that macroscopic and microphysical properties tend to follow similar spectral slope, particularly, microphysical spectra are consistent with that of vertical velocity. However, the Haar wavelet analysis shows that they also depend on position, and that detailed differences exist between multiscale structures of vertical velocity and particle concentration fluctuations. Such details that collective methods can not resolve are important for cloud physics. Whether they follow multifractal scaling awaits further research.

The following should be noted.

- (1). The data available can only permit to obtain multi-scale structures over about 100 m to 100 km. Data sets with larger scale ranges are desirable for further study.
- (2). The consistency between collective spectra of various quantities makes us ask further questions: Is it really a cirrus feature, or an artifact due to instruments, or a combination of both?

REFERENCES

Gao, W. and B. L. Li, 1993: Wavelet analysis of coherent structures at the atmosphere-forest interface. *J. Appl. Meteor.* 32, 1717-1725.

Gollmer, S. M. et al., 1995: Windowed and wavelet analysis of marine stratocumulus cloud inhomogeneity. *J. Atmos. Sci.*, 52, 3013-3030.

Gultepe, I. et al. 1995: Dynamical characteristics of cirrus clouds from aircraft and radar observations in micro and meso- γ scales. *J. Atmos. Sci.*, 52, 4060-4078.

Gultepe, I. and D. O'C. Starr, 1995: Dynamical structure and turbulence in cirrus clouds: Aircraft observations during FIRE. *J. Atmos. Sci.*, 52, 4159-4182.

Liu, Y. 1995: On the generalized theory of atmospheric particle systems. *Adv. Atmos. Sci.*, 12, 419-438.

Lovejoy, S., 1982: Area-perimeter relation for rain and cloud areas. *Science*, 216, 185-187.

Mahrt, L. 1991: Eddy asymmetry in the sheared heated boundary layer. *J. Atmos. Sci.*, 48, 472-492.

Mandelbrot, B.B. 1983: *The Fractal Geometry of Nature*, W. H. Freeman, 468pp.

Meneveau, C. 1991: Analysis of turbulence in the orthonormal wavelet representation. *J. Fluid Mech.*, 232, 469-520.

Nastrom, G.D. and K.S. Gage, 1985: A climatology of atmospheric wavenumber spectra of wind and temperature observed by commercial aircraft. *J. Atmos. Sci.*, 950-960.

Sreenivasan, K. R. , 1991: Fractals and multifractals in fluid turbulence. *Annu. Rev. Fluid Mech.*, 23, 539-600.

Stull, R. B., 1988: *An introduction to Boundary Layer Meteorology*. Klumer Academic Publishers. 655 pp.

VanZandt , T.E. 1982: A universal spectrum of buoyancy waves in the atmosphere. *Geophys. Res. Letter*, 9, 575-578.

Weng, H. and K. M. Lau, 1994: Wavelets, period doubling, and time-frequency localization with application to organization of convection over the tropical Western Pacific. *J. Atmos. Sci.*, 51, 2523-2541.

Yee, E. et al., 1996: Multiscaling properties of concentration fluctuations in dispersing plumes revealed using an orthonormal wavelet decomposition. *Boundary Layer Meteor.* (in press)

FEATURES OF FRONTAL CLOUDINESS STRUCTURE OVER UKRAINE IN WINTER SEASONS

Ludmila V. Palamarchuk¹ and Svetlana V. Krakovskaia²

¹Ukrainian State Pedagogical University, 9 Pirogova str., Kiev-252033, Ukraine;

²Ukrainian Hydrometeorological Research Institute, 37 Nauki Av., Kiev-252028, Ukraine

1. INTRODUCTION

As recently been pointed in Shapiro and Evelyn Donall Grell (1994):

A variant of the Bergeron-Hoskins paradigm for optimal methods of scientific inquiry includes theory, diagnosis, and observations as a union of elements in the search for physical understanding and its expression through conceptual models.

In our investigation we intend to fill some of the gaps in our knowledge of mesoscale processes in frontal winter cloud systems over Ukraine through diagnosis and with aid of numerical models and observations.

There are significant regional features of atmospheric processes in Ukraine due to her geographical situation. There are 3 main groups of frontal systems which determine the weather in Ukraine in winter seasons. They move from: South (S); South-West (SW); West and North-West (W-NW). S and SW cyclones play a principal role in cloudiness and precipitation formation there (Koshenko and Ponomarenko 1979, Palamarchuk 1990). In winter seasons, due to the activation of Mediterranean branch of the Polar frontal zone, synoptic situations with S and SW lows are more often and probable. It has to note such situations are corresponded to heavy highs over the far South-East of Europe.

On a base of 5-years synoptic data analysis Fig.1 shows averaged movements of cyclones in Ukraine from S, SW and SE. There are 71 cases of such replacing in total and 49% of cases corresponds to way I, 34% -- to way II and only 17% -- to way III.

To estimate of natural and probable enhanced precipitation formation of southern frontal cloud systems, thermodynamical conditions in frontal zones are analyzed with aid of radiosounding, aircraft and synoptic data and 2-D mesoscale diagnostic models. The reader is referred to Palamarchuk and Pirnach (1992) and (1994), Pirnach and Krakovskaya (1994) and Krakovskaia, Pirnach and Suhinsky (1994) for a

detailed presentation of the methodology, set of equations and numerics.

To study structure of thermodynamic characteristics' fields the active and passive thermodynamic zones (ATZ and PTZ) are distinguished. ATZ is a place where horizontal temperature gradients are not equal zero (hyperbaroclinic zones -- HBZ), thermodynamic condensation in grid points (ϵ) and updrafts ($w>0$) are present. PTZ is a place where these characteristics are opposite or absent. The great attention in the analysis of inner structure of frontal zones is devoted to computing of free for sublimation water vapor or ice supersaturation (Δ) and integral both thermodynamic condensation rate (E) and ice supersaturation (B).

2. RESULTS OF THE STUDY

From the synoptic data it was found that deep cloud systems with intense prolonged precipitation are

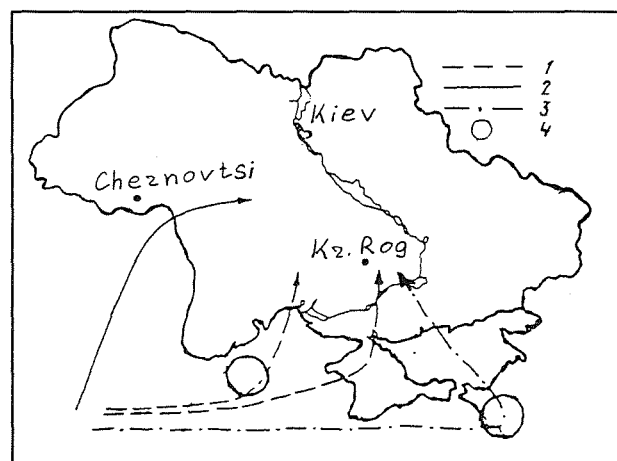


Fig.1. Ways of cyclones in their movements on Ukraine from: 1-- Mediterranean Sea to S of Ukraine; 2 -- North Mediterranean to SW of Ukraine; 3-- Mediterranean to W of Caucasus Mountains with low's sedimentation; 4-- places of generation of new local lows.

characteristic features for Southern cyclones of the I way (see Figs.1 and 2). Usually one or often couples of warm fronts of such cyclones affect and determine weather in Ukraine in winter seasons for a long time. Table 1 presents quantitative characteristics of some fronts simulated with aid of the 2-D mesoscale model on the basis of radiosounding ($X = 0$ is a place of a surface front line in all Tables). Significant vertical and horizontal zones with ice supersaturation are features of thermodynamic conditions of such frontal cloud systems. Averaged value of B is 0.13 mm and maximum is 0.59 mm. These zones are perspective for precipitation formation and located ahead of fronts. Sometimes analogous zones may be found behind of the first frontal line and probably it is determined by influencing of the second frontal section. The updrafts do not exceed 10 cm/s and averaged values of w are about 2-3 cm/s. The values of E in our simulations of such type of fronts oscillate in limits from 0.02 to 1.85 mm/h. Diverging of E and B maxima has been pointed here. Probably it is effect of active dynamical processes in the low troposphere when water vapor is taken out from place of its generation with air stream. For instance, at the level of maximum ε the normal component of wind speed is 9-10 m/s while the front velocity u_f is 5-6 m/s. In investigated frontal rainbands ice supersaturation (Δ) differs from value of 0.05 up to 0.2 g/kg. Sometimes computed Δ in some grid points exceeds this maximum but never achieves 0.3 g/kg.

As a rule SW cyclones over Ukraine (way II in Fig.1) are on a developing stage because they have significant warm sectors. Table 2 and Fig.3 present the results of such lows' study. Both warm and cold fronts of the SW cyclones influence and determine weather in Ukraine. Characteristic feature of the warm fronts of SW lows is absence of free water vapor zones accompanied by quite intense dynamic processes in frontal cloudiness. It is found in some grid points the simulated updrafts achieve 25 cm/s, $\varepsilon = 175 \cdot 10^{-6} \text{ mm (cm h)}^{-1}$ while normal to front velocity is 10-12 m/s. At the same time there is no ice supersaturation zones in the frontal cloudiness. Only a few frontal cloud systems are characterized by quite significant values of $B = 0.31 \text{ mm}$ (Fig.3). For the latter systems of way II values of w and ε are not much differ from the ones of corresponded fronts of the other ways.

Study of the III way's lows (see Fig.1) has shown that mostly occluded and rarely warm fronts are observed over Ukraine. Table 3 and Fig.4 with vertical cross sections of frontal zones present quantitative characteristics of investigated fronts. As a rule cloud systems of the occluded fronts have ice supersaturation layers and maxima of B achieve 0.67 mm. Most probable location of the zones in cloudiness is ahead of the surface fronts. Though simulated values of Δ for cloudiness of III way's lows are less than for S cyclones (way I), but deepness of such layers is greater. However the intensity of thermodynamic processes in the

cyclones of III way is less than in Southern ones. Thus values of E oscillate from 0.01 to 0.57 mm/h for the warm fronts and from 0.02 up to 0.96 mm/h for the occluded fronts of III way's lows.

It should be noted for all warm fronts of S and SW lows relationship $E \cong I$ is found (I is a natural precipitation rate). Nevertheless, existence of deep ATZ with ice supersaturation points on the possibility for a

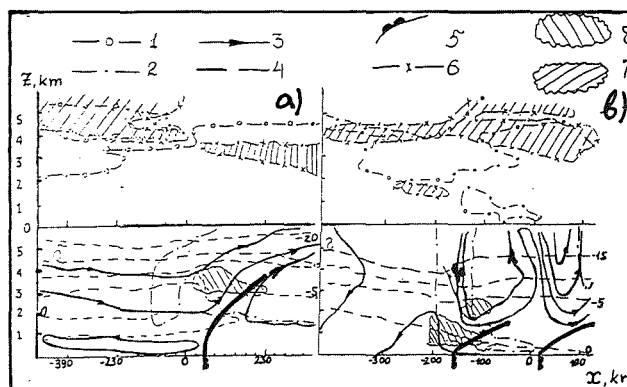


Fig.2. Vertical cross-sections of frontal zones of S lows. 1-- relative humidity $> 90\%$; 2 -- $\varepsilon = 10^{-5} \text{ mm/(cm h)}^{-1}$; 3-- flow function lines; 4 -- $T, ^\circ\text{C}$; 5 -- frontal lines; 6 -- $\Delta = 0.1 \text{ g/kg}$; 7-- $\Delta > 0$; 8 -- $|dT/dx| > 3^\circ\text{C}/100 \text{ km}$. (a) 28.03.80; (b) 12.02.81.

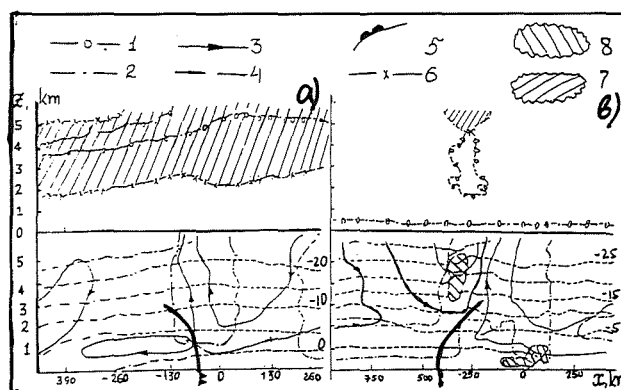


Fig.3. Vertical cross-sections of frontal zones of SW lows (all lines as for Fig.2). (a) 06.02.81; (b) 10.02.83

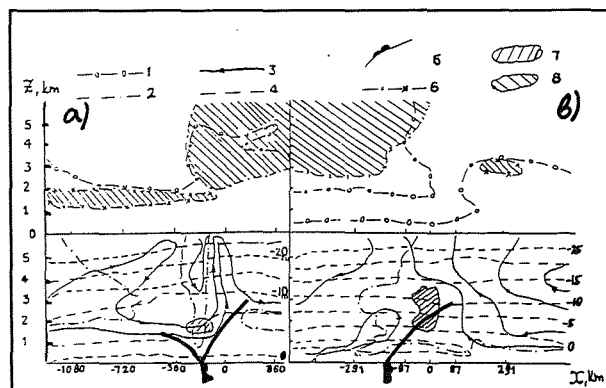


Fig.4. Vertical cross-sections of frontal zones of SE lows of III way from Fig.1 (all lines as for Fig.2). (a) 17.02.81; (b) 20.01.81.

Thermodynamical characteristics of some simulated frontal systems of S lows

Table 1

Date	Front type	Characteristics	X, km								
			-200	-150	-100	-50	0	50	100	150	200
28.03.80	WF	B, mm	0,07	0,08	0,09	0,09	0,00	0,04	0,05	0,09	0,11
		E, mm/h	0,05	0,06	0,03	0,17	0,26	0,24	0,34	0,38	0,40
		W, cm/s	2,30	0,80	1,00	1,10	2,30	2,40	3,10	2,60	2,60
		dT/dx,°C/100 km				-2,5		-2,5	-2,5		
16.11.81	WF	B, mm	0,29	0,31	0,34	0,36	0,27	0,15	0,13	0,11	0,17
		E, mm/h	0,03	0,04	0,06	0,18	0,46	0,41	0,03	0,08	0,15
		W, cm/s		1,10	1,20	2,20	3,80	3,10	0,50		
		dT/dx,°C/100 km				-2,1	-4,3	-2,1	-4,0	-2,0	
1.02.82	WF	B, mm	0,10	0,13	0,15	0,28	0,44	0,59	0,30	0,30	
		E, mm/h	0,03	0,03	0,01	0,00	0,39	1,19	1,05	0,49	
		W, cm/s		2,30	2,10		6,70	10,0	6,10	3,60	
		dT/dx,°C/100 km		-3,0	-8,0	-13,0	-14,5	-8,5	-5,5	-3,5	
20.01.85	WF	B, mm		0,02	0,02	0,01	0,01	0,05	0,03	0,09	
		E, mm/h		0,32	0,50	0,08	0,40	0,18	0,00	0,01	
		W, cm/s		3,90	6,00	1,60	3,30	5,50	3,20	0,10	
		dT/dx,°C/100 km				-2,5	-4,5	-2,0	-2,0	-2,0	

Thermodynamical characteristics of some simulated frontal systems of SW lows

Table 2

Date	Front type	Characteristics	X, km								
			-200	-150	-100	-50	0	50	100	150	200
3.11.80	WF	B,mm	0,00	0,00	0,00	0,00	0,01	0,00	0,00	0,00	0,01
		E,mm/h	0,74	0,67	0,60	0,37	0,17	0,25	0,31	0,17	0,08
		W,cm/s	4,50	4,00	3,50	2,20	1,10	1,20	1,10	0,90	0,40
		dT/dx, °C/100km	-3,0	-3,0	-4,0	-4,0	-3,0	-3,0	-1,0	-1,0	-1,0
7.11.80	WF	B,mm	0,00	0,00	0,00	0,00	0,00	0,00	0,00	0,00	0,00
		E,mm/h	0,04	0,03	0,03	0,03	0,04	0,03	0,02	0,02	0,02
		W,cm/s	0,50	0,50	0,40	0,40	0,40	0,40	0,40	0,40	0,40
		dT/dx, °C/100km	-1,0	-2,0	-2,0	-2,0	-2,0	-2,0	-2,0	-1,0	
13.12.82	WF	B,mm	0,00	0,00	0,00	0,00	0,00	0,00	0,01	0,12	0,37
		E,mm/h	0,03	0,01	0,03	0,76	0,86	1,45	0,82	0,72	0,33
		W,cm/s	0,60	0,20		0,20	2,90	6,10	4,10	3,60	1,40
		dT/dx,°C/100km	1,5	1,0	0,5	0,0	-2,8	-4,3	-3,0	-2,8	-1,5
10.02.83	WF	B,mm	0,00	0,00	0,00	0,00	0,00	0,01	0,01	0,00	0,00
		E,mm/h	0,06	0,07	0,08	0,10	0,15	0,33	0,28	0,25	0,29
		W,cm/s	0,60	0,60	0,60	0,60	0,50	2,30	2,70	2,60	2,70
		dT/dx,°C/100km	-1,0	-1,0	-1,6	-1,6	-1,6	-1,6	-1,6	-1,6	-3,0

Thermodynamical characteristics of some simulated frontal systems of SE lows

Table 3

Date	Front type	Characteristics	X, km								
			-200	-150	-100	-50	0	50	100	150	200
20.01.81	WF	B, mm	0,33	0,30	0,23	0,16	0,11	0,08	0,02	0,00	0,00
		E, mm/h	0,09	0,08	0,07	0,11	0,23	0,37	0,57	0,32	0,52
		W, cm/s	0,20	0,80	1,10	1,50	1,60	3,10	2,40	2,80	6,00
		dT/dx,°C/100 km						-2,0	-2,0	-2,0	-2,0
5.02.83	OF	B, mm	0,13	0,17	0,19	0,23	0,34	0,20	0,19	0,27	0,32
		E, mm/h	0,19	0,41	0,64	0,86	0,96	0,04	0,10	0,21	0,44
		W, cm/s	5,70	3,90	6,50	8,80	12,00	1,00	2,20	1,00	4,60
		dT/dx,°C/100 km		1,5	0,0	-2,8	-4,3	-1,5	0,0	0,0	1,5
20.02.83	OF	B, mm	0,01	0,02	0,04	0,08	0,12	0,15	0,06	0,05	0,05
		E, mm/h	0,00	0,07	0,34	0,22	0,03	0,04	0,09	0,06	0,31
		W, cm/s		0,70	2,30	1,50	0,50				4,80
		dT/dx,°C/100 km			1,8	3,7	-1,8	-3,7	-3,7	0,0	1,8
8.03.88	OF	B, mm	0,07	0,08	0,11	0,15	0,20	0,32	0,67	0,61	0,57
		E, mm/h	0,15	0,26	0,30	0,20	0,09	0,06	0,22	0,39	0,05
		W, cm/s	2,70	2,90	3,20	1,80	1,80	2,70	5,00	0,70	
		dT/dx,°C/100 km			0,0	-1,7	1,7	1,7	1,7	0,0	0,0

precipitation enhancement into those systems by seeding of artificial crystals (Palamarchuk 1990, Palamarchuk and Pirnach 1994).

Cloud systems and precipitation of W and NW cyclones over Ukraine are connected with occluded and cold fronts as a rule. Warm fronts are observed rarely and we studied them not enough. Though from obtained results mostly PTZ, absence of ice supersaturation and in a whole less intensive thermodynamical processes in comparison with occluded and cold fronts are found in cloud systems of warm fronts. Cloud systems of occluded fronts are characterized by ATZ into warm and less cold air masses. Values of E for such systems differ from 0.01--0.02 to 0.9--1.2 mm/h and exceed I usually ($E \gg I$). Significant deep layers of $\Delta > 0$ are found into the above ATZ ($B = 0.02\text{--}0.30$ mm). Cold fronts of W and NW cyclones are characterized by deep ATZ too occurred ahead of a front. But the ATZ is not coincided with layers of ice supersaturation. $E \gg I$ in such systems and can achieve 2.5 mm/h. Nevertheless, such cold frontal cloudinesses are less suitable for precipitation enhancement due to significant dynamical processes and narrowness of rainbands. While the occluded frontal cloudinesses are more suitable for artificial seeding due to storage of free water vapor in clouds (Palamarchuk and Pirnach 1994, Krakovskaia, Pirnach and Suhinsky 1994).

3. SUMMARY

Investigation of distributions of thermodynamical characteristics, which determine frontal cloudiness formation and structure, was carried out with aid of 2-D diagnostic numerical models. Radiosound, aircraft observations of frontal cloudiness and appropriate synoptic maps were initial data for the study and simulations of real fronts over Ukraine in winter seasons. More than 100 frontal zones which moved on the above region from S, SW, SE, W and NW were analyzed.

Frontal zones of the S lows frequently consist of pair warm fronts. Their thermodynamic structure is characterized by the large ATZ in both horizontal and vertical directions with significant ice supersaturation layers. Time development examination of such thermodynamic zones and connected with them cloudiness systems has pointed at keeping (12-15 h) of their movement directions and intensities of processes.

Frontal zones of the SW lows differ from previous ones by smaller ATZ's extents in both directions and by absence of significant ice supersaturation layers. Cloudiness of the SW fronts is insignificant, ragged and not precipitate.

Frontal zones of the W and NW group are divided into 2 parts. Thermodynamical characteristics and

cloudiness of the first one are similar to the above S cyclones. Thermodynamical structure of the second group is characterized by small smashed ATZ and PTZ and by ice supersaturation of significant streaking-out into small extent layers. Cloudiness of the latter group is insignificant, broken, but precipitate.

Obtained features of frontal cloudiness structure and thermodynamic characteristics can be used as a basis for to construct regional diagnostic and prognostic models of frontal cloudiness and precipitation. Obtained relationships for E and I and thermodynamical characteristics in frontal zones can be included in precipitation forecast schemes for Ukraine and be used for qualitative and quantitative estimation in precipitation enhancement experiments.

4. REFERENCES

- Krakovskaia, S.V., Pirnach, A.M. and A.N. Suhinsky, 1994: Simulation of seeded frontal clouds over Ukraine. In: Proc. of VIth WMO Sci. Conf. on Wea. Modif., Italy, WMO/TD-No.596, v.2, 499-502.
- Koshenko, A.M. and Ponomarenko, I.P., 1979: Some characteristics of frontal cloud and precipitation systems in Ukraine. Tr. UHRI, 176: 117-131 (in Russian).
- Palamarchuk L.V., 1990: Mesostructural features of the thermodynamic characteristics' distribution in frontal cloud systems of south and southwest cyclones over Ukraine. Tr. UHRI, 237, 96-117 (in Russian).
- Palamarchuk, L.V. and A.M. Pirnach, 1992: Study an internal structure of frontal zone with aid of three-dimensional numerical models. Tr. UHRI, 243: 107-124 (in Russian).
- Palamarchuk L.V. and A.M. Pirnach, 1994: Mesoscale structure of atmosphere fronts and potentialities of associated cloud systems for changing their precipitation over Ukraine. In: Proc. of VIth WMO Sci. Conf. on Wea. Modif., Italy, WMO/TD-No.596, V.2, 691- 694.
- Pirnach, A.M. and S.V. Krakovskaya, 1994: Numerical studies of dynamics and cloud microphysics of the frontal rainbands. Atmos. Res., 33: 333-365.
- Shapiro, M.A. and Evelyn Donall Grell, 1994: In search of synoptic / dynamic conceptualizations of fronts, jet streams, and the tropopause. In: Proc. of Int. Symp. "The Life Cycles of Extratropical Cyclones", Bergen- Norway, Vol.1: 163-181.

OROGRAPHIC INFLUENCE ON THE DISTRIBUTION OF ACCUMULATED RAINFALL FOR DIFFERENT WIND DIRECTIONS

Hermann Gysi

Inst. f. Meteorologie und Klimaforschung
Forschungszentrum Karlsruhe / Universität Karlsruhe
P.O. Box 3640 D-76021 Karlsruhe

1. INTRODUCTION

Orographic influence on the distribution of rain intensity in precipitation systems is a well known fact. However, due to the high variation of precipitation in space and time even in plain terrain e.g. through rain showers or convective systems its evidence is difficult to substantiate (Joss & Waldvogel, 1990). Additionally in orographic structured terrain the rainfall distribution is strongly affected by the structure of the terrain and its local wind-systems.

In order to determine the natural distribution of accumulated rainfall amount in such a terrain high resolution rainfall data are needed which are difficult to obtain from conventional rain gauge measurements. A suitable instrument for high resolution rain measurements is a C-band Doppler radar. The data used presented here are obtained by a radar located in the Rhine valley in the southwestern part of Germany. The orographic structure of this region is characterized by two parallel north-south orientated ridges of hills along the valley. Due to this feature many different orographic effects influencing the regional rainfall distribution become obvious. Not only well known phenomena as maxima of rainfall in the updraft region of the hills and minima in the lee of the hills, but also phenomena triggered by mesoscale flow systems such as parallel cloud bands (Gysi, 1995), preferred tracks of thunderstorms as well as vortices in the lee of hills can be observed.

These effects can often be very weak, occur rather seldom and depend strongly on the direction from which the clouds and rain systems move into the region of interest. Therefore they can usually not be recognized from the monthly accumulation of rain (neither by radar nor by ground based rain gauge measurements) which comprises a mixture of rainfall events from various wind directions.

2. DATA AND METHODOLOGY

To reveal the orographic influence on the distribution of the accumulated rain amount, the rain intensities detected at constant height (1.0 km) above ground were integrated in time:

- monthly without respect of the wind direction and
- the whole year 1994 considering eight different sectors of wind direction, where each sector is 45° wide.

Rain intensities were integrated with respect to a certain sector if the mean wind direction - measured between 2 and 2.5 km agl. in the vertical wind profile at the location of the radar - falls into that sector. The vertical wind profiles have been derived from Doppler velocity data with the VVP method of Waldteufel & Corbin (1979). Table 1 shows a list of hours of accumulated rainfall in 1994 for each of the eight sectors.

Table 1: Characteristics of the sectors of the wind direction and the hours of accumulation

Acronym	Wind direction	Duration of accumulation	
NNO	north-northeast	159 h	(4.5 %)
ONO	northeast-east	141 h	(3.9 %)
OSO	east-southeast	82 h	(2.2 %)
SSO	southeast-south	121 h	(3.4 %)
SSW	south-southwest	529 h	(14.6 %)
WSW	southwest-west	1745 h	(48.3 %)
WNW	west-northwest	572 h	(15.8 %)
NNW	northwest-north	208 h	(5.8 %)
NKL	not classifiable	53 h	(1.5 %)
Totale time of rainfall		3610 h	(100 %)

The data of radar reflectivity and Doppler velocity were available every 15 minutes as full volume scans with 15 elevations and a range of 120 km. For a larger range, reliable rain measurements by radar near the ground level are not possible anymore (Fabry et al. 1992). The radial resolution of the data is 0.5 km, the azimuthal resolution is 1°. Rain intensity is calculated at 1 km above ground, i.e. by using terrain-following surfaces, where the horizontal spacing is 1 km.

In order to transform the radar reflectivity (Z) into rain intensity (R), three different Z-R relations were assumed to be representative for different periods and meteorological situations (Sauvageot 1994):

- May until November $Z = 300R^{1.5}$ (only rain)
- December until April $Z = 200R^{1.6}$ (for rain)
 $Z = 1800R^{2.2}$ (for snow)

The reflectivity data of the radar have been corrected using a high pass Doppler filter to remove low frequency signals due to ground clutter and the rain intensities

have been corrected using measurements of a disdrometer located 15 km south of the radar.

3. RESULTS

Three monthly distributions (April, June and August) and three wind direction dependent (WSW, OSO and WNW) distributions of time integrated rainfall amount in mm are shown in Figs. 1-6. In all figures the location of the radar is in the center and marked with (+). The solid lines are isolines of the orographic height (100, 300, .. 900 m). West of the radar are the hills of the Pfälzerwald and in the Northeast those of the Odenwald (both with a maximum height of about 600 m). Southwest of the radar are the Vosges and in the South is the Black Forest (both with a maximum height of about 1100 m). Between the Vosges and the Black Forest is the wide and flat Rhine valley. East of the radar nearby trees lead to a drastic attenuation of the signal which is clearly seen in all figures.

In April (Fig.1), the month with the highest rainfall amount in 1994, only weak orographic effects occur. From Table 2 which shows the frequency of the different wind directions with rain one can see that this month is dominated by rain events from southwest-west.

Table 2. Frequency of the wind directions in the montly distribution of rainfall amount

	April	June	August
NNO	25	31	15
ONO	8	7	40
OSO	0	13	4
SSO	31	3	0
SSW	68	45	31
WSW	221	86	87
WNW	35	52	41
NNW	31	18	4
NKL	49	0	0
Total	468	255	222

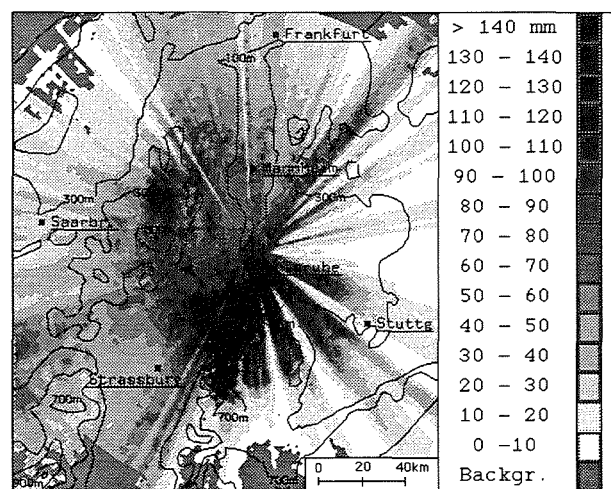


Fig.1: Distribution of rainfall amount, April 1994

Note that the maximum of the rain amount was in the Rhine valley between Karlsruhe and Strassburg and not at the slope of the Black Forest. A weak orographic influence on the rain distribution can be recognized at the hills of the Pfälzerwald.

The minimum rain amount, which usually appears east of the Vosges in the Rhine valley is weaker than in the distribution of rainfall accumulation of the whole year 1994 (Gysi, 1995) or in the climatological representations of this region (Klimaatlas, 1995).

Orographic effects in the rainfall distribution of June (Fig.2) are also not significant: large rainfall amounts have been measured not only in the Black Forest and the hills of the Pfälzerwald and Odenwald where they are expected but also in the Rhine valley. The maximum values northwest of the Black Forest as well as the minimum east of the Vosges are not significant.

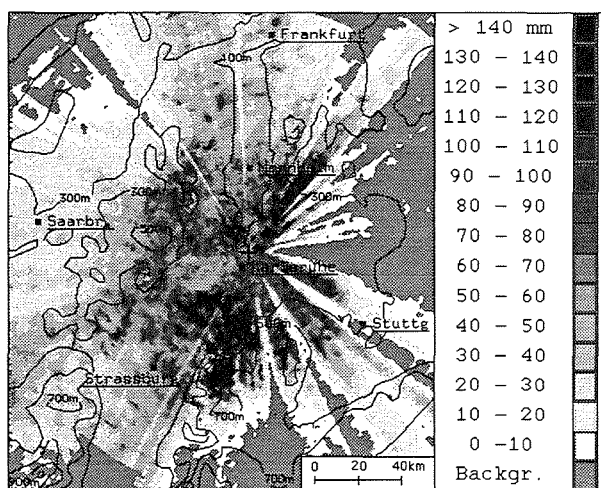


Fig.2: Distribution of rainfall amount, June 1994

This rainfall distribution is typical for a month, where a certain wind direction does not prevail (see Table 2). Nevertheless the inhomogeneous structure of the rainfall amount with horizontal gradients larger than 100 mm within 2 km in the Rhine valley is an interesting result. This is due to the occurrence of strong thunderstorms in this month. These strong gradients show how uncertain a comparison of ground based point measurements of rain with rainfall data from radar may be.

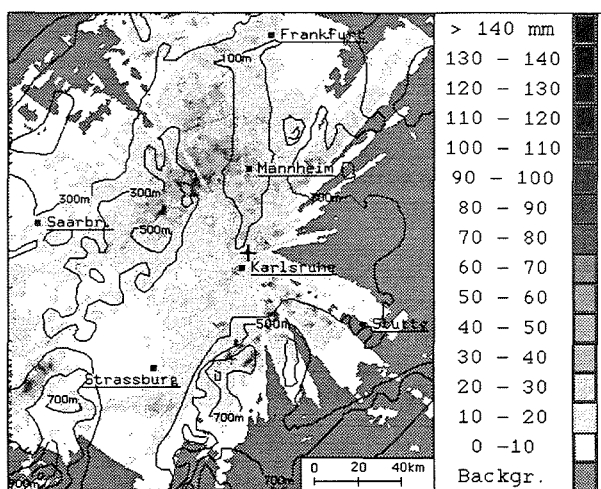


Fig.3: Distribution of rainfall amount, August 1994

In August (Fig. 3) the amount of rain was very small and again there is almost no orographic structure to be seen in the distribution of rain amount. Only in the northern part of the Pfälzerwald, the occurrence of rainfall is larger.

We turn now to the distributions of integrated rainfall amounts of all rain events within a certain sector of wind directions. Orographic effects then appear stronger and are very much better to recognize than in the monthly distributions. In Fig. 4 which shows the distribution of rainfall amount for the wind direction sector southwest-west (WSW) one can see a strong maximum of precipitation at the western slope of the Black Forest and a strong minimum at the eastern slope of the Vosges. Orographically induced maxima of rain are also seen in the

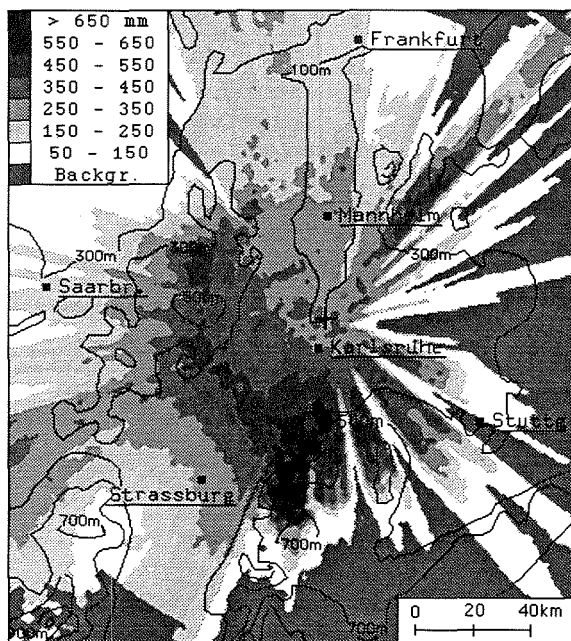


Fig.4: Distribution of rainfall amount with wind from southwest-west 1994

hills of the Odenwald, the Pfälzerwald and at the north-western slope of the Vosges. The maximum value in the Pfälzerwald is underestimated because it is on the luff side of the hills and therefore already invisible for the radar at 1 km agl.. It is interesting in this figure that the maximum of rain amount is southwest of the radar in the Rhine Valley. This is due to a depression between the Vosges and the Pfälzerwald which allows an undisturbed advection of moist air into the Rhine valley. Because of the high frequency of rain events in this sector (Tab.1) the distribution of Fig. 4 is representative of the whole year 1994.

In Fig. 5, which shows the distribution of rainfall amount for rain events within the wind direction sector east-southeast one can see that the whole area south of the radar is in the lee of the Black Forest and therefore very dry. The maximum rain amount is at the eastern and northeastern slope of the Pfälzerwald and in the Odenwald. Unfortunately the southeastern slope of the Odenwald is invisible for the radar because of attenuation by trees. The similarity of this distribution with that of August (Fig. 3) shows that the rain distribution of

August is dominated by rain events from the wind direction sector OSO, or vice versa that the rain distribution belonging to this sector is caused mainly by thunderstorms. The maximum at the northwestern slope of the Vosges as well as the inhomogeneous structure north of Mannheim are also due to thunderstorms.

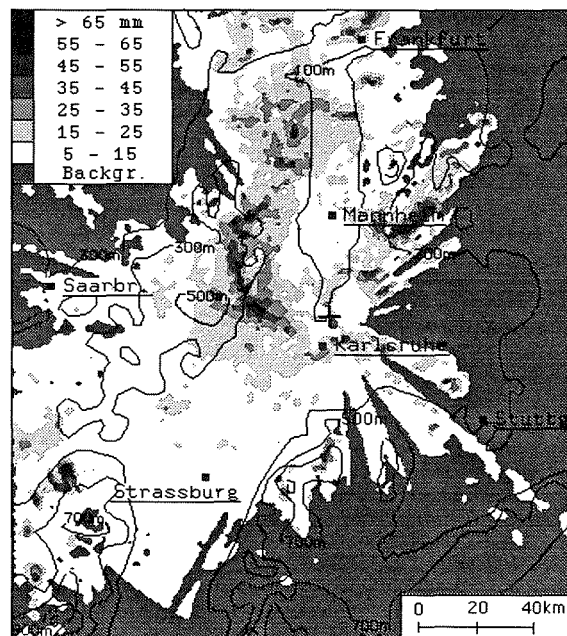


Fig.5: Distribution of rainfall amount with wind from east-southeast 1994

As a last example Fig. 6 shows the orographic influence on the distribution of rain amount with wind from the sector west-northwest. As expected, the accumulation effect of moist air in the updraft region at the north-western slopes of the Black Forest and the Odenwald leads to high rain amounts at the slopes themselves and in the eastern Rhine valley.

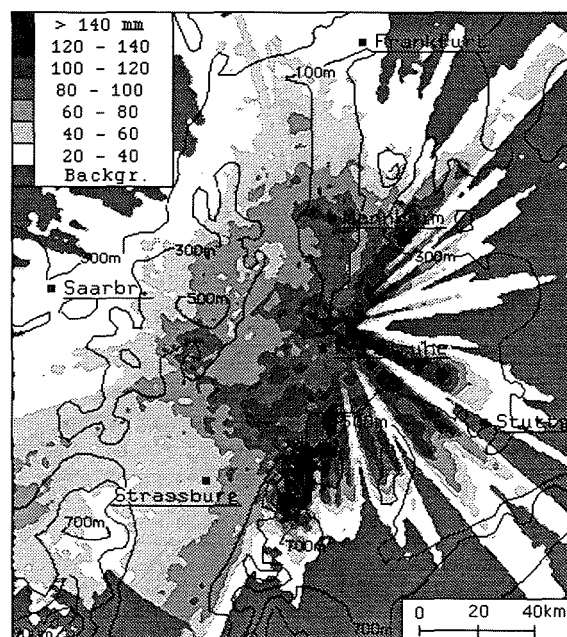


Fig.6: Distribution of rainfall amount with wind from west-northwest 1994

An interesting phenomenon in that distribution is the local maximum of integrated rainfall amount west of the radar and the local minimum northwest of it, both in the lee-side of the Pfälzerwald.

The local minimum is a nice example of a local föhn - effect in the lee of the 650 m high Kesselberg (which is not marked in the figure).

Unexpected with regards to this wind direction, on the other hand, is the local maximum of rainfall amount further south in the lee of the hills. The high rainfall intensities there seem to be triggered by a strong vertical windshear in the Rhine valley which often occurs during rain events according to this wind direction. It can be

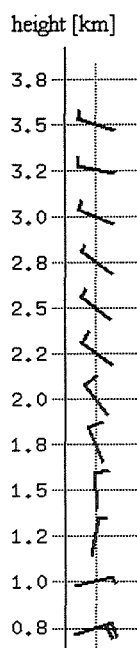


Fig.7: Vertical wind-profile at the location of the radar during the occurrence of the local maximum in the lee of the Pfälzerwald.

windspeed towards the slope of the Pfälzerwald (see arrows in Fig. 8). The northeasterly flow there reaches a height of almost 3 km above msl. (maybe through a forced raise at the hill). Above 2 km msl. it interacts with the northwesterly flow which leads to a strong anticyclonic rotation (dashed circle in Fig. 8).

Typical for this situation is the stationary precipitation cell at the location of the maximum in Fig 8 (and also in Fig. 6). The maximum of rain amount in Fig. 8 is formed by an eight hours time integration of horizontal cuts of the rain intensity (measured every 12 minutes) of a typical rain event from this wind direction in January.

No horizontal motion of the precipitation cell is recognizable. The precipitation at the northwestern slope of the Black Forest results from other precipitation cells.

clearly recognize in Fig. 7 which represents a typical vertical profile of the wind at the location of the radar for cases with the occurrence of rain cells in the lee of the Pfälzerwald. Near the ground, there is a rather strong flow from east-northeast. Between 1 and 2 km agl. it turns counterclockwise into a flow from northwest. Above 2 km the wind direction is west-northwest which causes that the rainfall event is counted into the sector west-northwest. Figure 8 shows a schematic representation of the typical local flow field around that maximum. The flow of moist and cold air from west-northwest over the Pfälzerwald in high levels is obviously disturbed and destabilized at the location of the maximum by a current of warm air coming from east-northeast near the ground in the Rhine valley. The evaluation of horizontal cuts of the Doppler velocity data shows an increase of

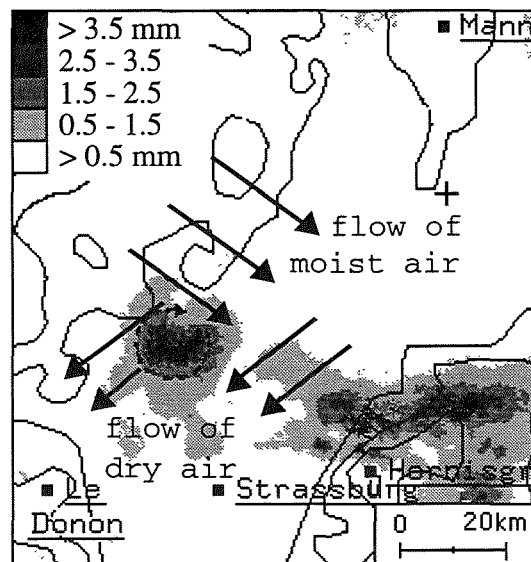


Fig.7: Schematic representation of the mesoscale flow near the local maximum in the lee of the Pfälzerwald.

4. SUMMARY

With the method of the wind direction dependent time integration of horizontal cuts of the rain intensity at 1 km agl. from radar data it is possible to reveal orographic effects dominating the distribution of rainfall amount. In contrast to time integrations of the precipitation over certain periods (month, year) which often shows very weak orographic influence on the rainfall amount, the wind direction dependent time integration elucidates even surprising meso- γ scale phenomena. A further step will be the comparison of these local phenomena with model simulations in the same area.

5. REFERENCES

- Fabry F., Austin G.L., Tees D., 1992: The accuracy of rainfall estimates by radar as a function of range. *Quart. J. Roy. Meteor. Soc.*, **118**, 435-453.
- Gysi H. 1995: Niederschlagsmessung mit Radar in orografisch gegliedertem Gelände. Dissertat., Univ. Karlsruhe.
- Joss J., Waldvogel A., 1990: Precipitation measurement and hydrology. Radar in Meteorology, *Amer. Meteor. Soc.*, D. Atlas, Editor, 577-606.
- Klimaatlas Oberrhein Mitte-Süd. IFG, Offenbach 1995.
- Sauvageot H. 1994: Rainfall measurement by radar: a review. *Atmos. Res.*, **35**, 27-54.
- Waldteufel P., Corbin H., 1979: On the analysis of single Doppler radar data. *J. Appl. Meteor.*, **18**, 532-542.

FRONTAL PRECIPITATION FIELD MORPHOLOGY AND IT'S POSSIBLE APPLICATION TO FORECASTING

Natalia A. Bezrukova and Alexander Ya. Naumov

Central Aerological Observatory
Dolgoprudny, Moscow Region 141700, RUSSIA

1. INTRODUCTION

Experimental data as given below have demonstrated the morphology of precipitation fields in frontal zones over the continental Russia. The morphology includes not just spatial characteristics (linear dimensions and form) but also movement of individual morphological features. We also discuss a relative contribution of widespread and convective precipitation to the total rainfall amount near the fronts over the European Territory of Russia (ETR). An attempt was made to apply the obtained information on morphology of precipitation structures and widespread/convective precipitation ratio to forecasting.

2. STUDY OBJECTIVES, DATA SOURCES AND METHODS

The objectives were to study morphology of precipitation fields, to obtain its quantitative characteristics and try to apply them to forecasting. Original field data obtained by rain recorders at the standard network and by the Meteorological radar-computing complex are analyzed.

In order to lessen effects of subjective perception in the precipitation field analysis, one needs to formalize the procedures for precipitation feature identification. Description of the form and localization of the mesoscale precipitation features was based on the following parameters: minimum (w), maximum size (l), "wave length" λ (a distance between local maxima), distance from front (d).

3. FREQUENCY OF OCCURRENCE

We have examined cloud and precipitation systems of about 100 fronts over ETR (Tabl. 1). The dimensions of large (L) mesoscale rainbands (Fig. 1) most frequently correspond to a boundary between α and β scales (150-250 km), while dimensions of mid (M) mesoscale rainbands have a two-mode frequency distribution: about 80-120 km (M1) and 30-50 km (M2). Small (S) mesoscale features correspond to γ -scale by Orlanski (1975).

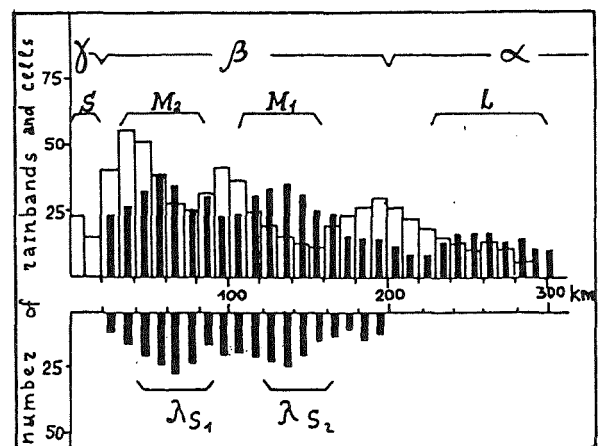


Fig.1 Frequency of occurrence of the frontal rainbands and cells (at the bottom). Open diagram - dimensions of the rainbands and the small features (cells), bold diagram - the distance between the axes of the rainbands (wavelengths). At the bottom - distance between the centers of the cells along the front.

Average wavelengths of mesoscale features are 200-300 (L), 100-150 (M1) and 50-70 km (M2). Distance between the centers of the small mesoscale features λ_{s1} is about the same both in cross and along the front directions (about 50-70 km).

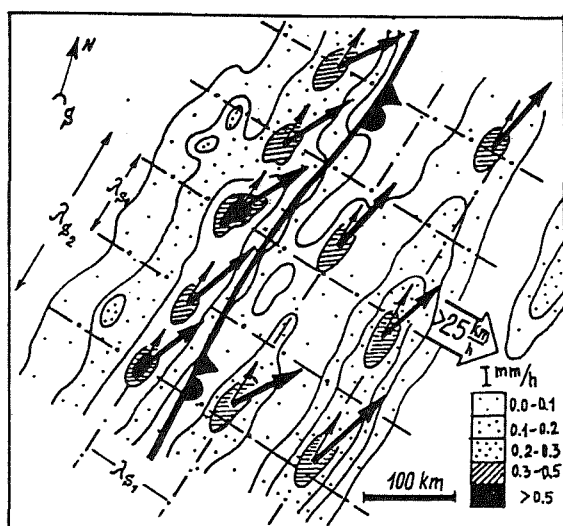


Fig. 2 Distribution of precipitation on January, 23 1986. The cells (shaded area) are located in the knots of a grid-like structure. Thin arrows indicate advection of the warm air in the warm sector. Thick arrows indicate displacement of high intensive precipitation cells. Open white arrow - direction of movement of the frontal precipitation system as a whole. It is an example of the cells of embedded convection that are developing in a thin layer.

Another maximum of occurrence of distance between cells along the front line λ_{s2} is observed in an interval of 120-160 km. Since the distance between the cells in both directions is almost the same, the cells are thought to be located in the knots of a grid-like structure (Fig. 2). Thus, besides a banded

structure there exists a regular cellular structure of the frontal precipitation fields.

4. SPATIAL DISTRIBUTION OF THE MESOSCALE FEATURES

Position of rainbands in relation to the frontal line are described by parameters: d and λ . Their quantitative values depend on the type of front. Accumulation and systematization of these data for local region is of important significance to forecasting. Two or three rainbands in precipitation field structure, well known in other regions, are also evident at ETR (Table 1). It is also shown that the mesoscale morphology structure of the rainfall and snowfall fields are identical.

5. MOVEMENT OF PRECIPITATION MESOSCALE FEATURES

Large (L) and mid-size (M) rainbands are moving along the frontal system as a whole. Small (S) scale cells near the cold fronts and occlusions are moving along rainband axis, thus following the direction of the strongest warm air advection in the warm sector. Low and mid-level jet streams in the warm air (warm sector) play an important role in the S-dimension cell movement.

Table 1. Rainband morphology characteristics for three type of fronts.

Type of front (number of cases)	Total width of precipitation zone, km	Distance (d) between front line and rainband, km	L-rainbands width, km (λ_L)	M-rainband width, km	
				(λ_{M1})	(λ_{M2})
Warm fronts (24)	200-250	150-160	150-200 (250-280)	80-120 (150-200)	30-40 (60-80)
Cold fronts (34)	300-350	230-240	-"-	-"-	-"-
	50-80 180-200	- 100-150	- 150-200	- 80-100 (120-160)	- 30-60 (40-80)
Occlusion fronts (23)	260-280	-	-	-"-	-"-
	250-300	100-150	-	-	30-60 (50-70, 120-160)

Mid-level jets with a mean velocity of 15-17 m/s (up to 25 m/s) exist in the warm sector of cyclones, even at the mature stage of occluding. No movement of precipitation cells along the warm fronts has been found.

It has been shown earlier (Bezrukova and Shmeter, 1989) that the precipitation cells are moving along the wind shear vector in a convection layer. The cells of embedded convection that are developing in thin layers, move at a speed equal to the vector sum of cold and warm air velocities.

6. CONTRIBUTION OF VARIOUS SNOW INTENSITIES TO TOTAL SNOWFALL

We examined 27 cases of winter-time frontal precipitation in various types of fronts and for different types of cyclone trajectories, which adequately reflect typical frontal processes in the European Russia. Described below are results of radar observations of various snow intensity contributions into the total snowfall and area covered by precipitation. Moreover, convective to widespread precipitation contribution ratios are estimated. For this purpose an assumption was made that light and heavy precipitation was produced mainly by widespread lifting on front, convective updrafts, respectively. A threshold of 0.3 mm/h was taken to distinguish between light and heavy precipitation (Bezrukova, 1994). In winter stratiform precipitation generally prevails. Ratio values strongly depend on the type of cyclone

trajectory. The frontal precipitation in the northern (N) and north-western (NW) cyclones is the lightest. The heaviest precipitation was observed in southern (S) and south-western (SW) cyclones. It has been found also, that in N, NW cyclones 90% of frontal precipitation is stratiform and covered 90% of total area. In the western (W) cyclones stratiform precipitation accounts for 70-80%. By contrast, in S and SW cyclones stratiform precipitation accounts for only 20-40% of the total amount and covers no more than 30-40% of the total area. Relative contribution of stratiform precipitation into the total snowfall amount, depends, to some degree, on the type of front. Stratiform precipitation contributes 90-92% in warm frontal snowfall, 70% in cold and occluded fronts.

7. POSSIBLE APPLICATION TO FORECASTING

The statistical characteristics of ETR precipitation field structure (Table 1) can be applied to forecasting. An example of such application (in case of a summer-time warm front) is described below. A site affected by an approaching warm front will experience the following sequence of the weather events. If the cloud system width exceeds 300 km and front velocity equals 20-50 km/h, the first 2 hour peak in precipitation rate and decrease of visibility to 6-8 km. Then the rain faints or ceases. The second rain peak is to be expected 1-2 hours after warm front passage. At this time

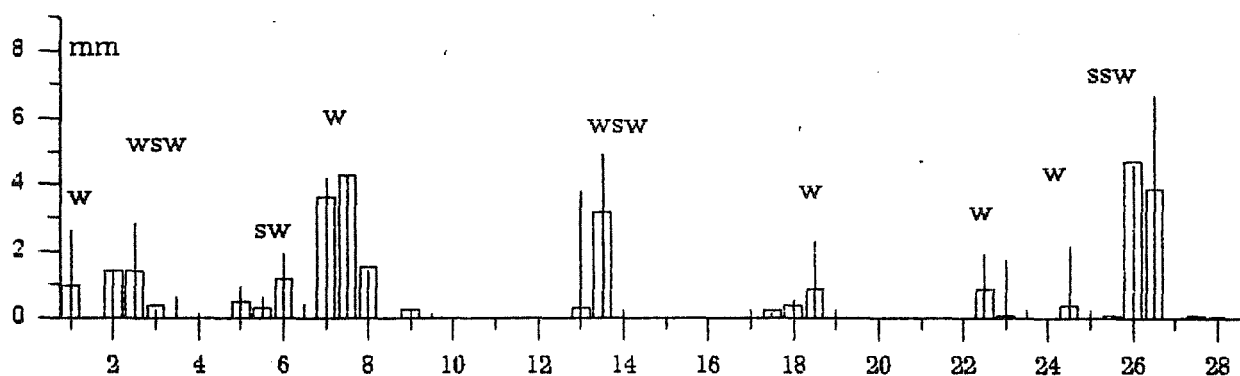


Fig. 3 The calculated (forecasted) versus observed precipitation amounts. February, 1995. Open diagram - calculated values of 12-hours sum of precipitation. Line diagram - observed precipitation amounts. The largest forecast errors corresponded to cases with W and SW trajectories.

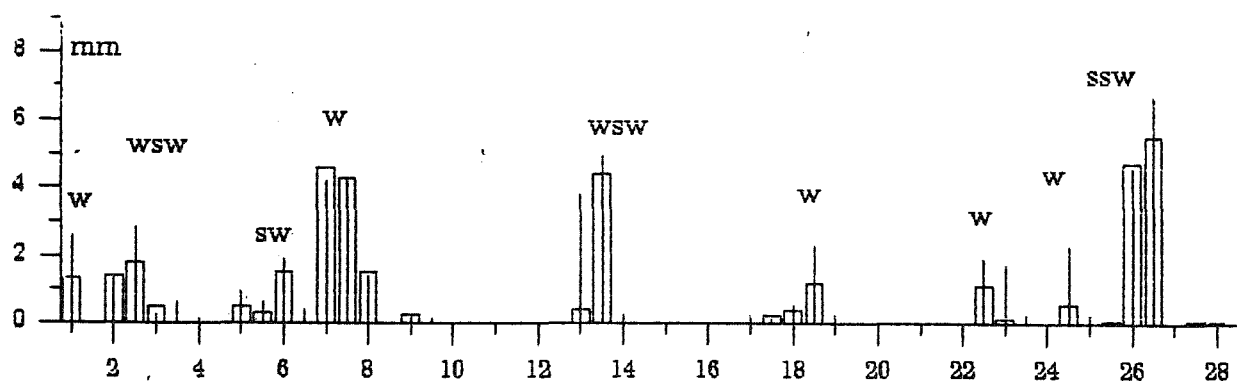


Fig. 4 The calculated values 12-hours sum of precipitation with correction for convective part of total amount.

the rain intensity undergoes drastic changes. Within 20-30 min it can rise to shower values it can rise to shower and lessen visibility to 1-2 km.

A quantitative forecast is also possible. Several series of calculations of stratiform snowfall (i.e., generated by widespread lifting) 12-hours in advance in Moscow Region were performed for February 1995 using diagnostic vertical motion derived from rawind-sonde observations. No direct calculations of the winter-time snowfall were involved. The latter was inferred from the above statistics of convective/stratiform precipitation ratio for various types of fronts and synoptic processes (trajectories).

The first stage involved calculation of the widespread precipitation which, as has been stated above prevails in winter. Fig. 3 shows the calculated (forecasted) versus observed precipitation amounts. Mean absolute (η) and relative (ϵ) errors of the forecast, according Manual (1986), were 0.40 mm and 34% respectively, the correlation coefficient (r) between calculated and observed values being 0.88. The largest forecast errors corresponded to cases of cyclones of southern and south-western trajectories.

At the second stage, a correction for convective precipitation contribution was made, based on the obtained widespread/convective precipitation ratios for cases with W and SW cyclone trajectories (Fig. 4), characteristic to the given region. The correction resulted in lessening of the forecast

error: η and ϵ 0.31mm and 23% respectively, $r=0.92$.

8. CONCLUSION

The principal findings include: existence and parameters of mesoscale inhomogeneities in precipitation intensity fields, their shape and size, characteristics of motion, regularities of their position in cyclone system relative to surface front boundary. Classification of mesoscale inhomogeneities within the fields of frontal precipitation over the ETR according to their linear dimensions is suggested. It is also shown that the cellular structures can be observed in precipitation fields alongside with the bands. An attempt was made to apply the obtained information to forecasting.

9. REFERENCES

- Bezrukova N.A., Shmeter S.M., 1989: Cloud and precipitation structure in the frontal zones. *Proc. 5-th Int. Weath. Mod. Conf.*, Beijing, 471-474.
- , 1994: Winter precipitation variability over European Russia in different types of fronts originated over Arctic, Atlantic and Mediterranean regions. *Atmospheric Research* 34, 153-168.
- Manual for Short-Range Forecasting., 1986. Gidrometeoizdat, Leningrad, 702.
- Orlanski I., 1975: A rational subdivision of scales for atmospheric properties. *Bull. Amer. Meteorol. Soc.* 5, 525-530.

CONVECTIVE VERSUS STRATIFORM RAINFALL — REVISITING THE DYNAMICAL AND MICROPHYSICAL BACKGROUND

Matthias Steiner and James A. Smith

Department of Civil Engineering and Operations Research
Princeton University, Princeton, New Jersey 08544

1. INTRODUCTION

The discussion of convective versus stratiform rainfall gained attention because of the distinct differences in the vertical profiles of latent heat released to the atmosphere between the two basic modes of precipitation (Houze 1989; Mapes and Houze 1995; Tao et al. 1993). This is important for climatological studies such as the Tropical Rainfall Measuring Mission (TRMM; Simpson et al. 1988) or the Coupled Ocean–Atmosphere Response Experiment (COARE; Webster and Lukas 1992).

On the other hand, there are arguments that tend to make a convective–stratiform separation also useful for the radar-rainfall measurement (Steiner et al. 1995). A classification of rainfall into convective and stratiform may also provide valuable information for hydrological modelling. For example, hydrologic modelling may be advanced by making use of statistical rainfall properties within a grid box (e.g., rain rate distributions, fractional coverage in time and space, or exceeding a given rain rate threshold); a convective–stratiform separation may provide useful information in that regard. In addition, global circulation models (GCM) generally incorporate some convective versus widespread precipitation parameterization (e.g., Donner 1993; Xu 1995).

Because of these different perspectives, however, and because there is no consensus on precisely how to define the terms *convective* and *stratiform*, there exists some confusion about the terminology and the use thereof. A convective–stratiform definition may need to be formulated scale dependent; for example, a physically-based classification that might be useful on the storm or mesoscale, may have to be parameterized as “subgrid-scale noise” for application in a GCM. Nonetheless, the definition should be consistent across scales. It appears very appropriate, therefore, to revisit the dynamical and especially the microphysical aspects of the precipitation formation and discuss their relevance to different scales.

2. BASIC DYNAMICAL CONSIDERATIONS

In order for a cloud to form, it is required that air becomes saturated. This is accomplished almost entirely by vertical motions (thermal, orographic, or along frontal boundaries), lifting air parcels to levels where condensation takes place and cloud droplets (or ice crystals) form. Mixing or radiational cooling of air masses may result in cloud formation (e.g., fog), though this is rarely accompanied with measurable amounts of precipitation. The vertical air motions have horizontal extents ranging from tens of meters to hundreds of

kilometers, and their magnitude may range from a few centimeters per second to tens of meters per second, dependent on the generating process. The horizontal extent of the vertical air motion is decreasing with increasing magnitude of the vertical velocity.

Vertical air motions are required for cloud formation and play a dominant role in determining the character and quantity of precipitation that a cloud may ultimately produce. Updrafts not only supply moisture to the cloud but also increase the time precipitation particles may reside within the cloud and thus have time to grow in size. On the other hand, the microphysical structure, describing the circumstances by which an individual cloud droplet (or ice crystal) can form from the vapor phase, grow to visible size, and interact with other cloud or precipitation particles, determines how receptive a cloud may be for producing rain and how much time may be required to do that.

The vigor of convection is primarily dependent on the magnitude of the vertical air motions and the moisture supply. In convective clouds, precipitation particles grow while being carried aloft by significant vertical air motions until they fall out of the updraft cores or become too big to be swept out. In contrast, in stratiform (or more widespread) precipitation the particles grow while they are settling down from higher levels in the cloud in mostly weaker, more mesoscale updrafts. It makes sense, therefore, to use the magnitude of the vertical air motions to classify precipitation into convective and stratiform elements. According to Houze (1993), for example, stratiform precipitation is defined to exist when the vertical air motion *above the freezing level* is much smaller than the terminal fall speed of snow particles. Thus updrafts in stratiform precipitation are bound to be smaller than maybe 1–3 m/s.

3. MICROPHYSICAL CONSIDERATIONS

From a microphysical point of view, cloud and precipitation particles may grow by vapor deposition (diffusional growth) or by particle interactions, namely the capture of other particles. On the other hand, the size of a particle may also be reduced due to breakup into smaller pieces, caused by instability or collisions.

Depending on whether the interacting particles are in solid or liquid form, the following microphysical processes may be distinguished: Coalescence of liquid particles, aggregation of ice particles, the capture of liquid particles by ice particles (riming or accretion), and vice versa, the capture of ice crystals by raindrops (freezing). Breakup may occur either spontaneously or

due to collisions among particles; for example, raindrops may become too big, unstable and thus break up into smaller drops, or satellite droplets may be created as a result of collisions (Komabayasi et al. 1964; Brazier-Smith et al. 1973; Low and List 1982). Large aggregates may break up into smaller pieces due to collisions (fragmentation), or as a result of a structural breakdown during the melting process (Mitra et al. 1990). And last but not least, under certain favorable circumstances, ice splinters may break away during the riming process (Hallett and Mossop 1974; Mason 1996) resulting in increased ice particle concentrations.

Hereafter, the key role of the mixed-phase process of riming, the pure ice-phase process of aggregation, and the competition among them will be highlighted. The discussion in Section 4 specifically emphasizes their role in shaping the raindrop spectra reaching the ground.

3.1 Riming and accretion (mixed phase)

The collection of supercooled cloud or rain droplets by ice particles is likely the most important growth mechanism of mixed-phased clouds. Based on the fall speed (difference) of the involved particles, the following distinction is made: The process by which precipitation-sized ice particles are collecting non-precipitating liquid particles (cloud or smaller drizzle droplets) is called *riming*, while the collection of precipitating particles (drizzle or raindrops) is termed *accretion*.

In mixed-phased clouds essentially every collision results in capture. The collection efficiency for colliding solid and liquid particles is therefore determined by the collision efficiency. The likelihood of a collision among liquid and ice particles is dependent on the size, shape, and number concentrations of the particles. A theoretical basis to calculate the riming efficiencies for complex particle shapes is provided by Böhm (1992, 1994).

The riming of ice crystals will not occur until they have reached a critical size by vapor depositional growth, which may vary with crystal habit, as pointed out by Ono (1969) and Harimaya (1975). Observations indicate a minimum size of cloud droplets on rimed crystals of about 10 μm (Harimaya 1975; Mosimann et al. 1994).

Experimental and theoretical studies indicate that ice particles smaller than maybe 100 μm in diameter are not collecting cloud droplets anymore; for example, Böhm (1992) estimates a corresponding collection efficiency of less than 10%. Once that critical size has been reached by the ice particle, the collection efficiency increases rapidly with increasing particle size. It appears to be maximal for cloud droplets with diameter of 20-30 μm . This is nicely reflected in the experimental data of Reinking (1979) and Mosimann et al. (1994). The latter study shows that columnar ice particles tend to collect larger cloud droplets (wide distribution peaking at 60 μm) than planar ice crystals, which collect predominantly smaller cloud droplets (narrow distribution peaking at 20 μm). Based on the results of Reinking (1979), cloud droplets larger than maybe 120 μm in diameter are not very significant to riming anymore.

Mosimann et al. (1994) objectively quantify the degree of riming on a scale from 0 (unrimed) to 5 (graupel). While lightly to moderately rimed crystals retain vestiges of their original crystal habit, the identity

of the collector becomes lost under heavy riming and the particle is referred to as graupel.

The fall speed of ice particles slowly increases with increasing degree of riming (increased mass), but starts to increase markedly beyond a riming degree of 3 (densely rimed) and higher (towards graupel). Intuitively, one would expect the ice particles to fall increasingly faster with increasing mass (rime); however, the accreted cloud droplets tend to increase the drag coefficient of the particle which may partially compensate the effect of an increased mass (Pflaum et al. 1978; Johnson 1987).

According to our previous definition, the boundary where accretion might start to occur is around updrafts of maybe 2 m/s, which is enough to sweep out drizzle droplets of 500 μm in diameter. Stronger updrafts may carry raindrops aloft and lead to significant accretion of graupel or frozen raindrops. The size of the resulting hailstones is dependent on the magnitude of the updraft, the availability of supercooled water, the fall behaviour, and the residence time in the updraft cores (García-García and List 1992).

The vertical depth within the cloud over which the processes of riming and accretion may occur is dependent on the magnitude of the updrafts among other factors. In weaker updrafts, riming tends to occur within a ~2 km thick layer directly above the freezing level. In contrast, given large enough updrafts, riming may take place over a significant fraction of the cloud depth. Accretion is likely not to be observed at temperatures colder than maybe -10 degree C, because of a high probability for supercooled raindrops to freeze (e.g., due to collection of small ice particles) before they reach higher levels in the cloud. Riming may be observed in widespread as well as convective cloud systems. Accretion, however, is clearly a process of convective nature.

3.2 Aggregation (ice phase)

The collection of ice particles by ice particles of similar habits is called *aggregation*. This is a typical process occurring in widespread precipitation and is easily identified in radar displays by the bright band, a thin horizontal layer of enhanced backscatter attached to the 0 degree C level. The aggregation of ice particles is dependent on temperature, but also on the shape (crystal type) and size of the particles. The likelihood that two colliding ice particles stick together becomes much greater when the temperature increases to above -5 degree C, at which the surface of ice crystals becomes adhesive. The largest aggregates are found close to or within the melting layer (Stewart et al. 1984; Willis and Heymsfield 1989), but a secondary maximum may occur between -10 and -16 degree C, caused by dendrites that easily entwine their branches (Magono 1953; Hobbs et al. 1974).

4. DISCUSSION AND IMPLICATIONS

Figure 1 shows an idealized schematic to illustrate the relative importance of some key microphysical processes in growing ice particles and how they affect the raindrop size distribution reaching the ground. The top panel shows the growth mechanisms in a parameter space spanned by the vertical air motion and the

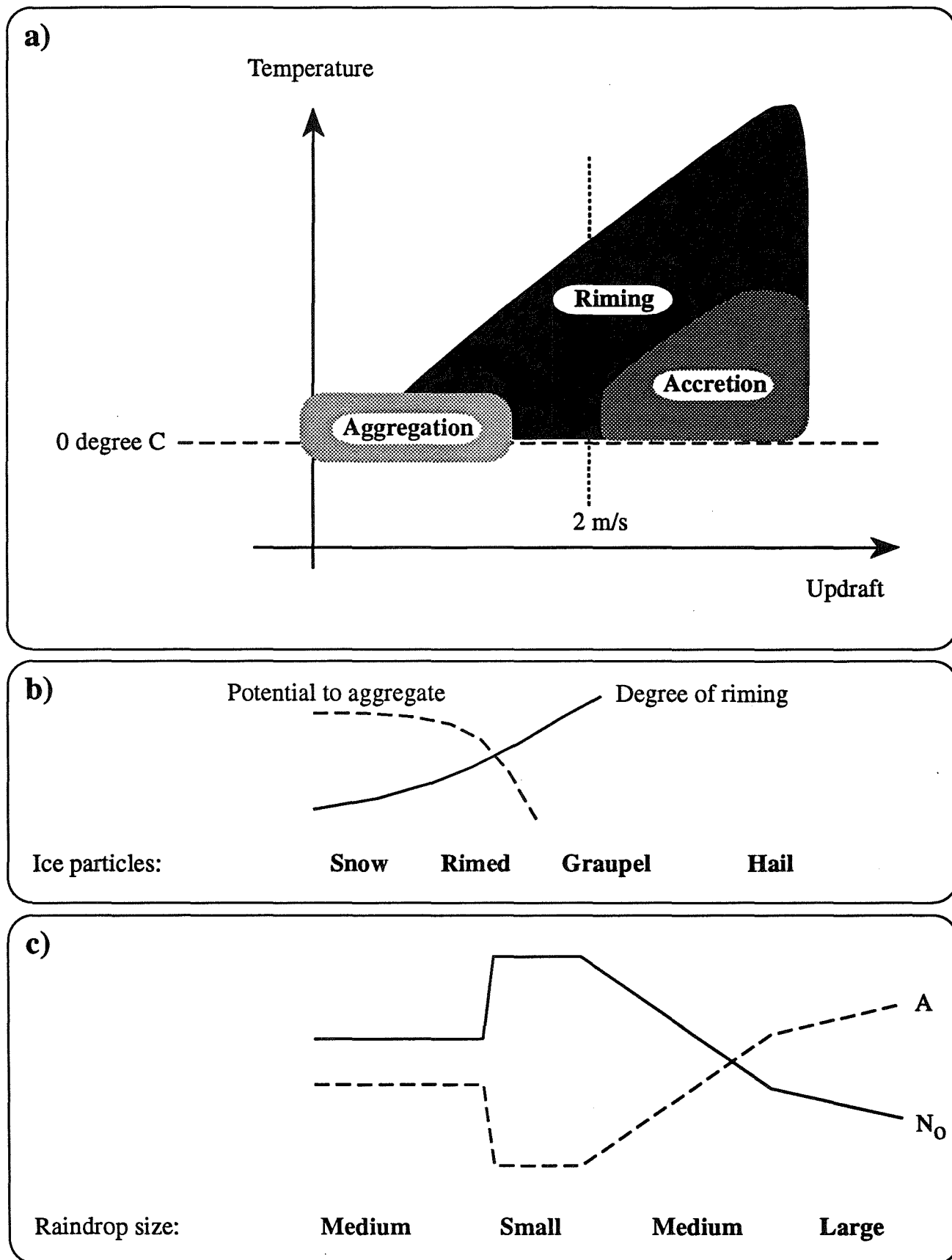


Figure 1. Schematic illustration of key ice-microphysical processes and their impact on raindrop size distributions reaching the ground.

temperature. The updraft given on the abscissa may as well indicate the magnitude of moisture supply to and/or the available liquid water content within the cloud. On the other hand, the temperature on the ordinate might also indicate height or depth of the cloud.

Evidently, in natural clouds there is a competition among the aggregation and riming processes (Wacker 1995). For example, heavily rimed particles or graupel are rarely observed together, while lightly or non-rimed ice particles may exist next to aggregates (Demos et al. 1993). A certain degree of riming appears to suppress the potential of ice crystals to aggregate (Fig. 1b).

The aggregation of ice crystals leads to snowflakes, which upon melting may result in decent sized raindrops. An increasing degree of riming will result in smaller and not aggregated ice particles, which eventually end up as smaller raindrops beneath the melting layer (Fig. 1c). In addition, the rime-splintering process may significantly enhance the number of smaller ice particles (Ferrier et al. 1995). On the other hand, graupel and smaller hailstones, if they completely melt before reaching the ground, will produce large raindrops. Using the intercept parameter N_0 of exponential raindrop spectra to indicate changes in the size distribution, we may thus observe a rapid increase in N_0 corresponding to a change of non or lightly rimed ice crystals or aggregates to moderately or densely rimed particles aloft (Waldvogel 1974; Waldvogel et al. 1993).

It can be shown that the multiplicative factor A of a power-law Z - R relationship is inversely related to the intercept parameter N_0 characterizing raindrop spectra (Fig. 1c). Therefore, any significant changes in the raindrop size distribution will be reflected in the Z - R relationship corresponding to these raindrop spectra. For example, Short et al. (1990) and Tokay and Short (1996) highlight such differences in Z - R relationships for intensities of 1-10 mm/h in tropical rainfall that are related to the competition between aggregation (results in medium-sized drops, and medium N_0 or A) and riming (smaller drops, high N_0 , smaller A). Similar effects have also been observed in midlatitude rainfall events. On the other hand, vigorous continental thunderstorms may produce raindrop spectra that result in low values for N_0 and high values for A .

The observations indicate that precipitation systems with extensive area coverage (i.e., significant area of stratiform rainfall), for example, mesoscale convective systems (MCS), produce raindrop size distributions that are in agreement with characteristics shown to the left in Fig. 1c, while multi-cellular, supercell, or thunderstorms associated with strong cold fronts are producing raindrop spectra that generally agree with the characteristics shown to the right in Fig. 1c (Waldvogel 1974; Waldvogel and Federer 1975). This may help to explain some of the difficulties encountered by Tokay and Short (1996) comparing Z - R relations for various geographical regions (their Fig. 11).

We have pretty much neglected warm-rain processes in the discussion so far. Below the melting layer, or in warm-rain clouds, size distributions of falling raindrops tend to evolve towards an equilibrium state (Srivastava 1971; List et al. 1987). The main processes of this evolution are binary raindrop interaction mechanisms like coalescence and breakup. While coalescence leads to

a production of larger drops reducing the number of smaller ones, breakup will restrict the maximum drop size to an upper limit. Warm-rain processes definitely occur in mixed-phase precipitation systems and they may actually be very important; for example, heavy rainfall events, characterized by low echo centroids (note the similarities to monsoonal-type rainfall), indicate that warm-rain processes are very efficiently at play (Maddox et al. 1978; Caracena et al. 1979; Smith et al. 1996). Such rainfall tends to be characterized by mediocre-sized raindrop spectra (lower A and higher N_0). The observed high rainfall rates are achieved by rather large number concentrations of raindrops. This results in numerous collisions and thus breakup, which may explain the somewhat reduced maximum drop size.

5. SUMMARY AND CONCLUSIONS

From a microphysical point of view, the existence of higher-density graupel is indicative for a convective nature of precipitation formation and growth. Graupel may thus be considered as particles marking the boundary between convective and stratiform precipitation. The growth of higher-density graupel particles requires updrafts of the order of 2-3 m/s, which is in support of the classification advocated by Houze (1993).

From a large scale point of view, such a definition might not be of great help. Convective-stratiform classifications have been attempted in the past for use in IR-based satellite rainfall estimation (Adler and Negri 1988). However, it appears that the more sophisticated satellites which are equipped with passive microwave sensors (e.g., SSM/I, MSU) might provide a better grip on classifying precipitation in convective and stratiform elements. For example, the 85 GHz signal exhibits a significant sensitivity to higher density ice particles (e.g., Wilheit et al. 1994).

The real challenge remains to find parameterizations of convective and stratiform rainfall for large-scale or global climate models that reflect how the subgrid-scale processes are felt on the grid-box and/or larger scales.

Acknowledgements. The very stimulating discussions with Brad S. Ferrier and Johannes P. Böhm are greatly acknowledged.

REFERENCES

- Adler, R. F., and A. J. Negri, 1988: A satellite infrared technique to estimate tropical convective and stratiform rainfall. *J. Appl. Meteor.*, **27**, 30-51.
- Böhm, J. P., 1992: A general hydrodynamic theory for mixed-phase microphysics. Part III: Riming and aggregation. *Atmos. Res.*, **28**, 103-123.
- Böhm, J. P., 1994: Theoretical collision efficiencies for riming and aerosol impaction. *Atmos. Res.*, **32**, 171-187.
- Brazier-Smith, P. R., S. G. Jennings, and J. Latham, 1973: Raindrop interactions and rainfall rates within clouds. *Quart. J. Roy. Meteor. Soc.*, **99**, 260-272.
- Caracena, F., R. A. Maddox, L. R. Hoxit, and C. F. Chappell, 1979: Mesoanalysis of the Big Thompson storm. *Mon. Wea. Rev.*, **107**, 1-17.

- Demoz, B. B., R. Zhang, and R. L. Pitter, 1993: An analysis of Sierra Nevada winter orographic storms: Ground-based ice-crystal observations. *J. Appl. Meteor.*, **32**, 1826-1836.
- Donner, L. J., 1993: A cumulus parameterization including mass fluxes, vertical momentum dynamics, and mesoscale effects. *J. Atmos. Sci.*, **50**, 889-906.
- Ferrier, B. S., W.-K. Tao, and J. Simpson, 1995: A double-moment multiple-phase four-class bulk ice scheme. Part II: Simulations of convective storms in different large-scale environments and comparisons with other bulk parameterizations. *J. Atmos. Sci.*, **52**, 1001-1033.
- García-García, F., and R. List, 1992: Laboratory measurements and parameterizations of supercooled water skin temperatures and bulk properties of gyrating hailstones. *J. Atmos. Sci.*, **49**, 2058-2073.
- Hallett, J., and S. C. Mossop, 1974: Production of secondary ice particles during the riming process. *Nature*, **249**, 26-28.
- Harimaya, T., 1975: The riming properties of snow crystals. *J. Atmos. Sci.*, **32**, 522-531.
- Hobbs, P. V., S. Chang, and J. D. Locatelli, 1974: The dimensions and aggregation of ice crystals in natural clouds. *J. Geophys. Res.*, **79**, 2199-2206.
- Houze, R. A., Jr., 1989: Observed structure of mesoscale convective systems and implications for large-scale heating. *Quart. J. Roy. Meteor. Soc.*, **115**, 425-461.
- Houze, R. A., Jr., 1993: *Cloud Dynamics*. Academic Press, San Diego, 573 pp.
- Johnson, D. B., 1987: On the relative efficiency of coalescence and riming. *J. Atmos. Sci.*, **44**, 1671-1680.
- Komabayashi, M., T. Gonda, and K. Isono, 1964: Life times of water drops before breaking and size distribution of fragment droplets. *J. Meteor. Soc. Japan*, **42**, 330-340.
- List, R., N. R. Donaldson, and R. E. Stewart, 1987: Temporal evolution of drop spectra to collisional equilibrium in steady and pulsating rain. *J. Atmos. Sci.*, **44**, 362-372.
- Low, T. B., and R. List, 1982a: Collision, coalescence, and breakup of raindrops. Part I: Experimentally established coalescence efficiencies and fragment size distribution in breakup. *J. Atmos. Sci.*, **39**, 1591-1606.
- Low, T. B., and R. List, 1982b: Collision, coalescence, and breakup of raindrops. Part II: Parameterization of fragment size distribution. *J. Atmos. Sci.*, **39**, 1607-1618.
- Maddox, R. A., L. R. Hoxit, C. F. Chappell, and F. Caracena, 1978: Comparison of meteorological aspects of the Big Thompson and Rapid City flash floods. *Mon. Wea. Rev.*, **106**, 375-389.
- Magono, C., 1953: On the growth of snowflakes and graupel. Science Report, Yokohama National University, Japan, Ser. I, No. 2, 18-40.
- Mapes, B. E., and R. A. Houze, Jr., 1995: Diabatic divergence profiles in western Pacific mesoscale convective systems. *J. Atmos. Sci.*, **52**, 1807-1828.
- Mason, B. J., 1996: The rapid glaciation of slightly supercooled cumulus clouds. *Quart. J. Roy. Meteor. Soc.*, **122**, 357-365.
- Mitra, S. K., O. Vohl, M. Ahr, and H. R. Pruppacher, 1990: A wind tunnel and theoretical study of the melting behavior of atmospheric ice particles. IV: Experiment and theory for snow flakes. *J. Atmos. Sci.*, **47**, 584-591.
- Mosimann, L., E. Weingartner, and A. Waldvogel, 1994: An analysis of accreted drop sizes and mass on rimed snow crystals. *J. Atmos. Sci.*, **51**, 1548-1558.
- Ono, A., 1969: The shape and riming properties of ice crystals in natural clouds. *J. Atmos. Sci.*, **26**, 138-147.
- Pflaum, J. C., Martin, J. J., and H. R. Pruppacher, 1978: A wind tunnel investigation of the hydrodynamic behaviour of growing, freely falling graupel. *Quart. J. Roy. Meteor. Soc.*, **104**, 179-188.
- Reinking, R. F., 1979: The onset and early growth of snow crystals by accretion of droplets. *J. Atmos. Sci.*, **36**, 870-881.
- Short, D. A., T. Kozu, and K. Nakamura, 1990: Rainrate and raindrop size distribution observations in Darwin, Australia. *Proc., URSI Commission F Open Symp. on Regional Factors in Predicting Radiowave Attenuation due to Rain*, Rio de Janeiro, Brazil, 35-40.
- Simpson, J., R. F. Adler, and G. R. North, 1988: A proposed Tropical Rainfall Measuring Mission (TRMM) satellite. *Bull. Amer. Meteor. Soc.*, **69**, 278-295.
- Smith, J. A., M. L. Baeck, M. Steiner, and A. J. Miller, 1996: Catastrophic rainfall from an upslope thunderstorm in the Central Appalachians: The Rapidan storm of June 27, 1995. *Water Resources Research* (submitted for publication).
- Srivastava, R. C., 1971: Size distribution of raindrops generated by their breakup and coalescence. *J. Atmos. Sci.*, **28**, 410-415.
- Steiner, M., R. A. Houze, Jr., and S. E. Yuter, 1995: Climatological characterization of three-dimensional storm structure from operational radar and rain gauge data. *J. Appl. Meteor.*, **34**, 1978-2007.
- Stewart, R. E., J. D. Marwitz, J. C. Pace, and R. E. Carbone, 1984: Characteristics through the melting layer of stratiform clouds. *J. Atmos. Sci.*, **41**, 3227-3237.
- Tao, W.-K., S. Lang, J. Simpson, and R. Adler, 1993: Retrieval algorithms for estimating the vertical profiles of latent heat release: Their applications for TRMM. *J. Meteor. Soc. Japan*, **71**, 685-700.
- Tokay, A., and D. A. Short, 1996: Evidence from tropical raindrop spectra of the origin of rain from stratiform versus convective clouds. *J. Appl. Meteor.*, **35**, 355-371.
- Wacker, U., 1995: Competition of precipitation particles in a model with parameterized cloud microphysics. *J. Atmos. Sci.*, **52**, 2577-2589.
- Waldvogel, A., 1974: The N_0 jump of raindrop spectra. *J. Atmos. Sci.*, **31**, 1067-1078.
- Waldvogel, A., and B. Federer, 1975: Raindrop spectra in severe local storms. *Preprints, 9th Conference on Severe Local Storms*, Norman, Oklahoma, Amer. Meteor. Soc., 431-435.
- Waldvogel, A., W. Henrich, and L. Mosimann, 1993: New insight into the coupling between snow spectra and raindrop size distributions. *Preprints, 26th Int. Conference on Radar Meteorology*, Norman, Oklahoma, Amer. Meteor. Soc., 602-604.
- Webster, P. J., and R. Lukas, 1992: TOGA COARE: The Coupled Ocean-Atmosphere Response Experiment. *Bull. Amer. Meteor. Soc.*, **73**, 1377-1416.
- Wilheit, T., R. Adler, S. Avery, E. Barrett, P. Bauer, W. Berg, A. Chang, J. Ferriday, N. Grody, S. Goodman, C. Kidd, D. Kniveton, C. Kummerow, A. Mugnai, W. Olson, G. Petty, A. Shibata, and E. Smith, 1994: Algorithms for the retrieval of rainfall from passive microwave measurements. *Remote Sensing Reviews*, **11**, 163-194.
- Willis, P. T., and A. J. Heymsfield, 1989: Structure of the melting layer in mesoscale convective system stratiform precipitation. *J. Atmos. Sci.*, **46**, 2008-2025.
- Xu, K.-M., 1995: Partitioning mass, heat, and moisture budgets of explicitly simulated cumulus ensembles into convective and stratiform components. *J. Atmos. Sci.*, **52**, 551-573.

CHARACTERISTICS OF THE CLOUD AND PRECIPITATION DURING THE DRY SUMMER SEASON IN SOUTH CHINA

Zeng Guang-ping¹, Tang Yu²
Feng Hong-fang³, Zhu Ding-hua⁴

(1,3,4 Fujian Meteorological Institute, Fuzhou, China
2 Jinjiang Meteorological Station, Jiangsu, China)

1. INTRODUCTION

Based on the theories of the synoptic meteorology, climatology and cloud physics and precipitation, the characteristics of the cloud and precipitation during the dry summer season in the south China were investigated, the cloud and precipitation model of different synoptic type were provided also.

2. DROUGHT

Fujian Province is located on the west-eastern coast of China. It has typical subtropical monsoon climate and abundant water, it's warm and wet. But rainfall is quite uneven to time and space, and serious drought usually happens because of the monsoon climate and the complex landscape. There are 2 — 6 millions mu which are threatened each year among the 18 million mu plough area of Fujian Province. The coast region is the most serious one. Drought happens all the year and the main drought is in summer. The drought causes great damage to the agriculture, the industrial manufacture and the people's living.

3. COLLECTION AND HANDLE OF THE MATERIALS

The materials of this paper come from:

- 1) The land routine meteorology datas:

The datas which are cloud form, temperature, atmosphere pressure, water-vapour content, rainfall, rainfall intensity and the duration of precipitation were collected by the dense precipitation stations and observation stations.

2) Radar probe materials:

The echo parameters of the cloud top and cloud base height, cloud thickness, cloud horizontal and vertical scale, echo intensity and cloud liquid-water content were gained by radar.

3) Satellite cloud picture:

From satellite cloud picture, we can get the materials such as the synoptic situation, synoptic system and it's changment and moisture flux, etc.

We can get the characteristics of the cloud and precipitation in different synoptic system after the handle to each physics quantity of the different synoptic system.

4. CONCLUSIONS

- 1) The major synoptic system dominating the coast area of the south China during the dry summer season can be classified into two categories: The first one is the subtropical high over the west Pacific; The second one is the cold front, tropical convergent zone, easterly wave and tropical cyclone, etc.

- 2) Under the influence of the first category synoptic system, the main cloud system and local thermal convective clouds, with a typical horizontal scale of 10—30 km, vertical extend of 6—10 km, radar echo intensity 25—40 dBZ, duration of precipitation 0.5—5 hours, maximum rainfall intensity 5—20 mm/h and process rainfall 2—30 mm.

3) Under the influence of the synoptic system of the second category, the main cloud system are convective cloud, the convective-stratiform mixed cloud and stratiform cloud. The convective-stratiform mixed cloud has a horizontal scale of 100 — 150 km, vertical extend of 4—6km for the large area stratiform cloud, and 6 — 10 km for the convective cell embeded in the stratiform cloud, duration of precipitation form 10^0 — 2×10^1 hours, maximum rainfall intensity 5—25 mm/hr and process rainfall 10^0 — 10^1 mm.

4) For the synoptic system of the first type, the efficiency of precipitation is about 30 — 40 %, while it is as high as 50 — 65 % under the weather condition of the second type.

5) By analysing the water vapor divergence, we found that under the first type weather situation, the whole layer of the atmosphere is divergent, while the whole layer of the atmosphere is convergent under the second type of the weather situation.

6) According to the airplane observation, rader, satellite data and numerical simulation, the vertical structures of the precipitating particles for various types of cloud under different weather conditions have been obtained. The vertical structures of the precipitating particles for the cumulonimbus cloud under the first category synoptic system, the stratiform cloud and convective-stratiform mixed cloud under the second category synoptic system are shown in Fig.1, Fig.2 and Fig.3.

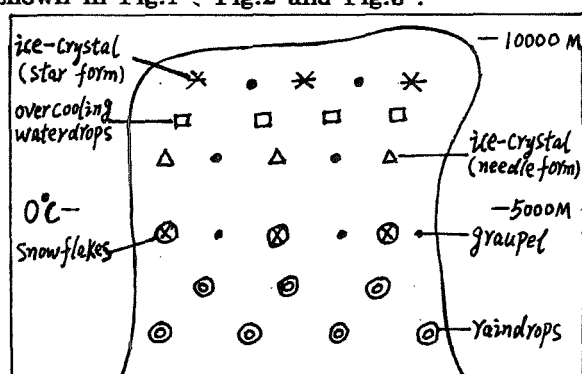


Fig.1: The vertical structures of the precipitating particles for the cumulonimbus cloud under the first category synoptic system.

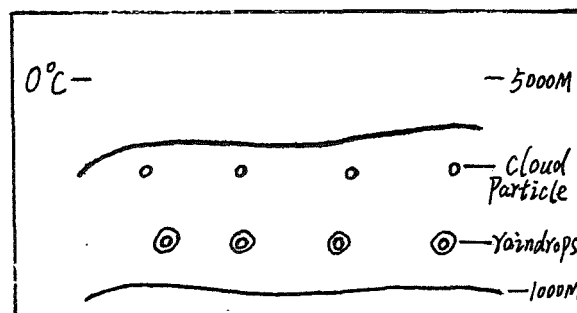


Fig.2: As in Fig.1 for the stratiform cloud under the second category synoptic system.

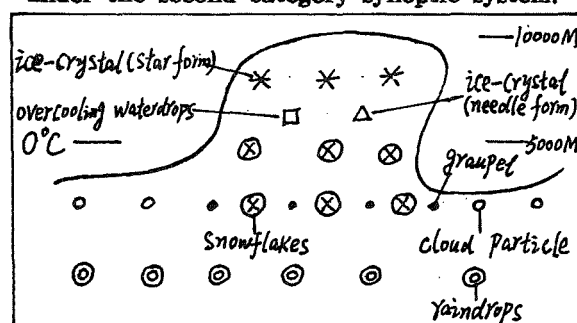


Fig.3: As in Fig.1 for the convective-stratiform cloud under the second type synoptic system.

REFERENCES

- Zeng Guang-Ping, Fang Shi-zhen, Linfen, 1991: The air water resources and the conditions for artificial precipitation in the summer drought periods in Fujian province, *meteorological(in Chinese)*, 1993.11, 25-30.
- Zeng Guang-ping, Xian Feng, 1991: Total analyses of the effect of artificial rainfall in the Gutian reservoir area during 1975—1986, *Chinese Journal of Atmosphere Sciences*, volume 15, No.3, 35-46.
- Zeng Guang-ping, Sui Ping, 1991: The radar-echo features of frontal cloud system during the Pre-rainy season in South China, *Scientia meteorologica sinica*, vol 11, No.3, 301—308.
- Zeng Guang-ping, Liu Jun, 1990: The precipitation efficiency and the precipitation stimulation possibility of frontal clouds during first rainy season in South China, vol.6, No.4, 365—371.
- Zeng Guang-ping, Yang Ben-ming: The meso and micro feature of preceding flood season's storm rainfall in Fujian. The Workshop on Mesoscale Meteorology in East Asia, 1995.11, FuZhou, China.

STUDIES ON THE CHARACTERISTICS OF PRECIPITATION PHENOMENA OBTAINED BY RADAR OBSERVATIONS AT SYOWA STATION, ANTARCTICA

Hirovuki Konishi¹, Makoto Wada² and Tatsuo Endoh³

1: Osaka Kyoiku University, Osaka 582, Japan

2: National Institute of Polar Research, Tokyo 173, Japan

3: Institute of Low Temperature Science, Hokkaido University, Sapporo, 060, Japan

1. INTRODUCTION

The Japanese Antarctic Research Expeditions (JARE) attempted for several years to comprehend the Antarctic climate system as a link in the Antarctic Climate Research (ACR) project, which is under the umbrella of World Climate Research Program (WCRP). The authors participated as the members in the JARE to study clouds and precipitation near the coast around Syowa Station by using meteorological radars and a microwave radiometer. The present paper describes the characteristics and of precipitation phenomena through analysis of observational data obtained in 1989.

The analysis of radar data provides useful information on meso-scale structure of clouds causing precipitation. Clouds and precipitation near Antarctica are thought to be produced by water vapor transported from the sea surface at lower latitudes surrounding Antarctica. Carleton (1992) noted that synoptic scale cyclones are important in the supply of moisture to Antarctica. The present study shows the characteristics of precipitation phenomena at Syowa Station and associates them with the precipitation clouds by using the data of synoptic charts and satellite images. The radar observations provided useful data to propose a conceptual model concerning the structure of cloud vortex associated with extratropical cyclones.

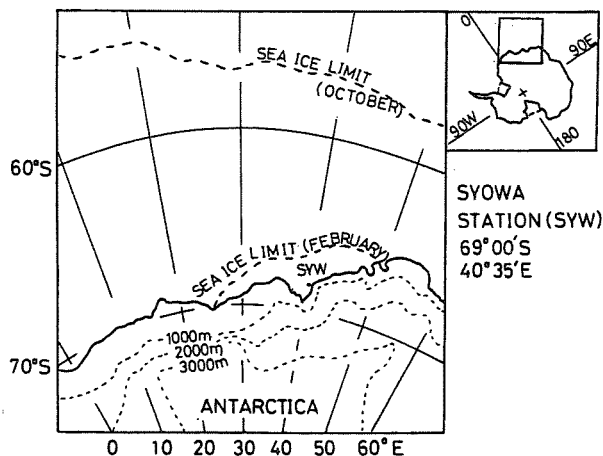


Figure 1. Location of Syowa Station (SYW)

2. METHODS OF OBSERVATION

Long-term observations of precipitating clouds were carried out by a vertical pointing radar and PPI radar at Syowa Station (69°00'S, 40°35'E), Antarctica in 1989. The location of Syowa Station is shown in Fig. 1. Syowa station is situated on the north side of the Ongul Islands near the east coast of Lutzow-Holm Bay. The vertical pointing radar gave reflectivity with a range interval of 50m up to 6.4 km at time intervals of 10 sec. The wavelength of the radar is 3.2 cm and the detailed characteristics of the radar are specified by Wada (1990). A PPI radar detects the horizontal distributions of precipitation and the evolution of precipitating clouds near the coast within a 64 km radius of Syowa Station. Radar data was recorded every 18 minutes at three different elevation angles of 2.0°, 3.5° and 6.0° in order to produce Constant Altitude PPI (CAPPI).

Surface synoptic data such as temperature, humidity, pressure and wind velocity and direction were measured every hour and upper air sounding data were obtained twice a day at 00Z(03LT) and 12Z(15LT) at Syowa Station. NOAA satellite data were also received and processed for at least one orbit per day at Syowa Station. The satellite carries several sensors including an Advanced Very High Resolution Radiometer (AVHRR), which views the earth's surface with the high resolution of about 1 km. The AVHRR image data was used to detect cloud vortices. Synoptic charts were used to trace the trajectories of low pressure center in the format depicted twice a day by using European Center for Medium-Range Weather Forecast (ECMWF) analysis grid data at 1000 hPa every 2.5 degrees.

3. RESULTS

The vertical structure of precipitating cloud was observed continuously from 1 January to 19 December in 1989 by vertical pointing radar at Syowa Station. Since the cloud system accompanied by low pressure is

usually as large as several hundred kilometers in diameter, the clouds associated with the low pressure system would cover Syowa Station for long duration. The occurrence frequency of duration longer than 10 hours is 53 cases in the observation period. The sum of appearance duration of the 53 cases is 50% of that of all cases and the total amount of precipitation of them 66% of that of all cases. Hence it is concluded that the cases of the long duration contribute large amounts of snowfall near Syowa Station to Antarctica.

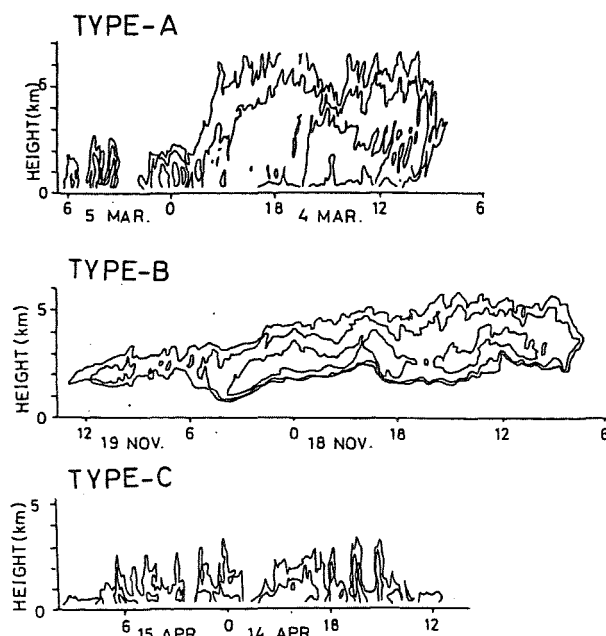
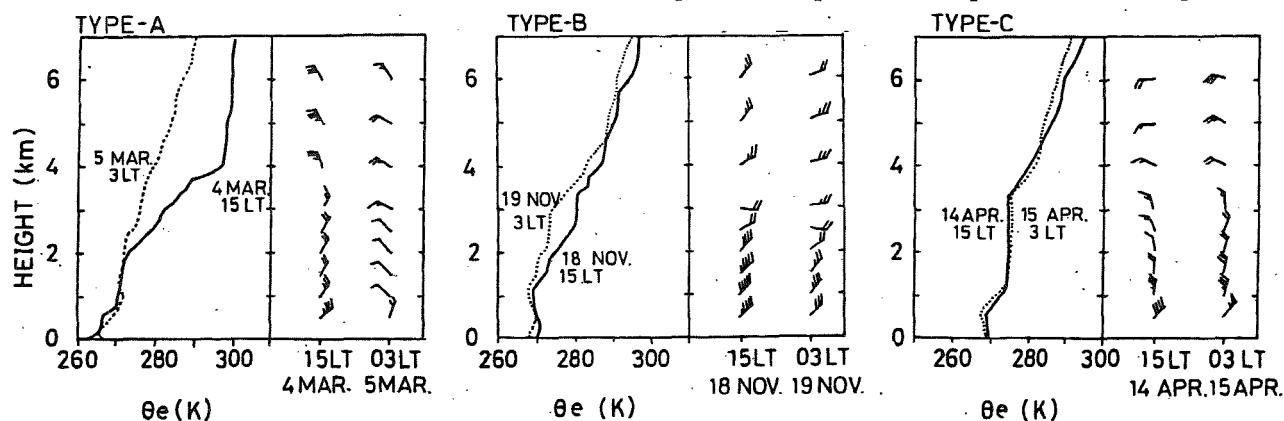


Figure 2. Three types of time-height cross section observed by vertical pointing radar. (a): A pair of early deep echoes and later shallow echoes defined as type-A echo in this paper. (b): A high level echo without precipitation on the ground for over 10 hours defined as type-B. (c): The shallow echo with short periodic convective cells defined as type-C. The radar echo intensity is contoured at 2, 12 and 20 dBZ.

Figure 3. Vertical profiles of equivalent potential temperature and wind for the same 3 cases shown in Fig. 2.



The 53 cases of long duration of echo are classified into three types by the time-height cross section showing the vertical structure of the echo observed by the vertical pointing radar. The typical time-height cross sections of three types are shown in Fig. 2. The echoes of the type-A consist of a pair of deep and shallow echoes. The deep echo appeared over 6 to 10 hours before the shallow echo appeared. Type-B echoes are composed of only high level echo without precipitation on the ground for long period over 10 hours. Type-C echoes show short periodic structure such as convective cells. The number frequencies of type-A, type-B, type-C and other types are 21, 11, 4 and 17, respectively.

The thermal and kinetic vertical structures corresponding to the cases in Fig. 2 are shown in Fig. 3 by equivalent potential temperature, wind speed and wind direction obtained from upper soundings. The equivalent potential temperature of type-A indicates that the warm air was present in the upper part of echoes at the beginning when the high level echo appeared; however, the air temperature decreased when the low level echo appeared. The temperature difference between both conditions was greater than 20 degrees around 4 km height at 15 LT on 4 March and at 3 LT on 5 March. Vertical stability was suspected to be small above 4 km at 15 LT on 4 March, but larger at 3 LT on 5 March. Therefore it is expected that the air mass was changed during the passage of the type-A echoes above Syowa Station. The neutral layer was observed in the warm air, around 6 km on 17 February. The equivalent potential temperature of type-B indicates that the echo exhibited in a stable layer and the profiles changed little with time. The wind profile suggested that the low pressure center was located north of Syowa Station because the wind blew westward at every height. On the contrary, the potential temperature of type-C shows that the echo was expected in the neutral layer of potential temperature after convective mixing.

The type-A echoes appeared most frequently in all seasons in 1989. Since the height of the deep echo top changes with season at about the -35°C level, the echo top would depend on temperature. The deep echo

appeared when the pressure decreased and the shallow echo appeared when the pressure increased. The time of the minimum surface pressure corresponds to roughly the change from the deep echo to the shallow echo. These facts suggest that boundary of two echoes seems to be a frontal structure dividing warm and cold air masses.

The horizontal structure of the type-A echoes was analyzed by using the PPI radar data. The composite charts of PPI radar for one of the typical cases observed on 4 March and 5 March 1989 are shown in Fig. 4. The lower part of the figure shows the horizontal structure of type-A echo composed of time-distance cross section using the PPI radar echoes along a line 10 km north of Syowa Station. The time-height cross section of radar echo using vertical pointing radar data is also shown for comparison in the upper part of the figure. The PPI radar data suggests that the type-A echoes consisted of layer echoes before 21 LT on 4 March and line echoes in the latter period. The former echoes were consistent with deep echoes and the latter line echoes were consistent with shallow convective echoes in comparison with time-height cross section. The corresponding NOAA/AVHRR image indicates that the cloud band of cloud vortex was above Syowa Station. The cloud band of cloud vortex passed above Syowa Station from north to south. The orientation of cloud band of cloud vortex extends from east to west at the southern periphery, when the type-A echo appeared above Syowa Station. On the other hand, the orientation changed to NE-SW around the rear edge of the band as the type-A echo passed away. The change of orientation of the band is also found in composite charts of PPI radar data. Hence it is expected from the NOAA image that the type-A echoes would be cross sections across the cloud band of cloud vortex associated with an extratropical cyclone.

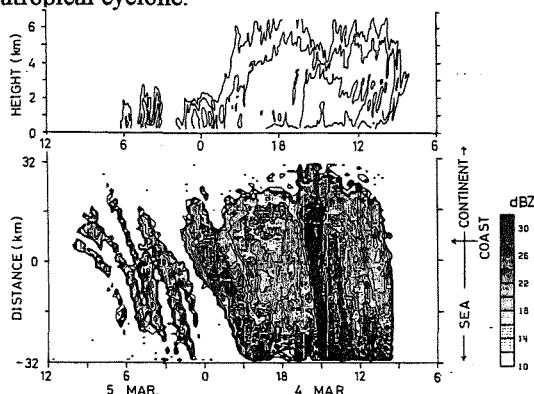


Figure 4. Echo structure of the type-A clouds observed on 4 March and 5 March 1989. The lower part of the figure shows a horizontal structure of type-A echo composed of time-distance cross section using the PPI radar echo along a line 10 km north of Syowa Station. The upper part of the figure shows the vertical structure of the type-A echo composed of time-height cross section using the vertical pointing radar echoes corresponding to the horizontal structure in the lower panel.

The trajectory of the center of the low is considered for each echo type. When the type-A echo appeared, the low center was usually northwest of Syowa Station. On the other hand when the type-B echo was observed at Syowa Station, the low center was usually north of Syowa Station.

4. DISCUSSION

The precipitation at Syowa Station mainly occurs from clouds associated with low pressure systems. Such a low pressure frequently appears as cloud vortex in the mature and dissipating stages. The conceptual model of cloud vortex structure is proposed in Fig. 5 incorporating the results described above. The cloud vortex is formed on the boundary between the easterly cold air stream and warm air in lower latitudes. If the center of the low stays in the northwest of Syowa Station where the lows appear most frequently in the circumpolar trough, the cloud vortex progresses toward Syowa Station from lower latitude and type-A echoes appear. The type-A echo is considered to be the normal cross section of the band such as an occluded front. On the contrary, if the low moves east along the coast near Syowa Station, the south edge of the cloud vortex covers Syowa Station and a type-B echo appears without precipitation on the ground surface. Hence the type-B echo would show a different section of the same band from the type-A echo. If the center of the low is in the vicinity of Syowa Station, the type-C echo appears as the convective cells. The convective cells correspond to the vertical mixing at the center of the low.

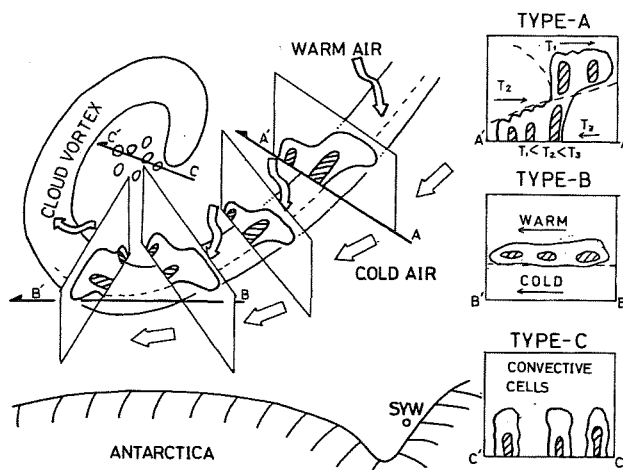


Figure 5. Conceptual model of structure of cloud vortex. The type-A echo corresponds to the cross section normal to the cloud vortex (i.e. A-A'); the type-B echo is from the south periphery of the cloud vortex (i.e. B-B'). The type-C echo is considered to be from convective cells near the low pressure center.

The cloud vortex is analogous to the rainbands associated with extratropical cyclones in the Northern Hemisphere described by Matejka et al. (1980). They describe the structures and microphysical structures of six types of rainbands. The structure of the former clouds of the type-A in the present study is expected to be the same as that of warm front in their study with an unstable layer above the cold stable layer. However the unstable layer in the former clouds of the type-A is not shown clearly in the present study. It is expected that the unstable layer would be present at lower latitude but changed to a neutral or stable layer by vertical convective mixing while the unstable layer was approaching Syowa Station. The structure of the latter clouds of the type-A is similar to the wavelike rainbands located in a potentially unstable layer behind a cold front aloft and near the surface occluded front. Wang and Hobbs (1983) note that the orientation of the band is parallel to the winds near their upper level, which correspond to the orientation of the line echo in the type-A echo shown in Fig. 4.

5. CONCLUSIONS

Precipitation phenomena at Syowa Station, Antarctica were observed continuously by using two kinds of radars in 1989. The results obtained include characteristics variations of snowfall.

It is concluded from the observations that precipitation near Syowa Station is mainly brought by cloud vortices associated with extratropical cyclones which advance to high latitude while developing to mature stage. Lows in their mature stage are accompanied by cloud vortices around a definite center (Streten and Troup, 1973). It is proposed that the outer side of the cloud vortex band is composed of layer clouds as that above the warm front formed by the warmer air advancing southward from low latitude and rising above the colder and drier air circulating westward around the polar high along the coast near Syowa Station. The inside of the vortex is composed of convective clouds formed in colder air rotating around the low center along the well-developed spiral. Therefore the cloud vortex is concluded to be created by the occluded front composed of the cold front up-gliding above the warm front.

Precipitation from an occluded front crossing over Syowa Station was often observed when the low pressure center stayed northwest of Syowa Station. The time-height cross sections of radar echoes in this case are considered to be normal cross sections of cloud vortex as shown in the type-A echo. No precipitation

echoes with high level clouds such as the type-B were observed when the low advanced eastward. The echoes are considered to be cross section along south periphery of the cloud vortex. Convective echoes such as type-C echo were observed when the low pressure center was located near Syowa Station. Therefore the echoes are expected from clouds near the low pressure center. The relative frequencies of echoes which appeared for the long duration greater than 10 hours were 40, 20 and 10% for the type A, B and C respectively. It is concluded from the observations that the necessary conditions are that the low pressure is in its mature stage, locates northwest of the station and is stationary in order to bring much precipitation to the coastal region near Syowa Station. Especially, a low pressure in its mature stage northwest of the station would bring a large amount of precipitation for a long time in case the low moves westward in accordance with the direction of the cloud vortex.

ACKNOWLEDGEMENTS

The authors would like to express thanks to Prof. K. Kikuchi, Dr. H. Uyeda and Dr. Y. Asuma, Graduate School of Science, Hokkaido University, for their valuable advice and useful suggestions.

This study was carried out as a link in the chain of the project of Antarctic Climate Research (ACR). The author also wish to thank the wintering all members of the 30th Japanese Antarctic Research Expedition for their supports in setting up and maintaining the observation instruments.

REFERENCES

- Carleton, A.M. (1992): Synoptic interactions between Antarctica and lower latitudes. *Aust. Meteor. Mag.*, **40**, 129-147.
- Matejka, T.J., Houze, R.A. and Hobbs, P.V. (1980): Microphysics and dynamics of clouds associate with mesoscale rainbands in extratropical cyclones. *Quart. J. R. Meteor. Soc.*, **106**, 29-56.
- Streten, N.A. and Troup, A.J. (1973): A synoptic climatology of satellite observed cloud vortices over Southern Hemisphere. *Quart. J. R. Meteor. Soc.*, **99**, 56-72.
- Wada, M. (1990): Antarctic climate research data, part 2. Radar and microwave radiometer data at Syowa Station, Antarctica from March to December 1988. *JARE Data Rep.*, **153**(Meteorology 24), 97pp.
- Wang, P.-Y. and Hobbs, P.V. (1983): The mesoscale and microscale structure and organization of clouds and precipitation in midlatitude cyclones. X: Wavelike rainband in an occlusion. *J. Atmos. Sci.*, **40**, 1950-1964

REMOTE MEASUREMENTS OF SUPERCOOLED LWC SPACE DISTRIBUTION IN WINTER FRONTAL CLOUD SYSTEMS

Koldaev A.V., Chernikov A.A., Melnichuk Yu.V.,
Koloskov B.P., Troitsky A.V.

Central Aerological Observatory, Roshidromet,
Russia

1. INTRODUCTION

It is well known the supercooled liquid water in frontal clouds has the greatest importance in the processes of precipitation formation and specially for clouds in which the crystal and liquid phases exist simultaneously. But at the same time there is not enough experimental data about temporal and space characteristics of the liquid water zones with respect of the same parameters of precipitation zones. In many regions over all the World year water balance is determined by the winter frontal clouds, that's why the investigations of such clouds has the prime interest.

This article reports the LWC zones parameters and relative space distribution of these zones and zones of precipitation observed during two winter storm experiments conducted by the Central Aerological Observatory (Hydrometeorological Service, Russia). One of them was carried out in the Moscow Region in the winter season 1989/1990 and another in Syria in winter season 1995/1996.

2. INSTRUMENTATION AND DESCRIPTION OF EXPERIMENTS

Both experiments were equipped with the same instruments: dual-wavelength (3 and

10 cm) weather radar MRL-5 and K-band microwave radiometer. The technical characteristics of radiometer system are presented in the Table 1.

N	Parameter	Value
1	Central frequency	37 GHz
2	Sensitivity	0.15 K
3	Bandwidth	2 GHz
4	Stability	1.5 K
5	Modulation rate	1 KHz
6	Integration time	1s
7	Recording rate	10s
8	Power supply (27V)	40W
9	Weight	3Kg

Table 1. Radiometer system parameters.

The radar was operated in automatic circular scanning mode collecting data of complete volume information about reflectivity of clouds and precipitation each 10 minute in 24 hours non-stop mode. The technique of radar observation was like a CAPPI and described in detail in (Melnichuk et.al. 1989). This technique possesses to receive horizontal cross-sections from the height 600m up to 15 km with height step about 500m. Horizontal dimensions of the observed area was chosen as 200km x 200km with spa-

ce resolution cell size 4km x 4km. The volume file the vertical cross section were available also. The Inertial Forecasting method was used for determination of a direction and velocity of cloud system transfer. Beside the two parameters above the next data were obtained: space position of the precipitation zone, intensity of precipitation, height of the clouds top, height of zero isotherm ("bright line") in cases when ground temperature was positive.

The microwave radiometer was pointed to the sky with elevation angle 45 deg looking through the radio transparent window directed opposite to the wind. The radiometer data were collected by the IBM/PC computer. Sample rate of the radiometer data was 30 Sec with 1 Sec integration time. From received brightness temperatures (T_b) the integral LWC (W) retrieved using two different procedures.

1. For the cases when ground temperature was below zero and dry snow precipitation observed the simple equation was used:

$$W = \frac{1}{b} \left[-\ln \left(1 - \frac{T_b}{T_a} \right) - \tau_g \right] \quad (1)$$

where T_a - average atmosphere temperature, b - absorption coefficient for 8mm wavelength, τ_g - water vapor and oxygen opacity.

2. For the cases when liquid precipitations observed, the measured brightness temperatures were reduced taking into account attenuation in precipitation. Attenuation in precipitation have been estimated on the basis of regression dependence of radar reflectivity

on 3 cm band measured at the lowest level and absorption on 8mm wavelength. Total attenuation in precipitation was calculated as production of the absorption and height of the zero degree isotherm. When the precipitation part have been eliminated from the measured T_b , the equation (1) was used for the retrieving of integral LWC.

In Moscow Region radar was installed 15 km apart from the place of radiometer installation and data were collected only for the time when ground temperature was below zero, so just equation (1) was used. The flat relief and large dimensions of the observed cloud systems permit us to assume the precipitation and cloud cells had not big changes during the time of transmission over the place of radiometer installation.

In Syria the radiometer and radar were installed on the top of the mountain at 45 km to the east from the coastal town Tartus. Such location was chosen because of two reasons: 1) the height of the mountain is about 1100 m and that reduce the liquid precipitation layer and consequential the influence of rain on the measured brightness temperatures; 2) cloud system passing from Meadlterrestrial Sea to the coastal mountain region has a small scale and very quick changes, so the assumption which we used for the Moscow Region experiment is not valid.

3. RESULTS

The experiment in the Moscow Region was conducted from

1 November 1989 up to 28 February 1990. The radar and radiometer have operated in 24 hours non-stop mode. From the total observation time just 9 situation with dry snow precipitation when cold front cloud systems passed over the point of measurements were chosen for the detail analysis. Example of one situation is shown in the fig.1. The synoptic surface analysis (fig. 1b) shows that at 1200 GMT the cold front stayed at the Moscow. The cloud radar characteristics along the vector of all cloud system transfer is presented on the fig. 1a as well as radiometer data about integral LWC. All parameters: snow precipitation intensity, radar echo top and integral LWC are presented as time series. Radar data is actually space distributed, but for the convenience of comparisons these parameters convert to time series by the use of velocity of cloud system trans-

fer. It is interesting to point out that the zone with supercooled LWC was observed on the back side of the cloud system, and maximum of precipitation intensity separated from the LWC zone, in terms of distance, on approximately 20 km. The same features were observed for all 9 cases and the separation distance varied from 10 to 30 km. In average during the experiment the mean value of integral LWC was 0.13 kg/m^2 with maximum value about 0.78 kg/m^2 . The mean horizontal dimension of the LWC zone was about 60 km and approximately the same mean dimension of precipitation zone with intensity more then 0.1 mm/h was observed. The radar echo top that corresponds to the upper altitude of the existing of large crystals had not a big variation, so the increase of the integral LWC can be explained only by increase of the absolute LWC value.

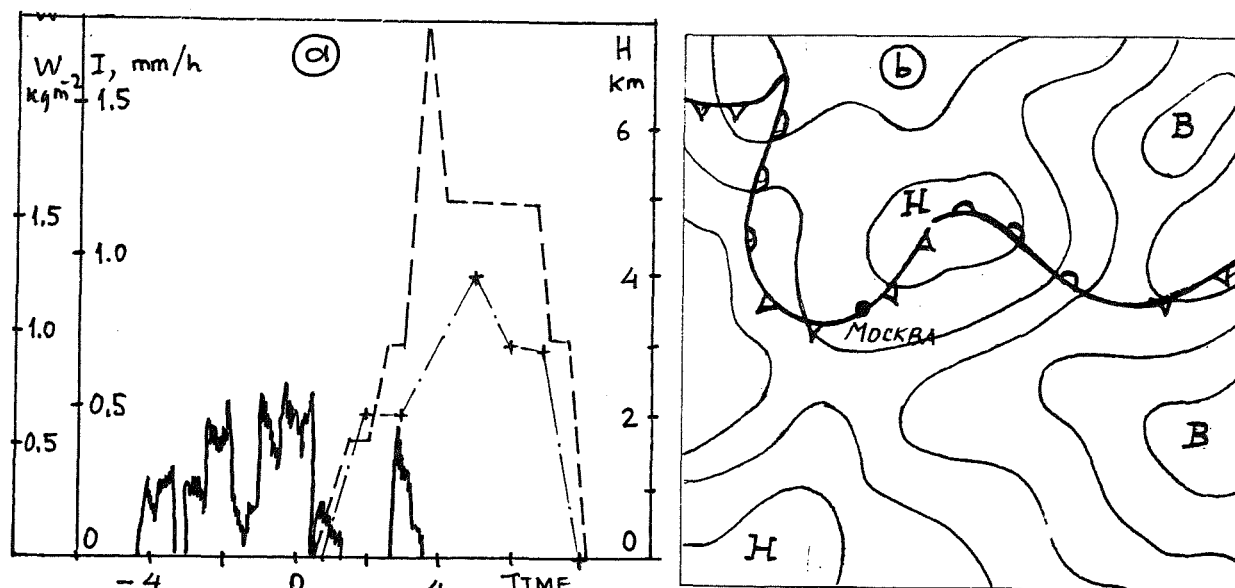


Fig.1. Time series of the integral LWC (—), radar echo top (+—+—+), radar intensity of precipitation (— · —) (a) and synoptic surface analysis (b), Moscow Region at 1200 GMT on 14 Nov. 1989.

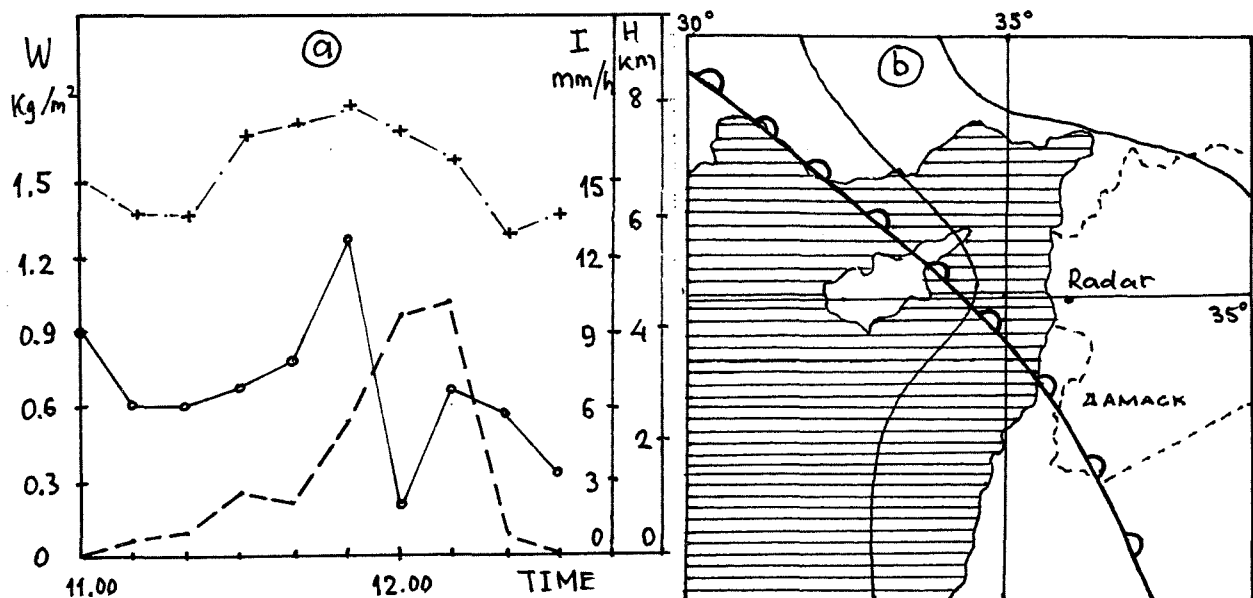


Fig.2. Time series of the integral LWC (\circ — \circ), radar echo top ($+$ — \cdot — $+$), radar intensity of precipitation ($- - -$) (a), presented at local time and synoptic surface analysis (b), Syria at 0000 GMT on 02 Jan. 1996.

The experiment in Syria have been conducted from 1 January up to 30 March 1996. The seven cloud systems were selected for the detail analysis. The rain or wet snow were observed for all the cases. One of the cases is shown in fig.2. The synoptic surface analysis shows that the clouds and precipitation in the region of observation was associated with the warm front. The radar characteristics of clouds along the vector of cloud system displacement are presented on the fig.1a as well as radiometer data about integral LWC. It is important to point out that the maximum of supercooled LWC was observed on the forward side of the cloud system, and maximum of precipitation intensity was separated from the LWC zone about 15 km. In the cases of cold fronts the maximum of LWC was observed as in the Moscow Region on the back side of the cloud system. The separation distance varied from 10 to 30 km. In average the mean value of integral LWC was 0.8 kg/m^2

with maximum value about 1.8 kg/m^2 . The mean horizontal dimension of the LWC zone was about 20-30 km. As in case of Moscow experiment the radar echo top had not a big variations, and increase of the integral LWC corresponds to the increase of the LWC value and not connected with the increase of LWC column.

4. DISCUSSION

As usual for the explanation of the precipitation formation in mixed clouds the Bergeron-Findeisen mechanism is used, but as it was observed in two series of winter experiment there was not any case when the maximum of precipitation intensity and maximum of supercooled liquid water were at the same space location. The authors have not the final version of explanation of the phenomena observed, but sure the facts above have to be tested with the numerical models and additional field experiments.

THE DEVELOPMENT PROCESS OF CONVECTIVE SNOW CLOUDS DURING THE WINTER MONSOON SURGE ALONG THE WEST COAST OF HOKKAIDO, JAPAN

Hiroyuki Yamada¹, Hiroshi Uyeda¹, Michael A. Menshov¹, Yoshio Asuma¹,
Katsuhiko Kikuchi¹, Masayuki Maki² and Koyuru Iwanami³

¹ Graduate School of Science, Hokkaido University, Sapporo 060, JAPAN

² National Research Institute for Earth Science and Disaster Prevention (NIED),
Tsukuba-shi, Ibaraki-ken, 305, JAPAN

³ Nagaoka Institute of Snow and Ice Studies, NIED, Nagaoka-shi, Niigata-ken, 940, JAPAN

1. Introduction

In the winter monsoon season, convective snow clouds are generated over the Japan sea and sometimes produce heavy snowfall locally on the west coast of northern Japan. In most cases the snow clouds are organized by convective cells which have a horizontal scale of about ten kilometers. Although each convective cell has a lifetime of about an hour (Yamada et al. 1994), the organized snow cloud which has shapes of band-like, line-like or vortex-like echoes has a lifetime of more than several hours. The phenomena wherein old dissipating cell is replaced by new cell is considered to occur frequently in the organized snow cloud. However the details of the process have not been determined yet.

A strong downdraft, which is often observed in the dissipating cell of a snow cloud, termed a 'Snowburst' by Shiroyuka and Uyeda (1990), often produces a strong outflow on the ground surface with snowfall. It is one of the origins of blowing snow over land, and it is also able to produce an updraft to form a new convective cell in the convective mixing layer over the sea surface.

An experiment to reveal the origin and source of blowing snow was carried out from 18 to 28 January 1995 around Ishikari Bay, on the west coast of Hokkaido Island, Japan. During this period, we observed several cases of developing snow clouds in the observation range over the Ishikari Bay. Specifically, in one case before dawn on 28 January, we observed the rapid development of a line of snow clouds and the temporal changes in the three dimensional structure of these clouds using three Doppler radars.

In this study, we examine the development process of this line of convective snow clouds from

the kinematic structure obtained by dual-Doppler radar analysis and discuss the interaction between a dissipating cloud and a developing cloud.

2. Observation and data processing

Three X-band Doppler radars, two of them belonging to National Research Institute of Earth Science and Disaster Prevention (NIED) and the other from the Hokkaido University Meteorological Laboratory (HUMI), were placed at Atsuta, Otaru and Sapporo around Ishikari Bay (Fig.1). A volume scan data of reflectivity and Doppler velocity was obtained at Atsuta and Otaru. Volume scan data of 11 elevation angles within 6 minutes was obtained at 12 minute intervals.

The raw data was interpolated to an orthogonal grid with 1.0km spacing in X, Y, and 0.25km in Z. Horizontal wind vectors were then computed from this grid data of reflectivity and Doppler velocity fields, and vertical winds were determined from

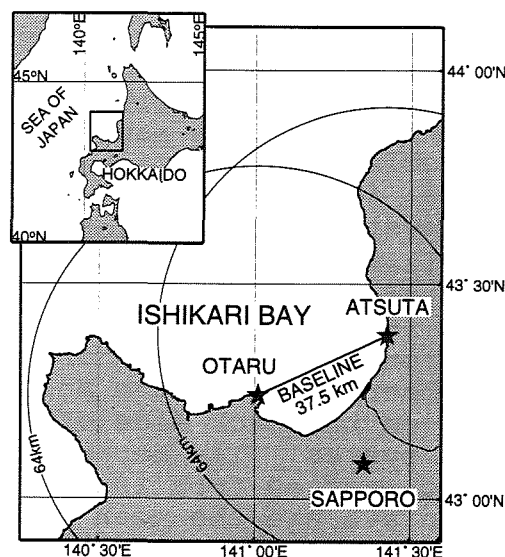


Fig.1 Map around Ishikari Bay, Hokkaido, Japan.

the upward integration of the horizontal divergence and were adjusted using the method of Ray et al. (1980).

3. Results

The rapid development of a line echo was observed before dawn on 28 January 1995. Figure 2 indicates the time series of PPI from 0000JST to 0100JST (JST is 9 hours earlier than UTC) at the elevation of 1.2 degree. A band-like echo (hereafter band-A) extending to a direction of north-south (N-S) existed from 40km to 60km east of Atsuta radar at 0000JST and moved slowly ($\sim 5\text{ms}^{-1}$) toward the direction of ENE. The horizontal gradient of reflectivity of this echo was much larger at the forward edge (eastern edge). At 0036JST, a line-like echo (hereafter line-B) suddenly formed ahead (east) of band-A and this echo was composed of eight convective cells. The reflectivity of this echo increased rapidly, and the maximum reflectivity reached 36dBZ at 0112JST which was as strong as a snow cloud.

The middle level (2.0km) of reflectivity and wind vector fields and the low level (0.25km) of wind vector, wind speed and divergence fields are shown in Fig.3. The mean wind was westerly at both levels. At 0.25km level, there are two shearlines (α and β) in two narrow convergence areas and a remarkable change of wind direction and wind speed is analyzed along shearline- α . Shearline- α was located about -25km east of Atsuta radar, and expanded parallel to the alignment of band-A and line-B at 2.0km level. The maximum convergence is approximately $3 \times 10^{-3}\text{s}^{-1}$ and was located at the east edge of the strong ESE wind area between band-A and line-B, in which wind speed exceeded 10ms^{-1} . The location of line-B coincided with that of shearline- α . On the other hand, shearline- β was located approximately -15km east of the Atsuta radar. Along

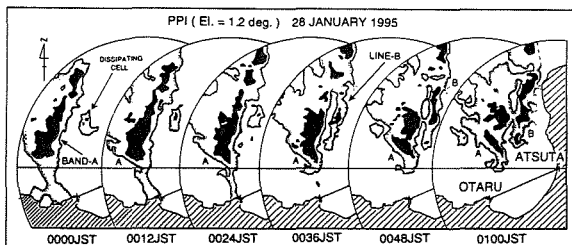


Fig.2 Reflectivity patterns of PPI scan at the elevation angle of 1.2 degree at Atsuta radar for 0000-0100JST. Contour intervals are 15 dBZ (outline), and 25 dBZ (shaded). Range circle indicate 64km

this shearline, the convergence is about $2 \times 10^{-3}\text{s}^{-1}$.

To notice a change in the vertical structure of line-B, time series of the east-west cross section through the cell which indicate the maximum reflectivity in line-B are shown in Fig.4. From a structure of radar reflectivity, the cell which organized line-B was formed at around 0024JST at the location between band-A and a dissipating single cell located about -25km east of Atsuta. This dissipating cell is recognized ahead of band-A at 0000JST and 0012JST in Fig.2. An echo top height of the developing cell reached near 5km, whereas the top of the mixing layer was 3.5km, as observed by sounding data in Sapporo at 2100JST 27 January. This overshoot of 1.5km suggests the strong development of a convection. The height of the core increased until 0036JST, decreased slightly

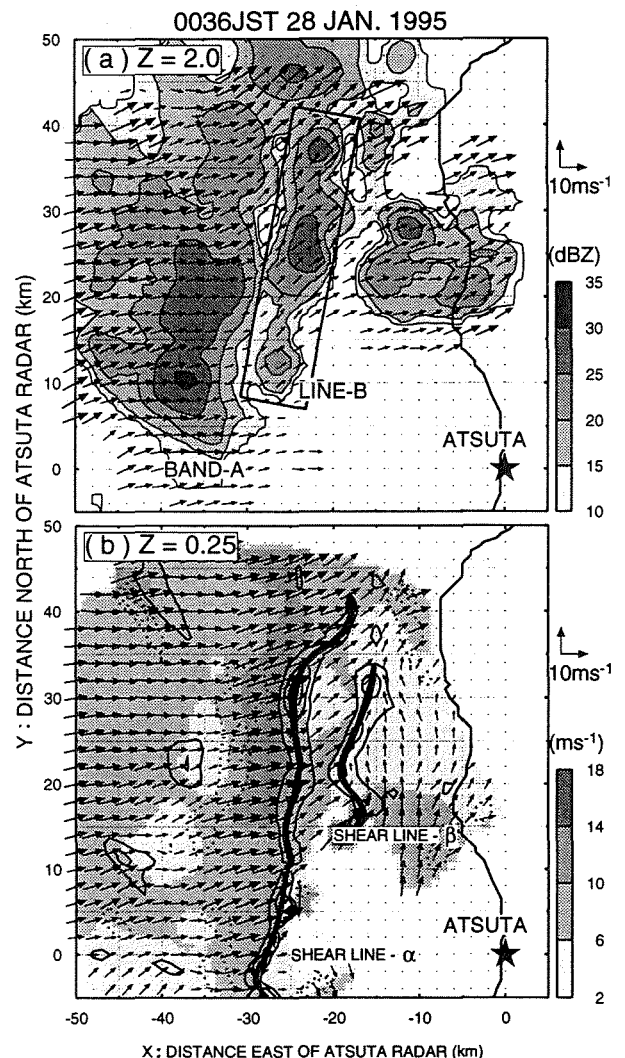


Fig.3 (a) Reflectivity and wind vector at 2.0km. (b) Wind vector and divergence at 0.25km. Shades indicate wind speed and contours indicate divergence (dotted line) and convergence (thin line) at an interval of $1.0 \times 10^{-3}\text{s}^{-1}$.

from 0036JST to 0100JST, and reached the surface at 0112JST. Consequently, line-B was at the stage of developing until about 0036JST, mature until about 0100JST and dissipating after 0112JST. In contrast, band-A was already dissipating stage at 0012JST, judging from the height of maximum reflectivity.

Shearlines α and β detected from the vertical structure of horizontal wind fields were already formed at 0012JST. An updraft of line-B had already appeared at about -30km, whereas a reflectivity

corresponding to line-B had not yet been detected. After 12 minutes, the location of shearline- α moving eastward coincided to that of line-B. It indicates that the updraft formed by shearline- α contributed to the rapid development of line-B. The area of strong wind produced by shearline- α was located between the dissipating band-A and the developing line-B, thus it corresponds to the outflow at low level formed by the downdraft of band-A.

In contrast to the above, shearline- β did not contribute to the development of line-B until 0036JST. It lingered at approximately -15km, whereas shearline- α and line-B moved eastward. Shearline- β was then caught up by the shearline- α at 0048JST. The location of line-B coincided with this location. The width of a convergence area and an updraft area then expanded. Although line-B was at a mature stage, a strong updraft was maintained by an enhanced convergence by the merging of the two shearlines.

At 0112JST, shearline- α dissipated though shearline- β still existed. The location of the updraft shifted to rear of the line-B. Line-B was considered to have dissipated after landing and its lifetime was put at about 2 hours, though this was not observed in a shadow area of two radars. This value of lifetime is as large as that of a snow cloud.

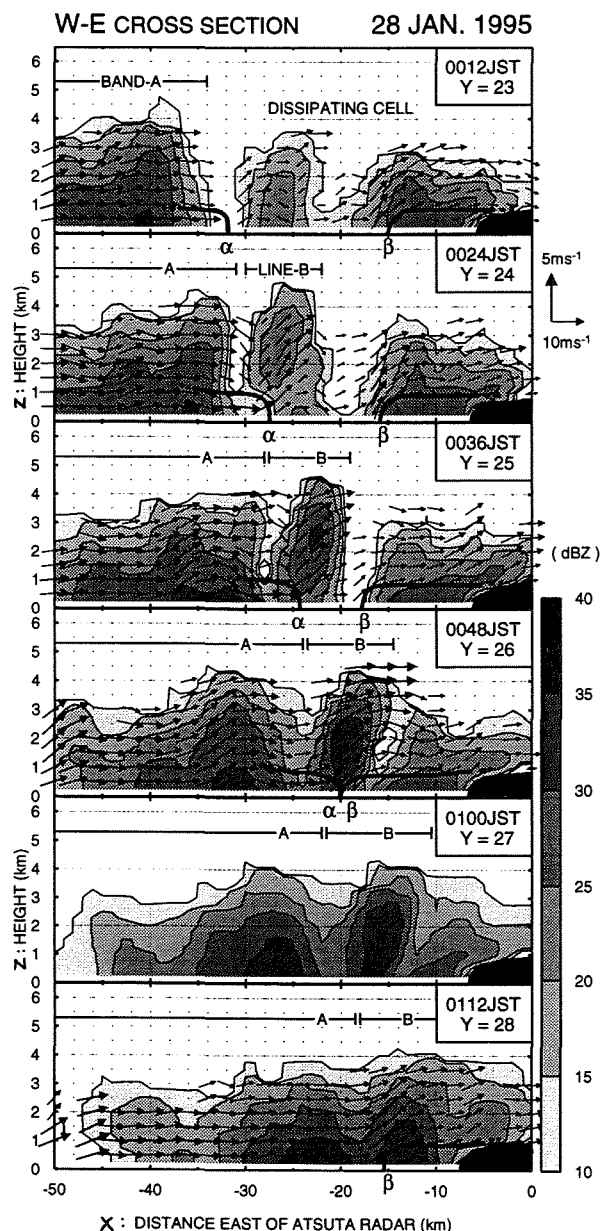


Fig.4 Structure of reflectivity and wind fields on the east-west vertical cross section from 0012JST to 0112JST. A value of Y indicates distance north of Atsuta radar. A wind vector at 0100JST is not indicated for a lack of the PPI data of the Otaru radar.

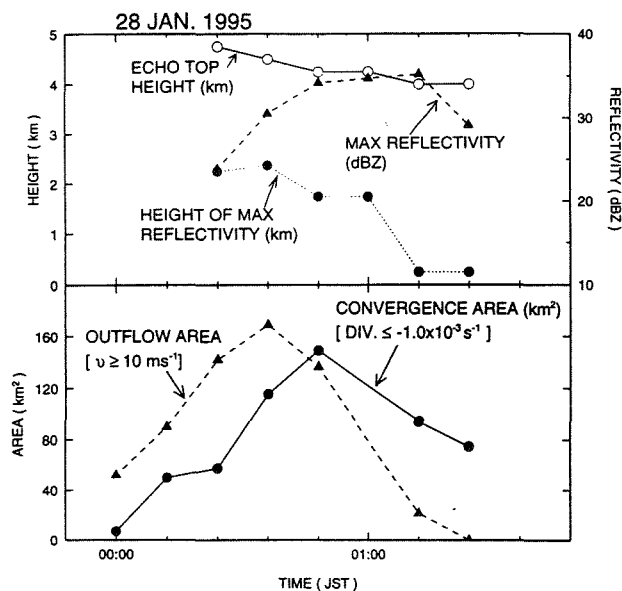


Fig.5 (a) Echo top height, maximum reflectivity and height of an echo peak of the convective cell in the line-B. (b) area of convergence zone ($< -1.0 \times 10^{-3} \text{ s}^{-1}$) and outflow region ($> 10 \text{ ms}^{-1}$) near the line-B detected from horizontal plane at $Z=0.25 \text{ km}$.

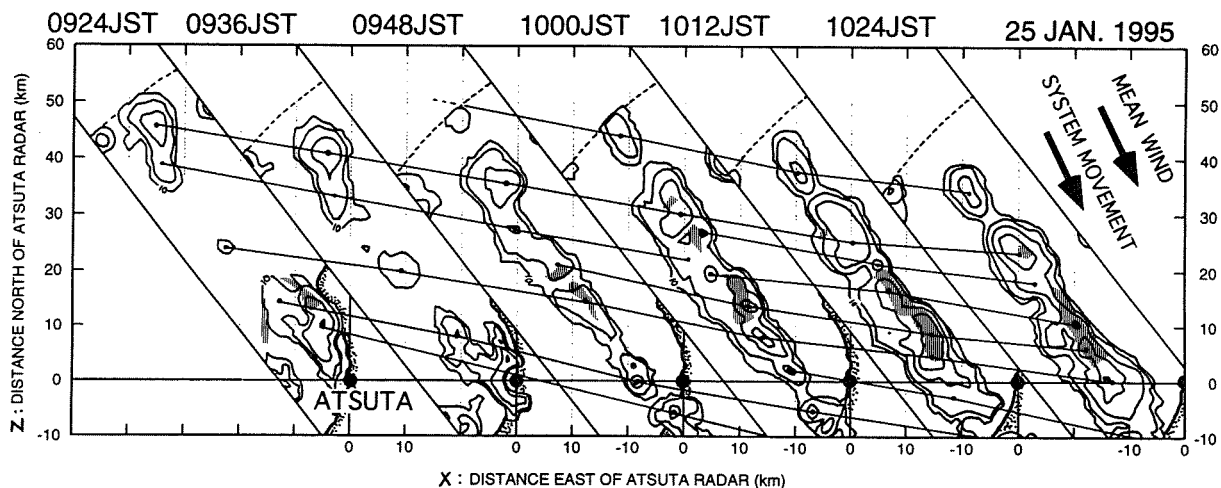


Fig.6 Reflectivity contours at 5dBZ interval and a location of convergence area observed 0924-1024JST 25 January 1995. The shaded area indicate convergence zone ($< -1.0 \times 10^{-3} \text{ s}^{-1}$).

4. Discussion and conclusion

To classify the development process of the line-like echo B, the temporal change of values detected from reflectivity and wind fields is shown in Fig.5. It is notable that the peak of the area of convergence is 12 minutes later than the peak of the outflow area. It is interpreted that the convergence area increased by adding a convergence with shearline- β after 0048JST although the outflow from band-A was declining from 0036JST. Consequently, the mechanisms of the rapid development and the maintenance of the line of snow clouds correspond to the updraft forced by the outflow from the dissipating cloud and the enhanced convergence by the merging of the two shearlines respectively.

Rapid cloud development associated with the outflow from a dissipating cloud was analyzed also on 25 January, in a line of clouds parallel to the mean wind around the center of Ishikari Bay (Fig.6). Similarly, in this case, the outflow from a dissipating cell formed convergence at a low level and contributed to new cell development which occurred one after another on the line echo. Therefore, outflow from a dissipating cell is considered to be a basic mechanism of new cell development and the maintenance of a snow cloud system having a

horizontal scale larger than several tens of kilometers and a lifetime of more than a few hours.

Acknowledgments

The author would like to thank Dr. Shinsuke Satoh of the Communication Research Laboratory for providing the program of a dual-Doppler radar analysis. These studies used the data observed at the Project Study of NIED, "Study on Areal Prediction Techniques of Drifting Snow and the Development of a Warning System".

References

- Ray, P. S., C. L. Ziegler, W. C. Bumgarner and R. J. Serafin, 1980: Single and multiple Doppler observations of tornadic storms. *Mon. Wea. Rev.*, **108**, 1607-1625.
- Shirooka, R. and H. Uyeda, 1990: Morphological structure of snowburst in the winter monsoon surges. *J. Meteor. Soc. Japan*, **68**, 677-686.
- Yamada, Y., T. Matsuo, M. Murakami, H. Mizuno and K. Iwanami, 1994: Mesoscale and microscale structures of snow clouds over the sea of Japan. Part II: Time change in airflow structures in isolated snow clouds derived from dual-Döppler radar observations - A case study -. *J. Meteor. Soc. Japan*, **72**, 695-708.

THE SPATIAL DISTRIBUTION CHARACTERISTICS OF MICROSTRUCTURE IN FRONTAL CLOUDS

Tamara N. Zabolotskaya

Ukrainian Hydrometeorological Research Institute, 252028 Kiev, Ukraine

1. INTRODUCTION

Cloud observations from the research aircrafts, synoptical and aerological data in different regions of Ukraine during the cold period 1960-85 inclusive were used to investigate the spatial distribution characteristics of microstructure and liquid water content in frontal clouds.

By data of the research aircraft were chosen the cases, when the measurements of microstructure and liquid water content were made from cloud base to cloud top. After these measurements were "tied up" to the line of front. Aerological data were used to build-up of the spatial sections of concrete fronts. The treatment of data was made with step by vertical-300 m and by horizontal - 50 km.

It being known, that the frontal clouds are extended on several hundreds km, but the measurements of microstructure or liquid water content usually are referred to more narrow parts. Because it was not a success to receive the complete picture of distribution in the whole cloud volume of separate concrete front. So the middle-statistic spatial sections were built for primary front types (warm, cold, occlusion) with the representation of the distribution characteristics of microstructure and liquid water content.

2. LIQUID WATER CONTENT

The spatial distribution of liquid water content in frontal clouds are given in fig.1 (used about 10000 measurements). In clouds of warm fronts (fig.1a) can choose three zones of the higher meanings of liquid water content ($W \geq 0.20 \text{ gm}^{-3}$). The first zone is placed along the front surface in warm air mass and extent for 300-400 km, $W_{\max} = 0.20 \text{ gm}^{-3}$. The second zone occur behind the front on distance $\sim 200 \text{ km}$ from the surface line of front in the layer from 0.8 to 1.5-2 km, $W_{\max} = 0.25 \text{ gm}^{-3}$. The third small zone occur before the front in the lower layer (to 1 km).

Zones of the lower meanings of liquid water

content are limited by isoline 0.10 gm^{-3} , the minimum meanings constitute $0.01-0.02 \text{ gm}^{-3}$. These zones mainly are placed in the layer from 3 to 5 km in whole cloud space. More over the similar zone is immediately above the front on distance $\sim 300 \text{ km}$ from the surface line of front.

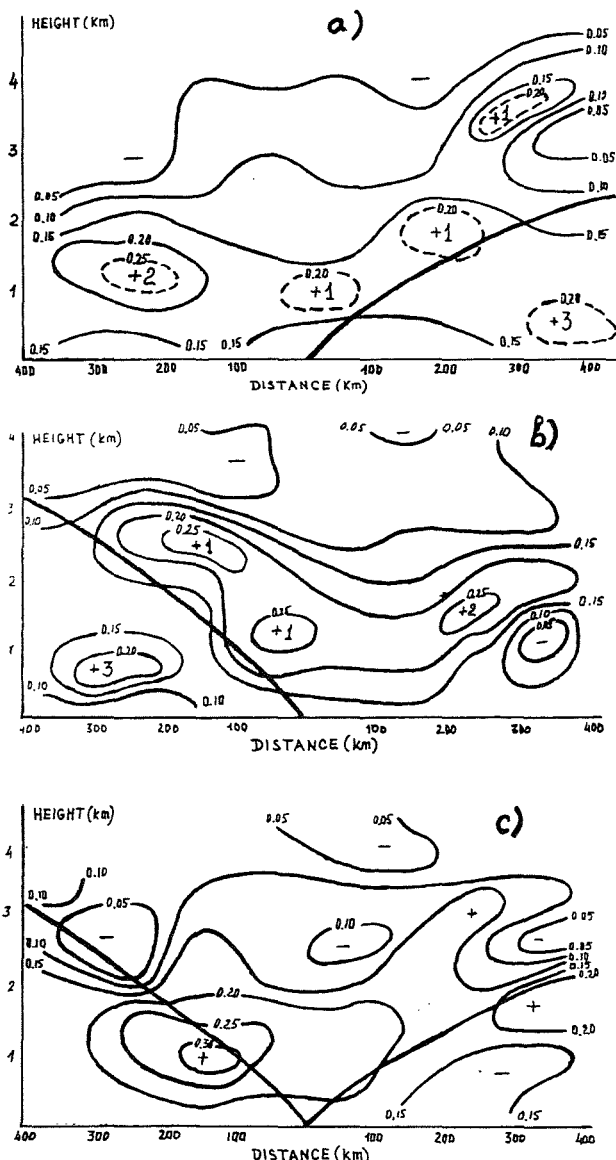


Fig.1. The distribution of liquid water content (gm^{-3}) in clouds of a) warm front, b) cold front, c) occlusion front.

In clouds of cold fronts (fig.1b) zones of the higher meanings of liquid water content in the main are concentrated before the front. The first zone occur in layer from 0.8 to 3.0 km in warm air mass and parallel of the surface front, $W_{\max} > 0.25 \text{ gm}^{-3}$. The second zone is placed before the front and extent for 300-400 km from the surface line of front. Here $W_{\max} > 0.25 \text{ gm}^{-3}$. The third zone occur in layer from 0.5 to 1.0 km behind the front on distance about 200 km from the surface line of front, $W_{\max} > 0.20 \text{ gm}^{-3}$. The zones of the lower meanings of liquid water content are observed above 3 km in the main, $W_{\min} = 0.01 - 0.02 \text{ gm}^{-3}$.

In clouds of occlusion fronts (fig.1c) zone of the higher meanings of liquid water content occur along the warm branch of the front and capture the occlusion region and the lower part of the cold branch (in the layer from 0.5 to 2 km). The horizontal extent of that zone is 500-600 km, W_{\max} is about 0.35 gm^{-3} . The zones of the lower meanings of liquid water content occur up 2 km above the cold branch and the occlusion region and up 3 km above the warm branch of front.

Such picture of the spatial distribution is kept independently from the direction of motion of frontal cloud masses: a) the west, b) the north-west, c) the south, the south-west. The differences there were, but it became apparent only in the absolute meanings of liquid water content.

3. PARAMETERS OF MICROSTRUCTURE

As parameters of microstructure were considered the size and concentration of cloud drops and the presence of crystals (table). The cloudiness of warm fronts mainly has the mixed structure in cold period, but behind the front on distance more 100 km from the surface line of front in lower layer by thickness 2 km there are the water clouds. The mixed structure of clouds is observed to 4.5-5 km, above 5 km there are crystal clouds. Only in the central parts of front (~100 km before the front) may be observed drops.

The lower surface layer by thickness 2 - 2.5 km the concentration drops (N) is about 300 m^{-3} . With increase of height the concentration is reduced and in layer from 2.5 to 4.5 km it consist 200 m^{-3} . Above 4.5-5 km N is about $50-100 \text{ m}^{-3}$.

The cloud drops were grouped into three classes by size: small ($d < 13 \text{ }\mu\text{m}$), middle ($d = 13-25 \text{ }\mu\text{m}$) and large ($d > 25 \text{ }\mu\text{m}$). It should be noted, that in whole cloud space all sizes of

drops are observed. The concentration of drops in abovementioned groups is approximately equal, but the middle drops prevail (100 m^{-3}), then small (90 m^{-3}) and after large drops (80 m^{-3}).

The cloudiness of cold fronts also has the mixed structure. Only in the lower layer by thickness 1 km (>100 km before the front and >200 km behind the it) are registered the water clouds. Before the front mixed clouds are observed to 4 km, above there are mainly the crystal clouds. In central part and behind the front the mixed clouds may be observed to 5 km.

The concentration of drops is less than in clouds of warm front. So in lower layer by thickness 1-1.5 km N is about 300 m^{-3} , in layer from 1.5 to 2.5 km - $200-250 \text{ m}^{-3}$, above 2.5 km - 100 m^{-3} . The small and middle drops are observed in whole cloud space, the large drops mainly are concentrated in the lower layer by thickness 2-2.5 km, above this level - only in central part of front. In clouds middle drops prevail ($\sim 100 \text{ m}^{-3}$), concentration of small and large drops is about 70 m^{-3} .

The occlusion frontal clouds have the mixed structure also. The water clouds are observed only far before the front (~300 km) and behind the front (~200 km) in lower layer by thickness 2-2.5 km. The crystal clouds are observed above 5-6 km in the occlusion zone. N_{\max} ($300-350 \text{ m}^{-3}$) is observed in layer from 1.5 to 2.5 km. In lower layer by thickness 1-1.5 km N is about $200-250 \text{ m}^{-3}$ and in layer from 2.5 to 5 km - $150-200 \text{ m}^{-3}$. Only above 5 km the small drops may be observed with $N = 50 \text{ m}^{-3}$. In clouds of occlusion fronts the drops of all sizes are observed also, its concentration is approximately equal ($90-100 \text{ m}^{-3}$). The process of cloud formation is intensive to height of 2.5-3 km. Above that layer the water mass in the main is placed only before the front.

4. CONCLUSION

The abovementioned data of the spatial distribution parameters of microstructure and liquid water content in cold period over Ukraine must be considered as more probable, because these distributions were received on large experimental material. These data can be used for the working up of the scientific works (such as the determination of mechanisms of cloud and precipitation formation; the build-up of climate models) and the applied works (for example, the planning and realization of precipitation enhancement and etc.).

Table. The spatial distribution of drop concentration (m^{-3}) in frontal clouds

Layer km	d μm	D i s t a n c e, km																	
		Behind the front									Before the front								
		300-201			200-101			100-0			0-100			101-200			201-300		
		warm	cold	occl	warm	cold	occl	warm	cold	occl	warm	cold	occl	warm	cold	occl	warm	cold	occl
0-1.2	<13	90	-	100	150	110	100	110	80	90	100	130	120	80	110	80	-		115
	13-25	120	50	100	90	110	110	100	90	80	100	110	80	95	150	100	110		100
	>25	50	50	90	50	60	125	70	80	50	70	80	60	80	175	60	125		50
	cryst.	-	-	-	-	+	+	+	+	+	+	+	+	+	-	+	+		+
1.21-2.4	<13	120	75	115	100	90	50	70	80	115	90	50	115	100	100	90	60		145
	13-25	140	100	50	150	130	200	95	105	100	115	100	90	50	70	105	130		115
	>25	130	-	50	100	-	200	90	90	200	80	50	50	50	50	90	130		-
	cryst.	-	+	-	-	+	+	+	+	+	+	+	+	+	+	+	+		+
2.41-3.6	<13		100			50	-	110	50	80	170	50	50	-	-	50	70		50
	13-25		-			-	-	110	50	50	150	50	80	50	50	-	75		120
	>25		-			-	-	50	50	-	50	50	50	-	-	-	75		80
	cryst.		-			+	+	+	+	+	+	+	+	+	+	+	+		+
3.61-4.8	<13					50		50	60	200	50	-	-	-	-	-	50		50
	13-25					-		125	125	125	100	-	100	100	-	50	-		100
	>25					-		125	100	-	100	50	-	100	-	-	-		80
	cryst.					+		+	+	+	+	+	+	+	+	+	+		-
4.81-6.0	<13					-		-	50		100	-	-	-	-	50	-		
	13-25					125		-	-		-	-	-	-	-	-	-		
	>25					-		-	-		-	-	-	-	-	-	-		
	cryst.					+		+	+		+	+	+	+	+	+	+		

SOME CHARACTERISTICS OF THE CLOUDS AND PRECIPITATION OF TRANSITIONAL SEASONS OF THE YEAR ON THE TERRITORY OF UKRAINE

Iraida A.Ocokina and Saveli V.Khusid

UHRI, 252028 Kiev, UKRAINE

1. INTRODUCTION

This very work reveal the peculiarities of the atmosphere circulation in days with precipitation; the classification of the falling precipitation on the form of clouds is done in this work; certain characteristics of the clouds and their precipitation in transitional seasons of a year (march-april, september-october) in forest-steppe and steppe zones of Ukraine is also given in this work.

The description of the clouds and precipitation were conducted early at the experimental meteorological ground (EMG) /Miroschnikova J.I., 1979, Osokina I.A., 1985/. In order to get the possibility of transportation of the results received in (EMG) to the other areas the new research has been done in the forest-steppe and steppe zones of Ukraine.

2. THE TRAJECTORIES OF DISPLACEMENT OF AIR MASSES IN UKRAINE

The trajectories of the transferring air masses on the barial topography maps 700 mb were built concerning the peri-

od of 11-years (1970-1980) for all the twenty four hours containing precipitation. The repetition in per cents of different transferrings is given in table 1.

Table 1

The repetition (%) of different transferrings

Month	Transfer			
	west	east	north	south
March	17	11	3	69
April	23	2	8	67
September	46	2	6	46
October	28	7	-	65
Spring	21	6	6	67
Autumn	39	4	4	53

The differences in circulation conditions of spring and autumn are in following the weather condition in spring in Ukraine was influenced by south-west outlying districts anticyclone; in autumn the west Europe and west Ukrainian zone were influenced by little gradient cyclone field connected with Island minimum. The rest Ukrainian territory was under the influ-

ence of the west outlying districts of siberian anticyclone.

3. MAIN CHARACTERISTICS OF THE PRECIPITATION OF TRANSITIONAL SEASONS OF A YEAR

Let's look through the Table 2, from which follows that the most average monthly quantity (R, mm) of precipitation were observed with south transfer. The contribution (P, %) of precipitation (table 2) of that transfer into the sum of the spring precipitation accounts in 72%. The contribution of the west transfer is also essential, which accounts in 22%.

Table 2

Main characteristics of the precipitation

Characteristic of precipitation	Transfer			
	west	east	north	south
Spring				
R, mm	19,0	1,9	2,8	48,8
P, %	22	3	3	72
Autumn				
R, mm	33,3	1,0	5,5	33,6
P, %	43	1	6	50

The autumn contribution of precipitation of south and west transfers reached the figure of 93% of the season sum of precipitation, taking to the account that the contribution of these both transfers is quite similar. The information of the duration (hour) of fall precipitation (table 3) is very important for the practice of the active inf-

luence. In general for Ukraine, all the precipitation falling within south and west transfers, are of the greatest interest.

Table 3

The duration (hour) of fall precipitation

Season	Transfer			
	west	east	north	south
Spring	10,3	9,4	6,4	11,1
Autumn	8,7	4,4	10,2	8,4

In springtime season strong precipitation (more 5 mm per twenty-four hours) was observed for 20% of cases only, however its contribution to season sum was 60% approximately. In autumnal season frequency of strong precipitation was observed in 25% of cases and its contribution in total sum of precipitation reach 70%. Average lifetime of the strong precipitation almost was twice average lifetime weak precipitation. In figure for EMC a frequency of lifetime of strong and weak precipitation is shown.

Any peculiarity for season spring-autumn was not exposed, and so data of two season were generalized.

By data of fig. 1 we can see, that for 70% of cases lifetime of falling weak precipitation not exceed 5 hour while for 80% of cases lifetime of strong exceed 5 hour. Of all month transitional season, with the

exception of march, precipitation mainly was liquid.

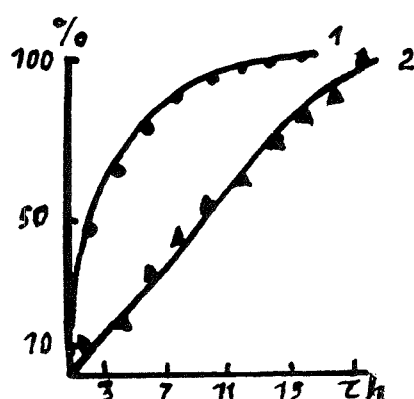


Fig.1

Accumulate recurrence lifetime precipitation in spring on EMG.

- 1 - weak precipitation
- 2 - strong precipitation

4. SOME CHARACTERISTICS OF THE CLOUDS GIVING PRECIPITATION

Various forms of cloudiness, which produce precipitation is observed in transitional seasons. In different month the number of cases with one or the other form of cloudiness is not similar. Due to aircraft investigation and weather-stations data during transitional seasons there was a combination of stratus clouds with convective for twenty-four hours. In spring the number of the days with cloudiness giving precipitation is more than in autumn. The contribution (%) of precipitation from each form of cloudiness into the sum of precipitation is not equal (table 4).

The stratus rain clouds make a considerable contribution to the precipitation of the

spring season. The cumulonimbus clouds make contribution to autumn season. The insidemass stra-

Table 4

The contribution (%) of precipitation from each form of cloudiness into the sum seasons

Season	Ns	Cb	Sc, St, Ac
Spring	55	37	8
Autumn	39	58	3

tus clouds make a small contribution, about 3-8%. The combination of stratus clouds with convective ones are determined in transitional seasons. In autumn there were about 50% of cases and in spring were less.

5. CONCLUSION

Due to there available data one can receive an information about the resources of cloudiness, suitable for sowing with the aim of receiving supplementary precipitation. For this reason the fitness coefficient of the clouds was used with crystallize reagents: Ns - 0,78 in spring and 0,49 in autumn; St, Sc - 0,50 in spring and 0,13 in autumn / Khysid S.V., 1986 /. The fitness coefficient for sowing Cb is equal to 1 (one). The average number of cases with resource cloud in every month of the season is given in table 5.

On the basis of the complete research one can come to the conclusion about the expediency of activities on the arti-

ficial increasing of precipitation during the transitional seasons of a year, so far as the fitness resource for the cloud

Table 5

The average number of cases with resource cloudiness

Season	Ns	Cb	Sc, St, Ac
Spring	4	5	2
Autumn	1	5	-

comparable with the winter season of a year.

6. REFERENCES

Miroschnikova Y.I., Solanek E.G., Khusid S.V. Some characteristics of the clouds and precipitation of transitional seasons of the year on the ste-

ppe part of Ukraine with the point of view of artificial regulation of precipitation. - The all Union conference physics of clouds and aggressive influence on them. Thesis lecture. Obninsk, 1979, p.101-102.

Ocokina I.A., Khusid S.V., Shedenenko I.P. About the distribution of precipitation on the praving ground of URI of the state meteorological committee of the USSR with different transfer of air masses in transitional seasons of a year. - Trudy UHRI, 1985, part 214, p.103-116.

Khusid S.V. Extent fitness of stratus clouds in transitional seasons of a year to the aggressive crystallization of reagent with the aim of receiving supplementary precipitation. - Trudy UHRI, 1986, part 218, p.27-31.

THE RESULTS OF INVESTIGATING CLOUDS AND PRECIPITATION REGIME OF THE COLD PERIOD IN LENINGRAD REGION

1 1
Yu. A. Dovgalyuk, E. V. Orenburgskaya,

2 1 1 1
A. M. Pirnach, D. D. Stalevich, A. A. Sinkevich, V. D. Stepanenko

1
Main Geophysical Observatory, Karbyshev Str. 7, St. Petersburg
Russia, 194018

2
Ukrainian Regional Hydrometeorological Institute,
Nauki Str. 37, Kiev, Ukrain, 252650

During 1986-1990 A. J. Voeikov Main Geophysical Observatory carried out investigations of clouds and precipitation produced by them in the cold season of the year (September to March) for Leningrad and its region. The necessity of those investigations was caused by the beginning of practical works on winter precipitation regulation to protect Leningrad from intensive snow-falls. Investigations on possibility of meteoroprotection of big industrial cities began earlier (Litvinov, 1967) and included investigations of clouds and precipitation in proposed region of experiments, as a necessary initial stage. To a great degree, it was caused by physical-geographic situation of the city (region) and by peculiarities of mesoscale atmospheric processes.

To evaluate climatological characteristics of clouds and precipitation the 1946-1982 data from ground based meteorological stations of Leningrad and its region, 1974-1982 data of radar observations, and 1946-1964 data of aircraft sounding for Leningrad station were used.

Statistical analysis of the data showed that the main cloud form for the period under consideration was stratiform, the recurrency of which reached 96% in some months. One-layer clouds predominated: more than 70% of cases. In multilayer clouds the upper layer was the thickest. At the same time, on 4 days a month one could observe the stratiform clouds with embeded convective clouds in the investigated region. The assessment showed that weak precipitation

predominates from the layer clouds (12mm/24 hours). Their frequency is about 70% of cases. The frequency of intensive precipitation (more than 10 mm/24 hours) is about 10% and they fall mainly from systems Ns-As and Cb-layer clouds. The contribution of considerable precipitation is not large, about 9% of the amount of the cold period of the year sum (Nicandrov, Orenburgskaya, 1987).

The comparison of precipitation data for the stations based in the city and its region showed that maximum difference between precipitation amounts appears to be in precipitation, falling from Ns. One can observe greater percent of heavy and considerable precipitation in the city (13 and 7% respectively), and there are 10 and 5% of such precipitation respectively in the region. We have not discovered differences in precipitation intensity distribution between the city and the region for the other forms of clouds. The comparison of precipitation amount falling in the city and its surroundings also confirms the influence of industrial city (Leningrad in our case) on precipitation field. The precipitation amount in the city occurred to be approximately 10% lower than in the surroundings. This regularity in precipitation amount between the city and region was not only for the whole cold period averaged over 1946 to 1981, but for every year. The comparison carried out, was based on the data of 3 groups of stations, chosen for different distances from the city center. The 1 group of stations was located in city, the 2 group of stations was located in radius of 30 km from

the city, the 3 group of stations was located in the distance of up to 100 km from the city.

In 1986-1990 additional investigations were carried out with the help of NGO aircraft laboratory (Zvonarov V.V. et al, 1986) in Leningrad region. The measurements of the upper and lower cloud boundaries heights, cloud layer thickness, LWC and cloud phase composition were made. It was found out that the lower boundary of the layer clouds (disregarding the types) were at the height from 0.1 up to 1.1 km, and the lower boundary of the middle height clouds - at the height from 2.0 to 2.5 km. Multilayer clouds (2 and more layers) developed on some days. The lower boundary heights of the 2 and 3 layers alter from 2.7 to 3.4 km and from 3.7 to 4.2 km respectively. The upper boundary of the cloud lower layer reaches the height 0.6-2.5 km, and when Ns-As takes place exceeds 8 km. Analyzing the cloud phase structure, one can notice that drops predominate for Sc. Ns, Ns-As usually have mixed structure. LWC of the lower level clouds does not exceed 0.3 g/m, while in Cb embedded in layer clouds LWC increases up to 0.6 g/m.

Besides the above-mentioned measurements the investigations were carried out of non-homogeneity of the temperature field and the field of vertical motions in clouds. It was found out, that maximum recurrence of thermal non-homogeneity scale in all parts of Sc and Ns clouds is within 0.2-0.6 km. (The data is obtained with the help of IR-radiometer (Sinkevich A.A., 1981).

More detailed information on cloud structure and cloud dynamics can be obtained with the help of numerical modeling. We used two numerical models: a) semi-empirical model of atmospheric front, b) two-dimensional unstable model of frontal layer clouds for typical situations. The choice of these models was caused by the fact that in investigated region one can observe mostly frontal layer clouds. The cyclones, passing over Leningrad, are mainly connected with south and west-south invasions.

The models were designed in UkrNIGMI (Pirnach A.M., 1984). Here we present the results of analysis of clouds development during the 7 November 1987 experiment. Complex observations of clouds with the help of aircrafts, radars and ground base stations were carried out that day.

The occluded front had passed over Leningrad on November 7, 1987. To construct its vertical profile, the radiosonde data obtained for 5 periods during 6-7 November was used. One can see the vertical front cut with the central point /t=0/ in Fig. 1. =

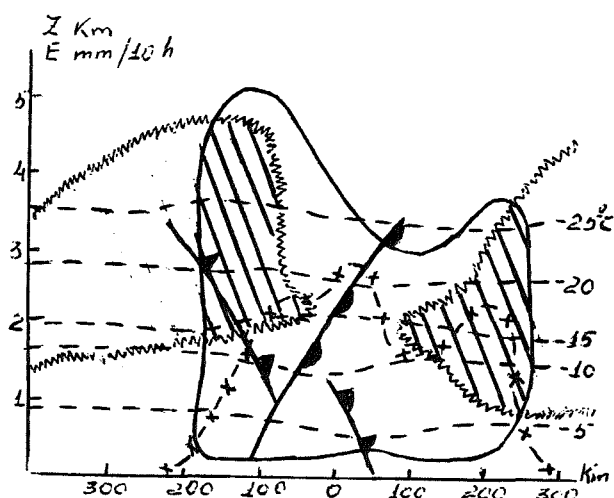


Fig.1. The vertical profile of the front passing over Leningrad on the 7.11.87.

isolines of local condensation velocity $e = 10^{-5}$ mm/h

isolines of super saturation to ice $D = 0$ g/kg,

--- air temperature (C),

—x— integral condensation speed E mm/h,

regions where $e > 0, D > 0, w > 0$.

One can see from the Figure that frontal system, has a wide region of updrafts ($w > 0$), which correspond to positive values of local condensation speed ($e > 0$). This region covers the central part of frontal system, including occluded front. There are two regions with supersaturation to ice ($D > 0$) in the system, i.e. containing water vapour able to sublimate. Regions with $e > 0$ and $D > 0$ do not coincide, but they partly overlap in the areas where $w > 0, D > 0$ and $e > 0$. The simultaneous presence of water vapour able to sublimate, intensive condensation and updrafts form favourable conditions for receiving additional precipitation (shaded region). There are two regions where $w > 0, D > 0, e > 0$ in the analyzed system. There are regions with $e < 0$ and $D > 0$ to the left and to the right from the region with $e > 0$. In the presence of clouds, these regions are favourable for cloud dissipation, because the existence of water vapour able to sublimate promotes

formation and growth of additional crystals which later fall as precipitation.

The calculations of cloud evolution show that the cloud consists of two layers. The layer with small concentrations of crystals was located between those two layers. The microphysical characteristics of the cloud noticeably vary during its development.

REFERENCES

1. Litvinov I. V., 1967: The Distribution of Precipitation During Cloud Seeding with Ice Forming Reagents. *Meteorology and Hydrology*, N. 9, 60-64.
2. Nikandrov V. Ya., Orenbureskaya E. V., 1987: The Recurrence of Strong Snowfalls and Investigation of their Regulation Possibility. *Questions of Cloud Physics*. Gidrometeoizdat, Leningrad, 31-36.
3. Pirnach A. M., 1984: A Numerical Simulation Processes in Frontal Clouds. *Proceedings of the 9 International Cloud Physics Conference*, Tallinn, v2, 637-640.
4. Sinkevich A. A., 1981: On the Analysis of IR-Radiometer Operation in Measuring Temperature of Cloudless and Cloudy Atmosphere. *Trudy MGO*, N439, 93-102.
5. Zvonaryov V. V., Lyadov V. S., Ponomarev Yu. F., Sinkevich A. A., Stepanenko V. D., 1986: Characteristic Features of the MGO Aircraft Laboratory IL-14, Leningrad, Gidrometeoizdat, *Trudy MGO*, v. 497, p. 51-52.

COUPLED ATMOSPHERIC-FIRE MODELLING: ROLE OF THE CONVECTIVE FROUDE NUMBER AND DYNAMIC FINGERING AT THE FIRE LINE

M. A. Jenkins¹, T. L. Clark², J. L. Coen², and D. R. Packham³

¹Earth and Atmospheric Science, York University, Toronto, Canada M3I 1P3

²NCAR/MMM, P.O. Box 3000, Boulder, CO 80307-3000

³Geography and Environmental Sciences, Monash University, Melbourne, Australia

1. INTRODUCTION

Until recently, studies on effects of forest fires on the atmosphere have treated the fire-atmosphere as an uncoupled system. Exceptions are Grishin (1992) and Clark et al. (1996), hereafter referred to as CJCP. These works point to a serious need to consider coupling between the fire and the atmospheric dynamics because the energy released by an intense fire is strong enough to drive the atmospheric dynamics over a wide range of spatial scales. CJCP argue that for idealized mean-flow conditions increasing the wind strength above some threshold value results in a decreased level of coupling between the atmospheric and fire dynamics. Their argument is based on the square of a convective Froude number

$$F_c^2 = \frac{(U - S_f)^2}{g \frac{\Delta\theta}{\theta} W_f}, \quad (1)$$

which provides a measure of the ratio of the kinetic energy of the air (relative to the fire) over the sensible heat flux provided by the fire. U and S_f represent wind speed and rate of fire spread, W_f is width of the fire, $\Delta\theta/\theta$ the convective buoyancy, θ potential temperature, and g gravity. For large wind speeds and corresponding large F_c^2 values, air parcels remain in the fire for such a short time that atmosphere-fire dynamic interactions are negligible. For small wind speeds and F_c^2 values, the air and fire should be strongly coupled.

CJCP have taken a three-dimensional non-hydrostatic mesoscale model and coupled it with a simple dry eucalyptus forest fire model to establish a time-dependent wildfire simulation model. Sensible and latent heat fluxes associated with the fire are introduced into the atmospheric model by modifying the equation for the conservation energy.

The present fire model is extremely simple and is treated as a homogeneous forest with both ground and canopy fuel. Fuels are assigned initial masses and fixed burn rates, and a single constant combustion coefficient is applied to each dry fuel type. Canopy fuel is given a moist/dry ratio. Of the sensible heat released, 3% dries the ground fuel, and 56% of the dry fuel's mass is converted to water vapor. Smoldering

is emulated. Fuel is ignited by contact, where ground tracers move following a simple empirical fire spread-rate formula (Noble et al., 1980). Heat flux from the ground fire first dries the canopy, and once canopy fuel is dry and the ground heat flux exceeds a threshold value, the canopy ignites. The effects of radiation and small scale turbulence are parameterized using a simple extinction depth of 50 m for sensible and latent heat fluxes.

Using CJCP's model, we present simulations of coupled fire and atmospheric dynamics performed over a range of ambient wind speeds to assess the utility of the convective Froude number in predicting short fire-line behavior. Please refer to CJCP for details.

2. DESCRIPTION OF EXPERIMENTS

Experiments are described in Table 1. The standard experiment starts with a 420 m long fire line and a constant ambient wind U_0 . In the following, S_f is fire spread rate calculated analytically following Nobel et al., S_{fa} actual fire speed due to fire front dynamics, and F_{ca}^2 the square of the actual convective Froude number calculated using S_{fa} . The arrows in figures represent wind vectors taken at the 15 m height.

TABLE 1. Fire experiments and parameters: U_0 = ambient wind speed; † fire lines are separated by 400 m.

Experiment	U_0 (m s ⁻¹)	$U(z)$ (m s ⁻¹)	Backfire	# fire lines
FIR7AR	1.	const	no	1
FIR7CR	3.	const	no	1
FIRE7C	3.	const	yes	1
FR7CS1	3.	tanh	no	1
FIRE7Z	4.	const	no	1
FIR7DR	5.	const	no	1
FIRE7E	10.	const	no	1
FIR7E2	10.	const	no	†2
FIRE7F	15.	const	no	1

3. RESULTS

3.1 Effect of backfire on short-line experiments

Backfire introduces convectively disturbed flow in boundary layer ventilation flow. Experiment FIRE7C has a backfire, FIR7CR does not (Table I). Figure 1 shows that turbulent forcing by backfire eddies produces significant variability in S_f for FIRE7C. If the region of burned out fuel behind the main fire cools, then convective downdrafts can penetrate closer to the surface to enhance near surface wind speeds. This buildup of low-level shear adds to the instability of the fire front and to the possibility for increased S_f . This is evident at $t \approx 4$ min in FIRE7C when S_f suddenly increases from ≈ 0.4 to 0.5 m s^{-1} and then drops back to $\approx 0.4 \text{ m s}^{-1}$. Unlike FIRE7C, S_f versus t for FIR7CR (no backfire) is extremely regular. It is also possible that the backfire preheats air coming into the fire, reducing low-level wind speeds and shear to stabilize the fire by reducing $\Delta\theta$ and increasing F_c^2 . Figure 1 shows that after the initial convective adjustment time, and other than the peak at ≈ 4 min, the maximum S_f for FIRE7C (backfire) remains temporally fairly uniform, while for FIR7CR (no backfire) the maximum S_f steadily increases.

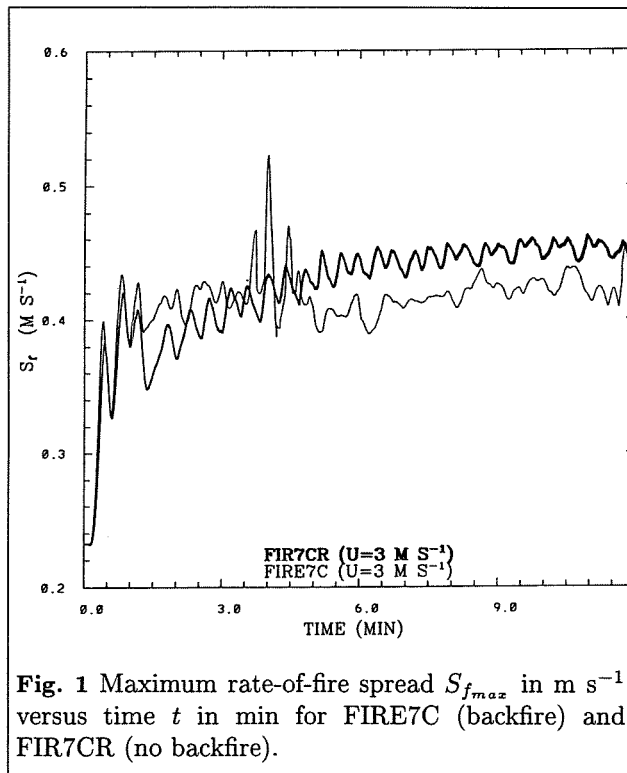


Fig. 1 Maximum rate-of-fire spread $S_{f,max}$ in m s^{-1} versus time t in min for FIRE7C (backfire) and FIR7CR (no backfire).

3.2 Effect of F_c^2 on flow pattern

Decoupling with increasing U_0 is seen in Fig. 2, a plot of the fire line's surface fuel ignition in constant ambient winds U_0 of 1, 3, 4, 5, 10, and 15 m s^{-1} at $t=6$ min. Lower wind speeds, $U_0 < 5 \text{ m s}^{-1}$, allow the buoyant column of hot air to lie just in front of the fire. The column draws air (normal to the fire line) much faster from the center of the fire than from its

sides and the fire line evolves a pronounced parabolic shape. If the wind speed is too strong, then the convection column is too far removed from the fire to allow any interaction. When $U_0 = 10$ and 15 m s^{-1} , the shape of the central portion of each fire line stays linear; the near surface convergence pattern of the convection column is decoupled from the fire. Simulations show that as U_0 increases, the wind tends to flow through the fire, while the air shows little vertical deflection.

A final variation is to set two fire lines to observe the effect of halving the F_c^2 by doubling the fire's heat flux for a fixed $U(z)$. FIR7E2 ($U_0 = 10 \text{ m s}^{-1}$, double fire line, $F_c^2 = 0.85$) is two fire lines initially spaced 400 m apart and perpendicular to U_0 . Although convection is initiated by two parallel fire lines, plots of buoyancy show that by $t = 2$ min the forward fire plume entrains the rear one and becomes a single plume, behaving as though a single line source is located beneath it and the source is essentially collocated with the forward line fire.

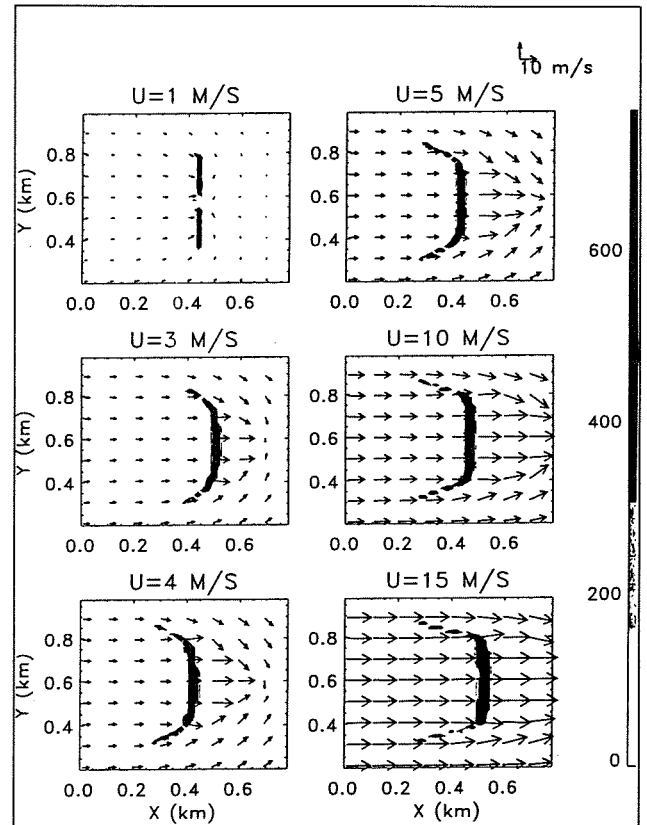


Fig. 2 Fire line ignition at $t = 6$ min for $U_0 = 1, 3, 4, 5, 10, \text{ \& } 15 \text{ m s}^{-1}$ corresponding to FIR7AR, FIR7CR, FIRE7Z, FIR7DR, FIRE7E, & FIRE7F, respectively. Shaded regions indicate fire fluxes in kW m^{-2} .

In the double fire line FIR7E2, the front fire moves much faster than in the single line FIRE7E. The fire-atmosphere coupling is also much greater in FIR7E2 ($F_{ca}^2 = 0.47$) than in FIRE7E ($F_{ca}^2 = 1.2$). In FIR7E2, coupling is weak for the rear fire line, significant for the forward fire line; buoyancy plots show little ver-

tical deflection in the air flowing over the rear fire; winds flow through the rear fire and are entrained by the forward, vertically-tilted, fire plume. Figure 3 shows that the shape of the central portion of the rear fire line stays linear, while the forward fire line evolves into a parabolic-like shape, indicating that the downstream near-surface convergence pattern of the single convective column is coupled with the forward fire, but is too far upstream to affect the shape of the rear fire line.

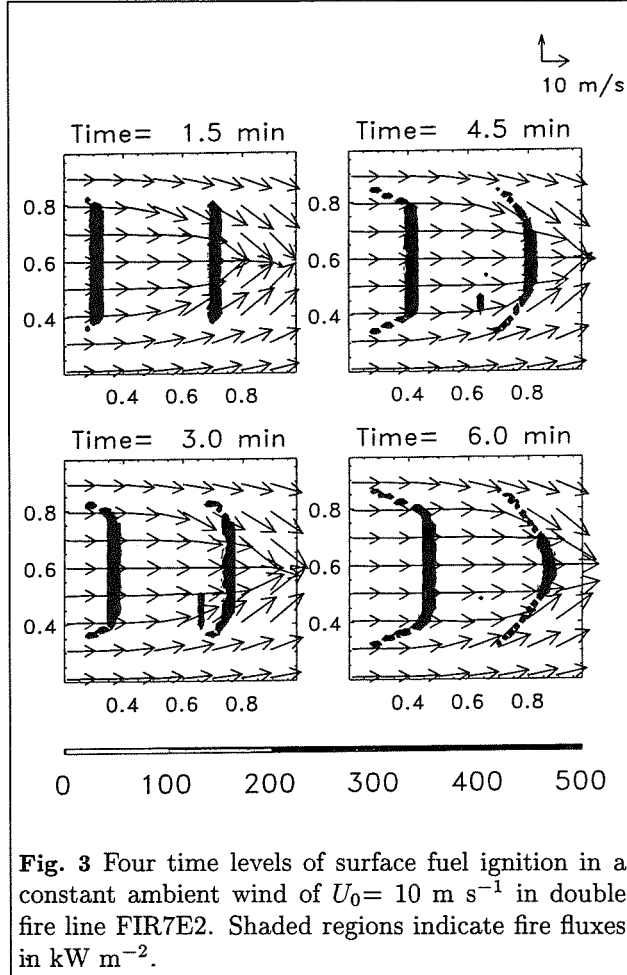


Fig. 3 Four time levels of surface fuel ignition in a constant ambient wind of $U_0 = 10 \text{ m s}^{-1}$ in double fire line FIR7E2. Shaded regions indicate fire fluxes in kW m^{-2} .

3.3 Effect of fire-induced motions on fire evolution

Experiments FIR7CR and FR7CS1 demonstrate the effect of long term feedback of the fire-induced convection on the fire. FIR7CR used a constant wind of $U_0 = 3 \text{ m s}^{-1}$, FR7CS1 used $U(z)$ set equal to an hyperbolic tangent profile where $U(z)$ is $+3 \text{ m s}^{-1}$ at the surface $z=0$, zero at $z=500 \text{ m}$, and asymptotic to -3 m s^{-1} for $z \gg 500 \text{ m}$. In FIR7CR the convective motions are advected downstream of the fire; in FR7CS1 the convective motions are eventually advected upstream, providing the opportunity to re-enter the fire.

A time series of $S_{f_{\max}}$ for these two cases shows that in FIR7CR, $S_{f_{\max}}$ remains steady, whereas in FR7CS1 $S_{f_{\max}}$ displays very nonuniform behavior over a period of 28 min. $S_{f_{\max}}$ departs dramatically from a steady value once $t > 15 \text{ min}$, the time re-

quired to recycle convective eddies on the scale of the fire, and at $t = 24.4 \text{ min}$ jumps erratically. As discussed next, this sudden increase in $S_{f_{\max}}$ corresponds to a dynamic fingering event.

The evolution of fire ignition for these two cases show that while FIR7CR retains its integrity throughout the integration period, FR7CS1 breaks up by $t = 20 \text{ min}$ as a result of the feedback of fire-induced motions. The break up of FR7CS1 is seen in Fig. 4. The curved shape of the fire line results in the development of two counter rotating vortices positioned at the mid-point of the fire line. In FR7CS1 the environmental hyperbolic tangent wind profile allows this vortex pair to eventually touch down within the fire line, where the opposing winds from the vortex pair blow air into the fire and break up the fire line. A similar vortex pair is produced in FIR7CR, that eventually touches down, but well in front of the fire line without strongly affecting fire line dynamics.

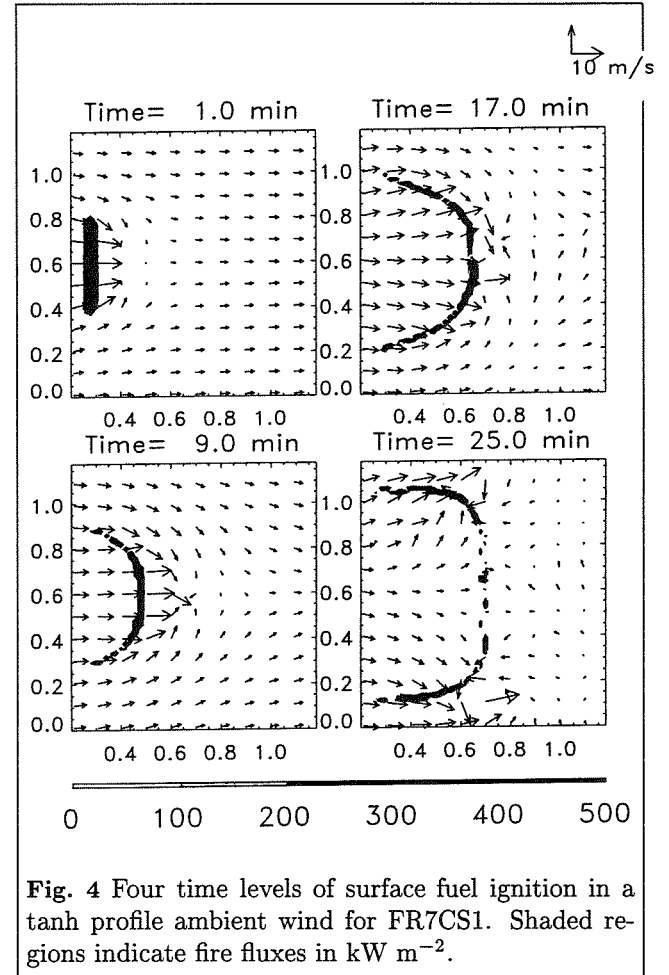


Fig. 4 Four time levels of surface fuel ignition in a tanh profile ambient wind for FR7CS1. Shaded regions indicate fire fluxes in kW m^{-2} .

3.4 A dynamic fingering event

One specific type of small-scale dynamical process occurring at fire fronts that may affect strong feedbacks between the atmosphere and fire dynamics is a process CJCP refers to as “dynamic fingering”. The vertical tilting of regions of intense horizontal negative shear at the fire front lead to narrow regions, or “fingers”, of high speed, hot air shooting out in

front of the fire. These small-scale fingers of hot gas may represent a major process in fire spread on the microscale that causes fires to “jump” as they spread.

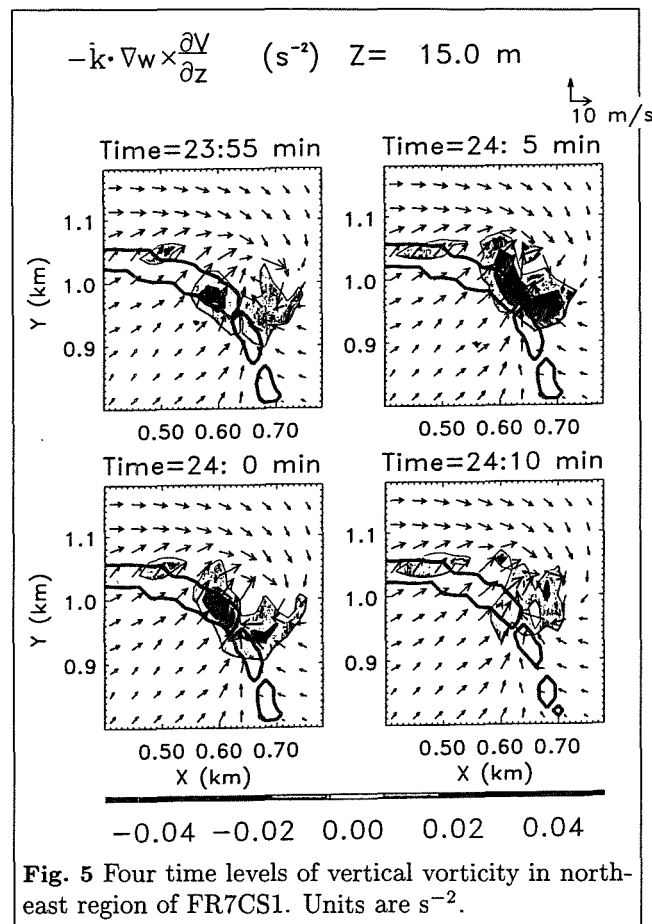


Fig. 5 Four time levels of vertical vorticity in north-east region of FR7CS1. Units are s^{-2} .

Probably a necessary, but not sufficient, condition for dynamic fingering to occur is that F_c^2 be small, i.e., the atmosphere-fire dynamics must be strongly coupled before any fire front vortices that are tilted can be near the fire. Our simulations to date suggest that even when the value of F_c^2 indicates strong coupling, fire-line dynamics remain stable, showing little dynamic fingering activity. Something besides small F_c^2 is needed before dynamic fingering can occur, and a likely candidate is low-level shear. Here we rely on a longer term integration to produce a variety of eddies to provide low-level shear in the boundary layer. A single dynamic fingering event is obtained with this procedure and is observed in the north-east sector of the fire front.

This particular fingering event is caused by the advection of a fire-induced downdraft into the rear ventilation flow. The downdraft produced a region of near surface vertical shear that moved through the fire front adjacent to an existing vertical rotor. The vertical tilting of this shear by local updrafts intensified the rotation rate of the vertical rotor leading to an anomalous wind speed maximum. Large maximum S_f values for $t > 18$ min resulted from this type of forcing. The intensified rotation rate of the fire vortex is seen in Fig. 5 which shows the vorticity

source $-\hat{k} \cdot \nabla w \times (\partial \vec{V} / \partial z)$ due to vortex tilting.

4. CONCLUSIONS

Simulations of coupled forest fire and atmospheric dynamics are performed over a range of mean ambient wind speeds to assess the utility of the square of the convective Froude number in predicting fire line behavior. The results show that for moderate to low wind speeds fire-atmosphere coupling is significant, leading to strong feedbacks between fire-induced motions and fire-line spread. Wind speeds of 10 m s^{-1} or greater result in faster rates of fire spread, but weaker fire-atmosphere coupling with no noticeable feedback between the fire and fire-induced motions. The results also reveal that backfire in short fire lines can either stabilize or destabilize fire-line dynamics.

For moderate ambient wind speeds, our simulations show three basic mechanisms affecting fire line behavior. The first, discussed in CJCP, is the effect of the near-surface convergence zone of the convection column inducing a parabolic-like shape to the wind-driven line fire. This is seen in the simulations with U_0 ranging from 2 to 5 m s^{-1} . The second mechanism is a longer term effect derived from the first, where the curved shape of the advancing fire front produces a vertically-oriented vortex pair situated in front of the fire. When the ambient wind reversed direction with height (FR7CS1), this vortex pair eventually touched down in the fire, resulting in a breakup of the fire line into two sections. When the wind speed remained constant with height (FIR7CR), the vortex pair touched down well in front of the fire line, allowing the fire line to retain its curved shape throughout the simulated time. The third mechanism is “dynamic fingering”, the result of vortex tilting at the small scales of the fire line. In this case the sense of vortex tilting amplifies the wind speed in the direction of fire spread resulting in a marked increase in the rate of spread. A single event of dynamic fingering is presented (FR7CS1) that resulted from the vertical tilting of a zone of negative wind shear produced by a fire-induced eddy at the fire front. The tilted zone of shear amplified an existing vertical vortex to locally increase the rate of spread.

5. REFERENCES

- Clark, T.L., M.A. Jenkins, J. Coen, and D. Packham, 1996: A coupled atmospheric-fire model: Convective feedback on fire line dynamics. *J. Appl. Meteor.* (In Press.)
- Grishin, A., *Matematicheskoye modelirovaniye lesnykh pozharov i novyye sposoby bor'by s nimi* (Mathematical modeling of forest fire and new methods of fighting them). Novosibirsk, “Nauka” Publishers, Siberian Division, 1992, 408 pp (Russian).
- Noble, I.R., G.A.V. Bary, and A.M. Gill, 1980: McArthur's fire-danger meters expressed as equations. *Aust. J. Ecology*, 5, 201-203.

A CASE STUDY OF SNOW CLOUDS INFLUENCED BY TOPOGRAPHY OBSERVED IN THE TOHOKU DISTRICT OF JAPAN

Sento Nakai¹, Yoshinori Yamada² and Masahiro Kajikawa³

¹National Research Institute for Earth Science and Disaster Prevention, STA, Tsukuba 305, Japan

²Meteorological Research Institute, JMA, Tsukuba 305, Japan

³Akita University, Akita 010, Japan

1. INTRODUCTION

Snow clouds developed over the Sea of Japan are modified by the topography in a variety of ways (e.g., Kikuchi et al. 1987; Takeda et al. 1982). After landing, the snow clouds lose the supply of sensible and latent heat, and affected by the orographically-forced airflow (Nakai and Endoh 1995). Inland areas of northern Japan suffer from heavy snowfall in winter seasons. Investigating the orographic modification of snow clouds is important to clarify the mechanism of the heavy snowfall.

The "Cooperative Japan Sea Snow Cloud Project" observations were carried out in the Tohoku District of Japan from 1989 to 1993. So far, the precipitation formation processes and airflow structures of snow clouds over the sea have been demonstrated (e.g., Murakami et al. 1994; Yamada et al. 1994). Observations of snowfall influenced by the topography over the land were also carried out as part of this project.

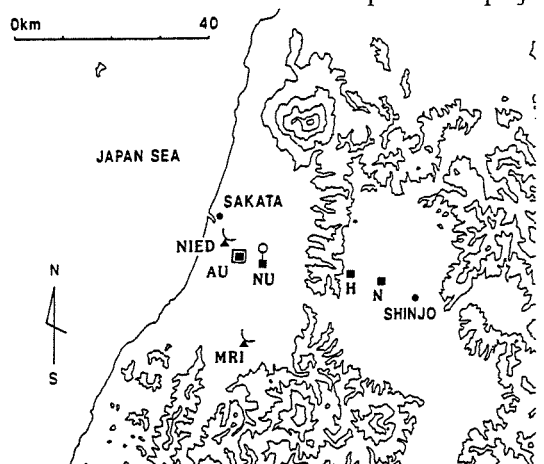


Fig. 1. Observation area. Contour lines are drawn by 400-meter intervals.

Within the observation area, there were many mountains at altitudes less than 1000 meters and a few mountains at more than 1500 meters. Figure 1 shows the observation area with the locations of the observation facilities. Two X-band Doppler radars were used by NIED (National Research Institute for Earth Science and Disaster Prevention) and MRI (Meteorological Research Institute). AU, located in the

coastal plain, indicates precipitation particle observation facilities of Akita University. NU indicates rawinsonde and HYVIS (Murakami and Matsuo 1990) launch site of Nagoya University. Photographs of precipitation particles are taken inland at H (Hanesawa) and N (Nikke) sites. Meteorological observatories at Sakata and Shinjo are indicated by closed circles. Sakata Meteorological Observatory is located at (38°54'N, 139°51'E).

2. ENVIRONMENTAL CONDITIONS DURING THE ANALYSIS PERIOD

We analyzed the snow clouds observed over the land on 13-19 February 1992. The analysis period was divided into two stages (stages I and II) based on the radar echo pattern and the rawinsonde data. Stage I is from 13 February to 17JST, 16 February. Stage II is from 17JST, 16 February to 19 February.

The cold outbreak was weak in stage I. Mean wind speed and the temperature at 850hPa were 9.7m/s and -7.3°C, respectively, according to the aerological data at Akita. VAD analysis indicated that vertical wind shear in the convective mixed layer was large (Fig. 2, 1022JST). Wind speed was often below 10m/s at a height less than 1500m, and the west-east component was very small in the lowest levels.

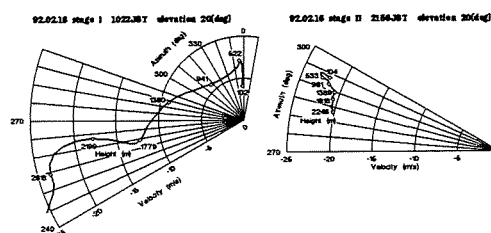


Fig. 2. Hodographs at 1022 and 2156JST.

Many cellular echoes were observed with larger wind speed and lower temperatures in stage II. Mean wind speed and the temperature at 850hPa were 15.1m/s and -11.4°C, respectively. The cold outbreak was strong. The wind in the convective mixed layer was almost uniform and the vertical wind shear was very small (Fig.2, 2156JST). The wind speed often exceeded 15m/s at levels less than 1000 meters, and the wind direction favored the orographic lifting.

3. STATISTICAL CHARACTERISTICS

Average reflectivity (I_A) of MRI radar is derived for each stage. Figure 3 is the vertical section of I_A along the direction of the average motion of snow clouds.

Hydrometeor type was observed at AU, H and N sites in Fig. 1. We paid attention to whether graupels existed or not on classifying the hydrometeor type. We have 67 data simultaneously observed at the three sites (Table 1) and 210 data observed at H and N sites by three-minute intervals (Table 2).

Table 1. Number of data classified by the hydrometeor types. Included are the data that hydrometeor types were observed at AU, H and N sites. AU site was on the windward side, H and N sites were on the lee side of the hills.

	stage I	stage II
graupels were observed on both sides of the hills	1	17
graupels were observed only at AU site	2	16
graupels were observed only on the lee side of the hills	0	3
graupels were not observed	24	4
total	27	40

Table 2. The same as Table 1, but for all data that hydrometeor types were observed at H and N sites. G, S, U and M indicate graupels, snowflakes, undistinguishable, and mixed, respectively. U includes the data of no precipitation.

H	N	stage I	stage II
G	G	0	10
S	G	1	4
G	S	5	4
G	U	0	8
U	G	2	11
M		1	4
S	S	33	13
S	U	14	5
U	S	6	8
U	U	42	39
total		104	106

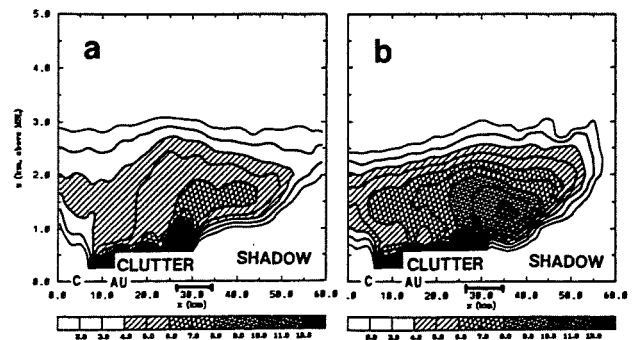


Fig. 3. Vertical section of average reflectivity (a) of stage I along 270° - 90° , and (b) of stage II along 287° - 107° . C is the position of the coastline. AU is the same as in Fig. 1. A bar around $x=30\text{km}$ indicates the area more than 400 meters high.

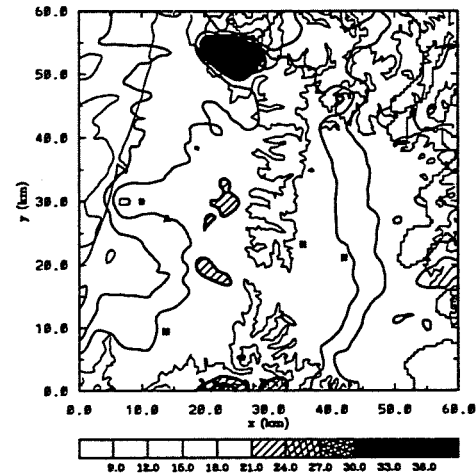


Fig. 4. Horizontal section of reflectivity at a height of 1500 meters at 1019JST.

3.1 Stage I

The radar echoes were often widespread as shown in Fig. 4 in stage I. These echoes were not stationary, and moved eastward. According to I_A distribution, the precipitation was intensified over the hills around $x=30\text{km}$. The increase of I_A over the hills was up to 2dB, and the concentration of large I_A values was weak. I_A decreased with height between the coast line and the hills ($4\text{km} < x < 26\text{km}$).

Snowflakes prevailed among the observed precipitation particles, especially on the lee side. Graupels were observed only 8% of the data in stage I (Table II), and less observed at inland observation sites. When graupels observed at H site, snowflakes were apt to be observed at N site. When snowflakes observed at H site, sometimes there were no precipitation at N site.

3.2 Stage II

The precipitation was also intensified over the hills around $x=30\text{km}$ in stage II, however, the increase

reached 5dB, which was much larger than in stage I. Large I_A values were concentrated in a narrow area centered at $x=35\text{km}$, suggesting strong orographic effect of the hills. I_A increased with height below 1500 meters level between the coast line and the hills ($4\text{km} < x < 26\text{km}$).

Graupels observed more frequently in stage II than in stage I, especially on the windward side (AU site) of the hills (Table 1). The frequency of graupel at H site was almost the same as that at N site (Table 2). They were lower than that at AU site, though, the class U on the lee side might include graupels so that only qualitative comparison is possible.

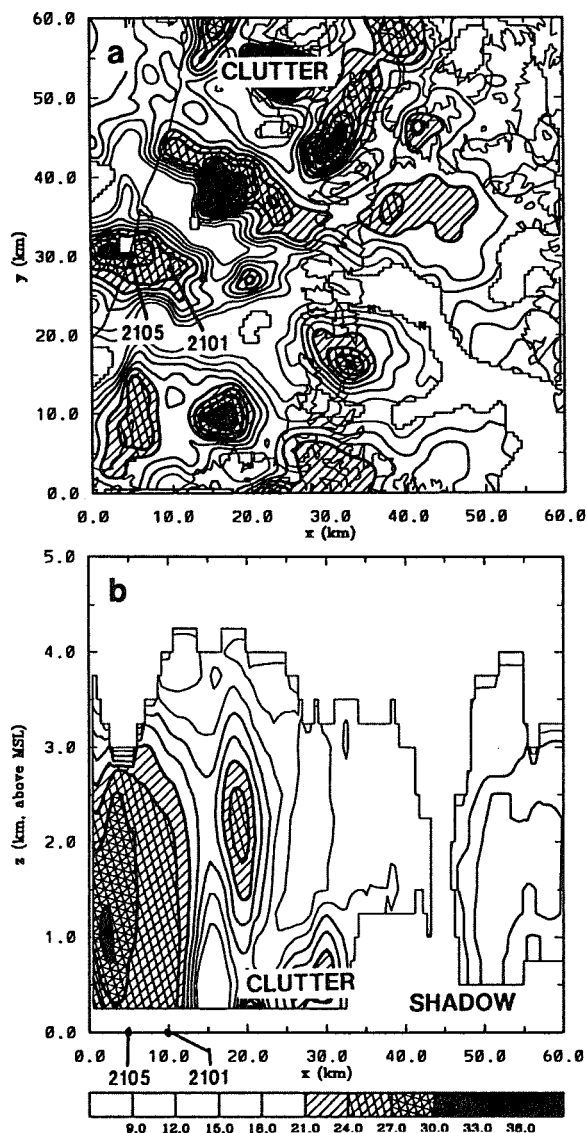


Fig. 5. Reflectivity fields at 2057JST. (a) is the horizontal section at a height of 1500 meters. (b) is the vertical section along the line between $(x,y)=(0.0, 30.2)$ and $(x,y)=(58.8, 18.0)$. 2101 and 2105 are the locations of AU site corrected by the moving speed of the radar echoes.

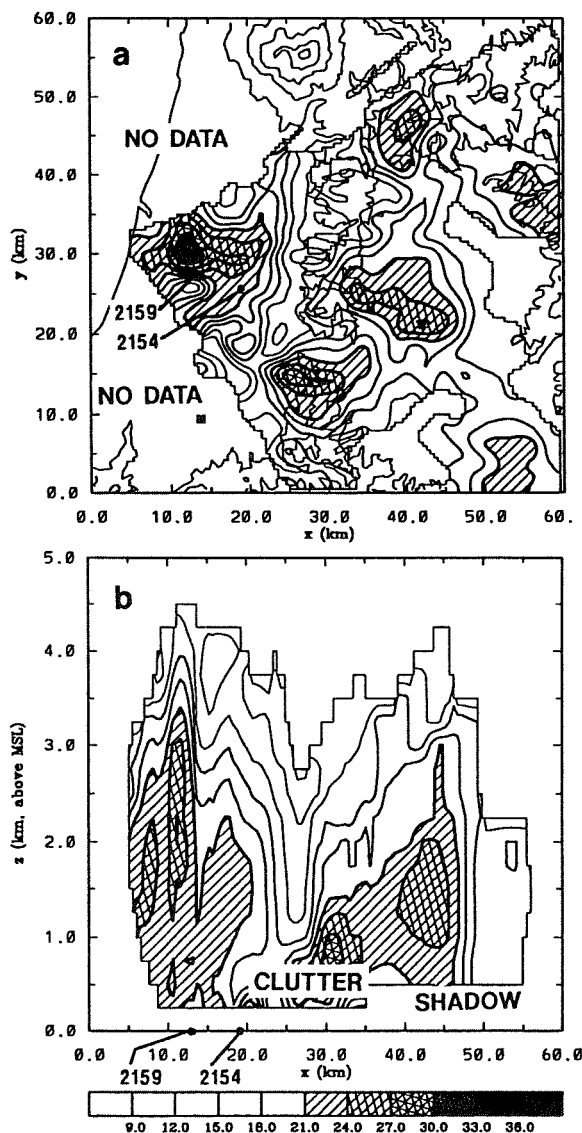


Fig. 6. The same as Fig. 5, except for at 2157JST.

The observation site tended to be off the center of the echo when snowflakes were observed. It is considered that the hydrometeor type depended on the position relative to the snow cloud not only to the topography.

4. HYDROMETEOR TYPES OF CELLULAR ECHOES

Intense observations of hydrometeors were carried out at AU site. Graupels were not only often observed in stage II, but significantly contributed to the precipitation amount. We compared the particle size distributions with the position of AU site relative to the cellular echoes.

Fig. 5 and Fig. 6 are the examples of reflectivity distribution in stage II. Both are the sections when a cellular echo was close to AU site. The vertical sections

are made along the direction of motion of cellular echoes. The locations of AU site corrected by the time-space conversion is indicated by the time of precipitation particle observations at AU site.

Comparing Fig. 6 with Fig. 7, it is inferred that the total precipitation rate was higher where the corresponding reflectivity was stronger. The contribution of graupels to the precipitation rate shows similar relation. However, the size distribution of 2154JST is the exception. The reflectivity is stronger than expected from the total precipitation rate, and the contribution of graupels are larger than other three panels in Fig. 7. The AU site was at the point where two echoes were merging at 2154JST. This indicates that the evolution of the cellular echo, not only the relative position within the echo, affects the hydrometeor type observed at the ground.

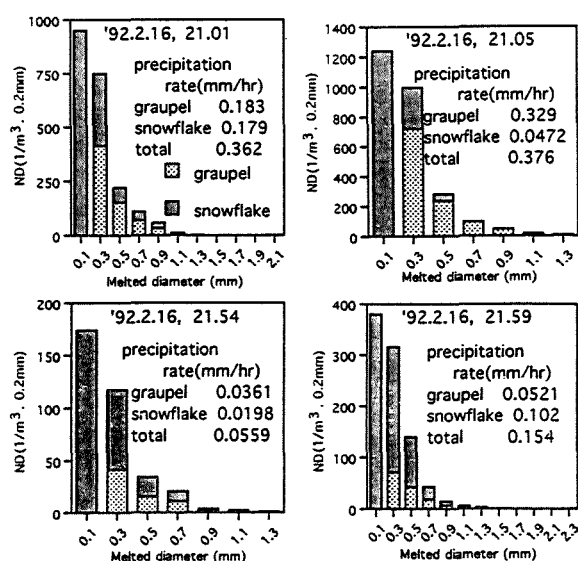


Fig. 7. The size distributions of precipitation particles at AU site.

5. SUMMARY

The observation of snow clouds over the land was conducted on 13-19 February 1992 in the Tohoku District of Japan. Two types (described as stage I and stage II) of snow clouds appeared during the analysis period. One appeared as the widespread echoes in a weak cold outbreak, when snowflakes dominated among the precipitation particles. The other appeared as the cellular echoes in a strong cold outbreak, when graupels contributed considerably to the precipitation amount. The contribution of graupels was higher when the observation site was closer to the center of the cellular

echo. The difference of cloud types clearly reflected the hydrometeor types. In both stages, the precipitation enhancement over the hills occurred, and the frequency of graupel at the lee side of the hills was lower than that at the windward side. However, the average reflectivity patterns suggest that the mechanisms were different between the stages. The evolution of each snow cloud may affect the type and amount of hydrometeors. Further analyses, including the analysis of the airflow within the cloud, are necessary to clarify the detailed structure of the snow clouds over the land and the mechanisms of the precipitation enhancement over the hills.

Acknowledgments. The authors would like to thank Dr. T. Matsuo of Japan Meteorological Agency, Dr. M. Murakami and Mr. H. Mizuno of Meteorological Research Institute, and Dr. T. Ishizaka of Nagoya University for their discussions and cooperation in the observation.

REFERENCES

- Kikuchi, K., S. Azumane, M. Murakami and T. Taniguchi, 1987: Precipitating snow clouds during winter monsoon seasons influenced by topography of the Shakotan Peninsula, Hokkaido Island, Japan (SHAROP). *Environ. Sci., Hokkaido*, 10, 109-128.
- Murakami, M. and T. Matsuo, 1990: Development of hydrometeor video sonde (HYVIS). *J. Atmos. Oceanic Technol.*, 7, 613-620.
- Murakami, M., T. Matsuo, H. Mizuno and Y. Yamada, 1994: Mesoscale and microscale structures of snow clouds over the Sea of Japan. Part I: Evolution of microphysical structures in short-lived convective snow clouds. *J. Meteor. Soc. Japan*, 72, 671-694.
- Nakai, S. and T. Endoh, 1995: Observation of snowfall and airflow over a low mountain barrier. *J. Meteor. Soc. Japan*, 73, 183-199.
- Takeda, T., K. Isono, M. Wada, Y. Ishizaka, K. Okada, Y. Fujiyoshi, M. Maruyama, Y. Izawa and K. Nagaya, 1982: Modification of convective snow—clouds in landing the Japan Sea coastal region. *J. Meteor. Soc. Japan*, 60, 967-977.
- Yamada, Y., T. Matsuo, M. Murakami and H. Mizuno, 1994: Mesoscale and microscale structures of snow clouds over the Sea of Japan. Part II: Time change in airflow structures in isolated snow clouds derived from dual-Doppler radar observations — A case study —. *J. Meteor. Soc. Japan*, 72, 695-708.

A STUDY OF PRECIPITATING CLOUDS IN THE VICINITY OF THREE FRONTS AND A CYCLONE OBTAINED FROM OBSERVATIONS OF MICROWAVE RADIOMETER AND VERTICALLY POINTING RADAR IN SVALBARD, ARCTIC

Makoto Wada¹ and Hiroyuki Konishi²

¹ NIPR, Itabashi-ku, Tokyo 173, Japan

² Osaka Kyoiku Univ., Kashihara, Osaka 582, Japan

1. INTRODUCTION

Developed cyclones or deeply occluded fronts can often be found on the weather maps or in the satellite images (e.g., Yamanouchi and Seko, 1992) in the polar regions. Many researchers have studied clouds associated with fronts and extratropical cyclones for a long time (e.g., Bergeron, 1959, Kreitzberg and Brown, 1970, Hobbs et al., 1975, Matkovskii and Shakina, 1982 and Matejka et al., 1980). Saarikivi and Puhakka (1989) also reported an occluded front passing through near Helsinki. They described the observation in their paper that it was done during winter when the temperature was below zero at all levels. Although there were many observations for investigating occluded fronts, few observations were carried out in the polar regions as Saarikivi and Puhakka emphasized the low temperature condition in their paper.

Amount of water vapour is normally a few in the polar regions, because of low temperature. When a disturbance such as front or cyclone moves up to the polar region, it brings much water vapour there. A drastic change might be raised, as a result, in the processes forming clouds or precipitation. Occluded fronts generally might be more deeply occluded in the polar regions than in the middle latitude. Temperature change at the ground when an occluded front passes through there might be less remarkable in the polar regions than in the middle latitude. This paper presents a case study for a series of three wintertime fronts and an cyclone observed in the polar region. Although our analyzing data were obtained at one place only and few information of aerological sounding was obtained, we analyze the data with special attention to column cloud liquid water data which observation has not been popular till recently. Since rain is scarcely observed and the temperatures of all altitudes are below 0C in the polar region, the cloud liquid water is a good indicator for knowing the cloud stage such as developing, mature and decaying stages.

2. INSTRUMENTS AND OBSERVATION

Main instruments for clouds and precipitation were a vertically pointing X-band radar (Wada and Konishi, 1992), a 37 GHz microwave radiometer (Wada, 1991) and an electric field meter. General meteorological data were referred, for example, temperature, pressure, humidity, wind speed and wind direction. Some other data listed next were also utilized: Total precipitation for 12 hours, cloud base temperature obtained from an infrared radiation thermometer, aerological observation using balloon and altitude of cloud base obtained from a ceilometer. Those observation were carried out in Ny-Ålesund (79N, 12E), Svalbard, Arctic. Our staying period was from 9th February to 16th March 1995, but a main studying period for this paper was from 5th March to 14th March.

3. RESULTS

We classified precipitating clouds observed in the main studying period as 4 categories of clouds having similar characteristics using special attention to the data of column cloud liquid water and electric field meter. For classification we checked the existence of column cloud liquid water at first. If the clouds contained liquid water, we checked the existence of short period variations in the column cloud liquid water data. Finally, we checked the existence of big

Table 1: Classification of clouds. The column "CLW" shows the existence of column cloud liquid water. The column "SPV in CLW" shows the existence of short period variations in the column cloud liquid water data. The column "BV in EF" shows the existence of big variations in the electric field data. Y means yes and N means no.

	CLW	SPV in CLW	BV in EF
Type A	N	N	Y*
Type B	Y	N	Y*
Type C	Y	Y	Y
Type D	Y	Y	N

* EF data were not involved in the classification.

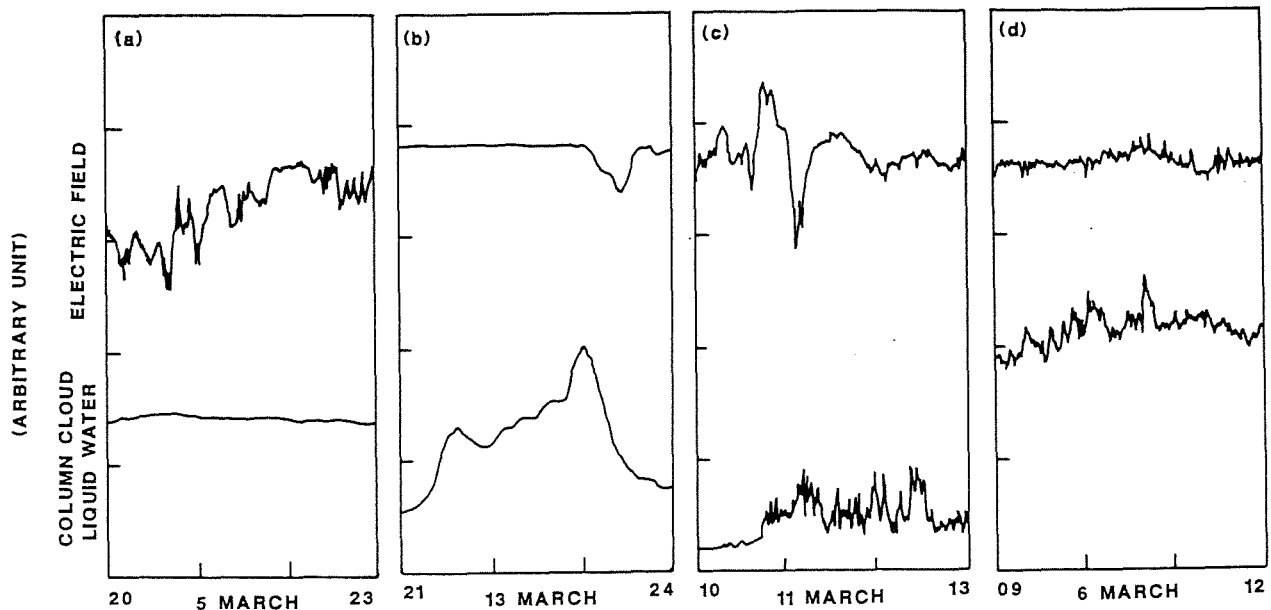


Fig. 1: Chart recorded data of microwave radiometer and electric field meter. (a) shows type A clouds from 20UTC to 23UTC on 5th, (b) shows type B clouds from 21UTC on 13th to 00UTC on 14th, (c) shows type C clouds from 11UTC to 14UTC and (d) shows type D clouds from 09UTC to 12UTC on 6th.

variations in the electric field data. As a result we classified the clouds as 4 types shown in Table 1. Combination of bullets crystals were main crystal type at the ground in the period of type A clouds, graupels were in type C clouds and graupels or heavy rimed crystals were in type D clouds. Crystal types in type B clouds were not reported, but probably snowflakes, we think. Figure 1 shows the 4 typical chart recorded data obtained from the data in the periods of 4 cloud types.

The snowfalls stopped sometimes in the main studying period. Judging from the cloud base temperature data obtained from an infrared radiation thermometer, the period can be classified as 4 periods, although no snowfall periods were found many. These 4 periods are divided using the periods in which there was no cloud or the heights of cloud base was relatively high. The first (1st) period is from 14UTC on 5th to 03UTC on 8th. The second (2nd) one is from 05UTC on 11th to 05UTC on 12th. The third (3rd) one is from 12UTC on 12th to 22UTC on 12th, and the last (4th) one is from 01UTC on 13th to 02UTC on 14th. Date-height cross section of temperature are shown in Fig. 2. Aerological sounders normally were launched once a day around 12UTC. It is, therefore, difficult to decide the actual time when the front passed through Ny-Ålesund. Four peaks are found in the -15C contour as shown in Fig. 2. The

first 3 peaks, which are shown around on 6th, 11th and 12th, were caused by passage of fronts and the last peak, which is shown around 13th, was caused by passage of cyclone. Cloud types and the times of fronts and cyclone passages in the 4 periods are described next.

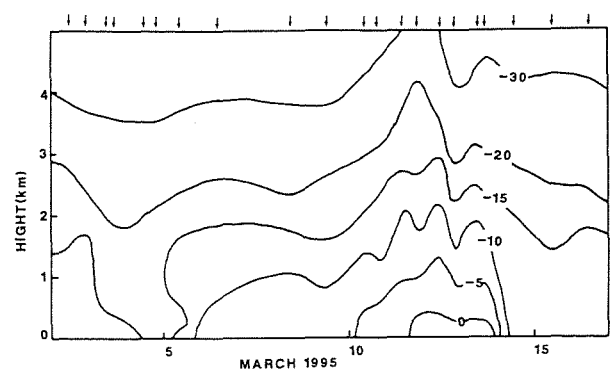


Fig. 2: Date-height cross section of temperature (C) from 2nd to 16th March 1995. Aerological soundings were carried out at the times shown by arrows (\downarrow) at the top of the figure.

According to the meteorological data, especially temperature and wind data, a front passed through Ny-Ålesund around 12UTC on 6th, roughly. Type A clouds were observed for 16 hours till 6 hours before the front passed through there, then, type D clouds covered there for 30 hours. After a short break of snowfall, type C clouds were observed for 5 hours till end of the 1st period. The 2nd front passed through around 12UTC on 11th, roughly, from surface meteorological data. Type C clouds were observed for 11 hours from 05UTC on 11th, that is a few hours before passage of the 2nd front, to 16UTC on 11th. Then, type D clouds were found for 13 hours from 16UTC on 11th to 05UTC on 12th. The 3rd front passed through around 12UTC on 12th, roughly, from meteorological data. type C clouds were observed for 4 hours from 12UTC to 16UTC on 12th, then, type D clouds were found for 6 hours from 16UTC to 22UTC on 12th. After a short break of snowfall, type D clouds were observed for 16 hours from 01UTC to 17UTC on 13th, in which a cyclone came near Ny-Ålesund around 15UTC. Then, type A clouds were observed for 4 hours from 17UTC to 21UTC. Moreover, type B clouds, which was observed only once in the main studying period, were found for 3 hours from 21UTC on 13th to 00UTC on 14th, then, type A clouds covered for 2 hours. Cloud types and how long the cloud types were lasting based on the results above are listed in Table 2.

Radar echo obtained from a vertically pointing radar has not been shown as yet. Four time-height cross sections of radar echo intensity larger than 0dBZ are shown in Fig. 3 in the same period as Fig. 1, but shown for 1 hour only. Echoes shown in (a) and (b) look like stratiform and tops of the echoes are relatively high. Echoes shown in (c) and (d) look like convective form. It is looked that lasting periods of their echo cells are different. Namely, the lasting periods of cells are shorter in (c) than in (d).

4. FEATURES OF PRECIPITATING CLOUDS ASSOCIATED WITH FRONTS AND CYCLONE

The 1st front was drawn as a warm front on the

Table 2: Cloud types and how long the cloud type were lasting in the each period. Last column shows which period the fronts or cyclone passed through or came near Ny-Ålesund.

Period	Type	Lasting hours	Front or Cyclone
1st	A	16	Front
	D	30	
	C	15	
2nd		74*	Front
	C	11	
	D	13	
3rd		7*	Front
	C	4	
	D	6	
4th		3*	Cyclone
	D	16	
	A	4	
	B	3	
	A	2	

* Hours without snowfall between each period.

weather map of 12UTC on 5th. We, however, cannot find a front near Svalbard on the weather map of 12UTC on 6th. The 2nd front was drawn as an occluded front and it passed through Svalbard between 12UTC 10th and 12UTC 11th, according to the weather maps. The 3rd front was drawn as also an occluded front associated with a cyclone described next. The cyclone was very developed and the surface pressure went down to 960 hPa at 15UTC on 13th in Ny-Ålesund.

The characteristic features of precipitating clouds associated with each front and a cyclone can be found out, referring to Table 2. The 2nd and 3rd fronts are nearly same occluded fronts and the 3rd one is little stronger than the 2nd one. We thought these 2 occluded fronts were general occluded fronts in this region because they contained similar types of clouds. Since the electric field in Ny-Ålesund varied largely around the passage of both fronts when type C clouds were observed, the relatively strong convective clouds with cloud liquid water would be embedded in or

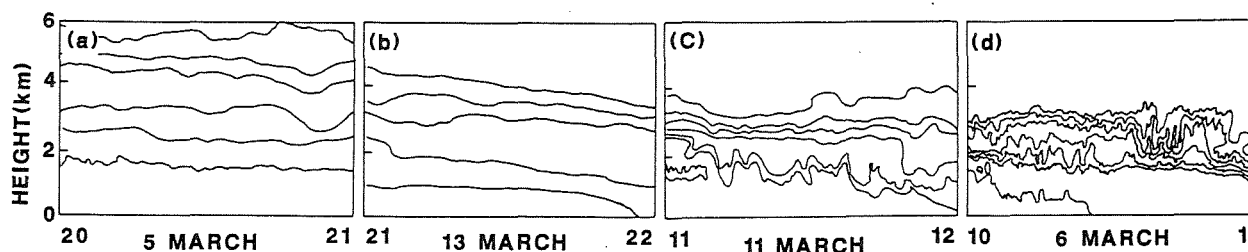


Fig. 3: Time height cross sections of radar echo intensity. (a) means the echo in the period of type A clouds and (b), (c) and (d) are type B, C, and D clouds, respectively.

around the occluded fronts. Besides, a cell of the type C clouds shown in Fig. 3 were lasting longer than that of the type D clouds. We consider that this means the convective scale of the type C clouds is stronger than that of the type D clouds, although both clouds contained cloud liquid water. Namely, it is considered that type D clouds were weak convective clouds comparing with type C clouds and type D clouds can be found after an occluded front has passed through.

The 1st front has different characteristics. Type A clouds continued for a long time before the front had passed through there. The type A clouds were clouds ahead of a warm front which would be formed as a result of airmass aloft along the warm front. The precipitating clouds were type D clouds, when the front passed through there. It is considered that the convection in this front was weaker than that in the 2nd and 3rd fronts, because this front was a warm front and the others were occluded fronts. The type D clouds were embedded in the warm front. Type C clouds are listed after the type D clouds in Table 2. The type C clouds were not so strong as the type C clouds in the 2nd and 3rd periods, because the variation of electric field was very small comparing with the cases of 2nd and 3rd periods. The type C clouds in the 1st period could be considered to resemble the type D clouds in the 1st period.

The cyclone has also different characteristics. According to the weather maps and the variation of wind direction at the ground, the cyclone passed near the west side of Svalbard along a track from southwest to northeast. The clouds near the centre and ahead of the cyclone were type D clouds. The first clouds behind of the cyclone were type A clouds and type B clouds followed. If a cyclone is already developed, strong convective clouds would not be formed near the centre. The type D clouds, which were not so convective, were observed near the centre of the cyclone, because the cyclone associating with the deeply occluded front mentioned above. It is difficult to discuss the formation of the type A and B clouds followed by the cyclone. The cyclone brings huge water vapour from the south to Arctic. We consider that a cold airmass from northwest would enter into behind of the cyclone. A warm airmass associated with the cyclone would rise over the cold airmass as the cyclone moves up to the north. We consider that the water vapour would not distribute uniformly. It could be considered, therefore, the cloud liquid water raises in the area behind of the cyclone where much water vapour are converged. The strong convection would not be occurred, since the influence of the cold airmass is weak. Namely, type A clouds would be observed in the area contained relatively few water vapour and type B clouds would be observed in the

area contained relatively much water vapour because of the irregularity of water vapour amount in the areas.

5. ACKNOWLEDGMENTS

The authors would like to express their sincere thanks to the Norwegian Meteorological Institute for sending their collected meteorological data of Ny-Ålesund and also sincerely thanks to the Alfred Wegener Institute for Polar and Marine Research for doing the aerological observations in Ny-Ålesund. We also thank to the Arctic Environment Research Center of National Institute of Polar Research for doing logistic and financial supports. A part of this work has been supported financially by the Ministry of Education, Science and Culture through Grant-in-Aids No.05044065 and No.06640564.

6. REFERENCES

- Bergeron, T., 1959: Methods in scientific weather analysis and forecasting. An outline in the history of ideas and hints at a program. In "The Atmosphere and the sea in Motion" (ed. B. Bolin), New York, Rockefeller Inst. Press, 440-474.
- Hobbs P. V., R. A. Houze, Jr. and T. J. Matejka, 1975: The dynamical and microphysical structure of an occluded frontal system and its modification by orography. *J. Atmos. Sci.*, 32, 1542-1562.
- Kreitzberg C. W. and H. A. Brown, 1970: Mesoscale weather systems within an occlusion. *J. Appl. Meteor.*, 9, 417-432.
- Matejka, T. J., R. A. Houze and P. V. Hobbs, 1980: Microphysics and dynamics of clouds associated with mesoscale rainbands in extratropical cyclones. *Quart. J. Met. Soc.*, 106, 29-56.
- Matkovskii, B. M. and N. P. Shakina, 1982: Mesoscale structure of an occluded front over the center of the European USSR from special measurements. *Meteorologiya i Gidrologiya*, No. 1, 24-33.
- Saarikivi, P. and T. Puhakka, 1989: The structure and evolution of a wintertime occluded front. Report from Dept. Met. in Univ. Helsinki, 30, 54p.
- Wada, M. and H. Konishi, 1992: A study of precipitation in the coastal area of Antarctica as observed at Syowa Station using a vertical pointing radar. *Antarctic Record*, 36, 341-349.
- Wada, M., 1991: Estimation of vertically integrated liquid water contents in the atmosphere. *Antarctic Record*, 35, 1-11.
- Yamanouchi, T. and K. Seko, 1992: Antarctica from NOAA Satellite. National Institute of Polar Research, Tokyo, 91p.

